

# Proceedings of the Second Conference on Advanced Materials for Alternative-Fuel-Capable Heat Engines

**EPRI**

EPRI RD-2369-SR  
Proceedings  
May 1982

Keywords:

Coal Gases  
Coal Liquids  
Gas Turbines  
Diesel Engines  
Metallic Materials  
Ceramic Materials

Prepared by  
Electric Power Research Institute  
Palo Alto, California

**ELECTRIC POWER RESEARCH INSTITUTE**

Proceedings of the Second Conference on  
Advanced Materials for Alternative-Fuel-Capable  
Heat Engines

---

RD-2369-SR

Proceedings, May 1982

Monterey, California  
August 24-28, 1981

Cochairmen

J. W. Fairbanks  
U.S. Department of Energy  
Washington, D.C.

and

J. Stringer  
Electric Power Research Institute  
Palo Alto, California

Compiled and Edited by

Meeting Planning Associates  
Menlo Park, California

Cosponsored by

U.S. Department of Energy  
Washington, D.C. 20585

and

Electric Power Research Institute  
3412 Hillview Avenue  
Palo Alto, California 94304

Materials Support Group  
R&D Staff

## ORDERING INFORMATION

Requests for copies of this report should be directed to Research Reports Center (RRC), Box 50490, Palo Alto, CA 94303, (415) 965-4081. There is no charge for reports requested by EPRI member utilities and affiliates, contributing nonmembers, U.S. utility associations, U.S. government agencies (federal, state, and local), media, and foreign organizations with which EPRI has an information exchange agreement. On request, RRC will send a catalog of EPRI reports.

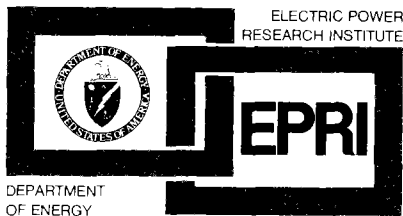
Copyright © 1982 Electric Power Research Institute, Inc. All rights reserved.

## NOTICE

This report was prepared by the Electric Power Research Institute, Inc. (EPRI). Neither EPRI, members of EPRI, nor any person acting on their behalf: (a) makes any warranty, express or implied, with respect to the use of any information, apparatus, method, or process disclosed in this report or that such use may not infringe privately owned rights; or (b) assumes any liabilities with respect to the use of, or for damages resulting from the use of, any information, apparatus, method, or process disclosed in this report.

## ABSTRACT

This conference, cosponsored by the Electric Power Research Institute and the U.S. Department of Energy, is the second to address the problems that may be encountered by structural materials in heat engine systems burning alternative fuels. Alternative fuels are those that will replace natural gas and distillate oils as price increases or diminishing availability restrict their use, and include residual oils, shale oil, coal, and coal-derived liquids and gases. The problems for heat engines in the change to these different fuels are primarily related to impurities, both those whose role is chemical, in increasing the corrosion of materials, and those that appear as solid or liquid particles in the combustion gases and may erode or deposit on component surfaces. A difficulty is that the impurities that may be present in the newer fuels when they appear in the market cannot be predicted with confidence; both the amount and the nature of the impurities will be a function of the preparation methods. The principal areas of concern are gas turbines and diesels, but heat exchangers and novel forms of direct combustion of coal are also discussed. Metallic materials, structural ceramics, and coatings are included; advanced cooling techniques, which may reduce problems of the interaction of the materials with their environment at the expense of greater fabrication problems, are also reviewed.



Since the first Conference two years ago, there have been significant changes in the alternative fuels field. The government role has been reassessed particularly with respect to demonstration plants. Government funding of alternative fuels has shifted to the newly created Synthetic Fuels Corporation and emphasizes cost sharing. The Department of Energy (DOE) projects that use of coal for energy purposes will increase almost ten-fold between 1985 and 2000, then double again by 2020. How coal derived liquids and coal gasification fit into this scenario is uncertain. In the near-term, DOE is developing beneficiated coal water slurry fuels in which the ash and sulfur levels are drastically reduced. This fuel presents major erosion/corrosion and combustion challenges for heat engine use but also the promise of an economical, abundantly available fuel.

Oil shale derived fuels will probably become significant heat engine fuels beginning in the late 80's. Early use of shale oil will probably be as feedstocks for petroleum refineries.

Coal gasification is proceeding at a slower pace than had been anticipated, however several demonstration plants will be built in the early '80's. Preliminary design has identified materials problem areas: (a) the gas as a heat engine fuel should be relatively clean, (b) directionally solidified and single crystal airfoils should produce major performance and durability improvements, (c) ceramic coatings have attractiveness for most hot-section components, (d) the gasifier vessel materials problems are primarily with the refractory linings.

Pressurized fluidized bed combustion with a gas turbine expander coupled with some form of steam cycle is attractive. Here, the materials problems in the combustor are principally erosion and corrosion of the in-bed components. The major issue is the level to which particulates can be removed from the exhaust gas and the expander turbines ability to tolerate the remaining particles.

Developments in gas turbines are still aimed at methods of improving the thermal efficiency by raising the turbine inlet temperature through improved cooling in the hot-section. However, three further aspects are becoming increasingly important. These are: improved reliability, reduced  $\text{NO}_x$  emissions and multi-fuel capability. There is considerable interest in the development of a new generation of coating systems.

The adiabatic diesel or thermally insulated combustion zone concept offers potential advantages of emissions reductions, improved combustion, high efficiency with waste heat utilization and multi-fuel capability. Ceramic or thermal barrier coatings, ceramics, particularly the composite ceramics are the materials requirements. This ceramic technology will logically emanate from the gas turbine materials technology base. The Norwegians are to be commended for their corrosion/erosion resistant coatings which are extending diesel component life.

The authors and session chairmen are to be congratulated for making this conference a great success. The pleasant surroundings and the many courtesies extended by the staff of the Naval Postgraduate School were very much appreciated. We are looking forward to the next conference in this series in the Summer of 1983 and quite possibly in the United Kingdom.

John Stringer  
Conference Co-Chairman  
Electric Power Research  
Institute

John Fairbanks  
Conference Co-Chairman  
Department of Energy

CONTENTS

	<u>Page</u>
SESSION I: ALTERNATE FUELS	
ALTERNATIVE LIQUID FUELS--S.B. Alpert and A. Cohn, Electric Power Research Institute	1-1
COAL GASIFICATION COMBINED CYCLE SYSTEMS - DEVELOPMENT STATUS, GAS QUALITY AND CONTROL CONSIDERATIONS--N. A. Holt, Electric Power Research Institute	1-25
ECONOMICS OF ALTERNATIVE FUELS FOR ELECTRIC POWER GENERATION--M. J. Gluckman, Electric Power Research Institute	1-53
SESSION II: ALTERNATE FUELS COMBUSTION	
A LOW EMISSION PRE-MIX TWIN REVERSAL GAS TURBINE COMBUSTOR--R. J. Taylor and D. McKnight, Rolls Royce Limited	2-1
ON FUEL ECONOMY AND THE USE OF ALTERNATIVE FUELS IN MEDIUM- AND SLOW-SPEED DIESEL ENGINES--A. Sarsten, G. Fiskaa, and H. Valland, The Norwegian Institute of Technology	2-29
DIESEL ENGINE OPERATIONAL TESTING ON EARLY ALTERNATIVE FUELS--John W. Fairbanks, DOE, and Dan Gurney, Bartlesville Energy Technology Center	2-53
MULTIFUEL CAPABILITY OF MODIFIED DIESEL ENGINES--R. Kamo, Cummins Engine Company, Inc.; T. Nakagaki, Komatsu, Ltd.; and T. Yamada, Yanmar Diesel, Ltd.	2-73
COMBINED CYCLE POWER PLANT BASED ON PRESSURISED FLUIDISED BED COMBUSTION--H. R. Hoy and A. Roberts, Coal Utilization Research Laboratory, and John Stringer, Electric Power Research Institute	2-115
SESSION III: HEAT ENGINES AND HEAT RECOVERY	
DIESEL ENGINE RESEARCH AND DEVELOPMENT FOR ALTERNATIVE FUEL OPERATION-- John W. Fairbanks, U.S. DOE	3-1
METALLIC HEAT EXCHANGERS--John Stringer, Electric Power Research Institute and Holger Lukas, Encotech, Inc.	3-27
ADVANCED COOLING OF UTILITY GAS TURBINE ENGINE COMPONENTS--Arthur Cohn, Electric Power Research Institute	3-43

	<u>Page</u>
THE U.S. DEPARTMENT OF ENERGY HIGH TEMPERATURE TURBINE TECHNOLOGY PROGRAM--George B. Manning and John Neal, U.S. Department of Energy	3-59
SESSION IV: HEAT ENGINE COMBUSTION ZONE MATERIALS PROBLEMS	
HIGH TEMPERATURE CORROSION IN HEAT ENGINES--John Stringer, Electric Power Research Institute	4-1
MATERIALS CONSTRAINTS FROM THE EROSION-CORROSION POTENTIAL OF ALTERNATIVE FUEL SOURCES--I.G. Wright and W.R. Pierson, Battelle Columbus Laboratories	4-27
CORRODANT SOURCES, CORROSION, AND DEPOSITION IN DISTILLATE AND HEAVY OIL-FIRED TURBINES--C. J. Spengler, Westinghouse Research and Development Center, and S. T. Scheirer, J. H. Marlow and J. J. Vitello, Westinghouse Combustion Turbine Systems Division	4-53
THE HIGH TEMPERATURE COMBUSTION OF RESIDUAL FUEL OIL - SOME DEPOSITION PRODUCT CONSIDERATIONS-- G.A. Whitlow, S. Y. Lee, P. R. Mulik, R. A. Wenglarz, Westinghouse Research and Development Center, T. P. Sherlock, Westinghouse Combustion Turbine Systems Division, and Arthur Cohn, Electric Power Research Institute	4-73
MECHANICAL PROPERTY REQUIREMENTS FOR HOT SECTION COMPONENTS IN GAS TURBINES--W. J. Ostergren and G. T. Embley, General Electric Company	4-109
PROBLEMS THAT MAY RESULT FROM BURNING COAL DERIVED FUELS IN GAS TURBINES-- P. Hancock and J.R. Nicholls, Cranfield Institute of Technology	4-137
TRIBOLOGICAL SCREENING OF CERAMIC MATERIALS FOR USE IN ADVANCED DIESEL ENGINES--Alan I. West and Walter D. Syniuta, Advanced Mechanical Technology, Inc.	4-163
COAL SLURRY TESTS WITH A SLOW SPEED TWO-STROKE CYCLE DIESEL ENGINE, CONCLUSIONS AND PREDICTIONS, H. A. Steiger, Sulzer Brothers Switzerland	4-175
TURBINE MATERIALS EROSION/CORROSION IN AN EXPERIMENTAL PFBC SIMULATOR--R.L. McCarron, A.M. Beltran, R.P. Brobst and D.R. Spriggs, General Electric Company	4-191

SESSION V: AIRFOIL COOLING

	<u>Page</u>
MATERIAL DEVELOPMENT FOR A WATER-COOLED GAS TURBINE--W.F. Schilling, M.C. Muth, P.W. Schilke, M.F. Collins and A. Caruvana, General Electric Company	5-1
TRANSPIRATION AIR COOLING FOR HIGH TEMPERATURE TURBINES OPERATING ON COAL DERIVED FUELS--J. Wolf, J. Mogul, S. Moskowitz, Curtiss-Wright Corporation, and G. Manning, U.S. DOE	5-23
WAFFER COOLING FOR INDUSTRIAL GAS TURBINE BLADES AND VANES--Bruce T. Brown and Daniel B. George, Pratt & Whitney Aircraft Division of United Technologies Corporation	5-43

SESSION VI: CERAMIC COATINGS AND MONOLITHIC CERAMICS

PROBLEMS ENCOUNTERED IN DEVELOPING AND USING THERMAL BARRIER COATINGS ON DIESEL ENGINE COMPONENTS--Ingard Kvernes, Central Institute for Industrial Research	6-1
DEVELOPMENT OF CERAMIC HEAT EXCHANGERS FOR INDIRECT FIRED GAS TURBINES--Wate T. Bakker, Electric Power Research Institute and Dave Kotchick, Airesearch Manufacturing Company of California	6-22
CERAMIC COATINGS FOR USE IN ALTERNATE FUEL APPLICATIONS--J.W. Vogan, L.L. Hsu and A.R. Stetson, Solar Turbines International	6-54
STUDIES OF THERMAL BARRIER COATINGS FOR HEAT ENGINES--R.J. Bratton, S.K. Lau, C.A. Andersson and S.Y. Lee, Westinghouse Research and Development Center	6-82
PROCESSING TECHNOLOGY FOR ADVANCED METALLIC AND CERAMIC TURBINE AIRFOIL COATINGS--D.S. Duvall, Commercial Products Division, Pratt and Whitney Aircraft	6-102
SPUTTERED CERAMIC COATINGS AND SEALING LAYERS--J.T. Prater, J.W. Patten, D.D. Hays and R.W. Moss, Battelle Pacific Northwest Laboratories	6-118
RESPONSE TO PLASMA SPRAYED MgO.ZrO <sub>2</sub> AND ZrO <sub>2</sub> -6·6Y <sub>2</sub> O <sub>3</sub> TO THERMAL BARRIER COATINGS TO THERMAL FATIGUE AND HOT CORROSION--T.A. Taylor, M.O. Price, and R.C. Tucker, Jr., Union Carbide Corporation, Linde Division	6-131
DEVELOPMENT OF ELECTRON BEAM PHYSICAL VAPOR DEPOSITION OF CERAMIC COATINGS--R.E. Demaray, W.K. Halnan and S. Shen, Turbine Coating Group, Airco Temescal Division	6-151
THERMAL BARRIER COATINGS RESEARCH AT NASA LEWIS--S.R. Levine, R.A. Miller, M.A. Gedwill, NASA Lewis Research Center	6-185

SESSION VII: METALLIC ALLOYS

PROTECTIVE COATINGS FOR ELECTRIC UTILITY GAS TURBINES--J.A. Goebel, C.S. Giggins, United Technologies Corporation, Pratt and Whitney Division; M. Krasij, United Technologies Corporation, Power Systems Division; and John Stringer, Electric Power Research Institute	7-1
---	-----



	<u>Page</u>
BEHAVIOR OF NiCrSi COATING ALLOYS IN Na <sub>2</sub> SO <sub>4</sub> , V <sub>2</sub> O <sub>5</sub> , AND MIXED SALT HOT CORROSION--R.G. Corey, R.H. Barkalow, A.S. Khan, and R.J. Hecth Pratt and Whitney Aircraft Group	7-17
CHANGES IN HOT CORROSION DUE TO COMPOSITION MODIFICATIONS IN CoCrAlY COATINGS--J.W. Patten, J.T. Prater, D.D. Hays and R.W. Moss, Battelle Northwest Laboratory and J.W. Fairbanks, U.S. DOE	7-29
DEVELOPMENT OF DIFFUSION BONDED CLADDINGS FOR LARGE GAS TURBINE APPLICATIONS--J.H. Wood, T.R. Farrell, A.M. Beltran, W.F. Schilling and W.J. Ostergren, General Electric Company	7-45
INTERACTIONS BETWEEN COATINGS AND SUBSTRATES AT ELEVATED TEMPERATURES--D.P. Whittle and D.H. Boone, Lawrence Berkeley Laboratory, University of California	7-69
TURBINE BLADE MATERIALS RESEARCH AT SANDIA NATIONAL LABORATORIES-- R.E. Benner, J.D. Hamilton, A.S. Nagelberg and P.L. Mattern, Sandia National Laboratories	7-83
RAPIDLY SOLIDIFIED SUPERALLOYS--E.C. van Reuth and L.A. Jacobson, Defense Advanced Research Projects Agency	7-105
DEVELOPMENT OF A DIRECTIONALLY SOLIDIFIED COMPOSITE INDUSTRIAL GAS TURBINE AIRFOIL--John W. Fairbanks, U.S. DOE and William Schilling, General Electric Company	7-119
LIST OF ATTENDEES	7-135

**Session I**  
**ALTERNATIVE FUELS**

ALTERNATIVE LIQUID FUELS

Prepared by

S.B. Alpert  
A. Cohn

Advanced Power Systems Division

Prepared for

Electric Power Research Institute  
3412 Hillview Avenue  
Palo Alto, CA 94304

## Introduction

In order to consider the utilization of synthetic liquid fuels for power production we need to first look at the quantities of liquid and gas used by the electricity industry today and projected in the future. Table 1 presents the capacity of the U.S. electricity industry by fuel category and indicates that oil and gas fired plants in the U.S. represent about 200,000 MW of capacity. Most of this capacity is located on the Atlantic and Pacific coasts. The major supply of residual fuel oil represents imports from foreign sources where large refineries are equipped to supply fuel oil for electricity plants. Historically, the U.S. refining industry does not satisfy a significant portion of domestic fuel oil demand and has concentrated refinery emphasis on production of gasoline and light distillate for home heating oil, jet fuel, and diesel oil markets. U.S. refineries have installed process technologies that convert the heavier portions of crude oil to higher valued products. Processes such as coking, and heavy oil conversion plants have been encouraged by the price differential that exists between distillate and residual fuel oil products and the much larger demand for gasoline in the U.S. than for heavy fuel oil. Currently, gasoline has a value that is higher than crude oil but fuel oil is still priced lower than crude oil as indicated in Table 2.

During this decade from 1980-1989 the capacity of oil and gas fired electric generation capacity is expected to be constant with capacity increases from nuclear and coal fired plants representing the largest growth. If the nuclear capacity increases cannot be realized then in order to attain the projected electric capacity there would be a higher requirement of up to an additional 1 million barrels per day of fuel oil. Only oil or gas fired electric capacity could be installed in time to meet the projected 1989 capacity requirements, presuming delays in nuclear plants. The technology which could be installed in time is represented by oil and gas fired combined cycle modular plants that can be ordered and installed in less than five years. It should be noted that indicated growth in capacity is projected assuming a growth rate of about 4% per year in electric demand, probably too high a rate.

Table 3 shows the portion of electricity generated by the major sources of energy. Petroleum fuels consumption will be constant in the amount required over the next decade, but gas requirement will decrease sharply as a result of higher gas prices that stem from deregulation and policy decisions on the use of natural gas for generating electric power. Table 4 translates the electricity generated into annual fossil fuel requirements. Liquid fuels will remain a significant fuel for power generation but are not expected to increase over the quantity used today. In contrast natural gas is expected to decrease sharply with a large increase in the use of coal.

For utilities heavily dependent on petroleum fuels such as Consolidated Edison of New York, Florida Power and Light, and Southern California Edison Co., liquid fuels will continue to represent important sources of fuel. In the U.S. such heavily oil dependent utilities are not able to make a transition to coal without colossal investments that are beyond their capabilities, and without jeopardizing reliability of electric supply to customers.

Table 5 shows a breakdown of the major consuming utilities that are dependent on petroleum liquid fuels and gas for generating electric power. The annual cost for fuel is in excess of \$2 billion for those utilities at the top of the list. For the next decade the preferred lowest cost alternate, would not be represented by synthetic liquid fuels from shale oil, coal, etc., but probably an orderly transition to coal fired plants on nuclear capacity. We believe that gasification combined cycle plants should enter in the late 1980s. When the development and demonstration is completed.

In the U.S. the realization of a supply of liquid fuels from indigenous resources cannot be achieved in this decade. Thus for the near future it is not likely that the technology options that can supply replacement fuels in a timely way to displace liquid fuels will have very much impact. Based on the status of the alternate energy technology, and the extant policies that have discouraged production capabilities to be installed, synthetic gases and liquid fuels cannot be counted on to reduce our dependency on unreliable suppliers in the near term.

Table 6 provides a list of the fuels that usually are assumed by the term "synthetic fuel". The list is an arbitrary one in that the products listed are no more synthetic than the rearranged isomerized, alkylated and cracked molecules that you obtain at the corner gasoline station that was derived from "natural" heavy petroleum fractions in modern refineries, or is it any more "synthetic" than

the "natural" gas you used to heat your house that was coproduced in an oil field and processed to remove acid gases to make it noncorrosive and acceptable before it was put into a transmission system.

## Technology Status

### Liquid Fuels

#### A. Coal Derived

Direct and indirect routes can be used to produce liquid fuels from coal. In each of the technologies there are variations of process technology that represent differing approaches to the same goal. Coal liquefaction as a science has been worked on since the 19th century. All of these routes were used before the modern day discoveries of low cost crude oil in the middle east and large reserves of natural gas that are readily transmitted to population centers. With low energy prices as a national policy and a reliable supply of fuels the use of coal to supply storable liquid fuels fell into disfavor by the 1950s. This capability in the U.S. had disappeared.

In the U.S. there are a number of projects again returning to these routes to produce liquid fuels from coal. Two large pilot plants are in operation to establish an engineering basis for pioneer direct coal liquefaction plants. By the mid 1980s technical readiness of H-Coal and the Exxon EDS processes will be established. Both the Exxon EDS and H-Coal pilot plants have operated and much has been learned regarding the requirements for pioneer commercial plants with regards to components and materials that are required.

The Exxon pilot plant has successfully completed operations on Illinois coal in a once through mode and is now in operation on a Western subbituminous coal from the Wyodek seam. The plant was reportedly successfully practicing bottoms recycle that increases the yields of distillates. This was introduced as a processing alternative by EPRI.

Table 7 summarizes the coal derived liquid development status in the U.S. The fate of the 6000 ton/day demonstration plants are uncertain. The SRC-II demonstration plant has been cancelled leaving only the funds for the SRC I demonstration plant design. There is no commitment to proceed with its construction. The 30 ton/day Fort Lewis pilot plant is to be shut down in the

next few months. While the design of a commercial H-Coal plant has been started its fate depends on successful application to the Synthetic Fuels Corporation. There is one other coal liquefaction pilot plant that is just starting up in Germany using the I.G. Neue process which is a modification of World War II technology. This plant has reportedly started up.

The policy of the current administration is to reduce federal involvement in this area and to turn the responsibility to industry. Since coal derived liquid fuels are unlikely to be competitive with petroleum fuels in that they are \$10-15 higher in cost, it is unlikely that the petroleum industry will proceed with pioneer plants at this time and progress in this field is stalled. Prudent strategies would recommend that initial pioneer plants be installed at this time in order to take advantage of the technical teams that have evolved over the last decade. The dispersal of the organized capability represents a serious set back, which will require considerable cost and time to reassemble when the OPEC nations return to escalating the oil price by controlling production in the middle east.

Nominal yields of fuel oil products (350-800°F) for several processes that are useful for utility applications is shown in Table 8. Major differences between coal derived liquid fuels and comparable petroleum fuel oils are indicated. The nitrogen content is two to five times higher than petroleum products and the aromaticity of the product is also higher as indicated by the hydrogen contents. Tables 9 and 9A provide additional detailed inspections for H-Coal, and Exxon products.

In petroleum derived fuel oil the hydrogen content is usually 8-10%. In contrast to petroleum derived fuel oils the organic metallic species are usually lower. Vanadium plus nickel content in petroleum fuels can represent up to 1000 ppm. In coal derived fuels those constituents are not present in such high concentrations. However, trace constituents of a different character, e.g., iron, titanium and soluble chlorides may present other problems when combustion turbines or boilers are operated for long periods. No long duration testing has been performed at utility sites because of the short supply of coal derived fuel which would delineate material issues.

Table 10 presents the coal which can be handled by different processes. Processes are specific to their flexibility and a prudent strategy recommends that several routes be developed.

## B. Shale Oil

Table 11 summarizes the situation with respect to production of liquid fuels from shale deposits in Colorado and Utah. Recently the administration decided to provide support to the Tosco Corporation who are partners with Exxon in the Colony project and to Union Oil Co. to allow them to proceed with demonstration plants which will retort shale using two alternate methods. In the next few years we should see the beginning of a shale oil industry that has been promised for many decades. Liquid fuels from shale will most probably be sent to refineries. Shale products are compatible with petroleum refinery processes. Because of this factor and their remote location it is unlikely the shale derived liquid fuels for a considerable period will be significant as a large supply for electricity plants. Shale oil is a relatively high grade feedstock useful for producing gasoline and jet fuels - the refiners bread and butter products-that are relatively high in value. Thus, for the materials engineer there is unlikely to be significant problem in adapting engines and combustion equipment to shale derived fuels since they most probably will enter the market as blends with petroleum fuels and will be indistinguishable from the usual fuels commercially handled.

## C. Pyrolysis of Coal

The pyrolysis of coal is analogous to shale retorting in that heating coal in the absence of air results in liquid products being produced. The yields are relatively low (1 Bbl/tons vs 3 Bbl/ton) compared to direct liquefaction processes. Generally, pyrolysis processes are suitable for noncaking western coals using techniques that employ fluid beds (Lurgi Ruhrgas) or kilns (Toscoal). Large plants of a capacity greater than 1000 tons/day have been operated and the technology is relatively mature. The raw liquid fuels are usually upgraded and are similar to other coal derived liquid fuels from direct liquefaction processes.

Pyrolysis processes coproduce 50-65% char that is relatively low in volatile matter and higher in ash content as compared with coal. Its utilization in coal burning stations and its value still needs to be determined.

The Utah Power and Light Co. is considering a pyrolysis project and is carrying out economic screening studies.



#### D. Methanol, Fischer Tropsch Liquids

Fuels represented by methanol and Fischer Tropsch liquids are produced from synthesis gas (CO and H<sub>2</sub>). They are clean burning liquid fuels with superior characteristics for use in combustion turbines and boilers. No severe materials problems are likely to be encountered in their utilization although adaptations are required in procedure since they have different characteristics (e.g., low lubricity). Table 12 presents a summary of status. Because of deregulation of natural gas prices the cost of methanol in the U.S. is expected to rise dramatically in the next few years, thereby, encouraging the production of methanol from coal. One methanol plant based on Texaco gasification is under construction by the Tennessee Eastman Co. Methanol is in the opinion of the authors not likely to represent a significant fuel supply for some time, although in the 1990s some production capabilities may be realized.

#### Fuel Testing

Short tests using methanol, shale oil, and derived liquids have been carried out by utility organizations under the EPRI program. Further test work is planned using fuels from the operating H-Coal and Exxon pilot plants. Tests performed are provided in Table 13.

The complete program for gaining acceptance of a new fuel in utility markets is likely to represent expenditures of \$10-50 million to carry out a detailed program as shown in Table 14. Short term tests that have thus far been performed in utility equipment have shown few problems with regards to materials of construction that are ordinarily used. However, long duration tests on synthetic fuels have not been performed and their timing must await the availability of production quantities. The realization of the test program is stalled and continued technical progress is uncertain.

#### Compatibility Of Fuels With Combustion Turbines

Combustion turbines, while usually utilizing kerosine or No. 2 oil can also be operated on crude or residual oil. Such equipment can be flexible and use a wide range of fuels. Critical fuel properties are: Ash, nitrogen content, hydrogen content and flame temperature. Other properties include viscosity, specific gravity, pour point, flash point, sulfur content, carbon residue, oxygen content, stability, lubricity, and heating value.

For residual oils the main corrosive elements are vanadium, sodium and potassium. Sodium and potassium are usually removed by water washing. However,

there is no economic way to remove the vanadium. Magnesium is added since it forms noncorrosive compounds with the vanadium.

Deposition and corrosion can occur from ash in the fuel. Turbines currently burning crude or residual oil are subject to high deposition rates, mainly of magnesium compounds. The magnesium is used for treatment of the vanadium in the fuel. The main ash deposit components from coal derived fuels are iron oxides. At temperatures of about 2000°F iron deposition has been at a comparatively low rate compared to deposition from magnesium compounds. At 2300°F gas temperature iron deposition has been relatively severe. Deposition with coal derived liquid fuels is less than that of residual oil at 2300°F. Distilled coal liquids should have very low ash levels. Deposition results indicate that fuels with ash content up to 500 ppm can be utilized by combustion turbines.

Coal liquids are relatively low in vanadium. They do contain sodium and potassium as organic constituents which can be removed by conventional washing.

Nitrogen bound in the fuel does not deleteriously effect the combustion turbine.  $\text{NO}_x$  emissions, however, will be higher than petroleum fuel.

To meet emission limitations a number of innovative combustor designs have been developed that are discussed in a following paper. These designs alleviate the  $\text{NO}_x$  emission problem but compound other areas of concern among which are smoke emission and combustor wall-cooling.

Low fuel hydrogen content tends to increase wall temperatures and deleteriously effect smoke emissions. These issues are being addressed in the EPRI program.

Table 1

## CAPACITY OF U.S. ELECTRIC PLANTS

Source: NERC

Year	<u>1980</u>		<u>1989</u>	
	<u>1000 MW</u>	<u>%</u>	<u>1000 MW</u>	<u>%</u>
Coal	220	41	357	46
Nuclear	48	9	140	18
Oil	139	25	140	18
Gas	56	11	49	6
Hydro	65	11	67	9
Other	<u>17</u>	<u>3</u>	<u>25</u>	<u>3</u>
Total	545	100	778	100

Table 2  
 INCENTIVES FOR UTILITY INTEREST  
 IN DIRECT LIQUEFACTION

	<u>1980 Wholesale Prices of Petroleum Products (\$/bbl-FOE)</u>	<u>1980 Prices of Equivalent Coal-Derived Liquid Products (\$/bbl-FOE)*</u>
Propane	27	25-34
Butane	37	34-47
Gasoline	49	46-62
No. 2 fuel oil -- low sulfur	33	31-42
No. 6 fuel oil -- 0.3% sulfur	<u>24</u>	<u>23-31</u>
Overall average for all products	-	33-45

FOE = Fuel oil equivalent =  $5.85 \times 10^6$  Btu/bbl

\* Assuming price ratios between petroleum products hold.

Table 3

SOURCE OF ELECTRICITY GENERATED  
Source: NERC

Year	<u>1980</u>		<u>1989</u>	
	<u>10<sup>12</sup> kW HR</u>	<u>%</u>	<u>10<sup>12</sup> kW HR</u>	<u>%</u>
Coal	1.16	49	1.77	52
Nuclear	0.30	13	0.81	24
Oil	0.33	14	0.32	10
Gas	0.27	12	0.16	5
Hydro	0.23	10	0.23	7
Other	<u>0.05</u>	<u>2</u>	<u>0.07</u>	<u>2</u>
Total	2.34	100	3.36	100

Table 4  
FOSSIL FUELS  
REQUIRED FOR ELECTRIC POWER

Year	<u>1980</u>	<u>1989</u>	<u>△.%</u>
Coal Million Tons	574	928	62
Distillate Oil, Million Bbls	52	61	
Residual Fuel, Million Bbls	<u>536</u>	<u>488</u>	
Total	588	549	-7
Gas, Trillion Cubic Feet	2.9	1.6	-44

Table 5  
ELECTRIC UTILITY USE OF OIL AND GAS  
(1979)

<u>Utility</u>	<u>Annual Consumption of Oil And Gas</u>		<u>Fraction of Total Gas and Oil, %</u>
	<u>Oil, Million Bbls</u>	<u>Gas, Billion CF</u>	
Houston Light and Power	1.3	480	7.6
So. Cal. Edison	47.7	152	6.8
Mid South Util.	24.0	268	6.4
Central and Southwest	0.4	399	6.2
Pacific Gas and Electric	26.2	215	5.8
Florida P & L	39.6	92	5.1
Texas Utilities	1.5	301	4.9
Gulf States	6.8	213	3.9
Cons. Edison, N.Y.	32.5	57	3.9
Oklahoma Gas and Elect.	0	167	2.6
Va. Electric	24.3	2	2.3
New England Power	19.2	2	1.8
L.A. Dept. of Water & Power	13.2	32	1.7
Long Island Lighting	16.7	11	1.7
Public Service N.J.	14.5	21	1.7

Table 6

LIST OF SYNTHETIC LIQUID FUELS

Shale Oil

Coal Derived Liquid Fuels

- Direct
- Indirect
- Pyrolysis

Tar Sands

Biomass



Table 7

TECHNICAL CONSTRAINTS - PROCESS DEVELOPMENT STATUS

- Coal Derived Liquids - Direct
  - Major Candidate Processes - Solvent Refined Coal (SRC-I, SRC-II), H-Coal, Exxon Donor Solvent
  - Two - 250 Ton/Day Pilot Plants Undergoing Operation in U.S.
  - Two - 6,000 Ton/Day Demonstration Plant Projects in Design
    - One 30 Ton/Day Pilot Plant and One Six Ton/Day Pilot Plant in Operation
  - One Commercial (60,000 BBLs/Day) Plant Design Underway
    - No Total Commitments to Commercial Plants

Table 8  
 NOMINAL YIELDS OF FUEL OIL PRODUCTS  
 FROM ILLINOIS NO. 6 COAL

Process	Exxon Donor Solvent	H-Coal	SRC-II	SRC-I
Yield of fuel oil product, ≈ 350-800°F Wt% on MAF coal	23-28	30-35	25-35	5-15
Wt% S	0.3-0.5	0.08	0.3	0.4
Wt% N	0.5-0.7	0.5	1.0	0.7
Hydrogen required Wt% on MAF coal	5-6	5-6	4-5	2-3
Light gas yield	Medium	Medium	High	Low
Naphtha yield		High	High	LowLow

Table 9

## FUEL CHARACTERISTICS

<u>BLEND M/H</u>	<u>H-COAL</u>	<u>EDS</u>
Gravity °API at 60°C	9.2	10.3
Flash Point, °F	280	172
Heating Value Btu/lb	17,860	17,770
Carbon wt %	88.52	88.66
Hydrogen wt %	9.14	9.14
Nitrogen wt %	0.57	0.39
Sulfur wt %	0.075	0.29
Oxygen (by diff) wt %	1.68	1.59
Ash wt %	0.017	0.008
Viscosity		
SSU AT 140°	43.5	37.7
SSU at 210°	35.7	-

Table 9A

## PRODUCT QUALITIES

Coal Technology Contractor Products	Illinois No. 6 H-Coal Fluor Raw	Illinois No. 6 H-Coal Stone & Webster Upgraded	Wyodak H-Coal Fluor Raw
Yield (vol. % of product)			
● LPG	14	14	-
● Naphtha	24	24	45
● Turbine	48	48	35
● Fuel oil	14	14	20
Nitrogen contents (wt%)			
● Naphtha	0.24	nil	0.10
● Turbine fuel	0.47	0.2	0.22
● Fuel oil	0.63	0.6	0.46
Sulfur contents (wt%)			
● Naphtha	0.07	nil	0.02
● Turbine fuel	0.08	< 0.1	0.03
● Fuel oil	0.08	0.1	0.03

Table 10

COALS ARE PROCESS SPECIFIC

Feedstocks	Processes	
	Suitable	Unsuitable
Eastern bituminous	SRC-I SRC-II H-Coal Exxon Donor Solvent Two-stage liquefaction	
Western subbituminous	H-Coal Exxon Donor Solvent Two-stage liquefaction	SRC-I SRC-II
Texas and North Dakota Lignites	H-Coal Exxon Donor Solvent	

Table 11

TECHNICAL CONSTRAINTS - PROCESS DEVELOPMENT STATUS

- Shale Oil
  - Reserves >200 Billion Barrels - 25 Gal/Ton or higher
  - Surface Retorting Demonstrated with Several Processes (300-1000 Ton/Day)
    - Union Oil Rock Pump - 10,000 Ton/Day Demo Unit Committed, 50,000 BbL/Day Expansion being Evaluated - Potential Expansion to 150,000 BBLS/Day
    - Colony Development - Exxon-Tosco-TOSCO-II Retort- 50,000 BBLS/Day
      - o Potential Expansion to 75,000 BBLS/Day
    - Rio Blanco-Gulf-AMOCO - 9,000 BBLS/Day Lurgi - Ruhrgas Retort, Potential Expansion to 150,000 BBLS/Day
    - Standard Oil of California - 350 Ton/Day Demonstration Units and 50,000-100,000 BBLS/Day Production Plans
    - Numerous Additional Developers
  - Modified in Situ
    - Occidental Petroleum Cathedral Bluffs, 56,000 BBLS/Day Initial Capacity - Excavation Well Underway - Potential Expansion to 150,000 BBLS/Day

Table 12

TECHNICAL CONSTRAINTS - PROCESS DEVELOPMENT STATUS

- Indirect Coal Liquids
  - Methanol
    - Numerous Commercial Plants Worldwide Using Natural Gas Feed - 300-3,000 Ton/Day Product
    - Few Old Commercial Plants Used Coal Gas Feed - 300 Ton/Day Product
    - Numerous Engineering Feasibility Studies Underway Using Lurgi, Texaco, Winkler Gasification Technologies
  - Fischer-Tropsch Liquid
    - SASOL-II Commercial Plant in South Africa Successfully Started-Up (  $\approx$  100,000 BBLs/Day Products)
    - Numerous Engineering Feasibility Studies Underway in U.S. - Lurgi Gasification Technology

Table 13

## EPRI EMISSIONS TESTING

<u>TEST CONDITIONS:</u>	DISTILLATE OIL FT-4 CIDF, 26 MWe BASE LOAD 0.6/1.0 Water/ FUEL RATIO	BLENDED RESIDUAL OIL W-501 PACE 62MWe BASE LOAD 0.5/1.0 Water/ FUEL RATIO	SHALE OIL BOTTOMS FT-4A 9DF 20 MWe BASE LOAD 1/0/1.0 Water/ FUEL RATIO	METHANOL FT-4A 1DF 26 MWe BASE LOAD 0.2/1.0 Water/ FUEL RATIO
<u>EMISSIONS</u>				
NO <sub>x</sub> PPM 15%O <sub>2</sub>				
H <sub>2</sub> O Injected	55	95	113	18
Not H <sub>2</sub> O Injected	207	200	275	50
Particulates, EPA-5 LB/10 <sup>6</sup> BTU	.008	.09	.01	.005
CO PPM 15%O <sub>2</sub>				
H <sub>2</sub> O Injected	60	98	439	116
Not H <sub>2</sub> O Injected	50	30	75	43
SO <sub>x</sub> PPM 15%O <sub>2</sub>	8-16(SO <sub>3</sub> <1.0)	110-133(SO <sub>3</sub> <1.0)	Not Available	0
SMOKE				
H <sub>2</sub> O Injected	0 Opacity	4 Smokespot	1.2 ARP1179	0 Opacity
Not H <sub>2</sub> O Injected	0 Opacity	3 Smokespot	2.2 ARP1179	0 Opacity



Table 14

PROGRAM OPPORTUNITIES NEEDING DEFINITION

- Scale of Operations, Test Plans, Test Duration
- Equipment Selection
  - ● Short Term Tests in Tangentially Fired Equipment - Designed for Coal Complete
  - ● Feasibility from Short Term Tests
  - ● Long Term Tests
    - ● ● Tangentially Fired Oil
    - ● ● Wall Fired Oil
- Burner Modifications or Staging
  - ● Control of Nitrogen Oxides
  - ● Smoke and Particulates
  - ● Hydrocarbon Emissions
- Stability and Compatibility
- Fuel Handling and Utilization Procedures
- Market Study Defining
  - ● Retrofit and New Plant
  - ● Costs and Experience
  - ● Industrial Hygiene
  - ● Fuel Handling

COAL GASIFICATION COMBINED CYCLE SYSTEMS  
DEVELOPMENT STATUS, GAS QUALITY AND CONTROL CONSIDERATIONS

This paper was prepared for the Second Conference on  
Advanced Materials for Alternative-Fuel-Capable Heat Engines

Neville A. Holt  
Program Manager

Prepared for  
Electric Power Research Institute  
3412 Hillview Avenue  
P.O. Box 10412  
Palo Alto, CA 94303

## SUMMARY

EPRI studies show Integrated Coal Gasification Combined Cycle (IGCC) plants equipped with currently commercial gas turbines to be economically competitive with direct coal fired units equipped with stack gas scrubbers. Further improvements in gasification and gas turbine technology should render such IGCC systems more attractive.

The status of development of the major candidate coal gasification processes is reviewed. The composition ranges of the product gases are discussed with reference to combustion characteristics in the gas turbine. The results of gas quality monitoring from EPRI test programs on gasification pilot plants are presented showing that current gas clean up technology should be more than adequate to meet gas turbine requirements. The control of IGCC systems is briefly discussed.

Finally, the major remaining IGCC development issues are addressed and a brief account given of the 100MW Texaco coal gasification combined cycle plant project to be located at Southern California Edison's Cool Water station near Barstow, California.

### Introduction and Incentives

The continued uncertainty surrounding nuclear power deployment, the rapidly increasing cost of oil, the need to reduce utility oil and gas usage, the Clean Air Act amendments and the Resource Conservation and Recovery Act argue strongly for the rapid development of alternative, coal fueled power systems.

Clean gaseous fuels from coal have the following potentially beneficial uses in electric power systems:

- Fuel for integrated combustion turbine combined-cycle power plants or fuel cell combined cycle systems.
- Fuel for direct firing in steam boilers.
- Fuel for retrofit to existing gas and oil fired boilers, combined cycles and turbines.
- Production of synthesis gas as a source of clean liquid fuels, such as methanol, for intermediate and peaking load duties in combustion turbines and fuel cells.

Of all of these uses, the integrated gasification combined cycle power plant has the largest potential impact in the power industry. It promises reduced heat rates, lower water consumption and land requirements, markedly reduced emissions, and capital and electric power costs competitive with conventional coal fired steam plants.

## Economics

EPRI studies show that integrated gasification combined cycles using commercially available combustion turbines (2000°F inlet temperature) and based on Texaco or BGC/Lurgi slagging gasifiers are competitive with conventional coal fired power plants with stack gas cleanup. Table 1 shows a performance comparison between conventional coal firing and gasification based power systems. The data presented in Table 1 reflect 1979 environmental control regulations. Cost estimates are also presented in Table 1 for cycles with advanced high temperature turbines to illustrate the further performance improvement potential of this technology. As environmental control regulations become more stringent, the economic advantages of gasification combined cycle (GCC) power plants will increase markedly. Table 2 shows the cost for the more stringent projected mid 1980's standards: GCCs clearly emerge as preferred coal fired baseload plants. They also have significant potential for additional improvements to heat rate and environmental performance. GCCs also offer reduced water consumption and land requirements, reduced fuel and chemicals consumption, and reduced solid waste volume. The solid waste from the Texaco and BGC/Lurgi slagger is in the form of extremely inert slag which should be readily disposable.

Table 1  
 Performance and Cost Comparison  
 Conventional/Gasification Combined Cycle Technologies  
 (1979 Federal Emission Control Requirements)

System	Net Heat Rate Btu/kWh	Capital <sup>(1)</sup> Investment \$/kW	Levelized Cost of Electricity Mills/kWh <sup>(2)</sup>
Reference Coal Fired Steam Plant with Limestone FGD	10,000	1095	90.6
Texaco - GCC 2000°F Turbine	9400	1080	80.2
Texaco - GCC 2600° Turbine	8460	1050	78.1
BGC/Lurgi GCC 2600° Turbine	7920	885	70.1

Notes:

- (1) December 1980 dollars, Illinois #6 coal  
 (2) Coal cost = \$1.65/MM Btu, capacity factor 65%

Table 2

Economic Comparison of Texaco Gasification Based  
Power Systems with Conventional Coal-Fired Steam Plants

	<u>1979 Federal Emission Control Requirements</u>	<u>Projected mid-1980s Emission Control Requirements</u>
Sulfur	90% removal	95% removal
Particulates	0.03 lb/10 <sup>6</sup> Btu	0.02 lb/10 <sup>6</sup> Btu
NO <sub>x</sub>	0.6 lb/10 <sup>6</sup> Btu	0.2 lb/10 <sup>6</sup> Btu
Waste Water		Zero discharge
Coal Ash		Special handling
 <u>Coal-Fired Steam Plant</u>		
Heat Rate Btu/kWh	10,000	10,180
Capital Requirements \$/kW <sup>(1)</sup>	1,095	1,300
30 Yr. Levelized Cost of Electricity Mills/kWh <sup>(2)</sup>	90.6	100.7
 <u>Texaco GCC - 2000°F Turbine</u>		
Heat Rate Btu/kW	9400	9550
Capital Requirement \$/kW <sup>(1)</sup>	1,080	1,160
30 Yr. Levelized Cost of Electricity Mills/kWh <sup>(2)</sup>	80.2	83.7

## Notes:

- (1) December 1980 dollars, Illinois #6 coal  
 (2) Coal Cost - \$1.65/MM Btu, capacity factor 65%

Gasification may also be used for retrofit to existing gas and oil fired boilers, combined cycles and combustion turbines. Gasifiers might be installed at an existing plant or some cases remotely, with fuel distributed by pipeline. Gasification may allow repowering existing boilers with combustion turbines to reduce the heat rate and provide increased generation capacity in convenient increments at an existing site with probably reduced permitting periods. The effects of retrofitting and repowering are illustrated in Table 3.

Table 3  
**RETROFITTING & REPOWERING**

Over-the-fence supply of intermediate Btu gas containing 5 ppm sulfur, costing \$4-\$5.50/10 <sup>6</sup> Btu if utility produced and \$6-\$8/10 <sup>6</sup> Btu if purchased (1980 \$).				
<i>System Description</i>	<i>Plant Capacity (MW)</i>	<i>Heat Rate (Btu/kWh)</i>	<i>Heat Rate Including Gas Plant (Btu/kWh)</i>	<i>Heat Rate of Added Equipment (Btu/kWh)</i>
Retrofit of oil-fired boiler	333	8,960	12,000	—
Repower oil-fired boiler with one gas turbine	436	8,105	10,800	5,345
Retrofit oil-fired combined cycle	400	7,600	10,100	—



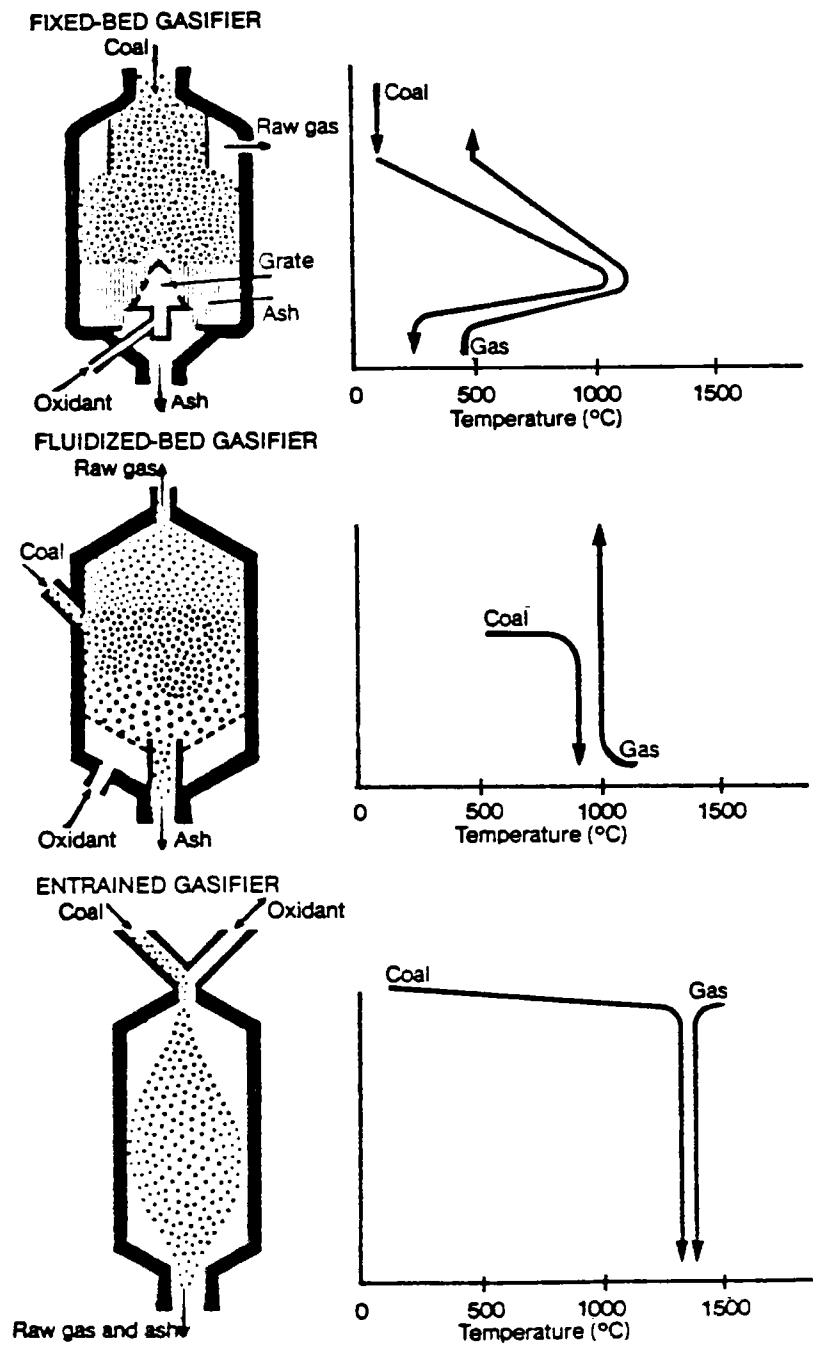
## Coal Gasification

The existing commercial coal gasification processes and most of those in an advanced state of development fall into three categories: fixed (or more correctly moving) bed, fluidized bed and entrained systems. Each of these types of reactors have distinctly different methods of contacting and temperature regimes which give rise to different product gas compositions and other characteristics. These are illustrated in Figure 1.

In moving bed gasifiers, such as the well known Lurgi dry ash (which is deployed commercially in South Africa and elsewhere) sized coal is introduced through lockhoppers to a pressurized (typically 450 psig) reactor and moves slowly downwards countercurrent to the ascending gases produced from the steam and oxygen (or possibly air) introduced through the distributor grate at the bottom. The grate also serves as a means of dry ash removal into another lockhopper system. A typical temperature profile for a moving bed gasifier is shown in the diagram in Figure 1. In the Lurgi, the higher temperature bottom zone is kept below the ash fusion temperature by excess steam injection. Being a countercurrent gasifier, the gases are cooled by the descending coal and the gas outlet temperature is much lower than other gasifier types so that devolatilization products such as tars and oils are present in the gasifier effluent. The British Gas Corporation (BGC) version of the Lurgi gasifier operates at slagging temperature where only the steam for the gasification reaction is required. Steam consumption is reduced, efficiency is greatly improved, and waste water treatment is markedly reduced. In addition the higher temperature increases the reaction rate so that throughput can be three or four times those of dry ash units. Fine coal and the tar by product can be gasified by injecting them into the slagging zone.

In fluidized bed systems, such as the Winkler, Westinghouse and 'U' Gas processes, coal (typically  $<1/8$ " size) is introduced into a fluid bed of partially gasified coal particles. Steam and oxygen are typically introduced through a grid plate.

Ash is removed at the bottom and a particulate laden gas leaves the top. The fluidized bed is a back-mixed reactor and has an almost uniform temperature throughout. The temperature clearly must not exceed the ash fusion temperature of the coal but should be high enough to ensure destruction of all tars. The currently commercial version of the Winkler process operates at atmospheric pressure and the gas has little methane content. The Westinghouse, 'U' Gas, and a new version of the Winkler under development by Rheinische Braun Kohlen (RBK) in West Germany, all operate at pressure and have increased methane contents. In the Westinghouse and 'U' Gas processes the ash is removed as ash agglomerates.



COAL GASIFICATION REACTORS

Figure 1

In entrained systems pulverized coal and oxidants are introduced together and flow co-currently through the reactor. These gasifiers operate above the slagging temperature typically at 1400-1500<sup>0</sup>C. There are several designs. The currently commercial Koppers Totzek (K-T) gasifier operates at atmospheric pressure and introduces the coal and oxidants horizontally through opposed heads and the gas flows upwards with some of the ash while the rest of the ash is removed from the bottom as slag.

Shell is developing a pressurized reactor of similar configuration to the K-T. In both the Shell, and K-T, and in most other entrained gasifiers, coal is introduced in dry pulverized form; whereas, the Texaco process is a downflow reactor and uses essentially the same kind of reactor as that successfully employed in more than 70 plants across the world for heavy oil gasification.

For the fluidized bed and entrained systems, a significant part of the energy leaving the gasifier is as sensible heat which must be recovered by steam raising or other gas heat exchange in order to obtain satisfactory overall efficiencies. Such heat exchange developments are of key importance for GCC commercialization.

## Coal Gas Compositions

The major components of the product gas are carbon monoxide, hydrogen, carbon dioxide, with some methane from certain gasifiers. Some typical gas compositions are shown in Table 4. The different gas compositions carry separate implications for gas cleanup. In most cases the gas composition is such that the flame temperature is higher than methane alone, and this carries implications for gas turbines. In order to meet the stringent NO<sub>x</sub> standards the gas turbine combustors will probably have to use either phased combustion, water/steam injection or possibly some admixture of such techniques.

Of the typical gas compositions listed in Table 4, all are from oxygen blown systems with the exception of Combustion Engineering (C-E). The C-E gasifier is an atmospheric pressure two staged air-blown gasifier so that the product gas is only about 100 Btu/SCF and is 60 percent nitrogen. The gas compositions are strongly functions of the outlet temperatures and pressures of the gasifiers. The CO/CO<sub>2</sub>/H<sub>2</sub>/H<sub>2</sub>O ratios are related to equilibrium of the shift reaction, so that gasifiers with significant excess steam, such as Lurgi (arising from ash fusion control) and Texaco (arising from water slurry feed), have higher CO<sub>2</sub> contents. Gasifiers such as BGC/Lurgi and Shell have low steam contents in the effluent gas hence CO<sub>2</sub> is quite low. Lower CO<sub>2</sub> contents can have economic advantages in the gas cleanup scheme since lower energy consuming acid gas removal processes can be used to produce acceptable Claus plant feedstocks. The moving bed gasifiers typically have outlet temperatures of 500°C or lower and the methane, largely produced by devolatilization of the coal, survives. The entrained gasifiers all operate at high temperatures and only traces of methane survive. In fluid bed gasifiers with outlet temperatures typically 850-1000°C depending on coal type, the methane content is influenced strongly by pressure with little present in an atmospheric Winkler, but up to about 8% in a pressurized Westinghouse at 350 psig.

## NO<sub>x</sub> Emissions

In Table 5 the flame temperatures of various gases are tabulated together with their NO<sub>x</sub> forming potential relative to natural gas. It can be seen that those gases containing substantial CO and H<sub>2</sub> will have higher flame temperatures and therefore produce more NO<sub>x</sub> unless that flame temperature is moderated either by phased combustion techniques or by reduction of the flame temperatures by CO<sub>2</sub> or steam/water. Later on in this paper some account will be given of the techniques to be used on the 100MW Texaco gasification combined cycle plant to be located at

Table 4

TYPICAL COAL GAS COMPOSITIONS  
Clean Dry Basis - Volume Present

	<u>Lurgi</u>	<u>BGC/Lurgi</u>	<u>Westinghouse</u>	<u>Texaco</u>	<u>Shell</u>	<u>Koppers</u>	<u>C-E</u>
CH <sub>4</sub>	9	7	8	--	--	--	--
H <sub>2</sub>	40	29	27	36	32	30	11
CO	20	60	54	47	65	58	22
CO <sub>2</sub>	30	3	10	16	2	11	7
N <sub>2</sub> etc.	1	1	1	1	1	1	60

Southern California Edison's Cool Water station in Southern California. Coal derived gas from an air-blown gasifier will have much lower flame temperature than natural gas due to the presence of so much nitrogen, and accordingly, as shown in Table 5, there should be no problem in meeting NOx emission standards with such a gas.

Additional Composition Considerations for Gas Turbines

Flamability limits are important in combustion stability and during start-up in ignition/blow out performance and cross firing capability. Blow out margin, CO emissions, efficiency and possible dynamic pressure pulsation are also of concern. The presence of liquid slugs, particulate matter or alkali metals must be avoided and will be addressed in a later section of this paper.

Table 5  
RELATIVE NOx EMISSIONS<sup>(1)</sup>  
OF VARIOUS GASES

Gas	Flame Temp. °F	Relative NOx <sup>(2)</sup>
Natural gas	4006	1.00
Methane	3982	0.95
Coke oven gas	4107	1.25
Carbon monoxide	4536	3.25
Hydrogen	4331	1.97
Coal-derived gas (air-blown)	2837	0.07

(1) Assuming the absence of nitrogen bearing compounds.  
(2) NOx/NOx (natural gas) - PPMV/PPMV

## Coal Gasification-Status of Development

In Table 6 the pattern of development for some of the existing commercial processes (Lurgi, K-T) and of several of the better known process currently under development are shown. Generally it has been found, pragmatically, that the scale up of the complex gas solid mixing reactions can most prudently be accomplished in steps of less than ten fold. Scale-ups greater than this are judged to be much greater risk. Obviously any time an opportunity arises for putting up a large unit at an existing commercial facility and using existing gas cleanup, coal handling, and utility connections there will be a chance for a larger scale up for a given expenditure than if a new grass roots facility has to be built. For most commercial gasification combined cycle (GCC) plants modules based on about 1000 ton/day coal gasifiers are typically planned. The output of such gasifiers corresponds approximately to the energy requirements of the currently commercial large frame size gas turbines operating with turbine inlet temperatures of about 1100°C. Some further economics could be expected from future 2000 ton/day gasifiers.

The currently commercial gasification processes do have gasifiers of about 1000 ton/day size. The Mark IV (4 meters) Lurgi's used in South Africa at Secunda, the four headed Koppers-Totzek units in India and the Winkler gasifiers in Turkey have capacities in the range of 500-1000 tons/day.

At Sasol a Mark V Lurgi (5 meters diameter) has also recently been tested. At Westfield, Scotland a 350 ton/day BGC/Lurgi slagging gasifier has been tested since 1974 and is currently undergoing a long term endurance run to prove out the mechanical and materials integrity in the slagging zone. A 700 ton/day unit is planned to be commissioned there in 1983.

A 165 ton/day Texaco oxygen blown unit has been successfully operated by Ruhrkohle/Ruhrchemie at Ruhrchemie's Oberhausen-Holten plant since 1978. This unit includes a heat recovery boiler to raise steam from the sensible heat in the gasifier effluents. This item is key for GCC applications and a similar unit is planned for the Cool Water 100MW Texaco GCC demonstration plant. Dow has been testing an air-blown Texaco gasifier at their Plaquemine, Louisiana division, and have also conducted test operations of a Westinghouse 10-15MW gas turbine on the low Btu gas. Dow has also recently announced scale up plans for a plant to supply power at one of their commercial plants.



Shell has operated a 150 ton/day unit at their Harburg refinery since 1979 and plans to scale up to a 1000 ton/day unit at Moerdijk in the Netherlands for commissioning in 1985. The gas from this larger unit is planned to be transported to fuel an existing combined cycle unit.

Combustion Engineering has a 120 ton/day gasifier at Windsor, Connecticut and under DOE funding is conducting the design of a larger unit to retrofit an existing 150MW boiler at Gulf States Utilities' Lake Charles station.

Westinghouse operates a 30 ton/day pilot plant at their Waltz Mill, Pennsylvania site and has recently announced that they plan to supply a 1200 ton/day unit with associated heat exchange and particulate cleanup, to Sasol by 1984.

IGT has operated a 15 ton/day pilot plant for several years, and a larger plant based on this technology was planned for Memphis LWG as part of the DOE demonstration plant program. With the demise of this latter program, a proposal has been submitted for support to the Synthetic Fuels Corporation (SFC).

The COGAS process which had been tested with coal chars in a unit of about 50 tons/day capacity in Leatherhead, England had been planned to be scaled up to a demonstration plant in Illinois under the DOE demonstration program. However, this project does not appear likely to proceed.

Allis Chalmers plans to test an air-blown pressurized rotary kiln gasifier of about 600 tons/day capacity to retrofit an existing boiler at Illinois Power's Wood River station. The unit is currently in construction for planned commissioning in 1983.

From the above status report it can be seen that the coal gasification field is extremely active with major organizations of considerable financial resources and technical capability undertaking major development programs.

Table 6

## THE PATTERN OF COAL GASIFICATION DEVELOPMENT

	10-50 t/d	100-400 t/d	500-1000 t/d
Lurgi	1930s	MK III (1950s)	MK IV (1970s)
Koppers-Totzek	Louisiana, Mo.	2 headed (1950s & 60s)	4 headed (1970s)
BGC/Lurgi	1948-62	1974	Planned 1983
Texaco	1950+ Montebello	Oberhausen 1978, DOW, TVA	Planned 1984
Shell	1977 Amsterdam	1979 Harburg	Planned 1985 Moerdijk
C-E	1962 (B&W)	1978 Windsor, CT.	Planned 1985
Westinghouse	1975		Planned 1984
IGT 'U' Gas	1976		Planned 1984
COGAS	1974		Planned 1984
Allis-Chalmers			Planned 1983

## Turbine Fuel Gas Specifications and EPRI Test Results on Gasification Pilot Plants

Over the past five years EPRI has conducted several test programs on various coal gasification pilot plants as shown in Table 7. Future planned test programs are also indicated. The objective of these programs has been to obtain steady state and dynamic (load change) data on the characteristics of these systems with coincident close monitoring of gas quality and environmental data on effluent streams.

EPRI has sampled raw fuel gas (before sulfur removal) from the BGC/Lurgi slagging gasification (350 ton/day) at Westfield, Scotland; Ruhrkohle/Ruhrchemie's 165 ton/day Texaco gasifier at Oberhausen, West Germany; and Texaco's 15 ton/day pilot plant at Montebello, California. The object was to determine the environmental acceptability of these processes and to determine the suitability of the gas for gas turbine fuel. The gas meets most turbine manufacturers' specifications for cleanliness despite the fact that in all cases it would undergo one additional thorough scrubbing step (and perhaps two) before being admitted to a turbine. This is illustrated in Table 8.

Turbines are intolerant of any liquid droplets in the fuel. These are eliminated by superheating the fuel gas (recommended at least 20 F superheat) and a final knock-out vessel just before the turbine to catch any liquid slugs. Superheating the fuel gas can have the added advantage of improving the efficiency of an IGCC power plant because it is a means to utilize relatively low level heat. The exact resaturation, reheat configuration to be used at Cool Water will be discussed in more depth later. This equipment was not available at any of the gasification pilot plants tested by EPRI, so testing for liquids in the fuel gas would have been meaningless.

Particulates can cause erosion of turbine internals and should be eliminated from the fuel gas as much as possible. Manufacturers recommend that all particulates  $>10\mu$  be filtered out. In one of our tests, we discovered a  $40\mu$  particle, (probably pipe scale) but most other particulates were at or below the  $10\mu$  limit. The total particulate loading is so low that conventional  $5\mu$  fuel filters should have no difficulty meeting manufacturers specifications with the gas from either process.

Table 7

## CLEAN GASEOUS FUELS: EPRI TEST PROGRAMS

Technology	Location	Year	Size(t/d)
<b>Conducted &amp; ongoing</b>			
● Texaco	Montebello, CA	1978+	15
	Oberhausen, W. Germany	1980	165
● BGC/Lurgi	Westfield, Scotland	1976	350
● Combustion- Engineering	Windsor, Connecticut	1978+	100
<b>Planned</b>			
● Texaco	Oberhausen, W. Germany	1981+	165
	Muscle Shoals, Alabama	1982+	160
● Shell	Amsterdam	1982+	6
	Harburg, W. Germany	1982+	150
● BGC/Lurgi	Westfield, Scotland	1983+	700
● Allis Chalmers	Wood River, Illinois	1984+	600

Table 8

COMPARISON OF EPRI GASIFICATION PILOT PLANT TEST RESULTS  
AND TURBINE FUEL GAS SPECIFICATIONS

<u>CONTAMINANT</u>	<u>SPECIFICATION</u>	<u>EPRI TEST RESULTS</u>
LIQUIDS	ELIMINATE ENTIRELY	NOT TESTED
PARTICULATES	30 PPM TOTAL ELIMINATE ALL $>10\mu$	ALL $< 2$ PPM, MOST $< .1$ PPM ONE PARTICLE $40\mu$
NA, K, (LI)	.5 PPM	ALL $< .3$ PPM, MOST $< .1$ PPM
V, PB, P	2 PPM	$< .1$ PPM
CA, SI	$< 10$ PPM EACH	$< 1.0$ PPM
CI	$< 10$ PPM	UP TO 50 PPM
FE, CU, NI	.1 PPM	$< .1$ PPM

The alkali metal sulfates (Na and K are the most prevalent) cause hot corrosion. V, Pb, and P can enhance alkali sulfate hot corrosion. Concentration of all of these elements are comfortably below the manufacturers recommended limits. Some sulfur removal processes (Benfield, Stretford) use solutions containing some of these elements, so if such a process is considered for sulfur removal, special precautions may be required. Testing for these elements downstream of existing commercial Benfield units is being considered by EPRI. If they are present in excessive concentrations, an additional water washing step may be necessary.

Ca and Si can form deposits. The main source of these elements is generally injected water for NO<sub>x</sub> control. Injected water should therefore be demineralized to limit the concentration of these elements in the fuel gas.

The chlorine content of the raw fuel gas exceeds turbine manufacturers' specifications. The high chlorine concentrations determined were due to the fact that this fuel gas was produced from high chlorine Illinois #6 coal. These high chlorine levels are potentially harmful not only to the turbine but also to all the upstream gasification equipment. In this case, an additional water scrubbing step is probably indicated to reduce the chlorine levels to 10 ppm. This can probably be accomplished in the resaturator as designed for Cool Water. (The Cool Water design coal is a lower chlorine Utah coal.)

It is possible that Fe, Cu, Ni can contribute to hot corrosion and for this reason, some manufacturers limit the concentration of these elements to .1 ppm. The raw fuel gas from the processes tested meets these specifications.

## Dynamic Test Results and Control Studies

Over the past five years EPRI has also conducted a series of modelling and simulation projects for GCC unit operations and complete systems to aid in defining characteristics important to integrated control system design. These studies are shown in Table 9.

Detailed computer models of entrained and moving bed gasifiers incorporating both hydrodynamic, thermodynamic and kinetic aspects have been assembled. The H<sub>2</sub>S removal system has similarly been modelled.

Computer simulations of both entrained and moving bed GCC systems have also been completed and exercised for EPRI by teams from Fluor/Westinghouse and General Electric respectively.

Considerable information on the dynamic characteristics of the Texaco gasifier has been determined from EPRI test runs of the Montebello and Oberhausen gasifiers. An almost instantaneous response of gas output to gasifier feed change was noted together with virtually no change in gas heating value over the 50-100% operating range.

Table 9

### EPRI GCC MODELLING & SIMULATION PROJECTS

---

#### SUBSYSTEM MODELS

Entrained Gasifier  
Moving Bed Gasifier  
H<sub>2</sub>S Removal System

#### GCC SYSTEM SIMULATION

Moving Bed System  
Texaco System

#### GCC SYSTEM TEST ON UTILITY SYSTEM MODEL

The Fluor/Westinghouse study drew attention to a potentially important factor with regard to oxygen plant response. Commercial oxygen plants had typically been designed to maintain high oxygen purity and only to change load at about 10% per hour. Therefore in 1980 EPRI conducted some load change trials on a commercial sized Air Products 1000 ton/day oxygen plant at La Porte, Texas. It was shown that with the Air Products closed loop computer control scheme that load changes of  $\pm 10\%$  were accomplished in one to two minutes, and ramp rates of 2% per minute over the 70-105% of rated load, could be accommodated with variations of only  $\pm 0.2\%$  in oxygen purity. This was an important test which demonstrated that oxygen plants should not limit the response of integrated oxygen blown IGCC systems.

In the GCC systems simulations studies EPRI's contractors evaluated two basically different GCC control modes, turbine-lead and gasifier-lead. The former is a familiar power plant control strategy: the combustion turbine fuel inlet valve moves in response to changing load on the power system, and the fuel gas flow is regulated accordingly by pressure control of the gasifier feed streams. In the gasifier-lead mode the gasifier feed valves first respond to changing load, and the combustion turbine valve subsequently responds to pressure control.

Review of both simulations under the two control modes permits some general conclusions. Closed loop operation was successful in both plants, because the combustion turbines responded rapidly and effectively handled much of the burden.

The fast response rate of the entrained flow gasifiers, with constant gas heating value, makes this option very suitable for closely coupled operation in a GCC plant. As a result, the entrained flow plant demonstrated excellent capability for cyclic operation to meet power system needs. Both control modes worked well in closed loop operation of this overall plant during normal transients and during emergencies after the simulated loss of key components.

As expected, the response rate of the moving bed gasifiers was slower because of the larger reacting masses of coal. Transient changes in fuel gas heating value also made control of these gasifiers more complex. Operation of the combined cycle plant, in turn, was accompanied by fuel system transients that inevitably limited the closed loop response rate during load changing operations. Nevertheless, in the turbine lead control mode, this plant was controlled satisfactorily to meet load following criteria. In the gasifier lead mode it was less responsive, making this mode less acceptable.



Perhaps the most significant conclusion from these analyses was that both the entrained flow and the moving bed GCC plants are capable of closely coupled operation without interposed gas storage buffers or supplementary fuels. On the basis of these simulation studies and the associated experimental work with pilot gasifiers, the load following maneuverability of GCC plants has now been established, and the design of the Cool Water 100MW demonstration plant is proceeding with improved confidence. The ultimate proof of the controllability of an integrated GCC plant is one of the prime, perhaps, the prime objective of the Cool Water Project.

## The First Integrated Coal Gasification Combined Cycle Demonstration Plant

The key issues remaining for resolution in GCC development are:

- Gasifier scale up
- Heat recovery boiler scale up
- Integral control
- Load following capability
- Gas turbine reliability and durability
- Gas turbine combustor design

In the preceding parts of this paper, (and certainly also else where) the data base preparatory for a larger project has been outlined; a project which constitutes the key to commercialization of of this technology.

The Cool Water project, referred to earlier, is such a project and is funded by Texaco, Southern California Edison, EPRI, Bechtel, General Electric, a Japanese consortium and ESEERCO. The overall block flow diagram for this plant is shown in Figure 2. It is based on the Texaco coal/water slurry gasification technology. An oxygen blown 1000 ton/day gasifier is to be employed, equipped with a heat recovery boiler (HRB) or syngas cooler which raises saturated steam from the sensible heat in the gasifier effluent. After particulate removal, and gas cooling  $H_2S$  is removed in a Selexol (Allied Chemical) unit as a rich stream which is fed to a modified Claus plant for sulfur recovery, and the clean fuel gas forwarded to the gas turbine for combustion and power generation. The sensible heat from the gas turbine exhaust gases is used to raise steam in the gas turbine heat recovery steam generator (HRSG). The steam system is integrated between the gasifier HRB and the gas turbine HRSG with the HRSG providing superheated steam which is then forwarded to the steam turbine for further power generation. Figure 3 focuses more specifically on the configuration which has been adopted in the gas cooling and gas cleanup sections of particular importance to the gas quality as delivered to the gas turbine.

Gasifier product gas leaves the gasifier HRB and is fed to the Texaco venturi scrubbing tower for removal of the remaining coal ash (or rather slag) particles. Most of the remaining sensible heat in the particle free gas is then recovered in a heat exchanger with a circulating water loop for reintroduction to the essentially  $H_2S$  free clean fuel gas prior to gas turbine. The gas is then further cooled by air and water cooling to the lower temperature necessary for the

Selexol H<sub>2</sub>S removal process. The clean fuel gas is then saturated and heated by the circulating hot water which has recovered some of the sensible heat of the raw product gas. Clean demineralized water is introduced as make up to the top of the saturator tower.

The gas, is further superheated with steam about 20°C before entering a knock out pot. This final guard chamber is also equipped with a demistor and a boot for detection of any inadvertent liquid that might survive the precautionary train.

This arrangement serves three major purposes. First of all raw product gas sensible heat is transferred to useful energy into the gas turbine thereby improving efficiency and heat rate. Secondly water or rather steam is introduced into the clean fuel gas to lower the flame temperature and provide NO<sub>x</sub> emission control. Thirdly, precautions against inadvertent entrainment of liquid slugs are provided.

Construction of this project should start in the Fall of 1981 with plant commissioning in early 1984. By 1985 a basis for the design of full commercial units should be established. Accordingly full commercial deployment of IGCC technology can be predicted for the early 1990's. With the parallel developments in other gasification technologies such as BGC/Lurgi, Shell and Westinghouse a healthy competitive environment promising further advances can also be anticipated.

BLOCK FLOW DIAGRAM FOR COOL WATER PROJECT

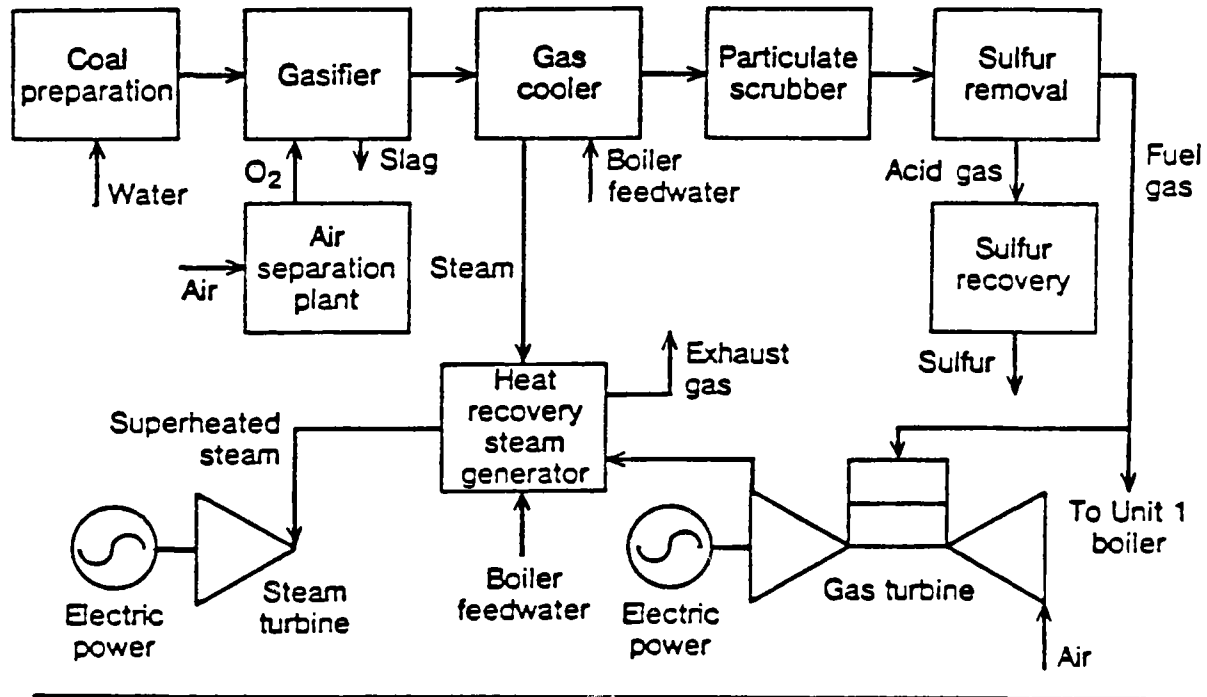


Figure 2

COOL WATER  
GAS CLEAN UP PROCESS SCHEME

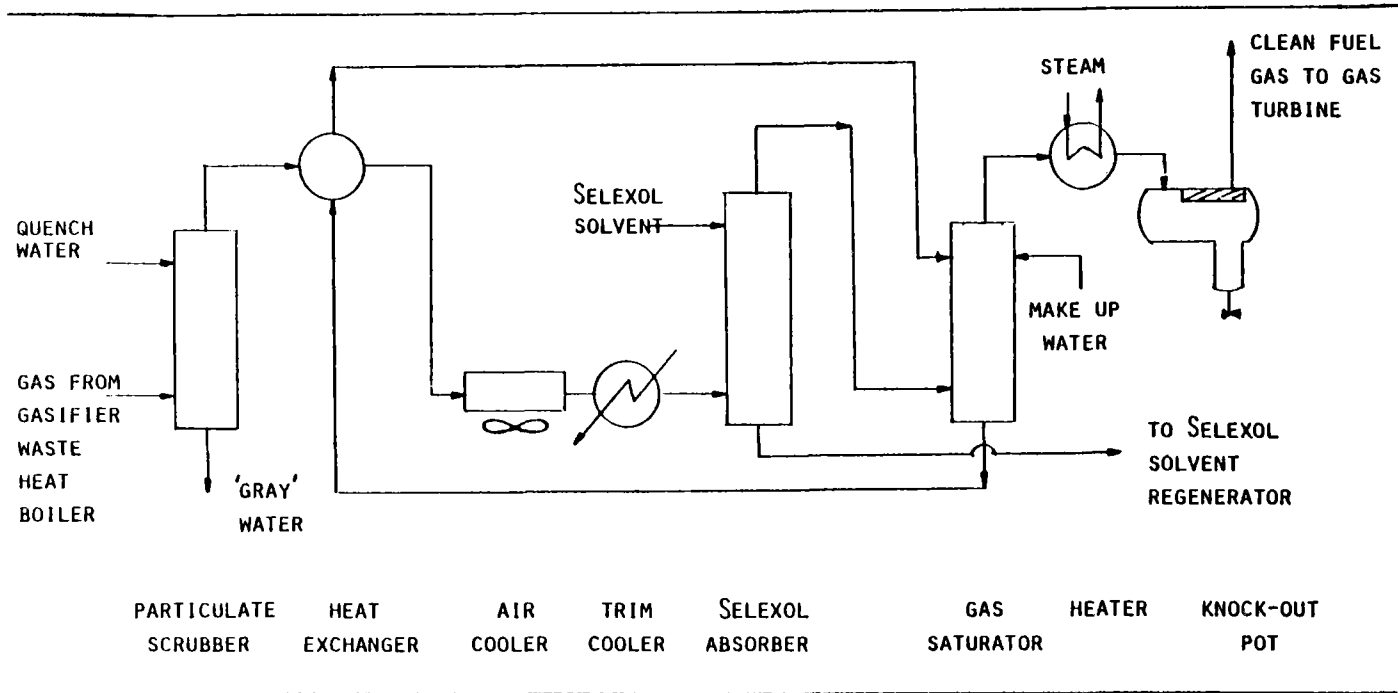


Figure 3

ECONOMICS OF ALTERNATIVE FUELS FOR  
ELECTRIC POWER GENERATION

M. J. Gluckman  
Electric Power Research Institute

INTRODUCTION

The era of synthetic fuels is about to commence. Isolated examples of the development of this new industry can be found throughout the world, i.e., a massive coal-to-gasoline plant (SASOL II) in South Africa (with a duplicate system currently under construction); a coal-based methanol plant in India; coal-based gasification-combined cycle power plants in West Germany and the U.S.A.; and a small coal-to-ammonia plant in the U.S.A. Recent actions by the U.S. Federal Government to dramatically reduce government support of emerging synthetic fuels technologies will certainly slow down these developments. However, it is this author's opinion that synthetic fuels development will be continued--albeit at a slower pace--by the private sector for the economic reasons outlined below.

The driving force behind this torturous emergence of a new, highly capital intensive technology, is a complex combination of economic, political, social and resource related factors. Diminishing world reserves of crude oil coupled with a variety of international political issues have driven the average market price of imported crude oil from less than \$3.50/bbl in 1971 to approximately \$36.00/bbl in 1981. Although it is not possible to project future crude oil price trends with much certainty for the remainder of this century, most energy companies are projecting a real annual growth in the market price for crude oil in the range 0% to 3% over the general inflation rate. Even at no real annual price growth, crude oil will be selling for more than \$220.00/bbl or \$37/10<sup>6</sup> BTU by the year 2000 assuming an annual general inflation rate of 10%. Coal, on the other hand, is currently selling for approximately \$1.50/10<sup>6</sup> BTU (\$9.00/bbl Fuel Oil Equivalent) in the U.S. Even if coal experiences the same fractional price increases as those anticipated for crude oil, it will cost approximately \$9.00/10<sup>6</sup> BTU or \$55.00/bbl Fuel Oil Equivalent by the year 2000. This enormous price differential between coal and crude oil will provide a major incentive for the world to reduce its consumption of expensive crude and to move in the direction of producing less expensive synthetic fuels from coal.

From a utility industry viewpoint, escalating prices and restrictive legislation are increasing the difficulty associated with continuing to operate or install new oil or natural gas fired capacity. Similarly, increasing stringent environmental and safety control requirements are resulting in excessively high capital costs for both conventional coal and nuclear power plants. For these reasons, the Advanced Power Systems Division of EPRI has been working for the past eight years, to develop a variety of environmentally acceptable and cost competitive coal derived synthetic fuel options for consideration by the electric utility industry.

Synthetic coal derived fuels can be categorized into two major groups, i.e., gaseous fuels and liquids. The ways in which utility companies can use these types of synthetic fuels will vary considerably as a function of region, existing capacity mix, and duty requirements.

The most probable initial application of coal derived gaseous fuels will be in the area of retrofitting and repowering a fraction of the currently existing 225,000 MW of oil and gas fired capacity. This can be accomplished by production of "over-the-fence" intermediate-BTU gas (having a gross heating value of 250 BTU/SCF-350 BTU/SCF). Later potential applications of coal gasification technology will involve the construction of integrated grass-roots gasification-combined cycle plants for baseload power generation. Such systems have the potential to be more efficient, more environmentally acceptable and less costly than conventional coal fired steam plants.

Coal derived liquid fuels will, in most cases, be too expensive for baseload power generation. They could, however, be applied to the fueling of intermediate and peak load generation equipment if they are competitively priced with respect to crude oil derived fuels and natural gas.

This paper presents estimates of both capital and production costs for coal gasification based power systems. Also presented will be estimates of the potential selling prices of coal derived liquid fuels (produced by direct and indirect techniques) as a function of plant ownership (regulated utility company or non-regulated producer). The competitive position of these coal derived liquids with respect to equivalent crude oil derived products will be addressed.

Finally, it is important for the reader to understand two limitations to the following discussions. First, as none of the synthetic fuels technologies addressed have been operated at commercial scale, all of the cost estimates presented must

be considered to be of a preliminary nature. Also, it must be realized that the purpose of this paper is to present cost and price estimates for synthetic fuels rather than to describe or discuss the technologies being evaluated. References will be provided for those readers interested in obtaining further information concerning the various synthetic fuels technologies evaluated.

#### PROCEDURES AND SYSTEMS STUDIED

All of the capital and operating cost estimates presented (with the exception of those for shale oil) are based on detailed engineering studies conducted by Fluor Engineers and Constructors, Inc., under contract to EPRI. It is important to realize that all of the Fluor designs have been based on the assumption of mature commercial technologies, i.e., they should be representative of the fifth or sixth plant built. They in no way are intended to represent the costs of the first plants built. The first-of-a-kind commercial plants for any of the technologies described will cost substantially more than the estimates presented here. It is not uncommon, for example, for first-of-a-kind new technology systems to cost up to 40% more than the mature technology plants. For additional caveats and explanations of the estimates presented in this paper, the reader is urged to refer to the source EPRI reports.

Two types of plants will be discussed. The first type, integrated gasification-combined cycle (IGCC) power systems employing Texaco's coal gasification technology, have been assumed to represent new grass roots facilities to be owned and operated by regulated utility companies. Detailed designs and cost estimates for systems of this nature can be found in references (1) and (2). The second type of system considered is one producing a synthetic fuel such as intermediate BTU (I-BTU) gas, direct coal derived liquids (H-Coal), indirect coal derived liquids (methanol) and shale oil. These fuel production facilities could be owned and operated by either regulated utilities or by non-regulated companies. Product production costs (for regulated utilities) or selling prices (for non-regulated owners) will be presented.

#### ECONOMIC CRITERIA

Before presenting the capital and operating cost results for the above systems, it is necessary to outline the economic criteria employed for the financial analyses. Table 1 presents the financial parameters used for the analysis of both regulated utility and non-regulated company ownership. It is important to realize that these financial criteria do not reflect the latest tax laws.



Table 1

## FINANCIAL PARAMETERS USED TO DETERMINE PRODUCT PRICES AND COSTS

	Regulated Utility Ownership	Non-Regulated Company Ownership
Plant Location	Southern Illinois	Southern Illinois <sup>(1)</sup>
Post-1980 General Inflation Rate	10%/Yr	10%/Yr
Plant Start-Up	1990	1990
Design and Construction Period	(2)	(2)
Project Book Life	30 Years	20 Years
Net Plant Salvage Value	10% of PFI <sup>(3)</sup>	10% of PFI <sup>(3)</sup>
Delivered Coal Cost in 1980\$	\$1.30/10 <sup>6</sup> BTU	\$1.30/10 <sup>6</sup> BTU
Real Coal Price Escalation	1%/Year	1%/Year
Federal Income Tax Rate	46%	46%
State Income Tax Rate	6%	6%
Investment Tax Credit	10% of PFI <sup>(3)</sup> Normalized Over Period of Commercial Operation	10% of PFI <sup>(3)</sup> Taken During the Construction Period
Common Equity	35% at 16%/Year After Tax Return	100% at 20%/Year After Tax Return
Preferred Stock	15% at 12.75%/Year Dividend	0
Debt	50% at 12.25%/Yr Interest	0

(1) Except for the shale oil plant.

(2) 4 Years for IGCC, I-BTU Gas and Shale Oil  
5 Years for Methanol and H-Coal

(3) PFI = Plant Facilities Investment

## INTEGRATED GASIFICATION-COMBINED CYCLE (IGCC) PLANTS

A block flow diagram for a Texaco-based IGCC system is shown in Figure 1. EPRI has been performing detailed engineering and economic assessments of such systems for a number of years. The basic advantages of such power systems for baseload generation is that they have the potential to be more efficient, more environmentally acceptable and lower in cost than conventional coal fired steam plants--particularly if environmental control requirements become more stringent.

Detailed cost estimates have been performed for Texaco-based IGCC power plants employing current technology (2,000<sup>0</sup>F) gas turbines and for conventional subcritical coal fired steam plants, both designed to comply with the 1979 Federal New Source Performance Standards (NSPS) shown in Table 2. Performance and cost comparisons for these two technologies are shown in Table 3 (1). It can be seen from Table 3 that Texaco-based IGCC systems are expected to be more efficient than and cost competitive with conventional, subcritical coal fired steam plants designed to comply with the 1979 NSPS.

If environmental control requirements become more stringent as time progresses, it is anticipated that the cost of producing electricity from coal fired plants will increase substantially. However, the cost of electricity produced by IGCC systems is not anticipated to change dramatically (in constant dollars) as the small cost increases due to stringent environmental requirements will probably be offset by technology advances, i.e., more efficient gas turbines and more reliable gasifiers. This situation is depicted graphically in Figure 2.

## SYNTHETIC FUEL PRODUCTION PLANTS

It has been stated earlier that synthetic liquid and gaseous fuels are needed by the electric utility industry to: a) retrofit and repower existing oil and gas fired generating capacity, and b) to provide a secure and stable source of fuel for the future that will not be subject to the instabilities created by international politics.

Technologies for synthetic fuels production (i.e., coal gasification and coal liquefaction) have been operated at large scale for a number of years, demonstrating that these technologies are viable from an engineering point of view. The key question to be faced by any corporation thinking of producing synthetic fuels is can they be profitably produced at a market price that is competitive with natural gas and petroleum derived liquids. All of the second generation coal gasification

### GASIFICATION-COMBINED-CYCLE SYSTEM

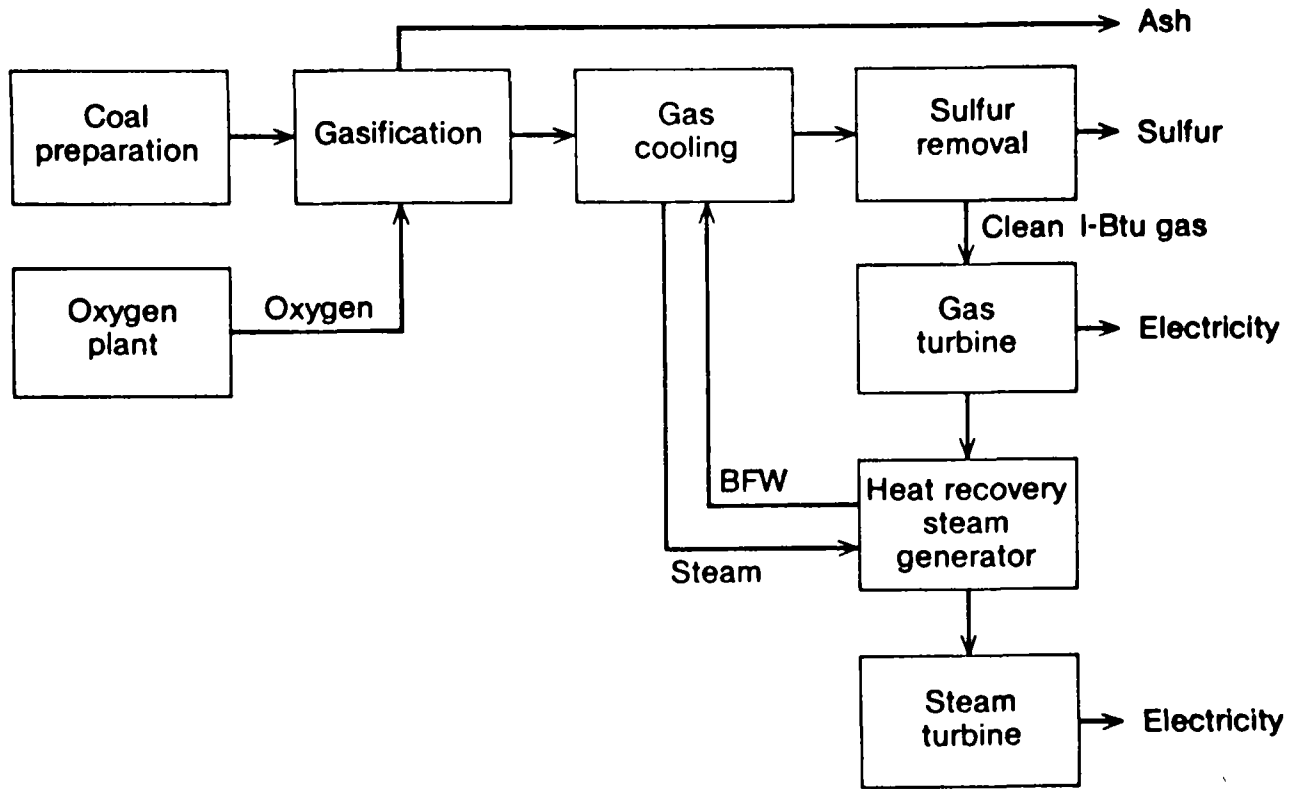


Figure 1

Table 2  
EMISSION CONTROL REQUIREMENTS

<u>Emission Being Controlled</u>	<u>1979 Federal Emission Control Requirements</u>
Sulfur	90% Removal
Particulates	0.03 lb/10 <sup>6</sup> BTU
NO <sub>x</sub>	0.6 lb/10 <sup>6</sup> BTU

Table 3

ECONOMIC COMPARISON OF TEXACO GASIFICATION-BASED  
POWER SYSTEMS WITH CONVENTIONAL COAL-FIRED STEAM PLANTS

<u>Current Technology Plants</u>	<u>1979 Federal Emission Control Requirements</u>
<u>Subcritical Coal-Fired Steam Plants</u>	
Heat Rate (BTU/kWh)	9,980.0
Capital Requirement (\$/kW) <sup>(1)</sup>	1,030.0
First Year Cost of Electricity (mills/kWh) <sup>(2)</sup>	52.6
<u>Texaco GCC Plant with 2000<sup>0</sup>F Turbine</u>	
Heat Rate (BTU/kWh)	9,400.0
Capital Requirement (\$/kW) <sup>(1)</sup>	1,010.0
First Year Cost of Electricity (mills/kWh) <sup>(2)</sup>	45.5

<sup>(1)</sup>Mid-1980 dollars.

<sup>(2)</sup>1990 cost of electricity in mid-1980 dollars based on a 70% capacity factor and high sulfur Illinois coal.

## INCENTIVES FOR GCC TECHNOLOGY

Cost of Electricity (mills/kWh)

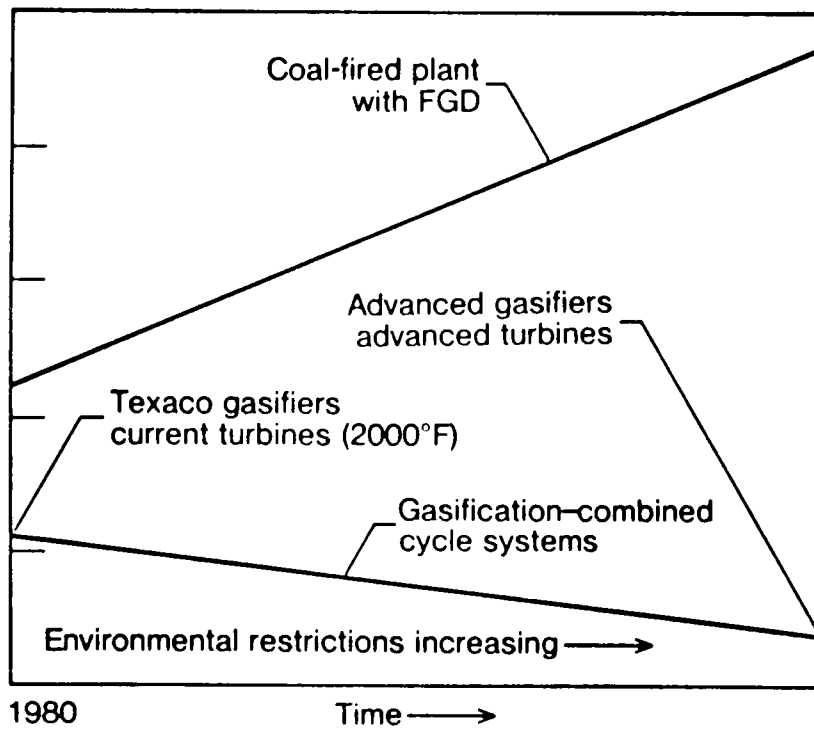


Figure 2

and liquefaction processes are being developed to reduce the cost of producing these fuels. The major problems at the moment that are preventing large scale investment in synthetic fuels plants are:

- Uncertainties concerning future availability and price of natural gas and crude oil.
- The financial risks associated with investment in the first few synthetic fuels plants.

The dilemma created by unknown future crude oil prices is shown graphically in Table 4. This table shows that by the year 2000, crude oil prices could range from \$6.00/10<sup>6</sup> BTU to \$11.00/10<sup>6</sup> BTU in constant mid-1980 dollars. At the \$6.00/10<sup>6</sup> BTU level, only some synthetic fuels will be marginally competitive with crude oil. However, at the \$11.00/10<sup>6</sup> BTU level, most of the synthetics will present extremely attractive business opportunities as will be shown shortly.

Over the years, EPRI has conducted a number of engineering and economic evaluations of coal derived synthetic fuel production facilities based on the assumption of mature, second generation technologies. Performance information and capital investment estimates for a sampling of these technologies are presented in Table 5. (The estimates for refined shale oil were not developed by EPRI.)

Product selling prices and production costs based on the performance and capital requirement estimates shown in Table 5 were developed. Table 6 presents estimated product selling prices for the various synthetic fuels assuming non-regulated company ownership and a minimum acceptable after tax return on common equity of 20%. Table 6 also presents sensitivity analyses to the base case price estimates. This table shows that I-BTU gas and shale oil represent the lowest cost synthetic fuels with coal derived liquid products being significantly more expensive.

Comparing the estimated selling prices shown in Table 6 with the potential future crude oil prices in Table 4, the synthetic fuel dilemma becomes clear. If crude oil experiences no real price growth between 1980 and 2000, thereby selling for \$6.00/10<sup>6</sup> BTU (mid-1980 dollars) in the year 2000, it appears that I-BTU gas and shale oil sold for \$5.10/10<sup>6</sup> BTU - \$6.50/10<sup>6</sup> BTU would be competitive, returning slightly more than 20% after taxes to the owners. However, under these conditions it appears that the coal derived liquids (H-Coal and methanol) would not be sufficiently profitable (if sold at \$6.00/10<sup>6</sup> BTU) to warrant the large capital investment required without some form of government support. On the other hand, if crude oil prices escalate at an annual average real rate of 3%, thereby

Table 4  
 FUTURE CRUDE OIL PRICES PRESENTED IN  
 CONSTANT MID-1980 DOLLARS

	<u>Assuming No Real Price Increase*</u>	<u>Assuming 1%/Year Real Price Increase*</u>	<u>Assuming 3%/Year Real Price Increase*</u>
Mid-1980 Price, $\$/10^6$ BTU	6.00**	--	--
Mid-1990 Price, $\$/10^6$ BTU	6.00	6.63	8.06
Mid-2000 Price, $\$/10^6$ BTU	6.00	7.32	10.84

---

\* Real price increases are those increases over and above the general inflation rate.

\*\*An average landed mid-1980 price of  $\$/10^6$  BTU has been assumed for imported crude oil.



Table 5

CAPITAL INVESTMENT ESTIMATES FOR SYNTHETIC FUELS PLANTS  
All Dollars are Mid-1980 Dollars

	Literature Reference	Production Capacity FOEB/D*	Net System Thermal Efficiency %	Capital Investment <sup>δ</sup>	
				\$/FOEB/D*	\$10 <sup>6</sup> Total
Texaco-Based I-BTU Fuel Gas (1,000 TPD Gasifiers)	(3)	27,338	64.67 <sup>#</sup>	31,003	848
Texaco-Based I-BTU Fuel Gas (2,000 TPD Gasifiers)	(3)	27,338	64.67 <sup>#</sup>	28,093	768
H-Coal	(4)	42,820	68.40	34,875	1,493
Texaco-Based Methanol	(5)	36,154	57.86	41,666	1,506
Refined Shale Oil	(6)	50,000	--	35,258	1,763

\*Barrels of distillate fuel oil per day ( $5.85 \times 10^6$  BTU/bbl) with higher heating value equivalent to above products.

<sup>δ</sup>Includes working capital, start-up costs, land and allowance for funds during construction.

<sup>#</sup>This plant also exports 79 MW of electricity. If the electricity is credited at a heat rate of 10,000 BTU/kWh, the thermal efficiency would increase to 72.4%.

Table 6

SELLING PRICE ESTIMATES FOR SYNTHETIC  
 FUELS PRODUCED BY NON-REGULATED COMPANIES  
 All Prices are 1990 Prices in Mid-1980 Dollars

	Base Case Selling Prices*	If Capital Investment Increases By 35%	If After Tax Return On Equity Is 30%	If Thermal Efficiency Decreases By 10%
	←————— \$/10 <sup>6</sup> BTU —————→			
Texaco-Based I-BTU Fuel Gas (1,000 TPD Gasifiers)	5.45	6.51	8.80	6.12
Texaco-Based I-BTU Fuel Gas (2,000 TPD Gasifiers)	5.11	6.06	8.14	5.74
H-Coal Liquids	6.59	7.79	10.65	7.33
Texaco-Based Methanol	7.87	9.30	12.72	8.75
Refined Shale Oil	5.15	6.34	9.00	5.72

\*Based on coal costing \$1.30/10<sup>6</sup> BTU (in Mid-1980), a required after tax return on equity of 20%, and an operating capacity factor of 90%.

reaching \$11.00/10<sup>6</sup> BTU (in mid-1980 dollars) by the year 2000, Table 6 shows that all of the synthetic fuels examined would look extremely attractive, having the potential to generate after tax returns on common equity in excess of 30%.

Finally, Table 7 presents production cost estimates for regulated utility ownership of synthetic fuels plants. It can be seen from this table that even if crude oil does not experience any real price growth between now and the year 2000, synthetic gaseous and liquid fuels could be produced at attractive costs by regulated utilities. There are a number of fundamental reasons why utility companies are not rushing headlong into the synthetic fuels business right now:

- As their rate of return on common equity is regulated to be no greater than approximately 16%, they feel that this marginal return does not warrant the risks associated with building the first synthetic fuels plants. This problem could possibly be alleviated if some fraction of the synthetic fuel product could be sold on the open market in competition with other energy companies resulting in a higher rate of return on common equity. This raises certain institutional barriers that must be overcome before the electric utility industry can invest large quantities of capital in first generation synthetic fuels plants.
- At the present time electric utility companies are facing severe capital raising problems. It seems unlikely that utilities, having difficulty raising the capital necessary to build new generating units, will attempt to extend their resources further to raise the vast quantities of capital necessary to build synthetic fuels plants.

## CONCLUSIONS

The following major conclusions result from the information presented in this paper:

- Texaco-based IGCC power plants offer the potential for being more efficient than and cost competitive with conventional coal fired steam plants designed to comply with 1979 Federal New Source Performance Standards (NSPS). For environmental control requirements that are more stringent than the 1979 NSPS, IGCC systems appear to represent an extremely attractive option for baseload power generation.
- The economic potential for coal derived synthetic fuels produced by non-regulated companies depends to a great extent on future prices for crude oil. If crude oil prices do not experience any real price growth in the next 20 years (a highly unlikely situation), the development of a synthetic fuels industry in the U.S. will probably be slow. On the other hand, if crude oil escalates at an annual real rate of 3%, both gaseous and liquid synthetic fuels plants could be extremely profitable by 1990.

Table 7

PRODUCTION COST ESTIMATES FOR SYNTHETIC  
 FUELS PRODUCED BY REGULATED UTILITIES  
 All Costs are in Constant Mid-1980 Dollars

	Base Case Costs*		If Capital Investment Increases by 35%		If Operating Capacity Factor Is 70%	
	First Year	Constant 1980 Dollar Levelized <sup>#</sup>	First Year	Constant 1980 Dollar Levelized <sup>#</sup>	First Year	Constant 1980 Dollar Levelized <sup>#</sup>
Texaco-Based I-BTU Fuel Gas (1,000 TPD Gasifiers)	4.83	3.65	5.72	4.06	5.74	4.16
Texaco-Based I-BTU Fuel Gas (2,000 TPD Gasifiers)	4.53	3.48	5.34	3.86	5.36	3.94
H-Coal Liquids	5.82	4.44	--	--	--	--
Texaco-Based Methanol	6.94	5.35	--	--	--	--

\*Based on coal costing \$1.30/10<sup>6</sup> BTU and an operating capacity factor of 90%.

<sup>#</sup>A levelized cost is one which if held constant will yield the same return on common equity as the varying year-by-year values.

- Regulated utility production of synthetic fuels--particularly I-BTU gas--represents a mechanism for utilities to limit their fuel costs at an attractive level while providing a secure source of fuel. Hindrances to this development are the relatively low rates of return allowed, the capital raising problems currently being faced by utilities and finally, the institutional problems faced by utilities planning to sell fuels on the open market.

## REFERENCES

1. R. F. Beckman, et al. Economic Evaluations of Energy Recovery Options for Oxygen- and Enriched Air-Blown Texaco GCC Power Plants. EPRI Report No. AP-1624, November, 1980.
2. M. J. Gluckman and B. M. Louks. Second-Generation Gasification Combined Cycle Power Plants for U.S. Utilities--Detailed Performance and Cost Estimates. EPRI Advanced Power Systems Division Staff Report, April, 1981.
3. Fluor Engineers & Constructors, Inc. An Economic Evaluation of Texaco Coal Gasification for Intermediate-BTU Fuel Gas Production. EPRI Research Project No. RP-239, Task 18. To be Published.
4. P. A. Buckingham, et al. Engineering Evaluation of Conceptual Coal Conversion Plant Using the H-Coal Liquefaction Process. EPRI Report No. AF-1297, December, 1979.
5. P. A. Buckingham, et al. Coal-To-Methanol--An Engineering Evaluation of Texaco Gasification and ICI Methanol Synthesis Route. EPRI Report No. AP-1962, August, 1981.
6. E. N. Cart, Jr., et al. Exxon Research and Engineering Company. Alternative Energy Sources for Non-Highway Transportation. Prepared for U.S. Department of Energy, Contract No. DE-AC05-77CS05438, DOE/CS/05438-T1. June, 1980.

Session II

**ALTERNATIVE FUELS COMBUSTION**

EPRI PAPER ABSTRACT

A LOW EMISSION PREMIX TWIN REVERSAL GAS TURBINE COMBUSTOR

CO-AUTHORS:                   D. MCKNIGHT  
                                  R. J. TAYLOR

The combined impact of energy conservation and air pollution control has led to the use of high pressure ratio fuel efficient gas turbines capable of burning a wide range of fossil fuels. High pressure operation, fuel tolerance and clean exhaust requirements have placed more stringent conditions on conventional gas turbine combustion systems and has promoted a requirement for innovative response.

This paper describes a combustion system which has been successfully used in a range of sizes for lightweight gas turbines, the principle features involving a novel aerodynamic fuel injection system combined with a vortex controlled twin reversal primary zone. The resultant performance has shown a significant improvement in exhaust emission levels whilst maintaining a wide degree of fuel tolerance.

Whilst it is admitted that this system does not provide a complete solution to low emission fuel tolerance targets than some of the more sophisticated concepts being developed, it does represent a major step forward in offering a viable, cost effective design with full production engine commitment.

ACKNOWLEDGMENTS

The authors wish to thank Rolls-Royce Limited for permission to publish the paper, and gratefully acknowledges the assistance of their colleagues in preparation of the data.



## ILLUSTRATIONS

<u>Figure</u>	<u>Page</u>
2.1 'Cuff' Combustor	2-4
3.1 Schematic of Conventional and RAB Combustors	2-7
3.2 RAB Combustor (RB244 Production)	2-9
3.3 RB244 RAB and Aero Smoke Emission	2-10
3.4 RB244 Combustion Efficiency	2-11
3.5 RB244 NO <sub>x</sub> Levels (Marine)	2-12
3.6 NO <sub>x</sub> Emissions Rolls-Royce Industrial Engines	2-13
4.1 10" dia. Olympus RAB Combustor	2-14
5.1 NO <sub>x</sub> Model Industrial RB244 Rapid Quench Combustor	2-18
5.2 NO <sub>x</sub> Model RAB Marine/RAB/Rapid Quench Combustor	2-18
6.1 10" dia. Olympus RAB Combustor Prior to Test	2-22
7.1 Dual Fuel RAB Combustor	2-23

## TABLES

6-1 Comparison of Diesel No.2 Oil with Residual Fuel Oil/ Surrogate C.D.L.	2-20
---	------

## SECTION 1

### INTRODUCTION

An increasing need for energy conservation has led to the development of more efficient industrial gas turbines capable of operation on a wide range of fuels. Higher cycle pressures and the influence of Clean Air Acts to reduce exhaust pollution levels have combined to place more stringent demands on conventional combustion systems.

The original combustion system designed for the RB244 lightweight gas turbine performed satisfactorily when operating on natural gas. When fired with diesel No.2 fuel, however, the same combustor gave unacceptable smoke emission levels at all power conditions. Previous experience with lower pressure ratio engines had shown that improved smoke emissions were obtainable by adjustment to 'lean burn' primary zone stoichiometry levels. These modified but conventional combustors, however, suffered from limitations of impaired weak stability and high idling exhaust emission. A solution was sought which was capable of retrofit, and avoided mechanical complexity and an innovative approach has produced a combustor employing novel primary zone aerodynamics and fuel premix methods, which has reduced exhaust emissions.

Work on a prototype aero version of a premix twin reversal combustor (RAB), was extended to cover the industrial/marine application for the RB244/SM1A marine project. The project, now jointly ordered by the Royal Navy and the Japanese Defence Agency, has reached the final development stages to a point of production hardware release. Subsequent development programmes have revealed additional emission advantages, principally in the area of  $\text{NO}_x$  emissions and has demonstrated improved tolerance to a wide range of fuel types.

## SECTION 2

### 'CUFF' COMBUSTOR

The exhaust smoke emission characteristics of diesel No.2 can be separated into two distinct categories; black smoke, which occurs at power conditions and is produced by fuel rich burning; white vaporous smoke which arises from unburnt hydrocarbons and is symptomatic of low combustion efficiency weak burning at the idling condition. Effective treatment of these characteristics has been obtained by modifications to a conventional swirler/flare primary zone. This was achieved by improved primary zone mixing by the addition of a swirler extension tube or 'cuff' (Fig. 2.1).

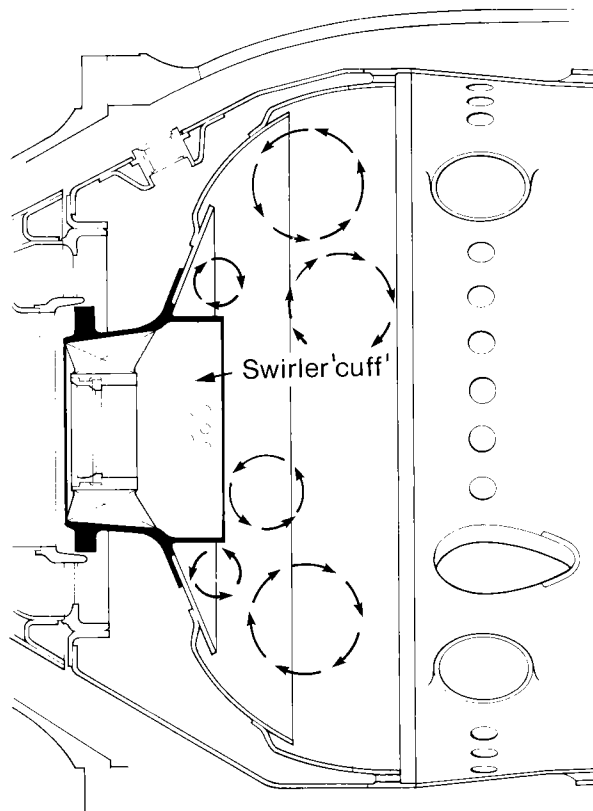


Figure 2.1 'Cuff' Combustor  
Source: Rolls-Royce Limited

The device has been successfully used on the Olympus 10" dia. combustor and a 12% point improvement in combustion efficiency was achieved. This same system has also successfully demonstrated engine operation on a residual fuel (220 Redwood secs. 8% Conradson Carbon). Combustion performance improvements were wholly related to the enhanced mixing characteristics obtained from a pattern of vortices promoted by the swirler extension 'cuff' as shown in the diagram. Although the modified combustor dealt adequately with carbon deposits, which were a feature of the unmodified combustor when operated on heavy fuel, smoke emission with heavy fuel was unacceptably high and subsequent rig trials showed that a modified "air assist" fuel nozzle was necessary to achieve satisfactory smoke levels. The fuel nozzle, however, suffered from weak stability problems and was replaced by a standard dual fuel nozzle for engine trials.

From this work it was realised that further improvements in emission performance could be expected from improved primary zone mixing if combined with re-organised and better ordered vortex patterns. The RAB combustor development fulfilled this requirement and further work on the 'cuff' was temporarily curtailed when the full potential and emission advantages of the RAB twin reversal development were realised. The 'cuff' system, however, though considered a less sophisticated version of a vortex controlled combustor, was seen to have potential, with further development, for other applications and was adopted in the role of "best available conventional technology", as a successful candidate design in recent USA RALFE I programme. In this exercise target values of  $\text{NO}_x$  were achieved and the design (5" dia. combustor) was selected as one of three candidates for the USA RALFE II programme.

## SECTION 3

### TWIN REVERSAL RAB COMBUSTOR

#### 3.1 COMBUSTOR OPERATING CRITERIA

In a conventional combustor which employs a swirler/flare single vortex mechanism, effective treatment of the emission characteristics are compromised by the choice of conflicting values of stoichiometry. In an attempt to obtain optimum smoke emission performance, at the power condition, a near stoichiometric primary zone is desirable. However, when the engine is turned down to idling power, the now "over-lean" condition created in the primary zone reduces the burning efficiency and creates problems of idling unburnt emissions and weak stability. These characteristics were recognised as an undesirable feature of the swirler/flare configuration and the alternative RAB arrangement was adopted.

#### 3.2 RAB MODE OF OPERATION

Improved methods of fuel preparation and fuel/air staging, have demonstrated that effective emission control can be obtained but often at the expense of mechanical complexity. In the RAB concept a method of air-staging has been achieved by aerodynamic placement of a twin reversal vortex pair in the primary zone, arranged so that the primary reversal is fuelled from the out-flow of a "premix" fuelling tube (Fig. 3.1). The secondary reversal is arranged to be axially in tandem, and forms a "geared" pair with the primary reversal.

Fuel enters the primary toroidal vortex from the premix tube outlet annulus, it makes a circuit(s) of the primary vortex, where depending on the power condition, varying degrees of burning efficiency is achieved. The partially burned fuel/air mixture is released and migrates to the secondary vortex, where a further stage of burning can occur. The primary zone is thus provided with an additional reaction stage which acts as a 'burn out' zone thus improving combustion efficiency, at the idling condition, and reducing the smoke producing carbon matter at the power condition.

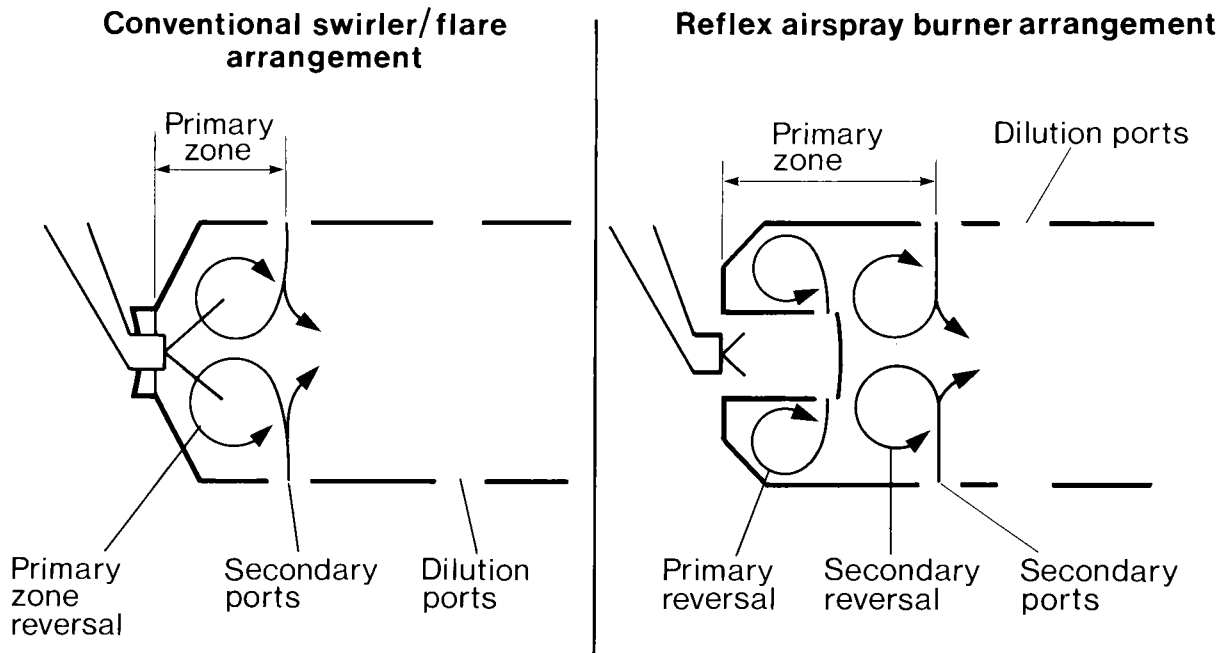


Figure 3.1 Schematic of Conventional and RAB Combustors

The premix tube operates as an air blast atomiser which provides air transportation and placement of the fuel whilst maintaining an acceptable level of atomisation quality. It is generally less sensitive to the physical changes in the fuel (viscosity, density), than a conventional swirl atomiser and is, therefore, most fuel tolerant.

The primary vortex is formed by strategic positioning of the premix tube outlet annulus, wall cooling jets and a bi-directional cooling device. This latter device controls the position of the separation point of the vortex pair. The secondary vortex position is fixed by the combined aerodynamic action of the downstream flowing section of the bi-directional cooling device and the secondary air holes which act as a zone cut-off point. The net effect is to ensure, by adjustment to air placement, that each reversal has the desired level of stoichiometry to give optimum emissions.

### 3.3 MECHANICAL BACKGROUND

The twin reversal concept has now been engineered into a final production standard for the RB244/SM1A marine application (Fig. 3.2) and has retrofit capability with the industrial combustor. The combustors are arranged in a 'cannular' array consisting of 10 inter-connected combustor liners each directly fuelled via the premix tube from a conventional pressure atomiser fuel nozzle. At the downstream end the combustor uses the production version of the industrial combustor dilution zone and turbine entry section. This arrangement has maintained outlet temperature traverse pattern factor at acceptable levels without modification.

#### 3.3.1. Fuel Nozzle

The fuel nozzle is a conventional dual orifice swirl pressure atomiser derived from the well-proven Spey aero engine. Fuel preparation quality and placement is wholly controlled by the premix fuel tube geometry (Reflex Air Spray Burner, RAB). This arrangement has the added benefit of protecting the fuel nozzle from exposure to the hostile primary zone environment, thus ensuring clean operation with all fuel types. The premix tube intake geometry also allows fitment of gas and dual fuel nozzle derivatives without modification to the RAB.

#### 3.3.2. Starting

Starting is achieved with conventional HE igniters combined with small atomisers which form an integral part of the combustor liner front mounting assembly.

#### 3.3.3. Programme Status

The production design standard has achieved all of the programme goals, viz. emissions, ignition, stability pattern factor and mechanical integrity &c. The development test programme has reached completion stage and the design is issued for production. A development set of combustors have successfully completed 1,000 hours of engine running, part of which included a 500 cyclic endurance test at power levels up to 10% above the design value.

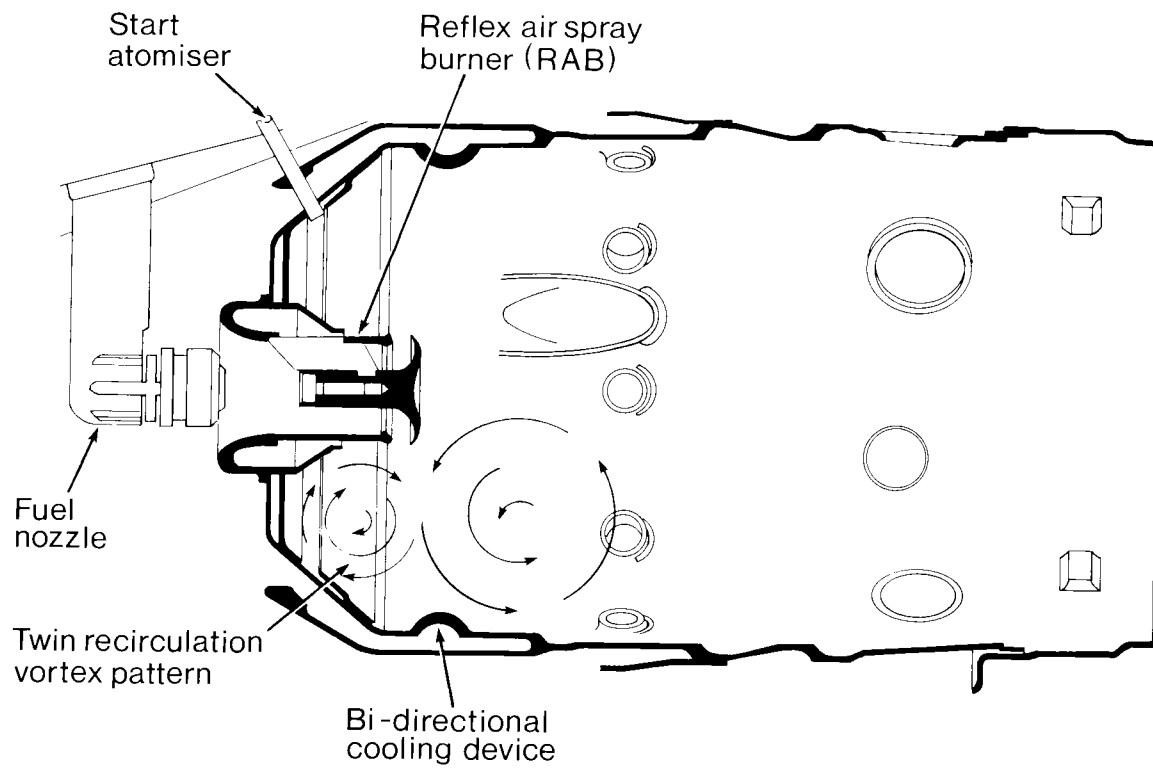


Figure 3.2 RAB Combustor  
(RB244 Production)



### 3.4 EMISSIONS

3.4.1. Black smoke emission targets when operating with diesel No.2 fuel were set at Bacharach Scale 3.5 (S.A.E. = 8). This level was determined from visual appraisal of the exhaust plume opacity and is defined as the lower limit of visual acceptability (i.e. virtually invisible). Smoke values are below target levels at 10% power and above (Fig. 3.3), and are significantly lower than the diesel fired aero combustor values.

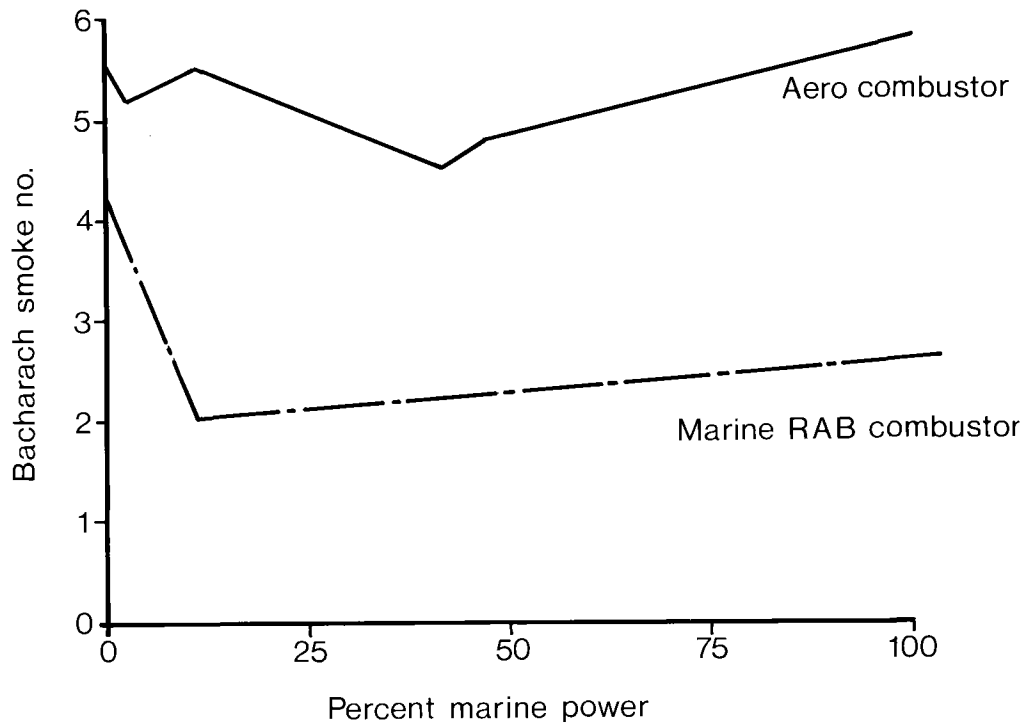


Figure 3.3 RB244 RAB and Aero Smoke Emission

3.4.2. Idling white smoke emissions are largely dictated by combustion efficiency levels and arise from sub-dewpoint precipitation of unburnt hydrocarbons in the exhaust plume when it is cooled by exposure to ambient conditions. A method which relates white smoke opacity to exhaust unburnts was used to establish minimum combustion efficiency targets of 94% at ISO conditions.

The achieved combustion efficiency levels are shown in Fig.3.4, a typical curve indicating a characteristic rapid rise approaching 100% values at 10% power levels and above. These emission achievements imply that the whole engine power spectrum is achieved with a virtually invisible exhaust.

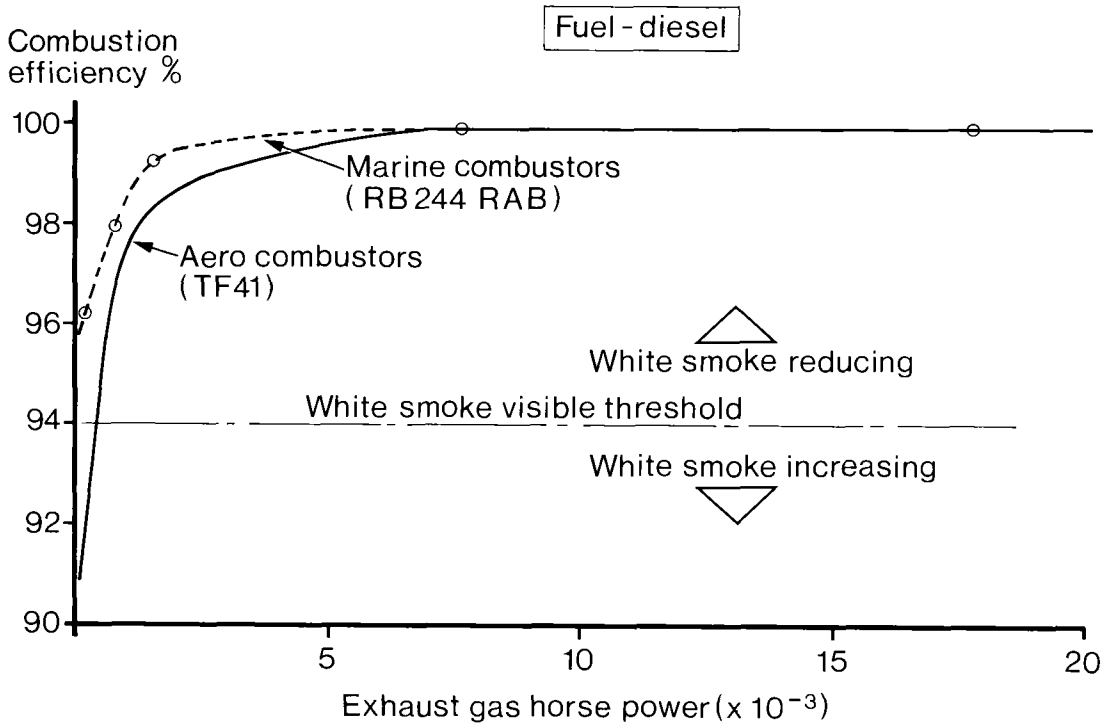


Figure 3.4 RB244  
Combustion Efficiency

### 3.4.3. NO<sub>x</sub> Levels (Marine)

The marine requirement does not specify any NO<sub>x</sub> emission targets; however, measurements made on the RB244 marine engine, showed thermal NO<sub>x</sub> reductions of 41% when compared with the industrial (original aero standard) combustor (Fig. 3.5).

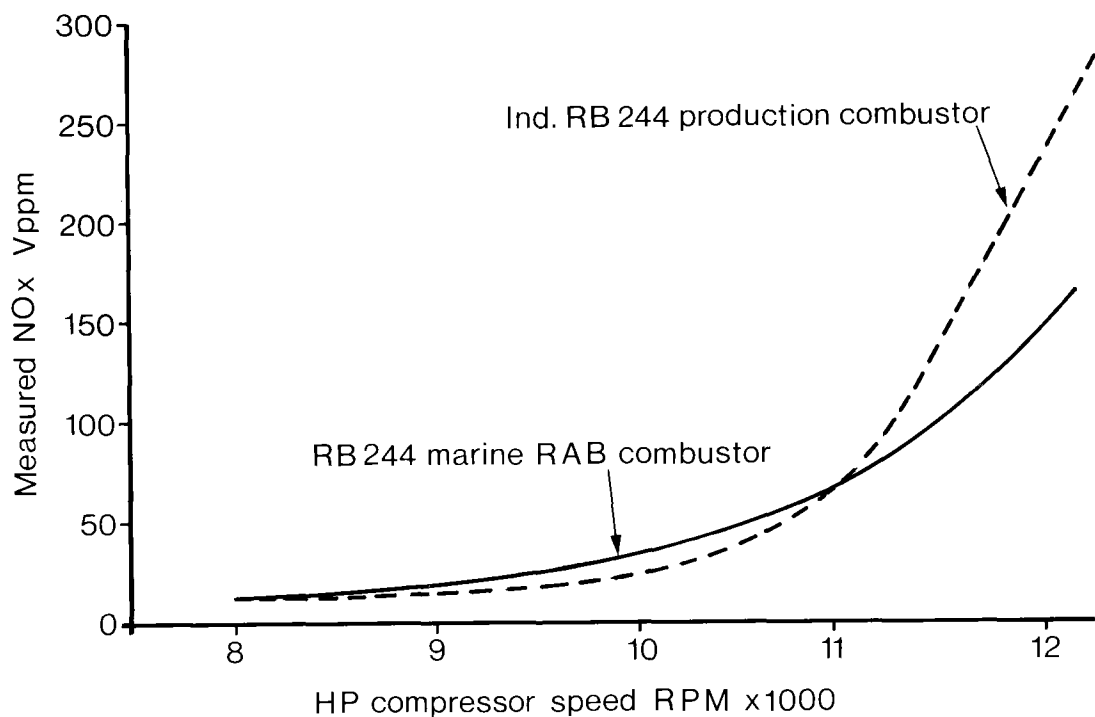


Figure 3.5 RB244 NO<sub>x</sub> Levels

### 3.5 NO<sub>x</sub> (All Engines)

Typical thermal NO<sub>x</sub> levels are shown for the complete range of Rolls-Royce Industrial engines (Fig. 3.6). The data was derived from rig and engine measured values when operating at the design power condition on diesel No.2 fuel. In general, NO<sub>x</sub> levels are much lower than typical heavy industrial gas turbines, this is thought to be attributable to shorter primary zone residence times and better mixing performance associated with aero-derived combustor technology. The RAB combustor result compares very favourably with other Rolls-Royce conventional combustion systems and is significantly lower than typical heavyweight gas turbine NO<sub>x</sub> emission levels.

Further examination of the data shows similar low NO<sub>x</sub> emission trends are present in the Avon and Olympus rig derivatives.

Also plotted is the NO<sub>x</sub> value obtained from a rig test on a surrogate nitrogen bearing fuel (FBN). This was obtained by doping a surrogate fuel with Quinoline to simulate a typical coal-derived liquid (the rig test fuel was 0.9%). The achieved NO<sub>x</sub> figure represents a 28% N<sub>2</sub>/NO<sub>x</sub> conversion and is thought to relate to the rich burning stoichiometry design of the primary reversal.

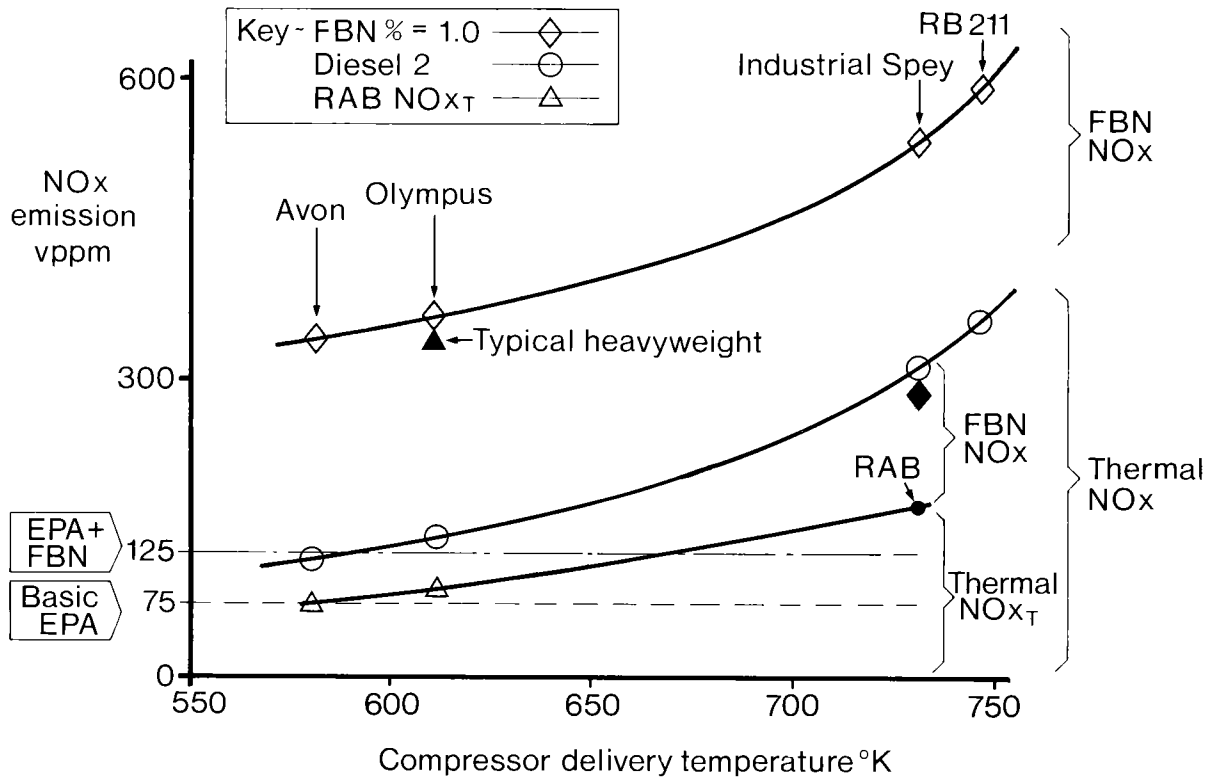


Figure 3.6 NO<sub>x</sub> Emissions  
Rolls-Royce Industrial Engines

## SECTION 4

### SCALING

It was decided to exploit the  $\text{NO}_x$  reduction potential of the 5" dia. RAB system by applying the concept to larger diameter combustors. Design rules established from the 5" dia. marine combustor programme were used to manufacture a 10" dia. version of the RAB for the Olympus engine (Fig. 4.1), a similar 9" dia. version of the Avon engine has also been rig tested. In each case, rig results gave a 25-30% reduction in thermal  $\text{NO}_x$  (Fig. 3.6).

Using correlating predictions a  $\text{NO}_x$  reduction in excess of 40% could be anticipated on an engine, thus achieving EPA Regulations.

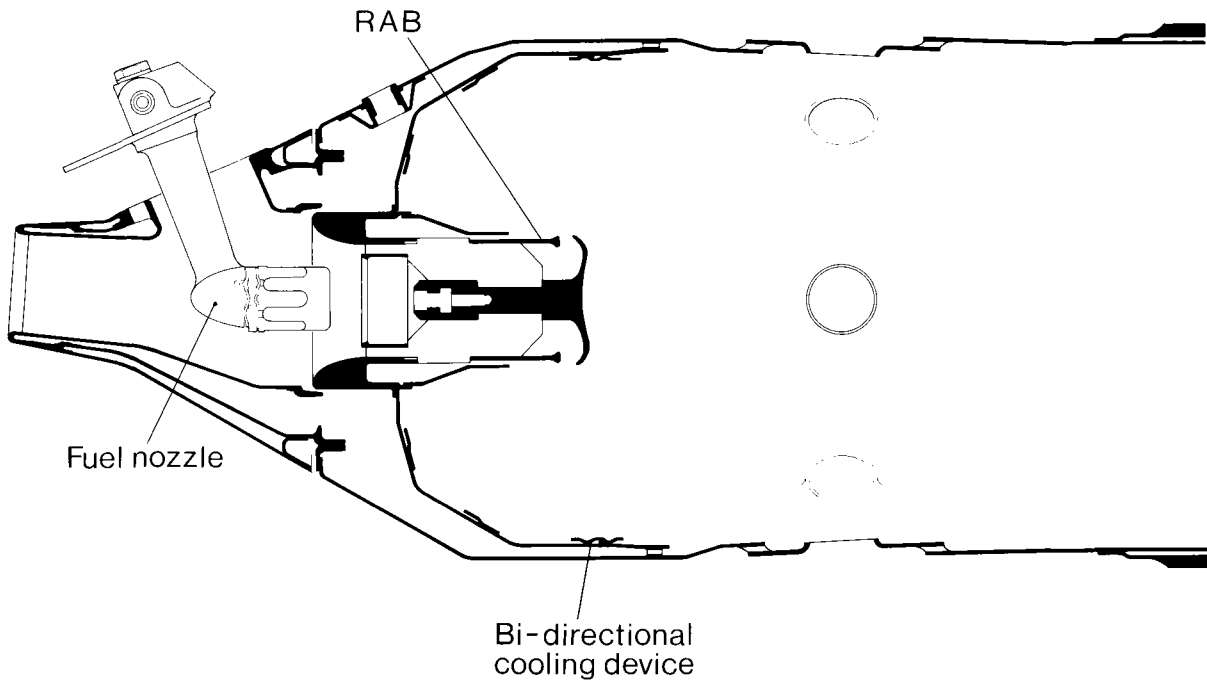


Figure 4.1 10" dia. Olympus RAB Combustor

The design factors employed in the scaling exercise were:-

- maintenance of zonal fuel/air ratios in the premix tube, primary and secondary reversals by re-arrangement of the air proportions
- optimisation of the primary zone length to ensure minimum residence time within the constraints of the combustor geometry
- retention of the relative positions of the air and fuel injection points, to ensure correct location of the primary and secondary vortices. The standard fuel nozzle was retained without modification

The modifications to a production combustor consisted of replacement of the conventional air swirler and flare assembly with the RAB premix tube and reverse flow flare cooling devices; installation of a bi-directional cooling device and re-positioning of the secondary air holes.

SECTION 5  
SIMPLISTIC NO<sub>x</sub> MODEL

A rationale of the NO<sub>x</sub> formation mechanism in the industrial and RAB combustor is hypothesised in the form of a histogram plot of temperature and combustor length (Figs. 5.1, 5.2). It is intended to be representative of the thermal NO<sub>x</sub> production parameters of residence time and temperature along the combustor gas path commencing at the most upstream plane of the primary zone and terminating at the turbine nozzle guide vane leading edge. In the model there are some recognised imperfections, these are:

- NO<sub>x</sub> production is known to be exponential with temperature, in this model it is assumed to be linear, but is considered only above a threshold point of 1900°K
- temperature rise computations assume 100% combustion efficiency at each plane, however in fuel rich areas efficiency is less than 100% and this partly compensates for the linear temperature assumptions

The model attempts to illustrate, using simple calculable parameters, the NO<sub>x</sub> formation mechanism within the production industrial and RAB combustors and shows the effect of applying rapid quench techniques to both systems. In Fig. 5.1, the Industrial Combustor, was modelled on the basis of rig NO<sub>x</sub> results obtained on propane. NO<sub>x</sub> comparisons are made with a version modified to include rapid quench holes installed immediately downstream of the secondary zone. This produced a 46% NO<sub>x</sub> reduction and correlates reasonably with the area reduction arising from subtracting the area under the curve for the rapid quench combustor (RQ) from the industrial combustor (Ind).

In similar manner, an analysis of the RAB combustor (Fig. 5.2) shows the dependence of NO<sub>x</sub> output and zone (reversal) stoichiometry e.g. the model indicates the temperature (NO<sub>x</sub>) reduction benefits arising from selection of the primary reversal stoichiometry. An engine measured NO<sub>x</sub> reduction of 40% correlates with an "area under curve" reduction of 42%.

The model is most useful in highlighting the zones in the combustor most likely to effectively respond to further NO<sub>x</sub> reduction modifications. These changes consist of adjustment to air flows to obtain optimum values of zonal fuel/air e.g a further

leaned off secondary reversal zone could produce NO<sub>x</sub> reduction benefits. These modifications can be combined with the most effective sitings of the rapid quench holes. The model suggests that a 72% reduction may be achieved by installation of a rapid quench zone located downstream of a 'leaned off' secondary reversal. If, optimistically, this was demonstrated, the modified RAB combustor would achieve NO<sub>x</sub> levels of 84 vppm and would comply with the EPA Regulation levels required of this engine operating on clean distillate fuels.



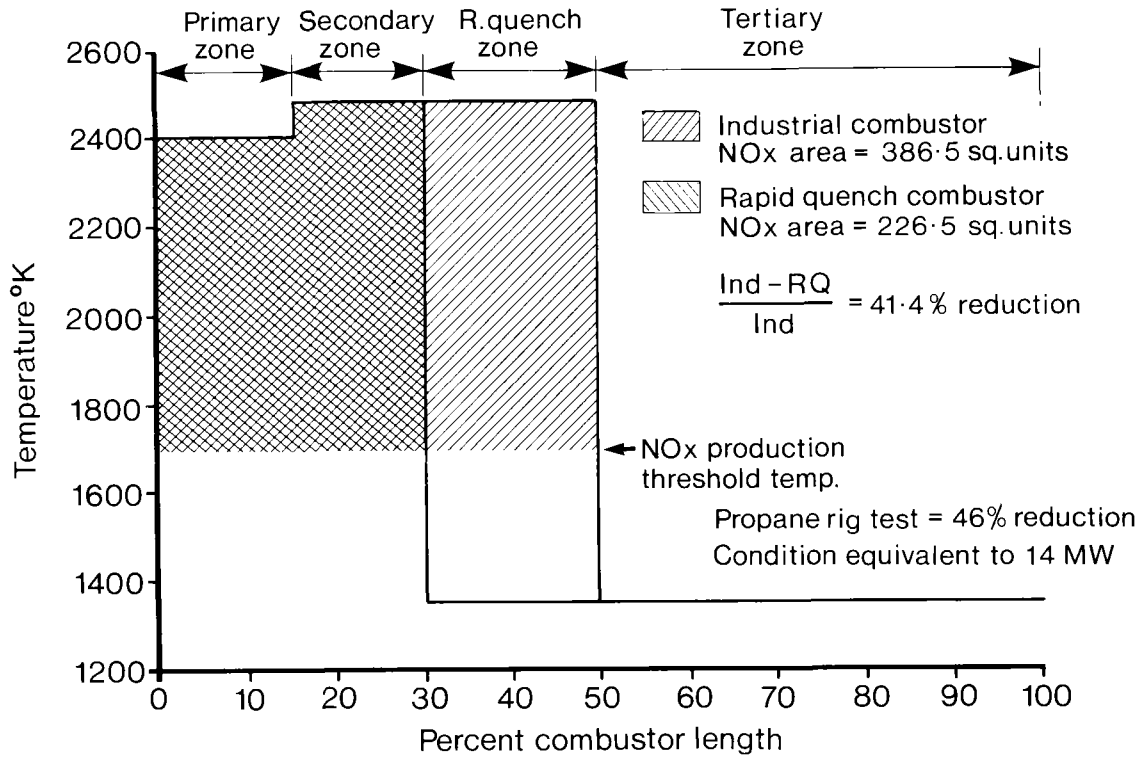


Figure 5.1 NO<sub>x</sub> Model Industrial RB244/Rapid Quench Combustor

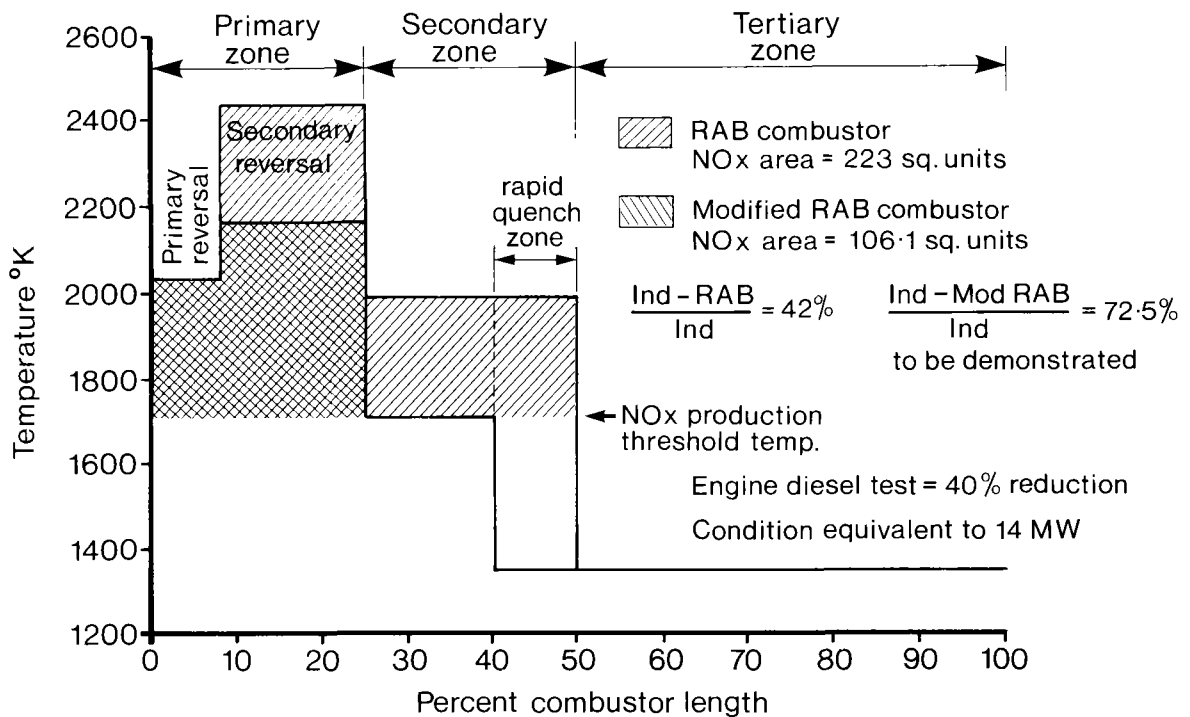


Figure 5.2 NO<sub>x</sub> Model RAB Marine/RAB Rapid Quench Combustor

## SECTION 6

### ALTERNATIVE FUELS

#### 6.1 Heavy Fuels

Rolls-Royce, through its alternative fuels programme, recognise fuel flexibility as a major design consideration for modern gas turbines. Heavy fuel burning has been rig and engine demonstrated on the 'Cuff' combustor development programme. The results showed the significance of improved fuel placement, primary zone mixing and stoichiometry in avoiding mechanical problems arising from carbon deposits. The RAB design had also indicated advantages in all of these parameters and was, therefore, considered a suitable candidate for further research into its propensity to burn heavy oil.

Heavy fuel can be characterised by comparison of the specific properties likely to influence combustion performance with similar properties in No. 2 fuel (Table 6.1): the most significant parameters being Viscosity, Conradson Carbon Value and Hydrogen Content. The test fuel was primarily chosen as being representative of a typical heavy fuel used by the Utilities and also for its on-site availability.

A photograph of the combustor before test is shown in Fig.6.1, further test evidence exists which shows the combustor cooling devices and internal surfaces virtually free of heavy carbon deposits, (photograph not shown because of reproduction difficulties). The result compares with a conventional combustor which, after a similar 1 hour period of rig running, showed heavy deposits over the air swirler, fuel nozzle and wall cooling devices. This evidence further underwrites the design advantage of protecting the fuel nozzle from exposure to the hostile combustor burning environment.

TABLE 6.1

COMPARISON OF DIESEL NO. 2 OIL WITH RESIDUAL FUEL OIL/SURROGATE CDL

## FUEL ANALYSIS

<u>PARAMETER</u>	<u>DIESEL NO. 2</u>	<u>RESIDUAL FUEL OIL</u>	<u>SURROGATE CDL</u>
Carbon Content (Conradson % wt 100% sample)	0.01	7.9	.01
Specific Gravity @ 15°C	0.85	0.95	.88
Kinematic Viscosity @ 40°C (CS)	3.0	61.8	3.0
Sodium Content (wppm)	0.2	32.0	0.2
Vanadium Content (wppm)	<1.0	50.0	<1.0
Lead Content (wppm)	Nil	Nil	Nil
Hydrogen Content (% wt)	13.5	10.76	10.5
Sulphur Content (% wt)	<1.3	2.48	3.0
Water Content (wppm)	< 50	500	< 50
Ash Content (wppm)	< 50	200	< 50
Nitrogen Content (wppm)	300	1700	8800
Calorific Value BTU/lb	18450	17679	18200

## 6.2 Fuel bound Nitrogen

Many coal-derived fuels and some heavy fuels contain appreciable amounts of chemically bound nitrogen, which converts in the primary zone burning process to  $\text{NO}_x$ . A technique of operating the primary zone rich of stoichiometric has been shown effective in reducing conversion rates. The amount of nitrogen converted into  $\text{NO}_x$  is expressed as a percentage of the  $\text{NO}_x$  which would be formed if all of the nitrogen was converted; low values are, therefore, indicative of improved  $\text{NO}_x$  conversion.

A 5" dia. RAB combustor was rig tested on a coal-derived surrogate fuel doped with Quinolene, which is a nitrogen rich aromatic hydrocarbon and contained a nitrogen level of approximately 1% (0.9% was the test measured value). Results showed that at the engine design point fuel/air value a  $\text{N}_2/\text{NO}_x$  conversion rate of 28% was achieved, (Fig. 3.6) thus indicating a significant improvement over a conventional combustor (typically  $\text{N}_2/\text{NO}_x = 60\%$ ).

In its latest form the RAB combustor can be categorised as an adaptation of a "rich burn/lean burn/ rapid quench" arrangement . Analysis of the primary reversal stoichiometry (.7 equivalence ratio) indicates that it complies with current "rich burn" concept recommended for dealing with fuel bound nitrogen. The secondary reversal equivalence ratio of 1.6 was selected as a compromise between minimum thermal  $\text{NO}_x$  and optimum 'burn out' of free carbon for smoke suppression reasons. The fuel bound nitrogen test data is, however, very limited and a full work programme will be required to examine how conversion rates vary with primary zone stoichiometry and how these characteristics interact with thermal  $\text{NO}_x$  design criteria.

## 6.3 Gaseous Fuels

An additional part of the Rolls-Royce Alternative Fuels Programme is an examination of the potential of the twin reversal combustor to operate on gaseous fuels. These are categorised under 3 headings:-

### (a) Low BTU Gases

This covers the gases in the range 100-300 BTU/ft.cu. typically produced in air-blown coal gasifiers and weak process gases associated with oil production and gas-gathering schemes &c.

(b) Medium BTU Gases

These fall in the range 300-600 BTU/ft.cu. and are produced typically from oxygen-blown coal gasifiers and oil production process gases subjected to methane stripping.

(c) High BTU Gases

These cover the range 600 BTU/ft.cu. and above and consist of natural gas and LP gases &c.

When operating the RAB system on gaseous fuel, it was assumed that the premix tube may suffer thermal distress, because of its reliance on the cooling potential of the vaporising liquid droplets. Further work, however, and an appraisal of the premix tube residence time, stoichiometry and temperature indicated that vaporisation rates are at minimal levels and would depend on achievement of fuel droplet sizes below those observed. Confirmatory natural gas rig trials using an industrial production standard gas fuel nozzle indicated no mechanical problems, and a 30% reduction in  $\text{NO}_x$  was observed.

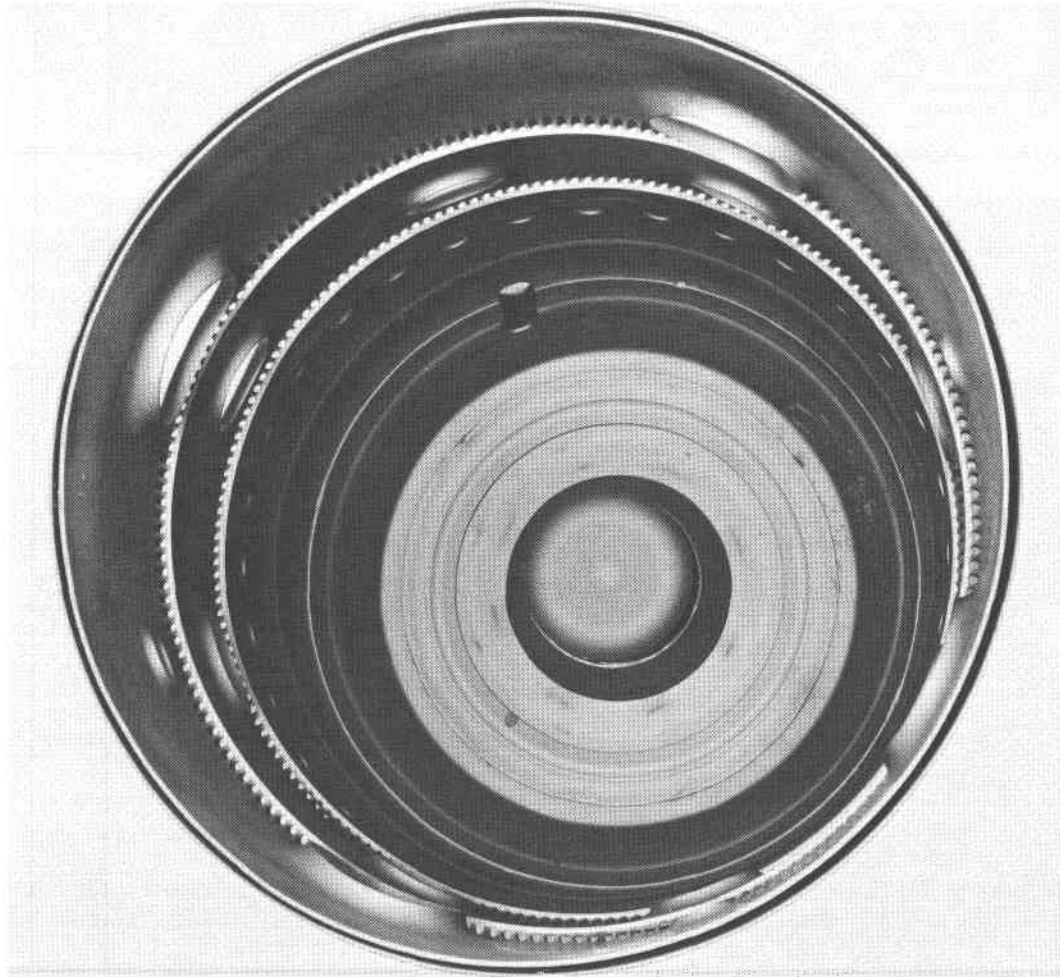


Figure 6.1 10" dia. Olympus RAB Prior to Test

SECTION 7

DUAL FUEL

Promising results from single fuel mode tests on gaseous and liquid fuels indicate that the RAB twin reversal combustor could be adapted to operate in the dual fuel mode. Major design changes affect the premix tube (Fig. 7.1), this is modified to a configuration where the liquid and gaseous fuel delivery tubes are arranged co-axially to avoid the risk of fuel 'back flow' when operating on either of the alternate fuels. The system was arranged to be self-purging to obviate the risk of carbon build-up in the fuel delivery passages at the point of fuel injection into the burning space. It is sized to accept low BTU gas (i.e. 150 BTU/ft.cu.) and has been scaled for both 5" dia. and 10" dia. combustors. Rig trials will be conducted on this system at the end of 1981 as part of the ongoing low BTU gas programme.

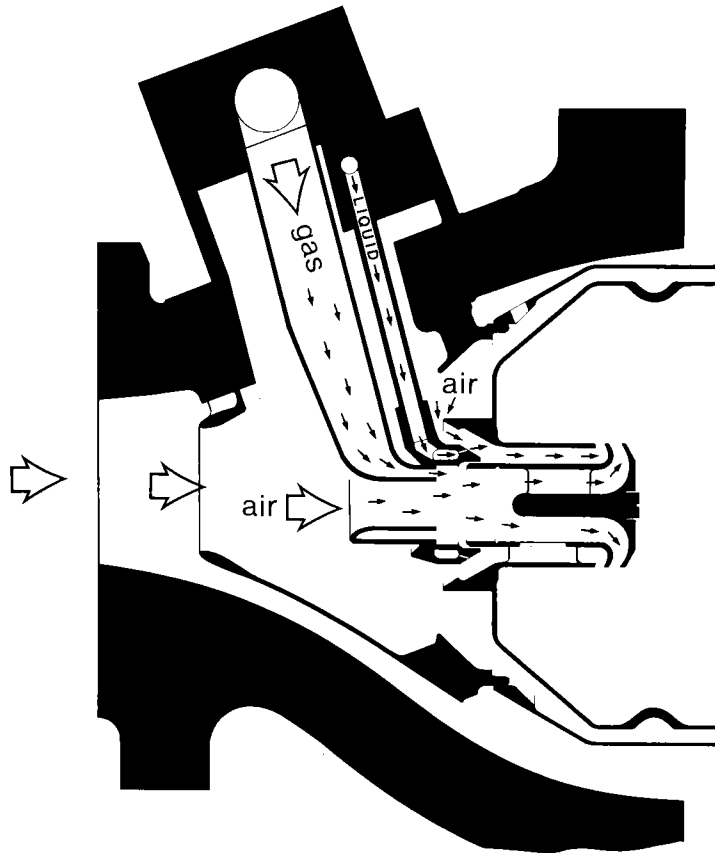


Figure 7.1 Dual Fuel RAB

## SECTION 8

### CONCLUSIONS

Experience with the twin reversal RAB combustor has indicated that significant improvement in emission performance can be obtained by control of the internal aerodynamics of the primary zone. The design has demonstrated that significant exhaust emission reductions can be obtained from the combined advantages of fuel premix and rich burn/lean burn/rapid quench technology. It has further indicated that this can be achieved with relatively simple engineering without reverting to complex variable geometry or fuel staging.

The 5" dia. twin reversal RAB has been adopted as the production hardware for the RB244 engine project which will be used in a marine application for the Royal Navy and the Japanese Defence Agency. In excess of 1,000 hours of engine development has been completed which included endurance and functional trials. The combustor system has engine demonstrated on diesel No. 2 fuel:-

- invisible smoke emissions throughout the complete engine power range
- high idling combustion efficiency levels, resulting in suppression of white vaporous smoke
- 40% reduction in high power NO<sub>x</sub> levels when compared with a conventional combustor
- acceptable levels of the standard combustor parameters, viz. pressure drop, pattern factor, stability, ignition, mechanical integrity
- design advantages of retrofit
- satisfactory operation of a standard fuel nozzle located in a clean environment isolated from the burning process

In supporting rig programmes, design rules have been established which have been successfully used to develop larger scale versions up to 10" in diameter. Rig tests have successfully demonstrated:-

- operation on natural gas with reduced NO<sub>x</sub> levels

- operation with heavy fuel on a 10" dia. scale version
- significantly reduced NO<sub>x</sub> conversion when operating on fuels containing 1% levels of bound nitrogen typical of coal-derived liquids
- design potential to convert to a dual fuel configuration sized to accommodate low BTU gas



## SECTION 9

### FUTURE WORK

The programmes planned for other twin reversal RAB derivatives are dependent on the acquisition of suitable funding. However, it is clear that the basic design concept has potential for adaptation to other larger scale combustor applications. Application of the RAB principle has featured in preliminary discussions with a manufacturer of heavy weight gas turbines.

Rolls-Royce have been in service for 7 years with industrial versions of the RB211 operating on natural gas. A dual fuel version of this engine has just been launched for an offshore and power generation application. This engine employs an annular combustor and great interest is being shown in the possible application of the twin reversal RAB concept to this project in anticipation of exploiting the NO<sub>x</sub> reduction advantages.

## SUMMARY

This is a status review of a gas turbine combustion programme aimed at producing a system capable of meeting the emission and life requirements of the RB244/SMLA marine gas turbine project. The engine and module, which was developed with MoD (PE) resources, has reached a stage of full production commitment for the Royal Navy and Japanese Defence Agency, and is based on a marine derivative of the Spey aero-engine.

The paper describes a combustor concept which uses 'novel' aerodynamic techniques to control fuel injection, primary zone mixing and stoichiometry levels. The resulting premix twin reversal RAB combustor which emerges is shown to have significant improvements in visible exhaust emission along with reduced NO<sub>x</sub> emission.

Further privately sponsored rig programmes are described which have objectives of exploiting the low NO<sub>x</sub> potential of the concept and exploring fuel tolerance advantages. Design rules established from the rig programme have been used to produce larger scale versions for other production industrial gas generators. A 5" dia. version has rig demonstrated improved emission levels with gaseous fuels, and fuels containing chemically bound nitrogen. Advantages of reduced levels of combustor carbon deposits and a clean fuel nozzle have been demonstrated with heavy fuels and dual fuel capability with low BTU gas is suggested.

A need for further research is indicated to understand the mechanisms influencing N<sub>2</sub>/NO<sub>x</sub> conversion rates with fuels containing bound nitrogen, and dual fuel operation with low BTU gas has been rig and engine demonstrated.

Research work so far has been confined to cannular systems but it is believed that the emission improvement potential could be read across to annular combustion systems. The rate of application of the RAB principle will be dictated by the commercial necessity to comply with future emission legislation.

ON FUEL ECONOMY AND THE USE OF ALTERNATIVE FUELS  
IN MEDIUM- AND SLOW-SPEED DIESEL ENGINES

A. Sarsten, G. Fiskaa, H. Valland  
Division of Combustion Engines and Marine Engineering  
The Norwegian Institute of Technology

INTRODUCTION

The increasing fuel oil prices and the prospect of deteriorating heavy fuel quality for shipboard use are problems of some importance in Norway. This country has traditionally had a relatively large, diesel-engined merchant marine engaged in foreign trade, the earnings of which still contributes significantly to the national economy.

This fact has led our country to emphasize research into the possible effects of future fuels on marine diesel engines, and the increase in energy bill has led to research into diesel engine fuel economy and a ship's energy economy in general. The objective of this paper is to present some aspects of this research as regards medium and slow speed diesel engines, and which was carried out at the Marine Technology Center (MTS) at Trondheim. This is a common facility shared by the Norwegian Institute of Technology (NTH), and by the Ship Research Institute of Norway (NSFI).

HEAVY FUEL RESEARCH

Research into use of current heavy fuels for diesel engines has been going on for some time. It has been shown that the quality of such fuels delivered world-wide will differ considerably from port to port, and it appears that operational problems, both for the pretreatment plant and engines on board, and due to fuel quality, are reported in increasing numbers.

Since 1975 this research has been coordinated in three sequential programs with participants both from the Trondheim milieu (NTH, NSFI), Det norske Veritas and the Central Institute (both of Oslo). Experimental activities have to a large extent been carried out in Trondheim laboratories of MTS by the Division of Combustion Engines and Marine Engineering. Here the use has been made of an extensively instrumented single-cylinder, two-stroke medium speed engine (Wichmann 1AX, bore 300 mm, stroke 450 mm 375 rpm). Lately we have included various rigs for detailed

studies of problems related to injection equipment and combustion (refer to next section).

Table I gives a survey of some typical heavy fuel qualities tested either at MTS, or on large-bore diesel engines (testbeds or shipboard).

Table 1  
HEAVY FUEL ANALYSIS DATA

Fuel no: →	1	2	3	4	5	8	9	10	11	12	
Spec. weight	.990	.953	.992	.953	.962	.97	.973	.977	0.966	1.108	
Viscosity (Cst)	357	298	685	401	197	242	216	180	122	306	
Water (weight %)	0.05	0	0	0.05	0.10	0.2	0	0	0.15	trace	
CCR	"	17.3	8.9	18.3	8.9	10.1	13.	17.5	16.8	14.2	10.1
Ash	"	0.04	0.02	0.04	0.02	0.04	.04	.05	.04	0.04	0.06
Asphaltenes	"	8.1	3.4	8.1	3.2	4.1	6.0	11.8	7.1	7.0	
Sulphur	"	2.95	2.61	3.07	2.42	2.36	-	2.94	3.26	2.21	3.91
SHF	"	0.02	0.01	0.02	0.01	0.02	0.0	0.05	.04	0.01	
Sodium (ppm)	3.6	2.8	3.6	2.0	38	-	34	9	15		
Vandium	"	69	42	75	42	30	-	96	53	72	
Silicon	"	2	2	2	1	4	-	0	23	5	

- Test fuel 1. Visbroken residue, blended with "cycle oil" from FC-cracker to a viscosity of app. 380 Cst at 50°C.
- Test fuel 2. Straight-run residue, blended with gasoil to a viscosity of app. 380 Cst at 50°C.
- Test fuel 3. Visbroken residue.
- Test fuel 4. Straight run residue.
- Test fuel 5. Problem fuel delivered from ship.
- Test fuel 8. Wärtsilä test fuel Por -230.
- Test fuel 9. Wärtsilä test fuel -Special (delivered from an oil company).
- Test fuel 10. Durban fuel delivered from sailing ship.
- Test fuel 11. Canada fuel delivered from sailing ship.
- Test fuel 12. Clarified slurry oil.

In addition to the above chemical analysis, three different chromatographic methods (GC, GPC, and HPLC) have been employed on some fuels. During the testing conventional Marine Diesel Oil has been used as reference fuel, and tests largely per-

formed as sandwich tests.

To attempt to find correlation between fuel data and combustion behavior, a variety of sensors are installed in the engine. For short-term combustion tests (3-4 hours duration), these include:

- Cylinder and injection pressure analysis
- Dynamic surface temperatures in combustion chamber
- Radiation from combustion at different locations
- Exhaust gas composition

In addition, longer tests (100 h) have been carried out in order to assess long-term effects (deposits, wear rates, etc.).

Based on the results from short-term combustion tests it can be stated that, generally, there are only small and insignificant deviations in the parameters measured for combustion characterization. This is the case when comparing the different heavy fuels, but also when comparing heavy fuels with marine diesel oil (MDO). Figure 1 gives a survey of some results obtained through an analysis of cylinder pressure. At part load the differences in combustion quality may appear as significant deviations in the parameters measured.

However, the combustion process, even at rated engine load, has to be different in one way or another since long-term tests with some of the test fuels show very different results. This indicates that parameters other than those chosen initially may be better suited for detection of combustion anomalies.

Test fuel 5 has been included in combustion tests on two different engines. In the smaller medium speed engine the fuel does not show combustion characteristics different from other heavy fuels or MDO. However, a 100 hour test supports the observations from the ship from which this fuel has been lifted. Very hard deposits were found on piston top land and in the piston ring zone, and the two uppermost piston rings were heavily worn. The wear of the top piston ring being as much as 1 mm during a 100 hour test and the wear of the second ring being only slightly less.

The same fuel, when tested in a larger slow-speed two-stroke engine showed, however, combustion characteristics somewhat different from the other heavy fuels and MDO tested, namely a later and slower combustion compared with the other fuels. Also

# DEVIATIONS IN CYLINDER PRESSURE DATA FROM MARINE DIESEL OIL (MDO)

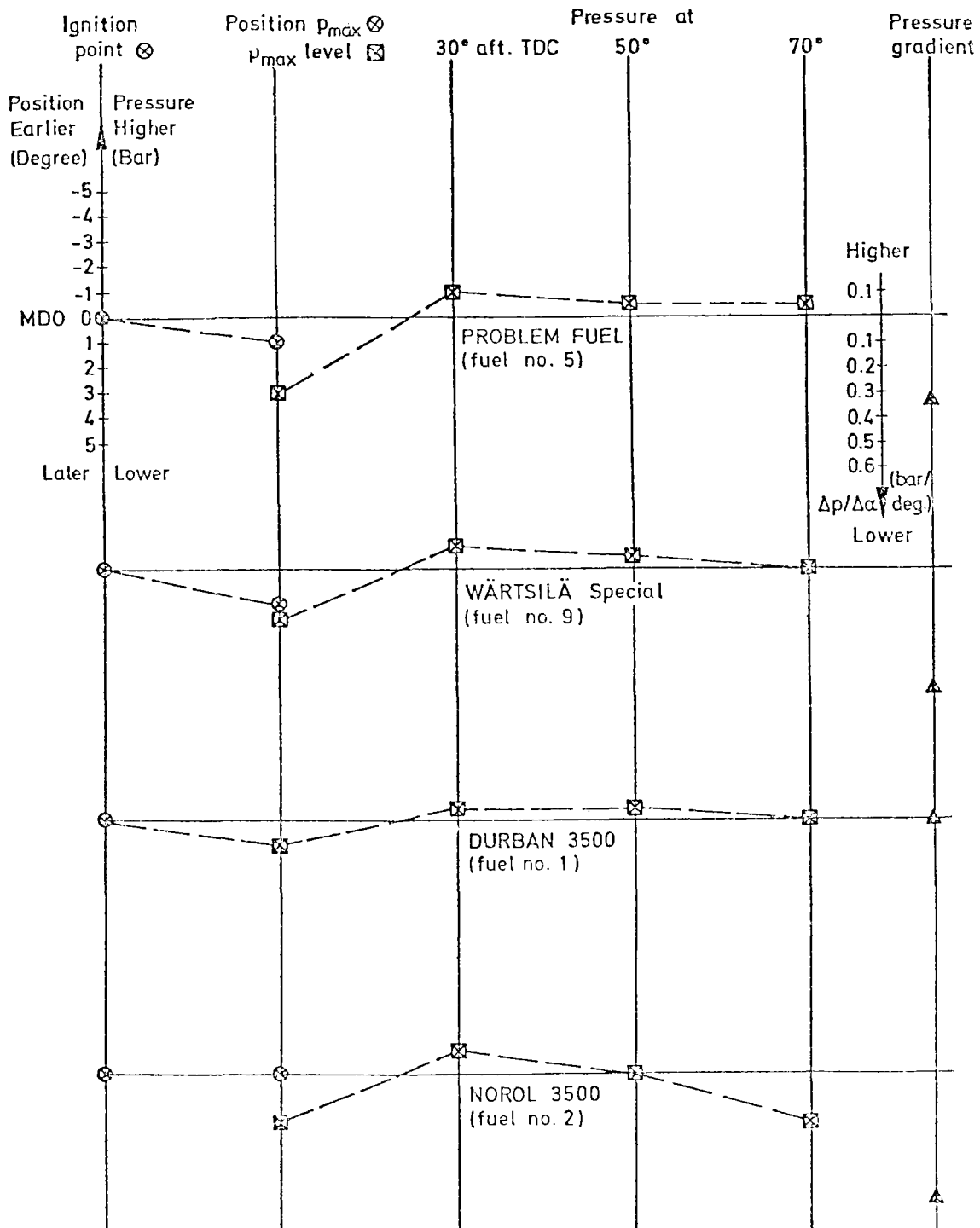


Figure 1.

the measurements of visible light showed longer burning time for test fuel 5 with strong indications of afterburning.

The test results with this "problem" fuel clearly show that the combustion characteristics obtained on one type of engine may not be the same of a different engine, even though the end result is the same (wear and heavy fouling). This means that the chosen measured parameters cannot be used for prediction of fuel behavior as far as long term effects are concerned.

Test fuel 9 has been run on two- and four-stroke medium speed engines, while long-term tests did not indicate operational problems. Thus two heavy fuels showing no significant deviation from other heavy fuels and MDO as regards registered combustion characteristics (except when burned in a large crosshead engine) have in these tests given different results as far as long term effects are concerned. This despite the extensive instrumentation of combustion process and computer evaluation employed for evaluation of thermodynamic events.

Conventional analytical fuel data (table I) does not always give a fair idea of the combustion qualities, at least at full load. On the other hand it seems that the gas chromatography profiles may be a more significant parameter when it comes to combustion properties and long term effects from the combustion of a fuel, according to the analysis work done at the Central Institute.

Data on fuel and operational problems have been collected from ships in service by Det norske Veritas who have performed a correlation analysis. This indicates some relevance between high CCR and asphaltene content and specific problems. However, conversely we have indications that operation on some heavy fuels with high CCR values can be accomplished without problems. A fuel analysis and problem data collection scheme on a much larger scale is now operated by DnV. It is hoped that this will give a good basis for valid conclusions.

Combustion tests on different heavy fuels will continue, with a slant towards direct investigation of combustion and more emphasis on various pretreatment methods for different heavy fuels. (1), (2).

## SYNTHETIC FUELS

Looking over the horizon, it appears that alternative fuels of some sort may become an alternative or supplement to increasingly expensive and poorer quality marine fuels. In cooperation with DoE in Washington, the research group at MTS have received for testing quantities of the following fuels:

- A. SRC II; blend of middle and heavy distillate (2,9:1)
- B. SRC II; middle distillate
- C. Shale derived diesel fuel

At the present moment fuel types A and C have been included in short-term tests on the laboratory engine and the following tests have been performed:

- Mixture of SRC II and Marine Diesel Oil (MDO) to determine the necessary amount of distillate mixed into this fuel to obtain satisfactory ignition and combustion at full load.
- Tests of combustion on the chosen mixture at part load.
- Study of the influence of preheating the mixture.
- Combustion tests of Shale Oil at different engine loads.

### SRC II Fuel Results (3)

For the SRC II fuel the following observations were made:

- The medium speed two-stroke diesel engine will run with acceptable combustion on a mixture of 75 % SRC II and 25 % MDO, on full and overload conditions. Figure 2 shows the changes in ignition delay when varying the contents of MDO in the fuel mixture. An injection delay in the magnitude of 2-2.5 msec. is acceptable, i.e. gives acceptable knocking level.
- A reduction of the engine load below 80 % of full load will necessitate an increased amount of MDO to be added. Low load and idle will not be possible unless a substantial amount of MDO is used in the mixture. Such tests have not been performed, but it may be estimated that necessary amount of MDO will lie in the order of 50 % to 60 %.
- Cold starting of the engine even with such large amounts of MDO may be difficult. No such tests have, however, been made so far.
- An increase in the fuel temperature prior to the injection has no influence on the fuel's ignition qualities. A slight reduction in the cylinder pressure is observed and the combustion seems to become slightly more stable.
- After having ignited there seems to be only insignificant differences in the combustion pattern of the synthetic fuel as compared to MDO.



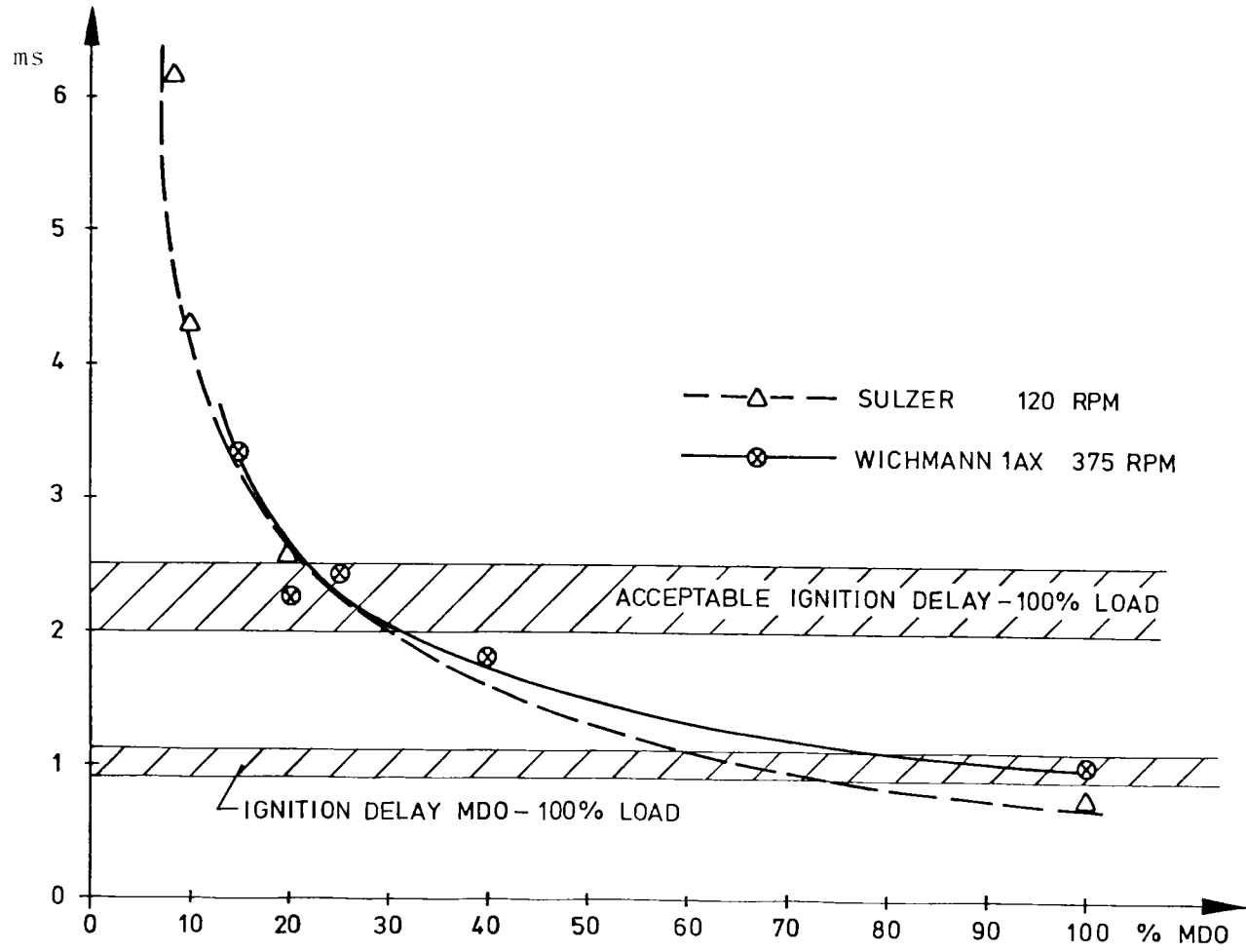


Figure 2.

- The handling of the fuel necessitates certain precautions, and further tests will have to include a separate and well ventilated fuel pretreatment room. Even so one will have to take measures to prevent leakages and spill of fuel, and try to keep the complete fuel system as leakproof as possible.
- It is hard to imagine how such fuel could be introduced in today's marine engine environment, and it is expected that a complete redesign of the fuel pretreatment and transporting system on board will be necessary before this type of fuel can be accepted.
- The odors are both obnoxious and ill effects have been claimed by operating personnel (headaches, etc.). We feel doubtful that the fumes would be tolerated by today's environmental standards unless kept to a very low level by special measures.

#### Shale Oil Results (4)

Our tests with Shale Oil are in progress, but the following preliminary conclusions seem valid:

- The medium-speed engine (at least our two-stroke version) will run satisfactorily on Shale Oil. No significant rearrangements and/or adjustment of the engine appear necessary when changing from MDO to Shale Oil.
- No differences of significant nature were found in the combustion process as compared to MDO (based on analysis of the cylinder pressure trace). A slight reduction of injection pressure was observed. This may lead to slightly different spray patterns and minor, local differences in the combustion. Such derivations appear to exist, but have no marked influence on the engine overall performance. Figure 3 shows some results achieved through an analysis of cylinder pressure.
- Conventional engine operating data (exhaust gas temperatures, turbo-charger performance etc.) do not change when shifting over to Shale Oil.

No long-term tests have been carried out on either fuel quality. It is not possible on the basis of our short tests to indicate if these fuels might lead to unexpected operational problems in the long run, as for example heavy wear of rings and/or liner.

#### INJECTION AND COMBUSTION TEST RIGS

In order to study both the actual injection spray pattern with different fuel types as well as their ignition and combustion characteristics under various conditions, a constant volume bomb has been developed. The bomb is equipped with a variety of sensors, while large quartz glass windows enable one to study the complete spray

# SHALE OIL TEST RESULTS

## ANALYSIS OF CYLINDER PRESSURE

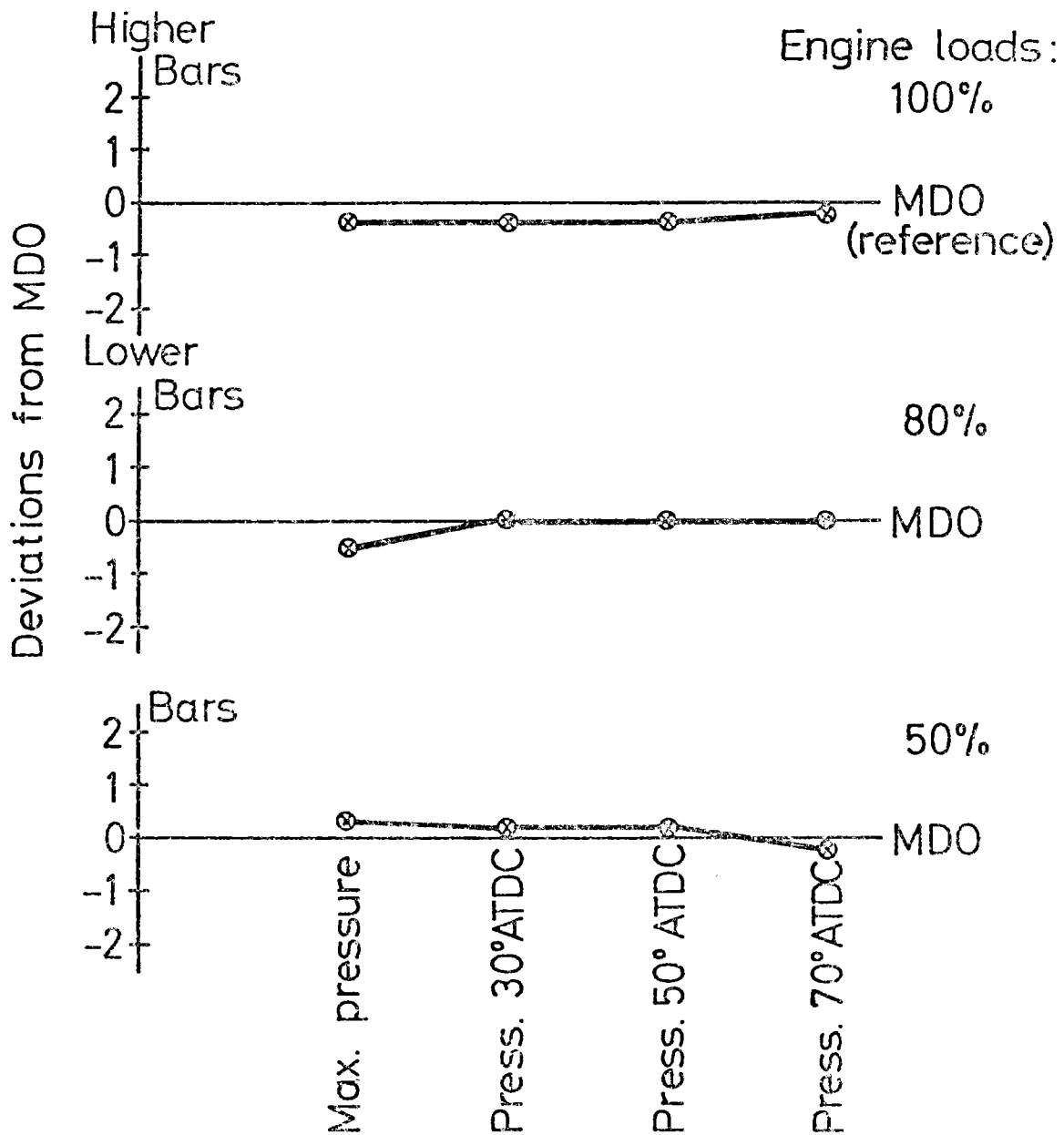


Figure 3.

development, ignition and combustion sequence. High-speed camera techniques are employed for these studies. The bomb is pressurized (max 130 bars) and internally heated (600°C) and charged with compressed air or other gases. The sensors installed include a number of newly developed radiation probes, surface thermocouples and dynamic pressure recording.

Currently the rig is being used for more detailed studies of the ignition and combustion of SRC II/MDO mixtures, under contract to DoE.

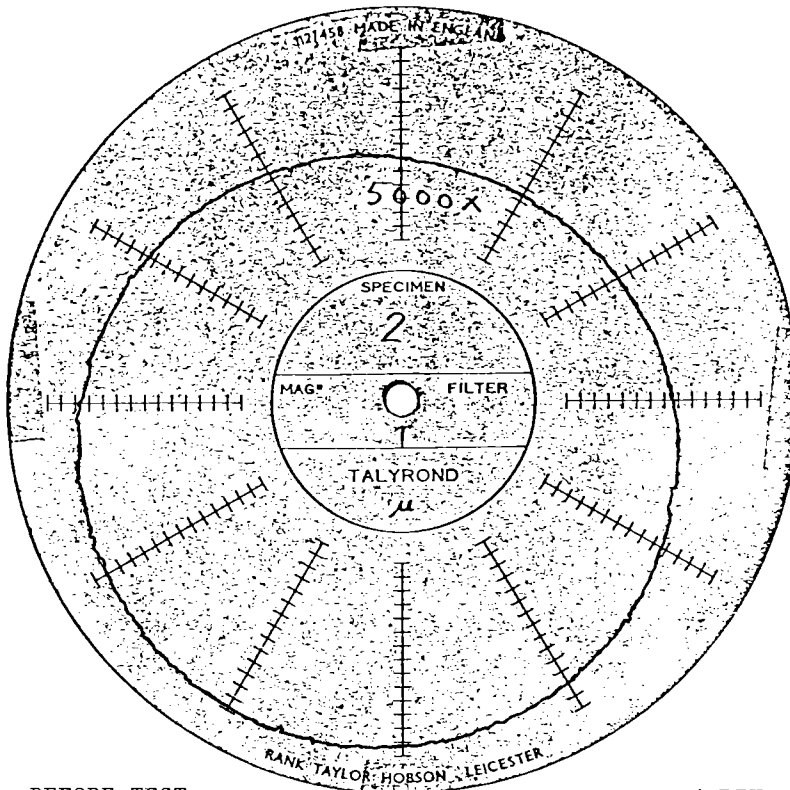
It is evident from ship reports of damage suspected due to fuel oil quality, that the injection equipment is vulnerable for certain qualities. Typical reports concern heavy wear due to catalytic fines. In order to study both the long term effects on the injection equipment itself and the resulting changes in spray pattern etc., a test rig consisting of a complete injection system for a smaller medium speed engine has been produced. The rig has recently been used to study the effects of a "problem fuel" creating severe operational disturbances after only a few hours of operation in the injection system of a large-bore engine.

Figure 4 gives an example of the changes in roundness and roughness of the sleeve surface in the high pressure injection pump on this test rig after only 60 hours operation with above fuel. Heavy scratching of the surface was observed. This rig is now included in more systematic research with different heavy and synthetic fuels as regards their long-term effects (1000 h operation).

#### THERMAL BARRIERS

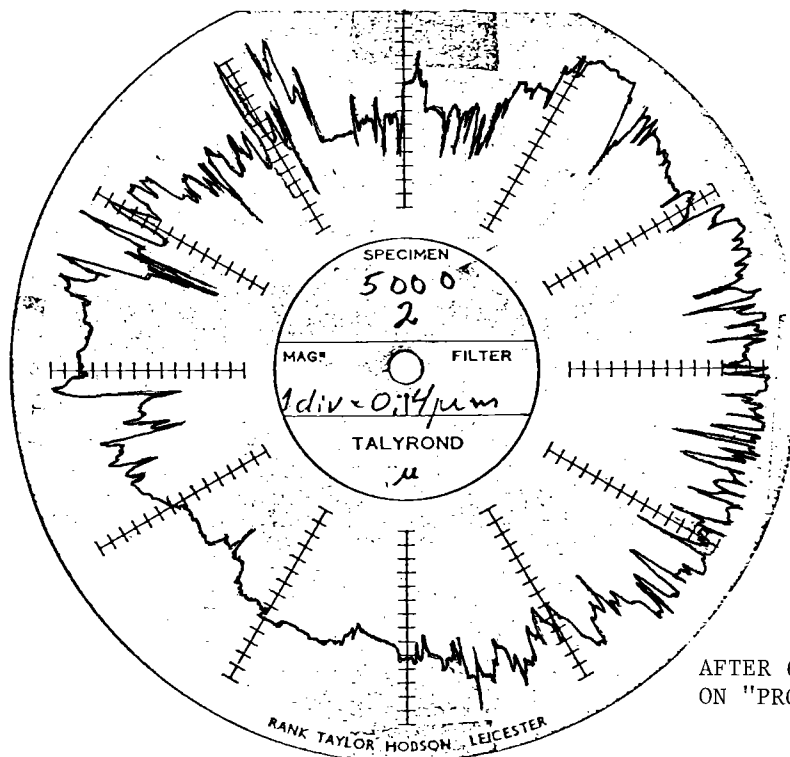
A group at the Central Institute for Industrial Research (SI) in Oslo, Norway, and which is headed by dr. Kvernes, has for a number of years been successfully addressing the problem of fuel-induced hot corrosion of piston crowns and exhaust valves via plasma sprayed coatings. The thermodynamic aspects of such coatings, which also act as thermal barriers, has been the subject of recent research at MTS in Trondheim.

When reviewing the possibilities for fuel consumption improvement of these engines, it was found that, apart from the obvious improvements to the pressure volume diagram obtained by squeezing pressures and heat release rates upwards, and which we are witnessing today in the form of increasingly lower specific fuel consumptions, only very minor improvements appeared possible in the conventional thermodynamic engine cycle.



BEFORE TEST

1 DIV = 0.4 μm



AFTER 60H OPERATION  
ON "PROBLEM FUEL"

Figure 4. Roundness and roughness of injec. pump liner

One unconventional alternative, however, is the suppression of heat loss to coolant via thermal insulation of the combustion chamber components. In view of the background in plasma-sprayed ceramic coatings at SI, it was natural to investigate theoretically such a thermally insulated engine in order to realistically assess its possibilities. This ceramic layer will also contribute to reduction of temperature and heat load of the metallic base under it, besides providing corrosion protection.

Reduced heat flow implies that a larger fraction of the fuel energy released during the combustion process will be converted into mechanical power and exhaust energy.

A perfectly insulated engine will reduce to zero the heat flow from the engine cylinders. Such an engine would work without any cooling system when mechanical losses are disregarded. These are the key properties of the Adiabatic Engine which is currently the target of worldwide research and development activities.

Research (5), (6), (7) shows that if heat loss could be eliminated in an adiabatic engine, only a part of it will be recoverable as work output. A true adiabatic process in the engine cylinder does not permit any heat transfer at all. A hypothetical thermal boundary for this case must have zero heat conductivity as well as zero heat capacity. In that case the surface temperature of the coating will instantaneously adjust to the gas temperature and thereby prevent any heat flow. The compression and expansion processes in the cylinder will not produce any change in entropy. We might therefore call this engine an Isentropic Engine.

The real thermal barrier, due to its heat capacity, does not prevent heat transfer between the working medium and the barrier. In the limiting case of perfect insulation the barrier will act as an energy buffer which absorbs and returns equal amounts of energy during one engine cycle. No heat will be transferred to the coolant.

#### Simulation

The present investigation of the effects of cylinder insulation on the diesel engine process was carried out using an engine cycle simulation program. The simulation model basically computes the process in the cylinder of a given engine when ambient conditions and operating conditions are given. As a part of the simulation, the transient heat flows between the cylinder gases and the surrounding surfaces are computed. The surface temperatures are subsequently computed from steady state heat flow through the metal walls.

In addition to the two limiting cases for a perfectly insulated engine, the numerical study presented in the paper also includes thermal barriers of uniform thickness obtained by plasma-sprayed coating based on zirconium oxide  $ZrO_2$ .

The purpose of the study was a comparative assessment of the impact of this type of materials on a hypothetical two-stroke and a four-stroke diesel engine cycle in cylinders of similar bore and stroke. Their thermal barrier aspect has been investigated over a broader range of thicknesses and surface combinations than it would be possible for experiments on real engines.

The cycle simulation program PROCES (8), (9) was employed in this investigation. This program is designed for computing the process in single-cylinder four-stroke or two-stroke diesel engines having an undivided combustion chamber. The heat transfer models are shown in figure 5. These resulted in a network of heat flow elements. For computational details refer to (10).

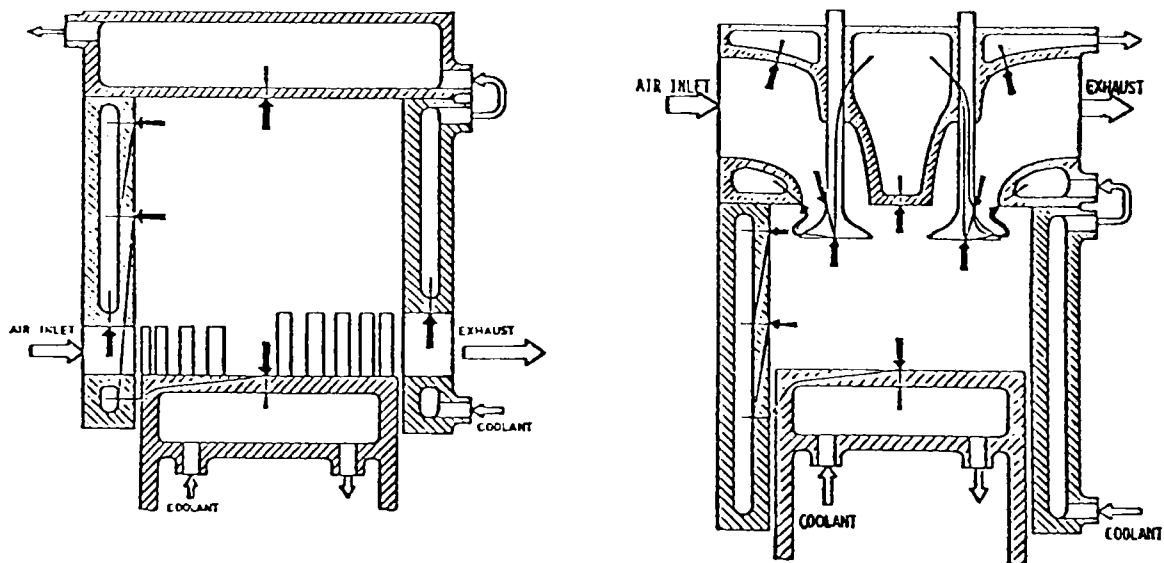


Figure 5. Heat Transfer Model Employed for Cycle Calculations

The PROCES program has three possibilities of describing the thermal barrier, controlled by the input data.

- A. Blocking all heat transfer by convection as well as by radiation. Alternative A will produce a true adiabatic process inside the control volumes.
- B. Using a very small non-zero value of the thermal conductivity  $\lambda$  for the heat conducting elements in the network. Alternative B permits heat transfer between the working medium and the exposed surfaces. The thermal barrier is perfectly insulating, i.e. no heat is transferred to the coolant. The heat capacity of the barrier is infinite since the surface temperature is assumed constant.
- C. Increasing the length of the heat conducting elements in the network. This approach will directly simulate the effects of an extra layer covering the original engine components assuming that their surface area is kept constant.

This method was used for all heat conductors having a ceramic insulating layer, and allowed us to account for any layer thickness. Alternative C represents the coating of infinite heat capacity, for the same reason as in alternative B. •

All other system parameters were kept constant during the simulation experiments.

#### Energy Balance

The various alternatives of heat insulation were compared and evaluated by means of simulated energy balance. The results are shown in figure 6. In these diagrams, the change relative to the reference cycle is shown to the left and the absolute values on the right hand scale.

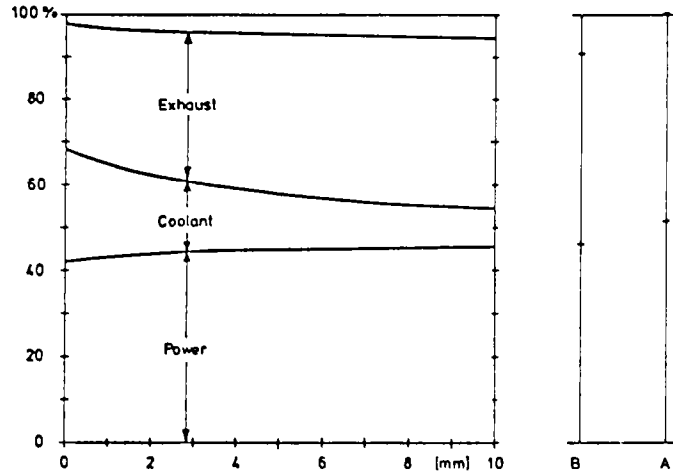
Figure 6 shows the effect of the coating thickness on the total energy balance of the cylinder unit. The individual energy flows called WORK, EXHAUST, COOLANT and REST refer to the energy carried by the fuel and released during combustion, see figure 7.

The delivered mechanical work, WORK, is the net indicated work done by the gases on the piston during one complete engine cycle. The energy carried away by the coolant, COOLANT, consists of contributions from piston crown, cylinder liner and cylinder cover. The energy carried out from the engine by the exhaust gases, EXHAUST, is defined as the difference between the enthalpy of the exhaust gases and the inlet air. The variable REST is an indicator of the computational accuracy and should ideally be equal to zero.

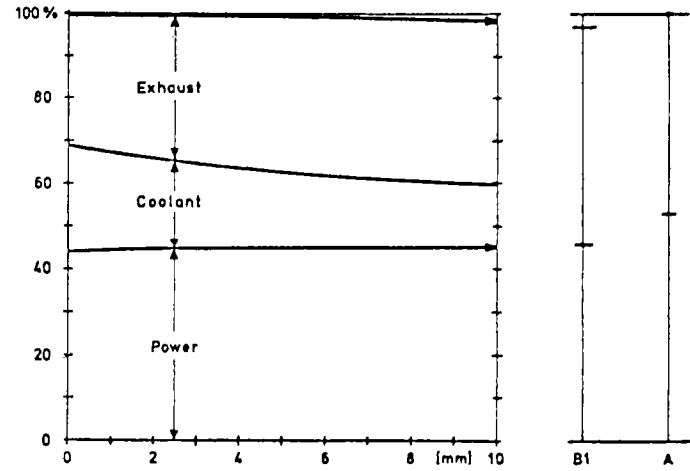
The overall energy balance shows clearly that when the coating thickness increases, less energy will be transferred to the coolant. The exhaust energy gets an approximately equal increase while the engine power is only slightly increased. Extremely



TWO-STROKE



FOUR-STROKE



2-43

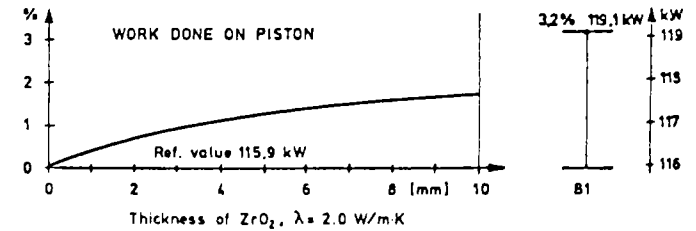
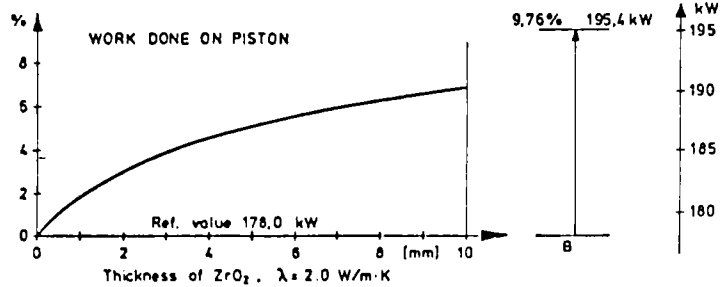
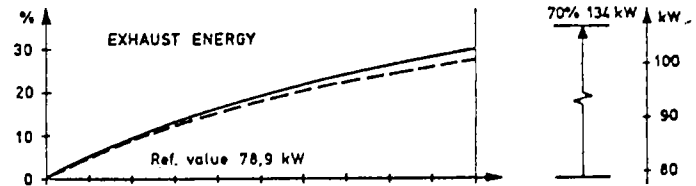
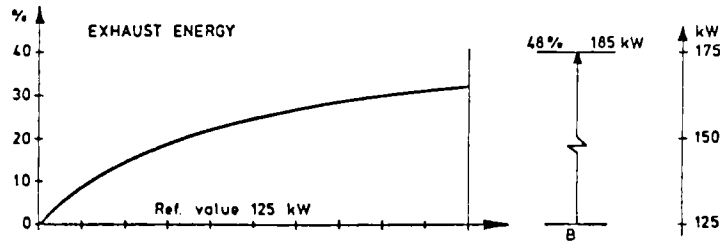


Figure 6. Change of the engine energy balance due to the thermal barrier

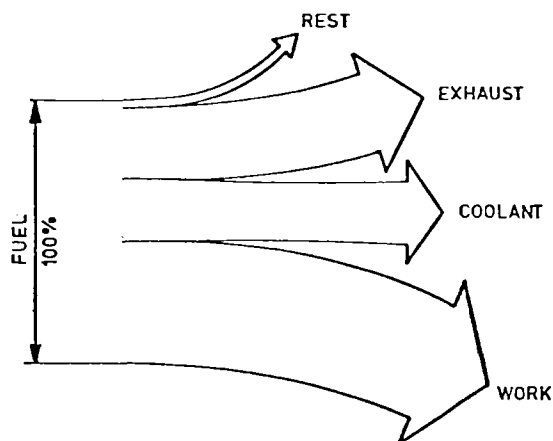


Figure 7. Energy Balance of Cylinder Unit

good insulation (B) will not improve the engine power by much, but will reduce to zero the energy transferred to the coolant.

A truly adiabatic process (A) could yield significantly higher mechanical power. The improvement, referred to the fuel energy, is approximately 9 % for both two-stroke and four-stroke cycles. The reason for the big difference between (B) and (A) comes from the fact that (B) allows a heat flow between the insulating layer and the gas whereas (A) prohibits any such energy flow as shown in figure 4.

It appears that the time variable heat flow in case (B) is large enough to prevent a significant increase of the thermal efficiency even if the net heat flow to the coolant is reduced to zero. Increasing the thickness of the ceramic coating is followed by an asymptotic change of the process variables and the limit values seem to be given by the insulation alternative B.

Curves in figure 6 show that about one third of the potential power increase is obtained by a coating of 2 mm in the two-stroke engine and 3 mm in the four-stroke engine. The improvement is then as large as 3 % and 1 % respectively in two-stroke and four-stroke cylinder unit.

Taking a round figure of say 1 mm as a practical case, coatings of this thickness will give increase of power of 1,8 % for the two-stroke engine and of 0.4 % for the four-stroke engine. This is equivalent to fuel savings of 3,6 g/kWh and 0,7 g/kWh respectively. The difference between the two-stroke and the four-stroke engine is

mainly due to the substantially higher thermal load of the former.

Figure 6 shows clearly that the reduction of energy flow to the coolant is accompanied by a corresponding increase in the exhaust energy. A 1 mm coating thickness yields an exhaust energy increase of approximately 9 % for two-stroke cycle and 6 % for four-stroke cycle.

#### Performance Data

Figure 8 shows that the specific indicated air consumption is considerably reduced when the thickness of coating is increased. The reduction of air throughput is sharper than the increase in indicated power. This is even more pronounced in the two-stroke cycle than in the four-stroke one. It thus demonstrates that the heating of the cylinder charge due to hotter surfaces adds to the air flow resistance through the cylinder.

Improved heat insulation results in higher temperatures of the cylinder gases. The gas temperature at the beginning of combustion is increased by approximately 60 K in the two-stroke cycle and by 30 K in the four-stroke cycle when the coating is 1 mm thick.

#### Surface Temperatures

The cylinder wall temperatures are highly sensitive to an insulating barrier. This is demonstrated in figure 9 for the piston crown and for the lower part of the liner. Similar results have been found for all other exposed surfaces.

The figure shows that the gas surface temperature of the coating will increase sharply when the coating thickness increases. Even a coating thickness of 1 mm may result in almost 180 K temperature rise for the two-stroke cycle. On the other hand, the temperature at the metal side of the coating will be reduced by approximately 50 K. For the four-stroke cycle the corresponding figures are 100 K and 25 K respectively.

This demonstrates that the ceramic coating gives very good heat protection of the metal parts provided that the thermal conductivity of the coating can be maintained under engine operating conditions.

In the limiting case of extremely good insulation, alternative B, the surface temperature on the gas side of the coating will be equal to the effective gas temperature for steady-state heat transfer. These high temperatures, which are 1401 K for the

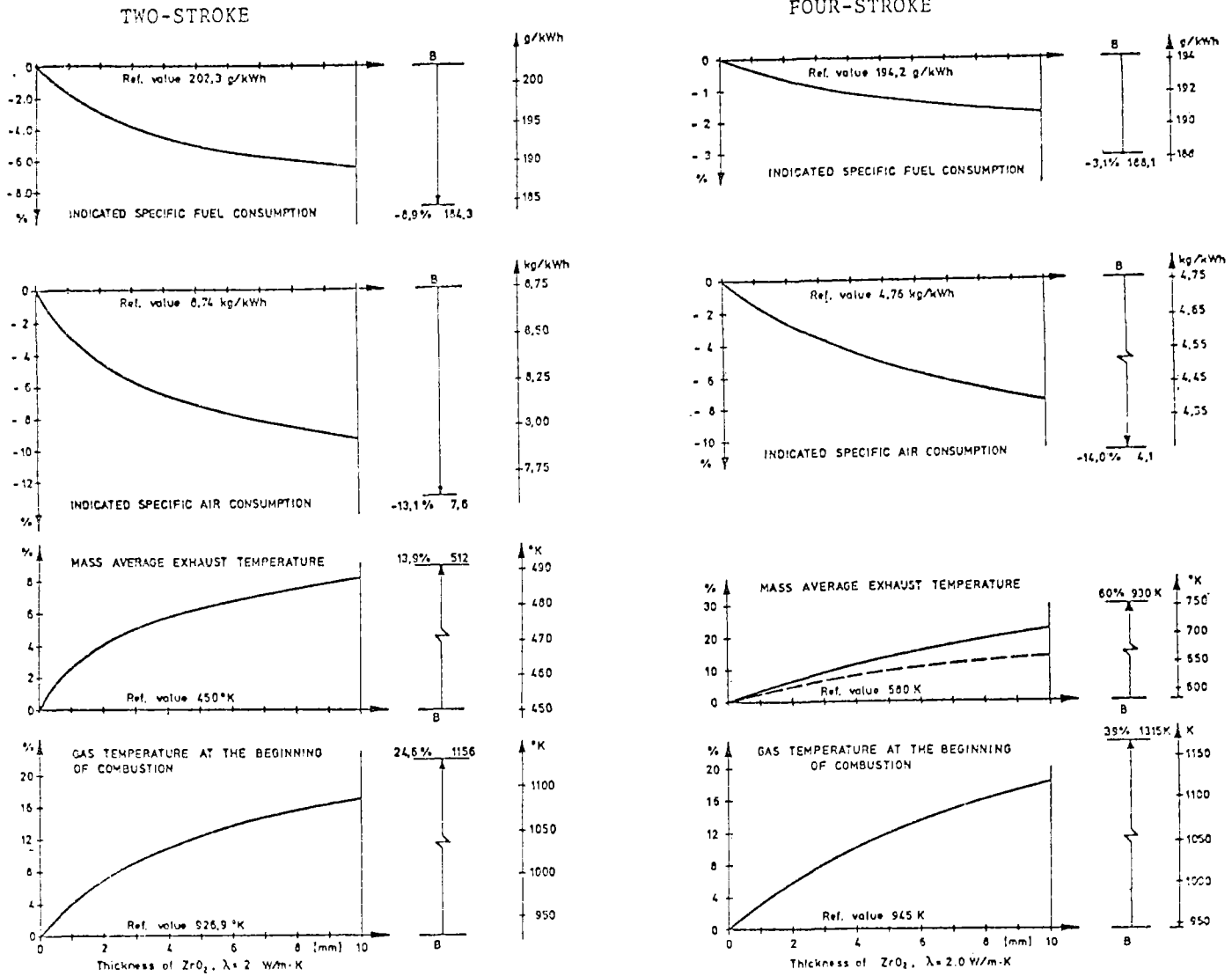


Figure 8. Change of Engine Performance and Process Parameters due to the Thermal Barrier

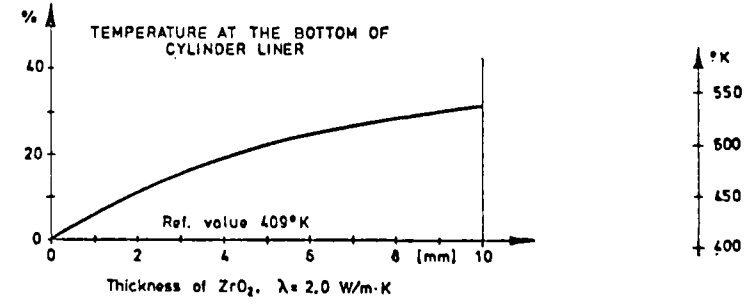
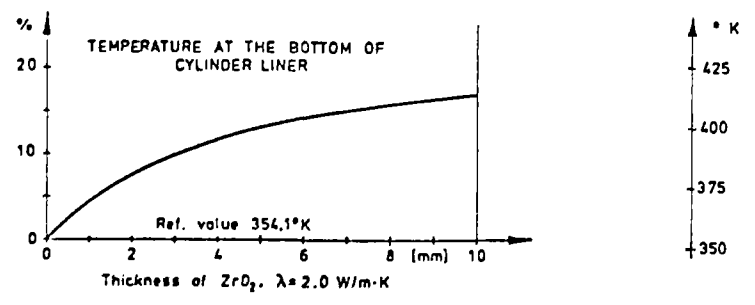
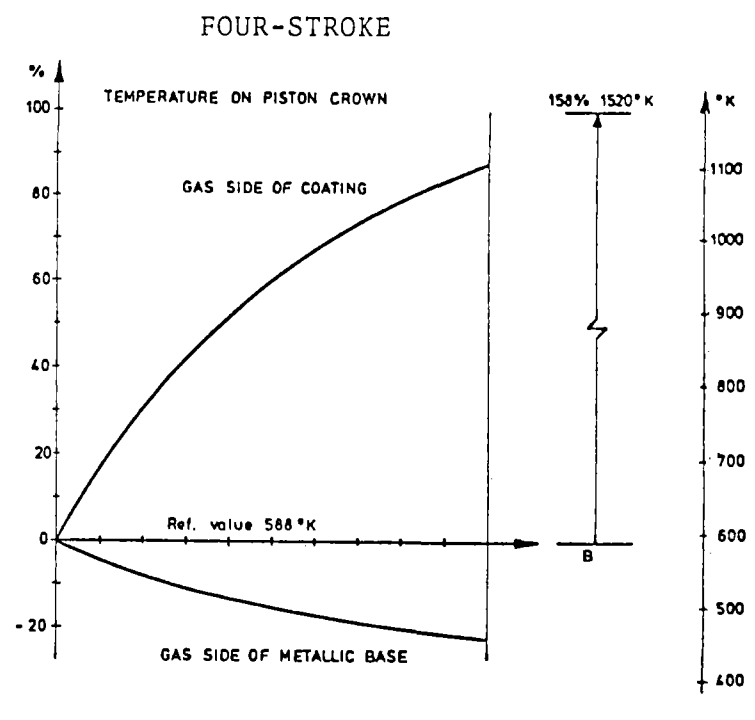
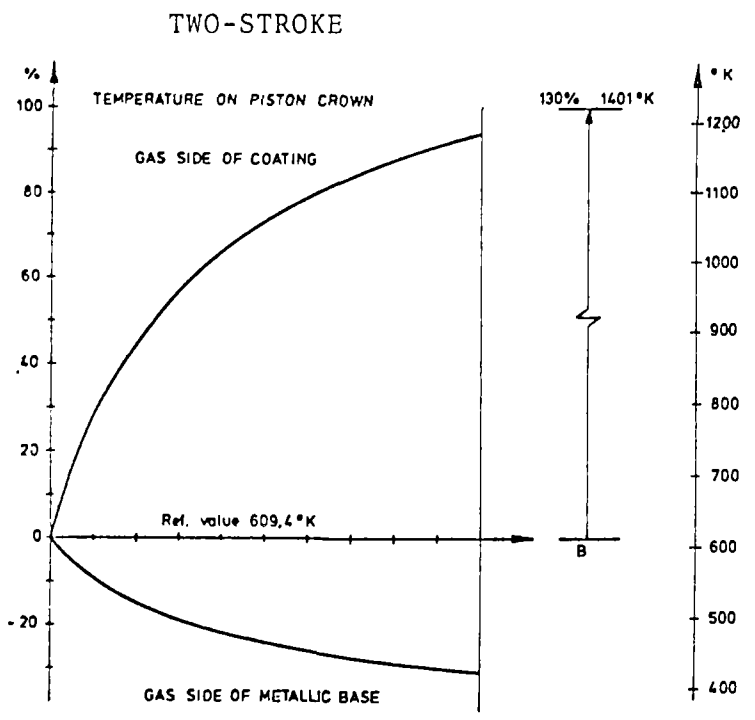


Figure 9. Change of the wall temperature due to the thermal barrier

two-stroke and 1520 K for the four-stroke cycles, may be critical even for the ceramic material used in the coating.

### Conclusions

Some general conclusions from the computations may be noted:

- Improved insulation reduces the heat flow to the coolant and increases the exhaust energy by approximately the same amount.
- The indicated power shows a small improvement when the insulation is increased. Perfect insulation yields an improvement in the order of 4 % and 2 % of supplied fuel energy respectively for two-stroke and four-stroke cycle. Significantly better results could still be obtained for a truly adiabatic barrier around the working medium.
- The insulation will produce higher surface temperatures and higher temperature level of the gases prior to ignition. This may have an advantageous effect on the ignition delay.
- The increase in exhaust energy is due to increased exhaust temperature. The air throughput is even reduced. Higher exhaust temperatures are advantageous for utilization of the exhaust energy. The two-stroke engine yields exhaust energy at substantially lower temperature level than the four-stroke engine.
- Even if the surface temperatures are increased, the temperatures of the base metal will be reduced when using ceramic coatings, thus reducing the thermal loading of the components.

### Relative Importance of Individual Surfaces

The preceding represent the maximum improvement attainable subject to given assumptions. In a real engine it may not be possible or practical to insulate all surfaces. Accordingly, an investigation of the relative improvement for the various surface area elements was carried out for four- and two-stroke engines. The results are shown in table 2.

It appears that the piston crown, the cylinder liner, and the cylinder cover each contributes by roughly 1/3 of the attainable improvements in two-stroke engines. In four-stroke engines the cylinder cover contribute somewhat more, mainly due to the greater surface area and high coefficient of heat transfer for exhaust valves and exhaust channels.

Lubrication problems may put a limit on the theoretical possibility of thermal isolation of the cylinder liner.

Table 2

RELATIVE IMPROVEMENTS DUE TO  
ISOLATION OF INDIVIDUAL SURFACES

	Four Stroke	Two Stroke
Piston crown	29 %	32 %
Cylinder liner	30 %	32 %
Cylinder cover, complete	41 %	36 %
Exh. valves	9 %	
Exh. channels	7 %	
Cover face	25 %	

The Effect of Transient Heat Conduction

In the preceding computations the heat flux between gases and surface was based upon the assumption of constant surface temperatures. The amplitude of the surface temperature depends on the gas temperature variation, the coefficient of heat transfer, and the thermal properties of the wall material. If the surface temperature could follow the gas temperature sufficiently close, the heat flux would decrease and in the limiting case we would approach an adiabatic surface.

The effect of surface material properties has been investigated in this context, the basic question being which material property values would yield a substantial reduction of the transient heat flux. This analysis was based upon one-dimensional heat conduction through the walls for a two-stroke cycle, with constant temperature on the coolant side. Numerical values of heat capacity ( $\rho c$ ) and thermal conductivity  $\lambda$  were systematically varied. The results showed that low values of the parameter  $b = \lambda \rho c$  will substantially influence the heat flux.

Remarks

It must be borne in mind that the preceding simulation and results were based on the in-cylinder process only, and the effect of the thermal barrier on the turbocharger system was ignored. Work is now in progress to include the complete engine in the simulation and to include the turbocharger.

The preceding has indicated that the possible gains in efficiency are small when practical limitations on layer thickness and areas are taken into account. The major benefit appears in the form of increased exhaust gas energy. This may be utilized as increased turbocharger work and improved gas exchange cycle. However, the greatest improvement in thermal efficiency probably lies in the use of compound cycles and waste heat utilization. Some of these possibilities will be investigated in the coming months. The long computer times for complete engine simulation limits the scope of such investigations and demands a judicious choice of alternatives.

Another important aspect of thermal barriers, already briefly touched upon, is the influence that increased gas and surface temperatures may have upon combustion. Combustion at low loads is a pronounced problem when running medium speed engines on heavy fuel. Increased temperature levels at low loads are beneficial in this respect. Ignition problems are even more pronounced with synthetic fuels such as SRC II. Thus the thermal barrier temperature effect, perhaps coupled with variable pilot injection, could be a possible means of providing acceptable ignition smoothness over the engine's load range without employing undue amounts of petroleum-based fuel together with SRC II. Laboratory research is planned in this area.

#### ELECTRONIC FUEL INJECTION

The combustion process, and thereby the cylinder pressure curve, the thermal loading and the fuel economy are greatly influenced by the fuel injection process. In theory the fuel injection process ought be tailored to the fuel at hand. However, a major adjustment of injection characteristics requires some hardware change, ideally a new fuel pump cam.

With the present prospect of deteriorating and variable fuel quality, adaptability of the injection system to changing fuel quality has recently been given attention by several builders of slow-speed crosshead engines using both electronic and mechanical means. NSFII tested a prototype digitally controlled injection system in the early 70's, and which we are now attempting to evaluate and develop at MTS.

The principle is shown in figure 10. Contrary to most accumulator systems, the delivery profile (injection rate), including the possibility of pilot injection, is under immediate, online control. Obviously such a system could prove a very useful research tool for developing injection cams. However, the real payoff could lie in shipboard use by tailoring the injection process to optimum conditions both for the speed and load at hand (when slow-steaming etc.), and especially for the fuel quality in the system. This latter aspect would be very valuable if future research



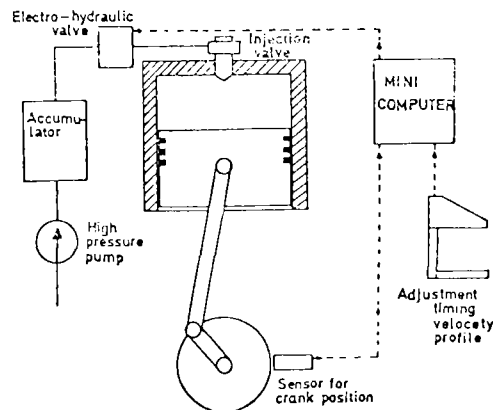


Figure 10. Digitally controlled accumulator injection.

could turn up some significant fuel quality parameters and determine their relationship to the optimum injection profile for each case. Improved combustion and slight increase in efficiency could result.

Taking the longer view to use of SRC II or other synthetic fuels of poor ignition quality, it appears, at least from our tests on a medium speed engine, that substantial amounts of fuel oil or ignition improvers must be mixed with SRC II for part load operation on present engines. The flexible pilot injection possibility of this electronic injection system should improve the ignition roughness problem and substantially reduce the fuel oil mixture required. An investigation of the effects of pilot injection on the medium speed engine are scheduled.

However fascinating the perspectives of the system may be, the hydraulic control valve has given us problems. We would like to operate at 1200 to 1500 bars max pressure for efficient combustion of heavy fuel in a medium speed engine. But standard units available of-the-shelf will tolerate less than half this pressure, due to extrusion problems with 'o'-ring seals. We have had difficulty in developing our own valves. The market does not appear to warrant the costly development of a supervalve. Reliability of such electronic hardware in a marine environment is another matter of concern.

Research in this area will continue with a view to assessing the possible advantages of the system with respect to inferior and synthetic fuels.

#### ACKNOWLEDGEMENTS

The authors wish to acknowledge the financial support for much of the work presented. Research grants have been given by The Norwegian Council for Scientific and Industrial Research (NTNF), while other portions of the work have been under contract to the Department of Energy. Thanks is also due to Bergens Mekaniske Verksteder and A/S Wichmann for support and cooperation, plus numerous other engine manufacturers. A number of staff and thesis students have contributed results. The heavy fuel activities have been carried out in close cooperation with T. Wiborg of Det norske Veritas (DnV) and dr. Kvernes' group at the Central Institute for Industrial Research (SI).

#### REFERENCES

1. G. Fiskaa. Short Term Tests on Four Different Heavy Fuels. Intermediate report 8-12.80. Damage Criteria Project, December 1980.
2. G. Fiskaa et al. The Effect of a Changing Heavy Fuel Quality on Diesel Engine Operation. Paper D62, CIMAC-81, June 1981.
3. G. Fiskaa. Combustion of SRC II (Solvent Refined Coal) in a Medium-Speed Two-Stroke Laboratory Engine. IFMM-81-07, Division of Combustion Engines and Marine Engineering, The Norwegian Institute of Technology, January 1981.
4. G. Fiskaa. Combustion of Shale Oil in a Medium-Speed Two-Stroke Laboratory Engine. (Under preparation) Division of Combustion Engines and Marine Engineering, The Norwegian Institute of Technology.
5. J.H. Stang. Designing Adiabatic Engine Components. SAE paper No. 780069.
6. W.J. Griffiths. Thermodynamic Simulation of the Diesel Engine Cycle to Show the Effect of Increasing Combustion Chamber Wall Temperatures on Thermal Efficiency and Heat Rejection. Diesel Engineering, summer 1977, pp 82-85.
7. F.J. Wallace, R.J.B. Way and M. Vollmert. Effects of Partial Suppression of Heat Loss to Coolant on the High Output Diesel Engine Cycle. SAE paper 790823.
8. H. Valland. Simulation of Thermodynamic Processes in Internal Combustion Engines. (In Norwegian) Lic.tech. thesis, The Norwegian Institute of Technology, Trondheim, December 1976.
9. H. Valland. User's Manual for PROCES, a Simulation Program of the Thermodynamic Process in a Four-Stroke Diesel Engine. (In Norwegian) The Norwegian Institute of Technology - Div. of Combustion Engines and Marine Engineering, Trondheim, December 1976.
10. H. Valland and G.K. Wyspianski. Thermal Barriers in Combustion Engine Cylinders. An Investigation of the Effects of Thermal Barriers Using the Cycle Simulation Program PROCES. Part I: Four-Stroke Diesel Engine, Report UR-80-12. Part II: Two-Stroke Diesel Engine, Report UR-80-13. Div. of Combustion Engines and Marine Engineering, The Norwegian Institute of Technology, Trondheim 1980.

## DIESEL ENGINE OPERATIONAL TESTING ON EARLY ALTERNATIVE FUELS

John Fairbanks  
Department of Energy  
Washington, D.C.

Dan Gurney  
Bartlesville Energy Technology Center  
Bartlesville, Oklahoma

### INTRODUCTION

The Department of Energy (DOE) has a major role in assisting and encouraging an early transition to non-petroleum or alternative fuels. Alternative fuels encompass gaseous, liquid or solid fuels and chemical feedstocks derived from coal, oil shale, tar sands, lignite and bio-mass fuels. Producers of candidate alternative fuels need to either make alternative fuels to current petroleum specifications or to develop a product slate of fuels which take best advantage of the molecular structure of the alternative fuels and mate these fuels with an appropriate market. Heat engine manufacturers are interested in understanding how their engines operate on alternative fuels and defining any research and development needed to adapt their engines to the new fuels. Many current production engines will still be in use when alternative fuels, or blends of the alternative fuels with petroleum fuels, replace straight petroleum fuels.

### ALTERNATIVE FUELS

The alternative fuel industry in the United States is in early stages of development. When the multi-billion dollar commitments to large scale production facilities are made, schedules and product slates for alternative fuel introduction will become realistic. The alternative fuel candidates which would be the initial potential fuels for the industrial/utility diesel engines will be derived from coal or oil shale based on the abundance of these resources and the developments underway in these areas.

Fuels derived from coal and shale have different hydrocarbon quantities and molecular structure than petroleum. While the overall hydrogen-carbon ratio (H/C) is about 2:1 for petroleum and close to that for shale oil, it is only about 0.75:1 for raw distillate coal derived fuel. This low H/C ratio results in a very low cetane number for raw distillate coal fuels. Also, the low H/C fuels burn with a considerably more luminous flame which results in a higher thermal radiation from the flame to the engine parts with a view factor of the flame. Analysis done at Westinghouse indicates this increased luminosity will increase metal temperatures in a gas turbine by over 100°F. This could be significant as diesels operating on light distillate petroleum fuels such as No. 2 diesel oil have temperatures on the exhaust valves just below the threshold of aggressive hot-corrosion. Determination of the extent of the hot-corrosion problem or of a synergistic erosion/hot-corrosion problem will have to await the availability of larger quantities of coal derived fuels for engine testing. The testing conducted with the early coal and shale derived fuels generally involves the handling, pumpability, lubrication, injection and combustion characteristics in diesel engines, developed for the characteristics of petroleum fuels, but operating with fuels with different physical and chemical properties.

The coal derived liquid fuels being tested in diesel engines are the SRC-II 2.9:1 Heavy to Middle Distillate Blend, SRC-II Middle Distillate, Exxon Donor Solvent (EDS), H-Coal, Char-Oil Energy Development (COED) and micronized coal in diesel oil mixtures (COM). The shale derived fuels are from the Navy sponsored refining of Paraho shale crude done by SOHIO in their Toledo refinery in 1978. In this operation 71,000 bbls of crude oil shale was refined to JP-5, JP-8, Marine Fuel Diesel (MFD), gasoline stocks and the remainder, a residual fuel.(1) DOE has made arrangements to test the shale derived MFD and the residual shale fuel. While the Navy sponsored refining of shale oil was not done to develop a commercialized product slate, it does provide insight into the potential of shale oil. In the case of SRC-II, the 2.9:1 blend is considered a large stationary boiler fuel requiring special handling. Middle Distillate SRC-II is considered a potential industrial/utility gas turbine and diesel engine fuel by Gulf and also requires special handling.(2) Various difficulties have resulted in cancellation of the planned SRC-II Demonstration Plant. One of the core difficulties is the Reagan Administration philosophy concerning Government support of demonstration plants. Apparently the percentage of commercial investment was too low in the SRC-II program fuels to be acceptable to the new Administration. However, the Exxon Donor Solvent, H-Coal and SRC-I fuels are being supported through the Synthetic Fuels Corporation with major cost-sharing arrangements. SRC-II has been relegated back to laboratory development status. If an SRC-II fuel were marketed for diesel engine use, it would be an upgraded version of SRC-II Middle Distillate (MD).(2) Thus, testing with SRC-II MD provides a worst case test for engine performance. That is to say, if a diesel engine designed to operate on petroleum base fuels can be modified or fuels can be modified or adjusted to operate on SRC-II MD over its full power range, it could most probably operate on the upgraded commercial version of this fuel, EDS or H-Coal with better performance and reliability. The major differences are between the petroleum fuels and the coal derived liquids, not between the coal derived liquids.

As a result of testing a wide range of fuels, Sarsten indicates that the combustion characteristics obtained with a fuel in one type of engine may not be the same in a different engine.(3) This anticipated engine difference factor with new fuels integrates into the DOE approach of having several organizations test small quantities of alternative fuels to assist in understanding the ability of diesel engines to operate on the fuel. This approach should identify R&D areas and provide the lead time to embark on long term solutions if these are necessary. Also, it helps focus a wide range of diesel engine talents on the alternative fuel engine compatibility problems.

#### SLOW SPEED DIESEL TESTING

The initial effort in coal derived fuel compatibility was with the slow-speed diesel engines on an Energy Research Development Agency (ERDA), which was later included in the DOE when it was established, contract with Thermo Electron/Sulzers. The multi-fuel capability reputation of the slow-speed diesel appeared to make this engine a reasonable starting point. Operating at 120 rpm, the slow-speed engine has virtually a "variable geometry combustor," which appears to provide advantages with coal base fuel combustion. Sulzers single cylinder test engine used in this program had a cylinder diameter of 760 mm, a speed of 120 rpm and was rated at 1500 KW.

Sulzers early testing with the COED fuel indicated this highly hydrotreated fuel could be directly substituted for petroleum MFD. The engine could be started

on COED and the exhaust smoke is undetectable to the eye. Performance was measured by a wide range of engine parameters and the data was very close to the comparative standard MFD test. At present the COED process is not being pursued. However, the COED fuel test indicates a coal fuel can be made to petroleum MFD specifications. The problem is the cost of adding hydrogen to the coal fuel to the petroleum fuel level hydrogen level. As an example, upgrading an SRC-II raw distillate from its 9.1 H level to the 12.8 level of petroleum MFD could require 10,000ft<sup>3</sup>H/bbl which could add \$20/barrel.

Sulzer measured the cetane number of the SRC-II 2.9:1 fuel as 0.8 which indicates very poor ignition quality. A variety of injection techniques were investigated. Satisfactory engine operation was achieved with pilot injection of 3.5% diesel fuel. The exhaust was smoke free and the engine could be cold started. Satisfactory engine operation was also achieved with a premixture containing 20% diesel fuel with the SRC-II 2.9:1 blend without pilot injection. Sulzer's data indicates SRC-II can be used with pilot injection to achieve virtually the same thermal efficiencies as that obtained with diesel fuel from 35% to 100% engine load.(4)

A slurry or mixture of finely ground coal and diesel oil (COM), where the coal comprised 32% of the slurry, was also tested. Seizure problems with the conventional Bosch-type diesel oil injector system were encountered when the slurry injection pressure exceeded 300 bar. Normal injector operation with diesel fuel is 735 bar. Seizure occurs in the plunger-barrel section of the fuel pump and in the stem-guide section of the injector valve. Under high pressure operating conditions, coal particles are forced into the close tolerance pressure sealing clearance spaces in these components. A wedge of particles accumulates that interferes with the sliding action of the pump plunger and valve stem. The powdered coal had 50% of the particles with diameters below 1.6 microns with the general distribution below 5 microns although a small fraction greater than 5 microns were measured. Sulzers developed a modified accumulator fuel injection system that satisfactorily introduced the COM into the engine.

Approximately 20 hours testing was achieved with this COM. Engine efficiencies measured during these tests were within a few percent of the reference testing with petroleum fuels. This satisfactory combustion was attributed to the low engine speed which provides a long residence time for particle burning. After 9-1/2 hours the engine was disassembled and examined. Extensive corrosion/erosion was noted in the injection nozzles and piston ring. The rings were bound in the ring grooves and there was extensive wear in the ring and cylinder wall contact area. Injection nozzles were changed at 1 hour intervals to minimize effects of nozzle deterioration.(5) This excessive wear is attributed to ash in the coal and unburned carbonaceous particulates. Sulzer recommends efforts to decrease the size of the coal particles and removal of most of the ash.

Sulzer also ran a second slurry composed of the same coal and ground to the same size but with diesel oil replaced by water. Since this fuel had an extremely low heating value, the capacity of the existing fuel injection system limited the engine loads to very low levels. Also this coal water mixture (CWM) was non-lubricating thereby limiting the operational time with existing auxiliary equipment. Nevertheless, the coal burned even at this low load with a correspondingly low temperature regime to a surprisingly high degree. Specifically, at 27% engine load using 17% pilot fuel, a 15% increase in heat rate was recorded. No increase

in smoke or cyclic speed variations was noted in spite of a 22% increase in cyclic pressure.(6) Tony Steiger reports in detail on these tests at Sulzers with alternative fuels at this conference.

Burmeister & Wain in a cooperative DOE project tested SRC-II 2.9:1 blend and a COM in their single cylinder, two-stroke turbo charged, uniflow scavenging, 120 rpm test engine. The test with SRC-II was conducted at full power while running on blends from 25% to 15% diesel fuel. The engine was started on diesel fuel then switched to either COM or SRC-II.

Operation on SRC-II was trouble free from a 25% blend of diesel oil in a gradual reduction to 15% diesel oil. SRC-II blended with diesel oil was considered an acceptable fuel for the slow-speed engine by Burmeister & Wain.

Operation with COM encountered significant clogging of fuel atomizers which caused a rise in injection pressures. After 4 hours of operation the engine was disassembled. Heavy scuffing was observed on the cylinder liner and piston rings. Large amounts of unburned particles and ashes saturated the cylinder lubricating oil resulted in a dry cylinder surface.

Burmeister & Wain's assessment of the COM test is that "if the abrasive particles in coal slurry can be prevented, such fuel may be feasible for diesel engines provided special fuel injection systems can be developed to solve the clogging problem. Also, a cylinder lube oil must be developed to cope with clogging tendencies of piston rings and cylinder parts experienced with cylinder lube oils developed for current petroleum fuels."(7)

Both Sulzers and Burmeister & Wain indicate coal slurries are candidate fuels for slow-speed diesels from a combustion perspective. Sulzers suggest a coal water slurry might be possible. The problems confronting the coal slurries are severe wear, need for non-conventional injector system such as Sulzer's accumulator approach and an appropriate cylinder lube oil. Since the inception of the diesel, people have tried to operate the engine on some form of coal but invariably they encountered severe wear. This should be a challenge to the gas turbine materials community who have the materials capability which could make considerable headway if focused on the diesel engine wear problems in the injector, ring-cylinder wall contact area, exhaust valve, piston crown and the auxiliary handling systems.

DOE is sponsoring work to develop a beneficiated coal water slurry (BCWM). Laboratory work suggests it is possible, within the framework of economical considerations to reduce the coal ash level from the average 10% down to about .5%. Also, the sulfur level can be reduced to this level. This work has not been thoroughly evaluated and scaled up for large quantity operation. A combination of improved erosion resistance and successful BCWM could be a very attractive alternative fuel-heat engine combination with world-wide applications.

#### MEDIUM SPEED DIESEL TESTING

The DOE has negotiated with the Norwegian Technical Institute to add three alternative fuels to the program supported by the Norwegian Council for Scientific and Industrial Research involving diesel engine testing with a wide range of fuels. This testing is done in a highly instrumented Wichmann IAX 2-stroke laboratory diesel engine which has a 300 mm bore and a 450 mm stroke and runs at 375 rpm. The Norwegian sponsored work was directed more at different qualities of heavy petroleum fuels and the importance of fuel oil parameters for a range of problems. Thus, this effort will provide a good comparison of SRC-II 2.9:1 blend of Middle to Heavy Distillate, the SRC-II Middle Distillate and Shale Oil

refined to Marine Fuel Diesel specifications. In addition DOE supported the modification of an existing diesel engine operational computer program to account for various thicknesses of ceramic coatings. Also, a ceramic coated exhaust valve is included in a test to validate the computer analysis.

Tests with the SRC-II 2.9:1 middle distillate to heavy distillate were done in the Wichmann 2-stroke medium speed test engine with various percentages of diesel fuel. This engine ran with acceptable combustion at full and overload conditions on a mixture of 75% SRC-II and 25% diesel oil. However, if the engine load was reduced below 80% excessive and violent knocking would result. It was estimated that blending 50-60% diesel fuel with the SRC-II would be necessary for full range operation although this was not verified by testing.

The Norwegian Technical Institute testing also identified the importance of the ignition delay parameter. Ignition delay is the period from the start of injection until ignition is measured by an increase in cylinder pressure. A long ignition delay will inevitably lead to:

- Rapid pressure rise after ignition
- Unstable combustion with large pressure variations
- High mechanical loads and noise (knocking)

Operation with long ignition delay can lead to severe engine damage. Ignition delay measurements with SRC-II 2.9:1 blended with various percentages of diesel oil are shown in figure 1 along with similar measurements made by Sulzer with the slow-speed engine all at full load. These data indicates an acceptable ignition delay for the Wichmann medium speed engine is in the range of 2 to 2.5 milliseconds which suggested the 25% diesel oil blend with SRC-II. Ignition delay measurements were made with the 25% diesel oil blend with SRC-II at 110%, 100% and 80% load. These data are plotted in figure 2. Extrapolating these data leads to an estimated ignition delay of 4.25 milliseconds at 60% load which would produce unacceptable engine knocking.(8)

A program was undertaken through the Bartlesville Energy Technology Center (BETC) in which five contracts were awarded to diesel engine manufacturers to determine the handling procedures, operational characteristics and emissions measurements of several alternative fuels. This testing has only recently begun. Testing scheduled to be accomplished is summarized in Table 1 for the five participating contractors. The diesel engines and their characteristics being used in this program are listed in Table 2. The matrix of alternative fuels being tested by the contractor's on the BETC project are identified as Table 3. Some of the properties of the alternative fuels being tested are shown in Table 4 along with comparative data for No. 2 diesel oil.

Initial results with SRC-II MD blended with No. 2 diesel oil indicated a higher percentage of SRC-II could be used at the higher power settings but the diesel oil content had to be increased as the throttle was moved back to idle. Trans-America DeLaval reports they could operate with 100% SRC-II at full load but had to blend 40% petroleum No. 2 diesel for knock free operation at idle. Similar testing with the Fairbanks Morse 38 TD-8 engine using a single cylinder indicated acceptable full power operation could be sustained with 80% SRC-II but that 50% No. 2 diesel oil was necessary at idle. General Electric's early work indicates 30% SRC-II MD blended with No. 2 diesel oil was satisfactory for all loads. Fuel consumption in these General Electric tests was generally within 5% of baseline operation with 100% No. 2 diesel oil.

Conventional injection of fuel into a diesel engine is begun at a crank angle of about  $10^{\circ}$  before the piston reaches top dead center (TDC) and sustained at an even rate until about  $20^{\circ}$  after TDC. Pilot injection involves an additional amount of second fuel injected before the main injection by about  $10^{\circ}$  of crank angle and only for a few degrees of crank angle. If the a quantity of the same fuel is injected early it is referred to as preinjection. If the early injection is injected over a large number of crank angle degrees, that is to say a small amount of fuel is introduced for a relatively long time, say over  $20^{\circ}$  of crank angle before main injection, it is referred to as dual rate injection.

Pilot injection of small quantities of No. 2 diesel fuel before the main injection of SRC-II is being investigated by A.D. Little in a Fairbanks-Morse 38 TD-8 and by TransAmerica DeLaval in their DSR 46 engine. Early work with the Fairbanks-Morse engine indicates a 2-1/2% pilot injection of diesel oil produces satisfactory operation at full load. DeLaval reports a 5% pilot injection was appropriate at full load with SRC-II.

Early results with preinjection are somewhat similar to the blended fuel results. However, a very intriguing test result has recently been reported by Southwest Research Institute (SWRI) in a test program for DOE's Office of Transportation Programs on medium and high speed diesels for transportation applications. They report that pilot injection of a small percentage of diesel oil  $115^{\circ}$  before TDC seems to improve engine operation when SRC-II Middle Distillate is the main injection fuel. The exhaust valve on this engine closes at  $119^{\circ}$  before TDC. This phenomena is not fully understood and is being further investigated. These results indicate there are marked differences in combustion of coal derived liquids in diesel engines and work should proceed to further understand the combustion process with these fuels.(9)

Shale oil refined to Marine Fuel Diesel (MFD) specifications appears to be an excellent diesel fuel. The high cetane number (49) shown in Table 4 is a good indicator of the suitability of this fuel for diesel engines. Testing of 100% Shale MFD was satisfactory over the full load range for both the GE FDL-8 and the Superior 40x6 engine. This fuel could be substituted for petroleum fuel in today's engines without modifications.

Shale oil MFD was also tested at the Norwegian Technical Institute in their Wichmann laboratory diesel engine. Their conclusions were that a medium-speed two-stroke diesel engine will operate on shale oil MFD with engine performance close to that obtained with diesel oil. A slight reduction in thermal efficiency was observed burning shale oil MDF which could probably be eliminated through optimization of the fuel injection equipment. The overall combustion process with shale oil MFD as analyzed by cylinder pressure diagrams does not differ from diesel oil. However, slight tendencies to incomplete combustion seem to be present in shale oil MFD. No differences in ignition delay were observable between the two fuels.(10)

#### HIGH SPEED DIESEL ENGINE TESTING

Grandi Motori Trieste (GMT) conducted tests with the SRC-II Middle Distillate in their four-stroke high speed (1200 rpm), 53 HP/single cylinder experimental engine. Additional testing is planned for their two-stroke, low-speed engine. GMT analyzed the SRC-II fuel they received and determined that the density was about 18% higher and the heating value was 11% lower than that of diesel oil. The cetane number measured was -8. The SRC-II and diesel oil were metered and homogeneously mixed.



Engine testing results were that a 67% SRC-II, with 33% diesel fuel encountered ignition failures in the cylinder and ignition was noted in the exhaust manifold. However, with a 50/50 SRC-II/diesel fuel blend, no operating irregularities were observed. The test results are summarized in figure 3. These data show that specific fuel consumption with the SRC-II blend is rather high at low loads but stabilizes at the higher loads.(11)

As part of a DOE contract with Cummins Engine Company, Yanmar Diesel of Japan is to scale-up their pre-combustion chamber for a Cummins medium speed diesel engine to determine the reduction in cetane sensitivity with coal derived fuels. Yanmar ran one barrel of SRC-II 2.9:1 fuel in their high-speed (2400 rpm) prechambered engine. They ran with a 50%-50% blend with diesel oil, SRC-II with 70% diesel oil and a baseline run with 100% diesel oil. Test data with these fuels are shown in figure 4. There was essentially no difference with the SRC-II blends and 100% diesel oil runs at full power. However at partial loads there was significant backfiring with both SRC-II blends. Surprisingly the smoke density with the 50% SRC-II, diesel oil blend was considerably lower than the baseline 100% diesel fuel or the other SRC-II blend.(12)

The Energy Research Group at the David Taylor Naval Ship Research and Development Center, Annapolis made arrangements with Caterpillar to run a single cylinder, turbo-charged precombustion chambered, 4-stroke, 1200 rpm diesel test engine with Shale Oil MFD. The same engine was tested with petroleum diesel oil for comparative purposes. The results from this testing were as follows: (a) the same power level was developed by both fuels, (b) the BSEC (brake specific energy consumption) was a minimum of 2.3% higher with the shale oil MFD i.e., the energy efficiency is lower with the shale derived fuel, (c) no significant difference in performance or emissions were measured with the two fuels.(13)

#### COAL DERIVED LIQUID FUEL HANDLING

Most of the early testing of coal derived liquid fuels has been done with the SRC-II fuel. This is a toxic fuel and special precautions need to be taken with the raw distillate cut of this fuel and other coal derived liquid fuels. Fumes from the SRC-II fuel are obnoxious and complaints of headaches and sore throats were numerous where special ventilation had not adequately removed the fumes.(8)(14) Gloves are recommended as well as dedicated clothing including face shields. Clothing used in the vicinity of SRC-II should be changed regularly and not worn outside of the facility. The intent is not to have prolonged exposure of SRC-II to the skin as might occur if the work clothes became saturated with the fuel and allowed to rub against the skin. You certainly would not want to clean deck plates with SRC-II as is the practice with diesel oil. Showering after working around SRC-II is prudent.

SRC-II attacks many materials including the conventional gasket materials, rubber hoses, seals, O-rings etc. Short term effects of SRC-II exposure to O-rings and hoses are shown in figures 5 and 6. Materials such as viton or teflon have to be substituted for these materials.(8) Also, SRC-II fuel will leach lead out of solder joints and copper out of brass. Stainless steel lines appear to be satisfactory for these fuels. SRC-II MD fuel has precipitated out many impurities after long term storage in tank cars.(15) It is strongly advised that these early fuels be characterized at a number of stages to determine handling, storage and stability effects.

It should be noted that the intended SRC-II fuel for the industrial/utility heat engine sector was anticipated to be hydrotreated to something like a 10% to 11% hydrogen level. This hydrotreating would significantly reduce the handling

problem and increase the cetane number and reduce the ignition delay. One of the reasons the raw distillate SRC-II was not hydrotreated was the unavailability of a refinery to hydrotreat the relatively small quantities produced by the pilot plant. The Exxon Donor Solvent process can produce a higher hydrogen level without a separate hydrotreating step since it uses recycling.

#### SUMMARY AND CONCLUSIONS

Alternative fuel development is in a formulative stage prior to commercialization. The most economical approach would be to modify engines to operate with the inexpensive grades of fuel as opposed to upgrading the fuels. Diesel engine operation with a specific fuel may well be different for each engine design of similar rating.

It has been demonstrated that a coal derived liquid fuel can be processed to about petroleum diesel oil specifications, such as the COED fuel and it can be substituted as a fuel in the low-speed diesel. Also, oil shale can be refined to Marine Fuel Diesel (MFD) specifications to produce an excellent diesel fuel with a cetane number of 50. This fuel can be substituted directly for the petroleum MFD in medium-speed and high-speed diesels with no significant difference noted in performance or emissions. Engine durability with COED and shale oil MFD have not been demonstrated due to lack of large quantities of the fuels. However, a review of the characteristics of these fuels does not suggest any serious problems.

The low quality cuts of raw distillate SRC-II 2.9:1, Middle Distillate: Heavy Distillate was tested early in the pilot plant operation in both slow-speed and medium speed diesel test engines. This fuel has a negative cetane number and it is necessary to blend this SRC-II with diesel oil or use pilot injection with diesel oil or to reduce the cetane number sensitivity of the engine. Operation at the full power level can be done with about 75% SRC-II blended with 25% diesel oil. However the percentage of diesel oil has to be increased as the power level is reduced or severe knocking is encountered. Probably something like 50-60% diesel fuel blended with SRC-II is necessary for full range operation. Electronic fuel control mated with an engine condition monitoring system could optimize the blend for the power setting. The ability of high speed engines to operate with the SRC-II 2.9:1 blend at full load was surprising. However, low power settings required 70% diesel fuel. Test results with the Exxon Donor Solvent fuel should be better as the cuts being tested have a 10.5% hydrogen level compared with the 9.1% H level of SRC-II. It should be noted that if Gulf commercializes SRC-II for the heat engines market, it would be hydrotreated making it easier to burn with reduced handling problems. However, these data obtained indicate that coal derived liquid fuels could be used in industrial/utility diesel engines with appropriate handling.

The coal derived liquid fuels tested in diesel engines must be handled as a toxic material. Contact with the skin should be avoided. Work clothes should be changed regularly and not worn outside the work area. Showers after working in close proximity with the fuels is prudent. Ventilation must be provided in storage areas and around the engine where leakage of seals, gaskets and/or valves occurs. Handling procedures adopted at the pilot plants has shown no abnormal medical problems compared to the national average with extensive medical examinations conducted quarterly.

## REFERENCES

- (1) Dr. Alan Roberts, NAVMAT - Personal communication.
- (2) Dr. John Freel, SRC International - Personal communication.
- (3) Sarsten, A.; Fiskaa, G. and Valland, H., "On Fuel Economy and the Use of Alternative Fuels in Medium- and Slow-Speed Diesel Engines," Division of Combustion Engines and Marine Engineering, the Norwegian Institute of Technology, August 1981.
- (4) Steiger, H.A.; Eberle, M.K.; Dunlay, J.B.; Davis and Maslen, P.L., "Economic and Technological Assessment of Diesel Engines Using Coal-Based Fuels for Electric Power Generation," Report No. TE 4234-37-80 performed on DOE Contract EF-77-C-01-2647, Waltham, Mass. September 1979.
- (5) Steiger, H.A.; et al, "Performance Tests of A Slow-Speed, Two-Stroke Diesel Engine Using Coal-Based Fuels" Report No. TE 7905-267-80, performed on DOE Contract EF-77-C-01-2647, Waltham, Mass. June 1980.
- (6) Steiger, H.A., "Coal Slurries and Synthetic Fuels in Diesel Engines," 14th CIMAC Conference - Helsinki Panel Discussion Future Fuels (Non-Crude) June 1981.
- (7) Henningsen, S. "B and W DE I.50 Operation on Coal Slurry and SRC-II" B and W Research Lab, Copenhagen, Denmark September 1979.
- (8) Fiskaa, G. "Combustion of SRC-II in a Medium-Speed Two-Stroke Laboratory Engine," Norwegian Technical Institute Report IFMM-81-07, Trondheim, Norway, January 1981.
- (9) Baker, Q.A., "Alternative Fuels for Medium Speed Diesel Engines," Progress Report No. 25 DOE Contract - Southwest Research Institute EM-78-C-01-4266 for period 11 March 1980 to 10 April 1980.
- (10) Fiskaa G. "Combustion of Shale Oil in a Medium-Speed Two-Stroke Laboratory Engine," Norwegian Technical Institute Report IFMM-81-10, Trondheim, Norway September 1981.
- (11) Anon "210.1 High Speed Four-Stroke Diesel Engine Operation on SRC-II Coal Derived Fuel," Grand Motori Trieste Report D10104 prepared for U.S. Department of Energy, Trieste, Italy, August 1981.
- (12) Roy Kamo, Cummins Engine Company, Personal communication.
- (13) Carl H. Hershner, David W. Taylor Naval Ship Research and Development Center, Personal communication.
- (14) Prof. Peter Hancock, Cranfield Institute of Technology, Personal communication.
- (15) Tom Sherlock, Westinghouse, Personal Communication.

TABLE 1

	TESTS TO BE PERFORMED				
	<u>ACUREX</u>	<u>A. D. LITTLE</u>	<u>EER</u>	<u>GENERAL ELECTRIC</u>	<u>TRANSAMERICA DELAVAL</u>
<u>Analytical</u>					
Determine Theoretical Limits					
Fuel Handling, Injection, Combustion	Yes	Yes	Yes	Yes	Yes
Examine Fuel System Modification Alternatives	Yes	Yes	Yes	Yes	Yes
Develop Procedures for Laboratory Stage	Yes	Yes	Yes	Yes	Yes
<u>Laboratory Testing</u>					
Determine Specific Fuel Properties	Yes	Yes	Yes	Yes	Yes
Select Components	Yes	Yes	Yes	Yes	Yes
Develop Fuel System Modifications	Minimum	Minimum	Minimum	No	Minimum
Perform Bench Tests	Yes	Yes	Yes	Yes	Yes
Conduct Injector Tests	Yes	Yes	Yes	Yes	Yes
<u>Engine Testing</u>					
Engine Starting	Yes	Yes	Yes	Yes	Yes
Fuel Injection Technique Evaluation					
Pilot Injection	Yes	Yes	Yes	No	Yes
Pre-Injection	Yes	No	No	No	Yes
Dual Rate Injection	Yes	No	No	No	No
Fumigation	No	Yes	No	No	No
Different Blend Ratio	Yes	Yes	Yes	Yes	Yes
Emissions Analysis	Yes	Yes	Yes	Yes	Yes
Extended Run Tests and Wear Analysis	100 hr.	No	100 hr.	200 hr.	100 hr.
Vary Load	Yes	Yes	Yes	Yes	Yes
Vary Compression Ratios	No	Yes	No	No	Yes
Measure Engine Parameters					
Combustion Pressures	Yes	Yes	Yes	Yes	Yes
Combustion Duration and Steadiness	Yes	Yes	Yes	Yes	Yes
Ignition Delay	Yes	Yes	Yes	Yes	Yes
Valve and Piston Temperatures	No	No	No	Yes	No
Vary Injection Timing and Rate					
Heat Air	Yes	Yes	No	No	Yes
Heat Fuel	Yes	Yes	Yes	Yes	Yes

TABLE 2

## DIESEL SELECTION FOR TEST PROGRAM

<u>PRIME CONTRACTOR/ SUBCONTRACTOR</u>	<u>ENGINE CHARACTERISTICS</u>				
	<u>MODEL</u>	<u>BHP @ RPM</u>	<u>B x S</u>	<u>CID</u>	<u>CR</u>
ACUREX/ RICARDO ENGINEERING	APE-ALLEN BSC 12 F 6-CYLINDER, IN LINE TURBOCHARGED, 4-STROKE	1402 @ 1000	9.5 x 12	5101	12.0
A. D. LITTLE	FAIRBANKS MORSE 38TD-8-1/8 6-CYLINDER, IN LINE TURBOCHARGED, 2-STROKE	1050 @ 900	8.5 x 10	3108	13.8
EER/ SUPERIOR INDUSTRIES	SUPERIOR 40-X-6 6-CYLINDER, IN LINE TURBOCHARGED, 4-STROKE	702 @ 900	9.125 x 10.5	4122	13.5
GENERAL ELECTRIC/ (NONE)	GE FDL-8 8-CYLINDER, V TURBOCHARGED, 4-STROKE	1750 @ 1050	9 x 10.5	5344	12.7
TRANSAMERICA DELAVAL/ (NONE)	DELAVAL DSR 46 6-CYLINDER, IN LINE TURBOCHARGED, 4-STROKE	3656 @ 450	17 x 21	28600	12.0

TABLE 3

## FUEL SELECTIONS FOR FIELD-TEST PROGRAM

<u>PRIME CONTRACTOR/SUBCONTRACTOR</u>	<u>FUEL SELECTION(S)</u>
Acurex/Ricardo Engineering	Shale Residual
A. D. Little/Colt Industries	SRC-II Middle Distillate, Exxon Donor Solvent, and H-Coal
EER/Superior Industries	Shale Distillate, Exxon Donor Solvent, and H-Coal
General Electric/(None)	SRC-II Middle Distillate and Shale Distillate with some Single Cylinder Work on Exxon Donor Solvent and H-Coal
Transamerica Delaval/(None)	SRC-II Middle Distillate

TABLE 4

Key Properties of Alternative Liquid Fuels

Property	Baseline Fuel No. 2 Diesel Oil (Petroleum Base)	SRC-II Middle Distillate	SOHIO Shale Oil (MFD)	H-Coal (High H <sub>2</sub> )	Exxon Donor Solvent (Middle Distillate)	Anticipated Problem Areas for Diesel Engines
Viscosity (SC)						
100° F	2.8 ± 0.8	3.2	2.7	2.2	4.4	Atomization (larger drops unless preheated)
210° F	1.1	1.1	1.2	1.1	1.3	
Distillation (°F)						
10%	430	390	450	430	422	Evaporation time affects sooting and NO <sub>x</sub>
90%	590	490	560	570	703	
C/H by Weight	6.80	9.45	6.75	7.6	8.6	Increased soot and thermal radiation from high C/H
Hydrogen, by wt.	12.0%	9.1%	12.8%	11.4%	10.2%	
Nitrogen, by wt.	<0.02%	1.0 ± 0.1%	0.06%	<0.3%	0.15%	Fuel-related NO <sub>x</sub>
Aromatics	20-30%	62-65%	30%	27%	65%	PAH emissions
Cetane	40-50	<20	49	44	<20	Delayed ignition, elev- ated rate of pres. rise
Heating value (HHV)						
Btu/gallon	136,700	137,100	137,300	143,400	148,800	No problem
Btu/lb	19,300	16,900	19,600	19,000	18,600	
Density						
API	35 ± 2	13.8	37	25	15	No problem
Specific gravity	0.85	0.974	0.84	0.905	0.96	

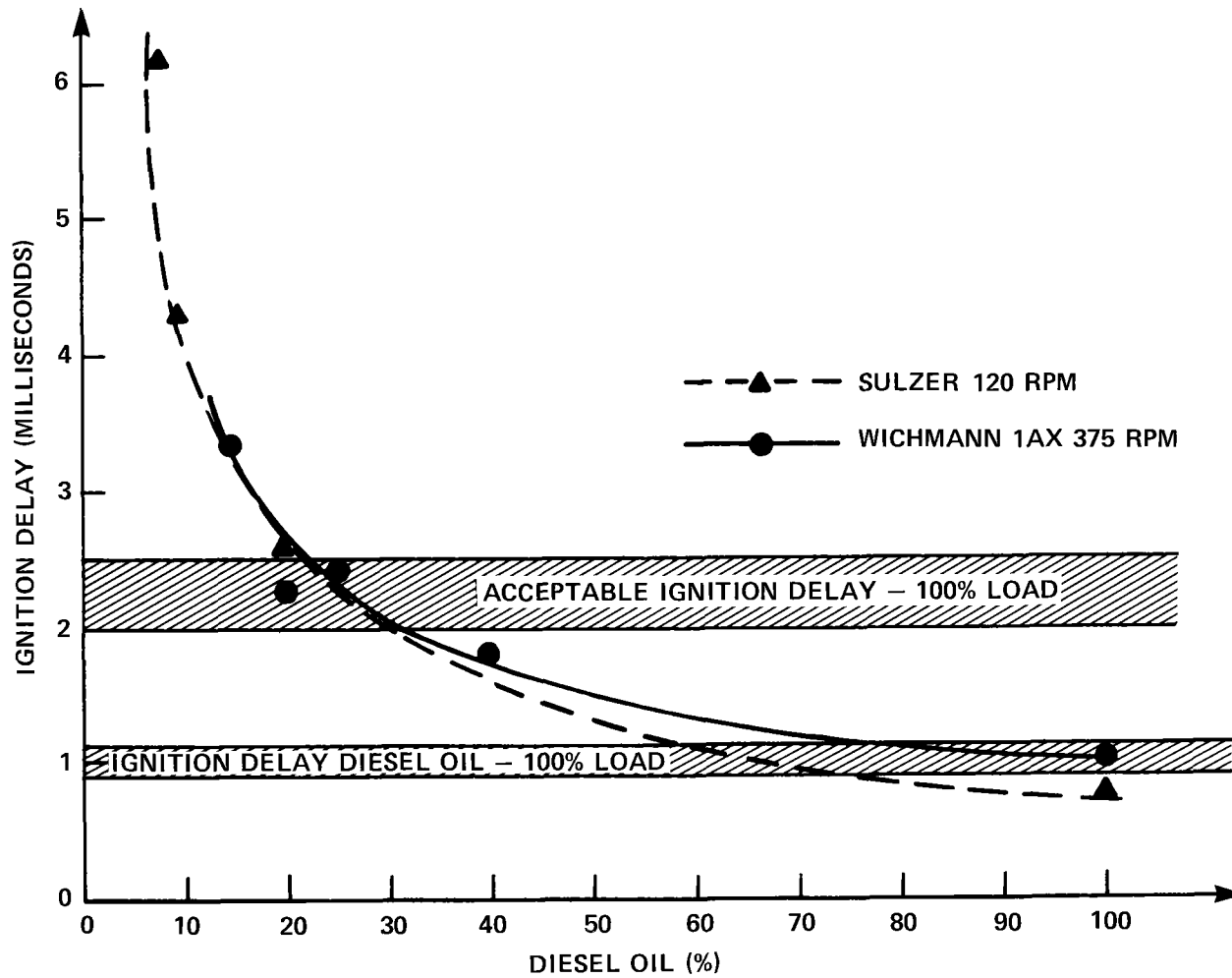


**FIGURE 1**  
**SRC-II BLENDED WITH VARYING AMOUNTS DIESEL OIL OPERATING AT FULL POWER**



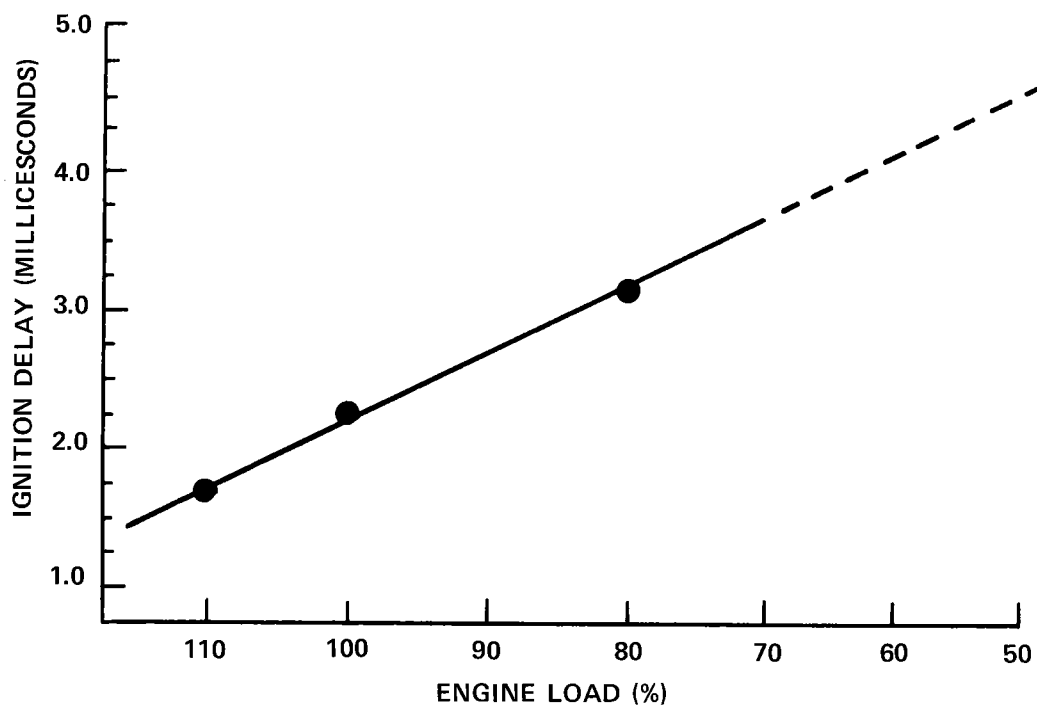


**FIGURE 2**  
**EFFECT OF ENGINE LOAD ON IGNITION DELAY**  
**IN MEDIUM SPEED DIESEL OPERATING ON SRC-II &**  
**DIESEL OIL (25%) BLEND**

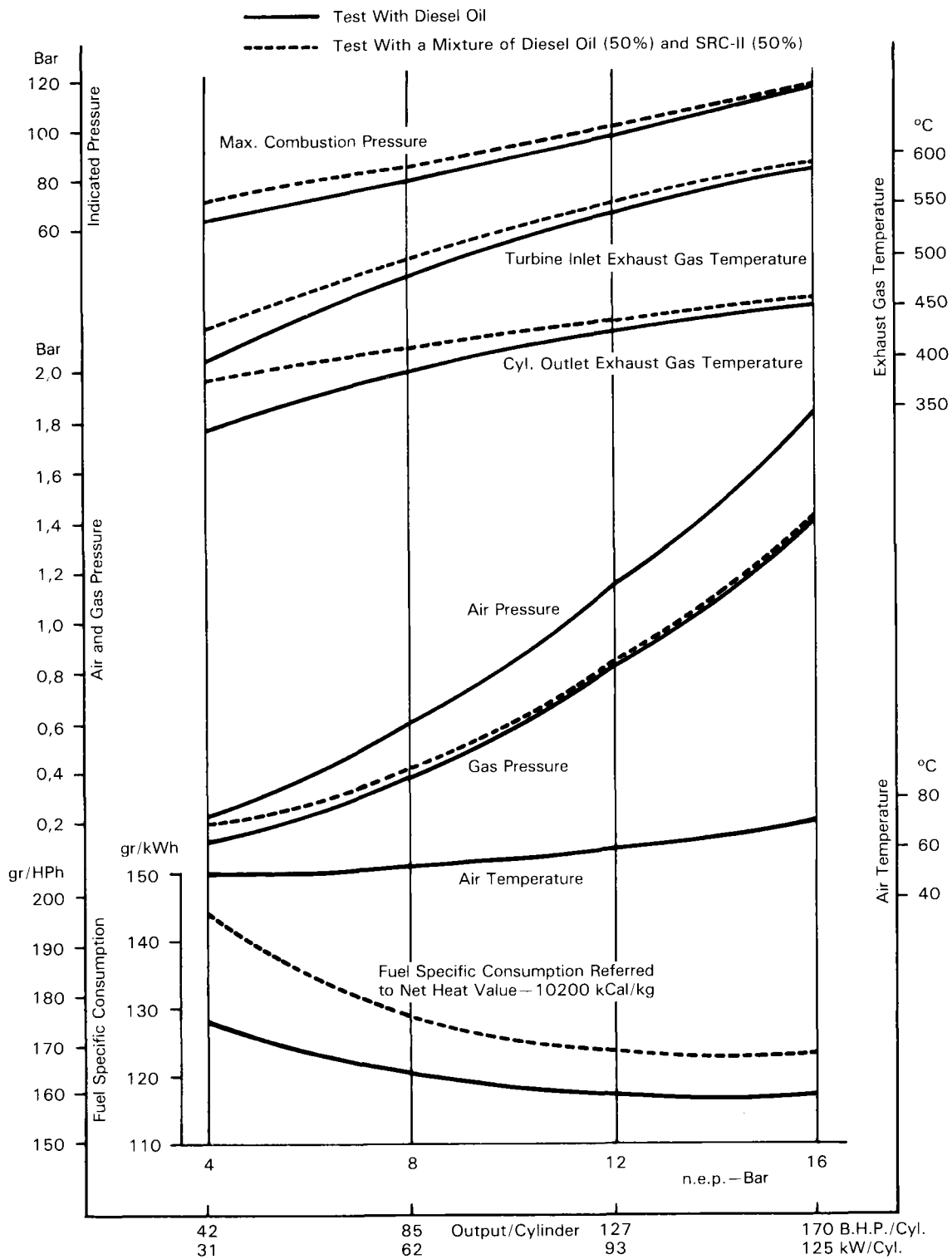
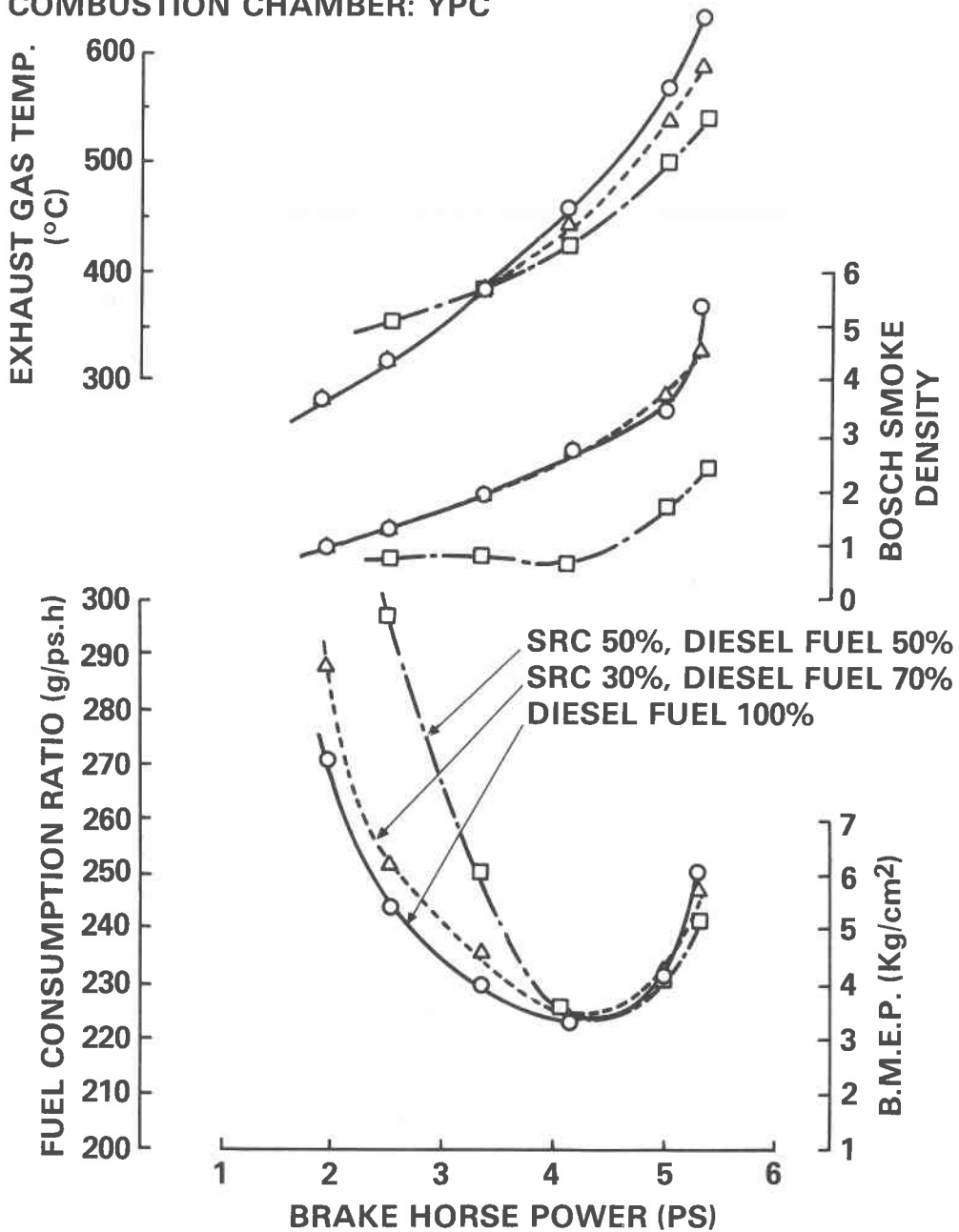


**Fig. 3 Comparison of Operation With Diesel Oil and Mixture of SRC-II/Diesel Oil in GMT Single Cylinder 210mm Bore Enging at 1200 rpm.**

## ENGINE SPEED: 2400 rpm

ENGINE: NSA50C (1-75 $\phi$ x75)  
 CHARGE AIR TEMP.: 25-27.5°C  
 COMBUSTION CHAMBER: YPC

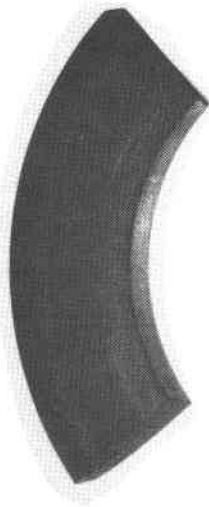


NO DIFF @ FULL LOAD  
 MISFIRING AT PART LOAD.

NO FIRING @ 100% SRC-II  
 SMOKE DENSITY LOW AT 50% SRC-II

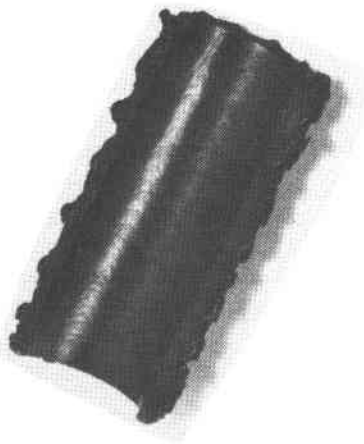
FIGURE 4 HIGH SPEED DIESEL WITH PRECHAMBER TEST WITH SRC-II FUEL

No. 2 DIESEL FUEL



7 DAY IMMERSION  
ROOM TEMPERATURE

FUEL HOSE LINING  
FUEL FILTER GASKET



100% SRC II

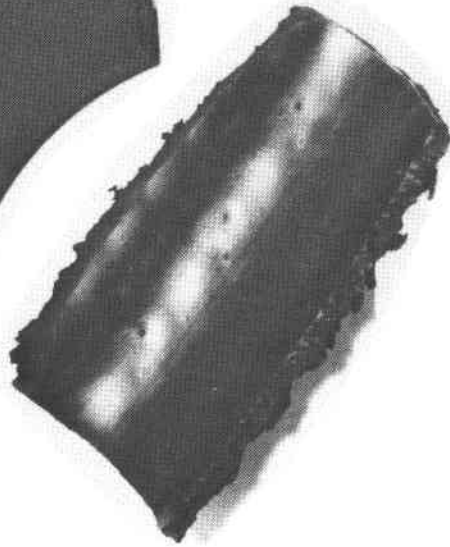
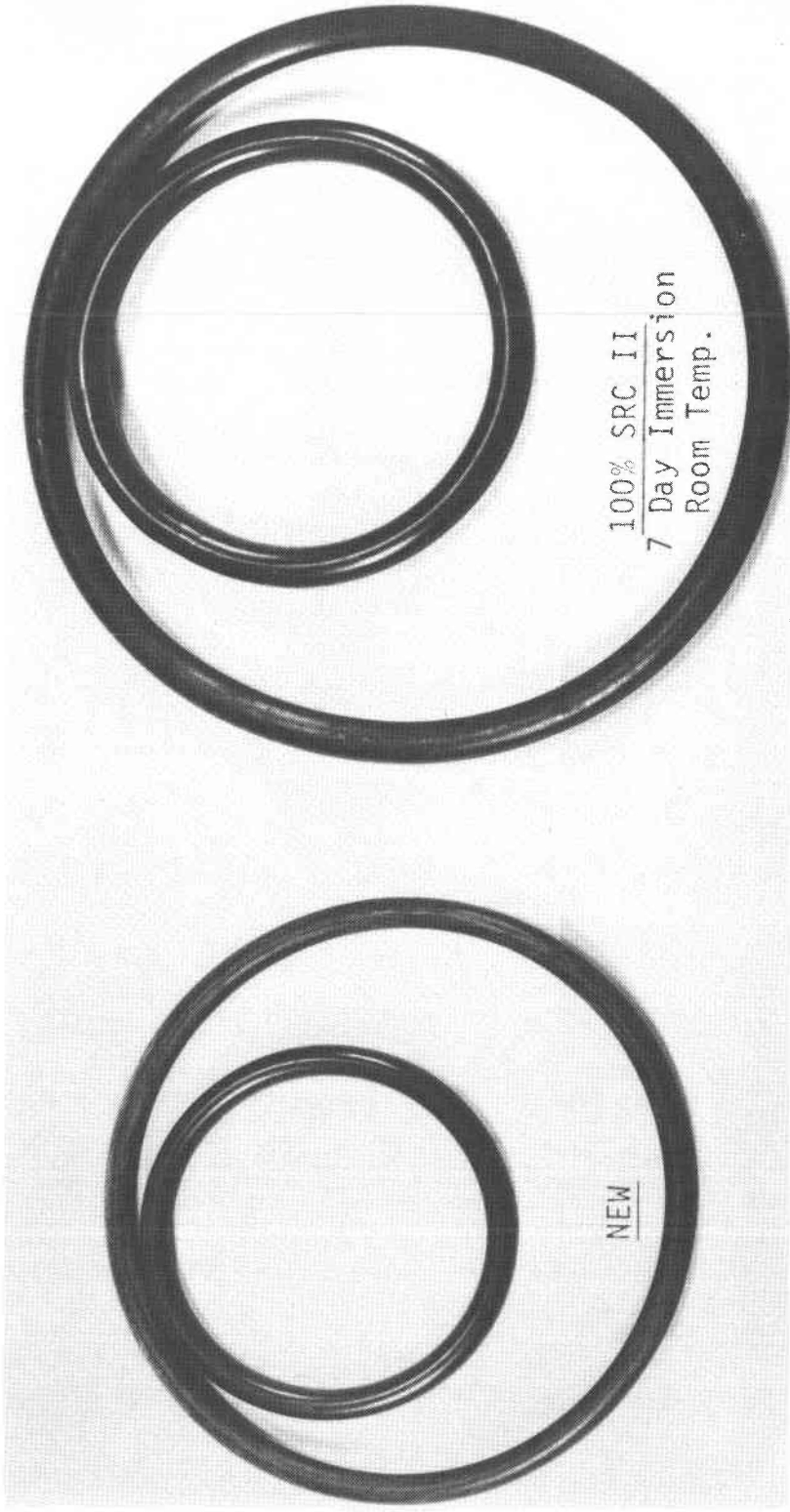


Figure 5. SRC-II Effect on Fuel Hose Compared with No. 2 Diesel.



FUEL SYSTEM "O" RINGS

- 10-328000-220
- 10-328000-209

Figure 6. Swelling of "O" rings with SRC II

## MULTIFUEL CAPABILITY OF MODIFIED DIESEL ENGINES

R. Kamo  
Cummins Engine Company, Inc.

T. Nakagaki  
Komatsu, Ltd.

T. Yamada  
Yanmar Diesel, Ltd.

The open chamber, prechamber, and spark assisted (prechamber) diesel engines with varying degrees of insulation were investigated for multifuel capability and emissions characteristics. The degree of engine insulation was achieved by operating the conventional water-cooled engine uncooled. Engine performance in terms of brake specific fuel consumption, rate of combustion pressure rise, and cold start was determined. Emissions measurements covered smoke, NO<sub>x</sub>, CO, UHC, and particulates. In general, the increasing degree of engine insulation improved the ability of the modified diesel to burn lower grade fuels such as coal-derived fuel oil, shale oil, and methanol without affecting engine performance and emissions. The spark assisted diesel improved operating characteristics, especially for alcohol fuels. Cold start will be a problem for all the engines tested and an intake manifold burner may be necessary for the adiabatic case and the spark assisted case. Increasing insulation to provide higher operating temperature offers best improvement for SRC-II combustion. In fact, the spark assisted adiabatic diesel with intake heater for cold start may be the best combination for diesel multifuel capability.

## MULTIFUEL CAPABILITY OF MODIFIED DIESEL ENGINES

### Introduction

Heat engines capable of burning all grades and types of alternative fuels are essential, as the supply of conventional petroleum-based fuels continues to dwindle all over the world. Politically and technically, the U.S. must develop heat engines capable of burning alternative fuels, such as coal-derived fuel oils, shale oil, and other lower grade residual fuel oils. The diesel engine, or the compression ignition engine, is still believed to be one of the primary heat engines capable of meeting this challenge.

However, it may be necessary to modify the existing diesel engine to provide the necessary requirement to ignite and burn the alternative fuels. Emissions and other future sociability goals must be met in order for the engine to be accepted. New materials, ignition sources, and novel injection systems should be investigated to determine their respective merits for adaptation in the diesel engine.

The uncooled, waterless diesel, the waterless, insulated adiabatic diesel, the spark assisted, and the dual fuel injection approach are just some of the recent advancements in the diesel engine technology which may satisfy the performance and emissions goals with alternative fuels.

### Technical Considerations

The diesel or the compression ignition engine today is divided into two main combustion chamber configurations; namely, direct injection engine and indirect injection or the prechamber diesel engine. These engines are predominantly four-stroke cycle except for the large slower speed stationary and marine engines, of which some are of two-

stroke design. In the conventional diesel, the prechamber engine design is usually lower in emission but higher in fuel consumption when compared to the direct injection design.

In burning lower grade fuels, the most important fuel properties are the cetane numbers. Lower cetane numbers usually imply poorer ignition qualities and lower ignition delays. In a compression ignition fuel injected engine, the long ignition delays are responsible for the sudden combustion of large quantity of already injected fuel. This combustion is accompanied by high pressure rise rate in the combustion chamber with subsequent higher engine noise levels. Continued engine operation under those conditions will result in premature engine failure.

There is a number of cetane improvers. However, the most simple and direct method of improving cetane number or achieving shorter ignition delays is through addition of heat or energy in the form of a spark, or early combustion of a small quantity of conventional fuels. The hot waterless and insulated adiabatic engine will also provide a hotter environment for improved combustion qualities.

#### The Uncooled Adiabatic Engine Concept

During the course of developing the insulated ceramic adiabatic engine, the waterless uncooled engine came as a spin-off from the high temperature lubrication investigation. Figure 1 shows the Cummins NTC-400 engine capable of pulling full speed and load without a water-cooling system. This means a simpler, lighter, smaller and lower cost engine installation. It should be emphasized that air cooling is also unnecessary. Only advanced materials, coatings and lubricants are used. Figure 2 shows the early stages of thermal barrier plasma sprayed piston (1) that failed, and Figure 3 shows a successful two-layered thermal barrier liner which was plasma sprayed. The thicker



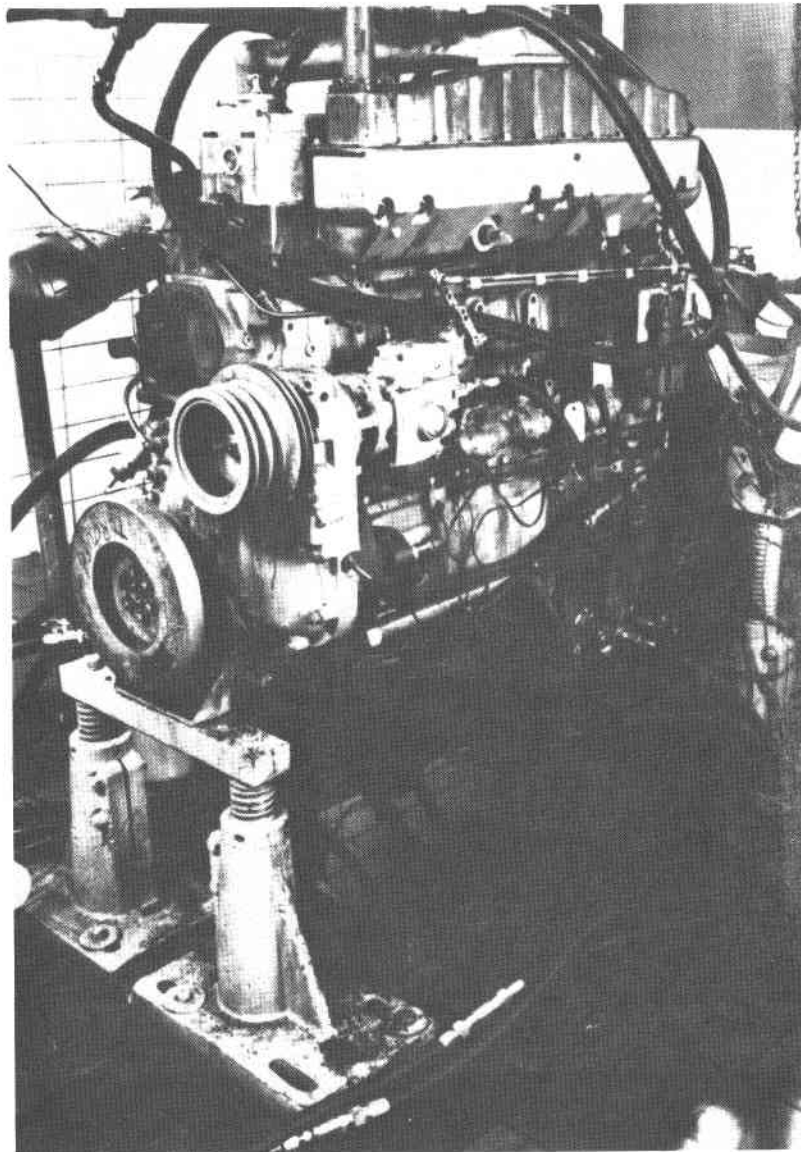


FIG. 1 - CUMMINS UNCOOLED NTC-400 ENGINE

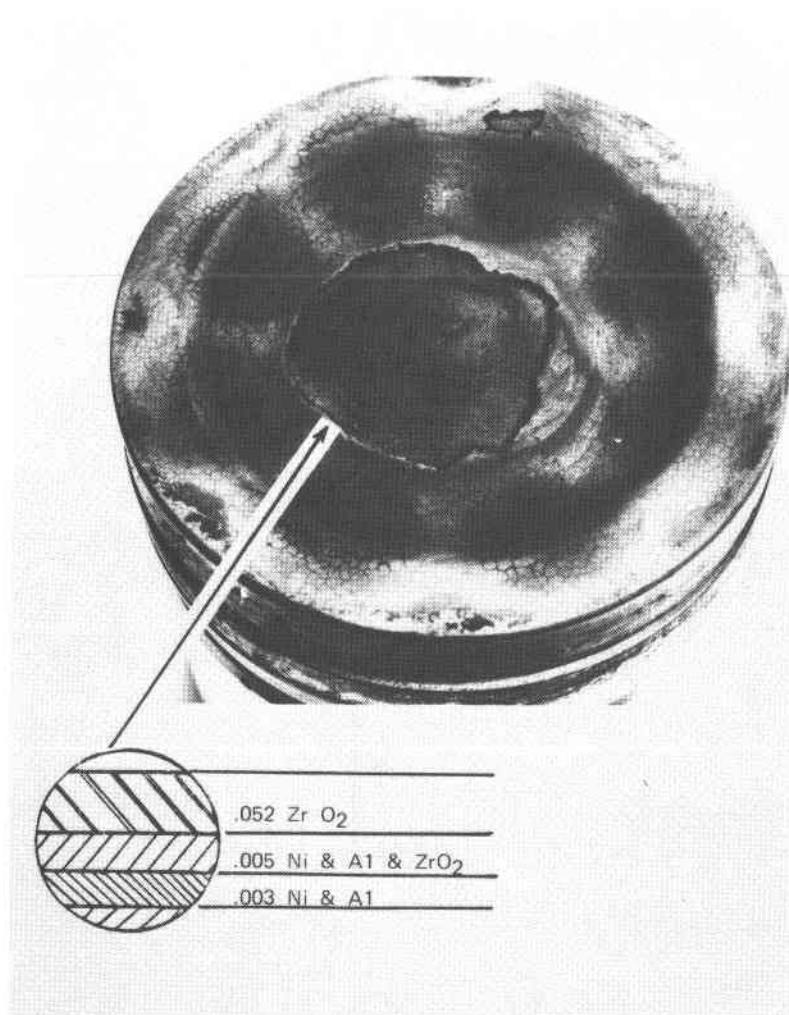


FIG. 2 - ZIRCONIA COATED PISTON SHOWS FLAKING OF CERAMIC COATING IN CENTRAL REGION OF PISTON CROWN

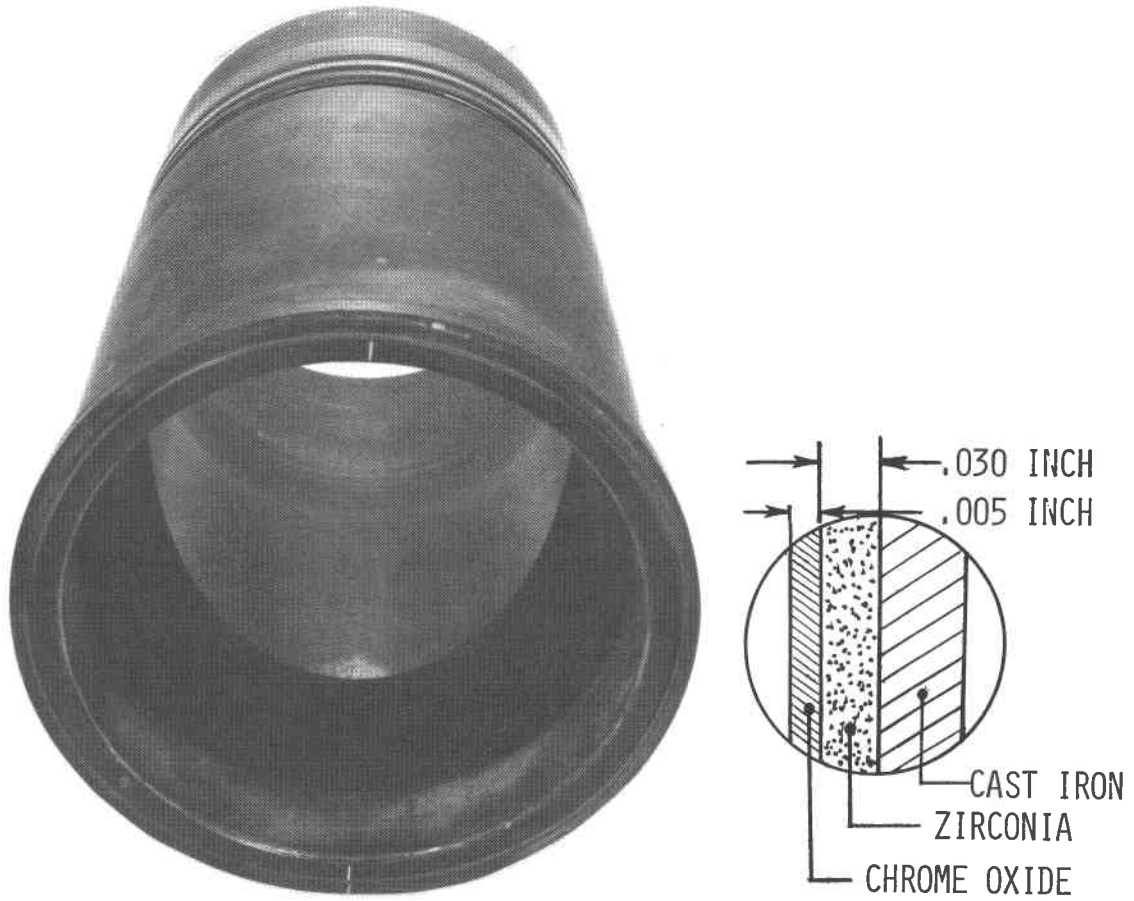


FIG. 3 - ZIRCONIA/CHROME OXIDE COATED CYLINDER LINER

zirconia layer provided the thermal barrier coating and the thin, hard outside chrome oxide layer provided the wear surface.

The fully adiabatic insulated diesel engine combustion chamber is built up with ceramic composite engine components. Figure 4 shows the cross-section of the basic adiabatic engine. The cylinder liners, cylinder heads, exhaust and intake ports, pistons, and engine manifolds are basically built up with partially stabilized zirconia and steel composite design. The resultant high temperature exhaust gases are then passed through the turbocharger turbine and the low pressure free power turbine. The free power turbine is geared to the crankshaft whereby the extracted exhaust energy is converted to mechanical energy to the crankshaft with resultant high engine thermal efficiency (2).

The insulated waterless engine provides significantly higher combustion chamber surface temperature when compared to the conventional water-cooled counterpart. Figure 5 shows the isotherm for a waterless silicon nitride cylinder liner. At the top ring reversal point, the surface temperature exceeds 1000°F. In the conventional water-cooled case, the surface temperature is about 375°F. The hotter surface temperature in the combustion chamber can now shorten the ignition delay of the lower cetane grade fuels considerably and avoid the undesired diesel knock. Thus, the "red-hot" diesel can provide good ignition qualities to the lower grade fuel while achieving outstanding thermal efficiency.

#### Objective of Investigation

The expected improvements in ignition qualities and thermal efficiencies of the uncooled adiabatic engine were shown in the previous section. What influence the hot chamber has on the emission is still unknown, especially with respect to particulates.

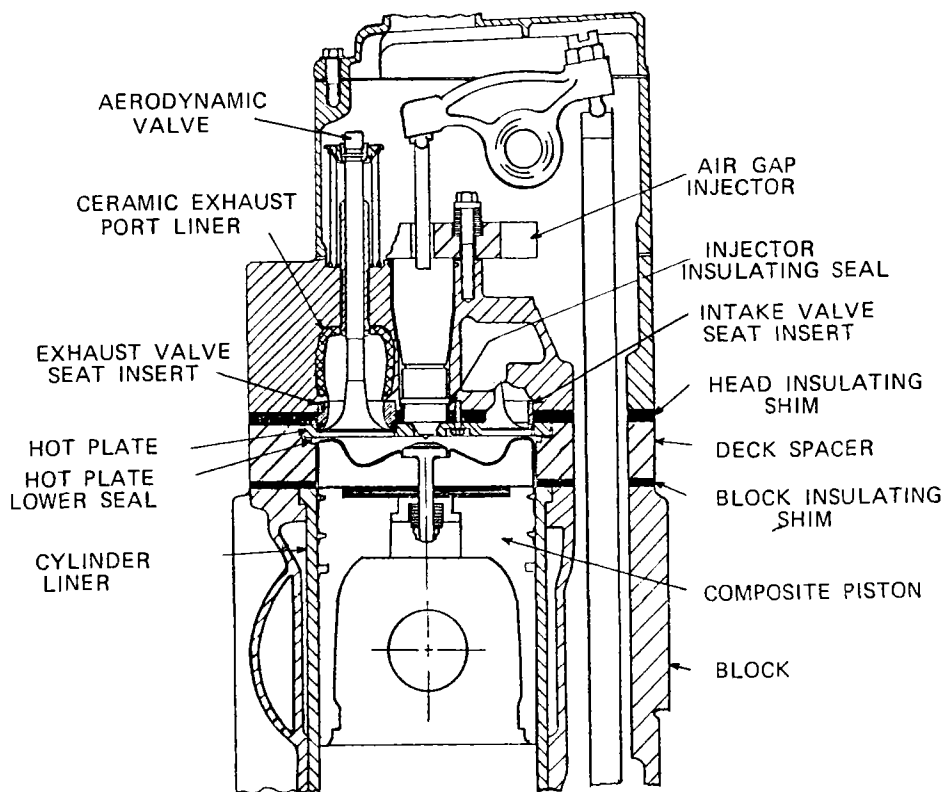


Fig.4-Cross section of Cummins basic adiabatic (insulated) diesel engine

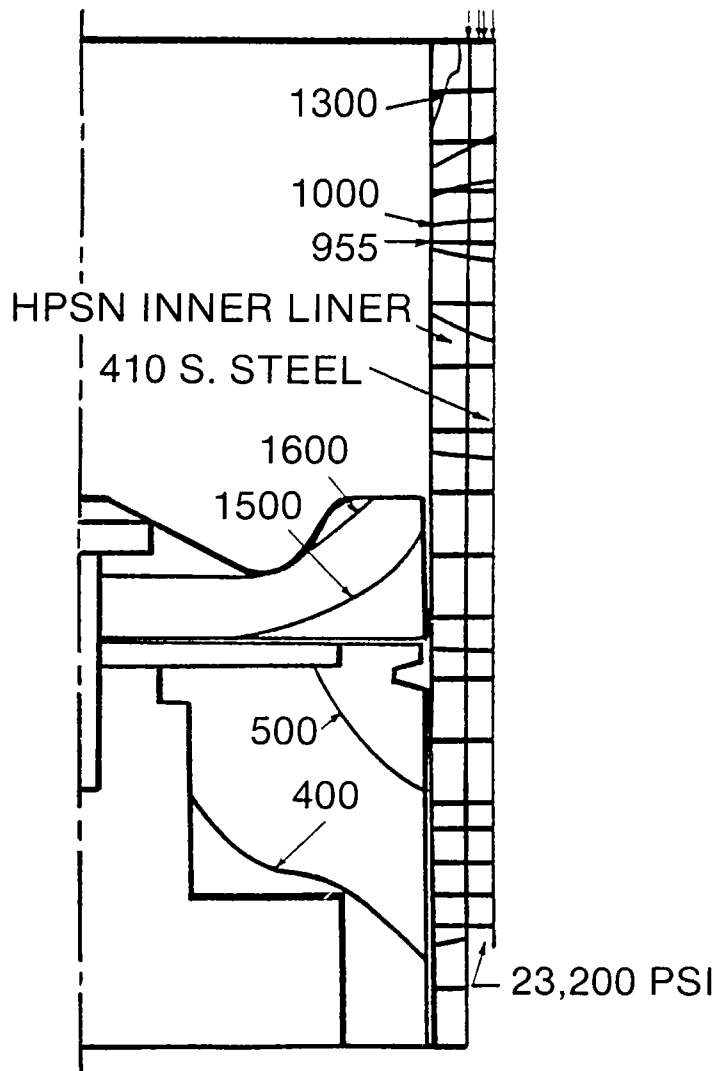


FIG. 5 - TEMPERATURE PREDICTION FOR HPSN COMPOSITE LINER

Thus, the purpose of this study was to determine the ignition qualities, performance, emissions, and noise characteristics of the modified direct injection and indirect injection diesel engine when operated on coal-derived fuel oil (SRC-II), shale oil, and other lower grade fuels. The engine modification includes spark assist, dual injection, waterless uncooled, and waterless adiabatic designs. Figure 6 shows the main combustion chamber configurations in the conventional water-cooler, waterless uncooled, and waterless adiabatic designs.

#### Fuel Investigated

This study is still in the early stages of investigation, thus all the fuels were not tested. The fuels that were tested are the conventional No. 2 diesel fuel (house fuel), SRC-II coal-derived fuel oil, and shale oil. Their properties are shown in Table 1 below.

Note in particular the aromatic content, the specific gravity, and the heating value of the SRC-II fuel oil when compared to petroleum base fuels.

#### Data Obtained

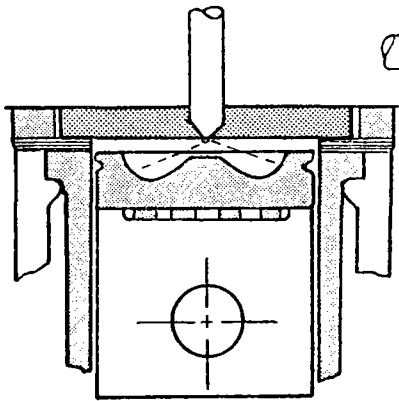
The investigation reported herein is mainly performance and emissions oriented. No long duration operation of the engine was contemplated; thus, erosion, corrosion and deposit data cannot be expected except for what was observed after each test. In addition to the usual engine data gathered in any good diesel test procedure, the following data were gathered:

1. Engine Performance Map
  - . BSFC
  - . BMEP
  - . Engine Speed

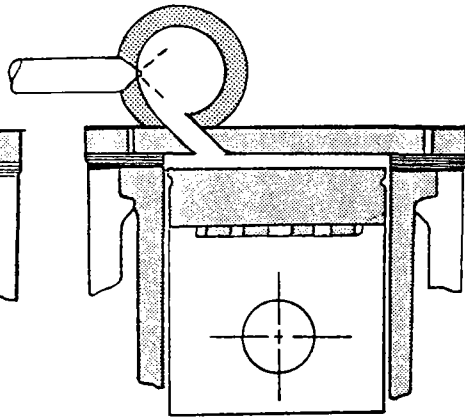
TABLE I  
COMPARISON DIESEL Vs. SYNTHETIC FUELS

FUEL PROPERTY	DIESEL FUEL	SRC II MIDDLE DISTILATE	SHALE
<b>PHYSICAL AND CHEMICAL PROPERTIES</b>			
ENERGYCONTENT BTU/LB GROSS	19,200	17,102	19,365
GRAVITY 60°F.	33	12.4	38.2
SPECIFIC GRAVITY 60/60 °F	.86	.983	.834
VISCOSITY	2.85	3.87	2.72
POUR POINT	-35	-65	- 5
FLASH POINT	167	175	178
CETANE NO	45-50	22	45
HYDROGEN/CARBON	1.75	1.24	1.86
- AROMATICS	36	79.1	30.5
- SATURATES	62	14.4	67.7
- OLEFINS	20	6.5	1.8
<b>ELEMENTAL ANALYSIS</b>			
- SULFUR	.29	.31	.07
- NITROGEN	.2-.4	1.0	.024

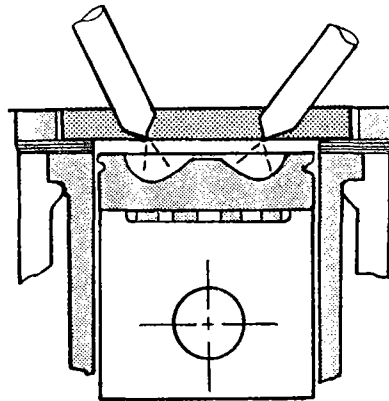




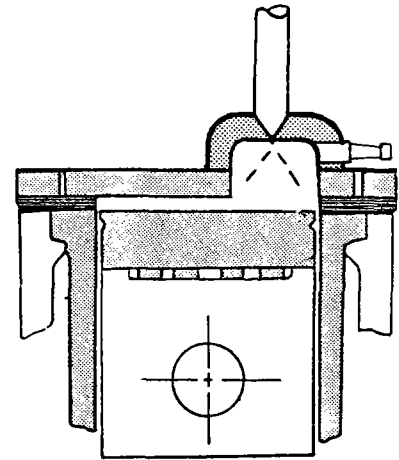
**DIRECT  
INJECTION**



**PRECHAMBER**



**DUAL FUEL  
INJECTION**



**SPARK ASSISTED  
DIESEL**

FIG. 6 - CUMMINS ALTERNATIVE FUELS PROGRAM

2. Emissions
  - . NOx
  - . Unburned Hydrocarbon
  - . CO
  - . Smoke
  - . Particulate
3. Operating Characteristics
  - . Combustion Pressure Diagram
  - . Noise
  - . Intake Air Temperatures and Pressures
  - . Exhaust Temperatures and Pressures
4. Mechanical
  - . Wear
  - . Deposits
  - . Fouling and Corrosion
5. Startability
  - . Determine Time to Sustained Idling Speed  
at Room Temperature

#### Instrumentation

Figure 7 shows schematically a typical single cylinder test set-up. The direct injection and the indirect injection tests were made on a single cylinder engine. The spark assisted diesel data were obtained on a multicylinder version. In the uncooled and the adiabatic engine tests, the cooling water system is unnecessary. Blending of SRC-II fuel with standard No. 2 diesel fuel was necessary in order to operate in the standard cooled engine. The blending instrumentation is also shown on the right side of Figure 7.

One instrument still in the infancy stage is the particulate sampling equipment. In order to assure consistency in data, Cummins,

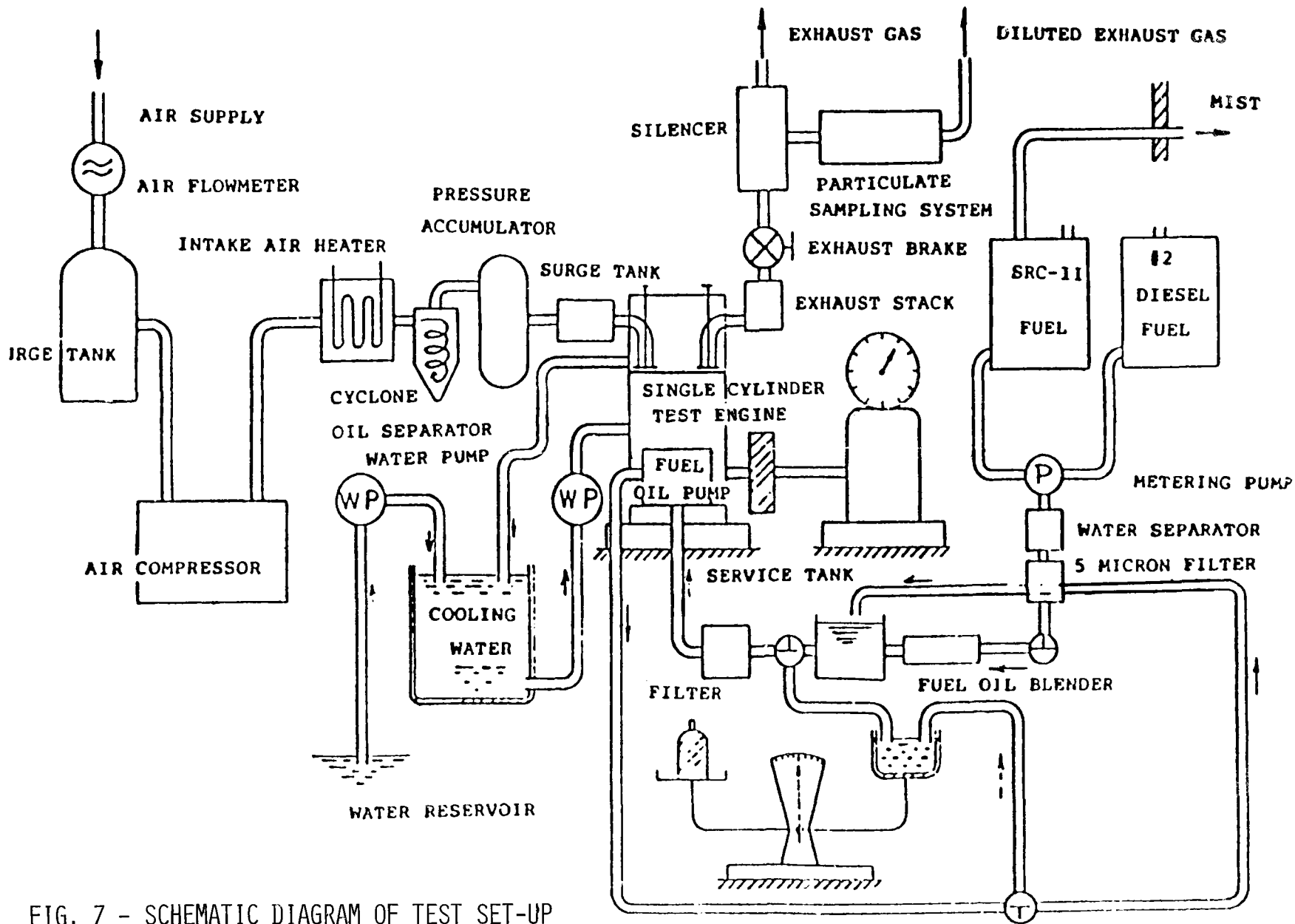


FIG. 7 - SCHEMATIC DIAGRAM OF TEST SET-UP

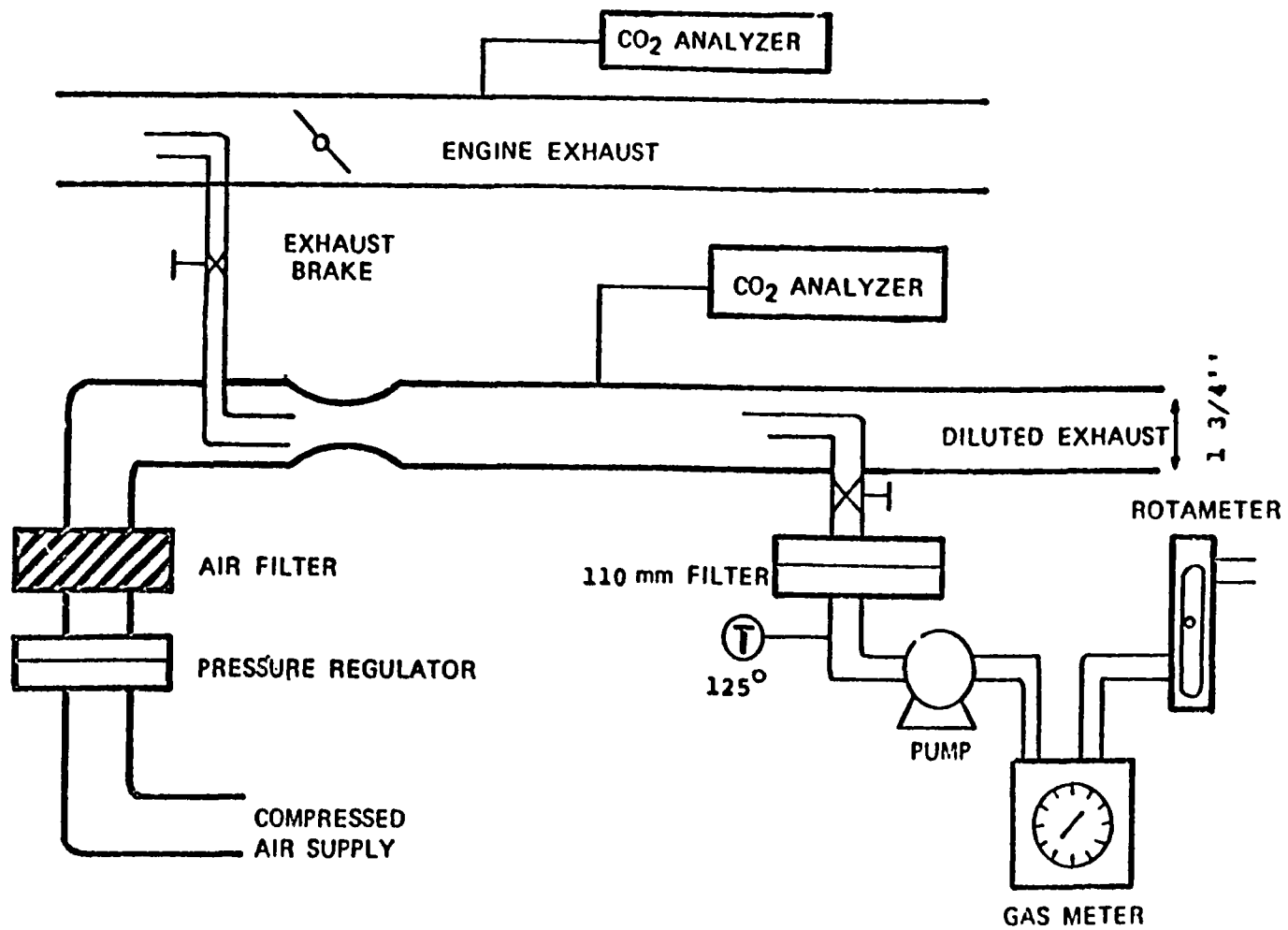


FIG. 8 - PARTICULATE SAMPLING SYSTEM

Yanmar, and Komatsu all used the EPA-approved particulate sampling system. The system is shown in Figure 8 indicating the dilution procedure. The sampling system is based on McDonald's design (3).

### Results of Investigation

#### Direct Injection Diesel

The direct injection single cylinder engine test was conducted by the Cummins Engine Company. Table II outlines the specifications of the engine tested. Figure 9 shows the laboratory set-up of the single cylinder engine in the waterless uncooled form as witnessed by the absence of the water pump. The particulate sampling device is photographed on the right side of Figure 9.

Figure 10 shows the improvement in ignition delay as a function of load for diesel fuel and SRC-II fuel. The shorter ignition delay of the diesel fuel in an uncooled engine is shown in solid square.

Figure 11 shows the trade-off between fuel consumption (abscissa) and emissions (NOx) for diesel fuel, shale fuel, DFM-2, and SRC-II fuel oil. The shale oil indicates the best BSFC-NOx trade-off. The SRC-II fuel, although indicating 10% worse fuel consumption, must be remembered that its heating value is 10% less on a mass basis. On a thermal efficiency basis, the SRC NOx trade-off should be no worse than the shale or diesel fuel oil.

Figures 12 and 13 show the BSFC fuel consumption and BSNOx emissions respectively as a function of engine load for various fuels and engine configurations. In Figure 12, the conventional diesel fuel, if it possessed 10% less heating value, would be depicted in the dotted line. The dotted line again compares similarly with the SRC-II data. Combustion of shale oil DFM-2 presents no problems and consistently shows slightly better fuel consumption and lower emissions. The cooled engine shows slightly better emissions than the uncooled up to rated

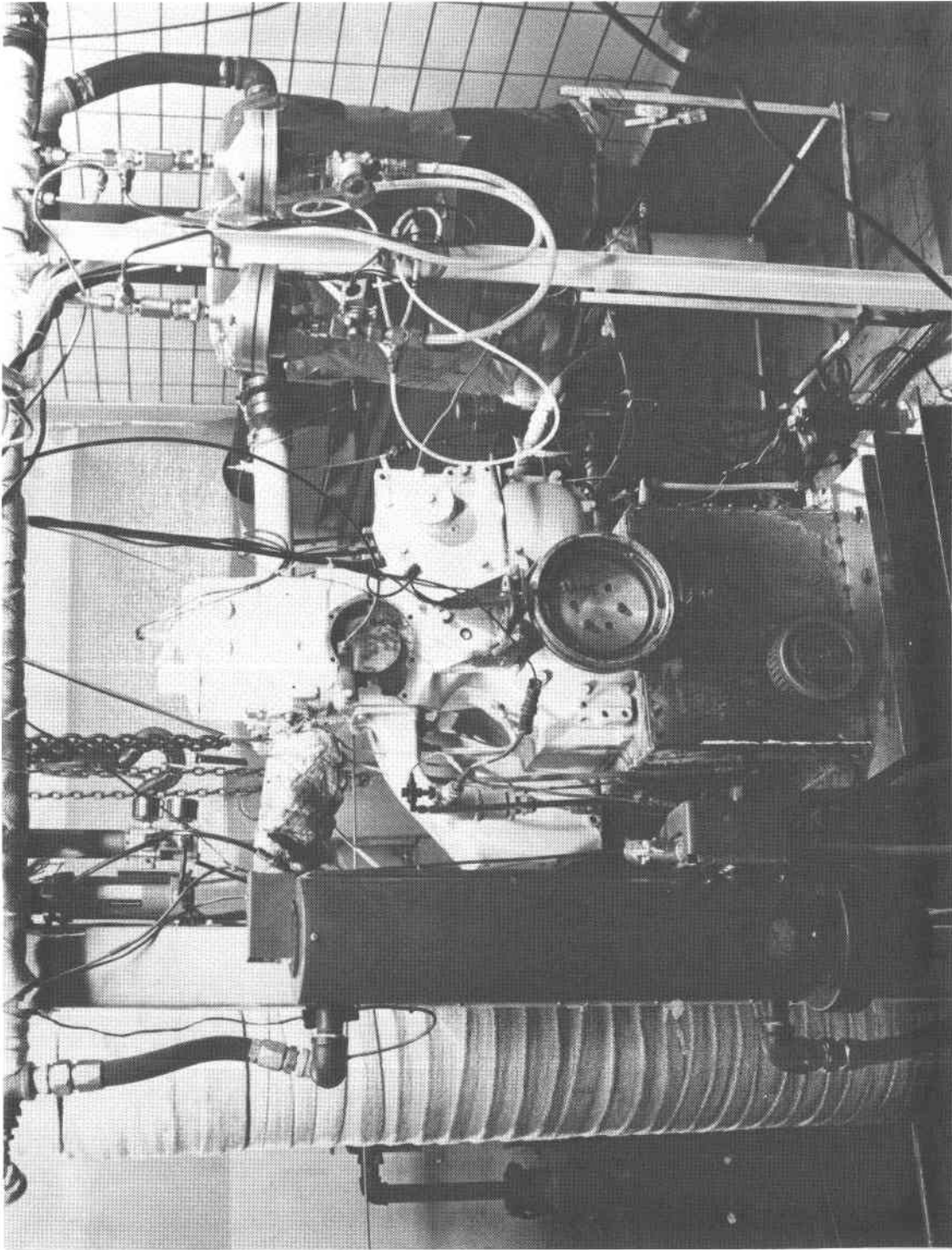


FIG. 9 - DIRECT INJECTION SINGLE CYLINDER UNCOOLED ENGINE WITH INSTRUMENTATION

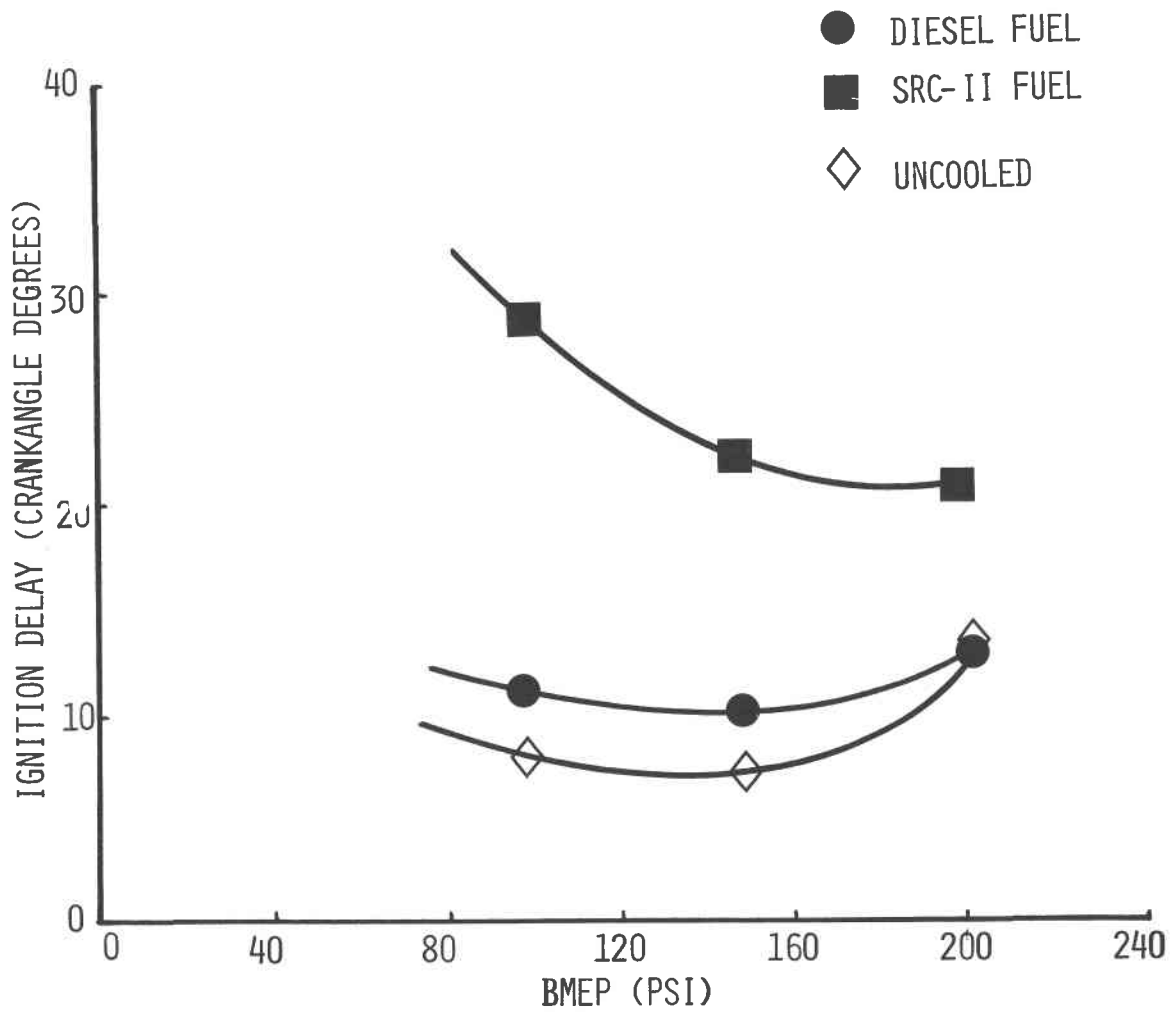


FIGURE 10.  
IGNITION DELAY Vs. BMEP  
1900 RPM .070 TIMING

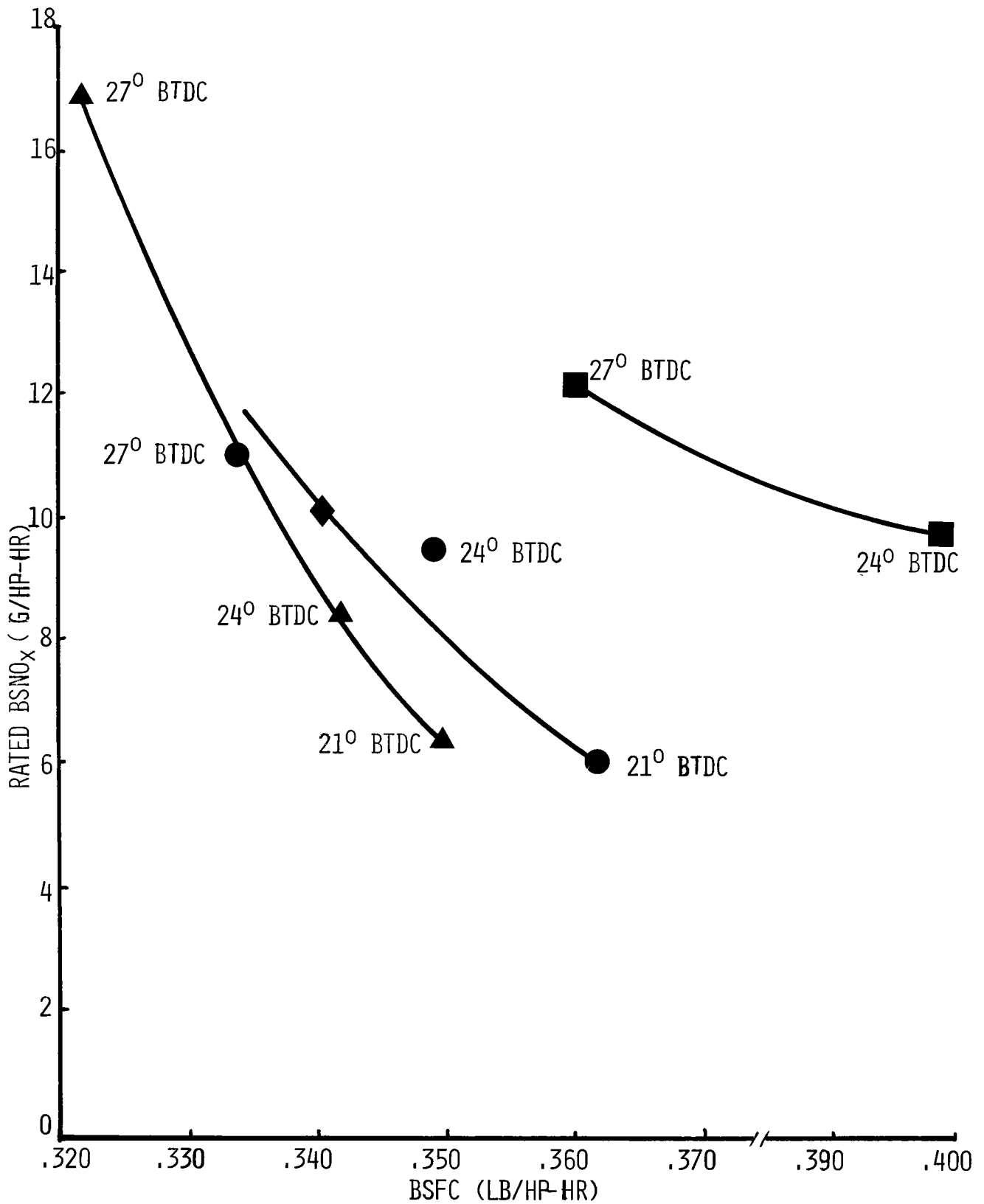


FIGURE 11. BSFC Vs. BSNO<sub>x</sub> RATED SPEED (1900 RPM ) AND LOAD



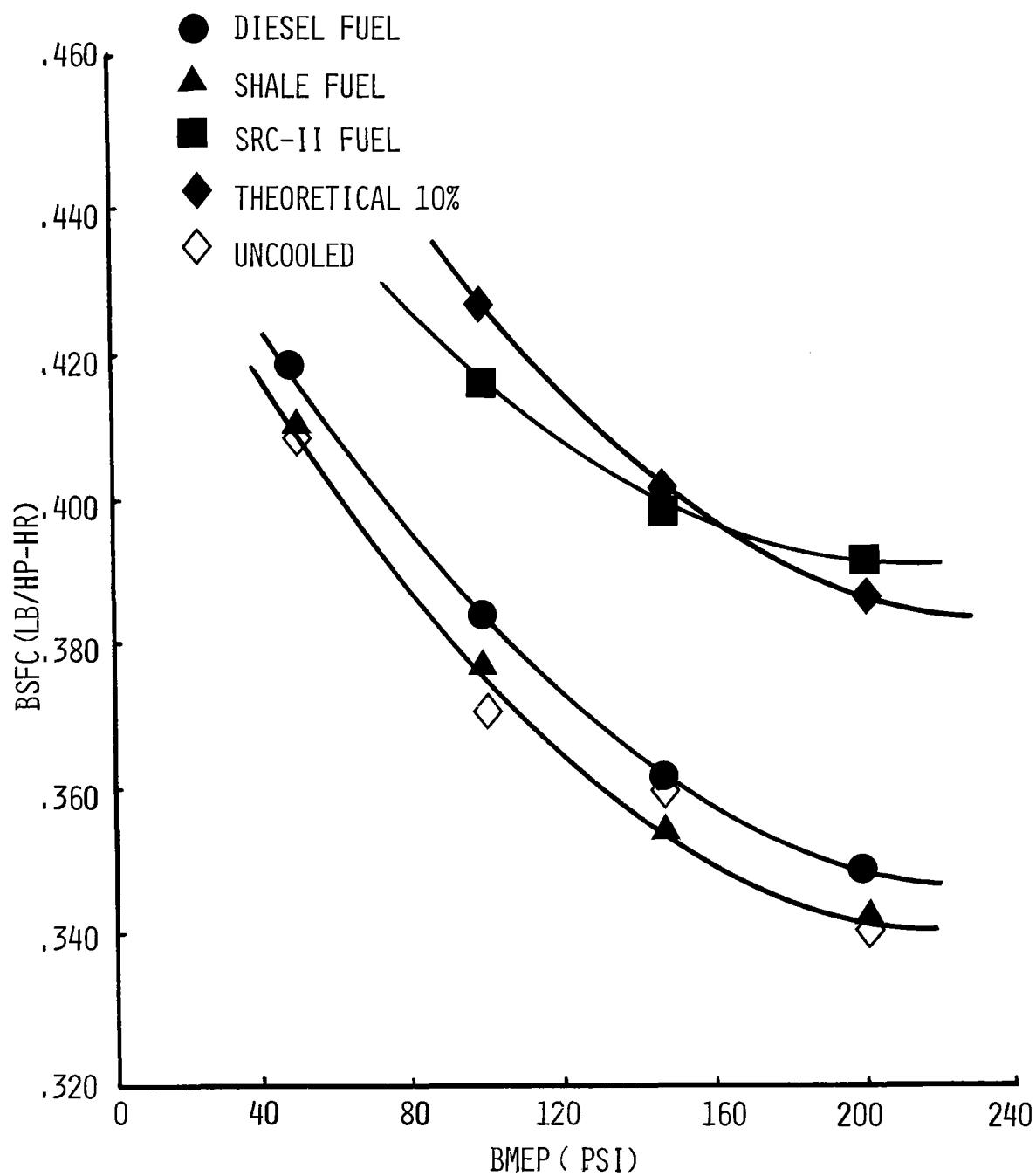


FIGURE 12. BSNO<sub>x</sub> Vs. BMEP COOLED Vs. UNCOOLED ENGINE DIESEL FUEL  
1900 RPM

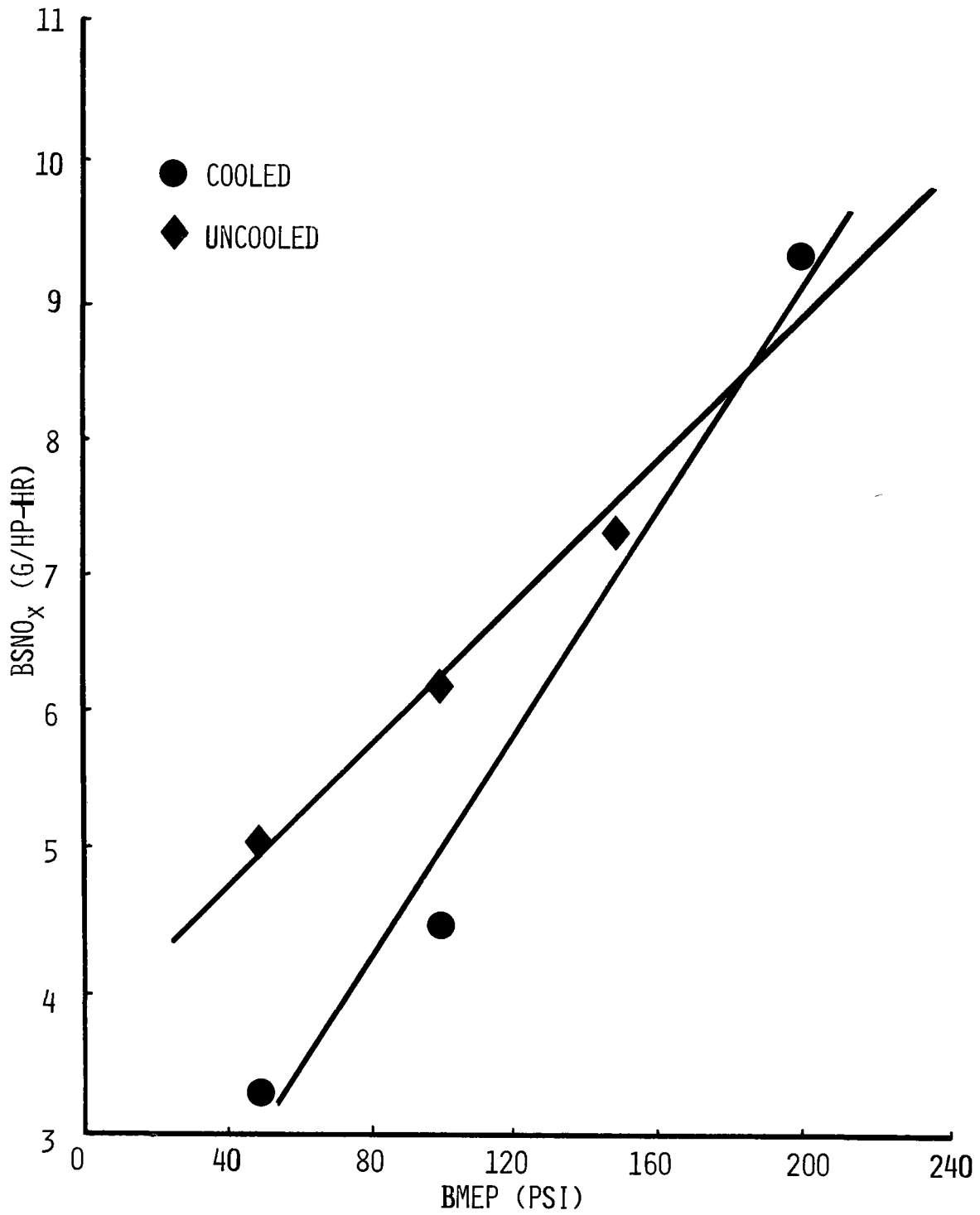


FIGURE 13. EFFICIENCY COMPARISON HOUSE FUEL Vs. SYNTHETICS 1900 RPM  
.085 STATIC TIMING

load. However, the uncooled engine has a slight edge on the fuel consumption.

Figure 14 shows the particulates plotted against load. In general, for diesel fuel and shale fuel, the particulates are consistent and drops slightly with load. On the other hand, the SRC-II fuel shows a rapid increase in particulates with increasing load. No data are available at the time of writing for the uncooled engine.

Table II. Direct Injection Diesel  
Cummins Engine Co.

Engine Specifications:

Model	NH Series
Compression Ratio	15.0:1
Number of Cylinders	Single
Bore x Stroke	5.5 x 6.0
Engine Speed, Rated RPM	1900
BHP @ Rated	67 BHP @ 1900
Injection Timing	Variable
Adiabacity (Uncooled)	30%

Indirect Injection Diesel

The indirect injection diesel engine tests with SRC-II fuel were conducted by the Yanmar Diesel Co., Ltd. Table III outlines the specifications of the engine tested. Figure 15 shows the cross-section of the prechamber combustion chamber. It was not possible to operate this engine on 100% SRC-II fuel. Thus, the tests were conducted with various blends of SRC-II and No. 2 diesel fuel. Only the standard water-cooled version was tested for the indirect injection tests.

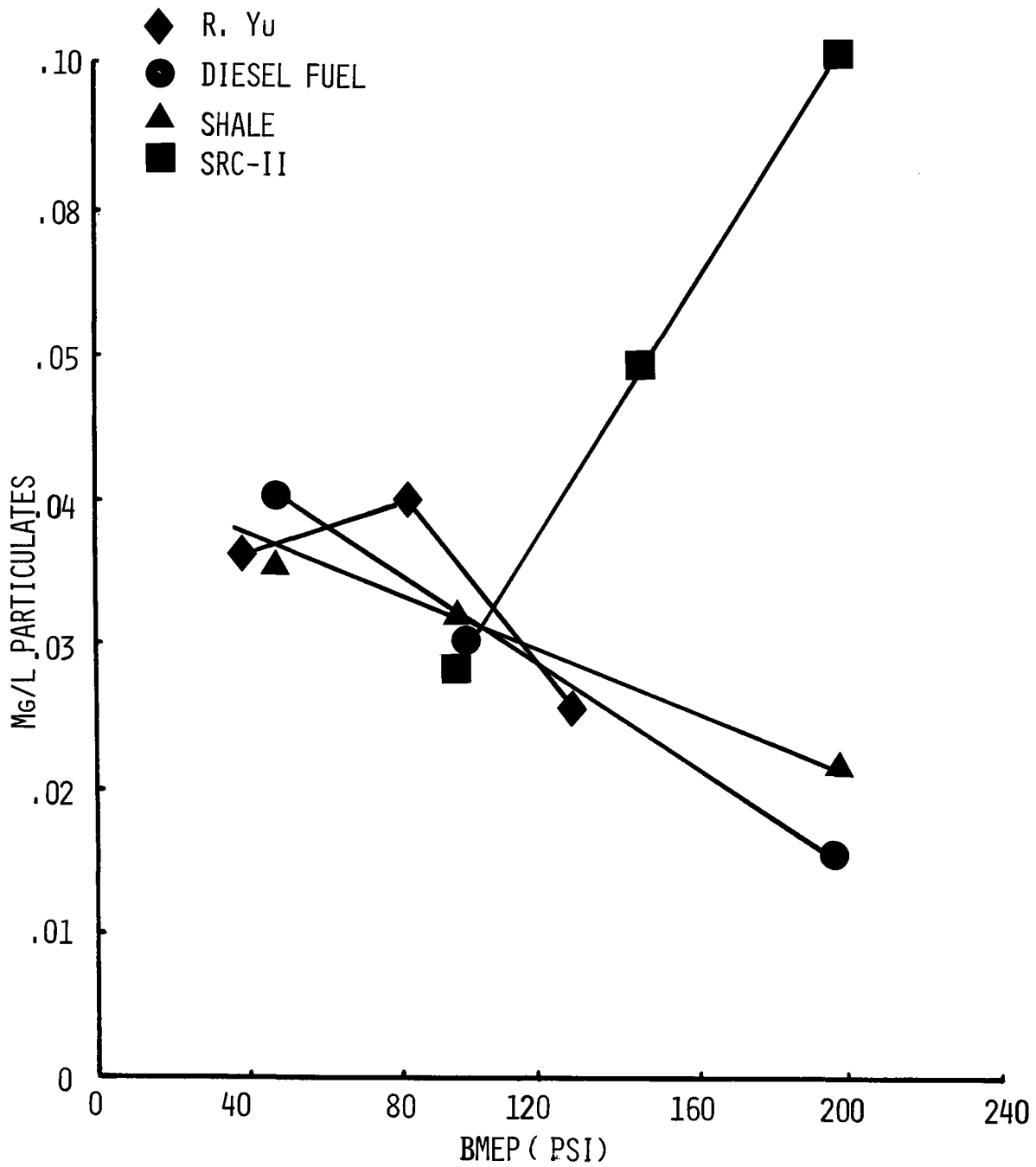


FIGURE 14. PARTICULATES Vs. BMEP

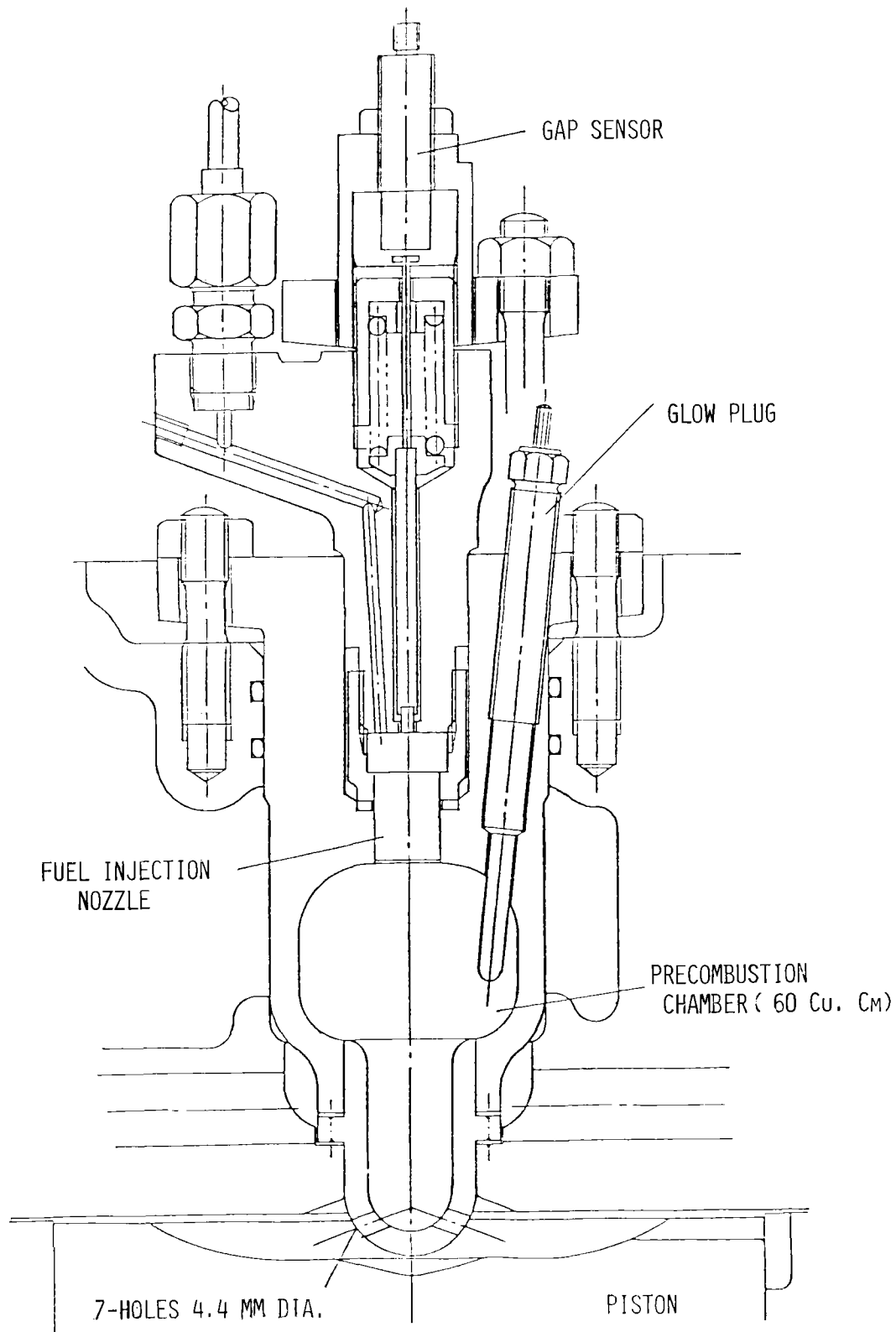


FIG. 15 - CROSS SECTION OF YANMAR DIESEL PRECHAMBER COMBUSTION CHAMBER

Figure 16 shows the operating range of SRC-II blended fuel for various load and speeds. Ninety percent (90%) SRC-II and 10% diesel fuel can only be operated at high loads and high speeds. Figure 17 shows the optimum injection timing as a function of engine speed for various blended SRC-II fuels at light and heavy load. The optimum timing converges with higher engine speed for various load and blended SRC-II fuel to a value of 19°BTC (before top center).

Figure 18 shows the combustion characteristics (BSFC, exhaust temperature, smoke, and Pmax) for various blends of SRC-II for 1200 and 1800 engine rpm as well as light and heavy loads. Table IV shows the emissions characteristics (BSNOx and BSHC) of the prechambered engine for various loads, speeds, and SRC-II blends. Figure 19 shows the change in the indicator diagram for various blends of SRC-fuel and loads. Again, it can be noted that the SRC-II fuel operates better at higher loads and speeds. The sudden rise in combustion pressures as shown in the top of Figure 19 is usually accompanied by high knocking noise level. In the early test phase, the injector nozzle tip broke off and piston and liner scuffing was noted.

Startability with SRC-II is also difficult. The following starting characteristics were observed at temperatures of 25 to 27 degrees centigrade:

26 vol. % SRC-II

Ignitable at the initial injection - same as for #2 diesel fuel.

49 vol. % SRC-II

Ignitable at the 5th or 6th injection.

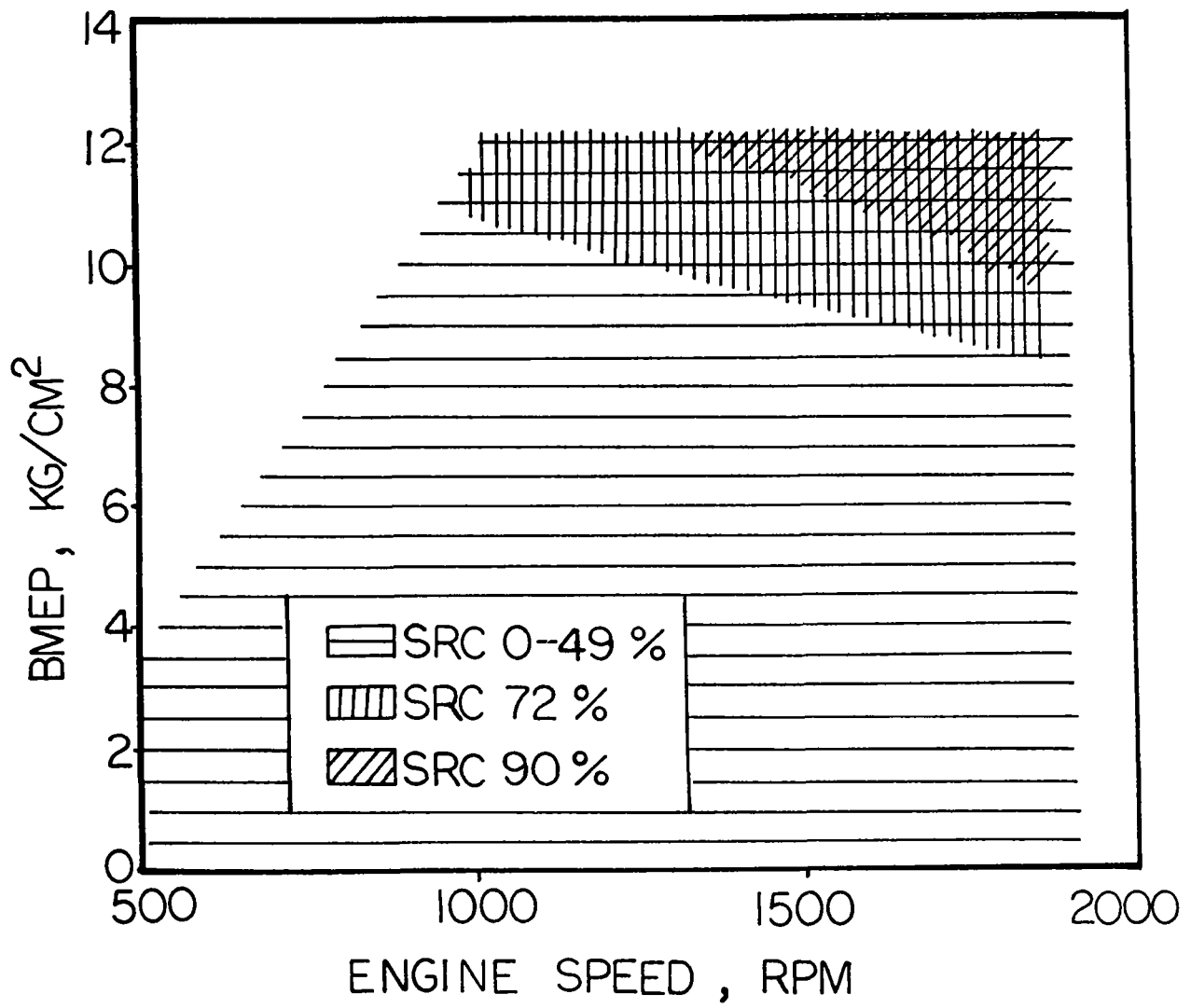


FIG. 16 - ENGINE OPERATING RANGE

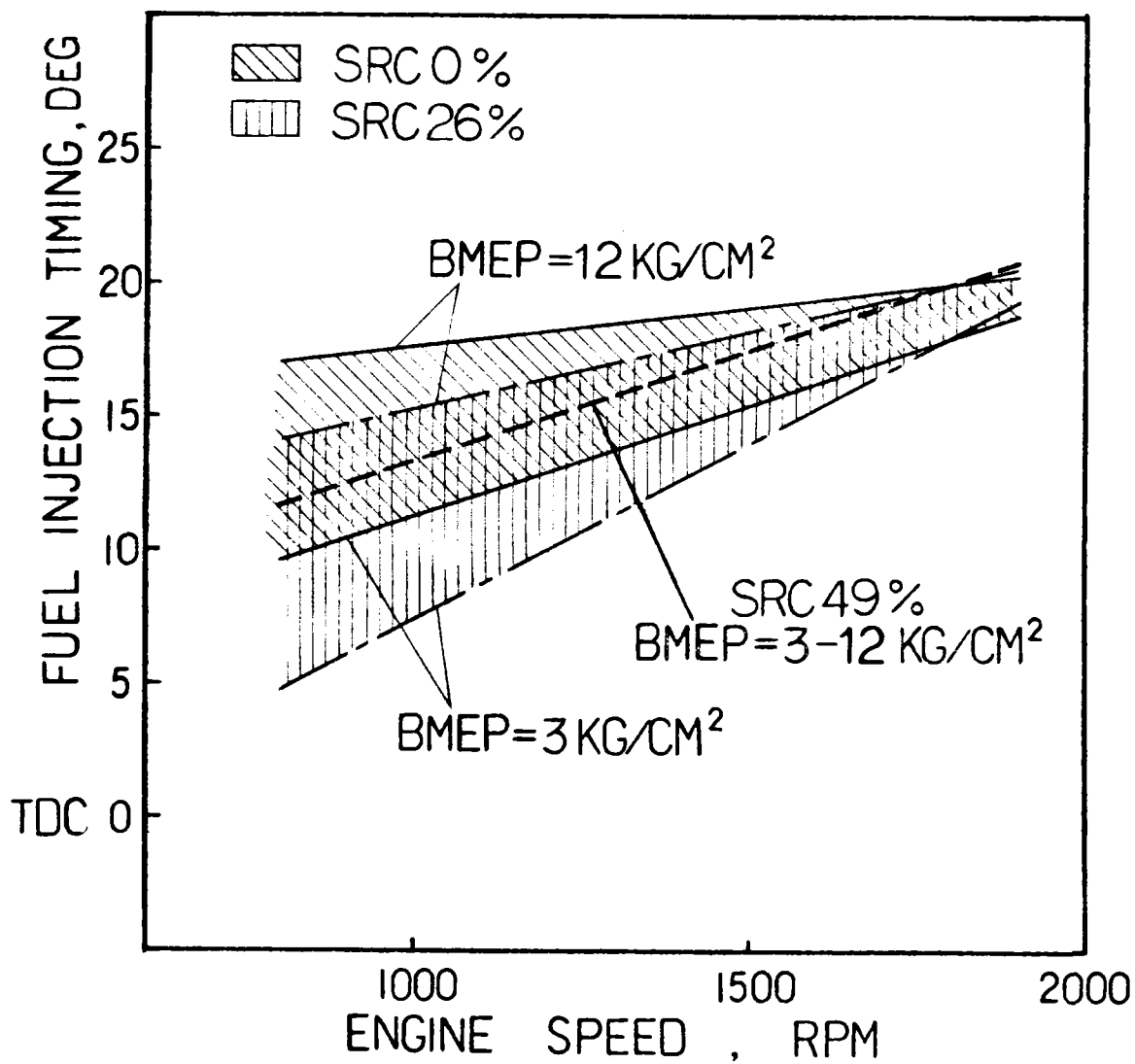


FIG.17 OPTIMUM INJECTION TIMING



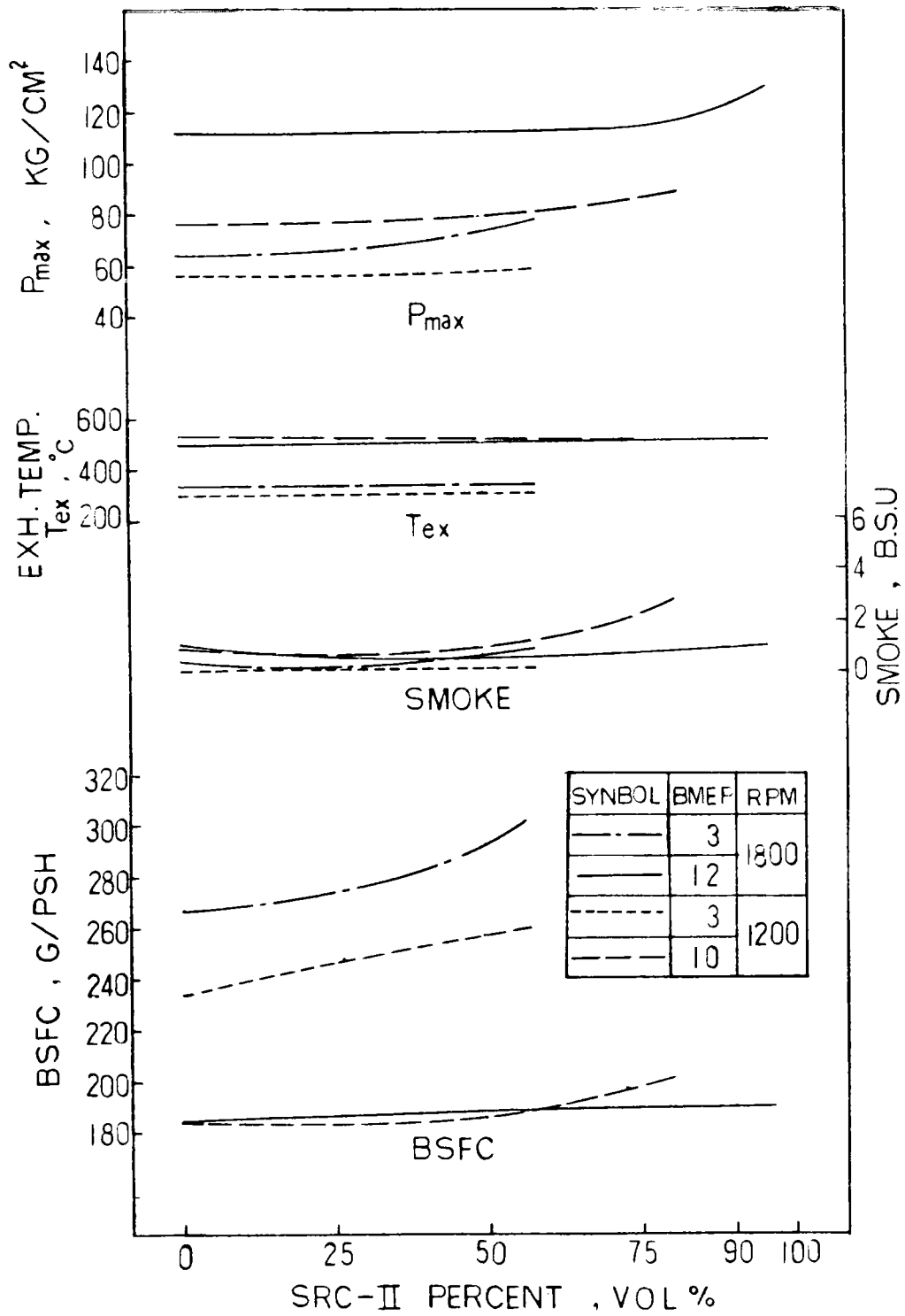


FIG. 18 - COMBUSTION CHARACTERISTICS

TABLE IV. EXHAUST EMISSIONS

(BSNO<sub>x</sub>/BSHC , G/PSH)

BMEP/ RPM	SRC-II VOL %				
	0	26	49	72	90
3/1200	6.2/0.2	11.3 /0.1	17.4 /0.2	—	—
10/1200	4.4 /0.1	4.4 /0.2	5.9 /0.1	6.3 /0.1	—
3/1800	8.3 /0.2	10.3/0.5	17.3 /0.9	—	—
12/1800	5.9 /0.4	6.6/0.3	7.8 /0.3	8.4 /0.2	9.6/0.1
13MODE	5.9 /0.6	7.1 /0.3	9.6 /1.0	—	—

BMEP , KG/CM<sup>2</sup>

TABLE VI. SUMMARY RESULT OF SPARK ASSISTED DIESEL COMPARED WITH CONVENTIONAL AND ADIABATIC ENGINE

ENGINE SPEED (RPM)	LOAD	CONVENTIONAL ENGINE*		SPARK ASSISTED ENGINE**		ADIABATIC ENGINE*	
		DIESEL FUEL (C.N. ≈ 55)	SRC-II (C.N. < 10)	SRC-II		DIESEL FUEL	SRC-II
				INJECTION TIMING			
				30°	22°		
2200 ~2500	HIGH MIDDLE LOW	OO		OO □	O △ □	OO	OO
1600 ~1800	HIGH MIDDLE LOW	OO		O △ □	□ □ □	OO	OO
1000	HIGH MIDDLE LOW	OO		□ □ □	□ □ □	OO	OO
IDLING		O		□	□	O	□
ROOM TEMP START- ABILITY	1 (SEC)	8				3	□

2-102

\* KOMATSU 1D105 ENGINE  
 \*\* KOMATSU 2D94 ENGINE  
 O NORMAL RUNNING  
 △ SEVERE KNOCKING  
 □ INOPERABLE  
 | DID NOT TEST

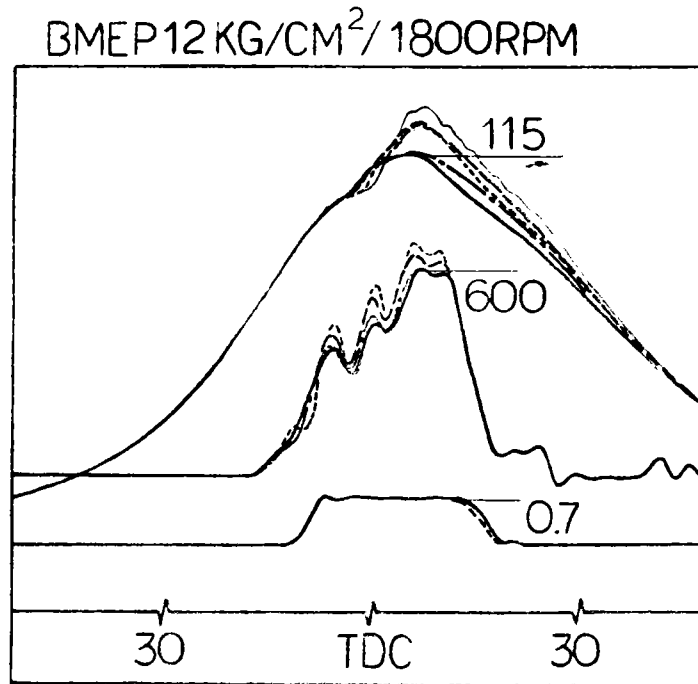
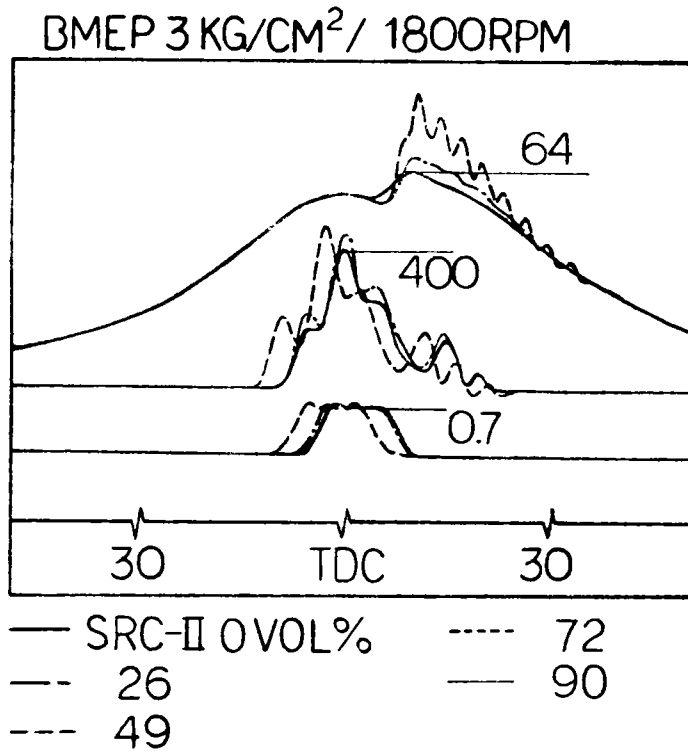


FIG. 19 CHANGES IN CYLINDER PRESSURE OSCILLOGRAM WITH INCREASE IN SRC-II CONTENT - 2

72 vol. % SRC-II

Ignitable by cranking after the use of a glow plug for 15 sec. but not sustained. A continued use of the glow plug was required to arrive at a sustained operation.

90 vol. % SRC-II

A sustained operation was achieved at the 2nd cranking after a 15 sec. use of the glow plug.

Table III. Prechamber (IDI) Diesel Engine  
Yanmar Diesel Ltd.

Engine Specifications:

Model	X1-150
Number of Cylinders	Three (3)
Bore x Stroke	150mm x 165mm
Compression Ratio	17:1
Adiabacity	
Injection Timing	
Prechamber Volume Ratio	
Fuel Injection Pressure	160 kg/cm <sup>2</sup>
Fuel Injection Nozzle	Pintle
Lube Oil	SAE #30 CD Class
PV Valve	11g kg/cm <sup>2</sup> x m/sec
Mean Piston Speed	9.9 m/sec
BMEP (1 MEP)	12.0 kg/cm <sup>2</sup> (15.0)
Rating	70 HP @ 180 RPM
Displacement	2.916 L

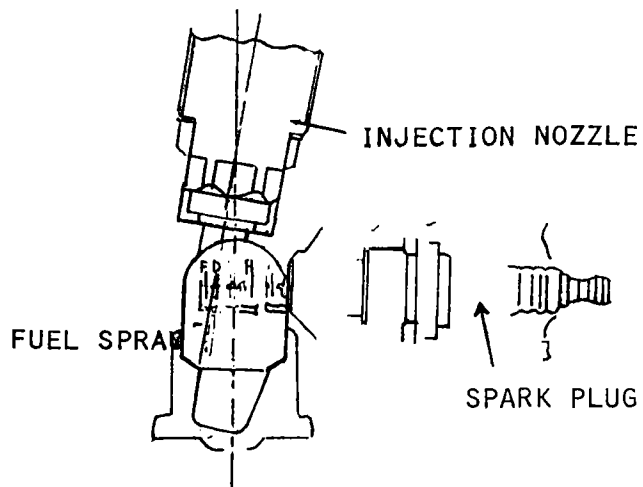
### Spark Assisted Diesel

The spark assisted diesel experiments with SRC-II fuel were conducted by Komatsu Ltd. Table V outlines the specification of the engine that was tested. The spark assisted engine made use of the prechamber version as shown in Figure 20. Figure 20 also shows the fuel injection period and the spark period of the engine under test. This engine was tested in the cooled version as well as the adiabatic form.

Figure 21 shows the operable range of the engine with and without spark assist when injecting SRC-II fuel oil. Again, the higher speeds and loads are conducive for SRC-II operating range. Table VI summarizes the result of spark assisted diesel compared with conventional and adiabatic engine with various fuels, loads, and speeds. The adiabatic engine with the hot combustion chamber offers the best operating range. Although spark assist does improve ignition quality, operation with SRC-II is difficult at best. However, for alcohol fuels, the spark assist is quite capable of operating over a wide range in spite of the low cetane number of alcohol fuels.

Figure 22 shows the combustion characteristics of the spark assisted diesel in terms of smoke, fuel consumption, maximum combustion pressure,  $P_m$ , and exhaust temperature. Again, the SRC-II fuel combustion is limited to the high load end. Figure 23 shows other important combustion characteristics of low cetane fuel in a conventional water-cooled, semi-insulated, and insulated combustion chamber. Conventional diesel fuel has the shortest ignition delay with consequent lowest combustion pressure rise rate,  $dp/d\theta$ .

Figure 24 shows the heat release rates for various engine configurations and fuels. With lower cetane fuels, the adiabatic engine shows more gradual heat release than the conventional engine. Figure 25 shows



INJECTION PERIOD ( $\approx 20^\circ$  C.A.)

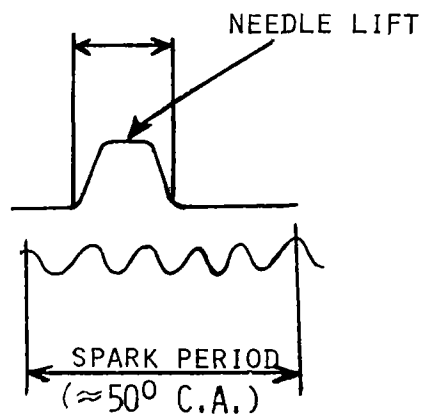


FIG. 20 - SPARK PLUG POSITION AND TIMING OF SPARK ASSISTED DIESEL

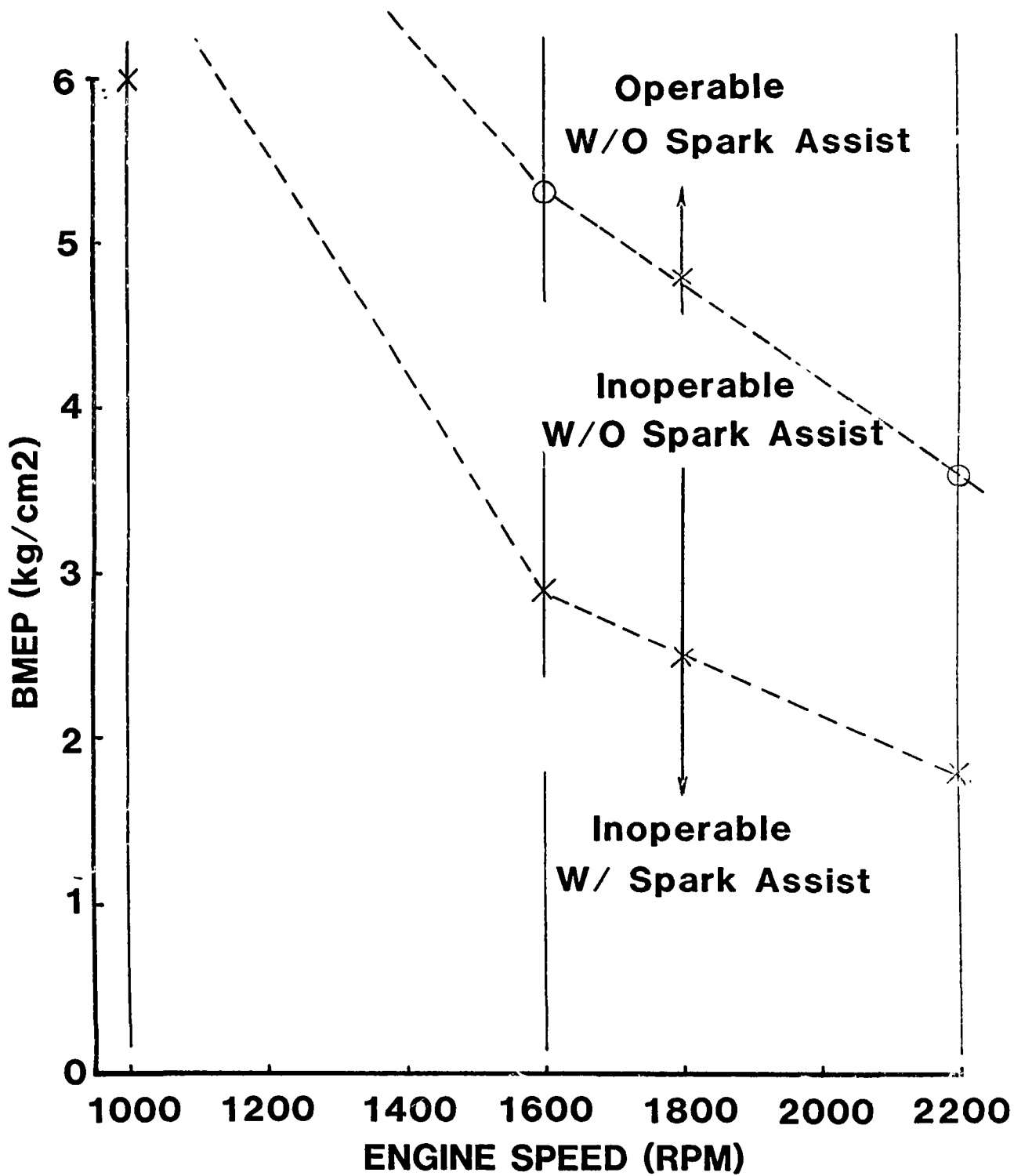


FIG. 21 - OPERATING RANGE OF SRC-II FUEL OIL WITH SPARK ASSISTED IGNITION



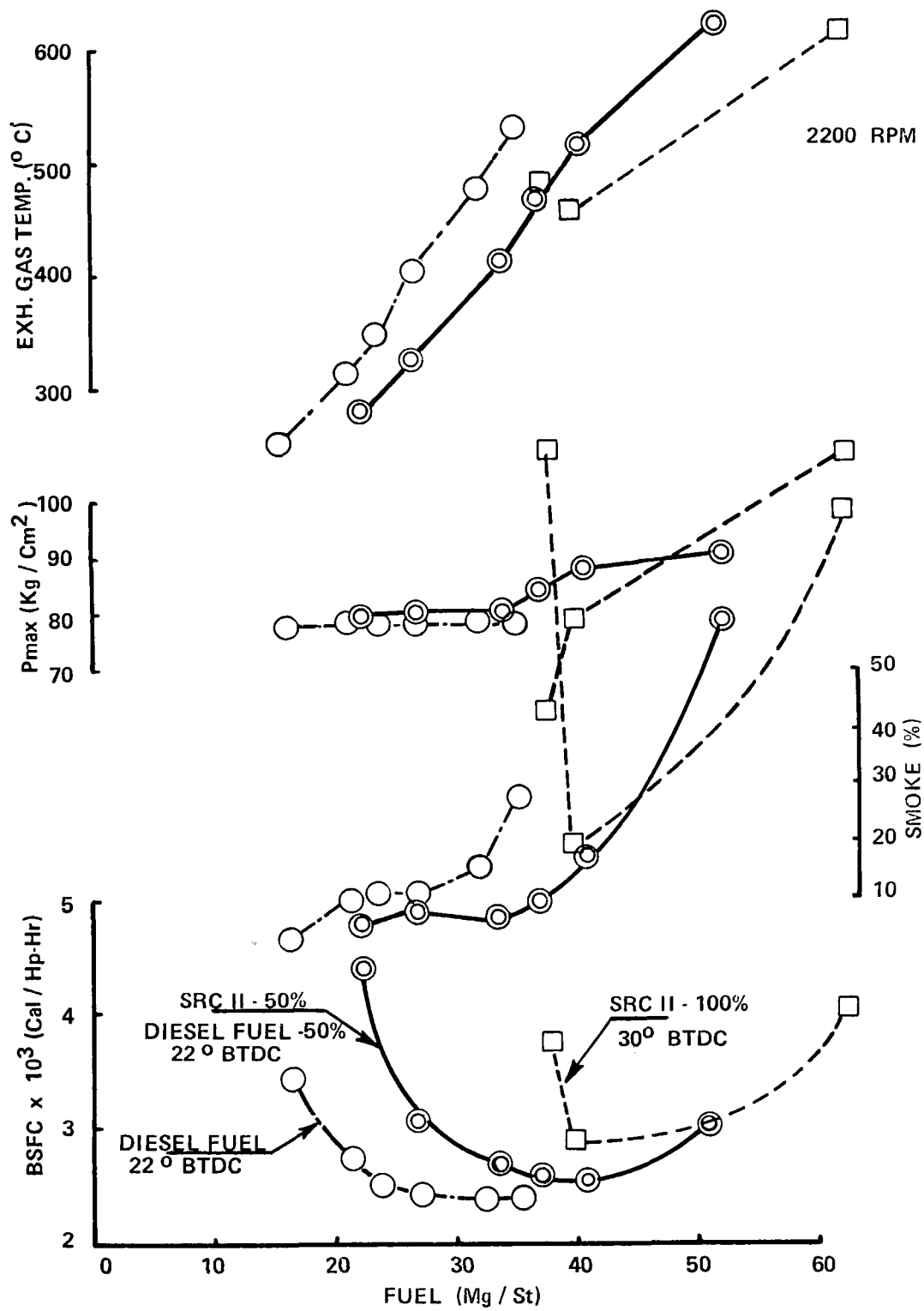


FIG. 22 - COMBUSTION CHARACTERISTICS OF DIESEL, 50% SRC-II BLEND, AND SRC-II FUEL OIL IN A SPARK ASSISTED DIESEL

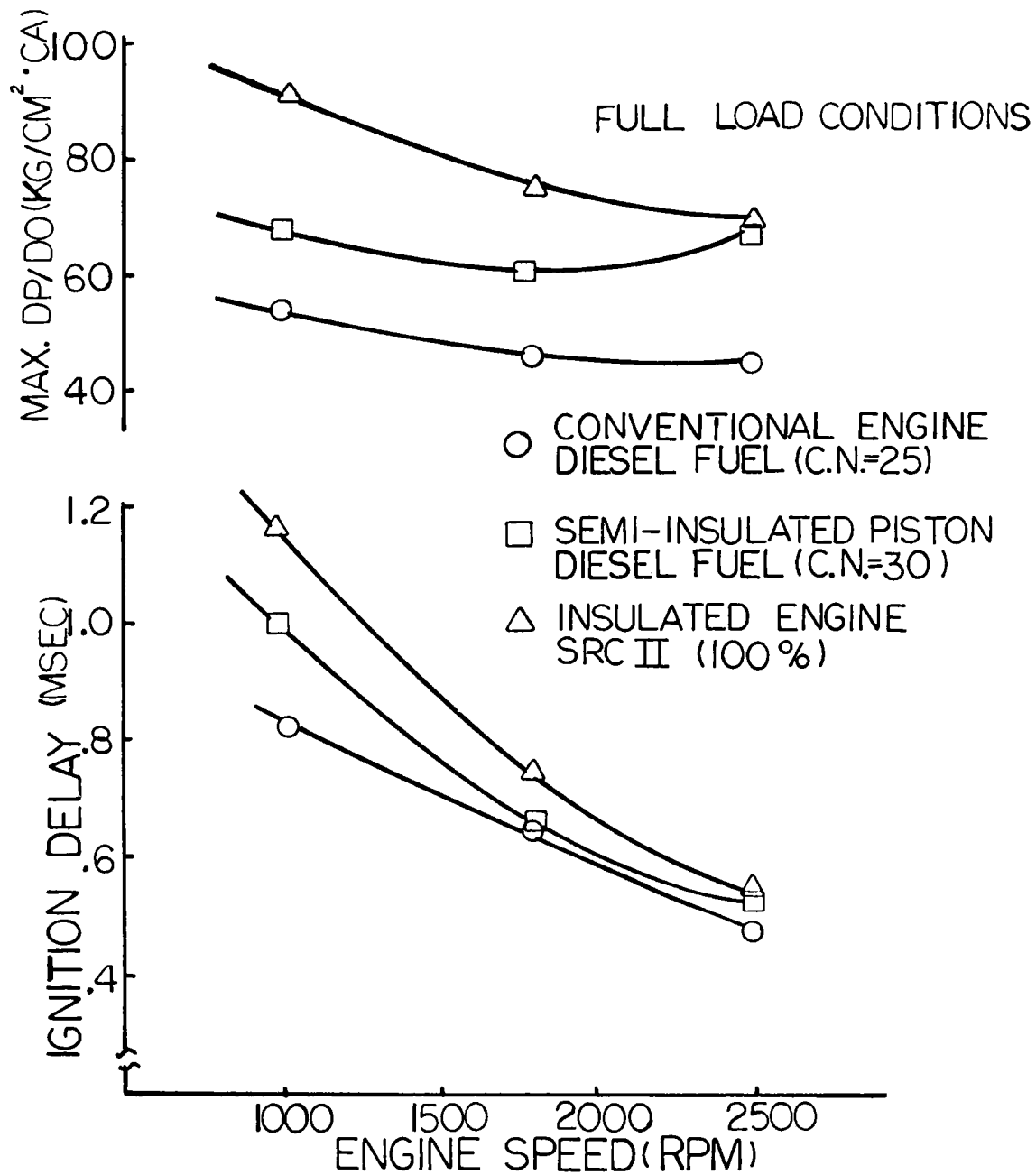


FIG. 23 - OTHER COMBUSTION CHARACTERISTICS OF LOW CETANE FUEL

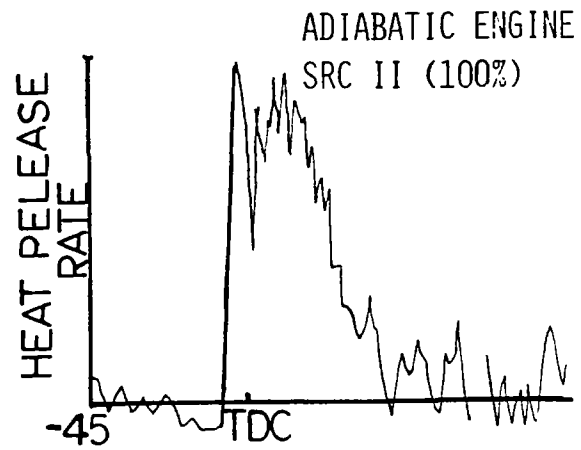
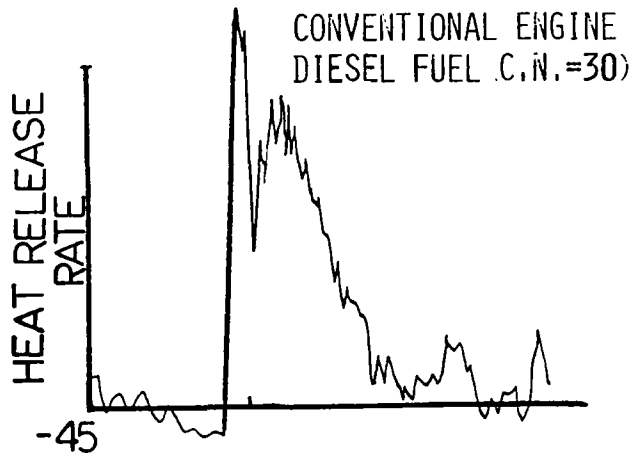
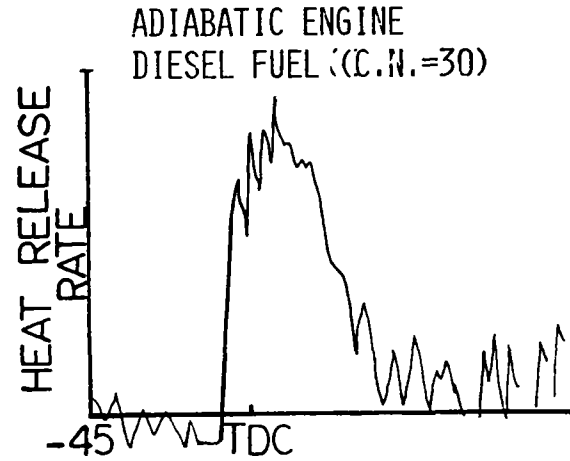
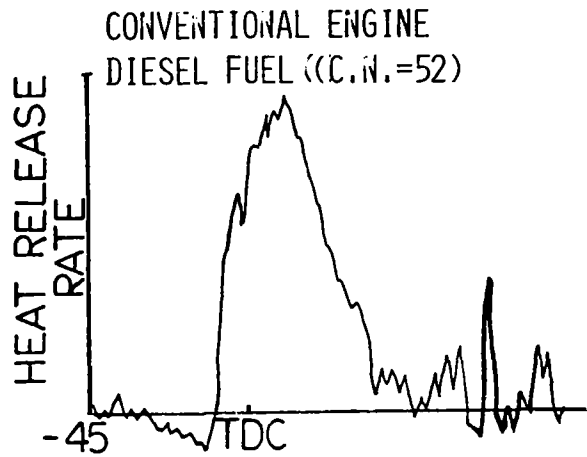


FIG.24 - HEAT RELEASE RATE (2500 RPM RATED CONDITION)

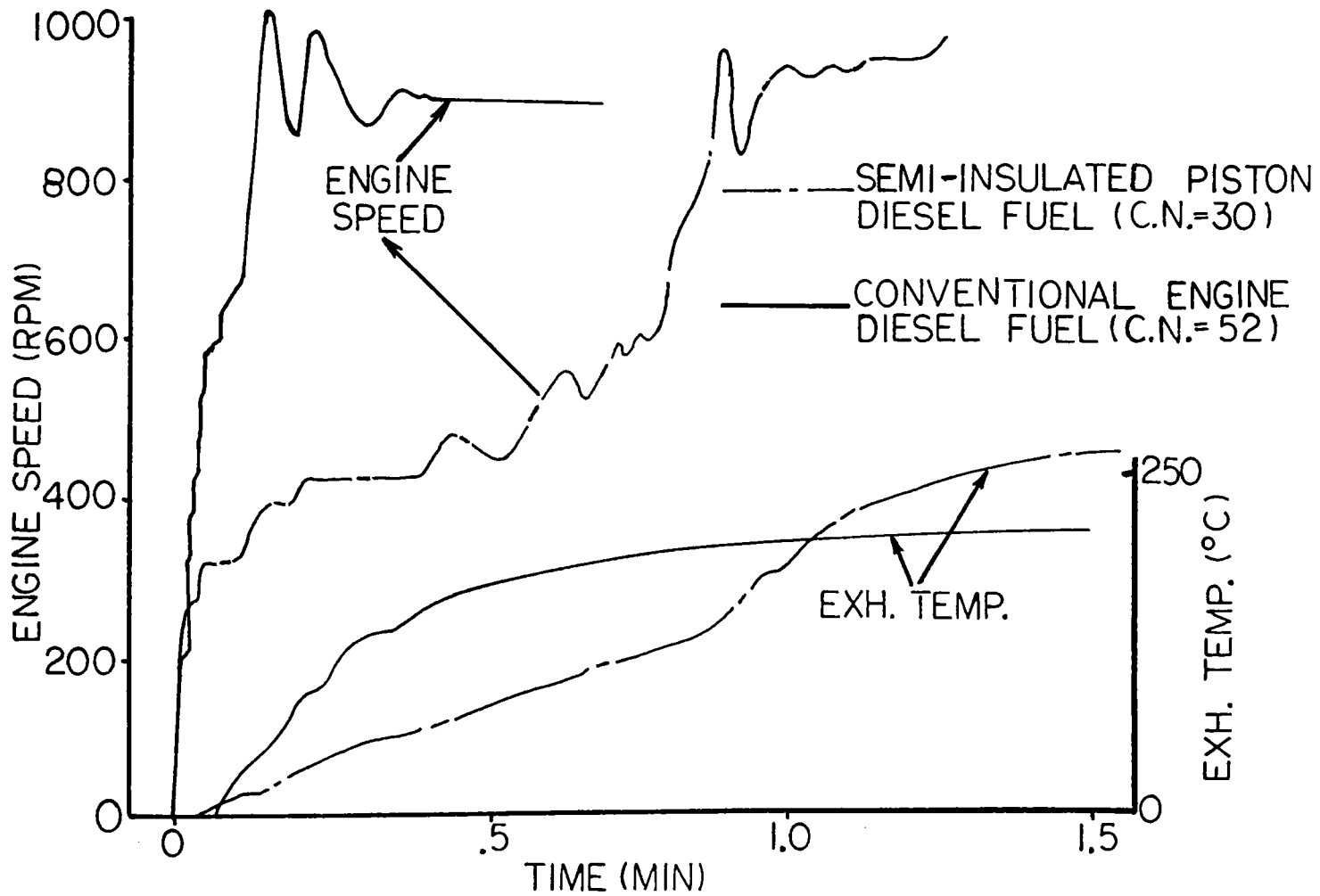


FIG. -25 STARTING CHARACTERISTICS OF LOW CETANE FUEL

the starting characteristics of low cetane fuel in a spark assisted diesel. The lower cetane number fuel does not reach equilibrium idling speed as quick as the conventional engine. A more gradual increase in engine speed is seen with low cetane fuel.

Table V. Spark Assisted Diesel  
Komatsu Ltd.

Engine Specifications:

Model	4D94
Number of Cylinders	Four (4)
Bore x Stroke	94 mm x 106 mm
Compression Ratio	16.0:1
Combustion Chamber Type	Prechamber
Prechamber Volume Ratio	
Adiabacity	
Injection and Ignition Timing	18°BTC
Engine Speed @ Rated	3100
BHP @ Rated	80

Conclusions

Based on preliminary test results from Cummins Engine Company, Yanmar Diesel, Ltd., and Komatsu, Ltd., the following can be concluded:

1. Combustion of SRC-II fuel in conventional water-cooled DI, IDI, or spark assisted diesel is difficult.
2. SRC-II fuel has narrow band of operation in conventional diesels. It likes higher operating speeds and loads.

3. Parameters improving SRC-II combustion in diesel engines are:
  - Increased Air Temperature
  - Increased Boost Pressure
  - Increased Jacket Water Temperature
  - Cetane improver
4. In terms of emissions, all fuels are comparable for UHC, and NOx-shale oil somewhat timing sensitive. For particulates, diesel fuel and shale oil are comparable but SRC-II has much higher value than diesel fuel.
5. Spark assisted diesel contributes to improved ignition, especially with alcohol fuels.
6. Increasing adiabacity of diesel offers best improvement in SRC-II combustion.

#### Acknowledgement

The authors wish to acknowledge the contributions made by the Research teams of Cummins Engine Company, Inc., Yanmar Diesel, Ltd., and Komatsu, Ltd.

#### References

1. M. Woods, R. Kamo                      Thermal barrier coating for diesel  
T. Yamada, M. Mori                      engine piston; ASME 80-DGP-14  
New Orleans, LA; Feb. 3-7, 1980
2. Kamo, R., Bryzik, W.                      Adiabatic turbocompound engine  
performance prediction; SAE paper  
780068; Detroit, MI; Feb. 27 -  
March 3, 1978

3. McDonald, J. Scott,            Experimental measurements of the  
Plee, Steven L.                    independent effects of dilution ratio  
D'Arcy, James B.                 and filter temperature on diesel  
Schreck, Richard M.             exhaust particulate samples;  
SAE paper 800185

COMBINED-CYCLE POWER PLANT VIA PRESSURISED FLUIDIZED-BED COMBUSTION

by

H.R. Hoy            National Coal Board, Leatherhead, England  
A.G. Roberts       National Coal Board, Leatherhead, England  
J. Stringer         Electric Power Research Institute

for Presentation at Session II.

Second Conference on Advanced Materials for Alternative-  
Fuel-Capable Heat Engines

Monterey, California, August 24-28, 1981

Sponsored by  
Electric Power Research Institute  
and  
Department of Energy



## Summary

Combined gas steam cycles have the capability of significantly increasing power generating efficiency. Pressurised fluidised bed combustion (PFBC) offers the possibility of direct combustion of coal for generating combustion gases that, after cleaning in cyclones, can be expanded through gas turbines without causing uneconomic rates of erosion, fouling, and corrosion of the turbine blades. Coal-to-bus-bar efficiencies of about 40% should be achievable with PFBC combined cycles incorporating reheat steam cycles, even with gas turbine inlet temperatures as low as 850°C.

Compared with conventional pulverised coal-fired plant with scrubbers to control SO<sub>2</sub> emission, the PFBC combined cycle plant potentially offer (i) around 5 percentage points higher generating efficiency, (ii) lower NO<sub>x</sub> emission, (iii) smaller plant size, and (iv) ultimately at least 10% lower capital costs.

Two main types of PFBC combined cycle are under consideration:

1. the supercharged boiler cycle, in which steam is generated superheated and reheated in tubes within the bed and the hot gases are passed through a gas turbine followed by a heat recovery system.
2. the airheater cycle, in which air is heated in tubes within the bed and then mixed with cleaned hot combustion gases before passing through a gas turbine followed by a waste heat boiler.

In both schemes, crushed coal is burned in a fluidised bed which is composed mainly of partially-sulphated dolomite together with some coal ash. The relatively low combustion temperature of 850 to 950°C minimises volatilisation of the alkali constituents and does not produce sintering of the ash. This feature, aided by three stages of efficient cyclone dustcollectors, is considered likely to result in combustion gases giving economically acceptable rates of erosion, corrosion and fouling of gas turbine blades.

The areas in which the choice of materials is vital are:

- (i) gas turbine blades and protective coatings for them.
- (ii) the tubes immersed in the bed for generating superheating and reheating steam, or for heating air together with their supporting structures which necessarily work at close to combustor temperatures.
- (iii) materials used in the hot gas cleaning equipment.

The paper discusses the operating conditions to which materials in the two cycles will be subjected and summarises investigations of the corrosion and erosion of in-bed materials and gas turbine blades which have been made during the course of tests of several thousand hours duration, in the UK and USA.

## 1. Introduction

It is expected that the bulk of new power-generating plant to be built in the foreseeable future will be coal-based. In an attempt to reduce the cost of electricity as currently produced from conventional pulverised-coal-fired stations with stack gas clean-up, several advanced power generating systems are being examined. In the near term the most promising systems appear to be those involving combined-cycle power plant that use both gas and steam turbines. Pressurised fluidised bed combustion (PFBC) offers the possibility of direct coal burning for such plant.

## 2. Combined cycles

The thermal efficiency of a heat engine cycle depends upon the maximum temperature at which heat is transferred to the working fluid and the minimum temperature at which it is rejected. Progressive increases in thermal efficiency have resulted from advances that have permitted higher maximum temperatures to be used. However, when steam is used as a working medium, limitations are imposed because high temperatures lead to corrosion problems and are accompanied by high steam pressures which result in highly-stressed parts.

With a gas turbine, the working fluid is heated directly by combustion of the fuel within it and the maximum permissible temperature is appreciably higher than the maximum temperature in the steam cycle. However, the efficiency of a cycle also depends on rejecting heat at the lowest possible temperature and although a steam plant is well suited for this, a gas turbine is not. A combined cycle therefore has the potential for increasing the range of temperature over which heat can be converted into power and for increasing the efficiency. The extent of the improvement over a steam cycle increases with the temperature at which the gas turbine operates.

There are two main forms of combined cycle of interest in PFBC applications (i) the supercharged boiler cycle and (ii) the airheater cycle. These are shown in simplified form in Fig. 1.

In the supercharged boiler cycle most of the steam is generated, superheated and reheated in tubes immersed in the bed. The steam is used to drive a steam turbine in a more or less conventional steam power generation loop and the hot pressurised combustion gases are expanded through a gas turbine.

In the airheater cycle, some of the air supply (about two-thirds) is heated in tubes immersed in the fluidised bed, the remainder being used to fluidise the bed and burn the coal. The two hot streams are then mixed and expanded through a gas turbine with steam being generated from the gas turbine exhaust. Depending on the operating conditions the gas turbine contributes at least 60% of the total power output compared with up to about 33% in the supercharged boiler cycle.

Groups such as

American Electric Power (AEP), Stal-Laval, Deutsche Babcock;  
General Electric, VKW, Boston Edison;  
Electric Power Research Institute, Brown Boveri, Babcock & Wilcox Co.

are involved in activities aimed at commercialising the supercharged boiler cycle. The current proponent of the airheater cycle is Curtiss-Wright under a contract from the Department of Energy.

It is not the purpose of this paper to compare the merits of either cycle. The intention is to discuss the metallurgical implications of the cycles, many of which are common to both cycles.

### 3. Pressurised fluidised bed combustion (PFBC)

In fluidised combustion systems, coal is normally burned in a fluidised bed of limestone or dolomite. The total amount of carbon in the bed is small - normally less than 0.1% of the bed weight when operating under pressure. The bulk temperature of the bed is maintained in the range 850 to 950°C by the transfer of heat to steam or air in the immersed tubes, although individual coal particles can attain temperatures up to 150°C higher than the bulk temperatures.

The main features of fluidised combustion are:

- 1) high heat transfer rates are obtained to surfaces in the bed, resulting in heat transfer surface area requirements that are low compared with conventional combustion systems.
- 2) because the operating temperature is far below the softening temperature of the ash, a large "radiation" chamber - such as is necessary in conventional combustion systems - is not required to cool the ash particles down to the gas temperature. Furthermore, the ash particles are not vitrified so that they are less abrasive.
- 3) SO<sub>2</sub> emissions can be reduced to a level low enough to meet any reasonable regulations by the addition of a sorbent, such as limestone or dolomite, to the bed.
- 4) the volatilisation of alkali compounds in the coal ash is low; such compounds contribute to the formation of deposits and cause corrosion at temperatures relevant to gas turbines.
- 5) NO<sub>x</sub> emissions are low.

One of the main physical differences between atmospheric and pressurised units is that, under pressure, the heat release rate per unit bed area is so high that deep beds will be necessary in order to accommodate sufficient heat transfer surface. Typically, PFBC units will have beds 3 to 5 metres deep compared with 1 - 1½ metres with AFBC, and as a consequence the transit time of the air/gas through the bed will be relatively long - typically 3 to 6 seconds. This has a beneficial effect on combustion efficiency and on items 3 and 5 above.

### 4. Materials problems

The main potentially corrosive elements associated with coal are sulphur, sodium, (1) potassium, and chlorine. These have their origins in the wide range of minerals associated with the coal substance and as might be expected the proportions vary considerably from one region to another.

The fractions of these elements released into the gas phase during combustion are greatly influenced by the type of process and the operating conditions. In normal pulverized coal combustion for example, typically 10% of the alkali associated with the coal will be in the gaseous phase whereas in fluidised bed combustion systems (which operate at much lower temperatures) only about 1-2% of the alkalis are likely to be in the gas phase. Nevertheless even at this low level the concentration is considerably above that considered to be acceptable for oil-fired gas turbines. Fig. 2 shows calculated equilibrium values of alkali vapour

concentrations for a specific set of operating conditions in a PFBC system. (11)

Impurities in the SO<sub>2</sub> sorbent (limestone or dolomite) fed to a fluidised bed also contribute alkali to the system and together with the CaSO<sub>4</sub> produced by sulphation of the lime can be considered to augment and/or modify the distribution of the potential corrodents.

Table 1 below shows an example of the distribution of the potential corrodents between the residual material in the combustor bed, the dust discharged by the cyclones and the material escaping the cyclones, for operation at 6 bar, 850°C when burning a typical Eastern US coal with dolomite fed to give 90% sulphur retention. (2)

Table 1. Distribution of Potential Corrodents  
% of Total Input of each Species.

	Na	K	Cl	S
Bed Material	35	24	4	64
<u>Elutriated Material</u>				
(a) Cyclone Discharge	62	73	3	25
(b) Exhaust Dust	2	2	-	1
Exhaust Gases	1 to 2	1 to 2	93	10

A general consideration of the different environments to which materials in a PFBC system are subjected indicates that for many US Eastern coals the following would apply:

For Materials Immersed in the Bed: i.e. steam generating, superheating, reheating tubes, etc. and their supports. PFBC fluidising velocities will be generally below 1.5 m/s, and the environment will therefore be a gently bubbling bed of material, typically with a mean size of about 1100 microns, comprising about 20% by weight of the ash of the coal, 80% of partly sulphated dolomite (MgO, CaO, CaSO<sub>4</sub>, CaCO<sub>3</sub>) and less than 0.5% of the carbon in the coal. The gaseous atmosphere (products of combustion) is likely to vary in composition across the cross section with the possibility of low oxygen potential in the regions directly above coal inlets but with an overall excess air above 20%.

In the supercharged boiler cycle, the maximum tube temperatures are likely to be in the order of 600 to 650°C and the excess air not less than about 30%; in the airheater cycle the maximum tube temperatures will be similar to the bed temperature (say 850°C) and the excess air is unlikely to be more than about 30%. Thus it can be expected that the tubes in the airheater cycle will be subjected to a more corrosive environment although the tubes will be less highly stressed. Uncooled support structures in both cycles will be operating at bed temperatures.

For Materials in the Ducting and Hot Gas Clean-Up System: i.e. up to the inlet of the first stage of hot gas clean-up. The environment is a combustion gas with free oxygen, typically containing up to 20,000 ppm by weight of particulate material, with particles up to 500 micron in size. With gas velocities desirably in the range 20-30 m/s to minimise the size of hot ducting, resistance to erosion

becomes an important consideration.

For Materials After Hot Gas Clean-Up: i.e. the ducting into the gas turbine and turbine blade materials. The dust concentration at this stage is likely to be below 500 ppm with only a small concentration of particles larger than 5 microns. Dust concentration will be lower in the air cycle because of the diluent effects of the heated air. As will be discussed later, particulate erosion in either cycle may not be a problem when high efficiency cyclones are used, but as the temperature of the combustion gas falls, condensation of volatilised alkali may lead to the formation of deposits and to highly corrosive conditions.

#### 5. Experience to date

Over recent years there have been three major programmes sponsored by the US DOE to investigate (amongst other factors) materials behaviour in these environments:

- (a) a 1000 hour test on the CURL pressurised combustor in England. (3,4,5)
- (b) a 1000 hour test on the Exxon Miniplant, Linden, New Jersey. (4,6,7)
- (c) a 1000 hour test on the Curtiss-Wright plant at Wood Ridge, New Jersey. (8)

In the following comments, these three will be referred to as the CURL, Exxon and Curtiss-Wright programmes.

In-bed tubes: Sufficient work has now been carried out in pilot-scale operation under pressure for periods of 1000 hours and at atmospheric pressure for periods up to 2000 hours, to confirm that the environment is potentially corrosive. Thin deposits are formed on the tubes, the deposits being fine-grained, compact, of low porosity and having a similar composition to the bed, i.e. to be mainly  $\text{CaSO}_4$ ,  $\text{CaCO}_3$ ,  $\text{CaO}$  and  $\text{MgO}$  with small amounts of coal ash. The reasons why deposits form on immersed tubes are not clear. Because of their low porosity it is tempting to postulate that a significant part of the material that is deposited is partially molten at the temperatures encountered during operation or that constituents of the ash released from burning coal particles act as a deposit-cementing agent. The main mechanism of corrosion is by sulphidation with the sulphur diffusing through the deposit and through the scale to react with the alloy elements to form chromium or nickel sulphides. As the alloying elements are consumed within the bulk of the alloy it becomes increasingly more difficult to form a protective oxide scale and breakaway corrosion may occur.

Whether or not corrosion occurs to a serious extent depends on the material chosen and on the operating temperature. Low chromium ferritic steels are suitable at metal temperatures up to  $400^\circ\text{C}$ ; from  $400$  to  $650^\circ\text{C}$  high-chromium ferritic steels or iron-based austenitic steels should be suitable. For higher temperatures or for uncooled support members, certain FeCrAlY steels (in cladding form) seem suitable while some iron-based austenitic steels may also be acceptable.

In general, corrosion tends to increase with metal temperature for a given alloy, but can reach a plateau (e.g. at about  $800^\circ\text{C}$  for Incoloy 800H) with a reduction in corrosion at higher metal temperatures.

The complex nature of in-bed corrosion is beginning to be understood through the extensive EPRI-sponsored investigations at atmospheric pressure<sup>(9)</sup>. Corrosion of in-bed tubes in PFBC appears to be similar to that in atmospheric fluid beds (AFBC's) although there are small, perhaps significant, differences. Tests in the CURL programme\* have shown that corrosion in a PFBC environment may be less severe.

\* EPRI Report still to be published.

Incoloy 800H had an improved performance (particular in uncooled specimens) whereas Type 347 SS was not quite as good as in AFBC's.

Sufficient work has been done to give a reasonable degree of confidence that materials are available for fabricating steam-generating systems. The main need is for longer term testing - 1000 to 2000 hours is too short a period in which to obtain a reliable prediction as to the likely performance over 100,000 hours and more.

Ducting and hot-gas clean-up: For the fabrication of ducting and cyclones, AISI 310 steel has been found to give good resistance to erosion and corrosion in pilot-scale plant but it can suffer from serious weakening by the formation of sigma phases. Hence the use of Incoloy 800H may be more appropriate.

Gas turbine blades: The crucial factor which will determine whether or not PFBC can be applied to combined cycles is the capability of the gas turbine for handling dirty gases. Practical experience at the moment is limited to the operation of a small gas turbine in the Curtiss-Wright programme and to the exposure of cascades of blades and target specimens in the Exxon and CURL programmes. These programmes have shown that erosion can occur if the performance of the gas cleaning equipment is inadequate but also that erosion is unlikely to occur over long periods of operation if two or more stages of highly efficient conventional cyclone dust collectors designed to avoid malfunctioning are used.

Based on the Exxon and CURL results, together with earlier coal-fired gas turbine experience and theoretical calculations, General Electric have proposed specific limitations on particle size concentrations to avoid erosion in one particular modern industrial gas turbine.<sup>(10)</sup> This is shown in Fig. 3. It is believed that the amount of dust smaller than 2 or 3 micron is not important, but that the stated amounts above 5 micron should not be exceeded. Experiences in the Curtiss-Wright, Exxon and CURL programmes suggest that it should be possible to meet this criterion in commercial applications using three stages of large cyclones.

A number of advanced gas cleaning devices, such as high temperature filters and precipitators, are currently being developed. If these are successful, even more confident statements could be made regarding particulate erosion in turbines.

Deposition and corrosion may be a greater risk to turbine life than particulate erosion. It has already been stated (see Fig. 2) that some alkali is volatilised from the coal ash in the bed. Amounts of vapour alkali measured in the CURL and Exxon rigs are in rough agreement with calculated values. Hot corrosion of a turbine blade can occur when this alkali reacts with  $\text{SO}_2$  and  $\text{O}_2$  to form complex alkali sulphates which condense on hot blade surfaces.

The alkali metal content of the gas phase is not in itself a sufficient measure of the tendency to condense alkali sulphate in the gas turbine, even though it is at least an order of magnitude higher than the present gas turbine limit for liquid fuels. This is because (i) the chlorine/alkali atom ratio in the PFBC is higher than with the oil products and this might be expected to suppress condensate (alkali chlorides are more volatile than sulphates), and (ii) reaction with the particulate alumino-silicates in the coal ash (known as "gettering") will tie up some of the alkali in a harmless form. Thermochemical calculations<sup>(11)</sup> indicate, however, that with typical  $\text{Cl}/(\text{Na} + \text{K})$  ratios, the alkali metal sulphate condensation will be many times that of a conventional liquid fuel-fired gas turbine, even with 90% gettering.

Thus, although only a small proportion of the input alkali (perhaps 1 or 2%) is vapourised from a PFBC, the efflux must be considered to be potentially corrosive. Whether corrosion of metal occurs depends, of course, on the temperature and on the corrosion resistance of the alloy. Experience in the Curtiss-Wright, Exxon and CURL programmes indicates that if the metal temperature is not higher than 800 to 850°C, then existing turbine alloys with existing corrosion-resistant coatings should give adequate life. This view is based however on a relatively few thousands of hours of operation. The General Electric facility shortly to begin long term testing of blade materials is an important stage in proving this. For higher gas turbine inlet temperatures (up to 950°C) a solution may be in the use of cooled blades and/or in the metallurgical development of more corrosion-resistant coatings and claddings.

The overall efficiency of the cycle increases as the gas turbine inlet temperature increases, although the type of gas turbine has some influence. Thus the Stal-Laval GT 120 achieves an adequate efficiency at a turbine entry temperature of 800-820°C by the use of high pressure with intercooling, whereas most other manufacturers produce non-intercooled engines which require inlet temperatures of c.900°C to achieve the same efficiency.

#### 6. Scope for Improvement

Improvements in metallurgy and gas cleaning (possibly incorporating alkali adsorbers) will enable the gas turbine entry temperature to be increased. However, there is likely to be a limit imposed by the maximum safe combustion temperature of 900°C above which volatilisation can lead to the formation of strongly-bonded deposits on the blades. One potential method of overcoming this problem is the use of the "After burner" cycle (Fig. 4) in which a cleaned gas produced from a preliminary pyrolysis/gasification stage is burned in the cleaned products from a combustor operating at a high excess air. Raising the turbine inlet temperature by about 200°C in this way (whilst still maintaining a combustor temperature of not more than 900°C) would increase the cycle efficiency by 3 to 4 percentage points.

#### 7. Commercial/Demonstration developments

The next important step in the commercialisation of the process is the need to demonstrate, on a reasonable scale, the ability of a gas turbine to handle the dirty gases. There appear to be four approaches to this problem.

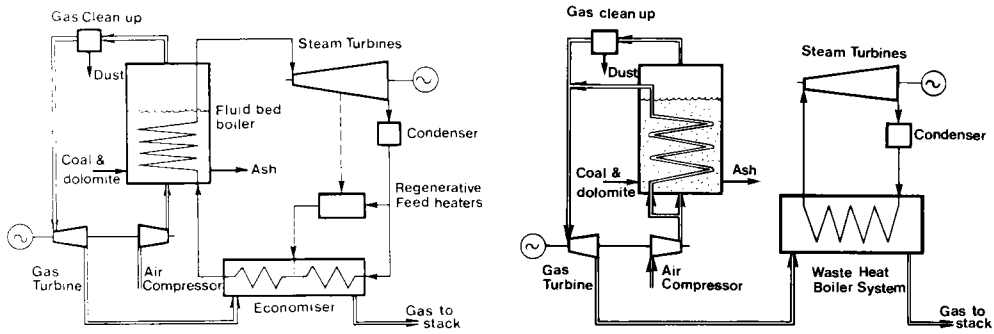
- 1) the operation of a pilot-scale plant with a small sized gas turbine. This is the approach adopted by Curtiss-Wright.
- 2) the operation of a demonstration-scale plant with a large gas turbine de-rated to run at a low turbine entry temperature - the proposed GE/VKW/Boston Edison approach.
- 3) the operation of a demonstration-scale plant with a large gas turbine operating at full inlet temperature - the AEP/Stal-Laval/Deutsche Babcock approach using the advantageous characteristics of the GT 120 engine.
- 4) the operation of a large PFBC with a large cascade of blades and target rods, i.e. a scale-up of the CURL and Exxon programmes. This is the initial approach of the IEA experimental facility at Grimethorpe which also has the capability of testing rotating turbine blade assemblies.

The potential of PFBC combined cycle plant is such that all four approaches can be justified.

## References

1. Hoy, H.R. & Watt, J.D., "Effect of inorganic matter on combustion". Paper D, Session II, North American Fuel Technology Conference, Ottawa, June 1970.
2. National Coal Board's Coal Utilisation Research Laboratory, "1000 hour test programme in a pressurised fluidised bed facility". Report to DOE, Nos. FE-3121-15-a, b, c, d.
3. Hoy, H.R. & Roberts, A.G., "Investigations on the Leatherhead pressurised facility". 6th International Conference on Fluidised Bed Combustion, Atlanta, April 1980.
4. Grey, D. et al. "High temperature corrosion/erosion in the effluent from pfbc", Ibid.
5. Jansson, S.A. et al, "Turbine materials performance in combustion gases from a coal fired pressurised fluidised bed combustor." Ibid.
6. Hoke, R.C. & Ernst, M., "Control of particulate emissions from the pressurised fluidised bed combustion of coal". Ibid.
7. Nutkis, M.S. et al, "Hot corrosion/erosion testing of materials for application to advanced power conversion systems using coal-derived fuels". Exxon Research & Engineering Co. Report to DOE FE-2452-39.
8. Mogul, J. et al, "Materials for pressurised fluidised bed air heater system". 6th International Conference on Fluidised Bed Combustion, Atlanta 1980.
9. National Coal Board's Coal Research Establishment, "Materials problems in fluidised-bed combustion systems." EPRI Reports CS-1449 (May 1980) and CS-1853 (May 1981).
10. Boericke, R.R. et al, "Assessment of gas turbine erosion by pressurised fluidised bed combustion products". 6th International Conference on Fluidised Bed Combustion, Atlanta, April 1980.
11. Roberts, R. "Technical planning study - PFBC". General Electric Report to EPRI, CS-1465 (July 1980).





Supercharged boiler cycle

Air cycle

Fig. 1 Combined cycles incorporating PFBC

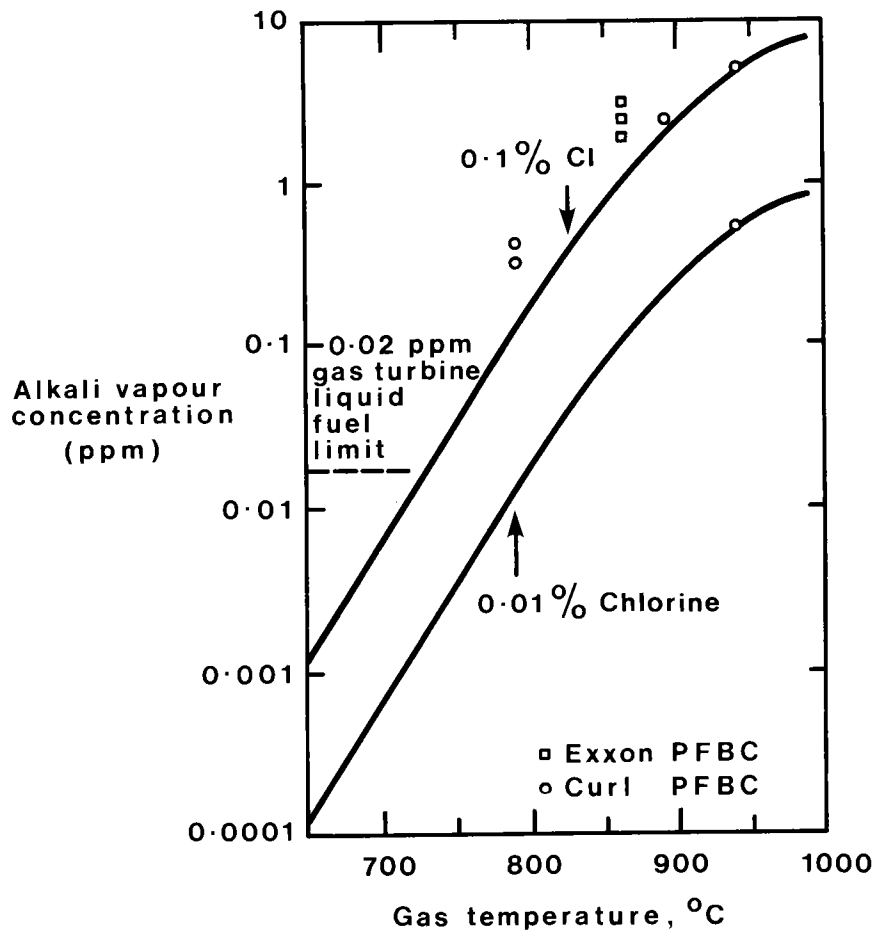


Fig. 2. Equilibrium alkali content of gas phase

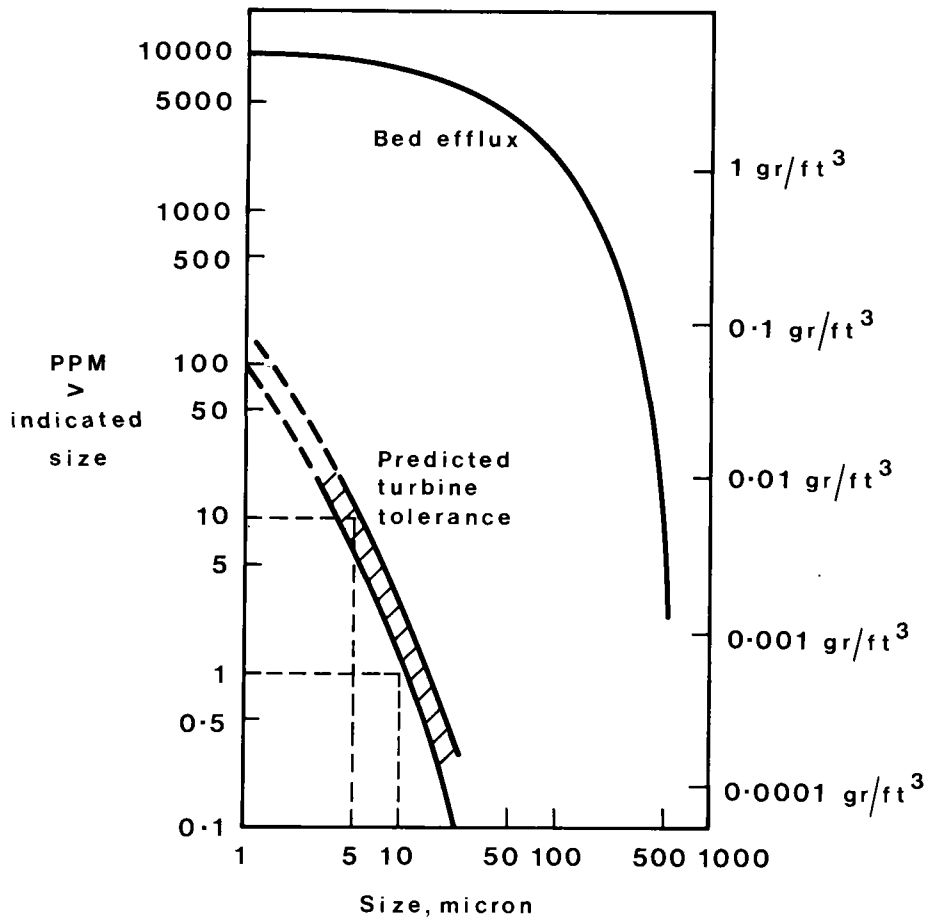


Fig. 3 Predicted dust size distribution for avoiding turbine corrosion

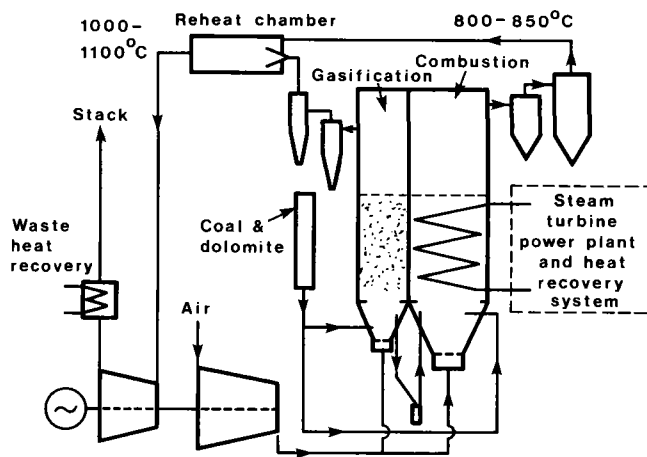


Fig. 4 Afterburner cycle

**Session III**

**HEAT ENGINES AND HEAT RECOVERY**

Diesel Engine Research and Development  
for Alternative Fuel Operation  
John Fairbanks  
U.S. Department of Energy  
Washington, D.C.

INTRODUCTION

Diesel engines currently being manufactured and many already in use may operate on some form of alternative fuel before the end of this century and quite possibly in this decade. The scenario for transition from current petroleum fuels to alternative fuels is imprecise as it is currently evolving. While the 70's saw considerable efforts in alternative fuel development, the multi-billion dollar commitments for large scale production facilities have yet to be made. Events in the Middle East could dramatically alter the rate of alternative fuel development. The U.S. has enormous coal and shale resources and we are the world's leading agricultural nation. Thus, coal derived, shale derived and biomass fuels are the primary sources of non-nuclear alternative fuels. Heat engines that can operate in a cost-effective manner on the alternative fuels that emerge will dominate the heat engine market place as we approach the 21st century.

Coal has to be considered a leading alternative fuel contender due to vast and widespread deposits and the established mining industry. Combustion of coal adversely affects the air quality and has downrange problems such as being a possible contributor to acid rain. Removal of the elements causing these problems at the centralized fuel processing stage is the basic theme of coal liquefaction and coal gasification. Techniques of beneficiation or removing ash and sulfur etc. from ground coal leading to fuels as coal dust, coal-water or coal-oil slurries are also being pursued. Near-term use of shale oil will probably be as a refinery feedstock mixed with petroleum crude such that the refinery product slate is essentially unchanged. Dedicated shale refineries appear an eventuality but require the financial commitment and environmental acceptance. Biomass fuels appear too expensive at this point, however blending small quantities of biomass fuels to improve certain aspects of coal liquid fuels could be attractive. The economics of these fuels were analyzed by Lou Conta in a DOE program at ESCOE and are summarized in Table 1. Candidate alternative fuels burn differently than petroleum fuels however some of them can be processed to virtual petroleum specifications such as Marine Fuel Diesel. This can be expensive processing, for example, coal derived raw distillate 350-500°F boiling point SRC-II would require roughly 10,000<sup>3</sup>ft of H to hydrotreat one barrel of this fuel from its 9.1% of H level to 12.8% H, which at commercial H rates of \$2/1000 ft<sup>2</sup> would be an additional \$20/barrel cost. Thus, the impetus should be to develop heat engines that can operate effectively with the more economical versions of the emerging alternative fuels rather than altering alternative fuels such that they burn as petroleum specification fuels. From the technical perspective, co-evolving the alternative fuels with the heat engines is the logical approach. Specifically for diesel engine research and development (R&D) four interrelated areas emerge: enhanced multi-fuel capability, acceptable emissions, improved performance and engine durability. The diesel engine has demonstrated an ability to operate on a wider range of fuels than other production engines, however diesels have emission problems.

A good indicator of how well a fuel will run in a diesel or compression ignition engine is the fuels cetane number. This number is measured in a special single-cylinder variable-compression test engine. Most U.S. diesel engines operate on No. 2 diesel fuel which has a cetane number of about 50. Coal-derived liquid fuels are characteristically high in aromatics which results in a low cetane number while the shale derived fuels are high in paraffins which tends to increase the

cetane number. If we concentrate on the coal-derived fuels for industrial/utility diesel engines the R&D may also provide advantages for shale derived fuels operation. Most DOE experience to date is with Solvent Refined Coal (SRC)-II from the pilot plant in Ft. Lewis, Washington. Experience with SRC-II should be applicable to the Exxon Donor Solvent and H-Coal fuels. The cetane number of SRC-II middle distillate has been determined to be -16 by Chevron. Thus, a general perspective for diesel R&D involves increasing the cetane number of coal-derived liquid fuels or reducing the engine's sensitivity to cetane number or a combination of the two.

#### DIESEL ENGINE CLASSIFICATION

Diesel engines are generally classified according to the rotational speed of the engine into three groups, slow speed, medium speed and high speed. This grouping does not take into account the stroke length and consequently the piston speed. Combustion characteristics of the alternative fuels may require use of the speed factor,  $C_s$ , which is defined as: (1)

$$C_s = \frac{nc}{100,000} \quad \text{and} \quad c = \frac{ln}{6}$$

where  $c$  = mean piston speed (ft/sec)  
 $l$  = length of stroke (in)  
 $n$  = engine speed (rpm)

Representative speed factors, engine sizes and ratings are listed in Table II.

Table II - Diesel Engine Classification

	<u>Slow Speed</u>	<u>Medium Speed</u>	<u>High Speed</u>
Speed Range (rpm)	90-250	250-1000	< 1000
Speed Factor	1-3	3-9	< 9
Power Ratings (HP)	7,500-50,000	4,000-20,000	600-5,000
Bore Size (mm)	700-1100	200-700	100-200

Most of the high-speed diesel engines have speed factors incompatible with ignition delay and combustion characteristics of the early coal-derived liquid fuels. Diesel R&D efforts at DOE are thus focused on medium and low-speed diesel engines for industrial/utility applications for early use of coal-derived fuels.

Most of the U.S. manufacturing and operating experience is with medium-speed diesels operating on No. 2 petroleum diesel fuel or natural gas. Low-speed diesel engines are primarily designed and built in Europe although a few of these engines are being built in the U.S. More than 94% of merchant ship construction in 1980 was diesel propulsion and 74% of these diesel engines were the low-speed type. This trend in marine propulsion began after the '73 Yom Kippur War when diesels accounted for only about 60% of propulsion horsepower. The advantageous fuel efficiency of the diesel in the range of up to 50,000 HP per shaft can be illustrated by ships that have had their boilers and steam turbines or gas turbine engines replaced by diesel engines. It may be somewhat ironic that some of the problems encountered with diesel engine operation on alternative fuels may be ameliorated by adapting gas turbine materials technology. Discussion of these problems may be assisted by a short review of diesel combustion.

## DIESEL ENGINE COMBUSTION

The combustion process in the diesel or compression ignition engine is an extremely complex physical and chemical process. Fuel is injected into the conventional diesel chamber at pressures of about 10,000 psi at a crank angle of about  $20^{\circ}$  before the piston is at top dead center (TDC). Ignition occurs about  $10^{\circ}$  before TDC which produces a very rapid pressure rise. This pressure is converted to power on the piston downstroke. The time between the start of fuel injection until there is a measurable pressure rise due to combustion is called the ignition delay time. Because ignition temperature, which is produced by the heat of the air being compressed, is reached well before the optimum time for ignition, ignition is controlled by the time of injection. Thus, the time available to vaporize the fuel and mix it with air being compressed by the piston to achieve complete combustion is very short. Burning substantially all the fuel under these conditions requires a precise correlation of air flow patterns, injector fuel spray characteristics, including atomization, distribution and penetration. The importance of ignition delay is that the only control over the rate of combustion, and consequently over the rate of pressure rise, is the rate of fuel injection. (2) There are many implications involved in ignition delay time, however in general reducing ignition delay is desirable. The most important variables affecting ignition delay period are fuel quality, pressure, temperature of the air and temperature of the surfaces of the engine parts the fuel contacts. The problem may change with time if the injector tip cokes up altering the spray pattern. This coking occurs much more frequently with low quality fuels. Fuels with high aromatic content, such as the coal-derived liquids have increased ignition delay. Combustion rate must be compatible with engine speed, or more precisely the speed factor.

R&D for improvement of diesel engine combustion and performance can be categorized into two general approaches: empirical and using sophisticated diagnostics. Most of the performance improvements to date have been achieved using empirical techniques with evolutionary changes in geometries, injector patterns, speed factor, air swirl, fuel-air mixing, and timing. Characteristically considerable art is applied with the science and much of the technology developed is proprietary. This empirical approach was effective with No. 2 petroleum fuels in the U.S. and with residual petroleum fuels in Europe.

A more scientifically sophisticated technology emerged in the seventies that is being adapted to understand the fundamental diesel combustion kinetics. Initial motivations were to reduce emissions with improved combustion followed by multi-fuel capability considerations also with emissions concerns.

Several types of laser diagnostic techniques are used including laser anemometry, laser scattering and laser Raman spectroscopy to understand the chemistry and dynamics of combustion within the diesel engine combustion chamber. Laser doppler anemometry is used to measure the speed and turbulence of the combustion gases. Laser scattering enables measurement of particle sizes. Laser Raman Spectroscopy provides a method for measure temperature and combustion of the fuel/air mixture as it undergoes combustion and as these parameters rapidly change. Laser beams are transmitted through the combustion chamber by way of appropriately installed quartz ports. Fiber optics are also used to transmit the laser beam into the engines.

Computational methods of combustion can be developed and validated with laser diagnostic measurements. These analytical techniques are still in developmental status but progress is very promising. Laser diagnostics could play a major role

in providing an expeditious understanding of diesel engine combustion with alternative fuels to lead to diesel engine modifications or incorporation of novel combustion concepts that lead to optimized engine efficiency with acceptable emissions.

This laser diagnostic approach requires engine designers to thoroughly understand the data being developed in terms of what it means for their specific engine. Engineering engine modifications based on advanced combustion diagnostics is a major challenge. Thus, laser diagnostics and computer modeling of combustion will have to be developed and validated in order to provide reliable data in a format useful to engine designers.

The mechanics and status of laser diagnostics at Sandia-Livermore are reported in Session II. DOE has supported development of a user oriented Combustion Research Facility at Sandia-Livermore featuring laser diagnostics available at several test bays which was completed this year. These facilities are available to gas turbine and diesel engine manufacturers to use in combustion research.

### EMISSIONS

Diesel engines must meet Federal, State and local emission regulations or the regulations must be modified to a technically achievable level. The primary emission problem with diesel engines are the oxides of nitrogen (NO<sub>x</sub>) which are difficult with light distillate No. 2 diesel fuel to meet emission regulations and more difficult with some alternative fuels. The reason for limiting NO<sub>x</sub> emissions is that nitrogen dioxide (NO<sub>2</sub>) reacts with hydrocarbons and ozone in light resulting in smog and compounds that irritate eyes, injure plants and may aggravate respiratory diseases. (3) Engine exhaust is primarily NO which combines with oxygen in the atmosphere to form NO<sub>2</sub>.

There are two sources of NO<sub>x</sub> formation in a diesel. Thermal NO<sub>x</sub> is formed with nitrogen in intake air, or atmospheric nitrogen. The amount of thermal NO<sub>x</sub> is determined by flame temperature, residence time and the fuel air ratio. A second source of NO<sub>x</sub> is from the fuel bound nitrogen which combines with oxygen during combustion and is referred to as organic NO<sub>x</sub>. The major part of NO<sub>x</sub> emission from light distillate No. 2 diesel fuel or natural gas combustion is thermal NO<sub>x</sub>. However, the levels of fuel bound nitrogen is considerably higher in raw distillate coal-derived liquid fuels, shale derived fuels and residual petroleum fuels than it is in No. 2 diesel fuel or natural gas.

Diesel engines using conventional direct fuel injection characteristically have a high heat release rate as the piston reaches about 10° crank angle BTDC which shows up as a tall spike when heat release rate is plotted as a function of crank angle or cycle time as shown in Figure 1 (4). A disproportionate amount of thermal NO<sub>x</sub> is formed in close proximity to this spike. Thermal NO<sub>x</sub> can be reduced by distorting this spike to much lower peak levels. One way this can be done is by retarding the time of fuel injection which causes higher compression temperatures resulting in reduced ignition delay. This effect of retarding the fuel injection when burning No. 2 diesel fuel is also shown in Figure 1.

### ALTERNATIVE FUEL/DIESEL ENGINE COMPATIBILITY

The Energy Research and Development Agency (ERDA), the forerunner of DOE, contracted with Thermolectron/Sulzer in 1976 to test and evaluate coal-derived liquified fuels and coal-oil mixtures in a low speed diesel. The results can be summarized as follows: Char-Oil Energy Development (COED) fuel could be virtually substituted for No. 2 diesel fuel. This result with COED fuel demonstrated that coal

could be made in a liquid form to petroleum No. 2 diesel specifications and operate satisfactorily in a diesel engine. However, COED was considered too expensive and the COED fuel process is not being pursued. A raw distillate blend of SRC-II in the ratio of 2.9:1.0 Middle to Heavy Distillate, which made a 350° - 850° boiling range fuel burned satisfactorily with either a blend of 20% No. 2 diesel fuel or pilot injection of about 3.5% No. 2 diesel. Sufficient fuel was not available to assess durability and emission measurements were lacking. Micronized coal mixed in No. 2 diesel also burned effectively; however, severe erosion was noted in the injector and cylinder liner. (5)

Burmeister and Wain ran SRC-II 2.9:1.0 fuel in their low-speed test engine successfully with a blend of 20% No. 2 diesel fuel. Operation for one hour on micronized coal in No. 2 diesel fuel essentially wore out the fuel oil injector, Figure 2, and produced considerable wear in the cylinder liner and piston rings as shown in Figure 3. These results are consistent with those encountered with all reported programs using pulverized coal in some form as a fuel and are further discussed in the Erosion section.

A program was initiated wherein U.S. medium speed diesel engines were tested with coal-derived and shale-derived fuels. This was essentially an empirical approach to vary parameters with existing engines to determine the fuel flexibility of cuts of alternative fuels considered candidates for industrial utility diesel engine use. These data are being provided to the fuel producer in real time. This work is also reported at this conference. Blending or pilot injection were both successful as far as operation. Handling of coal-derived fuels received considerable attention. Coal liquid fuels leach lead out of solder joints and copper out of brass. Coal liquid fuels also attack hoses, seals, etc., which should be replaced with materials like Teflon or Viton. Initial results justified investigation of several novel combustion techniques for the coal-derived fuels.

#### PRECOMBUSTION CHAMBER

The precombustion chamber or prechamber concept is somewhat akin to the rich-burn, lean-quench gas turbine combustor concept. The intent is to convert fuel bound nitrogen to N<sub>2</sub> initially in the prechamber and minimize thermal NO<sub>x</sub> formations in the combustion chamber. Prechambers are located between the fuel injector and the combustion chamber. Prechambers are typically 5-20% of the total "clearance volume," which is the volumetric space between the piston crown and the adjacent surface of the combustion chamber housing when the piston is at TDC. Prechambers reduce the NO<sub>x</sub> level by providing fuel rich conditions in the early ignited charge and by suppressing the peak of the heat rate spike. A problem with conventional prechambers is a 5-8% increase in fuel consumption attributed to heat losses to the increased surface area. Metal prechambers used in automobile diesel engines have an insert throat passage between the bowl of the prechamber and the cylinder. High nickel alloys are used for prechamber inserts but significant thermal stress cracking and erosion of the throat insert are encountered which significantly reduces life and effectiveness of these parts.

Ceramic or ceramic coated prechambers have the potential to reduce the heat loss and reduce the erosion. Reaction bonded silicon nitride prechambers have been initially tested in an Opel Reckord Car by Ricardo & Co. and Advanced Materials Ltd. and later in several other automotive diesel engines. These engines ran noticeably quieter on cold startup and light load operation.

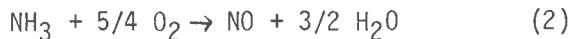
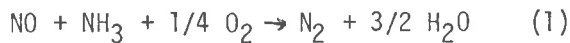
Most diesel engines with prechambers are high-speed engines used in autos or trucks. DOE is supporting investigating scaling up of a prechamber from a production small marine engine to a medium speed diesel. Ceramic and ceramic coated



prechambers will be investigated operating with SRC-II middle distillate, Exxon Donor Solvent and No. 2 diesel fuel as a comparative standard. Testing will be done with an adiabatic and conventional diesel. DOE objectives are to determine the effect of initially confined rich burn combustion in reducing both emissions and cetane No. sensitivity.

### NO<sub>x</sub> REDUCTION BY NH<sub>3</sub>

Exxon Research and Engineering has developed a process for reducing emissions of oxides of nitrogen (NO<sub>x</sub>) in combustion exhaust gases. In this process ammonia (NH<sub>3</sub>) reduces the NO<sub>x</sub> in a selective homogenous gas phase reaction, which means you don't need a catalyst. The reaction is simply the reduction of NO<sub>x</sub> by NH<sub>3</sub> and O<sub>2</sub> to N<sub>2</sub> and H<sub>2</sub>O. The process proceeds in the presence of excess oxygen within a critical temperature range. The overall NO<sub>x</sub> reduction and production reactions can be represented by the following competing reactions:



In typical flue gas environments, the NO<sub>x</sub> reduction of equation (1) dominates at temperatures around 950°C (1740°F). At higher temperatures reaction (2) becomes significant until the temperature exceeds 1090°C (2000°F) at which point injection of NH<sub>3</sub> is contraproductive causing increased NO. At flue gas temperatures below 850°C (1600°F) the rates of both reactions is extremely low, the NO reduction falls off drastically and the NH<sub>3</sub> flows through unreacted as shown in Figure 4. Hydrogen can be injected with NH<sub>3</sub> to shift the reaction to a lower temperature. At H<sub>2</sub>/NH<sub>3</sub> ratios of 2:1, the NO<sub>x</sub> reduction can proceed rapidly at 700°C (1290°F). Adjustments of this H<sub>2</sub>/NH<sub>3</sub> injection ratio can adjust the reaction for any intermediate temperature. (Figure 5) Costs are estimated in FY '77 dollars as 7-15 cents/10<sup>6</sup> BTU's fired. This NO<sub>x</sub> reduction by NH<sub>3</sub> has been demonstrated in twelve industrial/utility boilers. The effectiveness by which this process reduces NO<sub>x</sub> is illustrated in Figure 6 with 4 different coals and natural gas-firing. (7)

Mitsui Engineering & Shipbuilding Co. in Japan reported a series of tests in one of their medium speed diesel (530 rpm) burning coal tar. The two coal tar fuels used had fuel bound nitrogen levels of 1.12 to 1.33 wt. % and only 5 wt. % hydrogen. Mitsui used a NO<sub>x</sub> removal device in the exhaust in which NH<sub>3</sub> was injected. They report that this device reduced the NO<sub>x</sub> level from about 880 to 70 ppm, or a better than 90% reduction of NO<sub>x</sub>. This NO<sub>x</sub> reduction was achieved with exhaust gas entering the device at 400°C (752°F) and with a NH<sub>3</sub>/NO<sub>x</sub> ratio of about 1:3. (8) Comparing the Exxon and Mitsui data, it is clear that Mitsui is not using a homogenous gas phase reaction. Most likely they are using a catalyst in their device which is probably refractory metal oxides and/or transition metal oxides.

If a catalyst is used, the NO<sub>x</sub> removal device used by Mitsui appears outside the Exxon patent. In any event, diesel exhaust NO<sub>x</sub> emissions can be dramatically reduced by NH<sub>3</sub> or by baghouse systems. This should be very significant for operation with alternative fuels with high fuel bound nitrogen. There are insufficient data on the side effects of the process including the possible inhibition of the oxidation of CO to CO<sub>2</sub>. Is the CO oxidation complete before the exhaust gases reach the NH<sub>3</sub> injection point? Durability of the catalyst and the adequacy of NH<sub>3</sub> mixing throughout the power range are possible concerns. Ammonia handling, storage, injection and costs must be considered. In 1981 NH<sub>3</sub> costs about \$170/ton.

## CATALYTIC COMBUSTION

Gas turbine combustor development has used a catalytic converter for NO<sub>x</sub> reduction as shown schematically in Figure 7. Catalytic combustion dramatically reduces the combustion temperatures and thereby the thermal NO<sub>x</sub> formation. Logically the same effect should be possible with the diesel wherein heat release rate spike is reduced and spread out. In fact, that is essentially what Ricardo Consulting Engineers did in a joint program with Johnson Matthey & Co. As a bonus, since the start of combustion in the diesel is controlled by the catalyst rather than the heat of compression, the cetane number sensitivity of the engine is reduced.

Ricardo's first approach was two platinized catalyst grids installed in the combustion chamber which was a bowl in the piston crown. One Pt grid was installed on a radius of the bowl and the second one perpendicular to this grid such that it formed a cap for the piston bowl. Fuel was injected at an angle in the bowl such that it mixed with air and swirled through the bowl before encountering the vertical catalyst grid. Any unoxidized fuel would be consumed as it passed through the cap catalyst grid. This approach ran into power output problems attributed to insufficient movement in the bowl.

Ricardo was more successful with a Pt catalyst mesh installed in a prechamber as shown in Figure 8. This combustion system had a swirl ratio of 30 compared to a swirl ratio of 6 with direct injection. A photographic sequence of combustion events is shown in Figure 9. In the left of each frame is the prechamber viewed from the side and next to it is the simultaneous view looking down into the main chamber. The sequence of events is as follows:

- 1 - injection begins
- 2 - droplets of fuel pass down through catalyst and combustion starts
- 3,4 - combustion progresses to both sides of catalyst
- 5,6 - pre-mixed combustion is occurring around the periphery of the flame in the excess air in the piston cavities
- 7 - the bulk of combustion within the main chamber is complete but is still continuing in the prechamber
- 8 - combustion complete

This work indicated that combustion commenced catalytically during the latter part of heat release by droplet burning. The natural swirl of the combustion system was greatly reduced. The simple theory of fuel mixing with air and passing through the catalyst was not applicable to the photographed sequence. The Pt catalyst was shown to be necessary as the engine would not run with a stainless steel mesh of the same configuration installed in place of the Pt catalyst mesh.

A Pt catalyst in the prechamber has shown that NO<sub>x</sub> and hydrocarbons in the diesel exhaust are reduced, the engine runs quieter and the engine operates with reduced cetane sensitivity with methanol and gasoline. Additional work is needed to improve the power output, reduce fuel economy at high loads and extend the durability of the catalyst.

## NAHBE

The Naval Academy Heat Balance Engine (NAHBE) employs a mushroom shaped cap on the piston and a manifold modification to either a conventional spark assisted or

compression ignition engine. This cap separates the combustion volume from the secondary volume which ideally contains only air. Air precedes the fuel air charge entering the cylinder by a novel manifold change. During the compression stroke this separate charge of air enters the secondary chamber under the cap through a narrow annulus between the cap and the cylinder wall. On ignition, a compression wave precedes the flame front, compresses the air and pumps it to the upper combustion chamber. This provides air for a secondary combustion. Pressure and temperature of combustion are determined by the geometry of the cap. (10) The NAHBE Concept, primarily in the spark ignition mode has been supported by the Office of Naval Research for several years. DOE is interested in the capability of NAHBE to provide complete combustion with alternative fuels in the compression ignition version. The heat release spike can be blunted and the secondary air exchange may assist complete combustion.

A NAHBE variable compression lab engine was operated with a small quantity of SRC-II MD. In the compression ignition mode, the lower limit of compression ignition was at a compression ratio of 8.0:1, stable compression occurred at 9.05:1. At a compression ratio of 9.67:1 the engine operation was steady with good acceleration response. Exhaust temperatures were low, 1050°F at 1500 rpm and maximum power output. (11) A DOE program to investigate the advantages of the NAHBE concept with alternative fuels has been deferred due to budgetary limitations.

### EROSION

The patent for the combustion ignition or diesel engine was issued in 1892 to Rudolph Diesel. Early work by Diesel was directed at having his engine operate on coal dust. However, severe cylinder liner wear in short-term operation prompted early developers to change to liquid fuels. Diesel engines operating on coal encounter an abrasive wear problem from the ash in the fuel and unburned carbonaceous particulates. This severe abrasive wear problem was also encountered in Germany during World War II in development of coal burning diesel engines (12) to the extent it was a "show stopper." The British Army encountered engine wear which reduced engine life to under 100 hours in early operations in North African deserts in 1940. A solution developed was the chrome plated piston ring while retaining the cast iron liner which has been extensively used since. Micronized coal in No. 2 oil caused severe erosion in injectors and cylinder liners in tests at Sulzer, Burmeister & Wain and Virginia Tech. Durable operation with coal-derived fuels in micronized or dust, slurries or in liquid form requires abrasive erosion resistant cylinder liners, exhaust valves, injectors and fuel pumps. There are several efforts underway that have the potential to dramatically reduce these abrasive wear problems.

In the early '70's the British Army tried out their Chieftan main battle tank in Finland during winter months. These battle tanks are powered by the Leyland L-60, 2-stroke, 6 cylinder diesel with opposed pistons on twin crankshafts which is rated at 700 HP. The tank operators mixed kerosene with the fuel oil to obtain adequate viscosity in very cold weather. This kerosene blending with the fuel produced severe wear in the cylinder liners which significantly reduced their life below the normal 250 hours when replacement was normally required. (13) This cylinder wear problem was brought to the attention of the Royal Armament Establishment, Ft. Halstead. A very intriguing development emerged on this project on contract with Laystall Engineering. Laystall developed a 3-stage process of impregnating the porous cast iron cylinder liners with silicon carbide. Mechanical honing is used in the initial stage to physically force a slurry of coarse 200-grit silicon carbide into the liner surface under pressure. The next step involves lapping the first deposit with finer 400-grit silicon carbide using the same honing tool. This step also fills the remaining interstices. The third step involves replacing the iron inserts in the honing device with flexible plastic sticks and polishing the liner. The thickness of the carbided surface layer is 0.0003 to 0.0005" requiring machining

to account for this reduced bore diameter. Laystall reports tank engine life is extended beyond 4,000 hours with this process which is now in production status. Current work is underway investigating silicon carbide impregnation of various cast irons, steel and aluminum. (14)

DOE has several interests in silicon carbide impregnation of cylinder liners. It may provide the improved wear resistance necessary with some forms of coal fuels. In fact it could make some of the coal fuels viable! In addition, this carbiding process may be a replacement for chrome plating of rings which would reduce use of a critical material. DOE is having some cylinder liners and test specimens carbided by Laystall for test and evaluation in the U.S.

Some versions of silicon carbide and silicon nitride have outstanding resistance to wear. However, among the difficulties encountered in ceramic gas turbine developments, the inability of monolithic ceramics to distribute loadings was pre-eminent. What is needed is a "ductile ceramic." United Technologies Research Center (UTRC) is developing a range of fiber strengthened glass and glass-ceramic matrix composites which they call COMPGLAS. The glass matrix, because of its viscous flow characteristics, can be densified at high temperatures without damage to reinforcing fibers. Young's Modulus of Elasticity values for most glasses and glass-ceramics are considerably lower than those of many reinforcing fibers. This characteristic enables the load to be transferred from the glass matrix to the fibers. The current limitation of this material is the physical/chemical stability above 1000°C. While this temperature limit prevents use in most gas turbine hot-section applications, it is not a restriction for any diesel component with the possible exception of some prechambers.

DOE is starting a program with UTRC and International Harvester to examine the application of fiber reinforced ceramic materials as diesel engine combustion zone components. High on the priority list is an erosion resistant cylinder liner. These COMPGLAS components have the potential to provide durability with a wide range of alternative fuels, and might well contribute to making the adiabatic diesel engine concept achievable.

#### HOT-CORROSION

U.S. industrial/utility medium speed diesel engines operate primarily on No.2 diesel fuel or natural gas. The hottest engine components are the exhaust valves that operate at temperatures just below the threshold of aggressive hot-corrosion. Europeans and the Japanese operate slow-speed and medium-speed diesel engines on residual fuels because their refineries produce roughly 40% residual, while the product slate from U.S. refineries is only about 10% residuals, and the cost differential is substantial in Europe between residual and light distillate No. 2 diesel fuel.

After the "Yom Kippur War" in 1973, the quality of residual fuels from European and Japanese refineries decreased as the refiners attempted to extract more quality fuels. A very significant increase in hot-corrosion attack on diesel engine combustion zone components was noted as a result of fuel quality. This problem prompted the Norwegian Shipowners Association and the Norwegian Research Council to initiate a program with the Central Institute for Industrial Research in Oslo to investigate the problem and develop a solution. The problem was hot-corrosion, specifically  $\text{Na}_2\text{SO}_4$  attack enhanced by vanadium and  $\text{SO}_3$ . Some of the fuels used in Europe contain about 100 ppm vanadium, 50 ppm sodium and 4% sulfur. These levels vary significantly from the refinery and the crude feedstock. Some Venezuelan crudes have more than 300 ppm vanadium.

The Central Institute's solution was a series of coatings for exhaust valves and piston crowns that more than doubled the life of these components in service operating on the low-grade residual fuels. Most successful coatings have been variations of plasma spray deposited magnesia stabilized zirconia outerlayers over NiCoCrAlY bond coats. Early coatings on the exhaust valve covered the seating surface after the stellite overlay was undercut to accommodate the thermal barrier coating thickness. These coatings maintained mechanical integrity under thousands of hours of seat/face impacts, valve head flexure and thermal stresses. In fact the insulation was too good and later exhaust valves had only a NiCoCrAlY metallic coating on the valve seat face surface while the zirconia covered the valve head and the fillet up to the stem. This was done to increase the heat transfer from the valve seat face to the seat in the engine housing, which was water cooled, while the thermal barrier coating effectively reduced combustion heat transfer to the valves.

DOE anticipated the more economical versions of the alternative fuels would have more severe corrosion/erosion effects than experienced with No. 2 diesel fuel. Coal derived liquid fuels have about a 60% lower H/C ratio and consequently burn with a more luminescent flame. As a result, combustion zone components would run more than 38°C (100°F) hotter, which should enhance hot-corrosion. Some of the known aggressive hot-corrosion elements are anticipated in the alternative fuels in addition to higher levels of erosion causing particles than has been encountered. Engine intake air, particularly around coastal areas, will also introduce hot-corrosion active sea salts. Thus, as part of the DOE effort to ensure reasonable engine durability in order to encourage early use of alternative fuels, a program was initiated to test and evaluate in the U.S. the Central Institute's coatings that had performed well in marine propulsion with residual fuels.

Exhaust valves coated by the Central Institute with stabilized zirconia coatings were tested on DOE contract with DeLaval in engines operating on No. 4 fuel at Annamax Mining in Arizona, as part of Cummins Adiabatic Engine development and by Eaton in their laboratory equipment. In addition, a large number of specimens were provided to the Naval Research Laboratory (NRL) for mechanical property testing. Although these evaluations are not complete, preliminary assessments are quite favorable.

While there has been considerable use of plasma spray, the fundamental understanding of the process and the powders has not received adequate attention. Dr. Kvernes at the Central Institute has made several contributions to ceramic or thermal barrier coating development. Until recently only 10% H was the limit with H/AR gas used in plasma spray. With new power supplies, he was able to get 20-30% H levels which has a beneficial effect on the coating structure. Also, Dr. Kvernes has analyzed the ceramic powders more thoroughly for ceramic coating depositions than has been otherwise reported. Zirconia has by far been the most extensively used ceramic for thermal barrier and corrosion resistance primarily because of its thermal conductivity, which is fairly close to that of hot-section metals. Zirconia will undergo a phase change from monoclinic to tetragonal upon cooling from engine level temperatures. Thus it is necessary to add a stabilizer such as oxides of yttrium ( $Y_2O_3$ ), calcium (CaO) or magnesium (MgO) in the cubic phase. Kvernes' work indicates European powders are superior to U.S. powders with respect to chemical composition and homogeneity, grain size and shape, level of moisture and other contaminants. He points out that added stabilizing oxides frequently are not prereacted in powders obtained from U.S. sources. MgO stabilized zirconia powders show MgO-rich areas on every  $Zr_2$  particle. In one batch of 20%  $Y_2O_3$  stabilized powders, the powder was analyzed to be made of spherical particles, each particle being a mechanical mixture of the two oxide components. Thus, the stabilizing reaction must take place in the plasma flame. Powders of this type result in an inhomogeneous coating that has a varying extent of being stabilized or has regions that are not stabilized at all. (15)

The effects of stabilization on ceramic coating life needs to be further studied. Systematic analyses of ceramic powders for plasma spraying need to be conducted and assessed with respect to lab and engine testing. Better quality ceramic powders are available from Starck in Germany and Castolin in Switzerland than those analyzed from U. S. sources. (16)

The Russians are plasma spraying a coating system comprised of a 3 mil thick molybdenum bondcoat and a 3 mil aluminum silicate outer layer on 6" diameter piston crowns for truck diesel engines. The Russians indicate they are getting more complete combustion, less depositions in the combustion chamber and improved fuel economy which they attribute to this "catalytic coating." Aluminum silicate is actually a thermal barrier coating which provides a more stable combustion flame front. The improved performance may result from more complete and sustained combustion during the power stroke. They also claim diesel engines with these coatings are easier to start in cold weather. These ceramic results lend additional support to their adiabatic diesel concept.

### ADIABATIC DIESEL

The most intriguing development in the diesel engine field in recent years is the adiabatic diesel concept. Thermodynamicists postulated the adiabatic wall as an ideal perfectly insulated surface to assist in thermal analysis. The term adiabatic diesel has come to represent a diesel engine with a very well insulated combustion chamber. Army interest in the adiabatic diesel concept included improved efficiency and an uncooled engine. One impetus for the uncooled engine is the vulnerability of the engine's cooling system on a battle tank. Reducing the size of the radiator is attractive but elimination of all the cooling system is highly desirable. Improved efficiency in a cooled adiabatic engine accrues from reduced heat transfer to the cooling water, improved combustion efficiency and enhanced exhaust heat recovery from the resulting elevated exhaust gas temperature.

DOE is interested in the adiabatic engine concept to reduce cetane number sensitivity to alternative fuels, reduced emissions extended durability and improved efficiency. Combustion efficiency is increased as the ceramic piston or ceramic coated piston crown spreads the heat of combustion evenly and improves uniformity of the flame front travel. More complete combustion should reduce organic NOx and enhance even heat distribution with elimination of hot spots which may reduce thermal NOx. Some ceramic materials have excellent erosion resistant characteristics which could play a significant role in providing durability with alternative fuels that are corrosion problems.

Problems encountered developing ceramic gas turbine airfoils were very much more severe than those faced in early work with diesel pistons, cylinder liners and exhaust turbines. Geometries are much simpler, pressure loadings are more evenly distributed and temperatures are considerably lower in the diesel parts. A production line of ceramic parts for diesel engines could well provide the base needed to extend ceramic use to gas turbine engines. Ceramic roller bearings for wrist pins, crank pins and main bearings are being studied as well as solid lubricants for gears, valve guides, rocker arm and push tube assembly. (17) Lithium alumina silicate (LAS) is being used for a number of components. LAS has attractive low cost and a very low thermal expansion coefficient but has low strength. Ceramic fibers reinforcing the LAS matrix, such as the UTC COMPGLAS, improved the strength and load distribution of the glass ceramic.

The most comprehensive adiabatic diesel development reported has been done at Cummins under Army support. DOE is supporting work at Cummins to investigate performance and emission effects of the adiabatic diesel engines insulated combustion chamber with SRC-II middle distillate and Exxon Donor Solvent (EDS) compared with operation on No. 2 diesel fuel and with a conventional combustion chamber. Prechamber spark assisted and dual fuel systems will also be assessed with the adiabatic diesel and coal derived fuels.

### ELECTRONIC FUEL CONTROL

The major cost reduction achieved with microprocessors in the early '70's is a major factor in development of engine condition monitoring systems. A production version may shortly be introduced in automobiles. Engine condition monitoring has been used in some aircraft for a decade or more. The Navy developed fairly sophisticated engine condition monitoring systems for marine gas turbine engines. There have also been diesel engine condition monitoring systems developed. Alternative fuel use in diesel engines can be enhanced by engine condition monitoring.

It would be within the state-of-the-art to have an engine condition monitoring system calculate performance from measured parameters and optimize injection for virtually each stroke. Thus, the optimum blend of a coal-derived fuel and No. 2 diesel fuel could be maintained for each power setting. Pilot injection could be likewise optimized.

Pilot injection with SRC-II produced some very interesting, but not well understood, results in DOE work conducted at Southwest Research Institute (SRI). They found that pilot injection of 5% No. 2 diesel at  $115^{\circ}$  BTDC and a main injection of SRC-II MD at  $1^{\circ}$ ATDC produced smooth operation, rates of pressure rise and thermal efficiency equivalent to that obtained with 10% optimized pilot injection. Typically pilot injection is  $10^{\circ}$  to  $20^{\circ}$  before the main charge and the main charge is injected at  $4^{\circ}$  BTDC. SRI surmises that at the  $115^{\circ}$  BTDC pilot injection, which closely follows the exhaust valve closing at  $119^{\circ}$  BTDC, the pilot fuel does not compression ignite but disperses and evaporates. Through an unknown interaction between the main fuel charge and the pilot, combustion starts shortly after the start of main injection.

This SRI work suggests the pilot injection and main charge injection may vary with fuels, power setting and engines. Thus, electronic fuel control of fuel spray patterns, timing and pilot injection could play a major role in use of some coal derived fuels. A contract has just been initiated with the UTRC to determine the advantages of electronic fuel control with a precisely controllable fuel injection system. The logical progression would be to incorporate the electronic fuel control in an engine condition monitoring system adapted for alternative fuel use.

There has been some clever work done to determine the condition of the diesel engine internals without engine disassembly by condition monitoring. Abnormal wear rates caused by scuffing can be detected by a special surface thermocouple developed to measure the temperature flashes produced by microseizure between piston rings and the cylinder liner. The frequency of scuffing temperature flashes can be used as a parameter and can be programmed as an alarm. Piston ring condition can be measured by proximity sensors in the cylinder liner wall. These sensors measure the distance between the liner wall and piston ring surface and provide a means to detect sticking and broken piston rings. Computerized counting of ring passages per stroke will provide data on the number of failed rings. Thermal and pressure measurements will also provide condition and performance data on cylinders and injectors. (19) One of the problems is developing appropriate fault signatures.

As previously discussed,  $\text{NH}_3$  injection in the exhaust can dramatically reduce  $\text{NO}_x$ . The introduction of  $\text{NH}_3$  could be readily controlled by the microprocessor and exhaust sensors. The microprocessor could also be programmed to optimize bottoming cycles. Engine condition monitoring systems using state-of-the-art capabilities could be developed to pay their way in engine performance and maintenance.

## CONCLUSIONS

Alternative fuel commercialization is in the formative state. Coal in a pulverized benefacted state in a water slurry, coal gasification, coal derived liquid fuels shale and biomass fuels are the alternative fuel candidates for the next two decades. The heat engines that can operate in a cost-effective and an environmentally acceptable manner on these fuels will have major advantages over those engines that can not. Multi-fuel capability rapidly emerges as a top priority diesel engine R&D goal as long as it has superimposed appropriate engine durability, performance and emission concerns. Low-speed diesel engines and, to a lesser but still substantial degree, medium speed diesels have a multi-fuel capability unmatched by other production heat engines. The very attractive high efficiency of the diesel over a wide power range makes it virtually the unanimous choice for commercial marine propulsion of new construction and a strong option for replacing existing steam and gas turbine propulsion engines.

The problem with diesel engine operation on current fuels is primarily emissions and the problems encountered when burning coal based fuels such as pulverized coal slurries are erosion, complete combustion and emissions.  $\text{NO}_x$  emissions may be reduced by prechambers, catalytic prechambers, some form of the insulated combustion chamber or adiabatic engine, spark assisted, electronic fuel control with computerized engine diagnostic input, NAHBE concept or possibly some combination of these concepts. Exhaust gas  $\text{NO}_x$  can be reduced by more than 90% by use of a device that mixes  $\text{NH}_3$  with the gas in the presence of a catalyst. The conventional baghouse could also be used. Elevated exhaust temperatures from versions of the adiabatic engine concept are compatible with waste heat utilization bottoming systems or turbocompounding. Advanced materials and high temperature lubrication could make the adiabatic engine concept viable.

Rapid erosion in the cylinder liners and fuel injectors have prevented use of coal in diesel engines although this was the initial thrust of the inventor of the diesel engine. Germany devoted considerable effort to this problem in WWII but achieved only modest progress. The SiC impregnated cylinder liner work by the British is an intriguing erosion resistance improvement although not yet adequately assessed for coal derived fuels. Woven ceramic fibers in a glass matrix, such as COMPGLAS developed by UTRC, hold considerable promise for erosion resistance and insulation of the combustion chamber. Recent improvements in plasma spray, electron beam physical vapor deposition and sputtering of ceramic materials suggest that appropriately focused programs could ameliorate the erosion and hot-corrosion problems within a few years.

Hot-corrosion has become a significant problem with diesels operating on residual fuels of low quality. Hot-corrosion and erosion should be addressed in a coordinated materials effort including mechanisms investigations, which is flexible to address these problems with candidate alternative fuels as they emerge. Advanced materials could very well make an economic version of an alternative fuel viable for heat engines use. Materials development are the key to improvement in diesel engine performance, emissions reductions and durability. Ceramic materials



in monolithic, composite or as coatings hold a near-to-mid-term potential pay-off in diesels as the engine conditions are much less severe than those encountered in gas turbines. Materials technology that may enable the diesel to prevail as the most cost-effective heat engine with some forms of alternative fuels and applications is logically a cross-cut from the materials technology base developed to support gas turbines.

## References

- 1) Maleev, V.L., "Diesel Engine Operation and Maintenance," Page 26 McGraw Hill, New York, 1954
- 2) Thomas, R.L., "Alternate Fuels for Industrial Combustion Engines" ESCOE Report FE-2468-77 on DOE Contract No. EF-77-C-01-2468 Washington, June 1980
- 3) Pruce, L.M. "NO<sub>x</sub>-Reduction Efforts for Gas Turbines Continue; In Face of Stiff Regulations, Fuel Uncertainties," Power, Vol. 125 May 1981
- 4) Pischinger, R. & Cartellieri, W., "Combustion System Parameters and Their Effect Upon Diesel Engine Exhaust Emissions," SAE Paper 720756, 1972
- 5) Steiger, H.A., Eberle, M.K., Davis, J.P., and Dunlay, J.B., "Slow-Speed Two-Stroke Diesel Engine Tests Using Coal-Based Fuels," ASME Paper 81-DPE-12 presented at Energy Sources Technology Conference, Houston, Texas January 18-22, 1981
- 6) McLaughlin, D., "Ceramic Applications in the Diesel Engine" Advanced Materials Engineering, Ltd., Gateshead, UK 1978
- 7) Lyon, R.K., "Thermal DeNO<sub>x</sub>: How it Works," Hydrocarbon Processing, Pages 109-112, Oct. 1979
- 8) Anon, "Background of Mitsui - Developed M-Series 4-Stroke Medium Speed Diesel Engines" Mitsui Engineering & Shipbuilding Co., Ltd. TN-53206 - (presented at 13th CIMAC Meeting)
- 9) Thring, R.H., "The Catalytic Engine," Platinum Metals Review, Vol. 24, No. 4, London - Oct. 1980
- 10) Pouring, A.A. et al "Parametric Variations of a Heat Balanced Engine," U.S. Naval Academy Report No. EW-12-79 Annapolis, Md. Sept. 1979
- 11) Personal Communication, Prof. Pouring, U.S. Naval Academy, John Fairbanks, DOE, April 10, 1980
- 12) Soehngen, E.E., "Development of Coal Burning Diesel Engines in Germany" Report FE/WAPO/3387-1 prepared for ERDA, August 1976
- 13) Letter, J.E. Tanner, Laystall Engineering, Wolverhampton to J.W. Fairbanks, DOE, Washington, D.C., 31 July 1980
- 14) Scott, D., "Carbide Impregnation Cuts Cylinder Bore Wear," Automotive Engineering, Dec. 1976

- 15) Kvernes, I., Fartum, P., and Henriksen, R., "Powder Selection for Plasma Sprayed Coatings in Diesel Engine Applications," International Metallurgical Coatings Conference, AUS, San Diego, California, April 1980
- 16) Boone, Lawrence Berkeley Laboratory Trip Report, Europe, June 1981
- 17) Anon, "An Update on Turbocompound and Adiabatic Engine Programs", Diesel Progress North American, Vol, XLVII, No. 7, July 1981
- 18) Baker, Q. A., "Alternative Fuels for Medium Speed Diesel Engines," Monthly Progress Report No. 25, SWRI Project No. 11-5381, Contract No. EM-78-C-01-4266 with DOE, Aug. 1980
- 19) Riksheim, J. B., Wiborg, T., and Tuft, Q., "Condition Monitoring of Diesel Engine Cylinder Units - Experience - Economic Considerations," Det Norske Veritas Report No. 76-429, Oslo, December 1976

**TABLE 1: COMPARATIVE COSTS OF ALTERNATE ENGINE FUELS**  
**1980\$/10<sup>6</sup> Btu (LHV)**

	DISTILLATE				GASEOUS	
	SHALE OIL	COAL LIQUIDS	METHANOL (COAL)	ETHANOL (BIOMASS)	LOW BTU	SNG
RESOURCE	0.20*	1.50	2.10	9.00 - 13.50**	1.25	1.85
MINE	2.30					
RAILROAD	MINEMOUTH PLANT	MINEMOUTH PLANT	0.69		0.71	MINEMOUTH PLANT
CONVERSION***	1.70 - 1.90	2.55 - 4.60	5.00 - 9.05	7.70	2.40 - 3.00	4.20 - 6.05
PIPELINE	0.25	0.25				0.60
REFINERY	NIL***	1.60 - 2.70				
PRODUCT PIPELINE	0.11	0.11	0.40	0.91 (RAIL)		
TERMINAL STORAGE						
PIPELINE, TRUCK OR RAIL TO CUSTOMER	0.31	0.31	0.73	0.55		
CUSTOMER STORAGE						
1980\$/10 <sup>6</sup> BTU***	4.87 - 5.07 4.97	6.32 - 9.47 9.07	8.92 - 12.97 12.82	18.16 - 22.66 22.66	4.36 - 4.96 4.96	6.65 - 8.50 7.00

\* LEASE BONUS BID PAYMENT

\*\* INCLUDES COLLECTION AND TRANSPORT TO CONVERSION UNIT.

\*\*\* REFLECTS RANGE OF PUBLISHED STUDIES

\*\*\*\* MOST REPRESENTATIVE COST BASED ON AMOUNT OF DETAILED INFORMATION AVAILABLE

## LIST OF FIGURES

<u>Figure</u>	<u>Title</u>
1	Heat Release Rate at Three Injection Timings
2	Piston Ring Wear in Coal-Oil Slurry Test
3	Fuel Valve Nozzle after One Hour Coal Slurry Test
4	NO Reduction and NH <sub>3</sub> Consumption as a Function of Temperature
5	Addition of Hydrogen Decreases the Optimum Temperature for NO Reduction
6	Effectiveness of NO <sub>x</sub> Reduction by NH <sub>3</sub> in Boiler
7	Gas Turbine Catalytic Combustor
8	Precombustion Chamber
9	Sequence of Events with Pt Catalyst in Prechamber

### HEAT RELEASE RATE EFFECT AT THREE INJECTION TIMINGS

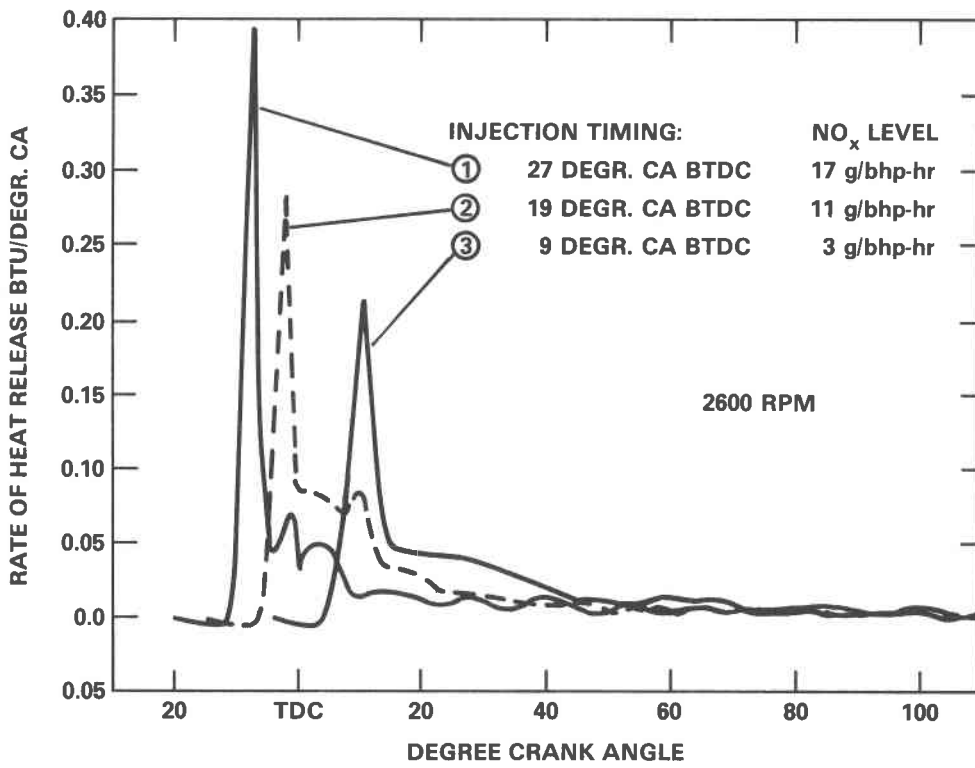
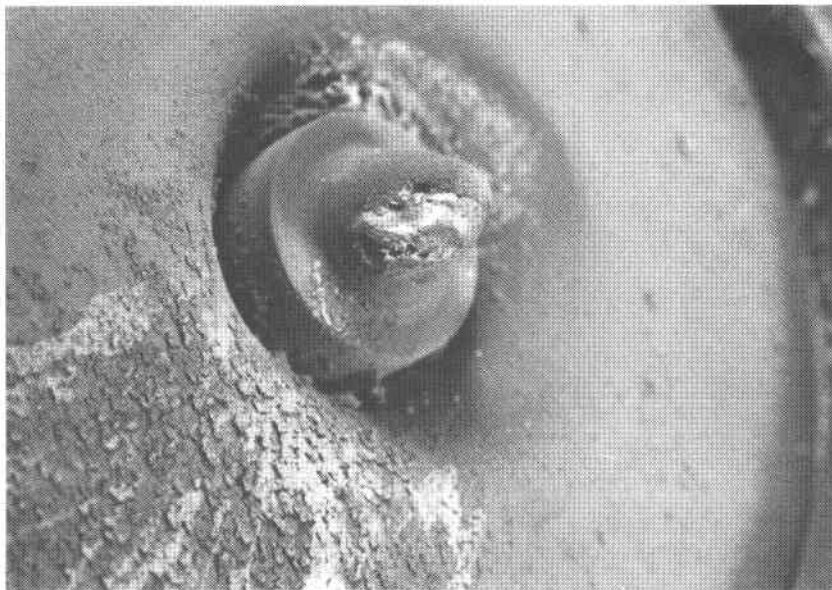


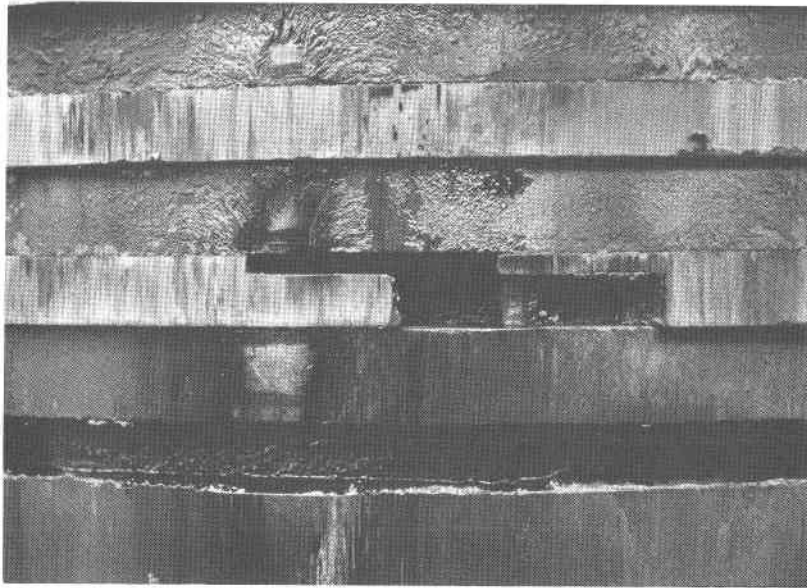
Figure 1 — Heat Release Rate Effect at  
Three Injection Timings



CONDITIONS:  
CONSTANT LOAD 100%  
CONSTANT RPM 150  
CONSTANT SCAVENGING  
PRESSURE 1.80 BAR  
SAME INJECTION TIMING

FUEL VALVES NOZZLE  
FUEL: COAL SLURRY  
AFTER TEST 1 HOURS  
SXH E 2320

Figure 2 – Fuel Valve Nozzle After 1 Hour Coal-Oil Slurry Test



CONDITIONS:  
CONSTANT LOAD 100%  
CONSTANT RPM 150  
CONSTANT SCAVENGING  
PRESSURE 1.80 BAR  
SAME INJECTION TIMING

PISTON RINGS  
FUEL: COAL SLURRY  
AFTER TEST 1 HOURS

Figure 3 – Piston Ring Wear In Coal-Oil Slurry Test



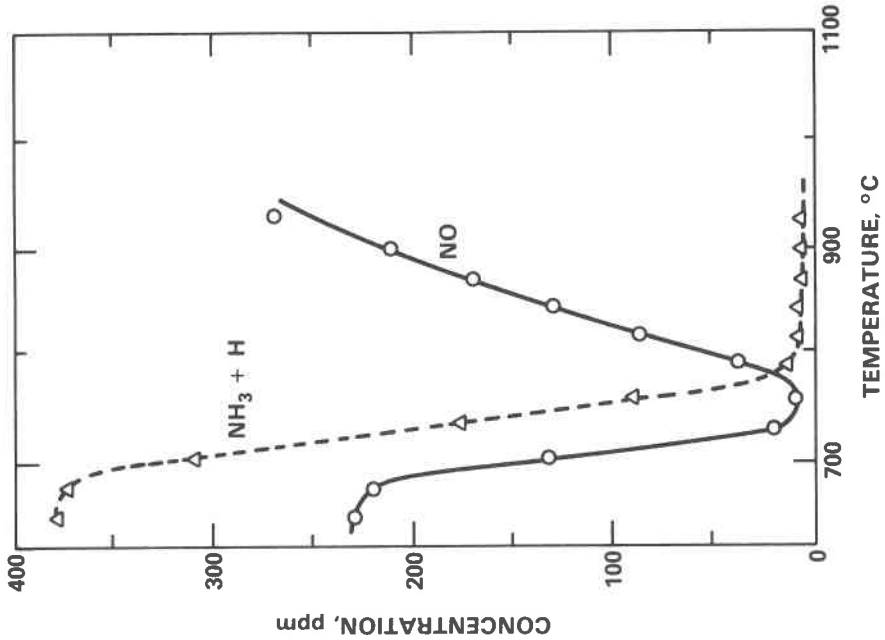


Figure 5 — Addition of Hydrogen Decreases the Optimum Temperature of NO Reduction

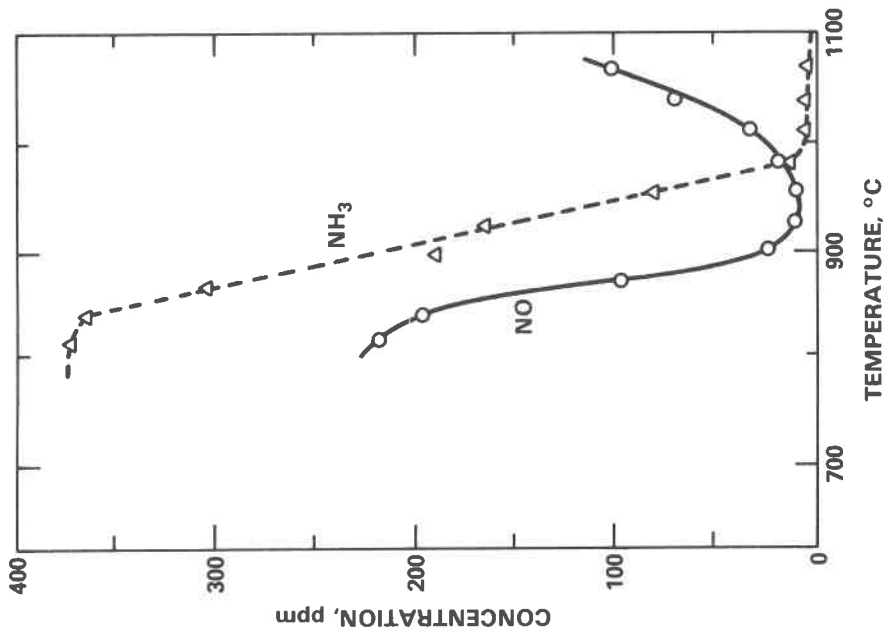


Figure 4 — NO Reduction and NH<sub>3</sub> Consumption as Function of Temperature (Lab Data for 2% O<sub>2</sub>; NH<sub>3</sub>/NO = 1.7 and Time is 0.2 Seconds.)

### EFFECTIVENESS OF NO<sub>x</sub> REDUCTION BY NH<sub>3</sub> IN BOILERS

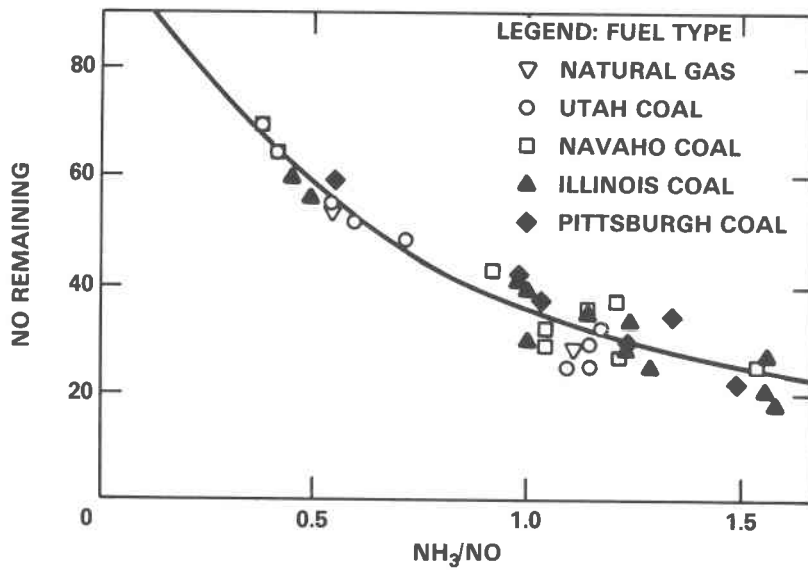


Figure 6 — Effectiveness of NO<sub>x</sub> Reduction  
by NH<sub>3</sub> in Boilers

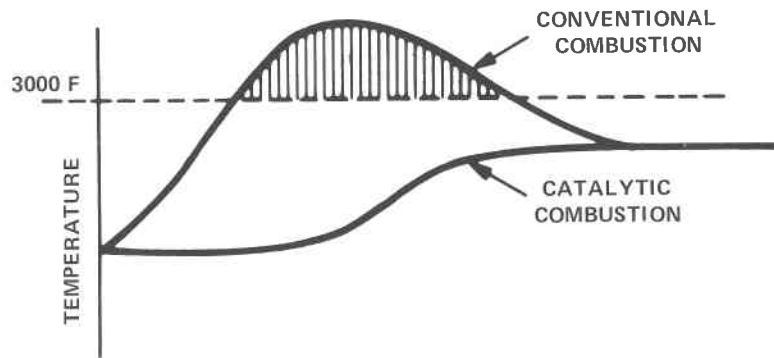
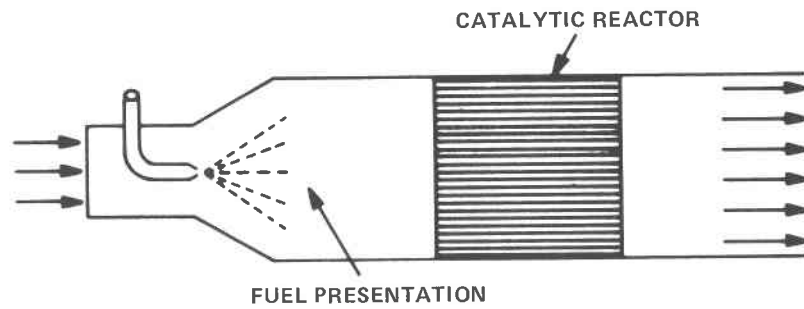
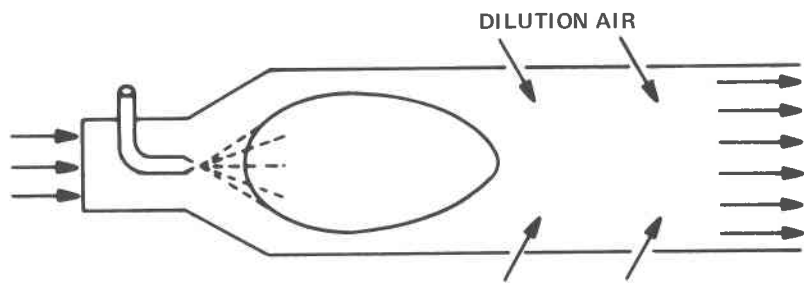


Figure 7 — Gas Turbine Catalytic Combustor

# PRECOMBUSTION CHAMBER

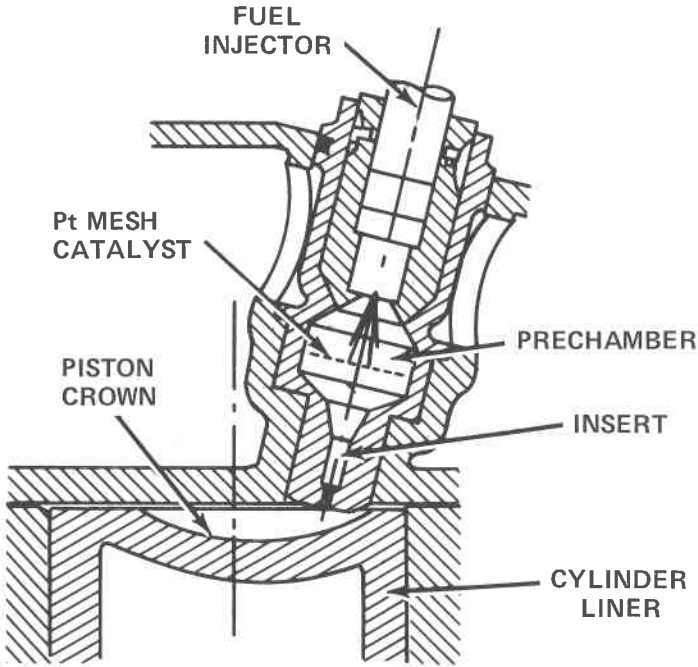
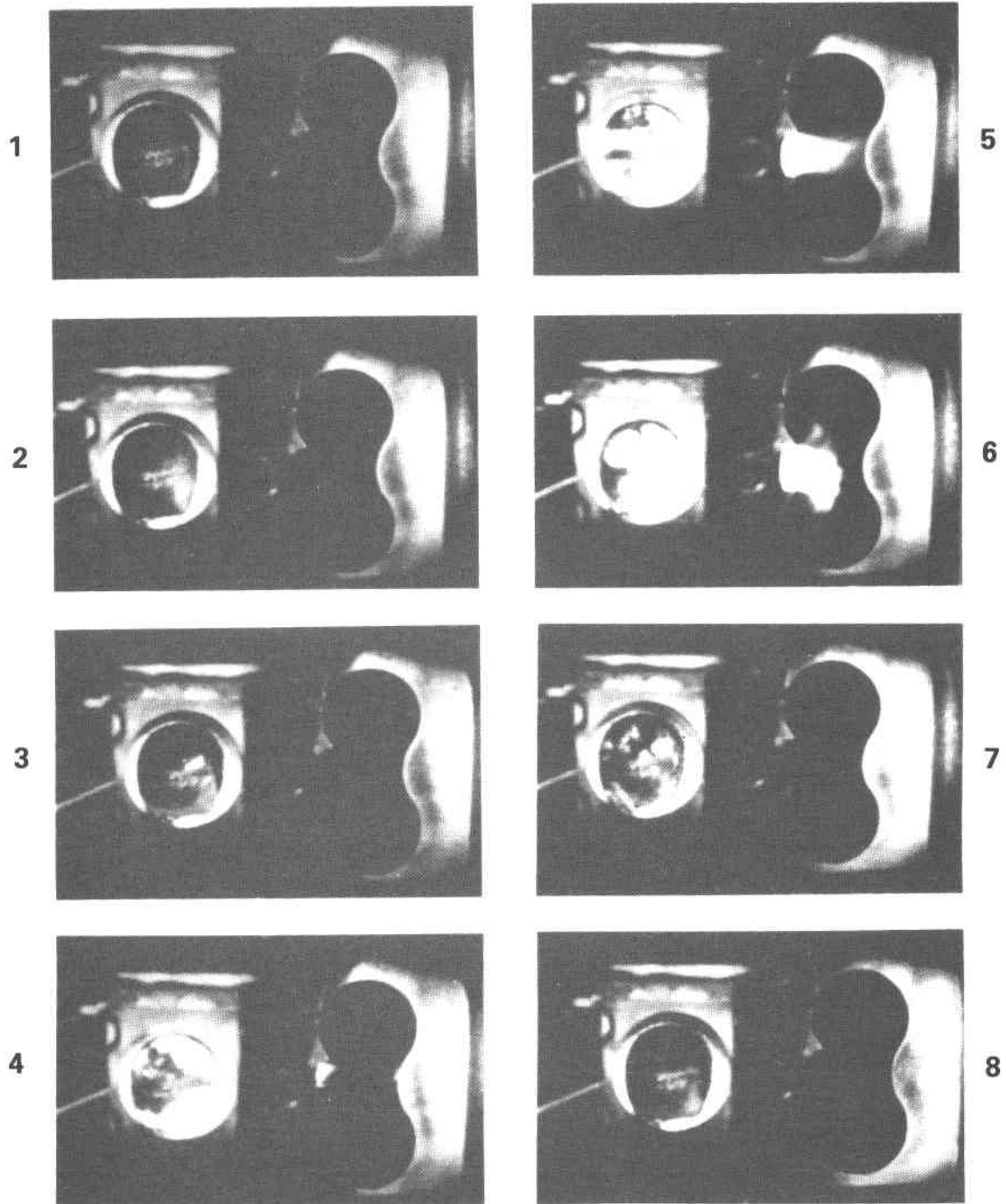


Figure 8 – Precombustion Chamber



**Figure 9 – Sequence of Events with Pt Catalyst in Prechamber.  
(Prechamber From Side Appears in Left of Each Photograph  
and Main Chamber From Above is Seen on Right)  
Courtesy Ricardo Consulting Engineers**

## METALLIC HEAT EXCHANGERS

John Stringer  
Electric Power Research Institute

and

Holger Lukas  
Encotech, Inc.

### INTRODUCTION

Within heat engine systems there are usually a number of heat exchangers whose function is to ensure the maximum conversion of the thermal energy. In particular, it is often convenient to use a secondary working fluid rather than the hot combustion products of the fuel itself, as for example in steam turbines, indirectly fired gas turbines or Stirling engines. The heat exchanger in which heat is exchanged between the combustion products and the secondary working fluid normally sees the most severe environment within the system and presents the most difficult materials problems. The stringent design requirements for recuperators in closed cycle engines, for air preheaters, or for condensers may also present significant materials problems. However, these are not problems which are different in alternative fuel capable systems from those in the more conventional systems and will not be discussed in this paper.

Heat exchangers are of two types. A recuperator has a continuous flow of heat from one fluid to another. Generally the two fluids are separated by a membrane through which heat passes; this may be metallic, the case considered in this paper; or ceramic, the case to be considered by Bakker and Kotchick. Efficient heat transfer requires the membrane to be as thin as possible, and its surface area relative to the fluid flow as large as possible. The thermal conductivity of the membrane may be a factor, and fouling by slag or deposits can have a significant effect. In a regenerator a thermal reservoir is heated for a time by the primary fluid, then the flow switches and the secondary fluid is heated up by passing over the heated reservoir. An example is the rotary Ljungstrom air heater. Again, a large surface area relative to the fluid flow is desirable, but in addition the thermal capacity of the reservoir material should be as high as possible.

Recuperators are of two principle types. In the tube and shell or tube and manifold type one fluid flows through tubes connected by a manifold of some kind. The other fluid flows over the outside of the tubes, contained within a larger vessel, the shell. In a plate and fin exchanger the two fluids flow on either side of thin flat plates, the general flow path being essentially symmetrical.

Recuperators and heat exchangers have been designed both with plain and extended surface heat transfer areas. The purpose for the use of extended surface area is to increase the rate of heat transfer. Ideally, the rate of heat transfer outside the surface or tube should be very close to that of the inside surface or tube. If one is much greater than the other, the lesser becomes the limiting or governing function. Extended surface heat transfer areas have a greater pressure drop than plain surfaces. When using extended surface heat transfer, an analysis must be made relative to the penalty of increased pressure drop to that of the increased heat transfer area and therefore reduced size.

The most important group of primary heat exchangers, those used for heating a secondary working fluid with hot combustion products, are tube and manifold types. Examples are conventional boilers, fluidized bed combustors used either as boilers or air heaters, syngas coolers, and fired air heaters for gas turbines. The combustion gases may be on the inside or the outside of the tubes (for example, fire-tube or water-tube boilers). The major problems with these heat exchangers include oxidation and corrosion on the fireside; creep rupture; thermo-mechanical fatigue; erosion by ash particles in the gas stream; and erosion by soot-blowers used to remove deposits. The construction involves some specific problems: junction of the tubes to the manifold or tube sheet and austenitic-to-ferritic welds, for example.

Many of these problems can be solved by appropriate selection of materials and proper design. In some cases however the limitations of available materials can have considerable significance in terms of the design relaxations which are forced. An example is the syngas cooler for entrained slagging gasifiers. It would obviously be desirable to attain the highest possible temperature in the secondary fluid in this cooler, but the actual maximum temperature is determined by the corrosion resistance of available materials in the syngas environment. Some aspects of corrosion and erosion relevant to specific heat exchangers will be presented in later papers.

## HEAT EXCHANGERS IN GAS TURBINE SYSTEMS

Recuperators have been used in gas turbines both in peaking (intermittent duty) and in base load (continuous duty) applications and not always successfully. Early recuperators were of the tubular type of the "gas in tubes" "air in shell" design. After those early tubular recuperators, the less expensive plate type recuperators appeared on the scene. These units were successful when used in continuous duty applications, but when used in cyclic applications, they started to fail both in metal fatigue and due to low temperature corrosion. The early type of plate fin regenerators were of the "compression braze" design (Figure 1). In this method of construction, a gas fin and two tube sheets are brazed together using copper as the brazing alloy. A spacer bar is welded between two such assemblies. The compressed air flows between the two tube sheets while the exhaust gas flows in the finned passages. The air pressure between the two tube sheets pushes the plates against the fins loading the joint in compression. The air pressure tends to separate the two plates and therefore must be restrained by what is referred to as a structural or pressurized strongback. In cyclic duty application, thermal fatigue is incurred due to the differences in thermal time constants of the thin plates and the heavy strongbacks. Failure of the tube sheets occurs. Additionally as the fins are loaded in compression, weakening of the fins resulted in buckling and subsequent rupture of the air passages. To reduce the problem of thermal fatigue, redesign of the strongback or pressure containing parts has been performed.

Recently another type of plate fin regenerator has come into use. This is the "tension braze" design. In this concept a fin is brazed in the air passage with a high temperature nickel braze alloy that is both strong and oxidation resistant at operating temperatures (Figure 2). The air passage pressure is balanced by the air fin, thus eliminating the need for a strongback. Since pressures are balanced, the casing does not have to be rigidly attached to the core. Expansion joints between the core and the casing allow the core to heat up independently of the case, thereby eliminating most of the restraints that lead to thermal fatigue.

The introduction of the less expensive plate type recuperator did not eliminate the use of the tubular recuperators. Two basic types are in use: the straight through design (Figure 3), except that now the air is in the tubes and the exhaust gas is in the shell; and the U-tube design (Figure 4). Both of these designs require consideration of the thermal stresses due to the difference in thickness of the tube and the tube sheet. The tube to tube sheet joints are welded and in some cases, both



rolled and welded. Two types of tube sheets are in use. One is based on standard heat exchanger design and consists of a flat plate into which the tubes are welded (Figure 5). The other design is based on boiler technology and consists of a circular tube sheet or drum. For high pressures, the circular tube sheet allows the use of thinner material therefore reducing the thermal cyclic stresses.

A further group of gas turbine heat exchangers are the primary exchangers used in closed-cycle machines which transfer heat from the fuel to the working fluid heating it to the turbine inlet temperature. Since a closed cycle gas turbine tends to be expensive because of the heat exchanger costs there are benefits in increasing the overall pressure in the system; and of course as high a turbine inlet temperature as possible is desirable. Garrett AiResearch have recently demonstrated a small unit using a fluidized bed combustor burning coal as the heat source; the primary heat exchanger essentially consists of a tube bundle within the bed. Indirectly fired open cycle turbines are also of current interest, and Curtiss-Wright, under the sponsorship of the Department of Energy, have developed a combined directly-indirectly fired unit using a pressurized fluidized combustor. Air is heated in an in-bed heat exchanger and mixed with the combustion gases before being expanded through the turbine. Their heat exchanger consists of vertical bayonet-type tubes: air flows in from the bottom up a central tube, and then down between this tube and the outer tube, the heated air being withdrawn from the bottom (Figure 6). Various types of extended surface, both on the inside and the outside have been tried; since the heat transfer is much better on the bed side than the air side it seems probable that the eventual configuration will consist of smooth outer walls with some form of extended surface between the two concentric tubes. The pressure in the system will be of the order of 150 psi (1.0 MPa).

One recent consideration is the use of a heat exchanger as a recuperator on compressed air storage gas turbine generating plants. In this duty, air is taken out of storage at 100 to 140 F (38-60 C) at up to 1000 psig (6.8 MPa) and heated by exhaust gases at 800 to 900 F (427-482 C). Due to the high pressures involved, thick tube sheets are required aggravating thermal cycling problems. As the heat transfer rate is very high inside the tubing as compared to the outside of the tube, the metal temperature is approximately at that of the air inside the tube. A major portion of the tubing is therefore below that of the dewpoint of sulfuric acid as well as possibly below that of sulfurous acid.

Heat exchangers are also used in many other applications. They have been used to recover waste heat from diesel engines, incinerators, petrochemical and other chemical

processes. The heat exchanger is an important part of fuel cell systems, heat pumps, solar heating systems and many other energy related systems. Many of those duties are made severe from both a cyclic as well as a corrosion standpoint, but all of the same design problems and considerations outlined above must apply.

#### MATERIALS ISSUES IN HEAT EXCHANGERS

The materials-related problems in heat exchangers are:

1. Fabrication problems, particularly welding and brazing.
2. Mechanical problems induced by thermal and mechanical cycling (thermomechanical fatigue, TMF).
3. Fouling and deposition. This can reduce the effectiveness of the heat transfer, increase the pressure drop across the heat exchanger and eventually block the passages.
4. Erosion of the metal by particles entrained in the gas stream.
5. Corrosion, which includes cold end corrosion due to the condensation of liquors such as sulfuric acid, and hot end corrosion such as oxidation or hot corrosion.

The first two of these have been briefly touched on in the previous section, and will not be discussed further here. EPRI currently has a project with Encotech, RP1791-5, to study the thermomechanical fatigue problem in the compressed air storage recuperator, and a project with the Materials Properties Council, RP1874-1, to study the dissimilar metals weld failure problem in boilers.

Fouling and deposition has been a continuing problem in fossil-fired systems. Reid<sup>(1)</sup> has reviewed most of the early work. In coal-fired boilers, the ash will fuse in the combustion zone. The molten ash droplets may deposit on the water walls, where they freeze; because of the consequent drop in heat transfer, later droplets may not completely freeze, and quite thick deposits with the outer layers molten may form. This is referred to as "slagging." In the upper part of the boiler the ash particles have mostly solidified, but some constituents may still be molten: these act as a "glue" and cement together deposits of the otherwise solid particles on the superheater and reheater. As the deposit thickens, the outer layers become hotter and sinter more readily; "beards" up to several inches in thickness can form on the tubes, pointing towards the gas stream. This is often called "fouling" to distinguish it from slagging, but in reality the differences are only of degree. The ash deposits can be removed by jets of steam or air; this is called soot blowing. In extreme cases, water jets may be used, but this can result in thermal shock damage. The slag

deposits on the walls are more difficult to remove because they are more solidly bonded: in some cases they are dislodged by shooting at them with shotguns.

An alternative approach is to control the ash chemistry by blending different coals. Various formulae exist which predict fouling tendency in terms of ash chemistry, and thus a feed can be synthesized which should not foul. This sometimes works. A more extreme version of the same thing is to use an additive. EPRI currently has a project with Battelle, Columbus Laboratories, RP1839, to study the effectiveness of additives in controlling fouling in coal-fired boilers. It is not simply the amount of deposition which must be controlled, but the physical characteristics of the deposit; a loosely-bonded deposit is easier to remove by soot blowing and thus may be preferable to a thinner but more tightly bonded deposit.

Deposition is experienced in oil-fired units as well; the ash content is a great deal lower, but again the deposition can be related to impurity chemistry. Additives are used to control both deposition and the associated corrosion. In other forms of heat exchanger deposition must be controlled by building in cleaning systems or using designs which are self-cleaning. It is sometimes stated that the higher turbulence of the flow in a corrugated plate heat exchanger discourages the deposition of particulates in the fluid stream and thus reduces fouling. Conversely, fins and other extended surface features can result in local stagnant areas, encouraging deposition, or regions that a deposit can bridge across, thus increasing the integrity of the deposit and making it less easy to remove.

Erosion arises when particles strike a metal surface at sufficiently high velocities. The erosion rate depends to some extent on the temperature, the nature of the metal surface, the character of the erodent particle, the size of the particle, the angle of impact and the velocity of impact. For high temperature heat exchangers, where other factors usually determine the choice of material, the erosion depends mainly on the nature of the particle and its velocity. For coal ashes, the amount of crystalline silica in the ash appears to be the most important characteristic, but things are unfortunately more complicated than this. In boilers, designers use empirical guidelines for the maximum permissible gas velocity which varies somewhat depending on the type of coal to be burnt. As a very rough guideline, with local velocities (which is not the same as the design velocity) in excess of 25 m/s (80 fps) erosion may well be a problem.

This must be remembered in relation to the cleaning system. If high velocity soot blowers are employed, ash will be entrained in the jet which may then erode the tube surfaces.

The jets should be of as low velocity as is consistent with effective cleaning, and they should not be left on longer than necessary.

Recently, erosion has been observed within the beds of fluidized bed combustors where the velocities should be far below the value quoted above. In these dense media, once the gas velocity exceeds 2 m/s erosion may appear, and seems to be probable above 4 m/s; local jets within the bed can be particularly damaging. The mechanism for in-bed erosion is not well-understood at present.

Erosion is usually a very localized phenomenon. So long as the well-known rules are followed in design and operation there should be no overall problem, but often a local high velocity region can develop, perhaps downstream of a deposit or at a location where there is an abrupt change in the cross section of the gas path. Severe local erosion can then result.

Cold-end corrosion is very common in heat exchangers in systems using sulfur-containing fuels. Generally, one tries to set a limit for the cold end temperature which lies above the dew point, but for various operational reasons it is not always possible to meet this criterion. The condensation can then cause corrosion itself, and it may also lead to deposition and fouling if the gas contains particulates. Since cold-end corrosion is a quite general problem and relatively well understood, it falls outside the range of this conference: the introduction of alternative fuels should introduce no new features.

Hot-end corrosion is also relatively well understood. The oxidation rate of metals clearly puts an upper limit on the temperature at which they can be used in an oxidizing environment; for plain carbon and low alloy steels this rather than strength limitations often determines their maximum use temperature. Once again, this is well known and need not be discussed further here.

In conventional boilers a further complication is the deposition of various materials on the hot surfaces. In the lower part of the boiler it is possible for fragments of iron sulfide and unburnt carbon to become incorporated in the slag deposit: this leads to a low oxygen activity environment which is highly sulfidizing, and rapid wastage of the tubes can take place. In the upper part of the boiler the deposit contains sulfates of the alkali metals sodium and potassium: these sulfates may also contain other elements, and appear to be molten at the tube surface temperature (650 C or so). Under these circumstances accelerated oxidation can take place, as will be described in the later paper by Stringer.

In-bed heat exchangers in fluidized bed combustion systems experience an environment in which there is an excess of calcium sulfate, with local oxygen activities which fluctuate from very low values, of the order of  $10^{-15}$  atm, to high values close to that of the intake air. If local equilibrium were established, dissociation of the calcium sulfate in the low oxygen activity periods would generate high sulfur activities, of the order of  $10^{-5}$  atm, and it is possible that sulfidation-oxidation corrosion of alloys could occur. This is in fact observed, and the mechanism for this process will also be discussed in more detail by Stringer.

In coal gasification systems the product gas has even lower oxygen activities, typically around  $10^{-20}$  atm, and sulfur activities which depend on the sulfur content of the coal but are typically of the order of  $10^{-7}$  atm. Again, the major problem is sulfidation-oxidation corrosion, and the maximum permissible metal temperature in large syngas cooler heat exchangers will be determined by the resistance of common structural alloys such as low alloy steels to this form of attack. Perkins is currently studying this problem under EPRI Project RP1655-3

The primary heat exchanger in indirectly fired gas turbines and the syngas cooler heat exchanger probably represent the major high temperature materials problems for alternative fuel fired systems. There are some heat exchangers in the petrochemical industry which see broadly similar conditions. These are typically tube and shell exchangers, with centrifugally cast tubes of austenitic steels such as HK40 (Fe-25Cr-20Ni-2Si-2Mn-0.4C) and commonly achieve lifetimes of 4-5 years. The working temperature is of the order of 1000 C, although at these temperatures the atmospheres do not contain any significant amount of sulfur. The pressure differential is around 1.8 MPa, depending on the particular application, and the gases do not normally contain particulates or slag. For more severe environments, there is little experience above approximately 750 C, which is the outlet temperature of the coal fired 14 MW air turbine at Oberhausen, and the relatively small number of hours accumulated at temperatures approaching 850 C in fluidized bed combustors.

#### SUMMARY

Large numbers of heat exchangers will be required in advanced energy systems to make the most effective use of expensive fuels. These will range from waste heat recovery units at the exhaust end, operating at lower temperatures and pressures, to the high temperature, high pressure primary heat exchangers in indirectly fired gas turbines. There are two types of heat exchangers: recuperators and regenerators. Most metallic recuperators are either plate and fin or tube and shell: the latter is probably better at high pressures, the former is likely to be more efficient and rather cheaper

at lower pressures. Materials problems are related to fabrication, particularly welding and brazing; thermomechanical fatigue; erosion; and low and high temperature corrosion. For alternative fuel fired systems the most severe problems will probably be encountered with the primary heat exchanger in indirectly fired systems and with the syngas cooler in entrained gasifier integrated combined cycle systems.

#### REFERENCE

1. W. T. Reid, "External Corrosion and Deposits, Boilers and Gas Turbines" (Elsevier, New York, 1971)

#### BIBLIOGRAPHY

- Barkley, J. F., et al. Corrosion and Deposits in Regenerative Air Preheaters. Bureau of Mines Report of Investigations, U.S. Department of Interior, August 1953.
- Boyen, J. L. Practical Heat Recovery. John Wiley & Sons, New York, London, Sidney, Toronto, 1975.
- Cuffe, K. W., Beatenough, P. K., Daskavitz, M. J. and Flower, R. J. Plate Fin Regenerators for Industrial Gas Turbines. J. Eng. for Power, ASME, 100 (1978) 576-585.
- Kind, R. W., and Rutte, E. Tubular Gas Turbine Recuperators. ASME Paper No. 77-WA/HT-8.
- Kretzinger, K., et al. Gas Turbine Regenerators. AiResearch Manufacturing Co., Technical Paper January 1981.
- McDonald, C. F. Gas Turbine Recuperator Technology Advancements. ASME Paper No. 72-GT-32.
- Radway, J. E. and Exley, L. M. A Practical Review of the Cause and Control of Cold End Acidic Stack Emissions in Oil-Fired Boilers. ASME Paper No. 75-WA/CD-8.
- Tennery, V. J. and Wei, G. C. Recuperator Materials Technology Assessment. Oak Ridge National Laboratory Report TM-6227 on DOE Contract No. W-7405-eng-26, (February 1978).

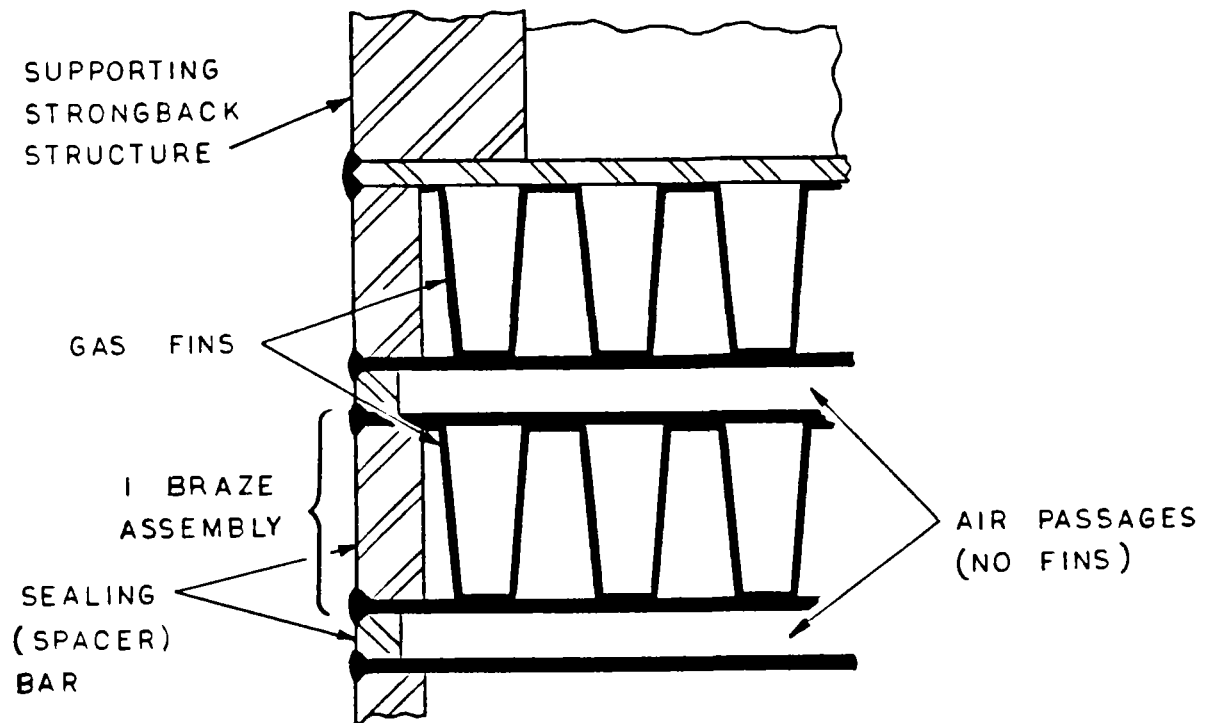


Figure 1. Compression Braze Design

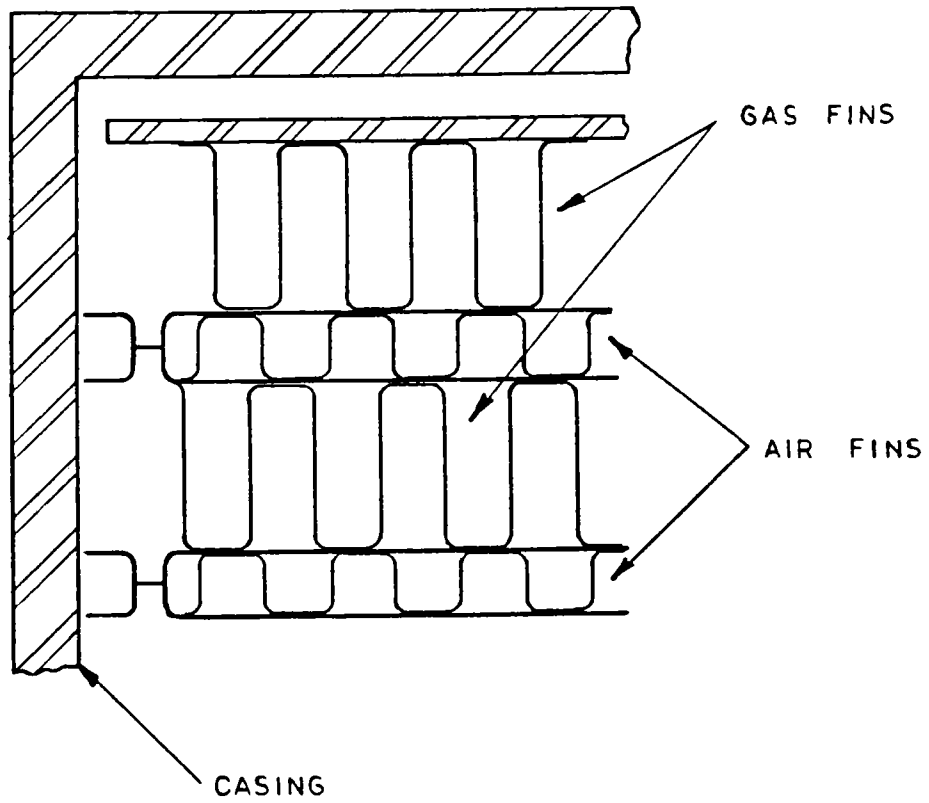


Figure 2. Tension Braze Design



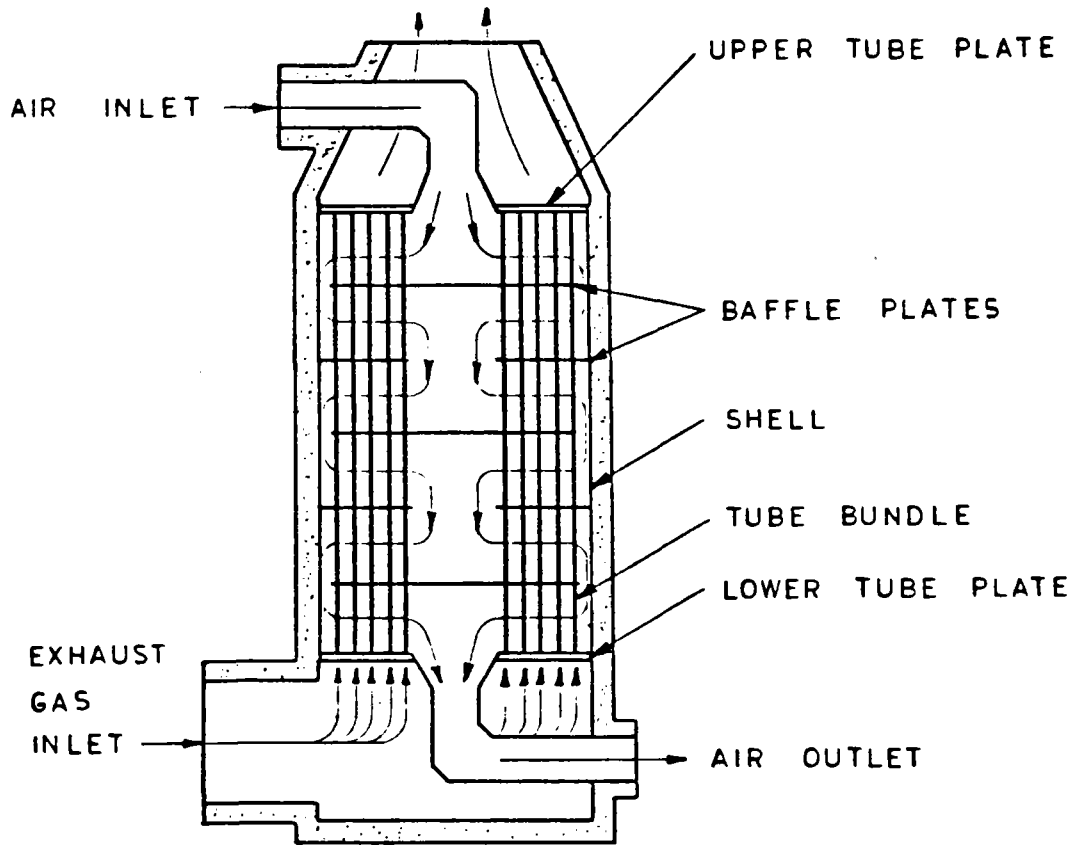


Figure 3. Straight Through Design

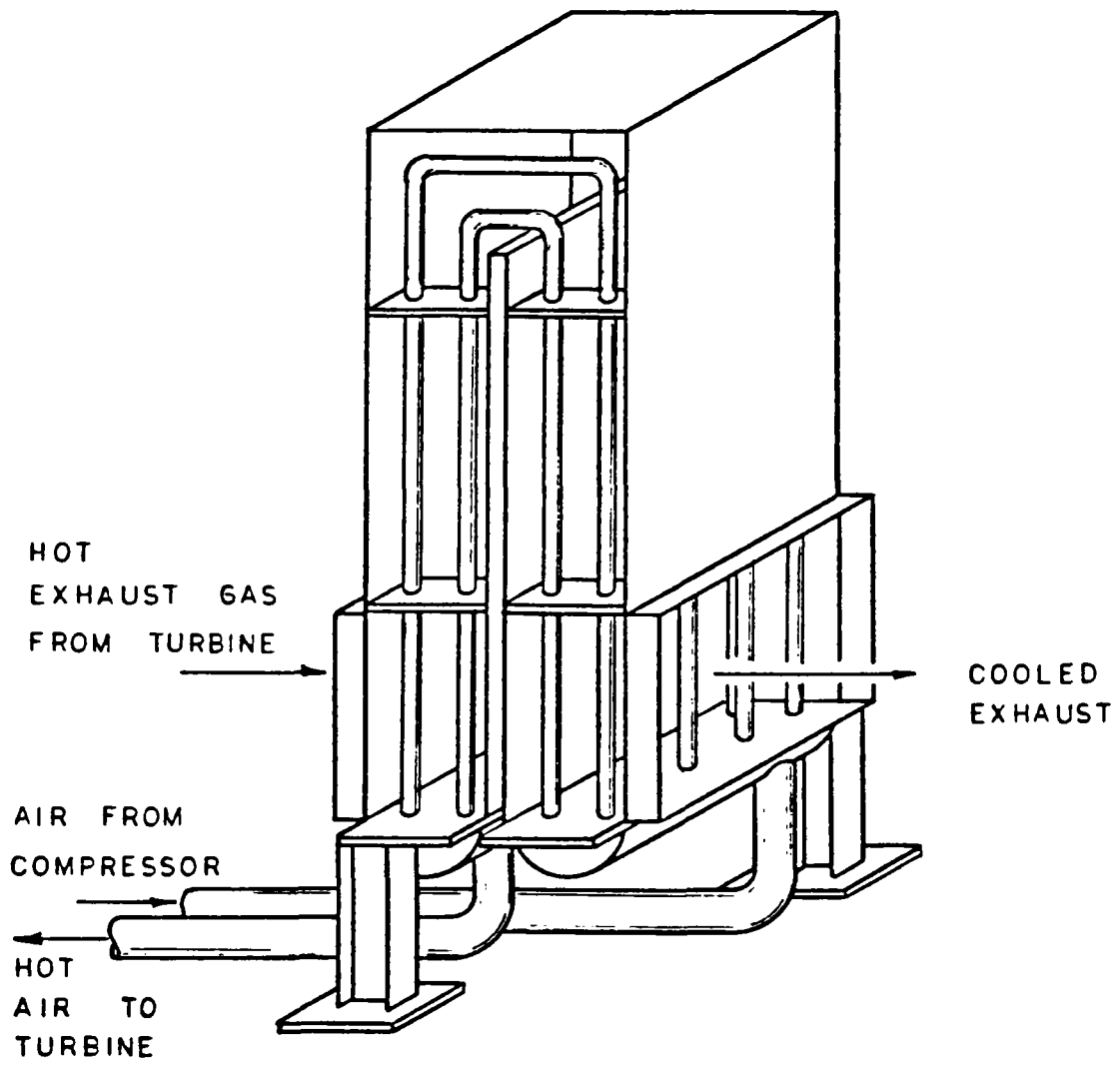
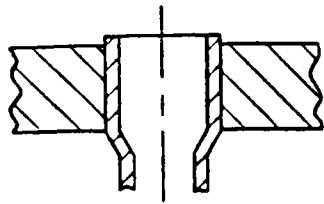
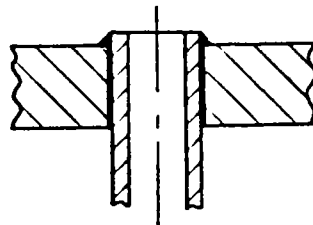


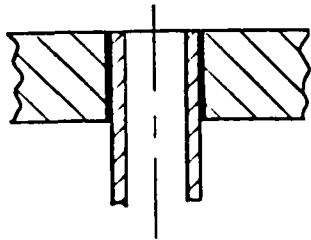
Figure 4. U - Tube Design



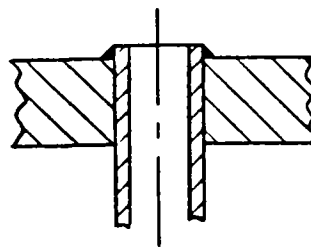
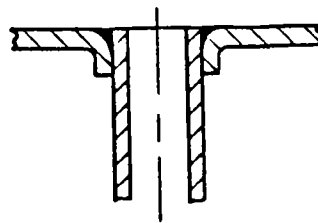
MECHANICALLY  
EXPANDED



WELDED AND  
BACKBRAZED JOINT



BRAZED  
JOINTS



WELDED  
JOINTS

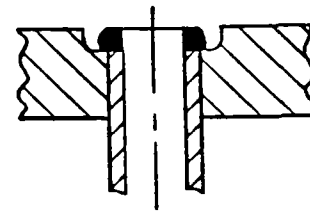
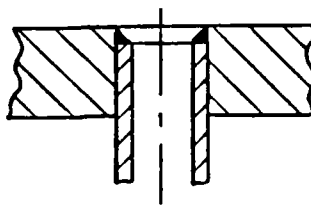
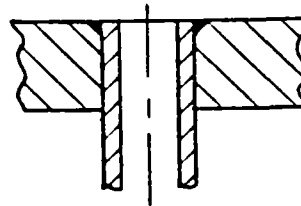


Figure 5. Typical End Seals Used in Tubular Heat Exchangers

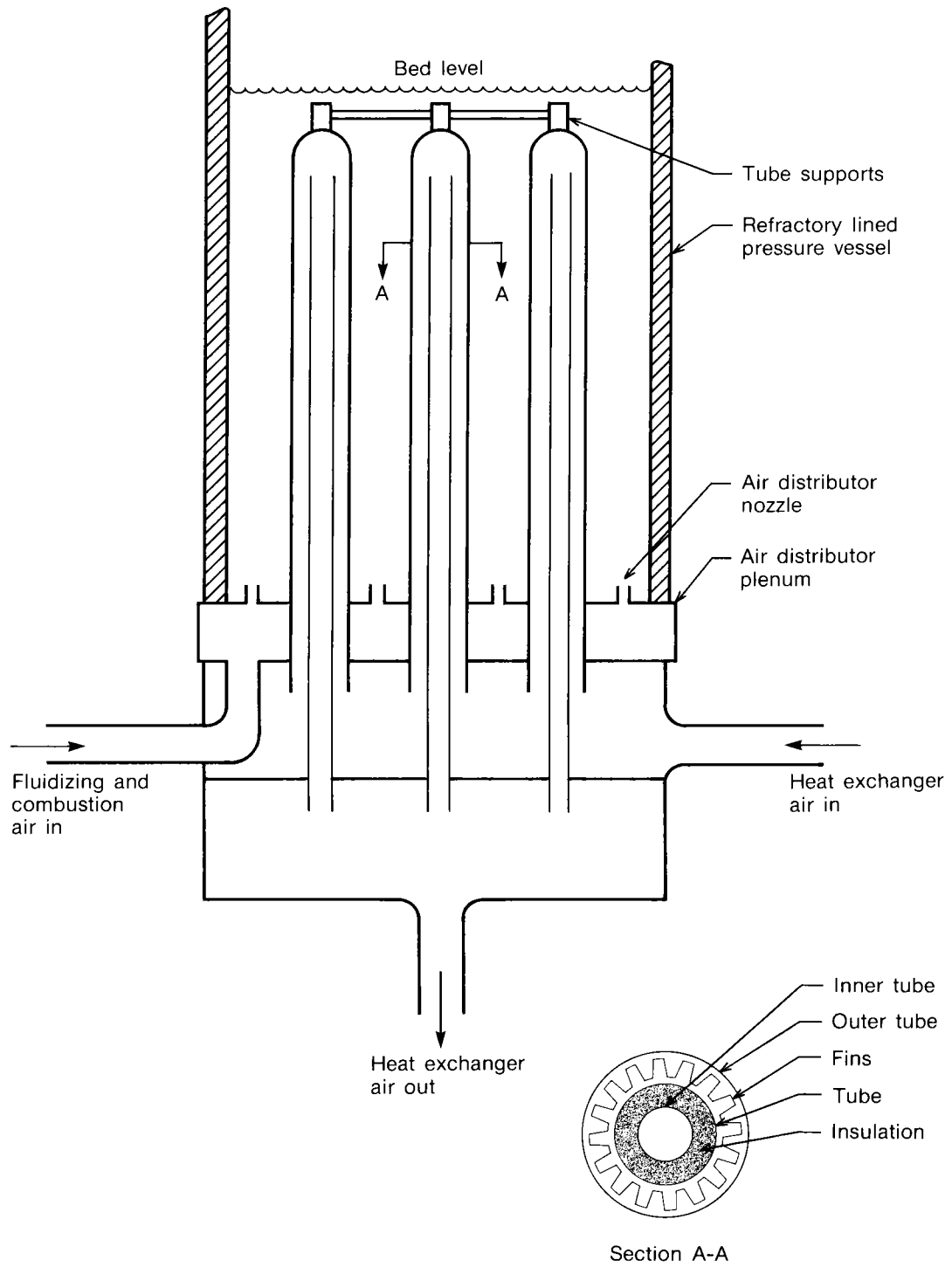


Figure 6. Schematic diagram of the Curtiss-Wright pressurized fluidized bed combustor air heater.

ADVANCED COOLING OF UTILITY GAS TURBINE ENGINE COMPONENTS

August 1981

Prepared by

ARTHUR COHN

Electric Power Research Institute  
3412 Hillview Avenue  
Palo Alto, CA 94304

## ADVANCED COOLING OF UTILITY GAS TURBINE ENGINE COMPONENTS

Arthur Cohn, EPRI

The major improvement desired by utilities for combustion turbine power plants is increased reliability. In order to assist the improvement in reliability, EPRI has the "High Reliability Gas Turbine", project RP1187. There is also the desire to lower heat rate and the cost of electricity. For combustion turbine combined cycle plants, this can be accomplished by raising the turbine inlet temperature. However, in the past an increase in turbine inlet temperature has been associated with a decrease in reliability and durability, especially as metal temperatures have risen. It is the purpose of the EPRI "Advanced Cooling Engine" project RP1319, to apply advanced cooling and fabrication techniques to the engine hot section in order to lower metal temperatures while allowing growth in turbine inlet temperatures to the competitive levels expected in the mid and late 1980's. It is also desired to increase the engine fuel flexibility. The improvements should be compatible with fuels of high ash contents and low hydrogen levels.

Some of the relationships of the gas and metal temperature to various effects which take place in a combustion temperature are summarized in Figure 1. There is a metal temperature "window" between approximately 1350° and 1550°F where sulfidation corrosion conducted by the alkalis has a relative minimum. Decreasing metal temperature below 1350°F is actually deleterious until below 1050°F where sulfidation corrosion is greatly reduced and there is evidence that vanadium can be tolerated without magnesium treatment of the fuel. Deposition has been found to increase with decreasing metal temperature to about 1100°F where it starts to decrease sharply until at about 700°F deposition tends to be nil. However, the heat rate rises with decreasing metal temperature, although with the improved cooling techniques that have a higher effectiveness, this deleterious effect is decreased.

A number of projects within RP1319 have been started. Phase I involved the preliminary design and analysis of advanced cooling components along with conceptual design and performance analysis of the overall engines and powerplants utilizing these components. There were four phase I contracts:

- RP1319-1 with GE investigated the use of a water cooled first stage turbine nozzle (stator).
- RP1319-2 with W/DDA investigated the use of skin-spar construction of the turbine blades and vanes
- RP1319-3 with UTC investigated the use of wafer and bonded construction of the turbine blades and vanes
- RP1319-4 with W/DDA investigated the application of lamilloy®\* impingement-full-film cooling to the combustion liner.

Phase II is for the detailed design, fabrication, and acceptability tests of these advanced cooling components. There are currently two phase II contracts:

- RP 1319-5 with W/DDA for first stage blades and vanes of shell-spar construction with impingement-convection cooling utilizing cooling slots in the outer surface of the spar under the thin skin.
- RP 1319-7 with W/DDA for detailed design, fabrication, and acceptance testing of the combustor using the lamilloy liner.
- Other phase II projects are expected to be approved.

Projected are the phase III of current projects where the advanced components will be installed into the engine for which they were designed. After short term shop tests the engines and components will be field tested at utility stations to hopefully demonstrate their durability and performance advantages.

The RP1319-1 project with GE has experimentally investigated the effect of very low metal temperatures on residual oil ash deposition and analytically compared the performance and economics of combustion turbine power plants having the first

\*Lamilloy is a registered trademark of Detroit Diesel Allison.

nozzle (stator) water-cooled versus similar machines with all air-cooling. During this project a water-cooled nozzle stator sector (Figure 2) was fabricated for the deposition tests, while the preliminary design drawings for modifying an engine to utilize the water-cooled nozzle stator were accomplished.

The water-cooled stator sector and a similar air-cooled sector were run in the combustion products of No. 2 distillate-doped to simulate high ash residual oil. Tests were run at 1850°F, 2050°F and 2300°F gas temperature for various metal temperatures. The results show (Figure 3) that there is a severe decrease in deposition at a metal of 700°F, but that for metal temperatures in the 1000-1200°F range the deposition rate is greater than occurs for the 1500-1600°F metal temperature range.

The comparison of performance showed that for equal turbine stator inlet temperatures up to 2300°F, the efficiency of combined cycle powerplant using an air cooled stator would be superior to that with a water-cooled stator at 800°F metal temperature (Figure 4) because of the cooling air mixing effect. This comparison corresponds to a lower "firing" (turbine rotor inlet) temperature for the air cooled machine with thus easier operating conditions on the first rotor and downstream stages. Therefore, in this temperature range the use of a water-cooled first stage nozzle stator appears disadvantageous. An exception would be where base load operation on high ash fuel is done. In that uncommon case, the plant with the water-cooled stage would have the economic advantage because of the much less frequent need to shutdown for water-washing in order to remove the deposits.

In project RP1319-3 with U.T.C. the aim was highly effective convection air cooling of the blades and vanes. This was aimed to hold metal temperatures to a maximum hot spot of 1500°F while minimizing the colder areas that would fall in the low temperature corrosion region. Two basic advanced construction techniques were investigated for both the blades and vanes. One technique was what is termed wafer blading. A large number of wafers (20-50) are etched with a segment of the cooling channel pattern. These are bonded together and then machined to the airfoil shape. The cooling patterns designed for these vanes are etched in chordwise wafers while for the blades they are etched in spanwise wafers (Figure 5). In the second technique, termed bonded blading, a multi-piece (2-3



pieces) casting is made which is then bonded into a single airfoil. These can contain high heat transfer coefficient and area cooling passages (Figure 6) that are practically as effective as that allowed by the wafer technique (Figure 7).

Contract RP 1319-2 with W using DDA as a very major subcontractor, was the first phase of the project that has continued into phase II as RP 1319-5. During the first phase a number of skin-spar concepts were designed for a modified W 251 engine. These were for blading with impervious shell type skin, with lamilloy multi-holed sandwich type skin, and for hybrid designs containing regions of both types of skin. Deposition tests using No. 2 oil-doped to simulate a high ash residual oil were run with a stator sector whose vanes had large areas of lamilloy skin. It was found that the air cooling holes tended to stay open clearing themselves of deposit. However, the overall deposit rate was very high, which may have been caused by the eddy type air flow from the cooling holes.

The shell-spar designs had spars containing three or five chambers (Figure 8). Cooling air entered through the odd chambers, passed under slots between the skin and the spar, then either into the even chambers where it exited at the other end of the blading or exited at the trailing edge. The original design had the cooling slots etched into the underside of the shell lying on the flat surface of the spar.

This type of design and the plan for incorporating it in a test engine were found to be satisfactory and have proceeded into Phase II. The blades and vanes are currently being detail designed. One design modification is that the cooling slots are now to be cast in the outer surface of the spar while the shell will be a flat sheet wrapped over the spar covering the cooling slots. The slots are cast in the chordwise direction. Each pair of slots are connected by manifolds in the spanwise direction that contain the holes that pass the cooling air between the spar chambers and the slots.

The design philosophy is to aim for the low corrosion window in the 1400-1500° F metal temperature region. The design is aimed at a low 200° F variation of the metal temperature over the surface of the blading. There is a minimum of cooling holes exiting through the surface skin. The shell material and coating is to be chosen for corrosion resistance and flexibility at 1500° F while the spar will be

chosen for castability, strength and corrosion resistance at 1400° F. They must also be compatible with respect to thermal expansion at their respective operating temperatures. These operating conditions are an attempt to find the best combination of the somewhat conflicting conditions of minimizing corrosion, deposition, and enthalpy loss to cooling, while maximizing the blading strength and durability.

The detailed design will be completed shortly. This will be followed by fabrication and acceptance testing of the blading. Simultaneously, a modified engine is being designed and will be manufactured to be compatible with this blading. In the projected Phase III, the complete engine with the shell-spar blading will be assembled. After in-house shop tests it is planned that a cooperative testing program with a host utility will be arranged. On the utility system the power produced can help pay towards the cost of the test. This field test unit should be completely equipped with diagnostic instrumentation such as thermocouples and strain gages. As far as possible, the testing should be run to a determined program which may override the utility's dispatch priority. The testing should be done jointly with the utility's and manufacturer's personnel.

The last advanced cooling project differs from the others in that it involves the combustor rather than the turbine section. This project, RP1319-7, superseding RP1319-4, has now moved into Phase II. A detailed design of a combustor compatible with the W 501 engine has been made. This combines the dome end of a standard combustor with a liner made of lamilloy. The lamilloy is a three-piece sandwich material rolled into the liner cylindrical shape. Cooling air passes through holes in the outer sheet, into the first grid area between sheets, then through holes in the middle sheet into the second grid area where it impinges on the inner sheet, finally passing out through holes in the inner sheet, providing full film coverage of the inner surface (Figure 9). This cooling technique eliminates the thermal stresses associated with the stepwise cooling used in normal combustion design.

The combustor has been designed for fuels containing only 9% hydrogen to have a maximum hot spot temperature of 1550°F. The lamilloy liner is being fabricated at present out of Hastelloy X alloy. Fabrication should be completed shortly.

The Phase III test program is currently being planned. Testing on fuels containing 13%, 11% and 9% hydrogen are projected. Inside and outside temperatures will be measured using thermal paint in conjunction with external thermocouples. The 11% hydrogen fuel test will be with a high ash residual oil which will also investigate the resistance of the lamilloy to hole plugging by deposition.

Additional projects dealing with cooling of the transition piece are under consideration. With this development, the overall RP1319 project will cover all the components of the turbine hot section. These project developments should provide proven designs that will operate reliably at lower metal temperatures with a wider range of acceptable fuels while using lower cooling air flows and yet allowing somewhat higher turbine inlet temperatures than current combustion turbine power plants.

# TEMPERATURE LEVEL CHART

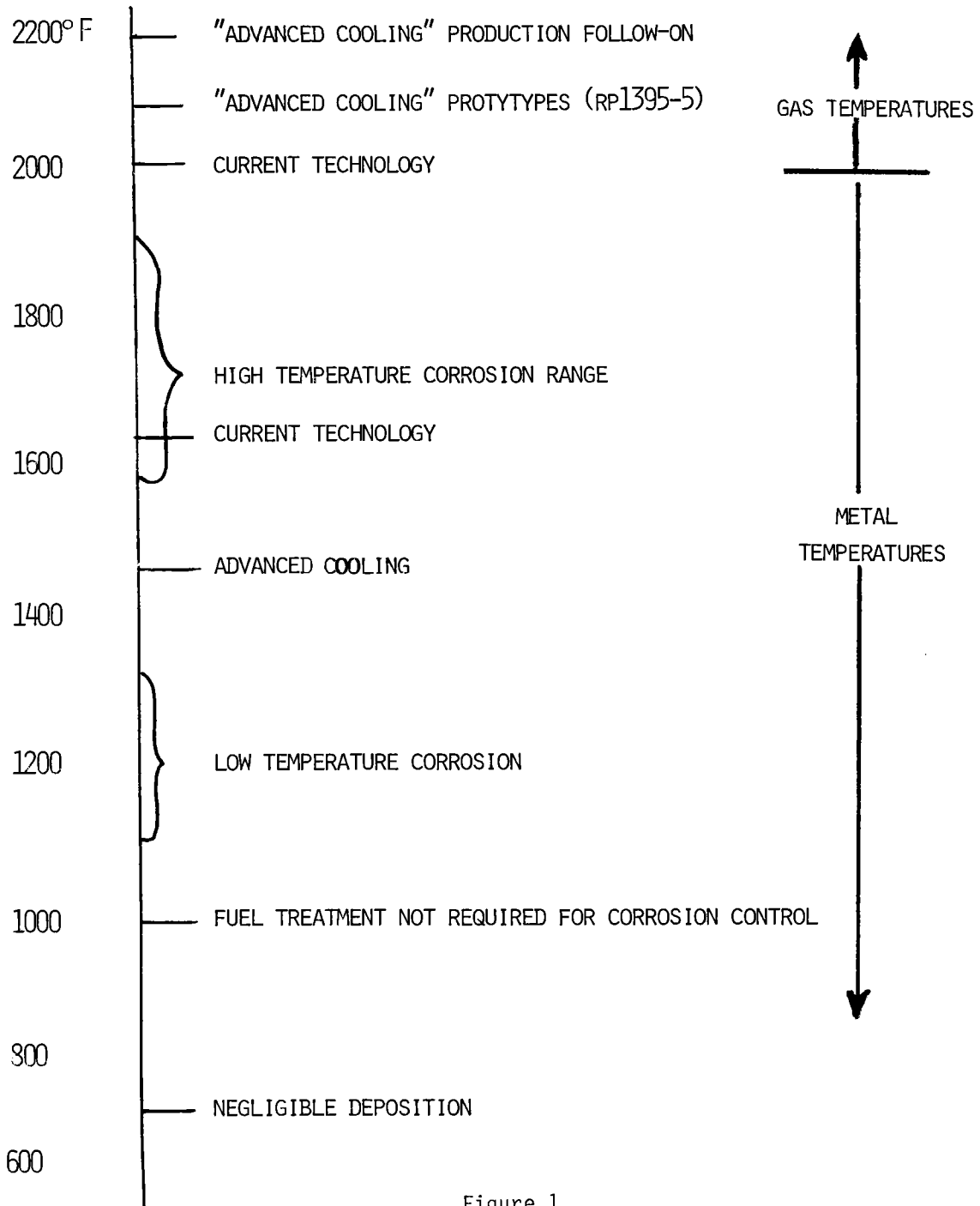
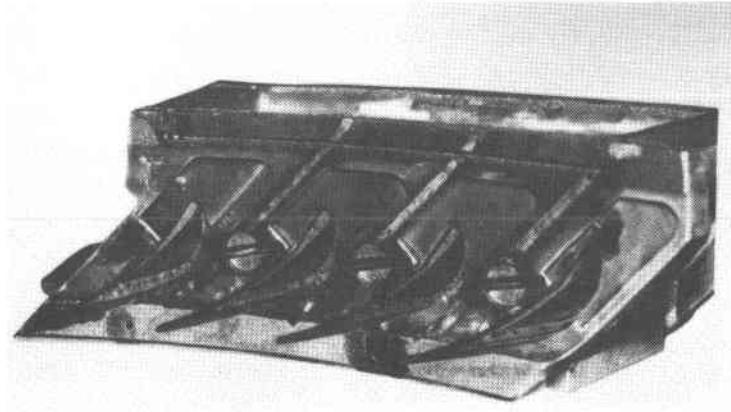
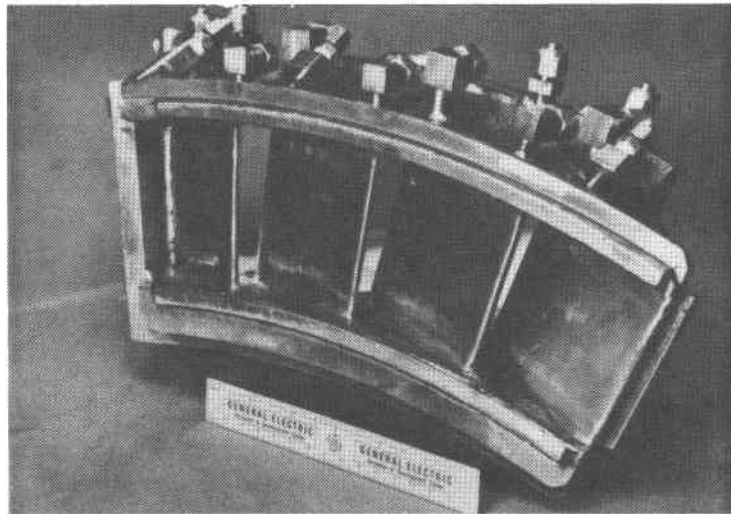


Figure 1

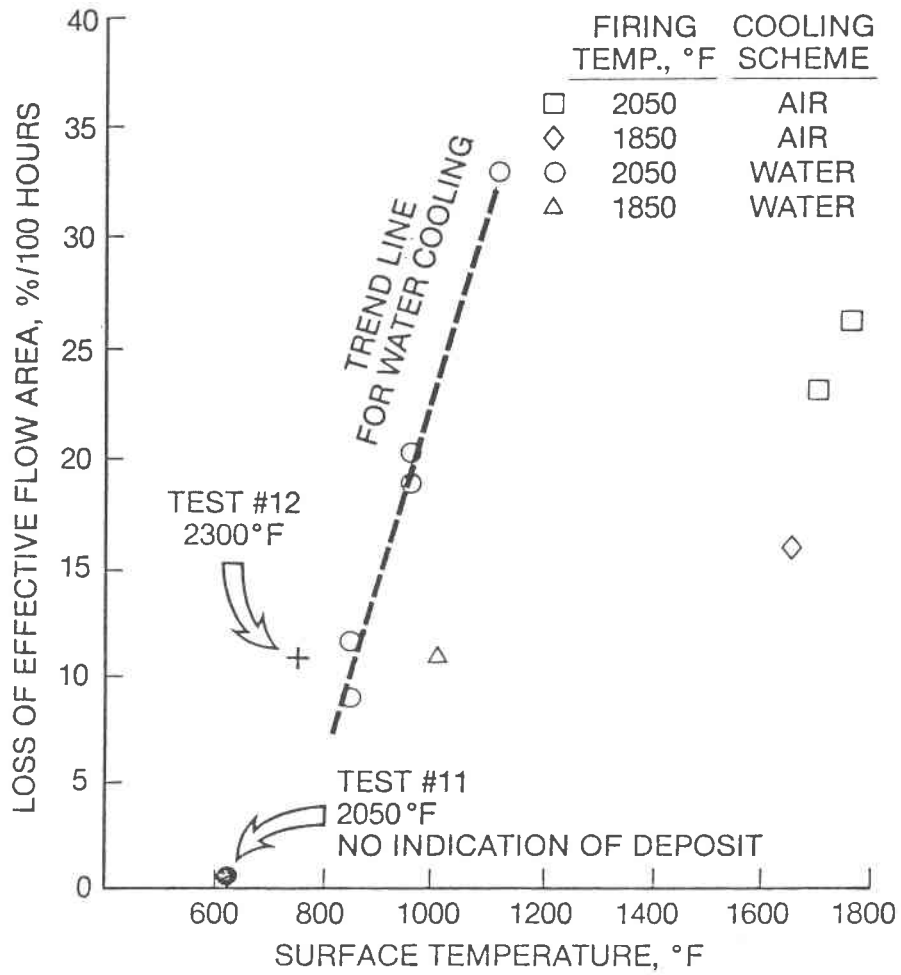


Welded Nozzle Segment Showing Airfoil  
Cooling Holes and Endwall Manifolds



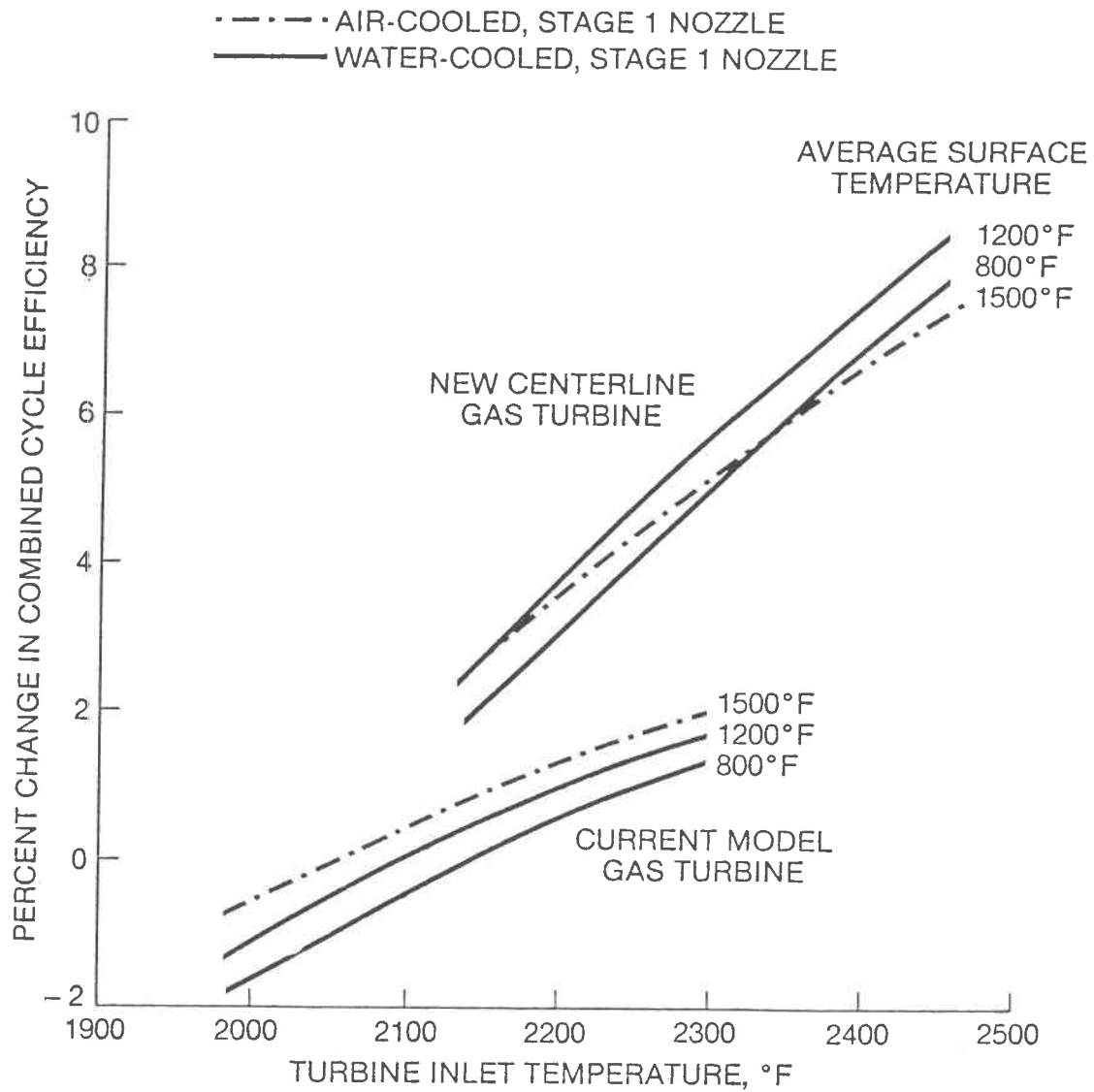
Completed Ash Deposition Nozzle with  
Water Fittings

Figure 2



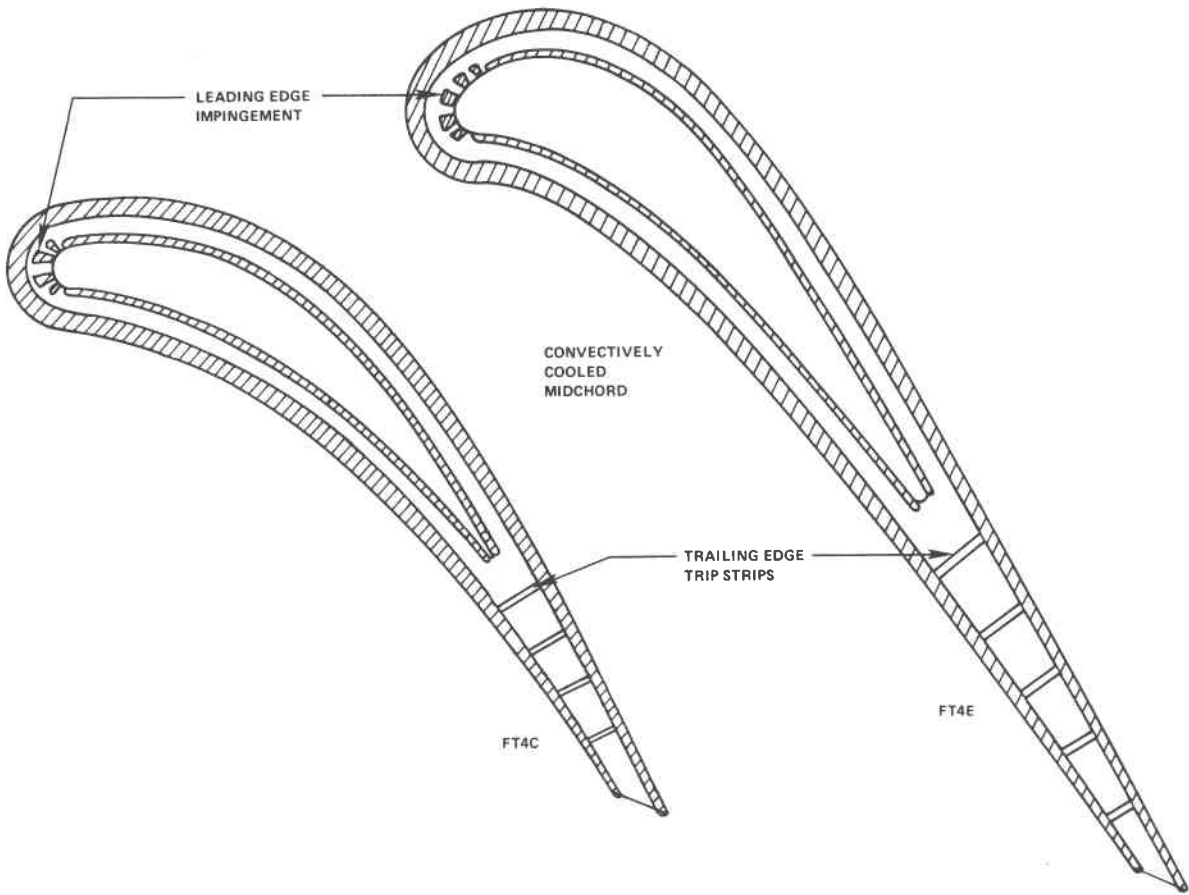
Ash Deposition Rate at 2300°F on a Water-Cooled Nozzle in Perspective

Figure 3

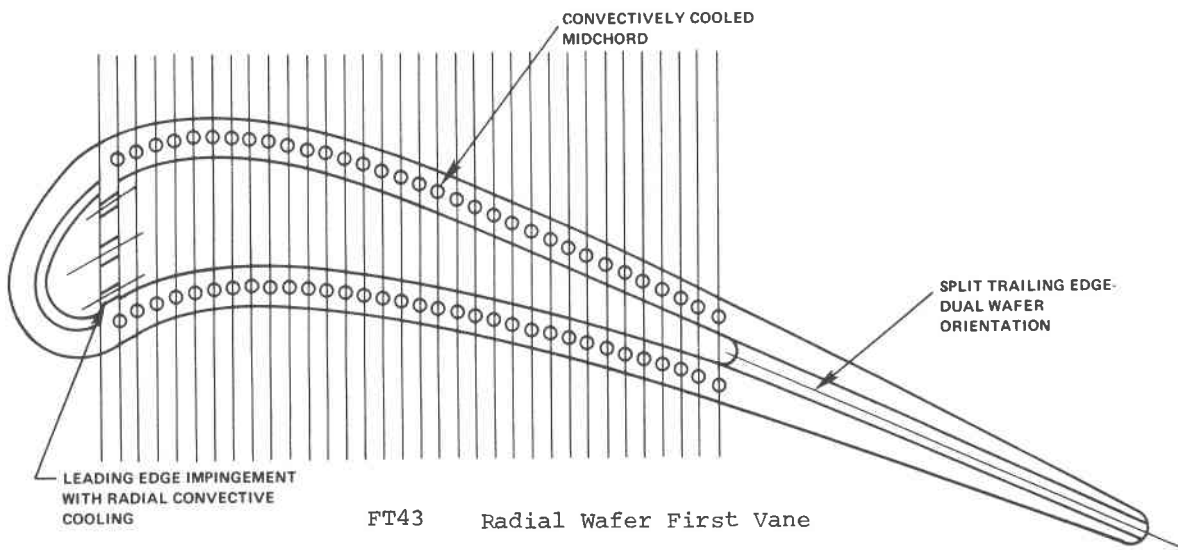


Effect of Turbine Inlet Temperature on Combined Cycle Efficiency

Figure 4



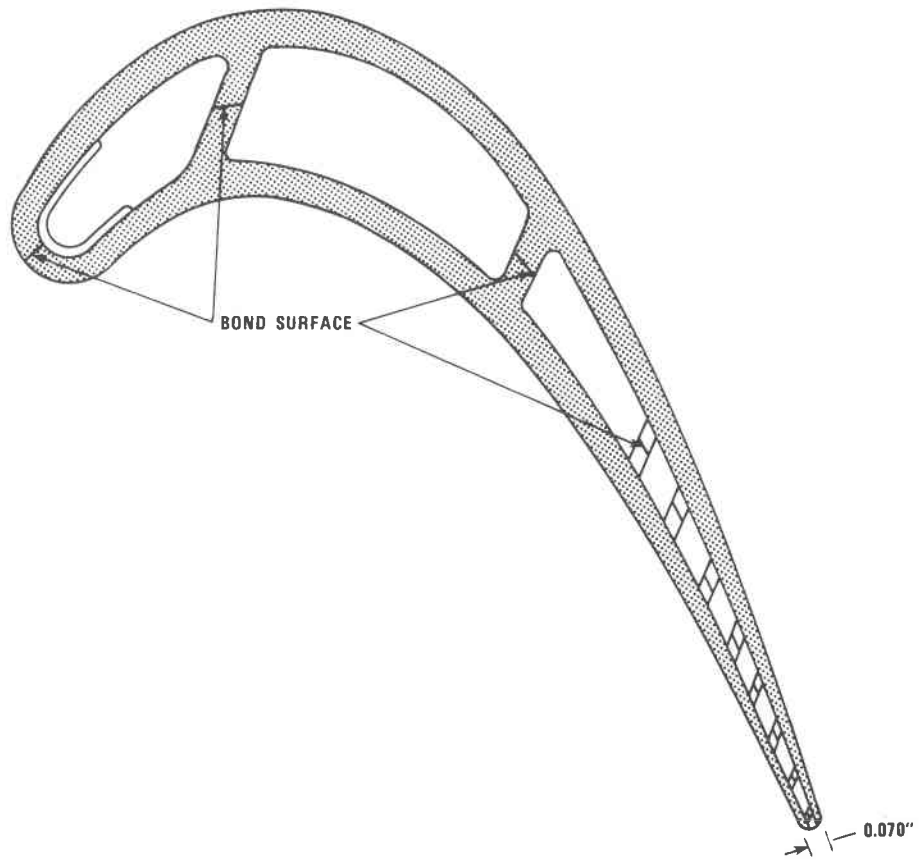
Comparison of FT4C and FT4E Chordwise Wafer First Vane



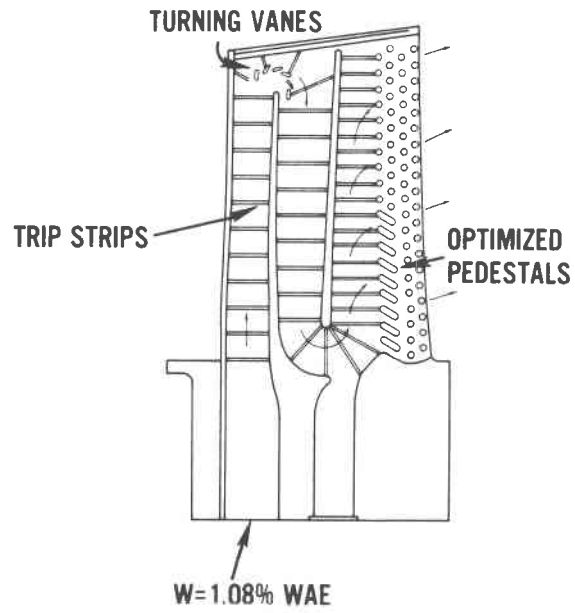
FT43 Radial Wafer First Vane

Figure 5





Bonded Blade Mean Section



Bonded Blade Cooling Configuration

Figure 6

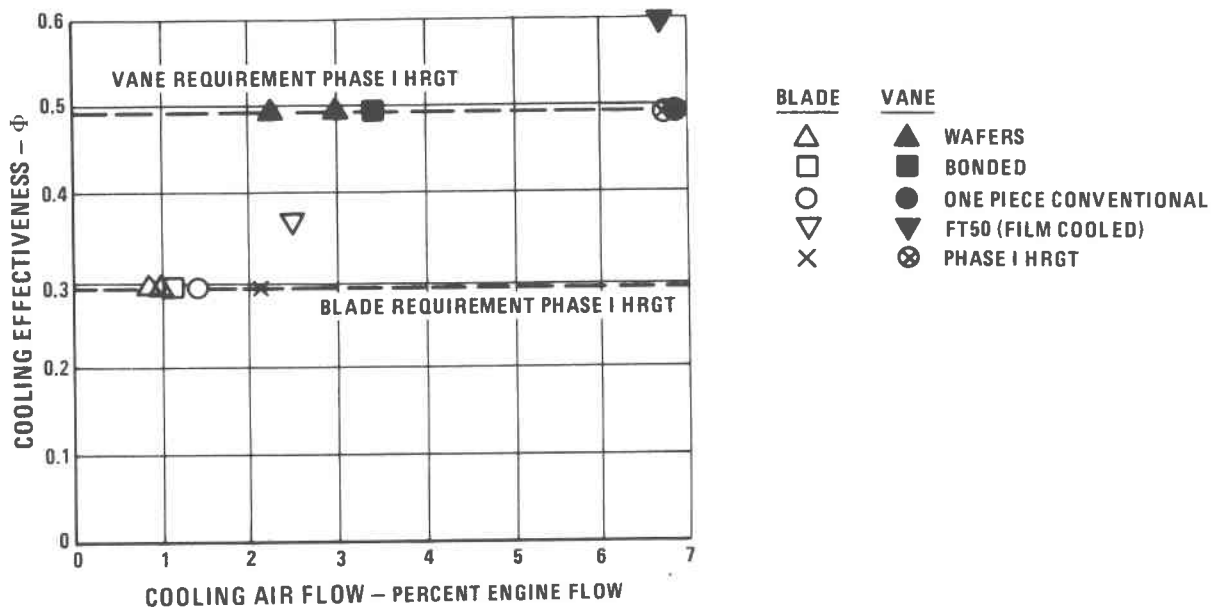
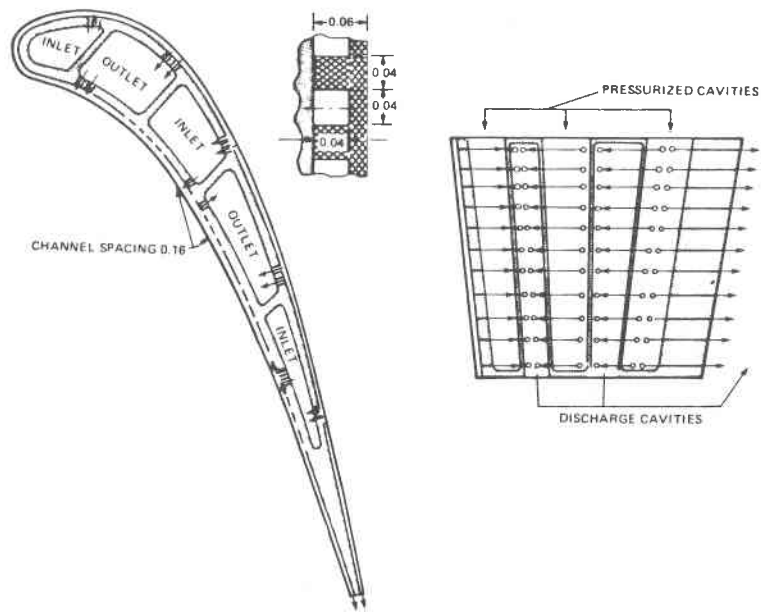
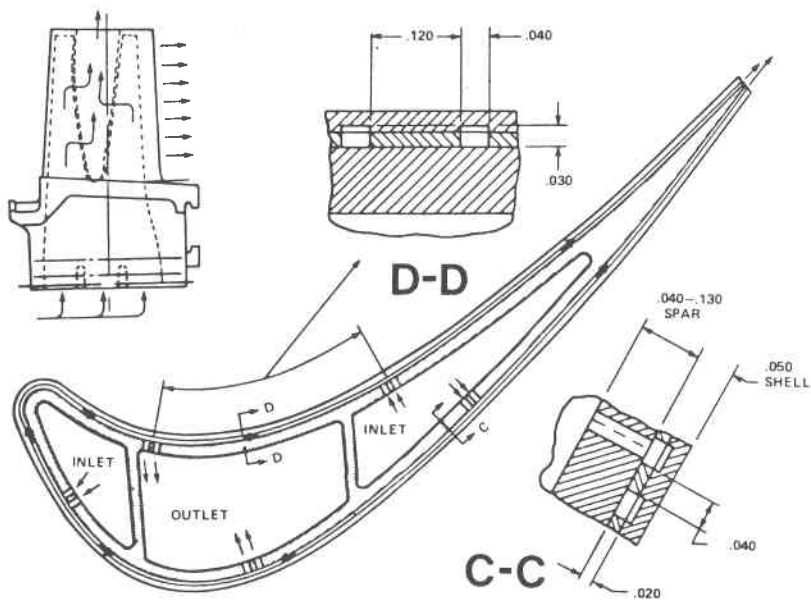


Figure 7

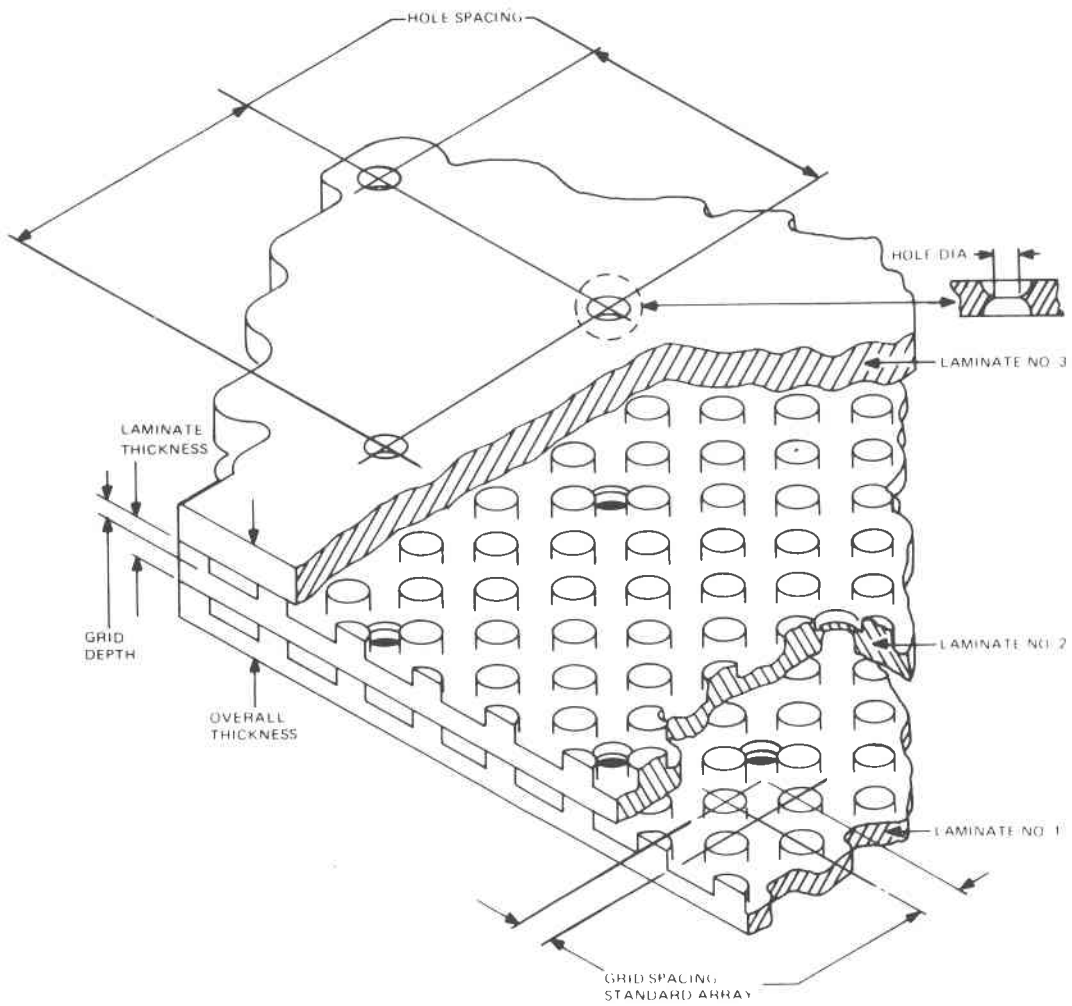
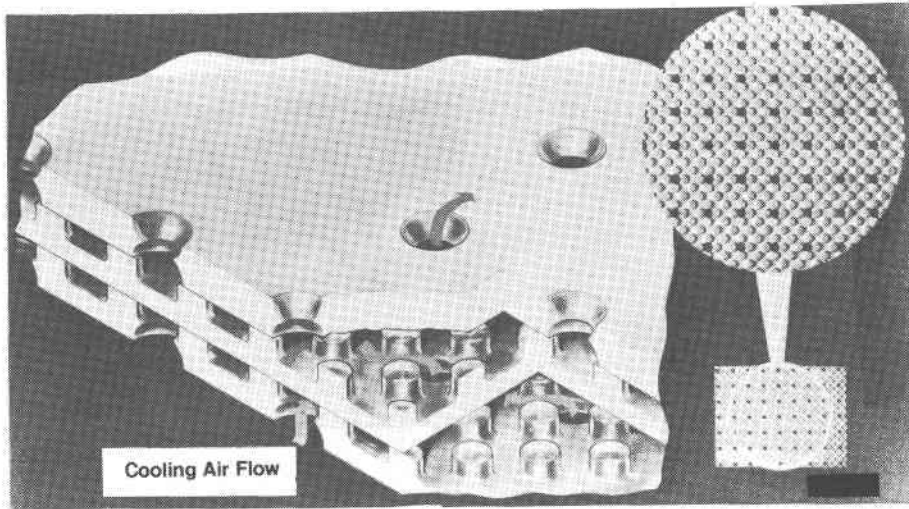


Conceptual Design of Shell/Spar First Stage Vane



Conceptual Design of Shell/Spar First Stage Blade

Figure 8



Cutaway and Schematic Views of Lamilloy Porous Material Structure  
Figure 9

THE U.S. DEPARTMENT OF ENERGY  
HIGH TEMPERATURE TURBINE TECHNOLOGY PROGRAM

George Manning, U.S. Department of Energy  
John Neal, U.S. Department of Energy

INTRODUCTION

One of the principal concerns with the increased use of coal is the environmental impact of its burning. New technologies must be developed in order to assure that utilities (which account for 75 percent of annual coal consumption) can continue to rely primarily on coal and can retain the flexibility to site coal plants in areas, that because of environmental problems, are candidates only for oil- and gas-fired generation. It is in the Nation's best interest that the utility sector be provided with the technological options that will allow coal to be burned more cleanly than current systems can achieve economically. In addition, clean environmental use of coal in the utility sector, by technology transfer will allow more coal to be used in the industrial sector where substantial oil and gas fuels are also consumed.

Of the various advanced technologies for the more economical and environmentally acceptable use of coal, the gasification-gas turbine combined cycle (GCC) (Fig. 1) promises to significantly increase thermodynamic efficiency and significantly reduce levels of pollution. Estimates of the environmental, thermodynamic and economic performance of this system are compared with other advanced coal systems in Fig. 2. It should be noted that the higher thermodynamic efficiency of advanced GCC results in this technology requiring 23 percent less coal than conventional technology. This efficiency improvement not only has implications for lower cost electricity (especially if delivered coal prices rise more rapidly than expected) but also results in reducing the environmental and potential health impacts associated with coal mining, transportation, disposal, and air emissions. Commercial availability of this technology would also improve the marketability of the higher sulfur Eastern coals, thus broadening the U.S. base of usable coal reserves.

Considering the advantages of the advanced GCC system, the Department of Energy initiated the High Temperature Turbine Technology (HTTT) Program in 1976. This technology effort seeks to increase the overall firing temperature of utility size gas turbines from today's 2000°F (1095°C) levels with clean fuels to 2600-3000°F (1427°C-1650°C) with coal-derived fuels containing a broader range of contaminants than current gas turbine specifications permit. These increases in turbine temperature levels, if successfully developed, will result in gasification combined cycle GCC systems with overall power generation economics 20 to 30 percent better than current technology pulverized-coal steam systems with flue gas desulfurization as shown in Fig. 3. Development of advanced turbine technologies are particularly important now that the private sector has made a commitment to demonstrate gasification combined cycle at full scale. This is because the private sector demonstration program will utilize current technology turbines and prove the superior emissions characteristics (i.e. better than oil-fired plants) of GCC. The private sector activities do

not include any support of high temperature turbines and associated components necessary for advanced GCC to have the significant economic advantages shown in Fig. 3. Thus, the Federal research and development (R&D) effort to develop high temperature turbine technology is critical in order for the turbine manufacturers to have the high-risk technology base necessary to commercialize second generation turbines that will allow GCC systems to attain superior economic performance as well as superior environmental performance.

The High Temperature Turbine Technology Program is structured in three phases as follows: Phase I - System and Program Definition; Phase II - Technology Testing and Test Support Studies; Phase III - Technology Readiness Verification Testing.

Technology Readiness is defined as "that point in the development cycle after which minimal risks would be involved in the development of the turbine subsystem for use in a full-scale open cycle gas turbine system." In other words, that point at which all technical problems appear to have a reasonable solution and no barrier problems appear to exist which would prevent taking the next developmental step into commercializing the subsystem. It does not mean that the turbine subsystem is ready yet for the commercial marketplace.

HTTT PHASE I

The Phase I system and program definition was begun in 1976 and was completed in 1977. Four contractor teams completed this phase.

The integrated gasifier combined cycle plants defined by the four Phase I contractors were as follows:

<u>Curtiss-Wright</u> 749 MW	<u>General Electric</u> 513 MW	<u>United Technologies</u> 955 MW	<u>Westinghouse</u> 925 MW
4 gas turbines	2 gas turbines	4 gas turbines	4 gas turbines
12 large gasifiers plus 2 spares	12 large gasifiers plus 2 spares	4 molten sodium carbonate gasifiers	4 fluidized bed gasifiers
1 steam turbine	1 steam turbine	1 steam turbine	1 steam turbine

The gas turbines proposed utilized the following advanced technology cooling methods.

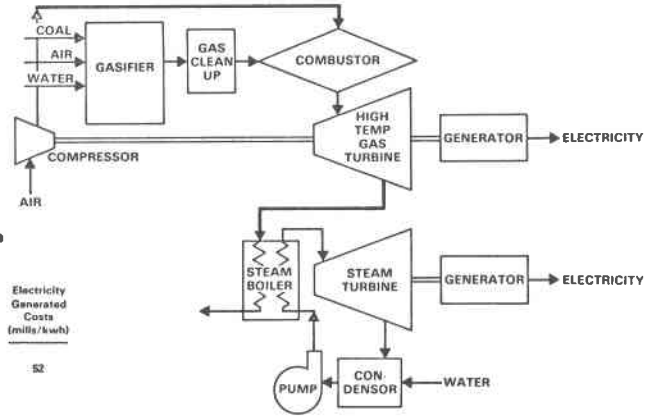
<u>Curtiss-Wright</u>	<u>General Electric</u>	<u>United Technologies</u>	<u>Westinghouse</u>
Air	Water	Water and Air	Air

There are currently only two contractors involved in Phase II, which was started in 1977 and should be completed at the end of 1981, G.E. and Curtiss-Wright. While the General Electric Company approach makes use of water cooling, the integrated system proposed by them creates fewer water and other environmental intrusions than conventional coal-fired steam plants. Fig. 4\* describes these intrusions.

The environmental intrusions projected by Curtiss-Wright are equally low.

\*Topical report FE-1806-83 "High Temperature Turbine Technology Program Overall Plant Design Description (OPDD) Low-Btu Coal Gas Electric Program Plant", March 1980, General Electric Company

Fig. 1 High Temperature Turbine Technology (HTTT) Program



Estimated Environmental And Cost Performance Of Utility Technologies

Parameter Technology	SO <sub>x</sub> Removal (Weight %)	NO <sub>x</sub> Remaining (Lb/10 <sup>6</sup> Btu)	Particulates Remaining (Lb/10 <sup>6</sup> Btu)	Efficiency (Percent)	Electricity Generated Costs (mills/kwh)
Conventional Flue Gas Desulfurization and Particulate Control	90	0.5 - 0.6	.03	34	52
Advanced Scrubbers and Particulate Control	95	0.3 - 0.4	.03	33 - 35	49 - 53
AFB	85 - 92	0.3 - 0.5	.03	36	46
PFB	90 - 95	0.08 - 0.12	.03	37 - 41	46
Gasification Combined Cycle	95 - 99	0.03 - 0.19	<.01	38 - 44	46
Molten Carbonate Fuel Cell	95 - 99	< 0.03	< .01	44 - 48	42

Fig. 2 Estimated Environmental and Cost Performance of Utility Technologies

Fig. 3 Gasification Combined Cycle Economics with Advanced Technology

GASIFICATION COMBINED CYCLE ECONOMICS WITH ADVANCED TECHNOLOGY

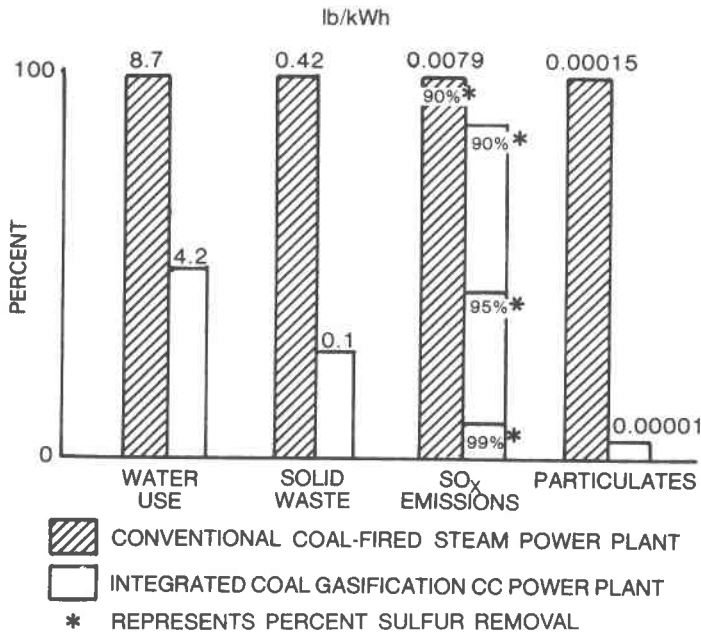
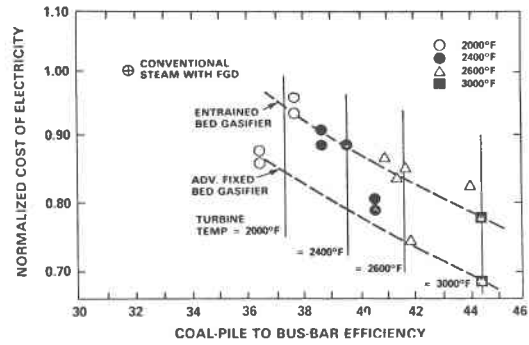


Fig. 4

## HTTT PHASE II

While both the Phase II contractors were required to structure their programs in compliance with identical program guidelines defining the design, fabrication and test of experimental components as well as test rig equipment, each contractor, because of his radically different approach from the other ended up with a different test program with respect to what they were to do specifically.

Several years prior to the beginning of this Department of Energy program the U.S. Navy had funded a program at Curtiss-Wright which had resulted in the construction and operation of a jet engine which made use of transpiration air cooling. Therefore, because this complete engine, plus most of the hardware for two more engines was available, it was transferred to the Department of Energy by the Navy. On account of this, the Curtiss-Wright Phase II program consists of several hundred hours of operation of one jet engine and the planned testing of a second engine at temperatures well above 2600°F (1427°C). It also includes the completion of a number of tests involving combustors, turbine vane cascade tests as well as materials compatibility tests.

The testing done by the General Electric Company involved no complete engine tests at all, rather their entire effort has involved the design and test of individual component parts intended for use in an as yet incompletely defined test vehicle. This vehicle will not be completely designed and fabricated until Phase III comes into being. A sectoral combustor will be tested. This is intended for use in the advanced machine and uses low Btu gas at operating temperatures above 2683°F. Phase II includes the design and test of composite water cooled stator vanes and monolithic rotor blades. One of the last tests to be completed during Phase II will be a mocked-up water delivery system intended to demonstrate how to get the cooling water on board the turbine rotor, then distribute it to all of the rotor blades so that they are all cooled evenly, and then discharges the water from the rotor.

### PHASE II - GENERAL ELECTRIC WATER COOLING APPROACH

The status of each of these test programs will now be discussed. There are eight categories of tests within the G.E. water cooled Phase II program. They will be discussed in the following paragraphs with the numerical identities shown below:

1. Hot Gas Path Test
2. Turbine Simulator Test
3. Low Btu gas cleanup test
4. Aerodynamic Test
5. Air turbine test
6. Shock tunnel test
7. Motorized test rig test
8. Water delivery and distribution test

#### 1. HOT GAS PATH TEST:

Fig. 5 is an artist's rendition of this test stand with a sectoral combustor in place. Fig. 6 is the actual fixture partly in place. Fig. 7 is the sectoral combustor designed to burn low Btu gas and is shown installed in Fig. 5. Fig. 8 is the composite nozzle identified in Fig. 5.



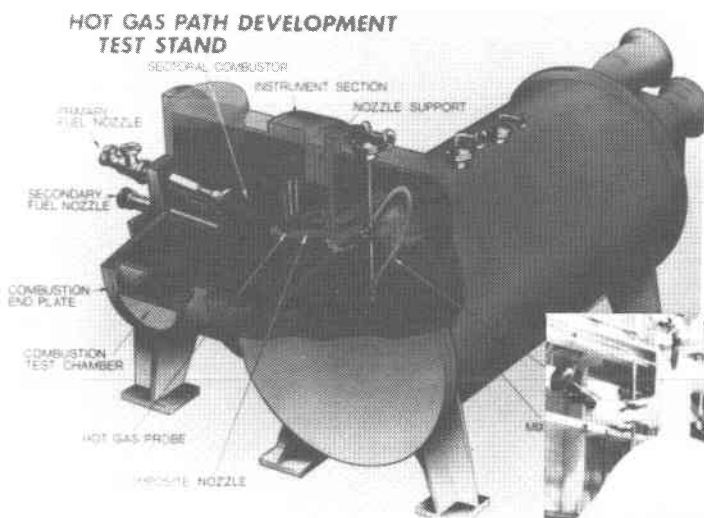


Fig. 5 Hot Gas Path Development Test Stand

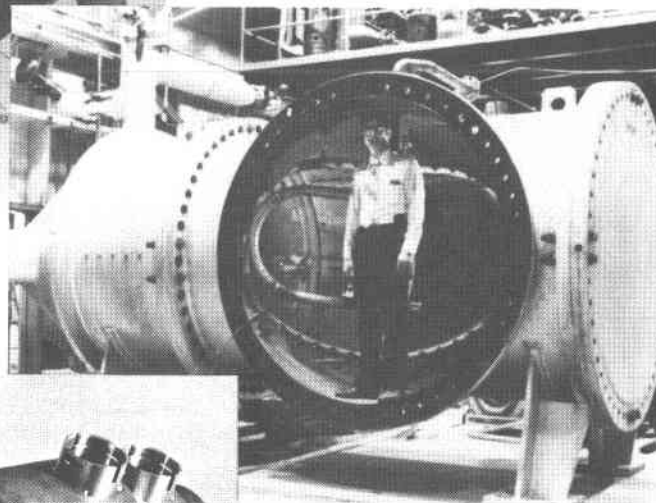


Fig. 6

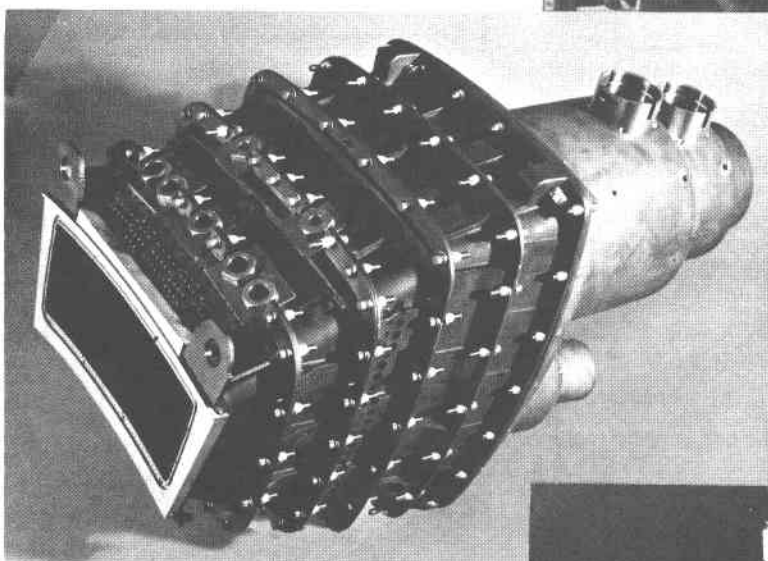
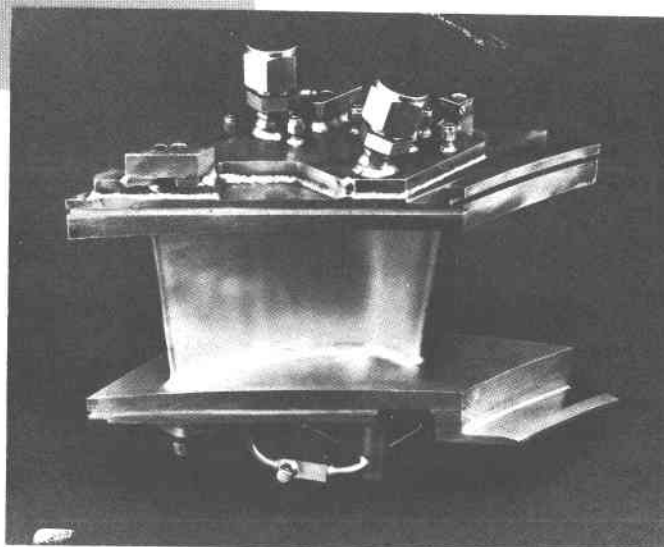


Fig. 7

Fig. 8



This entire assembly, sectoral combustor and composite first stage nozzle has not yet been tested together as shown in Fig. 5. However, the sectoral combustor has been tested in a separate test stand (not the one shown in Fig. 5) at 2600°F (1427°C) temperature and 12 atmospheres. The composite nozzle has also been tested in the Fig. 5 test stand using a substitute combustor at operating temperature for 42 hours and for 617 cycles up to 2600°F and at 12 atmospheres. The entire assembly as shown in Fig. 5 will be tested together by August 1981.

This same test fixture was used for testing the second stage monolithic nozzle also at second stage temperatures and pressures, 2082°F and approximately 5 atmospheres. Fig. 9 shows a second stage monolithic nozzle being assembled. Both second stage and third stage nozzles are made from Inconel 718 with drilled cooling passages. (Present plans do not include testing of the third stage.) A sample third stage rotor blade has been successfully fabricated, however, including the drilled cooling passages.

#### 2 & 3. TURBINE SIMULATOR TEST & LOW BTU GAS CLEANUP TEST:

The turbine simulator and low Btu gas cleanup test will be discussed together because they were tested together. At the G.E. corporate Research and Development Center, which is about 10 miles from the site where the Hot Gas Path tests were conducted using the Fig. 5 fixture, the G.E. Company has a small Gegas\* gasifier, which is really a stirred Lurgi. The entire installation, including the cleanup train is shown in Fig. 10. The cleanup train shown here includes a physical cleanup system consisting of two water washes, as well as a Benfield sulfur removal system, which is the high structure on the right. The Benfield removal system has already demonstrated its capability of removing 93% of the sulfur without any carryover during transients. This gasifier-cleanup system supplies low Btu gas to the turbine simulator, which is in a nearby test cell. The turbine simulator is only a combustor and a stator vane cascade test assembly as shown schematically in Fig. 11. The water cooled composite nozzle designed for this turbine simulator is shown in Fig. 12. This composite test nozzle was the first such nozzle assembled from the composite materials, and tested at 2600°F (1427°C). The composite first stage nozzle construction is shown schematically in Fig. 13. The monolithic construction is as shown in Fig. 14.

#### 4 & 5. AERODYNAMIC TEST AND AIR TURBINE TEST:

The Aerodynamic tests and the air turbine tests were tests designed to help refine the aerodynamic passageways within the turbine and to investigate the effects of gas stream wakes on heat transfer coefficients.

#### 6. SHOCK TUNNEL TEST:

The shock tunnel tests helped to refine the correct value of the air side heat transfer coefficients.

#### 7. MOTORIZED TEST RIG TEST:

The motorized test rig is shown schematically in Fig. 15. The actual test device is shown in Fig. 16. As a result of test results obtained with this fixture the bucket heat loads are as shown in Fig. 17.

\*General Electric trade name. Similar to a Lurgi except that the coal fines are fed into the gasifier by means of a patented screw feeder device.

Fig. 9

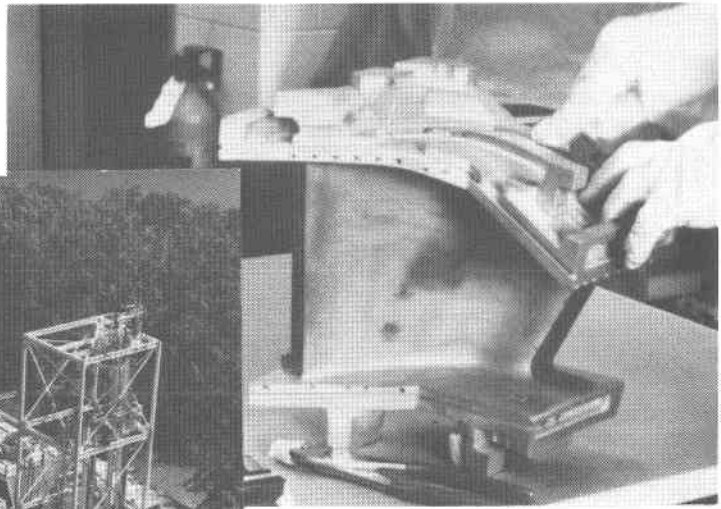
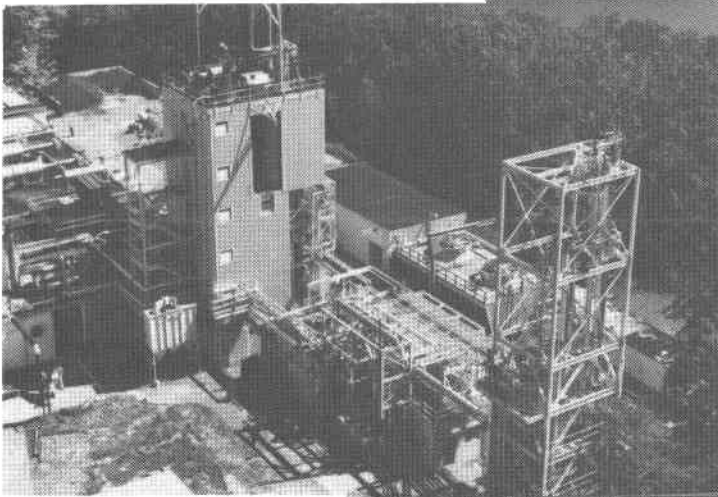


Fig. 10

Fig. 11

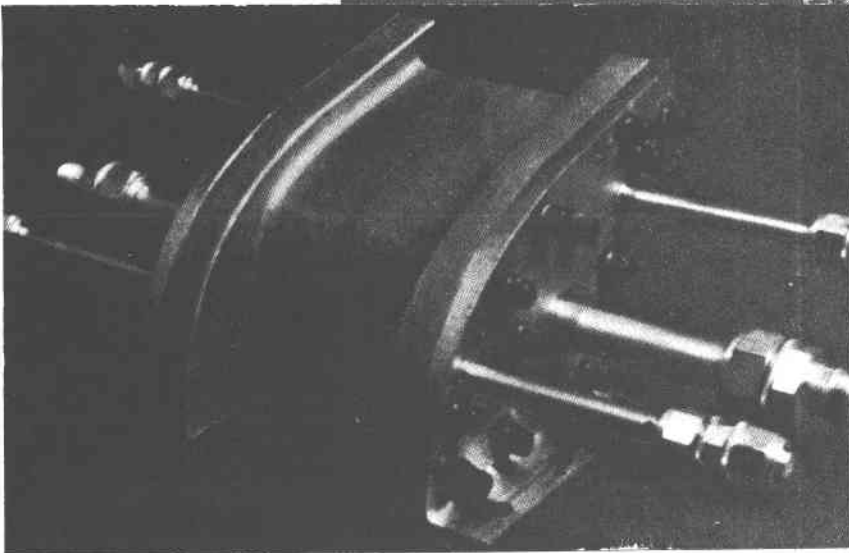
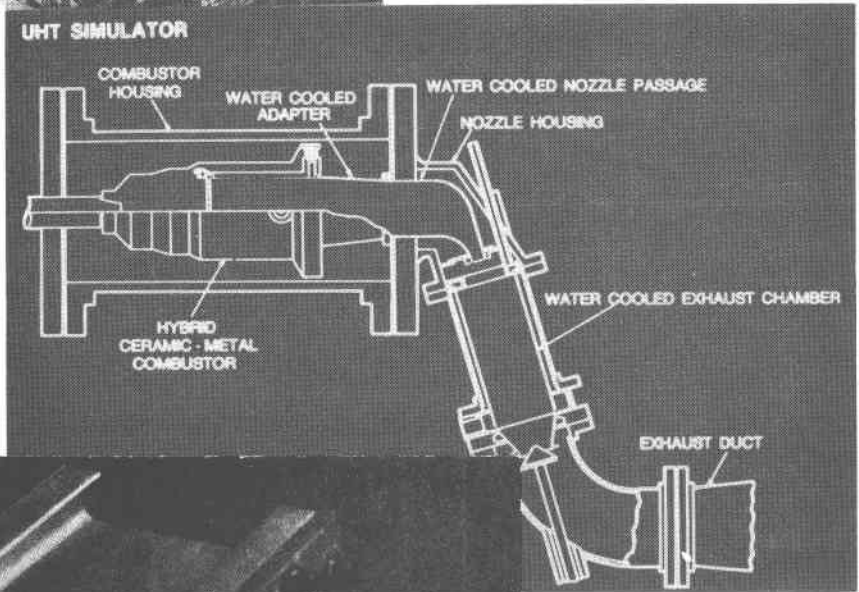


Fig. 12

Fig. 13

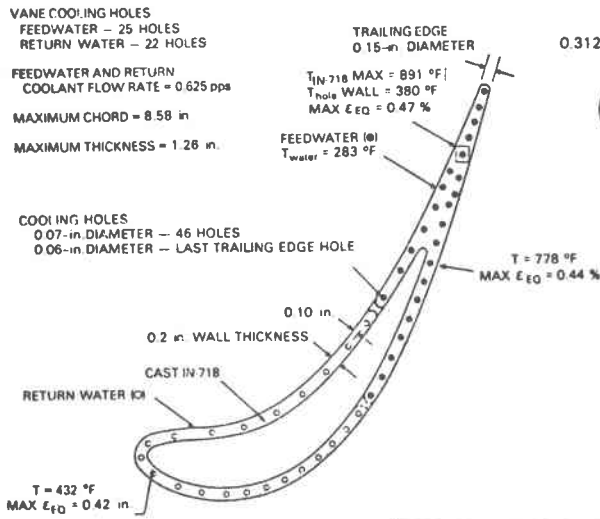
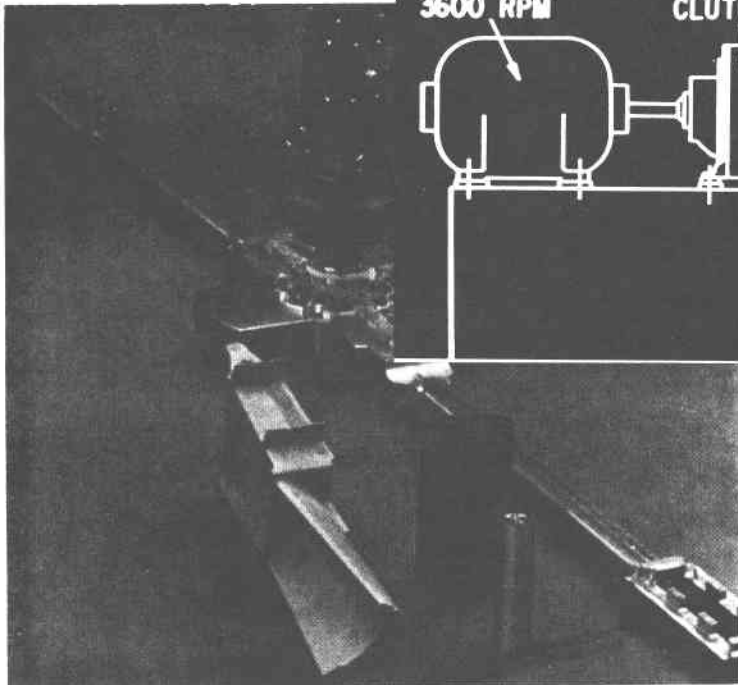


Fig. 15



$T_{\text{firing}} = 2600 \text{ }^\circ\text{F}$   
 $T_{\text{gas max}} = 3010 \text{ }^\circ\text{F}$ ,  $M_0 = 0.155$   
 $P_{T \text{ gas}} = 166.2 \text{ psia}$   
 $W_{\text{nozzle throat}} = 305.9 \text{ pps}$   
**NUMBER OF NOZZLES = 48**  
**NOZZLE AIRFOIL HEIGHT = 3.8 in.**  
**NOZZLE CHORD = 3.47 in.**  
**NOZZLE PITCH DIAMETER = 65 in.**  
**LOW-Btu GAS FUEL, LHV = 127.5 Btu/scf**

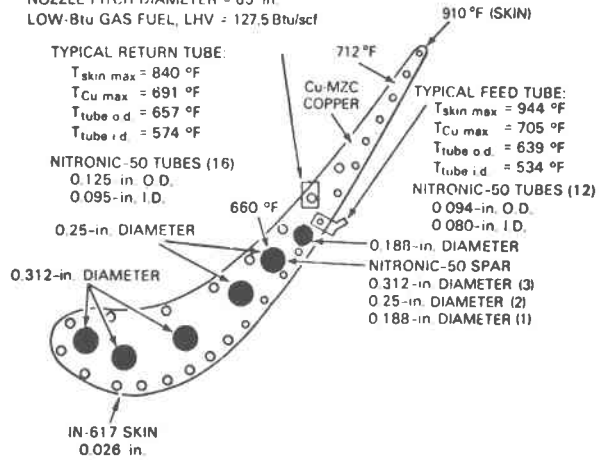


Fig. 14

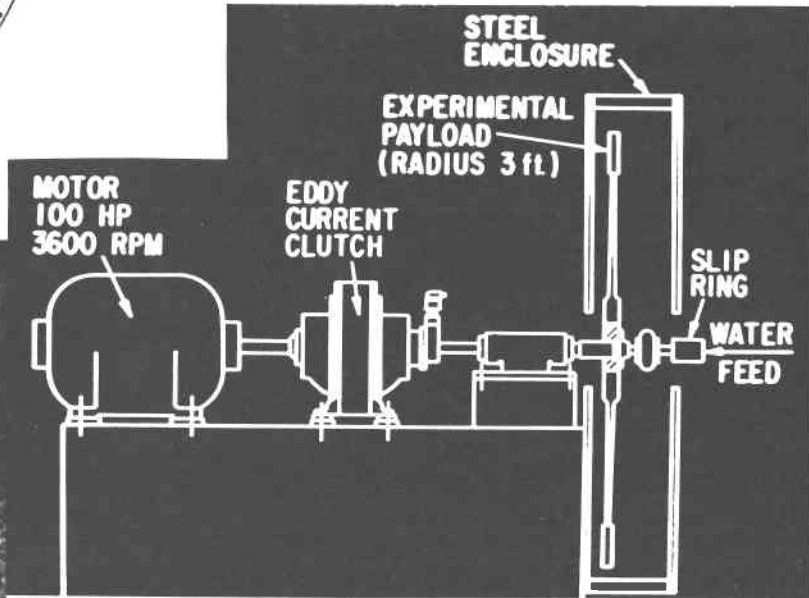


Fig. 16

## 8. WATER DELIVERY AND DISTRIBUTION TEST:

The fixture utilized to check the cooling water delivery system to the rotating turbine shaft is shown in Fig. 18.

This summarizes the test program for the G.E. Phase II program as of this date. The conceptualized test vehicle making use of the Phase II component designs is shown in Fig. 19.

### PHASE II - CURTISS WRIGHT AIR TRANSPIRATION COOLING APPROACH

The Curtiss-Wright Phase II program made extensive use of the Low Pressure Ratio Test Rig engine shown in Fig. 20. This is the jet engine mentioned earlier which came from the Navy program. All of the stator vanes and rotor blades are cooled by the transpiration air cooling method as shown in Fig. 21. Fig. 22\* is a graphical representation of the low pressure ratio engine test during operation on fuel contaminated with ground fly ash.

The fuel used at first was distillate, and later when distillate became unobtainable natural gas was substituted. It shows how the cooling air flow changed with time while the engine was operating on fuel which had 10 micron particulates added. After the first 200 hours of running, the blades and vanes were cleaned, and run again for 50 hours. They were then cleaned and run again with 2.7 micron fly ash for another 150 hours (for a total of 400 hours.) The actual particulate sizes were not all 10 micron or all 2.7 micron, rather, the size distribution was as shown in Fig. 23. The test summary beyond the 400 hours shown in Fig. 22 is shown in Table 1.

TABLE 1 LP Rig Engine Turbine Summary

- After 800:20 hours of operation in a 2600 - 3000°F gas stream environment there was no mechanical, thermal distress on any of the turbine components.
- In over 300 hours of cascade testing and 800 hours of LP operation, particulate deposition was minimal and there was no evidence of hot corrosion.
- Blades and vanes sustained foreign object damage (FOD) without mechanical failure. Fifty eight rotor blades and 65 stator vanes were repaired by replacing damaged skin panels. Repair cycle time was 6 weeks.

The annular combustor used in this engine is shown in Fig. 24. The combustor shown in Fig. 25 was operated with the simulated low Btu gas obtained by mixing the various gases in the mixing facility shown schematically in Fig. 26. While the testing of this combustor has demonstrated that it will light off and operate, the pattern factor is shown in Fig. 27. The appearance of the blades after this test described in Fig. 22 are as shown in Fig. 28.

\*"Proceedings of the Department of Energy Advanced Gas Turbine Central Power Systems Workshop", Conf-8004103, April 30-May 2, 1980.

Fig. 19 General Electric Test Vehicle

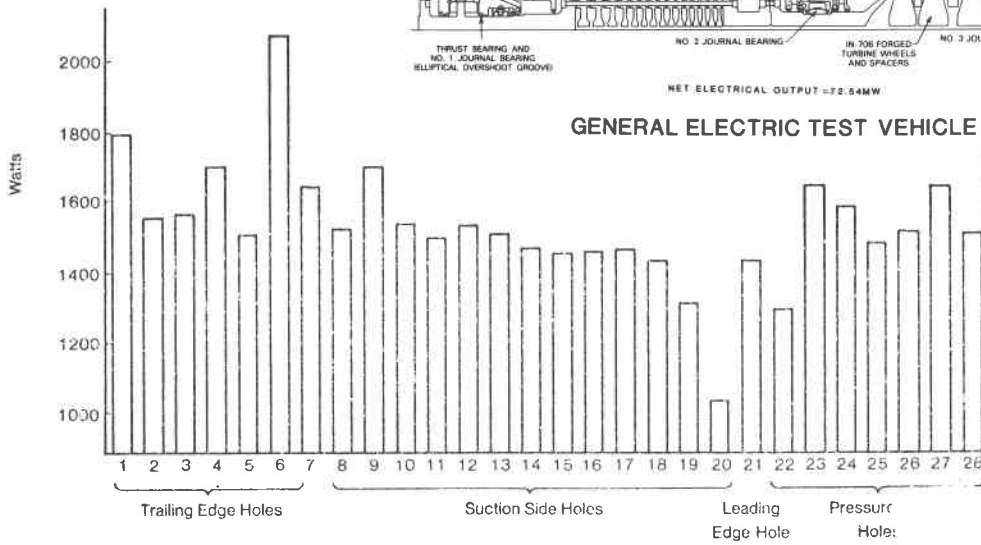
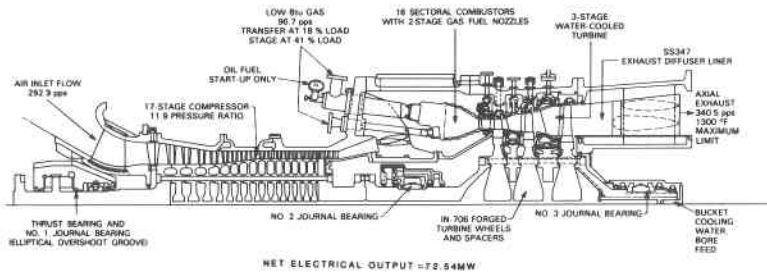


Fig. 17 Thermal Load per Hole

Thermal Load Per Hole

Fig. 18

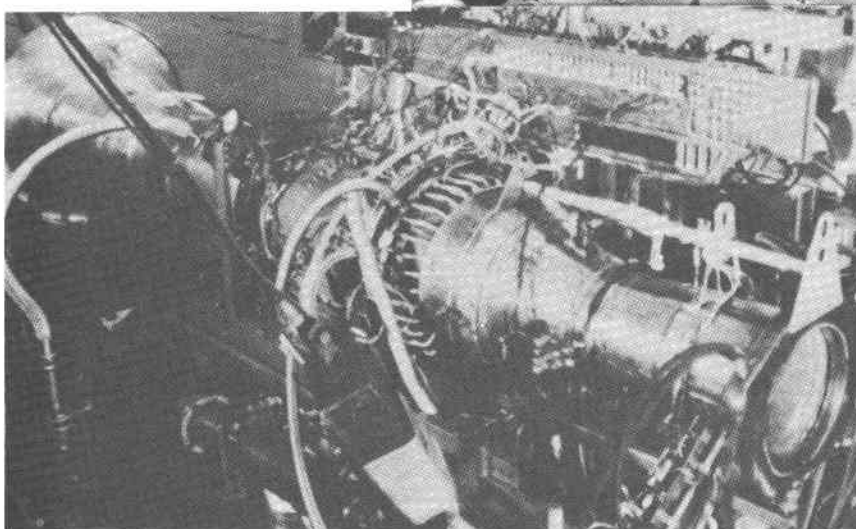
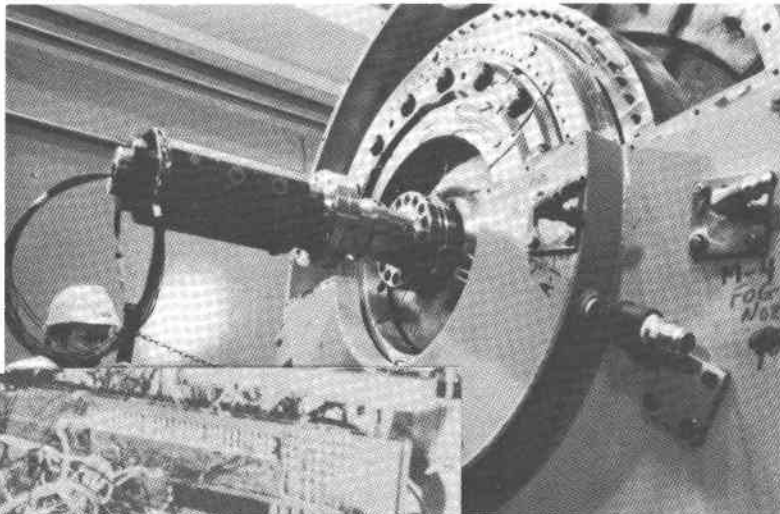


Fig. 20

Fig. 21 Transpiration Air Cooled Turbine Blade Concept

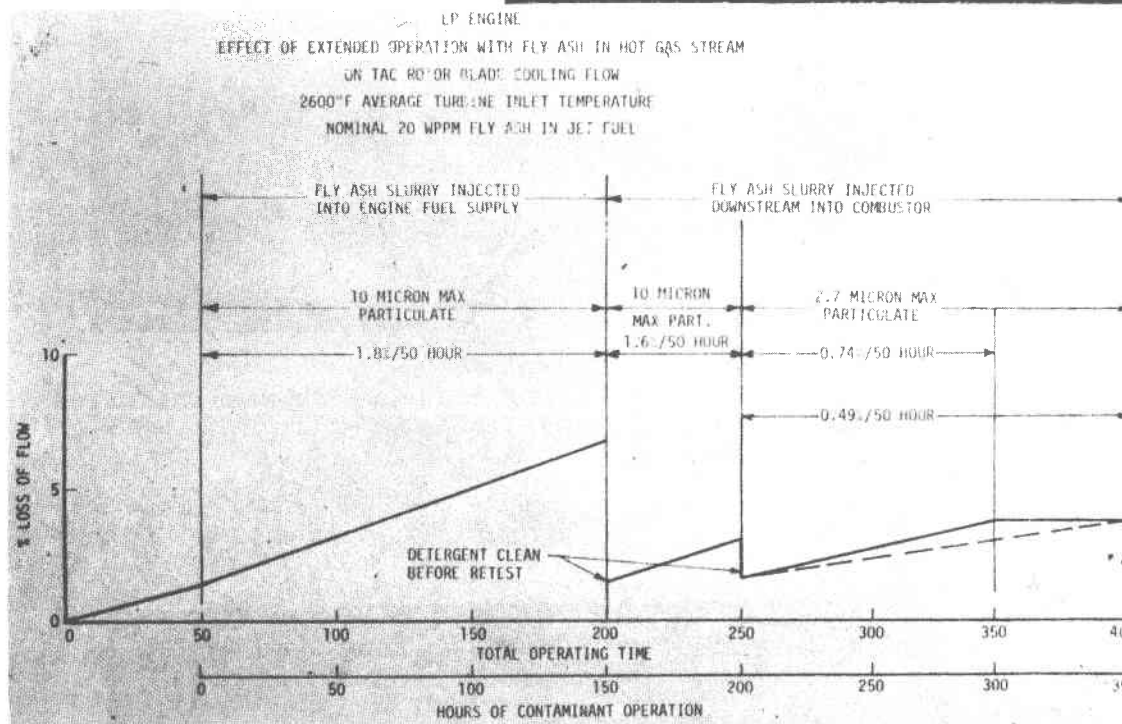
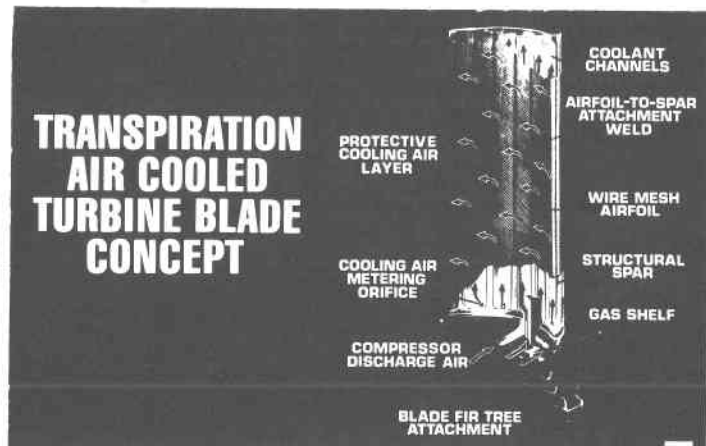


Fig. 22

EFFECT OF MILL TIME ON PARTICLE SIZE  
440 WPPM FLY ASH IN JET FUEL  
COUNTER ANALYSIS  
(NORMALIZED DISTRIBUTION)

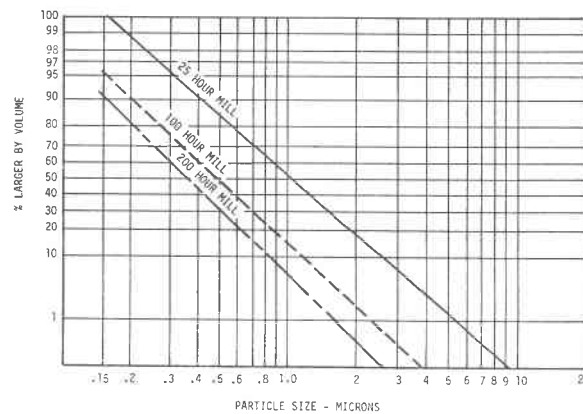


Fig. 23 Effect of Mill Time On Particle Size

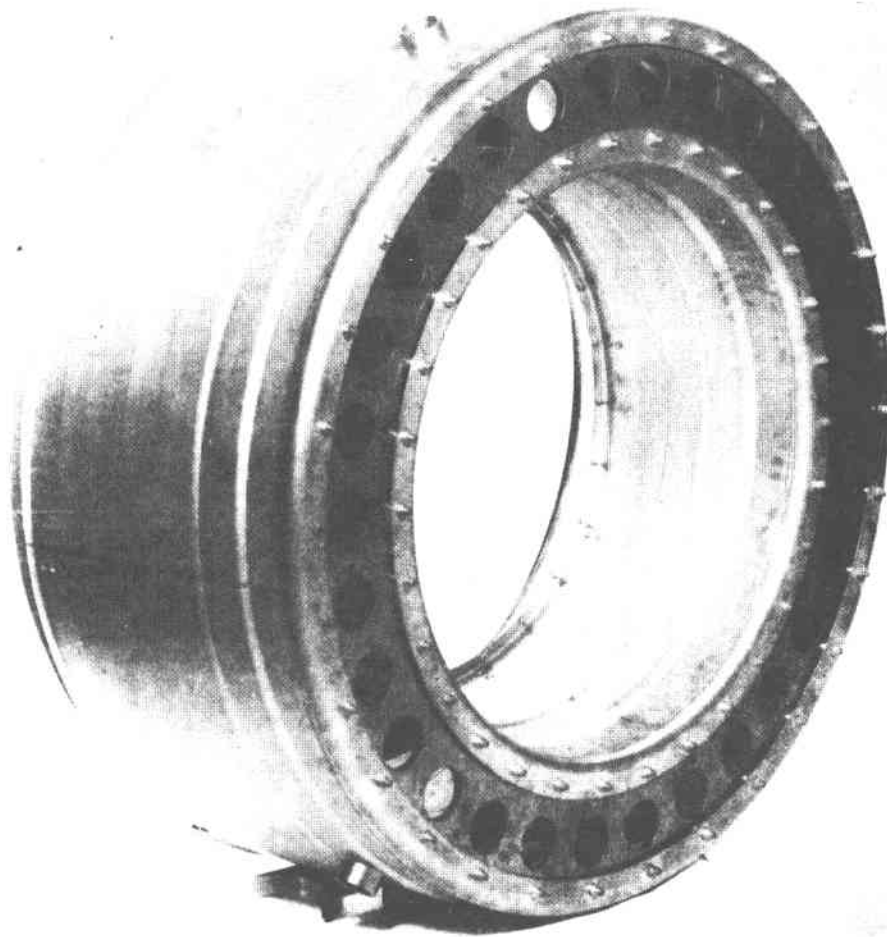
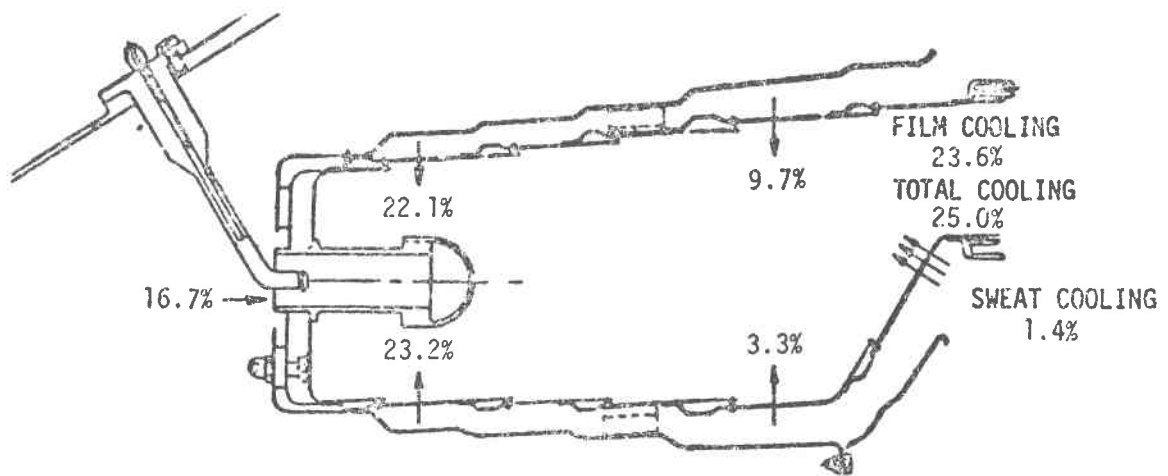


Fig. 24 TSTR Full Annular Low Btu Gas Fuel Combustor Basket with Cooling Shrouds Installed



CONFIGURATION Va

Fig. 25



Not shown is a material test fixture utilized to evaluate a number of turbine materials in simulated combustor outlet conditions.

The second gas turbine to be tested by Curtiss-Wright is shown in Fig. 29. This engine is identified as the Turbine Spool Technology Rig engine (TSTR). It is very nearly the same 6515 engine as the low pressure ratio engine mentioned earlier except the earlier engine had three stages in the compressor removed and this one did not. Consequently, this latter engine has a pressure ratio of 7:1 where the earlier engine only had a 3.5 to 1. The hot section turbine vanes and blades are somewhat different also. The transpiration cooling method is the same.

This latter TSTR engine has been assembled with much tighter clearances than the earlier engine in order to be able to operate with as good aerodynamic efficiency as possible so that the changes in performance can be measured and evaluated. It is planned to calibrate this engine on clean fuel then operate several hundred hours with contaminated fuel much like the earlier engine and then to measure the change in performance caused by the particulate laden fuel. The earlier engine was not calibrated because it has large clearances; it was only intended for measuring the changes in the cooling air flow caused by the dirty fuel.

The latest conceptual design for a transpiration air cooled engine to meet the power requirements which were originally defined in Phase I is shown in Fig. 30.

#### DISCUSSION

From the status discussion presented it can be seen that the two Phase II High Temperature Turbine Technology contractors have programs which are quite different from each other and each approached his program differently because of the status of past testing being quite different, where one is operating complete engines, the other is not. The basic thrust in both programs is an attempt to learn enough so that when Phase III begins to be able to design an advanced technology machine incorporating all that has been learned in Phase II and to reasonably expect that these advanced machines will operate. Both contractors were required to publish all of their technical results so that all the technology enters the public domain as quickly as it is published. Once the Phase III machines are operated, a considerable amount of testing and modification should eventually result in machines which can then later be commercialized. At the same time other contractors using published data should be able to conceptualize an advanced design machine using the information available to the general public. Proprietary concepts and approaches will undoubtedly vary.

#### HTTT PHASE III

The Phase III procurement is to be completely competitive. It is not the intent that only the present Phase II participants be the only ones qualified to compete for Phase III, rather, it is to be open to all who have the manufacturing capability.

NASA is to release the RFP and manage the project under DOE program control.

#### ACKNOWLEDGEMENT

The authors would like to express their gratitude to the HTTT program managers from the General Electric Company and Curtiss-Wright Corporation for the use of the figures and data which came from the technical reports published in their program reports.

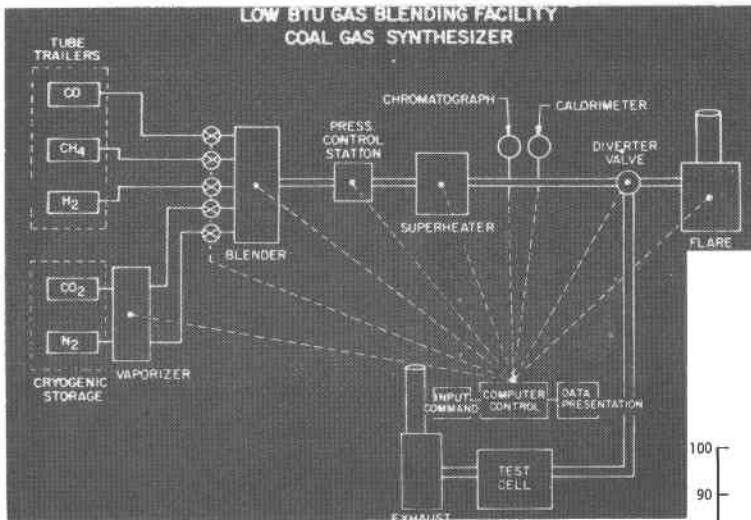


Fig. 26 Low Btu Gas Blending Facility Coal Gas Synthesizer

TSTR 60° SECTOR COMBUSTOR  
 AVERAGE RADIAL PROFILE  
 COMBUSTOR CONFIGURATION Va

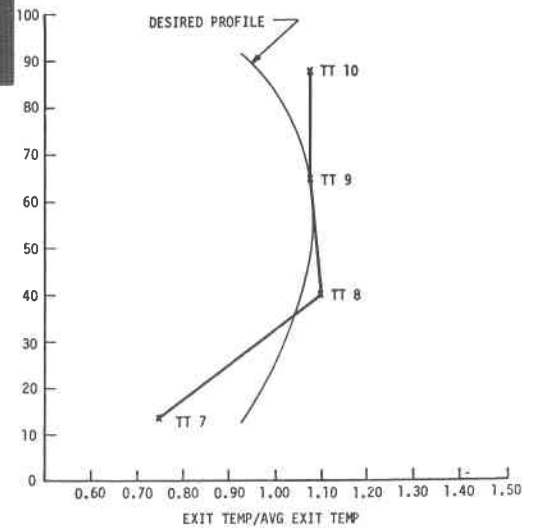


Fig. 27

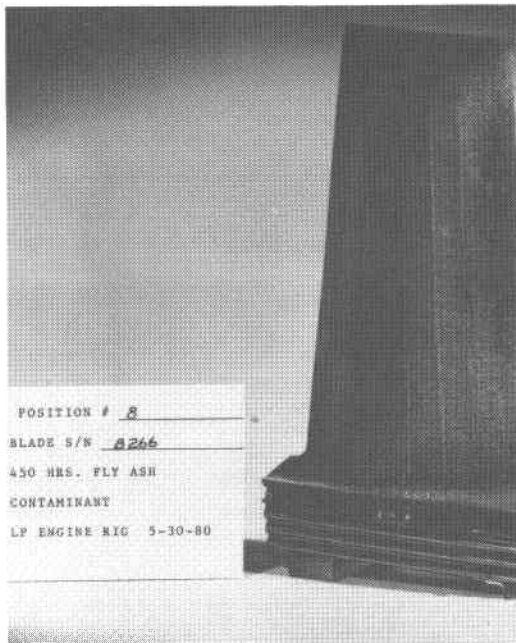
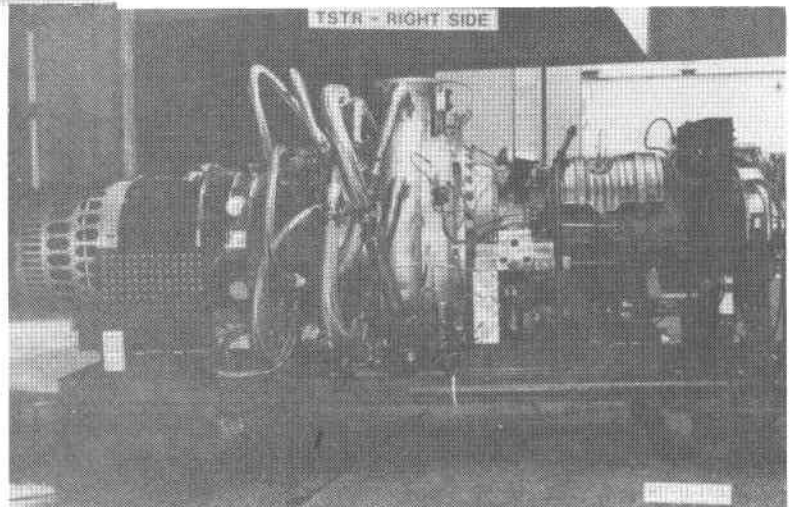


Fig. 28

Fig. 29



HTTT PROGRAM  
REFERENCE TURBINE SUBSYSTEM PRELIMINARY DESIGN  
OVERALL SYSTEM LONGITUDINAL SECTION

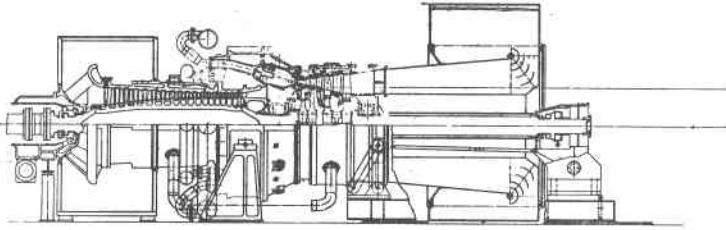
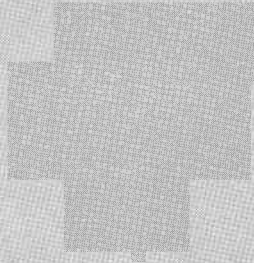


Fig. 30 Reference Turbine Subsystem Preliminary Design Overall System Longitudinal Section



Session IV

HEAT ENGINE COMBUSTION ZONE  
MATERIALS PROBLEMS

## HIGH TEMPERATURE CORROSION IN HEAT ENGINES

John Stringer

Electric Power Research Institute  
3412 Hillview Avenue  
Palo Alto, California 94304

### Synopsis

The use of alternate fuels in heat engines will introduce some new problems in high temperature corrosion and extend the range of some already well-known problems. It is shown that the majority of the high temperature corrosion problems can be categorized as either mixed oxidant corrosion or salt-induced accelerated oxidation. The most important case of the former is sulfidation-oxidation corrosion in gasifier environments and in fluidized bed combustion; the most important example of the second is alkali sulfate induced hot corrosion. The general mechanisms of the corrosion processes are summarized; examples are given of different practical problem areas; and the various approaches to the solution of the problems are outlined.

### Introduction

The products of combustion of all but the purest of fuels form an aggressive environment for most structural alloys. The desire for improved efficiency has resulted in higher and higher working fluid temperatures in heat engines. The combination of these factors has resulted in an increasing incidence of high temperature corrosion problems and these can be expected to increase further with the introduction of other fuels to replace oil and natural gas.

Some alloys are not developed for oxidation resistance. They are used up to a limiting temperature, which may be determined by mechanical strength criteria, or by high temperature corrosion criteria. This is true of the low-alloy ferritic steels used in boilers: in a coal-fired boiler burning a typical American coal, 2 1/4 Cr-1Mo steel (T22) can be used up to a metal surface temperature of approximately 600°C. This is an oxidation limit temperature. If conditions are a little more severe, it may be decided to switch to an austenitic stainless steel, such as Type 304, at a slightly lower temperature. But if a very high chlorine coal (this implies high volatile alkali) is to be burnt, the lifetime of a superheater constructed of these materials may be only 5 years. In this case, tubes clad on

the exterior with a more corrosion resistant material such as Type 310 SS or Inconel 671 (50Ni-50Cr) by coextrusion may be more economical.

However, in more demanding situations, such as that in a gas turbine, relatively small amounts of metal are exposed to the most severe environments, and their performance is critical. Again, both strength criteria and corrosion criteria are involved, and to some extent it proved possible to develop alloys which met both. The early nickel-based superalloys were developed from the oxidation-resistant heater alloy Ni-20Cr strengthened by  $\gamma'$  precipitates ( $\text{Ni}_3(\text{Al}, \text{Ti})$ ). However, increasing the strength required a progressive decrease in the amount of chromium, the solid solution strengthening being provided instead by molybdenum. Eventually these alloys reached a point at which they had poor corrosion resistance in the presence of alkali salts. Two possible paths diverged at this point. One was to attempt to produce an alloy with adequate strength, but sufficient chromium to confer inherent corrosion resistance. This approach resulted in IN738 (Ni-16Cr-8.5Co-3.4Al-3.4Ti-1.75Mo-2.6W-1.75Ta-0.9Nb) and a group of generally similar alloys. The alternative was to separate the functions of strength and corrosion resistance, and use a corrosion-resistant coating on a strong substrate. This approach resulted in the platinum aluminides and the MCrAlY coatings.

In very severe conditions (marine gas turbines, turbines burning blast furnace gas or sour natural gas) it has been common practice to lower the turbine inlet temperature to avoid severe corrosion. However, this resulted in the discovery of an accelerated form of corrosion at somewhat lower temperatures which, as luck would have it, was particularly severe on the low chromium, high aluminum CoCrAlY coatings which were then the state-of-art for aircraft turbines. Avoiding corrosion by cooling the component sufficiently is still a valid method of approach, but in the case of alkali sulfate induced attack, as we shall see, the definition of a "safe" temperature is a little difficult. In the extreme case, it appears that the surface temperature may have to be as low as 550°C; others think that 650°C may be sufficient. To achieve this with a turbine inlet temperature of at least 1200°C and perhaps as high as 1425°C is clearly very difficult: this issue is the subject of other papers in this conference.

Although coal gasification is a process of considerable antiquity, modern gasifiers present severe materials problems. Since the gas may be produced at 1300°C or more, and since the equipment must last for perhaps 200,000 operating hours, some early studies attempted to find alloys which could last for this sort

of time in the syngas at very high temperatures. While it would obviously have been very desirable to find such a material, it could have been predicted with some confidence that such efforts were doomed to failure. It is important to recognize that there are several methods of approach to a problem of this kind. First, the process may be modified to make the conditions less severe. Second, the system may be designed to avoid having metals in contact with the severe environment at elevated temperatures, for example by using a cooled refractory-lined vessel. Third, the metallic components may be cooled. Fourth, if all else fails, shorter lifetimes may be acceptable if the component can be quickly replaced without causing a major interruption in the operation of the plant. For practical problems of this kind, it is not possible to separate the corrosion science from the engineering.

The accelerated high-temperature corrosion boilers and in gas turbines involve the presence of deposits on the metal surface. These contain the alkali metals, usually as sulfates, and frequently other elements such as vanadium, phosphorus, lead, calcium and magnesium. The deposits are often at least partially molten. The corrosion in gasifiers however need not involve a deposit at all: the accelerated attack takes place because of the simultaneous reaction of the metal with two or more oxidants. The next sections of this paper will discuss these two forms of accelerated corrosion in more detail, although in some practical cases both processes may be involved at the same time.

#### Oxidation in Mixed Oxidants

Alloys designed to be resistant to high temperature oxidation generally rely on the development of an oxide layer which acts as a barrier to further transport of the reactants. The protective oxide has to be continuous, to prevent the transport of one or other of the reactants through discontinuities such as pores. It should be adherent: not because this is required to be a transport barrier, but because it means that the oxide is less likely to fail mechanically. It should be resistant to thermal cycling, and to reaction with other constituents of the environment. It should not transport minor constituents of either the alloy or the environment at significant rates. In practice, it turns out that there are a limited number of possible protective oxides. The large majority of high temperature alloys rely on the formation of  $\text{Cr}_2\text{O}_3$  or  $\text{Al}_2\text{O}_3$ ; some depend on  $\text{SiO}_2$ . A few authorities believe that compound oxides, particularly spinels such as  $(\text{Ni,Fe})\text{O} \cdot \text{Cr}_2\text{O}_3$  can also behave as protective oxides: others believe that it is very unlikely that continuous protective layers of spinels can develop.

For a given alloy, there is a minimum amount,  $N_C$ , of the oxide-forming element (Cr, Al or Si) that must be present to develop an external protective oxide.  $N_C$  is determined by four criteria. First, it is clear that the desired protective oxide must be the thermodynamically most stable oxide phase in equilibrium with the alloy. Second, since the oxide will grow at a certain (slow) rate, it must be possible for the oxide-forming element to diffuse from the body of the alloy to the oxide/metal interface fast enough to balance the growth rate without the concentration at the interface falling below that required by the first criterion. Thirdly, the oxide must form externally, rather than internally. This is related to the relative diffusion of oxygen into the alloy and the oxide-forming alloy element out. It appears that the critical amount is related to the volume fraction of the oxide that would be formed within the alloy, it being postulated that the internally-formed oxide acts as a barrier to the inward diffusion of oxygen. Lastly, when oxygen is admitted to a clean metal surface all possible oxides will nucleate, not only the most stable. The less-stable oxides will frequently grow more rapidly, although the most stable oxide will tend to spread over the metal surface eventually cutting off the supply of metal ions to the other phases. However, if the lateral spreading of the protective oxide is too slow, the recession of the metal surface under the more rapidly growing oxides can lead to the nuclei of the stable oxide being undermined and carried off into the scale: it will then not be possible to develop a continuous protective layer. This fourth criterion is less easy to express as a quantitative function for  $N_C$ , since it depends not only on the lateral growth rate of the protective oxide but on the mean internuclear spacing.

If a pure metal is exposed to a mixture of two oxidants, the thermodynamic criteria can be expressed in terms of the relative stability of the oxidation products of the two oxidants with the metal, and a two-dimensional thermodynamic stability diagram can be constructed: an example is shown in Figure 1 for the Fe-O-S system taken from the compilation of Hemmings and Perkins<sup>(1)</sup>. If the activities of the two oxidants are such that the point representing the atmosphere in this diagram falls (for example) within the oxide-stable region, it follows that the phase in equilibrium with the atmosphere is the oxide. It is not however possible to determine what is the phase in equilibrium with the metal, although from an oxidation point of view this is the more important issue. Rapp<sup>(2)</sup> has made the point that if the sulfur activity in the atmosphere lies above the extrapolation of the Fe-FeS line, then it is possible for the sulfide to form below the oxide: Rapp refers to the sulfide as being "metastable" under these



circumstances. Whittle and Stringer<sup>(3)</sup> following on these ideas and similar suggestions of Rahmel<sup>(4)</sup> introduced the concept of a "reaction path" which could be drawn on the diagram, and Stringer<sup>(5)</sup> has shown qualitatively how, depending on the relative activity gradients within the product phases, a number of different phase distributions may be possible.

It is not uncommon to speculate on the behavior of alloys by superimposing the stability diagrams for the various elements within the alloy, perhaps modifying them to allow for the activity of the element in the bulk alloy. Giggins and Pettit<sup>(6)</sup> point out that this is formally incorrect: for a binary alloy a three dimensional stability diagram must be constructed. The possible form of the reaction path in such a diagram is very difficult to predict, and it is thus hard to use these diagrams for obtaining a qualitative rationalization of possible phase distributions in the corroding system. At our present state of knowledge, this is as much as can be asked from a thermodynamic stability diagram.

Why does the formation of sulfide matter? If a continuous layer of chromium sulfide is grown on pure chromium, and then the specimen is exposed to oxygen, chromium oxide forms on the outside of the sulfide layer and grows at virtually the same rate it would on pure chromium. The sulfur released by the oxidation does not escape through the oxide: it reacts with more chromium at the metal surface. If a nickel-chromium alloy is first sulfidized at low sulfur potentials it too may form a continuous external layer of chromium sulfide<sup>(7)</sup>; and if the sulfidized specimen is exposed to oxygen it will again form an external chromium oxide layer. Once again, the sulfur released by the oxidation does not escape through the oxide, but migrates inward to form fresh chromium sulfide. So far, the presulfidation has very little effect on the corrosion. However, it appears that as time goes by the chromium sulfide layer ceases to be uniform in thickness. It develops protrusions into the metal, and eventually becomes discontinuous. The sulfide oxidizes in situ, and thus eventually one forms an oxide layer with intrusions into the metal beneath which are discontinuous colonies of chromium sulfides. Because of the chromium depletion near the metal surface, it is possible for the sulfur activity to rise above the original value, and eventually nickel sulfides may form.

The sulfides tie up the chromium. It is not obvious how a two-phase material will oxidize<sup>(8)</sup>, but in this case, since the sulfides oxidize in situ, it is clear that the ability of the external chromium oxide to heal itself will be diminished, and eventually the oxidation rate increases with nickel oxides forming. In addition,

the nickel sulfides are liquid at relatively low temperatures, so that if these form the reaction may become catastrophic.

The point of this description is to show that, in this case at least, the presence of the sulfide does not of itself lead to rapid corrosion. It is the development of a structure which is incapable of forming a protective scale that is the significant process, and this is determined by kinetic and structural factors in addition to the thermodynamic concepts contained in stability diagrams. It can be said that the process is a break-away corrosion, which will eventually become rapid; and all the kinetic and structural factors determine is when this will happen. This may be true, but from a practical point of view the time to breakaway is the important parameter: if it is sufficiently delayed, and sufficiently reproducible, an acceptable lifetime may be possible. A second objection is that the nature of the corrosion when the two oxidants are present simultaneously is very different from the sequential scenario outlined above. This is true, and the differences may well be of great importance.

If the atmosphere is such that (for example) chromium oxide is the phase in equilibrium with the atmosphere but chromium sulfide and nickel sulfide are "metastable" in the sense used above, then the oxygen activity will fall going through the scale towards the metal. The sulfur activity may remain constant or also fall. At some point the activities will correspond to a sulfide phase (probably chromium sulfide, but it depends on the variation of metal activities and the magnitudes of the solubility products) becoming stable. If the system were perfectly uniform, this would form as an inner layer, but in practice heterogeneities will probably result in either sulfide intrusions into the metal, perhaps along alloy grain boundaries, or sulfides depositing at the oxide grain boundaries. The first case will eventually result in oxide breakdown, as described above; again, lowering the chromium activity within the surface layer of the metal may ultimately allow nickel sulfides to form and the reaction may become catastrophic. In the second case the sulfide paths may eventually extend effectively to the gas interface for kinetic reasons and then may act as rapid diffusion paths for the metal atoms leading to rapid external oxide growth and loss of adhesion of the protective oxide.

However, it has also been observed that sulfides can form even though the sulfur activity in the atmosphere lies well below the sulfide "metastability" range. This is thermodynamically impossible in terms of simple transport processes, and implies that there must be some process capable of developing local enhancement of

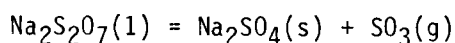
the sulfur activity. Several authors have discussed this problem, and one simple case (following Wootton and Birks<sup>(9)</sup>) is as follows. The scale contains pores. O<sub>2</sub> and SO<sub>2</sub> migrate down the pore. Whether the reaction is with the oxygen, increasing the SO<sub>2</sub> partial pressure, or with the SO<sub>2</sub> reacting with metal at the base to form oxide and releasing sulfur vapor, which has to diffuse out to the surface to react with oxygen to form SO<sub>2</sub> again, the sulfur activity increases from the atmosphere towards the metal surface, and may thus exceed the critical value required to form sulfide. Similar models have been suggested for other gas mixtures, and other possibilities have been postulated.

Holmes and Stringer<sup>(10)</sup> have discussed the specific problem of the corrosion of alloys in low oxygen activity, high sulfur activity atmospheres, and the processes responsible for the breakdown of the protective oxide scale. The possibilities of developing a quantitative model for the breakdown are discussed, but no model is presented.

#### Corrosion Associated with Molten Salt Deposits

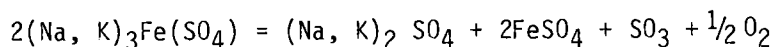
It has been known for many years that in combustion systems burning sulfur-containing fuels, it is sometimes possible to deposit on the metal surfaces alkali sulfates (Na,K)<sub>2</sub>SO<sub>4</sub>. The alkali metals may derive from the fuel or from impurities in the combustion air. It is generally assumed that the solid sulfates do not induce corrosion, although it will appear later that this is not necessarily true. Part of the problem is then to identify a molten phase derived from the alkali sulfates.

In gas turbines, the usual source of the alkali is sea salt, and the deposits are rich in sodium with relatively little potassium. In coal-fired boilers, the deposits contain much more potassium, the relative amounts depending on the coal. Sodium sulfate melts at 884°C; potassium sulfate melts at 1071°C; and the minimum melting point of a mixture of the salts is at 823°C for a Na:K ratio of 4:1. In practice, corrosion is observed at much lower temperatures. Early investigators suggested that the corrosion in coal-fired boilers, which is observed in the temperature range 535-725°C, might be due to the presence of sodium pyrosulfate, Na<sub>2</sub>S<sub>2</sub>O<sub>7</sub>, which deliquesces at 460°C. However, this compound is relatively unstable, tending to dissociate according to the reaction



and at these temperatures, partial pressures of  $\text{SO}_3$  in excess of  $2 \times 10^{-3}$  atm. would be required for there to be a significant activity of the pyrosulfate.

Reid and his co-workers<sup>(11)</sup> suggested that the molten phase was a complex alkali iron trisulfate,  $(\text{Na}, \text{K})_3\text{Fe}(\text{SO}_4)_3$ . This also tends to dissociate

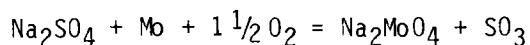


and a pressure of  $\text{SO}_3$  of the order of  $2 \times 10^{-4}$  atm is required for the liquid to be stable at the lower temperatures. As a result, the low temperature limit is associated with the melting point of the complex salt, and the high temperature limit is associated with its dissociation to form a solid product. This range clearly depends on the local  $\text{SO}_3$  partial pressure, but it also depends on the Na:K ratio.

Many other species can result in low melting point phases being present. Thus,  $\text{V}_2\text{O}_5$  is molten at  $672^\circ\text{C}$ , and in the  $\text{Na}_2\text{SO}_4 - \text{V}_2\text{O}_5$  system the minimum melting point is at  $630^\circ\text{C}$ .  $\text{MoO}_3$  evaporates at low temperatures, but is capable of forming low melting point complexes with  $\text{Na}_2\text{SO}_4$ , with melting points as low as  $672^\circ\text{C}$ . Other transition metal sulfates may also stabilize low melting point phases.

Frequently, these liquid phases are stable over fairly narrow ranges of conditions, and consequently the corrosion they induce is also present over a restricted range of temperature,  $\text{SO}_3$  partial pressure, and perhaps metal ion activity.

Given that a liquid salt phase is present, it is necessarily aggressive? The answer is no. Reagent grade  $\text{Na}_2\text{SO}_4$  at  $900^\circ\text{C}$  in oxygen at 1 atm pressure in the absence of any added  $\text{SO}_3$ , is relatively innocuous to most metals: the exceptions are those that can form compounds more stable than  $\text{Na}_2\text{SO}_4$ . Thus, the refractory metals Nb, Ta, Mo and W react readily with  $\text{Na}_2\text{SO}_4$  to form (for example) sodium molybdate  $\text{Na}_2\text{MoO}_4$  releasing sulfur vapor in copious clouds. The reactions with tantalum and niobium are particularly violent. If the reaction is written



it is apparent that the violence of the reaction implies that a very high  $\text{SO}_3$  partial pressure would be required to make the reaction go to the left. For sulfate melts one can define an acidity in terms of the dissociation pressure of

the acid species  $\text{SO}_3$  which is then analogous to the practice of expressing the acidity of aqueous media in terms of the partial pressure of the hydrogen ion  $P_{\text{H}}$ . However, while  $P_{\text{H}} \cdot P_{\text{OH}} = 10^{-14}$  for dilute solutions, there is no similarly well defined product for the molten sulfates and thus no value of  $P_{\text{SO}_3}$  which can be said to correspond to neutrality: it can be expected that the neutrality condition will vary with composition in these complex molten salt mixtures. There is a further significant difference. Because we are concerned with high temperature processes, if the environment contains less than the equilibrium partial pressure of  $\text{SO}_3$  for a given salt, the salt will tend to dissociate until the balance is restored, and vice versa. The partial pressure of  $\text{SO}_3$  in the local environment thus wholly defines the value for the salt mixture, and relative to the neutrality condition thus defines the acidity of the salt mixture. However, given that the neutrality condition may change except for systems based on nearly pure  $\text{Na}_2\text{SO}_4$  it follows that as the composition of the salt changes for a fixed external partial pressure of  $\text{SO}_3$ , the salt acidity may also change.

This concept of salt acidity is the basis for one model of molten salt corrosion. The model appears to have been suggested first by Bornstein and De Crescente<sup>(12)</sup> and developed further by Goebel et al<sup>(13)</sup>. The idea is that while neutral salt may not be very aggressive, the acidic or basic salt may be. Thus, reagent grade  $\text{Na}_2\text{SO}_4$  may be melted in a high purity alumina crucible in air with no problem. However, if  $\text{Na}_2\text{O}$  is added to the melt (displacing it in the basic direction) the crucible dissolves rapidly; sodium aluminate can be recovered from the melt. The metal itself will not be attacked very much by this basic melt ( $\text{Na}_2\text{O}$ -rich melts are used for descaling metals). However, if the salt is made more acid (for example, by bubbling  $\text{SO}_3$  through it, or by adding molybdenum or vanadium) the metal will dissolve readily, and aluminum sulfate can be recovered from the melt. Figure 2 shows a diagram developed by Goebel et al<sup>(13)</sup> which is similar to a Pourbaix diagram mapping the phases of aluminum stable in a sodium sulfate melt as a function of the acidity, expressed as  $P_{\text{SO}_3}$ , and the oxygen partial pressure.

On the basis of this model, the protective oxide may be removed by fluxing in either an acidic or a basic salt. This is not in itself enough.

Suppose a sodium sulfate layer is applied to the surface of nickel in oxygen at elevated temperatures. The model for the corrosion is shown in Figure 3, due to Pettit et al.<sup>(14)</sup> Near the metal surface the oxygen activity is low and the metal reacts with the salt to form  $\text{NiS}$ . This removes sulfur from the sulfate, and so moves it locally in a basic direction. The nickel oxide on the original surface

(or the nickel metal) enters solution as an anionic species: Pettit suggests the nickelate ion  $\text{NiO}_2^-$ . This then migrates to the outer part of the salt deposit, but here the salt is still approximately stoichiometric. The nickelate ion is not stable, and dissociates to precipitate NiO. Thus, in the early stages of the reaction a loose, porous NiO scale develops and the reaction rate is rapid. However, eventually the system reaches steady state: further removal of sulfur is not possible because the activity has fallen too low for NiS to form; the salt is saturated with the nickelate ion so no more will dissolve. At this point, a dense, compact NiO scale starts to develop at the metal surface and the reaction rate drops to approximately that in the absence of the salt layer. The real problem in a salt-fluxing model is therefore how to make the reaction a continuing process, rather than one which quickly saturates.

Reid understood this problem well, although his formalism is different. He suggested that the salt with the corrosion products periodically fell off the surface, and was replenished by fresh salt, allowing the process to repeat. Similar suggestions have been made more recently.

Acid fluxing is less likely to saturate, because the acidity has to be provided elsewhere, by  $\text{SO}_3$  outside the salt or refractory metal within the alloy: there is thus no particular reason why the salt should saturate.

An alternative view has been developed by Rapp and his co-workers.<sup>(15)</sup> They were able to demonstrate that the solubility of various oxides in sodium sulfate melts exhibited a minimum at certain values of the acidity, different for each oxide, and rose rapidly on either side (Figure 4). They suggest that continued reaction is only possible if the solubility of the oxide decreases through the salt layer from the oxide/salt interface to the salt/atmosphere interface, since this allows continued precipitation of the oxide away from the interface. Whether this condition is satisfied will depend on the local condition in the salt and the form of the solubility curve for the particular oxide. They show that for normal conditions, the solubility of chromium oxide will increase from metal towards the atmosphere, so the salt will saturate without the precipitation of the oxide. This seems to account for the beneficial effect of chromium on resistance to this form of attack.<sup>(16)</sup>

The acidity of the salt can be modified in several different ways. Obviously, the partial pressure of  $\text{SO}_3$  in the external atmosphere is important, and for quasi-steady state experiments it is vital; but it is clear from the analysis presented

above that there is the possibility of a gradient of acidity through the molten salt layer with the outer surface being (perhaps) effectively neutral. In this case, the external  $P_{SO_3}$  is largely irrelevant. The removal of sulfur by the sulfidation of a constituent of the alloy will render the salt near the metal surface less acidic (more basic). The lowering of the activity of  $Na_2O$  in the salt by the presence of species which form strong compounds with it ( $MoO_3$ ,  $WO_3$ ,  $Nb_2O_5$ ,  $Ta_2O_5$ ,  $V_2O_5$ ,  $P_2O_5$ , and perhaps  $PbO_2$  etc.) will make the salt more acid. The acidity of the salt can also be displaced electrochemically either by imposing a potential or as a result of local cell action.

It should not be assumed that the salt-fluxing model has universal acceptance. There are a number of anomalous results. For example, it is clear that if  $MoO_3$  is added to  $Na_2SO_4$ , there is a displacement reaction forming  $Na_2MoO_4$  and releasing  $SO_3$ ; the acidity of the salt increases. However, if  $Na_2MoO_4$  is added to  $Na_2SO_4$ , it would appear that there should be little change in acidity, and certainly no  $SO_3$  will be evolved. Obviously, since the ionization behavior of the molybdate will be different from that of the sulfate, there may be some displacement; but the model would appear to suggest that the resulting salt would be much less corrosive than that to which an equivalent amount of  $MoO_3$  had been added. In fact, there appears to be very little difference in behavior, at least for cobalt-chromium alloys; in both cases there is an acceleration of attack compared to the simple sulfate to a very similar degree<sup>(17)</sup>. A molybdenum-containing compound is formed with the alloy constituents (probably an oxide: it contains no sulfur) at the metal surface, and it appears that this may be a factor in the corrosion process. It is well known that  $MoO_3$  by itself can cause accelerated oxidation of many high-temperature alloys.

It has been pointed out several times<sup>(16)</sup> that the salt-induced hot corrosion of alloys appears to involve two steps: an initiation step and a propagation step. For a time, a specimen coated with salt will oxidize at the same rate as it would without the coating, or even a little slower. There is no (or very little) sulfidation; the oxide appears to be continuous and protective. Then over a relatively short time the oxidation accelerates; the oxide becomes porous and non-protective, and sulfides may be formed within the metal. It is believed that the attack initiates as a result of the failure of the initially protective oxide scale, and it has been shown that this failure is very local. Pettit<sup>(18)</sup> used a hot-stage microscope to study the process. A specimen of Ni-15%Cr was heated with crystals of  $Na_2SO_4$  lying on the surface. Eventually they melted, forming a thin liquid layer over the surface of the oxide; and for a time nothing happened.

Then, quite abruptly the liquid vanished from the surface, and the scale started to undulate. Pettit suggested that the liquid had penetrated the scale, and the scale had separated from the metal so that the scale was now floating on a molten salt layer in contact with the metal. No apparent change in the scale could be detected in the microscope. Thereafter, hot corrosion proceeded rapidly.

The onset of hot corrosion has been induced by thermal cycling<sup>(17)</sup> and by mechanical stressing<sup>(20)</sup>; it is generally believed that it can also be induced by erosion.

The presence of very small amounts of sodium chloride in the vapor phase appears to be able to induce scale failure<sup>(21)</sup>, and it is claimed that it can also induce the onset of hot corrosion.

Obviously, the fluxing processes discussed above could also remove the protective scale. One would expect this to be a broad-front process rather than a local effect, but perhaps local inhomogeneities in the scale or the alloy might account for that.

The fluxing mechanisms are most frequently involved in discussions of the propagation stage, and there is good evidence that often these processes are involved. However, caution must be used. It has been pointed out that once the liquid sulfate-containing salt penetrates beneath the scale, it is in a region of low oxygen activity, and as a consequence may dissociate to generate a high sulfur activity. The subsequent corrosion is then a sulfidation-oxidation process of the sort described in the previous section, and it has been possible to duplicate most, if not all, of the morphological features of propagating high temperature sulfate-induced hot corrosion by oxidizing a pre-sulfidized specimen in the complete absence of any salt<sup>(22)</sup>.

Rapid corrosion has been observed in the presence of other compounds.  $\text{MoO}_3$  in the vapor phase has been referred to above. Vanadium apparently present as  $\text{V}_2\text{O}_5$ ; lead, present as  $\text{PbO}_2$ ; and phosphorus as  $\text{P}_2\text{O}_5$  have all been shown to result in rapid attack. In all cases, the mixture of these compounds with sodium sulfate results in increased severity of attack, but all are capable of corroding alloys in the absence of sulfate. Liquid vanadium pentoxide is the best-documented example; it appears to be almost a universal solvent for oxides. It is difficult to find an oxide crucible capable of holding it, and it readily wets most if not all oxides. The process appears to be a classic acid dissolution: the vanadates



of most elements appear to be very stable in solution in the melt. It is possible that lead oxide can behave the same way, but it has been suggested<sup>(23)</sup> that the lead-induced "burning" of exhaust valves may involve the presence of sodium sulfate as well rather more commonly than had been supposed.

The attack by the highly acid melts such as vanadium pentoxide typically produces hemispherical pits filled with the corrodent and having a fairly smooth interface with the metal; the rapidity of the attack usually means that the substrate shows very few metallurgical changes. There is little or no internal attack, and a very thin depletion layer, if any. In the case of lead oxide melt the relatively low stability of lead oxide can result in actual metallic lead being present in the pit; but this is not, of course, observed in the case of vanadium or phosphorus. It does show, as might be expected, that the melt in the pit has a low oxygen activity. Giggins and Pettit<sup>(24)</sup> suggest that this pit morphology, which they report for the corrosion of CoCrAlY coating alloys by  $\text{Na}_2\text{SO}_4$  in the presence of  $\text{SO}_3$ , is a characteristic of acid attack.

To summarize: molten salt-induced attack may require the initially formed oxide to be penetrated. This penetration can be achieved mechanically or by the participation of other species such as sodium chloride. Coarse second-phase particles may provide points of weakness in the scale which lead to local failure. Local cell action may be significant, and local inhomogeneities (particularly, for example, coarse refractory metal carbides in the alloy) may allow the scale to be penetrated by solution in the salt. In some cases, the protective scale may actually be dissolved generally (fluxed) by the salt. Following this initiation stage, the corrosion proceeds rapidly. A key aspect of the reaction is the nature of the alloy element species which is thermodynamically stable in the salt. One model suggests that if the oxide is stable, the metal will not be attacked since a stable protective oxide can develop on the metal surface. However, if an anionic or cationic species is stable, attack may be rapid, provided a process exists to prevent the salt becoming saturated in the species. A related view discusses the oxide solubility in the salt as a function of acidity and suggests that rapid attack depends on the solubility falling from the metal interface to the atmosphere interface, thus allowing the precipitation of the oxide in the outer layer of the salt and preventing the establishment of a protective layer.

Another view regards the important step, for sulfate melts, to be the penetration of the salt into a low-oxygen activity region near the metal, allowing the development of a sulfidation-oxidation attack.

On the basis of all of these differing views, there appear to be two quite different factors. The first relates to the melting point of the salt, which is also connected with the stability of the low melting point phase. It may be that the viscosity of the melt and its surface tension are also important. The second is the acidity of the salt, which for sulfate melts is related to the local  $\text{SO}_3$  activity, which can be identified with the  $\text{SO}_3$  partial pressure,  $P_{\text{SO}_3}$ . It is important to remember that usually the most important factor is the acidity at the oxide/salt or metal/salt interface, and this may be different to the value at the atmosphere/salt interface which will be determined by the  $\text{SO}_3$  partial pressure in the atmosphere at the interface. It should also be remembered that, unlike dilute aqueous solutions, the neutrality condition in terms of a value of  $P_{\text{SO}_3}$  will not be independent of the other species in the salt.

Both acid and basic deviations from neutrality can result in accelerated attack. There is some reason to believe that acid deviations are more common, but basic fluxing processes are known to exist and will certainly be of major importance in specific situations. A process may be initiated by a basic fluxing (dissolving a protective  $\text{Al}_2\text{O}_3$  scale), and then the salt may react with molybdenum in the alloy to become acid so the propagation stage is an acidic fluxing process.

There may be morphological differences which will help in distinguishing acid fluxing, basic fluxing, and sulfidation-oxidation corrosion; but in many practical cases the complexity of the situation makes the distinction difficult.

#### Some Practical Examples of High-Temperature Corrosion in Energy Systems

(1) Superheater corrosion in coal-fired boilers. As described earlier, there has been a great deal of study of this problem. An excellent summary of the early work is contained in the proceedings of the Marchwood conference<sup>(25)</sup>; the American work from the same period is described by Reid<sup>(11)</sup>. Following the studies described in these two sources, which extend up to about 1965, the effort has diminished because there was a recession in maximum steam temperature and a number of practical solutions were developed. In the United States the problem has been relatively less severe, because the coals burned by the utilities have not been very corrosive. This situation may change as a result of three developments: first, the increasing economic pressure to burn less acceptable coals; second, the pressure for utilities to burn refuse-derived fuel; and third, the deliberate

addition of sodium sulfate to the coal to improve the performance of hot-side precipitators. There has been some talk of improving steam conditions again, and this too would increase the severity of the problem.

It seems likely that the low melting point of the corrosive salt is produced by a relatively high local  $\text{SO}_3$  partial pressure near the metal, and the participation of iron in forming a complex melt. Other elements may well be involved in specific situations. The high local  $\text{SO}_3$  is probably produced as a result of the presence of a thick outer ash deposit, the outer surface of which may be close to the gas temperature. In this region, sulfate species may dissociate, and the  $\text{SO}_3$  released migrate towards the inner regions of the deposit. As a result, the corrosion will be related to the tendency to form thick ash deposits and to the gas temperature near the superheater as well as the metal temperature.

The corrosion itself is probably an acid fluxing process. The local  $\text{SO}_3$  partial pressures are clearly again of importance, and other acid species in the ash ( $\text{As}_2\text{O}_3$ ,  $\text{P}_2\text{O}_5$ , etc.) may also be important. The actual range of temperatures over which the reaction is important in a boiler may well be somewhat different from those reported in the literature which are based largely on laboratory studies.

Methods of reducing the corrosion include careful selection or blending of coals to avoid low melting point ashes or ashes high in the alkali metals; the use of additives, particularly lime; and moving the hotter components back along the gas path to reduce the temperature difference between the metal surface and the gas. Screens designed to catch the ash before it reaches the superheater have been used; bandages of corrosion-resistant alloys wrapped fairly loosely around parts of the tubes at risk have also been very effective. In severe cases, coextruded tubes with a corrosion-resistant outer layer (type 310 SS or Ni-50%Cr) over a strong inner layer have been used with great success.

(2) Water-wall corrosion in coal-fired boilers. Commonly, slag deposits form on the water walls in coal-fired boilers. In some cases, the combustion pattern may be such that in the vicinity of the walls the conditions are "reducing" (low oxygen partial pressure). The slag deposit may then include unoxidized pyrite ( $\text{FeS}_2$ ) from the coal ash, and uncombusted carbon particles. Under these circumstances, there may be very rapid wastage of the water-wall tubes, even though the metal temperature may be as low as  $400^\circ\text{C}$  or so. English authors suggest that chlorine in some form is essential for this type of attack<sup>(26)</sup>, with iron chloride being formed at the metal surface: it is said that the corrosion is

not encountered with coals containing less than 0.3% Cl. However, U.S. experience is that water-wall corrosion is encountered with low chlorine coals, and authors suggest that liquid alkali iron trisulfates, alkali pyrosulfates, or simply reducing conditions leading to direct sulfidation of the iron are important.

Methods of solution include: improving the combustion in the furnace to prevent the development of reducing zones at the walls; bleeding air through the walls; and the application of coatings in affected areas. The commercial coatings are usually plasma sprayed in situ, and may have several layers.

(3) Superheater corrosion in oil-fired boilers. The ash deposits are typically much thinner in oil-fired boilers, but may contain significant amounts of vanadium oxides, leading to severe corrosion. Again, moving the superheater surface back along the gas path and the use of coextruded tubes are solutions. Additives, particularly magnesium oxide, are beneficial. Reducing the excess air to the lowest value consistent with efficient combustion helps a great deal in limiting the corrosion. This can be done with oil, but not with pulverized coal.

(4) Hot corrosion in aircraft gas turbines. The temperature range over which this is important has been a subject for considerable debate. The majority view is that it is seldom observed below 750°C (perhaps 800°C) and seldom above 950°C. The range appears to depend on the alloy composition. The lower temperature is often regarded as the melting point of the deposit (essentially  $\text{Na}_2\text{SO}_4$  with the melting point reduced by  $\text{MgSO}_4$  and  $\text{CaSO}_4$ , which should have little effect on the chemistry). The higher temperature is often interpreted as the dew point of the salt: above this temperature the salt is in the vapor phase and molten deposits are not stable. Increasing the chromium content in an alloy increases its resistance to hot corrosion: in general, nickel-base alloys with more than approximately 14% chromium are resistant. Above a certain limit, molybdenum appears to be harmful. For lower chromium alloys, the critical concentration is about 4% Mo; higher chromium alloys can tolerate rather more molybdenum. The response of an alloy depends critically on the physical distribution of the molybdenum-rich phases: if they are fine and uniformly dispersed, the alloy may have excellent resistance. If they are present as coarse carbides, for example, corrosion may be severe. Other elements have less well-defined effects. It has sometimes been suggested that niobium may be harmful, but it is generally agreed that tantalum and tungsten have little effect. In purely chemical terms, this is difficult to explain. As a result, the more corrosion-resistant alloys now replace part of the molybdenum with other refractory metals,

to retain the solid solution strengthening. The other strengthening mechanism in nickel-base superalloys is the precipitation of gamma prime,  $Ni_3(Al, Ti)$ . The Al:Ti ratio is varied to alter the interface coherency and the precipitate shape. It has been suggested that this ratio has an effect on hot corrosion resistance, with high titanium reducing the corrosion resistance. The evidence for this seems fragile, and it is probably a second-order effect at best.

If a nickel-base superalloy contains more than 5 wt% Al, it will usually form an  $Al_2O_3$  scale rather than  $Cr_2O_3$  at elevated temperatures. This greatly improves the high-temperature oxidation resistance, but it appears to have virtually no effect on the hot-corrosion resistance: the hot corrosion correlates with chromium content irrespective of the oxide formed.

The hot components are normally protected with a coating. The simplest is an aluminum diffusion coating, with the outer layer being NiAl or CoAl. In more recent coatings, platinum or rhodium is added. These coatings are principally for oxidation resistance. An alternative approach is to use an overlay coating, usually applied by physical vapor deposition from a pool melted by an electron beam (EB-PVD). Low pressure (or vacuum) plasma spray is another method which appears to have much promise. For aircraft engines, the most common coatings are the "MCoCrAlY" series, where M is usually cobalt, but may be a mixture of cobalt and nickel. Usually, these coatings contain 10 wt% Cr, and 14 wt% Al or so, with 0.5-1.0% Y. More recently, small amounts of hafnium have been added as well. These coatings confer adequate resistance to hot corrosion in aircraft engines.

(5) Hot corrosion in marine or industrial gas turbines. A different form of corrosion was encountered in aircraft gas turbines modified for marine service. These engines customarily run at rather lower temperatures than the aircraft engines from which they are derived, and may at times see rather higher salt loadings. The MCoCrAlY coatings which had been so effective in aircraft use were sometimes very severely corroded in the marine engines, with the deep hemispherical pits with the smooth metal surfaces referred to above as typical of acid corrosion. It appeared that this form of attack was most severe at a little over 700°C, and was probably confined to a very narrow temperature range. The nickel-based superalloy beneath the coating appeared to be much more resistant than the coating itself. In the laboratory, duplication of the attack required the furnace atmosphere to contain significant amounts of sulfur oxides, and analysis of the deposits suggests that a low melting point phase involving cobalt sulfate as well as the alkali sulfate is formed. Nickel sulfate does not appear

to act in the same way. The parallels with the superheater corrosion mechanism described above are obvious.

The cobalt sulfate model is not universally accepted. Some sources consider that chlorine may play a role; that the presence of potassium may be important; and that uncombusted carbon incorporation in the deposit may also be a factor. However, while the simultaneous contributions of other factors cannot be ruled out, there seems little doubt that the major effect is the formation of an acidic sulfate melt containing transition elements (Co, Fe and perhaps Ni). The thermodynamics of these melts have been analyzed by Misra, et al.<sup>(27)</sup>

The method of solution is to modify the coating composition. The major single effect is the chromium content, but there is some indication that simultaneously reducing the aluminum content may help. However, an alloy such as Co-25Cr-5Al-1Y may have unacceptable resistance at the higher temperatures. Several programs are currently in progress to optimize coating compositions for the best compromise between the resistance at the two temperatures.

(6) Corrosion of in-bed superheaters in fluidized bed combustion. Because the combustion temperature in a fluidized bed combustor (fbc) is so low (the bed is usually 850-900°C), it seemed improbable that conditions could be satisfied for the formation of the low-melting alkali sulfate containing phases. However, it was shown by Cooke, et al.<sup>(28)</sup> that extensive low oxygen activity regions were present in the bed, and this observation has now been confirmed by several investigators. The bed contains considerable amounts of calcium sulfate, and it was pointed out<sup>(29)</sup> that in a low oxygen activity it would be possible for a CaO/CaSO<sub>4</sub> mixture to develop a sulfur activity high enough to produce a sulfidation/oxidation corrosion by the "mixed oxidant" method, without there being any necessity for the formation of a molten phase at all. Subsequent laboratory experiments<sup>(30)</sup> confirmed the essential features of this mechanism, and several studies in fluidized bed combustion<sup>(31)</sup> have shown that this form of attack can, indeed, take place.

It is possible that the mixing conditions within the bed could be modified to minimize the risk of the corrosion, but work on this approach has scarcely started. At the moment, designers are relying on a careful choice of materials: the 18-10 type stainless steels such Type 304 and Type 347 appear to have good resistance; nickel-base alloys should be avoided. Claddings would be a possible route: the alloy GE 2541 (Fe-25Cr-4Al-1Y) has exhibited exceptional resistance, but such an expensive approach may not be necessary.

(7) Corrosion in coal-gasification systems. Detailed analysis of coal-gasification systems suggests that relatively few uncooled metal components will be exposed to the gas stream. The overall situation has been summarized by Holmes and Stringer<sup>(10)</sup>. The most demanding problems are posed by the gas cooler heat exchanger which will certainly be required for systems using entrained gasifiers and perhaps also by other systems. Chemically, the situation may not be all that different from the water-wall corrosion problem discussed above. As yet, there is very little practical experience; laboratory experiments are currently being conducted by Perkins<sup>(32)</sup>.

### Summary

High-temperature corrosion is a serious problem in heat engines, and in a number of cases limits the maximum temperature (and hence the efficiency) of the system. It is possible to distinguish two areas: mixed oxidant corrosion and molten salt induced corrosion. Mixed oxidant corrosion is damaging because the oxidants other than oxygen may, by reacting with the protective oxide forming alloy elements, eventually destroy the alloy's ability to regenerate its protective scale. Molten salt corrosion can involve two stages: an incubation period during which reaction is slow, followed by a relatively rapid propagation stage. Again, the transition is probably associated with the destruction of an initially protective oxide scale. This destruction may be mechanically induced, or it may result from the dissolution of the oxide by the salt. So far as the salt-induced part of the reaction is concerned, the two factors are the stabilization of a low melting point phase, and the "acidity" of this phase. These two aspects are separate, although not necessarily independent. For a sulfate melt, the local  $SO_3$  partial pressure is a major factor.

Methods of dealing with the problems of high-temperature corrosion include changes in design, changes in the combustion pattern, fuel treatment, combustion air treatment, careful materials selection, and coatings of various kinds. Careful analysis of particular systems is required to determine the most effective solution.

## References

1. P. L. Hemmings and R. A. Perkins, "Thermodynamic Phase Stability Diagrams for the Analysis of Corrosion Reactions in Coal Gasification Combustion Atmospheres," EPRI Report FP-539 (1979).
2. R. A. Rapp, Proc. Workshop on Materials Problems and Research Opportunities in Coal Conversion, Vol. II (Ohio State University, Columbus, Ohio, April 1974) 313.
3. J. Stringer and D. P. Whittle, Rev. int. Htes. Temp. et Refract., 14 (1977) 6; Proc. First Petten Colloquium on Advanced High Temperature Materials: Technological and Industrial Aspects (Joint Res. Centre, Comm. Euro. Commun., Petten, The Netherlands, Jan. 1976).
4. A. Rahmel, Corr. Sci. 13 (1973) 125.
5. J. Stringer in "Behavior of High Temperature Alloys in Aggressive Environments," I. Kirman, J. B. Marriott, M. Merz, P. R. Sahm and D. P. Whittle (eds.) (The Metals Society, London, England, 1980) 739.
6. C. Giggins and F. S. Pettit, Oxidation of Metals 14 (1980) 739.
7. M. E. El-Dahshan, D. P. Whittle and J. Stringer, Oxidation of Metals 8 (1974) 179; 211.
8. J. Stringer, P. S. Corkish and D. P. Whittle in "Stress Effects and the Oxidation of Metals" ed. J. V. Cathcart (Met. Soc AIME, New York, 1975) 75.
9. M. R. Wootton and N. Birks, Corrosion Science 12 (1972) 829.
10. D. R. Holmes and J. Stringer in "Materials to Supply the Energy Demand" ed. E. B. Hawbolt and A. Mitchell (ASM, Metals Park, Ohio, 1981) 165.
11. W. T. Reid, "External Corrosion and Deposits: Boilers and Gas Turbines" (Elsevier, New York, U.S.A., 1971).
12. N. S. Bornstein and M. A. DeCrescente, Trans. AIME, 245 (1969) 1947; Met. Trans., 2 (1971) 1971.
13. J. A. Goebel and F. S. Pettit, Met. Trans., 1 (1970) 1943, 3421; J. A. Goebel, F. S. Pettit and G. W. Goward, Met. Trans., 4 (1975) 261.
14. F. S. Pettit, J. A. Goebel and G. W. Goward, Corrosion Science 9 (1969) 903.
15. R. A. Rapp and K. S. Goto, in Proc. Symp. on Corrosion in Fused Salts (Electrochemical Soc., Princeton, N.J., 1979).
16. See, for example, a review of the available information in J. Stringer, Ann. Rev. Mater. Scie., 7 (1977) 477.
17. D. M. Johnson, D. P. Whittle and J. Stringer, Corrosion Science 15 (1975) 649.
18. F. S. Pettit, personal communication.
19. J. Stringer, D. P. Whittle and R. K. Hughes, Corrosion Science 17 (1977) 529.



20. P. Hancock, personal communication.
21. R. C. Hurst, J. B. Johnson, M. Davies and P. Hancock, in "Deposition and Corrosion in Gas Turbines" ed. A. B. Hart and A. J. B. Cutler (Applied Science Publishers, London, 1973) 143.
22. C. Spengler and R. Viswanathan, *Met. Trans.*, 3 (1972) 161; see also ref. 7.
23. A. S. Radcliff and J. Stringer, *Corrosion Science* 14 (1974) 483.
24. C. S. Giggins and F. S. Pettit, Final Report to AFOSR on Contract F44620-76-C-0123, Report No. FR-11545 (June 1979).
25. L. M. Wyatt and G. J. Evans (eds.) "The Mechanism of Corrosion by Fuel Impurities" (Butterworth's, London, England, 1963).
26. See, for example, A. J. B. Cutler, T. Flatley and K. A. Hay, CEGB Research (October 1978) 13.
27. A. K. Misra, D. P. Whittle and W. L. Worrell, *J. Electrochem. Soc.* (in press).
28. M. J. Cooke, A. J. B. Cutler and E. Raask, *J. Inst. Fuel* 45 (1972) 153.
29. J. Stringer and S. Ehrlich, ASME Paper No. 76-WA/ED-4 (1976).
30. J. Stringer and D. P. Whittle, Proc. Intl. VGB Conf. on Corrosion and Deposition in Power Plants, Essen, Germany (June 1977).
31. EPRI Reports on various projects concerned with corrosion in fluidized beds: Report numbers CS 1449 (May 1980), CS 1475 (August 1980), CS 1935 (July 1981), and CS 2118 (November 1981).
32. R. A. Perkins, work in progress on EPRI Contract RP2048.

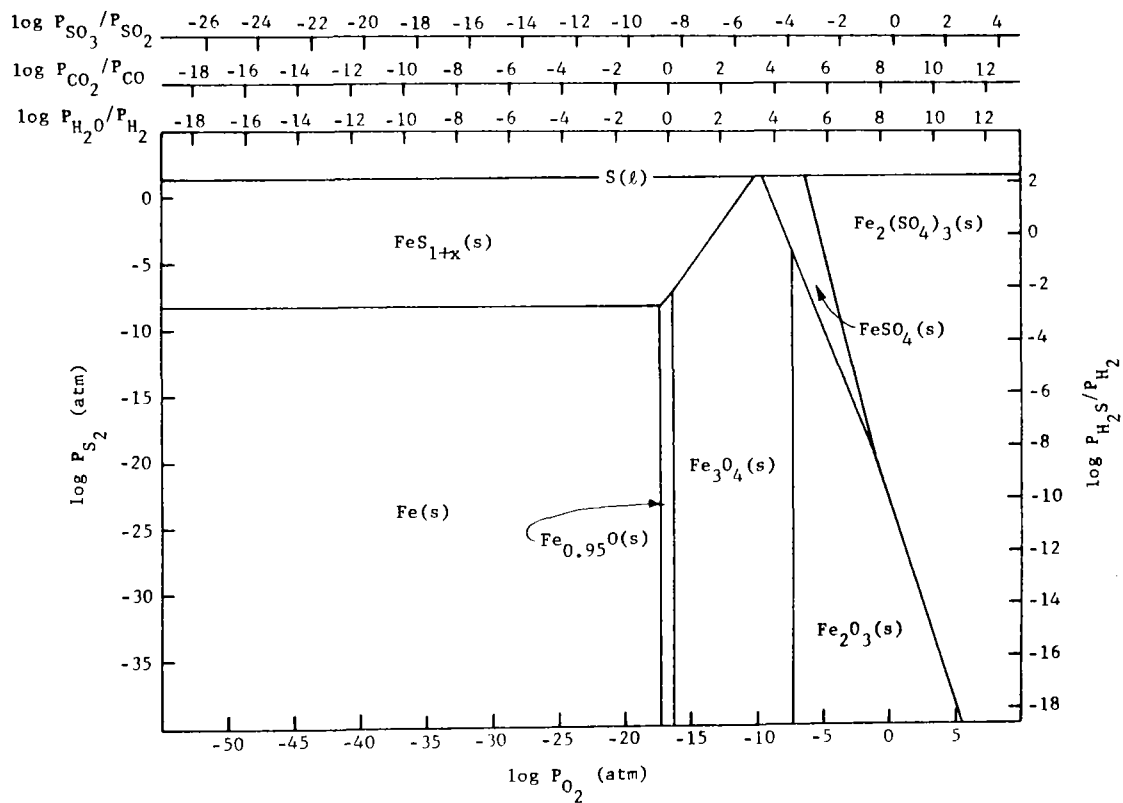


Figure 1. The Fe-S-O stability diagram at 871°C. From Hemmings and Perkins<sup>(11)</sup>.

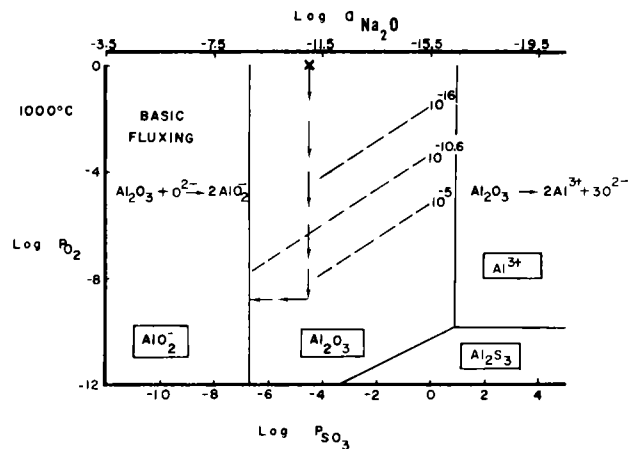


Figure 2. Stability diagram showing the phases of aluminum that are stable in  $\text{Na}_2\text{SO}_4$  at  $1000^\circ\text{C}$ . The arrows show how the composition of  $\text{Na}_2\text{SO}_4$  can change because of removal of oxygen and sulphur. The broken lines are sulphur isobars and the isobar of  $10^{-10.6}$  is the sulphur pressure required to form aluminum sulphide beneath an  $\text{Al}_2\text{O}_3$  scale on a Ni-31 wt.%Al alloy. This diagram shows that  $\text{Al}_2\text{O}_3$  is stable in  $\text{Na}_2\text{SO}_4$  for certain compositions, and that  $\text{Al}_2\text{O}_3$  reacts with  $\text{Na}_2\text{SO}_4$  which has either high or low activities of  $\text{Na}_2\text{O}$  (after Goebel et al<sup>13</sup>).

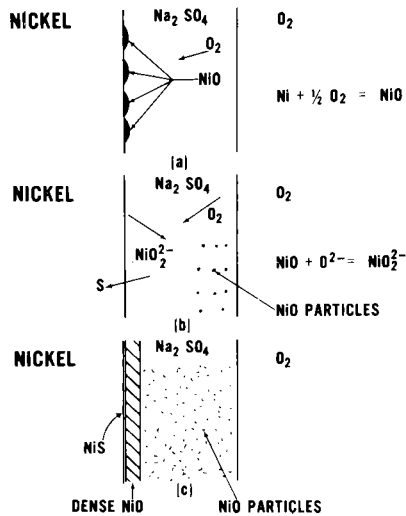


Figure 3. A model proposed by Pettit et al.<sup>14</sup> for the hot corrosion of nickel by sodium sulphate. Initially, the metal oxidises to form a layer of NiO, liberating sulphur. This diffuses through the oxide to form nickel sulphide. Continuing sulphidation produces an increase in oxygen ion activity in the salt adjacent to the oxide surface, eventually allowing solution of the oxide as nickelate ions (basic fluxing). Towards the salt/atmosphere interface the oxygen ion activity falls and the ions are reduced to form a loose non-continuous oxide. Eventually, however, the reaction achieves a steady state in which a continuous oxide layer again develops by transport of oxygen through the salt.

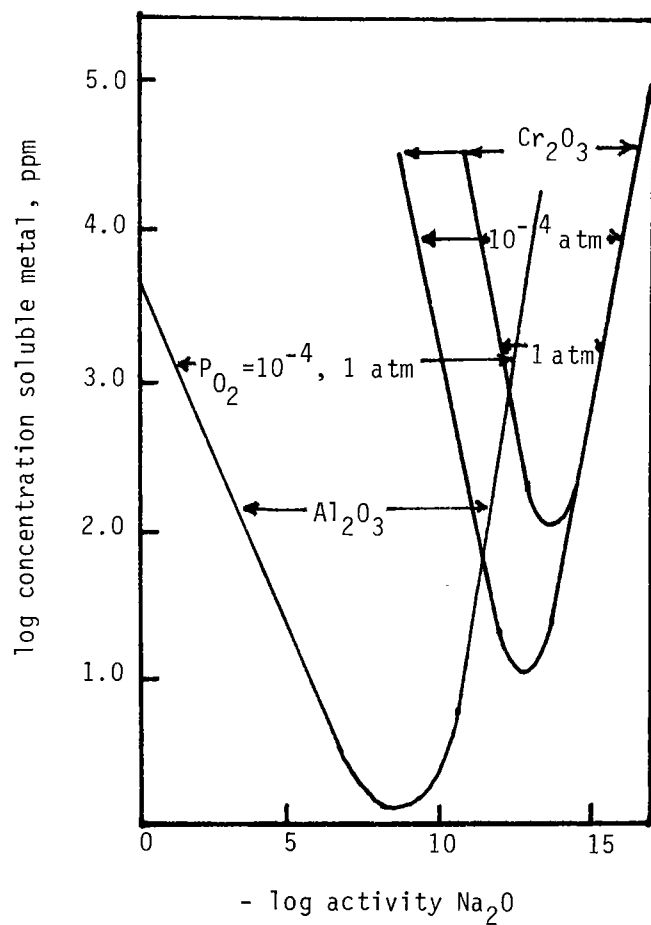


Figure 4. Solubilities of Al<sub>2</sub>O<sub>3</sub> and Cr<sub>2</sub>O<sub>3</sub> in molten Na<sub>2</sub>SO<sub>4</sub> at 1200 K (from Rapp and Goto<sup>(15)</sup>). Basic dissolution occurs to the left of the minima in the curves, acidic dissolution to the right.

MATERIALS CONSTRAINTS FROM THE EROSION-CORROSION  
POTENTIAL OF ALTERNATIVE FUEL SOURCES

I. G. Wright  
W. R. Pierson  
Battelle, Columbus Laboratories

Paper presented at the Second Conference on Advanced  
Materials for Alternative-Fuel-Capable Heat Engines, Monterey, California,  
August 24-28, 1981.

BATTELLE  
Columbus Laboratories  
505 King Avenue  
Columbus, Ohio 43201

## Section 1

### INTRODUCTION

The design or modification of heat engines to operate on alternative fuels requires some definition of the types and seriousness of the problems expected to be encountered by the critical components from handling and combusting the fuels. In the first instance, alternative fuels will be made to meet existing fuel standards for a given duty, which provide some limitations on, for instance, properties such as viscosity and boiling point, and on impurity contents such as sulfur, alkali metal, and ash levels. A cursory examination of the fuel types likely to be derived from the processing of coal suggests that the ranges of impurity types, and the forms of the contained solids, may be considerably different from those regulated by current fuel specifications. In some cases this will necessitate a redefinition of tolerable limits of ash, for instance, and an examination of the effects of impurities for which there is no established experience.

As an aid to developing a strategy to address these needs, an attempt has been made in this paper to examine the types of processes utilizing coal which may provide fuel for gas turbine engines, and to define the duties and therefore the specific environments likely to be encountered by hot gas-path components. The results of actual turbine tests or related laboratory studies under conditions simulating aspects of specific alternative fuel usage have also been considered, with a view to finding common problems and solutions.

Section 2  
ALTERNATIVE FUEL CAPABLE ENERGY CONVERSION  
SYSTEMS EMPLOYING OPEN CYCLE GAS TURBINES

The energy conversion systems discussed in this paper have been limited to those utilizing coal as the energy source and heat engines have been limited to the open cycle gas turbine. Since advanced materials constraints from the erosion/corrosion potential of alternative fuel sources is the topic of this paper, these limitations are appropriate.

The coal utilization systems of interest are those pressurized systems that convert coal to the more usable forms of synthetic gaseous and liquid fuels. The timely implementation of coal utilization and conversion is of great importance in the reduction of the import rate of gaseous and liquid fuels. The term "coal utilization" will be hereafter used to include both "direct utilization" to convert coal to useful energy or to "more usable forms of gaseous and liquid fuels".

In order to identify the role of the open cycle gas turbine in coal utilization systems, over 30 processes were considered. These processes converted coal (chemical energy) to flue gas (stored energy) or to synthetic gaseous or liquid fuels (chemical energy). After "dirty coal" has been converted to other forms of chemical stored energy, there are at least 33 processes available to produce exportable energy in the form of high BTU gas, electric power, steam, hot water, etc. The processes of particular interest were extracted and presented in Figure 2-1. The lines and arrows indicate the direction of the process. The final energy utilization processes are not shown since they are generally familiar.

Utilization of the open cycle gas turbine (OCGT) is shown in Figure 2-1. Each system was categorized by driving fluid and assigned an arbitrary type number. Table 2-1 lists the seven gas turbine systems by type numbers and notes driving fluid and exhaust gas utilization, and identifies the system as open (OCGT) or closed cycle (CCGT). Closed cycle systems, Types V, VI, and VII, associated with "atmospheric combustion", are not included in this paper due to the considerably lower potential for erosion/corrosion.



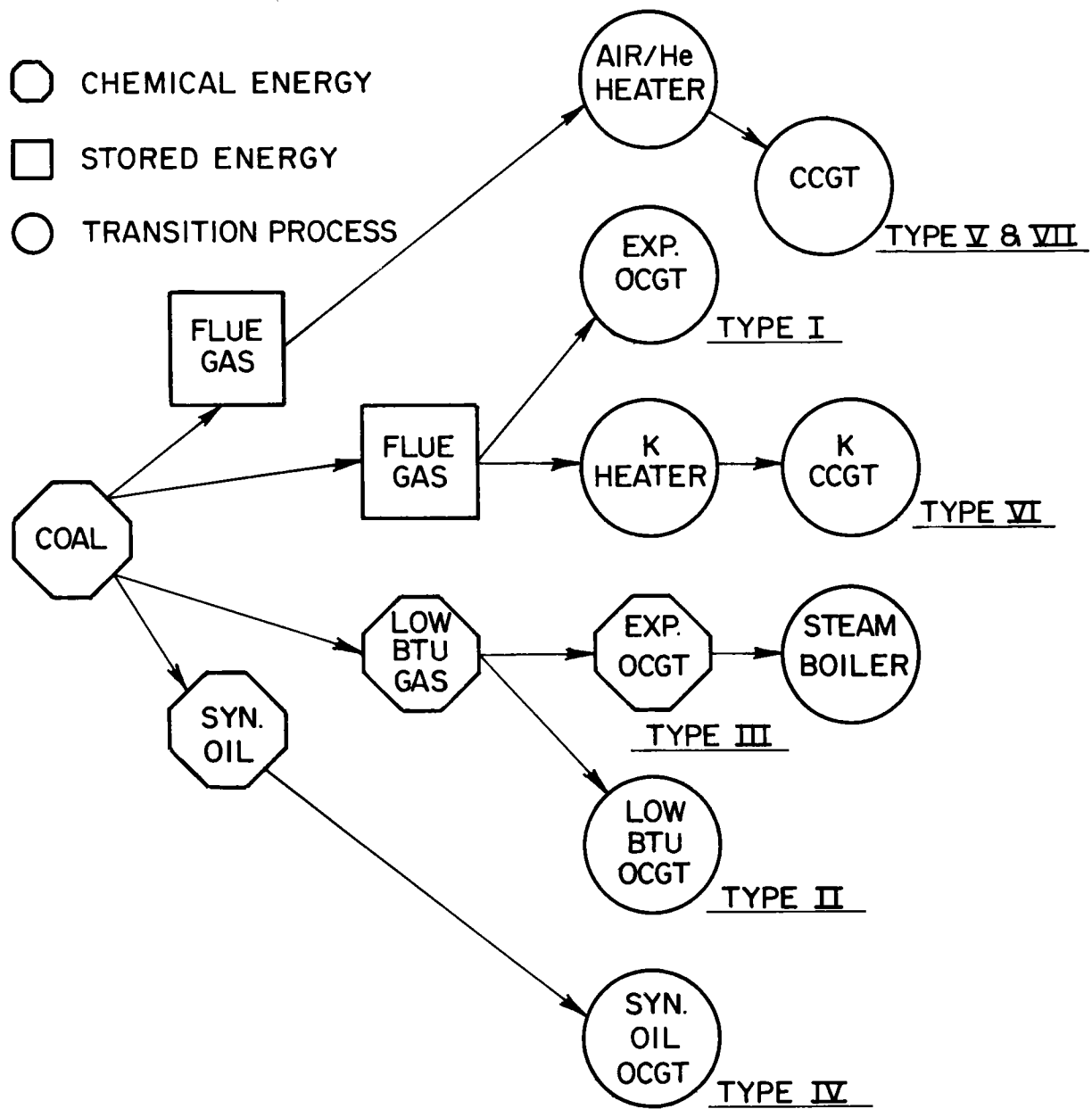


Figure 2-1. Coal Utilization Systems

Table 2-1

## GAS TURBINE SYSTEM CATEGORIES

Type No.	Driving Fluid	Cycle	Exhaust Gas Utilization
I	Flue Gas	O	WHB/ECON
II	Low Btu Gas	O	WHB
III	Uncombusted LBG	O	SB
IV	CDL	O	WHB
V	He	C	OBC
VI	K	C	SBC
VII	Air	C	WH

In regard to turbine nomenclature, there has been a trend to label the turbine an "expansion turbine", if no combustion takes place immediately upstream of the first stage, and to label it a "power generation" turbine if combustion does occur and the turbine drives an electrical generator. Regardless of the end use of the shaft power generated, or where the combustion occurs, all open cycle gas turbines being developed for use in a pressurized coal utilization system have common materials problems in regard to hot gas path components. An examination of the factors which influence erosion/corrosion indicate these factors to be influenced by the specific coal utilization process (as noted in the following sections) and not a function of the end use of the shaft power generated.

Examples of shaft power utilization, considering all seven types of gas turbine systems, includes electric generator drive, air compressor drive, and process gas compressor drive, in that order of importance.

In consideration of materials constraints based on erosion/corrosion potential of alternate fuel sources, it is useful to review the four types of coal utilization systems which employ open cycle gas turbines and to note their similarities and differences. Systems types I through IV, which generate shaft power through the use of open cycle gas turbines, are described.

## TYPE I - EXPANSION OF NONCOMBUSTIBLE FLUE GAS

Type I systems are characterized by expansion of a dirty, oxidizing flue gas through a gas turbine to produce shaft power. Examples of flue gas sources are as follows:

- Flue gas from a pressurized fluidized bed combustor
- Flue gas from the COGAS Gasifier Combustor
- Flue gas from the fluidized bed burner side of the Agglomerating Burner Gasification process
- Flue gas from the regenerator side of the CO<sub>2</sub> Acceptor High Btu Coal Gasification Process
- Flue gas from the IGT Steam-Iron Coal Gasification process

Examples of Type I pressurized coal utilization systems currently under active development are the DOE/Curtiss Wright PFBC Combined Cycle Power Generation System and the AEP/Stal-Laval PFBC Combined Cycle demonstration plant.

## TYPE II - COMBUSTION OF LOW/MEDIUM BTU COMBUSTIBLE GAS

Type II systems are characterized by combustion of a relatively clean synthetic gas in a gas turbine combustor in the conventional manner to produce shaft power. The generic gasifier types which produce low or medium BTU gas are listed in Table 2-2.

Table 2-2

### GENERIC TYPES OF LOW/MEDIUM BTU GASIFIERS

<u>Category</u>	<u>Examples</u>	<u>Sponsors/Operators</u>
Fixed bed	STEAG/Lurgi	STEAG AG (W. Germany)
Entrained Bed	SOCE/Texaco	SOCE/Texaco/EPRI/GE
Fluidized Bed	Westinghouse Fluidized Bed Gasification Process	DOE/Westinghouse
Molten-Salt	RI/AI/Molten-Salt	DOE/RI

Examples of Type II systems currently under active operation or construction include the Dow Chemical-Westinghouse/Texaco unit in operation and the SOCE/Texaco unit under construction. A third unit, the DOE/Conoco BGC/Lurgi Slagger Combined Cycle (CO<sub>2</sub>Blown) is currently under consideration.

#### TYPE III - EXPANSION OF UNCOMBUSTED LOW-BTU GAS

Type III systems are characterized by the expansion of dirty nonoxidizing gas, without prior combustion, through an open cycle gas turbine to produce shaft power. The sources of such gas are the same as Type II. The gas leaving the turbine is then burned in a boiler or in a Type II gas turbine, depending on the pressure level at the Type III turbine discharge. The purpose of the Type III turbine is to recover shaft power from a combustible gas stream when a suitable pressure ratio is available and when the turbine discharge pressure is sufficient for the remaining functions.

An example of Type III is one version of the Texaco Entrained Bed system in which the high pressure, medium BTU gas stream, is expanded through a gas turbine to recover power to drive air or oxygen compressors. This application was described in Reference 29 and is not currently under development. Other examples of Type III are the expansion of off-gas streams from catalytic cracking units in the petrochemical industry and from blast furnaces in the steel industry.

#### TYPE IV - COMBUSTION OF COAL DERIVED LIQUID FUELS

Type IV systems are characterized by the combustion of coal-derived liquid (CDL) fuels in an open cycle gas turbine combustor in the conventional manner. While CDL fuels have been burned in experimental burners under laboratory conditions, there are no known examples of full scale gas turbines having operated on CDL fuels.

Section 3  
SPECIFIC ENVIRONMENTS ASSOCIATED  
WITH ALTERNATIVE FUEL SOURCES

Consideration of the actual environments to be encountered by the hot gas path components of open-cycle gas turbines fired by the various possible alternative fuel sources suggests that basically three different sets of conditions will prevail. These are:

- Expansion of a dirty, oxidizing gas, such as that from a fluidized-bed combustor (Type I)
- Expansion of a dirty nonoxidizing gas (low  $PO_2$ , possibly high  $PS_2$ ), such as that from a gasification process (Type III)
- Combustion of a relatively clean gas, or liquid, such as those derived from gasification or liquefaction processes (Types II and IV)

The extent to which existing turbine technology can be used with, perhaps, minor modifications in mechanical design or materials deployment, will be determined by the concentration and types of solids and reactive species in the fuel, and the combustion characteristics of the fuel.

#### EXPANSION OF PFBC FLUE GAS (TYPE I)

##### Static Cascade Tests

A number of test runs have been made using static cascades in the off-gas stream from small, coal-fired pfbc's. These have generally indicated some deposition of ash, but erosion damage has been very variable. Early work using the BCURA 3 ft x 2 ft PFBC (1), operated at 4.5-5.0 atm (66-73 psig) with a bed temperature of 1650-1750°F, involved the exposure of a nozzle guide vane segment in the exhaust gas such that the gas velocity at the vanes was approximately Mach 0.6. The cascade temperature was 1600°F or 1650-1700°F, when the bed temperature was 1650 or 1750°F, respectively. The gas was passed through two stages of 12-in-diameter cyclones before entering the cascade, and the resulting dust loading at the cascade was about 250 ppm. Typically, the dust was 95 percent less than 10  $\mu$ m. The alloy tested as vanes was aluminized X-40 (cobalt-base), while rods of Nimonic 75 and EPK-55 were exposed downstream of the vanes.

A total of 204 hours of exposure was accumulated in four tests. No significant deposition took place at a bed temperature of 1650°F, but at 1750°F the deposits were sufficient to be a potential source of operating problems. However, a 'soft-blast' cleaning with fruit stones removed most of the deposits. No enrichment of alkali was found in the deposits, which were essentially the same composition as the dust which passed over the cascade. Slight accumulation of dust occurred on the leading edges of the rods.

Very little attack attributable to erosion was observed. However, significant hot corrosion attack occurred on the Nimonic 75 alloy (204 hours + 600 hours of previous exposure at a bed temperature of 1450°F), while EPK-55 (exposed for 204 hours) showed a form of attack considered to be a precursor to hot corrosion. The X-40 alloy was very severely attacked along the carbide network, also suggesting the imminent onset of typical hot corrosion. Measurements upstream of the cascade indicated that the sodium level ranged from 1.5 to 5.2 ppm, and the potassium level from 1.2 to 2.7 ppm, and also that more than 87 percent of the alkali was contained in the solids.

A series of reaction and impulse airfoil specimens were exposed for a total of 1000 hours in the exhaust stream from the Exxon Miniplant PFBC (2), which was run at 8.7-9.1 atm (113-119 psig), with a bed temperature of 1700-1750°F. Three cyclones were employed before the cascade section, and the gas entered the test section at 5.0 atm and 1550-1570°F (augmented by burning methane), at a velocity of about 800 feet per second. Corrosion, erosion and deposition occurred, the first two to different extents on a given alloy specimen. A dense, adherent, apparently stratified deposit of essentially  $\text{CaSO}_4$ , and fly ash (silicates and alumino silicates) formed on the leading edges and pressure surfaces, and attained a thickness of about 0.01 in. The deposit was thought to be amenable to nut shelling. Quite severe erosion-corrosion of IN-738, U-700 and FSX-414 occurred, especially on the leading edges, but coatings or cladding of FeCrAlY and CoCrAlY showed considerably less attack. The nominal dust loading was 65 ppm (0.034 gr/SCF), with 3-5 percent of the particles greater than 10  $\mu\text{m}$ . However during short periods of upset operations, the particle loading increased to 860 ppm (0.46 gr/SCF) at the same particle size, and the particle size distribution shifted to 10 percent greater than 10  $\mu\text{m}$ , with 2 percent greater than 25  $\mu\text{m}$ .

A similar set of test specimens was exposed in a recent 1000-hour test in the CURL PFBC (4). This bed was operated at 1560-1585°F and 6 atm (73.5 psig) pressure. The use of three conventional cyclones in series and a skimmer resulted

in a consistent particle loading of about 250 ppm (0.13 gr/SCF) particles 99.2 percent < 10  $\mu\text{m}$  fed to the cascade section. The specimen temperatures were maintained at 1475°F, and 1350°F in the case of internally cooled specimens, and the gas velocity at the inlet was 1400 feet per second. Deposits formed on the airfoils were structurally and compositionally similar to those in the Exxon Miniplant. No effort was made to remove the deposits, and, in fact, the thickness was not significantly different after 1000 hours than at intermediate inspection times. This self-limiting feature was possibly the result of thermal cycling, or the system aerodynamics.

Some corrosion attack of IN-738 occurred, but it was much less severe than in the Exxon test. The CoCrAlY and FeCrAlY-clad specimens suffered only mild oxidation. Virtually no evidence of erosion (or erosion accelerated corrosion) was found in this test, not even on pin specimens located downstream of the fourth cascade where the leading edge velocity was about 1400 feet per second.

Concurrently with the test just discussed, another cascade rig was run on the CURL PFBC, using a portion of the bed exhaust gas (3). The gas cleaning system used here consisted of two cyclones and one high-efficiency cyclone in series. The test specimens consisted of three sections of a Stal Laval GT 120 first-stage turbine blades (U-500), two of which were PVD-coated with FeCrAlY and CoCrAlY, together with a number of specimens of U-500, IN-671 and Alloy 713C. The specimens' temperatures were 1418-1436°F, and the gas velocity over the blades was 755 feet per second (entering) and 1247 feet per second (leaving), while the other specimens experienced velocities in the range 590-1760 feet per second. The dust loading of the gas entering the cascade was maintained at around 100-120 ppm, with particles essentially smaller than 5  $\mu\text{m}$ , and an average particle size around 2  $\mu\text{m}$ . There was no measurable erosion damage observed on any of the specimens in this test. Neither were there any problems with build-up of deposits.

Some evidence of corrosion of U-500 blades to form subscale sulfides of variable extent attested to the corrosive potential of the environment. However, Alloy 713C formed a protective oxide scale, whereas IN-671 showed severe hot-corrosion attack, apparently associated with its tendency to loss of oxide scale by spallation under these conditions. Some surface damage on the coated specimens had apparently resulted from impact of metal oxide particles, which had exfoliated from upstream surfaces and became entrained in the gas stream.

## Turbine Tests

Although early attempts to coal-fire turbines generated voluminous and practically useful data, the fly ash in question is thought likely to have been more closely related to the sintered glassy spheres of standard pulverized-coal combustion fly ash than that from PFBC. Nevertheless, the experience is worthy of careful consideration.

No full-scale turbine tests have yet been run on PFBC off-gas. Some short tests have used small turbines or turbine-type rigs, and a considerable volume of data has been accumulated for turbines operated on blast-furnace gas, and from attempts to directly fire pulverized coal. In work by the Locomotive Development Committee of Bituminous Coal Research and later by the Bureau of Mines, major difficulties in separating the PC fly ash from the hot gas resulted in severe erosion of vanes and blades, and in fouling by heavy deposits, as extremes of behavior. Modifications were made to provide space for separation of ash after the first row of vanes by centrifuging to the outer side wall of the turbine, by minimizing radially-inward secondary gas flows, and by using wear inserts of TiC at the upstream base of the first five rows of vanes and blades. In this form the turbine ran for 878 hours, with an ash loading of 228 ppm (0.12 gr/SCF), with a particle size range of 2-20  $\mu\text{m}$ , until shutdown was caused by heavy fouling of the first-stage blades. No serious erosion of the blade roots or vane tips was observed, although some polishing of the blades in the last three rows, near the roots, had occurred. As expected from the design, however, the most heavily eroded areas were the blade tips and the bases of the vanes, in spite of the wear inserts (which showed no significant erosion). Little or no corrosion was found.

It was concluded that satisfactory turbine life could be obtained if the ash loading were reduced to 19 ppm (0.01 gr/SCF). Since some plugging of the multicyclone separator had occurred for a significant period during these tests, General Electric reassessed the results, and concluded that acceptable life (25,000 hours) could be achieved by reducing the dust loading (particles  $> 2 \mu\text{m}$ ) to 68 ppm (0.036 gr/SCF).

Similar experience was gained in the Australian Coal-Burning Gas Turbine Project. Initial experience of catastrophic erosion when firing Callide coal (lignite) without conscious attention to ash separation led to improvements through very fine grinding of the coal, and then incorporation of multicyclone separators (overall efficiency  $\sim 70$  percent). In runs with the cyclones, locations which had previously suffered erosion were covered with deposits. Comparison of the performance of the



high pressure turbine (1100 feet per second) components with those in the low pressure (800 feet per second) turbine suggested that the rate of erosion/corrosion at the lower velocity was sufficiently reduced to allow acceptable turbine life (> 10,000 hours). Corrosion was also a significant factor beneath deposits; Nimonic 80A was corroded, HS31 and C242 showed oxide scale spallation. Chromium plating provided good erosion protection, was not significantly corroded, but suffered cracking (thermal fatigue).

A redesigned turbine was run with better results in a 125-hour test using bituminous coal. This machine used three stages instead of two and a gas velocity of 800 feet per second, thickened trailing edges in the blades, mid-span fences on the vanes to minimize particulate concentration at the outer casing, and HS31 blades (coated and uncoated). The feed coal was finely pulverized, and the ash leaving the multi-cyclone separator had an average particle size of 4-7  $\mu\text{m}$ , and a maximum size of  $\sim 20 \mu\text{m}$ . The loading is unknown. The first and second stages of blades were eroded on the trailing edge on the pressure side. The vane fences successfully reduced erosion of the inner wall, and recessing the vane tips below the blade bases effectively reduced erosion at the blade roots. The chromized-coated and aluminized-coated blades apparently showed less attack than uncoated blades. Only slight deposition occurred on the leading edges on the vanes and blades. The overall effect of these design changes was a projected 50 percent reduction in erosion loss, leading to the conclusion that velocity, mean particle size, particle concentration, and materials selection can significantly affect the rates of erosion-corrosion. A trend to increasing erosion rates with increasing particle size was noted, but beyond a limiting size of about 7  $\mu\text{m}$ , the rate of increase of erosion was considerably reduced.

The NASA-Lewis Research Center ran tests with an integrally cast, 5.5-inch diameter, turbine rotor in the exhaust gas stream from a 15-inch average diameter (conical section) PFBC (5). The combustor was run at 65-68 psig, and the bed temperature (at the top) was approximately 1832°F. The exhaust gases passed through a single Aerodyne cyclone and then into the turbine, which was operated at 6 percent partial admission to maintain an inlet flow rate of  $\sim 984$  feet per second. These runs were made with different coal/sorbent combinations. These gave cyclone inlet and outlet particle loadings of 1900/600, 7300/2600, and 4100/2800 ppm, and the  $\text{SO}_2$  content of the gas streams was 218, 669 and 112 ppm, respectively. The corresponding rotor inlet gas temperatures and relative gas velocities were 1274°F/853 feet per second; 1436°F/1083 feet per second and 1436°F/1083 feet per second. Severe erosion was observed in all three tests,

which were run for 164, 13 and 12 hours, respectively. Metal loss occurred in a pattern which reflected stratification of the particles in the gas stream immediately before it entered the turbine section, and by the trajectories of the particles through the test section. Maximum loss occurred at the leading edge near the hub, over most of the pressure side, and on the suction side trailing edge near the tip. Deposition occurred at the lighter particle impact sites, near the leading edge on the pressure side, and extensively on the suction side. Some interaction of erosion with the corrosion behavior of the alloys used (IN-792 + Hf) and Alloy 713LC), occurred to produce typical oxide scales, which grew some 10 to 100 times more rapidly than in clean air. While damage may be much less in large turbines run at lower particle concentrations, these data suggest that care should be taken to avoid conditions of particle stratification even at low particle loadings.

Complete small turbines have actually been powered by PFBC's in two programs, conducted by Combustion Power Company (CPC), and by Curtiss-Wright. In the tests by CPC (6), a Ruston turbine similar to that used by the Australian Coal-Burning Gas Turbine Project was fed by a 7 ft diameter, 44 psig, 1470°F PFBC burning high-sulfur coal with selected sulfur sorbents. Almost 600 hours of operation were accumulated with various configurations of gas cleanup equipment, which comprised combinations of cyclones in series, together with inertial separation, and a granular-bed filter. Deposition of ash especially on the first-stage vanes, and erosion were major problems, and stemmed largely from malfunctioning of the particle separation equipment. Although data on particulate loading or size distribution fed to the turbine were sparse, it appears that particle sizes ranged from 1 to 11  $\mu\text{m}$  and that the average particle size was < 3.5  $\mu\text{m}$ . Apparent total loading ranged from 250 ppm (0.13 gr/SCF) to 625 ppm (0.33 gr/SCF).

Supporting studies (6,7), using a smaller atmospheric pressure FBC, indicated that of the potentially condensable species in the combustion gases, K was low (0.01-0.06 ppm vol.), while Na was high (3-14 ppm) as was Cl (3.3-43.7 ppm). The sulfate level ranged from 0.07 to 8.11 ppm. Some hot corrosion attack of Nimonic 80A, FSX-414 and IN-738 was observed, but was much less important than the losses due to erosion. Other laboratory work indicated a strong temperature dependence of the erosion rate, erosion decreasing with increasing temperature from 77 to 1800°F. The fly ash formed an adherent deposit at 1500°F, so that based on predictions of the best practical cleanup of the gas (granular filter), a deposition rate of 16  $\mu\text{m}$  per hour of ash would be expected on hot surfaces. Experience at CPC is that deposits grow to a particular thickness and then spall, leading to possible erosion

problems. A further extrapolation of the erosion rate-temperature results was that erosion could be a problem in the second, third and fourth turbine stages if the particle trajectories were such that impact could occur.

Curtiss-Wright have run a small Rover turbine (IS/60) on a 94 psi, 1650°F PFBC burning coal with dolomite for up to 1000 hours (8). The gas cleanup train consisted of (after the recycle cyclone) a Dynatherm "Whirlaway" separator, A Ducon high-efficiency tangential entrance cyclone, and an Aerodyne split-flow cyclone using clean air from the bed heating tubes for secondary air augmentation. The gas entering the cleanup train contained 6800 ppm (3.6 gr/SCF) particles with a mean and maximum size of 8  $\mu\text{m}$  and 30-50  $\mu\text{m}$ , respectively. In an initial 150-hour test, malfunctioning of the first two cleanup units resulted in a dust loading at the turbine entrance of 283 ppm (0.15 gr/SCF), with a particle/mean/maximum size of 3.2 and 27  $\mu\text{m}$ , respectively. Erosion of the trailing edge tip of the rotor blades (Nimonic 90) had occurred, together with similar erosion of vanes (Nimonic 80) located 180 degrees away from the gas inlet scroll.

Modifications to correct the cleanup deficiencies produced a particle concentration of about 94 ppm (0.05 gr/SCF), with a mean/maximum size of 1.3/8  $\mu\text{m}$ , entering the turbine. After inspections at 160 and 368 hours, no signs of erosion at any location were reported. The vanes and blades used in these tests used revised materials and coatings. Blades of U720 were used both bare, and with Al-diffusion or Pt-Al diffusion coatings. The vanes were of IN-738 or FSX-414, with coatings of Al-diffusion, Pt-Al diffusion, Rh-Al diffusion, and PVD coatings of NiCrAlY, CoCrAlY and FeCrAlY.

#### Expansion of Dirty, Oxygen-Deficient Gases (Type III)

Very extensive experience has been gained in the operation of gas turbines on the off-gas or flue-gas streams of blast furnaces, and of catalytic cracking units in the petrochemical industry. A major difference between the operational modes of these machines and those anticipated for use in coal gasification systems, however, is the relatively low (1400°F max) turbine inlet temperatures of the former. Nevertheless, this useful body of experience is worth noting.

Gas turbines utilizing blast furnace gas generally operate with a turbine inlet temperature range 1200-1400°F, and accept dust loadings of 2-19 ppm (0.001-0.01 gr/SCF) (9,10). These low concentrations result from cold gas cleanup procedures, which usually utilize a two-stage wet scrubber, and possibly an electrostatic

precipitator. Deposition and fouling, rather than erosion, is the major problem in these turbines, occurring mainly on the later stages, and apparently depends more on the nature of the ash than on the ash loading. Cleaning is practiced and is effective in restoring efficiency when used at  $\sim 8000$  hours intervals. Some erosion and/or corrosion loss from the first-stage blades and vanes is usual, requiring their replacement at about 30-40,000 hours, although lives of up to 81,000 hours have been reported. The composition and size range of the ash in the blast furnace gas can vary considerably, and is not easily characterized. It is presumed to be different from PFBC-generated fly ash.

The use of gas turbines on catalytic cracking units has become fairly widespread since the early 1960's. In these systems, an expander turbine is driven by the regenerator off-gas and used to compress air for spent catalyst regeneration. Early efforts by Elliott Company (11) to run such a unit on an untreated off-gas, fed at 1000°F, 18 psig, and containing around 500,000 ppm (260 gr/SCF) of basically alumina catalyst with a particle size less than 20  $\mu\text{m}$ , met with very severe erosion such that the turbine was inoperative after 750 hours. The trailing edges suffered most damage and segregation of the solids before entering and within the turbine was considered a major problem. Revised systems using usually two or three cyclones separators ahead of the turbine, and having a turbine gas path (axial flow) designed to achieve uniform particle distribution, typically operate for four years between maintenance shutdowns (12-15). This performance is achieved with a turbine inlet temperature ranging from 1000-1400°F, a relative gas velocity of 500-1400 feet per second, and a particle concentration of less than 160 ppm (0.08 gr/SCF), with about 97 percent less than 10  $\mu\text{m}$ , and a mean particle size of 2-4  $\mu\text{m}$ . Without an effective final cleanup stage, particle concentration to the turbine is around 800 ppm with a mean/maximum size of 20/80  $\mu\text{m}$ , and erosion losses, then limit the blade life to around 450 hours.

The gaseous environments expanded by these turbines have equilibrium oxygen partial pressures in the range  $10^{-20}$  to  $10^{-22}$  atm, and sulfur partial pressures of around  $10^{-10}$  atm at 1200°F, such that they are potentially highly sulfidizing. Deposit formation has not been a problem in this application presumably because of the nature of the catalyst dust, and chromium oxide scale-forming alloys have generally performed well. Blades are A286, Inconel X-750 or Waspaloy depending on the temperature, while vanes are usually Haynes 31. Conceivably, as higher temperatures are attempted in these machines, erosion-assisted sulfidation attack may become a significant factor with some of the low-chromium (15 percent) alloys. Additionally, coatings of flame-sprayed WC which have been used for erosion

resistance in this oxygen-deficient environment may be expected to undergo oxidation-degradation in higher-temperature, oxidizing conditions.

Expansion of higher-temperature (1500-1800°F) Low BTU gas streams from coal gasification plants for power recovery purposes will undoubtedly require the use of materials with much improved resistance to sulfidation attack at low oxygen partial pressures, in addition to some means of resisting erosion. The alternate routes of injecting oxygen or steam to modify the environments, and of improving the particulate removal are attractive but in most cases not practical. High-temperature and high-pressure corrosion testing (17-19) of candidate alloys in simulated gas mixtures have indicated that high-chromium, high-aluminum, alumina scale-forming alloys can develop reasonable resistance to corrosion in these environments. Modifications of state-of-the-art turbine overlay coatings might therefore be expected to find application here, provided there are no overwhelming detrimental effects of erosion. Unfortunately, there are no available erosion data relevant to this environment. There are currently no commercial systems under design which require the expansion of Low BTU Gas.

#### COMBUSTION OF LOW/MEDIUM BTU GAS (TYPE II)

The coal gasification processes under serious consideration for integrated gasification combined cycle operation can be divided into three main types: fixed bed, entrained bed, and fluidized bed. Typical examples of each process are the Lurgi gasifier, the Texaco gasifier, and the Westinghouse Low BTU Process, respectively. While the operating conditions of these different systems may vary widely, the desired trends for optimizing the match-up with a gas turbine are towards high-pressure, high-temperature operation. All the processes are aimed at the production of a low-to-medium BTU fuel gas, which translates to a gas with high contents of  $H_2$ , CO (and some  $CH_4$ ) and in the raw state,  $H_2S$ , with prevailing oxygen and sulfur partial pressures in the range  $10^{-15}$  to  $10^{-17}$ , and  $10^{-5}$  to  $10^{-7}$  atm., respectively, at 1800°F. Before use in a turbine, the sulfur obviously must be removed, together with the particulate matter derived from the coal, and any condensable salts.

Currently available sulfur removal systems operate at low ambient temperatures, so that the gas must be cooled, with the inherent loss in system efficiency. Cooling will probably involve a water spray quenching step, and the sulfur removal systems involve contact with aqueous or organic reagents, so that particulate removal could also be effectively accomplished here. In practical systems, and as experienced with blast furnace gas cleanup, some ash invariably passes through the

system and could enter the turbine. In this eventuality, the gases derived from different gasification processes might pose different problems of erosion, corrosion or deposition. Intrinsic differences in the ash carried over from the various processes could extend to a number of those properties that affect erosivity, such as hardness, shape, density; those that affect corrosivity, such as composition, alkali metal content; and those that affect deposition characteristics, such as shape and melting/softening point. In its present form, however, the integrated gasification combined cycle appears to present few problems, indeed the initial experience with the DOW/Westinghouse 15MW unit has been very favorable (20). Whether the hot sulfur and hot particulate cleanup systems required for higher cycle efficiencies can be developed remains to be seen.

#### COMBUSTION OF COAL-DERIVED LIQUID FUELS (TYPE IV)

Coal-derived liquid (CDL) fuels contain a diverse array of metallic element impurities which are present after processing at the trace level. There is virtually no documented experience of the behavior of many of these impurities during combustion under gas turbine conditions, and in view of the problems associated with trace levels of Na, for instance, there is a need for systematic characterization of these fuels. The formation of inorganic ash particles or of corrosive, condensable salts during combustion could lead to erosion, deposition and fouling, or hot corrosion, by analogy to the well-researched problems resulting from the presence of Na and S in current fuels. Research under the Gas Turbine Critical Research and Advanced Technology Research Project (21), and in other programs has attempted to characterize the effects on gas turbine hot gas path components through the use of doped fuel oils, and by using some actual coal-derived liquid fuels.

The main problem encountered in turbine simulator rigs with actual CDL fuels has been deposition and fouling (22,23). The deposits were mainly metal oxides, containing Cu, Fe, Cr, Ca, Al, Ni, Si, Ti, Zn and Na, which was apparently in excellent agreement with equilibrium thermodynamic predictions. No hot corrosion was observed, mainly because of the very small amounts of Na and K in the deposits, and because of the dilution effects of the more inert oxides. Where the effects of some of the individual fuel impurities were studied in combination with Na, additions of K, V, Mo, W, P and Pb were each found to cause corrosion greater than Na alone under some conditions (24), essentially by lowering of the hot corrosion threshold temperature. If indeed variations in CDL fuel composition, combustion conditions, or changes occurring in deposits with time can lead to such

augmentation of hot corrosion attack in practice, then a whole new area of characterization and research will have to be undertaken in order to regain the rational base for materials selection currently enjoyed.

Methods used to combat the corrosivity might include the use of inhibitors, though this may aggravate the fouling tendency of the fuel. Some beneficial effects of additives such as Ba, Sr or Si have been noted (25), and some pretreatment techniques investigated to minimize fouling.

The CDL fuels have been found to be corrosive towards some of the components in the usual storage and fuel handling systems. While strategies can be employed to circumvent this problem, there is a possibility of further and variable contamination of the fuel with metallic species, which could modify its deposition and corrosion characteristics.

These coal-derived fuels exhibit different combustion characteristics to the usual distillate fuels. Different fuel-to-air ratios are required, together with possibly different flame control strategies. Experience to date has revealed some difficulties in maintaining clean combustion conditions; carbon deposition has been noted, which if uncontrolled could contribute to the deposition problem or possibly to erosion through spallation of hard, deposited particles and entrainment in the gas stream.

## Section 4

### GENERAL TRENDS

Pertinent data from the tests and studies discussed are listed in Table 4-1 for review and comparison. In general, velocity was found to exert the expected, large effect on erosion behavior, with metal loss proportional to velocity raised to some power around 2. Particle size and loading in the gas stream constituted important variables which might be controlled through process changes. While some progress towards definition of maximum tolerable particle sizes and concentrations has been made for specific systems, attention must also be focused on preventing stratification of the particulate flow inside a gas turbine, since the total number of impacts per unit area, or impact frequency, are important in determining erosion losses. An important feature that has been amply demonstrated is that excursions to particle sizes or loadings above certain levels can lead to very rapid loss of hardware intercepting the fluid stream. Where plant upsets may cause such fluctuations in the alternative fuel flow to the turbine, some form of erosion sensor to provide early warning to the turbine control equipment should be considered. Detailed design changes evolved for fluidized-bed catalytic cracker-duty turbines also provide an important example in strategies for accommodating particulates.

While different test types and different systems have been considered together in this overall assessment, it should be remembered that some twenty or more variables influence erosion/corrosion/deposition behavior (26), and specific differences in, for instance, particulate type may be very important. Under a given set of conditions, therefore, the parameters that determine whether particles will erode or deposit on a surface may include particle shape, composition, temperature, in addition to the more easily measured velocity, size and concentration.

In situations where erosion is a factor, harder alloys, such as Haynes 31, have shown better resistance than softer alloys such as Nimonic 75; such observations are relative, and have been found to be essentially reversed under conditions where oxidation is a significant factor (27). Ceramics have been used successfully as wear inserts, but the specific conditions of their application were such that oxidation-degradation was negligible. However, ceramics such as silicon nitride



have shown good promise in erosive, high-temperature turbine tests (28). Aluminide coatings and overlay metallic coatings consistently showed improved performance over bare alloys, and have demonstrated similar superiority in erosion rig tests (28).

TABLE 4-1  
SUMMARY OF PFBC-GT DATA

Test	T, °F	P, psig	V, ft/sec	W, ppm	dp, μm	t, hr	Remarks
<u>CASCADE TESTS</u>							
BCURA (1)	1600 1700	66-73 "	1338	250 "	95% < 10 85% < 5	204 "	No D, E; Hot Corr No E; D + Hot Corr
EXXON/GE (2)	1550-1570	113-119	800	65 → 860	95% < 10 (10% > 10, 2% > 25)	1000	D, E/C
CURL/GE (4)	1475 1350	73.5 "	1400 "	250 "	99% < 10 "	1000 "	D, some C, no E D, some C, no E
CURL/S-L (3)	1418-36 "	73.5 "	755-1247 590-1760	100-120 "	99% < 5 Av = 2	1000 "	No, E, D, slight C
<u>TURBINE TESTS</u>							
LDC-BCR/BM (30)	1229			210	10% > 10 2% > 20	878	E of blade tips, vane Blades. No C.C, Heavy D on 15th stage
AUST. CBGT (31)	1202		1100 800	650	4.3-7.8	125 125	{ No D, some E of trailing edges of 1 and 2 blades
NASA-LEREC (5)	1274 1436 1436	65-68 " "	853 1083 1083	600 (20-2500) 2600 2800	{ 98% < 50 90% < 30 50% < 10	164 13 12	E, C, D E, C, D E, C, D
CPC (6,7)	1400	44	1470	250 → 625	1-11 Av=3.5	600	E, D, C
C-W (8)	1600	94	1650	283	{ 3.2 Av 27 max	150	E trailing edge tip-blades and vanes
		"	"	94	{ 1.3 Av 8 max	1000	Slight E, E/C

TABLE 4-1 (Continued)

## SUMMARY OF PFBC-GT DATA

Test	T, °F	P, psig	V, ft/sec	W, ppm	dp, μm	t, hr	Remarks
<u>EXPANSION-OXYGEN DEFICIENT GAS</u>							
BFG (9,10)	1200-1400	"	"	2-19	"	8000 30-40K	D on later stages E/C on 1st V&B
CC (11-15)	1000	18	"	500,000	< 20	750	E, trailing edges
	1000-1400	"	500-1400	< 160	{ 97% 10 2-4 Av	32,000	E, same C at high T
	"	"	"	800	{ 20Av 80 max	450	E
<u>COMBUSTION OF COAL-DERIVED GAS</u>							
Coolwater-GE DOW-WH (20)	1985	150	"	3.5	"	"	"
<u>COMBUSTION OF COAL-DERIVED LIQUIDS</u>							
NASA-LeReC (21, 22,24,25)	"	"	"	"	"	"	D, no E, C
UC (32)	70	"	450	"	{ 38.4 (PC) 28 (PC) 15 (PC) 3.9 (PFBC)	"	E similar E ~ 0.1 of PC
PWA (28)	1600	0	789	300	0.3 (Al <sub>2</sub> O <sub>3</sub> )	-	D
	1600	0	845	300	2.5 (Al <sub>2</sub> O <sub>3</sub> )	28	E/C (synergism), Al <sub>2</sub> O <sub>3</sub> < Cr <sub>2</sub> O <sub>3</sub>
	1600	0	~ 600	300	8 (MgO)	28	< E/C
	1600	0	673	130	20 (Al <sub>2</sub> O <sub>3</sub> )	50	E, no effect of C
	1600	0	~ 600	130	20 (PFB)	-	D, no E
BCL (33)	1400	"	927	177	75% < 25 AV = 14	3	E
	1420	"	1040	53	98% < 9 AV = 4.3	3	E ~ 0.1 E AT 177 ppm

Section 5  
CONCLUSIONS

Erosion appears to be an overriding materials constraint for Types I and III turbines. A threshold condition related to particulate velocity, concentration in the gas stream, and density (or impact frequency) is apparent but has not been adequately defined. Above the threshold, essentially all hot gas-path materials are degraded at an unacceptable rate; ceramics may have some promise in requiring higher threshold conditions. Below the threshold, harder alloys have shown some advantages in certain circumstances, while ceramics and oxidation-resistant coatings appear superior to bare superalloys.

Corrosion resistance may be the main criterion for Type III turbines, in that these are expected to experience conditions more severe (higher temperature) than those of catalytic cracker turbines, which represent the only current use of this type. Corrosion may also be an important consideration for Type II turbines, since water-washing is expected to remove the erosion threat. These alternative fuels contain a different spectrum of trace elements from those with which the gas turbine community has experience, so that the extent of the corrosion potential must be determined. The use of additives is a possibility. A further feature of some alternative fuels is related to their combustion characteristics. Increased flame luminosity can result in higher metal surface temperatures for hot gas-path components, hence possible modifications of their corrosion behavior.

Deposition appears to be of major importance for Type IV turbines, and may also require consideration in Types I and III. Much depends on the nature of the ash; hence, on conditions of combustion some deposits may lead to corrosion, while others may pose problems because of their adherence. All may be amenable to periodic cleaning treatments. In some cases deposit thicknesses have been found to reach a steady state, such that wider machine passage tolerances might be advantageous.

## Section 6

### REFERENCES

1. Fluidized Combustion Control Group, NCB. "Reduction of Atmospheric Pollution." Final Report of National Coal Board to EPA Reference No. DHB 060971, 1971.
2. D. A. Grey, A. M. Beltran, R. P. Brobst, and R. L. McCarron. "High Temperature Corrosion/Erosion in the Effluent from Pressurized Fluidized-Bed Combustors." Proc. 6th Int. Conf. on Fluidized Bed Combustion, Atlanta, April, 1980, NTIS CONF-800428, Vol. 2, August, 1980.
3. S. A. Jansson, N. G., Nilsson, and B. O. Malm. "Turbine Materials Performance in Combustion Gases from a Coal-Fired PFBC." Ibid.
4. R. L. McCarron, A. M. Beltran, and D. A. Grey. "The Degradation of High-Temperature Materials in a Test Cascade Exposed to a High-Velocity PFBC Effluent." Proc. First Conf. on Advanced Materials for Alternative Fuel-Capable Directly-Fired Heat Engines, NTIS CONF-790749, December, 1979.
5. G. R. Zellas, S. M. Benford, A. P. Rowe, and C. E. Lowell. "The Erosion/Corrosion of Small Superalloy Turbine Rotors Operating in the Effluent of a PFB Coal Combustor." Proc. First Conf. on Advanced Materials for Alternative Fuel-Capable Directly-Fired Heat Engines, NTIS CONF-790749, December, 1979.
6. K. E., Phillips. "Energy Conservation from Coal Utilizing CPU-400 Technology." ERDA Contract No. EX-76-C-01-1536, 1976.
7. W. G. Stevens and A. R. Stetson. "Corrosion and Erosion Evaluation of Turbine Materials in an Environment Simulating the CPU-400 Combustor Operating on Coal." Contract No. OCR/ERDA E (49-18)-1536, 1977.
8. S. Moskowitz, G. Weth, and A. Leon. "Development of a Coal-Fired PFB for Combined Cycle Power Generation." ASME Paper 80-GT-189, 1980.
9. E. Aguet and J. VonSalis. "Three Years' Experience with 7500 KW Gas Turbine Plants in Belgian Steelworks." ASME Paper No. 60-GTP-3, 1960.
10. A. J. Jaumotte and J. Hustin. "Experience Gained from Ten-Year Operation of a Gas Turbine Working With Blast Furnace Gas." ASME Paper No. 66-GT-97, 1966.
11. J. R. Shields. "Power Recovery from 'Dirty' Gases." Powerfax, September, 1958.
12. J. C. Dygert and I. S. Bjorklund. "Integration of the Power Recovery Gas Turbine with Fluid Bed Processes." ASME Paper No. 59-A-231, 1959.
13. J. G. Wilson. Oil and Gas Journal, 64 (16), 1966, p. 77.
14. H. L. Franzel and D. W. Miller. Oil and Gas Journal, 67 (12), 1969, p. 95.
15. L. W. Stettenbenz. Oil and Gas Journal, 70 (51), 1972, p. 60.

16. W. G. Mathers and R. Schonewald. "Fluid Catalytic Cracker Power Recovery Expander Applied to Pressurized Fluidized Bed Combustion." Proc. 6th Int. Conf on Fluidized Bed Combustion, CONF-800428, Vol. II, 1980, p. 737.
17. K. Natesan. "Corrosion and Mechanical Behavior of Materials for Coal Gasification Applications." Argonne National Lab. Report, No. ANL-80-5, 1980.
18. R. A. Perkins and M. S. Bhat. "Sulfidation-Resistant Alloy for Coal Gasification Service." DOE Report No. FE-2299-12, 1977.
19. See ongoing research at IITRI on MPC-directed program entitled, "A Program to Discover Materials Suitable for Service Under Hostile Conditions Obtained in Equipment for the Gasification of Coal and Other Solid Fuels."
20. See Gas Turbine World. Engineering News and Trends, 11 (3), 1981, p. 61.
21. J. S. Clark. "Status of the DOE/NASA Critical Gas Turbine R and T Project." ASME Paper No. 80-GT-104, 1980.
22. G. J. Santoro, et al. "Deposition and Material Response from Mach 0.3 Burner Rig Combustion of SRC-11 Fuels." NASA TM-81634, 1980.
23. C. T. Simis, H. E. Doering, and D. P. Smith. "Effects of the Combustion Products of Coal-Derived Fuels on Gas Turbine Hot-Stage Hardware." ASME Paper 79-GT-160, 1979.
24. D. L. Deadmore and C. E. Lowell. "Effects of Impurities in Coal-Derived Liquids on Accelerated Hot Corrosion of Superalloys." NASA TM-81384, 1980.
25. D. L. Deadmore and C. E. Lowell. "Fouling and the Inhibition of Salt Corrosion." NASA TM-81469, 1980.
26. W. R. Pierson. "Superalloys in Coal Utilization Systems." ASME 22nd Annual International Gas Turbine Conf., 1977.
27. I. G. Wright, V. Nagarajan, W. E. Merz, and J. Stringer. "The Kinetics of High-Temperature Erosion-Corrosion of Oxidation-Resistant Alloys." Paper No. 3, Corrosion-81, NACE, 1981.
28. R. H. Barkalow, J. A. Goebel, and F. S. Pettit. "Materials Problems in Fluidized-Bed Combustion Systems: High-Temperature Erosion-Corrosion by High-Velocity (200 m/sec) Particles." EPRI Report No. CS-1448, 1980.
29. "Economic Studies of Coal/Gasification Combined Cycle System for Electric Power Generation." EPRI AF-642, Research Project 239, January, 1978.
30. J. P. McGee, A. J. Liberatore, D. C. Strimbeck, and G. B. Goff. "Turbine Blade Wear by Coal Ash in Working Fluid at 1200°F." U. S. Dept. of the Interior-BOM, Report of Investigation 7255.
31. "The Coal-Burning Gas Turbine Project." Report of the Interdepartmental Gas Turbine Steering Committee, Advocate Press Pty, Ltd., Melbourne, Australia, 1973
32. R. Kotwal and W. Tabakoff. "A New Approach for Erosion Prediction Due to Fly Ash." ASME Paper 80-67-96, 1980.
33. W. M. Goldberger. "Collection of Fly Ash in a Self Agglomerating Fluidized Bed Coal/Burner." ASME Paper 67-WA/FU-3, 1967.

CORRODANT SOURCES, CORROSION AND DEPOSITION  
IN DISTILLATE AND HEAVY OIL-FIRED TURBINES

C. J. Spengler  
Westinghouse Research and Development Center  
Pittsburgh, Pennsylvania 15235

S. T. Scheirer, J. H. Marlow and J. J. Vitello  
Westinghouse Combustion Turbine Systems Division  
Concordville, Pennsylvania 19331

ABSTRACT

This study was undertaken to compare the corrosion behavior of hot gas path turbine parts from Florida Power and Light's East Palatka Plant when turbines were operated with either a distillate oil or a combination of distillate and a heavy fuel oil. The study included the determination of corrodant sources, characteristics of deposition of corrodants in the compressor and the combustion turbine, and the correlation of the deposits to the initiation of hot corrosion attack in the turbine. It was found that elements concentrated in the compressor entered the combustion turbine. The deposits which formed in the turbines as a result of use of a heavy fuel oil with a magnesium additive depended on the temperature of the substrate. Corrosion attack due to vanadium compounds in the heavy fuel-fired machines was nil; however, some indication of hot corrosion attack was found in all of the turbines. The corrodants were mainly attributed to the ingestion of contaminated mist from adjacent cooling towers through the compressors. It was concluded that hot part corrosion degradation was not increased from heavy fuel operation.

INTRODUCTION

The objective of this study was to compare the corrosion behavior of hot gas path turbine parts when turbines were operated with either a distillate oil or a combination of distillate and a heavy fuel oil. The study included the determination of corrodant sources, characteristics of deposition of corrodants in the compressor and the combustion turbine, and the correlation of the deposits to the initiation of hot corrosion attack in the turbine. The study, part of a project co-funded by the Electric Power Research Institute, Florida Power and Light Company (FP&L) and Westinghouse Electric Corporation, was initiated in August 1978 at the Putnam Plant of FP&L at Palatka, Florida. Each 260-MW(e) unit included two W-501 Westinghouse combustion turbine engines, each exhausting into its own afterburner-equipped heat recovery steam generator.

The plant was designed with the capability of burning both light distillate fuel as well as heavy residual fuel and had a dual liquid fuel storage and forwarding system. The heavy fuel system was equipped with a water wash system and electrostatic desalter to remove water-soluble salts from the oil. The desalted fuel was blended with an oil soluble vanadium inhibitor at a rate of 3.0 ppm Mg for each ppm of vanadium in the fuel. The test called for a 3500 hour run during which data would be collected from each unit to quantify its operating and maintenance costs; the costs would be compared to define the relative economics of using each fuel. During the test, certain hot gas path components from each unit were to be examined to determine the relative effect of the two fuels. Emissions measurements were also planned. However, several factors combined to modify the initially planned tasks. A rapid escalation in the fuel cost differential between the No. 2 oil and the heavy oil resulted in early termination of distillate oil firing. Operating problems encountered during the early period of heavy fuel use caused this unit to accumulate only about 900 hours burn on heavy fuel oil. Since completion of the test, the Putnam Plant has operated almost exclusively on heavy oil because of the favorable overall economics.

The Westinghouse studies included metallographic and deposit analyses of selected turbine blades and vanes from each of the four W501B turbines, fuel and ambient air analyses, investigations of combustion and transition components, as well as characterization of various compressor deposits. The results of these studies are described and discussed to interpret the interaction of various operating parameters on the blade and vane materials performance.

## RESULTS AND DISCUSSION

### Plant Site Description

Shown in Figure 1 is the 500 MW station. To the top in a westerly direction is the brackish St. John River along which are the fuel storage and treatment installations. The power block area lies to the west of the cooling towers, water plant and waste water treatment basins which use St. John river water. When analyzed in August, 1979, the river water samples contained 45-115 ppm Na, 2.3-5.6 ppm K, 47-90 ppm Ca, 5.5-13.5 ppm Mg, 210-260 ppm Cl<sup>-</sup> and 95-195 ppm SO<sub>4</sub><sup>=</sup>. The turbine compressors had no inlet air filters or demister systems.



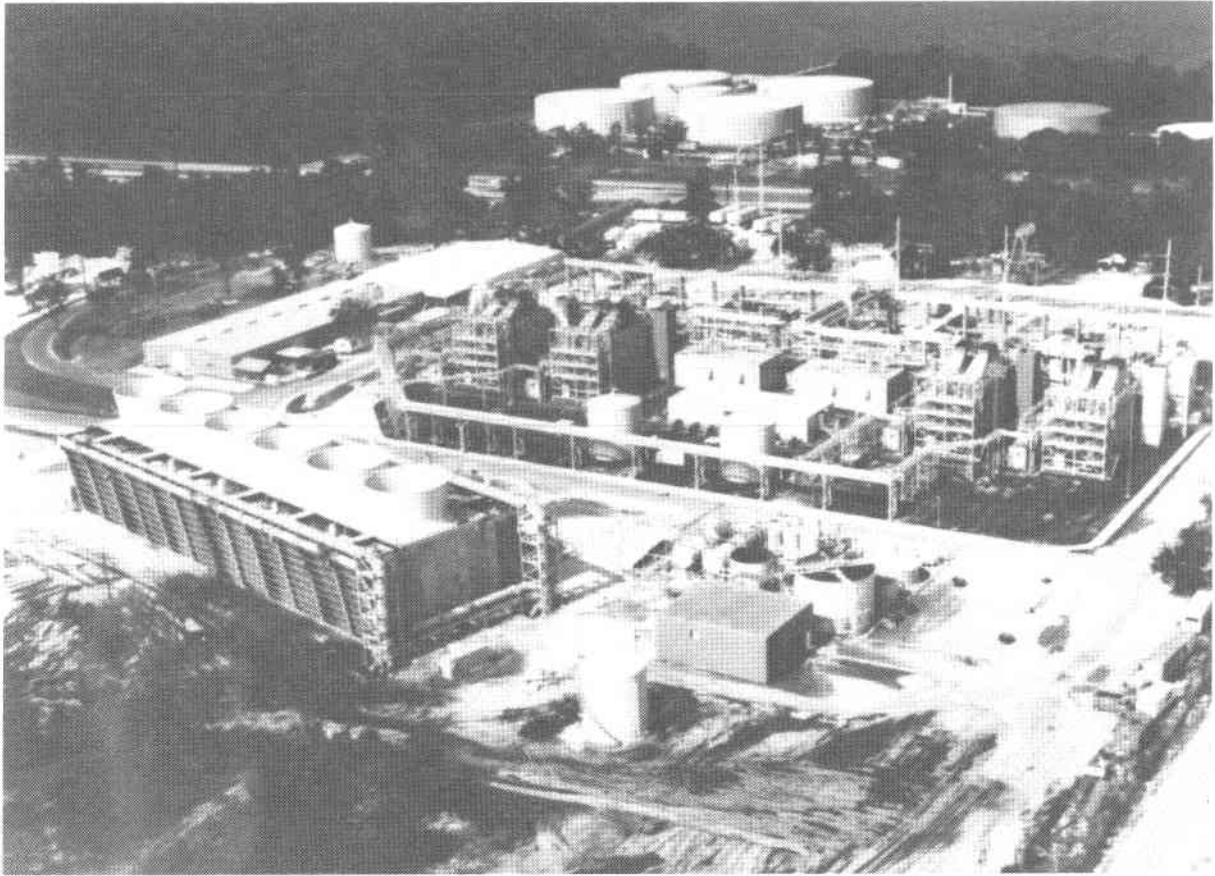


Figure 1. Florida Power and Light, Putnam Station, Palatka, Florida. This 500 MW station consists of two Westinghouse combined cycle plants. Each plant has two combustion turbines with heat recovery boilers and a steam turbine.

#### Ambient Air Quality

Two different samples of ambient air, as shown in Table 1, in January and August of 1979, revealed levels of sodium and potassium in excess of fuel specification allowances. The amount of material in the ambient air is converted to fuel basis (approximately 50 parts of air per part of fuel consumed during turbine operation). High concentrations, especially of sodium, were detected in the water of the nearby cooling tower system during both winter and summer test periods. Contamination of the compressor inlet air due to this source should occur only when the mist in the cooling tower plume drifts over the power block area. This situation occurred approximately 12 percent of the time during the winter and 44 percent of the time during the summer test periods. While the prevailing westerly wind direction will carry cooling tower plume away from the turbines the majority of the time, the

ambient air measurements are reasonable evidence that for short periods the plume was blown in the vicinity of the turbine inlets.

TABLE 1  
Ambient Air and Cooling Tower Water Samplings  
(Units 1-2 and 2-2)

	January '79		August '79	
	Ambient Air*	CTW**	Ambient Air	CTW
Na	0.3-0.85	297-574	0.33-1.00	132-640
K	0.04-0.18	9.1-15.7	0.03-0.10	8-20
Ca	0.24-0.55	113-190	0.10-0.16	32-275
Mg	0.04-0.08	36.7-62.4	0.02-0.04	19-41
SO <sub>4</sub>	---	459-918	---	455-649

\*ppm equivalents in combustion turbine fuel. ASTM fuel specification for Na+K is 0.5 ppm, max.

\*\*Cooling tower water in ppm.

Table 2 lists the ambient air and cooling tower water samplings as ratios with sodium. The Na/K, Na/Mg and Na/Ca ratios for the cooling tower water are generally consistent with the use of the brackish St. John river water in the cooling tower. The Na/K ratios for the ambient air especially for January indicate a separate source of potassium relative to the cooling tower water, perhaps from airborne potash from fertilizer. The Na/Mg and Na/Ca ratios of the ambient air remains relatively consistent with the plume as the source. Because the cooling tower plume is high in sodium, it is the likely principal source of sodium to enter the turbine compressors.

#### Compressor Deposits

In March of 1979 deposits were scraped off various components of the Unit 1-1 axial flow compressor. The unit had had 752 starts, 3960 total fired hours (28 hours peak operation) and had operated for 838 hours on heavy fuel. Table 3 lists the deposit locations and also the approximate air temperatures and static pressures for the locations during compressor operation.

TABLE 2

Sodium Ratios to Potassium, Calcium and Magnesium  
for Various Contaminant Sources

Ratio	January '79		August '79		St. John River Water**	Sea Salt
	Ambient Air	CTW*	Ambient Air	CTW		
Na/K	4.7-7.5	32.6-36.5	10-11	16-32	19.6-20.5	27.8
Na/Ca	1.25-1.5	2.6-3.0	3.3-6.7	2.3-11	0.96-1.3	26.6
Na/Mg	7.5-10.6	8.1-9.2	16.5-25	6.9-15.6	8.2-8.5	8.3

\*Cooling tower water.

\*\*Ratios determined in August 1979.

TABLE 3

Compressor Deposit Locations and Temperature  
and Pressure Conditions

Deposit Location	Approximate Conditions		
	Temperature (°F)	Static Pressure (atm abs)	
Row 1 and 2 blade airfoils	120	1.2	<u>INLET</u>
Row 2 diaphragm	140	1.2	
Rows 9, 10 and 11 blade airfoils	440	4.8	
Rows 13 and 17 diaphragms	585	7.8	
Row 17 blade airfoil	640	9.0	<u>DISCHARGE</u>

The deposits consisted of the phases listed in Table 4. The principal phase found in the inlet was  $(\text{NH}_4)_2\text{Co}(\text{SO}_4)_2 \cdot 4\text{H}_2\text{O}$ . This compound appeared in several additional stages of the compressor (Table 4) but only as a high minor or a trace constituent. Several other compounds, notably  $(\text{NH}_4)_2\text{Mg}(\text{SO}_4)_2 \cdot 4\text{H}_2\text{O}$  and  $(\text{Na})_2\text{Mg}(\text{SO}_4) \cdot 4\text{H}_2\text{O}$  are quite similar in the value of the X-ray diffraction constants. It is obvious that the ammonia compound detected is a complex solid solution that contains significant substitutions of K and Na in the mono-valent cation and Zn and Mg in the divalent

cation sites but little Co since only 0.003 w/o was present in the inlet deposits. Ammonia is present up to 5.1 w/o of the solute in the inlet section but drops off to lower values in successive stages (Table 6). It is in these latter stages that mono-valent cation substitutions take place in the double sulfate, especially K which has a crystal ionic radius (1.33 Å) close to that of  $\text{NH}_4^+$  (1.42 Å) (1).

TABLE 4  
Phases Identified in Compressor Deposits

	INLET				DISCHARGE
	Temp. °F Atm. ab.	120 1.2	140 1.2	440 4.8	585 7.8
$(\text{NH}_4)_2\text{Co}(\text{SO}_4)_2 \cdot 4\text{H}_2\text{O}$	Major	Trace	-	Trace	High Minor
$\text{CaSO}_4 \cdot 2\text{H}_2\text{O}$	-	Major	High Minor	Minor	-
$\text{SiO}_2$	-	Minor	-	-	-
$\text{Na}_2\text{SO}_4$	-	-	Minor	Major	Major
$\text{Na}_2\text{Mg}(\text{SO}_4)_2 \cdot 4\text{H}_2\text{O}$	-	-	Trace	-	-

The deposits formed in the inlet region contained significant Fe, Si, and Ca which is reflected in the identification of  $\text{SiO}_2$  (quartz) and  $\text{CaSO}_4 \cdot 2\text{H}_2\text{O}$  (gypsum); however, no iron-containing compounds were detected. The deposits, except for one stage, all contained significant sodium and, interestingly, zinc (Table 6).

Not all of the alkalis and alkaline earth elements present in the compressor deposits are in compounds that are likely to react in the combustion stream and result in condensed sulfates on turbine parts. The compounds less likely to react are alumino-silicates (feldspars, clay minerals) which are water insoluble. Therefore, we assumed that the potential sulfate-formers (in the hot gas path of the turbine), if present in the compressor deposits, would be in compounds that dissolve in water. The deposits were water leached and the results are shown in Tables 5 and 6. Almost all had greater than 50 w/o solubility in water and significant amounts of Na, Ca, Zn and K. The principal anion was sulfate but some chloride (up to 2.6 w/o of the bulk) was present. No carbonate, nitrate, phosphate or other sulfur-oxygen species such as sulfites, pyrosulfates or thiosulfates were detected.

TABLE 5

## Water Soluble Sulfate and Water Content of Deposits

	<u>INLET</u>				<u>DISCHARGE</u>
Temp. °F	120	140	440	585	640
<u>Atm. ab.</u>	<u>1.2</u>	<u>1.2</u>	<u>4.8</u>	<u>7.8</u>	<u>9.0</u>
Percent Sol.	57.1	27.7	54.1	54.6	74.7
SO <sub>4</sub> <sup>-2</sup>	19.0	9.0	23.0	31.0	42.5
H <sub>2</sub> O	28.7	14.2	16.4	8.0	12.8

TABLE 6

Composition of the Water Soluble Fraction  
of the Compressor Deposits (w/o)

	<u>INLET</u>				<u>DISCHARGE</u>
Temp. °F	120	140	440	585	640
<u>Atm. ab.</u>	<u>1.2</u>	<u>1.2</u>	<u>4.8</u>	<u>7.8</u>	<u>9.0</u>
Na	4.0	2.4	11.1	18.1	15.1
K	0.7	0.6	0.9	2.2	2.1
Mg	0.7	0.6	1.4	1.2	1.3
Ca	1.9	7.2	4.8	5.3	4.0
NH <sub>4</sub>	5.1	1.8	0.2	0.15	0.3
Zn	2.4	0.6	4.1	1.5	3.1
Cl	1.6	2.9	4.8	0.13	0.05
SO <sub>4</sub>	33.3	32.5	42.5	56.8	56.9

The sulfates present in the lower temperature-pressure region (inlet) of the compressor are more highly hydrated than the sulfates toward the discharge end. This is shown in Table 5 where the weight percent of H<sub>2</sub>O is calculated by difference. The compound Na<sub>2</sub>SO<sub>4</sub> is anhydrous, therefore, the water at the discharge end, the inlet region and rows 9, 10 and 11 is associated with the double salts. The double salts probably dehydrate at operational temperature and rehydrate on the daily shut down cycle.

The ammonia derives from several sources: (1) the putrefaction of the dead organisms observed to coat the inlet vanes, especially in the warmer months; (2) fertilizer dust; and (3) the ubiquitous  $(\text{NH}_4)_2\text{SO}_4$  aerosol.

The site is about 16 miles (25.7 km) directly west of the ocean across very flat land. Marine aerosols and their derivatives can travel distances inland from the oceans especially over a flat, featureless landscape. These aerosols (2) are influenced chemically by continental and anthropogenic processes but are mainly NaCl,  $\text{CaSO}_4$  and  $(\text{NH}_4)_2\text{SO}_4$  with no identified  $\text{Na}_2\text{SO}_4$  constituent. The  $(\text{NH}_4)_2\text{SO}_4$  is thought to form under low humidity conditions when gaseous sulfur species combine with ammonia gas released from soils. If the aerosol (3) is larger than  $1 \mu\text{m}$  in radius, it is NaCl and  $\text{CaSO}_4$ , with some  $\text{MgCl}_2$  and  $\text{K}_2\text{SO}_4$ ; however, below  $1 \mu\text{m}$  and  $>0.1 \mu\text{m}$  radius it is a mixture with  $(\text{NH}_4)_2\text{SO}_4$  and under  $0.1 \mu\text{m}$  radius the aerosol is  $(\text{NH}_4)_2\text{SO}_4$ . The aerosols derived from sea water become liquid at  $>40\%$  RH and continental salt-derived aerosols remain crystalline up to  $70\%$  RH.

The zinc content of the bulk samples was found to range from 0.5 to 1 w/o, based on emission spectroscopy (1/3 to 3X amount reported); however, as w/o of the solute fraction the zinc is present from 0.65 to 4.07 w/o (Table 6). The possible sources include: (1) rust inhibitors (zinc chromate-silicate compounds); (2) fungicides and bactericides used in the cooling water treatment (however, analyses in August 1979 showed only 0-0.065 ppm Zn in the CTW); (3) corroded galvanized steel and; (4) zinc oxide from such varied sources as paint and automobile tire dust. Regardless of the source, the zinc forms a complex water soluble double sulfate.

The alkalis (Na, K) and alkaline earth elements (Ca, Mg), potentially, are the most troublesome elements in terms of corrosion attack in the turbine when as sulfates. As is evident in Table 6, these elements constitute the majority of the cations detected. The sodium level of the deposit (bulk) increases from 2.3 at the inlet to 11.3 w/o at the discharge. The same is true for the solute fraction. The sodium content clearly increased toward the discharge.

It is interesting to examine the ratios of Na to the cations K, Mg and Ca as a function of combined increasing temperature and pressure. Table 7 compares the ratios in the various compressor stages with ratios of Na to the other cations for various contaminant sources. The Na/K, Na/Mg and Na/Ca ratios for deposits at the inlet are much lower than sea water and St. John River water but close for ambient air. The Na/Ca ratio is lower on the second stage vane ( $140^\circ\text{F}$ , 1.2 atms) than the ambient air ratio due to the larger amount of  $\text{CaSO}_4 \cdot 2\text{H}_2\text{O}$  relative to other

sulfates. The deposit on this vane had half the solubility compared to most of the other deposits.

TABLE 7  
Comparison of Water-Soluble Elemental Ratios of  
Compressor Deposits with Possible Sources

Ratio	St. John River Water*	Sea Water	Ambient Air (Jan.)	Temp. °F Atm. ab.	INLET				DISCHARGE
					120	140	440	585	640
					1.2	1.2	4.8	7.8	9.0
Na/K	19.6-20.5	27.8	4.7-7.5		5.7	4.0	12.3	8.2	7.2
Na/Mg	8.2-8.5	9.3	7.5-10.6		5.7	4.0	7.9	15.1	11.6
Na/Ca	0.96-1.3	26.6	1.2-1.5		2.1	0.33	2.3	3.4	3.8
SO <sub>4</sub> /Cl	--	0.14	--		20.8	11.2	8.8	437	~1140

\*Ratios determined in August, 1979.

The increase of Na on an absolute basis from inlet to discharge can be explained by the evaporation of NaCl at temperatures higher than 446°F (230°C) (4) and subsequent sulfation of the gaseous NaCl to form in successive stages the stable condensed solid Na<sub>2</sub>SO<sub>4</sub>. The ratio of water soluble sulfate to chloride (Table 7) initially decreases in the compressor and then sharply increases as the absolute concentration of chloride drops toward zero.

Bornstein and DeCrescente (5) have hypothesized that the deposition of salt onto compressor components is related to the solubility of salt in the water droplet entering the compressor. Their studies showed that the predominant salts that adhered to the low end of the compressor were chloride rich. In the FP&L site the principal source of the sodium was from the cooling tower plume which had a much higher sulfate/chloride ratio than sea water; therefore, the principal deposited phases in the low end of the compressor were sulfates. The chloride was ultimately precipitated in the compressor but remained a minor anion relative to sulfate.

#### Turbine Deposits

Distillate Fired Units. The deposits and reaction products collected from the Row 1 vanes and Row 1 and 2 blades contained single and double sulfates but were of

variable chemistry (Table 8). Many of the Na-Mg, -Ni, -Co and -Zn sulfate compounds, as well as Mg-Co-Zn sulfate, are isomorphous when hydrated and are very difficult to distinguish with X-ray diffraction techniques. Chemical analyses are, therefore, necessary for reliable identification. The water-soluble component of the deposit from a row 2 blade contained 9.2 w/o Na, 0.6 w/o K, 1.9 w/o Mg, 6.2 w/o Ca, 1.7 w/o Ni, 0.9 w/o Co, 3.4 w/o Zn, 0.5 w/o Cl, 0.1 w/o F and 75.5 w/o  $SO_4$ . If it is assumed that these cations and anions form a homogeneous mixture of equilibrium compounds then on the basis of ternary phase relationships (6) of the major species present there can be a possible molten phase at temperatures below 1450°F (790°C). Interestingly, some of the Na-Mg and Na-Co double sulfates and  $Na_2SO_4$  and  $CoSO_4$  were found on the airfoil that was normally at temperatures greater than 1450°F (790°C), and the corrosion attack was type I (classic high temperature hot corrosion attack).

TABLE 8  
Sulfates Identified in Distillate Fired Turbines

Row 1 Vanes	$CaSO_4$ (anhydrite)
Row 1 Blades	$CaSO_4$ $Na_2SO_4$ $Na_2M(SO_4) \cdot 4H_2O$ (M is Mg, Ni, Co, Zn)
Row 2 Blades	$Na_2SO_4$ $Na_2M(SO_4)_2 \cdot 4H_2O$ (M is Mg, Ni, Co, Zn) $CaSO_4$ $MSO_4 \cdot 2H_2O$ (M is Co, Mg, Zn) $CoSO_4$

The ratios of sodium to the potassium, magnesium and calcium, 15.3, 4.8 and 1.5, respectively, are somewhat close to those in the mid range of the compressor (Table 7) but the presence of zinc signifies that the compressor was the source of the contaminants. Anhydrite ( $CaSO_4$ ) is sparingly soluble in water, therefore, the 6.2 w/o water soluble Ca found in the deposit was in a mixed sulfate.

Heavy Fuel Fired Units. The turbine blade and vane deposits from the units operated on heavy fuel had similar physical features; flaky, soft and voluminous. The compounds present in these deposits were all similar with major magnesium



sulfate, some magnesium-vanadium compounds and calcium sulfate. The vanadium and alkali-alkaline earth compounds are listed in Table 9.

TABLE 9  
Vanadium and Alkali-Alkaline Earth Compounds  
Identified in Heavy Fuel Fired Turbines

Row 1 Vanes	$MgSO_4 \cdot 6H_2O$
	$MgSO_4 \cdot 7H_2O$
	CaO
	$CaSO_4 \cdot 2H_2O$
	$V_2O_5 \cdot H_2O$
	$Mg_{1.5}VO_4$
Row 1 Blades	$MgSO_4 \cdot 6H_2O$
	$MgSO_4 \cdot 7H_2O$
	$CaSO_4 \cdot 2H_2O$
	$V_2O_5 \cdot H_2O$ (root section)
Row 2 Blades	$MgSO_4 \cdot 6H_2O$
	$V_2O_5 \cdot H_2O$
	$Mg_{1.5}VO_4$
	$Mg_3V_2O_8$

The turbines operated on a daily basis with a start-up and shut-down each day. The machines were water washed periodically during a scheduled shutdown interval; therefore, the majority of the deposit analyzed subsequently was formed since the last wash cycle. An indepth examination was made of deposits collected from a row 1 vane that had operated 400 hours on heavy fuel. X-ray diffraction analysis of the pressure side airfoils showed major  $MgSO_4 \cdot 6H_2O$  and traces of  $Mg_3V_2O_8$  and MgO. The suction side airfoils had minor to major  $Mg_3V_2O_8$ , minor to major MgO and trace to minor  $MgSO_4 \cdot 6H_2O$ . The inner shroud surfaces had major  $MgSO_4 \cdot 6H_2O$ , minor  $Mg_3V_2O_8$  and minor MgO.

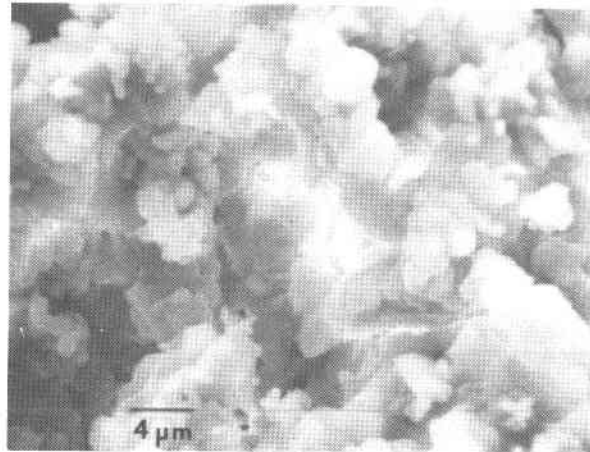
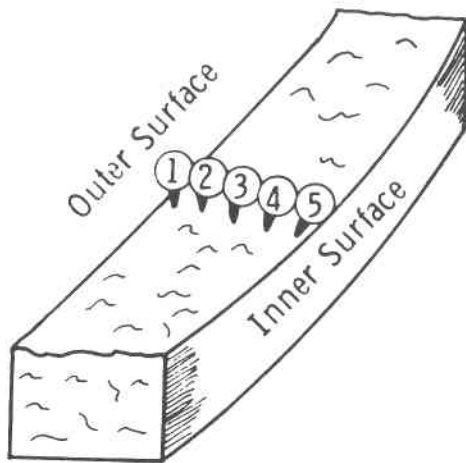
There is considerable interest in the formation and removal of residual fuel ash deposits that form at firing temperatures above 1800°F (980°C) in combustion turbines. Published work (7) states that sodium compounds can act as a "glue" to make magnesium-containing particles stick together and that deposits formed at

high firing temperatures do not wash off as readily compared to those formed at lower temperature. Deposits from the unit 1-1, first stage vane airfoil were examined with use of the SEM-EDAX system in order to ascertain the structure and chemistry of the deposits. The pieces selected were the thickest pieces that exhibited both original inner and outer surfaces. Figures 2 and 3 show the areas on the freshly fractured slab-like cross sections where analyses were made. Figure 2 contains areas 1 and 5, respectively, in the cross-sectional surface of the deposit on the vane pressure side. Area 1 near the outer surface is porous and is mostly  $MgSO_4$  with a little  $Mg_3V_2O_8$  and free  $V_2O_5$ . The deposit also contains Si, Al and Ti. There is a gradual change in the structure and chemistry from area 1 to 5 with area 5 somewhat sintered but still porous and mostly  $MgSO_4$  with a little  $Mg_3V_2O_8$  and  $MgO$ .

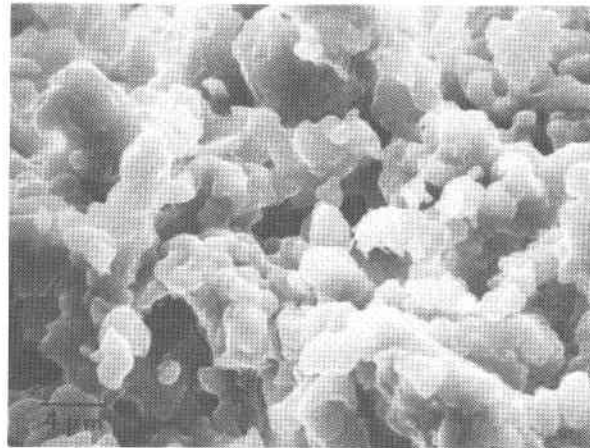
Figure 3 contains areas 2 and 5, respectively, of the cross-sectional surface of deposit from the vane suction side. Area 2 near the outer surface is porous and mainly  $MgSO_4$  with a little  $Mg_3V_2O_8$  and  $MgO$ ; however, area 5 approximately in the mid thickness shows an abrupt change in the structure where the deposit is all  $Mg_3V_2O_8$  and  $MgO$ . The suction side deposit is two-layered with probably freshly deposited  $MgSO_4$  over  $Mg_3V_2O_8$  and  $MgO$ .

Quantitative chemical analyses of water-leachable constituents of deposits were made on collections from combustor baskets, transition sections and from the first stage vanes. The Na (based on the bulk sample) ranged from 0.05 to 0.95 w/o, averaged 0.25 in the basket, 0.18 in the transition duct, 0.95 for the vane inner shroud, 0.5 for the vane suction side and 0.4 for the vane pressure surface. The SEM-EDAX analyses of first stage vane deposits did not locate any Na as part of any "glue" phase.

Deposits from a combustor basket, first stage vane, and fourth row blades were sampled and evaluated with X-ray diffraction. The deposits (Table 10) consisted of various proportions of  $MgSO_4 \cdot 6H_2O$  (hydrates on shutdown of turbine),  $MgO$  and  $Mg_3V_2O_8$  depending on the temperature at which the deposit formed. The major phase in the deposits agreed usually with that thermodynamically predicted based on the work of Lay (8) who described a graphical method for representing the condensed phases present in the deposit for any Mg:V ratio and for temperatures and equilibrium  $SO_3$  pressures of interest in combustion turbines. It was found in our study that the presence of major  $MgSO_4$  in the surface of a deposit was sensitive to the substrate temperature and not the local gas temperature even at the gas/deposit interface. It is interesting to note that the phase  $Mg_3V_2O_7$  was not detected in



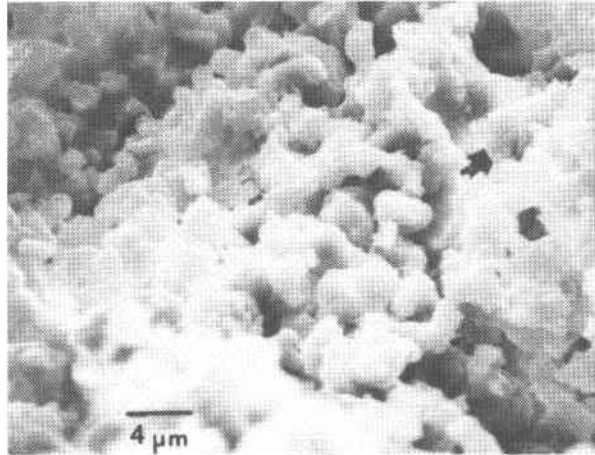
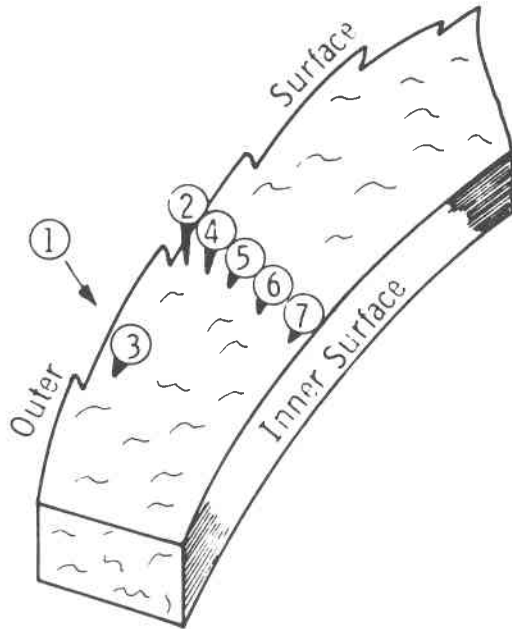
Area 1: Vane pressure side  $\text{MgSO}_4$ ,  $\text{Mg}_3\text{V}_2\text{O}_8$  and  $\text{V}_2\text{O}_5$ .



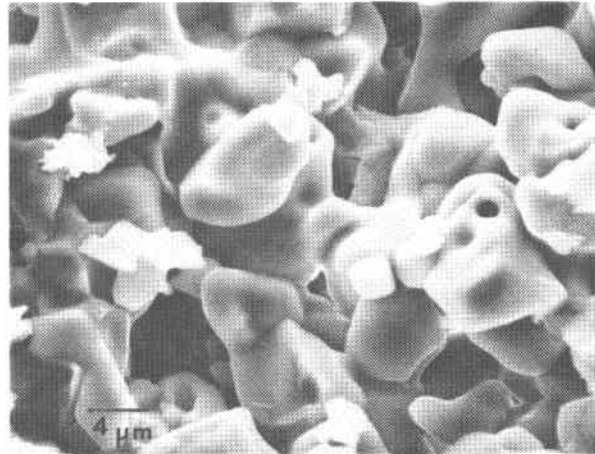
Area 5: Vane pressure side  $\text{MgSO}_4$ ,  $\text{Mg}_3\text{V}_2\text{O}_8$  and  $\text{MgO}$ .

Figure 2. Areas analyzed on cross-sectional surfaces of deposit from Unit 1-1 vane pressure side.

any of the deposits where it is predicted to be stable. Possibly this phase was not detected because the vanadium content of these lower temperature deposits ( $\sim 1550^\circ\text{F}$  [ $843^\circ\text{C}$ ]) was too low. The phase  $\text{Mg}_3\text{V}_2\text{O}_8$  was detected where the vanadium averaged 10 w/o but at the lower temperatures the deposits only had 0.3 w/o V. The detection of  $\text{V}_2\text{O}_5$  by X-ray diffraction was due to condensation on the shutdown cycle as well as condensation in deposits formed at very low temperatures ( $\sim 1300^\circ\text{F}$  [ $704^\circ\text{C}$ ]).



Area 2: Vane suction side  $MgSO_4$ ,  $Mg_3V_2O_8$  and  $MgO$ .



Area 5: Vane suction side  $Mg_3V_2O_8$  and  $MgO$ .

Figure 3. Areas analyzed on cross-sectional surfaces of deposit from Unit 1-1 vane suction side.

Hot Corrosion Attack. The original intent of this field study was to determine any potential differences on hot component service between combustion turbine operation with heavy and distillate fuel. Important to note is that the heavy fuel fired machines operated on heavy fuel approximately one-fourth of the test time and distillate fuel for the remainder. It would be expected then that the heavy fuel fired components would exhibit hot corrosion features similar to the all-distillate fired parts.

TABLE 10  
Heavy Fuel Deposits Associated with Different  
Component Temperatures

Component	Estimated Surface Temp. (°F)	Phases		
		$MgSO_4 \cdot 6H_2O$	MgO	$Mg_3V_2O_8$
Combustor				
Ring 1	1350	major	trace	pos. trace
Ring 2	1500	low minor	major	minor
Ring 3	1450	major	low minor	trace
Ring 4	1300	major	low minor	trace
Ring 5 & 5	1275	major	minor	trace
First Stage vane				
Inner shroud	1400	major	minor	low minor
Pressure side	1550	major	minor	trace
Suction side	1460	trace	major	minor
Fourth Row Blade	<1200	major	-	-

The degree of metal loss was used to gage corrosion attack. The degradation is the total metal thickness loss plus any affected superalloy microstructure. Measurements of metal loss were made relative to the minimum drawing contour dimensions.

Row 1 Vanes. All row 1 vanes (a cobalt-based cast superalloy) had some intergranular surface attack on the pressure airfoil and outer shroud surfaces, as listed in Table 11, but had only slight evidence of metal loss. There was some hot corrosion on all components without regard to fuel history.

Row 1 Blades. Some metal loss was observed on certain areas of all row 1 nickel-based wrought superalloy blade airfoils. Table 12 lists the observations from the four different units. Figure 4 shows the distribution of metal loss on blades from the two different units in the same PACE plant. There was slightly more hot corrosion attack on the distillate-fired units than the heavy oil-fired units. The corrosion morphology was of the type I with a depleted alloy region that contained chromium and titanium sulfides in advance of internal oxides.

TABLE 11  
Metal Loss of Row 1 Vanes

<u>Unit</u>	<u>Fuel Usage History (hrs)</u>		<u>Metallographic Observations</u>
	<u>Distillate</u>	<u>Heavy</u>	
1-1	3122	838	General corrosion (10 mils) and intergranular oxidation (10-20 mils)
1-2	3152	1122	General corrosion (10 mils), intergranular oxidation (10-20 mils), oxidation spikes (30 mils)
2-1	4240	0	General corrosion (10 mils), intergranular oxidation (10-20 mils), oxidation spikes (15 mils)
2-2	4252	0	Same as 2-1

TABLE 12  
Metal Loss of Row 1 Blades

<u>Unit</u>	<u>Fuel Usage History (hrs)</u>		<u>Metallographic Observations</u>
	<u>Distillate</u>	<u>Heavy</u>	
1-1	3122	838	Maximum of 3 mils of hot corrosion attack with some intergranular spiking on lower leading edge pressure side.
1-2	3152	1122	Similar to above.
2-1	4240	0	Maximum of 6 mils of hot corrosion attack with some intergranular spiking near base along leading edge.
2-2	4252	0	Maximum depth of 3 mils of hot corrosion attack at the leading edge at mid span.

Row 2 Blades. Table 13 lists the metallographic observations from both the heavy oil and distillate oil fired units. Figure 5 shows the type I attack with use of the distillate oil where the metal temperatures were above about 1400°F (760°C). In the region where the metal temperatures were generally below about 1400°F (760°C), there was type II attack as shown in Figure 6. This type of hot corrosion attack is

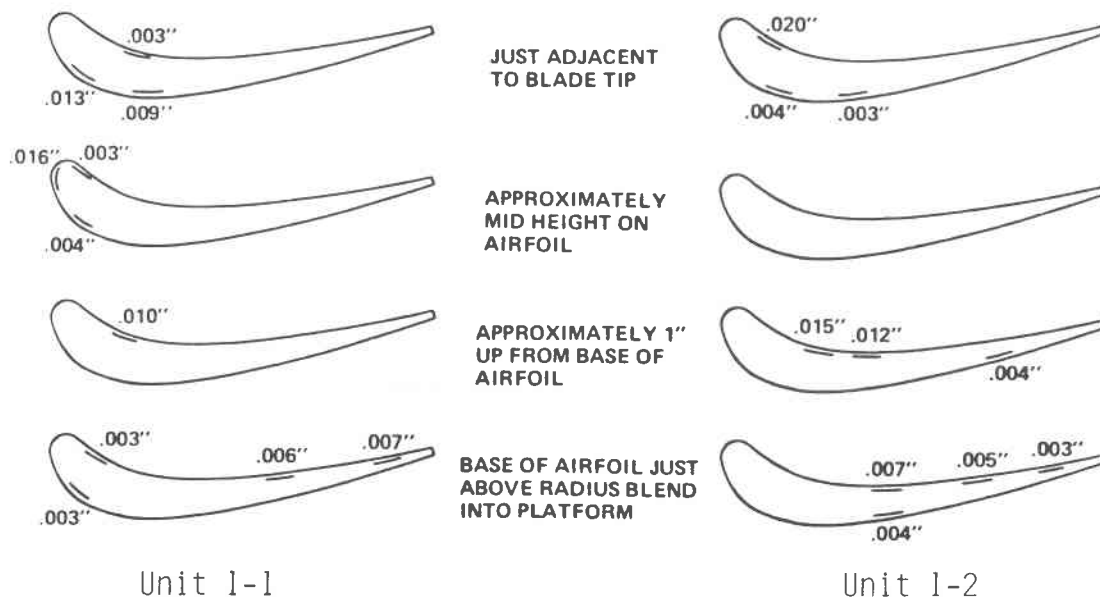


Figure 4. Metal stock losses of row 1 blades from both units in the same combined cycle plant. Measurements made on basis of minimum wall thickness tolerances. High temperature corrosion (type I).

TABLE 13  
Metal Loss of Row 2 Blades

Unit	Fuel Usage History (hrs)		Metallographic Observations
	Distillate	Heavy	
1-1	3122	838	Maximum of 2.5 mils of hot corrosion on the pressure airfoil at mid-span at the trailing edge. Some intergranular attack.
1-2	3152	1122	Similar to 1-1.
2-1	4240	0	Maximum of 2 mils of hot corrosion at leading edge at mid-span. Type II attack with intergranular attack to a maximum of 3 mils along trailing edge.
2-2	4252	0	Similar to 2-1.

characterized by a layer-type scale that contains a (Ti-Al)-rich sulfide layer at the scale/metal interface. This type of attack has been reported in other land based turbines (9). Slight variations in corrosion penetration between the residual

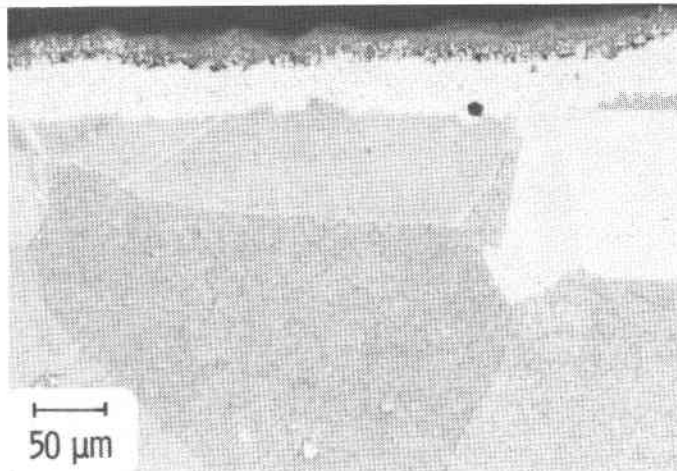


Figure 5. Corrosion microstructure on nickel-based superalloy blade at leading edge, mid-airfoil height. Row 2 blade from Unit 2-1 (4240 hours on distillate fuel).

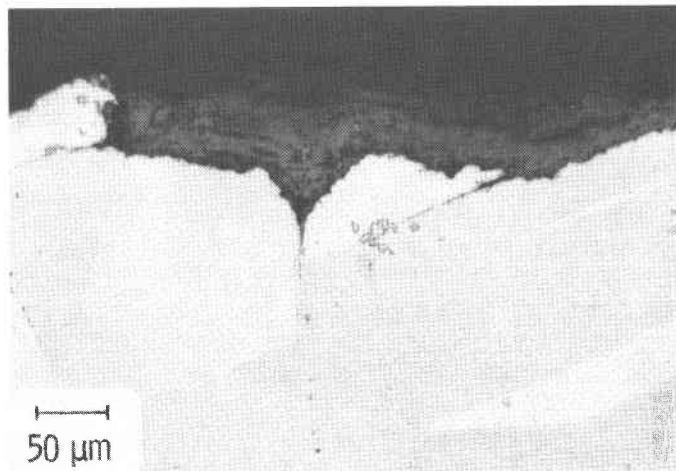


Figure 6. Low temperature (type II) corrosion microstructure on nickel-based superalloy blade near airfoil platform radius. Row 2 blade from Unit 2-1 (4240 hours on distillate fuel).

versus distillate run components can be attributed to water washing of the heavy oil-fired machines that removes water soluble sulfates such as  $\text{Na}_2\text{SO}_4$  on a periodic basis, consequently reducing the amount of corroding sulfates. Magnesium additives also form a large volume of deposit that dilutes the corroding sulfates.



## CONCLUSIONS

As part of another program, fuel from the FP&L Putnam Plant was sampled periodically and in nearly all cases during the test period, as-fired, met the total sodium and potassium of less than 0.5 ppm fuel specification. There was no indication of sodium contamination from the washed and treated heavy fuel. While there is always some possibility that oil contamination contributed to the observed hot corrosion attack in all four units, the generally clean oil makes it likely that the source of the corrodants was the inlet air.

The compressor deposits toward the discharge end were enriched in Na and Zn relative to total Na and Zn available from external sources and since both of these elements were found in the turbine it is logical to assume that shedding of compressor deposits contaminated the turbine. Moreover, the easily hydratable double sulfates probably shed more readily during each daily duty cycle than the  $\text{Na}_2\text{SO}_4$ -rich high pressure stage compressor deposits. Hence, the alkali/alkaline earth ratios of the hot gas path sulfates may reflect the ratios of these elements in the mid range of the compressor.

The source of contaminants in the axial flow compressors was likely the plume from the nearby cooling towers. These towers used the brackish St. John river which is subject to recycle concentration. The ammonia-containing double sulfate in the low pressure end of the compressor may have had a role in the formation of the readily hydratable sodium-containing double sulfates in the mid range of the compressor.

The deposits formed in the turbines, as a result of heavy fuel use with a magnesium additive consisted of various proportions of  $\text{MgSO}_4 \cdot 6\text{H}_2\text{O}$ ,  $\text{MgO}$  and  $\text{Mg}_3\text{V}_2\text{O}_8$ , depending on the temperature of the substrate rather than the local combustion gas temperature. The compound  $\text{Mg}_2\text{V}_2\text{O}_7$  was not detected even though it is predicted thermodynamically at temperatures below 1550°F (843°C).

Some indication of hot corrosion attack, types I and II, was found in all of the combustion turbines. The type II corrosion attack was in cooler regions of the blades where the temperature was lower than about 1400°F (760°C). Associated deposits were  $\text{Na}_2\text{SO}_4$ ,  $\text{CaSO}_4$ ,  $\text{MSO}_4$  (M is Co, Mg, Zn) and  $\text{Na}_2\text{M}(\text{SO}_4)_2$  (M is Co, Mg, Zn). The corrodants were derived from ingestion of contaminated mist from the adjacent cooling towers through the turbine compressors. Corrosion attack due to vanadium compounds in the heavy fuel fired machines was nil, which indicates that a heavy fuel oil is satisfactory for use in combustion turbine plants.

## ACKNOWLEDGMENTS

Part of this study was supported by the Electric Power Research Institute as Research Project 1079-2. We thank the personnel at the Florida Power and Light Company for their cooperation. The following Westinghouse personnel provided vital contributions to the content of this paper:

- T. A. Manion for the X-ray diffraction analyses and C. W. Hughes for the SEM-EDAX studies.
- G. Gidick and M. A. Fulmer for the chemical analyses.
- S. Y. Lee, C. Hussey, W. Hays, C. Rohr and M. A. Alvin for samples, details of turbine operation, calculations and helpful discussion.
- E. S. Obidinski and D. Gavin for the ambient sampling and analyses.
- H. D. Clements for the fuel analyses.

## REFERENCES

1. B. Mason, Principals of Geochemistry, Second Edition, John Wiley and Sons, Inc., New York, NY, 1958.
2. F. K. Lepple, P. E. Wilkniss and W. H. Cullen, "The Chemistry of the Marine Aerosol Near the Sea-Air Interface," Proceedings of the Third Conference on Gas Turbine Materials in a Marine Environment, Bath, U.K., 1976.
3. C. Frazier et al., "Status of Marine Gas Turbine Inlet Systems-Development Program," *ibid.*
4. D. L. Keairns et al., "Corrosion/Deposition in Fluidized Bed Combustion Power Plant Systems," Ash Deposits and Corrosion Due to Impurities in Combustion Gases, R. W. Bryers, Editor, Hemisphere Publishing Corp., Washington, DC, 1978.
5. N. S. Bornstein and M. A. DeCrescente, "Deposition - Hot Corrosion in Gas Turbine Engines," ASME Publication 81-GT-153, March 1981.
6. E. M. Levin, C. R. Robbins and H. F. McMurdie, Phase Diagrams for Ceramists, The American Ceramic Society, Inc., Columbus, OH, 1964.
7. T. A. Urbas and L. H. Tomlinson, "Formation and Removal of Residual Fuel Ash Deposits in Gas Turbines Formed at Firing Temperatures Below 982°C (1800°F)," Ash Deposits and Corrosion Due to Impurities in Combustion Gases, R. W. Bryers, Editor, Hemisphere Publishing Corp., Washington, DC, 1978.
8. K. Lay, "Ash in Gas Turbines Burning Magnesium-Treated Residual Fuel," ASME Paper No. 73-WA/CD-3, 1973.
9. C. J. Spengler, "Characterization of Corrosion Attack of Superalloys in Combustion Turbines in the Temperature Range 600-760°C (1110-1400°F)," Superalloys 1980, American Society of Metals, Metals Park, OH, 1980.

Paper presented at the EPRI/DOE 2nd Conference on Advanced Materials for Alternative Fuel-Capable Heat Engines, Monterey, CA, August 1981.

THE HIGH-TEMPERATURE COMBUSTION OF RESIDUAL FUEL OIL -  
SOME DEPOSITION PRODUCT CONSIDERATIONS

G. A. Whitlow, S. Y. Lee, P. R. Mulik, R. A. Wenglarz  
Westinghouse Research and Development Center  
Pittsburgh, Pennsylvania 15235

T. P. Sherlock  
Combustion Turbine Systems Division  
Concordville, Pennsylvania 19331

A. Cohn  
Electric Power Research Institute  
Palo Alto, California 94303

ABSTRACT

As traditional combustion turbine fuels such as natural gas and distillate oil become less abundant and more costly, the use of alternatives such as lower-grade oils and coal-derived products will intensify. There is some concern that the higher levels of impurities in these future fuels may well lead to enhanced corrosion and/or deposition of hot gas path components, resulting in less efficient machines. A joint Westinghouse/Electric Power Research Institute (EPRI) program, therefore, was initiated, whose objective was to develop information on operational and materials considerations associated with the combustion of residual fuel oil and coal-derived liquids in utility gas turbines. In this paper data on corrosion and deposition effects from the combustion of washed and treated residual oil are described and interpreted in the light of next generation machines operating at high gas temperatures [2300°F (1260°C)]. Information is presented on the nature and extent of these effects and their implications with respect to deposition mechanisms and subsequent turbine maintenance requirements.

INTRODUCTION

The deposition of combustion products from ash-bearing fuels, such as residual fuel oil and coal-derived liquids, may impose such restrictions on the design and operation of utility gas turbines that lower efficiencies and power outputs will result. Deposition may cause the operating temperatures of both the combustion gases and the turbine metal component surfaces to be so limited that maintenance costs increase, and, hence, engine availability is reduced.

The burning of these nontraditional fuels in large utility gas turbines, and the consequences thereto, particularly with corrosion and deposition, resulted in the initiation of a test program between the Electric Power Research Institute (EPRI) and Westinghouse. Both residual fuel and coal-derived liquids are being studied in the program, with the data from the first two phases of the residual fuel studies having already been disseminated(1-3). The initial observations on coal-derived liquid presented at the recent EPRI-sponsored deposition workshop(3) will be supplemented with the data from the current test program when they are available.

Deposition and corrosion data for combustion turbine materials have been obtained through dynamic testing in pressurized passages. The threefold objective of this research program was to:

- Optimize metal component temperatures on the basis of corrosion/deposition considerations.
- Establish trade-offs between metal temperature, performance, maintenance, and reliability.
- Develop a predictive model for deposition rates in combustion turbines burning low-grade, ash-bearing fuel that is capable of integrating laboratory data and field experience.

In this paper we have emphasized tests 9 and 10 (see Table 1), conducted with residual oil at burner outlet temperatures representative of future machines [2300°F (1260°C)], where very severe deposition was noted. However, brief reviews are presented of the corrosion and deposition data from the first phase (tests 1 through 4), on washed and unwashed residual oil(1), together with data from the second phase (tests 5 through 8) which compared deposition behavior observed in washed residual oil and distillate doped to simulate washed residual oil(2,3). The deposition data from all phases of the program were modeled on the basis of inertial impaction and thermophoresis. Maintenance intervals were calculated from this model and proved to be consistent with current operating experience.

#### PRIOR WORK ON DEPOSITION FROM RESIDUAL OIL COMBUSTION

A recent survey conducted with users of over 100 combustion turbines burning residual or crude oil(4) concluded that improperly washed or inhibited fuel or impurities in the inlet air were responsible for the hot gas path corrosion observed. Burning properly treated residual fuel, however, still presents problems with respect to deposition. The major means now available to restore full power and efficiency after deposition has occurred is to wash the turbine with water, but

Table 1  
SUMMARY OF TEST CONDITIONS

Test	Specimen <sup>a</sup> Material	Gas Temp., °F(°C)	Metal Temp., °F(°C)	Fuel and Additive	Exposure Time, h	Weight Gain, g	Deposition Rate, mg/h	Maximum Deposit Thickness	
								mil	mm
1	U	2000 (1093)	1100 (593)	Unwashed residual	20	0.45	22.5	10.6	0.27
						0.55	27.5	14.4	0.37
2	U	2000 (1093)	1350 (732)	Unwashed residual	20	0.06	3	6.1 <sup>b</sup>	0.16
						0.02	1	5.0 <sup>c</sup>	0.13
3	U	2000 (1093)	1350 (732)	Washed residual with Mg additive	10	0.30	30	9.0	0.23
						0.32	32	9.0	0.23
4	U	2000 (1093)	1600 (871)	Washed residual with Mg additive	10	0.14	14	3.4	0.09
						0.13	13	3.5	0.09
5	U	1900 (1038)	1250 (677)	No. 2 distillate with std. dopant	20	1.21	60.5	26.0	0.66
						1.20	60	27.6	0.70
6	U	1900 (1038)	1350 (732)	Washed residual with Mg additive	17.5	0.30	17.1	10.0	0.25
						0.23	13.1	5.5	0.14
7	U	1900 (1038)	1350 (732)	Washed residual with Mg additive	20	0.58	29.1	8.2	0.20
						0.43	21.4	9.7	0.25
8	U	1900 (1038)	1350 (732)	No. 2 distillate with zero Ca dopant	20	0.45	22.6	25.0 <sup>d</sup>	0.64
						0.56	28.1	55.5 <sup>d</sup>	1.41

<sup>a</sup>Duplicate specimens were tested; those denoted as U and I were Udimet 500 and IN-738, respectively; the (C) suffix denotes specimens coated with LDC-2E. For test 10 materials were I(IN-738), E(ECY-768), and H(Haynes 188).

<sup>b,c</sup>Metal recession of <sup>b</sup> 5.0 and <sup>c</sup> 24.5 mil was also reported.

<sup>d</sup>These represent high points in the deposit - typical thicknesses were of the order 1-5 mil.

Table 1 (Cont'd)

Test	Specimen <sup>a</sup> Material	Gas Temp., °F(°C)	Metal Temp., °F(°C)	Fuel and Additive	Exposure, Time, h	Weight Gain, g	Deposition Rate, mg/h	Maximum Deposit Thickness	
								mil	mm
9	I	2300 (1260)	1350 (732)	Washed residual with Mg additive	60	1.50	25	35.0	0.89
					106	1.79	16.9		
					150	1.07	7.1		
	I (C)	2300 (1260)	1350 (732)	Washed residual with Mg additive	60	1.04	17.3		
					106	0.98	9.2		
					150	0.86	5.7		
10	I I E E H H	2300 (1260)	1600 (871)	Washed residual with Mg additive	300	9.18	30.6	800 <sup>e</sup>	20.3 <sup>e</sup>
						12.22	40.7	1187	47.5
						5.07	16.9	483	12.3
						5.70	19.0	515	13.1
						8.70	29.0	850	21.6
						2.50	8.3	264	6.7

<sup>a</sup>Duplicate specimens were tested; those denoted as U and I were Udimet 500 and IN-738, respectively; the (C) suffix denotes specimens coated with LDC-2E. For test 10 materials were I(IN-738), E(ECY-768), and H(Haynes 188).

<sup>e</sup>Specimens in test 10 exhibited a range of deposit thicknesses - these are maximum measured values.

first the unit must be cooled down, rendering it unavailable for the duration of the procedure. Two additional considerations in the use of residual fuel are:

- The attention necessarily given to fuel handling, since the high fuel viscosity requires continuous heating and circulation
- Reduced combustor life.

This fuel burns with a more luminous flame than does diesel oil or natural gas, resulting in higher combustor wall temperatures and reduced combustor life. The consensus in the combustion turbine industry, however, is that burning residual fuels generates problems for which there are solutions and that the decision to burn residual oil will be one dictated by economic conditions.

Much of the available data in the open literature on the effects of residual fuel oil combustion on deposition consists of field experience from utility operation (4-7). Controlled experiments have been performed by several companies using simulated residual oil in the form of a doped distillate oil (8-11), but there is some question on the direct comparison of data obtained in this way and that from testing residual oil. Parametric studies oriented to gas turbine (as opposed to boiler) applications are not readily available. One example is the General Electric study on a deposition comparison of synthetic and real residual oil (10), which was for real residual fuel, unfortunately limited to firing temperatures  $\leq 1800^{\circ}\text{F}$  ( $982^{\circ}\text{C}$ ). Another example is the work of Nomura et al. (11) in which deposition from unwashed untreated, residual fuel oil was examined. Deposits were found to be principally sodium-vanadium-containing compounds. The current study, therefore, is designed to satisfy some of the deficiencies in the data base regarding the effects of the combustion of residual fuel oil. Some of the initial data were very encouraging (1), since corrosion was not evident with treated fuel, but deposition from treated residual oil was such that it necessitates better understanding if reliable, continuous turbine operation is to be attained (2). For future combustion turbines operating at higher gas temperatures, e.g.,  $\geq 2300^{\circ}\text{F}$  ( $1260^{\circ}\text{C}$ ), information on deposition considerations is unavailable.

Currently, Florida Power and Light (FPL) is burning residual oil in their 500 MW combined-cycle plant located in Palatka. An evaluation (5,12) of corrosion and deposition on various components from this plant concluded that the combination of fuel treatment, corrosion inhibitors, and metal surface temperature control can effectively inhibit vanadium-induced corrosion. Deposition of magnesium vanadate

and sulfate was not excessive and, indeed, FPL has now converted all four units to residual oil operation. The combustion turbines are operated at full power, and high starting reliability and overall availability have been achieved.

Although thousands of hours of successful operation with Westinghouse turbines has generated confidence, deposition will always be a concern when residual fuels are burned because of the addition of magnesium to control vanadium corrosion. The deposits formed can be removed by water washing the turbine, but only with the unit off line, with consequently reduced unit availability. On-line cleaning techniques such as nutshell injection and thermal cycling have been less effective than water washing in removing deposits, but they will continue to be developed to avoid the loss of availability.

#### MATERIALS AND EXPERIMENTAL TECHNIQUES

The washed residual oil used in our experiments was obtained from the Putnam station of FPL and was treated with KI-16 magnesium additive (supplied by the Tretolite Division of Petrolite) to inhibit vanadium corrosion. The magnesium-to-vanadium ratio was three on a weight basis. The two doped distillate fuels used in the second phase of this program(2), were prepared by blending given quantities of dopant (supplied by Tretolite) and No. 2 diesel fuel. Trace element analyses for both fuels are detailed in Table 2.

These fuels were burned in the Westinghouse Research and Development Center pressurized-turbine test passages (3 atm, abs), which utilize preheated compressed air in a 6 in. (15.24 cm) diameter, film-cooled combustor. Fuel is injected into the primary combustion zone and burned with compressed air. Combustion gases are then mixed with secondary cooling air to attain the desired turbine inlet temperature. Downstream of the combustor exit thermocouples, the flow area is reduced and the gas velocity increased to ~600 fps (~183 m/s). In the tests conducted at gas temperatures of  $\leq 2000^{\circ}\text{F}$  ( $1093^{\circ}\text{C}$ ) (tests 1-8 in Table 1), duplicate test specimens, located ~24 in. (61 cm) from the combustor outlet, were exposed to the combustion gases. These cylindrical Udimet 500 alloy specimens [2 in. (5.1 cm) long x 1 in. (2.5 cm) diameter x 1/8 in. (3.2 mm) wall thickness] were cooled with ambient compressed air introduced from the top and instrumented with thermocouples in the specimen wall to measure metal surface temperature.

For the tests conducted at  $2300^{\circ}\text{F}$  ( $1260^{\circ}\text{C}$ ) (tests 9 and 10, Table 1), the standard combustor was shortened by eliminating the secondary combustion section and retaining only the film-cooled section. The portion of the passage between the combustor



Table 2  
FUEL TYPES AND TRACE ELEMENT ANALYSES, ppm

Fuel	Mg	Ca	V	Pb	Na	K	S*
Washed Residual Oil with KI-16 Magnesium Additive	255	0.9	85.0	0.5	3.0	0.2	0.67
Simulated Residual Oil							
(a) No. 2 distillate oil plus th standard dopant	171.9	5.9	57.3	--	0.6	--	0.33
(b) No. 2 distillate oil plus the zero-Ca-containing dopant	171.9	0	57.3	--	0.6	--	0.33

\*wt%

and the transition section and the test section was also cooled with air. The cooling airflow was adjusted to maintain the finned liner below a maximum temperature of 1300°F (704°C), while the gas temperature was maintained at 2300°F (1260°C). Figure 1 is a schematic of the modified passage that was used to increase from two to six the number of specimens exposed per test. Each test specimen was 0.5 in. (12.7 mm) in diameter x 2.75 in. (70 mm) long x 1/8 in. (3 mm) wall thickness and was instrumented with five thermocouples located at various distances from the top of the specimen within the wall to measure the metal temperature. The specimens were placed in two rows of a staggered configuration with a spacing of 1.20 in. (31 mm) center-to-center within a row and a 1.10 in. (28 mm) center line between rows to prevent contact between the thermal boundary layer and aerodynamic wakes. Nominal chemistries of the alloys used in the short- and long-term exposures are shown in Table 3.

Within a given test the number of shutdowns was a function of factors such as fuel procurement and equipment maintenance. The overall average metal surface temperature could be adjusted by changing the cooling airflow rate, but the temperature distribution within a specimen was dependent on the gas temperature pattern factor.

A water-cooled, isokinetic, retractable sampling probe was used to provide information on particulates in the gas stream and has been described elsewhere(2,3). The use of such in-situ gas stream testing has been shown to be of great importance in understanding the deposition/corrosion phenomena observed in this program.

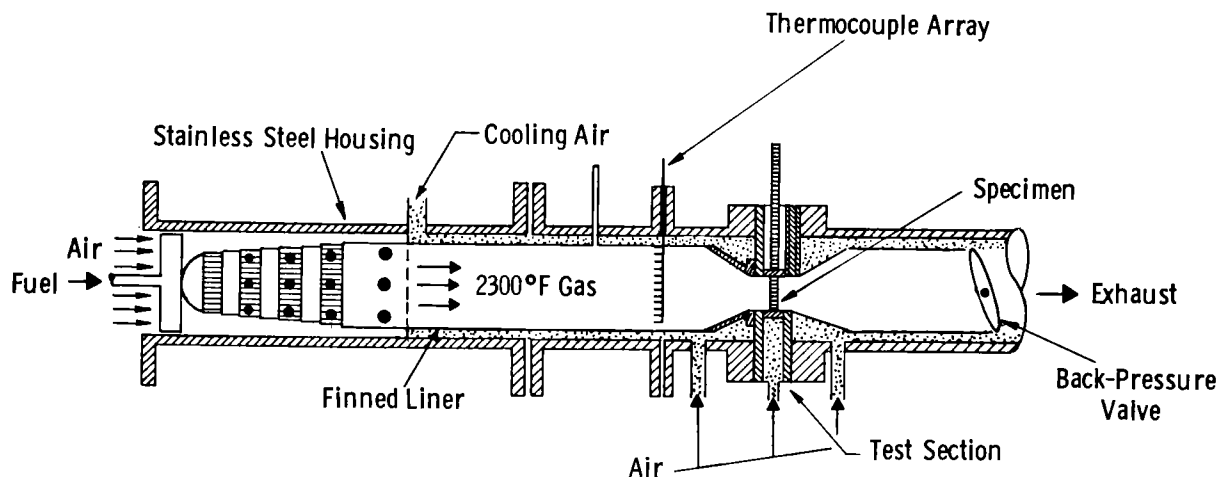


Figure 1. Air-Cooled Test Passage for 2300°F (1260°C) Tests

Table 3  
NOMINAL CHEMISTRIES OF SUBSTRATE MATERIALS

Material	Analyses, wt%						
	Ni	Co	Cr	Al	Ti	Mo	W
Udimet 500	54	19	18	3	3	4	--
IN-738	61	9	16	3	3	2	3
ECY-768	10	61	23	--	--	--	6
HA-188	22	42	22	--	--	--	14

Great care was necessary in evaluating the deposition products because of their fragility and their tenuous adherence to the specimens. After determining the weight change, we measured the deposit thicknesses at different locations on the specimens to relate deposition to gas impingement and flow perturbations. Both X-ray diffraction and scanning electron metallography were used to provide information on deposit chemistry and morphology. Selected specimens were examined metallographically for corrosion and deposition. A kerosene lubricant was used in preparing the sample to prevent loss of water/alcohol soluble components from the deposit. These experimental data on deposition were compared with theoretical predictions to permit calculation of turbine maintenance intervals and a comparison to field experience.

## RESULTS

Deposition data for the various phases of this study are shown in Table 1 for the sake of comparison. Although reference to the first two phases (tests 1-8) will be made in the subsequent sections of this paper, only the data from the long-term tests 9 and 10 will be presented and reviewed in detail.

The initial series were conducted to establish allowable operating limits (tests 1-4). Not surprisingly, the data showed that operation with untreated residual oil caused excessive corrosion as turbine metal temperatures exceeded 1000°F (538°C), but that operation with properly treated residual oil did not, even in the 1400 to 1600°F (760-870°C) range(1). Deposition of ash on the cooled test pin surfaces was shown to be a function of the difference between gas stream and metal temperatures and was explained by inertial impaction and thermophoresis. The latter is the movement of small particles in a gas, due to the influence of a temperature gradient, toward the cooler regions.

In a companion EPRI program with a distillate fuel doped to simulate a treated residual fuel(8), very heavy deposition was noted during a cascade test, so a decision was made to run the second series (tests 5-8, Table 1) in order to understand the cause of the excessive deposition. These tests clearly showed that a relatively small (~6 ppm) amount of calcium in the dopant promoted greater deposition and that the doped distillate may produce deposits different from those produced by residual oil. The in-stream, isokinetic, particulate probe was used to sample in-situ the constituents of the combustion gases at a gas temperature of 1900°F (1038°C) with residual fuel and doped distillates. Differences in the size distributions and types of particles generated with residual fuels (spheres), doped distillates without calcium (platelets), and doped distillates with calcium (fused, shapeless masses) were noted. The chemistry of the larger particles was also found to differ from that of the other particles, thus shedding considerable light on the differences in deposition rates noted in doped fuel versus residual oil tests. The deposition results from both the cascade tests and the test pins followed the model predicted by thermophoresis and inertial impaction(2).

The results from tests 1-8 accentuated the potential deposition problems in modern turbines with cooled blades and vanes and provided the impetus to study the problem for the next generation of turbines, which may utilize even more highly cooled components. Two, longer-term tests were conducted at a gas temperature [2300°F (1260°C)] representative of the next generation of combustion turbines.

## Test 9

In this test two IN-738 samples, one of which was coated with an LDC-2E\* platinum-containing, aluminide diffusion coating, were exposed to hot combustion gases in the pressurized test passage under the following design conditions:

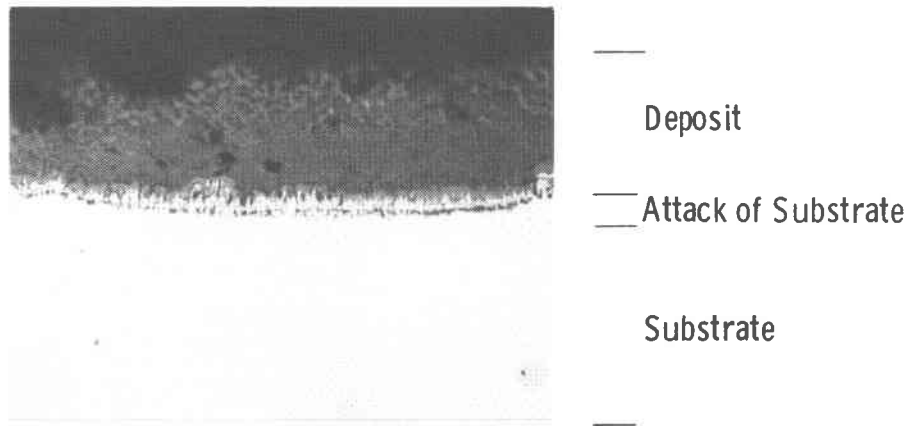
Average combustion gas temperature	2300°F (1260°C)
Average metal temperature	1350°F (732°C)
gas pressure	3 atm absolute
gas velocity	600 fps (~183 m/s)
exposure times	60, 106, 150 h

The surface of the two specimens after 150 h exposure to the hot combustion gases exhibited large amounts of both fine powdery and flaky deposits, and some spallation of the deposits occurred during the handling of the specimens for posttest characterization. The color of the deposits varied from off-white through green to black, and in some cases took the form of hard, buttonlike protuberances. No differences in the physical appearance of the deposits on the coated and uncoated samples were apparent. Maximum deposit thicknesses were observed on the front of the sample, i.e., the surface on which the hot gas stream impinged, but heavy deposition was also noted on the back of the samples. For uncoated IN-738 the maximum deposit thickness was 35 mils (890  $\mu\text{m}$ ) and for LDC-2E coated IN-738, 33.7 mils (860  $\mu\text{m}$ ). Average thicknesses for the uncoated specimen were 20 mils (510  $\mu\text{m}$ ) on the front and 11 mils (280  $\mu\text{m}$ ) on the back surface, and for the coated specimen 22 mils (560  $\mu\text{m}$ ) and 10 mils (250  $\mu\text{m}$ ). These thicknesses exceeded any measured in the preceding tests in this program.

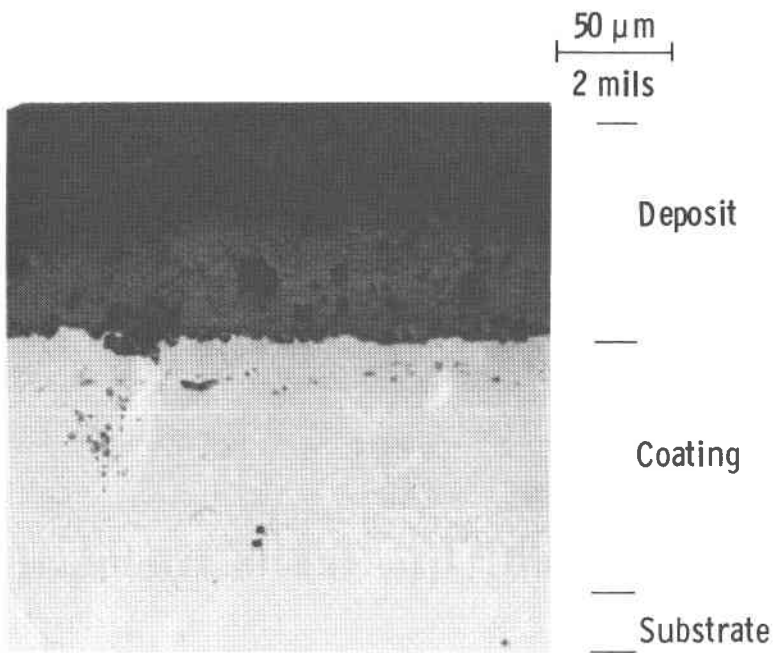
Deposition was monitored as a function of exposure time, and reference to Table 1 indicates that most of the deposition occurred early in the exposure (the first 60 h), with spallation and redeposition taking place during the subsequent exposure time. Deposition was greater by 20 to 30% on the uncoated sample. The morphology of the deposits and the degree of corrosion protection afforded to the IN-738 substrate by the aluminide coating is apparent from a comparison of Figures 2(a) and 2(b). Subsurface attack was seen on the uncoated IN-738 sample, together with a surface scale resulting from hot corrosion. No attack at the LDC-2E coating surface was observed except for one region at the bottom of the sample.

---

\*Trademark of TEW, West Germany, produced by Howmet Corporation.



(a) Uncoated IN-738



(b) LDC-2E Coated IN-738

50  $\mu\text{m}$   
2 mils

Figure 2. Metallographic appearance of cross-sections of the bottom front region of samples after exposure to hot combustion gases in the pressurized test passage under the following design conditions:

Test 9 - Average combustion gas temperature: 2300°F (1260°C)  
 Average metal temperature: 1350°F (732°C)  
 gas pressure: 3 atm absolute  
 gas velocity: 600 fps (183 m/s)  
 exposure time: 150 h  
 fuel: washed residual + KI-16 Mg

X-ray diffraction analyses indicated that the magnesium additive to the fuel resulted in the formation of MgO and  $Mg_3V_2O_8$  seen in earlier tests(1,2). No real difference was detected in the composition of the deposits on the two substrates tested in these analyses or in electron microprobe evaluations. The latter did confirm the observed hot corrosion attack of the uncoated IN-738 and the resulting subsurface layer of chromium and titanium sulfide (probably associated with oxide).

#### Test 10

Six specimens consisting of duplicates of the alloys IN-738, HA-188, and ECV-768 were exposed to the following conditions:

Nominal gas temperature	2300°F (1260°C)
Nominal metal temperature	1600°F (870°C)
Gas velocity	600 fps (183 m/s)
Gas pressure	3 atm absolute
Test duration	300 h (total)
Fuel type	Washed residual with KI-16 Mg additive

During each shutdown cycle the specimens were inspected visually. It was evident that heavy deposits built up during each period of continuous operation and that some spallation occurred after each terminal cycle. The appearance of the specimens at the end of the 300 h test is shown in Figure 3(a). The buildup of the deposits probably accumulated during the last 58 h of continuous operation. It was confined mostly to the front face of each specimen, taking the typical, dense, triangular wedge shape seen in cross section in Figure 3(b), because of the impingement of the gases on this face. The striated, glazed appearance of the side surface suggested impaction of molten particles; subsequent streaming of liquid deposit phases down the side surface resulted in an aerodynamically stable wedge shape. Colors ranged from a light gray-brown for the bulk of the surface, to an off-white, powdery deposit with some green areas on the back surface. The amount of deposition far exceeded that seen in previous runs using residual fuel oil and was probably a reflection of both the high gas temperature, the temperature difference, and the length of testing.

The weight gains (Table 1) were an order of magnitude higher than those measured in previous tests, but the overall (average over 300 h) deposition rates were comparable to previously measured rates from residual oil combustion(1,2). Because of the spallation occurring during shutdown, it may be more accurate to consider the weight gain data in Table 1 for this test as representing the deposition rates for the final 58 h of continuous operation.

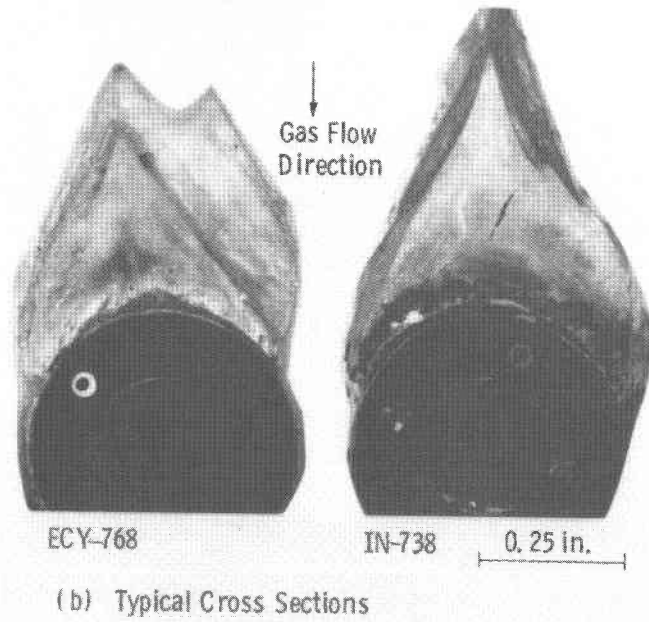
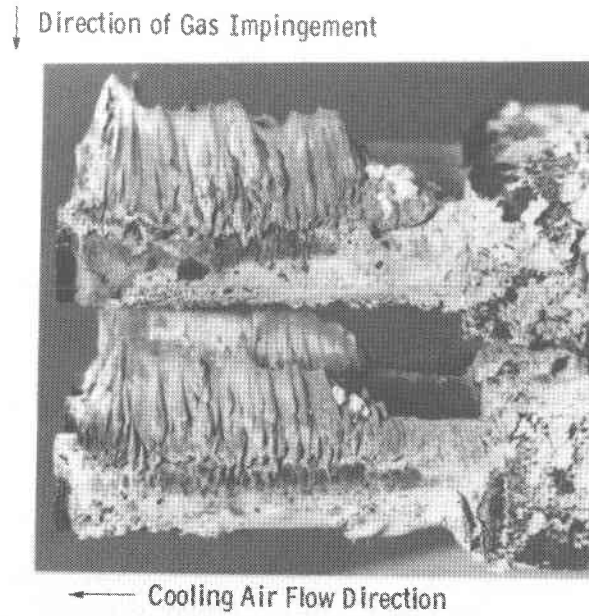


Figure 3. Deposition products on specimens exposed to hot combustion gases in the pressurized test passage during test 10

Deposits on the front surface reached peak thicknesses greater than 1 in. (25 mm) but on the back surface of these cylindrical specimens was typically 1/8 in. (3 mm) in thickness and reflected the comparatively stagnant air mass at this location.

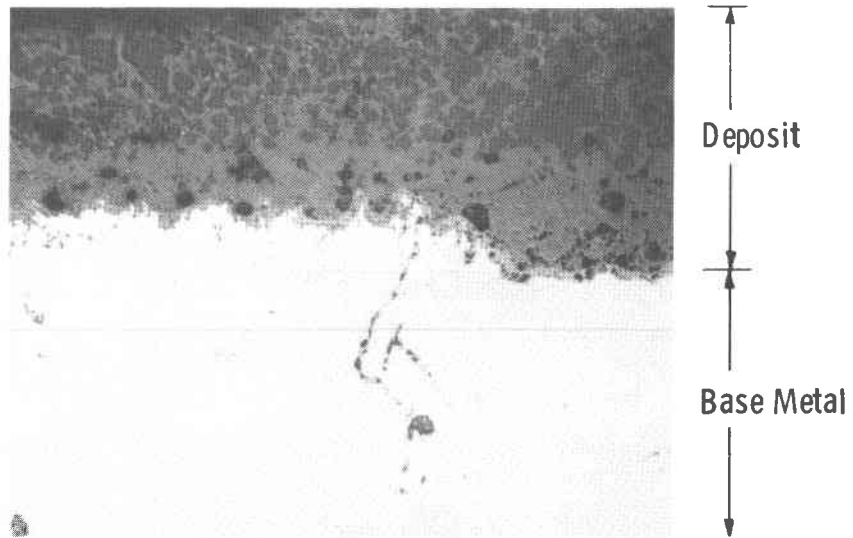
Examples of the microstructure, morphology, and composition of several deposit wedge cross sections are illustrated in Figures 3 through 6. Deposits retained the color range (pea green outside to white inside) previously noted, and porosity was generally very low, indicative perhaps of their previous high-temperature, molten stage.

In Figure 4(a), deposits on a cobalt alloy specimen (ECY-768) were accompanied by some subsurface sulfidation/oxidation and grain boundary attack at the substrate/deposit interface. A light gray reaction zone was present, on top of which was a particle-free region that in turn changed to a light gray matrix area containing darker gray particles. These particles varied in size and shape, but near the peak region of the deposit many were roughly spherical, in the size range of 10 to 30  $\mu\text{m}$ . Particle size determinations for this fuel, using the isokinetic removable probe device, were in the range of 4 to 12  $\mu\text{m}$ (2), but the gas temperature in the latter was only 1900°F (1038°C).

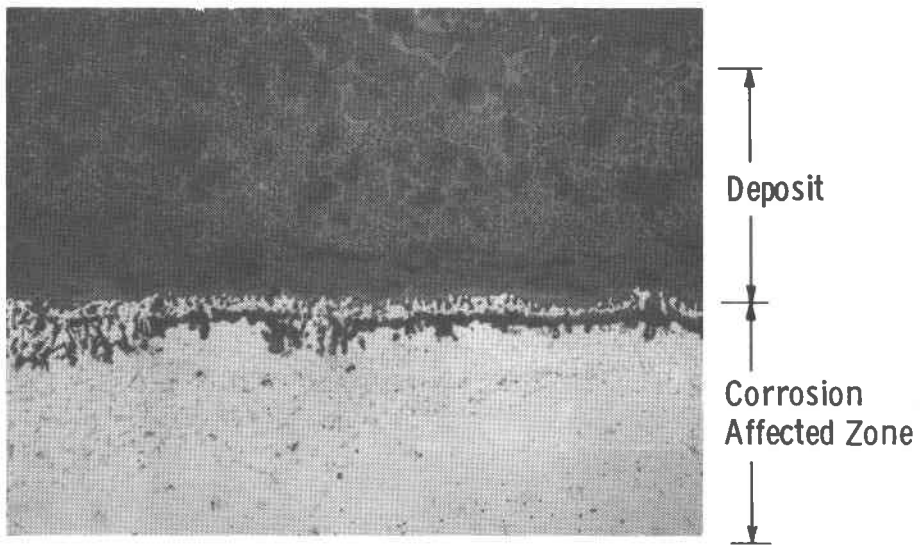
The deposit formed on the nickel alloy, IN-738, during this test is shown in Figure 4(b). Subsurface attack was again evident but to a greater degree than with the cobalt alloy. Oxidation of the substrate resulted in a corrosion-affected zone typically 4 mils (100  $\mu\text{m}$ ) in thickness. Selective attack occurred in other areas near the front of the specimen, where corrosion affected the microstructure to depths in excess of 10 mils (250  $\mu\text{m}$ ), most likely related to porosity from the casting process for the IN-738 alloy. The spherical morphology of the particles in the deposits can be confirmed by reference to Figure 4(b). Immediately above the surface oxide layer small particles were present, but in moving further away from the cooled surface of the metal, i.e., to a higher temperature regime of the deposit, the particle size increased.

Selected areas of polished cross sections of the cobalt alloys ECY-768 and HA-188 examined in the electron microprobe are shown in Figure 5. Irrespective of location or identity of the deposit, a particulate phase, generally darker gray in color and very rich in magnesium and nickel with some oxygen, was surrounded by a light gray phase rich in vanadium and chromium and some oxygen. The particulate phase was frequently spherical in shape and consisted of both 1 to 4  $\mu\text{m}$  particles [Figure 5(b)] and larger particles [Figure 5(a)]. It was most likely  $\text{MgO/NiO}$ , with the





(a) Unetched ECY-768



(b) Unetched IN-738

50  $\mu\text{m}$   
2 mils

Figure 4. Interface region between deposits and substrate for specimens exposed to hot gases in test 10

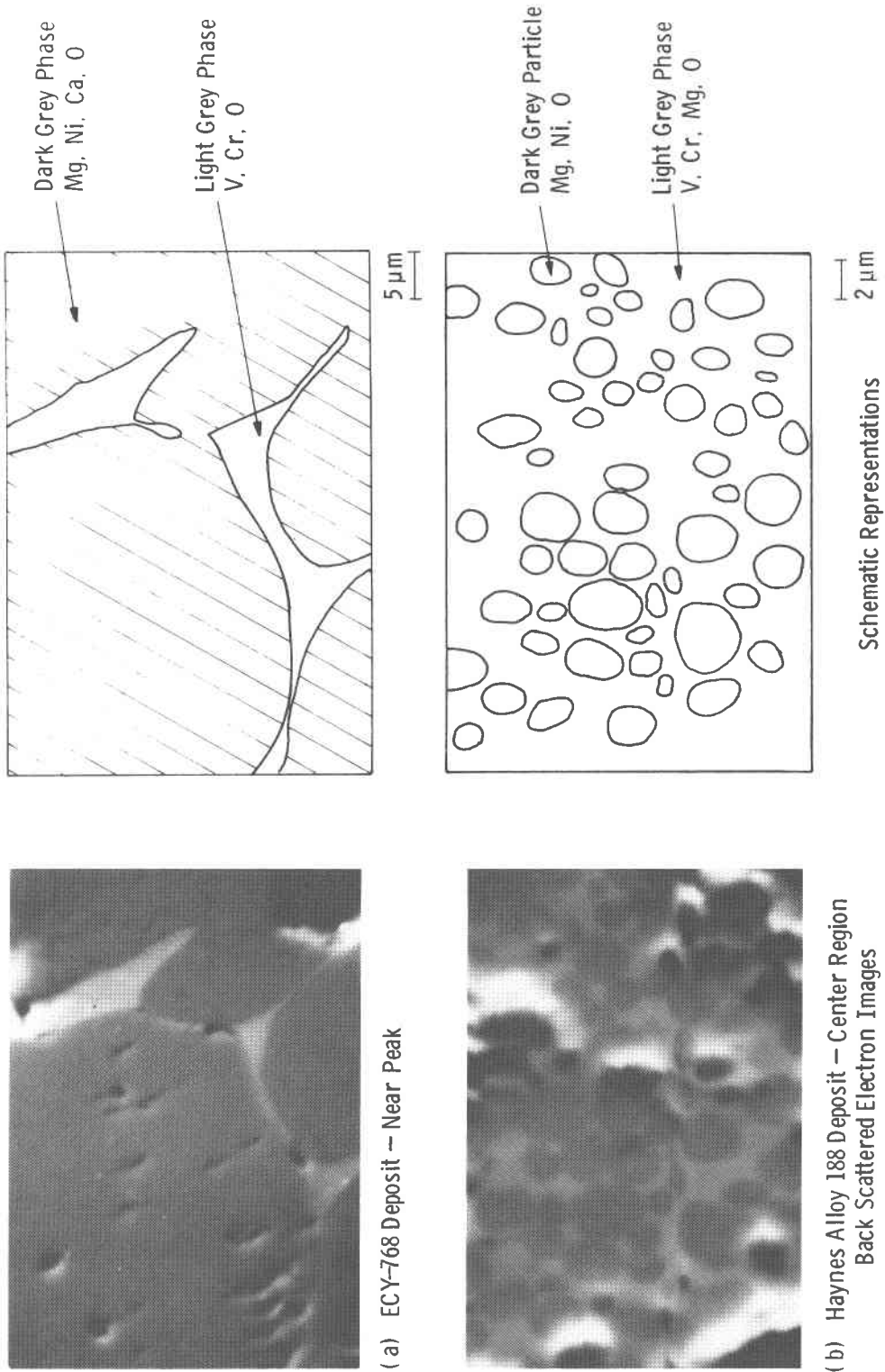
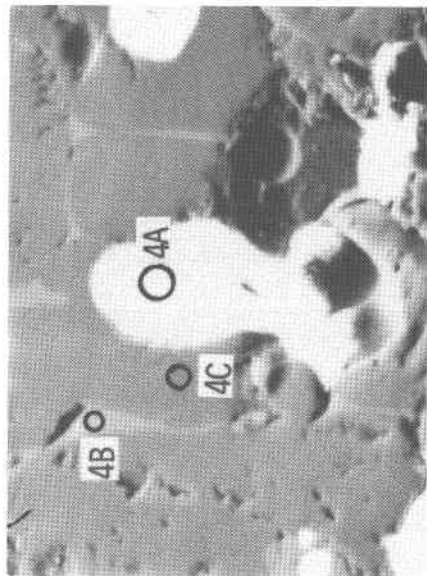
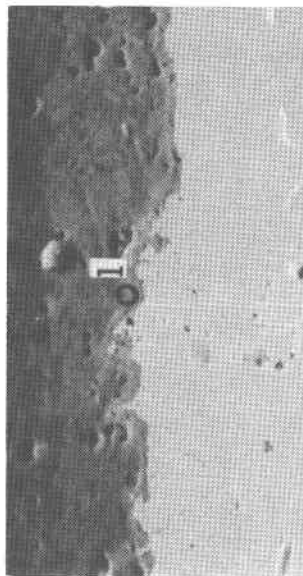


Figure 5. Electron microprobe data from polished cross sections of the deposits formed on alloy specimens exposed to hot combustion gases in test 10 (washed residual oil with KI-16 Mg additive)



Near Top of Deposit Wedge



Deposit/Substrate Interface

Major SEM-EDAX Analyses (w/o) \*

Analyzed Area	Mg	V	Cr	Si	S	Cl	Ni
4A, White Phase	26.7	17.7	5.2	23.7	3.9	4.2	6.7
4B, Light Grey (Glue) Phase	28.3	71.0		0.6			
4C, Darker Grey Phase	87.2			3.8			9.0

1, Grey Layer at Interface

2.3 0.7 95.7 1.3

Nominal ECY-768 Composition: 61 Co, 23 Cr, 10 Ni, 6 W

25 μm

\* Analyses do not include eg. Oxygen and Elements of Atomic Number < 11

Figure 6. Microstructure and analyses of selected areas of the deposit formed on an ECY-768 specimen exposed to hot combustion gases during test 10.

interstitial light gray phase a mixture of  $V_2O_5$ ,  $Mg_3V_2O_8$ , and V/Cr/Mg spinel. Identifying an exact phase was difficult because of the proximity of the oxygen  $K_\alpha$  absorption peak and the vanadium  $L_\alpha$  absorption peak.

The principal constituents of these deposits as identified by X-ray diffraction were MgO and  $Mg_3V_2O_8$ . The presence of  $MgSO_4$  on cooler regions of the specimen holder was thought to be related to the temperature of the deposit, on which fresh material was laid down, because at  $\sim 2055^\circ F$  ( $\sim 1120^\circ C$ ) the sulfate decomposes to the oxide. On the specimen holder, for example, where temperatures were less than  $2055^\circ F$  ( $1120^\circ C$ ), there were areas covered with a heavy white powder, the principal constituent of which was  $MgSO_4$ .

Energy dispersive analysis (SEM/EDAX) information also was generated from polished cross sections of deposits and used to indicate trends, but not for quantitative interpretation, because of the normalization of the data and its limitation to elements of atomic number greater than sodium. The SEM/EDAX, the X-ray diffraction, and the electron microprobe data reviewed in conjunction with each other, however, have permitted us to determine the following data trends:

- Oxidation occurred near the metal surface, and a thin adherent layer of chromium oxide ( $Cr_2O_3$ ) was formed on the surface.
- The deposits consisted of individual and agglomerated particles with some limited porosity.
- These particles in many areas appeared to be surrounded by another phase, frequently in the interstices between adjacent particulates.
- The microstructural appearance suggested that at operating temperature the deposit consisted of a molten phase containing many particulates of other phases.
- Particle sizes in the deposit varied up to  $30\ \mu m$  in diameter.
- A region such as 4C in Figure 6, the dark gray phase, was an MgO particle.
- Magnesium vanadates were the other major constituent of the deposits; see, for example, the white phase (4A in Figure 6).
- Other constituents that may have been present were in the form of spinels containing iron, chromium, and probably magnesium and vanadium.

- The light gray phase located in the interstices between particles, termed the "glue phase" (area 4B, Figure 6), contained vanadium in excess of that required to form vanadates with magnesium or calcium and may be the low melting point [1243°F (672°C)] phase  $V_2O_5$ , which was the last constituent to solidify.
- Because of the presence of sulfur in some areas, some  $MgSO_4$  was probably present, but only in a limited quantity.

## INTERPRETATION OF RESULTS AND DISCUSSION

### Metallurgical Evaluation

Deposition effects have been heavily emphasized and corrosion effects assigned relatively less importance in this study. The data have confirmed this division in that deposition was a major consideration in all the tests, and corrosion of the test specimens was only of concern in the early, unwashed residual fuel tests and the long-term 2300°F (1260°C), test 10.

### Deposition Rates

The effects of the different fuels used and the various test conditions examined are summarized in Table 1. For comparison purposes only the respective deposition rates in mg/h have been determined, bearing in mind that uniform deposition probably does not occur, because spallation can continuously occur during operation and at shutdown. For the unwashed residual fuel tests deposition appeared to increase with increased temperature difference ( $\Delta T$ ) between the metal surface and the gas, probably because of increase in the particulate capture efficiency with the lower metal temperature(1). Interpretation in this case is complicated, however, by the observed metal recession in test 2. The same kind of  $\Delta T$  effect was observed for the short-term tests with residual fuel (test 3 and 4). For tests involving the combustion of doped distillate fuel (i.e., simulated residual oil), deposition rates were found to be dependent on the dopant chemistry(2).

For the longer-term tests, where the gas temperatures were  $\geq 300^\circ F$  (167°C) higher than the previous short-term residual fuel tests, a clear statement on the effect of time on deposition rate cannot be made. In test 9, for example, rates after 60 h were comparable to those of shorter-term tests. Over the longer term (150 h), however, the fact that lower rates were measured can be interpreted to mean that once a critical deposit thickness was reached, spallation ensued. In test 10 rates varied from 8 to 40 mg/h, but the average rate for the six specimens (24 mg/h) was comparable to that measured in shorter-term, lower-gas-temperature tests with

residual oil. It would seem reasonable, however, to suppose that the generally excessive deposition observed in test 10 resulted primarily from the high gas temperature, with a significantly higher liquid/vapor phase loading, even though this test experienced the longest continuous period of operation (58 h) prior to termination.

In any one test several planned shutdowns took place, which resulted in some deposit spallation. At this time, however, we cannot correlate deposition rates and continuous operating hours. In rationalizing this sequential operation, one can say that it approximates actual practice in a stationary gas turbine operating at peaking load. Future testing should address the question of deposition-spallation effects resulting from intermittent operation.

Table 1 for tests 9 and 10 provides some information on the influence of substrate chemistry on deposition. For both nickel-based and cobalt-based alloy specimens and for both coated and uncoated surfaces upon which particles were deposited, we noted no difference in the rate of deposition. The exception to this observation may be the relatively high deposition rate (35 mg/h average) for the IN-738 specimens compared to the other materials exposed in test 10. Our data, with this exception, tend to support the hypothesis that, after the initial deposit has formed, one could expect that the substrate composition would have no effect on the amount of deposit because subsequent deposition is occurring on a ceramic surface rather than on bare metal.

#### Deposit Characterization

The deposits in the short-term tests with both residual and simulated residual fuels were generally very loosely adherent to the substrate. Although samples were examined metallographically, we did not obtain information on individual particle sizes.

The combustion of residual fuel containing the magnesium additive produced both large (6-12  $\mu\text{m}$ ) and smaller (<2  $\mu\text{m}$ ) particulates in the gas stream at 1900°F (1038°C), and many of these probably ended up in the deposits subsequently examined on the specimens from test 6 and 7. The higher gas temperature test [2300°F (1260°C)] produced deposits containing particles predominately in two size ranges: 10 to 30  $\mu\text{m}$  and 1 to 4  $\mu\text{m}$ . Because liquid phases were possibly present in these deposits for significant time periods, the possibility of particle growth within the deposit, i.e., after deposition from the gas stream, should be considered.

Unfortunately, particulate capture experiments in the gas stream at 2300°F (1260°C) were outside the scope of this study, so we have no experimental confirmation.

### Analyses of Deposits

For the short-term, low-temperature tests X-ray diffraction confirmed that MgO was the major constituent deposited, with  $Mg_3V_2O_8$  and  $MgSO_4$  also present. These compounds developed from the reaction of the magnesium additive, the combustion air, and the fuel impurities, vanadium and sulfur. Other compounds detected included vanadium pentoxide ( $V_2O_5$ ), with a relatively low melting point [1240°F (671°C)], and a magnesium phosphate (probably originating from the dopant or the distillate fuel).

X-ray diffraction data from deposits in the 2300°F (1260°C) tests confirmed the presence of MgO and  $Mg_3V_2O_8$ , but no other phases, such as  $V_2O_5$  or  $MgSO_4$ , were indicated, suggesting that these other phases, if present, were below the limits of detection (~5-10% by weight).

### Interpretation of the Deposition Observations

In an attempt to gain a better theoretical understanding of phases present in these deposits, we refer to the work of Lay(13), which in a modified format is shown in Figure 7. The condensed phases to be expected under the conditions of test 10 ( $pSO_3$ :  $7.5 \times 10^{-5}$  atm; 30 psi; 0.7 wt% S in fuel) are seen to be MgO +  $Mg_3V_2O_8$ . This situation is probably only true for the surface of the deposit, where free access to the hot combustion gases containing  $SO_3$  is available. Because of the buildup in deposit thickness with exposure time and the insulating properties of the surface crust, there will be a temperature gradient through the deposit from the gas temperature of 2300°F (1260°C) at the surface of the deposit to 1600°F (870°C), the cooled metal temperature at the deposit/substrate interface. We assumed that cyclical deposition and spallation would occur but that the latter would be partial and incomplete after each cycle. Temperatures in the deposit center will fluctuate with the deposit thickness, but over a narrow range. Particles of magnesia and  $Mg_3V_2O_8$  will be found in the molten deposit below the surface of the deposit, and, as the temperature falls at the end of the test, the condensed phases may form along the lines indicated in the diagram taken from Sperenskaya(14) shown in Figure 8. From the SEM/EDAX data the ratio of atomic percentages of Mg/Mg + V for the several different areas examined has been tabulated in Table 4, along with the phases present at ambient temperatures based on the MgO- $V_2O_5$  equilibrium diagram of Figure 8. This diagram does not take into account the influence of the  $SO_3$  partial pressure. We can assume, however, that, below the deposit surface, phase

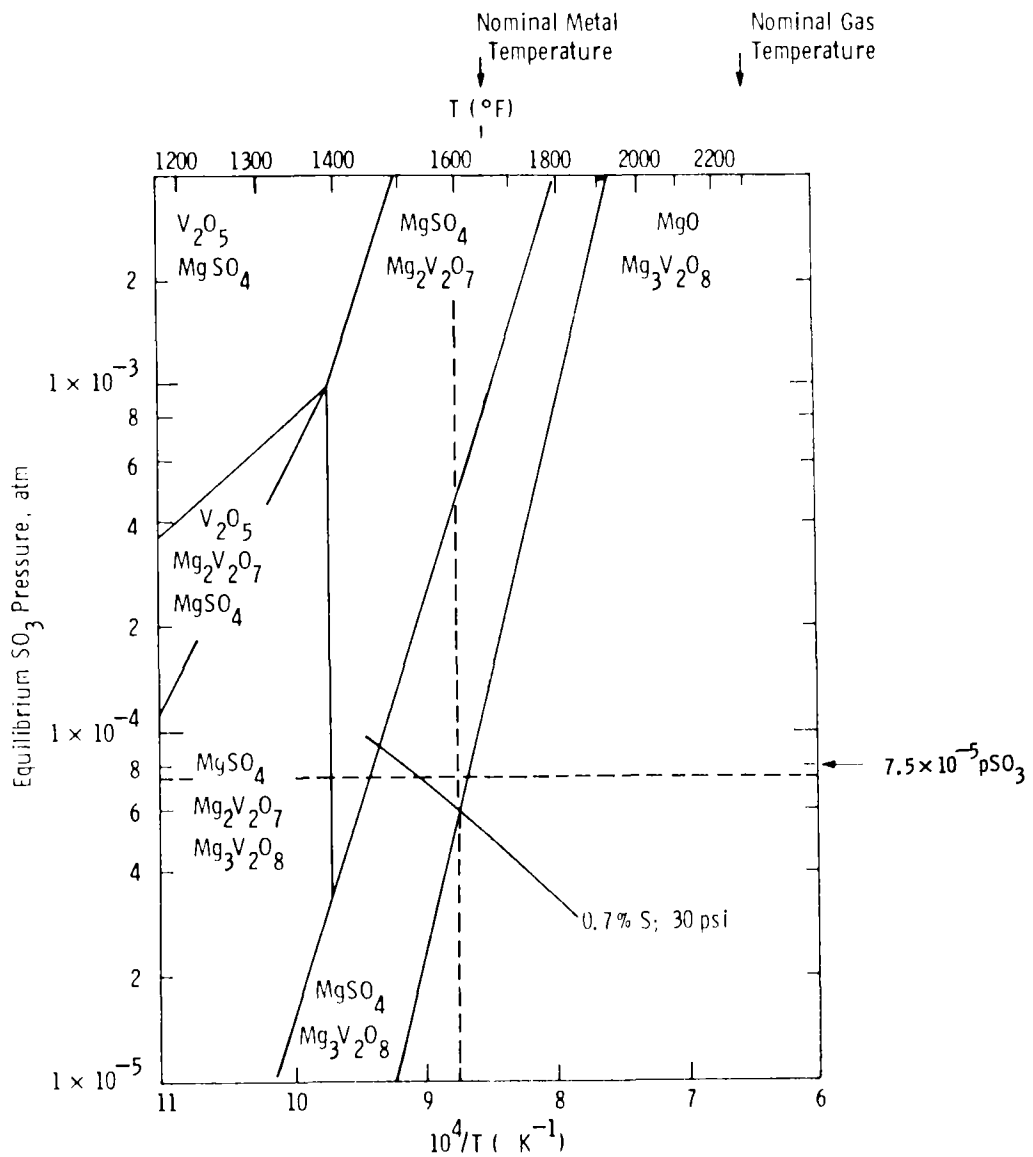


Figure 7. The condensed phases in the MgO-V<sub>2</sub>O<sub>5</sub> SO<sub>2</sub> system at SO<sub>3</sub> pressures and temperatures found in combustion turbines. Curved lines is pSO<sub>3</sub> trace for a 0.7% sulfur level in the fuel at 30 psi gas pressure (test 10). After K. W. Lay, Trans. ASME, J of Eng. for Power, 134, April 1974)



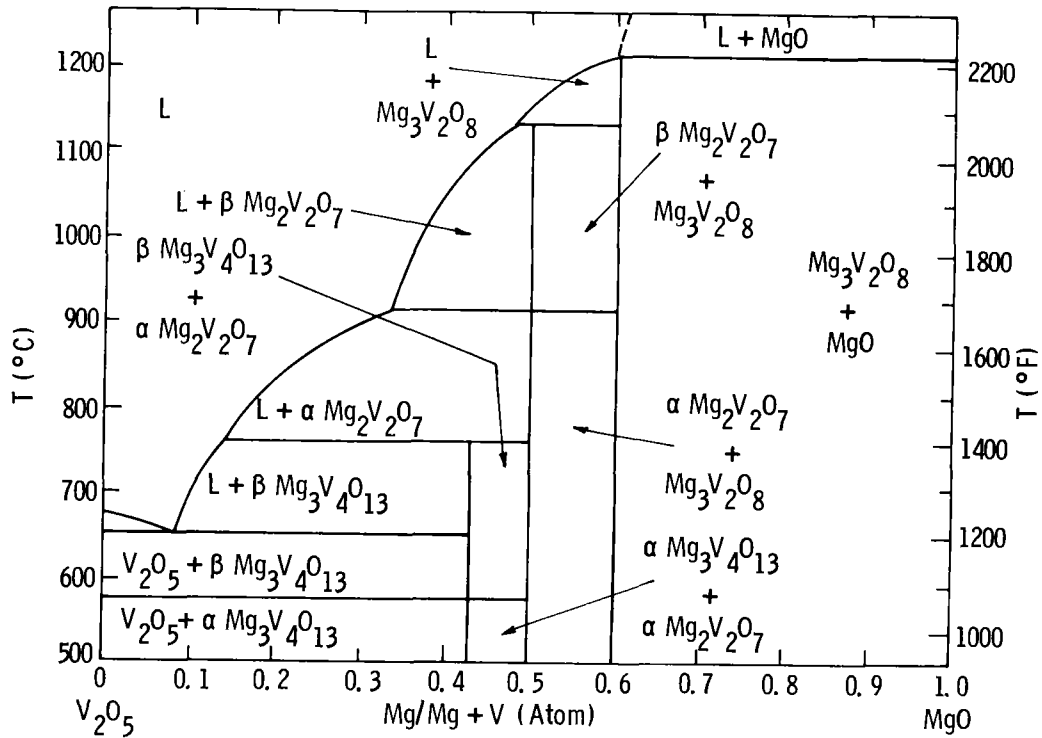


Figure 8. The MgO-V<sub>2</sub>O<sub>5</sub> phase diagram according to Sperenskaya(14)

Table 4  
DEPOSIT PHASE IDENTIFICATION FROM AN ECY-768  
SPECIMEN EXPOSED TO 2300°F (1260°C)  
COMBUSTION GASES IN TEST 10<sup>a</sup>

Area Analyzed In Figure 6	Mg/Mg+V Atom % <sup>b</sup>	Phases Present @ Ambient Temperature
4A White Phase	0.76	MgO + Mg <sub>3</sub> V <sub>2</sub> O <sub>8</sub>
4B Light Grey Phase	0.45	V <sub>2</sub> O <sub>5</sub> + Mg <sub>3</sub> V <sub>4</sub> O <sub>13</sub>
4C Darker Grey Phase	1.0	MgO

<sup>a</sup>From Sperenskaya(14) MgO-V<sub>2</sub>O<sub>5</sub> diagram (Figure 8).

<sup>b</sup>Obtained from SEM/EDAX information (Figure 6).

stability is not governed by the  $\text{SO}_3$  partial pressure. Thus, from Table 4 we can see that within the deposit there are particles of  $\text{MgO}$  and magnesium vanadates and, in the interstices, the light gray phase. The latter phase, which seems to act as a binder or glue phase, may be  $\text{V}_2\text{O}_5$  but may also be lower melting point magnesium vanadates.

In summary, particles of both  $\text{MgO}$  and  $\text{Mg}_3\text{V}_2\text{O}_8$  were probably present in the  $2300^\circ\text{F}$  ( $1260^\circ\text{C}$ ) gas stream and on the cooled metal surface [ $1600^\circ\text{F}$  ( $871^\circ\text{C}$ )] in the deposit. In the latter, they appear to be cemented together by a low melting point, V-rich phase (possibly  $\text{V}_2\text{O}_5$ ), which was a molten constituent of the deposit during the test. These factors are compatible with the formation of a hard, relatively dense deposit resulting from the combustion of this residual oil treated with a magnesium additive.

Characterization of the glue phase in the deposits and its neutralization may result in a reduction of stable deposition buildup, with associated reductions in blockage rates.

#### Issues Arising from the Deposition Observations

One question that has arisen from this study concerns the use of the magnesium additive with residual oil to control the adverse corrosion effects of the vanadium present as an impurity in the fuel. The relatively dense deposition products, particularly for test 10, suggest that conventional deposit removal methods may not suffice. In order to facilitate deposit removal from blades and vanes, it may be necessary to produce the fluffier deposits frequently observed with the combustion of a residual oil containing a silicon additive in conjunction with the magnesium. Florida Power and Light at their Putnam Station(5,12) were burning residual fuel oil containing only the KI-16 Mg additive used in this study. In peaking load operation they encountered no problems with deposit removal using periodic water washing of the turbine, but their gas temperature was only  $2000^\circ\text{F}$  ( $1093^\circ\text{C}$ ). Likewise, Florida Power Corporation at their DeBary plant reported excellent service: deposits spalled off during start-up, and the turbine thus required no water washing(15).

Another concern that may require attention as a result of the observation that  $\text{V}_2\text{O}_5$  may be present in the deposits, is the suitability of the accepted Mg/V ratio of 3. Apparently, even though the magnesium is present in excess of that required to combine with the vanadium impurity level, there is still free  $\text{V}_2\text{O}_5$  present that can act as a binder phase in these deposits. If  $\text{V}_2\text{O}_5$ , a relatively low melting point

constituent of deposits, can be completely combined with magnesium in the form of a vanadate or maybe in some other preferred form, then the so-called glue will be absent and deposit buildup may be reduced.

In this program, tests on doped No. 2 distillate fuel simulating residual fuel oil were run in order to compare them with the results from a parallel program on doped distillate fuel at Detroit Diesel Allison (DDA)(8). Considerable differences were noted in deposition behavior for simulated and real residual fuel, and a good simulation does not seem to have been achieved by the use of dopants(2). The fact that the deposition rate for the fuel containing the standard dopant was comparable to that for the residual fuel in short-term tests is fortuitous, because significant differences were noted in particle sizes and shapes in the particulate probe studies. Indeed, particle arrival rates are known to be sensitive to size and shape. The lack of good simulation with the doped fuels is in contrast to the data of Urbas and Tomlinson(10), who found that, at firing temperatures up to 1800°F (982°C), the chemical and physical nature of deposits from a synthetic fuel were the same as those from a real residual fuel oil.

#### Corrosion Observations

The nickel- and cobalt-based alloys exposed to hot combustion gases were not found to be significantly affected by corrosion when washed residual fuel containing the magnesium additive or the doped distillate fuel was used. In the long-term test with residual fuel, after 300 h exposure, the typical corrosion-affected layer was 4 mils (100  $\mu\text{m}$ ) in depth. The only exception to this was in the initial tests with unwashed, untreated fuel, where the vanadium impurity and the alkali metal content of the fuel most likely resulted in corrosion and  $\text{Na}_2\text{SO}_4$ -induced attack. No rapid corrosion was observed with metal temperatures  $<1000^\circ\text{F}$  ( $538^\circ\text{C}$ ), even in the absence of the corrosion inhibitor. In test 9, where the behavior of an LDC-2E-coated IN-738 and an uncoated IN-738, specimen was evaluated, the coating generally behaved satisfactorily. In summary, corrosion was not a problem in the test conducted with either washed residual oil or distillate doped to simulate residual fuel oil.

#### DATA EXTRAPOLATION TO UTILITY TURBINES

The data obtained during this test program, together with evaluations of the dominant deposition mechanisms, have enabled initial estimates to be made of deposit buildup rates and maintenance intervals for turbines burning washed residual oil treated with a magnesium additive.

## Deposition Mechanisms

Deposition buildup in combustion turbines depends on several types of mechanisms such as:

- Particle delivery to turbine surfaces
- Adherence and removal of particles delivered to turbine surfaces
- Gross detachment (spallation) of previously built-up deposits.

The primary mechanisms of particle delivery in turbines are inertial impaction, turbulent eddy diffusion, Brownian diffusion, and thermophoresis(16). The dominant delivery mechanism depends on particle sizes entrained in the turbine expansion gas. Inertial impaction dominates on vane and blade pressure surfaces for particle diameters larger than a few microns(17). Turbulent eddy diffusion tends to dominate for diameters of about 1  $\mu\text{m}$  down to a diameter that depends on the degree of vane or blade cooling. For highly cooled surfaces thermophoretic(18) delivery (which increases with the temperature differential between the gas and surface) becomes important for particle diameters perhaps as large as 0.5  $\mu\text{m}$ , while for uncooled surfaces Brownian diffusion begins to dominate in the 0.1 to 0.5  $\mu\text{m}$  particle diameter range. Once particles arrive at a turbine surface, deposit buildup depends on the balance of adherence forces versus removal forces on the particles at the surface. For hard particles adherence forces tend to be weak. Molten or semimolten particles, however, can adhere to vane and blade surfaces with attachment forces and deposit growth rates much greater than for hard particles. Finally, even should removal forces be insufficient to dislodge individual particles from turbine surfaces, forces and stresses can occur within the bulk deposit formed that can eventually result in spallation (gross deposit detachment), thereby restricting deposit net growth rates. These stresses can be caused by such factors as differential thermal expansion and chemical reactions producing volumetric changes in underlying deposit layers.

The above considerations suggest the difficulties in producing doped fuels to simulate deposition environments resulting from residual oils or other fuels. Not only must the elemental fractions of contaminants be reproduced in doped fuel, but the particles formed during combustion should also have the same size distribution and chemical composition with the same melting points as for the fuel being simulated. The differences in pin specimen deposition characteristics of the residual oil and doped (to simulate residual oil) distillate tests discussed earlier are not surprising, considering the differences in sizes, shapes, and chemistries of gas stream particles observed using the particulate probe(2).

Information from these particulate probe measurements and the delivery mechanism observations have helped to identify the primary modes of particle delivery to turbine surfaces for operation with residual oils. Particle probe measurements revealed particles predominantly 4 to 12  $\mu\text{m}$  in diameter, with some particles ranging in diameter up to 15  $\mu\text{m}$  and down to less than 0.1  $\mu\text{m}$ . Since most of the particulate mass is above a few microns in diameter, the bulk of the particles is expected to arrive on turbine surfaces (and the pin specimen tested) by inertial impaction. The small mass fraction in the size range smaller than a few tenths of a micron, however, where thermophoretic effects are significant, appears to affect deposition rates. Comparison of deposit buildup rates on the pin specimens for tests 1 through 8 in this program at 1900-2000°F (1038-1093°C) gas temperatures but with various specimen surface temperatures shows that deposition increases with gas/metal surface temperature differentials (see Table 1).

A plausible explanation may be that even though a small mass fraction of gas stream particles is in the few tenths of a micron and smaller size range, where thermophoretic effects are significant, those gas stream particles that are molten are predominantly in this size range. These smaller particles, delivered by thermophoresis, can then act as a molten "glue" to bond the larger, solid particles arriving by inertial impaction to test specimen (and turbine) surfaces. Apart from MgO, the major compound formed for residual fuels containing a magnesium inhibitor for vanadium is  $\text{Mg}_3\text{V}_2\text{O}_8$ , which has a melting point of about 2200°F (1204°C); smaller amounts of magnesium pyrovanadate ( $\text{Mg}_2\text{V}_2\text{O}_7$ ) and magnesium metavanadate ( $\text{MgV}_2\text{O}_6$ ) may be formed, with melting points of about 1700°F (927°C) and 1400°F (760°C), respectively(19). Low levels of  $\text{V}_2\text{O}_5$  (1204°F [671°C] melting point) may also occur in the gas stream because of incomplete reaction of the available vanadium with the magnesium. Any of these compounds could be the low mass fraction "glues" in the small size range, where the thermophoretic effects are significant. Vanadium pentoxide was detected in deposits following tests in this program. Whether the deposit bonding "glue" was  $\text{V}_2\text{O}_5$ , or a  $\text{Mg}_2\text{V}_2\text{O}_7$  or  $\text{MgV}_2\text{O}_6$  compound that decomposed during test cool-down, however, is uncertain. Further evidence for the above explanation is given in Figure 9, which indicates that deposition on test cascades and cylindrical specimens is correlated with the gas/metal surface temperature differential for gas temperatures below 2000°F (1093°C).

As indicated earlier, above a gas temperature of 2200°F (1204°C), not only the lesser mass fractions of  $\text{V}_2\text{O}_5$ ,  $\text{MgV}_2\text{O}_7$ , and  $\text{MgV}_2\text{O}_6$  are molten, but also the predominant orthovanadate,  $\text{Mg}_3\text{V}_2\text{O}_8$ . At these temperatures the bulk of the particles (other than MgO) in the size range above a few microns in diameter can be expected

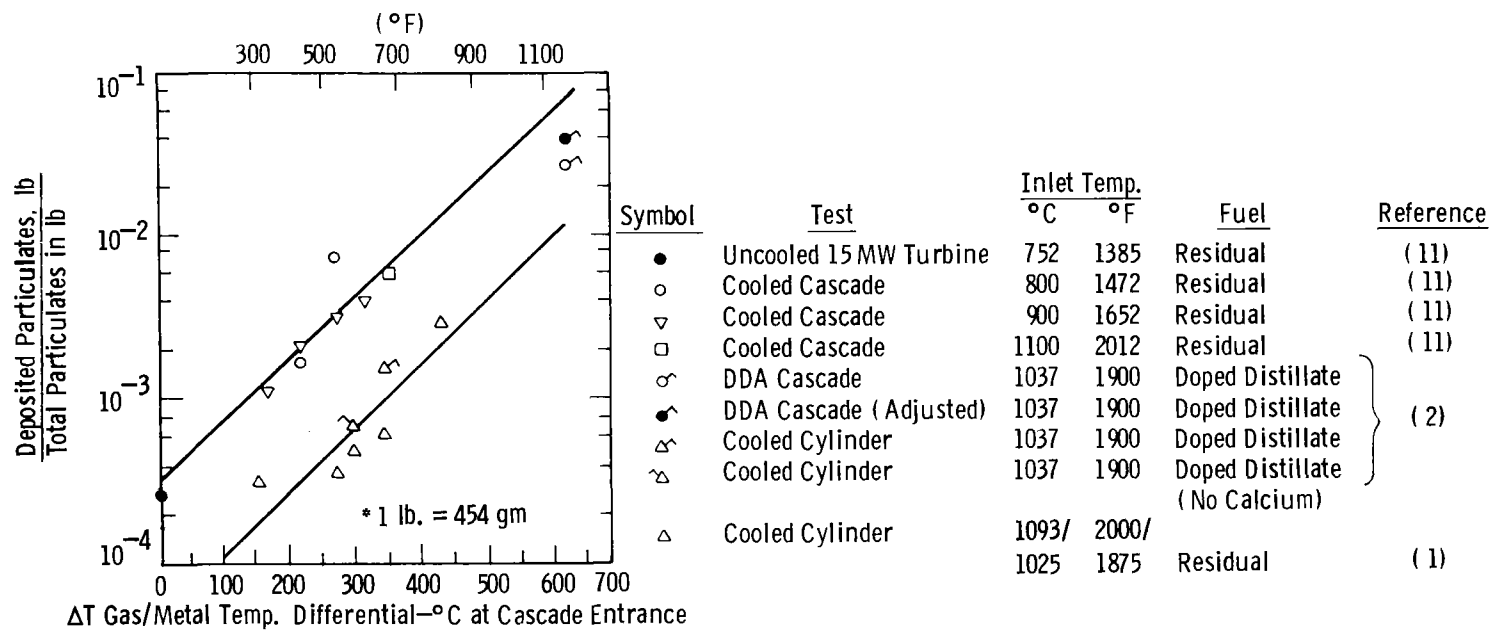


Figure 9. Deposition results on cascades and cylinders, after (1).

to be molten. While deposit buildup rates appear to be greatly influenced by thermophoretic delivery of small molten particles to turbine surfaces at gas temperatures lower than 2000°F (1093°C), deposit buildup rates are likely to be dominated by inertial impaction delivery of larger particles above a 2200°F (1204°C) gas temperature. Because of the much higher delivery rates (than in thermophoresis) due to inertial impaction for the much higher mass fractions of larger particles, turbine gas temperatures above 2200°F (1204°C) result in a potential for much higher deposit buildup rates than do lower temperatures.

This potential for high deposition rates, however, is greatly affected by the degree of particle cooling in boundary layers as they approach vane and blade surfaces. For increased surface cooling more particles of varying sizes are frozen before arriving on a turbine surface, resulting in fewer particles adhering to that surface. Consequently, at gas temperatures above about 2200°F (1204°C), increased surface cooling can decrease deposit buildup rates, while at lower gas temperatures increased cooling (perhaps down to somewhat lower than 1240°F [671°C]) can increase deposit buildup rates by increasing particle delivery due to thermophoresis. These trends have been observed in the magnesium-treated residual oil tests of this program (see Table 1). Further cooling of vane and blade surfaces to perhaps 100 to 200°F below the 1240°F (671°C) melting point of  $V_2O_5$  is expected to result in a rapid drop in deposit buildup rates. A surface temperature lower than the melting point of the lowest molten compound is required to freeze all of the arriving particles because of their short residence times in the cooled boundary layers and their thermal inertia. Initial deposit buildup, however, will result in an insulating layer, which will lower the tendency for arriving particles to freeze on impaction, resulting in accelerated deposition rates.

In addition to particle delivery and surface adherence factors, a third factor affecting net deposit buildup rates is spallation. Deposits formed on specimens in test 3 conducted at a 2000°F (1093°C) gas temperature and a 1350°F (732°C) specimen surface temperature exhibited a greater tendency to spall than did deposits formed in test 4 at the same gas temperature but at 1600°F (871°C) surface temperatures. On the other hand, a higher spallation rate in test 4 may be due to the thicker deposit. Similarly, deposits formed at a 2300°F (1260°C) gas temperature on 1350°F (732°C) specimen surfaces in test 9 were much more porous and fragile and appeared to experience greater spallation during test operation than did deposits formed in test 10 at the same gas temperature but at a 1600°F (871°C) surface temperature. In test 10 the molten nature of the deposits probably resulted in a denser, more securely attached deposit. These test results suggest that, for gas

temperatures representative of both current turbines (2000°F [1093°C]) and future, higher-temperature turbines (up to 2300°F [1260°C]), decreasing vane and blade surface temperatures may result in enhanced spallation. In fact, the data for both test 3 (2000°F [1093°C] gas) and test 9 (2300°F [1260°C] gas) with 1350°F (732°C) specimen surface temperatures may indicate the growth of deposits to a maximum thickness, after which further growth is prevented by spallation.

#### Deposition Model

A turbine deposition model is being developed, using information such as that described above concerning dominant residual oil deposition mechanisms. It will extrapolate the deposit buildup rates measured on the specimens during the tests in order to obtain estimates of deposit buildup rates and deposit removal maintenance intervals for utility turbines. The turbine deposition model described elsewhere (2) relates measured deposit buildup rates on the circular, cylindrical pin specimens (after proper adjustments for pressure and physical scale effects) to deposit buildup rates on stator vane throat regions, where flow blockage by deposits most degrades turbine performance. Turbine maintenance for deposit removal is assumed necessary when stator passage throat blockage results in 10% drop in power output for the flow-path geometry of a 10:1 pressure ratio turbine chosen for evaluation.

This modeling approach has been used to estimate maintenance intervals for turbines operating with washed residual oil treated with KI-16 magnesium additive. These turbines are:

- A current utility turbine with an inlet temperature of about 2000°F (1093°C) and first stator vanes cooled to about 1600°F (871°C)
- Future, high-temperature turbines with inlet temperatures exceeding 2300°F (1260°C) and first stator vanes cooled to 1350 (732) to 1600°F (871°C).

The estimated maintenance intervals, using data from tests 4, 10, and 9, respectively are:

- 580 hours for a current utility turbine with a 1600°F (871°C) stator vane surface temperature
- 25 to 250 hours for future, high-temperature turbines with 1350 (732) to 1600°F (871°C) stator vane surface temperatures.



The maintenance interval for current turbine operating conditions was determined in order to check the modeling approach projections with field experience. The projected 580 h interval agrees with the range of water-washing intervals from 200 to 1500 h determined in a survey(4) of turbine operators using residual and crude oils.

The above maintenance intervals do not consider long-term deposit spallation effects. For the high-temperature turbine with highly cooled stator vane surfaces, these spallation effects may be very important, as in test 9. Because of spallation, only very small deposit weight changes occurred after 60 h of test operation to termination of 150 h. Whether this spallation occurred during operation or during test shutdown and start-up is uncertain. If spallation occurred mainly during operation, the data may suggest that future high-temperature turbines with highly cooled surfaces burn washed and magnesium-treated residual oils under baseload conditions for very long durations, with only an initial, fairly rapid drop in power to a tolerable steady-state value. If spallation in test 9 occurred mainly during shutdown and start-up, the data may suggest that future high-temperature turbines with highly cooled surfaces burn washed and treated residual oils in peaking operation for very long, accumulated run times without requiring deposit cleaning maintenance. Longer-duration tests, however, designed to identify spallation sources, are necessary to learn whether long-term deposit growth reaches tolerable steady-state thicknesses.

A future, high-temperature turbine may experience acceptable deposit buildup rates with readily removable deposits from vanadium inhibitor additives other than the KI-16 additive used in this program. Laboratory burner tests (20) using residual oils treated with additives containing silicon, both alone and with magnesium, have produced vanadium complexes with much higher ash-softening temperatures (up to 2800°F [1538°C]) than the melting point (2200°F [1204°C]) of  $Mg_3V_2O_8$  produced by additives containing only magnesium. The deposits formed were loose and flaky and probably could be removed from turbine surfaces by conventional water washing or abrasive cleaning maintenance approaches.

#### Deposition in Future Turbines

Experimental results reported here for residual oil and from companion tests to be reported later for coal-derived liquids demonstrate greatly enhanced deposition for conditions representative of planned future turbines with high firing temperatures ( $\geq 2300^\circ\text{F}$  [1260°C]). This enhanced deposition is associated with the tendency for the much greater mass fraction of particulates formed during combustion to be in a molten phase, which results in a much higher fraction of the particles that arrive

on aerodynamic surfaces to adhere to those surfaces. Depending on the temperature of the surfaces, the deposits formed may be more tenacious and difficult to remove than deposits formed in current turbines with inlet temperatures in the 2000°F (1093°C) range.

Similar deposition effects are expected for turbines operating at inlet temperatures greater than 2300°F (1260°C) with coal-derived gases. Although integrated coal gasifier cleanup systems will remove the bulk of particulates from the product gases, a quantity of particulates will be carried over to the combustion turbines. Since the ash-softening temperature (indicative of molten subspecies) for many types of coals is less than 2300°F, the potential exists for high rates of deposition and tenacious deposits in future turbines operating with coal-derived gases.

Finally, higher turbine inlet temperatures may result in significant deposition even for typical clean fuels (distillate oils, natural gas) for which deposition has previously been of little consequence, again due to increased formation of molten particles. U.S. Navy experience with aircraft-derivative turbines operated on land has shown significant deposition (probably due to airborne particles) for inlet temperatures as low as 2100°F (1149°C) but insignificant deposition for inlet temperatures in the 2000°F (1093°C) and lower range.

Consequently, future generations of combustion turbines operating at inlet temperatures greater than 2300°F (1260°C) are likely to have a much higher potential for deposition than do current turbines operating at inlet temperatures in the 2000°F (1093°C) range. A greater understanding of turbine deposition phenomena and deposition control may be required to assure operation with acceptable reliability and availability for these high firing temperatures.

#### CONCLUSIONS

- In the initial tests the data showed that operation with untreated residual oil caused excessive corrosion when turbine metal temperatures exceeded 1000°F (583°C), but that operation with properly treated residual oil did not, even in the 1400° to 1600°F (760-870°C) range(1). For gas temperatures  $\leq$ 2000°F (1093°C), deposition of ash on the cooled test pin surfaces was shown to be a function of the difference between gas stream and metal temperatures and was explained by thermophoresis, the movement of small particles in a gas, due to the influence of a temperature gradient, toward the cooler regions.

- In the second series of tests in which deposition from simulated and real residual oil was evaluated, a relatively small ( $\sim 6$  ppm) amount of calcium in the dopant promoted greater deposition, and we noted that the doped distillate may produce deposits different from those produced by residual oil. The deposition results from both the cascade tests and the test pins followed the model predicted by thermophoresis and inertial impaction(2). An in-stream, isokinetic, particulate probe was used to sample in situ the constituents of the combustion gases of residual fuel and doped distillates at a gas temperature of 1900°F (1038°C). Differences in the type of particle generated with residual fuels (spheres), doped distillates without calcium (platelets), and doped distillates with calcium (fused, shapeless masses) were noted. The chemistry of the larger particles was also found to differ from that of the other particles, thus shedding considerable light on the differences in deposition rates noted in doped fuel and residual oil tests in this program(2).
- In a test conducted at gas temperatures representative of the next generation of combustion turbines (2300°F [1260°C]), a balance was shown to have been eventually achieved between deposition and spallation, as the total weight gain remained relatively constant for a metal temperature of 1350°F (732°C). Coated and uncoated specimens showed no major differences, except for some corrosion of the IN-738 alloy.
- At 2300°F (1260°C) and a somewhat higher metal temperature (1600° versus 1350°F [870° versus 732°C]), and for a longer time period, 300 h, excessive deposition was found after the final 58 h of continuous running. The dense deposits were unlike others from the short-term, lower-temperature tests. Possibly  $V_2O_5$ , a low-melting compound, was present in the deposit and may have been the "glue" that caused the excessive deposition. Treatment of residual fuel with magnesium additive normally will combine the  $V_2O_5$  in the form of a vanadate, and this test suggests that the treatment currently used may not be sufficient at higher turbine operating temperatures.
- Deposition and corrosion in combustion turbines operating on residual oil depend strongly on both the firing temperature and the operating metal temperature. For current gas temperatures (1800-2100°F [982-1150°C]) deposition appears to be greatly influenced by thermophoretic effects, and adequate corrosion control can be maintained with

magnesium additives and metal temperatures of 1650°F (900°C) or less. At higher firing temperatures a greater portion of the larger (>1 μm) particles are molten or semimolten, and inertial impact may predominate over thermophoretic effects.

- A model used to estimate maintenance intervals for current turbines operating with washed and treated residual oil produced times consistent with field experience. Future turbines, however, operating at inlet temperatures  $\geq 2300^\circ\text{F}$  (1260°C), will probably experience deposition of greater magnitude and substrate tenacity, requiring a better understanding of the phenomenology of deposit formation and removal.

#### REFERENCES

1. S. M. DeCorso, G. Vermes, S. Y. Lee, S. C. Singhal and A. Cohn, "Combustion Turbine Design Guidelines Based on Deposition/Corrosion Considerations," ASME Paper 80 GT-72.
2. G. A. Whitlow, S. Y. Lee, P. R. Mulik, R. A. Wenglarz, T. P. Sherlock and A. Cohn, "Combustion Turbine Deposition Observations from Residual and Simulated Residual Oil Studies," paper submitted to ASME Gas Turbine Conference, London, April 1982.
3. "Workshop Proceedings: Deposition in Utility Gas Turbines," EPRI Report WS-80-121, Proceedings May, 1981.
4. "Worldwide Survey of Current Experience Burning Residual and Crude Oils in Gas Turbines," EPRI Report AF-1243, TPS 78-833, Dec., 1979.
5. R. E. Strong and T. P. Sherlock, "Residual Oil Operating Experience with Westinghouse Industrial Combustion Turbines," presented at the EPRI Combustion Turbine Residual Oil Workshop, Atlanta, GA, July, 1980.
6. P. C. Felix, "Practical Experience with Crude and Heavy Oil in Stationary Gas Turbines," BBC Report No. CH-T113333E, 1980; also ASME Paper 78-GT-103.
7. W. J. Hefner and F. D. Lordi, "Progress in Heavy Fuels," General Electric Report GER-3110A, 1979.
8. D. A. Nealy and W. H. Timmerman, "Investigation of the Influence of Contaminated Fuel on Turbine Vane Surface Deposition," Paper No. AIAA-80-1113, AIAA/SAE/ASME 16th Joint Propulsion Conference, Hartford, CT, June, 1980.
9. T. A. Urbas and L. H. Tomlinson, "Part II, Formation and Removal of Residual Fuel Ash Deposits in Gas Turbines Formed at Firing Temperatures Above 982°C (1800°F)," Proceedings of Int. Conf. on Ash Deposits and Corrosion from Impurities in Combustion Gases, Engineering Foundation, Henniker, NH, Hemisphere Publishing Corp.; 1977.

10. T. A. Urbas and L. H. Tomlinson, "Part I, Formation and Removal of Residual Fuel Ash Deposits in Gas Turbines Formed at Firing Temperatures Below 982°C (1800°F)," Proceedings of Int. Conf. on Ash Deposits and Corrosion from Impurities in Combustion Gases, Engineering Foundation, Henniker, NH, Hemisphere Publishing Corp.; 1977.
11. M. Nomura et al., "An Experiment on Deposit Formation on Surface of an Air Cooled Gas Turbine Blade," Paper No. 69, Gas Turbine Soc. of Japan/The Japanese Soc. of Mech. Engineers/ASME, Tokyo, May 1977.
12. J. J. Vitello and S. T. Scheirer, "Hot Component Corrosion Evaluation to Obtain Baseline Data for Utilization of Low Grade Fuels in Combustion Turbine Applications," Westinghouse Final Report on EPRI Research Project 1079-2, September 1980.
13. K. W. Lay, Trans. ASME, J. of Eng. for Power, 134, April 1974.
14. E. I. Sperenskaya, Bull. of the Head of Sciences, USSR, Inorganic Materials, 7: 605; 1971.
15. H. L. Allen, "Florida Power Corporation Experience Operating Gas Turbines on Residual Fuel," presented at the EPRI Combustion Turbine Residual Oil Workshop, Atlanta, GA, July 1980.
16. M. J. Moore and R. I. Crane, "Aerodynamic Aspects of Gas Turbine Blade Corrosion," from Deposition and Corrosion in Gas Turbines, edited by A. B. Hart and A. J. B. Cutler, Halstead Press: New York, 1973.
17. R. A. Wenglarz, "An Assessment of Deposition in PFBC Power Plant Turbines," ASME Paper 80-WA/CD-1, also to appear in Transactions of the ASME, Journal of Engineering for Power, 1981.
18. G. Vermes, "Thermophoresis - Enhanced Deposition Rates in Combustion Turbine Blade Passages," ASME Paper 78-WA/GT-1, 1978.
19. G. E. Krulls, "Gas Turbine Vanadium Inhibition," ASME paper 81-GT-187, 1981.
20. G. K. Lee, E. R. Mitchel, R. G. Grimsey, and S. E. Hopkins, "An Investigation of Fuel-Oil Additives to Prevent Superheater Slagging in Naval Boilers," Vol. 26, Proceedings of the Americal Power Conference, 1964, pp. 531-47.

#### ACKNOWLEDGMENTS

This work was performed with the support of the Electric Power Research Institute, Contract No. RP 1345-1. Many persons contributed to the success of this research effort, and particular thanks are due to the technical staff of the Metallurgy and Chemical Engineering Research Departments of the Research and Development Center. The contributions of S. M. DeCorso of the Westinghouse Combustion Turbine Systems Division and P. P. Singh of the Chemical Engineering Research Department are especially gratefully acknowledged.

# MECHANICAL PROPERTY REQUIREMENTS FOR HOT SECTION COMPONENTS IN GAS TURBINES

W.J. Ostergren  
G.T. Embley  
General Electric Company, Schenectady, N.Y.

## INTRODUCTION

Requirements for improved efficiency and output have led gas turbines in the past to continually higher firing temperatures and increased sizes. This has been achieved through the use of high-strength, creep-resistant superalloy materials together with advanced cooling of critical hot-gas-path components (buckets, nozzles, and combustors). As shown in Figure 1 for the case of bucket materials, improvements in alloy creep resistance accounted for more of the increase in firing temperature up until about 1970. Use of air cooling and improvements in hot corrosion resistance have been responsible for more recent increases. Intricate cooling schemes, together with advanced material processing techniques, have made the task of selecting and evaluating materials for hot turbine sections increasingly complex.

Critical hot section components detailed in Figure 2 include the combustor, buckets, and nozzles. The wide variety in sizes of these components is illustrated in Figures 3 and 4. Designs and material properties must be balanced so as to achieve adequate resistance to a variety of potential failure mechanisms. Air-cooled buckets must possess both adequate low-cycle fatigue life and resistance to creep rupture (due to centrifugal and gas bending loads). Design against low-cycle fatigue crack initiation must be considered for the airfoil, where there are high thermal strains, as well as regions of high stress concentration, such as the dovetail. Combustor hardware, such as that shown in Figure 5, must be carefully designed to avoid creep distortion problems as well as fatigue cracking in welded joints and cooling hole regions.

Because of the competing influences of numerous potential mechanical failure modes, significant tradeoffs in properties must be made. Such tradeoffs will vary depending upon the expected operating conditions of the turbine. This, in turn, has required the development of sophisticated mechanics of materials approaches for predicting component life under cyclic and steady loading conditions in varied environments. These approaches must be flexible enough to account for the effect on life criteria of advanced processing techniques such as coatings, claddings, composite constructions, etc. Thus, it is the purpose of this paper to illustrate the role of mechanics of materials in development of mechanical property requirements for advanced hot-gas-path components.

## FATIGUE

Advanced cooling, while reducing bulk section temperatures, does produce larger thermal gradients in turbine hardware. Because of the resultant thermal strains, low-cycle fatigue becomes a potential failure mode of increased concern. At low temperatures, well below the creep regime, cycles to failure can be correlated with total strain range, and test results for an air environment are relatively insensitive to temperature and frequency. However, as temperature is increased, constitutive behavior (e.g., increases in plastic strain and stress relaxation) and environmental effects (e.g., oxidation) become increasingly important. At some point, an effect of temperature on life can be expected, as illustrated for the case of Alloy 718 in Figure 6 (1). Additionally, because of the time-dependent nature of constitutive and environmental effects, frequency and wave shape can also be expected to influence cyclic life. The effect of frequency has been considered by Coffin (2), who has shown that for a given wave shape and within certain ranges of strain the following relationship between strain range ( $\Delta\epsilon$ ), frequency ( $\nu$ ), and cyclic life ( $N_i$ ) holds

$$\Delta\epsilon = \Delta\epsilon_p + \Delta\epsilon_e \quad (1)$$

The plastic and elastic strain components ( $\Delta\epsilon_p$  and  $\Delta\epsilon_e$ ) are given by the expressions

$$\Delta\epsilon_p = C_2 N_i^{-\beta} \nu^{\beta(1-k)} \quad (2a)$$

$$\Delta\epsilon_e = \frac{A'}{E} N_i^{-\beta'} \nu^{k_1} \quad (2b)$$

where  $C_2$ ,  $A'$ ,  $\beta$ ,  $\beta'$ ,  $k$ , and  $k_1$  are empirically determined parameters and  $E$  is Young's Modulus of Elasticity.

This approach appears most applicable to cases where an oxidizing environment is the dominant factor. However, other factors, such as stress relaxation and creep damage, are also dominant at high temperatures and their effects must be considered as well.

Figure 7 represents strain-controlled cycles that are typically employed in isothermal low-cycle fatigue testing to assess the influence of strain wave shape on cycles to failure. The effect of wave shape varies with both material and temperature. On one hand, test results for AISI 304 stainless steel (3) indicated that tension hold times are more damaging than equivalent hold times in compression or tension plus compression. In other cases, testing of Hastelloy X and IN-738 (nickel base alloys typically utilized in combustor and bucket applications) has found compression hold times to be the most damaging (4, 5). Figure 8 shows typical results for IN-738 at 871 °C (1600 °F).

Predictive models (5, 6, 7) that account for these effects have been developed and used to establish cyclic lives of hot section components. In particular, the role of stress relaxation during the strain-controlled hold time has been identified. As shown in Figure 7, during hold times a biased stress develops, leading to a mean stress opposite the hold direction. This mean stress develops as a result of stress relaxation which drives the stress in a direction opposite the hold direction. A damage function based on the peak tensile stress ( $\sigma_T$ ) and plastic strain range was developed in Reference 5 to incorporate this deformation behavior. The relationship between this damage function and cycles to failure can be expressed as

$$\sigma_T \Delta \epsilon_p N_f^\beta = C \quad (3)$$

where  $C$  and  $\beta$  are empirically determined constants.

In cases where environmental or creep damage is not significant, the above relationship correlates strain-controlled hold time results very well. This is illustrated in Figure 9 for the case of IN-738 at 871 °C (1600 °F). Note that these are the same test results that were plotted as a function of total strain in Figure 8.

Often low-cycle fatigue behavior at elevated temperature involves some combination of time-dependent environmental or creep damage together with the mean stress effects discussed above. A correction for time-dependent damage can be included in Equation 3 in a similar fashion to that in Eq. 2b. That is

$$\sigma_T \Delta \epsilon_p N_f^\beta \nu^{\beta(k-1)} = C_1 \quad (4)$$

In cases where such damage is independent of wave shape, such as might be expected in the case of environmental reactions (e.g., oxidation), the frequency may simply be set equal to the inverse of the period of the waveform. Test data for Hastelloy X at 704 °C (1300 °F) which are plotted in Figure 10 for a variety of waveforms and frequencies, can be correlated within a factor of two on life using this approach.

The frequency modified approach outlined above can also be used in certain cases where the time-dependent damage depends upon waveform. When creep damage occurs, time-dependent damage associated with a tension hold time can be reduced by time spent in compressive hold. In these cases, data can be correlated by replacing the frequency in Eq. 4 with an effective value which is

$$\begin{aligned} \nu &= 1/(\tau_0 + \tau_T - \tau_C) \quad \tau_T > \tau_C \\ \nu &= 1/\tau_0 \quad \tau_T \leq \tau_C \end{aligned} \quad (5)$$

where

$\tau_0$  = time per cycle of continuous cycling

$\tau_T$  = tension hold time

$\tau_C$  = compression hold time

It was found in Reference 5 that this was an appropriate means for correlating 304 stainless steel at 650 °C (1200 °F).

Thus, for predicting fatigue behavior of hot section parts, sufficient low-cycle fatigue data must be generated to characterize the effect of frequency and wave shape as well as temperature on cyclic life. Predictive models such as those represented by Eq. 1 to 4 or other approaches (6, 7) can then be used to extrapolate results to low frequencies and long lives characteristic of the part.

Prediction of cyclic life at a single temperature is not alone sufficient to predict life in a hot section part. Consider the complex relationship between cyclic strain and temperature that is representative of a local region at the leading edge of a turbine bucket (see Figure 11). In this case, the temperature at which the maximum cyclic strain occurs is not the maximum temperature. Furthermore, intermediate temperatures may be the region where maximum environmental damage occurs. A reasonable design approach is one in which life is predicted by considering the combination of maximum strain range with the most damaging temperature and wave shape. Although such an approach can be expected to be conservative in most cases, this may not always be true. Alternatively, it may be overly conservative, causing undue penalties on design. Therefore, this approach has recently been evaluated through use of complex thermal mechanical testing.

Initial thermal fatigue work (8 and 9) emphasized use of the Glenn Disk specimen (Figure 12). Through alternate immersions in hot and cold fluidized beds (Figure 13), this specimen can develop thermal strain-temperature profiles that are similar to those produced in trailing edges of uncooled vanes and buckets (see Figure 14). Thermal strains develop because the thin edge of the disk heats up and cools down faster than the bulk of the section. The strain and temperature variation are computed as shown in Figure 15 for various peripheral radii ( $R_p$ ) of the disk. Bath temperatures and immersion times may also be varied. The number of cycles to crack initiation for various materials are measured and the rankings of these alloys compared as seen in Figure 16 for cobalt-base alloys. This permits identification of alloys possessing inadequate thermal fatigue resistance and provides a preliminary indication of design material properties.

While the Glenn specimen is useful for alloy screening, it does not provide proper simulation of more complex strain-temperature cycles such as that shown in Figure 11. Thus, more recent work has emphasized thermal-mechanical fatigue testing, in which actual component local strain-temperature transients are imposed on simple specimens. To evaluate the impact of these complex actual thermal-mechanical cycles on component life, closed loop electro-hydraulic test systems with dual control of strain and temperature have been developed.

These dual loop computer controlled test systems provide independent control of both strain and temperature. A hollow cylindrical test specimen is heated by an induction coil and air cooled down its centerline, with strain monitored by a longitudinal extensometer in the gage section (Figure 17). Test results for actual bucket cycles imposed on these simple specimens indicate considerable variation in measured cycles to cracking from those predicted by isothermal test data. Figure 18 presents a comparison of test result trends for two different bucket cycles with isothermal data at the maximum temperature, indicating that actual cyclic lives may be either conservatively or non-conservatively predicted utilizing isothermal predictions.

In summary, development of low-cycle fatigue properties for materials used in hot section components is a complex issue and must include consideration of

- The effect of temperature
- The effect of frequency and wave shape
- The effect of the actual strain-temperature-time cycle



Since determination of frequency and hold time effects using the actual design cycle is generally impractical, the present philosophy is to satisfy the first two considerations through isothermal testing and to confirm a reasonable design approach through use of limited thermal mechanical testing. In the future, it is anticipated that test programs will continue to be developed to expand the understanding of the relationship between isothermal and complex thermal mechanical cycles.

#### CREEP FAILURE CRITERIA

In heavy duty land-based gas turbine applications, reliable operation for many thousands of hours is important. The structure of sophisticated nickel and cobalt base superalloy materials, with their complex  $\gamma'$  and carbide strengthening mechanisms, can alter significantly with time at temperature. As illustrated in Figure 19, long-time trends in rupture data may deviate substantially from short-time extrapolations, due to changing cracking modes and alloy structure (10). Therefore, it is necessary to conduct long-term creep/rupture testing to determine the behavior of turbine alloys which will be subjected to long-time high-temperature exposure. Testing beyond 30,000 hours is typically performed at General Electric for combustor, bucket, and nozzle alloys.

Testing at General Electric (11) of the nickel base superalloy IN-738 determined that in the brittle behavior regime associated with long exposures, intergranular surface cracking may occur at strains and times considerably lower than those required for complete separation of the test specimen. This is a typical characteristic of cast nickel base superalloys. These alloys display excellent creep rupture strength up to high homologous temperatures, but the ductilities are low. The ductility often continues to decrease with exposure, due in part to attack by oxidation. Oxidation, attack occurs preferentially at grain boundaries, with micro cracks eventually linking up to form macro cracks as shown in Figure 20.

Failure criteria in terms of rupture time may be appropriate for a structure where loads are reasonably constant (as in the creep test). Where dynamic loadings also occur (as in a turbine section), a crack which is initiated by creep may propagate to failure in fatigue. This has caused emphasis to switch toward identifying material creep failure criteria which include the time or strain to produce a crack of sufficient size to propagate in fatigue. Ongoing work at the General Electric Company (11) has attempted to define a high-temperature creep failure criterion for cast nickel-base superalloys based upon these surface cracking observations. Specimens of IN-738 were pre-exposed to creep strains at varied temperatures and subsequently tested in fatigue. Results shown in Figure 21 indicate a reduction in fatigue life with creep pre-exposure, the effect increasing as the magnitude of creep strain or exposure temperature increases. The greater effect associated with higher temperature creep exposure appears to be attributed to an increased environmental attack with temperature. The role of the environment in producing this surface damage is indicated by Figure 22, which compares the results of fatigue testing for specimens creep-exposed in air and in vacuum at 982 °C (1800 °F). The vacuum exposed bars exhibit longer lives and apparently less surface damage than equivalent air exposures. Figure 23 compares the microscopic surface damage observed with air and vacuum exposures, the latter showing reduced damage due to the inhibiting of the surface/environment interaction by the relatively inert environment.

In view of the above, it is necessary to consider the trends toward surface cracking in long-time high-temperature applications and the possibility of interactive failure modes, i.e., the possibility of crack initiation by creep and subsequent propagation in fatigue. This suggests the need to identify the cracking strain-time-temperature envelope for potential turbine alloys as well as the creep strength trends. In IN-738, crack initiation appeared to occur at creep strains in the region just prior to the onset of tertiary creep. Thus, time to onset of tertiary creep might serve to define such an envelope for this alloy. This is illustrated in Figure 24.

While creep crack initiation serves to define a strain-time limit for cast superalloys that are used in turbine blades, different considerations become more dominant for other materials. For example, Hastelloy X, which is used extensively in combustor applications, possesses excellent rupture ductility in the temperature ranges of interest (12). However, in structures such as the combustor transition piece, relatively small creep strains could cause excessive structural distortion. A creep test program designed to provide long-term rupture data may not provide long-term prediction of the small creep strains (up to 0.5%) of interest to such a design. In these cases, long-term data should be obtained for the design application and, since the objective is determination of time to a given low creep strain, the test would of necessity be terminated well before rupture or the onset of tertiary creep.

Thus, critical creep/rupture property requirements will depend on both the details of the design and the characteristics of the materials. The nature of these requirements will dictate the emphasis to be placed in creep test programs.

#### **DEFECT TOLERANCE AND FRACTURE PROPERTIES**

Turbine parts may contain material or processing defects, i.e., inhomogeneities or discontinuities such as nonmetallic inclusions, voids, shrink, etc. which when sufficiently small will not affect the capability of the part to perform its function. To this end it is essential to establish inspection techniques and requirements for limiting the size of defects which may be accepted for actual components. The approach of linear elastic fracture mechanics has been utilized and adapted for use in hot turbine sections.

Beginning in the mid-1950's, fracture mechanics procedures were developed at General Electric for dealing with natural defects occurring in large rotor forgings (13). These techniques have been refined as our understanding of the relationship between defect growth and cycling, plasticity effects, etc. has increased (14). The extension of fracture mechanics techniques to the hot-gas-path components has been a natural outgrowth of these developments.

In large investment castings such as nozzles and buckets, shrinkage porosity (Figure 25) is a natural occurrence during solidification. A fracture mechanics approach similar to that outlined in Reference 14 can be conservatively applied to ensure that no risk exists that typical levels of porosity will propagate to a deleterious crack size. Additionally, this approach can be utilized to assess the subsequent growth and potential impact of cracks initiated by any number of modes (e.g., creep crack initiation). In hot-gas-path sections, one must consider the impact on defect growth of temperature, hold time, and environment. In addition, the dynamic loadings of a turbine environment must be acknowledged in defining operating stress-intensity factor levels.

In support of these evaluations, both fracture toughness data and crack growth data are being generated for cast superalloy materials at high temperatures. Figure 26 illustrates the effect of temperature on crack growth of IN-738. Changes in frequency at 871 °C (1600 °F) appeared to have little effect on crack growth rates. One means of assessing the effect of thermal-mechanical cycling on fatigue is through use of the Glenn Disk specimen (9). When a sharp notch is placed on the outer periphery of the disk (Figure 12) crack initiation occurs very early and subsequent crack growth can be monitored by periodic visual inspection. The stress-intensity factors corresponding to various thermal cycles and crack lengths have been computed for this specimen and crack growth rate curves, such as shown in Figure 27, have been generated for a variety of materials. This particular set of data is for a thermal cycle over a temperature range of 21-920 °C (70-1688 °F). Note that the data for IN-738, while generated for higher  $\Delta K$  values, are quite compatible with the isothermal data at 871 °C (1600 °F) (Figure 26). Consideration of crack growth characteristics of wrought alloys, such as Hastelloy X, has also been important to the evaluation of combustor components where fracture mechanics has been applied to the evaluation of brazed and welded joints, as well as the assessment of cooling hole manufacturing techniques.

Recent developments in the area of elastic-plastic fracture mechanics [(15) and (16), for example] are currently being utilized in gas turbine applications. For example, the J-integral test procedure currently under consideration by ASTM is being used to determine valid fracture toughness values for superalloys using subsize specimens. Emphasis (17) has also been placed on defining the relationship between crack initiation and crack growth behavior utilizing non-linear parameters such as  $\Delta J$  (18). This represents the opportunity for utilizing one type of test or property to define other major mechanical properties.

#### **THE EFFECT OF ENVIRONMENT AND THE ROLE OF COATINGS AND CLADDINGS**

Environment has a significant effect on mechanical properties of hot-gas-path alloys. Discussions in previous sections have illustrated the severe environmental effects that exposure to high-temperature air can have on low-cycle fatigue and creep rupture properties. Exposure to hot corrosion products typical of gas turbine applications causes further loss in life.

Coatings and cladding designed to inhibit oxidation and hot corrosion attack have been found to be quite effective in reducing the effect of the environment on creep and fatigue properties. Con-

sider the case of IN-738 discussed earlier, where creep cracking results from an oxidation attack which occurs preferentially at grain boundaries. In Figure 28, a comparison is made between long-time creep exposures of IN-738 with and without the presence of a PtCrAl coating. The coating has prevented the occurrence of surface cracking which is apparent in the bare sample.

The effect of hot corrosion products on low-cycle fatigue (LCF) life has been determined through tests of material pre-exposed in burner rigs. Figure 29 presents the effect on IN-738 LCF life of pre-exposure to a very aggressive 1% sulfur distillate fuel which contains a dispersing agent to keep enough synthetic seawater in suspension to maintain 125 ppm sodium in the fuel. This particular condition is more severe than would be expected in service. Pre-exposure to oxidation at the same temperature can also cause LCF life reduction. This together with the beneficial effect of a PtCrAl coating in preventing such damage is illustrated in Figure 30. It is interesting to note that shorter term exposures at several frequencies that occurred during LCF testing of this alloy did not result in any significant environmental effect (see section on fatigue). Thus, a lack of an observed frequency dependent effect in short-time LCF testing does not necessarily imply that such damage will not occur as a result of lower frequencies or long-term exposure to environment.

Although coating and cladding systems can prevent environmental degradation of mechanical properties in nickel base superalloys, it is important that these systems have adequate strength and ductility to withstand the cyclic strain conditions associated with hot-gas-path hardware. Premature cracking from inadequate strain capability in the coating or cladding system could, in fact, promote environmental attack. Furthermore, as coating and cladding thicknesses increase, it is necessary to account for the interactive role they play in the stress-strain behavior of the underlying component. As discussed in (19) a clad bucket or test specimen can be treated as a two-member composite element. The uniform load on the test specimen or the centrifugal load on a bucket will be shared by these two members based on their relative cross-sectional areas and properties. Also, the load distribution will change with time as a function of the differences in creep behavior between the cladding and the substrate alloy. The resultant creep behavior of the composite is depicted in Figure 31.

Thermal strains can also be reduced or magnified depending on the relative values of physical properties between coatings and claddings and the underlying substrate alloy. This causes one to ascribe considerable significance to the physical and mechanical properties of coating and clad alloys as well as the oxidation and hot corrosion resistance upon which they usually are judged.

#### COMPOSITE CONSTRUCTIONS AND ADVANCED PROCESSING TECHNIQUES

Advanced processing techniques, such as hot isostatic pressing, directional solidification, and high-strength powder production, offer new opportunities for producing composite constructions in which mechanical properties can be maximized in those locations where they are most needed. As an example, ductile, corrosion-resistant claddings can be diffusion bonded to high-strength load carrying buckets and nozzles, maximizing surface fatigue resistance.

Currently, General Electric is developing composite technology as part of a water-cooled turbine (HTTT) program (20). The program is aimed at achieving firing temperatures in the range of 1260-1650 °C (2300-3000 °F) with corresponding metal surface temperatures of nozzles and buckets of 540 °C (1000 °F) or less. To meet these objectives a composite water-cooled nozzle, whose vane cross section is illustrated in Figure 32, has been developed. High-strength spars along the centerline provide resistance to gas bending loads. These are surrounded by a high-strength copper alloy which provides high thermal conductivity to distribute heat fluxes and minimize surface temperatures. Erosion and stress corrosion resistant cooling tubes pass through the copper matrix. Finally, a hot corrosion resistant outer skin encloses the vane. The entire assembly is diffusion bonded to provide close thermal contact between the various elements.

A critical issue in design of such components is the behavior under the severe cyclic strains anticipated in hot-gas-path operation. To evaluate the copper composite life under cyclic straining, composite cylindrical thermal-mechanical test specimens, shown in Figure 33, were produced and cycled to failure (21). Results, shown in Figure 34, demonstrate that the composite life is dictated by the properties of the individual materials. Cracking initiated first in the copper alloy adjoining the bondline. No deleterious effects were identified in the bondline itself.

A similar issue was raised relative to creep strength of a composite nozzle or bucket. In this case, composite sandwich-type specimens with a copper matrix and IN-617 skin were constructed and tested in both uniform tension and pure bending (22). Here again results indicated that composite life can be evaluated in terms of the properties of the individual materials. This is shown by a Larson-Miller plot of both composite and monolithic copper test results in Figure 35. Additionally, test specimens removed from test prior to rupture were metallographically examined in detail and, in all cases, grain boundary void nucleation or cracking was observed in the copper matrix. Figure 36 illustrates features that are common to these specimens. Number 1 denotes a region denuded of precipitates in the copper substrate. This region is 0.003 to 0.004 inch in width. Number 2 identifies the bondline, the clarity of which is associated with a distinct step between the IN-617 surface and the copper surface (which etches away more rapidly). Number 3 denotes a region in the IN-617 in which the grain boundaries are rich in copper and nickel. Number 4 identifies grain boundary cracking in the MZC substrate. Cracking along the bondline (delamination) or along the copper-rich grain boundaries in the IN-617 region near the bondline was not observed in any of the specimens examined.

The above serves to highlight the potential for utilizing composite constructions to zone key mechanical properties. Diffusion bonding can produce excellent quality bondlines with negligible impact on life. In situations where bondline defects are likely, the bond joint can be located in lower stressed regions to prevent significant impact on life.

#### SUMMARY

Mechanical property requirements have become considerably more complex than the simple tensile and rupture properties that have been utilized in the past as tools in selecting and in developing hot-gas-path alloys. Today, sophisticated mechanics of materials approaches have been developed for defining component lives and relating the design needs to the material. This, in turn, has led to more refined property requirements which must be considered in material selection and development.

In summary, the key mechanical property requirements for hot turbine sections are:

- Thermal-mechanical fatigue capability under actual strain-temperature transients.
- Assessment of the impact of hold time, frequency of cycling, and environment on fatigue properties.
- Creep strain cracking resistance and strength capability under long-term service condition.
- Coating and cladding systems capable of inhibiting environmental attack and enhancing long-term mechanical properties.
- Adequate tolerance of defects from normal processing sequences.
- Composite constructions capable of maximizing mechanical properties at the desired locations of the component.

#### ACKNOWLEDGMENTS

A portion of the work discussed in this paper was conducted under United States Department of Energy Contract Number EX-76-C-01-1806. The financial support of DOE is gratefully acknowledged.

We also wish to acknowledge the valued contributions of our many co-workers at the General Electric Company who performed much of the work discussed in this paper.

#### REFERENCES

- [1] T.H. Sanders Jr., R.E. Frishmuth, and G.T. Embley, "Temperature Dependent Deformation Mechanisms of Alloy 718 in Low Cycle Fatigue," *Met. Trans. A 12A*, June 1981, pp. 1003-1010.
- [2] L.F. Coffin, Jr., "A Note on Low-Cycle Fatigue Laws," *J. Mater.* 6, 1971, pp. 388-402.

- [3] J.T. Berling and J.B. Conway, "Effect of Hold Time on the Low Cycle Fatigue Resistance of 304 Stainless Steel at 1200F," presented at the First International Conference on Pressure Vessel Technology, Delft, 1969.
- [4] D.W. Seaver, "Low Cycle Fatigue Properties of Hastelloy X at 704C (1300F)," in *Methods for Predicting Material Life on Fatigue* (ed., W.J. Ostergren and J.R. Whitehead), ASME, New York, 1979.
- [5] W.J. Ostergren, "A Damage Function and Associated Failure Equation for Predicting Hold Time and Frequency Effects in Elevated Temperature, Low Cycle Fatigue," *Journal of Testing and Evaluation JTEVA* 4 (5), Sept. 1976, pp. 327-339.
- [6] B.N. Leis, "An Energy Based Fatigue and Creep-Fatigue Damage Parameter," *Journal of Pressure Vessel Technology, Trans: ASME* 99 (4), Nov. 1977, pp. 524-533.
- [7] S.S. Manson, G.R. Halford, and M.A. Hirshberg, "Creep Fatigue Analysis by Strain Range Partitioning," Symposium on Design for Elevated Temperature Environment, ASME, 1971, pp. 12-24.
- [8] R.J.E. Glenny, "Thermal Fatigue," in *High Temperature Materials in Gas Turbines* (ed., P.R. Sahn and M.O. Speidel), Elsevier Pub., Amsterdam, 1974.
- [9] D.F. Mowbray, D.A. Woodford, and D.E. Brandt, "Thermal Fatigue Characterization of Cast Cobalt and Nickel-Base Superalloys," in *Fatigue at Elevated Temperatures ASTM STP 520*, 1973.
- [10] J.B. Conway, "Pre-Analysis Assessment of Creep-Rupture Data," *MCP-7, Characterizations of Materials for Elevated Temperatures*, 1978 – ASME/CSME Montreal PVP Conference, Montreal, Canada, June 1978.
- [11] W.L. Chambers, W.J. Ostergren, and J.R. Wood, "Creep Failure Criteria for High Temperature Alloys," *Trans. ASME* 101, October 1979.
- [12] M.K. Booker, "Evaluation of Creep and Relaxation Data for Hastelloy X Sheet," ORNL – 5749, February 1979.
- [13] A.F. Rubio, D. Timo, and S. Yukawa, "Fracture Design Practices for Rotating Equipment," in Volume 5 of *Fracture, An Advanced Treatise* (ed., H. Liebowitz), Academic Press Publishers.
- [14] R.E. Frishmuth, "Use of Fracture Mechanics Methods for Establishing Inspection Levels for Turbine Wheels," *Journal of Engineering Materials and Technology* 101, Jan. 1979, pp. 75-79.
- [15] J.A. Begley and J.D. Landes, "The J-Integral as a Fracture Criterion" in *Fracture Toughness*, ASTM STP 514, Philadelphia, 1972, pp. 24-39.
- [16] G.A. Clarke, W.R. Andrews, J.A. Begley, J.A. Donald, G.T. Embley, J.D. Landes, D.E. McCabe, and J.H. Underwood, "A Procedure for Determination of Ductile Fracture Toughness Values Using J-Integral Techniques," *Journal of Testing and Evaluation* 7 (1), Jan. 1979, pp. 49-56.
- [17] D.F. Mowbray, "Derivation of a Low-cycle Fatigue Relationship Employing the J-Integral Approach to Crack Growth and Fracture," ASTM STP 601, American Society for Testing and Materials, 1976, pp. 33-46.
- [18] N.E. Dowling and J.A. Begley, "Fatigue Crack Growth During Gross Plasticity and the J-Integral," *Mechanics of Crack Growth*, ASTM STP 590, American Society for Testing and Materials, 1976, pp. 82-103.
- [19] J.H. Wood, A.M. Beltran, T.R. Farrell, W.J. Ostergren, and W.F. Schilling, "Development of Diffusion Bonded Claddings for Large Gas Turbine Applications," to be presented at Second Conference on Advanced Materials for Alternative-Fuel-Capable Heat Engines," EPRI, August 24-28, 1981.
- [20] M.W. Horner et al., "Water-Cooled Gas Turbine Technology Development," ASME Paper 79-GT-72, March 1979.

- [21] "Development of High Temperature Turbine Subsystem Technology to a Technology Readiness Status – Phase II," Quarterly Report for the Period October-December 1979, FE-1806-76, Feb. 1980.
- [22] "Development of High Temperature Turbine System Technology to a Technology Readiness Status – Phase II," Quarterly Report for the Period January-March 1980, FE-1806-86, May 1980.

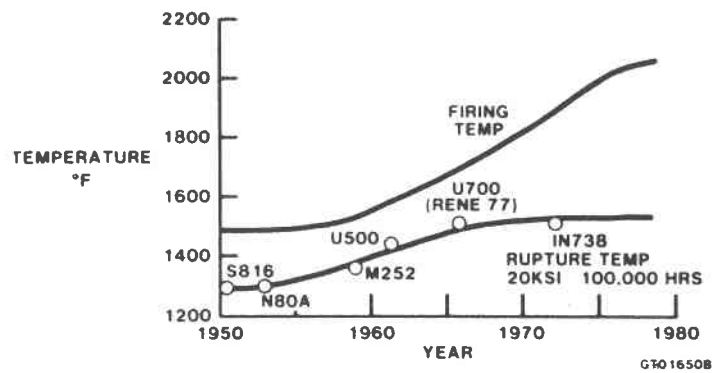


Figure 1. Past Trend Firing Temperature and Bucket Material Capability

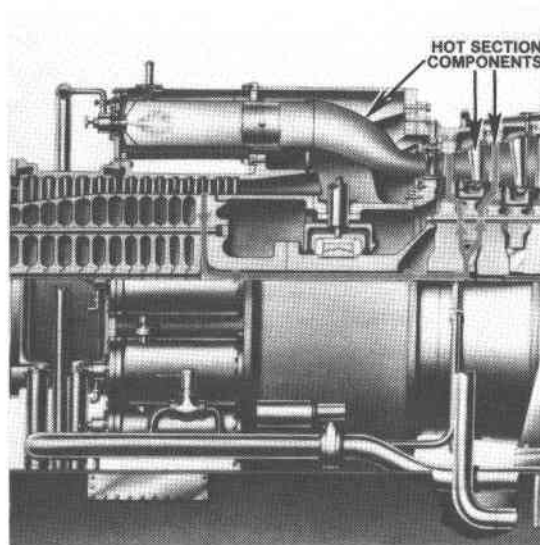


Figure 2. MS7001 Hot Gas Path

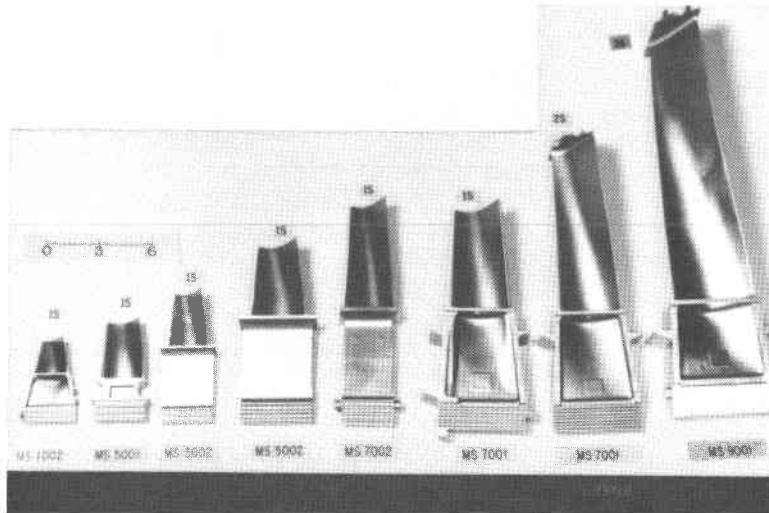


Figure 3. Investment Cast Buckets

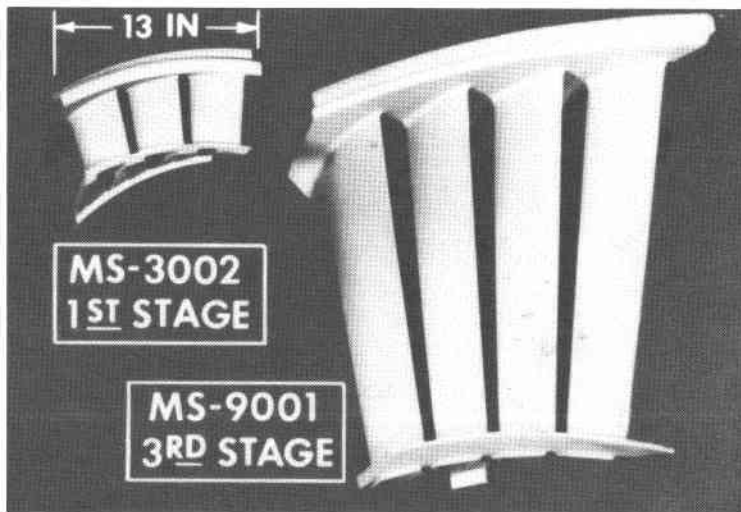


Figure 4. Investment Cast Nozzles



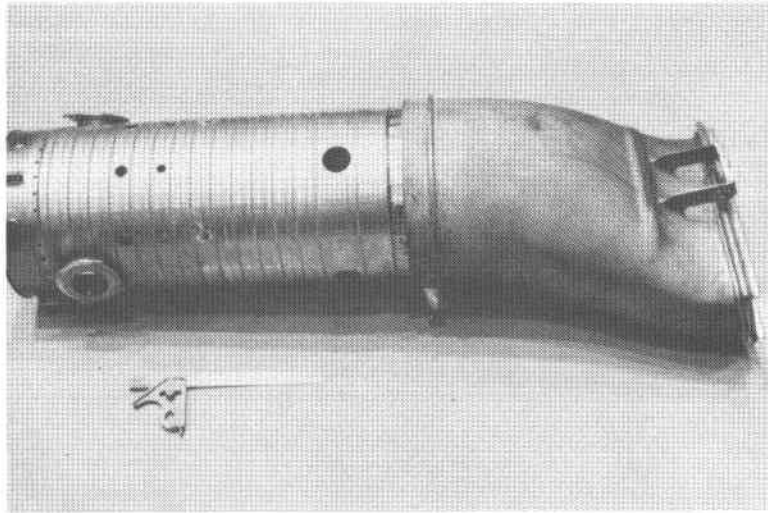


Figure 5. MS6001 Combustion System

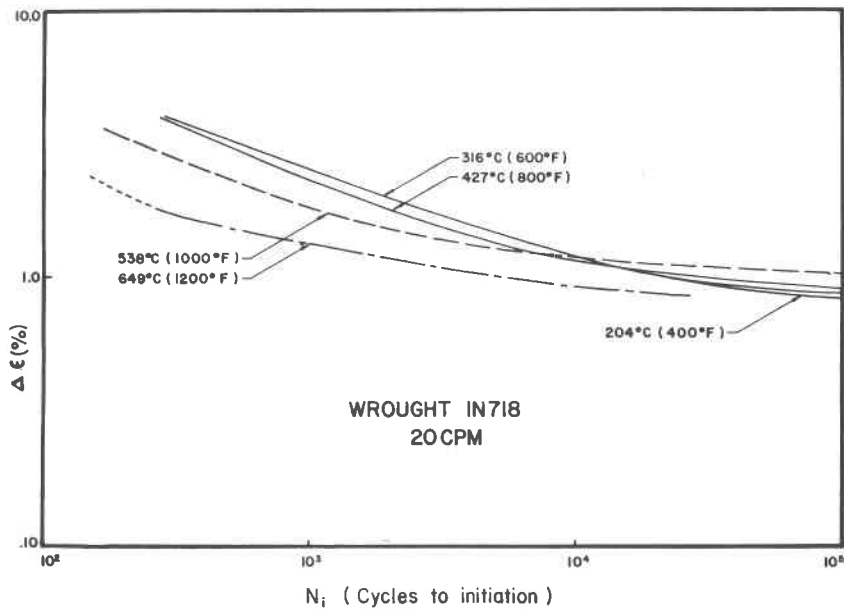


Figure 6. Total Strain Range vs Number of Cycles to Initiation for IN718 at Various Temperatures

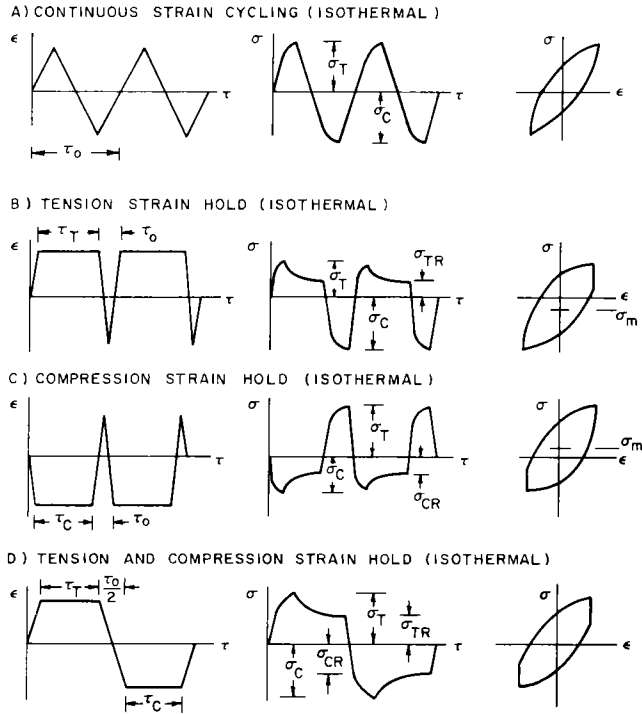


Figure 7. Schematic of Strain-Controlled Fatigue Cycles

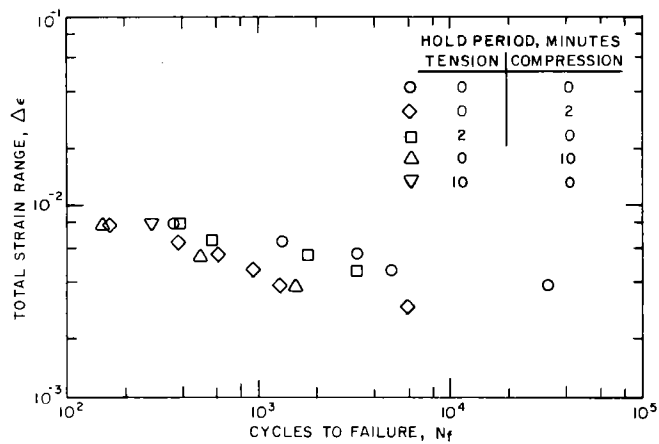


Figure 8. Total Strain Range vs Cycles to Failure for the Cast Nickel Base Superalloy IN-738 at 871 °C (1600 °F)

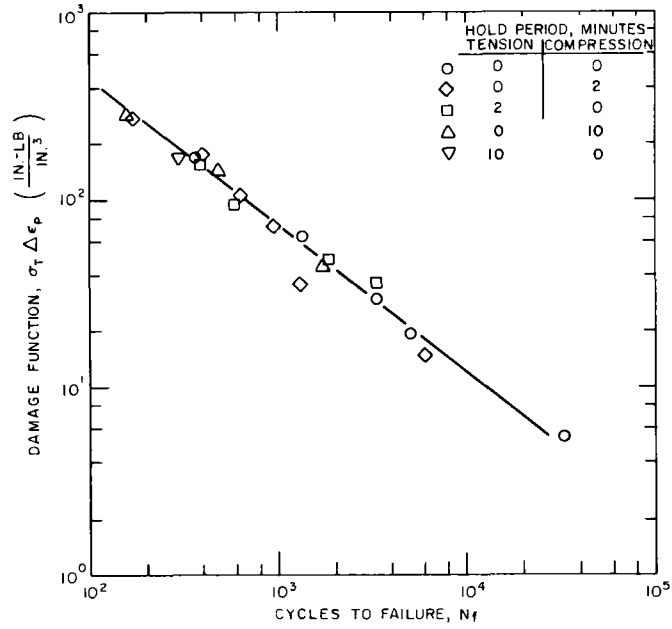


Figure 9. Damage Function,  $\sigma_T \Delta \epsilon_p$ , vs Cycles to Failure for IN-738 at 871 °C (1600 °F)

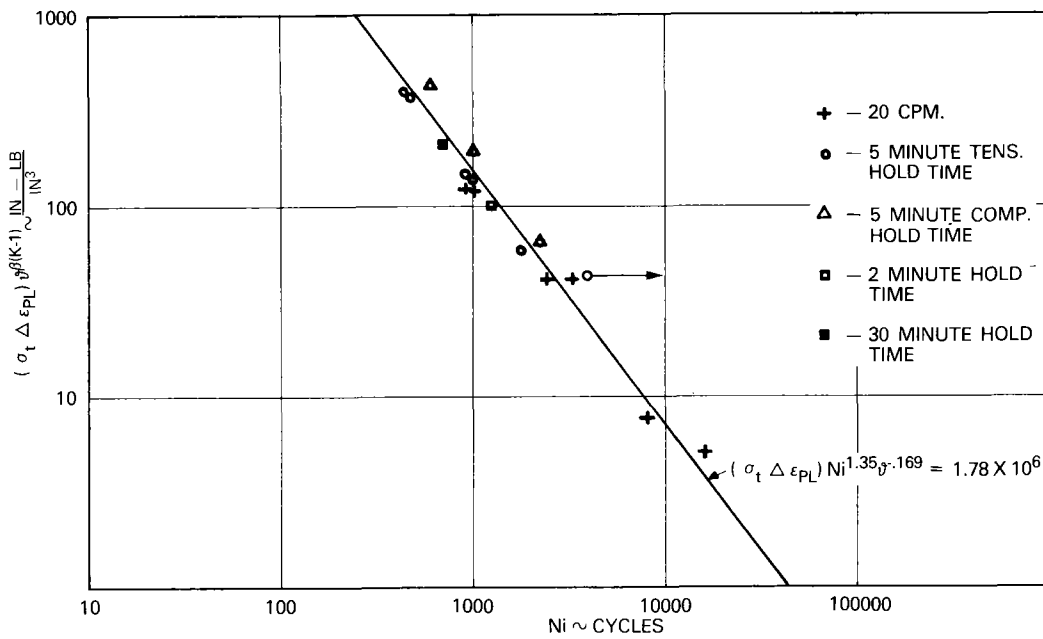


Figure 10. Correlation of Hastelloy X Data with Ostergren's Damage Function

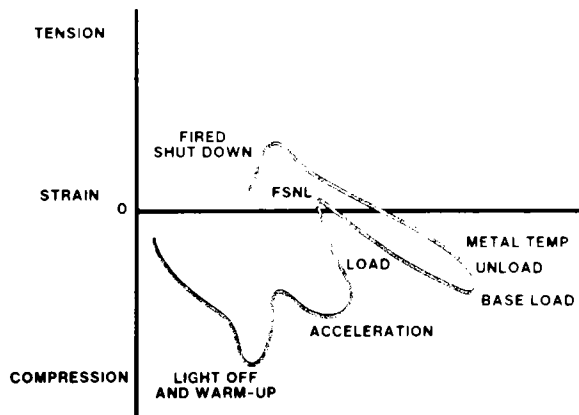


Figure 11. MS7001 Stage 1 Bucket Leading Edge Strain Temperature Variation for a Normal Startup and Shutdown

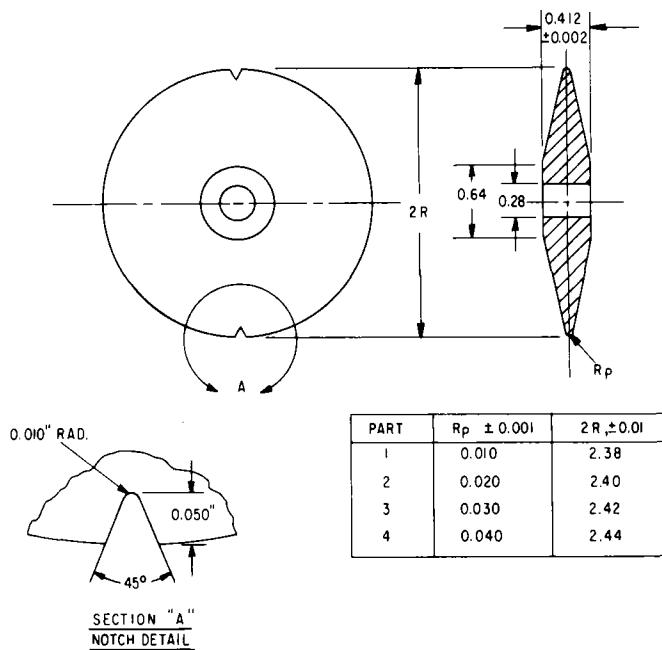


Figure 12. Tapered Disk (Glenny) Specimen

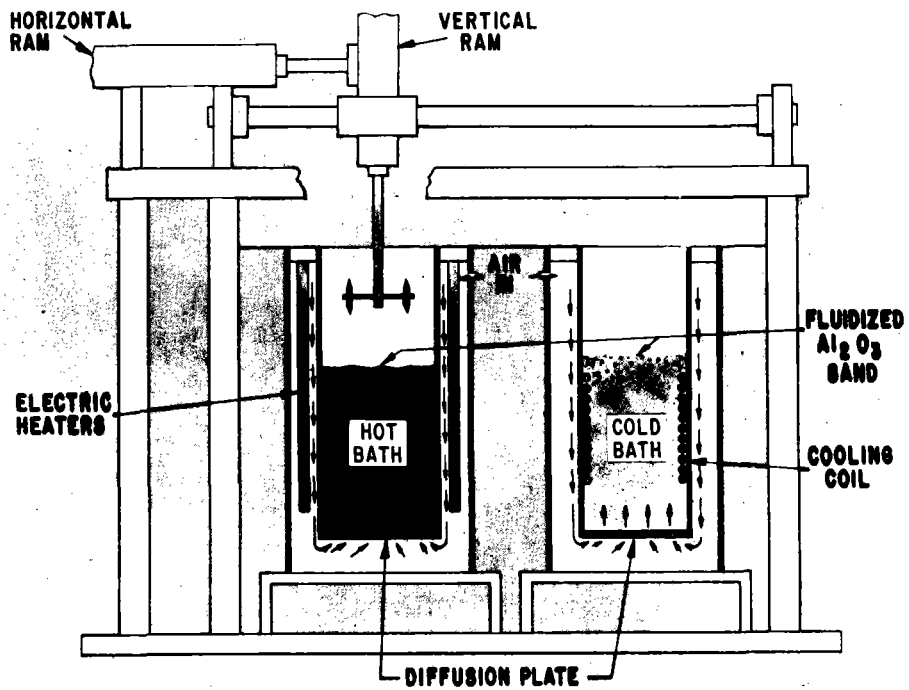


Figure 13. Schematic Illustration of Thermal Fatigue Equipment

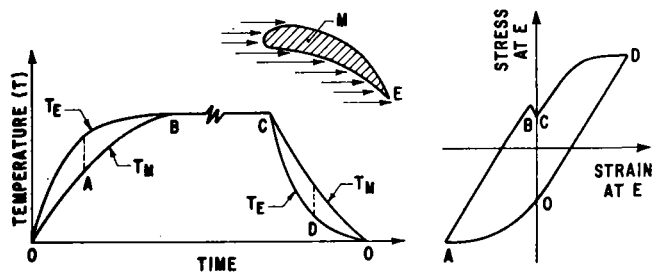


Figure 14. Origin of Thermal Fatigue Problem in Gas Turbine Airfoil Shapes

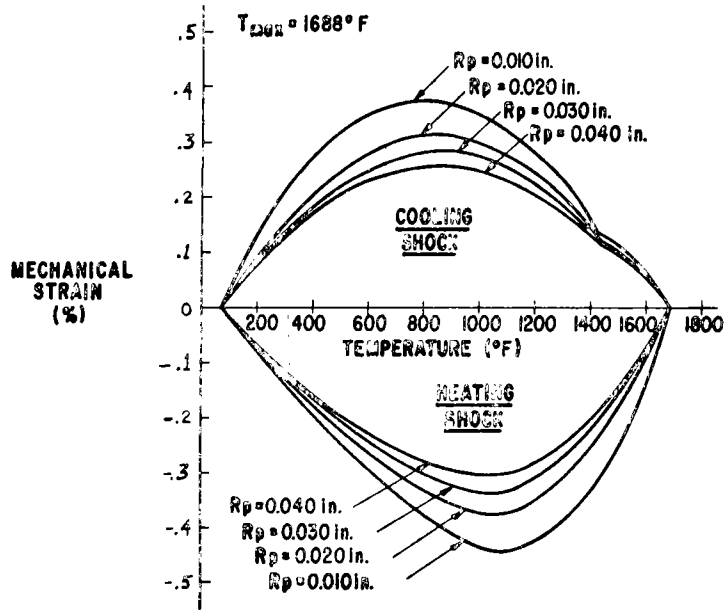


Figure 15. Example Strain-Temperature Cycles for Disk Periphery

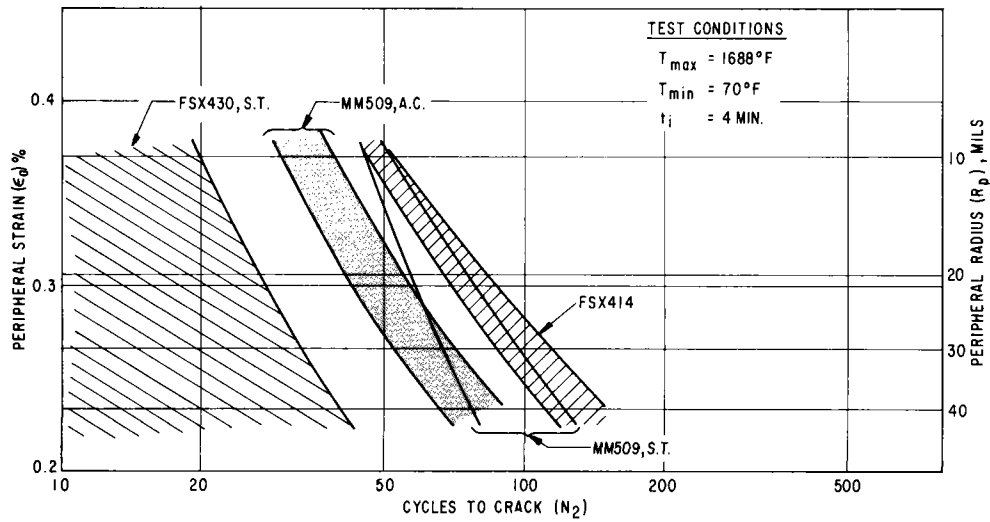


Figure 16. Crack Initiation Data Scatter Bands; Co-Base Alloys

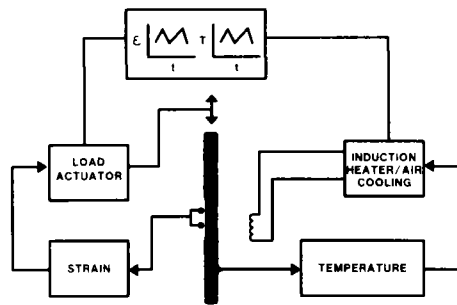


Figure 17. Thermal Mechanical Test System;  
Dual Loop Control

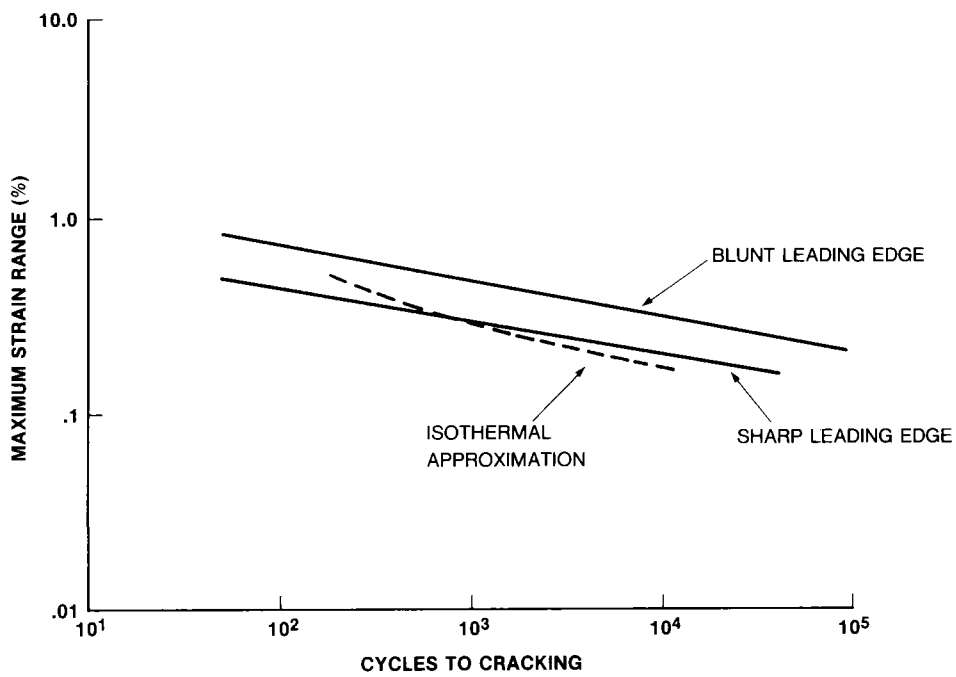


Figure 18. Test Results for IN-738 Thermal Mechanical Leading Edge Simulation  
of Bucket Cycle

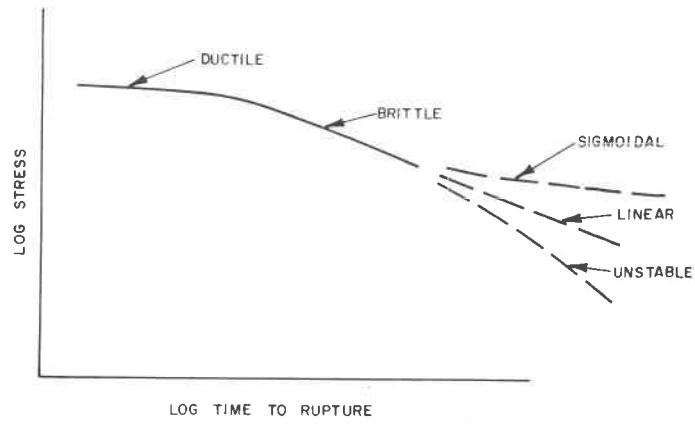


Figure 19. Characteristic Stress Rupture Response of High-Temperature Metals

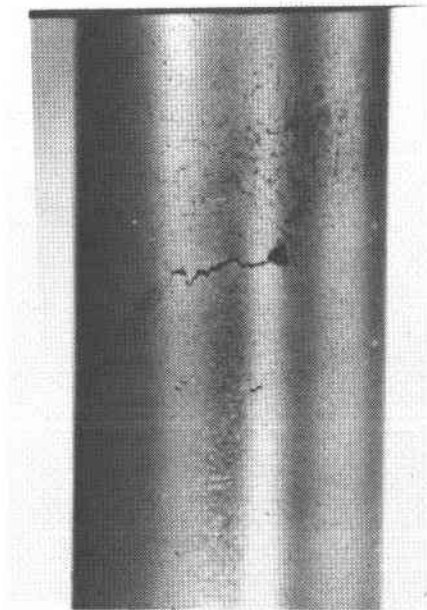


Figure 20. Surface Cracking in IN-738 After 1.2% Creep Strain at 732 °C (1350 °F)



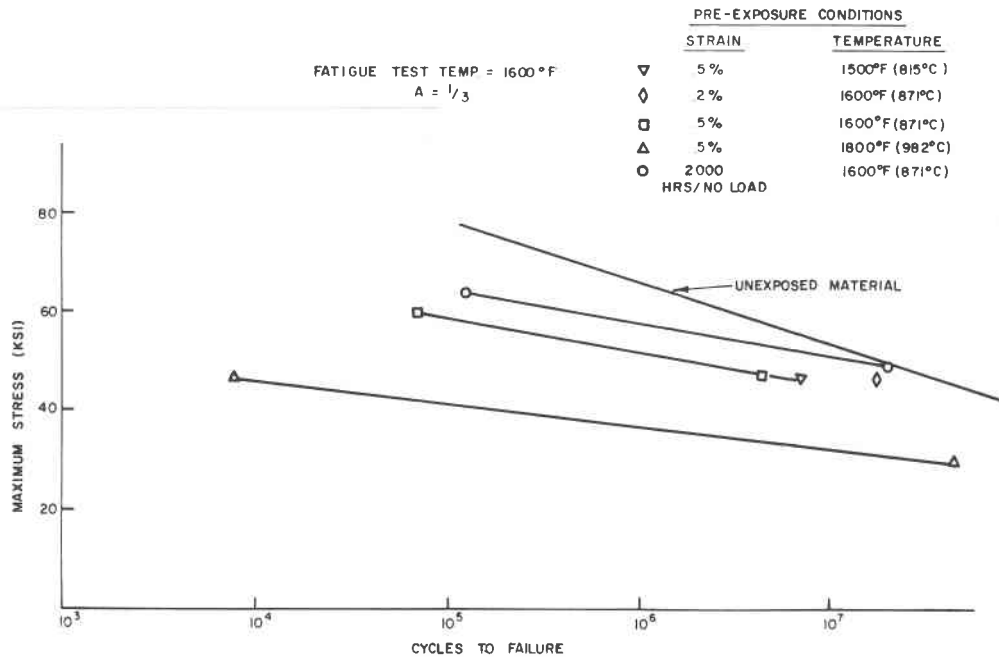


Figure 21. Effect of Pre-Exposure in Air on 871 °C (1600 °F) High-Cycle Fatigue Life of Cast IN-738

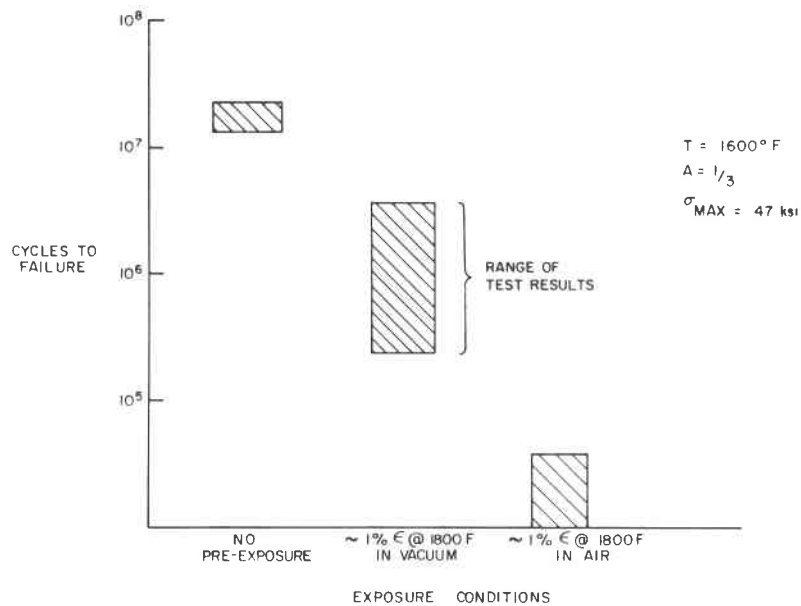
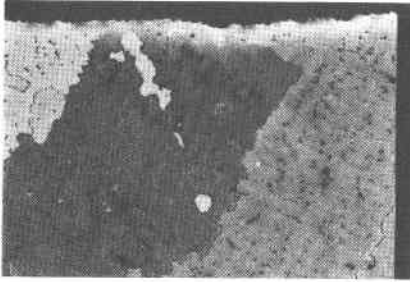
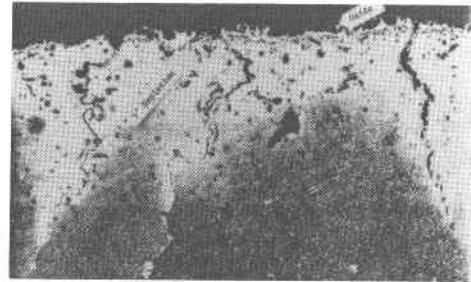


Figure 22. Effect of Creep Exposure Environment on Subsequent 871 °C (1600 °F) High- Cycle Fatigue Testing of Cast IN-738



(a) Specimen 7-145  
 Creep - 1800°F/211 hr/1% strain  
 (Vac -  $2.5 \times 10^{-6}$  torr)  
 HCF -  $1600^\circ\text{F}/\sigma_{\text{max}} = 47 \text{ ksi}/N_f = 2.62 \times 10^5$



(b) Spec. #45-145  
 Creep - 1800°F/834.1 hrs/0.55% strain (Air)  
 No HCF

Figure 23. Examples of Surface Damage Exhibited by Specimens Creep-Exposed in Air vs Vacuum Environments. Etchant: 2-2-1 (HCl-Glycerol-HNO<sub>3</sub>)

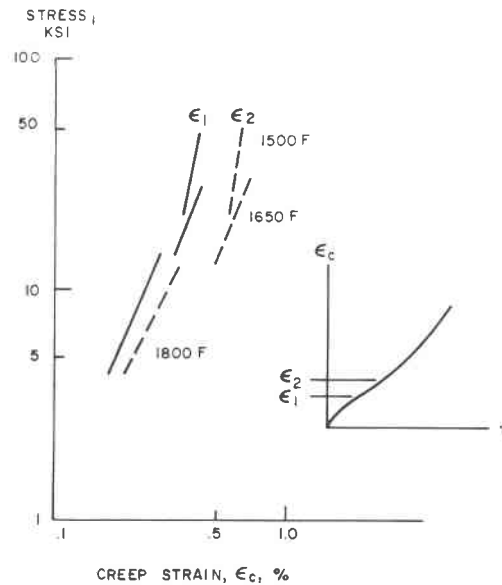


Figure 24. IN-738 Creep Curve Transition Strains

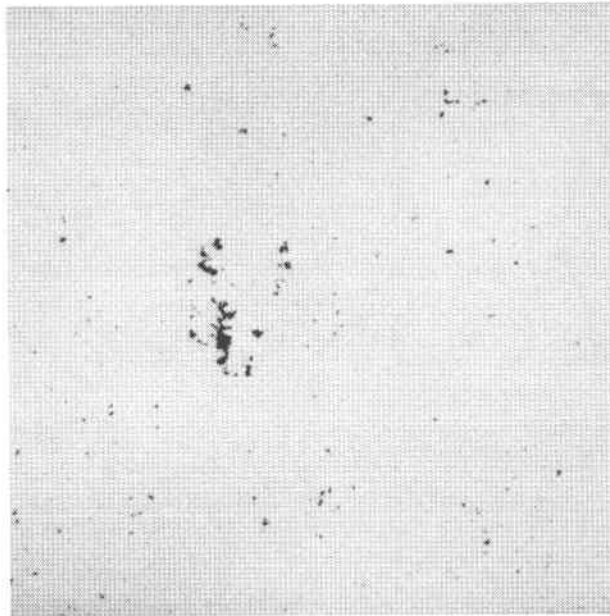


Figure 25. Shrinkage Porosity in a Cast IN-738 Bucket

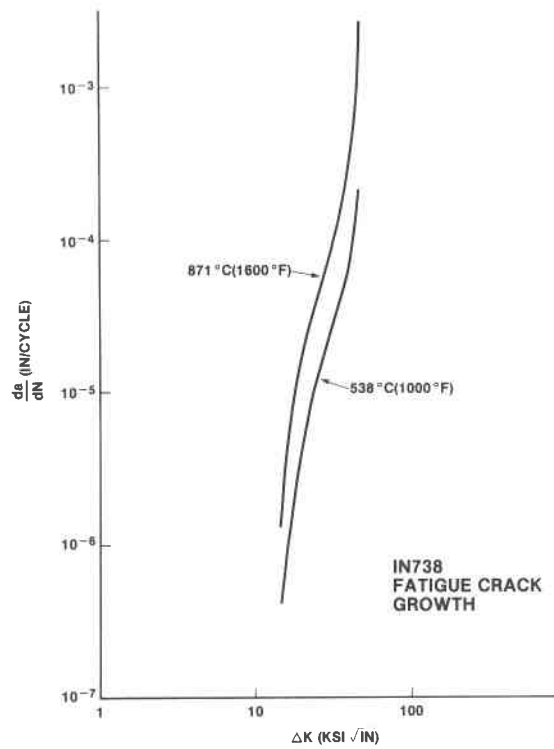


Figure 26. Effect of Temperature on Crack Growth Behavior of IN-738

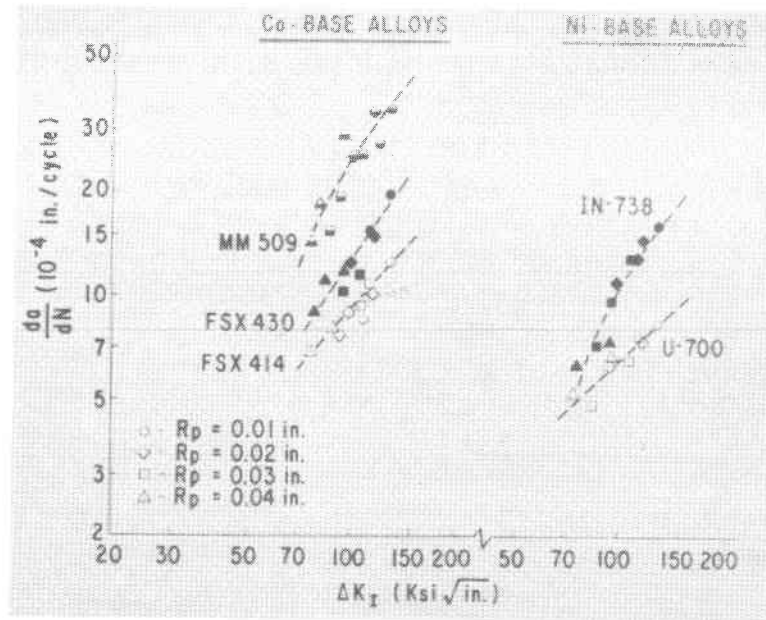
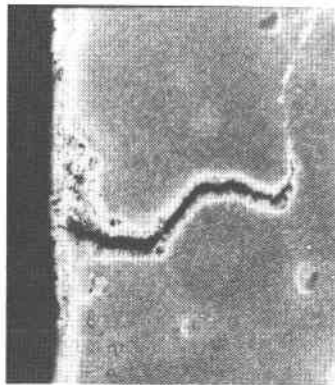
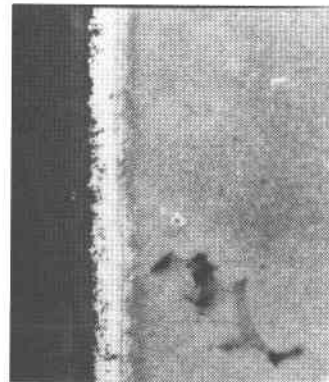


Figure 27. Comparison of Crack Growth Rates for Nickel and Cobalt Based Alloys



(a) Exposed without coating; 21,300 hr; 25 ksi



(b) Exposed with coating; 21,300 hr; 25 ksi

Figure 28. The Effect of Coating on Creep Cracking of IN-738 at 816 °C (1500 °F)

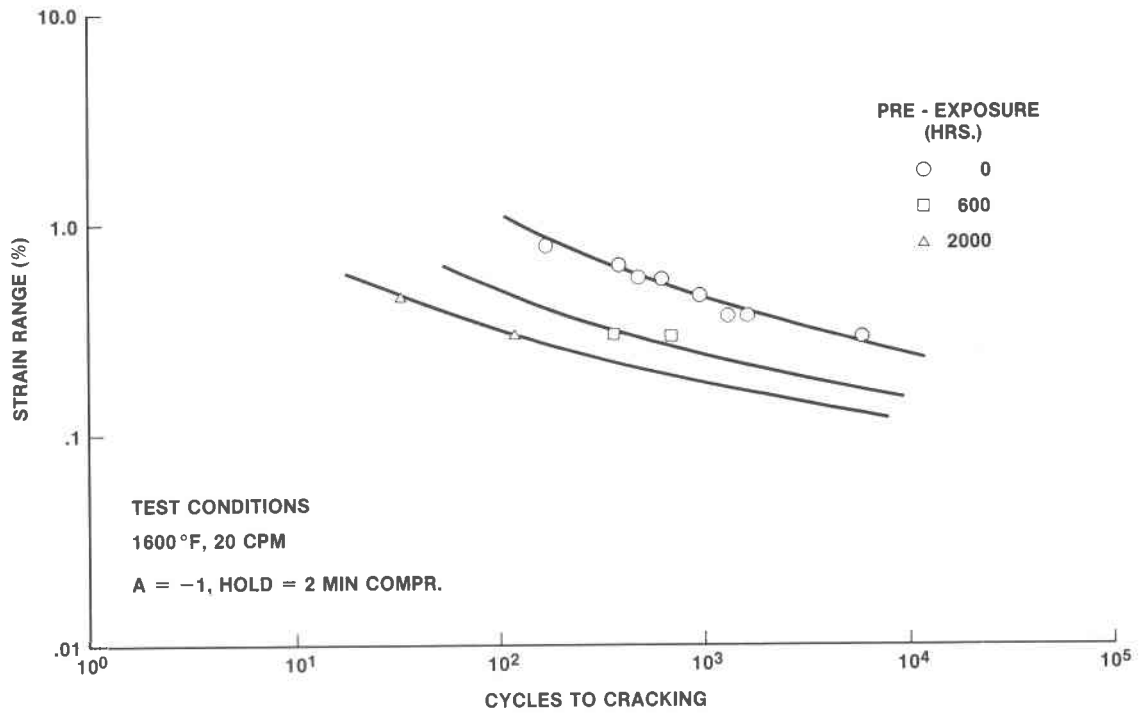


Figure 29. Effect of Pre-Exposure to Severe Hot Corrosion Environment on IN-738 at 871 °C (1600 °F)

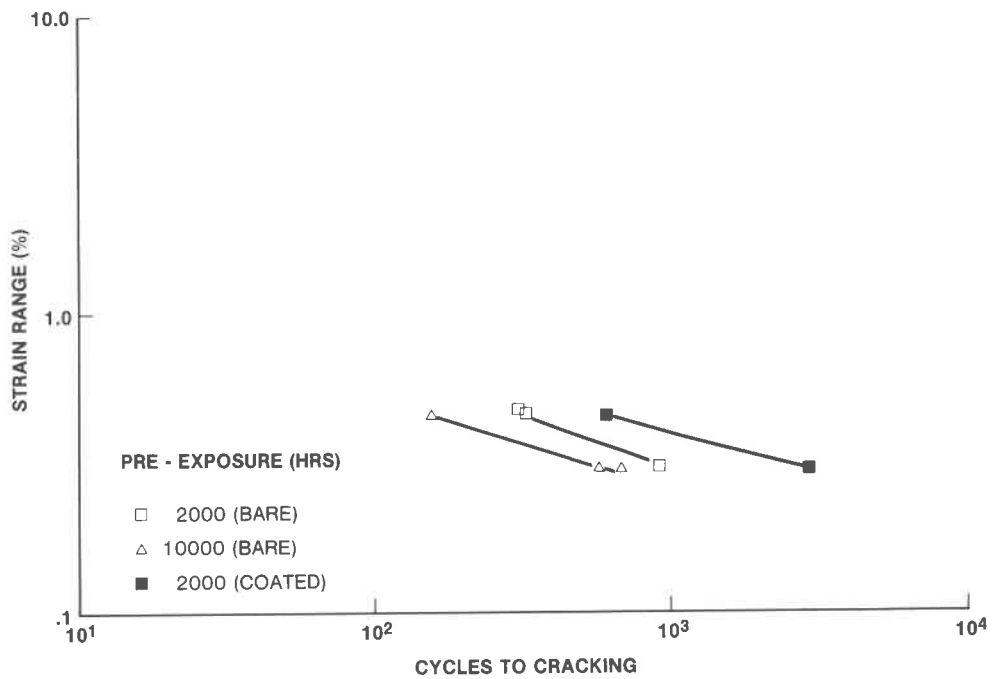


Figure 30. Effect of Oxidation Pre-Exposure on IN-738 Fatigue Properties at 871 °C (1600 °F)

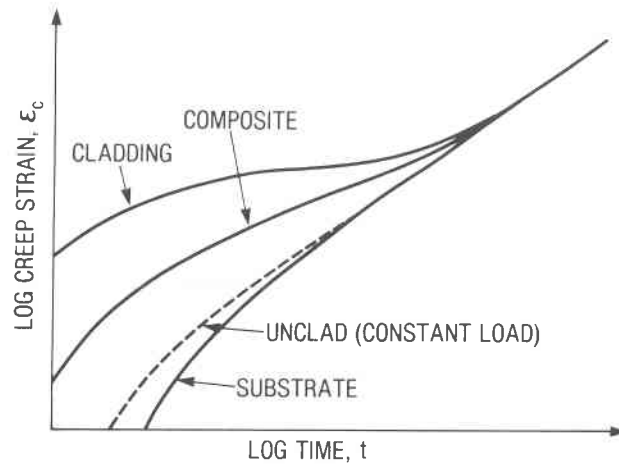


Figure 31. Typical Creep Response of a Clad Test Specimen

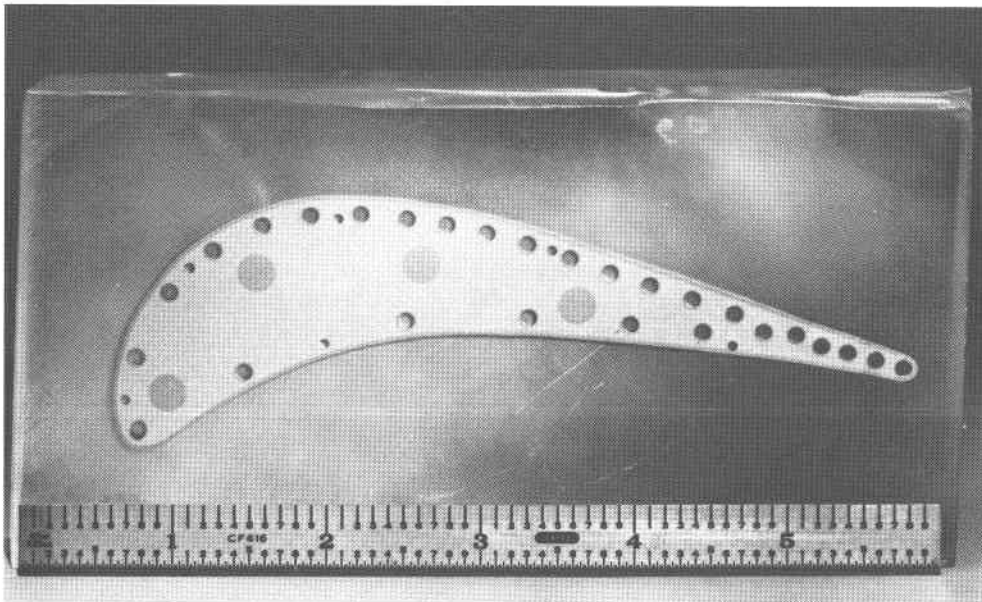


Figure 32. Composite Nozzle Cross Section through the Vane Section



Figure 33. MZC Copper Composite LCF Specimen with IN-617 Outer Skin and IN-718 Inner Tube

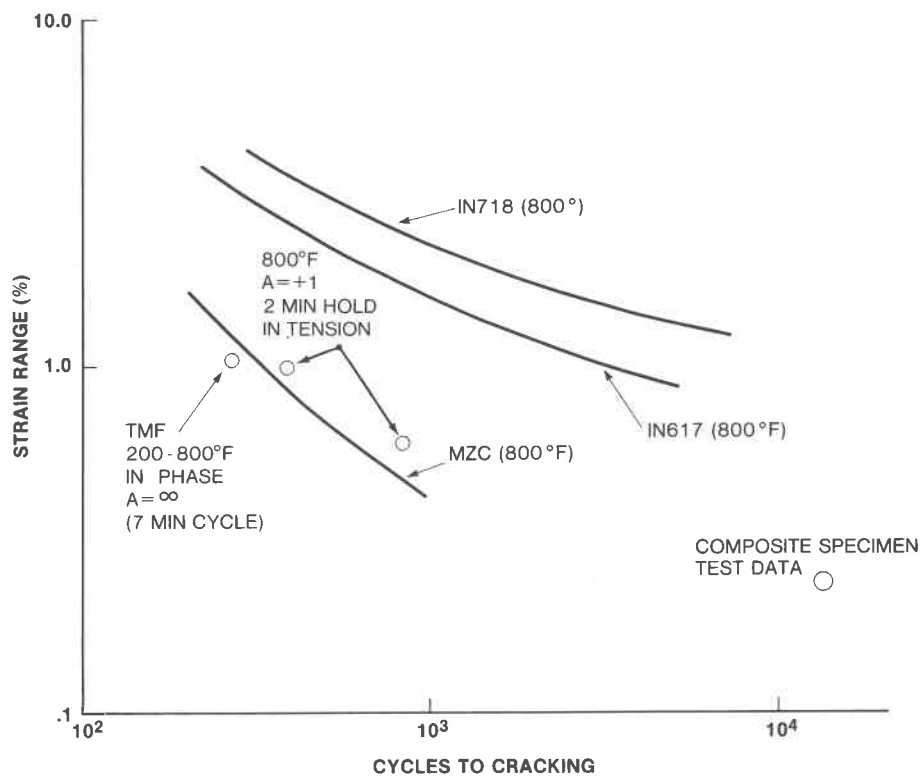


Figure 34. Composite LCF Specimen Test Results Versus Base Material Properties

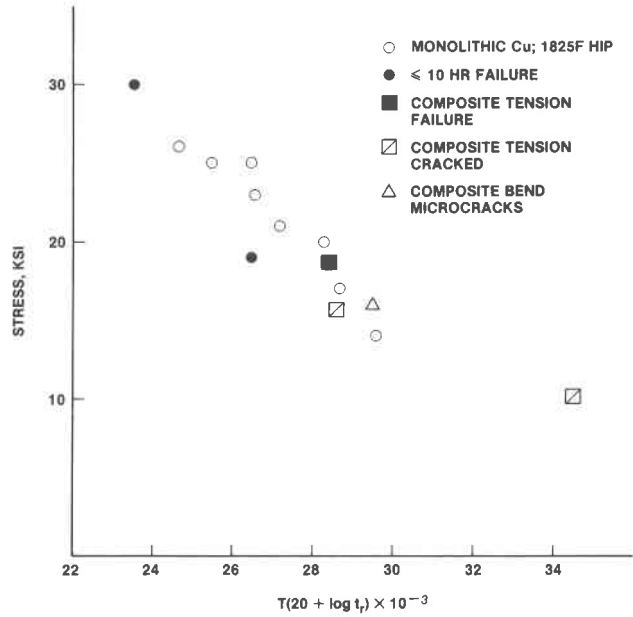


Figure 35. Comparison of Composite and Monolithic MZC Copper Creep Rupture Results

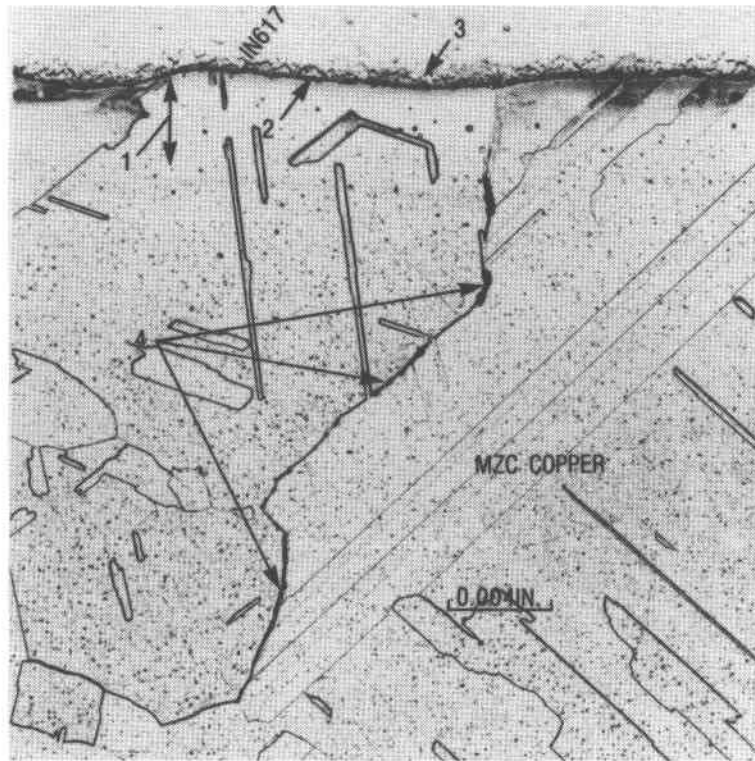


Figure 36. Metallographic Features of the Copper Composite Creep Specimens Which Did Not Fail



PROBLEMS THAT MAY RESULT FROM BURNING  
COAL DERIVED FUELS IN GAS TURBINES

P. Hancock and J.R. Nicholls  
Cranfield Institute of Technology

ABSTRACT

The problems likely to be encountered in burning coal derived fuels in gas turbines have been examined and some preliminary experiments have been made, using the Cranfield burner rigs with a solvent refined distillate SRCII fuel, supplied as a blend of 2.9 to 1 mid distillate to heavy distillate fractions. The characteristics of the solvent refined fuels have been studied. Their high carbon to hydrogen ratios are shown to cause carbon deposition on the burner can, which can only be alleviated by substantial modification of conventional combustors. The high aromatic content of the fuel causes handling and effluent problems and the precautions to be taken are examined. The fuel supplied surprisingly had a high vanadium content (30 ppm) and this caused characteristic vanadic corrosion of CoCrAlY coated specimens exposed to the combusted fuel at 750°C for 100 hours. Various types of CoCrAlY coatings have been examined under these conditions on IN792, Mar M509 and X40 substrates. The graded sputter coatings and proprietary PVD CoCrAlY coatings were more resistant to corrosive attack than sputter coatings of fixed composition and IN792 was the best of the substrate materials tested. Platinum underlay coatings were not found to give the beneficial effects reported in other test environments.

1.

INTRODUCTION

To ascertain the problems likely to be encountered in burning coal derived fuels in gas turbines, some preliminary experiments have been made using the Cranfield burner rigs with a solvent refined distillate SRCII fuel. The fuel supplied was a 2.9 to 1 blend of mid distillate and heavy distillate fractions. As it now appears likely that only middle distillate fractions will be contemplated for use in the foreseeable future, the blend supplied can be considered to constitute a more aggressive environment than will be used in potential initial applications. The difficulties

encountered may therefore be less severe than the initial experimental results indicate but the problem areas will remain the same and, if the heavy distillates are ultimately contemplated for financial reasons, the running problems will be exacerbated.

The solvent refined fuels have characteristics that differ significantly from those of conventional industrial diesel fuels. In particular, they have a high carbon to hydrogen ratio, are higher in fuel bound nitrogen and they contain an appreciably higher proportion of aromatic compounds than their petroleum based counterparts. Furthermore, although the coal derived fuels may be low in sulphur, the levels of ash and metallic elements can be high and this suggests that considerable corrosion and erosion problems may be encountered when burning these fuels in conventional industrial turbines.

The high aromatic content will tend to increase the build up of pyrolytic carbon in the combustor, which may then spall causing a significant increase in erosion problems on both vane and blades within the turbine section.

There are obvious problems in handling a new fuel of this type. The liquid has to be treated with extreme caution and good housekeeping is essential in storage and transmission. After combustion care must also be taken concerning the combustion products for these may give rise to environmental concern, if the effluent is not correctly controlled, particularly if inefficient combustion occurs.

It would be an obvious advantage if this fuel could be substituted directly into conventional industrial turbines, but this is not possible without some modification to the combustion equipment.

This paper covers the problems encountered in handling and burning a solvent refined distillate SRCII fuel in one of the Cranfield burner rigs. The corrosion problems posed by the combustion products of SRCII fuel at 750°C have been investigated by examining their effect on a range of CoCrAlY coatings deposited on IN792 and other substrates.

One of the Cranfield Gas Turbine Combustion Rigs has been modified to study the corrosion problems in the SRCII fuel. The rig has been described previously (1) and is shown schematically in Figure 1. Essentially, it consists of a high velocity fan feeding a Derwent 5 combustion can which has been modified to receive SRCII fuel. After combustion the hot gasses pass along a short flame tube into an exposure chamber which contains the specimen holder assembly. The specimens are small cylindrical pins ~ 3.2 mm diameter and 35 mm long. They are mounted in a carousel at one end and held with a retaining screw. The outer ends of the specimens are domed. The carousel can take 20 specimens and revolves at 10 revs per minute in the gas stream.

The fuel used was a blend of 2.9 parts middle distillate to one part heavy distillate SRCII. Details of the fuel analysis are given later in this paper. For this first test it was decided to run the burner rig under conditions similar to that used with conventional industrial diesel fuels to ascertain the problems that would be experienced in industrial plant if straight substitute of the fuel was contemplated. It was evident early in the test that some modification to the combustion equipment would be required to ensure successful operation of the equipment over 100 hours. These modifications will be dealt with in the section entitled combustion problems.

Problems were also encountered in both handling the fuel and in controlling exhaust emission and both of these aspects are covered later in this paper.

The rig test was run for an accumulated exposure of 100 hours at 750°C, with specimens rotating in a carousel through the exhaust gas. The rate of fuel consumption was approximately 8.1 US gals/hour to maintain a temperature of 750°C at the specimen carousel. The specimens (provided by Battelle Pacific Northwest Laboratories) were sputter deposited versions of CoCrAlY coatings with and without platinum underlay coatings. One set of CoCrAlY coatings was made with graded chromium and aluminium composition on IN792 substrate specimens. Similar specimens were also made on different substrate materials X40 and Mar M 509. Some specimens were made with constant chromium and aluminium levels through the coating and finally two PVD, CoCrAlY coatings were included, for comparison purposes. Detailed results of these exposure tests are discussed in this paper.

3.

### ANALYSIS OF 2.9:1 BLEND OF MID DISTILLATE AND HEAVY DISTILLATE SRCII COAL DERIVED FUEL

Samples of the 2.9:1 blended fuel were analysed to determine the fuel properties Metal elements present in both the fuel and ash and the more likely hydrocarbons present in the fuel have been determined.

#### 3.1 PROPERTIES OF SRCII BLENDED FUEL

The properties of this fuel are quite different from that of commercial dieso, as can be seen from Table I where the properties of this blend of SRCII fuels are compared with the specification limits (Def-Stan 91-4 (Dieso) Limits) for a commercial distillate gas oil.

The fuel sample has a dark brown/opaque appearance probably due to the presence of coal tar derivatives and contains a high proportion of compounds not soluble in n-Heptane (650 mg/l), of which an appreciable fraction were also insoluble in Toluene (160 mg/l), which implies that a large proportion of this fuel is aromatic in nature with an appreciable proportion of large polycyclic molecules. This, together with the low hydrogen content, low smoke point and high residual carbon indicated a high carbon to hydrogen ratio (confirming the fuel properties provided by the suppliers) and hence it was expected that some difficulty would be encountered in attempting to burn this fuel cleanly in a burner rig designed for gas oil fuels.

The sulphur content of this fuel was determined by two methods, by flask combustion/filtration and by X-ray fluorescence analysis. Both methods gave sulphur levels (0.32 and 0.21 wt % respectively) lower than the maximum permissible in gas oil distillates.

#### 3.2 METALLIC CONTENT OF SRCII BLENDED FUEL

Analyses of the fuel ash for metal content using X-ray fluorescence in an SEM (Figure 2) indicated that the ash was high in silicon, vanadium and iron, contained calcium and potassium plus traces of copper and zinc. Although the method of analysis is not quantitative, the high levels of iron and vanadium detected in the ash are indisputable and were totally unexpected in a fuel derived from coal. High vanadium levels are usually associated with fuels derived from the distillation of crude oils.

Atomic adsorption analysis of the whole fuel (i.e. a wet fuel sample, Table II,

confirmed the presence of both vanadium (30 ppm) and iron (9 ppm).

As mentioned above, high levels of vanadium are normally associated with petroleum based distillates and are unexpected in coals and coal derived fuels. An obvious conclusion is that the SRCII provided was not derived solely from coal but may have been derived from a blend of coal and crude or residual oil. The presence of a high proportion of aliphatic compounds (see later in this section) tends to support this hypothesis. However, it has been suggested that the high levels of iron and vanadium were the result of leaching of metallic elements from the reaction vessels, during the solvent refining process (2). The presence of both nickel and chromium in addition to iron and vanadium (Table II) adds weight to this argument as nickel, chromium and vanadium are present in many corrosion resistant steels.

It is not the aim of this paper to determine the source of heavy metal content in this fuel, but it was certainly present, and it had a significant influence on the corrosion environment generated during combustion of this fuel.

### 3.3 MOLECULAR COMPOSITION OF SRCII BLENDED FUEL

It was evident from earlier tests on the fuel properties that this fuel contained a high proportion of aromatic compounds. As many of these compounds are known to be toxic (3), a detailed analysis of the fuel using chromatographic and mass spectrometric techniques was undertaken.

As a preliminary step the fuel was separated into 5 fractions using an activated silica gel column, with elution by Pentane (250 mm x 0.45 mm Partisil PXS 10, elution rate ~ 3 ml/minutes). Elution of each fraction was monitored using a refractive index detector. Two samples were separated into fractions using this technique. The corresponding fractions from each sample were combined and the pentane was allowed to evaporate off overnight at room temperature.

It should be noted that the separation of fractions by this technique is not perfect and hence some overlap between fractions will be observed. The final fraction (fraction 5) was obtained by back flushing (i.e. reversing the flow) the eluant through the column.

The resulting fractions were colourless or light yellow with the exception of fraction 5 which was dark in colour and smelled strongly of coal tar. Each fraction was then analysed using combined gas chromatography and mass spectroscopy. The results of this analysis gave the most probable identities of the peaks detected

and the species which formed major components within a fraction. It should be emphasised that the species identified may not be the only compounds present in this fuel, as some substances may be present as traces below the resolution of this analytical system, while other very polar or pentane insoluble fractions may not have been eluted from the column at all. A summary of the results of this analysis is given below.

Fraction 1 (the lightest fraction) contains a range of aliphatic compounds typical of those found in petroleum derived fuel oils, namely decane ( $C_{10}H_{22}$ ) through to Tricotane ( $C_{30}H_{62}$ ). Dekahydro naphthalene, a likely saturated hydrocarbon from coal hydrogenation, was also identified in this fraction.

The principal components in fraction 2 were bicyclic, having either one aromatic and one aliphatic ring (Indanes) or two fused aromatic rings (Naphthalenes). Considerable overlap between fractions 2 and 3 are observed with naphthalene and phenalene derivatives forming the lower boiling point peaks. The higher boiling point peaks are associated with various polycyclic aromatic compounds (e.g. Anthracene and Pyrene derivatives). Dibenzofuran, a compound closely related to Diphenyl ether (in fraction 4), has also been identified in this fraction.

Fraction 4 is predominantly Diphenyl ether with traces of anthracene/phenanthrene derivatives from fraction 3. The presence of such a large proportion of diphenyl ether in the fuel is noteworthy, suggesting that this compound may be used in the production of SRCII, possibly as a solvent.

Finally, fraction 5, consisted mainly of phenolic compounds, normally associated with coal tar.

#### 3.4 CONCLUSIONS FROM FUEL ANALYSES

The analysis of this blend of mid to heavy distillate SRCII, indicates a fuel with low hydrogen to carbon ratio, whose hydrocarbon content is predominantly aromatic containing major amounts of condensed aromatic species. Strangely the aliphatic components of this fuel appear very similar to that found in petroleum derived fuels, which may suggest that this fuel is not wholly derived from coal.

Analysis of the metal content of the fuel and ash, indicates a high level of vanadium (30 ppm) and iron (9 ppm) in the fuel. Should the fuel contain some petroleum derivatives, then this in turn may account for the high vanadium level. Alternatively, the vanadium and iron may have been a result of metal element dissolution

during fuel manufacture.

Finally, on the basis of the elemental analysis, molecular analysis and measured properties (such as smoke point, etc.) it is anticipated that clean combustion of this blend of SRCII in a conventional gas turbine combustor, designed for gas oil, will be extremely difficult to attain.

#### 4. PROBLEMS ENCOUNTERED IN THE HANDLING AND COMBUSTION OF SRCII

For the successful operation of an engine or burner rig with a new fuel, problems associated with the handling of the fuel, its supply to the burner rig or engine, its combustion within the rig or engine and the subsequent removal of combustion products, have to be solved. In this section of the paper, consideration is given to problems encountered in the handling and combustion of this fuel in the Cranfield burner rigs, together with possible solutions and recommendations for the future use of this particular blend of SRCII fuel.

##### 4.1 HANDLING OF SRCII FUEL

The SRCII fuel was supplied to Cranfield in 55 US gal. drums and had to be transferred by hand into bulk storage containers from which the burner rig was fed. At the time of delivery no detailed analysis of the fuel was available. However, it was suspected that the fuel would be difficult to handle as each barrel had a notice attached whereby the supplying company disclaimed any liability resulting from the handling or use of the fuel. No data was available on the exact nature of SRCII, however coal tars and pitches from coal coking, gasification and combustion are known to be carcinogenic (4 - 6). Hence it was recommended that staff involved in handling the fuel should wear protective overalls and footwear, and handle the containers using protective rubber gloves. In accordance with the notice on each barrel fuel was transferred in a well ventilated area and operators were warned against prolonged breathing of the vapour.

Barrels that had contained the SRCII fuel were easily recognisable by the strong coal tar smell which remained long after these had been emptied into the bulk storage tanks. Vapour from the fuel was found to cling to operators' overalls and protective clothing, to such an extent that a complete change of protective clothing was necessary after handling the fuel.

After this early experience in handling SRCII, samples of the fuel were analysed for molecular content, Section 3.3. Toxicity levels for many of the compounds found in SRCII have been extracted from published literature. Table III - it is evident from this table that some of the components are very toxic, with exposure levels as low as 1 ppm vapour in air or 0.1 - 0.2 mg of particulates per m<sup>3</sup>. For comparison purposes the threshold limit value (i.e. the concentration of air-borne toxic substances for which a daily 8 hour exposure produces no detrimental effects) of a number of common combustion products is listed below :-

Carbon dioxide	5,000 ppm	9,000 mg/m <sup>3</sup>
Carbon monoxide	50 ppm	55 mg/m <sup>3</sup>
Nitrogen dioxide	5 ppm	9 mg/m <sup>3</sup>
Sulphur dioxide	5 ppm	13 mg/m <sup>3</sup>

It can be seen from a comparison of these values that some of the components in SRCII are more toxic than exposure to comparable levels of CO, NO<sub>2</sub> or SO<sub>2</sub>. Hence the authors can only reiterate earlier statements that SRCII fuel should be handled with caution, protective clothing must be worn and if prolonged exposure to the vapour is to be expected then either respirators, containing the correct filter element for hydro carbon gas (e.g. DIN 3181, type A, colour brown or equivalent) should be worn or self contained breathing apparatus should be provided.

#### 4.2 COMBUSTION OF SRCII BLENDED FUEL

Combustion trials showed that ignition was not a problem, but the flame was found to be burning away from the nozzle and, after an initial period, considerable coke deposits on the burner-can occurred, as experienced by other workers (7)(8).

Several tests were therefore carried out using different burner nozzles and flame tubes from both Tyne and Derwent combustors. Finally, the best burner characteristics were obtained by using the Derwent 5 combustor with extra holes drilled in the flame tube.

In spite of these initial combustion trials considerable coke build up occurred and the combustor had to be stripped every 2 hours to remove the deposits. Figure 3 shows the inside of a Derwent 5 combustor after 2 hours running time and illustrates this coking problem. Every endeavour was made to ensure that the rig was stopped when appreciable carbon deposits were formed, but there is no doubt that amounts of coke spalled throughout the test and impinged on the specimens. This means that



apart from the corrosive environment the specimens were also subjected to considerable erosive attack. Figure 4 shows a typical spectrum of coke particles collected from the exhaust tube during one of these 2 hourly combustor cleans near the end of 100 hours' running time and indicates the magnitude of this erosive problem.

Grossly simplified, the process of combustion of hydrocarbon fuels is a two step reaction. The first step involves the production of intermediary species, mainly carbon monoxide but also soot, which react further to produce carbon dioxide and steam in the second step. Carbon monoxide is always produced in this intermediary reaction, but the level of carbon production depends on the chemical composition of the fuel and the local fuel - air ratio at which combustion takes place. Polycyclic aromatic hydrocarbons with a high carbon to hydrogen ratio are known to produce large quantities of soot and this is the main reason for coke formation during the combustion of SRCII.

To overcome completely this coking problem, a complete redesign of the combustor system would be necessary. The design for low soot levels would involve the development of a system with low fuel - air ratios in the main combustion zone and/or intermediate combustion zones of sufficient temperature, residence time and oxygen concentration levels to permit oxidation of soot to  $\text{CO}_2$ .

Further, the long residence time required to completely burn the heavier fractions of this fuel means that many intermediary combustion products are present in the exhaust emission when SRCII is burnt in combustion chambers designed for petroleum based products. With the high level of carbon present in the combustion products it is possible that higher than normal levels of  $\text{NO}_x$  and CO may be present in the exhaust gas, together with partially oxidised hydrocarbons.

Although the control room is totally separated from the working area which houses the combustion rigs at Cranfield, it was decided to pressurise the control room to slightly above ambient pressure to ensure that no exhaust emission would enter the control room. In addition, when operators were required to service the burner, protective clothing similar to that provided for fuel handling had to be worn together with respirators containing an approved hydrocarbon filter. With these precautions no major difficulties were found in running the burner rig for the total of 100 hours.

5.

CORROSION OF CoCrAlY COATINGS EXPOSED TO  
SRC COMBUSTION PRODUCTS

The CoCrAlY specimens used in this investigation are detailed in Table IV. The first six compositions are graded sputter deposited coatings. The next two are fixed composition sputter deposited whilst the final composition (No. 9) is a standard PVD coating. Most coatings were on substrates of IN792, but X40 and MarM509 substrates were also included. The graded coatings and conventional PVD were tested with and without a platinum underlay coating as shown in Table IV. Full details of the development of these graded coatings by the Battelle Northwest Laboratory have been given in a previous paper in this conference series (9).

After an accumulated 100 hours exposure time at 750°C to the combustion products of SRCII fuel, specimens were removed from the rig and examined macroscopically for corrosion and damage. After macro examination, specimens were coated with copper to retain the corrosion deposits and sectioned for subsequent metallographic examination. Organic coolants were used throughout sample preparation so minimising the loss of water soluble corrosion deposits. Finally, all samples were etched using 2 : 10 HF/HNO<sub>3</sub> in water to reveal the coating structure. The degree of corrosion was assessed by measuring the coating thickness following exposure (~ 40 readings per section) and comparing these measurements with the original coating dimensions. Where only approximate original coating dimensions were available, measured corrosion loss was referenced to the maximum measured coating thickness following rig exposure. (In all cases this value was close to the quoted coating thickness).

Visual examination of the pins after exposure highlighted the problems of impact damage due to carbon spalling from the combustor can. Two of the pins had cracked through at the fixing holes at the base of each pin and a third pin was bent through some 10 - 15° at a similar position.

Deposition of combustion products was found on all pins. Microscopic examination of each coated pin was made and measured values of corrosion pit depth for the graded coating compositions (Types 1 - 4), coatings of fixed composition (Types 7 and 8), and a PVD coating (Type 9) are given in Figure 5 (10) for specimens without a platinum underlay on IN792 pins. This shows that the graded coated compositions (Types 1 - 4, Nos. 2019, 2021, 2022 and 2024) and the PVD coating Type 9 (specimen No. 2039) have considerably better corrosion resistance than the fixed coating

compositions Types 8 and 9 (specimens Nos. 2028, 2029, 2037 and 2053). The types of attack produced are significantly different and are shown in Figures 6 (a - e). Figures 6a and 6b show the extent of attack on typical graded coatings (Types 1 and 4, specimen Nos. 2019 and 2024) and should be compared with the type of attack that was observed on the fixed coating compositions (Type 7 and 8, specimens 2028 and 2037). Figures 6c and 6d illustrate the corrosion morphology found on fixed coating, which show well defined pits typical of vanadic attack or of Type II hot salt corrosion. The general attack on the PVD samples (Type 9 specimen No. 2039) was typical of a coating showing excellent corrosion resistance, Figure 6e.

As reported in a previous paper by the authors (10), the form of pitting observed on these specimens is very reminiscent of vanadic corrosion and, as the fuel contained 30 ppm vanadium, it was considered that vanadic attack was a very serious possibility. The deposits were analysed using microprobe analysis techniques and the results are shown in Figure 7 for a typical specimen (Type 1, No. 2019).

The X-ray maps show large concentrations of vanadium and minor concentrations of iron within the corrosion scale, together with concentrations of cobalt chromium and aluminium a result of coating attack. In addition some traces of carbon were detected near the outer scale surface and at localised points within the scale. Analysis of the scale using the EDAX facility attached to the microprobe, gave the metal contents listed in Table V. Assuming the most probably oxide compositions formed in the scale, a typical analysis of corrosion deposits can be calculated, Table V. It can be seen from this analysis, that the deposits formed contain a high percentage of vanadium salts. This was typical of the corrosion products observed on all specimens, with coatings showing a tendency for localised pitting which is characteristic of vanadic attack at the concentration level found in the analysis of this blend of SRCII fuel.

The influence of the substrate material under similar graded CoCrAlY sputtered coatings is shown in Figure 8. This shows that the coating performance is better on IN792 than on Mar M 509, and considerably better than on X40. The pitting is more severe on Mar M 509 and particularly severe on X40, Figure 9. It is well known that the performance of coatings can depend markedly on the underlying alloy substrate and this set of specimens confirms that this is happening under the corrosion conditions experienced in burning a 2.9 : 1 blend of SRCII fuel.

To check whether an underlay coating of 0.2 mils (5 $\mu$ m) of platinum would have a significant effect on the corrosion resistance of both graded sputter coated and proprietary PVD coatings, similar specimens with and without an underlay coating have been compared in Figure 10. These results show that under these particular corrosion conditions the specimens with a platinum underlay coating are slightly less resistant than the comparable specimens tested without a platinum underlay. This trend is confirmed for both maximum and average corrosion figures. The significance of these findings has been analysed in detail using statistical techniques in a previous paper by the authors (10).

## 6.

### CONCLUSIONS

1. Combustion characteristics of SRCII fuel are very different from standard diesel fuel so that combustion in equipment designed for conventional fuel oil proved to be extremely difficult. The major practical problem was associated with the high carbon : hydrogen ratio of the fuel which caused coke build up in the combustion chamber necessitating regular coke removal and causing erosive conditions in the flue gas. If this fuel is to be used, specially designed combustion systems are necessary.
2. The molecular composition of the fuel requires that extreme care must be taken during handling of the liquid. The high aromatic level means that efficient combustion is essential to minimise effluent problems and care must be taken to protect the operators from direct effluent exposure.
3. Analysis of the SRCII fuel showed that it had a high heavy metal content, particularly vanadium which is known to cause accelerated corrosive attack and vanadate corrosion has been observed on the coated specimens at the test temperature of 750°C.
4. In spite of these unusually aggressive conditions all the coatings examined provided protection to the underlying metal as long as the coating was free from severe processing defects.
5. The Battelle graded sputter coatings and the proprietary PVD coatings were more resistant to corrosive attack in SRCII fuel than the sputtered coatings of fixed composition that were examined.
6. There was a significant influence of metal substrate on the corrosive resistance of the graded coatings. The coatings on IN792 being more resistant than those on Mar M 509 which were better than the coatings on X40.
7. The difference between the corrosion resistance of both graded sputtered coatings and PVD coatings with and without platinum was small, but under these particular conditions a platinum underlay does not offer any significant advantage, in fact it appears to be slightly deleterious.

7.

#### ACKNOWLEDGEMENTS

This work was performed under contract for the Battelle Pacific Northwest Laboratories as part of the EPRI research programme. The authors would like to thank these organisations for permission to publish this work and would also like to acknowledge Dr. R.W. Hiley for the work on chemical analysis and for helpful discussions on the fuel characteristics.

8.

#### REFERENCES

1. J.F.G. Conde, B.A. Wareham, P. Hancock, R.C. Hurst and J.C. Clelland. Inhibition of Hot Corrosion. 3rd Conference on Gas Turbine Materials in a Marine Environment. Bath, England. September 1976.
2. J. Patten. Private communication.
3. 'Handbook of Chemistry and Physics', 59th Edition. 1978 - 79. CRC Press, pp. D161 - 166.
4. C.S. Weil and N.I. Condra. Arch. Environ. Health 9, 1960, pp. 137 - 193.
5. R.J. Sexton. Arch. Environ. Health 9, 1960, pp. 208 - 231.
6. R. Doll et al, Br. J. Ind. Med. 29, 1972, pp. 394 - 406.
7. P.W. Pittsbury, A. Cohn, P.R. Mulik and T.R. Stein, 'Investigating Combustion Turbine Burner Performance with Coal Derived Liquid Having High Fuel Bound Nitrogen'. ASTM 78-GT-126. Paper given at Gas Turbine Conference, London, April 9 - 13, 1978.
8. P.W. Pittsbury, A. Cohn, P.R. Mulik, P.P. Singh and T.R. Stain. 'Fuel Effects in Recent Combustion Turbine Burner Tests of Six Coal Liquids'. ASME Gas Turbine Conference, March 11 - 15, 1979.
9. J.W. Patten, R.W. Moss, D.D. Hays and J.W. Fairbanks. 'Development of Graded Composition CoCrAlY (+ Pt) Sputtered Coatings in the Proceedings of the First Conference on Advanced Materials for Alternative Fuel Capable Directly Fired Heat Engines. 31 July - 3 August 1979, Castine Maine, pp. 459 - 472.
10. P. Hancock and J.R. Nicholls. Paper presented at the International Conference on Metallurgical Coatings, San Diego, April 1980. Awaiting publication.
11. P. Hancock, 'Corrosion of Alloys at High Temperatures in Atmospheres Consisting of Fuel Combustion Products on Associated Impurities', HMSO Review, 1968.

Table I

 PROPERTIES OF 2.9:1 MID/HEAVY DISTILLATE SRCII COMPARED  
 WITH STANDARD DIESO FUELS

Property	SRCII* (Independent Analysis)	SRCII* (Shipment Analysis)	Dieso (Limits)
Appearance	Dark brown/opaque	-	Clear and bright
Density @ 15°C	0.999	0.999 (@ 15.6°C, 60°F)	0.82 → 0.86
Flash point °C	80	71 → 73	66 min
Pour point °C	-	-48 → -43	-
Viscosity at 40°C cSt	4.37	4.53 → 4.61 (@ 37.8°C, 100°F)	1.7 → 4.1
n-Heptane Insol- ubles mg/l	650	-	-
Toluene Insol- ubles mg/l	160	-	-
Organic Acidity mg KOH/ml	0.41	-	0.5 max
Conradson Carbon %	-	0.23 → 0.34	-
Rambottom Carbon Residue on Centrifuged Whole Sample %	0.44	-	0.2 max (on 10% residue)
Water % wt	trace	trace	0.05 max
Ash % wt	0.018	0.02	0.01 max
Sulphur % wt	0.32(a) 0.21(b)	0.21 → 0.23	1.00 max
Oxygen % wt	-	3.36 → 3.99	-
Hydrogen % wt	8.73	8.64 → 8.75	12.8 → 13.5 (typical)
Carbon % wt	-	86.21 → 86.72	-
Nitrogen % wt	-	0.92 → 0.95	-
Smoke point mm	5 → 8 (flame unstable)	-	14 → 16 (typical)

\* Shipment analysis is from laboratory test reports issued by Pittsburg & Midway Coal Mining Company - Solvent Refining Coal Pilot Plant. Independent analysis was undertaken for Cranfield by R.W. Hiley, Chemistry & Petroleum Technology Dept., N.G.T.E.

(a) determined using flask combustion/filtration (b) determined by X-ray fluorescence

Table II

ATOMIC ADSORPTION ANALYSIS ON FUEL SAMPLE  
OF SRCII TO DETERMINE METAL CONTENT

Metallic Element	Al	Cu	Cr	Fe	Pb	Na	Sn	Ni	Si	V	K
Content ppm	N.D.	N.D.	3	9	N.D.	0.2	N.D.	0.2	N.D.	30	N.D.

N.D. = not detectable

Table III

TOXITIES OF COMPOUNDS IN SRCII  
(Limits for human exposure to air contaminants (3))

Compound	Contaminant Level	
	ppm vapour in air	mg/m <sup>3</sup> of particulates in air
Alkanes (e.g. Heptane)	500	2,000
Methyl butyl benzene	10	60
Diphenyl ether (vapour)	1	7
Naphthalene	10	50
Naptha (coal tar)	100	400
Coal tar pitch volatiles (benzene soluble fraction; anthracene, phenanthrene, acridine, chrysene, pyrene)		0.2
Cresol (all isomers)	5 (skin)	22 (skin)
V <sub>2</sub> O <sub>5</sub> fume		0.1
Benzene	10 ppm	} 8 hour weighted average (Threshold limit values)
Toluene	220 ppm	

Table IV

## TYPES OF COATINGS EXAMINED. SUPPLIED BY BATTELLE PACIFIC NORTHWEST LABORATORIES

Type No. Sputter Depos- ited	Sample No.	Pin Alloy	Pit under- layer thickness mils	CoCrAlY thickness mils	Deposit Composition	Run No.	Cr Target Voltage Ramp	Thermal Treatment of Pins
1	2002	IN792	0.2 (~5 $\mu$ m)	~4.6(~117 $\mu$ m)	{Cr 25-30% est Al 10- 8% est	5	50' @ 500,600,700V,5' @ 800V " " " " " " " "	Vac HT 4hrs @ 1080 $^{\circ}$ C " " " " "
	2019	IN792	0	~4.6(~117 $\mu$ m)				
2	2004	IN792	0.2	~5.5(~140 $\mu$ m)	{Cr 25-30% est Al 10- 8% est	6	55' @ 500,600,700,800V " " " " " " "	Vac HT 4hrs @ 1080 $^{\circ}$ C " " " " "
	202L	IN792	0	~5.5(~150 $\mu$ m)				
3	2006	IN792	0.2 ( 5 m)	~4.2(~107 $\mu$ m)	{Cr 24.1-32.6%est Al 9.8- 8.4%est	7	60' @ 600,700,800,10' @ 900V " " " " " " "	Vac HT 4hrs @ 1080 $^{\circ}$ C " " " " "
	2022	IN792	0	~4.2(~107 $\mu$ m)				
4	2007	IN792	0.2 ( 5 m)	~7.0(~178 $\mu$ m)	{Cr 25 - 35% Al 10 - 8%	7	60' @ 600,700,800,900,1000V " " " " " " " " " " " " " "	Vac HT 4hrs @ 1080 $^{\circ}$ C " " " " " Vac HT 4hrs @ 1080 $^{\circ}$ C + 1 hr in air @ 1080 $^{\circ}$ C
	2008	IN792	0.2 ( 5 m)	~7.0(~178 $\mu$ m)				
	2024	IN792	0	~7.0(~178 $\mu$ m)				
5	5028	Mar.M	0	~7.0(~178 $\mu$ m)	{Al 10 - 8% Cr 25 - 35%	9	60' @ 600,700,800,900,1000V " " " " " " "	None (as-deposited) " " "
		509		0				
6	1038	X40	0	~7.0(~178 $\mu$ m)				
7	2028	IN792	0	6.5(~165 $\mu$ m)	{Cr 32.6% Al 9.4%	13	1000V "	Vac HT 4hrs @ 1080 $^{\circ}$ C " " " " "
	2029	IN792	0	6.5(~165 $\mu$ m)				
8	2037	IN792	0	6 (~152 $\mu$ m)	{Cr 30% Al 9.5%	14	800V "	Vac HT 4hrs @ 1080 $^{\circ}$ C " " " " "
	2053	IN792	0	6 (~152 $\mu$ m)				
PVD 9	2059	IN792	0.2 ( 5 m)	3.5(~89 $\mu$ m)	{Cr 23% Al 9.1% Y 0.3%			
	2039	IN792	0	3.5(~89 $\mu$ m)				



Table V  
ANALYSIS OF CORROSION SCALE ON A TYPICAL CoCrAlY COATED SAMPLE  
(Specimen No. 2019)(10)

	<u>Elements detected in the scale</u>		<u>Most probable oxides in the scale</u> *	
	Wt %	At %		Wt %
Al	7.92	14.85	Al <sub>2</sub> O <sub>3</sub>	10.29
Si	0.87	1.56	SiO <sub>2</sub>	1.27
S	0.18	0.28	SO <sub>3</sub>	0.30
K	0.27	0.35	K <sub>2</sub> O	0.22
Ca	0.64	0.81	CaO	0.62
V	13.08	12.89	V <sub>2</sub> O <sub>5</sub>	15.92
Cr	29.54	28.51	Cr <sub>2</sub> O <sub>3</sub>	29.43
Fe	7.91	7.11	Fe <sub>2</sub> O <sub>3</sub>	7.71
Co	39.52	36.65	CoO	34.24

\* Many of the oxides could be found in combination, for example the following are known to occur in combustion deposits (11)  
CaSO<sub>4</sub>; K<sub>2</sub>SO<sub>4</sub>; Fe<sub>3</sub>O<sub>4</sub>.2V<sub>2</sub>O<sub>5</sub>; K Al Si<sub>3</sub>O<sub>8</sub> (ash).

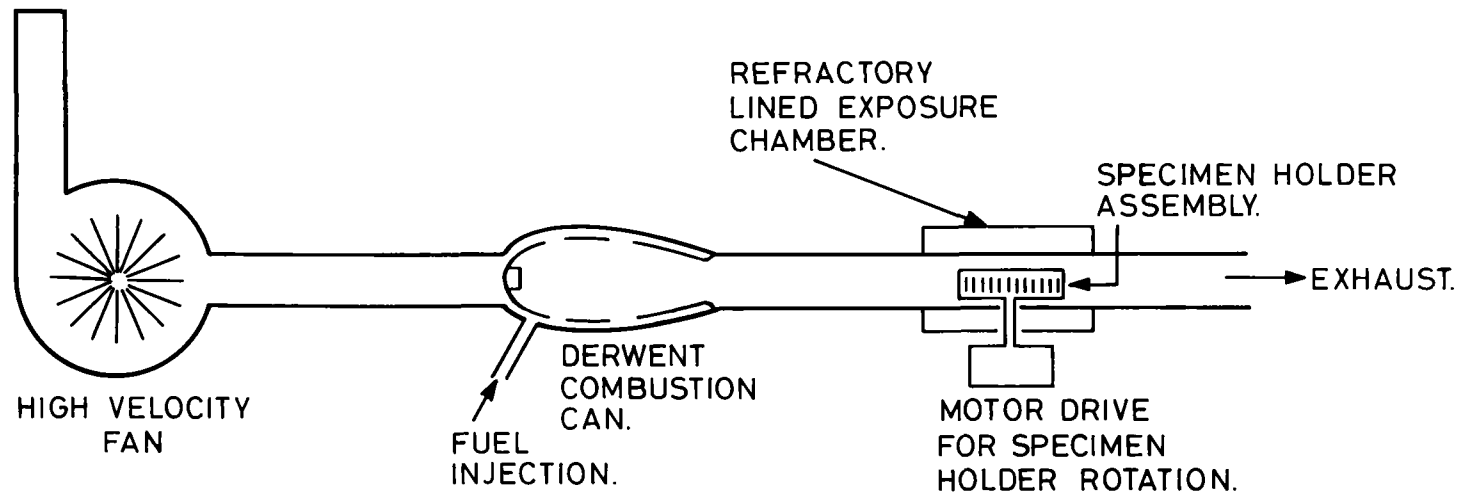


Figure 1. Schematic diagram of turbine simulator rig.

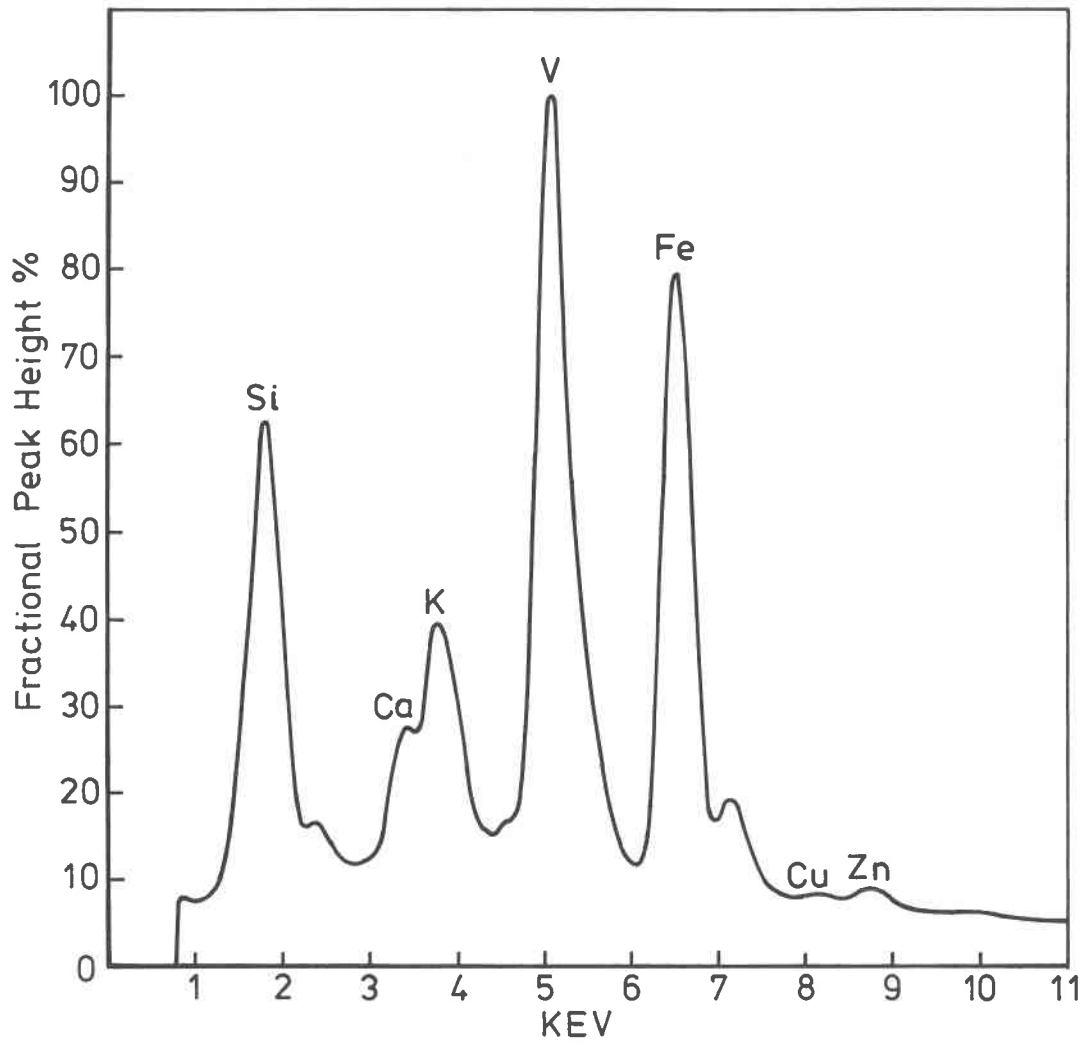


Figure 2. Analysis of ash from SRCII blended fuel.

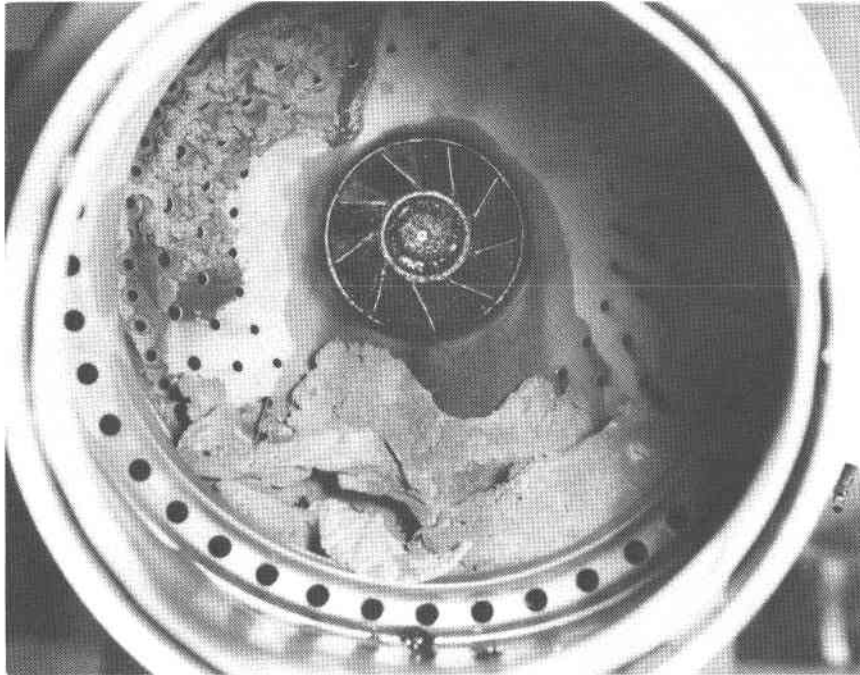


Figure 3. View into the combustion chamber, showing the build up of pyrolytic carbon

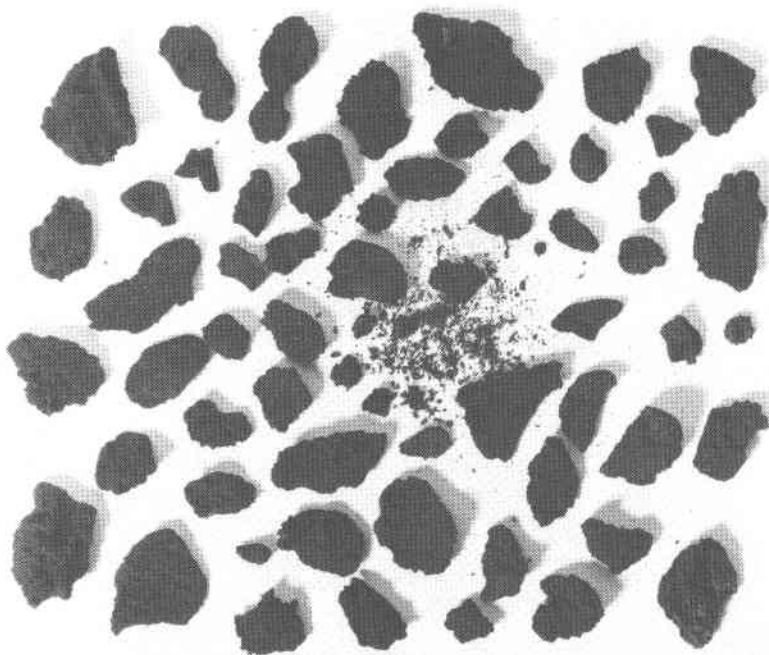


Figure 4. Typical carbon deposits removed from the exhaust duct  $X_{\frac{1}{2}}$ \*  
Carbon deposits formed during 2 hours combustion of SRC II at 750°C  
\*Please note that the illustration(s) on this page has been reduced 10% in printing.

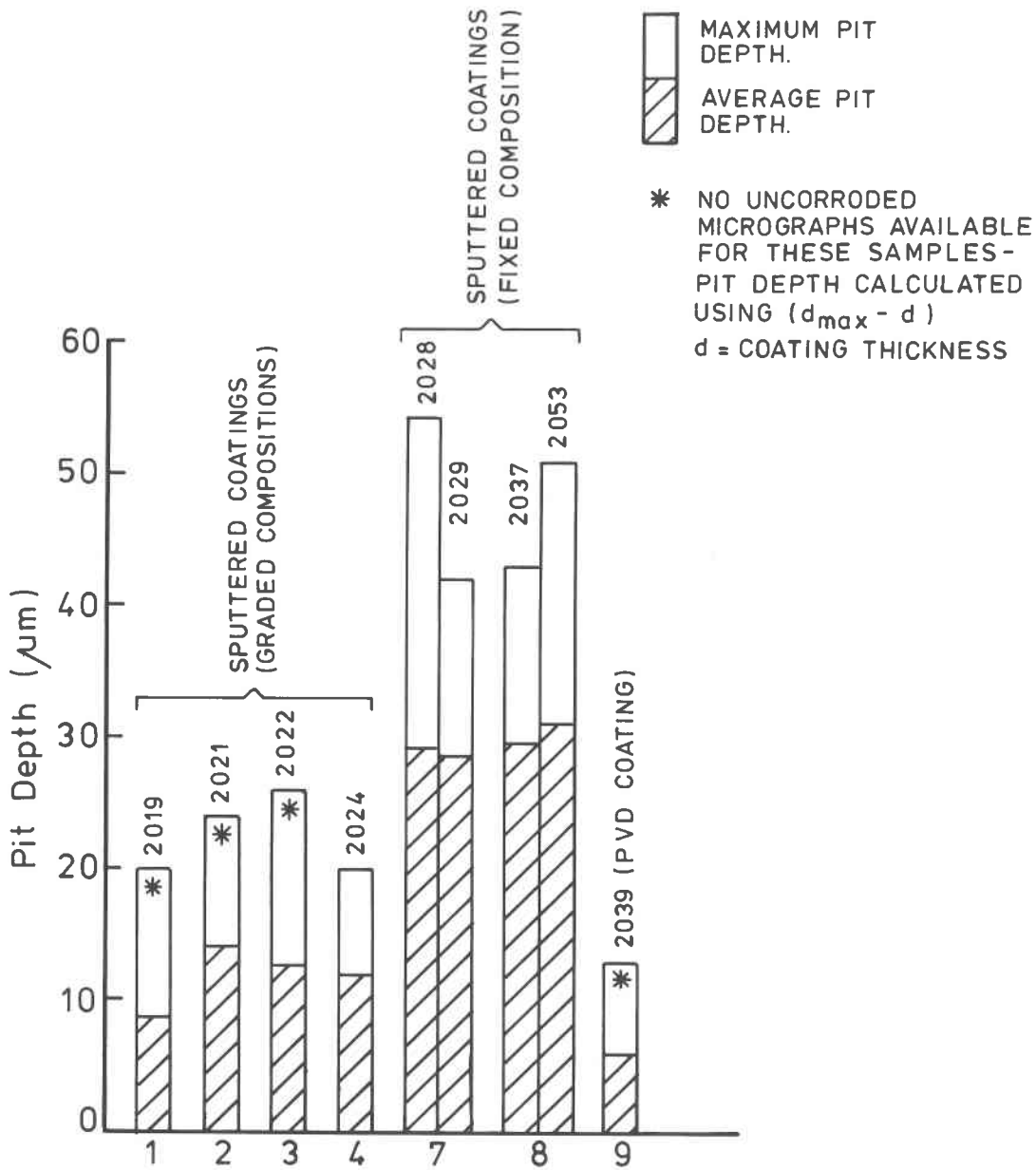
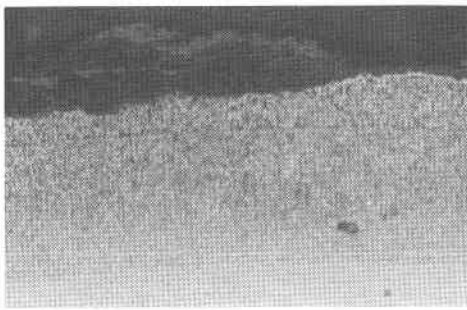
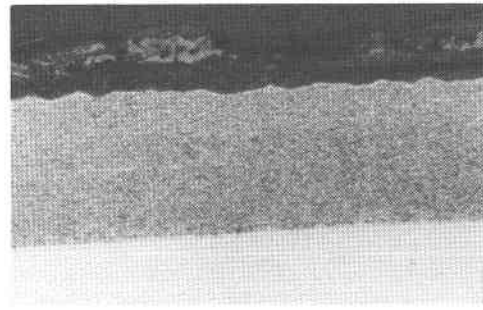


Figure 5. Comparison of coating loss, due to corrosion, for a range of CoCrAlY coatings, deposited using sputtering and PVD techniques. (10)

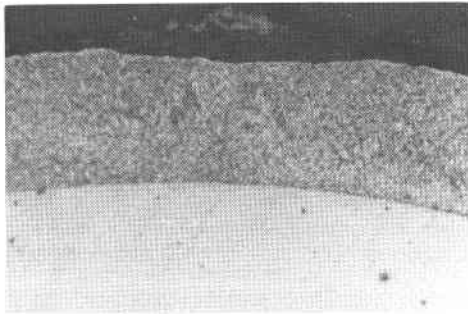


(a) Sample 2019

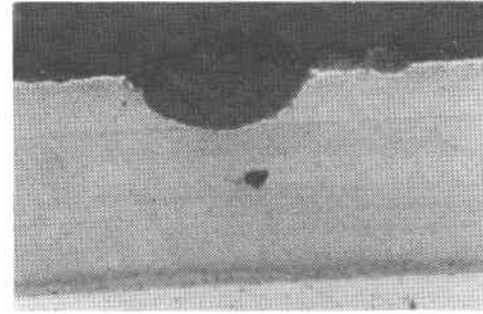


(b) Sample 2024

Sputter deposited coatings of graded composition

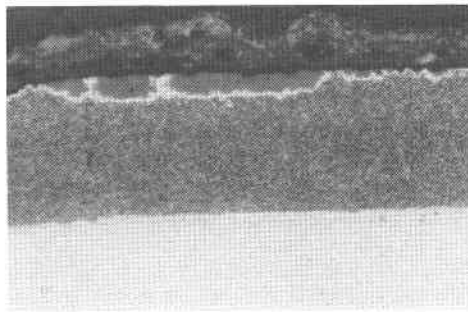


(c) Sample 2037



(d) Sample 2028

Sputter deposited coatings of fixed composition



(e) Sample 2039 - a proprietary PVD coating

Figure 6. Corrosion morphologies of CoCrAlY overlay coatings as a function of processing route on an IN792 substrate

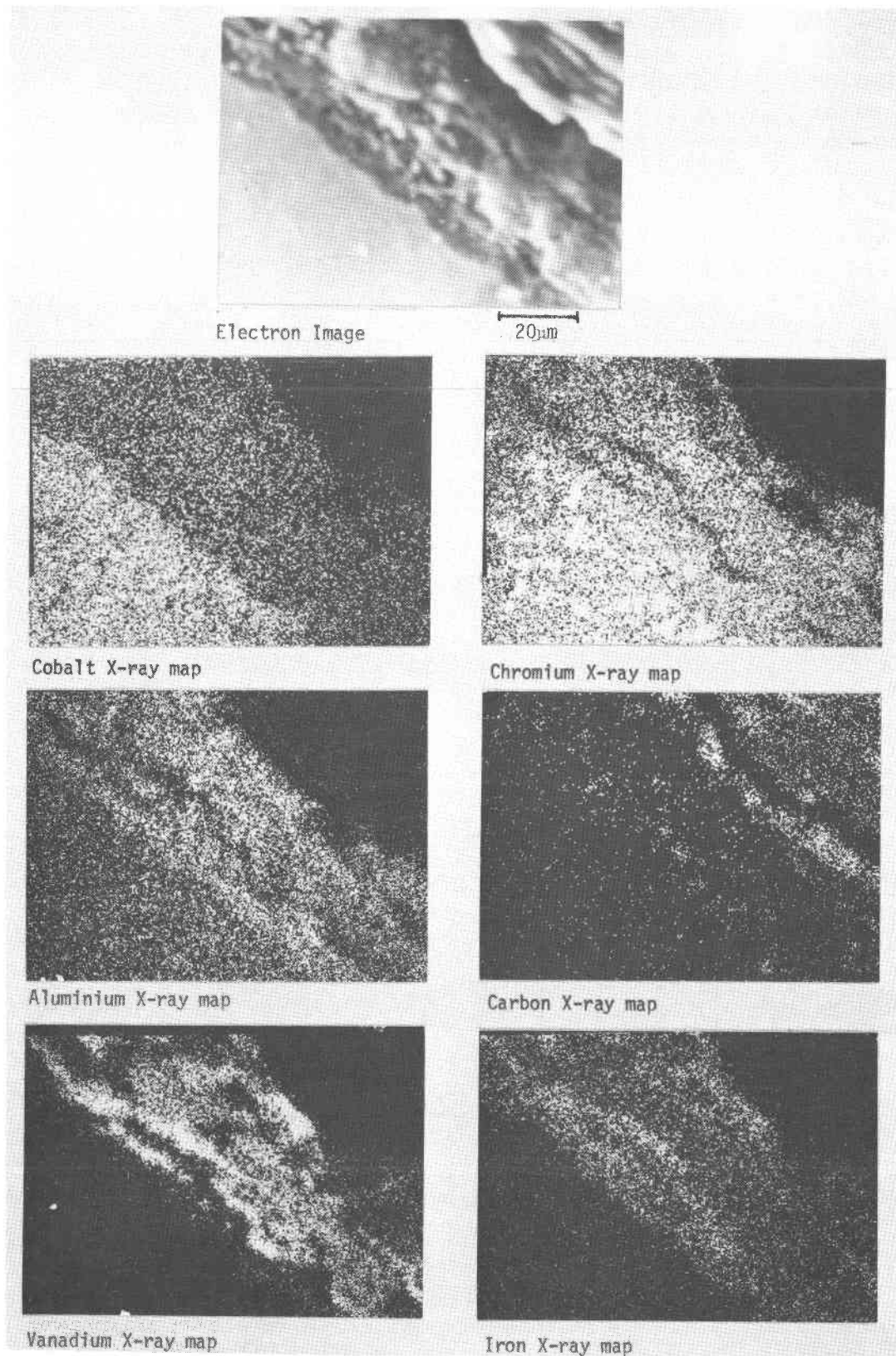


Figure 7. Microprobe analysis of corrosion deposits on CoCrAlY coated IN792 (Specimen 2019)

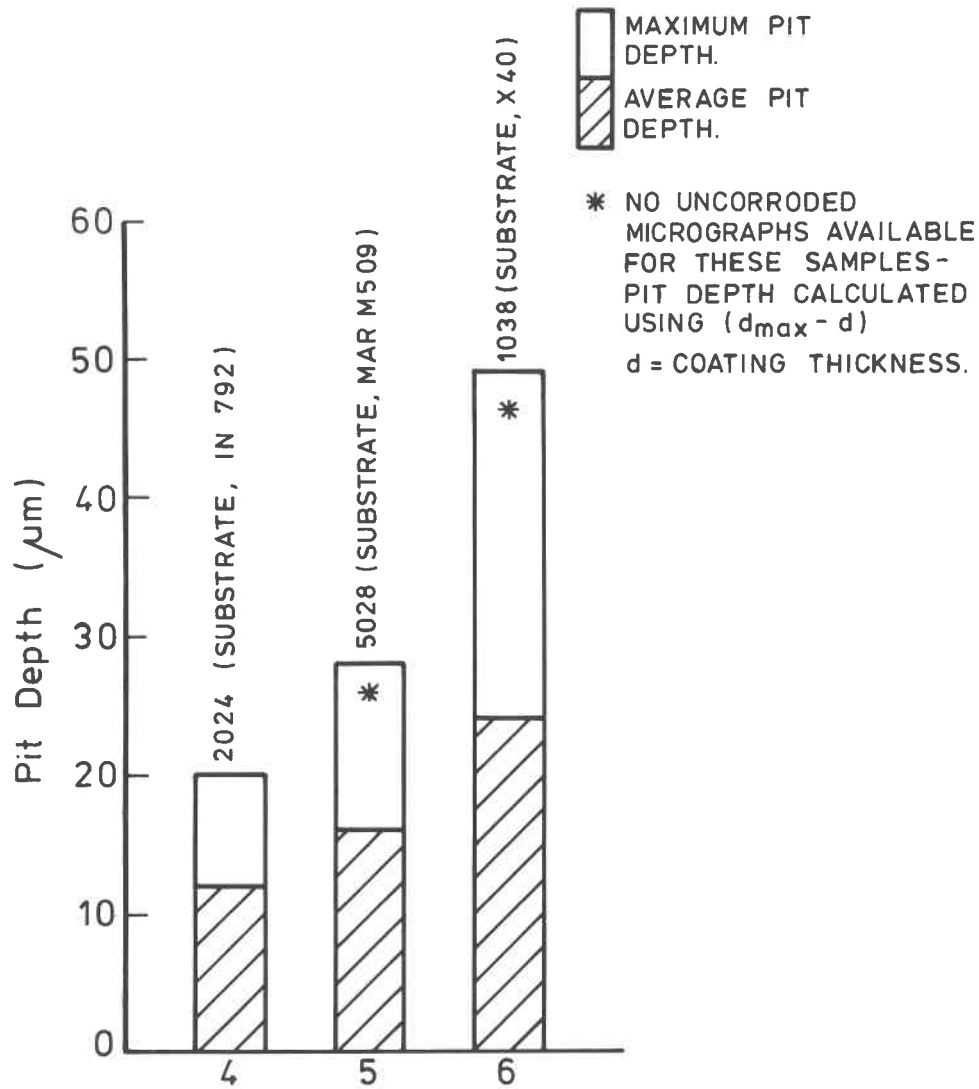
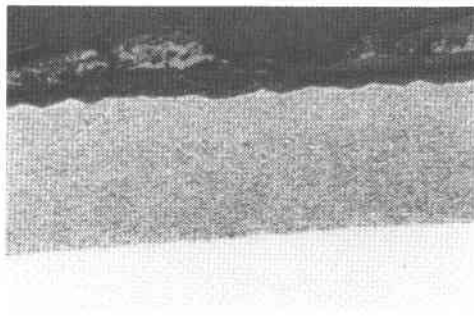


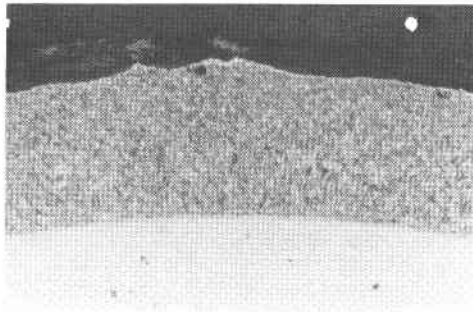
Figure 8. Comparison of coating loss, due to corrosion, of a graded CoCrAlY coating, deposited on a range of substrates. (10)





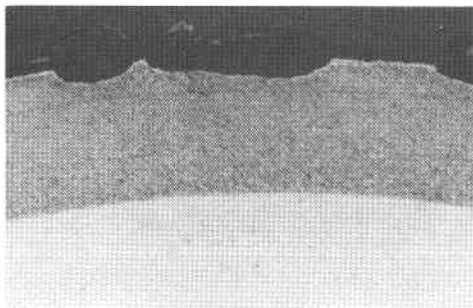
(a) on a IN792 substrate

100 $\mu$ m



(b) on a Mar M 509 substrate

100 $\mu$ m



(c) on a X40 substrate

100 $\mu$ m

Figure 9 Corrosion morphologies of graded, sputtered CoCrAlY coatings (composition 25-35% Cr, 10-8% Al) on a range of substrates.

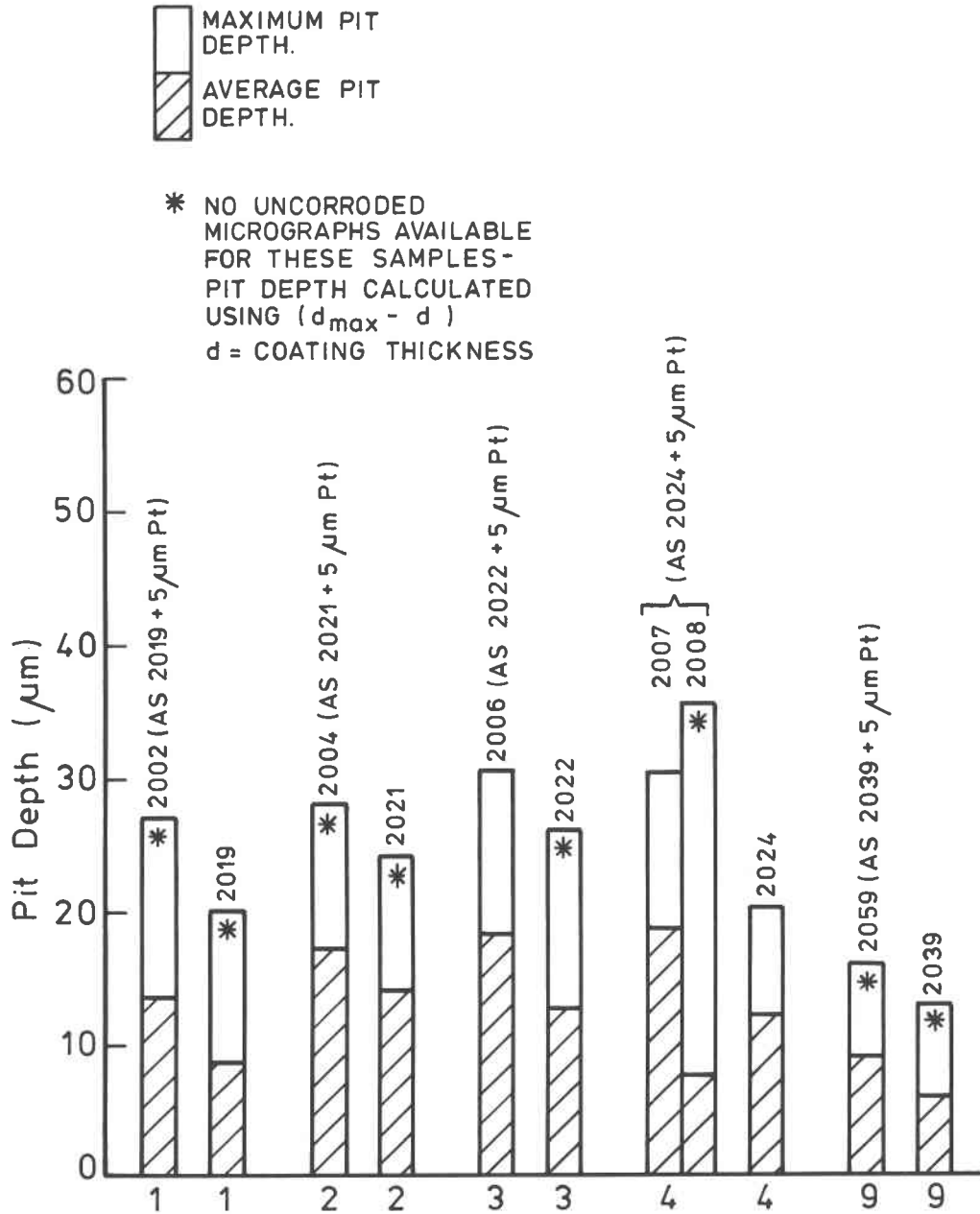


Figure 10. Comparison of coating loss, due to corrosion, of a range of sputtered, graded CoCrAlY and PVD CoCrAlY coatings, with and without a platinum underlay coating. (10)

## TRIBOLOGICAL SCREENING OF CERAMIC MATERIALS FOR USE IN ADVANCED DIESEL ENGINES

Alan I. West  
Walter D. Syniuta  
Advanced Mechanical Technology, Inc.  
141 California Street  
Newton, Massachusetts 02158

### INTRODUCTION

As residual fuels, coal-based liquid fuels, and coal-oil slurries replace the more highly refined petroleum-based engine fuels, advances in engine component tribology will be needed. The objective of this program was to evaluate ceramics as alternative materials for use in large, stationary diesel engines. Such material improvements would allow the following:

- The use of fuels which have considerably more corrosive and abrasive contaminants than allowed by current standards.
- Operation at higher mean effective pressure (MEP), thereby increasing efficiency and reducing engine size.
- Reduction in wear of critical components with a consequent increase in service life.

Recognizing the complexity of a subject such as friction and wear in a reciprocating engine with the many possible interactions of wear mechanisms, materials, lubricants, surface conditions, operating conditions, etc, this research included the identification and characterization of potential materials which might be incorporated into existing engine designs; screening of these materials with relatively simple laboratory apparatus especially designed for this purpose; SEM analysis of the wear surfaces; and the development of an accelerated wear test utilizing a single-cylinder diesel engine burning No. 2 diesel oil while ingesting coal dust. This paper will present results of the tribological screening tests and some of the conclusions drawn. No results of diesel tests are reported in this paper because the work is not yet completed.

### BACKGROUND/DIESEL ENGINE OPERATING CONDITIONS

The major area of concern for wear in diesel engines is the top piston ring. At top dead center (TDC), this ring is exposed not only to the high pressures and temperatures resulting from combustion, but also to a condition of marginal lubrication.

In large, stationary diesels, the operating temperature of the top ring is between 300-400°F, while the operating temperature of the cylinder liner is 300-340°F. The service life of rings is between 12,000 and 50,000 hours of operation, and the average replacement interval is 16,000-20,000 hours. The service life of the cylinder liners is better: from 60,000 to 100,000 hours with the common replacement in the order of 100,000 hours.

The most probable factors affecting ring and liner wear are fuel quality, MEP, piston speed, amount and type of lubricating oil used, and materials. Of these factors, fuel quality and materials present the most difficult design constraints.

European and Japanese oil refineries have traditionally used a straight run process resulting in almost 50% of the fuel produced being residuals of good quality, but it is expected that economics will force them to follow the philosophy of the United States which utilizes a catalytic cracking process that results in 10% of the fuel being residuals of poor quality. Future demands will certainly create fuels of lower quality.

The life-limiting factor in fuels relative to rings and liners appears to be sulphur, and currently manufacturers combat this by specifying high TBN lubricating oils. This necessitates a greater amount of oil usage because present engine designs wash down the sulphur by spraying oil onto the cylinder walls. The positive results of such high oil consumption are two-fold: the detrimental effect of sulphur is lessened, and the ring itself is kept well lubricated. It appears that sulphur has a more drastic effect on the wear rate of chromium than it does on the plasma coatings. Ring and liner wear have been reported to increase by as much as a factor of 30 when the sulphur content becomes greater than 0.6% (2-4), and presently 70% of the crude oils worldwide have sulphur contents exceeding 0.6%, whereas in the United States, 70% contain less than 0.3% sulphur.

Other wear-related fuel characteristics are the fuel viscosity, ash content, carbon (Conradson) and asphaltene content, and the presence of vanadium, sodium, and aluminum salts. The presence of vanadium, sodium and aluminum salts reduces exhaust valve life. Additionally, the chrome-plated top ring appears to break down chemically under conditions of marginal lubrication when these impurities are present (1). The presence of ash and carbon (Conradson) contributes to abrasive wear of the ring and liner. Asphaltene reduces the combustion rate and leads to higher thermal loading, and carbon and asphaltene both contribute to an increase in solid emissions.

Fuel viscosity is not a major problem as long as an appropriate heating system is used; insufficient heating can lead to poor atomization and slow burning resulting in higher thermal loading.

Presently, large stationary diesels utilize a chromium top ring and a cast iron liner. An advantage to an improved ring/liner material would be improved initial run-in wear; the run-in time is a critical period for piston ring scuffing. In the smaller diesels graphite impregnated molybdenum-coated rings have been used experimentally, and a marked improvement in run-in protection has been demonstrated (6).

The majority of engines surveyed were turbocharged, which is a highly effective way to increase MEP or output of the engine. Higher and higher pressures will no doubt be used in the future as increased operating temperatures are allowed.

There is another motive for increasing the safe working temperatures of the ring and liner. When chrome reaches a certain temperature, its hardness deteriorates rapidly (7). This temperature is about 700°F and can be reached locally on the ring by friction generated while running unlubricated or with the marginal lubrication that may occur at top dead center. Once chrome has softened, the process is irreversible and the degradation of the chrome continues. As such, chrome does not have the capability to operate under emergency (unlubricated) conditions.

At this time, however, the impetus to find new materials does not appear to be to achieve higher temperatures but rather to combat wear problems, especially those encountered with high sulphur fuels.

#### FRICION AND WEAR SCREENING

A pin-on-disk type testing machine was designed and built for material screening and testing. A general assembly drawing of this device is shown in Figure 1. A rotating faceplate was provided upon which could be clamped plate or disk specimens, and the pins were held in a collet-type holder which was mounted on the end of a two-axis force transducer. The test chamber allowed for testing at temperatures from ambient up to 1000°F. During each test the friction force and normal force were monitored continuously.

The material samples were fashioned into pins and disks. Each pin was fabricated with a 0.25 inch spherical radius at one end, and upon completion of a test the volume loss was calculated by measuring the diameter of the wear flat. The wear rate ( $W^*$ ) is defined as follows:

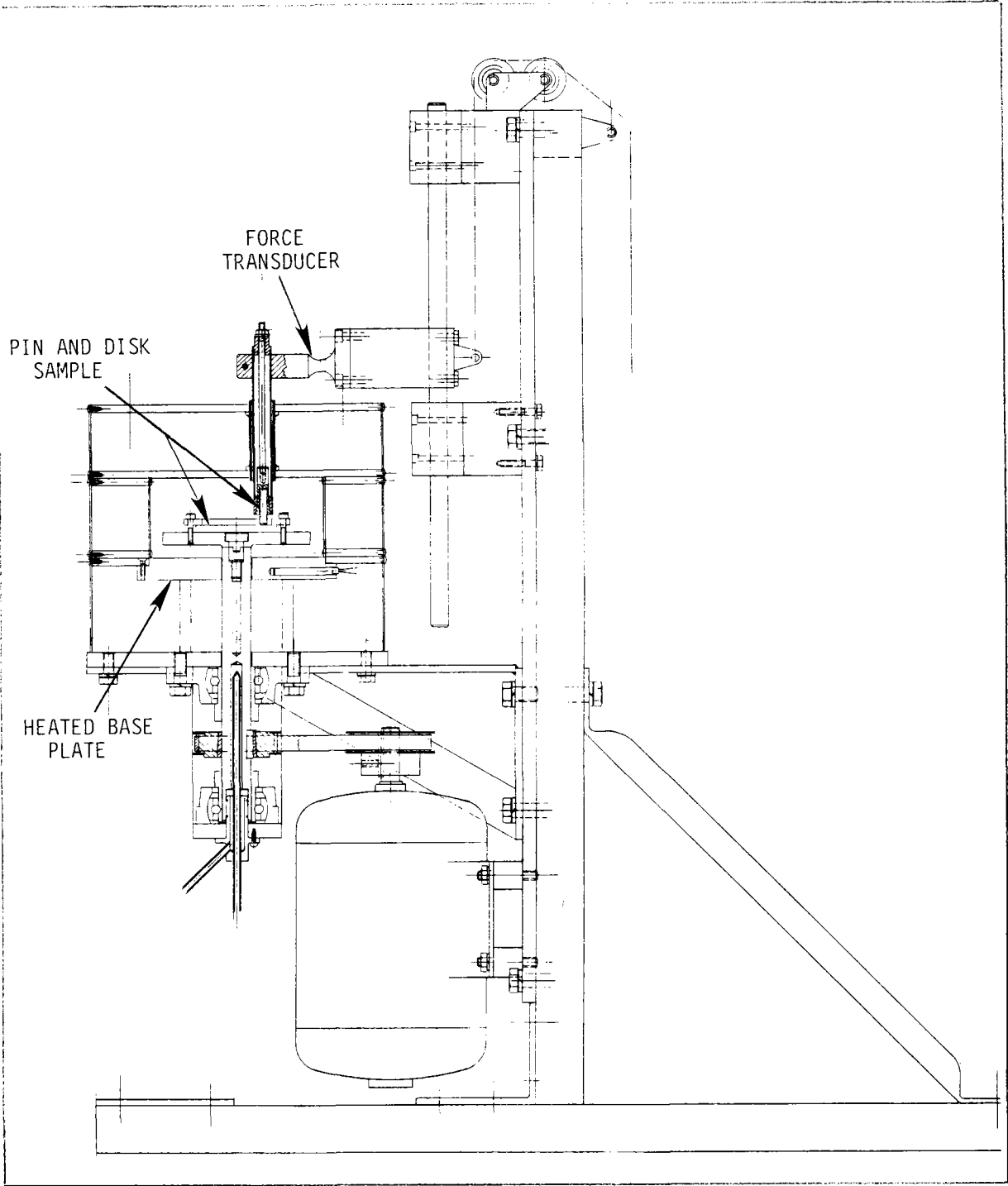


Figure 1. Pin-on-Disk Tester

$$W^* = \frac{V}{LX}$$

where:

$W^*$  = wear rate,  $\text{in}^3/\text{lb}\cdot\text{in}$

$V$  = wear volume,  $\text{in}^3$

$L$  = normal test load, lb

$X$  = total distance slid, in

Time is not explicitly included in the wear rate ( $W^*$ ) because it is not the actual time but the distance slid which is relevant.

Upon completion of each test, the mean coefficient of friction ( $\bar{\mu}$ ) and the wear rate ( $W^*$ ) were tabulated along with the test temperature, normal load, and test duration.

#### MATERIAL SELECTION

Design criteria for ceramic materials have not been established nor are the wear mechanisms well understood. In general, for a hard material the material properties which are relevant for a high temperature environment are Young's modulus  $E$ , modulus of rupture  $\sigma$ , thermal shock parameter  $K\sigma/\alpha E$ , thermal coefficient of expansion  $\alpha$ , hardness  $H$ , fracture toughness  $K_{IC}$ , thermal conductivity  $k$ , and corrosion/oxidation resistance.

To obtain a uniform, flaw-free surface as well as high hardness and strength, a candidate material should possess a fine grain size. The presence of porosity in sintered or plasma deposited materials will give rise to stress concentrations and consequently reduce the material's fracture toughness. Conversely, such porosity might provide containment for oil during conditions of marginal lubrication such as that incurred at top dead center.

A candidate material should be homogeneous as to its phase content, and the phase distribution and impurity content should be consistent between material heats.

Materials were selected for testing from a review of material properties, research previously published, and from the recommendations of suppliers. To facilitate the testing of a large number of materials, candidate materials were initially screened by testing at room temperature for one hour without lubrication. A total of 30 different ceramic and cermet materials were tested against themselves. Table 1 lists these materials along with the suppliers and designations. Materials passing this screening

were then tested for one hour in a lubricated condition. A material's rank order was then calculated by adding the dry and lubricated ranks. Additional one-hour tests were then completed at temperatures of 400°, 600°, and 800°F on the top 15 materials.

Table 1  
MATERIAL CANDIDATES

<u>Material</u>	<u>Type</u>	<u>Designation</u>	<u>Supplier</u>
SiC	S	Alpha	Carborundum
SiC	RS	KT	Carborundum
SiC	S	SC201	Kyocera
SiC	RS	SC410	Kyocera
SiC	HP	NC203	Norton
SiC	RS	NC435	Norton
SiC	S	EC422	NTK
SiC	RS	EC412	NTK
Si <sub>3</sub> N <sub>4</sub>	RS	Nitrasil	AED
Si <sub>3</sub> N <sub>4</sub>	RS	SN201	Kyocera
Si <sub>3</sub> N <sub>4</sub>	RS	SN220	Kyocera
Si <sub>3</sub> N <sub>4</sub>	RS	SN501	Kyocera
Si <sub>3</sub> N <sub>4</sub>	HP	NC132	Norton
Si <sub>3</sub> N <sub>4</sub>	RS	EC111S	NTK
Si <sub>3</sub> N <sub>4</sub>	RS	EC128	NTK
Si <sub>3</sub> N <sub>4</sub>	HP	EC131	NTK
Al <sub>2</sub> O <sub>3</sub>	S	A473	Kyocera
Al <sub>2</sub> O <sub>3</sub>	S	A479	Kyocera
Al <sub>2</sub> O <sub>3</sub>	S	UHA-99	NTK
Al <sub>2</sub> O <sub>3</sub> -TiO <sub>2</sub>	PS	110-256	Perfect Circle
Al <sub>2</sub> O <sub>3</sub> -BN	HP	ALOVHN96	USNRL
AlN	HP	137	Ceradyne
NbC-TaC	HP	---	Los Alamos
ZMgO•SiO <sub>2</sub>	--	F1120	Kyocera
B <sub>4</sub> C	HP	---	AVCO
Sialon	HP	---	AVCO
TiC	Cer	K162B	Kennametal
TiC	HP	---	AFWAL
ZrO <sub>2</sub> , full stability	HP	---	AFWAL
ZrO <sub>2</sub> , partial stability	HP	---	Kyocera

RS: reaction sintered  
S: sintered  
Cer: cermet  
PS: plasma sprayed



## RESULTS

Table 2 lists the top 15 materials in wear by their combined rank ordering score (room temperature screening).

Table 2  
COMBINED RANK ORDERING SCORES

<u>Material</u>	<u>Lubricated Rank</u>	<u>Dry Rank</u>	<u>Combined</u>	<u>Overall Rank</u>
TiC, HP	10	5	15	1
SiC (SC201), S	7	9	16	2
TiC (K162B), Cer	11	6	17	3
Al <sub>2</sub> O <sub>3</sub> (UHA99), S	16	1	17	4
Si <sub>3</sub> N <sub>4</sub> (SN220), S	1	16	17	5
SiC (EC422), S	15	3	18	6
SiC (EC410), RS	4	15	19	7
B <sub>4</sub> C, HP	13	7	20	8
SiC (NC435), RS	3	19	22	9
SiC (KT) , RS	5	18	23	10
Sialon, HP	9	14	23	11
Al <sub>2</sub> O <sub>3</sub> (A473) , S	22	4	26	12
Si <sub>3</sub> N <sub>4</sub> (NC143), HP	8	20	28	13
Si <sub>3</sub> N <sub>4</sub> (SN501), S	6	22	28	14
Si <sub>3</sub> N <sub>4</sub> (EC128), S	12	17	29	15

In addition to the top 15 materials, two other ceramic materials were evaluated in the heated tests: Carborundum's Alpha SiC was tested due to the widespread interest in this material, and Kyocera's partially stabilized zirconia was examined for comparison with fully stabilized cubic zirconia which had been tested earlier. Table 3 lists the observed friction and wear data for the hot tests.

Table 3  
HEATED FRICTION AND WEAR ( $W^* \times 10^{-10}$ ) DATA

Material	400°F		600°F		800°F	
	$W^*$	$\bar{\mu}$	$W^*$	$\bar{\mu}$	$W^*$	$\bar{\mu}$
TiC, HP	0.019	0.51	0.025	0.39	0.079	0.37
TiC (K162B), Cer	0.019	0.56	0.29	0.67	0.44	0.55
ZrO <sub>2</sub> (p. stab), HP	0.17	0.71	0.15	0.70	1.0	0.74
Si <sub>3</sub> N <sub>4</sub> (SN501), S	0.99	0.85	2.1	0.89	4.6	0.92
SiC (SC201), S	2.6	0.73	8.0	0.73	9.5	0.77
SiC (EC422), S	2.7	0.34	8.2	0.52	11.0	0.66
SiC (SC410), RS	3.1	0.66	12.0	0.63	11.0	0.70
SiC (KT) , RS	3.1	0.66	15.0	0.75	15.0	0.85
Al <sub>2</sub> O <sub>3</sub> (UHA99), S	3.7	0.72	7.9	0.90	8.6	0.71
SiC (NC435), RS	4.9	0.69	9.0	0.75	11.0	0.75
Si <sub>3</sub> N <sub>4</sub> (NC132), HP	5.3	0.61	5.9	0.60	6.9	0.74
B <sub>4</sub> C, HP	0.04-5.7	0.26-1.0	1.7	0.34-0.81	0.46-15.0	0.55-0.87
Al <sub>2</sub> O <sub>3</sub> (A473), S	8.6	0.79	6.8	1.0	11.3	0.96
Si <sub>3</sub> N <sub>4</sub> (SN220), S	12.5	0.64	7.2	0.66	9.3	0.71
Si <sub>3</sub> N <sub>4</sub> (EC128), S	12.5	0.73	19.0	0.69	8.3	0.78
Sialon, HP	13.0	0.70	19.0	0.84	18.0	0.79
SiC (Alpha), S	94.0	0.70	74.0	0.76	58.0	0.86

It is apparent from Table 3 that wear resistance is not only dependent upon the material and processing method, but also the manufacturer. For example, Kyocera's SN501 Si<sub>3</sub>N<sub>4</sub> material was significantly better in wear than other sintered Si<sub>3</sub>N<sub>4</sub> materials. It appears that factors such as sintering agents, powder size, and impurities all affect the wear resistance of the resulting material.

Seven of the top ten materials in wear are carbides. Boron carbide, the hardest ceramic tested, did not perform as well as expected and exhibited erratic, unrepeatable friction and wear data.

Five of the materials listed in Table 3 exhibit temperature dependent wear. SC201, K162B, SC410, SN501, and ZrO<sub>2</sub> all appear to wear more at 800°F than at 400° or 600°. The

K162B, a TiC cermet, exhibited a bright blue oxide after the 600° test which may account for the ten-fold increase in wear observed between the 400° and 600° tests. The HP TiC also demonstrated the formation of a blue oxide after the 600° test, and the wear rate appears to have increased, but not significantly (less than a factor of 3). The SN501 Si<sub>3</sub>N<sub>4</sub> exhibited a brown oxide after the 600° and 800° tests. The two SiC materials, SC201 and SC410, and the ZrO<sub>2</sub> did not appear visually tarnished, although the wear rate increased significantly.

Table 3 also shows no apparent correlation between a material's wear rate and the associated coefficient of friction ( $\bar{\mu}$ ). The magnitude of  $\bar{\mu}$  ranged from a low of 0.34 (EC422, 400°) to a high of 1.0 (A473 Al<sub>2</sub>O<sub>3</sub>, 600°).

Changes in the coefficients of friction ( $\bar{\mu}$ ) with temperature are also evident in Table 3.  $\bar{\mu}$  appears to increase significantly after 600° for HP TiC and the TiC cermet, and this is accompanied by the blue oxide formation. Changes can also be noted for SN220 and UHA99.

There were no dramatic changes in rank for a material when the testing temperature was raised, with the exception of SN501 Si<sub>3</sub>N<sub>4</sub> which ranked poorly at room temperature (14) but was much better under heated conditions (4). This Si<sub>3</sub>N<sub>4</sub> material, UHA99 Al<sub>2</sub>O<sub>3</sub>, and partially stabilized zirconia were the only non-carbide materials in the top 10 (Table 3).

#### DISCUSSION

There appeared to be little correlation between a material's tribological characteristics and its mechanical properties. The best correlation noted was between friction ( $\bar{\mu}$ ) and hardness (Figure 2), and an inverse relationship is apparent (correlation coefficient, R = 0.51). A similar plot for the wear values (W\*) resulted in a much poorer correlation (0.19).

An unexpected trend was observed between the measured wear and the processing method. After hot tests the wear was generally higher for hot pressed (HP) than sintered (S) materials. It appears that the presence of some small flaws improves the wear resistance of a material. This may be due to the formation of shallower cone cracks upon unloading, thus resulting in the formation of smaller wear particles.

The presence of impurities, porosity, and the manufacturing technique are all consequential in their effect on the material's tribological properties. It may be possible to design a material for use at a given temperature by including measured

amounts of impurities. For the SN501  $\text{Si}_2\text{N}_4$ , the wear rate at  $800^\circ$  was approximately the same as that observed at room temperature; EDAX results showed the presence of iron impurities in the SN501, and these impurities may have optimized its wear properties at  $400^\circ\text{F}$ . The oxides formed in this example appeared to have altered the wear mechanism from one of brittle fracture to a sloughing off of the oxide. One might optimize a material's wear rate by creating sufficient oxide to reduce the brittle wear, but not enough to increase the wear rate from oxidation removal. In a similar fashion, oxidation can be used to reduce the friction between surfaces by the creation of a solid lubricating film (e.g., HP TiC).

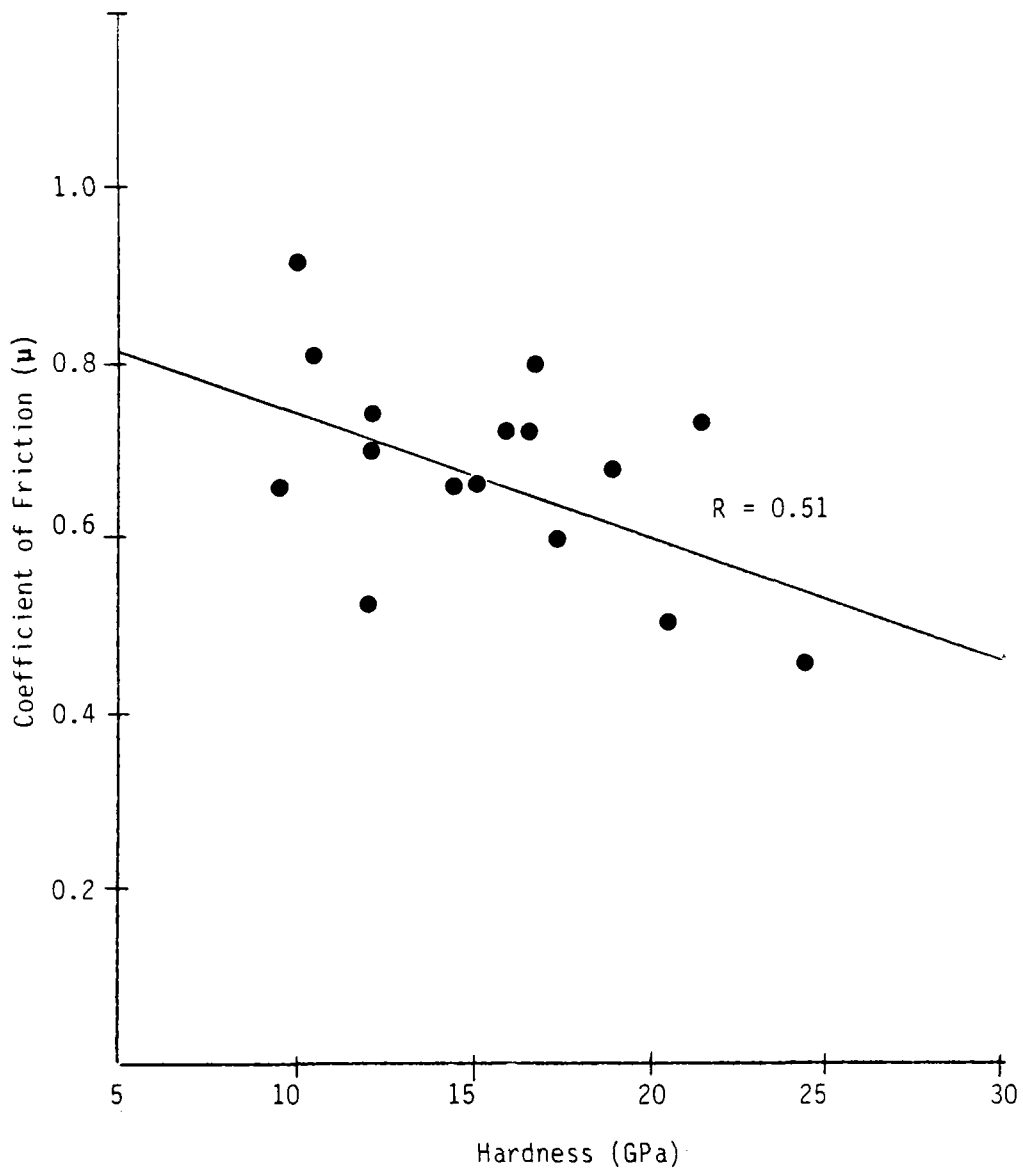


Figure 2. Effect of Hardness on Friction

Boron carbide ( $B_4C$ ), the hardest material tested, performed relatively poorly, and was the material with the least repeatability in friction and wear data. It would be useful to examine other  $B_4C$  materials with higher fracture toughness and the existence of a second phase to assess the nature of the variance observed in the data.

Titanium carbide (TiC) performed extremely well at high temperatures, and it appears that the formation of an oxide ( $Ti_2O_3$ ) changes the wear mechanisms by the addition of a soft, compliant layer. Much recent interest has been shown in the use of TiC as a wear resistant material (8). It would also be interesting to examine a composite material ( $Al_2O_3$ -TiC), given the relatively good ranking of TiC and  $Al_2O_3$ .

Zirconia ( $ZrO_2$ ) had a surprisingly low wear rate in the partially stabilized condition. Although this material was received late and consequently not characterized, the high fracture toughness reported by the supplier ( $6.9 MN/m^{3/2}$ ) is near its upper limit, although further toughening by heat treating may be possible. In view of this, a composite material such as  $Al_2O_3$ - $ZrO_2$  would be useful to examine.

Test results indicate promise for the use of ceramic materials in diesel applications. One of the major problems in applying the research results to engine components will be the difficulty of fabricating rings and liners out of hard and brittle materials. Some of the better materials, however, are sintered and therefore easier to work with than hot-pressed materials.

This work was supported by the U.S. Department of Energy under Contract No. DE-AC03-79ET15444, John Fairbanks, Technical Project Officer, and Contract No. DE-AC19-80BC10362, Dan Gurney, Technical Project Officer.

#### REFERENCES

1. J. Gallois, "Operational and Development Experience with the Pielstick Engine". Diesel Engineers and Users Association. Pub. 367 (1975).
2. G.F. Hyde, J.E. Cromwell, and J.H. Barnes, "Piston Ring Coatings for Internal Combustion Engines". SAE paper 790865 (1979).
3. G.F. Hyde, F.A. Robbins, and P.R. Shepler, "Piston Rings for Transportation Diesels". SAE Transactions, pp 285-285 (1961).
4. W.E. Martus and W.B. Young, "Compatibility Study of Piston Ring Coatings and Cylinders in Diesel Engines". ASME paper presented at the Energy Technology Conference and Exhibition, Houston, Texas, November 5-9, 1978.
5. B. Pearson and W.B. Wallace, "Medium Speed Diesel Engines Using Residual Fuels". Diesel Engineers and Users Association. Pub. 330 (1969).

6. H.F. Prasse, H.E. McCormick, and R.D. Anderson, "New Piston Ring Innovations to Help Control Automotive Engine Emissions". SAE paper 730006 (1973).
7. G.F. Hyde, J.E. Cromwell, and W.C. Arnold, "Piston Ring Coating for High Performance Diesel Engines". SAE Transactions. 76:3107-3139.
8. B. Aufderhaar. Now Available: TiC Wear Surfacing Powders. Metals Progress, 119(7):30-33, June 1981.

COAL SLURRY TESTS WITH A SLOW SPEED TWO-STROKE CYCLE  
DIESEL ENGINE, CONCLUSIONS AND PREDICTIONS

H. A. Steiger  
Sulzer Brothers, Switzerland

ABSTRACT

Since the slow speed large bore Diesel engine has until recently been absent from the US market scene, few people in the States are actually familiar with this type of energy converter. The paper therefore starts out with a brief characterisation of such engines. The reason for entering the US market in both fields, marine and stationary, is to be found in the new economic situation, favoring slightly more expensive machinery using less fuel. An added argument is its potential for burning coal-based fuels in the future. The later feature represents actually the central theme of this paper.

Tests are described which were conducted with such an engine using coal slurries provided by the US Department of Energy. This includes engine performance and the findings after dismantling the engine and inspecting piston, piston rings and liner as well as the injection nozzle. The analysis of these results point to the need for further R+D work in order to reduce wear and erosion problems caused by the high ash content of this kind of fuel. It is expected, however, that this work will lead to satisfactory results by reducing the ash content of the fuel on one hand, and increasing the hardness of liners, piston rings and fuel spray-nozzles on the other hand.

## Section 1

### BACKGROUND OF THE LARGE BORE SLOW SPEED DIESEL ENGINE

#### Characteristic of the engine

The most striking impression when one is physically confronted with this type of engine is its bulk and weight. (Fig. 1, P. 10) Typically such engines are 40 - 80 ft. long, 43 ft. high and 13 ft. wide, while providing 17 - 35 MW at around 100 RPM. The low RPM although being one of the advantages of this prime mover, as will be seen later, is, on the other hand, responsible for its large geometrical dimensions. But the outstanding advantage, which makes this energy converter so attractive, is its thermal efficiency, which amounts to 45 % without, and up to 50 %, with a bottoming plant. In this power range, there is absolutely no match for it in view of its fuel saving capability, particularly in connection with its extremely broad fuel spectrum, ranging from No. 2 to a No. 6 fuel oil and beyond.

#### Typical applications

This is foremost the marine propulsion application with directly driven single propellers and, in increasing numbers, stationary power plants for utilities and for industrial cogeneration. The fact, that only in such marine applications, where over 35 MW are required, more than one engine is installed, points to another positive feature of this power plant, namely to its outstanding reliability.

#### Reasons for the recent introduction of this type of engine in the US-market

The first large-bore engines have been built in the U.S. in 1980. These engines, being of the valvless Sulzer design, have entered the marine market in 1981 and are now followed by two stationary applications. The first one is an industrial cogeneration plant (Fig. 2, P. 10), and the second one is a small utility which is utilizing bottoming plants to get maximum efficiency in order to reduce power costs to a very competitive level (Fig. 3, P. 11 ).

What has caused this sudden surge of practical applications of slow speed engines in the US? Firstly, there is the new economic situation favoring slightly more expensive machinery using less fuel. Secondly, and particularly in the stationary case, the potential of the Sulzer engine to be converted in the future to coal based fuels. It is, of course, the latter aspect which will be dealt with extensively in this paper. The reason why, in those cases, Sulzer engines have been selected, is the following: From Fig. 4, where a cross section through this engine is depicted, it can be seen that due to the loop-type scavenging method employed -



whereby inlet and exhaust is controlled by the piston itself - exhaust valves are completely eliminated. This contrasts with the uniflow scavenged engine, which also requires a central air-swirl which does have a strong centrifuging effect upon the ash particles introduced with most coal-fuels.

## Section 2

### COAL SLURRY OPERATION

#### Characterisation of fuels

There are several coal-based fuels which can be considered for the slow speed Diesel engine. On account of its low RPM does this engine type provide a sufficiently long dwell-period for the slower burning coal. Synthetic coal liquids are rather unproblematic fuels when burned in such engines, however, their price and uncertain availability puts a big question mark to their practical application.

On the other hand, a so-called microslurry, consisting of finely ground coal and Diesel oil, or coal and water or both, is relatively cheap with a high likelihood of becoming commercially available. It is for these reasons that the focus of attention is clearly on the latter fuel. As part of a contract sponsored by DOE and solicited by Thermo Electron, Waltham, Mass., Sulzer has tested several slurries of this kind in their engine laboratories in Winterthur, Switzerland, under active participation of Thermo Electron.

The first of the fuels tested was a coal-oil microslurry. Its composition may be gathered from table 1. Two points in this table are of particular significance: Namely that the slurry consisted of 32 % of coal by weight and 68 % of Diesel oil and the fact that the coal contained over 8 % ash consisting largely of silicon-oxides which are quite known for their extreme hardness. The particle size as shown in Fig. 5 is a prerequisite when burning a mixture of particles in a fluid by a Diesel engine. Firstly, it enables the fuel injection valve to maintain its gas-tight seal, since such small particles do not interfere with the seating. Secondly, the large surface area obtained by the small particle size is essential for efficient burning in a reasonable time frame.

The second slurry tested consisted of the same amount of coal but mixed with water instead of fuel oil.

### Bench test results

These tests were conducted prior to actual engine work (Fig. 6, P. 12). The tests themselves revealed that an unmodified injection system was not compatible with the slurry operation at pressures beyond 4000 psi whereas the minimum pressure required for injection amounts to 8000 psi. Above the 4000 psi level the needle valve was quickly blocked by the so-called particle-wedge action as seen from Fig. 7. To overcome this problem, a new injection system had to be developed. Tests with this improved system were entirely free from this phenomena. Additional tests showed that even higher concentrations than 32 % of coal could be successfully injected. In fact, as Fig. 8 shows, only a very modest increase in injection pressure was experienced when going to a 40 % slurry, although this slurry does not pour any more at ambient conditions.

### Engine test results

The actual engine tests with these slurries were conducted on a single cylinder experimental slow-speed 2-stroke cycle crosshead engine having a bore of 30", a stroke of 61" and an output of 1500 KW at 120 RPM. This engine was run for a total of 15 hours at full load on the coal-oil slurry without any sign of either ring or piston seizure or ring blockage.

The performance results are shown in Fig. 9. The uppermost fuel curve shows the fuel consumption corrected to normalized heating values for the various fuels, whereas the middle curve resulted from a check-run with Diesel oil after the slurry test. The resulting increase in fuel consumption amounts to only 2 %. Functionally speaking, we may therefore consider these tests as being very satisfactory.

The consecutive engine tests with the coal-water slurry were, due to its extremely low heating value, limited to a very low engine output as a consequence of the existing capacity of the fuel injection system. Operating time was also very limited due to the fact that none of the auxiliary systems was suited for this non-lubricating type of fuel. Nevertheless, it could be demonstrated that the coal burned - even at this low load level with a correspondingly low temperature range - to a surprisingly high degree. Fig. 10 outlines some of the results obtained at 27 % engine load utilizing 17 % pilot fuel. A 15 % increase in heat rate was recorded. No increase in smoke, and in rotative speed was noticed in spite of the fact, that a 22 % increase in cyclic pressure was recorded. Due to the limited operating time available, no attempt could be made to minimize the amount of pilot fuel injection. Sketchy as this test may have been, it still represents the beginning of something which few spectators of the scene have even thought possible.

### Dismantling results

Upon disassembling injection nozzle and piston after these test runs, it became quite clear why the check run with Diesel oil (middle curve in Fig. 9, P. 13) did not correspond with the lowermost curve on this graph, which was the Diesel fuel test prior to the slurry run. The fuel nozzle was completely eroded (Fig. 11, P 13) and rings (Fig. 12, P. 13) and liner (Fig. 13, P. 14) terribly worn. The sharp knife-edge corners of the uppermost ring (Fig. 12, P. 13) must have scraped off the cylinder lubricating oil, thus leading to such high friction values that an increase of 200 BTU/KW-hr in the heat rate has occurred.

### Section 3

#### REQUIREMENTS FOR ADDITIONAL R & D WORK

##### Improvement on fuel side

The ash content of the slurries tested was about 100 times higher than what is normally encountered when operating such an engine on an extremely bad heavy fuel-oil. It is therefore quite obvious, that with measures on the engine side alone, it would never be possible to obtain wear rates comparable to those which are regarded acceptable today. Consequently, the ash content of the fuel must be reduced to about 10 % of the present value in order to make success a likelihood. Fortunately, it is well-known that a cleaning process carried to 90 % purity is quite feasible, whereas going to 99 % becomes completely impractical. Therefore, it appears that the goal which has been set should be achievable in practice. Still, technical success does not necessarily imply that it is also economically feasible.

Fortunately enough, even this appears possible since the measures required for de-ashing such a microslurry are involving only removal of ash by physical means, since, due to the micron size of the particles, over 99 % of the ash is already separated from the coal particles.

##### Improvement on engine side

On the other hand, as pointed out before, we than will still deal with a fuel having 10 times the ash content being customary today. Therefore, it is very plain that a large effort is required to improve wear properties of ring and liner as well as the erosion resistance of the injection nozzle. Since this paper is primarily concerned with measures on the engine side, it is this phase of the future R+D work which will be dealt with in some detail in the following sections.

## Section 4

### UTILIZATION OF EXISTING KNOWLEDGE WITH COAL-DUST BURNING ENGINES

The foremost source of information in this respect is the extensive development work carried out in Germany beginning practically with the invention of the Diesel engine and terminating with the end of the 2nd world war. Figure 14 depicts the extent of this work by indicating the many patents taken out for coal-dust Diesel engines by black dots and actual engine development by hatched areas. It also reminds us that Diesel himself intended to operate his first engine with coaldust. However, after an unsuccessful attempt, he discarded the idea altogether. However, his co-worker Pawlikowski stuck to it and, 20 years later, he started successfully the first coal-dust burning Diesel engine. At the beginning of the 2nd world war, 5 companies were engaged in this development. A total of 19 test engines have been operating, all of them typically slow-speed versions operating at 100 to 200 RPM. One of them was a Sulzer engine built under a license agreement with the "First Bruenner Maschinenfabrik". This particular engine achieved 1260 hours of operation on lignite-dust and obtained a thermal efficiency 10 % below the hence customary value for oil burning Diesel engines of this size. Fortunately, all records from this engine have been saved by Prof. Jehlicka who is still active at the Institute of Technology of Stuttgart.

Nevertheless, not one of these engines entered the market place on account of high wear rates. Consequently, this aspect of the coal burning engine caught the focus of attention of all its active proponents.

#### Wear reduction by design measures

It was quickly discovered that one of the main reasons for the high wear rates are the hard ash particles caught between ring and liner (Fig. 15, P.14 ). With conventional slotted sealing rings, the force acting upon these particles is primarily determined by the gas pressure behind the open rings. If this action could be prevented by using closed rings, one of the major causes for the wear would be eliminated. Attempts to this extent have actually been made with satisfactory results regarding wear, but being quite unsatisfactory with respect to sealing properties, since at that time, the thermal sealing ring invented by Junkers and successfully applied to the Junkers aircraft Diesel, has not yet been known. The design of this ring is shown in Fig. 16. Picture "a" shows the clearance in the cold condition of this closed ring with its typical high-collar design. When the engine

warms up, the collar reacts quickly to the gas temperature (picture "b") and extends until it is nearly touching the much cooler liner wall. The close proximity to this wall exerts a cooling effect upon the ring which causes it to retract slightly again into a balanced condition as shown in picture "c". Obviously, the practical limitation of this design depends on the liner wear.

Another design approach has been the rinsing of the gap between ring carrier and liner in the bottom dead center of the piston (Fig. 17, P. 15 ) Here on each piston stroke water is injected during the short time interval available through the lower bore and drawn off again by the upper one. By this action, the hope was to be able to carry away any loose ash particles which have accumulated in this gap. However, little success has been reported as a result of this measure.

#### Improved lubrication techniques

The piston and piston rings of crosshead engines must be lubricated by timed oil-injection into the cylinder. Consequently, it was a simple matter to increase the amount of lubrication over and above the normal rates which are in the order of 1 g/kW·hr and below. However, in order to meet with success, the lubrication rate had to be increased until 1 kg and over had been reached, which, of course, makes such an approach completely uneconomical.

There is a clear conclusion we can draw from these attempts: The lubrication method would have to become far more sophisticated in order to make such a system practical, since it is known, that the major liner wear takes place around top dead centre of the piston. This corresponds to the point where boundary lubrication exists. Consequently, a high pressure lubricating system injecting lubricant at the very instant where the top piston ring is at its uppermost position, could - at least theoretically - change the boundary type to a fully lubricated condition at this critical spot.

#### Wear reduction by technological measures

The German records show very clearly, that this approach was the only practical one. The most successful measures taken were the following:

As far as the liner is concerned, an inner liner made from chilled cast iron with a hardness of around 500 Vickers with an outer steel lining for strength and ductility, proved to be very successful. Fig. 18 shows the significant reduction obtained in liner wear due to this measure.

Similarly, piston rings made from a nickel-iron alloy whose composition is shown in table 2, and which were hardened after machining to also around 500 Vickers, resulted in an increase in life expectancy from originally 100 hours and below, to 1000, and in certain cases even 2000 operating hours.

In both cases, liner and ring, the improvement amounts to an order of 10, which was achieved with very modest additional manufacturing costs. Although this factor of improvement is very impressive, it must be pointed out, once more, that a factor of 200 would be required in order to obtain acceptable wear rates without deashing of the fuel to a sufficiently low level.

It is obvious that any new development will have to follow this course of action, making the most of the present day technologies available. The requirements for new materials for liners and piston rings are therefore as follows:

1. The highest possible hardness available at sufficient strength and ductility.
2. Sufficient penetration depth allowing unaltered surface conditions even if considerable wear takes place.

The last mentioned requirement automatically excludes any surface treatment or hardening procedure which has penetration depths below 1/8 of an inch. The requirement for a high degree of ductility serves to ensure that no hard particles may break out of the surface during operation.

## Section 5

### POTENTIAL FOR EROSION RESISTANT INJECTION NOZZLES

#### Technology available

It is well-known that the major cause for erosive abrasion is the weakness in the bonds of crystalline materials such as metals. Monocrystals are consequently much better suited as a design material for such applications. If at the same time such monocrystals provide a higher hardness than metals, a combined effect can be expected. A typical monocrystal of this type which is available in sufficiently large monocrystals and frequently used in industry is sapphire. The hardness of sapphire, which amounts to 2500 to 3000 Vickers, is so much higher than that of

silicates (approx. 1000 Vickers), that it appears very likely to obtain in this way an acceptable life expectancy.

#### Typical solution

A possible realization of an injection nozzle utilizing this technology is shown in Fig. 19, which represents a proprietary Sulzer design. It would of course be extremely impractical to make the entire nozzle tip out of sapphire since the quality of this material is only necessary in the immediate vicinity of the nozzle holes themselves.

The solution to the problem is to be found by a two pronged approach: Firstly, to find sufficient space for at least a dozen nozzle holes surrounded by sapphire crystals, and secondly, to hold these sapphire elements in place in spite of the high temperature gradient in this area and the much smaller temperature expansion coefficient of sapphire relative to steel.

The first problem area is solved by adopting a double-row arrangement, whereas the second one has been approached by utilizing an insert containing the sapphire elements and consisting of a metal which approaches the thermal expansion coefficient of the monocrystal. The conical arrangement of this insert allows the adaptation of considerable thermal expansion differences between the outer con-cealing part and the insert without giving raise to stresses or physical separation. The conical insert is firmly held in place in a fully flexible manner by the hydraulic forces exerted by the needle seat which is executed as a floating piston in the nozzle holder itself. The difference in hydraulic pressure above and below the needle seat presses under all condition the insert into the nozzle bay.

It is hoped that this design will practically eliminate erosion problems stemming from the coal-slurry operation.

#### SUMMARY

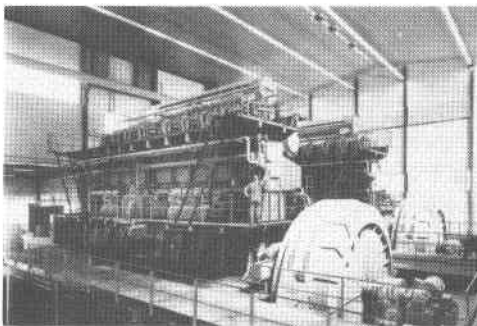
The slow-speed two-stroke cycle Diesel engine with its tremendous background in marine and stationary applications has recently been introduced on the US market, due to the new economic situation, favouring slightly more expensive machinery using less fuel. An additional advantage is its potential to burn coal based fuels in the future.

Tests conducted to substantiate this claim with the so-called coal "micro-slurry" have shown that, functionally speaking, there is no serious problem which would prevent this engine from burning successfully such fuels. However, it also showed that further development is required with respect to reducing wear and erosion problems arising from the high ash-content of this kind of fuel.

A two pronged approach to achieve this goal is required. On the one hand, a substantial reduction of the ash content of the fuel prior to entering the engine is an absolute necessity. The fact that in a micro-slurry over 99 % of the ash particles are already physically separated from the coal, is a tremendous advantage to achieve this end with simple means and in an economical fashion.

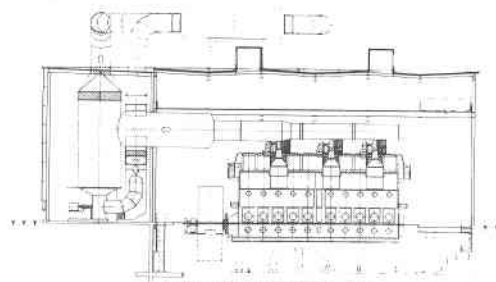
On the other hand, the wear and erosion resistance of the respective engine parts must be substantially increased. The lesson from the very extensive earlier tests of the German Diesel industry with coal-dust engines shows conclusively, that the path to success is to utilize harder materials for the sliding partners in order to reduce wear rates by a factor of 10 and over. The up-to-date knowledge on erosion problems allows the design of injection nozzles whose critical parts are made from extremely hard monocrystals which should all but eliminate this problem.

Finally, we can safely state that the slurry tests conducted up to now have conclusively shown that the valveless slow-speed engine concept with central fuel injection is particularly well suited for this kind of fuel.



POWER PLANT WITH SULZER SLOW-SPEED ENGINES

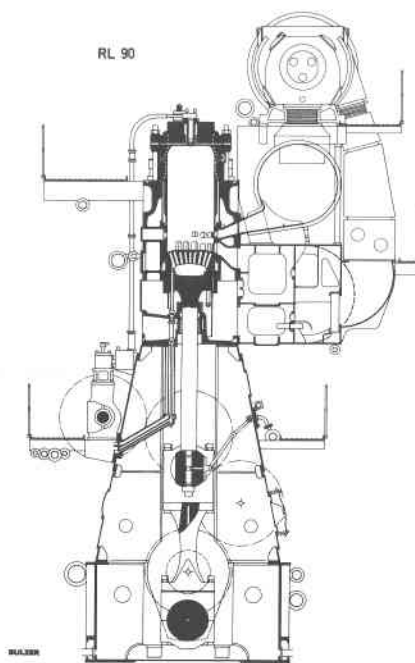
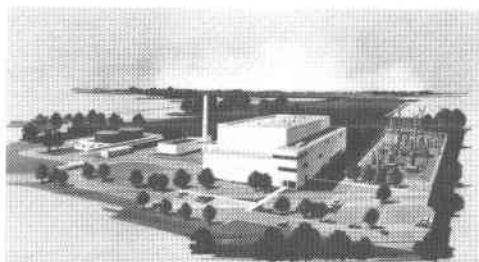
FIG 1



HOFFMANN-LA ROCHE COGENERATION PLANT

FIG 2





CROSS-SECTION OF SULZER SLOW-SPEED TWO-STROKE  
CYCLE CROSS-HEAD ENGINE  
FIG. 4

#### COAL ANALYSIS

Lower Freeport Pennsylvania Seam

	Coal (As Received)	Coal (Moisture Free)	Coal (Moisture / Ash Free)
	(Percent by weight)		
<u>Proximate Analysis</u>			
Moisture	1,6	0	0
Volatile Matter	26,2	26,6	29,1
Fixed Carbon	63,8	64,8	70,9
Ash	8,4	8,6	0
<u>Ultimate Analysis</u>			
Hydrogen	4,6	4,5	5,0
Carbon	79,8	81,1	88,7
Nitrogen	1,4	1,4	1,6
Oxygen	4,7	3,4	3,7
Sulfur	1,0	1,0	1,1
Ash	8,4	8,6	0
HHV (DOE) (BTU/lb)	14013	14237	15573

#### COAL/OIL SLURRY

Slurry Proportions  
(by weight)

- 68% Diesel oil
- 32% Coal
- Lecithin (4,5% of coal fraction)

HHV (DOE) :	17791 (BTU/lb)
HHV (EMPA) :	17370 (BTU/lb)
LHV (EMPA) :	16525 (BTU/lb)

TABLE 1 SLURRY-FUEL ANALYSIS

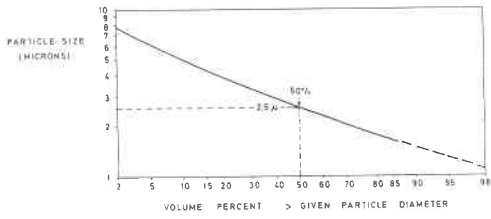


FIG 5 PARTICLE SIZE DISTRIBUTION (BY VOLUME)

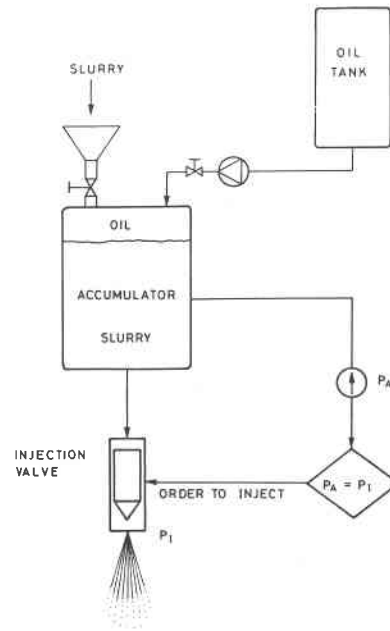


FIG 6 BENCH TEST ARRANGEMENT

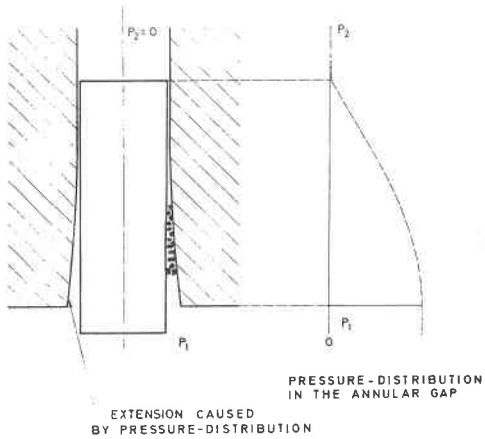


FIG 7 SEALING CLEARANCE WITH PARTICLE-WEDGE EFFECT

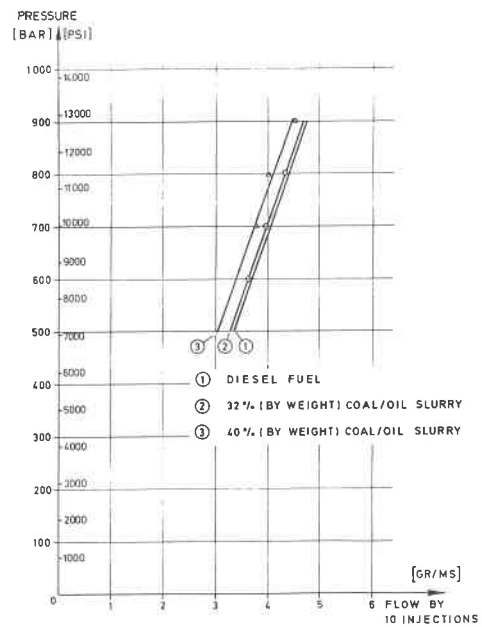


FIG 8 PRESSURE/FLOW RELATION

1 RSA 76 TESTS WITH COAL/OIL SLURRY  
CONSTANT SPEED N = 120 REV/MIN

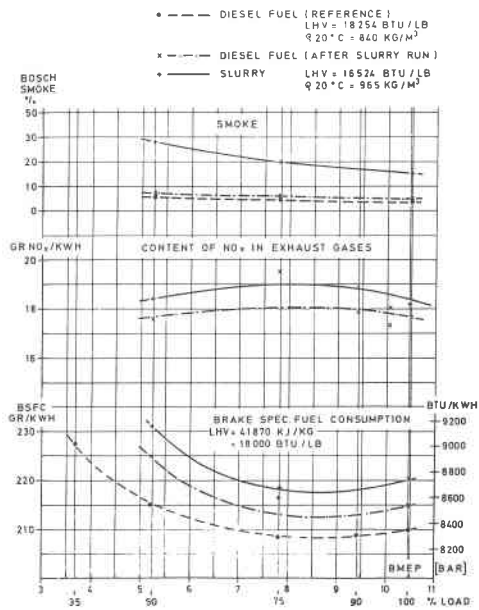
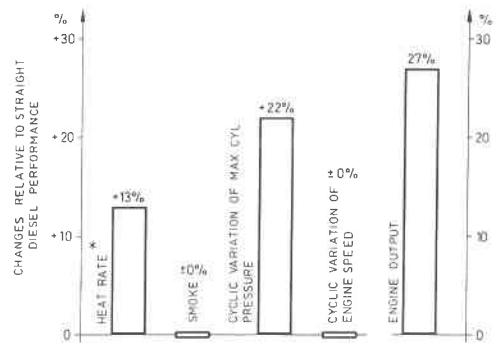


FIG 9 EXPERIMENTAL RESULTS

SULZER 1RS76 EXPERIMENTAL ENGINE

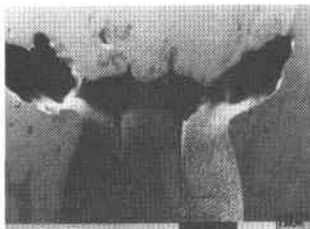
WATER-COAL MICROSLURRY TEST:  
(34% COAL CONTENT)

PILOT-OIL QUANTITY: APPR 17% OF TOTAL HEAT INPUT AT OPERATING POINT

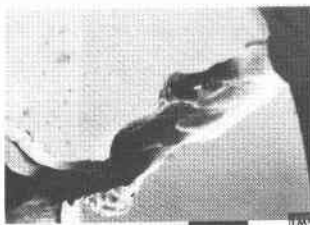


\*) NOTE PILOT FUEL INCLUDED AND CORRECTED FOR DIFFERENCE IN MAX CYLINDER PRESSURE

FIG 10



SECTION A  
(ENLARGEMENT 19:1)



SECTION B  
(ENLARGEMENT 20:1)

FIG 11 ERODED NOZZLE

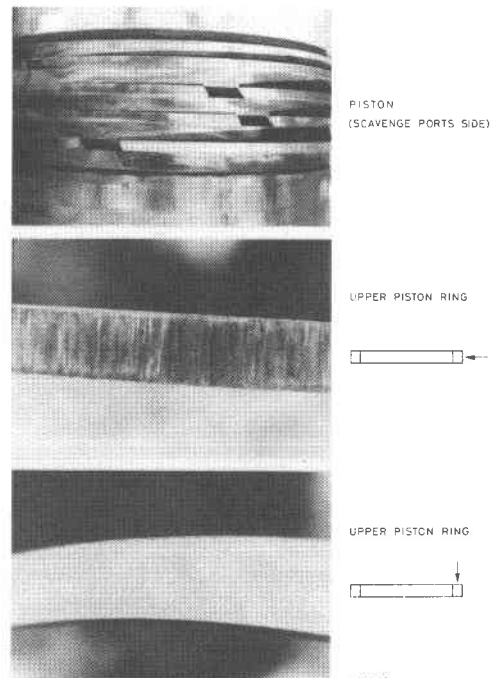
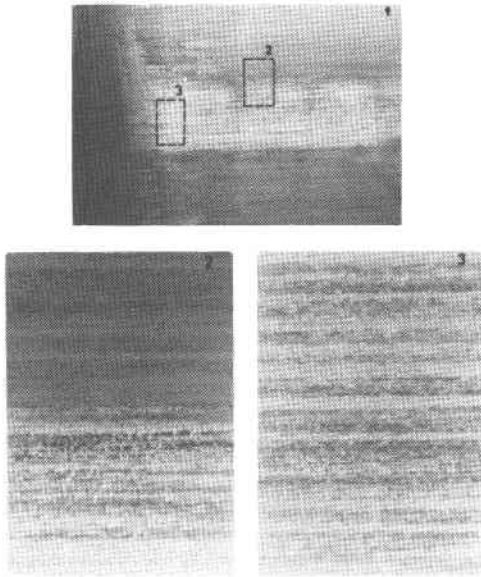
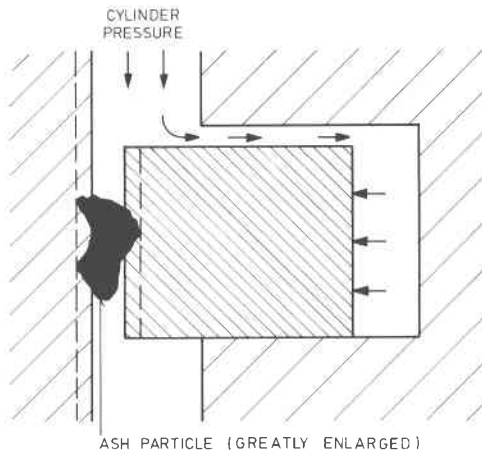
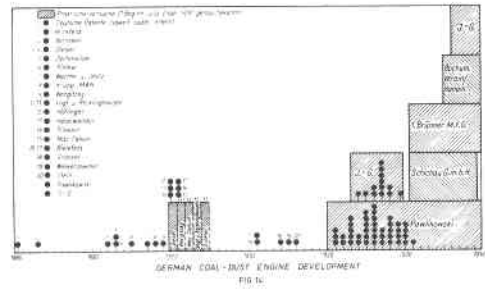


FIG 12  
WORN PISTON RINGS

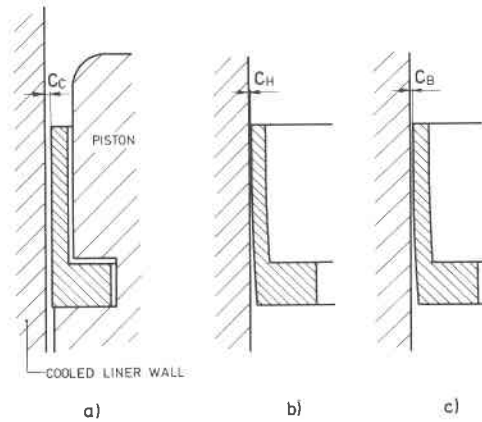


NO 1 WEAR MARKS BEFORE CLEANING  
 NO 2 DETAIL OF NO 1 AFTER CLEANING  
 NO 3 DETAIL OF NO 2 AFTER CLEANING  
 FIG 13 WEAR MARKS ON LINER



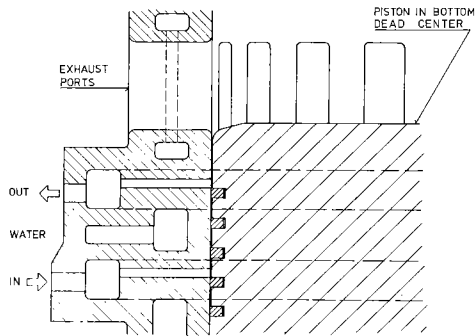
FORMING OF WEAR-SCARS BY  
 HARD PARTICLES

FIG 15



"JUNKERS" THERMALLY CONTROLLED  
 CLOSED PISTON RING

FIG 16



WATER-SCAVENGING ARRANGEMENT OF CLEARANCE SPACE BETWEEN PISTON AND LINER

FIG. 17

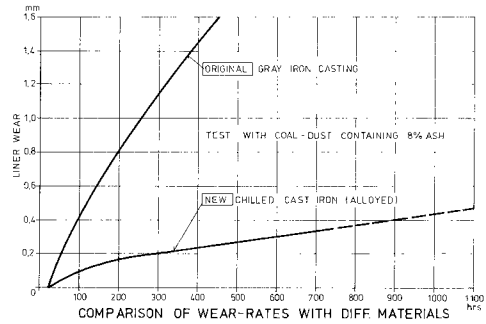


FIG. 18

### WEAR RESISTANT MATERIALS FOR PISTON RINGS:

MOST SUCCESSFUL COMPOSITION OF GERMAN COAL-DUST ENGINE DEVELOPMENT

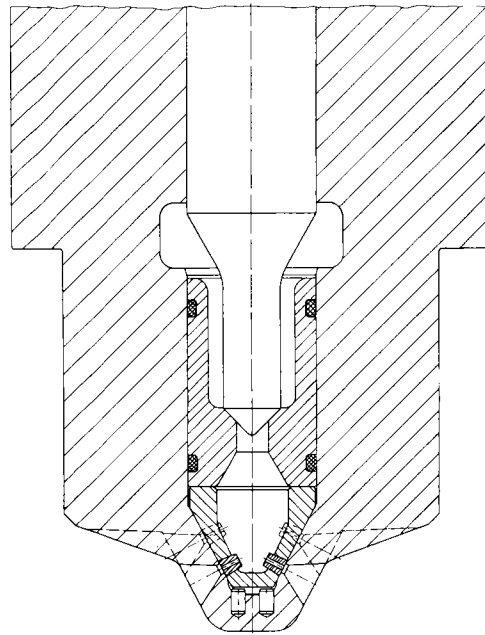
C : 2.0 ÷ 4.0 %

Si: 1.0 ÷ 2.0 %

Ni: .5 ÷ 1.5 %

Cr: .3 ÷ .7 %

TABLE 2



EROSION RESISTANT FUEL INJECTION NOZZLE  
FIG. 19

TURBINE MATERIALS EROSION/CORROSION

IN AN EXPERIMENTAL PFBC SIMULATOR

by

R.L. McCARRON, A.M. BELTRAN, R.P. BROBST, D.R. SPRIGGS

GENERAL ELECTRIC COMPANY

SCHENECTADY, NY 12345

## INTRODUCTION

The direct combustion of coal in pressurized fluidized bed combustor (PFBC) combined cycle power plants is a promising near-term solution to the national need to use coal more effectively for electric power generation. One of the key questions regarding the development of this system involves the life of gas turbine hot section components in the effluent from the PFBC. The potentially corrosive alkali (Na+K) vapor from a PFBC is estimated to be greater than the acceptable limit for present gas turbine superalloys based upon conventional liquid fuel experience. The loading and size distribution of the PFBC particulate effluent may cause degradation of gas turbine superalloys by erosion, if limits are exceeded.

During the past four years, the General Electric Company has participated in two experimental programs to evaluate turbine materials' durability in the effluent from pressurized fluidized bed combustors (PFBC). Candidate alloys for gas turbine applications were exposed to the high temperature, high velocity PFBC exhaust gas stream for up to 1000 hours and evaluated for erosion/corrosion/deposition. These programs were funded by the U.S. Department of Energy and involved the cooperative efforts of the General Electric Company, which provided the turbine test sections, specimens, and material evaluations and both the Exxon Research Engineering Co., Linden, N.J., and the National Coal Board's Coal Utilization Research Laboratory (CURL), Leatherhead, England, which provided the experimental test facilities.

The Electric Power Research Institute (EPRI) recognized the need for a test rig which allowed for flexibility in simulating the significant aspects of erosion, corrosion, or combined processes in PFBCs at lower operating costs than those experienced with the Exxon and CURL tests. The simulator was to be used to evaluate the effects of changes in key operating conditions on erosion/corrosion of turbine materials and to evaluate the erosion/corrosion behavior of advanced coatings/claddings in the simulated PFBC environment for the purpose of selecting the best materials. The General Electric Company was selected by EPRI to carry out this program (EPRI RP1337-1).

To date, a total of 2500 hours of erosion, corrosion, and erosion-corrosion testing has been conducted on the simulator at a gas temperature of 1600 °F and gas/particle velocities of 960 f/s and 1170 f/s using PFBC particulate as the erosive medium. 250-hour simulation tests have been conducted to evaluate the effect of gas/particle velocity, particle size distribution, and alkali sulfate flux level on the degradation of a variety of candidate gas turbine materials. Some of these early test results are reviewed along with a brief summary of the two 1000-hour PFBC cascade tests conducted at Exxon and CURL.

## PFBC CASCADE TESTS

### TEST CONDITIONS

Results of the Exxon and CURL tests have already been reported in detail<sup>1,2</sup> and will be summarized here. Both PFBC cascade tests incorporated static subscale airfoil specimens of impulse and reaction design exposed to leading edge gas velocities between 800 and 900 feet per second (f/s). The airfoil specimens were arranged in four-turn cascade test sections with six (6) specimens per cascade as shown in Figure 1. Two additional design features were introduced in the test section for the CURL 1000-hour test including:

- Straight-through air cooling of nine (9) selected impulse specimens to evaluate the effect of reduced metal temperature in reducing erosion/corrosion degradation;
- Insertion of three pin specimens downstream of the fourth cascade where the gas velocity at the specimen leading edge was approximately 1400 f/s.

The candidate gas turbine materials common to the CURL and/or Exxon and Simulator Tests (to be discussed later) are listed in Table 1. These include base alloys and protective coatings/claddings. The platinum-aluminide (RT-22) coating was applied by the pack cementation process while the FeCrAlY, CoCrAlY, and INCONEL 671 claddings were applied to IN-738 substrates by hot isostatic pressing (HIP).

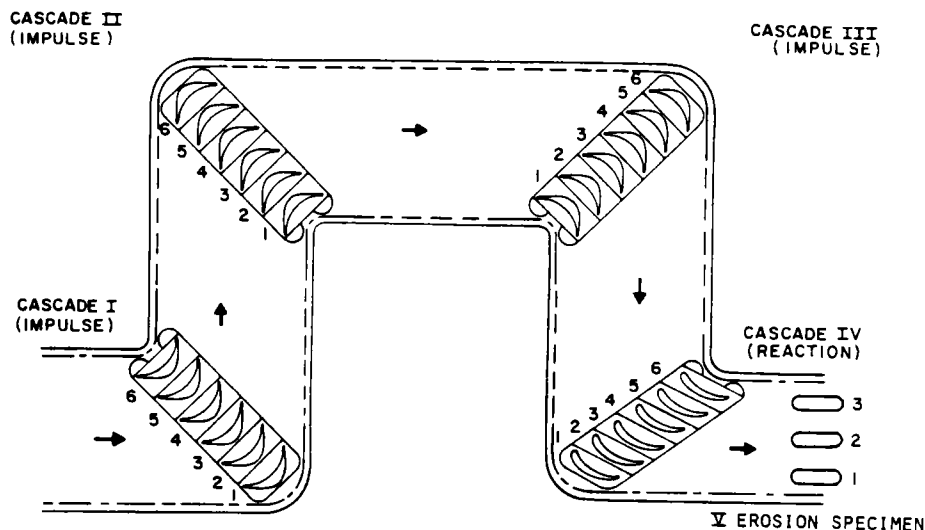


Figure 1. Schematic of Static Turbine Test Section

Table 1  
COMPOSITIONS OF ALLOYS  
(NOMINAL WEIGHT PERCENT)

	Ni	Cr	Co	Mo	W	Ta	Cb	Al	Ti	Fe	Mn	Si	C	B	Zn	Y
IN-738	Bal.	16.0	8.5	1.7	2.6	1.7	0.9	3.4	3.4	--	--	--	0.17	0.010	0.10	--
FSX-414	10.0	29.0	Bal.	--	7.5	--	--	--	--	1.0	--	--	0.25	0.010	--	--
Ni-50CR (IN-671)	52.0	48.0	--	--	--	--	--	--	--	--	--	--	--	--	--	--
FeCrAlY	--	25.0	--	--	--	--	--	4.0	--	Bal.	--	--	--	--	--	--
CoCrAlY	10.0	25.0	Bal.	--	--	--	--	5.0	--	--	--	--	--	--	--	0.15
RT-22	ALUMINIDED + Pt + Cr															

The salient conditions for each of the tests are summarized in Table 2. The Exxon test was conducted with a bed temperature between 1700° and 1770°F and a pressure of 10 atmospheres. The CURL bed operated at significantly different conditions, with the bed temperature at 1560°-1585°F and 6 atmospheres pressure. Specimen temperature during the Exxon 1000-hour test was maintained at about 1550°F, while the CURL specimens were maintained between 1350° and 1475°F. As previously indicated, nine (9) of the CURL impulse specimens were air cooled to obtain the 1350°F metal temperature. The pressure in the cascade channel was approximately 5 atmospheres in both the Exxon and CURL tests.

Measurements of the particulate loading and size distribution entering the turbine cascade sections were made during each test. These measurements revealed that a wide range of particle loading and size distribution occurred during the Exxon test, while a consistently higher but uniform and fine distribution was achieved in the CURL test (see Table 2). The nominal dust loading in the Exxon test was approximately 0.035 gr/scf (65 ppm), with 3-5% of the particles greater than 10 μm. However, during one brief period of approximately 6-8 hours' duration, although the size distribution did not change significantly, the total particulate loading increased dramatically to 0.46 gr/scf (860 ppm). In addition, at other short intervals the particulate size distribution shifted to 10% greater than 10 μm, with a smaller fraction (<2%) greater than 25 μm. By comparison, the CURL test ran for the full 1000 hours at a uniform, stable particulate loading of 0.13/ gr/scf (250 ppm), with only 0.8% greater than 10 μm.



**Table 2**  
**SALIENT TEST CONDITIONS**  
**OF EXXON/FIRESIDE II-CURL TESTS**

EXXON	CONDITION	CURL
III. No. 6	Coal (wt%)	Glen Brook
4.01	S	3.2-4.5
0.05	Na	0.05
0.19	K	0.47
0.08	Cl	0.08
Dolomite 1337	Sorbent (wt%)	Dolomite Plum Run
0.03	Na	0.06
0.04	K	0.05
0.09	Cl	0.05
1700°-1770°F	Bed temperature	1560°-1585°F
10 Atms	Pressure	6 Atms
6 f/s	Superficial fluidizing velocity	3 f/s
~1.8 sec	Bed residence time	~2.8 sec
3 cyclones	Particle separators	3 cyclones plus skimmer
35-820 ppm	Particle loading	~250 ppm
3-5% > 10 μm	Particle size	0.8% > 10 μm
1550°F	Specimen temperature	1350°-1475°F
900 f/s	Maximum specimen inlet velocity	1400 f/s

## TEST RESULTS

### *Deposition*

Chemical analyses of deposits from both tests were very similar, consisting of fly ash and spent sorbent. During the CURL test, no intentional effort was made to remove the deposits from the airfoils at the inspection intervals in order to assess buildup rate with exposure time. It was found that deposit thickness was not significantly different at the end of 1000 hours compared to the appearance at intermediate times.

### *Erosion/Corrosion*

Materials degradation by combined erosion/corrosion was more severe in the Exxon test due to the combined effects of the greater number of particles larger than 10 μm, the higher bed temperature, and higher specimen temperature. After 1000 hours, impulse specimens of bare IN-738, and FSX-414 experienced up to 0.015 inch of metal wastage and exhibited complete loss of leading edge radius due to the synergistic erosion/corrosion effects. Up to 0.030 inch of metal loss was measured at the leading edge of a bare IN-738 reaction airfoil. Although not attacked by corrosion, the thin platinum-chromium-aluminide coating was breached by the erosion process, exposing the IN-738 substrate material. A finding of great significance is that the FeCrAlY and CoCrAlY claddings performed well in this very aggressive environment. Only 0.001-0.002 inch of metal loss due to erosion/corrosion occurred at the leading edge of the clad impulse airfoils, with 0.003-0.006 inch loss on the corresponding reaction airfoils. Figures 2 and 3 show comparative photomicrographs of the leading edges of bare IN-738 and FeCrAlY clad on IN-738 impulse airfoils from the Exxon and CURL tests. Very clearly, good corrosion resistance is a prerequisite for satisfactory parts life in an erosive environment. Neither the bare nor protected impulse or reaction airfoils experienced any detectable erosion/corrosion in the CURL test. In addition, the three pin specimens located downstream of the fourth cascade, where the leading edge gas velocity was about 1400 f/s, showed no evidence of erosion.

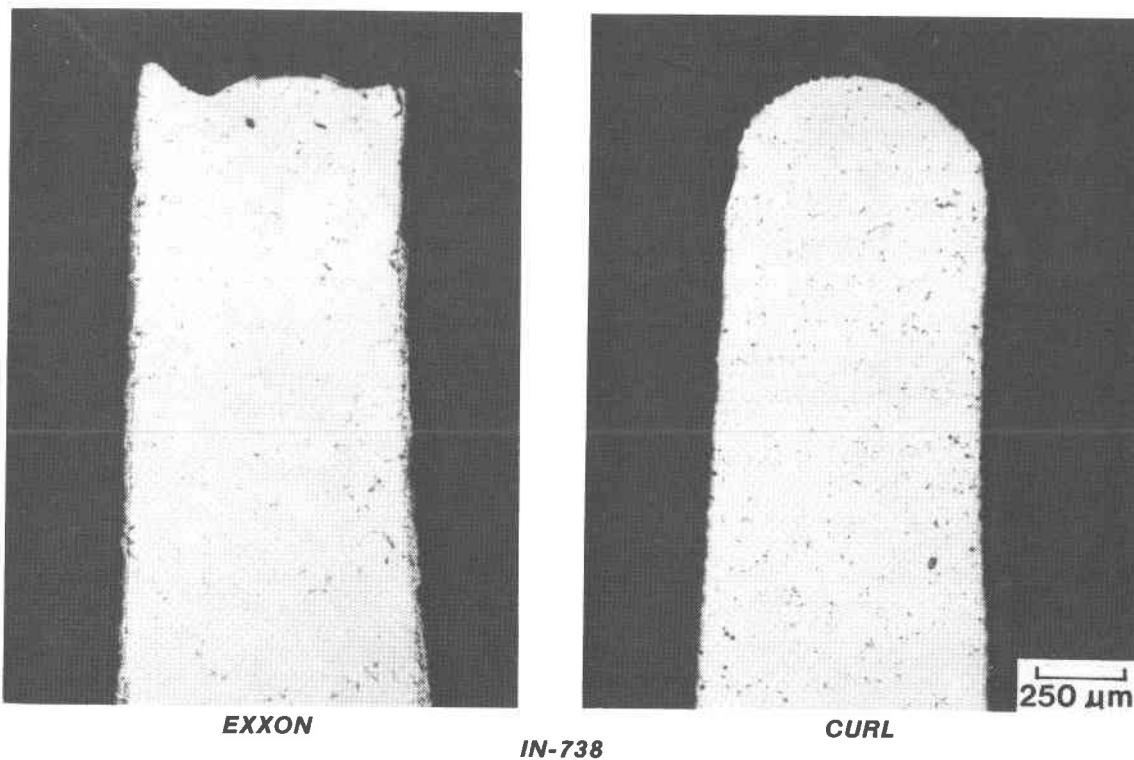


**Figure 2. Leading Edges of Bare IN-738 Impulse Airfoils After 1000 Hours' Exposure in the Exxon and CURL Tests**

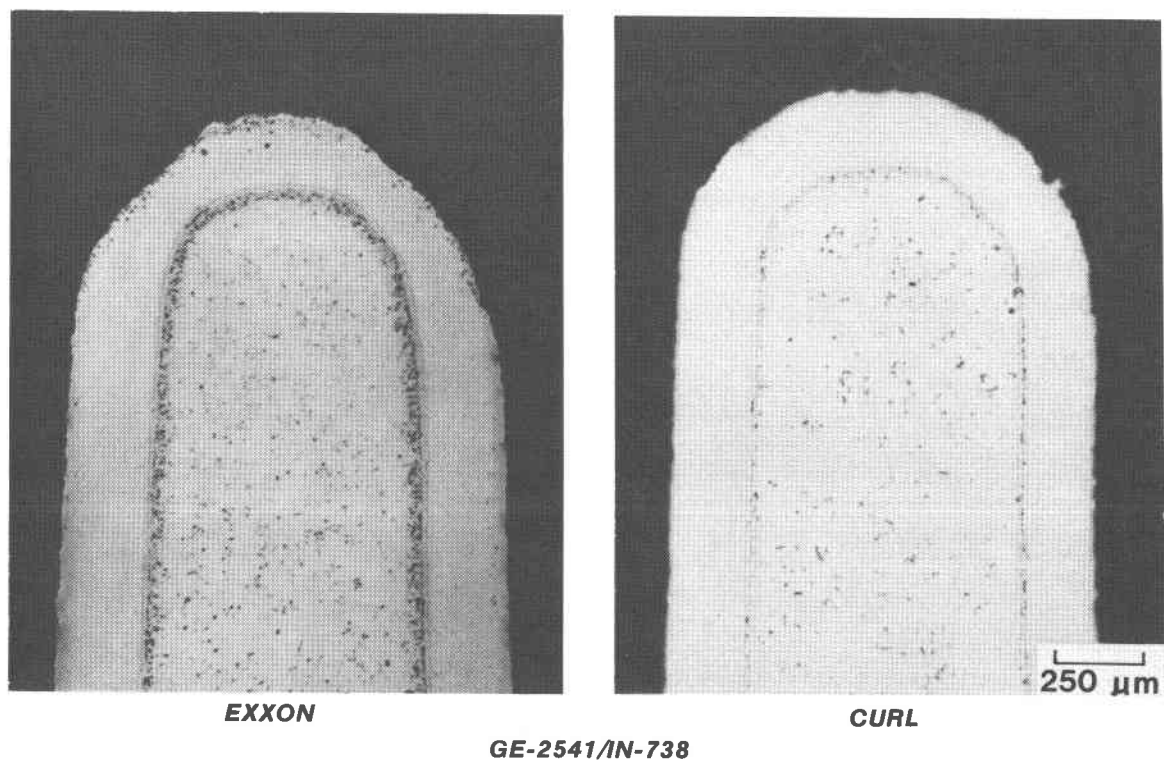


**Figure 3. Leading Edges of FeCrAlY CLAD IN-738 Impulse Airfoil After 1000 Hours' Exposure in the Exxon and CURL Tests**

## Corrosion

Corrosion attack alone, as determined by examining areas on specimen/cross sections not affected by erosion, was much greater in the Exxon test than in the CURL test. The maximum corrosion attack on IN-738 in the CURL test was only 0.0016 inch/1000 hours, while in the Exxon test it was 0.0042 inch/1000 hours. Similarly, the FeCrAlY and CoCrAlY claddings experienced corrosion of less than 0.001 inch/1000 hours in the CURL test, while corrosion in the Exxon Test was 0.002 inch/1000 hours and 0.004 inch/1000 hours, respectively.

In summary, the lower temperature and smaller number of particles greater than 10  $\mu\text{m}$  combined to make the CURL test much less aggressive toward turbine materials than the Exxon test. In the description of work which follows, the Exxon results are used for the purpose of qualifying the erosion/corrosion simulator since the Exxon conditions produced measurable degradation.

## PFBC SIMULATOR TESTING

### SIMULATOR TESTS – OBJECTIVES AND RIG REQUIREMENTS AND DESIGN

The main objectives of the PFBC simulator test program (EPRI RP 1337-1) are to:

- Determine a safe operating envelope to minimize erosion of gas turbine materials by quantifying the effects of key variables such as particulate loading and size distribution, particulate velocity, temperature and airfoil size. These tests will typically be of short duration ( $\sim 250$  hours) and include several materials which are known to exhibit varying degrees of resistance to erosion/corrosion.
- Evaluate the resistance of a variety of advanced protective systems (coatings/claddings) to the simulated PFBC environment for the purpose of identifying promising new materials and acquiring the background on compositional and structural effects to guide the development of new protective systems.

A PFBC erosion-corrosion rig (simulator) capable of simulating the significant aspects of the PFBC gas stream environment has been constructed. The simulator was funded and built by the General Electric Company and applied to the EPRI RP 1337-1 Program. Briefly, the simulator is an atmospheric pressure, high temperature, high velocity, combustion rig into which PFBC fly ash is injected at a temperature which does not exceed the maximum expected PFBC bed temperature ( $\sim 1750^\circ\text{F}$ ). The fly ash is accelerated to gas velocities representative of gas turbine operation. Alkali salts are also introduced into the simulator and the hot particulate laden gas stream impinges on a cascade of 14 airfoil-shaped specimens. The erosion-corrosion simulator is depicted schematically in Figure 4, and the nominal range of operating parameters is listed in Table 3. As shown in the schematic, the simulator is equipped with a quartz view-port which permits intermittent measurement of particle velocities by laser doppler velocimetry. A complete description of the facility appears in Reference 3.

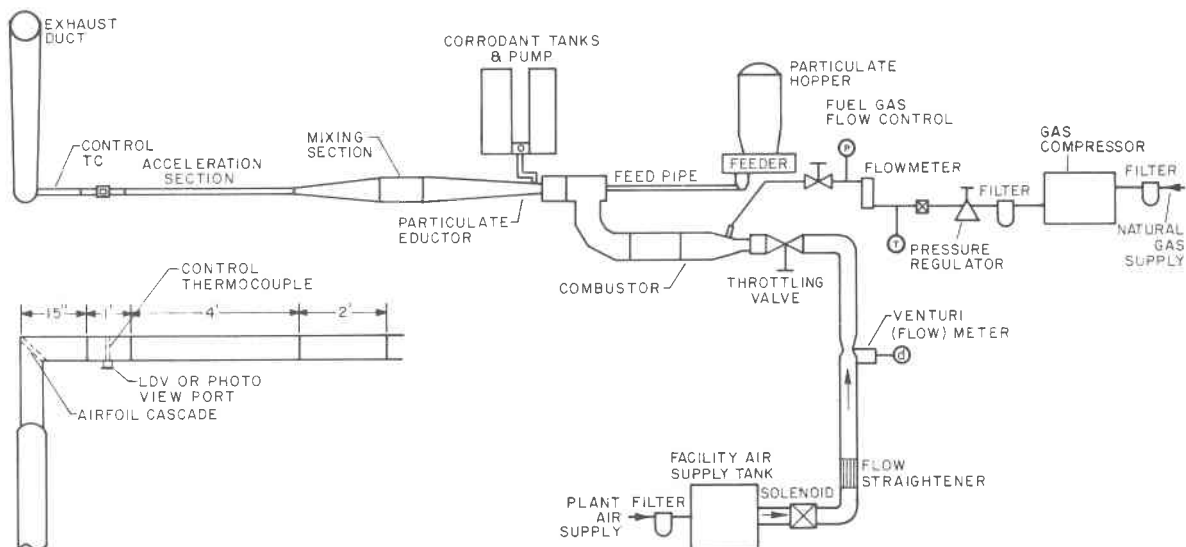


Figure 4. Erosion-Corrosion Simulator (ECS) Schematic

**Table 3**  
**NOMINAL SIMULATOR OPERATING PARAMETERS**

GAS VELOCITY	960 - 1170 f/s
TEMPERATURE	1350 <sup>o</sup> - 1600 <sup>o</sup> F
PARTICULATE LOADING	60 - 600 ppm
CORRODENT LEVEL	4 ppm
PRESSURE	1 atm

A total of 2500 hours of erosion, corrosion and erosion-corrosion testing has been conducted on the simulator at a gas temperature of 1600 °F, and gas/particle velocities of 960 f/s and 1170 f/s using PFBC particulate as the erosive media. Qualification of the simulator has been achieved through a series of experiments which successfully reproduced the erosion-corrosion effects observed during the PFBC test conducted at the Exxon Miniplant PFB Facility, Linden, N.J. Six 250-hour simulation tests have been conducted to date to evaluate the effect of gas/particle velocity, particle size distribution, and alkali sulfate flux level on the degradation of a variety of candidate gas turbine materials. Throughout the simulation tests, a ranking of alloy performance has been achieved which is consistent with the results of the Exxon 1000-hour PFBC test.

### **SIMULATOR TEST CONDITIONS**

#### ***Particulate/Erosive Environment***

The PFBC particulate used for both the qualification and simulation phases of this program was collected during the two 1000-hour materials tests conducted at Exxon and CURL. This particulate consisted of 900 lb of Exxon third cyclone dust, 1400 lb of CURL third cyclone dust and 2000 lb of CURL second cyclone dust.

As described in Reference 3, the 900 lb of Exxon third cyclone material was air classified into two size fractions: a fine fraction having a mean particle size of 3.4  $\mu\text{m}$  and  $\sim 5\%$  of the distribution greater than 10  $\mu\text{m}$ , and a coarse fraction having a mean particle size of 7.8  $\mu\text{m}$  with 25% of the particles greater than 10  $\mu\text{m}$ .

The CURL second and third cyclone particulate was not air classified; however, Coulter counter size analyses verified that the size distributions were as reported during the CURL 1000-hour test. CURL third cyclone dust has a mean particle size of 2.9  $\mu\text{m}$  and 1-2% greater than 10  $\mu\text{m}$ ; CURL second cyclone dust has a mean particle size of 5.8  $\mu\text{m}$  and 8% greater than 10  $\mu\text{m}$ . The Coulter counter size distributions for each of the four fractions of particulate are shown in Figure 5.

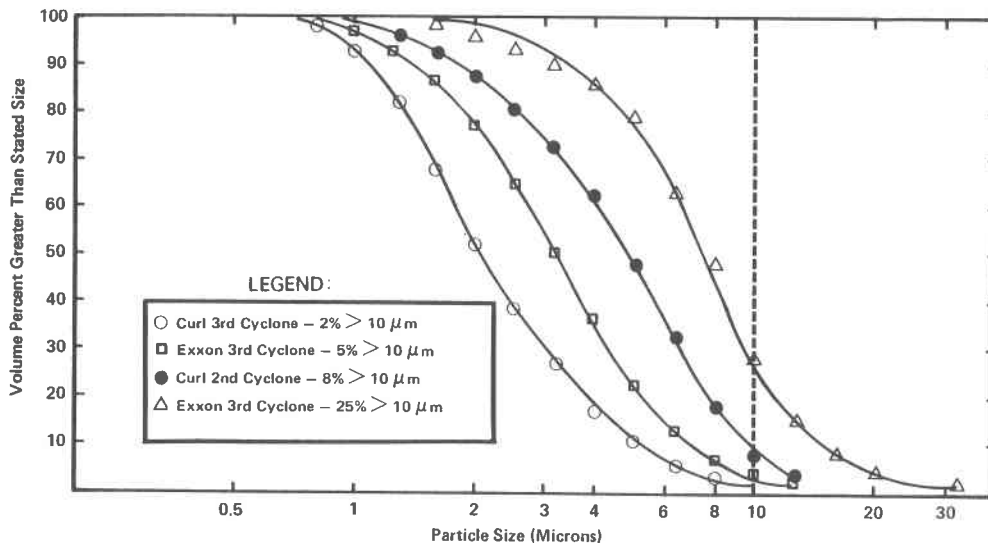


**Figure 5. Coulter Analysis Size Distributions for PFB Particulate**

The Exxon fine fraction was used to perform 500 hours of qualification testing and 750 hours of simulation testing. This dust has now been exhausted. The coarse fraction of Exxon dust and the CURL second cyclone material each have been used for one 250-hour simulation test, while the CURL third cyclone material was used for one 250-hour simulation test and a 100-hour qualification test.

**Corrosion Environment**

The complexity of the chemical environment generated during the PFB combustion of coal makes it impossible to completely account for all the chemical components of the environment in a simulation test. The water-soluble alkali sulfates,  $\text{Na}_2\text{SO}_4$  and  $\text{K}_2\text{SO}_4$ , are generally considered to represent the components of the PFBC effluent associated with hot corrosion. Therefore, this corrosive component of the PFBC effluent was simulated by injecting an aqueous solution of  $\text{Na}_2\text{SO}_4$  and  $\text{K}_2\text{SO}_4$  at concentration levels which resulted in an alkali sulfate flux to the specimens equivalent to that expected under real conditions. This flux level was established based on thermochemical calculations and several experimental runs followed by chemical analysis of the deposit. Finally, the flux was modified to produce material corrosion rates and corrosion morphologies comparable to those observed in the Exxon test.

**Gas/Particle Dynamics**

To verify that the erosion-corrosion simulator could reproduce the erosive environment anticipated in a gas turbine fired by a PFBC, a series of gas and particle velocity measurements was carried out.

Gas velocities were determined by pitot-tube measurements, mass flow and total and static pressure measurements, and computer analytical techniques. Particle velocities were determined by trajectory analyses using computer analytical techniques and via direct measurements using laser doppler velocimetry (LDV). LDV experiments were performed on both a laboratory free-jet and in the erosion-corrosion simulator at various temperatures (RT-1600°F) and gas velocities (200-1180 f/s) using a variety of seed materials ( $1\ \mu\text{m}\ \text{Al}_2\text{O}_3$ ,  $70\ \mu\text{m}\ \text{Al}_2\text{O}_3$ ,  $53\text{-}106\ \mu\text{m}\ \text{SiO}_2$ ) and PFB particulate. Gas and particle velocities were determined simultaneously to provide a direct correlation between the pitot-tube and the LDV velocity data. The test data is shown in Figure 6. Results of these experiments indicate that the PFB particulate is moving at the gas velocity while approaching the cascade of airfoil-shaped specimens being evaluated for erosion-corrosion degradation.

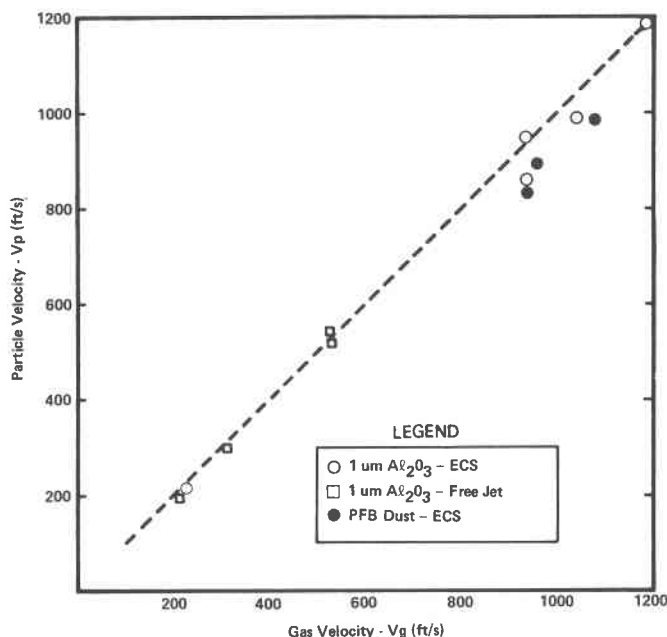


**Figure 6. Gas vs. Particle Velocity Data**

**Specimen Design and Evaluation Procedure**

The specimen configuration for simulator testing is identical to the impulse airfoils used during the two 1000-hour PFBC cascade tests conducted at Exxon and CURL, as shown in Figure 7.

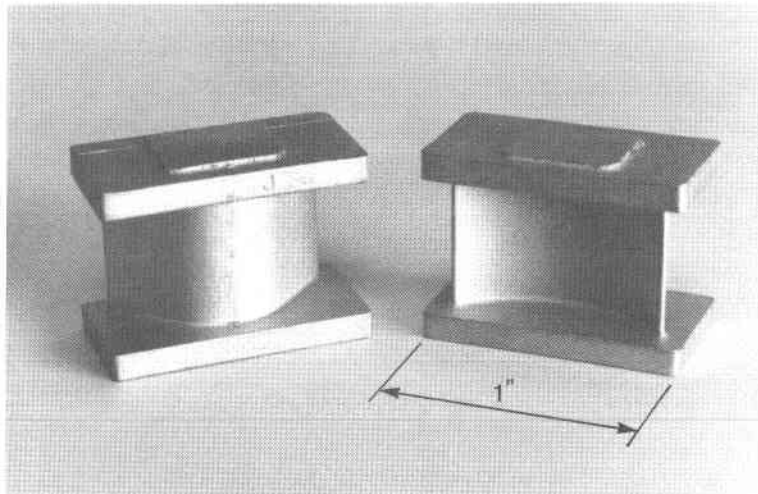


**Figure 7. Impulse Airfoil-Shaped Test Specimens**

**Characterization of Erosion/Corrosion/Deposition**

The mini-airfoil specimen design was selected to provide a closer simulation of actual turbine operating conditions than could be obtained with simple disc, pin, or wedge shaped specimens. Selection of this specimen design introduced, however, a number of analytical problems associated with quantitatively determining erosion, corrosion, and deposition on base alloy specimens and coated specimens.

Metal recession due to erosion and the thickness of adherent deposits were determined using a dimensional contour tracing technique. Prior to installation in the erosion-corrosion simulator, a 20X magnification tracing of each airfoil was made. Contour tracing was performed by profiling the mid-plane surface of each airfoil using two mechanical probes electronically connected to a strip chart recorder. The tracings are reportedly accurate to  $\pm 0.001$  inch. Statistical analysis of dimensions measured on 10 as-cast parts yielded a one  $\sigma$  standard deviation of  $\pm 0.0015$  inch. This variation is well within the dimensional tolerances of the as-cast parts. In addition, prior to exposure each part was weighed and thoroughly cleaned to remove potential sources of contamination.

Following exposure in the simulator tests, each airfoil was soft bristle-brushed, rinsed first in distilled water followed by an isopropanol rinse to remove all loose deposits, dried, and weighed. The parts were then profile traced, and measurements of metal recession and/or deposition were made by comparing the pre-test and post-test profiles. Figure 8 shows the general form of the erosion/deposition effects. Erosion is measured as the metal recession at the tip of the leading edge and along the pressure surface. The maximum metal recession generally occurred at the leading edge. The contour tracing technique was not used on clad specimens since the cladding is a uniform 0.010 inch thick and provides a good reference for post-test measurements.

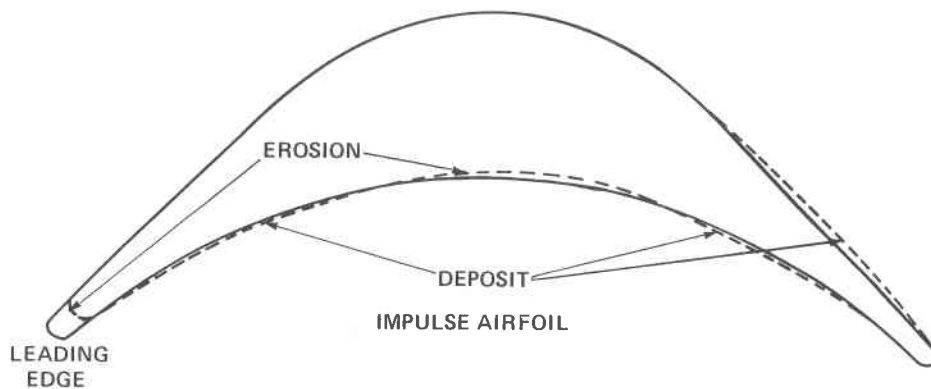


**Figure 8. Schematic of Impulse Airfoils Showing Areas Where Erosion and Deposition Generally Occurred**

Following post-test contour tracing, each specimen was sectioned at the midplane where the tracing had been made. One-half of each specimen was then mounted and metallographically prepared and evaluated. The microscopic evaluation was carried out to measure for corrosion attack (i.e., oxide or sulfide penetration), deposit thickness, and metal recession. Recession measurements on the base and coated specimens were compared with measurements from the contour tracings. Corrosion penetration was measured as the maximum depth of sulfide or oxide penetration below the existing metal surface; see Figure 9.

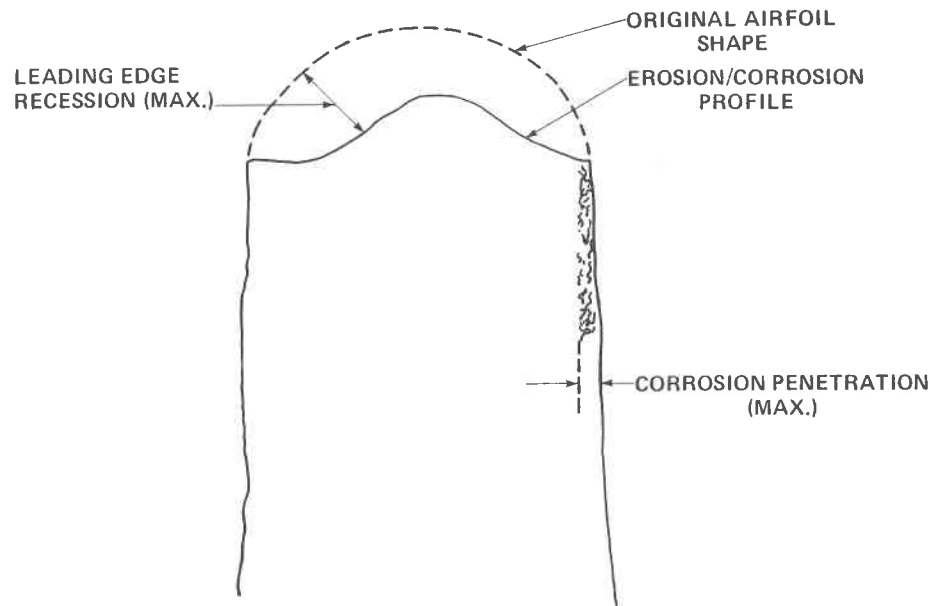


**Figure 9. Erosion and Corrosion Measurements**

## **SIMULATOR TEST RESULTS**

### **Qualification Tests**

The objective of the qualification tests was to evaluate the erosion, corrosion, and erosion-corrosion characteristics of the simulator for comparison with actual PFBC test results. Changes in test procedures were made during the qualification phase until the observed degradation of materials matched as closely as possible that observed under real PFBC conditions. Comparisons with the Exxon test results were used to calibrate and qualify the simulator, since the CURL test was not severe enough to cause measurable erosion/corrosion on any of the materials tested.

Throughout the qualification tests, the nickel-base alloy IN-738 and cobalt base alloy FSX-414 were used to measure the degree to which the individual tests satisfied their intended purpose: erosion, corrosion or combined erosion/corrosion. Several candidate gas turbine coatings and claddings also were evaluated (see Table 1) with the overall objective of achieving the same ranking of alloy performance as observed during the Exxon test.

The qualification test matrix is presented in Table 4. A series of seven tests, from 50-250 hours duration and totaling 1000 hours were performed during this phase of the program for comparison with results of the Exxon test. Operating conditions for each test were modified based on the materials degradation observed in the preceding tests.

Table 4

QUALIFICATION TEST MATRIX

Test No.	Description (Primary Effect Investigated)	Hours	Gas Temp. °F	Gas Velocity fps	Part. Loading ppm	Part. Size Dist. Percent Greater Than 10 micron	Alkali Sulfate Flux moles/cm <sup>2</sup> -sec (Contaminants)
Q1	Erosion	50	1600	960	960	5 <sup>(1)</sup>	---
Q2	Erosion	200	1600	960	60	5 <sup>(1)</sup>	---
Q3	Corrosion	150	1600	960	--	--	5x10 <sup>-10</sup> (Na <sub>2</sub> SO <sub>4</sub> ,K <sub>2</sub> SO <sub>4</sub> ,H <sub>2</sub> SO <sub>4</sub> *)
Q4	Corrosion	150	1600	960	--	--	1x10 <sup>-10</sup> (Na <sub>2</sub> SO <sub>4</sub> ,K <sub>2</sub> SO <sub>4</sub> ,H <sub>2</sub> SO <sub>4</sub> *)
Q5	Corrosion	100	1600	950	--	--	1x10 <sup>-10</sup> (Na <sub>2</sub> SO <sub>4</sub> ,K <sub>2</sub> SO <sub>4</sub> )
Q6	Erosion/Corrosion	250	1600	960	60	5 <sup>(1)</sup>	1x10 <sup>-10</sup> (Na <sub>2</sub> SO <sub>4</sub> ,K <sub>2</sub> SO <sub>4</sub> )
Q7	Erosion/Corrosion	100	1600	960	100	2 <sup>(2)</sup>	0.2x10 <sup>-10</sup> (Na <sub>2</sub> SO <sub>4</sub> ,K <sub>2</sub> SO <sub>4</sub> )

(1) Exxon third cyclone particulate-air classified fine fraction.

(2) CURL third cyclone particulate.

\* H<sub>2</sub>SO<sub>4</sub> added to increase sulfur activity in environment. Excessive corrosion/sulfidation of airfoils during these tests indicated this was not necessary; therefore, H<sub>2</sub>SO<sub>4</sub> was removed as a contaminant.

**Erosion.** Tests Q1 and Q2 were designed as baseline erosion trials (using Exxon PFBC particulate) to evaluate material degradation in the absence of any intentional corrodent additions. Each of these tests used PFBC particulate from the Exxon third cyclone catch, air classified to an average particle size of 3.4 μm and ~5% of the distribution greater than 10 μm. Two levels of particulate loading, which represent the following conditions (see Figure 5), were selected for study:

1. A high loading of approximately 600 ppm (0.32 gr/scf) representative of upset conditions during cyclone plugging as encountered during the Exxon 1000-hour test
2. A loading of approximately 60 ppm (0.032 gr/scf) more typical of the nominal conditions experienced during the Exxon test.

Both tests were performed at 1600°F and at a gas velocity of 960 f/s for 50 and 200 hours, respectively. Salient results were:

- Erosion, corrosion, and deposition effects in the simulator were generally similar to those observed in actual PFBC tests, even though no additional alkali sulfate contaminant was introduced in these tests
- The Exxon PFBC particulate was found to contain sufficient alkali to produce significant corrosion on Inconel 671 and IN-738
- The erosive-corrosive environment in the simulator was particularly detrimental to FSX-414
- Erosion characterized by leading edge metal loss was greater for the 50-hour exposure at 600 ppm than for the 200-hour exposure at 60 ppm and, in general, the damage was comparable to that observed in the Exxon test under similar conditions

**Corrosion.** The basis for setting corrodent levels in the qualification tests was reviewed briefly in an earlier section and is discussed in detail in Reference 1. Corrodent levels are specified in terms of the flux of alkali sulfate onto the airfoil specimens. Short term corrodent condensation trials were run to experimentally verify alkali sulfate flux levels which had been predicted by theory. Then three corrosion tests were run, tests Q3, Q4 and Q5 (Table 4), at three levels (decreasing) of alkali sulfate flux in order to achieve the most realistic corrosion simulation. Based upon the results of these three tests it



was determined that the corrosion attack achieved in test Q5 was suitable for a baseline corrosion level and that additional adjustment to the corrosive environment would be based upon the results of combined erosion/corrosion testing. The relative ranking of performance of materials tested in Q3, Q4, Q5 was consistent with the results of the Exxon test.

**Erosion/Corrosion.** A combined erosion/corrosion test, Q6, was run next under conditions shown in Table 4. The results of test Q6 indicated that material wastage due to corrosion was in excess of that observed in the Exxon test for similar times. However, the overall ranking of alloys in test Q6 was the same as that observed in the Exxon test. A second combined erosion/corrosion test, test Q7, was then run at a further reduced alkali sulfate flux, and this was selected as the baseline level for use in subsequent simulation tests.

One additional observation is appropriate in support of the ability of the simulator to reproduce erosion/corrosion effects representative of those actually observed in the Exxon test. Conditions for simulation test S2 (discussed in the next section and listed in Table 5) were selected to simulate the first 250-hour segment of the Exxon test. A comparison of IN-738 and FSX-414 after 250 hours of exposure in both the simulator and the Exxon test is shown in Figure 10. The level of erosion at the leading edge is insignificant in both tests. Similarly, the corrosion attack (see Figure 11) on both materials shows a close correspondence in morphology and depth of penetration between the two tests. These results are considered further proof that the simulator, operating under conditions which are nominally similar to those in an actual PFBC test, is capable of reproducing the essential features of erosion/corrosion damage observed in the real PFBC environment.

**Table 5**

**SIMULATION TESTING SUMMARY**

Test No.	Description (Primary Effect Investigated)	Hours	Gas Temp. °F	Gas Velocity fps	Part. Loading ppm	Part Size Dist. Percent Greater Than 10 Micron	Corrodent Flux moles/cm <sup>2</sup> -sec (Contaminants)
S1	Coarse Distribution	250	1600	960	100	25 <sup>(3)</sup>	0.2×10 <sup>-10</sup> (Na <sub>2</sub> SO <sub>4</sub> ,K <sub>2</sub> SO <sub>4</sub> )
S2	"Baseline" (Exxon PFBC Condition)	250	1600	960	100	5 <sup>(1)</sup>	0.2×10 <sup>-10</sup> (Na <sub>2</sub> SO <sub>4</sub> ,K <sub>2</sub> SO <sub>4</sub> )
S3	High Velocity/Corrosion (Exxon)	250	1600	1170	100	5 <sup>(1)</sup>	0.2×10 <sup>-10</sup> (Na <sub>2</sub> SO <sub>4</sub> ,K <sub>2</sub> SO <sub>4</sub> )
S4	High Velocity/Fine Distribution	250	1600	1170	100	5 <sup>(1)</sup>	---
S5	High Velocity/Coarse	250	1600	1170	100	8 <sup>(2)</sup>	---
S6	High Velocity/CURL Fine	250	1600	1170	100	2 <sup>(4)</sup>	0.2×10 <sup>-10</sup> (Na <sub>2</sub> SO <sub>4</sub> ,K <sub>2</sub> SO <sub>4</sub> )

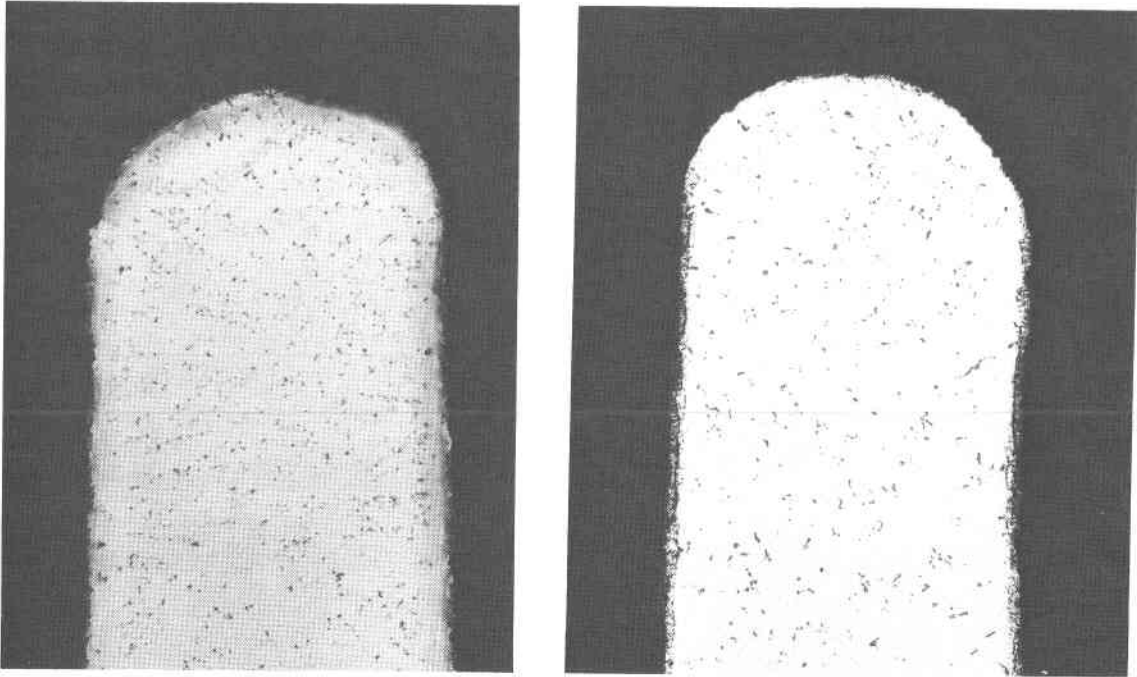
(1) Exxon third cyclone particulate-air classified fine fraction.  
 (2) CURL second cyclone particulate.  
 (3) Exxon third cyclone particulate-air classified coarse fraction.  
 (4) CURL third cyclone particulate.

**Deposition.** In tests Q6 and Q7, specimens were covered with a loose, powdery deposit on the tip of the leading edge and on the suction surface toward the trailing edge, while the pressure surface was covered with an adherent reddish-brown deposit. These deposits were very similar to those observed during both the Exxon and CURL PFBC tests.

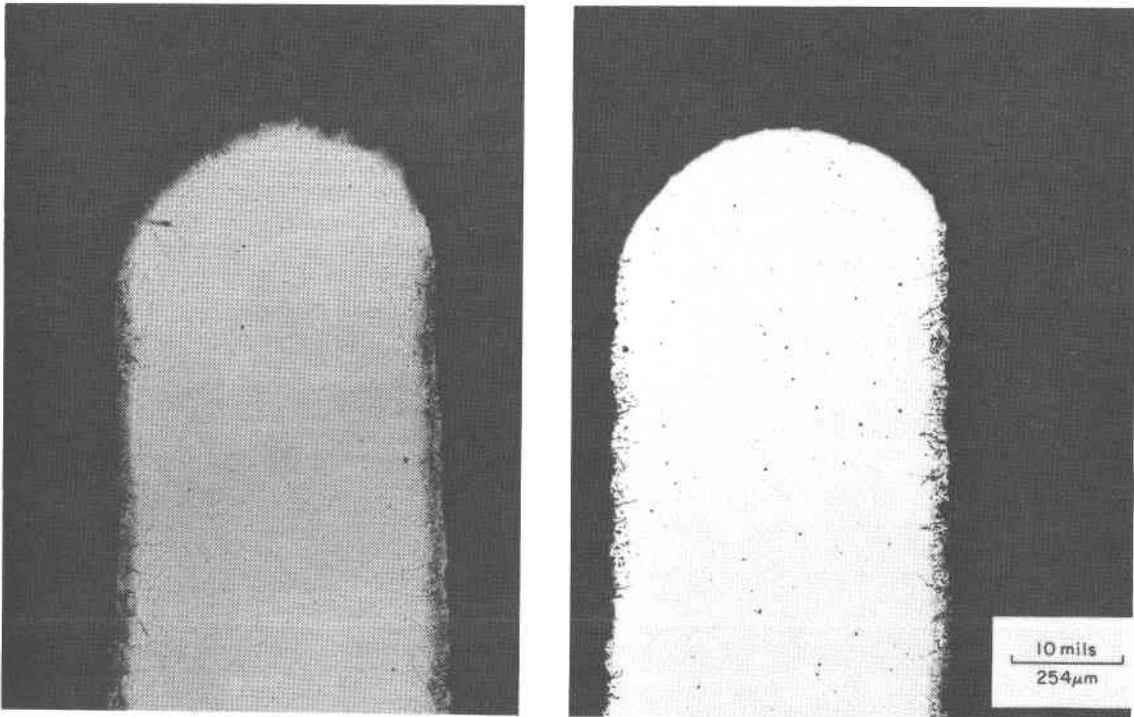
**Simulation Tests**

The objectives of the simulation tests are to:

- Evaluate the effects of changes in key PFBC variables (gas/particle velocity, particulate loading and size distribution, temperature, and alkali contaminant level) on the erosion/corrosion behavior of several state-of-the-art gas turbine base alloys, coatings and claddings (see Table 1);
- Evaluate the erosion/corrosion resistance of advanced coatings and claddings in a simulated PFBC environment for times up to 1000 hours.



**IN-738**



**(a)**

**FSX-414**

**(b)**

**Figure 10. Leading Edges of IN-738 and FSX-414 After 250 Hours Exposure in (a) Simulator Test S2 and (b) Exxon PFBC Test**

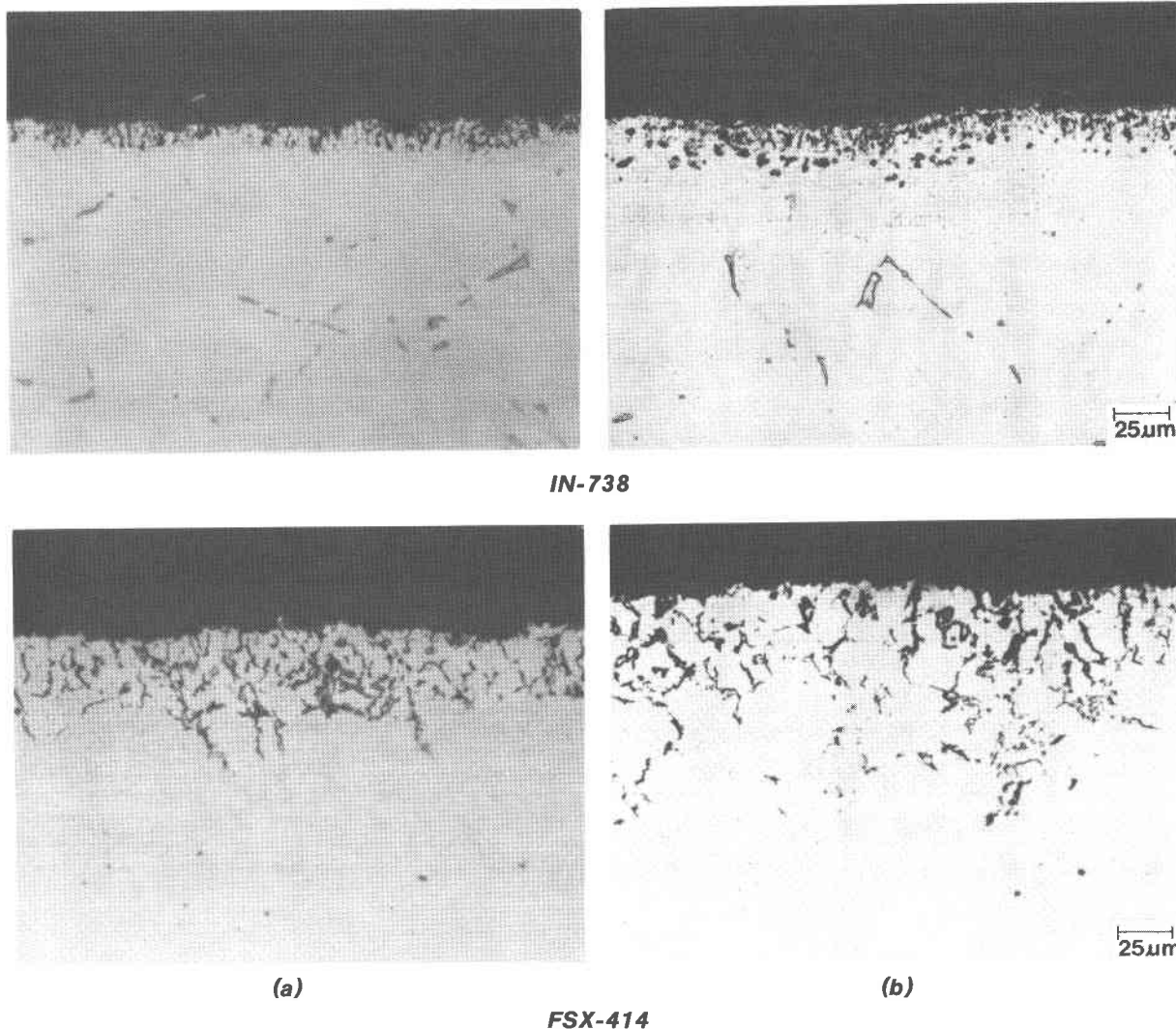


**Figure 11. Hot Corrosion of IN-738 and FSX-414 After 250 Hours Exposure in (a) Simulator Test S2, and (b) Exxon PFBC Test.**

To date six 250-hour simulation tests have been run to evaluate the effects of changes in key PFBC variables. Materials tested are listed in Table 1. A summary of the operating conditions and effects investigated in each of the six 250-hour tests is given in Table 5.

Tests S1 and S2 were run to determine the materials' response to significant changes in particle size distribution under combined erosive/corrosive conditions. As described under the section on test conditions, the Exxon third cyclone catch was air classified to produce fractions of particulate having a wide range of size distributions, i.e., ~5% > 10  $\mu\text{m}$  and 25% > 10  $\mu\text{m}$ . Each distribution was used in conjunction with the alkali flux level established during qualification test Q7,  $0.2 \times 10^{-10}$  moles/cm<sup>2</sup>-sec Na<sub>2</sub>SO<sub>4</sub>-K<sub>2</sub>SO<sub>4</sub>.

The purpose of the third test, S3, was to evaluate the effect of increased gas/particle velocity (1170 f/s) on erosion/corrosion degradation. The alkali flux level and particle size distribution were the same as in test S2. The fourth and fifth tests, S4 and S5, also were run at the high velocity using two size distributions of PFBC particulate, but the alkali flux introduced as the aqueous salt solution was not included in these tests. Therefore, a comparison of results of test S3 to test S4 provides data on erosion/corrosion degradation with and without the alkali sulfate addition. Test S6 can be compared to test S3 in that conditions were the same except the particulate was CURL third cyclone dust (see Figure 5) in place of the Exxon fine fraction. All future tests will be run with the CURL particulate since the Exxon material has been used up.

**Deposition.** Deposition patterns and structure on the airfoils were generally consistent throughout the simulation tests. The amount of deposit varied significantly, particularly on the pressure surface, depending upon the velocity and particle size distribution used for the individual tests; i.e., lower velocity and finer particle size distributions increased pressure surface deposit buildup.

**Erosion/Corrosion.** Table 6 summarizes the leading edge metal recession data and maximum corrosion penetration data measured on each of the airfoils exposed during the six simulation tests. Metal recession is reported for the leading edges, as these generally show the greatest damage. Test S5, high velocity plus coarse particle size distribution, did cause severe erosion to the (concave) surface as well. Consequently, two metal recession measurements are listed for each material. Corrosion penetration was measured at its maximum value on the airfoil.

**Table 6**

**SIMULATION TEST MATRIX EROSION/CORROSION DATA AFTER 250 HOURS  
Maximum Leading Edge Recession (Inch)/Maximum Corrosion Penetration (Inch)**

Test No.	FSX-414	IN-738	IN-671 Clad IN-738	GE-2541 Clad IN-738	PFB-6 Clad IN-738	RT-22 Coated IN-738
S1	0.005/0.002	0.001/0.002	0.002/0.006	0.001/0.002	0.001/<0.001	N.D./N.D.
S2	0.001/0.002	0.001/0.002	0.002/0.003	N.D./N.D.	N.D./N.D.	N.D./N.D.
S3	0.015/0.005	0.010/0.004	0.005/0.003	0.002/0.003	0.003/0.002	--/--
S4	0.006/0.002	0.002/0.001	0.002/0.002	0.001/0.002	0.002/0.001	0.001/N.D.
S5	(0.023/0.025)*/ 0.010	(0.010/0.006)/ 0.002	(0.004/0.010)/ 0.002	(0.004/0.010)/ 0.003	(0.004/0.006)/ 0.001	(0.003/0.003)/ N.D.
S6	0.007/0.002	0.002/0.002	0.002/0.002	0.003/0.004	0.002/0.002	0.001/N.D.
<hr/> <p>N.D. - None Determined</p> <p>* - Leading Edge Recession/Pressure Surface Recession</p>						

The six alloy systems with few exceptions exhibited the same relative performance throughout the six tests: platinum-aluminided IN-738 most resistant to erosion/corrosion followed in order by CoCrAlY-clad IN-738, FeCrAlY-clad IN-738, unprotected IN-738, Inconel 671-clad IN-738, and FSX-414, and this ranking compares favorably with that observed in the Exxon test. The primary type of corrosion attack, i.e., oxidation or sulfidation, exhibited by each alloy remained essentially unchanged throughout the six simulation tests independent of the addition or omission of an alkali sulfate flux to the hot gas stream.

Metallographic results and discussion for each of the six alloys in the six tests will not be presented here. This detailed data will be available in Reference 4. The effects of changes in key PFBC variables for each of the six tests are documented here by referring to the response of the cobalt-base alloy FSX-414. This is an ideal index alloy for this purpose since it was exposed in all six tests, responded sharply to changes in PFBC parameters, and was evaluated in the Exxon test.

### DISCUSSION

Gas turbine materials degradation in a PFBC environment is expected to take one of three forms:

- 1) *Corrosion* of gas turbine components primarily by sodium sulfate-induced hot corrosion due to the presence of alkali metals and sulfur from the burning of coal.
- 2) *Erosion* of gas turbine components by particulate matter (made up of coal combustion ash and PFB sorbent) not entirely removed by the hot gas cleanup train.
- 3) *Erosion-Corrosion* of gas turbine components emanating from a synergism of processes (1) and (2) above.

Conceivably, (1), (2), or (3) may each be operative at different times during PFBC operation. Steady state operating conditions such as used in the simulator test may best be regarded as a baseline on which to assess the effects of parametric changes. It should not be expected that any single simulation test at a discrete set of parameters will be totally simulative of a complete PFBC operating cycle.

The simulation tests run to date can each be classified according to the above criteria by their effects on the test materials. Erosion-dominated attack can be somewhat arbitrarily interpreted as metal recession in excess of the depth of corrosion penetration. Corrosion-dominated attack is defined for the purposes of these simulation tests as a hot corrosion surface morphology and/or sulfide penetration greater than 0.001 inch per 100 hours. Erosion-corrosion attack represents a combination of metal recession, corrosion product removal, and significant corrosion penetration. Viewed in this manner, the test results are summarized in Table 7.

**Table 7**  
**SIMULATION TEST CLASSIFICATION**

Test No.	Velocity (f/s)	Hours	Particulate Condition	Corrosion Condition	Predominant Degradation Mode
S1	960	250	100 ppm Exxon (25% > 10 $\mu$ m)	$0.2 \times 10^{-10}$ moles/cm <sup>2</sup> -sec Na <sub>2</sub> SO <sub>4</sub> -K <sub>2</sub> SO <sub>4</sub>	Erosion/Corrosion
S2	960	250	100 ppm Exxon ( 5% > 10 $\mu$ m)	$0.2 \times 10^{-10}$ moles/cm <sup>2</sup> -sec Na <sub>2</sub> SO <sub>4</sub> -K <sub>2</sub> SO <sub>4</sub>	Erosion/Corrosion
S3	1170	250	100 ppm Exxon ( 5% > 10 $\mu$ m)	$0.2 \times 10^{-10}$ moles/cm <sup>2</sup> -sec Na <sub>2</sub> SO <sub>4</sub> -K <sub>2</sub> SO <sub>4</sub>	Erosion/Corrosion
S4	1170	250	100 ppm Exxon ( 5% > 10 $\mu$ m)	None	Erosion/Corrosion
S5	1170	250	100 ppm CURL ( 8% > 10 $\mu$ m)	None	Erosion
S6	1170	250	100 ppm CURL ( 2% > 10 $\mu$ m)	$0.2 \times 10^{-10}$ moles/cm <sup>2</sup> -sec Na <sub>2</sub> SO <sub>4</sub> -K <sub>2</sub> SO <sub>4</sub>	Erosion/Corrosion

From the test data given in Table 6 and comparative micrographs of FSX-414 in the simulation tests, the effects of changes in key variables on erosion/corrosion can be assessed. In the comparisons which follow in Figures 12-15, all are cross sections of FSX414 leading edges tested for 250 hours at 1600 °F. The dashed white lines on the micrographs show the original leading edge profile before testing.

1. All other test conditions being held constant, an increase in the gas/particulate velocity resulted in a significant increase in erosion damage as measured by leading edge metal recession. This is evident from a comparison of data in Table 6 and the comparative micrographs in Figure 12 for FSX-414 in test S2 (960 f/s) and test S3 (1170 f/s). In the case of FSX-414, the 20% increase in velocity resulted in an approximate 14-fold increase in erosion damage at the leading edge. Although it would be inappropriate to quote a velocity exponent from the one comparison given here, it is apparent that the value of this exponent for FSX-414 in this experiment is much higher (> 10) than the value of 2 to 5 which is generally suggested.<sup>(5)</sup>
2. The 10  $\mu$ m particle is considered by some to be a critical size below which particles generally do not cause significant erosion. Therefore, in PFBC dust an increase in the number of particles greater than 10  $\mu$ m, everything else being constant, should result in increased erosion damage. This effect is in fact noted by comparing the damage to FSX-414 in tests S4 and S5 in Figure 13. In test S4, 5% of the particles were greater than 10  $\mu$ m, while in test S5, 8% were greater than 10  $\mu$ m.

3. Introduction of the alkali sulfate flux into the simulator test (an increase in the corrosion component) increases the level of erosion/corrosion damage. This effect on FSX-414 is documented in Figure 14 where specimens from test S3 (alkali sulfate added) and S4 (particulate alone) are compared. The effect of the presence of the alkali sulfate is obvious.
4. A comparison of the Exxon third cyclone fine fraction dust (5% > 10  $\mu\text{m}$ ) with the CURL third cyclone dust (2% > 10  $\mu\text{m}$ ) shows that the CURL fine ash is less erosive. The comparative micrographs for FSX-414 in tests S3 and S6 (Figure 15) illustrate this effect. A comparison of actual results from the Exxon and CURL tests confirms this observation.

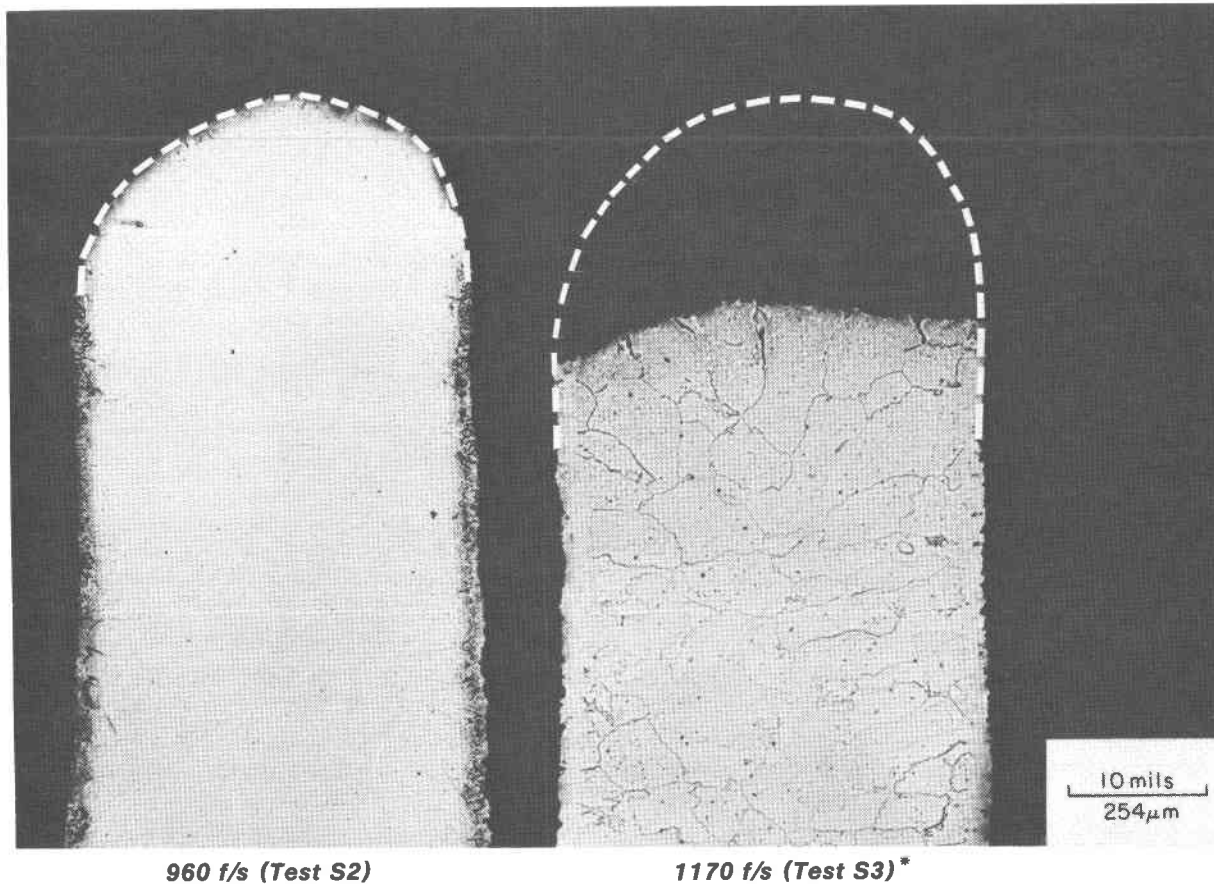
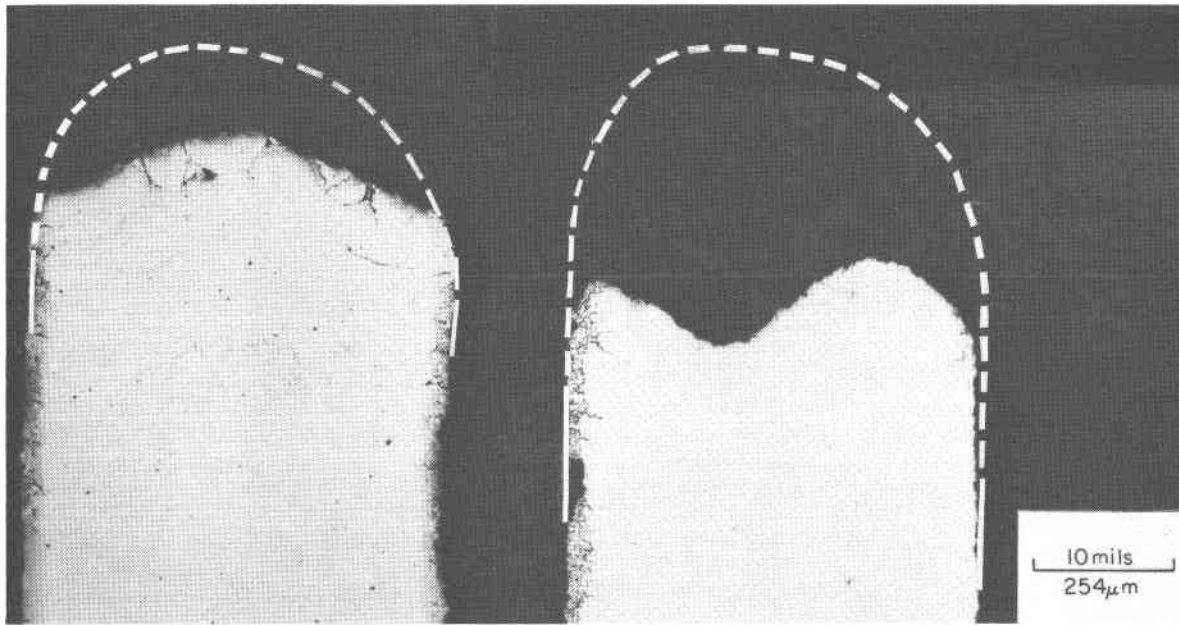


**Figure 12. Effect of Velocity [100 ppm Exxon PFBC Particulate (5% > 10  $\mu\text{m}$ ), with Alkali Sulfate Contaminants]**

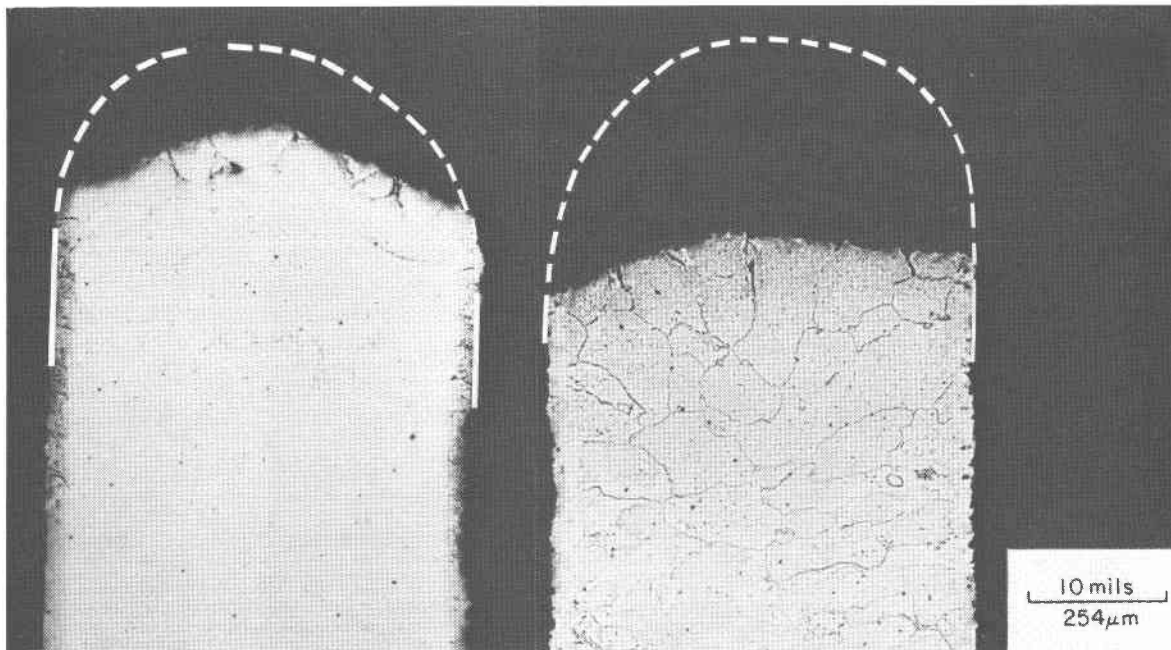
**\*The appearance of grain boundaries on this micrograph is a result of variations in metallographic preparation; it was not caused by the test exposure.**



5% > 10 μm (Exxon Fine, Test S4)

8% > 10 μm (CURL Coarse, Test S5)

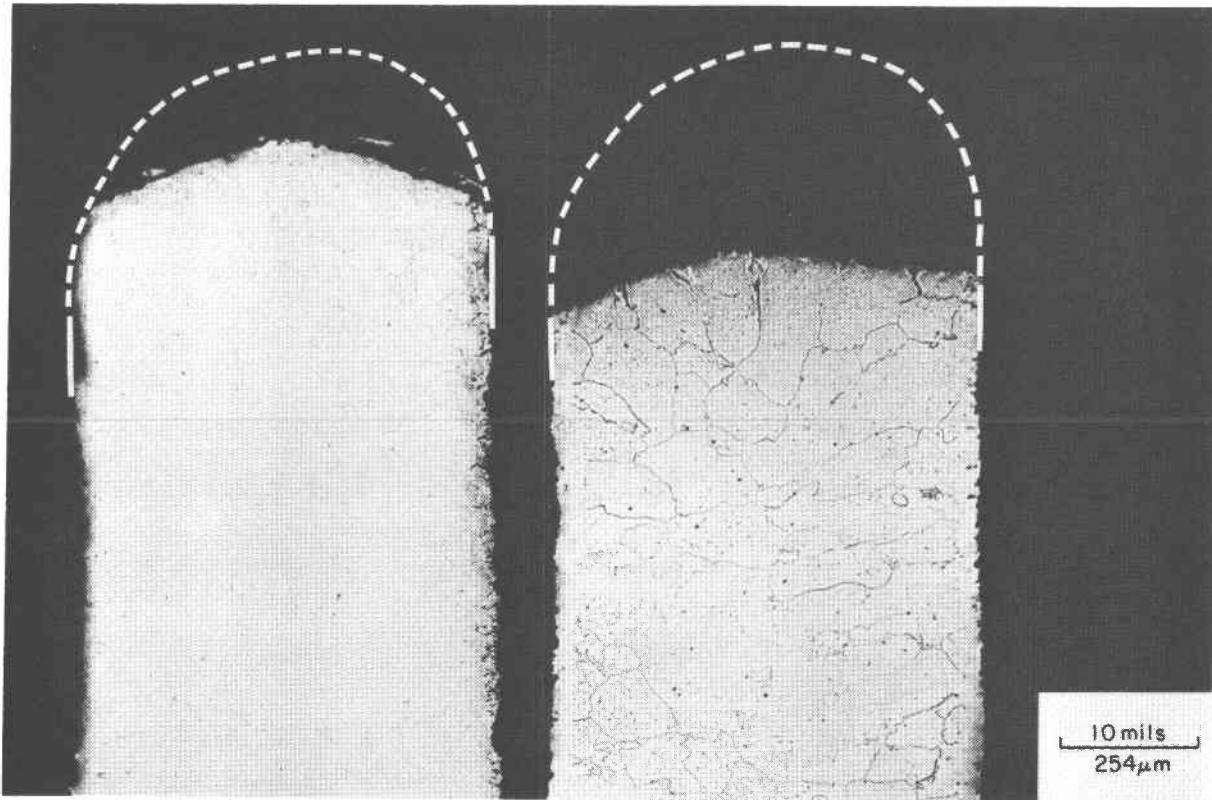
Figure 13. Effect of Particles Greater than 10 μm (100 ppm PFBC Particulate, 1170 f/s, No Alkali Sulfate Additions)



No Alkali Sulfate Addition (Test S4)

$0.2 \times 10^{-10}$  moles/cm<sup>2</sup>sec of Na<sub>2</sub>SO<sub>4</sub>-K<sub>2</sub>SO<sub>4</sub> (Test S3)

Figure 14. Effect of Corrodent Addition [ 1170 f/s, 100 ppm Exxon PFBC Particulate (5% > 10 μm) ]



**CURL 3<sup>rd</sup> Cyclone PFBC Particulate (2% > 10 μm, Test S6)**

**Exxon 3<sup>rd</sup> Cyclone Fine PFBC Particulate (5% > 10 μm, Test S3)**

**Figure 15. Exxon vs CURL 3<sup>rd</sup> Cyclone Particulate (100 ppm PFBC Particulate, 1170 f/s, with Alkali Sulfate Added)**

In addition to the results highlighted above, the following more general observations can be made.

- There is good correspondence between the ranking of alloys in the simulation tests reported here and in the Exxon PFBC test. In decreasing order of erosion/corrosion resistance, the ranking of the six materials tested here is:

<b>SIMULATOR</b>	<b>EXXON</b>
Pt-Cr-Al COATING (RT22)	Pt-Cr-Al COATING (RT22)
CoCrAlY CLADDING	CoCrAlY CLADDING
FeCrAlY CLADDING	FeCrAlY CLADDING
IN-738	IN-738
Ni-50Cr CLADDING	FSX-414
FSX-414	Ni-50Cr CLADDING

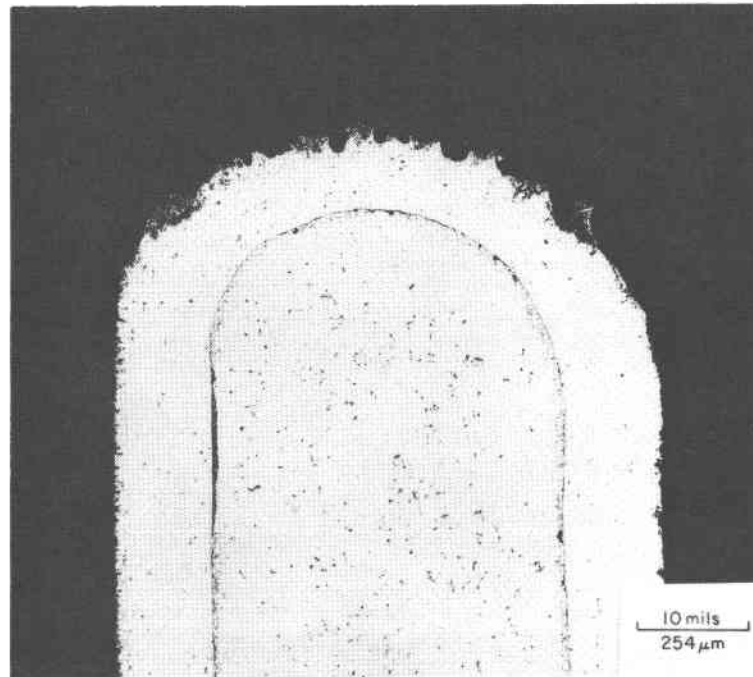
(Note that the most corrosion resistant materials are also the most erosion/corrosion resistant.)

- PFBC particulate alone contains a sufficient alkali concentration to cause hot corrosion/sulfidation even in the absence of additional alkali contaminants.
- In the high velocity tests S3, S4, S5, S6 (see Figures 12 through 15) the leading edge of the FSX-414 tended towards blunting as a result of erosion/corrosion rather than maintaining a knife edge configuration with maximum attack at ~45° angle. This feature was also observed in the Exxon test on FSX-414 and IN-738. The traditional theories of erosion suggest that

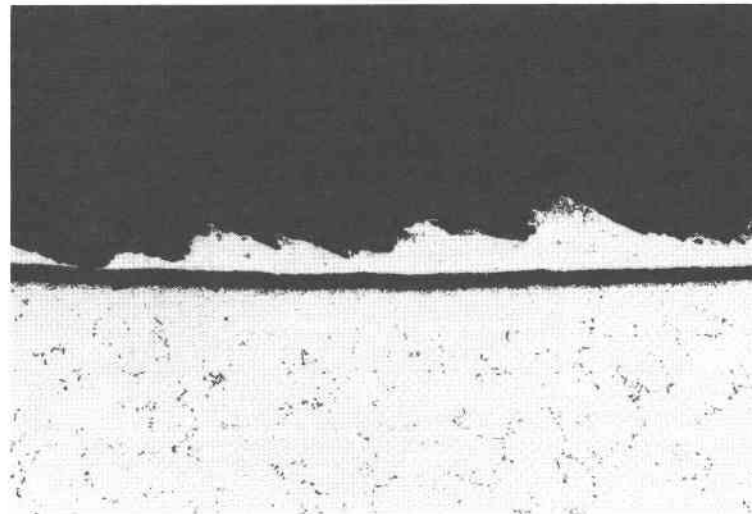


maximum erosion of ductile materials should occur at angles of 20°-45°, while erosion of brittle surfaces is a maximum at impingement angles of 90°. These departures from theory are noted here but at this time are unexplained.

- Lastly, there were instances, particularly at conditions of high velocity and a greater number of particles larger than 10  $\mu\text{m}$  (test S5), where the claddings exhibited a jagged and scalloped appearance at the leading edge and along the pressure surface. This effect is illustrated in Figure 16 for Inconel 671 clad on IN-738 after exposure in test S5.



**a) Leading Edge**



**b) Pressure Surface**

**Figure 16. Inconel 671 Cladding, 250 Hours, 1600°F, 1170 f/s, 100 ppm CURL PFBC Particulate, No Alkali Sulfate Additions (Test S5), ( $85 > 10 \mu\text{m}$ )**

## SUMMARY AND CONCLUSIONS

- A PFBC erosion/corrosion rig (simulator) has been built and qualified
- To date 2500 hours of testing have been completed
- Significant conclusions from the simulation testing to date are as follows:
  - An increase in PFBC particulate velocity of 20% caused erosion/corrosion damage to increase by a minimum of several fold
  - An increase in the number of particles  $> 10 \mu\text{m}$  caused a corresponding increase in erosion damage
  - Introduction of alkali sulfate over and above that present in the PFBC particulate caused an increase in erosion/corrosion damage
  - Exxon 3rd cyclone PFBC particulate is more erosive than CURL 3rd cyclone PFBC particulate
  - There is excellent correspondence between the ranking of materials in the simulation tests and in the Exxon test

## ACKNOWLEDGMENTS

The support of the Electric Power Research Institute is gratefully acknowledged together with the consultation and guidance of the EPRI Program Manager, Dr. John Stringer.

## REFERENCES

1. "Hot Corrosion/Erosion Testing of Materials for Applications for Advanced Power Conversion Systems Using Coal-Derived Fuels," Task II Final Report, Department of Energy Contract No. DE-AC01-76ET10547, General Electric Company, Schenectady, N.Y., September 1980.
2. "High Temperature Corrosion/Erosion in the Effluent from Pressurized Fluidized Bed Combustors," D.A. Grey, A.M. Beltran, R.P. Brobst, R.L. McCarron, Proceedings of Sixth International Conference on Fluidized Bed Combustion, Sponsored by DOE, Atlanta, GA., April 1980.
3. "Protective Coatings or Claddings for Turbines for Use with Pressurized Fluidized-Bed Combustors (PFBC)," Annual Report for Period April 1979 — March 1980, EPRI Contract No. RP1337-1, General Electric Company, Schenectady, N.Y., December 1980.
4. "Protective Coatings or Claddings for Turbines for Use with Pressurized Fluidized-Bed Combustors (PFBC)," Second Annual Report for Period April 1980 — March 1981, EPRI Contract No. RP1337-1, General Electric Company, Schenectady, N.Y., in preparation.
5. "Materials Problems in Fluidized-Bed Combustion Systems: Review of the Information on Gas Turbine Materials in Coal Combustion Environments," Electric Power Research Institute Report CS 1469, EPRI Project RP1337-1, General Electric Company, Schenectady, N.Y., August 1980.

Session V

AIRFOIL COOLING

## MATERIALS DEVELOPMENT FOR A WATER-COOLED GAS TURBINE

W.F. Schilling, M.C. Muth, P.W. Schilke,  
M.F. Collins, and A. Caruvana

General Electric Company, Schenectady, New York

### 1. INTRODUCTION

The DOE-sponsored High-Temperature Turbine Technology (HTTT) Program for a water-cooled gas turbine at firing temperatures (defined as the inlet temperature to the first-stage rotor) in the 1427-1649 °C range is now nearing the completion of the component demonstration phase. A major portion of this effort was based on a comprehensive materials development program, which is the principal focus of this paper.

The primary application of this technology is in an Integrated Gasification Combined Cycle (IGCC). An IGCC incorporating water-cooled gas turbines offers significant incentives to the utilities, and ultimately to the consumers, in the form of higher efficiencies and the associated lower cost of electricity (see Figure 1-1). In addition, it also provides for the utilization of our nation's abundant coal resources in an environmentally acceptable manner that is cost competitive and that reduces our dependence on foreign oil imports.

The major advantages of water-cooling in a high-temperature gas turbine are the following:

- There are no cooling holes susceptible to plugging by contaminants in the inlet air or by fuel ash in the combustion products.
- Metal surface temperatures are maintained below 538 °C, thereby providing maximum protection against hot corrosion.
- The low metal temperature allows the designer a wider choice of materials than has been available to date.

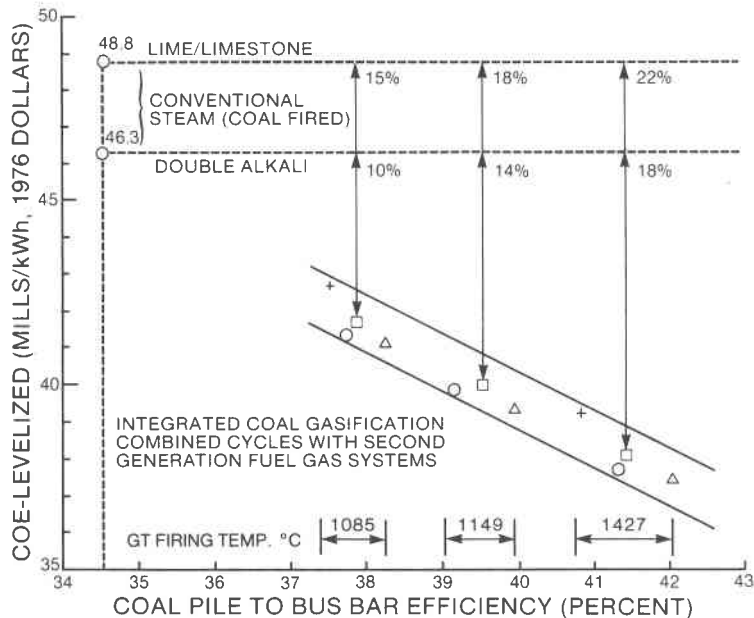


Figure 1-1. Cost of electricity projection vs efficiency.

- Lower metal temperatures also provide for selection of alloys which utilize up to an order of magnitude less critical materials such as cobalt.
- The use of low metal temperatures and the absence of external cooling holes also enhances the turbine's tolerance to fuel-system upsets such as carryover of alkali and vanadium contaminants.
- Actual test data have demonstrated significantly reduced ash deposition rates when burning heavy fuels such as a petroleum-based residual fuel.
- Removal of ash is much more effective when the metal temperatures are maintained below 538 °C.

This technology has been demonstrated effectively on the component level, and it provides the basis for the demonstration of the entire system during planned Phase III DOE program.

## 1.1 PROGRAM STATUS

Water-cooling technology has been demonstrated over the past ten years in a number of stages. Early in the 1970s fired tests of small, one-foot diameter, water-cooled wheels were conducted at sustained temperatures of 1538 °C and pressures of 12 atmospheres. Recently completed, under EPRI sponsorship, were water delivery and distribution tests on a MS7000-size wheel (approximately 10 feet in diameter). These and other associated tests have been previously reported (1-11). The program status reported in this paper concentrates on the test results of components that are equivalent *in size* to those that would be incorporated in a 73 MW water-cooled gas turbine and that have been tested at the same gas flow conditions, pressures, and temperatures that would be experienced in this turbine at a firing temperature of 1427 °C. These components and a summary of the test results are given in Table 1-1. The remaining portion of this paper is dedicated to key materials technology programs that were instrumental in the successful completion of these demonstrations.

## 2. MATERIALS AND PROCESSES OVERVIEW

The materials and process development efforts associated with the General Electric Gas Turbine Division's HTTT Phase II program have as their goals the resolution of key barrier problems. These problems are related to the fabrication of reliable water-cooled gas turbine hardware that will experience 1427 °C gas temperatures while maintaining metal surface temperatures below 538 °C. Water-cooling of large-scale industrial gas turbine hot section components presents unique issues which focus on materials selection and subsequent integration with fabrication processes to produce hardware with the required configuration of water passageways and mechanical properties.

A composite design was selected for the first-stage nozzle consisting of a load carrying spar surrounded by, and bonded to, a layer of high-strength, high thermal conductivity copper alloy into which are imbedded the bonded water-carrying tubes. The entire hot gas path portion of the nozzle is then clad with a corrosion-resistant skin. The copper inner layer distributes the high-heat fluxes to the water-carrying tubes while minimizing thermal gradients within the component. The first-stage bucket as well as the second and third turbine stages are of a more conventional monolithic design containing appropriate water-cooling passages. Lower heat fluxes associated with first-stage bucket and latter turbine stages permit the use of monolithic structures while meeting design life goals.

A summary of key program elements and results to date is given in Table 2-1. Basically, the overall program effort was separated according to technical issues associated with specific hardware such as alloy selection, casting or forging process development, joining development, etc., and issues more general in nature such as stress corrosion cracking susceptibility, nondestructive evaluation, low-temperature corrosion behavior, and water and particulate erosion.

A major objective of the Phase II program was the design and fabrication of key turbine components. These included the composite first-stage nozzle, a subscale composite nozzle, the monolithic second-stage nozzle, a sectoral combustor, and simulated testing of monolithic buckets. The scope of this paper does not permit a detailed review of all the programs listed in Table 2-1. Instead, selected topics are reviewed and key results reported. Emphasis has been placed on hardware fabrication and testing; however, certain key physical metallurgy issues are

Table 1-1

Test	Major HTTT Component Tested	Test Conditions	Test Results
Simulated IGCC system using advanced fixed gasifier, particulate removal system, sulphur removal and high-temperature low-BTU gas combustor	Water-cooled composite nozzle	<ul style="list-style-type: none"> <li>Actual coal gas from gasifier <math>5.58 \times 10^6</math> joule/m<sup>3</sup></li> <li>Gas temperature up to 1650 °C</li> <li>Pressure—12 atmospheres</li> <li>Flow rate—3.6 kg/s</li> </ul>	Nozzle in excellent condition after 75 hours of test. No erosion/corrosion observed.
Component test duplicating TRV first-stage nozzle environment	TRV first-stage composite nozzle	<ul style="list-style-type: none"> <li>Simulated coal gas</li> <li>Gas temperature up to 1480 °C</li> <li>Pressure up to 12 atmospheres</li> <li>Flow rate up to 9.5 kg/s</li> </ul>	Nozzle in excellent condition after 617 simulated startup/shutdown cycles.
Component test duplicating TRV second-stage nozzle environment	TRV second-stage monolithic nozzle	<ul style="list-style-type: none"> <li>Simulated coal gas</li> <li>Gas temperature up to 1150 °C</li> <li>Pressure—0.039 kg/mm<sup>2</sup></li> <li>Flow rate—10.9 kg/s</li> </ul>	Nozzle in excellent condition after 52 startup/shutdown cycles.
Component test of TRV Sectoral combustor	TRV combustion system	<ul style="list-style-type: none"> <li>Simulated coal gas</li> <li>Gas temperature up to 1510 °C combustor exit</li> <li>Pressure—12 atmospheres</li> <li>Flow rate—9.5 kg/s</li> <li>Gas HHV <math>4.71 \times 10^6</math> joule/m<sup>3</sup></li> </ul>	<ul style="list-style-type: none"> <li>Successful light-off and staging of three nozzles on distillate and transfer to LBTU gas</li> <li>Combustion eff.—96%-99%</li> <li>Low NO<sub>x</sub>—10 ppm</li> <li>Good thermal and structural design</li> <li>Low pressure oscillations</li> </ul>

discussed. These center on the development of a copper alloy for the first-stage nozzle and the evaluation of diffusion bonding behavior of the three alloys used in the composite nozzle. Thick section investment cast alloy 718 was investigated with the goal of improved properties and producibility for monolithic second- and third-stage nozzles. Wrought alloy 718, which has been chosen as the bucket alloy for all three turbine stages, was evaluated for precision forging behavior and subsequent heat-treat optimization. An evaluation of the aqueous stress-corrosion cracking (SCC) behavior of all materials in contact with the cooling water was made utilizing water chemistries that simulate both design and off-design conditions to assess the SCC potential.

Finally, fabrication and testing of actual turbine hardware are described and utilized to provide examples of how the materials and process effort has been integrated into the design of the hardware to yield a “materials systems” approach to advanced gas turbine hardware.

### 3. WATER-COOLED NOZZLES

#### 3.1 COPPER ALLOY DEVELOPMENT

The first-stage nozzle utilizes a composite design that consists of a high-strength, high thermal conductivity copper alloy as an inner layer to distribute effectively the heat flux to water-carrying tubes and thus minimize the thermal strains arising from the operation of such a part in large temperature gradients. Figure 3-1 shows a schematic diagram of the key design features of this nozzle. The multialloy, or composite structure, of the part mandated that diffusion bonding be utilized for its fabrication. Further, the complicated geometry normally associated with hardware of this type precludes uniaxial diffusion bonding. Gas pressure bonding, utilizing a hot isostatic press (HIP), was selected as the diffusion bonding technique due to its insensitivity to geometry.

Table 2-1  
HTTT MATERIALS AND PROCESS PROGRAM SUMMARY

Program	Phase II Results
● High strength/conductivity copper	● The Cu-MZC alloy has been shown to possess the required properties of strength and conductivity. First-stage nozzle testing confirms this conclusion.
● High-strength bondline	● Testing confirms that Cu-MZC can be gas-pressure bonded to IN-617 and Nitronic 50. Bondline performance exceeds Cu-MZC properties.
● Clad alloy processing	● IN-617 selected as clad alloy. Forming/joining processes demonstrated through first-stage nozzle construction and testing.
● Advanced investment casting	● Second-stage nozzle cast utilizing a split mold technique with improved dimensional tolerances over conventional methods.
● Forged and drilled alloy 718	● Prototype third-stage bucket with design property goals, precision forged.
● Nondestructive evaluation	● First-stage nozzles evaluated successfully using X-ray, ultrasonic C-scan, eddy current, and fluorescent penetrant inspection.
● Low-temperature corrosion	<ul style="list-style-type: none"> <li>● Pot furnace testing demonstrated capability for further improved clad corrosion resistance at reduced metal temperatures for contaminated fuels.</li> <li>● A water-cooled composite nozzle demonstrated the tolerance of IN-617 to combustion gases from low-BTU coal gas.</li> </ul>
● Stress-corrosion cracking behavior	● Selected materials in contact with cooling water demonstrated to have excellent resistance to SCC in design range expected.

Thus, it became apparent at an early stage of the program that the selected copper alloy must be capable of achieving mechanical property goals *after* a relatively severe thermal cycle. Property goals are given in Table 3-1. A design limit of 427 °C operating temperature was set for the copper inner layer. This limit was based on the fact that most age-hardenable copper alloys begin to lose strength rapidly through overaging at temperatures above 427 °C and that little is known about the long-time stability of these materials at elevated temperatures. This application represents a major change in the way copper alloys have been used for structural components. Historically, high-strength, high electrical and thermal conductivity copper alloys have been utilized for specialized electrical applications and have derived their strength from a combination of age

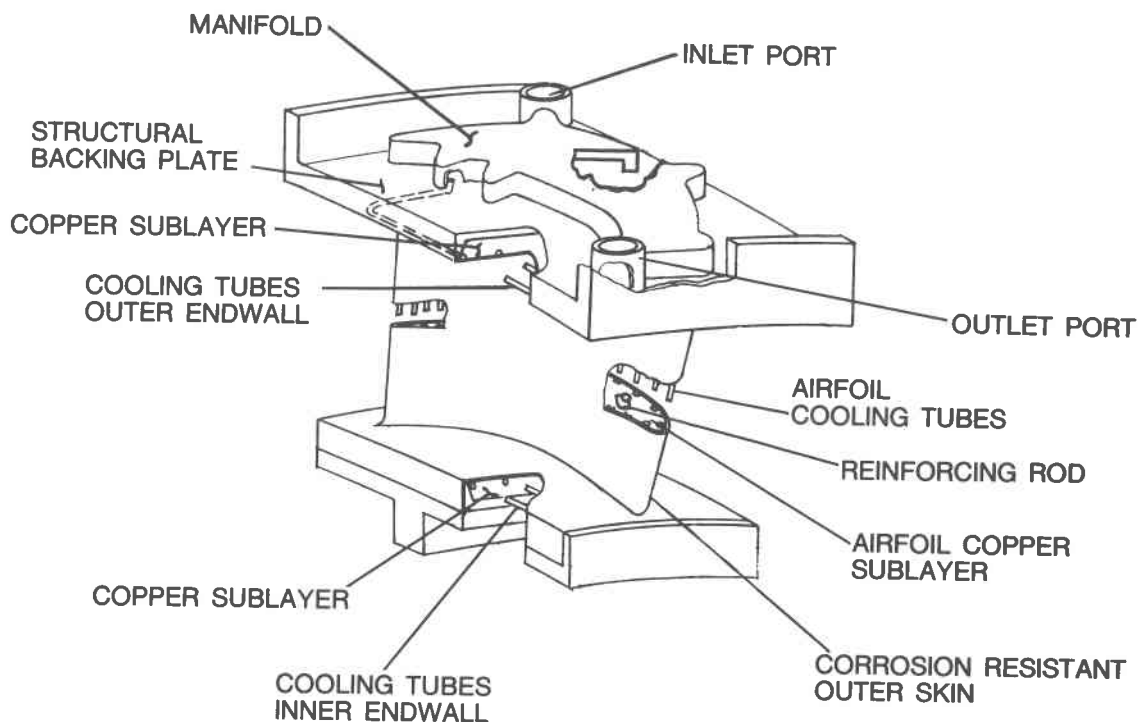


Figure 3-1. Composite nozzle concept.

Table 3-1  
COPPER ALLOY PROPERTY GOALS

Property @ 427 °C <sup>a</sup>	Goal <sup>a</sup>	Cu-MZC
Thermal conductivity	277 W/m·K	331 W/m·K
Coefficient of thermal expansion	$17 \times 10^{-6}$ cm/cm·K	16.4 cm/cm·K
Tensile strength	276 MPa	214 MPa
1000-hour rupture strength	172 MPa	103 MPa
Low cycle fatigue life	$N_f = 3350$ @ $\epsilon_T = 0.3\%$ 2 min tensile hold	$\epsilon_T = 0.45\%$

<sup>a</sup>Heat-treated properties after simulated diffusion-bonding cycle of 945 °C/2 hours.

hardening and cold working. Typically, these alloy systems contain elements that have low solid solubility in copper at the use temperature in order to maintain high levels of electrical conductivity. As is well known, the mechanical properties of this class of materials decrease significantly with increasing exposure temperature and time. Anticipated bonding cycles of 954-1010 °C/2-3 hours for the composite nozzle represent severe exposure conditions for copper alloys. Several types of copper alloys were considered for this application including oxide dispersion strengthened materials, alloys strengthened by thermo mechanical processing and precipitation hardenable alloys. Table 3-2 lists specific compositions and strengthening mechanisms.

Detailed evaluations were conducted of the behavior of the candidate alloys after the bonding thermal cycle. Tensile and stress-rupture properties were evaluated as well as postexposure microstructural stability. Figure 3-2 clearly shows the effect of 954 °C/2 hour exposure on subsequent strength and ductility of candidate materials at 427 °C. Yield strength behavior in the



Table 3-2  
COPPER ALLOYS EVALUATED

Alloy Composition (w/o)	Strengthening Mechanisms
Cu - 1.4 Al <sub>2</sub> O <sub>3</sub>	Dispersed fine (< 1000 Å) Al <sub>2</sub> O <sub>3</sub> + cold working
Cu - 0.17 Zr	Dispersed Cu <sub>3</sub> Z <sub>4</sub> , αZr + cold working
Cu - 5.0 Ni - 2.5 Ti	(Coherent?) Ni <sub>3</sub> Ti, Ni <sub>2</sub> Ti precipitation
Cu - 2.5 Co - 0.6 Be	Coherent αCo, αBe precipitation
Cu - 0.06 Mg - .15 Zr - .4 Cr	Dispersed Cu <sub>3</sub> Zr, αZr, coherent αCr precipitation + cold working

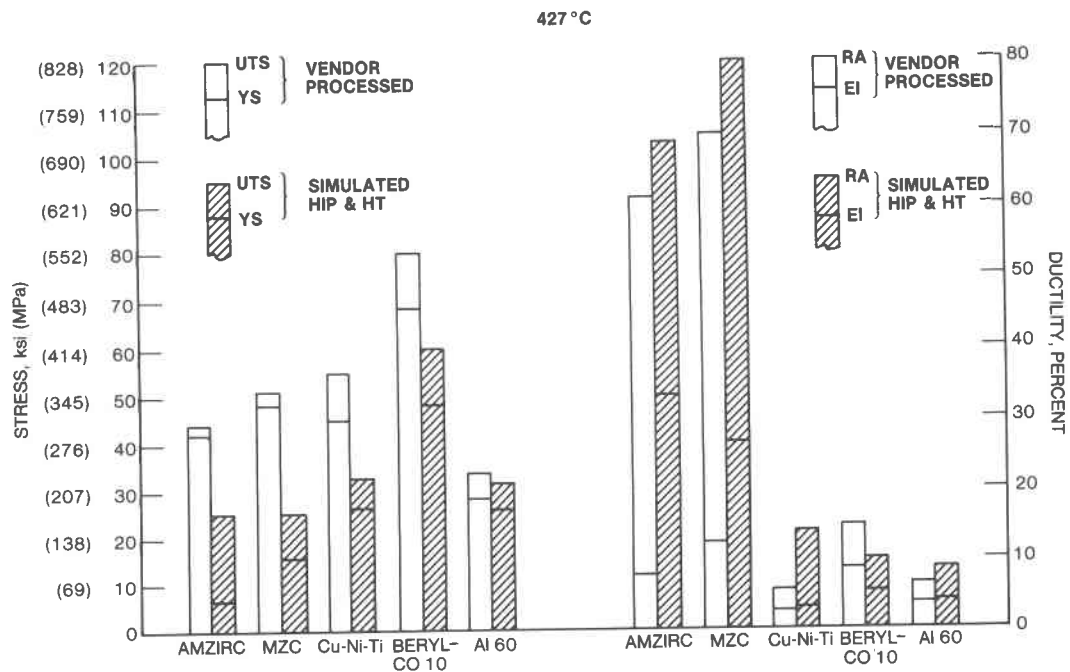


Figure 3-2. Comparison of 427 °C strength and ductility for various copper alloys in the vendor-processed condition vs after a simulated HIP exposure plus HT.

exposed and heat-treated condition as a function of temperature is shown in Figure 3-3, while Figure 3-4 shows stress-rupture performance. Inspection of the data reveals some important trends. All of the age-hardenable alloys suffered a loss in tensile and yield strength as a result of the thermal exposure. The oxide dispersion strengthened alloy Al-60 showed the highest resistance to the thermal exposure. Ductility was improved for all alloys after the simulated diffusion-bonding thermal cycle. The Cu-Zr and Cu-MZC alloys displayed very high ductility levels, while the remaining materials possessed elongations and RAs in the 5%-10% range. The stress-rupture strengths of the candidate alloys showed Al-60 to be superior and Cu-MZC somewhat stronger than the other age-hardenable alloys at the higher Larson-Miller parameter values.

The Cu-MZC alloy was selected as the prime candidate for the composite nozzle on the basis of its possessing the best overall combination of desired properties (see Table 3-1). Additional studies on the Cu-MZC alloy have yielded improvements in strength through modification of heat treatment. Basically, higher solutioning temperatures and increased cooling rates resulted in more effective use of Cr in the aging reaction, thus increasing strength. Stress-rupture strength was similarly improved.

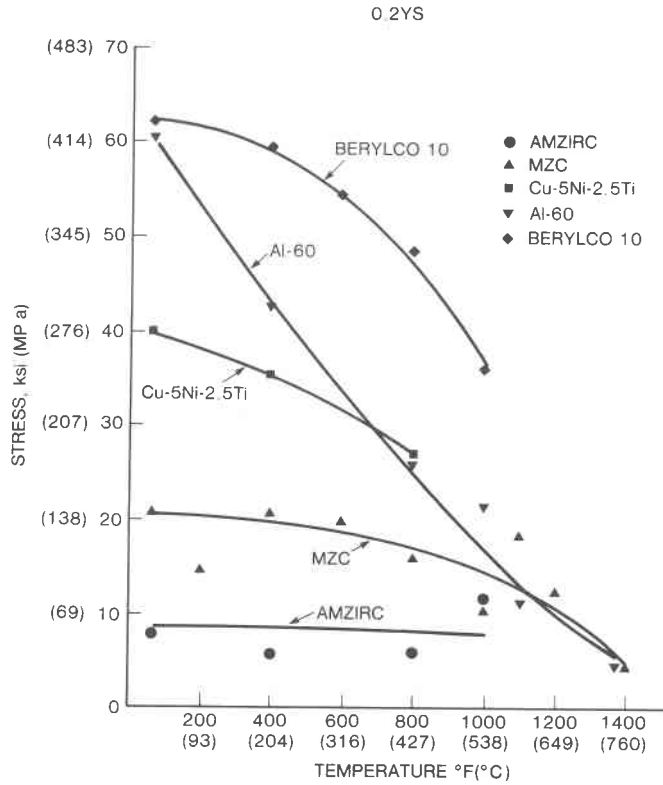


Figure 3-3. Tensile yield strength for various Cu alloys after a simulated HIP exposure followed by aging.

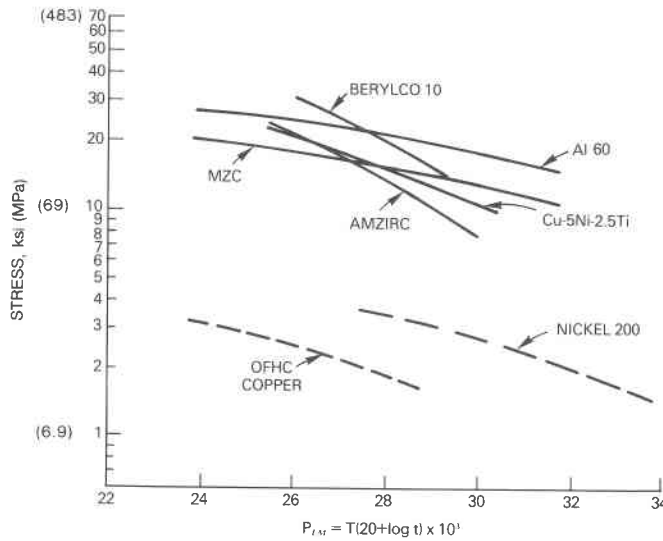


Figure 3-4. Estimated Larson-Miller stress-rupture curves for Cu alloys after a simulated HIP exposure at 954 °C followed by aging.

Final acceptance of the Cu-MZC alloy as the prime material for the composite nozzle was based on strain-controlled, low cycle fatigue (LCF) testing. Figure 3-5 shows the LCF behavior of the Cu-MZC alloy and compares to OFHC copper.

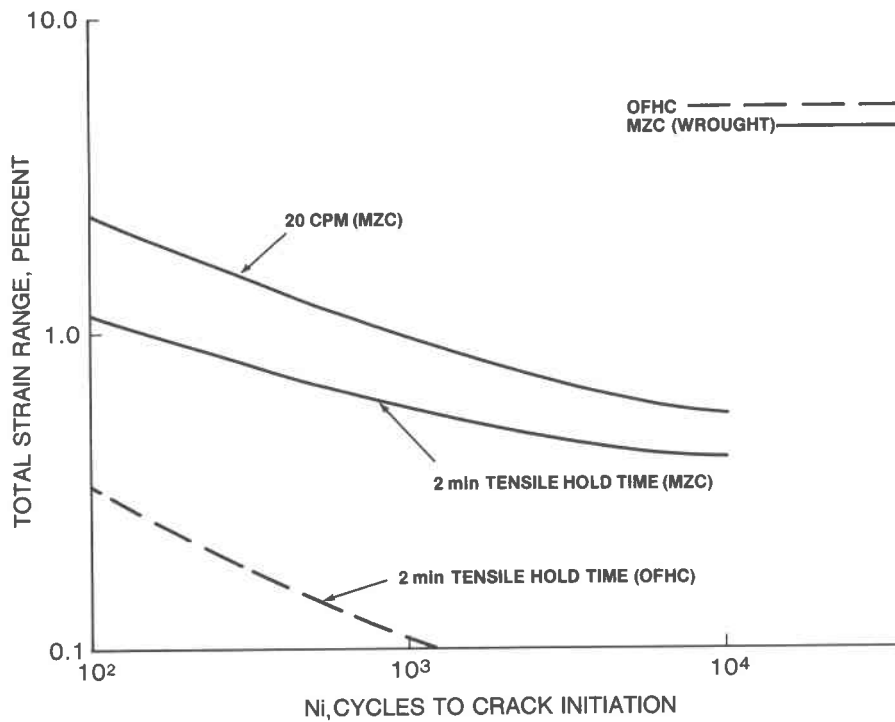


Figure 3-5. LCF results for wrought MZC Cu at 316 °C.

### 3.2 BONDLINE EVALUATION

A study was undertaken to characterize the HIP-diffusion-bonded interfaces of the materials utilized for the first-stage nozzle, i.e., IN-617, Nitronic 50, and MZC copper bonded to each other (17). The specific objectives were to

- Investigate pre-HIP surface preparation techniques that could promote or improve bonding.
- Characterize metallurgically the resultant bondlines.
- Evaluate the tensile strength and ductility of the bonds at anticipated operating temperatures.

The nozzle design (Figure 3-6) incorporates Nitronic 50 spar rods, endwall caps, and cooling tubes; MZC copper as a heat conductive airfoil and endwall body; and IN-617 as an

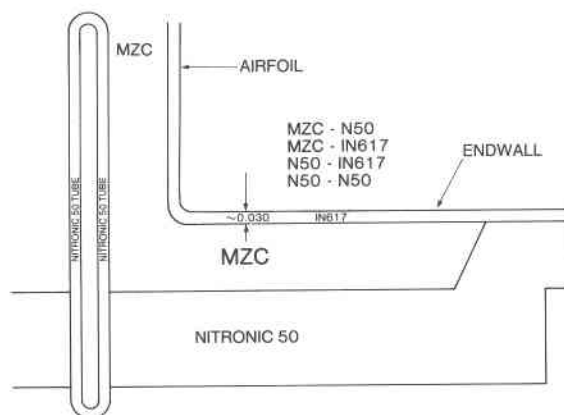


Figure 3-6. Schematic of HTTT nozzle composite interfaces.

erosion/corrosion resistant cladding. The bonding study was conducted to evaluate the fully processed bondline interfaces of the dissimilar materials and to assess potential composite bonding procedures and their attendant limitations. HIP-diffusion-bonded blocks incorporating the joint combinations in question were fabricated utilizing a 954 °C/103.4 MPa/2 hour cycle. Subsequently they were heat treated at 996 °C/2 hour/fast cool to 454 °C/hold for 24 hours to duplicate the nozzle heat-treat cycle. Tensile and metallographic specimens were removed from these blocks for testing and analysis. Various interlayers and cleaning procedures were evaluated in this manner.

A nickel-plate interlayer (nominally 25 μm thick) on one of the mating surfaces proved to be the best universal surface treatment. Resultant tensile properties at room temperature and anticipated operating temperatures can be seen in Table 3-3. A representative MZC/IN-617 bondline can be seen in Figure 3-7 wherein the cleanliness of the bond can be noted.

**Table 3-3**  
**BONDLINE TENSILE TEST RESULTS**  
**WITH NICKEL-PLATE INTERLAYERS**

HIP: 954 °C/103.4 MPa/2 hours  
Heat treated: 996 °C/2 hours  
Aged: 454 °C/24 hours

Specimen	Test Temperature (°F)	Ultimate Tensile Strength (ksi)	0.2 Yield Strength (ksi)	Elongation (percent)	Reduction of Area (percent)
Nitronic 50 to Nitronic 50	Room temp. 350 (177 °C)	105 (724 MPa)	63 (434 MPa)	13	15
		92 (634 MPa)	45 (310 MPa)	20	15
Nitronic 50 to IN-617	Room temp. 800 (427 °C)	100 (689 MPa)	66 (455 MPa)	12	18
		79 (545 MPa)	37 (255 MPa)	20	17
IN-617 to MZC Cu	800 (427 °C)	30 (207 MPa)	22 (152 MPa)	10	8
Nitronic 50 to MZC Cu	600 (316 °C)	35 (241 MPa)	28 (193 MPa)	26	60
<b>Reference Data</b>					
Nitronic 50	Room temp. 350 (177 °C) 800 (427 °C)	120 (827 MPa)	75 (517 MPa)	40	67
		100 (689 MPa)	55 (379 MPa)	38	67
		93 (641 MPa)	48 (331 MPa)	39	60
IN-617	Room temp. 800 (427 °C)	130 (896 MPa)	64 (441 MPa)	35	40
		110 (758 MPa)	52 (359 MPa)	45	40
MZC Cu	Room temp. 800 (427 °C)	54 (372 MPa)	35 (241 MPa)	25	73
		33 (228 MPa)	24 (165 MPa)	21	68

### 3.3 CAST ALLOY 718

Cast nickel-base alloy 718 is the material selected for the second- and third-stage nozzles and for the combustor pressure shell to satisfy the unique combination of thermal strain capability, corrosion resistance, and fabricability requirements of these components. The processes identified for the manufacture of these components include investment casting, hot isostatic pressing (HIP), conventional and electric discharge machining (EDM), shaped tube electrolytic machining (STEM) drilling, brazing, and welding. To ensure the successful fabrication and testing of these components, work was performed to understand and optimize the microstructure of investment-cast, thick-section 718 alloy.

Quantitative metallography indicated that the as-cast alloy 718 structure can contain about 1.5 volume percent carbide and nitride phase, about 0.4 volume porosity, and up to about

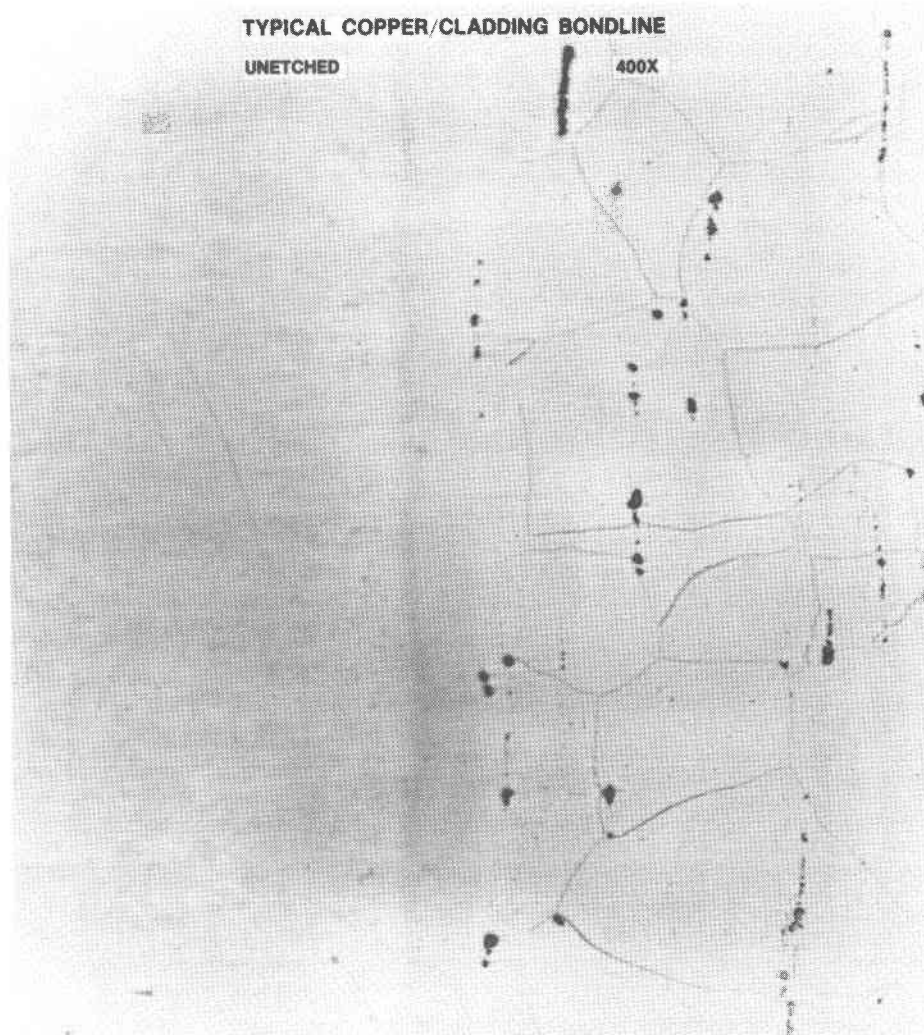


**Figure 3-7. Photomicrograph of IN-617/Ni-plated MZC bondline following 954 °C/15 ksi/2 hours, then 996 °C/2 hours and 454 °C/24 hours.**

17 volume percent Laves phase, which is a Cb-rich segregant that readily forms in this alloy (12). Samples of as-cast alloy 718 were hot isostatic pressed (HIPed) at different temperatures and times to determine the optimum HIP cycle. A HIP cycle of 1191 °C/103 MPa/4 hours was found to be optimum and eliminated all segregation and porosity, allowing ultimate tensile strengths up to 1240 MPa to be obtained. Subsequent differential thermal analysis (DTA) showed that the presence of Laves phase reduced the incipient melting point of the alloy by 100 °C compared to fully homogenized alloy 718 samples. Significant benefits to alloy tensile ductility were also achieved by use of this HIP cycle (see Figure 3-8). Brazing studies were also conducted to determine braze joint strengths and ductilities using a number of different brazing alloys. AMS 4786, gold-nickel-palladium alloy, was found to satisfy all mechanical property requirements and was selected for use on the second- and third-stage nozzles. Evaluations of STEM drilling and EDM parameters were also conducted on HIPed samples of alloy 718 using surface roughness and metallographic measurements, which resulted in the selection of preferred machining parameters.

#### **4. WATER-COOLED BUCKETS**

##### **4.1 FORGED ALLOY 718**

The third-stage water-cooled bucket design utilizes camber-line radial cooling channels that vary in diameter from 3.175 mm to 2.03 mm to achieve maximum metal temperatures below 538 °C.

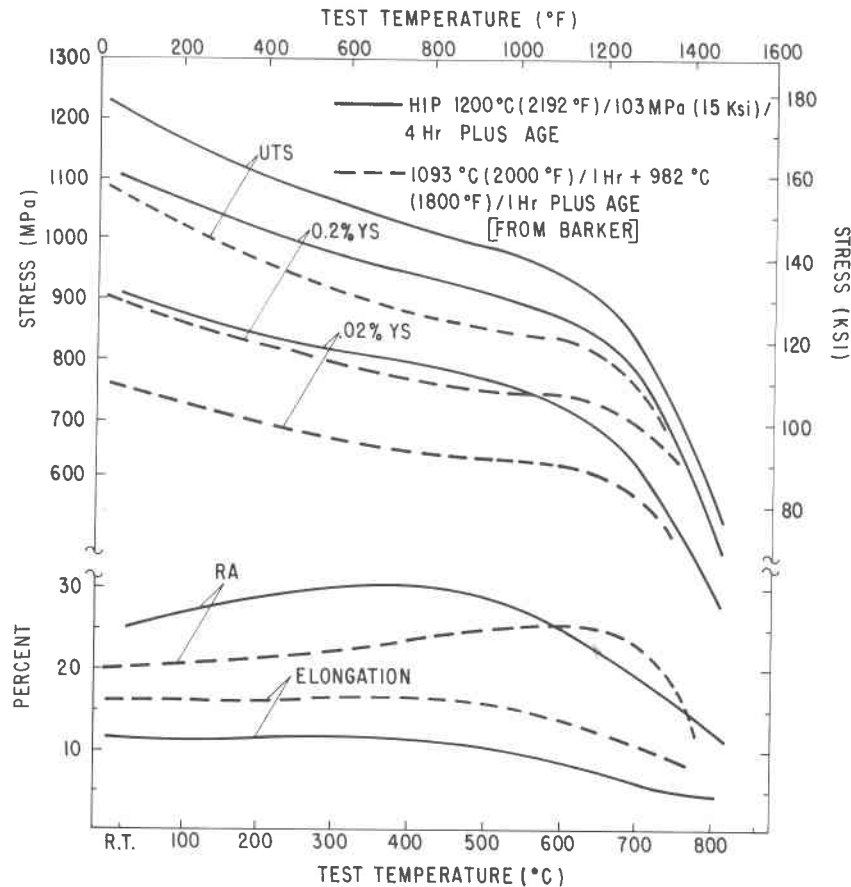


Figure 3-8. Elevated tensile properties of properly homogenized alloy (solid lines) compared to traditional data (dashed lines).

The bucket has a 332 mm linear airfoil with a shrouded tip and a 102 mm shank.

The third-stage bucket presents two critical processing-related characteristics. First, holes having a very high length-to-diameter ratio must be accurately located in the airfoil section; and second, high mechanical properties (room temperature 0.2% yield in excess of 966 MPa) are required due to large root stresses developed as a result of the bucket size and weight.

Because of the airfoil size, the complexity, and the expected service conditions of the third-stage bucket, an alloy having a unique combination of properties was required. The criteria for alloy selection included the following:

- Low cycle fatigue (LCF) life
- Fabricability
- Tensile strength
- Brazability
- Weldability
- Corrosion resistance
- Long-term stability
- Stress-rupture strength

An extensive evaluation determined that forged alloy 718 met the criteria stated above and therefore was selected as the third-stage bucket alloy.

Since alloy 718 is a nickel-base, precipitation-hardenable superalloy, the thermal mechanical processing (TMP) of the third-stage bucket can significantly affect the properties of the part. Both the primary strengthening gamma double prime  $[\text{Ni}_x(\text{Cb,Al,Ti})$  where  $x$  is about 3] phase and the delta ( $\text{Ni}_3\text{Cb}$ ) phase deplete the matrix composition of Cb when they form. Since the delta phase contributes little or nothing to the strengthening of the alloy, precipitation of this phase should be limited to avoid tying up Cb at the expense of gamma double prime formation.

Work at Kelsey-Hayes Corporation was aimed at developing the technology necessary to precision-forge wrought alloy 718 billets using conventional and fine-grain forging techniques. Twenty-four buckets were forged on a 6000-ton press in two iterations. A single heat of double vacuum melted bar stock 47.6 mm in diameter was used for all forging.

During the first iteration, five buckets were forged at the conventional alloy 718 forging temperature of 1093 °C, one bucket forged at 1010 °C, and six buckets at 968 °C.

The bucket forged at 1010 °C was used to assess the impact of lower temperature on the forgeability of the third-stage bucket. It was determined that the low-temperature forging would require several additional reductions to reach final shape. The conventional forging exhibited grain size and tensile properties typical for alloy 718. The 968 °C forgings exhibited a fine grain size (ASTM 8-9); however, the tensile properties were lower than expected. Although the grain size goal of ASTM 10-12 was nearly achieved, the 0.2% yield strength failed to equal conventional forging yield strength levels (see Table 4-1).

The low yield strength is thought to be the result of excessive exposure time at low temperature during upsetting and forging operations. The total time at low temperature during hot working operations for the 968 °C forgings was approximately 6-8 hours. An excessive amount of the stable, Cb-rich delta phase is precipitated at this temperature, thereby depleting Cb from the

**Table 4-1**  
**TENSILE TESTING RESULTS—FIRST ITERATION**

Forging Temperature	Testing Temperature				
	YS (MPa)	UTS (MPa)	EI (%)	(RA (%)	
1093 °C/1052 °C	21 °C				
	Airfoil at shroud	1207	1331	17.3	29.4
	Airfoil at root	1186	1344	17.2	27.0
	Root	1179	1289	18.0	29.1
	538 °C				
	Airfoil at shroud	1076	1145	17.0	40.2
	Airfoil at root	1076	1131	18.7	39.4
	Root	1014	1089	18.7	40.3
	968 °C	21 °C			
Airfoil at shroud		1014	1344	24.3	34.6
Airfoil at root		993	1358	21.3	36.2
Root		1117	1379	18.3	30.5
538 °C					
Airfoil at shroud		1076	1220	20.8	36.6
Airfoil at root		958	1200	22.8	34.7
Root		1076	1248	17.0	33.2
1010 °C		21 °C			
	Airfoil at shroud	1151	1372	19	26.6
	Airfoil at root	1172	1379	19	33.6

matrix gamma phase. This subsequently lowers the amount of strengthening gamma prime and gamma double prime developed during the aging heat treatment.

Parallel to the forging effort, an evaluation of thermal mechanical processing (TMP) of alloy 718 was conducted by the General Electric Company. Results of this work showed that reductions of 50% at 954 °C after a 24-hour delta phase precipitation cycle would produce the finest grain size and optimum mechanical properties. However, it was observed that mechanical properties did not vary significantly with grain sizes smaller than ASTM 10, and overaging prior to forging increased the forging temperature at which grain growth occurred.

Based on these data, the final 12 buckets were forged under two conditions. Six buckets were forged in the range of 993-1010 °C, which is just above the Ni<sub>3</sub>Cb solvus, and six buckets were forged in a temperature range just below the Ni<sub>3</sub>Cb solvus (982-988 °C). Buckets forged at the lower temperature received a 24-hour overage at 899 °C prior to the forging operation. This heat treatment precipitated needle-like Ni<sub>3</sub>Cb at the grain boundaries. It was hoped that this structure would restrict grain growth during the forging process.

Tensile properties for the buckets forged in this iteration are shown in Table 4-2. The buckets forged above the Ni<sub>3</sub>Cb solvus had grain sizes of ASTM 5-6 while the buckets overaged and forged below the Ni<sub>3</sub>Cb solvus had grain sizes of ASTM 9-10. The buckets that were overaged and then forged below the Ni<sub>3</sub>Cb solvus showed uniform grain size and significantly better properties than wrought or conventionally forged alloy 718.

This program has developed the technology to fabricate the third-stage water-cooled HTTT bucket. Dimensionally acceptable precision forgings were produced with the required mechanical properties. Since the current design calls for all three stages to be fabricated from forged alloy 718, the results of this program are being used in the design and eventual fabrication of the first- and second-stage bucket as well.

**Table 4-2**  
**TENSILE TESTING RESULTS—SECOND ITERATION**

Forging Temperature	Testing Temperature			
	UTS (MPa)	0.2% YS	EI (%)	RA (%)
993-1010 °C	21 °C			
Airfoil at shroud	1365	1186	22.8	38.4
Airfoil at root	1387	1220	21.5	35.8
Root	1344	1179	24.2	33.9
	538 °C			
Airfoil at shroud	1193	1076	17.2	37.4
Airfoil at root	1193	1096	16.3	36.0
Root	1138	1014	20.3	37.9
982-988 °C	21 °C			
Airfoil at shroud	1372	1069	24.2	39.8
Airfoil at root	1421	1188	23.0	28.2
Root	1390	1193	19.5	31.6
	538 °C			
Airfoil at shroud	1213	986	20.2	34.1
Airfoil at root	1234	986	21.3	36
Root	1234	1062	18.3	29.0



## 4.2 STRESS CORROSION TESTING

The purpose of this program is to determine whether the materials to be used that come into contact with water are susceptible to stress corrosion cracking (SCC), and if so, to what extent they are susceptible. Once susceptibility is identified as a problem, water chemistry variations and material modifications that eliminate this problem can be recommended. Those parameters which successfully control the problem will be recommended for implementation into a Test Readiness Vehicle (TRV).

The possibility of stress-corrosion cracking of alloy 718 in high-temperature, high-purity water was evaluated based on the experience of nickel-base alloy 600 in similar environments. It has been long known that alloy 600 experiences SCC in a variety of high-temperature water environments (13). A study by Mizla (14) indicated that 718, under certain heat treatments, might be susceptible to SCC in environments similar to those specified for the HTTT program. An evaluation of the SCC resistance of cast and wrought alloy 718 is required since all three hot gas path rotating stages and two of the three hot gas path stationary stages will be fabricated from it.

Nitronic 50 will be used as the water-carrying member of the first-stage composite nozzle. No problems are anticipated with this alloy, based on the extensive amount of testing conducted by the Nuclear Energy Division of General Electric (15).

Test parameters and test vehicles were chosen so as to obtain as many data as possible early in the HTT program. Constant extension rate testing (CERT), Figures 4-1 and 4-2, was chosen as the test vehicle since tests could be run in as little time as two weeks. To start CERT quickly, facilities used by the General Electric Boiling Water Reactor Division (BWR) were utilized. Water chemistry for this system included deionized high-purity water with 8 ppm oxygen and 5.5 pH.

Test temperature and pressure were 288 °C and 0.84 kg/mm<sup>2</sup>, respectively. With respect to HTTT water-chemistry requirements, these conditions represent a conservative aqueous test environment. Additional facilities, which more accurately represent HTTT water chemistry requirements of 9.3 pH with oxygen levels in the parts per billion range, were also incorporated into the stress-corrosion test program.

Although CERT testing has been shown to be a viable test vehicle for evaluating 304SS (16) its usefulness as a screening test on nickel-base alloys had not been confirmed. As an alternate loading technique, constant elongation tests were also run on alloy 718. Figure 4-3 shows the type of specimen and loading fixture utilized for this program.

Conditions that classically cause SCC were tried with both testing techniques. These included notches, crevices, welds, abusive grinding, electrochemical machining, and high applied stresses ( $\sigma > \sigma_y$ ).

Material testing included all prime candidate alloys that would be exposed to high-temperature water. These included IN-718 in rolled, cast, and forged conditions; IN-706 in a forged condition; and Nitronic 50 in rolled conditions (see Table 4-3). Heat treatments were given to each alloy to

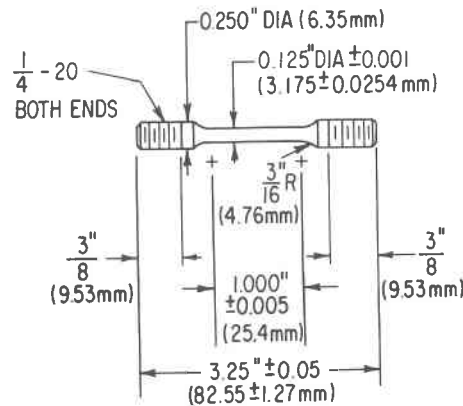


Figure 4-1. Standard CERT specimen.

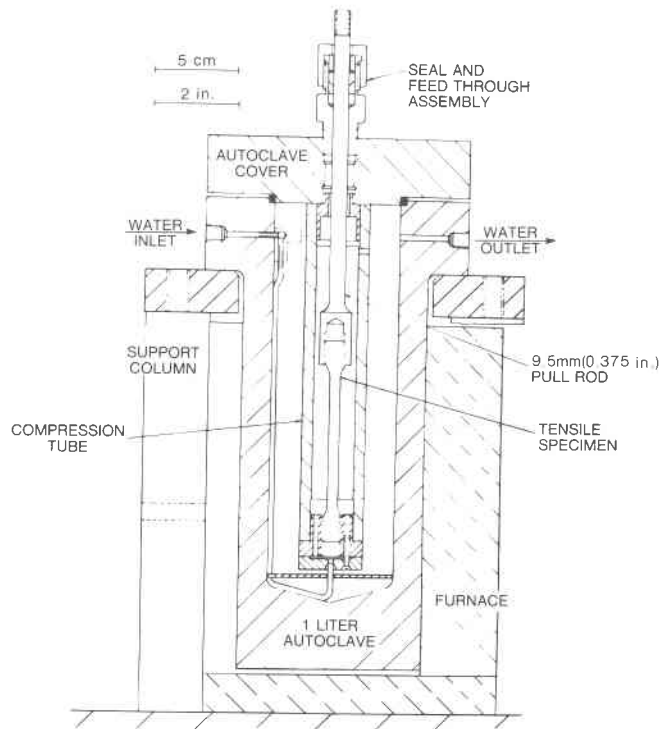


Figure 4-2. Autoclave schematic for CERT testing.

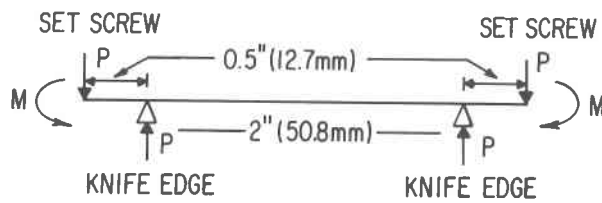
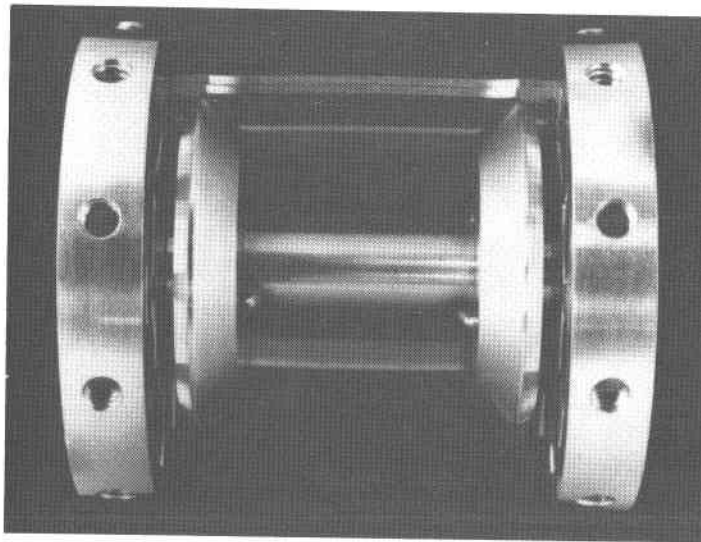


Figure 4-3. Test apparatus and specimen for constant strain testing.

Table 4-3  
MATERIALS USED IN STRESS CORROSION STUDY

A. Wrought alloy 718, heat No. HT16H3EK, lot No. P67870 Hot rolled and annealed (1800 °F), 0.375 in. (9.525 mm) plate Chemical Analysis (wt%)							
Ni	Fe	Cr	Mo	Cb+TA	Ti	AL	C
53.01	18.2	18.33	3.04	5.14	1.07	0.56	0.04
Mn	Co	Cu	Si	P	B	S	
0.13	0.13	0.18	0.17	0.013	0.003	0.003	

B. Alloy sheet Annealed, 0.125 in. (3.175 mm) sheet Chemical Analysis (wt%)							
Ni	Fe	Cr	Mo	Cb+TA	Ti	AL	C
53.06	Bal	18.23	3.10	5.15	0.98	0.54	0.007
Mn	Co	Cu	Si	P	B	S	
0.21	0.29	0.05	0.20	0.005	0.003	0.002	

C. Cast alloy 718 (from an as-cast MS9000 nozzle) Chemical Analysis (wt%)							
Ni	Fe	Cr	Mo	Cb+TA	Ti	AL	C
53.52	Bal	18.3	3.1	—	1.05	0.62	0.04
Mn	Co	Cu	Si	P	B	S	
0.1	0.60	0.1	0.13	0.009	0.003	43ppm	

D. Forged alloy 718 (UDIMET 718) Chemical Analysis (wt%) Ladle Analysis							
Ni	Fe	Cr	Mo	Cb+TA	AL	C	
53.0	18.5	17.6	3.0	5.37	0.52	0.07	
Mn	Co	Cu	Si	P	B	S	
0.13	0.50	0.10	0.12	0.01	0.004	0.003	

E. Forged alloy 706 Chemical Analysis (wt%)							
Ni	Fe	Cr	Mo	Cb+TA	AL	C	
42.18	36.45	16.3	—	2.94	0.24	0.04	
Mn	Co	Cu	Si	P	B	S	
0.19	—	—	0.14	0.006	0.004	0.002	

attempt to optimize mechanical properties and at the same time to be compatible with processing steps that would be used during fabrication of hot gas path parts.

As a result of this program the following conclusions were drawn:

- IN-718 will undergo stress-corrosion cracking in air-saturated water with a pH of 5.5. Testing was done with high-purity, deionized water heated to 288 °C and pressurized to 8.2 MPa. However, it required the presence of a crevice on an abusively ground surface (machined dry) with high applied surface tensile stresses (greater than the material yield strength).
- Other materials, including Nitronic 50, and 706, showed no signs of intergranular stress-corrosion cracking.
- For high nickel-base alloys a constant extension rate test does not seem to be capable of detecting SCC behavior. However, constant extension tests (four-point-bent-beam), which produce much lower creep rates (by at least two orders of magnitude)

then the slowest CERT, are better suited for initiating and propagating stress-corrosion cracks in nickel-base alloys.

- No cracking occurred in deaerated pH 9.3 water.
- All materials evaluated and selected for the TRV showed excellent SCC behavior and are thus deemed suitable for use.

## 5. HARDWARE TESTING

### 5.1 COMPOSITE NOZZLE

#### Turbine Simulator Nozzle Test

Testing conducted on the two different composite nozzle designs was addressed at differing objectives. The objective of the *Turbine Simulator Test* was to evaluate erosion, ash deposition, and corrosion characteristics of the composite nozzle concept in an environment representative of a high-temperature gas turbine burning coal-derived low-BTU gas fuel. The primary objective of the *First-Stage Nozzle Test* was to demonstrate technology readiness. It was desired that sufficient data be taken to develop an understanding of nozzle performance as a function of the various turbine system parameters and to verify the validity of the nozzle design analysis and fabrication technique. It is important to note that this part represents actual turbine hardware in design, shape, and size.

For the Turbine Simulator Test, low-BTU gas was generated in the General Electric gasifier, cleaned in a low-temperature, sulfur-removal (Benfield) system, fired in a special combustor to a 1427 °C firing temperature, and directed onto the nozzle. The test full-fired conditions were

Firing temperature	1427 °C
Combustor shell pressure	12 atmospheres
Compressor discharge airflow	2.5 kg/s
LBTU gas fuel flow	0.7 kg/s
Total test duration	~75 hours

Posttest evaluation of the composite nozzle was divided into four phases: visual, ultrasonic, eddy current, and metallographic. The visual examination showed the nozzle to be intact, without breach of its surface or internal integrity, even though there were extensive foreign object impacts due to an upstream system malfunction. Ultrasonic and eddy current testing indicated the nozzle was fully bonded. Metallographic examination of airfoil and endwall sections revealed a totally bonded and fully satisfactory structure (see Figure 5-1).

#### TRV First-Stage Nozzle Test

The First-Stage Nozzle Test was designed to accomplish the following objectives:

- Show that the heat flux at the critical trailing edge and airfoil suction surfaces and the total heat flux reasonably agree with values anticipated for similar operating conditions anticipated in the Technology Readiness Vehicle (TRV).
- Show that the cooling effectiveness of the water matches the anticipated effectiveness.
- Show that the measured thermal gradients and temperatures derived from measurements during simulated startup/shutdown cycles fall within the bounds determined by analysis and materials testing to ensure the desired low cycle fatigue life (LCF) in the TRV.
- Determine through intermediate and posttest inspections (visual, physical measurement, and ultrasonic) whether weaknesses not anticipated by earlier analysis and/or test are likely to be encountered during the TRV life.

The test plan formulated to accomplish the preceding objectives consisted of three parts: an unfired nozzle and test-facility checkout, steady-state fired testing, and cyclic testing. Fired test conditions were as follows:

Firing temperature	1427 °C
Combustor shell pressure	11.2 atmospheres
Airflow (choked)	2.9 kg/s throat
Propane fuel flow	0.26 kg/min
Time at 1427 °C	42 hours
Thermal cycles	617

All measured test data tended to confirm design analysis predictions. A hot spot on the nozzle inner endwall near the airfoil leading edge was detected and corrected for the TRV design. Preliminary visual and ultrasonic posttest inspections show that minimal distress occurring during test. A comprehensive posttest examination is in progress.

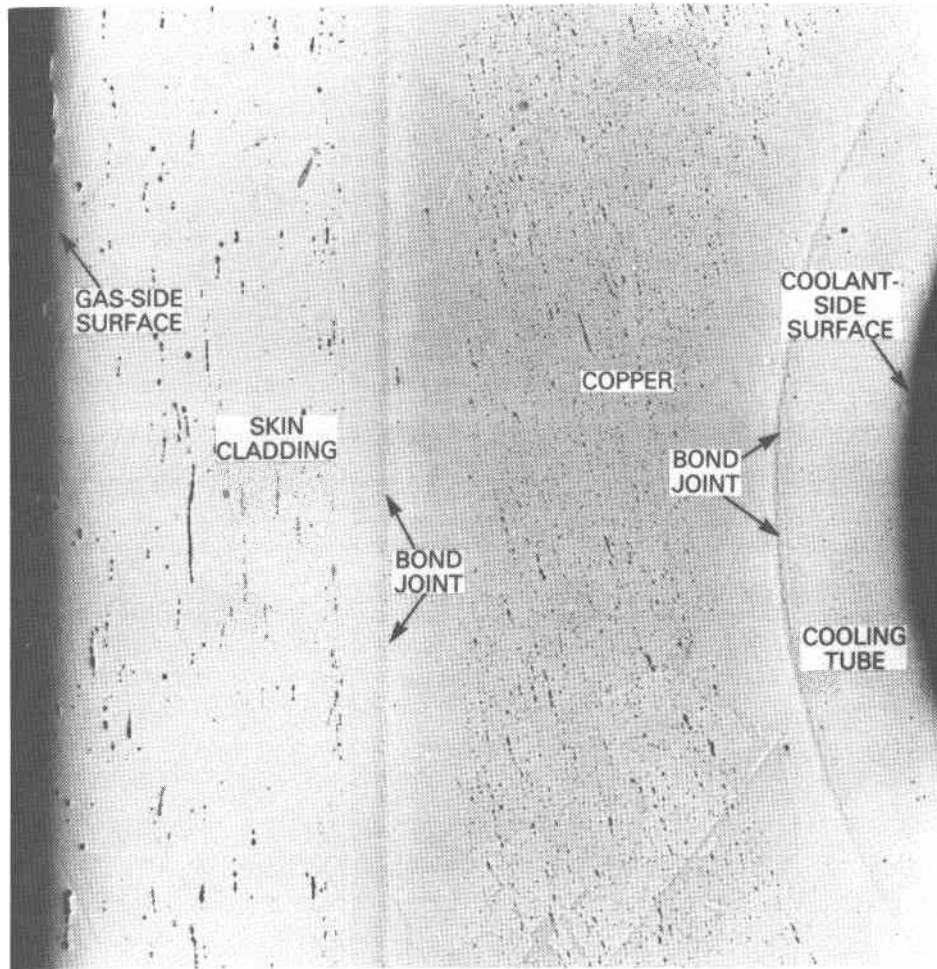


Figure 5-1. Airfoil cladding/Cu tube bond.

## 5.2 MONOMETALLIC NOZZLE TESTING

### Test Objectives

The primary objective of the second-stage nozzle test program was to verify the design in a simulated gas turbine environment (hot gas path cascade test apparatus) and to compare the observed

performance with the design predictions (10). The cooling water and metal temperatures were monitored during testing and compared with design predictions for each of these test points.

Design analysis has indicated that the life-limiting factor for a water-cooled monometallic nozzle is low cycle fatigue (LCF) due to machine startup and shutdown thermal cycles. Therefore, the test plan also included enough cycles to demonstrate that sufficient LCF life was present in the nozzles for successful testing in a prototype water-cooled gas turbine.

During the cyclic portion of the test, all instrumentation readings were recorded on magnetic tape at 35 second intervals. An infrared pyrometer was also used to measure the response to the transient. This measurement was achieved by focusing the pyrometer on a single point on the suction side of the airfoil during the entire cycle and plotting the temperatures as a function of time.

### Test Results

**Unfired Testing.** The results of the cooling-water flow test indicated that sufficient flow was being supplied to all passages in the nozzle-cooling circuit. The total measured pressure drop across the nozzle-cooling circuit was 0.85 MPa at the design flow rate of 0.283 kg/s and average cooling water temperature of 149 °C. This result compared to a calculated pressure drop of 0.81 MPa.

**Steady-State Fired Testing.** Data for the 1139 °C design point correlated well with the temperatures predicted by analysis. The largest discrepancy occurred with the infrared pyrometer measurements of airfoil suction surface temperatures forward of the trailing edge.

**Cyclic Testing.** The cyclic portion of the test was of particular importance since, in current production, air-cooled nozzle fatigue life is a function of how the part responds to a transient. The significant feature of the nozzle response was that neither the gas path surface temperature nor the core surface temperature lagged the gas temperature during the cycle. This implies that the temperature gradient and resulting thermal stress reach a maximum at steady state rather than during the transient. Therefore a water-cooled turbine should be able to tolerate a more rapid startup sequence than an air-cooled turbine and might also be far less affected by trips.

### Posttest Inspection

After each part of the testing program, a close visual examination of the second-stage nozzles was made. The inspection after the hot-air testing (unfired testing) showed no discernable change in the appearance of the nozzles. Obvious visual changes did occur after the steady-state and cyclic portions of the testing.

Examination after the steady-state and cyclic testing of the nozzles showed surface areas which were discolored in between the cooling passages of the nozzles. These markings clearly showed the pattern of cooling passages inside the nozzles. It is believed these areas were discolored as a result of a very slight oxidation of the hot surfaces in between the water-cooling passages. Since the fuel used in this testing was propane, no deposits would be expected. No indications of cracking, overheating, or other distress were observed during these inspections. In addition, a total water system leakage test at 8.6 MPa showed no change compared to the measurement taken at the start of the testing. The nozzles appeared to be in excellent condition after the testing with no discernable indications of cracking or any other distress.

## 5.3 COMBUSTOR HARDWARE TESTING

The combustor for the HTTT turbine is designed to meet a demanding set of requirements. It must be able to burn low-BTU gas while producing combustor exit temperatures of 1482 °C. The sectoral combustor is constructed with a double wall to allow for isolation of the thermal from the pressure stresses. The combustion air flows countercurrent in the channel between the two walls, first cooling the liner and then dividing and serving as cooling flow or mixing with the fuel for combustion.

The pressure shell, sectoral panels, and head end casting required extensive process development. In order to meet the test schedule, an abbreviated casting development and qualification program was initiated for all three components.

The pressure shell is identified as a one-piece alloy 718 casting in the TRV machine. For the hot gas path tests, the decision was made to manufacture the shell in five pieces and bolt them

together. This greatly reduced the gating problems and cycle time for fabrication of this component. A great deal of information was available on cast alloy 718 as a result of the successful work with the second-stage nozzle. Mold chemistry gating locations, pouring temperature, and inoculant levels were established in order to minimize segregation and maximize mechanical properties. Extensive NDE enabled the selection of the best castings for machining and final fabrication.

The sectoral panels provide the internal surface for the double-wall combustor, allowing air to flow inside the pressure shell and into the combustion chamber. High surface temperatures and thermal stresses resulted in the selection of cast U500 for these parts. The size and geometry of the panels required very close control of the casting parameters in order to obtain an acceptable end product. Casting process qualification included master heat chemistry check, gating and pour temperature experiments, heat treat qualification, and straightening guidelines. Review of macroetched samples revealed a uniform, fine-grain structure without the need of inoculants. X-rays and zygo inspections showed those panels with shrink or surface defects. Each panel was evaluated and rated prior to machining.

The head end castings were made of IN-718 using the Shaw casting process. A concern existed that the large mass of sand around the casting would act as an insulator and result in a slow cooling rate, subsequent segregation, and drop in mechanical properties. Increasing wall thicknesses and pouring temperature minimized segregation and shrink. Multiple X-rays of each part were used to evaluate the quality of each casting. Repairs were made in areas of concern.

Two full-size combustors have been constructed and tested at full temperature and pressure conditions (see Figure 5-2). The combustors have been ignited on distillate fuel oil, brought to full flow, transferred to a propane-steam mixture at the pilot, staged, and loaded to the design point. These tests have successfully demonstrated the capability of the sectoral combustor to operate at extremely high temperatures and design pressures.

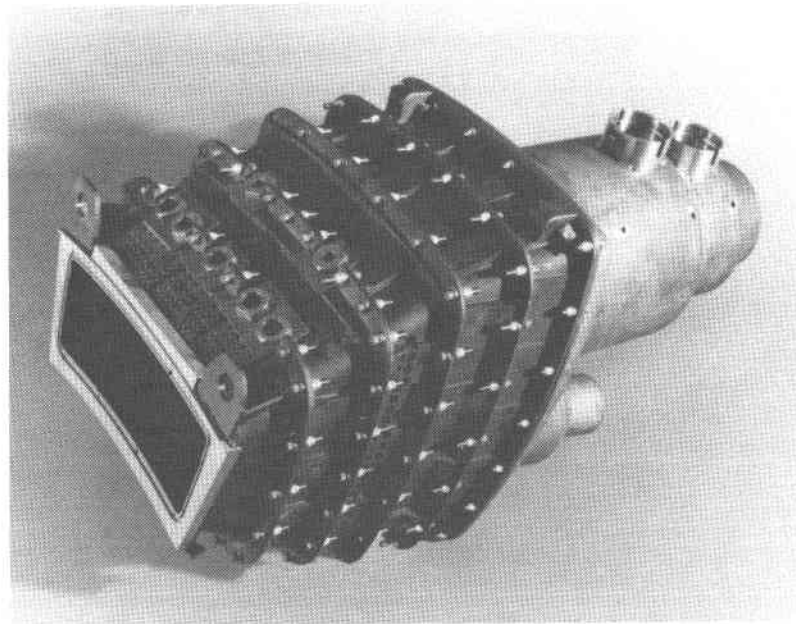


Figure 5-2. Combustor—corrugated shell region.

## 6. SUMMARY

This paper has presented a review of the key materials development programs associated with the U.S. Department of Energy's High-Temperature Turbine Technology—Phase II program as conducted by the General Electric Company under prime contract No. DE-AC01-76ET-10340. Materials and processes for all of the hot section turbine components have been selected during this phase. These selections have been verified through extensive metallurgical evaluations, fabrication, and testing of actual turbine hardware. Hardware testing was conducted at the design point and off-design conditions for key components. Materials and process "barrier" problems were resolved during this program and include the following:

- Verification of the suitability of the Cu-MZC alloy for the stage-one composite nozzle.
- Verification of diffusion-bonding methods for fabrication of a composite, water-cooled nozzle.
- Optimization of cast alloy 718 for second- and third-stage nozzles.
- Selection of forging parameters for alloy 718 for use in all three stages of turbine buckets.
- Verification of excellent stress-corrosion cracking resistance for the selected materials that will be in contact with water.

More important, these results, coupled with the output of other technical efforts contained in the Phase II program, form the basis for bringing water-cooling technology to a "technology readiness status" now.

## 7. ACKNOWLEDGMENTS

The authors would like to acknowledge the U.S. Department of Energy, Division of Fossil Fuel Utilization, for its support of this work. Thanks are also due to Dr. L.G. Peterson for his assistance in parts of this work and for review of this paper. The contributions to this program of the design and manufacturing organizations within the General Electric Gas Turbine Division are gratefully appreciated.

## 8. REFERENCES

1. P.H. Kydd and W.H. Day. *An Ultra High Temperature Turbine for Maximum Performance and Fuels Flexibility*. ASME Paper No. 75-GT-77, March 1975.
2. M.W. Horner et al. *Development of a Water Cooled Gas Turbine*. ASME Paper No. 78-GT-72, April 1978.
3. M.W. Horner et al. *Water-Cooled Gas Turbine Technology Development*. ASME Paper No. 79-GT-22, March 1979.
4. M.W. Horner et al. *Near Term Application of Water Cooling*. ASME Paper No. 80-GT-159, April 1980.
5. *Development of High Temperature Turbine Subsystem Technology to a Technology Readiness Status, Phase I*. Final Report, GE/DOE Report No. GE-1806-22, June 1977.
6. A. Caruvana et al. *Evaluation of a Water Cooled Gas Turbine Combined Plant*. ASME Paper No. 78-GT-77, April 1978.
7. A. Caruvana et al. *Subsystem Status of the Water-Cooled Gas Turbine for the High-Temperature Technology Program*. ASME Paper No. 79-GT-39, April 1979.
8. A. Caruvana et al. *Design and Test of a 73 MW Water-Cooled Gas Turbine*. ASME Paper No. 80-GT-112, April 1980.
9. P.W. Schilke et al. *Water-Cooled Gas Turbine Monometallic Nozzle Development*. ASME Paper No. 80-GT-97, April 1980.
10. P.W. Schilke et al. *Water-Cooled Turbine Monometallic Nozzle Fabrication and Testing*. ASME Paper No. 81-GT-162, December 1980.



11. D.W. Geiling, R.P. Chiu, and N. Klompas. *Mechanical, Thermal and Hydraulic Design of a Composite Construction Water-Cooled Gas Turbine Nozzle*. ASME Paper No. 81-JPGC-GT-3, June 1981.
12. G.K. Bouse and P.W. Schilke, "Process Optimization of Cast Alloy 718 for Water Cooled Gas Turbine Application," Proceedings of the Fourth International Symposium on Superalloys, September 1980.
13. R.M. Latonision and R.W. Staehle. "Stress Corrosion Cracking of Iron Nickel-Chromium Alloys," *Proceedings of the 1967 Conference on Fundamental Aspects of Stress Corrosion Cracking*. Ohio State University, Columbus, Ohio, 1969.
14. W.A. Mizla. *Corrosion Properties of NiCrFe Alloy 718 and Microbrazed -50 (BNi-7)*. WAPD-TM-1049, June 1973.
15. *XM-19 Materials Qualification Report*. NEDE -21653, July 1977.
16. H.D. Solomon and M.J. Povich. *Constant Extension Rate Testing in High Temperature Water*. General Electric Report No. 77CRD252, January 1978.

TRANSPIRATION AIR COOLING FOR HIGH TEMPERATURE  
TURBINES OPERATING ON COAL DERIVED FUELS

J. Wolf

J. Mogul

S. Moskowitz

CURTISS-WRIGHT CORPORATION

1 PASSAIC STREET

WOOD-RIDGE, N.J. 07075

G. Manning

U.S. DEPARTMENT OF ENERGY

GERMANTOWN, MARYLAND 20545

## INTRODUCTION

In 1976, the U.S. Department of Energy initiated the High Temperature Turbine Technology (HTTT) Program with the goal of developing to technology readiness, the turbine component of an industrial gas turbine capable of operation at gas stream temperatures of 2600<sup>0</sup>F and above. This turbine component, operating on coal-derived liquid or gaseous fuel, will provide Electric Utilities with an economically and environmentally viable alternative to the use of petroleum, natural gas or pulverized coal with stack scrubbers.

Analyses of both conventional liquid-fueled and more advanced combined cycles have shown that increasing the firing temperature and pressure ratio of the gas turbine can substantially improve the specific power output as well as the gas turbine efficiency and therefore also the combined-cycle plant efficiency. The results of one study, shown in Figure 1, clearly show the benefit to the cycle by increasing the gas turbine firing temperature above that of contemporary equipment. In this chart, the range of plant efficiency at a specific firing temperature is a function of the conversion efficiency of the gasifier and the gas cleanup system.

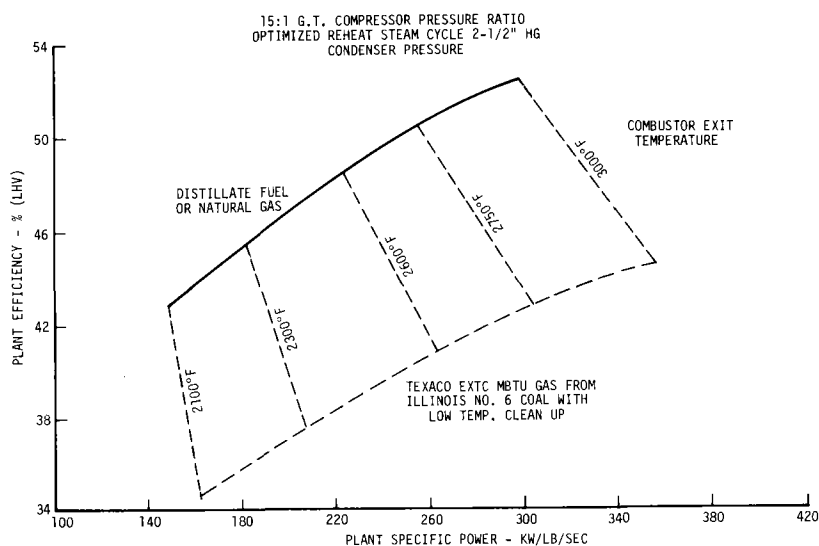


Figure 1. Combined Cycle Powerplant Analysis

To successfully operate on coal-derived fuel, the high temperature turbine must withstand, in addition to gas temperatures above the melting point of its constituent materials, entrained gas stream particulates and corrosive compounds which are capable of severely degrading structure and performance through erosion, corrosion and deposition of the turbine blading.

### TRANSPIRATION AIR COOLING CONCEPT

Curtiss-Wright has selected Transpiration Air-Cooling for the critical high temperature turbine blade and vane airfoils. In this concept, cooling air effuses through a porous skin to create an insulating film of cool air on the outer airfoil surfaces. The air for cooling is obtained from the gas turbine compressor component. The turbine porous airfoil skin is attached to an internal structural spar by hub and tip circumferential welds plus spanwise welds which also enclose internal longitudinal cooling air passages between adjacent welds. Figure 2 illustrates the concept. To optimize air usage, each passage is orificed to provide only that quantity of air required to meet design criteria at the local gas stream temperature and pressure conditions. Cooling air is obtained from the lowest compressor stage consistent with each turbine blade row pressure level.

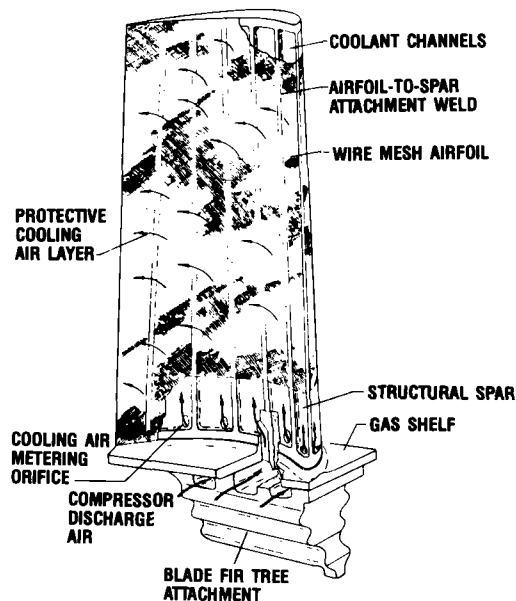


Figure 2. Transpiration Air-Cooled Turbine Blade Concept

The transpiration air-cooling arrangement protects the turbine airfoils from the degrading characteristics of the hot gas stream created by the combustion of coal-derived fuels by providing a continuous protective air blanket surrounding the airfoil so that:

- Metal temperatures of the skin and spar are maintained at levels commensurate with structural strength requirements.
- Solid and liquid particulates in the gas stream are deflected from the airfoil surface thereby minimizing or eliminating sulfidation, erosion and deposition.
- Skin temperature is cooled below the hot corrosion threshold and skin material oxidation is controlled within predictable and acceptable levels.

#### AIRFOIL MATERIALS & FABRICATION TECHNOLOGY

Early design studies indicated that a strut-supported configuration was the most promising approach for constructing reliable and cost-effective blades and vanes. The considerations for materials and fabrication technology were separated into three categories:

- The porous metal airfoil skin
- The load supporting strut
- The skin-to-strut attachment

#### POROUS METAL AIRFOIL

A number of porous metal configurations were identified as potential candidates for the airfoil. These included:

- Powder and foamed metals
- Perforated metals
- Random wire compacts
- Woven wire compacts
- Wound wire compacts

Laboratory, rig and engine tests, conducted over a number of years showed that compressed and sintered mesh, made from both woven and wound wire compacts, produced the optimum combination of properties and porosity control required. In addition, the fabrication technology was proven and commercially available.

The selection of alloy systems for the woven and wound mesh was clearly to be a compromise among mechanical properties, fabricability, and resistance to the turbine environment. The ability of the material to be drawn into wire and then fabricated into a skin structure was of course a primary consideration. The major property concern was oxidation resistance so as to provide a predictable permeability and cooling air flow through the skin at high temperature and with long operating times. Strength of the skin alloy was of secondary importance since the airfoil is essentially a non-load carrying member, and the design of the strut-skin composite can accommodate relatively low strength skin alloys. Ductility of the alloy was important, however, from both the fabrication standpoint and the ability to resist cyclic cracking due to thermal strains. Metallurgical stability, i.e. no structural changes that reduce ductility during operation, was another major requirement for resistance to thermal fatigue cracking. This latter requirement, which was made evident early in the development testing, provided the most severe restriction in alloy selection, since most candidate alloys were prone to such reductions in ductility with time at elevated temperatures. Finally, the alloy selection needed to consider the ability of the skin to be attached to the strut.

A significant number of candidate iron, nickel and cobalt-base alloys were fabricated into both woven and wound mesh and evaluated in both laboratory and full scale blade/vane tests. To date the best combination of fabricability, mechanical and environmental properties has been exhibited by Nichrome V-Cb (Ni-20Cr-1Si-1Cb). More recent investigations have identified and evaluated two other promising alloys which can be utilized in specific areas: Hastelloy S (Ni-base superalloy) where higher strength is desired, or for higher oxidation resistance, AL 16-5Y (FeCrAlY).

#### BLADE/VANE STRUTS

Because the load carrying struts of transpiration air-cooled blades and vanes are protected from the combustion gases and operate at moderate temperatures, neither rupture strength nor oxidation/hot-corrosion resistance is critical. The dampening effect of the porous airfoil also contributes to improved fatigue resistance. A number of commercially available nickel and cobalt-base turbine alloys have successfully

served as strut materials. Struts have been fabricated from both forgings and investment castings, with the latter being more cost effective in producing the required external and internal configurations required by the design.

#### SKIN-TO-STRUT ATTACHMENT

Brazing, resistance seam welding, electron-beam welding, laser welding, and a modified diffusion bonding process have all been utilized to attach the porous metal airfoil to the blade/vane strut. The most reliable and cost effective attachment process developed to date has been electron beam welding. The process has been optimized to the point where it is utilized for all skin-to-strut joints. It has also been utilized for repair and refurbishment through replacement of entire airfoils, individual airfoil panels, and sections of porous metal within individual panels. Ultrasonic chemical cleaning methods have been developed prior to welding which allow the process to be performed both on new and engine operated components.

Laser welding remains an attractive, potentially lower cost joining method, which has demonstrated an ability to produce skin strut joints equal in quality to the electron beam welded joints. Its use will depend on the continued development and optimization of laser welding equipment.

Several thousand transpiration air-cooled blades and vanes have been fabricated by Curtiss-Wright in various sizes ranging up to those of the planned commercial powerplant gas turbine prior to the current HTTT program. Stationary turbine cascades and rotating rig engines have been operated for hundreds of hours burning clean distillate fuels at steady state and cyclic conditions with inlet temperatures of 3000<sup>0</sup>F (1649<sup>0</sup>C) and above.

#### RECENT TURBINE DEVELOPMENT TESTING

Since the ability of a transpiration air-cooled turbine to operate in a high temperature gas stream has already been demonstrated, emphasis in recent testing under the DOE-sponsored HTTT program has been on evaluation of the erosion, corrosion and deposition characteristics of the

turbine in the aggressive atmosphere expected from the combustion of coal-derived fuel.

Principal test vehicles were a 7-vane turbine cascade and a low pressure rotating rig engine incorporating a complete single stage turbine.

Because of the difficulty in obtaining coal-derived fuel in the quantities required to operate large scale engines, a simulation was made by seeding initially distillate jet fuel and later natural gas, with contaminants. Early cascade tests utilized aluminum oxide particles and fuel-soluble alkali metal compounds; later cascade and rig engine tests were conducted with ground fly ash obtained from the electrostatic precipitator of a coal-fired utility boiler. Table 1 shows the composition of the ground fly ash used.

TABLE 1  
CHEMICAL ANALYSIS OF ILLINOIS NO.6 COAL FLY ASH  
USED IN TESTING TRANSPIRATION AIR-COOLED AIRFOILS

	<u>% By Wt.</u>
C	2.37
S	2.20
SiO <sub>2</sub>	28.9
Al <sub>2</sub> O <sub>3</sub>	29.4
Fe <sub>2</sub> O <sub>3</sub>	25.6
TiO <sub>2</sub>	1.67
P <sub>2</sub> O <sub>5</sub>	0.69
CaO	0.27
MgO	1.10
Na <sub>2</sub> O	2.20
K <sub>2</sub> O	2.77



The original test plan included operation at three levels of particulate size and loading selected on the basis of limited published data and estimates of gasifier output conditions and then-existing and developmental gas clean up systems. Later data presented for a fixed bed gasifier and "physical" (particulate scrubbing and gas cooling elements) cleanup system correlated well with the lowest particle size range and loading selected to simulate the output from a cold gas cleanup. The earlier developmental DOE/MERC high temperature gas cleanup system on which the higher specification values were based is no longer being actively pursued, leaving only the lowest category as representative of current technology. More recent data presented for the Texaco medium Btu coal gasification process with water scrubbing indicate even lower hot gas stream particulate loading and smaller particle sizing than those of our lowest-selected values. Accordingly, the test program was revised to emphasize the lower two particulate levels. Tables 2 and 3 show, respectively, these particulate loadings and sizes.

TABLE 2  
PARTICULATE LOADING FOR TURBINE CASCADE AND RIG ENGINE TESTS

Level	Specification Loading in LBG Fuel		Seeding Distillate Fuel	
	Grains Per SCF	WPPM	Turbine Cascade WPPM	Rig Engine WPPM
1	.001	2	42	16
2	.005	11	208	81

TABLE 3  
PARTICULATE SIZE DISTRIBUTION

Level	LBG Spec.	Aluminum Oxide	Ground Fly Ash
	% Micron	% Micron	% Micron
1	100 < 2	100 < 1.6	100 < 2.5
	80 < 1	99.8 < 1	88 < 1
2	100 < 5	100 < 6.3	100 < 6.3
	80 < 2	97 < 2	98 < 2

Over 800 hours of rotating rig engine testing were accomplished, preceded by almost 400 hours of stationary turbine vane cascade tests. In all of the testing, blade and vane airfoil skin oxidation was minimal, and there was no evidence of sulfidation, corrosion or erosion. Some light deposition of particulates was observed, but this produced only a slight reduction in skin permeability and had no measurable effect on turbine performance.

As discussed earlier, all of the test turbine blades and vanes incorporated porous airfoils made of columbium-stabilized Nichrome V wire and internal structural spars of Stellite 31 material. Airfoil construction was either wound or woven. In the former, the wire is flattened and wound in multiple layers on a conical mandrel. The conically wound tube is then sintered to join the layers, rolled to specific thickness and porosity requirements and die formed to the airfoil shape before being joined to the internal structural spar by electron beam welding. Woven skins are made up of multiple layers of flat-woven sheets similarly sintered, rolled, formed and welded to the spar. Basic wire sizes are either .005" and .010" diameter.

## TURBINE VANE CASCADE TESTS

Three 100-hour turbine vane cascade tests were conducted. The first two tests were intended to simulate in 100 hours the equivalent of 300 hours in the forthcoming rig engine. To accomplish this, the specification particulate loadings were trebled, to 120 and 600 wppm, respectively.

Because aluminum oxide particulate was used, appropriate amounts of sodium and potassium compounds were added to the fuel to achieve the level of alkali metal salts expected in a coal-derived gaseous fuel.

Results of the two 100-hour cascade tests with aluminum oxide particulate were quite similar. Visual and microscopic examination of the vane airfoils after test found slight dusting on the convex, or suction sides. The dusting was less than 5 microns thick after the first test at 120 wppm and approximately 15 microns maximum thickness after the second test at 600 wppm particulate loading. After the second test there was also some particulate on the trailing edge surfaces up to a maximum thickness of 15 microns.

Energy dispersive X-ray analysis (EXDA) for elemental composition of the particulate found on the vane surfaces after the first test indicated a preponderance of silicon, with a significantly lesser amount of the injected alumina particles. Subsequent investigations found that silica had eroded from the flat side walls of the 65° sector of the annular combustor used for the turbine cascade. Since the eroded silica could not be quantified, the test was considered significantly more severe than intended in that the amount of particulate passing through the turbine cascade exceeded the controlled quantity of aluminum oxide particulate injected into the combustor fuel supply.

Tests of the vane airfoils to determine cooling air flow characteristics at intervals during and after the tests showed flow capacity reductions in the same range as could be expected from oxidation alone at the skin operating temperature of approximately 1300°F. This indicates that the surface dusting of particulate had no effect on the flow capacity of the porous skin. Results from the first test indicated a maximum of

5 percent reduction in flow which compares with the low end of the mesh oxidation characteristic as determined by furnace exposure testing. The flow reduction data from the second 100 hour test with 600 wppm particulate loading was similar. Both characteristics become asymptotic with exposure time in the 50 hour range. Figure 3 shows the flow reductions of the vanes using airfoils made from 0.005 inch (0.013 cm) wire. The flow reduction rates shown for both cascade tests as well as the subsequent test with fly ash particulates, are highest during the first 50 hours but rapidly decrease to the area of the lower limit of the oxidation characteristics for these porous materials.

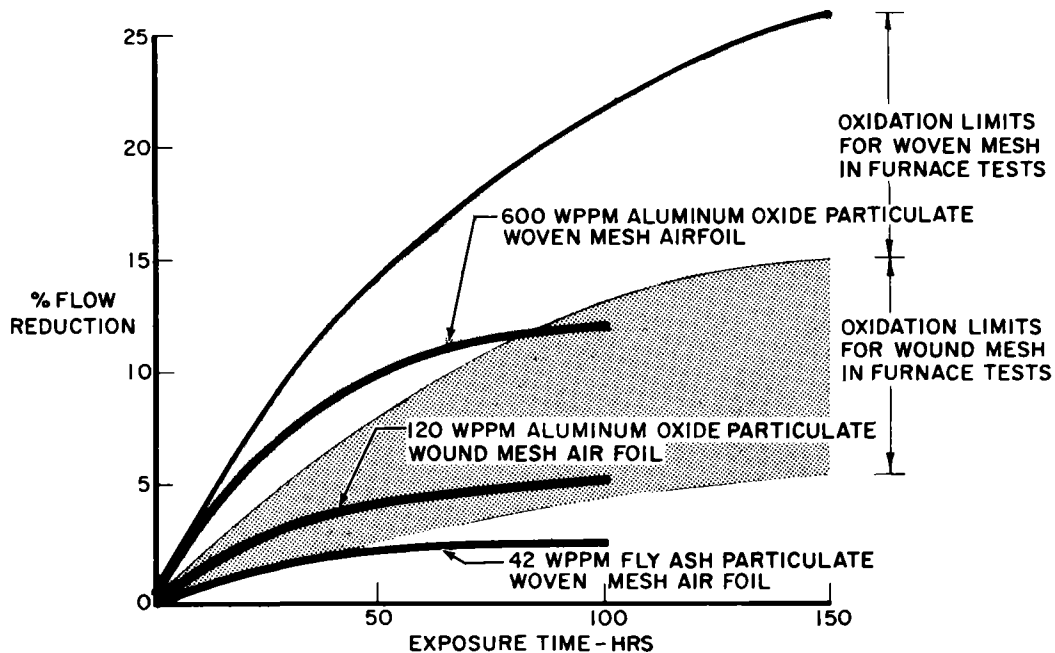


Figure 3. Vane Cooling Air Flow Reduction During Turbine Cascade Contamination Test

There was no evidence of either erosion or corrosion of the airfoil skin after the two tests. The lack of erosion was particularly gratifying in that the injected sharp-edged aluminum oxide particulate remained hard and abrasive at the rig engine firing temperature, whereas the particulates generated from the combustion of coal-derived fuel would melt and probably vaporize at these temperatures. The test time is considered too short to draw meaningful conclusions regarding the lack of corrosion or sulfidation.

The third 100-hour test was conducted with ground fly ash particulate at the originally specified rate of 42 wppm. The level of particulate loading was reduced from that of the previous tests to simulate the level to be used for the rig engine test.

Because of a facility malfunction, the vane cooling air temperature for this test was somewhat lower than that of the previous tests. Cooling air flow was increased slightly from the design value to achieve the same velocity exiting the skin into the main air stream as would have been achieved with design flow at the higher temperature. The combination of lower cooling air temperature and slightly higher flow rate produced a lower vane skin temperature and thus lower oxidation than was experienced in the two prior tests.

The results of the periodic flow tests obtained during this test with fly ash particulate in the gas stream are presented in summary with the preceding tests in Figure 3. The furnace oxidation characteristic at the lower skin temperature of this test is just above the lower limit of the oxidation range shown for wound mesh.

#### RIG ENGINE TESTS

Following a checkout on clean fuel, 650 hours of testing were conducted with fly ash particulates in the hot gas stream. All testing was at a particulate loading between 20 to 28 wppm, or the equivalent of .001 + grains per standard cubic foot of low Btu gas fuel. Maximum measured particle size for the first 200 hours of testing was 10 microns, and for the remainder of testing was about 3 microns.

The first 350 hours of testing were with distillate fuel (Jet A) and the final 300 hours were run on natural gas. As noted above, particulate loading was held constant, irrespective of fuel type or particulate size change.

Periodic visual examinations of the outside surfaces of the blades and vanes found varying light amounts of particulate, primarily on the leading edge. Even the lightest deposits created an orange coloration from the iron oxide content of the fly ash. Closer examination of individual airfoils reveals the shallow nature of the deposits in that the individual wire strands remain clearly visible. Generally, it appeared that the airfoil deposits accumulated primarily during the first 50 hours of exposure and then increased only minimally after that.

Microscopic examination of particulate from the surfaces of the airfoils after early testing revealed a high percentage of discrete particles in the size range of 5 microns and above. A short series of tests was conducted on an atmospheric discharge combustor rig to determine whether the injected particles undergo size change or agglomeration either when passing through the combustion zone, or residing in the storage tank and piping system.

For this test, the particulate was introduced into the combustor by means of the same system utilized on the rig engine. The size distribution of the injected flyash was the same as was used in the rig engine; the loading was increased to expedite sampling. Exhaust samples were collected isokinetically using a modified stack sampling probe behind the combustor exit station and subjected to SEM analysis for determination of particle size. The particle size distribution in the exhaust samples was found to be in close accord with the measured size distribution of the injected flyash. It was therefore concluded that there is no significant agglomeration of fly ash particles passing through the combustor, and that the major portion of large particles found on the airfoil surfaces represent the particle size found in the basic flyash supply. Conversely, it was concluded that the majority of the smaller particles in the hot gas stream were successfully deflected away from the blade and vane airfoil) surfaces by the transpiration cooling air.

The conclusion that the transpiration cooling air successfully deflects low micron size particulate from the airfoil surface is corroborated by comparison of the SEM photographs in Figure 4. The photomicrograph of a sample of the gas stream particulate from the combustor test shows primarily one micron size and smaller particles, with only occasionally larger particles. The photomicrograph of the sample taken from the surface of a rig engine tested turbine vane shows that for the most part only larger gas stream particles penetrated the cooling air barrier to deposit on the airfoil surface.

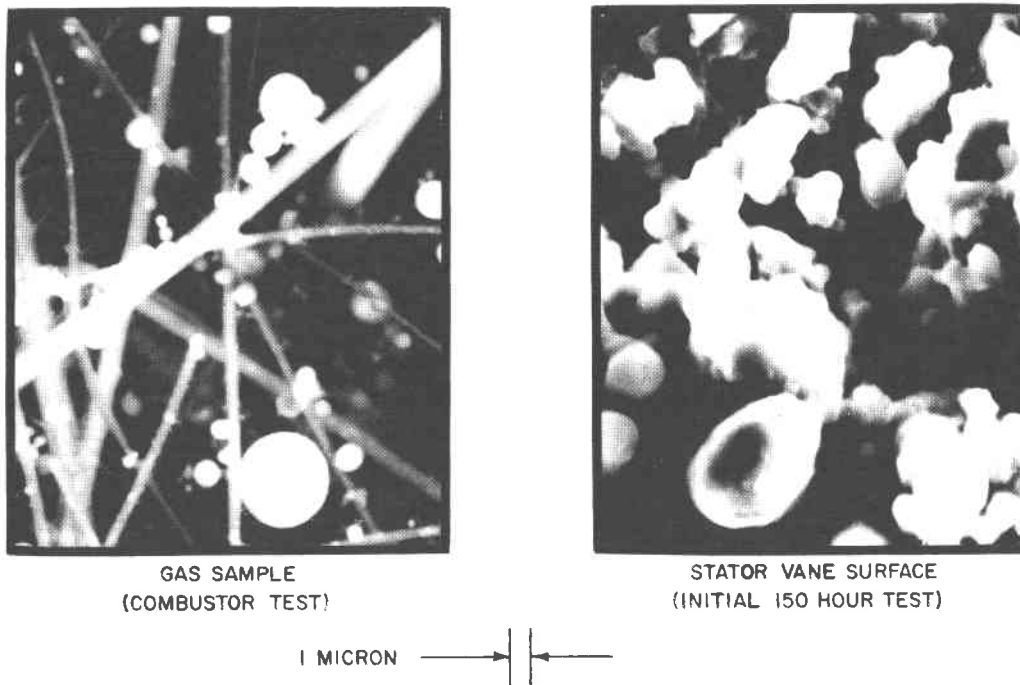


Figure 4. SEM Analysis of Particulate Size Distribution

Further metallographic analysis revealed that the gas stream particulate which penetrates the airfoil cooling air blanket produces only a surface deposit on the porous mesh airfoil skin. Figure 5 is an enlarged photomicrograph of a section through a vane leading edge after 50 hours of rig engine test with flyash particulate in the gas stream. Examination of this photomicrograph shows that the particulate has settled only on the outer wires of the first layer of skin material, with virtually no evidence of bridging over the cooling air pores or particle migration into the sub-surface layers.

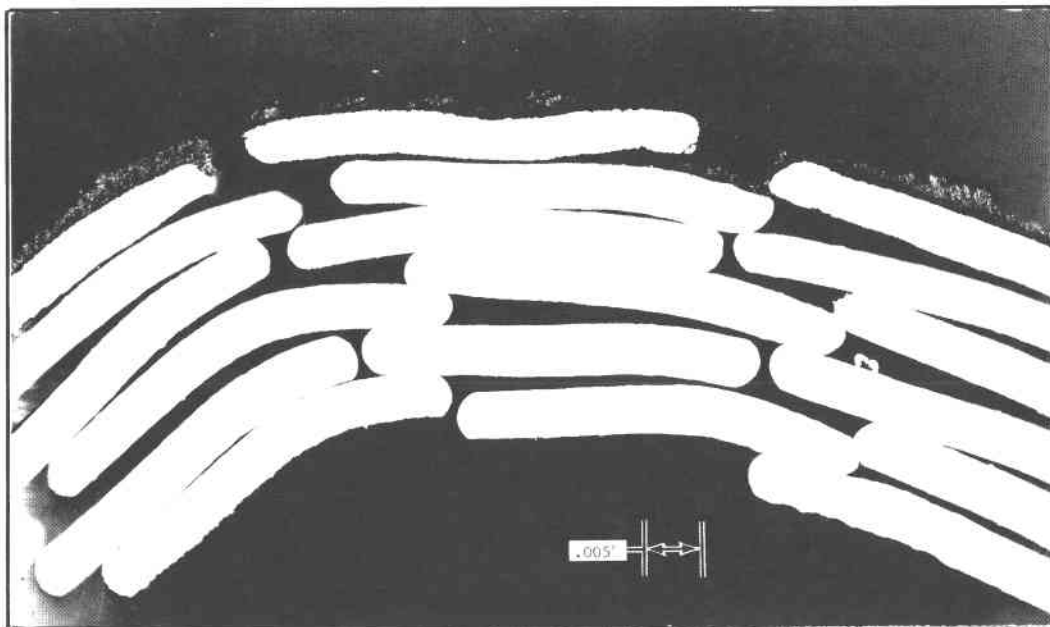


Figure 5. Photomicrograph of Section Through Transpiration Air-Cooled Turbine Rotor Blade Leading Edge



The particulates on all surfaces appeared to have melted or vaporized in the hot gas stream and then resolidified as they passed through the boundary layer of cooling air surrounding the airfoil. These deposited particles show little adhesive force and can easily be brushed off. At the vane leading edge only, the outer layers of particulate appear to have remelted or softened from combustor radiant heat to a more slag-like appearance.

Periodic flow bench tests were performed on vane and blade airfoils to determine changes in cooling air flow capacity with operating time. Significantly more flow checks were obtained on blades than on vanes because of ease of removal and reinstallation. The vane test results were quite consistent with those of the earlier cascade test program in which it was concluded that the operating flow loss characteristic levels off after the first 50 to 100 hours of exposure and is close to that produced by oxidation alone. The results of the rotor blade flow checks show a leveling off of flow loss at well under 10%, which is well within the requirements for extended operational life and is consistent with that which can be expected from oxidation alone. The flow bench results also corroborate the visual observations of surface deposition discussed above.

A typical rotor blade was destructively analyzed, using metallographic, SEM, and EDXA examinations, after completing 500 hours of rig engine operation with fly ash particulate in the hot gas stream. The results of the analysis are summarized in Table 4. Figure 6 is a photomicrograph of a typical section of the woven airfoil leading edge illustrating the minimal amount of oxidation, and the absence of any evidence of either erosion or hot-corrosion.

To obtain higher time oxidation characteristics of the porous airfoil skin, a laboratory program is in progress utilizing flat mesh samples exposed to flowing elevated temperature air in a furnace. Comparison of these data with similar permeability loss data taken on instrumented vanes from both cascade and engine tests has shown that laboratory furnace oxidation provides a satisfactory, conservative estimate of the airfoil material oxidation rate in engine operation. Figure 7 is a curve of the permeability reduction experienced by the wound .010"

(.254 mm) dia. wire Nichrome V Cb skin sample at 1350<sup>0</sup>F (732<sup>0</sup>C). To date, 2000 hours of exposure have been completed, with a total of 10,000 hours planned. Extrapolation of these data to 50,000 hours without any intermediate servicing indicates a flow capacity loss of 20%. From the curve of Figure 8, this flow capacity reduction would produce an increase in maximum skin temperature to 1400<sup>0</sup>F (760<sup>0</sup>C). This analysis indicates that a 50,000 hour blade life is feasible.

TABLE 4  
METALLURGICAL EXAMINATION OF LP RIG ENGINE TURBINE ROTOR BLADE AIRFOIL

TOTAL OPERATING TIME - 644 HOURS	MATERIAL - NICHROME V Cb	
CONTAMINANT EXPOSURE - 500 HOURS	12 X 64 WOVEN	
	OXIDATION DEPTH INCHES	
	PRESSURE SURFACE	SUCTION SURFACE
SECTION LOCATION		
4 5/8" ABOVE PLATFORM	.0016(MAX)	.0005
2 5/8" ABOVE PLATFORM	.0005	.0005
1/2" ABOVE PLATFORM	.001	.001

NO EVIDENCE OF EROSION

NO EVIDENCE OF SULFIDATION

FLY ASH DID NOT PENETRATE BEYOND SURFACE WIRES

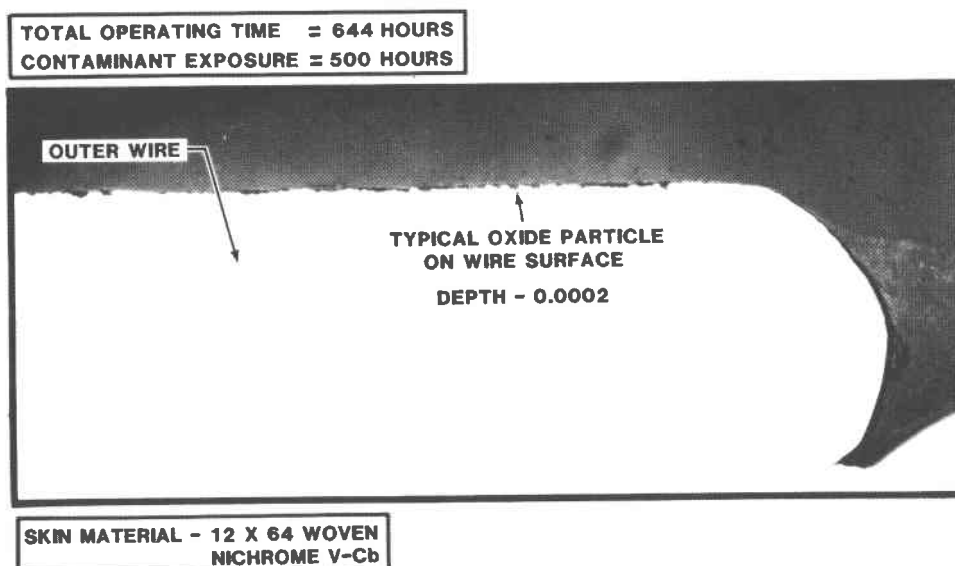


Figure 6. Photomicrograph of a Transpiration Air-Cooled Blade Leading Edge Outer Wire

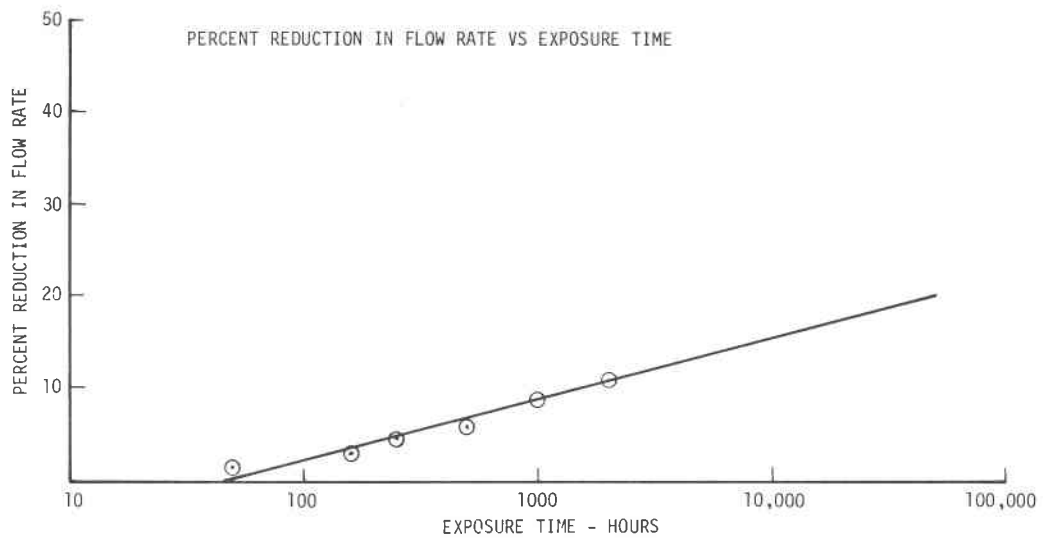


Figure 7. 1350<sup>o</sup>F Furnace Oxidation Results-Nichrome V-Cb Wound Mesh

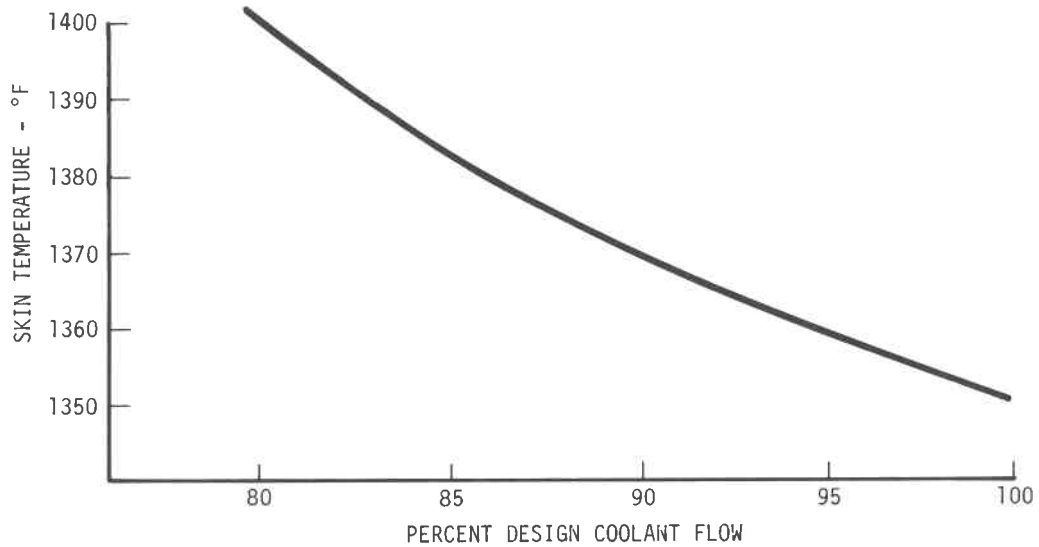


Figure 8. Effect of Reduced Coolant Flow on Transpiration Air-Cooled Blade Temperature

One other characteristic of transpiration air-cooled airfoils should be mentioned. After approximately 500 hours of testing, the turbine suffered foreign object damage from a rear bearing heat shield bolt which failed and exited the engine through the turbine annulus. All but one of the 59 rotor blades and 65 of the 70 stator vanes suffered damage to the leading and trailing edge porous skins respectively. There was no damage to the internal structural spars. In contrast to solid airfoils, which if similarly damaged would have had to be replaced, the porous skins were completely repaired by local replacement of damaged skin sections. Figure 9 is a photograph showing typical airfoil skin repairs.

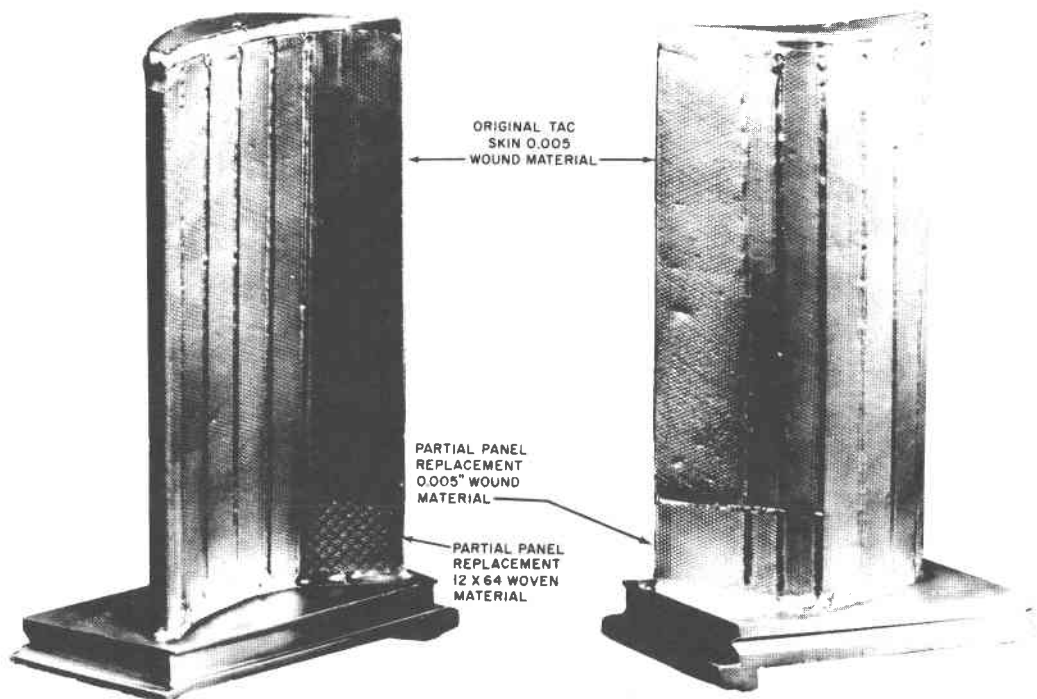


Figure 9. Transpiration Air-Cooled Vane Airfoil Repair

## SUMMARY AND CONCLUSIONS

The rig engine was operated for over 800 hours. Of this time, more than 650 hours were at a turbine inlet temperature between 2600<sup>o</sup>F and 3000<sup>o</sup>F and with fly ash particulates in the hot gas stream at a loading of (or equivalent to) 20 to 28 WPPM in the distillate fuel supply. Maximum particulate size was 10 microns. Preliminary test experience with hot gas stream contaminants was also gained by 300 hours of turbine vane cascade testing using aluminum oxide and fly ash particles at loadings up to 15 times the level expected in commercial operation. Based on the results of the tests, the following observations and conclusions were made:

1. There was no mechanical or thermal distress in any of the turbine components as a result of the hot gas stream temperature and particulates.
2. Oxidation on transpiration air-cooled components was minimal and generally less than that predicted for 2600<sup>o</sup> operation.
3. There was no evidence of erosion, corrosion or sulfidation on the transpiration air-cooled components.
4. Particle deposition on transpiration air-cooled materials was minimal and limited to the outer strands of the mesh. There was virtually no clogging of the cooling air pores.
5. Performance deterioration of the rig engine related to the minor deposition of particulates on the airfoil surfaces was negligible.
6. The flow loss vs operating time characteristic for the transpiration air-cooled airfoils operating in a particulate laden hot gas stream resembles the oxidation characteristic, i.e., the rate of cooling airflow capacity loss decreases with operating time, approaching zero after several hundred hours. Absolute values of flow loss are within a satisfactory range for long term operation. Based on the rig engine results and supporting metallurgical studies, an operational life of 50,000 hours appears feasible.
7. Blades and vanes were able to sustain FOD without catastrophic results. There was no evidence of overtemperature or damage to structural spars associated with the FOD.

## **WAFER COOLING FOR INDUSTRIAL GAS TURBINE BLADES AND VANES**

**Bruce T. Brown and Daniel B. George**

**Pratt & Whitney Aircraft Division of United Technologies Corporation**

### **ABSTRACT**

The application of wafer construction techniques to turbine vanes and blades offers significant potential increases in reliability, durability, and “dirty” fuel tolerance for marine and industrial gas turbine engines. In programs with DOE and EPRI, Pratt & Whitney Aircraft has demonstrated the feasibility of wafer cooling and confirmed the ability to produce wafers in industrial engine sizes using current industrial engine turbine alloys. Wafer construction provides highly effective cooling and reduced airfoil temperature gradients without requiring airfoil surface discharge film holes which are susceptible to plugging from “dirty” fuels.

Wafer airfoil construction consists of making a vane or blade from a stack of relatively thin wafers whose surfaces are individually photo-etched to produce cooling flow passages that are impossible with any other form of construction. The cooling of each wafer can be individually tailored for the local heat input at any point on the airfoil. The wafers are then stacked, joined and final machined to produce the final vane or blade contours. The wafers can be oriented either radially or chordwise. Blades produced from wafers have twice been demonstrated in the highly advanced F100 military aircraft engine. Recently demonstrated high-strength joining techniques have made wafer construction viable for gas turbine application. New alloys being produced by the Pratt & Whitney Aircraft Rapid Solidification Rate Process in combination with wafer construction could produce blades and vanes with temperature capabilities superior to anything produced today.

In this paper, wafer construction is discussed with an emphasis on industrial/marine applications. The DOE and EPRI programs are reviewed as well as alloys which have and could be used along with a proposed method of producing low cost wafer vanes.

### **INTRODUCTION**

The United Technologies wafer construction technique offers to the marine and industrial gas turbine engine an innovative turbine vane and blade fabrication method which eliminates many of the shortcomings of current production airfoil construction techniques. Wafer airfoils achieve high effectiveness cooling by virtue of the unique fabrication process. By constructing an airfoil from a stack of flat, thin wafers, an additional degree of freedom is available to the turbine designer. The wafers may be etched individually to produce cooling flow passages that are impossible with any other form of construction. This allows the airfoil interior to become an extended surface heat exchanger: heat transfer area is multiplied several fold; turbulence generating “trip strips” can be located as desired; cooling passages can be located closer to airfoil surfaces; and impingement cooling can be tailored to high heat flux locations. The individual wafers are then stacked, joined and final machined to produce the final airfoil contour. For turbine vanes where strength is not critical, the wafers can be oriented in either the radial or chordwise direction. For turbine blades where strength is of primary consideration, the wafers are oriented radially or parallel to the centrifugal load direction. Figure 1 shows a sample chordwise wafer vane and radial wafer blade.

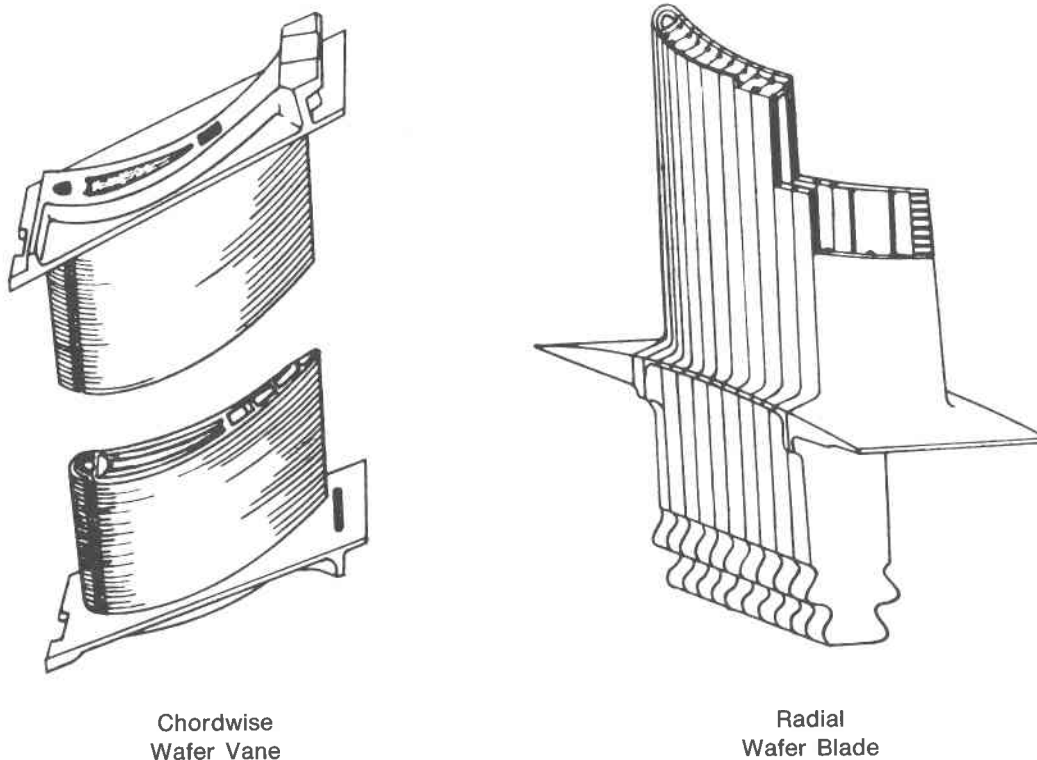


Figure 1. Wafer Vane and Blade

The wafer construction technique was initiated and underwent original development for use in advanced military aircraft gas turbine engines. In military aircraft engines the impetus is to increase the combustor exit temperature. This increase results in higher engine cycle efficiencies and higher engine thrust-to-weight ratios. The wafer vanes and blades built and tested as part of the military effort yielded the highest cooling efficiencies of any type of airfoil previously built and tested by United Technologies. Blades were built and tested in the F100 engine and vanes in the J58 engine.

The emphasis in military aircraft engine airfoil cooling has been focused on increasing the use of film-cooling to achieve improved high temperature operation. Marine/industrial turbines designed to tolerate a variety of fuels must be cooled by techniques that maintain low airfoil metal temperatures without the use of small coolant airfoil surface discharge holes which are susceptible to plugging. Plugging results in a degradation of airfoil life due to local coolant flow blockage with an associated increase in surface metal temperatures. The airfoil leading edge and pressure surfaces are most susceptible to plugging due to direct particle impingement. The suction surface is less susceptible, while the trailing edge and tip are relatively safe from plugging. The all-convective airfoil design philosophy discussed in this paper uses only the trailing edge and tip for coolant discharge, and offers a hole-free surface for application of corrosion/erosion resistant coatings. Coatings also tend to plug surface holes thereby requiring special precautions during application. Wafer construction enables the use of all-convective designs which achieve high cooling efficiency levels without the use of holes susceptible to plugging.

Current production blade and vane fabrication techniques severely limit the ability to direct the flow streams inside the airfoils to most effectively use the coolant. Since the coolant is compressor discharge air that is not burned in the combustor, any waste causes severe cycle efficiency and power output penalties. Wafer construction, because of its inherent design flexibility, has shown that all-convectively cooled vane and blade airfoils can be built that have highly effective cooling. This was illustrated when the Department of Energy funded a program in which advanced military component technology was investigated for use in industrial gas turbine engines. In this program, wafer airfoil cooling and high-pressure compressor technology were combined to achieve increased efficiency and improved durability in a 15,000 shp/10 MW industrial gas turbine study engine.

A follow-on program sponsored by the Electric Power Research Institute extended the technology to an existing large industrial/marine gas turbine engine. These programs will be discussed in detail in this paper. The benefits of wafer construction which have been demonstrated in the DOE and EPRI programs as well as military aircraft associated programs include:

- Maximum cooling effectiveness achieved through flexibility in design of airfoil internal heat transfer surfaces.
- Elimination of cooling air discharge holes from the airfoil surfaces most susceptible to plugging by the combustion products of heavy fuels.
- Reduction of airfoil temperature gradients, thus reducing airfoil cyclic stress and increasing life.
- Ability to produce wafers and construct airfoils from all alloys considered to date.
- Ability to produce wafers of the size required for industrial gas turbines.
- Ease of application of corrosion coatings and thermal barrier coatings due to elimination of surface holes and extended coating lives due to flatter airfoil temperature profiles.
- Improved turbine aerodynamic performance achieved by elimination of the airfoil surface cooling holes.

## **DISCUSSION**

### **WAFER CONSTRUCTION**

The application of wafer construction to achieve efficient cooling of turbine blades and vanes has been investigated for more than 12 years; however, it wasn't until reliable, high-strength joining techniques were developed that the wafer concept became truly feasible. The attainment of structural integrity in turbine blades joined by bonding techniques was demonstrated recently when two-piece turbine blades were tested extensively and qualified for production in the F100 engine which powers the F-15 and F-16 fighter aircraft.



Those blades were bonded using the Transient Liquid Phase (TLP®) process developed at United Technologies. This same process has been used on all the wafer blades and test airfoils built at UTC except those from the new RSR alloys which utilize solid-state diffusion bonding.

The TLP process, as illustrated in Figure 2, uses an interlayer which partially melts to fill surface irregularities of the surfaces to be joined. This interlayer, which is tailored to closely match the composition of the parent material, resolidifies isothermally, and during heat treatment goes through homogenization with the parent alloy to form a high-strength joint comparable in strength to that of the parent material (see Figure 3). Two full sets of two-piece TLP bonded blades successfully completed 3600 cycle ( $\approx 2000$  hr) Accelerated Mission Testing (AMT) without evidence of bond distress. In doing so they substantiated the viability of bonded multipiece airfoil construction.

Laminated or wafer airfoil construction is an extension of the two-piece airfoil concept that offers further improvements in both overall and local cooling effectiveness. Radial wafer blades built for experimental test in the F100 engine will serve to illustrate the wafer construction process. Figure 4 shows the fourteen wafers and two end blocks which make up the main part of the blade, and Figure 5 details the steps required for fabrication. The wafers are sliced from blocks of directionally solidified IN 100 by a multiple wire Electrical Discharge Machining (EDM) process. The wafers are preconditioned prior to joining by double disc grinding. Two wafer locating holes are then machined for use as reference points for all subsequent etching and machining operations to insure the accurate location of wafer features. The individual 64 mil thick wafers are then photo-etched to provide the desired blade cooling features. The blade root internal coolant feed area is then EDM cut and the wafers are TLP bonded together. The bonded stack of wafers (Figure 6) is machined to provide the airfoil internal cavity and subsequently bonded together with a cooled tip cap formed by two transverse wafers. External machining of the airfoil, platform, two rows of showerhead leading edge holes and

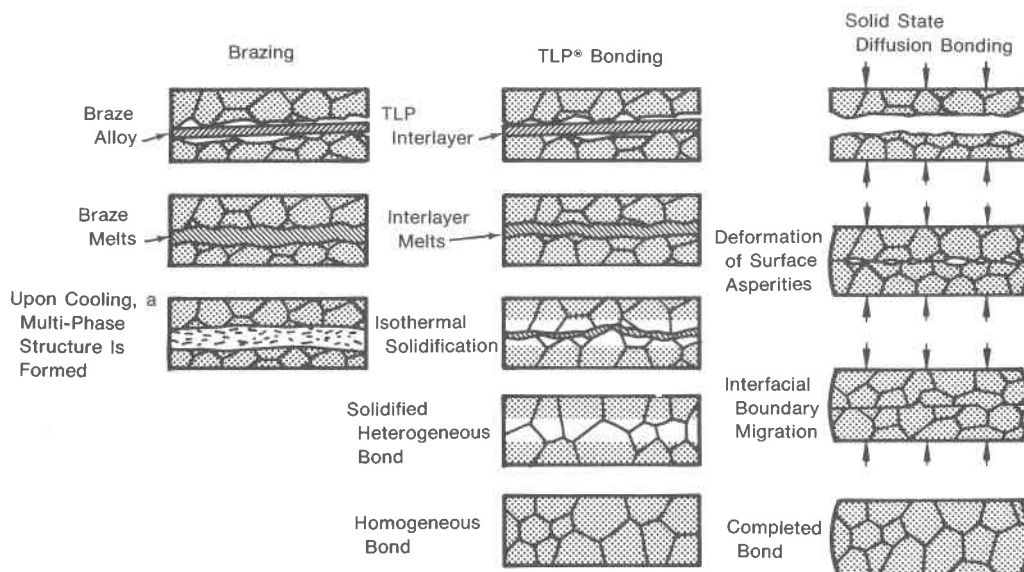


Figure 2. Comparison of Advanced and Conventional Joining Techniques

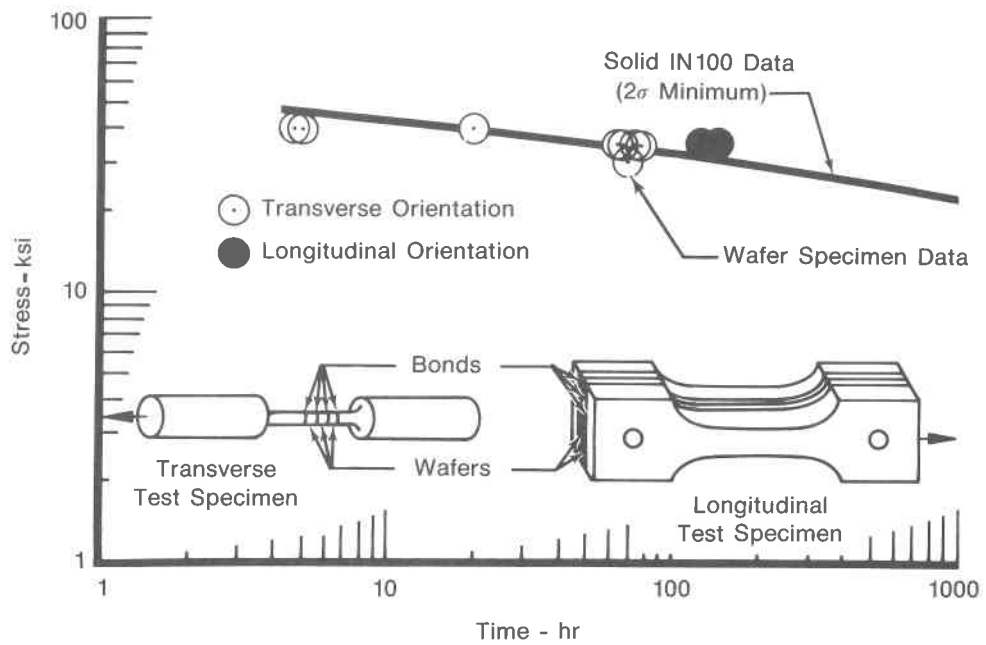


Figure 3. Stress Rupture Data for Bonded Joints

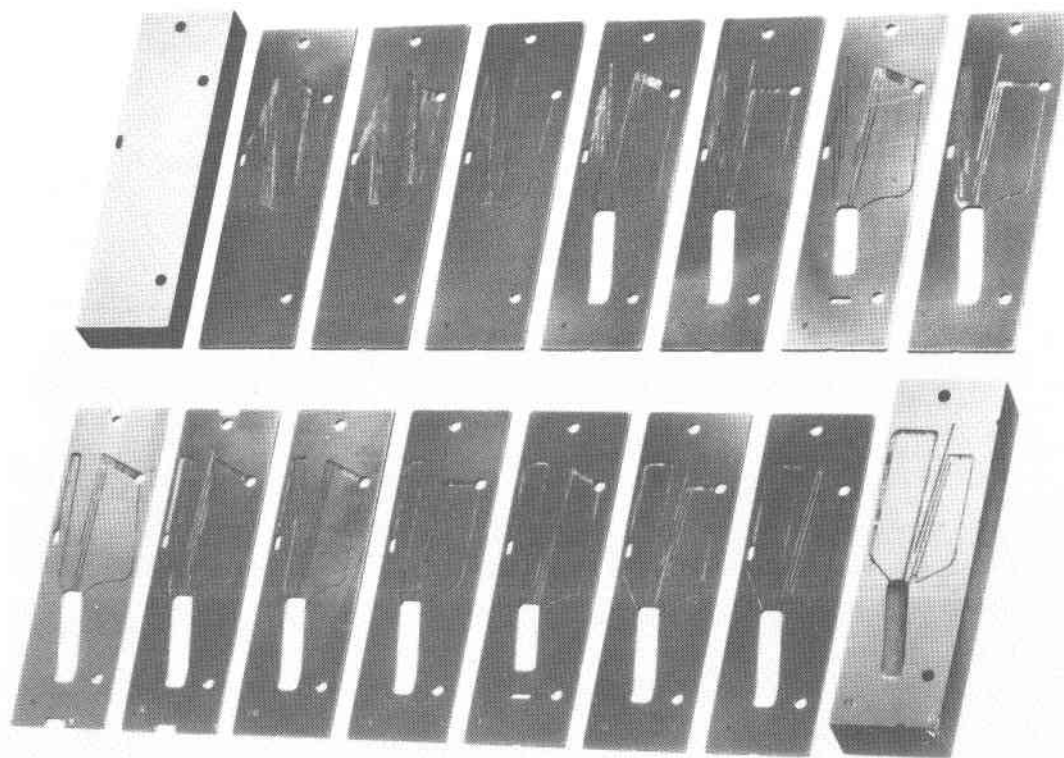


Figure 4. Wafers and End Blocks for F100 Blade

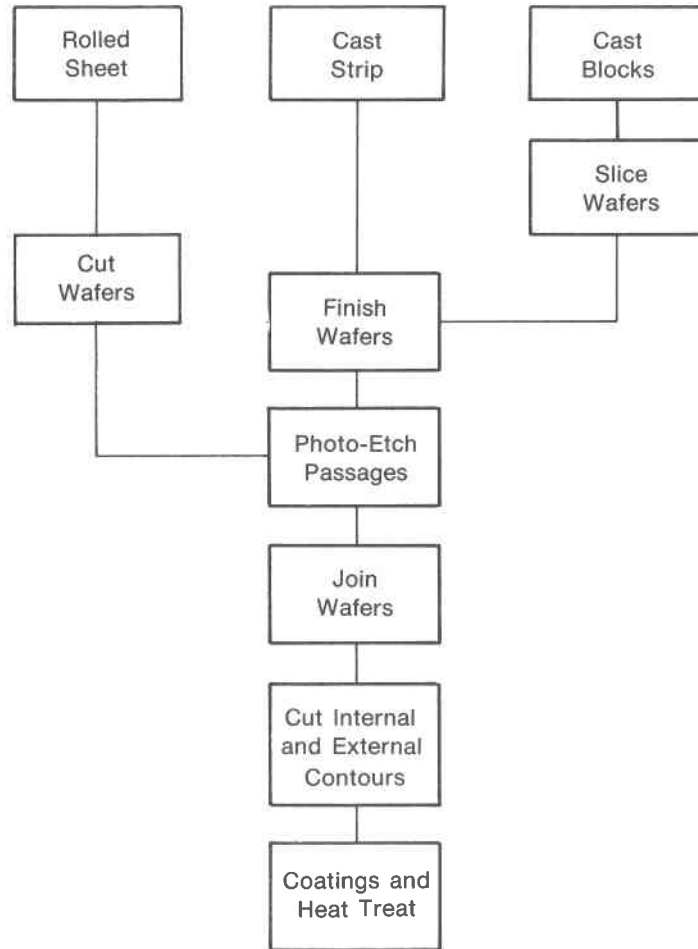
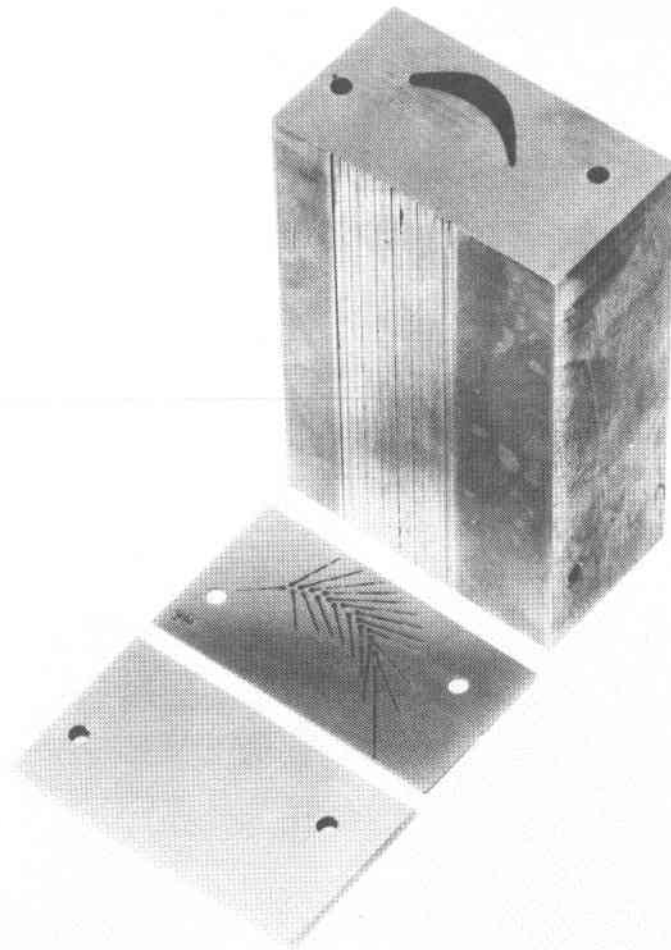


Figure 5. Wafer Airfoil Fabrication Sequence

fir-tree attachment completes the part. For experimental hardware, EDM is used for both the internal cavity and external contour machining. In production, Electro-Chemical Machining (ECM) would be utilized because of faster metal removal rates; the wafers would also be sized closer to blade final dimensions to minimize both the amount of alloy and final machining. A final machined blade is shown in Figure 7. The blade shown was engine tested for a total of 30 hours of which approximately 5 hours were at turbine inlet temperatures in excess of 2550°F. Based on thermal paint results the wafer blades showed an increase in turbine inlet temperature capability of more than 250°F over the Bill-of-Material (B/M) conventionally cast blades tested simultaneously with the same amount of cooling air. The detailed midspan surface temperature profiles are illustrated in Figure 8. This data shows a definite advantage for the radial wafer blade. Not only is the mass average temperature reduced but the peak temperature is much lower and the overall temperature profile shows much lower max-to-min thermal gradients. All of these features could be utilized to advantage in a marine/industrial blade application. The F100 blade described above illustrates the wafer airfoil fabrication process; however, the cooling design is not representative of that required for marine/industrial application since it utilizes extensive film cooling.



*Figure 6. Bonded Wafers with Internal Contour and Tip Cap Wafers*

Numerous other military aircraft wafer programs conducted under Air Force and NASA sponsorship in conjunction with Independent Research and Development (IR&D) programs at United Technologies have demonstrated both the cooling ability and basic structural integrity of the wafer concept. Blades twice have been demonstrated in the advanced F100 military aircraft engine to combustor exit temperatures over 2550°F. Vanes have accumulated 135 hours of testing in the J58 engine and have been rig tested to 3600°F. Although the engine testing to date has been highly successful, it has been of relatively short duration. Marine/industrial engine experience is totally lacking.

#### **DOE PROGRAM**

The Department of Energy was the first to explore the possibility of using advanced aircraft gas turbine engine technologies in industrial/marine engines. In a contract with DOE, Pratt & Whitney Aircraft examined the benefits of wafer airfoil cooling and advanced high-pressure compressor technology to a 15,000 shp/10 MW industrial gas turbine study engine. Emphasis was placed on durability and fuel flexibility. First-stage turbine

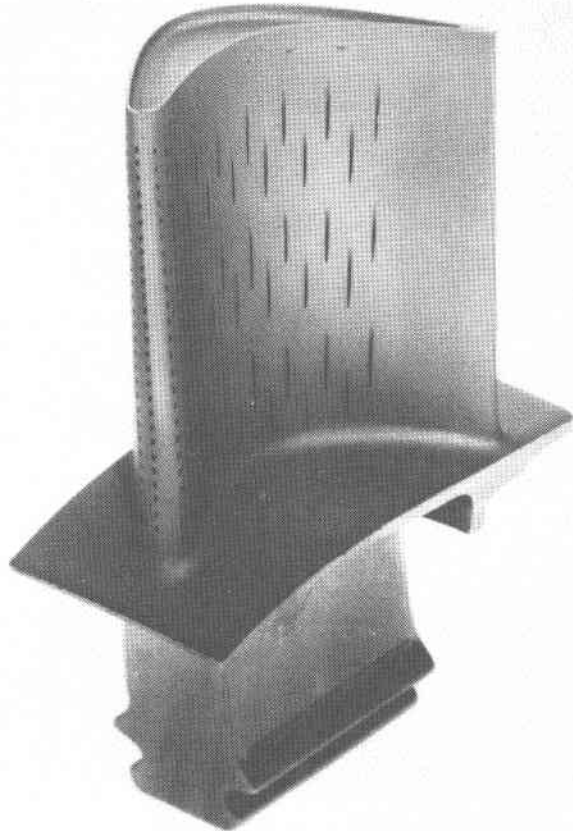


*Figure 7. F100 Radial Wafer Turbine Blade*

wafer vane and blade designs were generated for the engine and cascade tested to verify the predicted cooling. Turbine vane and blade design goals included durability requirements of 20,000 hours at a 2500°F combustor exit temperature (CET) for 10,000 normal duty cycles and 250 emergency shutdowns. Airfoil design maximum allowable surface temperatures were set at 1500°F, the suspected threshold temperature for sulfidation attack. The vane inlet hot spot temperature was established at 2970°F. This was the design gas temperature for the vane.

### **Vane Design**

The chordwise wafer vane cooling design is shown in Figure 9. Each of the 49 chordwise wafers is 0.031 in. thick. The vane was designed to be fabricated from Mar M-509, a cobalt-based alloy, with a CoCrAlY coating to resist sulfidation attack. Individual cooling air circuits were designed for leading edge, midchord, and trailing edge regions of the airfoil. Each of the three circuits is supplied by a large spanwise cavity that routes cooling air from the OD and ID ends of the vane with a low pressure loss. Although an all-convective cooling design was desired, it was necessary to provide film coverage on the suction surface near the leading edge to maintain the surface temperature below the 1500°F goal. Elsewhere the surface temperature could be controlled by impingement and convection techniques. The film-cooling holes on the suction surface were shown in previous testing to be relatively safe from plugging since they are not subject to direct impingement. Also, the holes were located forward of the gage point thereby minimizing aerodynamic losses.

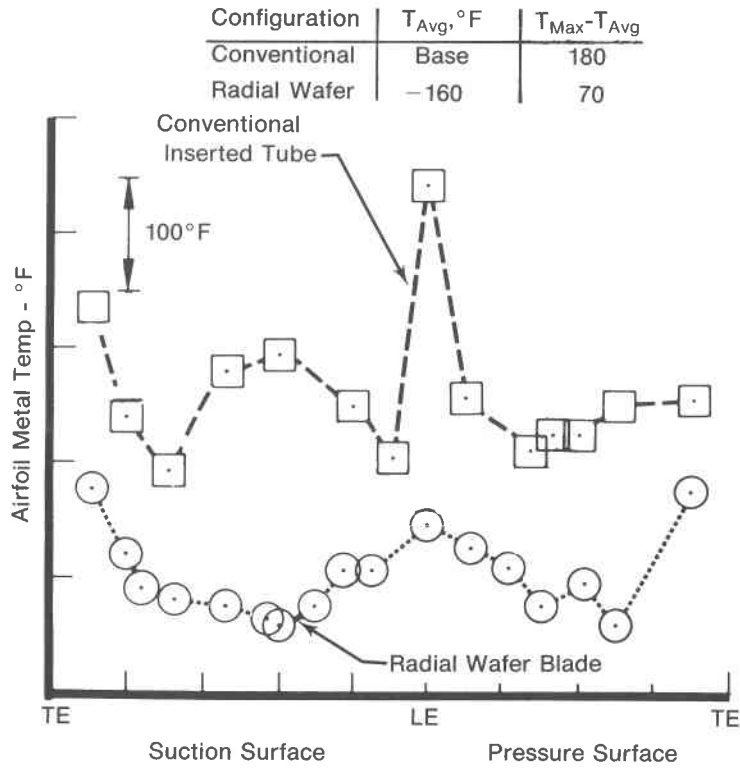


Figure 8. Improved Cooling and Reduced Thermal Gradients

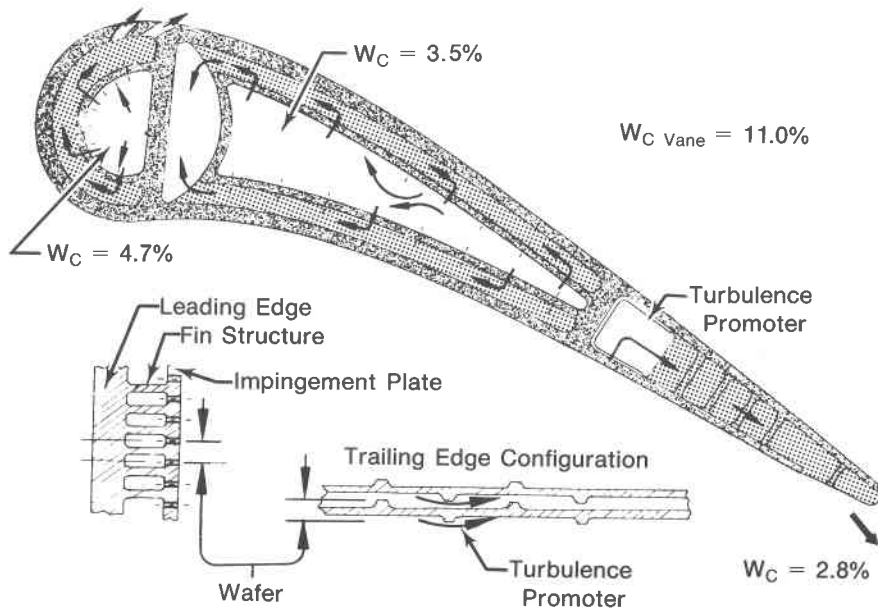


Figure 9. DOE Vane Cooling Configuration

The leading edge circuit and the pressure and suction sides of the midchord circuit are cooled by crossflow impingement augmented by internal fin surfaces formed by the wafers. In the leading edge circuit, impingement air flows around the fins between the inner wall of the airfoil and the impingement baffle plate and discharges through two rows of shaped film holes on the suction side of the airfoil. The internal fin structure connecting the inner wall of the airfoil to the impingement baffle plate increases the heat transfer area and strength of the leading edge section. After being used to cool the airfoil, the midchord coolant is routed through a spanwise cavity to the ID and OD platforms to cool these areas prior to being discharged aft of the airfoil.

The trailing edge flow circuit consists of chordwise fin surface cooling supplemented with turbulence promoters and coolant discharge at the trailing edge. The turbulence promoters are photo-etched into each fin surface with a spacing to height ratio of 10:1. Pressure side discharge of the air reduces the required trailing edge thickness and minimizes the hot spot occurring at the pressure side base region.

The vane cooling design was verified in a reduced temperature cascade rig using a test airfoil that closely simulated the engine vane design. Figure 10 shows the complete set of wafers for the cascade vane and Figure 11 shows the finished part. The slots in the vane surface are for installation of thermocouples required for heat transfer testing. The airfoil heat transfer performance was evaluated in terms of the cooling effectiveness ( $\phi$ ). Cooling effectiveness is a measure of how efficiently the airfoil cooling air reduces the external surface metal temperature. It is defined locally as the ratio of the difference between the relative inlet gas temperature and surface metal temperature divided by the relative gas temperature to cooling air temperature differential:

$$\phi = \frac{T_G - T_M}{T_G - T_C}$$

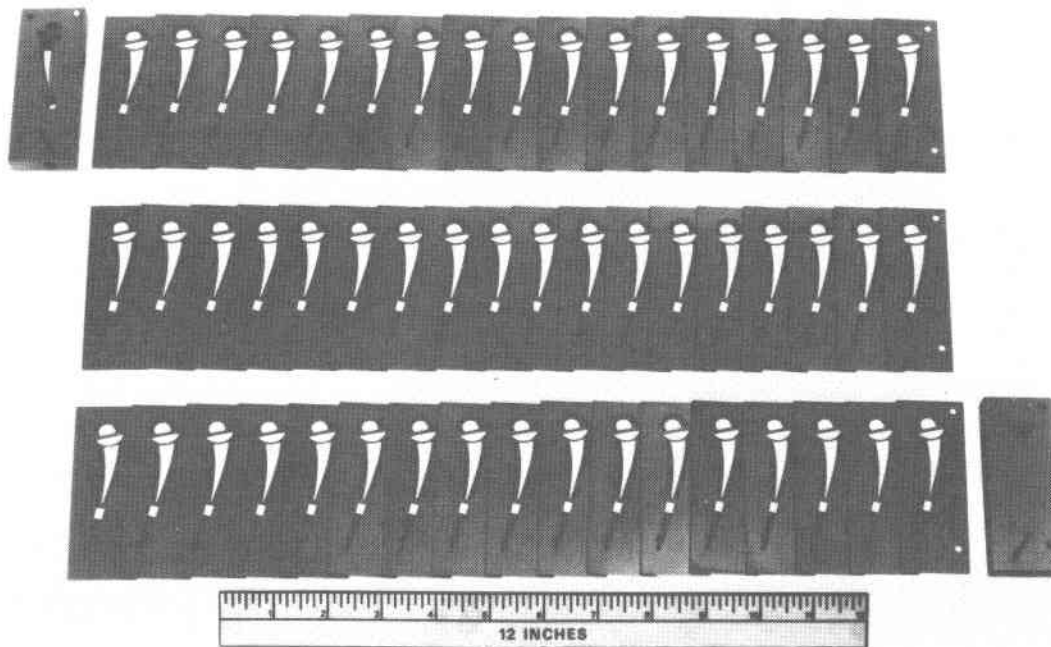
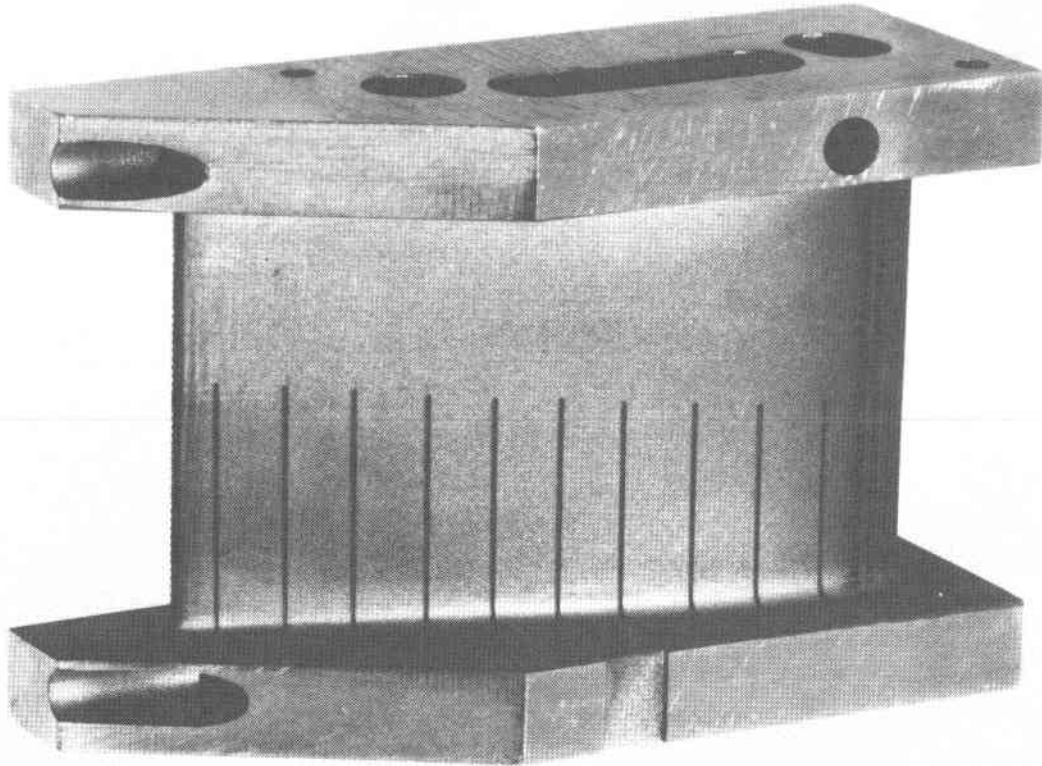


Figure 10. Test Vane Wafers and Platform Blocks



*Figure 11. Test Vane with Thermocouple Slots*

The local cooling effectiveness ( $\phi_{local}$ ) values are area-weighted and averaged to yield the average airfoil cooling effectiveness ( $\phi$ ). Figure 12 shows that the vane exceeded its design average cooling effectiveness (0.72) by achieving 0.74 at the design flowrate. Also shown for comparison is a current aircraft engine cast showerhead vane. The wafer vane exceeded the aircraft vane cooling effectiveness by 25%.

### **Blade Design**

The design of the first-stage blade (Figure 13) features radially oriented 0.065 in. wafers of INCONEL® 792, a nickel-based alloy, with a CoCrAlY coating. Sixteen wafers in the midchord section are combined with leading and trailing edge blocks to form the blade. The trailing edge section is a subassembly of two pieces joined at the mean camber surface. Similar to the vane design, three individual cooling air circuits are used to distribute the cooling air.

The leading edge flow circuit consists of a single-pass radial channel. Turbulence promoting trip strips with a spacing to height ratio of 10:1 are provided in the cooling passage to enhance the heat transfer. Coolant is supplied from the blade root and discharges at the tip.

The midchord section is cooled by etched radial passages in the airfoil wall. The coolant flow routing is identical to the leading edge circuit. Stepping of the suction side holes is provided to promote turbulence and increase cooling effectiveness in the critical blade midspan region.



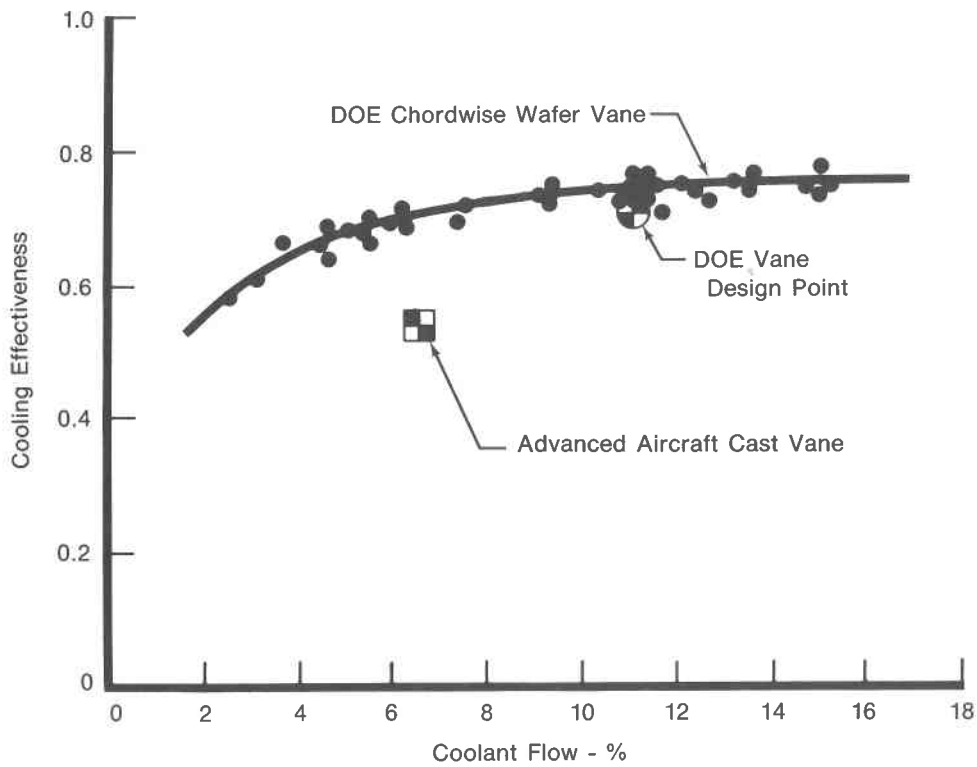


Figure 12. Chordwise Wafer Vane Cascade Test Results

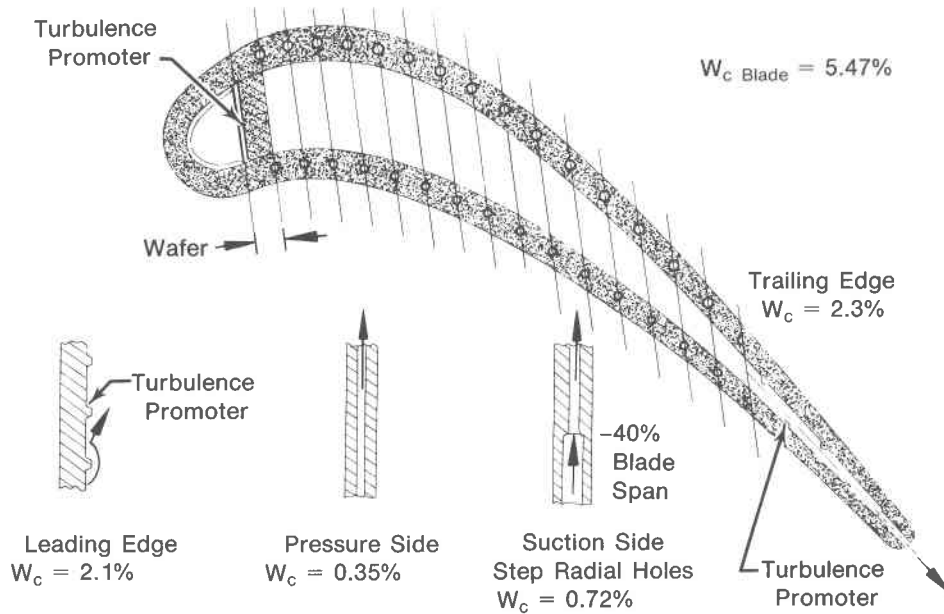


Figure 13. DOE Blade Cooling Configuration

The trailing edge circuit is similar to that for the vane. Coolant is fed from the radial midchord plenum, routed through the mean camber slot that is provided with turbulence promoters, and discharged through a row of 40 metering holes at the trailing edge.

As with the vane, a blade cascade airfoil was fabricated simulating the engine blade design. Figure 14 shows the 16 blade wafers and leading and trailing edge blocks. Figure 15 shows the finished blade airfoil fabricated for cascade testing. Figure 16 shows that blade also exceeded design expectations (0.56) by demonstrating a  $\phi$  of 0.60. Also shown on the figure for comparison is an advanced aircraft cast blade. The gain, although significant, is less dramatic for the blade than the vane for several reasons. The wafers were more than twice the thickness (0.065 vs 0.031) of those for the vane, and chordwise (as opposed to radial) wafer construction is usually more efficient since it allows more heat transfer area to be designed into the airfoil. The blade radial wafer orientation is used to allow the wafers to directly support the centrifugal loads without subjecting the bonded joints to the high loads.

This highly successful program vividly illustrated the direct application of wafer technology to industrial/marine gas turbine engines. The size of the engine studied was similar to that of aircraft engine sizes for which wafers were first made, but these sizes are much smaller than the most widely used industrial/marine engines.

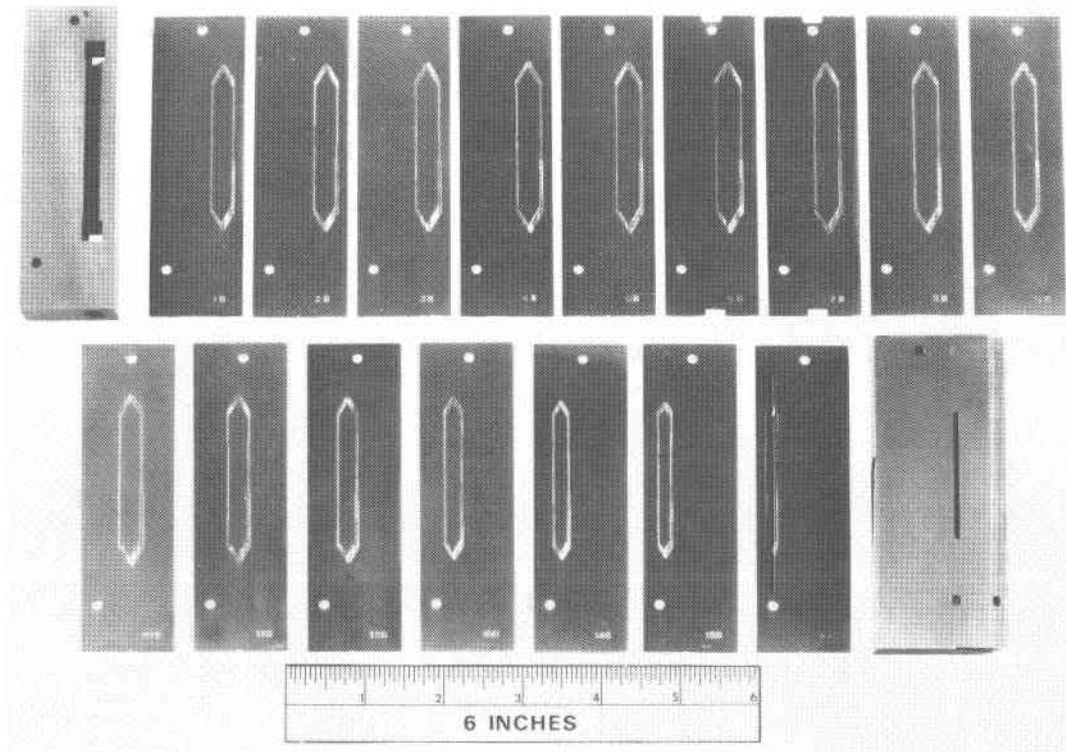


Figure 14. Test Blade Wafers and End Blocks

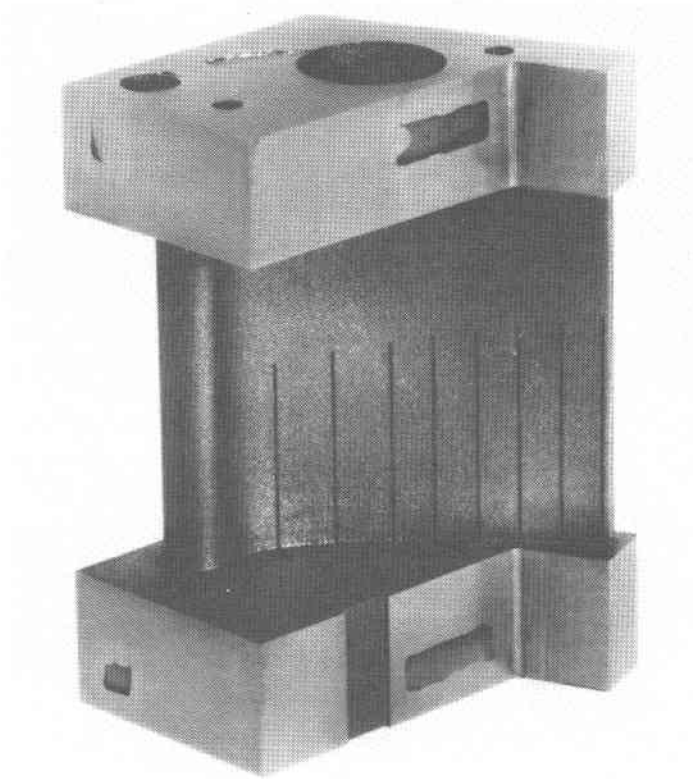


Figure 15. Test Blade with Thermocouple Slots

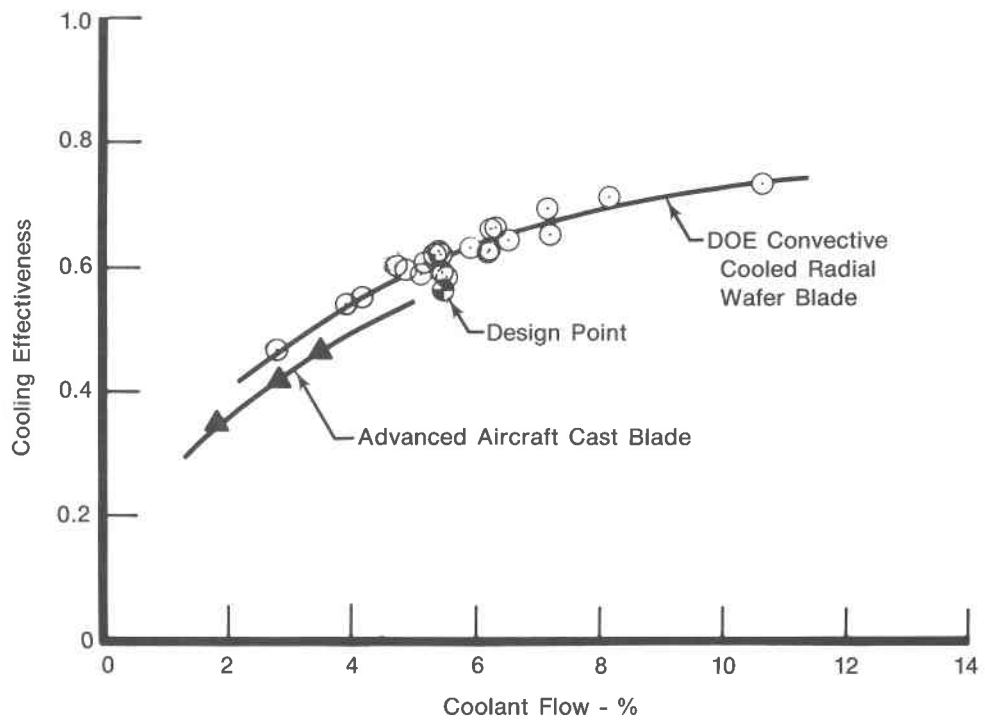


Figure 16. Radial Wafer Blade Cascade Test Results

## EPRI PROGRAM

Under a contract with EPRI, United Technologies extended wafer technology to the larger size industrial/utility gas turbine engines. The purpose of the contract was to demonstrate extended service of wafer vanes and blades in an existing industrial/utility engine to build confidence in wafer construction for eventual application to an Advanced High Reliability Engine. The contractual effort consisted of four basic tasks: (1) design of first-stage vane and blade airfoils for an FT4 engine, (2) heat transfer cascade testing including testing with heavy fuels to show the dirty fuel tolerance of the all-convective cooling designs, (3) a fabrication demonstration for FT4-size wafer vanes and blades, and (4) a scale-up feasibility study for gas turbines of the FT50 size (100 MW). The following paragraphs summarize the work completed.

### Vane and Blade Designs

The wafer vane and blade cooling designs for the FT4 are shown in Figures 17 and 18. Both are all-convective designs to enable a wide range of fuel capability and were designed to be interchangeable with bill-of-material FT4 airfoils. The chordwise wafer vane design utilizes a multiple passage leading edge, suction and pressure

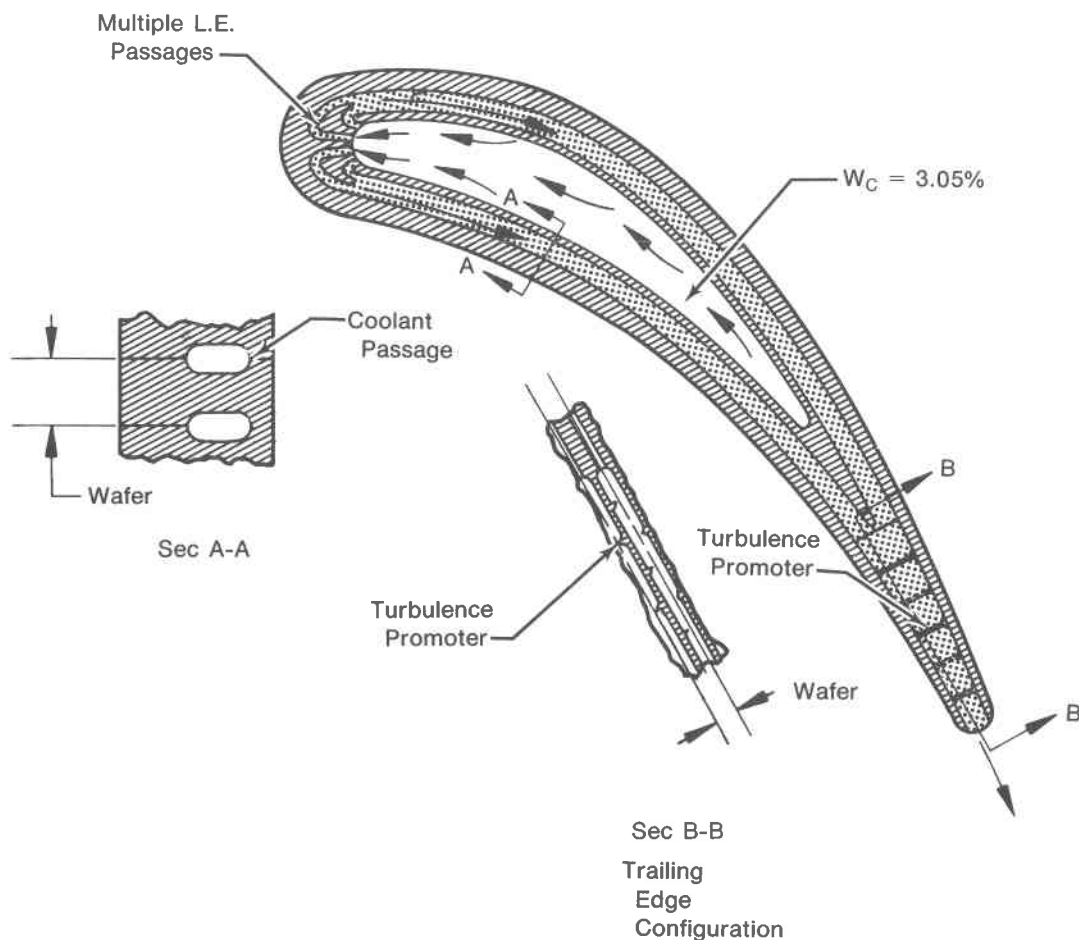


Figure 17. EPRI Vane Cooling Configuration

surface wall cooling passages and trailing edge discharge. The leading edge cooling fins provide higher flow velocities and a larger internal heat transfer area than a comparable vane without cooling fins and thereby increases the cooling efficiency in the leading edge. The trailing edge region uses trip strips to promote turbulence thereby augmenting the cooling in this region. The vane wafers are 60 mils thick, and the chordwise construction provides finned areas between wafers which again increases internal heat transfer area. In the leading edge region the ratio of internal area to external area is 4 to 1. This provides highly effective convective cooling. Using the same coolant flow rate as the bill-of-material FT4 vane (3.05%), the wafer design reduces the vane hot spot surface temperature by 185°F and has a 3.4X life factor improvement relative to the bill-of-material vane.

The radial wafer blade design (Figure 18) utilizes wafers 65 mils thick. The design is based entirely on in-wall cooling passages with the coolant entering at the root and exiting at the blade tip and trailing edge. The blade is shrouded, enabling the tip coolant discharge to be located aft of the shroud seal to utilize a more favorable and uniform discharge pressure. The leading edge passage has trip strips to improve the heat transfer. With the orientation of the wafers parallel to the leading edge, the aft wafers intersect the trailing edge providing an exit for the cooling air and trailing edge cooling. The wafer blade design will provide a 173°F reduction in hot spot temperature with an increased life factor of 3.1 at the 1.39% bill-of-material coolant flow rate.

**Cascade Test Evaluation**

Both the vane and blade life predictions exceeded the program goals. Cascade test airfoils were built simulating both the wafer vane and blade cooling designs along with a rig for testing the airfoils. The program was discontinued prior to heat transfer testing.

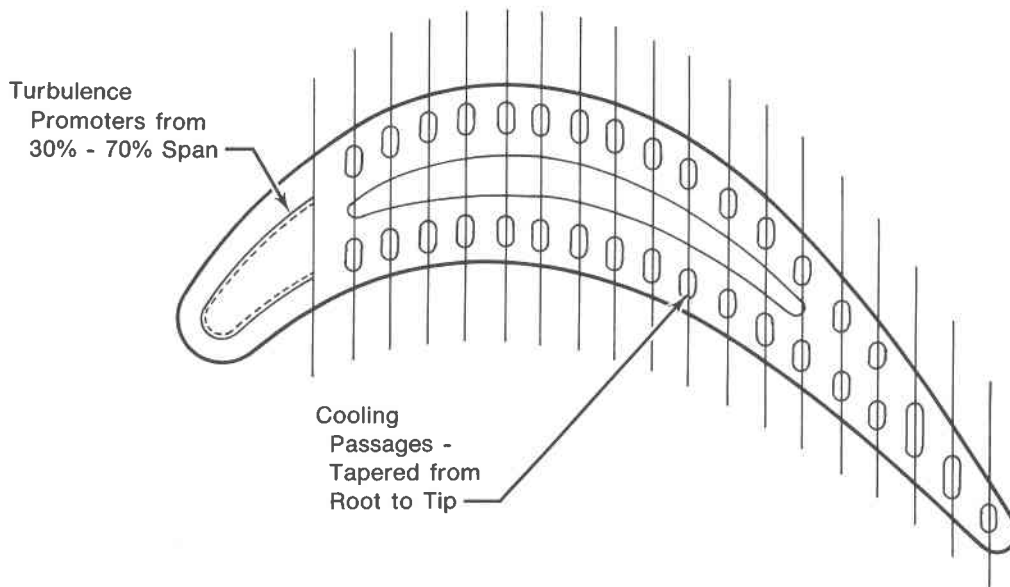
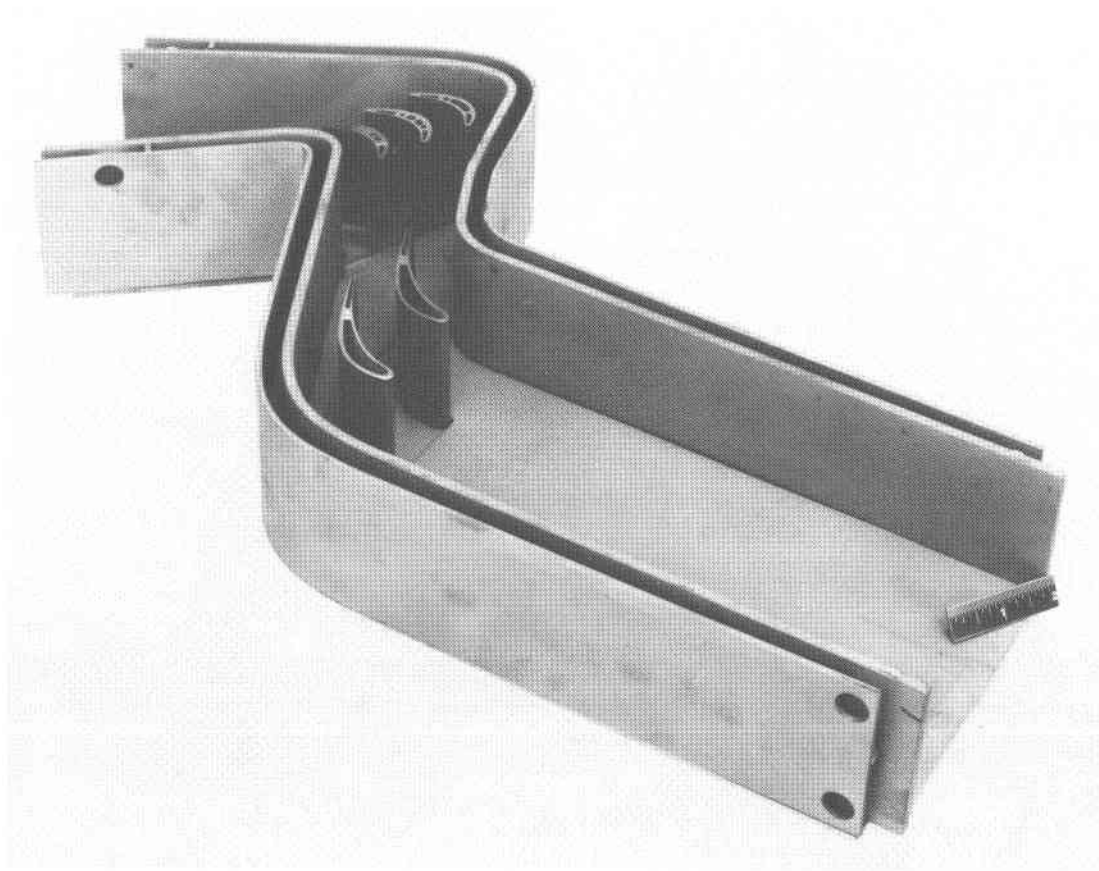
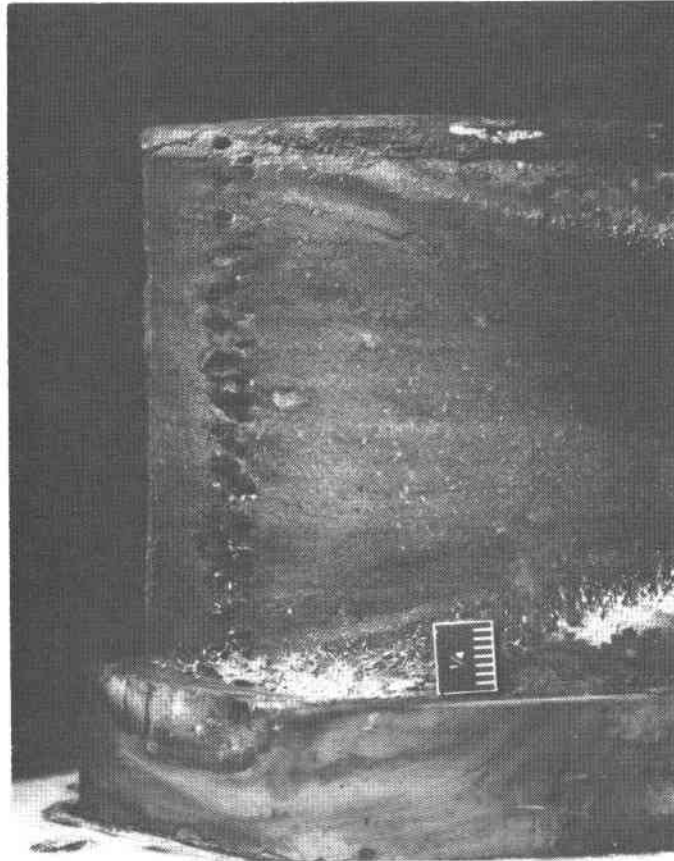


Figure 18. EPRI Blade Cooling Configuration

The corrosion erosion deposition (CED) testing was performed using simulated wafer airfoils featuring only trailing edge cooling discharge for the vanes and trailing edge and tip discharge for the blades. These airfoils were tested alongside an FT4 bill-of-material (B/M) blade, a B/M blade with added showerhead holes, and a B/M vane. Simulated number 5 fuel was the test fuel. Testing was at ambient discharge pressure and an inlet temperature of 1884°F. The combustion gas was passed through a vane and blade cascade flow rig, shown in Figure 19. Individual cooling airflows were adjusted to yield the predicted blade and vane metal temperatures for the B/M and wafer airfoils permitting an evaluation of corrosion rate differences as a function of temperature. Excessive contaminant concentration levels, aggravated by low-pressure testing, yielded excessively high rates of contaminant deposition on the airfoils. A total of 60 hours of test time was accumulated on the airfoils. The airfoils were repeatedly water washed and cleaned. Despite the artificially high rate of corrosion, it was evident that corrosion was less on the cooler wafer airfoils and that the trailing edge and tip discharge regions were not prone to plugging, whereas the B/M FT4 vane suction side film holes plugged and the blade leading edge holes plugged. Figure 20 shows the plugged B/M vane suction side film holes and Figure 21 shows the open wafer vane trailing edge.



*Figure 19. EPRI Vane and Blade Cascade*



*Figure 20. Vane Suction Side Film Holes*

### **Fabrication Feasibility Investigation**

The fabrication scale-up portions of the program focused on working with the Mar M-509 and Inconel 792 vane and blade materials and producing the larger wafers required for the FT4. The FT4 wafers have twice the area of wafers previously produced. The blade wafer is  $1.5 \times 6.0$  inches and the vane wafer is  $2.0 \times 4.5$  inches. The wafer surface flatness, parallelism and surface finish requirements needed to be maintained despite the size increase to produce acceptable joint strength. Wafer processing proceeded per Figure 5. The wafers were cut from cast blocks by a multi-wire EDM process. Ten wafers were cut at one time using thin copper wire. The rough-cut wafers were double disc-ground to final dimensions. Figure 22 shows a typical sliced and ground wafer. No difficulties were encountered in producing the larger wafers, and the industrial/utility alloys presented no special problems.

The larger wafers were successfully joined by the TLP® bonding process using previously developed nickel-based interlayer foils. Bonding trials were performed on stacks of five wafers. Following bonding, the stacks were X-rayed and cut up for metallurgical examination. A bond coverage of 96% minimum with no single void exceeding 5 mils in diameter was considered acceptable; all the specimens met the criteria.

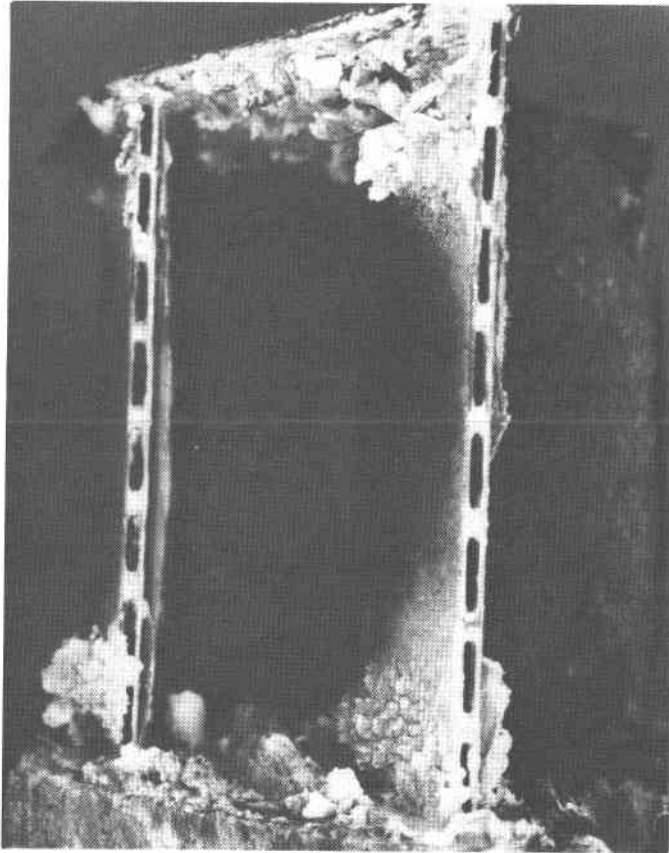


*Figure 21. Wafer Vane Trailing Edge*

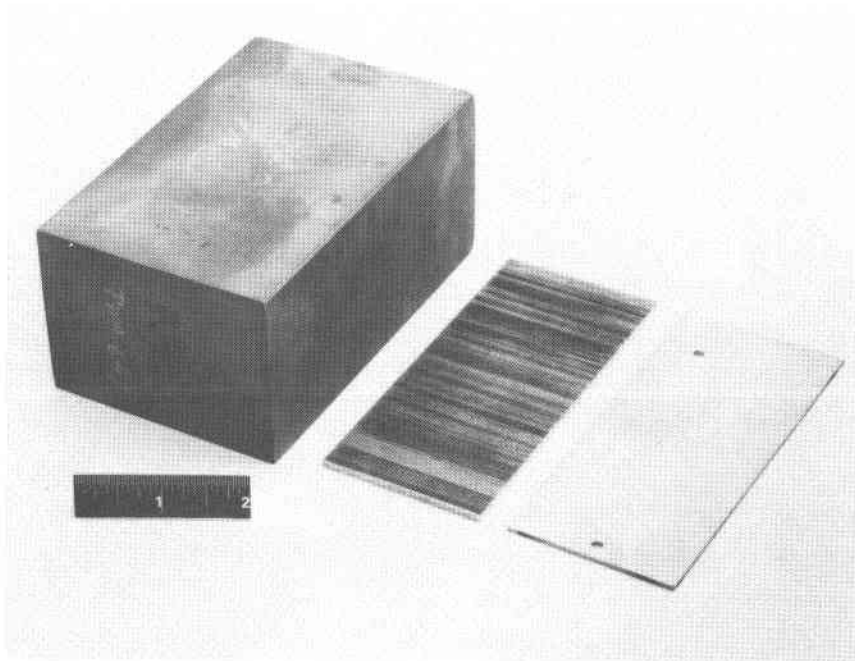


*Figure 22. Vane Wafer Slicing and Grinding*



Another study evaluated the impact of a further size increase to wafers for a 100 MW class industrial engine (FT50 size). The study showed no fundamental scale-up problems with the wafer construction technique that could not be resolved during a normal development cycle. Analytical work showed that the cooling advantages of wafer construction could be extended to these larger airfoils.

### **WAFER ALLOYS**

Wafers have been produced from a wide variety of raw material forms: (a) wrought sheet, (b) individual wafer castings, (c) sliced cast blocks, (d) cast strip, (e) sliced wrought powder metal extrusions, and (f) wrought powder metal rolled stock. From a cost standpoint, sheet alloys can most easily be converted into wafers. For cast alloys, cast strip is the most economical. Wafers have been produced from the following alloys:

1. Directionally-Solidified IN 100
2. Directionally-Solidified Mar M-200
3. Directionally-Solidified INCO 792
4. Mar M-509
5. Astroloy Sheet
6. Rolled IN 100
7. Inconel 600 Sheet (as rolled)
8. IN 100
9. Extruded Rapid Solidification Rate (RSR) Alloy 143
10. Extruded RSR 185
11. Extruded and Rolled RSR 185

INCO 792 and Mar M-509 are commonly used for industrial/marine applications. With the exception of the RSR alloys, all of the above alloys have been successfully joined using TLP® bonding. Solid-state diffusion bonding is the preferred joining method for the RSR alloys (see Figure 2).

Based on the alloys from which wafers have been produced it is apparent that wafer airfoils can be produced from any nickel- or cobalt-based superalloy being used or being considered for turbine blade and vane use. The most promising future nickel-based superalloys being developed at United Technologies are the RSR alloys.

### **RSR Powder Processing**

Under sponsorship of the Defense Advanced Research Projects Agency and the Air Force (AFML), Pratt & Whitney Aircraft has developed Rapid Solidification Rate Powder Processing which promises to revolutionize alloys available for gas turbine engines. RSR Powder Process alloys exhibit increased strength, increased temperature capability and increased life, with reduced dependence on strategic elements such as cobalt and chromium. RSR powder is produced by flowing molten metal onto a disc spinning at approximately 24,000 rpm and then cooling the atomized metal at rates on the order of 1,000,000°F per second. This rapid cooling allows the molten metal to be frozen into a supersaturated solid solution, providing alloy compositions which cannot

be produced by other means. This Pratt & Whitney Aircraft developed process also produces a highly uniform powder product which meets or exceeds all standards established for superalloy powder quality. Further details on the process and powder are available in Reference 1 or in a paper to be presented at this conference by E. C. van Reuth.

To convert the RSR powder into a form useful for the production of turbine components it must be compacted and worked. Powder consolidation is achieved in a vacuum by uniaxial loading to about 25,000 psi and at temperatures in excess of 2000°F. Effective working of the alloys has been achieved by such conventional processes as extrusion, rolling or forging. Subsequently, the alloys can be heat treated to an aligned grain structure by zone annealing at temperatures on the order of 0.9 of the melting point temperature.

Diffusion bonding is the preferred joining method for RSR alloys. Since the RSR alloy product consists of numerous small pieces of powder diffusion bonded together, it is not surprising that the alloy would be amenable to diffusion bonding.

#### **Application of RSR Alloys to Wafer Airfoils**

A group of RSR alloys which are potentially applicable to industrial/marine use are currently under DARPA/AFML development as aircraft turbine vane alloys. The most interesting feature of this group is that the alloys have exhibited outstanding oxidation and corrosion resistance, as shown in Figure 23, when compared with INCO 792 and an advanced single-crystal alloy. These alloys have high percentages of aluminum ( $\approx 7\%$ ) with no cobalt. The elimination of cobalt is especially of note because of the cost and scarcity of cobalt. Rapid solidification rate technology offers the potential to lessen our dependence on cobalt, and various other strategic elements, without jeopardizing hardware capability. As a wrought alloy capable of being rolled into sheet or plate form, RSR Powder Process material is ideal for wafer application. With the potential of combining the improved RSR vane alloy properties with the improved cooling ability of wafer airfoils, the possibility exists of producing airfoils far superior to present cast airfoils for industrial/marine applications.

#### **Low Cost Vane**

It is anticipated that the most cost effective method of wafer fabrication will feature the direct use of rolled sheet material in the as-rolled condition. It would further be desirable to use a commercially available rolled alloy. In the last five years a number of new wrought nickel- and cobalt-base "Super" alloys have become available. Several of these alloys have the potential for direct application to a chordwise wafer vane for industrial/marine turbine use. Using rolled sheet directly eliminates the slicing and finishing steps in Figure 5 for cast wafers and reduces raw material requirements which account for a large portion of the vane costs. High machining rate processes, such as coining for wafer details and production etching, should be done in the sheet form. The simplicity of the wafer shape lends itself to high production rate processing. Final machining would be accomplished by ECM fast metal removal processing. Vanes fabricated using such high production rate processing methods could be produced at lower cost than present cast vanes.

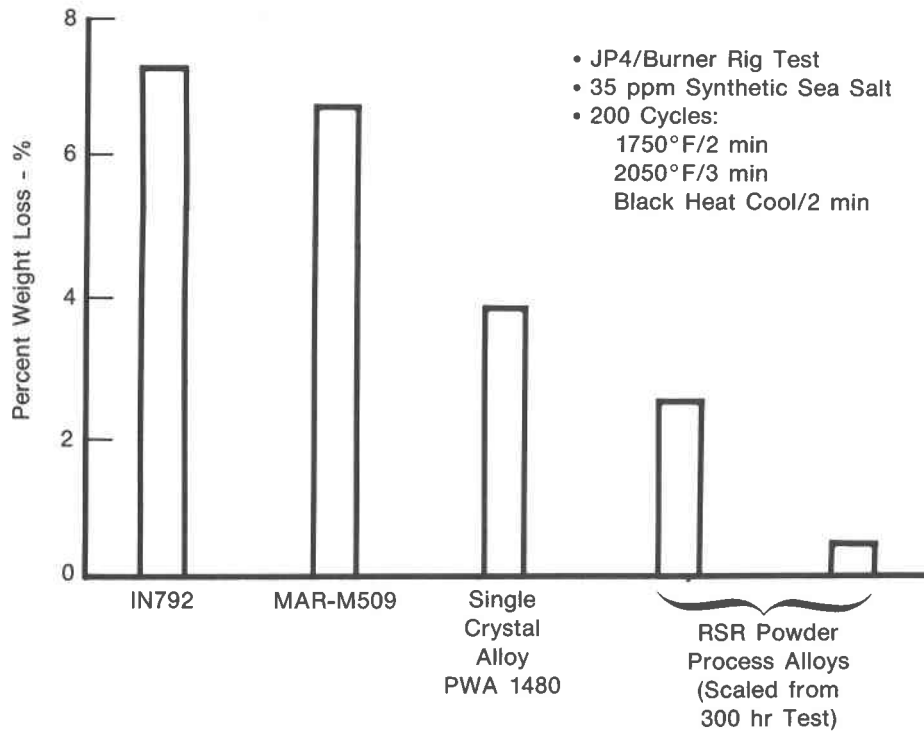


Figure 23. Cyclic Hot Corrosion Test Results

A screening of commercially available wrought alloys for direct wafer application is warranted for potential industrial/marine exploitation. Oxidation, sulfidation, and structural characteristics need to be investigated as well as the alloy joining properties and retention of strength properties through the joining and heat treatment cycles. The alloys' ability to be coated and the coating life would be evaluated. A typical industrial engine application would need to be selected for optimization and development purposes. The resulting wafer vanes would feature superior cooling capabilities, lower acquisition cost, and be tolerant of "dirty" fuels.

### CONCLUSIONS

The application of wafer construction techniques to turbine vane and blade airfoils offers a number of unique advantages over conventionally cast airfoils for high temperature industrial/marine environments. Wafer construction enables vanes and blades to be designed with "dirty" fuel tolerance by employing all-convective cooling designs (no surface cooling holes) while retaining high levels of cooling efficiency. Wafer construction allows the incorporation of intricate cooling designs featuring the creation of large internal cooling surface areas and coolant flow distribution control yielding high average effectiveness levels together with flat airfoil surface metal temperature profiles. Flat profiles reduce stress-causing temperature gradients and prolong the life of corrosion-resistant and/or thermal barrier coatings. Wafers have been produced from a wide variety of turbine alloy types and forms. The inherent flexibility of wafer airfoil construction in conjunction with the broadened range of corrosion-resistant alloy candidates available for airfoil construction afforded by the wafer technique warrant the further investigation of this unique fabrication method for potential industrial/marine

applications. Unsolved questions relative to production costs and long-term durability, reliability and maintainability need to be resolved in an ongoing R&D effort. The program started under DOE and EPRI should be continued to further refine and develop the potential afforded by wafer construction to future industrial/marine engines.

#### REFERENCES

1. George, D. B., B. T. Brown and A. R. Cox, "The Application of Rapid Solidification Rate Superalloys to Radial Wafer Turbine Blades," AIAA Paper 79-1226, AIAA/SAE/ASME 15th Joint Propulsion Conference, Las Vegas, Nevada, June 1979.
2. Sellers, R. R., D. E. Dahlberg, and G. S. Calvert, "New Approaches to Turbine Airfoil Cooling and Manufacturing," AIAA Paper 77-948, July 1977.
3. Schweitzer, J. K., and B. T. Brown, "DOE/P&WA Program for Demonstration of Advanced Industrial Gas Turbine Cooling and High Pressure Compressor Technology," Proceedings of the 12th Intersociety Energy Conversion Engineering Conference, Washington, D.C., 28 August 1977.
4. Brown, B. T., J. K. Schweitzer and J. W. Fairbanks, "Advanced Industrial Gas Turbine Cooling and High Pressure Compressor Technology," Proceedings of the 13th Intersociety Energy Conversion Engineering Conference, San Diego, August 1978.
5. Eckler, T., B. Manty and B. Brown, "Advanced Photoengraving Techniques for Nickel Superalloys," presented to Photo Chemical Machining Seminar, Anaheim, 27 February 1978.

Session VI

CERAMIC COATINGS AND MONOLITHIC  
CERAMICS

PROBLEMS ENCOUNTERED IN DEVELOPING AND USING  
THERMAL BARRIER COATINGS ON DIESEL ENGINE COMPONENTS

Ingard Kvernes  
Central Institute for Industrial Research  
Oslo - Norway

Users of larger diesel engines and gas turbines are facing poorer qualities of residual fuels. These contain high levels of impurities and complex molecules that cause hot corrosion wear and thermal load. Due to general cost increase and the cost differential of fuel types, the shipowners today operate the diesel engines on residual fuels. This has, however, caused increased damages of engine parts.

MAINTENANCE COSTS FOR DIESEL ENGINE COMPONENTS

Exhaust valves are today among the most cost effective parts in medium as well as in large bore diesel engines. Examinations which have been carried out show that maintenance of the exhaust valves in large bore engines amounts to about 60% of the total maintenance cost of the main engine (1). The maintenance costs are high for the following components:

- \* exhaust valves
- \* pistons
- \* liners
- \* cylinder covers, and
- \* fuel pump valves

Measures to reduce these problems will only be successful if a detailed understanding is available of how the components deteriorate. In this respect a good knowledge of fuel oil qualities and alloy qualities is necessary.

The following counter measures may be carried out:

- \* remove the aggressive impurity from fuel oil
- \* improve the combustion quality by using combustion improver or increasing the combustion temperature by using thermal barrier coatings
- \* change design of the components in order to reduce the metal temperature
- \* introduce cooling of the engine components
- \* improve the corrosion and wear properties of the alloy

Only the coating aspects will be considered and discussed in this report.

#### DEVELOPMENT OF COATINGS

The selection of materials for coatings depends on a number of factors: the base alloy, the chemical and physical properties of the ambient combustion gases and condensations of liquid salts, temperature in the combustion chamber, and mechanical load on the components. These inter-relationships are illustrated in Fig. 1. It is shown that the properties of the base alloy, the coating system and the environment have to be mutually adjusted in order to obtain a practical system.

The material properties which are relevant for high temperature diesel environment are Young's modulus, creep/fatigue, thermal shock parameter, thermal coefficient of expansion, hardness, fracture toughness, thermal conductivity and corrosion/oxidation resistance. Results have shown that it is not sufficient to look at the chemical composition of the coating powders. The spraying parameters and the physical properties of the powders have to be adjusted to each other in order to obtain a satisfactory microstructure of the coating. This is illustrated with the loop in Fig. 2 (2).

The three probably most important advantages of the plasma-sprayed coatings are:

- \* fine grain size or partly amorphous materials
- \* the presence of porosities and voids in a variety of size distributions and configurations
- \* the possibility of producing non-equilibrium phases and non-conventional phase combination

This report focuses on fuel oil contaminants, deposits and corrosion mechanisms mainly of coated exhausted valves, but also on coated guide vanes tested in small gas turbines. The goal of the work was to gain experiences from operating conditions in order to be able to obtain microstructure in the coating with superior properties. The engine tests are presented at the end of this report. Both laboratory and diesel engine tests were carried out. Most of the results discussed were obtained in the Scandinavian and the DOE research programs (3,4).

#### RELEVANT MICROSTRUCTURES AND PROPERTIES OF COATINGS

The properties of plasma spray powder as well as the deposition parameters affect the resultant coating properties. Minor variation in the chemical composition of a given plasma powder may have a pronounced effect on the sprayability of the powder.

### ENVIRONMENT/ APPLICATION

- Combustion gases (flow rate, chemical composition)
- Temperature 20 -1100°C and temperature cycling
- Geometry
- Erosion
- Abrasion



### BASE ALLOY PROPERTIES

- Mechanical, physical, chemical and thermal properties
  - thermal expansion
  - chemical composition
  - thermal conductivity
- Microstructure etc.
- Surface finish

### PROTECTION SYSTEM/COATING

- o Mechanical, chemical, physical and thermal properties
  - high temperature stability
  - chemical composition
  - adherence
  - composite coating
  - thermal shock

Figure 1. The selection of coating materials must be adjusted both to the properties of the environment and the base metals.

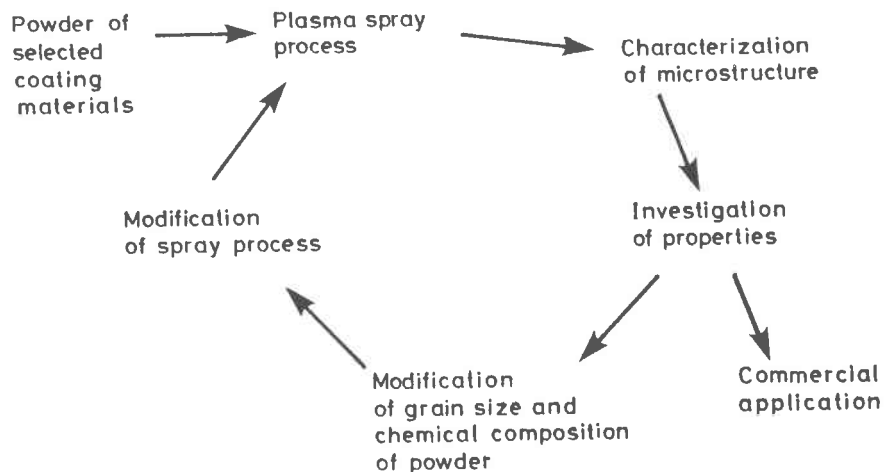


Figure 2. An advanced coating depends on a good coordination of various factors.



The coating quality depends further on the spray unit. Based on our experience the requirements of the spray unit are that it must

- \* be easy to operate
- \* produce a concentrated flame (as shown in Fig. 3)
- \* produce a high powder velocity

Commercial uses of coatings require reproducible microstructures. This has prompted the development of computer controlled spraying operation. Other important advantages of using robots are that they also remove much of the operator strain, increase the productivity, product reliability, and process safety.

Besides the chemical composition and the process parameters, the powder grains must have a narrow size distribution range. In addition, a concentrated plasma flame is necessary in order to obtain completely melted particles.

Two - or more component powders should be chemically pre-reacted in order to avoid separation of the powder components in the flame giving an inhomogeneous coating.

The powder specifications must include the following (5):

- \* chemical composition and homogeneity
- \* grain size
- \* shape
- \* flowability
- \* melting point
- \* level of moisture and other contaminations

Today there is a lack of information on the relationship between the microstructure and properties of the coating and the powder quality, the spraying parameters and heat treatments.

The microstructure of the plasma deposited oxide coatings is quite complex. Changes in pore sizes and shapes, chemical homogeneity, particle to particle bond strength, etc. influence the microstructure and thereby the properties of the coatings. The operational tests which have been carried out reveal that the pores usually present in plasma sprayed coatings grow when the coating is heated.

The corrosion mechanisms described by Levine is confirmed (6). As reported by Levine it is believed that liquid salts enter the open pores and penetrate the coating when the temperature exceeds the melting point of salt. Inside the pores

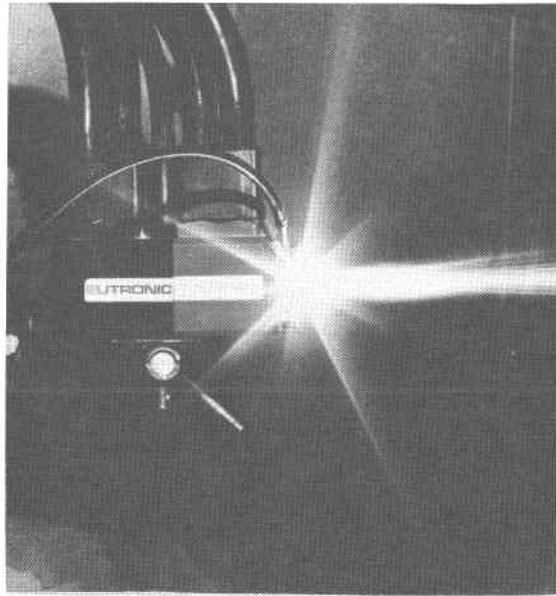


Figure 3. A concentrated plasma flame with oxide particles.

the salt may react with components in the coating. The mechanisms may involve the infiltration of molten salts into the pores and microcracks of the plasma sprayed ceramic coating and thereby greatly decrease its thermal stress resistance. A completely dense coating will reduce the corrosion attack. But without any controlled microcracks the shock resistance will be reduced. The experiments in the Scandinavian research program have shown that a ("Cr") chromium-enriched metal coating gave excellent protection against high temperature corrosion. A 1000 hrs test of an exhaust valve coated with Cr operated in an engine shows no attack at all.

Dense and chemically homogeneous microstructure is essential in the production of advanced coatings. Figs. 4a-d show the microstructure of MgO-stabilized  $ZrO_2$ , modified  $ZrO_2$ ,  $Al_2O_3$ , and  $Al_2O_3 + ZrO_2$ . Note the lamellar and dense structure formed as a result of the deposition of individual particles. The lamellar structure is important for ductility of the coating. The Zr-distribution in the cross section is superimposed in the micrographs in Fig. 4d.

The properties of stabilized  $ZrO_2$  and NiCrAlY coatings are given in Table 1. All properties are measured on plasma sprayed samples as sprayed conditions.

Table 1.  
Properties of plasma sprayed coatings.

Coating	Hardness HSR 15T	Bond strength N/mm <sup>2</sup>	Fracture toughness $K_{1C} = [N/mm^{3/2}]$	Thermal expans.coef. $\times 10^{-6} \text{ } ^\circ\text{C}$ 20 - 900 $^\circ\text{C}$	Thermal conductivity $\lambda = [w/m^\circ\text{K}]$
ZrO <sub>2</sub> +MgO	> 94	20 - 25	70 - 100*	9,0	1,5 - 2
ZrO <sub>2</sub> +CaO	> 94	25 - 35			
NiCrAlY	> 87	50 - 65			

\* $K_{1C}$  by 0,4 mm thick coating

It is seen that a  $\sim 0,1$  mm NiCrAlY bond layer is of advantage - particularly for coatings thicker than 0,5 mm.

In order to avoid thermal cracking during spraying of layers - particularly coatings thicker than about 0,4 mm, it is necessary to keep the coating at a constant temperature level during spraying. The first pass should not be cooled due to the high cooling effect from the base metal. The next pass must, however, be strongly cooled.

A dense microstructure of a CaO-stabilized zirconia layer produced under strong cooling is shown in Fig. 5a, and thermally cracked coating is shown in Fig. 5b. The regularly formed cracks in the coating structure of Fig. 5b are typical for thermal stresses. The cracks relieve the residual stresses and the thermal shock resistance is increased. The samples shown in Fig. 5a have been thermal cycled in combustion at 900  $^\circ\text{C}$  for 200 hrs without cracking.

#### FUEL OIL CONTAMINANTS CAUSING PROBLEMS

Ash-forming materials may be present in a fuel as oil soluble organometallic compounds, as water soluble salts in water dispersed in the fuel or as solid contaminants. The most common ash-forming elements which can be present are aluminium, calcium, iron, magnesium, nickel, potassium, sodium, silicon and vanadium. Ash-forming materials are present to varying degrees in crude oils depending on their geographical origin. They are concentrated in the residual fractions during the refining process, leaving the light distillates practically free of contaminants. However, ash-forming materials may also be introduced later by contamination with salt water or with other petroleum products during transportation and storage.

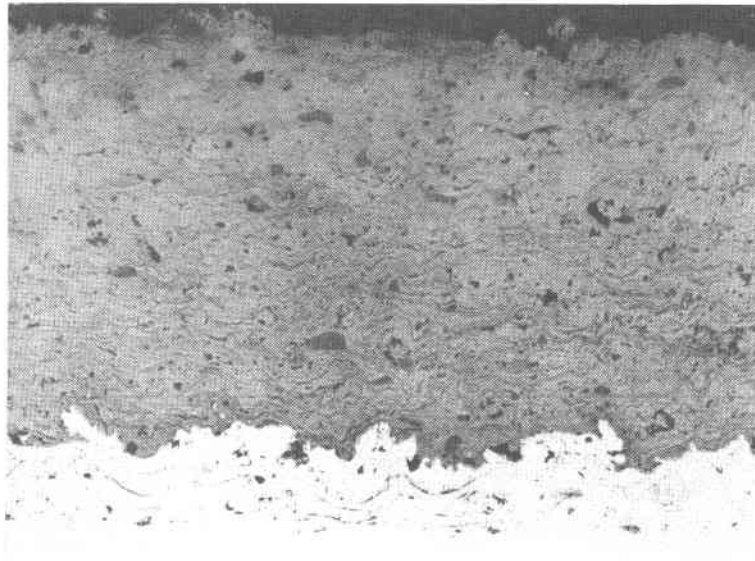


Figure 4a.  $\text{MgO} + \text{ZrO}_2$ . (200 x)\*

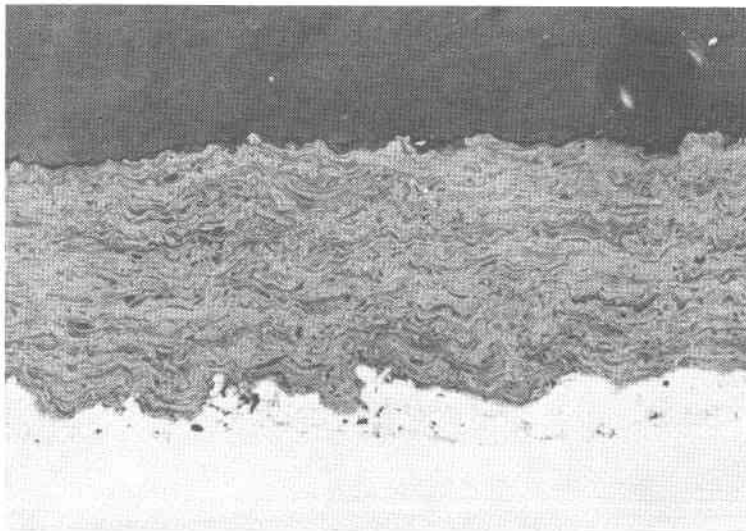


Figure 4b. Modified  $\text{ZrO}_2$  powder. (200 x)\*

Figures 4a-b. A dense microstructure of coatings based on Zirconia powder.

\*Please note that the illustration(s) on this page have been reduced 10% in printing.

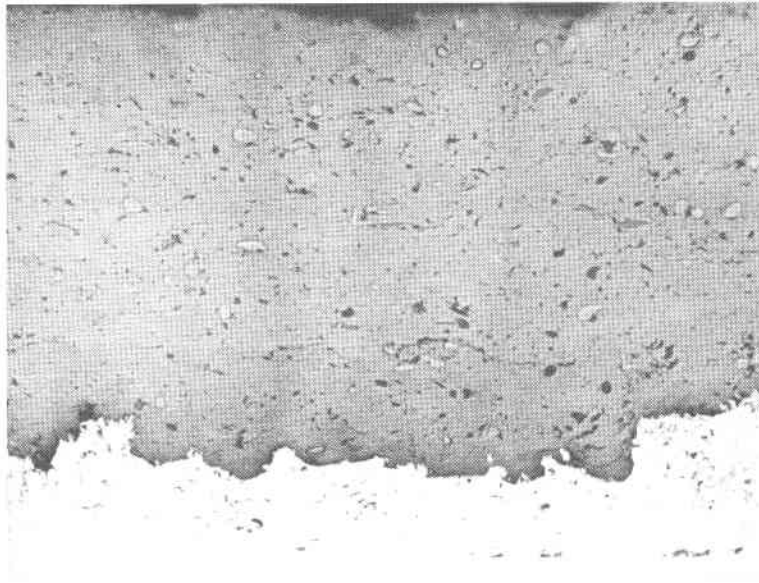
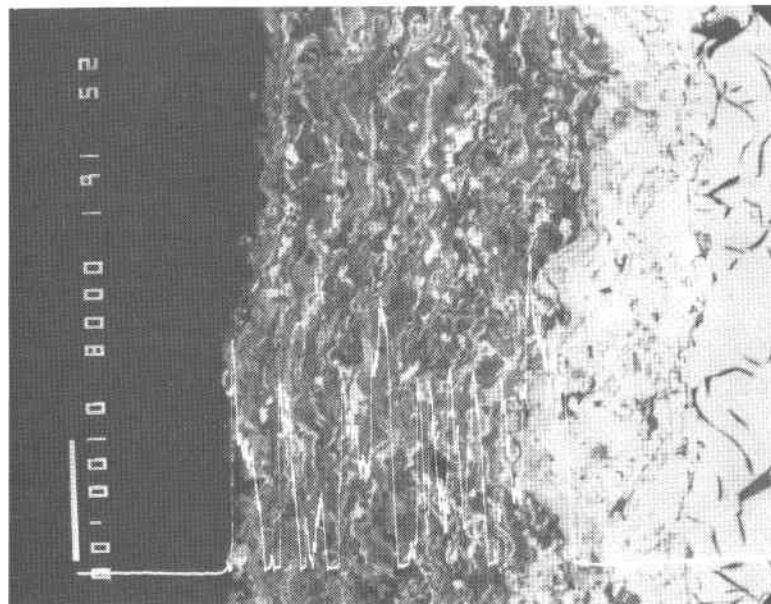


Figure 4c.  $\text{Al}_2\text{O}_3$ . (200 x)\*



Zr, La $\beta$

Figure 4d. Modified  $\text{Al}_2\text{O}_3$  powder.

Figures 4c-d. A dense microstructure of a coating based on Alumina powder.

\*Please note that the illustration(s) on this page have been reduced 10% in printing.

The experience gained in operating diesel engines has shown that some of the ash-forming substances that may be present in the fuel can lead to severe corrosion problems. These are most acute for residual fuels, which contain larger quantities of the troublesome substances than diesel oil. Wear causing substances will be the main problem when using residual and synthetic fuel oils in the future.

#### FORMATION OF DEPOSITS ON THE SURFACE DEPENDS ON THE SURFACE MATERIALS

##### Experiments

The diesel engine was operating during the various tests on diesel and heavy fuel oils. The load on the engine was up to 110%. An example of a load diagram during 24 hrs operation is shown in Fig. 6. The tested valves mainly consisted of austenitic steel, Nimonic with and without coating of stabilized zirconia or chromium on the valve fillet and head top. The seat faces had an overlay of Stellite or Deloro Alloy 60 materials.

##### Results

The deposits on steel valves consisted of at least two layers. The outer layer has a drop-like appearance as shown in Fig. 7.

The droplets mainly consisted of  $\text{Na}_2\text{SO}_4$  with some  $\text{CaSO}_4$ ,  $\text{SiO}_2$ ,  $\text{Al}_2\text{O}_3$  and sodium vanadates. The inner layer consisted of sodium vanadates (sticktion point  $\sim 400^\circ\text{C}$ ) of varying compositions,  $\text{Na}_2\text{SO}_4$ , some  $\text{CaSO}_4$ , and sulfides and oxides of the alloying elements.

On Nimonic 80A valves the deposits consisted only of a few droplets on the valve fillets. The deposits on the Nimonic compared to the deposits on steel valves is characterized as follows:

- \* an increased amount of deposits
- \* no defined border between the outer and inner layer
- \* the overall concentration of sulfates ( $\text{Na}_2\text{SO}_4$ ) in the deposits is higher

The analysis of deposits on Cr and  $\text{ZrO}_2$  coated valves show that they mainly consisted of  $\text{Na}_2\text{O} \cdot \text{V}_2\text{O}_4 \cdot 5\text{V}_2\text{O}_5$ , and probably of  $\text{Ca}_{0.7}\text{V}_2\text{O}_5$ . The valve plates had in addition  $\text{CaSO}_4$ . The chemical analyses of the fuel oil used in this test is shown in Table 3 (POR 380 or 230).

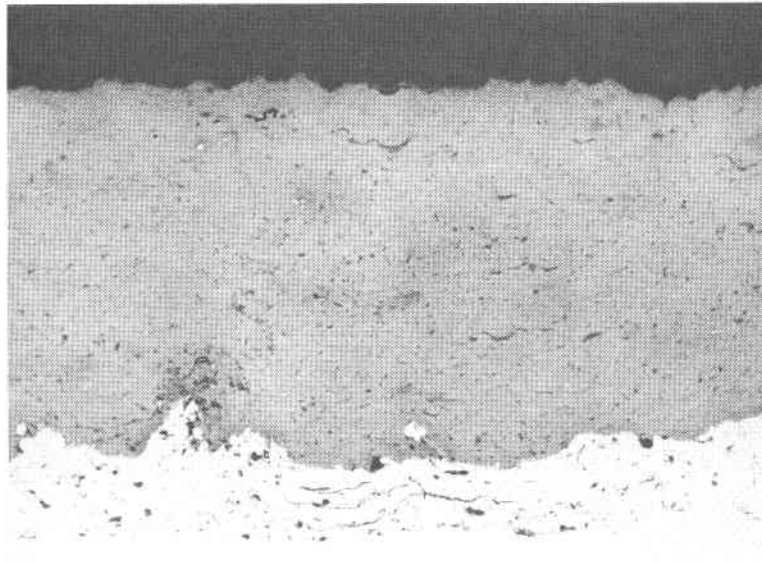


Figure 5a. A dense  $ZrO_2$  coating. (200 x)\*

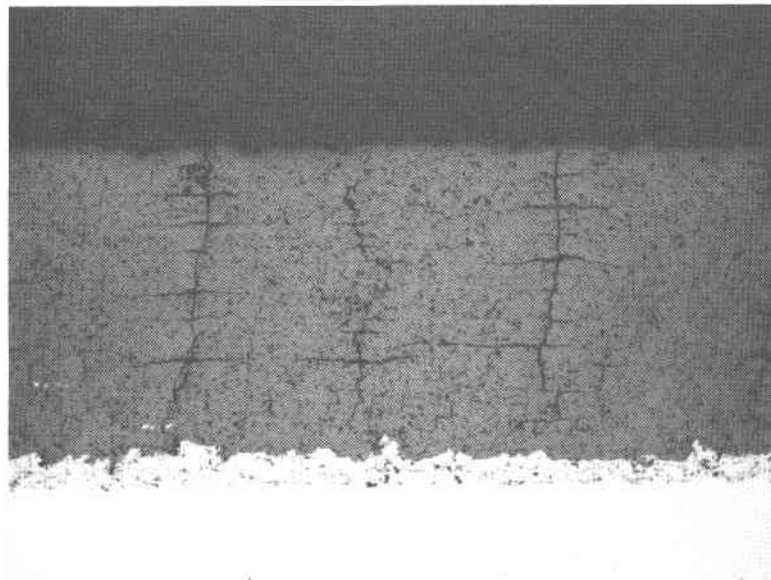


Figure 5b. A thermal cracked coating of CaO stabilized  $ZrO_2$ . Thickness  $\sim 2$  mm.

\*Please note that the illustration(s) on this page have been reduced 10% in printing.

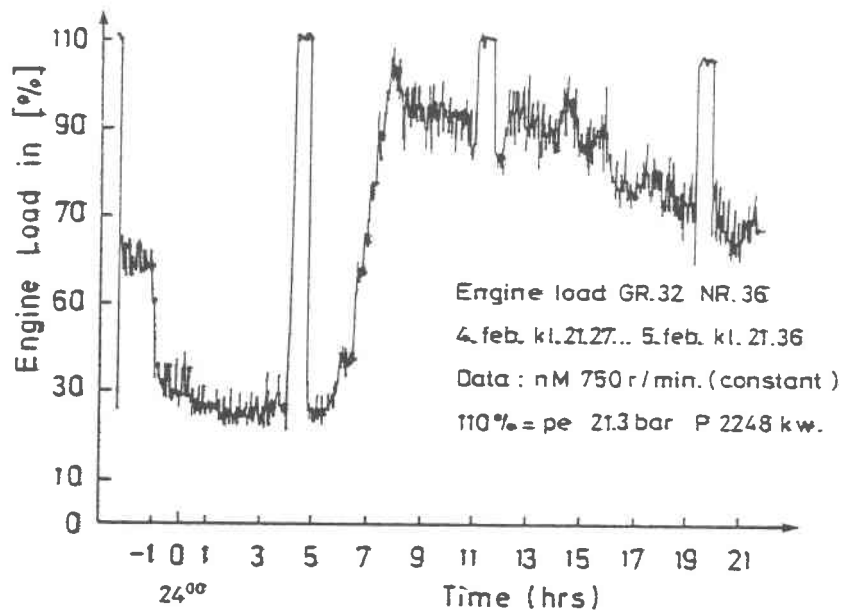


Figure 6. The engine load during a 24 hrs period.



Figure 7. Condensed salt droplet above the valve seat.



On the chromium coated valves there was evidently a relatively high concentration of chromium-ion in the liquid salt layer. Fig. 8 shows the microstructure in the cross section of the "Cr" coating covered with a deposit containing of soot,  $\text{Na}_2\text{SO}_4$ , and vanadium containing compounds. According to Bornstein, dissolved Cr in the salt reduces the assessibility of the deposits related to corrosion (7). This is confirmed by the Scandinavian test program in a 1000 hrs test with a Cr-coated valve in a diesel engine (3). A homogeneous vanadium distribution throughout the whole deposits was found. This is not the case for deposits on  $\text{ZrO}_2$ -coated valves. The deposits on a stabilized zirconia coating exposed to the same condition as described for the chromium coating show a different morphology. It is evident that the underlying base materials influence the morphology and also to a certain degree the chemical composition of the coating.

#### DETERIORATION OF EXHAUST VALVE MATERIALS

Corrosion of heat loaded components in a diesel engine takes place in three steps:

- i) deposition of liquid salt on cooler surface
- ii) dissolution of protective oxides on the surface
- iii) catalytic acceleration of the oxidation/sulfidation process

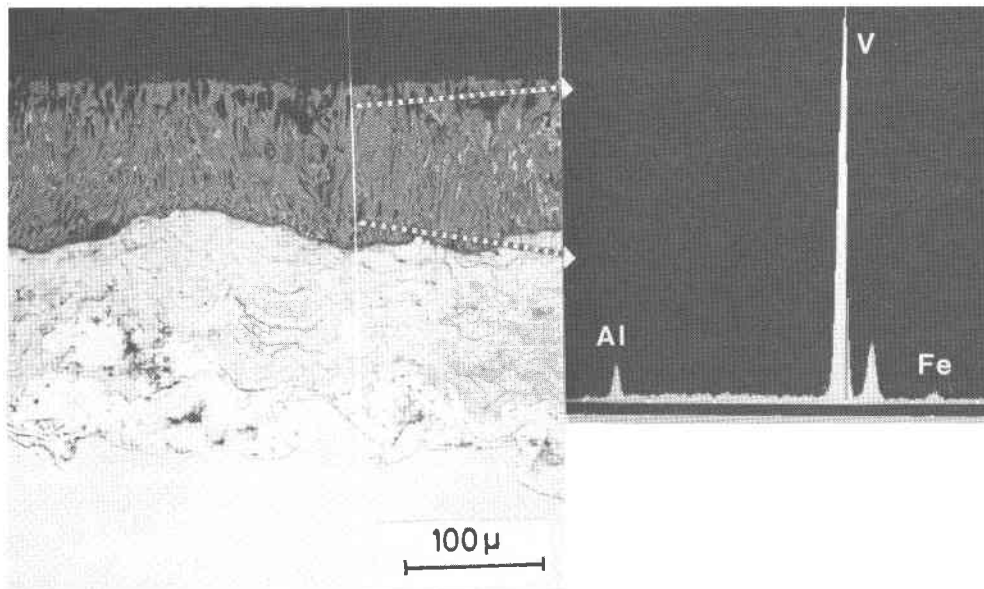


Figure 8. A micrograph of the deposits formed on a chromium coating.

The impurities in the fuels affecting the corrosion are mainly sodium, vanadium, sulphur and chlorine. We have, however, to be aware that all impurities forming salts with low melting point may initiate an accelerated corrosion attack.

The corrosion resistance of coatings is paramount in order to improve the surface stability and thereby the life time of exhaust valves.

#### Hard face materials

The main degradations of exhaust valves take place at the valve seat by the following mechanisms:

- \* mechanically formed dents
- \* partial spallation of salt layers on the valve seat
- \* corrosion on the seat and beneath the valve plates

An open question is if a local temperature increase occurs. How big must a temperature difference be in order to influence on the corrosion rate of practical consequences?

Valve seat materials such as Stellite 6, 12 and 20, Deloro Alloy 60 and Nimonic 80 have been tested in service in this program. The alloys tested have different hardness and corrosion resistance. The Stellite types show increased resistance to deterioration from Stellite 6 to 20. The chromium and carbon concentration and the hardness are also increased from No. 6 to 20. Nimonic 80A without seat-facing was insufficient, mainly due to low hardness. The best results were obtained by using Deloro Alloy 60 type alloy on the seat. This alloy is harder than the other tested materials and the tests have shown that the alloy with this composition has a relatively high corrosion resistance. The microstructure of a welded hardface sample (Eutroloy 12496 = Alloy 60) is shown in Fig. 9.

#### PERFORMANCE OF ZIRCONIA COATINGS ON EXHAUST VALVES

##### Zirconia coatings on the valve fillet and head top

The various test programs carried out on diesel engines show that ceramic materials corrode in engines running on residual fuels. It is found that the stabilizing components in  $ZrO_2$  react with the impurities in the fuel and form more stable components such as yttrium vanadate, calcium sulfate and magnesium sulfate. MgO-stabilized  $ZrO_2$  seems to be the most stable compound in vanadium and sulphur containing gases. It is believed that the reactions discussed above take

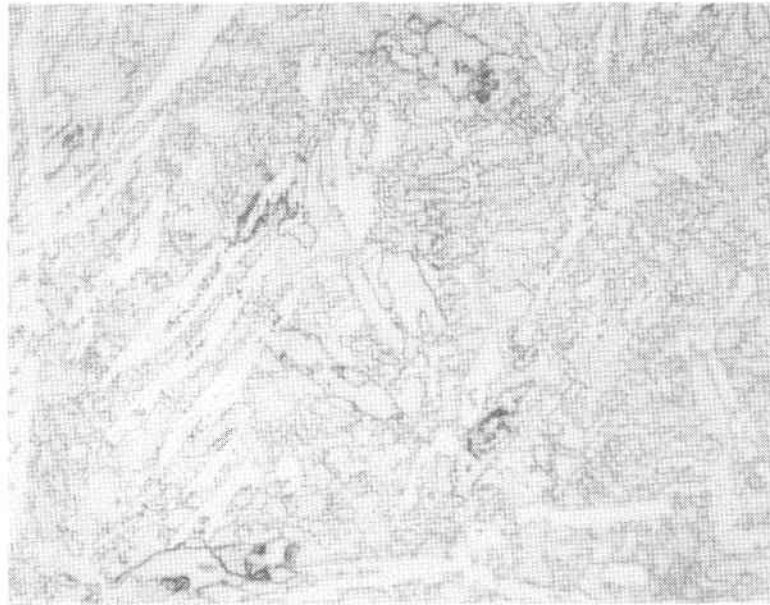


Figure 9. The microstructure of Eutroloy 12496 powder plasma welded. (500 x)\*

place with the stabilizing element which is not dissolved in the lattice of  $ZrO_2$ . Presently we assume that the corrosion will be much slower if we have a single phase compound and a completely dense coating, as shown in the microstructure in Fig. 4.

1. A 500 hrs diesel engine test (Vasa 32)

The objective of this test was to evaluate the thermal insulation effect of a 0,7-0,9 mm coating on the valve plate (CIIR tripple-layered coating). Five thermocouples were located just inside the valve plate surface. The engine parameters were:

- \* effective middle pressure     $P_e = 17,6$  bar
- \* revolution                       $Rev = 720-800$  rev/min

The chemical composition of the fuel oil is shown in Table 2.

\*Please note that the illustration(s) on this page have been reduced 10% in printing.

Table 2.  
Chemical composition on the fuel oils.

Density 15 °C .....	0,95
Sulphur W% .....	2,6
Vanadium ppm .....	150
Sodium ppm .....	30
Viscosity mm <sup>2</sup> /s at 50 °C	200

The results show that the metal temperature was about 50 °C lower in a coated valve than in an uncoated one. This is demonstrated in Fig. 10. The temperature is highest in the center of the valve plate. At the valve seat the temperature of the coating is reduced due to the heat flow through the seat area. Thermal fatigue problems create a crack in the ceramic in the center of the valve plate. In this case a round piece of the ceramic spalls off.

2. A 1000 hrs diesel engine test (Vasa 6R32) using residual fuels

The goal of the tests was to evaluate the effect of engine load on thin ZrO<sub>2</sub> coating (CIIR double-layered coating). The thickness was approximately 0,3 mm.

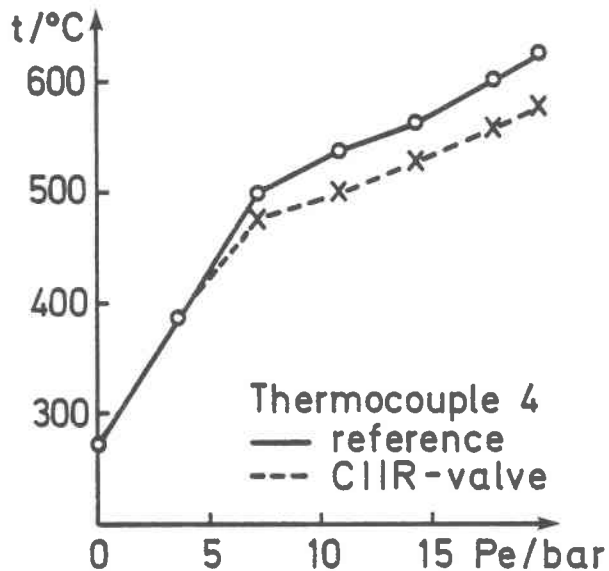


Figure 10. The average metal temperature measured in the center of the valve v.s. increasing load of the engine.

The engine load for a 24 hrs period is illustrated in Fig. 6. Other engine data are:

The effective middle pressure at 110% load : 21,3 bar (2248 kw);  
the revolution: 750 rev/min

The chemical composition of the fuel oils (POR 380 and POR 230) is shown in Table 3.

Table 3.  
Chemical composition of the fuel oils.

	<u>POR 380</u>	<u>POR 230</u>
Density 15 °C Kg/m <sup>3</sup>	-	0,959
Sulphur %	2,90	2,7%
Vanadium ppm	80	134
Sodium ppm	21	35
Nickel ppm	27	-
Aluminium ppm	2	-
Silicon ppm	2	-
Viscosity mm <sup>2</sup> /s 50 °C	380	280

A preliminary examination of the coating after the completion of the test showed the coating to be in excellent condition. No cracks or spallation of parts of the coating were observed. However, a more detailed investigation of cross sections of the coating revealed an unsatisfactory microstructure. Cracks had been formed, and pores had grown. Corrosion had taken place.

### 3. A 12000 hrs test program in an engine running on clean fuels

The objective of this present test program is to study the long term test of a 0,3 mm thick ZrO<sub>2</sub> coating (CIIR double-layered coating) (8).

The test engine is Anamax Engine Number 73034, Unit Number Average load (4,75 megawatt). The chemical composition of the fuel oil is shown in Table 4.

Table 4.  
Chemical composition of the fuel oil.

Sulphur % .....	0,92
Vanadium ppm .....	5
Viscosity mm <sup>2</sup> /s .....	9,7

The test is not completed and only a preliminary examination after 1000 hrs is reported.

The condition of two coated valves after 1000 hrs of operation was good. Both valves showed signs of good seat contact with only minor pitting of the valve face. There was no indication of chipping or deterioration of the ceramic coating. The valve seats for these valves are in excellent condition. One of the standard exhaust valves has shown signs of deterioration; larger areas on the valve face were eroded away. However, the valve appears to have sufficient seat control to continue testing. The other standard exhaust valve was in excellent condition. Thus, so far, the ceramic coatings have performed satisfactorily.

#### 4. Tests of exhaust valves under laboratory conditions

The objective of the study was to evaluate the integrity and properties of the double layered coatings on diesel engine exhaust valves under laboratory conditions (9). The ceramic thickness varied from 1,0 mm near the center to 0,4 mm near the circumference. The NiCrAlY bond layer was 0,1 mm. Specific evaluation included assessing coating integrity under seat/face impacts, valves head flexure and thermal gradient representative of the medium to high speed industrial/utility diesel engine valve environments.

The three test fixtures utilized in the test program at Eaton Corporation (9), were seat face wear, structural fatigue and thermal cycle. These were designed to separate the three stress environments to facilitate independent evaluation of each. It was believed that valve coatings could be more effectively screened because if a coating was rated a failure at this level of test evaluation, the probability of failure in an operating engine environment would be high because of the synergistic effect of stress input and material response.

At this place only the conclusion of the results on an MgO-stabilized zirconia will be given below. The detail and discussion of the experiments and results are given elsewhere (9).

The zirconia coatings demonstrated sufficient resistance to seat face wear, head flexural fatigue and thermal cycle shock to justify additional coating integrity evaluation testing in a firing engine (medium and high speed engine).

#### PERFORMANCE OF STABILIZED ZIRCONIA COATING ON GUIDE VANES

##### Tests in gas turbines

The stabilized zirconia coatings as described for diesel engines were tested in service on guide vanes in a gas turbine on an oil platform in the North Sea for 5000 hours. Distilled fuel was used. During the tests most of the  $Y_2O_3$ - and CaO-stabilized  $ZrO_2$  ceramic layer spalled off. The ceramic coating was intact only in areas with slag depositions. The slag seemed to protect the coating against erosion. The MgO-stabilized  $ZrO_2$  coating spalled off to a much smaller extent.

Cracks parallel to the surface appeared in the  $Y_2O_3$ - and CaO-stabilized coatings. As in the rig tests, cracks were located in the ceramic layer near the bond layer. In one sample with a cermet ( $NiCrAl/ZrO_2-Y_2O_3$ ) layer between the bond layer and the ceramic coating, the cracks were smaller and more of the coating remained after the test.

Characterization of the tested coating showed that  $CaSO_4$  was formed on CaO-stabilized  $ZrO_2$  evidently by a reaction between CaO in the coating and  $SO_2/SO_3$  in the combustion gases. Liquid salts also seemed to penetrate into cracks and large amounts of  $CaSO_4$  were found in the end of the cracks.

Fig. 11 shows the microstructure of the MgO-stabilized  $ZrO_2$  coating after  $\sim 25$  hrs in operation. The surface of the  $ZrO_2$  coating was covered with a very thin film of  $MgSO_4$ . No cracks or other corrosion reaction products were observed, but the erosion attack was severe. The porosity is too high and must be reduced.

It may be concluded that the salt mixture has a smaller tendency to react with MgO in MgO-stabilized  $ZrO_2$  than with CaO or  $Y_2O_3$  in correspondingly stabilized  $ZrO_2$  coatings.

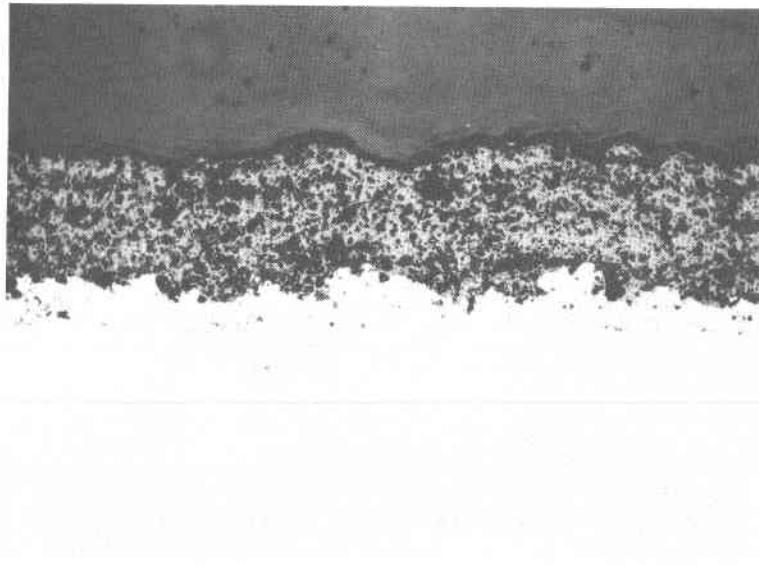


Figure 11. The microstructure of MgO stabilized  $ZrO_2$  coating tested 25 hrs in a gas turbine in operation.

#### CONCLUSION

All coatings used in the tests discussed above were made according to the specifications developed at Central Institute for Industrial Research, SI. The results suggest that the plasma sprayed coatings show acceptable performance. The tests have mainly been made on various steel qualities and different sizes of exhaust valves in diesel engine. Laboratory tests have also been carried out. X-40 alloys were used as base materials in the guide vanes for the coating tests in the gas turbine. The gas turbine tests have shown that the erosion properties of the coating must be improved.

The stabilized  $ZrO_2$  coating seems to have unique properties as thermal barrier coating. The corrosion resistance of the coating in engines running on residual fuel is poor. MgO stabilized  $ZrO_2$  seems to have better corrosion resistance than  $ZrO_2$  stabilized with  $Y_2O_3$  and CaO. This depends to a certain degree on powder quality. The degree of stabilization plays a major role regarding reaction between the stabilizing element and the species in the combustion gases or the liquid salt layer. Critical properties for a ceramic coating besides corrosion are thermal shock, fatigue, wear and fracture toughness. These properties depend on the microstructure and thereby on the spray parameters and the pre-treatment procedure.



The performance of the MgO-stabilized  $ZrO_2$  coating on exhaust valves tested under various engine conditions has resulted in the following conclusion:

Spraying of thin coatings (< 0,6 mm) of MgO stabilized  $ZrO_2$  after the CIIR specification creates a relatively low level of residual stresses. This type of coating seems to be acceptable on valves used in engines running on relatively clean fuels.

In order to extend the limitation for using these coatings in service the following problem listed in Table 5 must be solved. This is particularly important for coating thickness in the range 0,6-2,0 mm and combustion gases, enriched in vanadium, sulfur and sodium (residual fuel oils).

The ceramic coatings seem to exhibit a larger corrosion problem than expected. A detailed understanding of the corrosion problems on ceramic is required. The correlation between powders, spray parameter and microstructure is relatively complex, and more information is needed.

Table 5.  
Limitation of existing coatings used in diesel engines.

<u>Problems</u>	<u>Measures</u>
- High Residual stresses	- Better cooling during spraying
- Poor reproduction of the microstructure	- Using robot - Using chemical homogeneous powders - Control the flame temperature
- Low corrosion resistance	- Tighten the pores in the surface - Dence coating
- Insufficient fracture toughness	- Microcracking, controlled porosity

#### ACKNOWLEDGMENTS

The author wishes to express his appreciation to Mr. John Fairbanks, Department of Energy, Washington, for partly financial support and interesting discussions during the whole program. Furthermore I wish to express my gratitude to Mr. F. Prandstätter, Austria, for optimizing the spraying parameters, and to Professor Per Kofstad, University of Oslo, and all colleagues at my institute who have taken part in the program in various ways. I want to give a particularly

thank to the Scandinavian diesel and gas turbine engine manufacturers for carrying out the engine tests.

#### REFERENCES

1. I. Kvernes. "High Temperature Corrosion and Protection of Thermally loaded Components in Diesel Engines". Marine Diesel Engines - Fuel oil Qualities, No. 7560. NTH, Trondheim, 7th-9th January 1981.
2. B. Jacobson. "Methods for Characterization of coating Microstructure." Thin Solid Films 73, p. 331-345 (1980).
3. P. Kofstad and I. Kvernes. "Corrosion in Combustion Gases, a Scandinavian Research Program". Nordforsk, Stockholm, Sept. 1980.
4. I. Kvernes et al. "Characterization of the microstructure of stabilized Zirconia used on Diesel Engine Components" (1981) and "Problems by Developing and Using Thermal Barrier Coatings on Metals." U.S. Dep. of Energy Reports, Washington, 1981.
5. I. Kvernes et al. "Powder Selection for Plasma sprayed coatings in Diesel Engine Applications (1980)". U.S. Dep. of Energy Report, Washington, 1980.
6. S.R. Levine et al. "Improved Performance of Thermal Barrier Coatings". International Conf. on High Temperature Corrosion, NACE, San Diego, March 1981.
7. N.S. Bornstein et al. "The Relationship between  $V_2O_5$ ,  $Na_2SO_4$  and Sulfidation Attack", pp 70 in Deposition & Corrosion in Gas Turbines edited by A.B. Hart and A.J.B. Cutler, Applied Science Publishers Ltd., London, 1973.
8. K. Pearce. "Engine Test and Evaluation of Ceramic Diesel Engine Valves on Blended Residual Fuels." Transamerica Delaval. U.S. DOE Contract No DE-ACO3 - 79ET15436.
9. D.H. Scharnweber. "Laboratory Evaluation of Ceramic Coatings for Diesel Exhaust Valves." Eaton Corporation. VC-96, 79ET15320-80/1, ERC 80203.

DEVELOPMENT OF CERAMIC HEAT EXCHANGERS  
FOR  
INDIRECT FIRED GAS TURBINES

By

Wate T. Bakker  
Electric Power Research Institute

and

Dave Kotchick  
Airesearch Manufacturing Co. of California

## SUMMARY

Utilizing dirty fuels such as coal in gas turbine engines requires that heat input to the cycle working fluid occur through a heat exchanger. For high cycle efficiencies such a heat exchanger must operate in the 700-1400 KPA, 1100-1200°C (100-200 psi, 2000-2200°F) range. In this temperature range, ceramic heat exchangers are required. Ceramic heat exchangers that can operate in this regime have been under development for several years on a very modest scale. These programs are briefly reviewed. Major material issues are reviewed and the status of each is presented. Mechanical reliability and joining technology have been successfully demonstrated in short term tests. Long-term durability and the manufacturing technology to produce large scale components reproducibly remains to be demonstrated in the future.

Section 1  
INTRODUCTION

The service limit of metallic heat exchangers is 850-900°C in clean environments and considerably lower in corrosive gas streams. Since the inlet temperature of modern stationary open cycle gas turbines is about 1100°C, indirect fired turbines must be derated significantly, if metallic heat exchangers are used. Moreover, indirect fired turbines only make sense when solid or corrosive fuels, which cannot be used directly in gas turbines, are used. The use of these fuels will reduce the operating temperature to less than 800°C. and will result in a further decrease in efficiency. It is theoretically possible to recoup most of this loss in efficiency through the use of a closed cycle gas turbine operating at a high pressure (1).\* However, large size closed cycle turbines (10 MW or more) do not presently exist and will not be available in the near future. It appears therefore more advantageous to develop high temperature ceramic heat exchangers, capable of producing hot air at 1000-1100°C to be used in currently available open cycle gas turbines. It appears likely that the temperature capability of ceramic heat exchangers will be able to keep pace with future increases in turbine inlet temperature.

Figure 1 (1) shows an indirect fired open cycle gas turbine power plant in its most simple form. A recuperator is used to preheat the working fluid prior to entry in the ceramic heat exchanger. Further improvements in efficiency can be made through the use of a bottoming steam cycle as shown in Figure 2 (2). Possibilities for cogeneration also exist. Since the turbine exhaust consists of clean air, it can be used directly as preheated air for burners or as process heat for processes requiring temperatures up to 900°F. Alternately part or all of the steam generated in the bottoming cycle can be used for cogeneration purposes. In this manner an overall system efficiency of 75% may be obtained (2).

---

\*Numbers in parentheses indicate references on page 5-1.

Another promising use of pressurized ceramic heat exchangers is in solar-thermal applications (3). Here the capital cost per MWE is very high. Thus an efficient, high temperature heat conversion system is needed such as a ceramic heat exchanger/receiver coupled with an open cycle gas turbine. To provide a constant amount of electricity the turbine can be designed to run partially or completely on fossil fuels at night or on cloudy days. A schematic of such an installation is shown in Figure 3 (3).

In this presentation we will discuss the status of the development of ceramic heat exchangers in the USA, with emphasis on materials issues. First the major development projects currently in progress will be described. Then major materials and design issues will be discussed including mechanical reliability, joining technology, environmental compatibility and manufacturing technology.

## Section 2

### PRESENT DEVELOPMENT PROJECTS

One of the first efforts to develop a high pressure heat exchanger for an indirect fired gas turbine was carried out by the Garret AirResearch Manufacturing Company under EPRI sponsorship (4,5). The study included all major elements needed to design and build a ceramic heat exchanger.

- development of a preliminary design
- acquisition of a materials data base
- development of manufacturing technology
- component and module testing
- development of analytical techniques to assess the reliability of large ceramic systems

The overall development plan is shown in Figure 4 (4). It gives a good illustration of what it takes to design a reliable ceramic heat exchanger.

The AiResearch ceramic heat exchanger consists of bundles of ceramic U-tubes, permanently bonded to ceramic header modules. For a 150 KW (200 HP) closed cycle gas turbine 6 modules with 30 U-tubes each are needed (Figure 5). The hot airflow is across the tubes. U-tubes were chosen as the preferred design to avoid stress concentrations due to differences in expansion between the hot and the cold legs of the heat exchanger module and to decrease the number of tube-manifold joints.

Most objectives of the project have been achieved. The development of high-temperature (1800°F), high pressure (250 psi) mechanical seals between the header modules is presently underway. A 10-tube module similar to the module shown in Figure 6 will be tested under full design temperature and pressure to conclude the program in 1981.

The development of a high pressure ceramic heat exchanger at Solar Turbines International dates back to 1977. It has been sponsored mainly by U.S.D.O.E. and its predecessors (6). The design features an array of straight tubes connected to

a metal inlet header and a ceramic outlet header. Bellows on the cold end of the tubes, before the metal-ceramic mechanical joint, compensate for differences in thermal expansion. A hydraulic jack below the metal header provides the compressive force to keep the mechanical ball and socket joints leaktight. A module containing one set of headers and 28 fifteen foot long tubes has been constructed (Figure 7).

The fifteen foot tubes are made from two 7.5' tubes, joined by a silicon brazed sleeve. The combustion air flow is parallel to the heat exchange tubes. A 7 hour test at full pressure and temperature was successfully completed in 1980. This included several starts and stops as well as an emergency shutdown with heating and cooling rates as high as 1000°F/minute. A 500 hour endurance test and a 14 day test using a newly developed coal burner are planned in 1981. The latter test is sponsored by E.P.R.I.

A joint venture between Hague International and Ruston gas turbines proposes to develop an indirect fired gas turbine power plant, using a high pressure version of the Hague ceramic heat exchanger, originally designed for forging furnaces and a Ruston gas turbine. The low pressure ceramic heat exchanger developed by Hague International has been installed in several forge furnaces. The oldest unit has successfully accumulated 6,500 hours of service as of September, 1980. The high pressure version is still under development. Few details are publicly available, since the development is privately funded.

A one megawatt (thermal) ceramic solar-thermal receiver has been designed by Black and Veatch for EPRI and constructed by the Thermal Transfer Co. in 1978-1979 (3). Figure 8 shows one of the five heat exchanger panels of the receiver. The use of ceramics is limited to the straight tubes directly exposed to the sunlight. The headers and U-tubes connected to the hot and cold legs are made of stainless steel. The outlet header is carrying 1900°F air and is internally insulated. The most critical design feature is the joint between the ceramic tubes and the hot header (Figure 8). This concept was successfully tested at Atlantic Research Co. (8). Further testing of the solar-thermal receiver has been deferred due to lack of funds.



### Section 3

#### MATERIALS ISSUES

##### MECHANICAL RELIABILITY

During the last 10 years our understanding of the mechanical behavior of brittle solids has increased markedly. The use of finite element stress analysis allows us to pinpoint local areas of high stresses under thermal or mechanical loads, which may cause catastrophic failure, since the elastic modulus is very high and stress relief through plastic deformation cannot occur until temperatures very near the melting point are reached. Overstressed areas can thus be eliminated through redesign. Statistical techniques are generally used to determine the failure probability of individual stressed ceramic components and whole systems. The Weibull distribution (9) is the most commonly used method to characterize strength variations. The mathematics of the procedures are discussed in detail elsewhere (10) and will not be repeated here. Briefly the following steps are needed to calculate the failure probability of a ceramic structure.

1. The characteristic strength and strength variation of the material is determined.
2. The stress distribution in each component is determined using finite element analysis.
3. The probability of failure of each component is calculated using the characteristic strength and Weibull modulus obtained in (1).
4. The failure probability of key components is verified to make sure that the flaw size distribution is the same in all components. Correction factors must be applied if this is not the case.
5. From the failure probabilities of the individual components the overall probability of failure of the complete structure is calculated.
6. If the overall failure probability of the structure is considered too high, it can be improved by redesign of critical components to remove stress concentrations, by prooftesting critical components in an overstress test to ensure reliability, or by using an improved material with a higher characteristic strength and Weibull modulus.

The design process described above is illustrated in the development of the AiResearch ceramic heat exchanger. Siliconized Silicon Carbide\* was selected as the material for all components as this was the only available ceramic which could be fabricated into the required shapes at that time. Figure 9 (10) shows how the Weibull modulus and strength of the material varies with different size components. It is noted first that ground modulus of rupture bars are not suitable as test specimens, as one distribution of surface flaws is removed during the grinding process and generally replaced by a more uniform smaller size and distribution of flaws. This increases both the strength and the Weibull modulus and thus gives unrealistically high values which cannot be used for design purposes (curve 1 vs. 2) when designing as-fired, as-formed components. When scaling up to large, but relatively uncomplicated shapes, the Weibull modulus stays the same and the decrease in observed average strength is entirely due to the increase in stressed volume of the larger component (curve 2 vs. 3). The strength and Weibull modulus of complicated shapes like U-tubes and finned tubes is lower than expected, indicating that the flaw size distribution has changed or more likely because the complex shape has caused variations in the material during processing - that is both the characteristic strength and flaw populations have been altered. An experimentally determined correction factor is needed to calculate the failure probability of these components.

Figure 10 shows the reliability model of a heat exchanger for a small 150 KW turbine, based on the materials database and component verification tests. It is noted that the overall reliability of the system is relatively low, despite the high reliability of most components. Prooftesting of critical components like the manifold sections is needed to increase the overall systems reliability. Reducing the stress, for instance by reducing the diameter of the manifold, will also increase the reliability.

For long-term, high-temperature operation static fatigue of ceramics must also be taken into account. Delayed failure under stress in structural ceramics is due to the extension of subcritical cracks or flaws to a critical size where catastrophic failure can occur spontaneously by the release of stored elastic strain energy during continued crack extension. Several theories and limited evidence exist to prove the exact mechanisms for slow crack growth (SCG) in ceramics. However, SCG

---

\*NC 430, manufactured by Norton Co., Worcester, MA

is generally more prevalent at high temperatures, high stresses, and in moist environments. At high temperatures, mechanisms such as grain boundary sliding, liquid phase cavitation at the grain boundaries and grain boundary reactions are believed to control SCG.

The preferred material for heat exchangers, siliconized silicon carbide, is a two-phase material which contains about 10% free silicon as a second phase. For NC-430, the grain size is also quite variable. The silicon which has a melting point of 1410°C (pure silicon) complicates any SCG theory which might be applied. The onset of SCG is also stress and temperature dependent. The characterization of this material is further complicated by short term strengthening due to oxidation and slight plastic deformation of the silicon phase. Oxidation of the surface causes blunting of sharp surface cracks. This usually increases the characteristic strength and sometimes increases the Weibull modulus as shown in Figure 11 (11) for the siliconized silicon carbide. In addition, a slight plastic deformation of the silicon phase can cause very significant increases in fracture toughness as shown in Figure 12, especially at slow loading rates (12). In the same experiment the slow crack growth rate exponent,  $n$ , was found to be 131, which indicates a very slow crack growth rate. Experiments carried out by Trantina (13) indicate that the strength of siliconized silicon carbide increases about 20% at 1200°C when the samples are pre-oxidized at this temperature under stress for several hundred hours. During 500 hour stress rupture tests, at 1250°C, carried out recently at AiResearch, no failures occurred at stress levels ranging from 70-85% of the short term fracture strength. Some creep did occur during the test as shown by a slight deflection of the MOR bars.

Siliconized silicon carbide was also subjected to cyclic fatigue experiments. At 1250°C specimens did not fail when cycled from 0 to 70% of the fracture strength for 3600 cycles in one hour. The strength after the cyclic fatigue test was about 10% higher than before and the Weibull modulus increased from 9 to 17. Cyclic tests at higher temperature generally show a decrease in strength after the test, indicating that slow crack growth occurs during the test. Figure 13 summarizes all the data obtained so far.

All the tests described above indicate that siliconized silicon carbide will be able to operate reliably for long periods of time in the 1000-1200°C temperature range, both under steady state and cyclic conditions, at least in clean environments. Both strength and fracture toughness appear to increase when exposed to oxidizing conditions under stress. This provides an extra margin of safety for heat exchangers operating in this temperature range, which is not taken into

account in reliability calculations based on room temperature data. At temperatures over 1250°C, crack growth becomes more pronounced with increasing temperature. Fortunately present turbine inlet temperatures are generally below 1100°C and do not required heat exchanger temperatures much above 1200°C.

#### JOINING TECHNOLOGY

Mechanical joining, brazing and solid state bonding appear to be the joining methods with the highest potential for successful use in heat exchangers (14). Mechanical joining is used where component repair and replaceability are desired. Brazing and bonding are used for component or module buildup as they are permanent bonding techniques.

Mechanical joints can be either rigid or flexible. Flexible joints are of special interest for heat exchangers, as they provide a means for relieving stress concentrations caused by thermal cycling. Ball and socket joints are especially popular and are used in most heat exchanger designs. Mechanical joints are also used almost exclusively for metal-ceramic contacts. Diffusion of metal into the ceramic and vice versa is generally prevented by coating the metal surface with a relatively inert material such as flame sprayed  $Al_2O_3$ . Mechanical joints are limited to systems where the internal pressures and imposed loads are moderate. They should be adequate for the pressure range of modern gas turbines, where the maximum systems pressure generally does not exceed 250 psi.

The main drawback of brazed joints is that the brazing material generally has a much lower service temperature than the ceramic itself. Silicon metal is the most commonly used brazing material for high temperature applications. Its use limits the maximum steady state operating temperature to about 1200°C and short term exposures to about 1350°C. Silicon brazing works especially well for siliconized silicon carbide, which contains already 10% free silicon. Solar turbines (6) has demonstrated that a silicon brazed sleeve joint can be fabricated with the same strength as the parent ceramic tube. The ceramic surfaces to be joined must be completely wetted by the silicon, otherwise the joint will leak. An important advantage of silicon brazed joints is that they can be installed and repaired in the field.

Solid state bonding is usually achieved by using a cement of the same composition as the ceramic. The joints have to be fired at the same temperature as the ceramic. Unfired ceramic components can also be joined in this manner to avoid firing the material twice. The strength of solid state bonded joints is 10-20%

less than that of the original ceramics due to differences in percent Si content, number of SiC bonds formed and joint irregularity at the surface. This must be taken into account when computing the failure probability of the heat exchanger. Solid state joints cannot be installed or repaired in the field. This is a major drawback.

It is concluded that joining technology for the present generation of heat exchangers, using siliconized silicon carbide, is adequate. For future systems based on high purity silicon carbide or silicon nitride, joining systems which can match the high temperature capabilities of the ceramics and which can also be installed and repaired in the field remain to be developed.

#### ENVIRONMENTAL COMPATIBILITY

Both silicon carbide and nitride are thermodynamically unstable under oxidizing conditions. In clean oxidizing environments a protective  $\text{SiO}_2$  scale is usually formed. Available data generally indicate that the oxidation rates of carbides and nitrides are considerably lower than those of alloys in the same temperature range (15). However, data for temperatures over  $1200^\circ\text{C}$  are rather scarce. There are also many reports that localized pitting corrosion may occur during high temperature oxidation, especially in MgO doped, hot pressed silicon nitride. The pitting causes a significant drop in hot strength at temperatures over  $1000^\circ\text{C}$ , as the pits act as crack starters. There are no reports that siliconized silicon carbide suffers from pitting corrosion during high temperature oxidation up to  $1200^\circ\text{C}$ .

The corrosive effects of contaminants on the stability of silicon carbide or nitride is mainly caused by their ability to modify or destroy the protective  $\text{SiO}_2$  scale, a process similar to hot corrosion of super alloys by sodium sulfate. Long term data at high temperatures are again rather scarce and often conflicting. A paper by Brooks and Meadowcraft (16) indicates that siliconized silicon carbide corrodes very rapidly at temperatures as low as  $900^\circ\text{C}$  in a combustion environment containing vanadium oxide and sodium sulfate. A 1000 hour corrosion/erosion test at  $1200^\circ\text{C}$  carried out by Ward et al. (6), using flyash, sea salt and  $\text{V}_2\text{O}_5$  as contaminants showed no corrosion of siliconized silicon carbide, but significant corrosion or erosion of alpha silicon carbide. Five hundred hour corrosion tests were carried out by Tennery et al. (17) at  $1200^\circ\text{C}$  using Va containing #6 fuel oil and coal-oil slurries. No significant corrosion loss was reported in either test. The room temperature fracture strength of alpha silicon carbide decreased,

while that of siliconized silicon carbide increased. However, SEM examination revealed considerable diffusion of Fe and Ni in the silicon phase of the ceramic essentially forming a Fe, Ni, Si eutectic. This may reduce the hot strength of the ceramic. Unexplained changes in thermal expansion were also noted. These may increase thermal stresses during cycling and require further study.

Temperature cycling tests (5 cycles/hour) were carried out by Carruthers et al. (18) in a burner rig using #2 fuel oil at 1200°C. The room temperature fracture strength of siliconized silicon carbide decreased about linearly with time. After 2100 hours a 33% strength loss was noted (Figure 14). Alpha silicon carbide, on the other hand, showed no loss in strength after 3700 hour testing at 1200°C and a significant increase in Weibull modulus. After 3500 hours at 1370°C the room temperature fracture strength remained constant, but the 1200°C strength dropped 36%. Work carried out at Stanford under EPRI sponsorship indicates that the room temperature strength of siliconized silicon carbide is adversely affected by  $\text{Na}_2\text{SO}_4$ - $\text{Na}_2\text{CO}_3$  coatings (19), as shown in Figure 15. The effect is most pronounced at 800°C where the salt mixture is liquid. At higher temperatures the salt vaporizes and the drop in strength is less pronounced. Weber et al. (20) tested siliconized silicon carbide heat exchanger tubes in glass tank recuperators, where the combustion air contains large amounts of alkali salts, usually sulfates. Rapid corrosion was observed at 1200°C, but less at 1400°C.

All the references cited above indicate that silicon carbide and nitride are frequently adversely affected by common impurities in combustion environments, such as  $\text{Na}_2\text{SO}_4$  and  $\text{V}_2\text{O}_5$ . There appears to be a large variation in test results, some of which are quite encouraging. A more fundamental study is needed to investigate the corrosion mechanism and to establish safe operating conditions:

#### MANUFACTURING TECHNOLOGY

Ceramic heat exchanger components are usually made by slipcasting, a well established ceramic forming process, which lends itself well for the production of relatively complex shapes, such as manifolds. However for the production of tubes, this process is less suitable. Presently the maximum tube length available commercially is about 8 feet. When slipcasting the inside surface of the tube tends to be rough and irregular. This will affect the heat transfer coefficients in an unpredictable manner, by causing or enhancing turbulent flow. It will also

increase the pressure drop across the heat exchanger. Overall dimensional control also needs further development. Some warpage usually occurs during drying and firing, thus the resulting tubes are not straight. This cannot be tolerated to a large extent as the heat exchanger tubes are usually packed rather closely together. The inside and outside diameters of slipcast tubes are also not always concentric. This may cause leakage in ball and socket joints. It appears to the present authors that improvements in tube quality should result when an extrusion process is used instead of slipcasting.

Quality control of large components is also an area which needs improvements. For instance, a domestic grade of siliconized silicon carbide has an average fracture strength on as-fired, as-formed surfaces of 28 ksi and a Weibull modulus of 7-10. When fabricated in 8 foot tubes, the strength of equivalent size MOR bars, cut from the tubes, was found to be only 17.8 ksi, with a Weibull modulus of 5. Microscopic examination revealed the presence of a dense surface layer of large SiC grains on some of the specimens. Sharp microcracks through the depth of the dense layer apparently lowered the fracture strength. The strength of individual specimens was found to decrease with increasing thickness of the dense surface layer (Figure 15). It is obvious that uncontrolled strength variations as described here cannot be tolerated.

Non-destructive evaluation and prooftesting are additional areas which need further development. NDE is presently limited to techniques which are slow and expensive and only capable of discovering large flaws. Critical flaws are generally in the 100  $\mu$ m range. Dye penetrant inspection is generally limited to finding relatively large flaws such as machining cracks and surface pores. Proof-testing is considered by many to be the most promising technique to boost the overall reliability of ceramic heat exchangers. However, most prooftesting so far has been carried out on relatively small components such as turbine blades, not on large heat exchanger components. For a prooftest to be valid it must exactly duplicate the over stress condition of the component in operation including both thermal and mechanical stress contributions. An elegant way of combining proof-testing with strengthening of siliconized silicon carbide parts has recently been proposed by Trantina (13), based on his observation that a significant increase in strength occurs when this material is kept under stress at 1200°C in air. Much more work is needed in this area to arrive at commercially acceptable methods.

## CONCLUSIONS

1. Siliconized silicon carbide is at present the preferred material for use in ceramic heat exchangers. It shows good long term stability up to 1200°C, at least in clean environments. It can be fabricated by slip casting, extrusion and pressing to allow components of sufficient size and complexity for heat exchanger development.
2. The technical feasibility of pressurized ceramic heat exchangers has been demonstrated in short term tests on small modules representative of larger sized units, designed to operate with industrial gas turbines.
3. The materials data base, joining technology and design methodology now exists to construct mechanically reliable heat exchangers of moderate size, using siliconized silicon carbide. Maximum safe steady state operating temperature is about 1200°C.
4. The response of structural ceramics to common impurities in combustion gases such as  $\text{Na}_2\text{SO}_4$ ,  $\text{V}_2\text{O}_5$  and flyash is insufficiently known at this time, especially the effect on high temperature strength, creep resistance and slow crack growth. Presently available data are often conflicting, most data are encouraging, but there are also reports of rapid corrosion. An in-depth study of hot corrosion of structural ceramics is needed to develop models, which can predict the long term stability of ceramic heat exchangers in dirty combustion environments.
5. Manufacturing technology of ceramic heat exchanger components needs evolutionary improvements in many areas to assure reliable routine commercial production, but no radical breakthroughs are required.



## REFERENCES

1. E. A. Mock, L. D. Six. Comparison of Open and Closed Gas Turbines for Utility Power Systems - Internal Report. EPRI Contract RP545-2 from Airesearch Co. of Arizona, November, 1979. Not published.
2. P. G. Carlson, T. E. Duffy, P. B. Roberts. Description of Efficient, Fuel Flexible Combustion Turbine Plants for Small Electric Utilities. EPRI Report AF 1308, December 1979.
3. J. C. Grosskreutz. Solar Thermal Conversion to Electricity Utilizing a Central Receiver, Open Cycle Gas Turbine Design. EPRI Report ER-387-54, March 1977.
4. A. Pietsch. Coal Fired Prototype High Temperature Continuous Flow Heat Exchanger. EPRI Report AF 684, February 1978.
5. M. Coombs, D. Kotchick, H. Warren. High Temperature Ceramic Heat Exchanger. EPRI Report FP 1127, July 1979.
6. M. E. Ward, W. Solomon, M. E. Gulden, C. E. Smeltzer. Development of a Ceramic Tube Heat Exchanger with Relaxing Joint. DOE Report FE 2556-30, June 1980.
7. Hague International, S. Portland, Maine. Sales Literature.
8. E. L. Paquette. Final Report Project A - 1882. Gas Cooled Central Receiver, 1 MW Benchscale Model. September 1977. To be published.
9. W. Weibull. A Statistical Distribution Function of Wide Applicability. J. of Applied Mechanics. Vol. 18, September 1951, p. 293-297.
10. W. T. Bakker, G. G. Trantina, D. Kotchick. Requirements for Structural Ceramics in Advanced Power Plants. J. Materials for Energy Systems, Vol. 2, No. 2, September 1980, p. 41-50.
11. Norton Co. NC430, Densified Silicon Carbide Sales Literature, 1979.
12. G. Popp, R. F. Pabst. Fracture Behavior of Ceramic Materials at High Temperatures. Metal Science. March 1981, p. 130-132.
13. G. G. Trantina, G. Hopkins, J. Corelli. Ceramic Materials for Fusion Reactors. EPRI Report AP 1702, February 1981.
14. G. W. Brassell, V. J. Tennery. Technology Assessment of Ceramic Joining Applicable to Heat Exchangers. EPRI report AP1586, TPS77-748, October 1980.

15. C. T. Sims, J. E. Palko. Surface Stability of Ceramics Applied to Energy Conversion Systems. Proc. Workshop on Ceramics for Advanced Heat Engines, January 26-27, Orlando, Florida, 1977. ERDA report, Conf 770110, p. 187.
16. S. Brooks, D. B. Meadowcraft. Corrosion of Hot Pressed and Reaction Bonded  $\text{Si}_3\text{N}_4$  and Self-bonded SIC in Oil Fired Environments. Royal Navy, U.S. Navy Gas Turbine Mats Conf., Bath, England, September 1976.
17. V. J. Tennery, G. C. Wei, M. K. Ferber. High Temperature Behavior of Silicon Carbide, SIALON and  $\text{Al}_2\text{O}_3$  Ceramics in Coal and Residual Oil Slag. Proc. Am. Cer Soc September 1982<sup>2</sup> In print.
18. W. D. Carruthers, D. W. Richerson, K. W. Benn. 3500 Hours Durability Testing of Commercial Ceramic Materials. Interim Report DOE/NASA 0027-80/1, NASA Cr. 159785, July 1980.
19. A. L. Holk, W. D. Nix. The Effect of High Temperature Exposure in Different Environments on the Fracture Strength of SIC. EPRI Project RP 545-3. To be published.
20. G. W. Weber, V. J. Tennery. Materials Analysis of Ceramics for Gas Furnace Recuperators. ORNL TM 6970, November 1979.

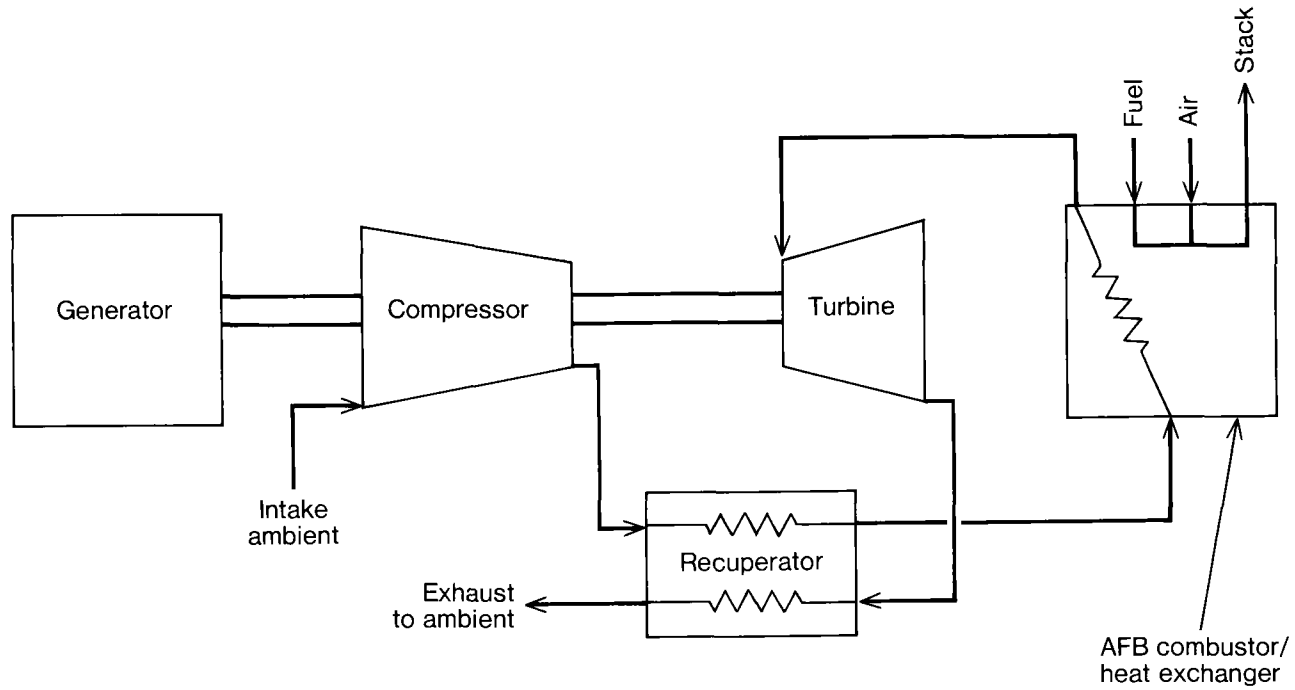


Figure 1. Open cycle indirect-fired gas turbine power plant.

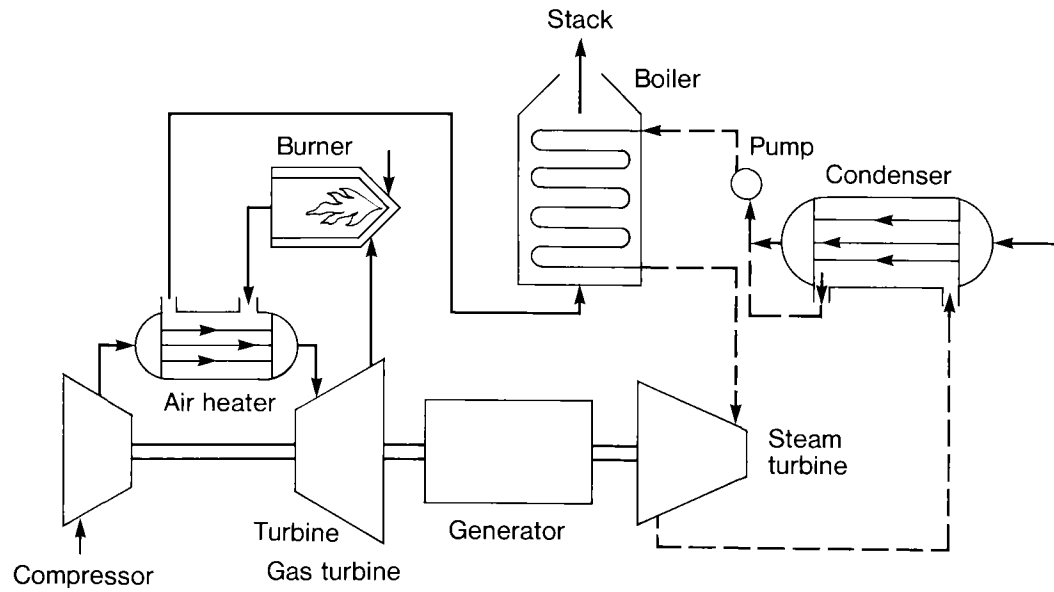
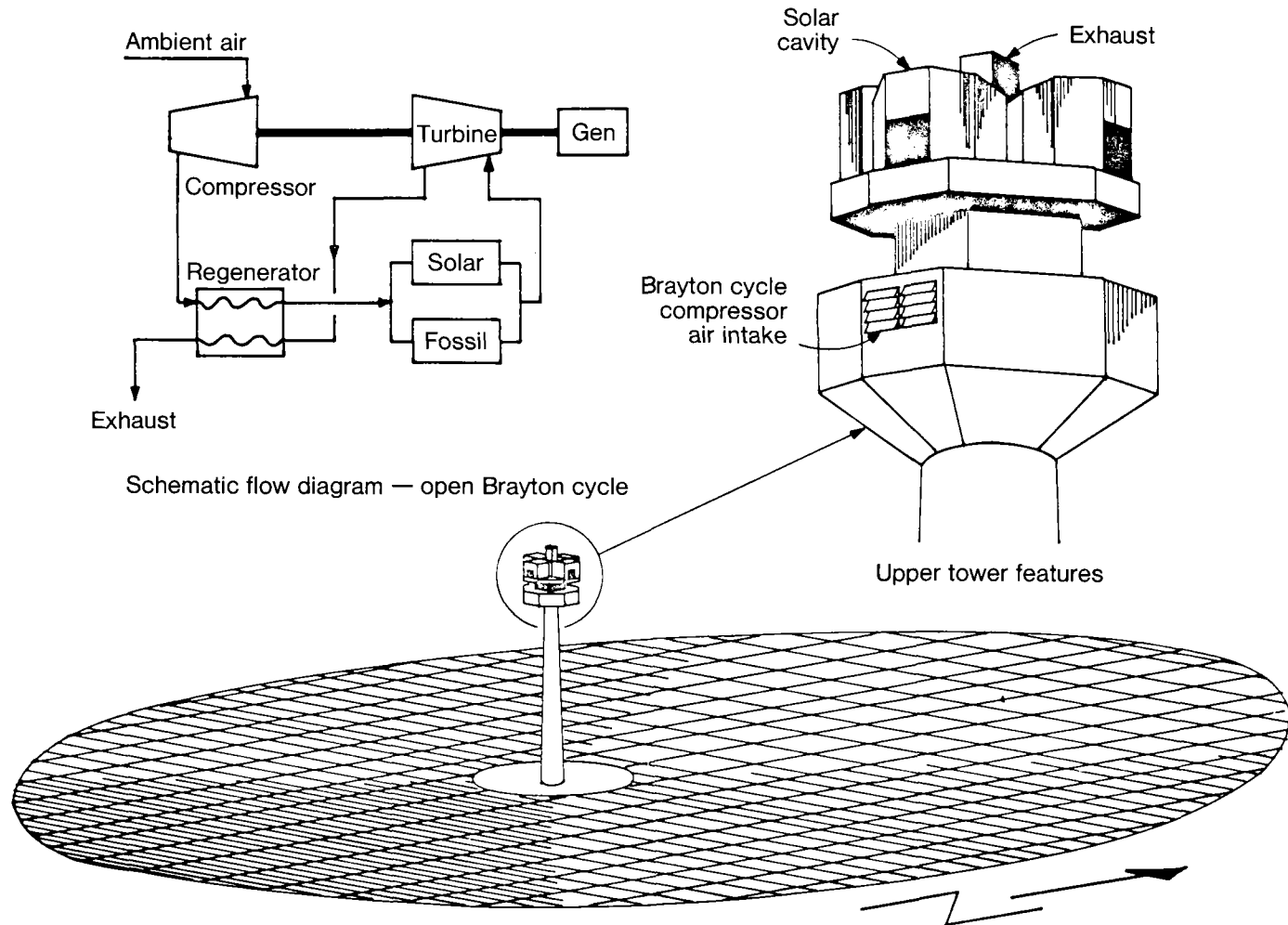


Figure 2. Combined cycle indirect-fired gas turbine power plant.



Schematic flow diagram — open Brayton cycle

Figure 3. Open cycle solar central receiver system.

## PROJECT PLAN FOR THE DEVELOPMENT OF A CERAMIC HEAT EXCHANGER

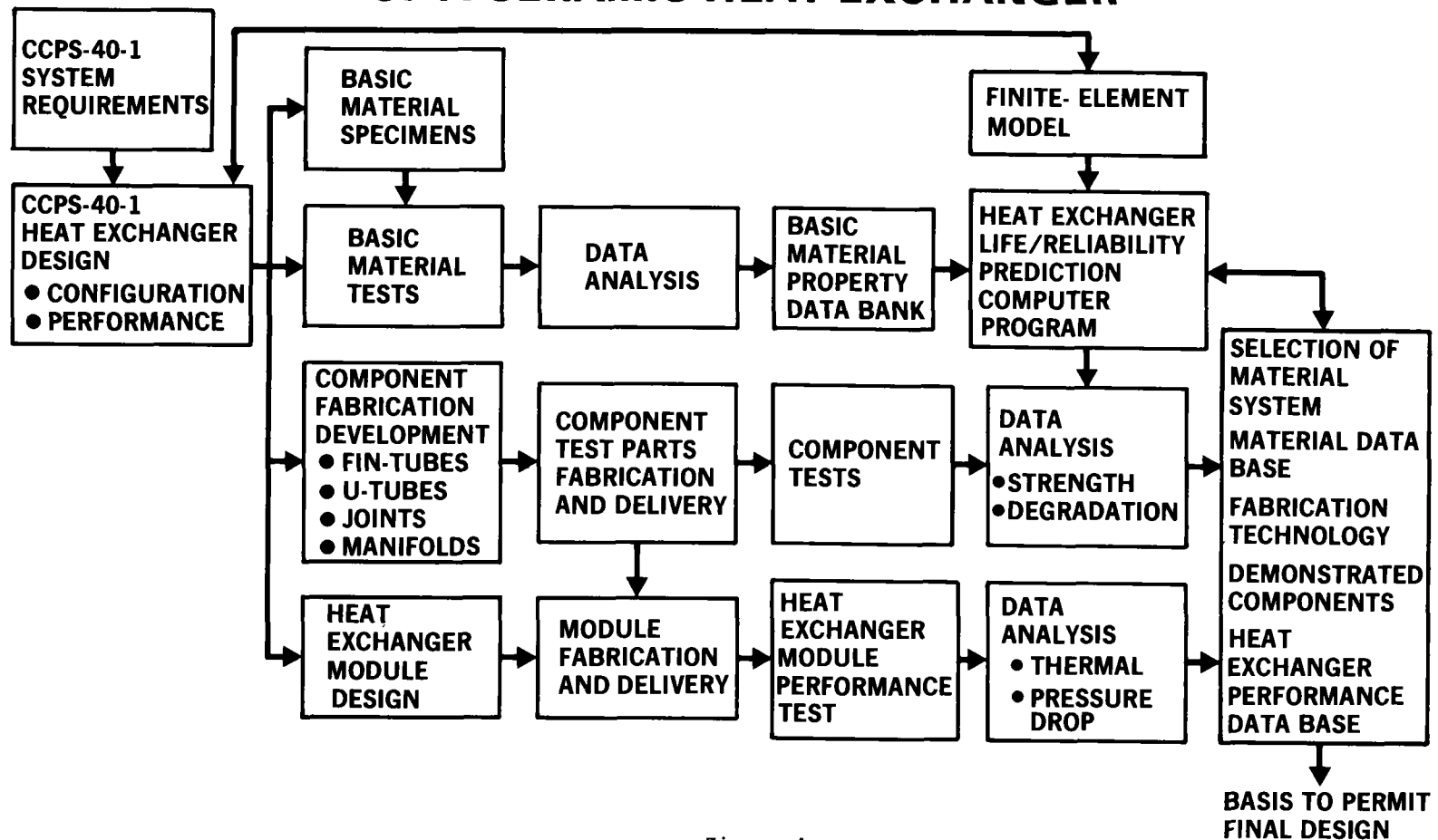


Figure 4

**CERAMIC HEAT EXCHANGER  
PRELIMINARY DESIGN  
CONCEPT**

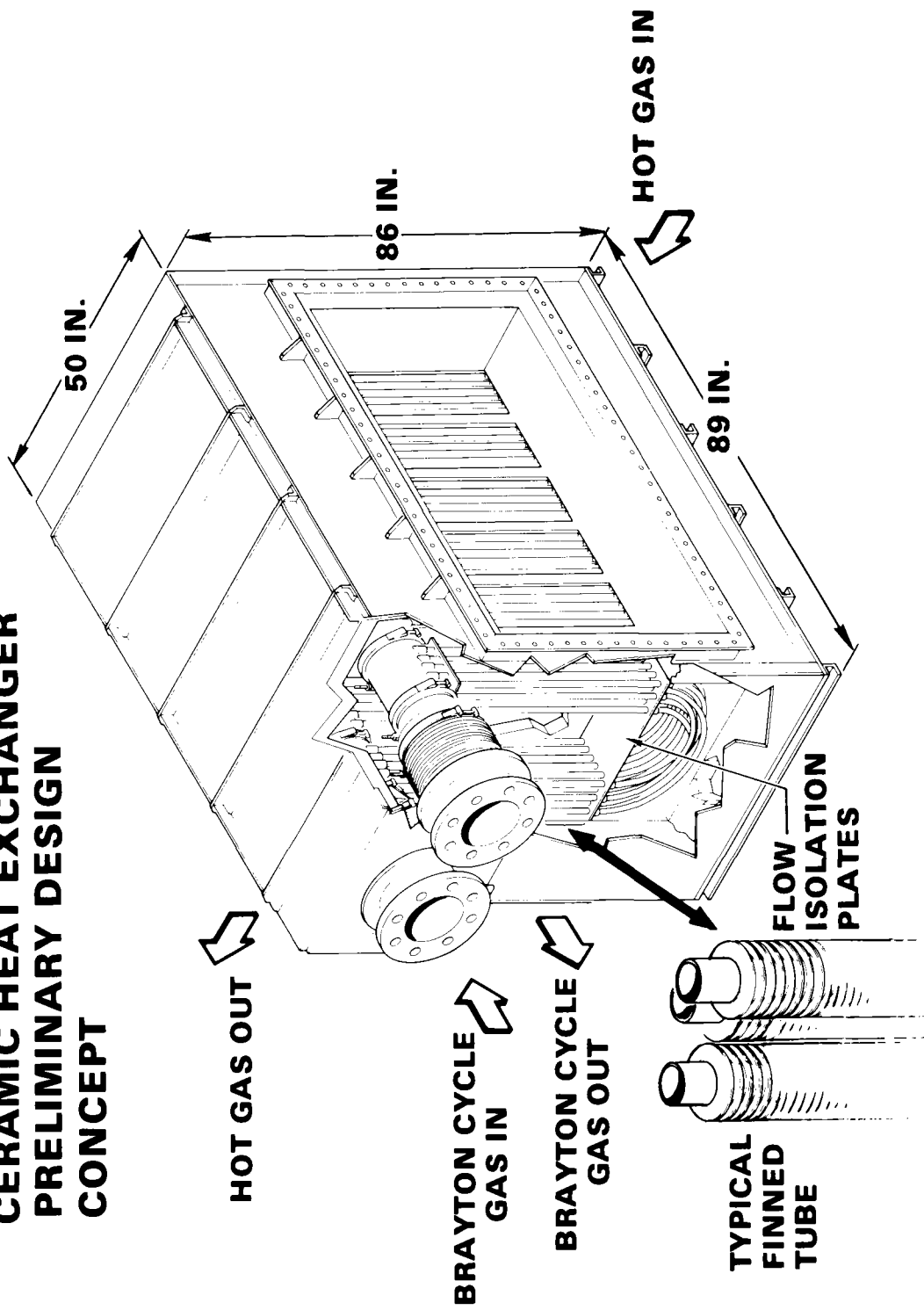


Figure 5



Figure 6. Heat exchanger module for AiResearch Design



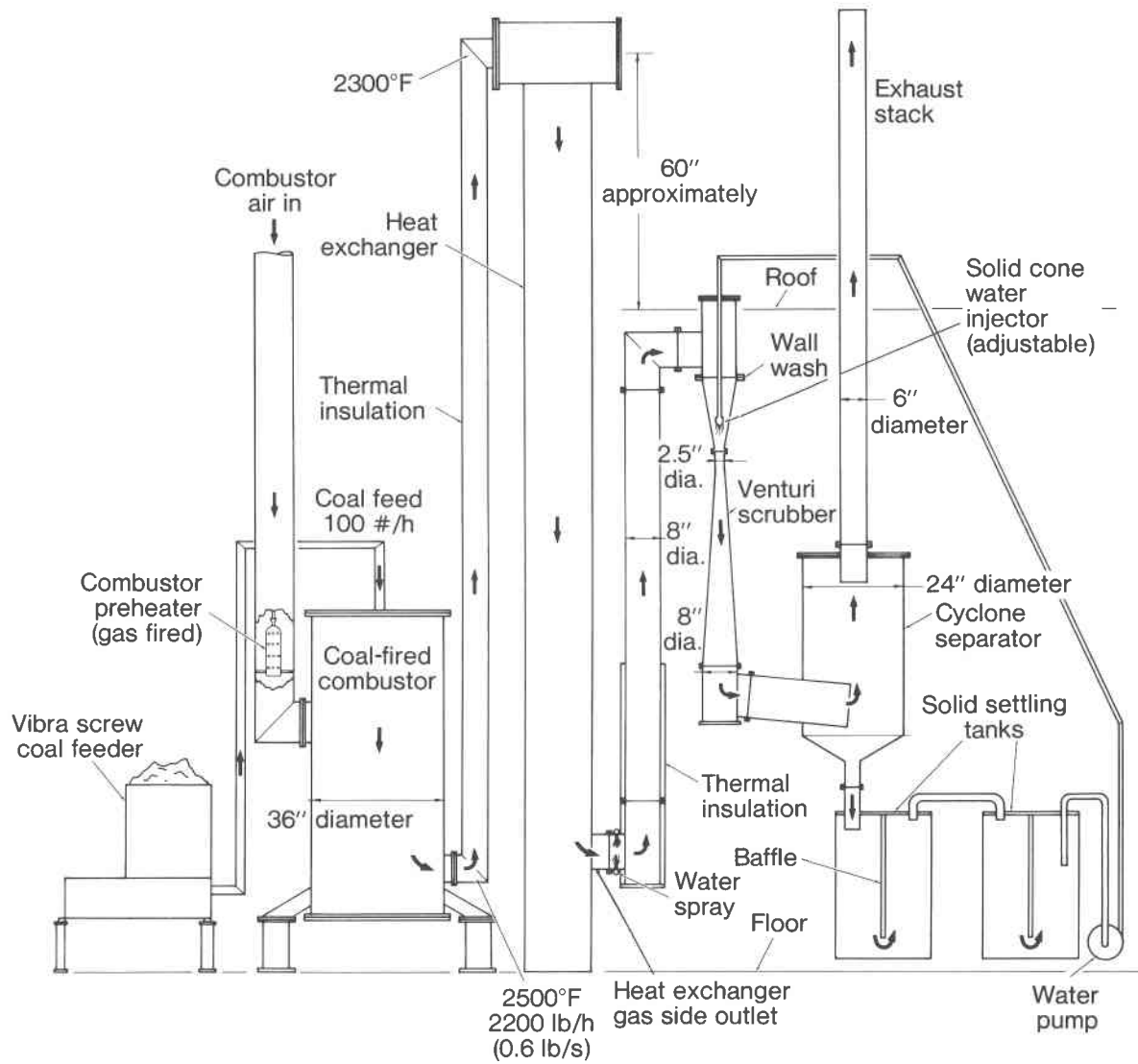


Figure 7. Coal-fired heat exchanger test facility.

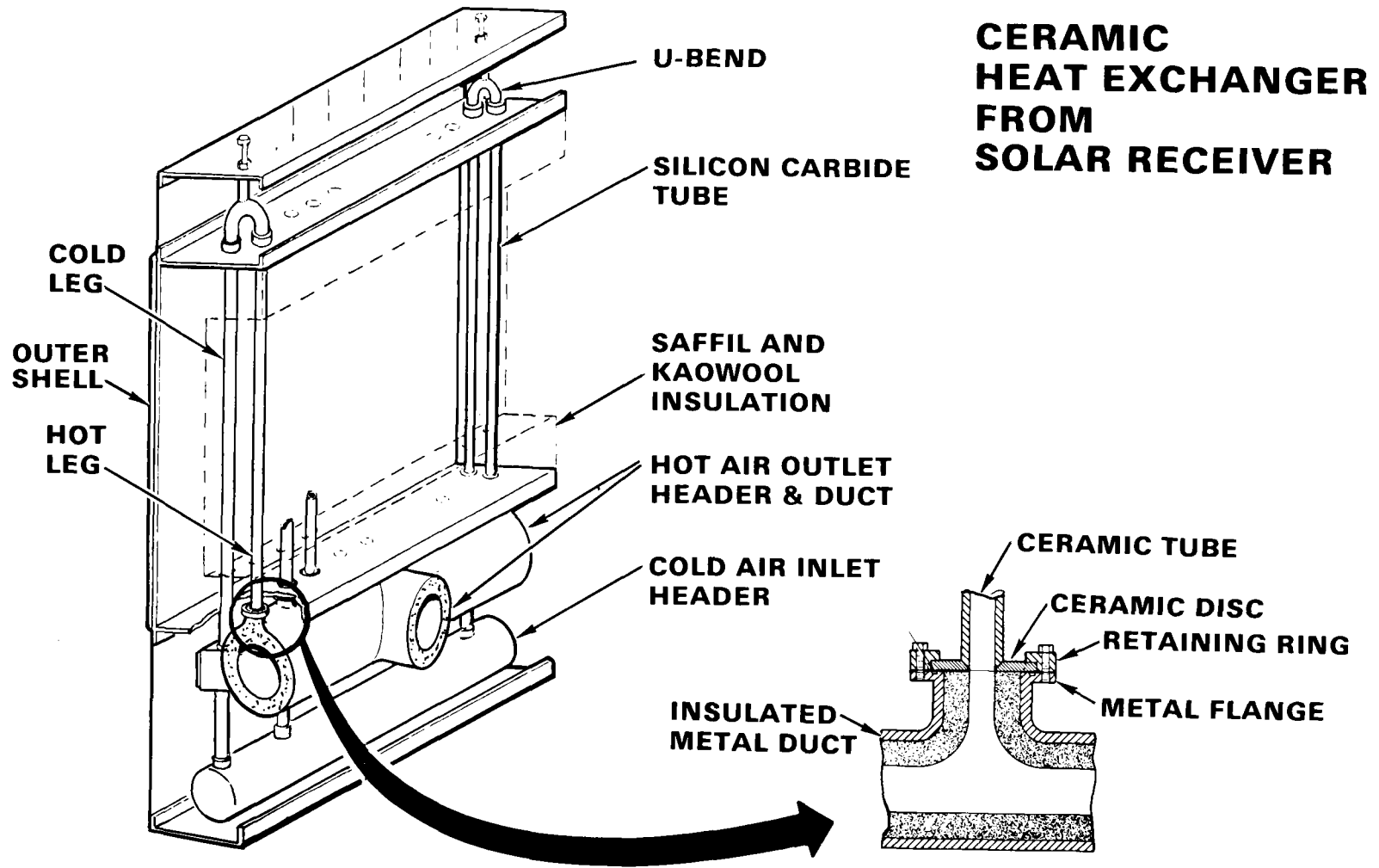


Figure 8

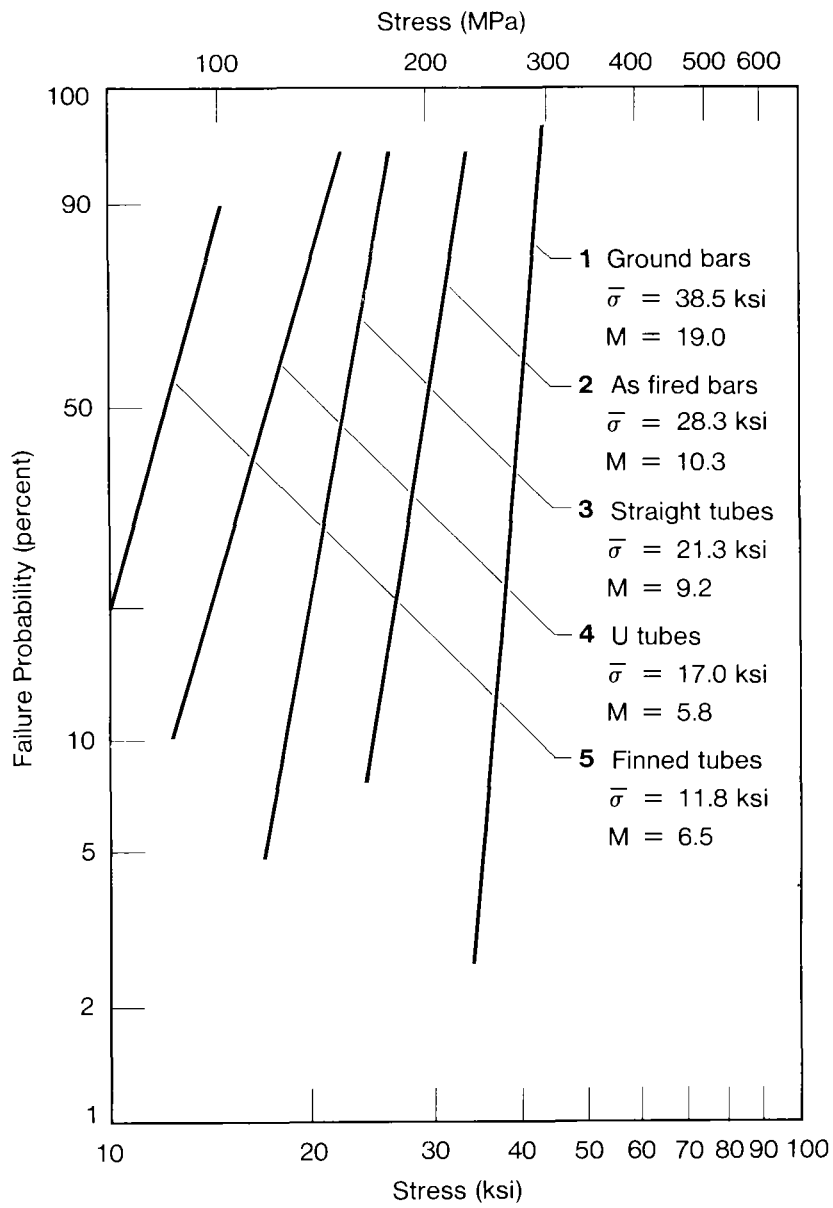
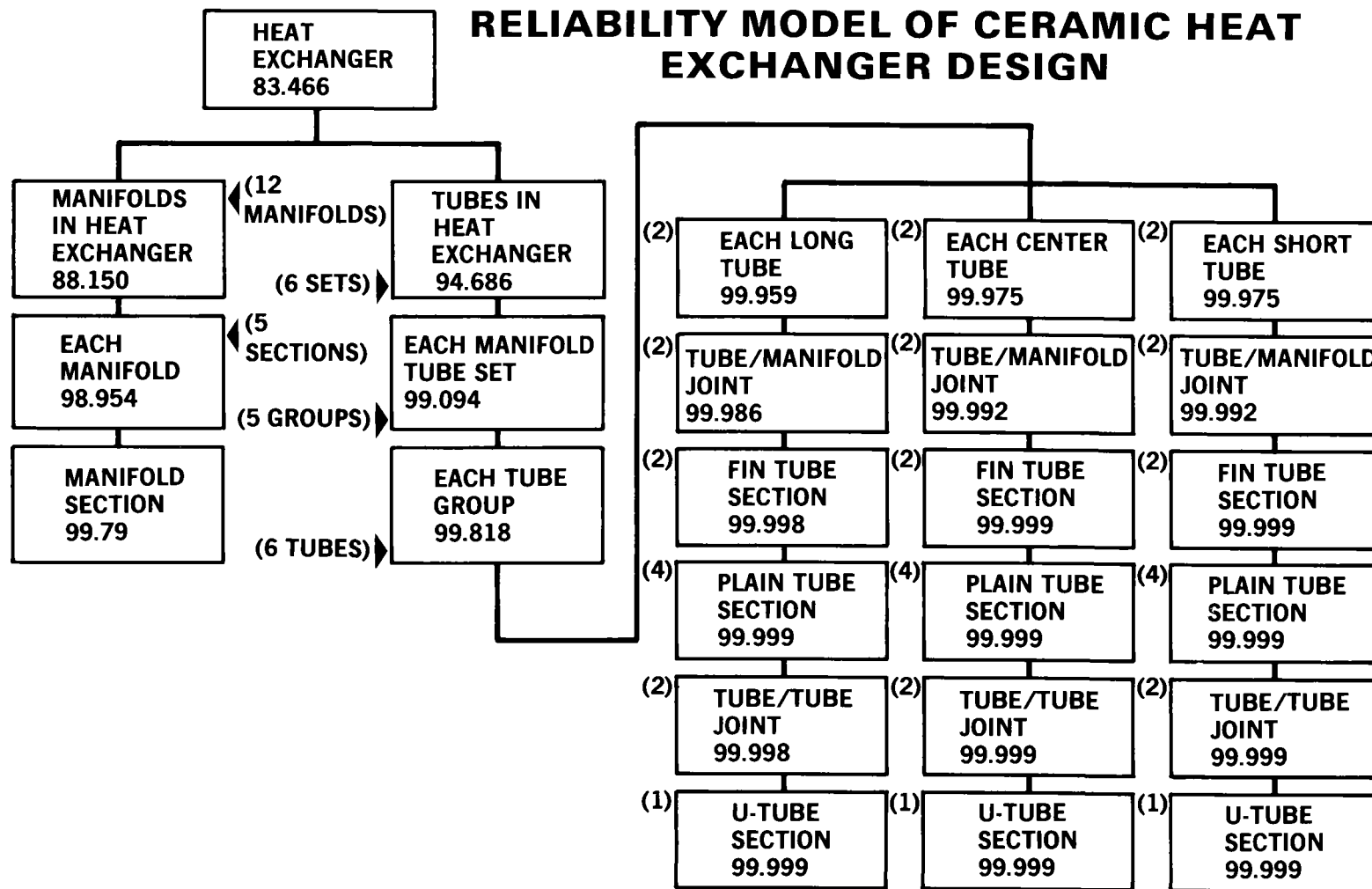


Figure 9. Effect of component size and complexity on fracture strength and variability of silicon carbide.



6-47

Figure 10

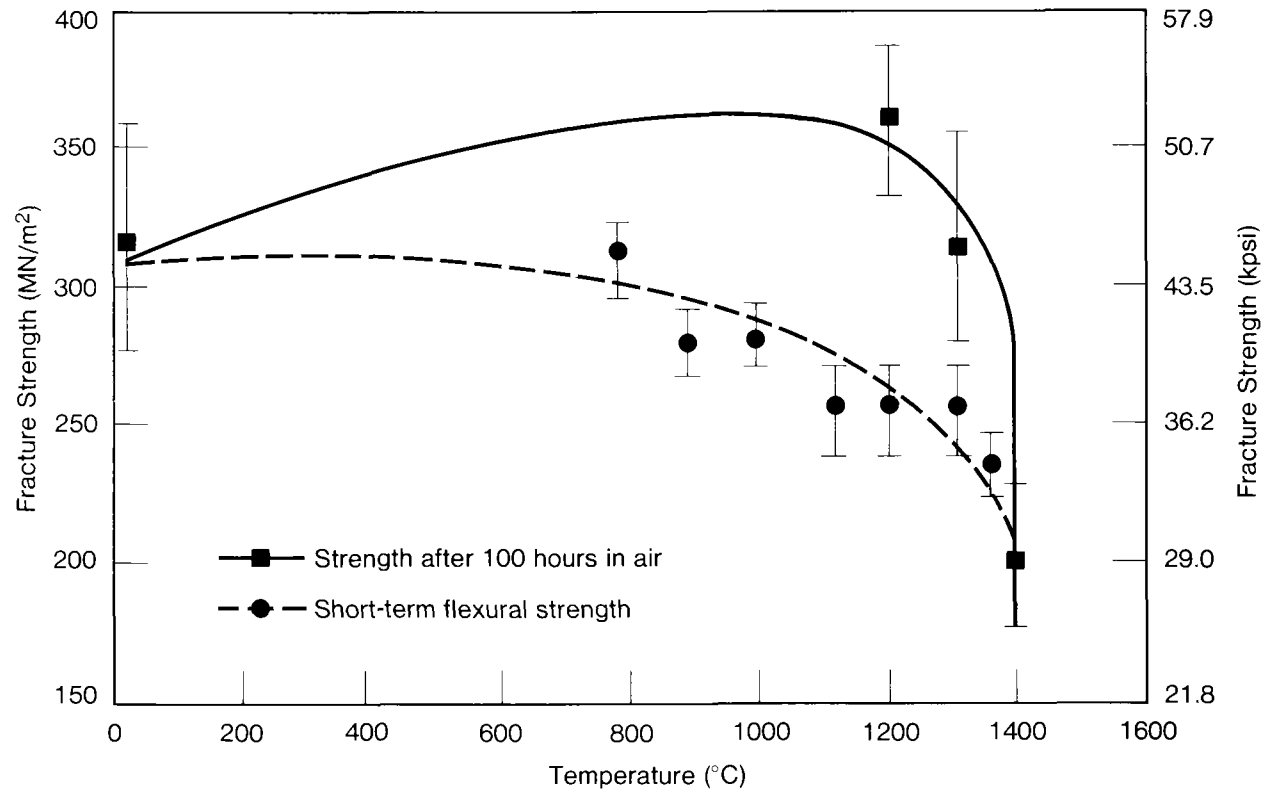


Figure 11. Strength increase in siliconized silicon carbide caused by oxidation at elevated temperature.

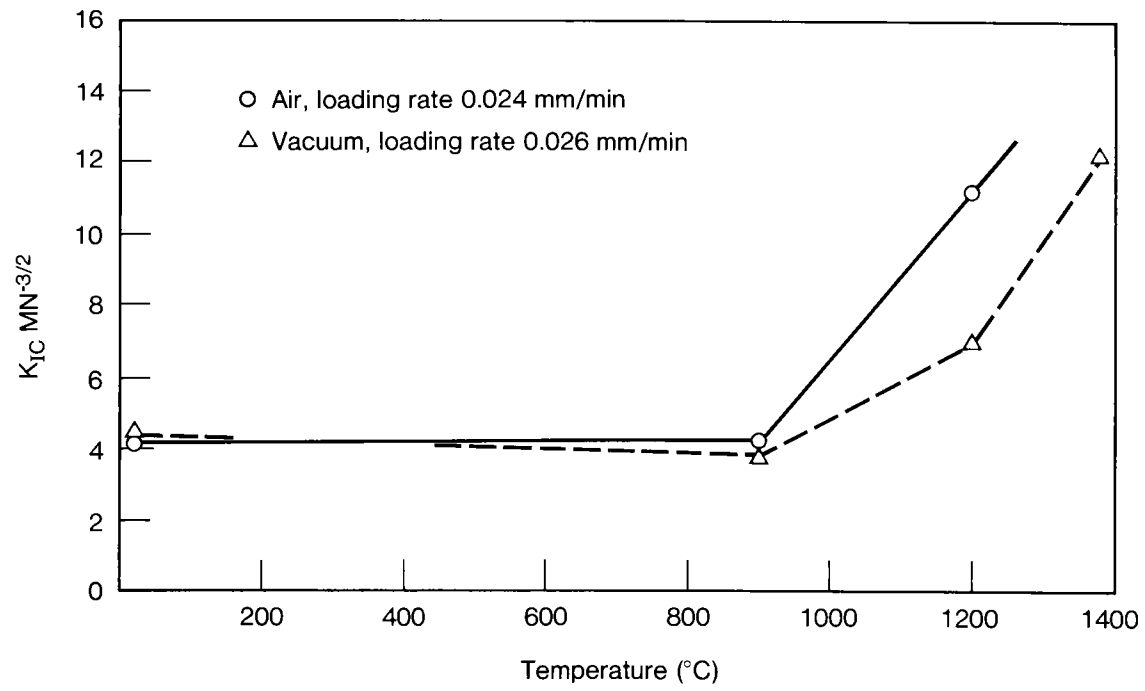


Figure 12. Fracture toughness of siliconized silicon carbide as a function of temperature (slow loading rate).

## SUMMARY OF CYCLIC FATIGUE RESULTS FOR SILICONIZED SILICON CARBIDE

### LEGEND:

- ◆ = BASELINE STENGTH DATA (WEIBULL m)
- = STRENGTH AFTER CYCLIC FATIGUE TESTING (WEIBULL m)
- = MAXIMUM STRESS DURING 1-HR, 1-Hz CYCLING

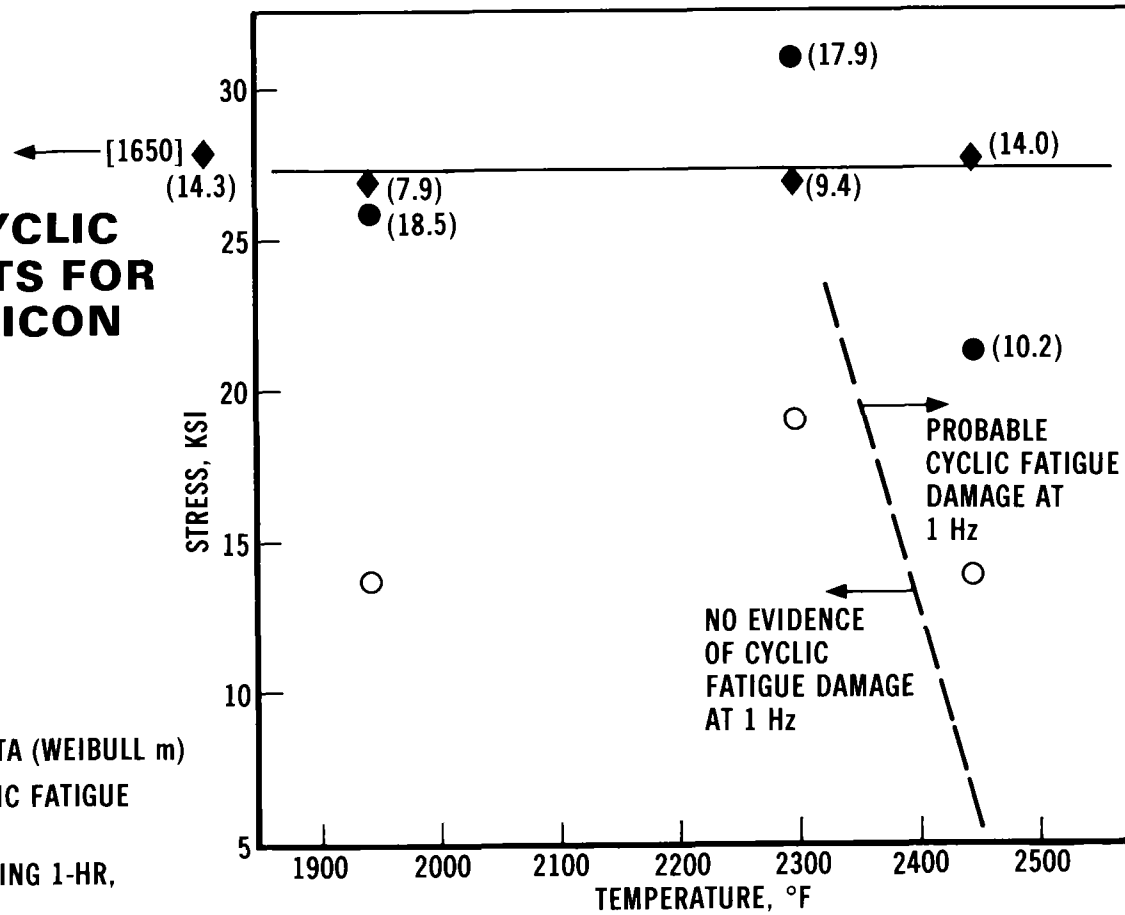


Figure 13

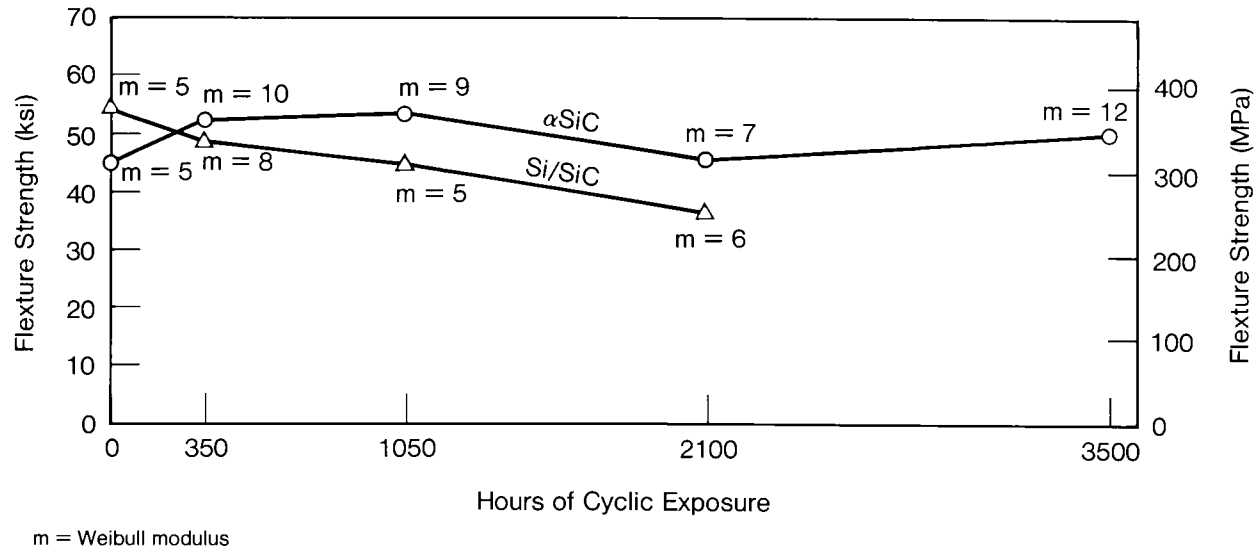


Figure 14. Room temperature fracture strength of siliconized SiC and  $\alpha$ -SiC after cyclic exposure at 1200°C.



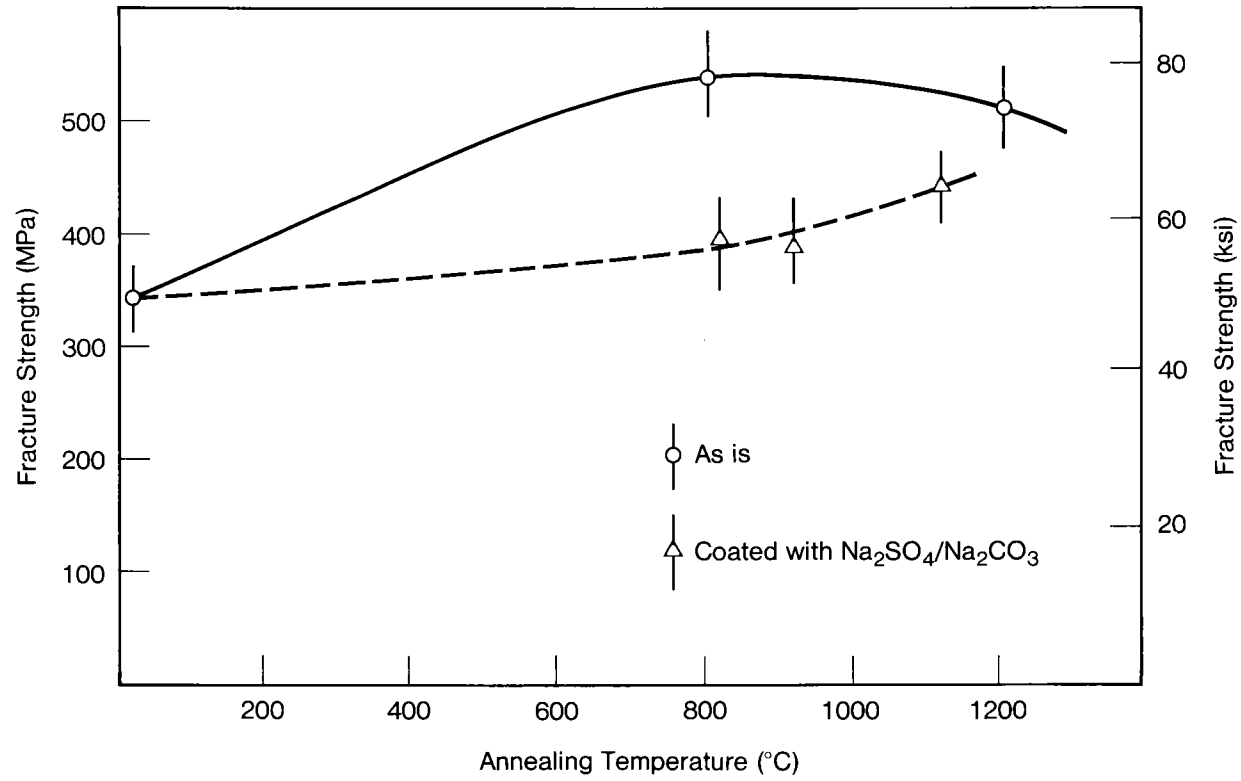


Figure 15. Fracture strength of siliconized silicon carbide after 48 hours annealing.

**MICROSTRUCTURE (100X)  
OF SURFACE AND AVERAGE  
FRACTURE STRESS FOR  
SELECTED SAMPLES OF  
NC-430**

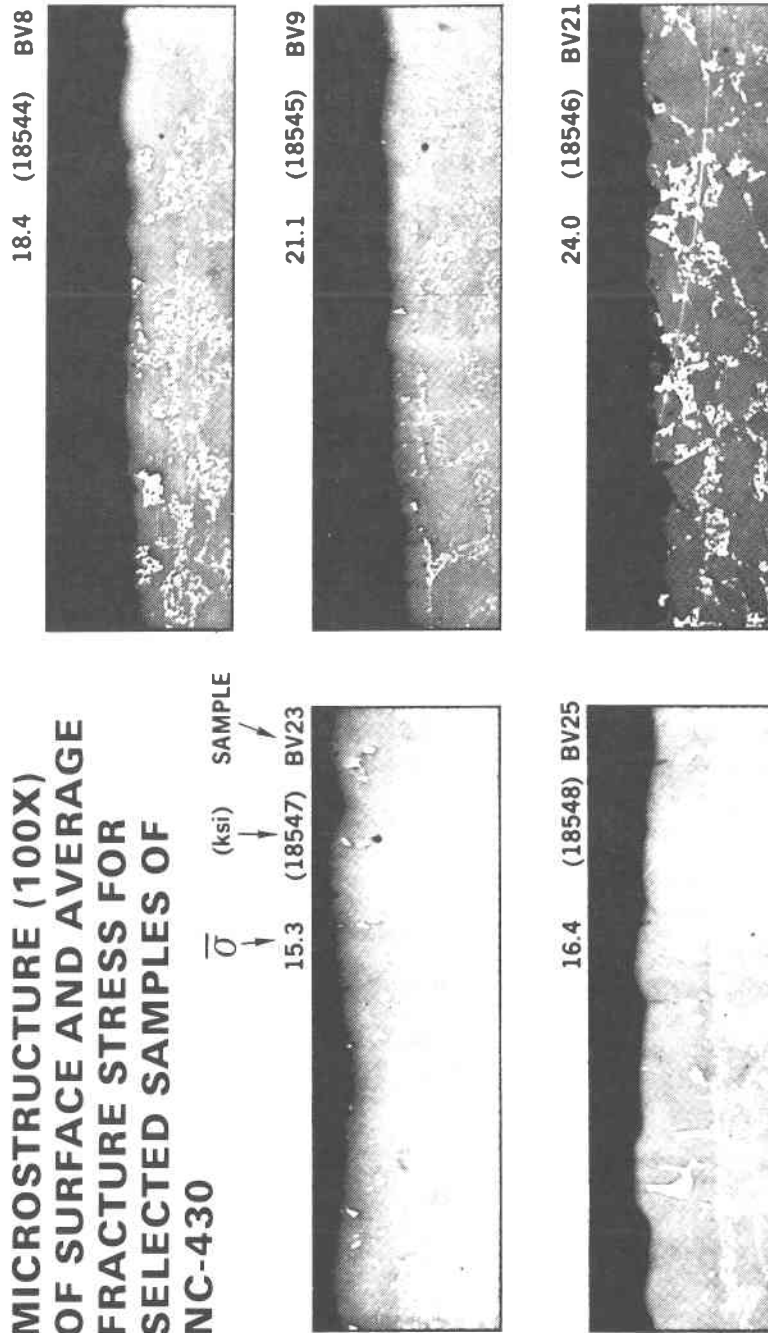


Figure 16

## CERAMIC COATINGS FOR USE IN ALTERNATE FUEL APPLICATIONS

by

J. W. Vogan, L. L. Hsu and A. R. Stetson

### ABSTRACT

The results of tests conducted on ceramic coatings in combustion environments generated by several different fuels are presented. Evaluations were made using municipal waste, solvent refined coal, Diesel No. 2 with controlled contamination levels of elements such as sodium, sulfur and vanadium as the fuel. Test methods employed municipal waste combustors, gas turbine engines, laboratory burner rigs and furnaces. Vitreous and plasma sprayed coatings were compared.

It was found that no single coating system was best in all environments. Vitreous coatings gave the best performance at lower temperatures (<600°F), high ash (municipal waste) combustion products while the plasma sprayed coatings were selected for gas turbine applications. A plasma sprayed coating greatly extended the life of a low NO<sub>x</sub> combustor and components with a vitreous coating were unaffected by conditions that destroyed corrosion resistant steel in a municipal waste incinerator.

### INTRODUCTION

Vitreous and plasma sprayed coatings were evaluated by field and laboratory testing in the products of combustion of alternate fuels. Test and coating combinations evaluated were:

- Municipal waste - vitreous ceramics
- Municipal waste - plasma sprayed ceramics
- SRC-II (low NO<sub>x</sub> combustors) - plasma sprayed ceramics
- Doped Diesel No. 2 (burner rig) - plasma sprayed ceramics
- Chemical corrodants (furnace) - plasma sprayed ceramics
- Diesel No. 2 (gas turbines) - plasma sprayed ceramics

This paper summarizes the results. Each of the environments differs widely from the others and, as a result, each is presented as a separate investigation of the effectiveness of ceramic coatings in protecting alloys from attack by alternate fuels.

The coating systems tested are given in Table 1. Table 2 lists the alternate fuels. The test data provides a basis for selecting coating types for investigation in new applications and indicates areas now under investigation at Solar.

Table 1  
Coating Types Evaluated

<u>Type</u>	<u>Designation</u>	<u>Thickness (mils)</u>
Vitreous	S5210-2C(1)	1-2
Vitreous	S6100M	1-2
Vitreous	S1600(1)	1-2
Vitreous/Metal	S20-180NC-1(2)	2-3
Vitreous	A418(3)	
$\text{CaTiO}_3/\text{NiCrAlY}$ base(4)		5 Base + 10 Ceramic
$\text{ZrO}_2\cdot 8\text{Y}_2\text{O}_3/\text{NiCrAlY}$ base(4)		5 Base + 10 Ceramic

- (1) Complex barium silicate glasses with various mill additions (Solar)
- (2) Complex barium silicate glass with Ni-20Cr addition (Solar)
- (3) Barium borosilicate glass coating developed at the National Bureau of Standards (applied at Solar)
- (4) Under development at Solar on NASA-Lewis/DOE Contract DEN3-109

Table 2  
General Type of Fuels Used in Test

1. Municipal Waste
2. SRC-II Using Stage Combustion
3. Diesel No. 2 with Additives

## CERAMIC COATINGS FOR COMBUSTION OF MUNICIPAL SOLID WASTE

There is an increasing need throughout the world to dispose of municipal waste in a manner that is energy efficient, maximizes scrap reclamation, and minimizes the requirement for landfill. The European countries have pursued this course for years primarily to reduce the requirement for landfill space and to reduce storage of toxic waste, thus minimizing the "Love Canal" type problems.

In Europe, super-heated steam is produced for the generation of electricity or for process, industrial, or residential heating. In many potential use areas in the United States, the need for process steam does not exist at the plant locations and a more cost-effective technique for electric power generation is required. The indirectly fired gas turbine, driving electric generators, is a candidate for this application.

Before one can undertake such a major step, from the steam turbine to the gas turbine, a major materials and coating evaluation program will be required to determine the upper and lower limits of operation for the heat exchanger in the Brayton cycle system.

Preliminary work was conducted to determine corrosion in the temperature range of 1300° to 1600°F for two alloys (AISI 310 and Incoloy 800), the type of coatings required to afford protection for a cost-effective period of time (greater than 1 year), and the amount of deposit to be anticipated.

The evaluation program was conducted in an actual waste burner in cooperation with U.S. Fiber Cycle, a firm engaged in energy recovery from municipal waste. The waste burner is one of the batch types manufactured by Consumat, Inc. The unit is located in Bellingham, Washington and burns essentially any type of waste with no separation of the waste material.

The cycle for this burner was 12 hours of burning each day for 5 days. A month, a standard test period, thus averaged about 240 hours.

The specimens for this test were either 3/4" diameter AISI 310 or 5/8" diameter Incoloy 800 tubing, 54" long. The test section was the center 18" which was made up of three 6" sections - the center one uncoated and the other two coated. Some variations of the test section length were included to maximize data from a 1-month run.

The initial 18 specimens (9 per alloy each with uncoated and an H9-109A and Solaramic 5210-2C coated 6" sections) were instrumented with Type K MagPak thermocouples as illustrated in Figure 1, and provision was made to internally cool the tubes to obtain temperatures of 1300°, 1500° and 1600°F, the range of interest for a heat exchanger to be used for Solar's Saturn or Centaur turbine engines.

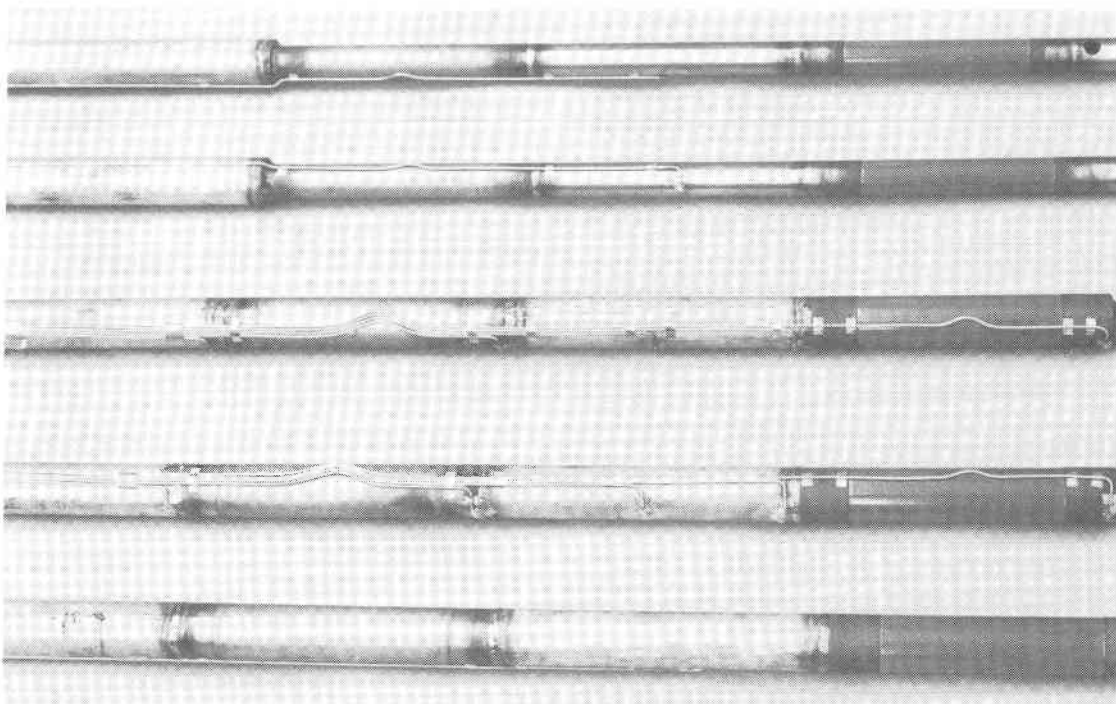


Figure 1. Typical Test Specimens Used in First Test in Municipal Waste Combustion Environment in Bellingham, Washington

The tubes were installed in the stack of the waste burner (gas temperature ~1800°F) as shown in Figure 2. The tubes were connected to an air supply and valving arrangement, Figure 3, to adjust individual tubes to the desired temperature - 1300°, 1500° and 1600°F. In the initial test all thermocouples failed within 24 hours (2 days) and most within 12 hours due to corrosion of both the sheath and thermocouples. The test was stopped and all tubes returned for rework. The rework consisted of removing all external thermocouples and replacing them with internal couples, i.e., couples in the clean cooling air section of the tubes. The thermocouples were, however, welded to the tube outer surface.

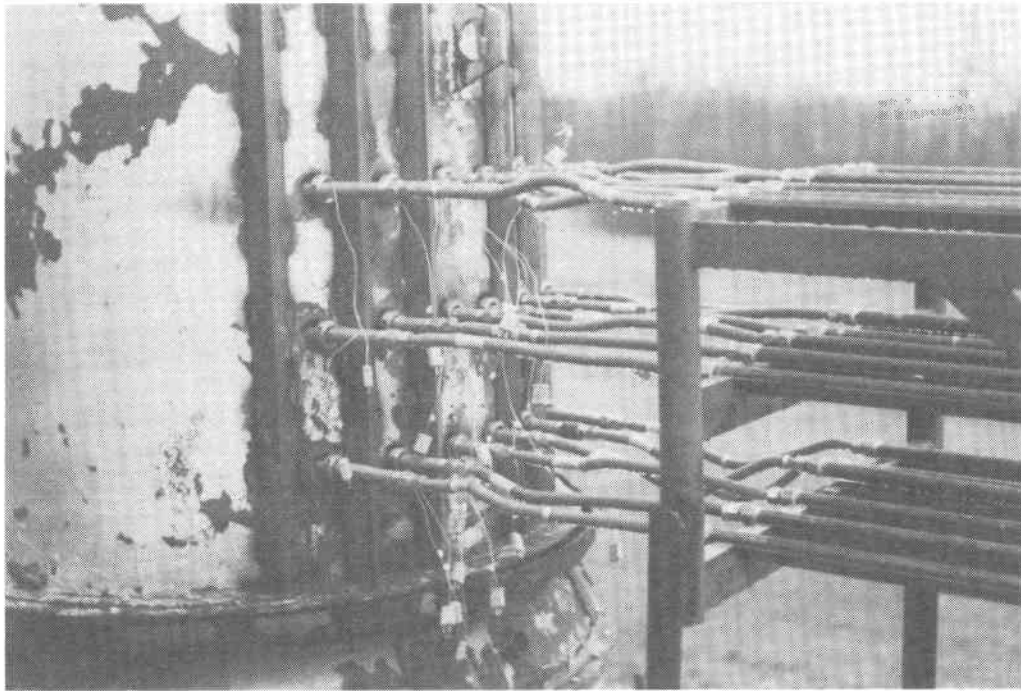


Figure 2. Closeup of the Test Section Connector and Thermocouple Leads

The temperature readout during the burning cycle was so variable due to the temperature fluctuation in the combustor that in the evaluation of results it is better to consider that all tubes were exposed to similar temperatures varying between 1300° and 1600°F during each burning cycle.

The evidence of corrosion was quite severe on the tubes after only the 2-day run. One Incoloy 800 tube was cut up for metallographic examination of the uncoated area and the areas coated with the H9-109A (aluminizing) and S5210-2C vitreous refractory enamel. A cross section is shown through the aluminized and the uncoated area in Figure 4. The uncoated Incoloy 800 was penetrated to a depth greater than 8 mils and the aluminized coating was completely penetrated. Sulfidation is evident, both by the appearance of the microstructure and by SEM/EDX analysis of the microstructure, which shows high sulfur and chromium contents, Figure 5.

The Solaramic S5210-2C coating afforded complete protection to the Incoloy 800 alloy for this short exposure. The appearance of this coating after wire brushing on the upstream side (facing the flame) and downstream side is shown in Figure 6 on both 310 SS and Incoloy 800. There was some adherence of flyash to the coating on the upstream side and essentially none on the downstream side. Figure 7 is a section through the S5210-2C coated area showing the complete protection of the substrate and complete retention of the coating on the downstream side.

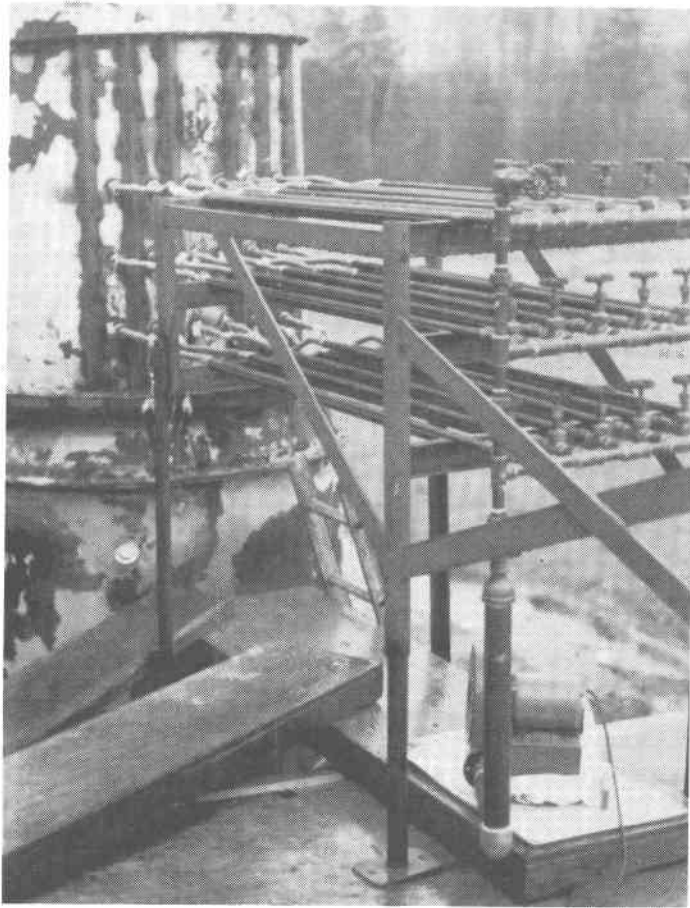
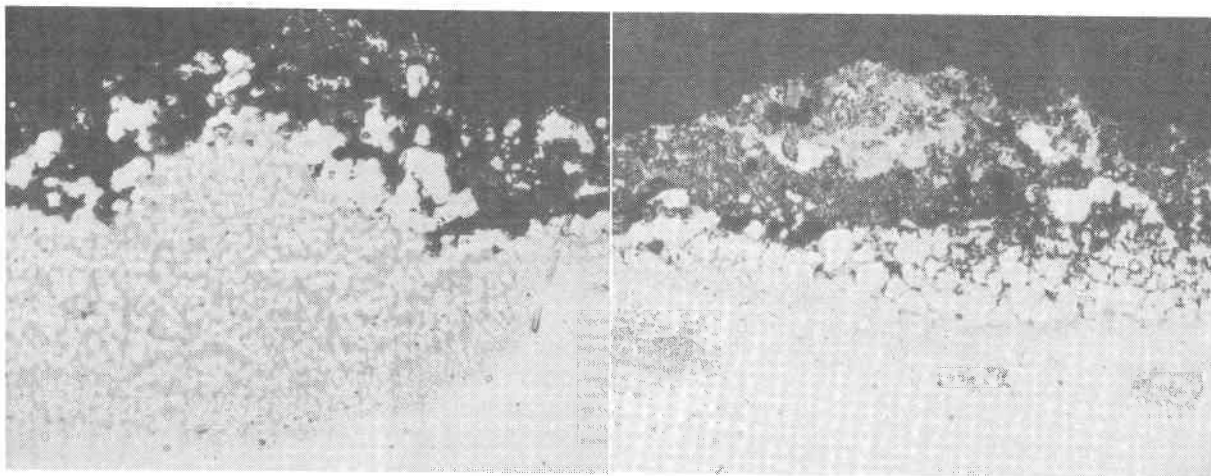


Figure 3. Installation With 18 Tubes in Place

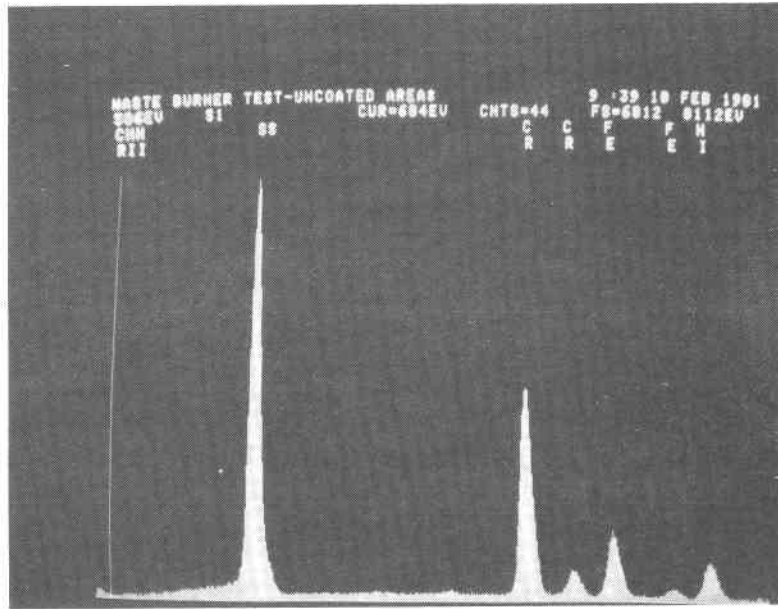


Uncoated

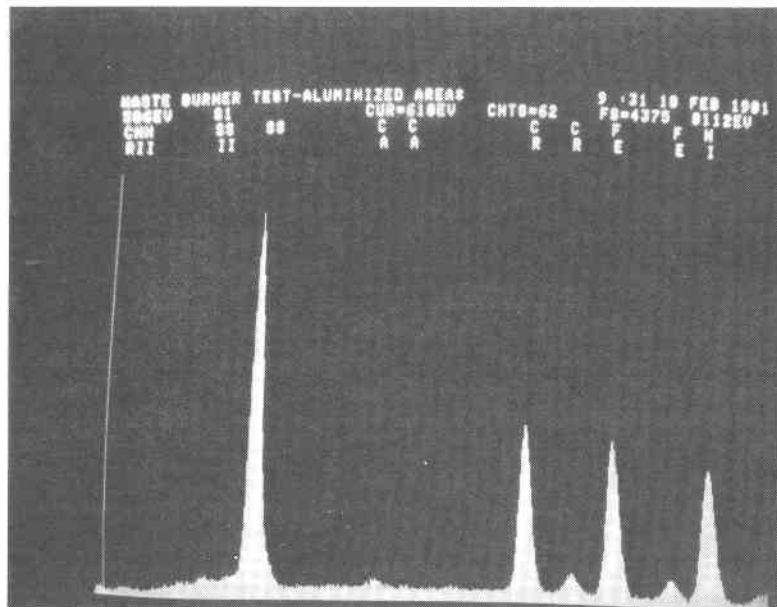
H9-109A Aluminized

Figure 4. Uncoated and H9-109A Aluminized Incoloy 800 - 24 Hours





Uncoated Incoloy 800



Aluminized Incoloy 800

Figure 5. EDX Analysis of Corrosion Product on Uncoated and Aluminized Incoloy 800

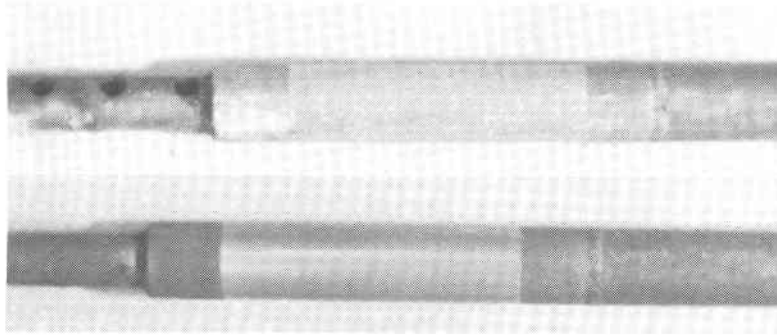
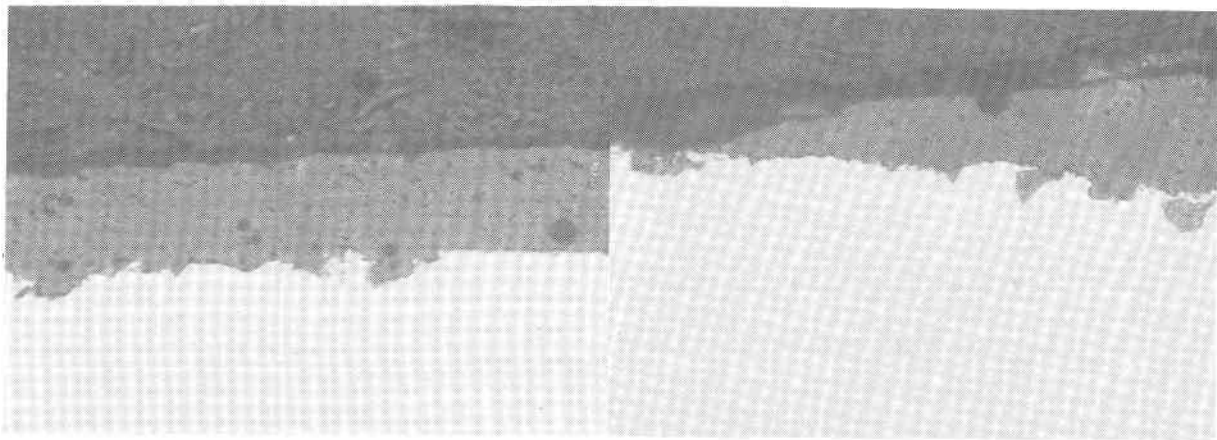
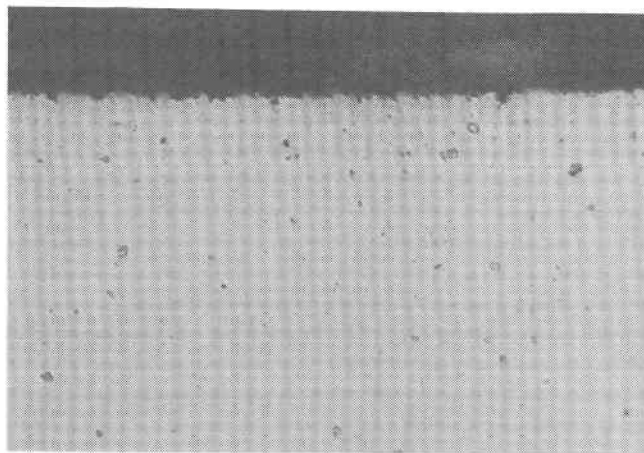


Figure 6. S5210-2C Coating After 14 Hours



Trailing Edge

Leading Edge



Internal

Figure 7. Solaramic S5210-2C Coated Tube - 24 Hours Exposure in Combustion Products of Solid Waste

Because of the short exposure time the tubes were re-instrumented without recoating except that the one sectioned tube was repaired and a slightly more refractory vitreous coating was applied to a short section of tubing, Figure 8. The coating is Solaramic S6100M, which is a minor mill addition modification of S5210-2C. The 18 tubes were placed back in service for 1 month with two ceramic tubes of NC430 silicon carbide also included.

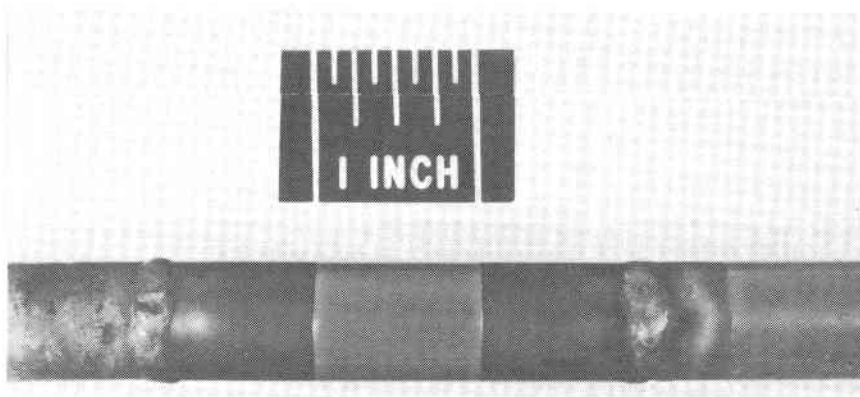


Figure 8. Vitreous Coating Closeup - First Rework - Coating S6100M

Several tubes were removed after 230 hours of additional testing with all thermocouples functioning, but with the continuation of the fluctuating temperatures in the tubes (1300° to 1600°F). Figure 9 provides an adequate overview of how the coatings performed on Incoloy 800 after 230 hours. The uncoated alloys and the aluminized alloys were deeply attacked and the Solaramic S5210-2C and S6100M coated tube sections fully protected. The external appearance of the two coatings is shown in Figure 10. Again, as noted previously, the upstream side was contaminated with ash and the downstream side was unaffected. Much less ash adhered to the ceramic coatings than to the oxidized uncoated or aluminized surfaces. The AISI 310 tubes performed identically to the Incoloy 800 tubes.

The NC430 tube after 1 month, Figure 11, showed only slight surface attack. Microphotographs were not available for this tubing at the time of writing of this paper.

At a 2-month interval or a total of 400 fired hours, a second group of tubes were removed; primarily those coated with S5210-2C, S6100M and H9-109A aluminizing. Many of our test sections had been lost by falling into the combustion chamber due to the complete penetration of the uncoated alloy. The remnant of one that was retrieved is shown in Figure 12. As illustrated, the uncoated Incoloy 800 was completely penetrated, the H9-109A aluminizing severely attacked. The vitreous ceramic coating, S5210-2C, provided essentially complete protection.

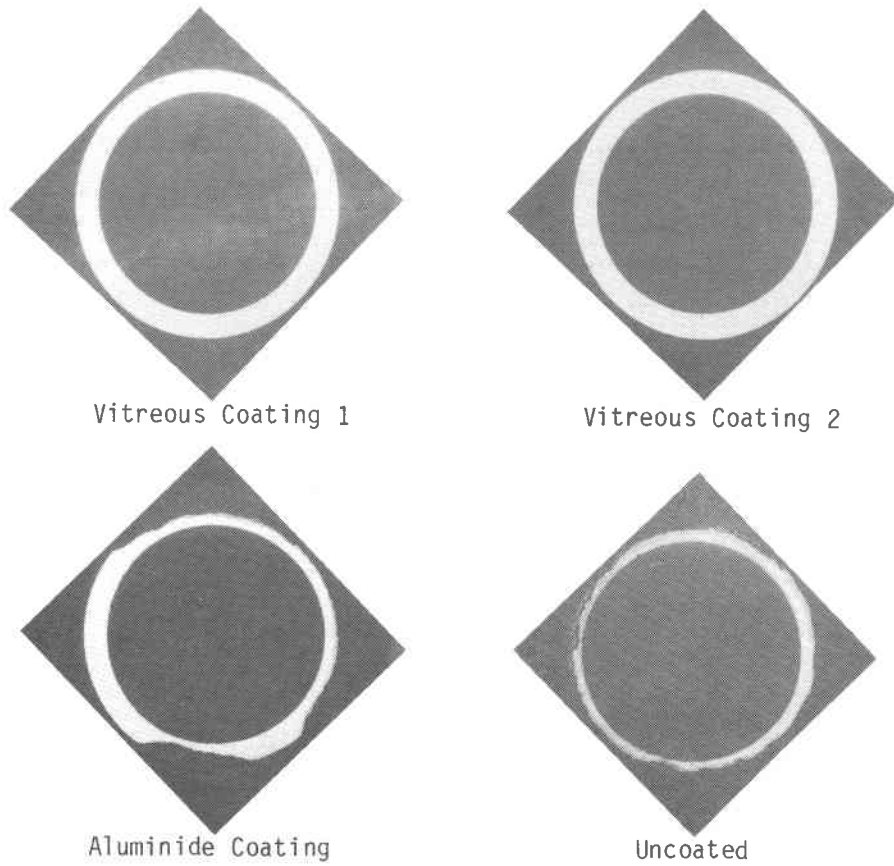


Figure 9. Typical Cross Section of Incoloy After One-Month Exposure (230 Hrs)

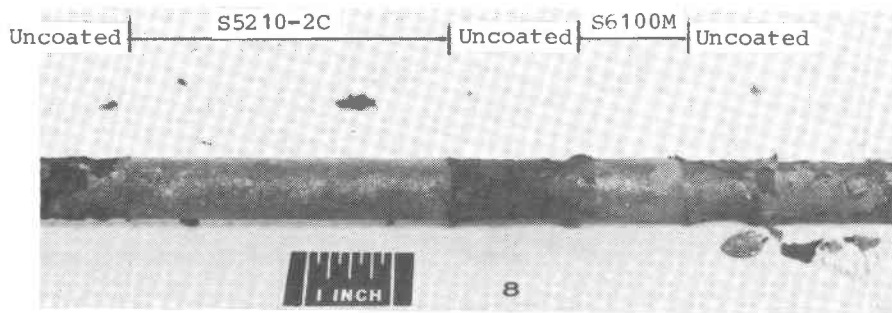


Figure 10. Physical Appearance of Incoloy 800 Tube After One-Month Exposure (230 Hrs)

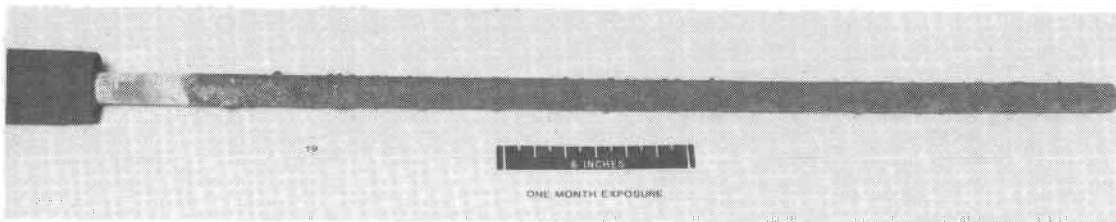


Figure 11. NC-430 SiC - One Month in Combustion Products of Municipal Waste

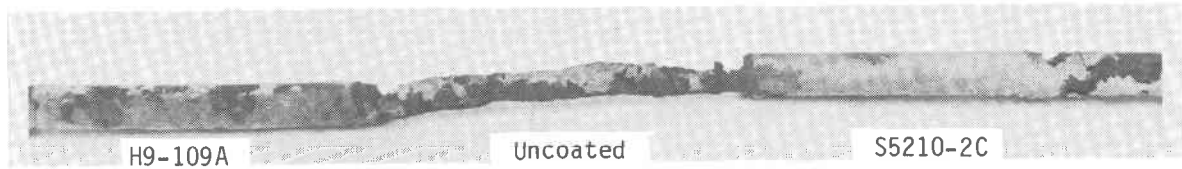


Figure 12. Two-Month Exposure - Municipal Waste Combustion Products

At this point in the investigation it was concluded that to avoid flyash reaction on the upstream side, more refractory ceramic coatings were required. Two new tubes were prepared to test this premise. Tube No. 1 (actually No. 21) was prepared with four 4.5" Incoloy 800 coated pieces welded into the center section. The coatings applied to the sections were as follows and were all of the vitreous type and more refractory than S5210-2C:

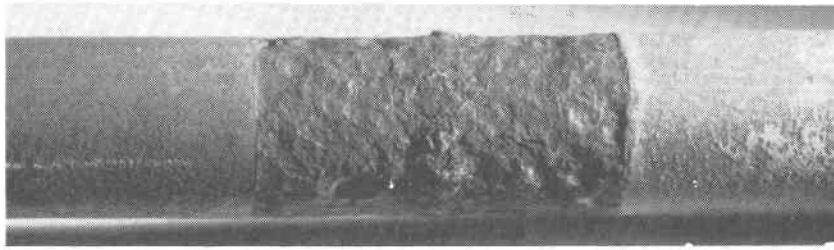
- S6100M (Solar)
- S6100 (Solar)
- A418 (70 NBS frit and 30 Cr<sub>2</sub>O<sub>3</sub>)
- S20-180NC-1 (50 v/o 320-180 frit - 50 v/o Ni-20Cr powder) S20-180 is an alkali-free barium borosilicate type frit

The second tube (No. 22) was prepared with three small areas coated by plasma spraying with the following compositions:

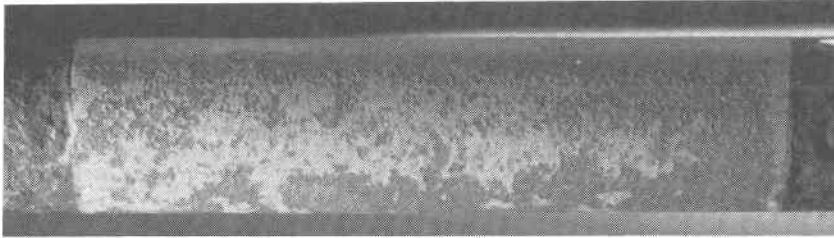
- NiCrAlY + ZrO<sub>2</sub>.8Y<sub>2</sub>O<sub>3</sub>
- CoCrAlY + ZrO<sub>2</sub>.8Y<sub>2</sub>O<sub>3</sub>
- NiCrAlY + CaTiO<sub>3</sub>.

The tubes were installed and exposed for 1 month under the standard conditions. The uncoated Incoloy 800 corroded in the normal manner. After wire brushing the vitreous coating, the upstream and downstream sides of the coated areas could not be distinguished. Visual examination would indicate that the more refractory A418 and S20-180NC-1 were unaffected. The other two coatings, S6100M and S6100, showed only some slight mottling, which is probably due to localized crystallization in to the presence of the flyash. Macrophotographs of the four coatings after the 240-hour test (1 month) are shown in Figure 13.

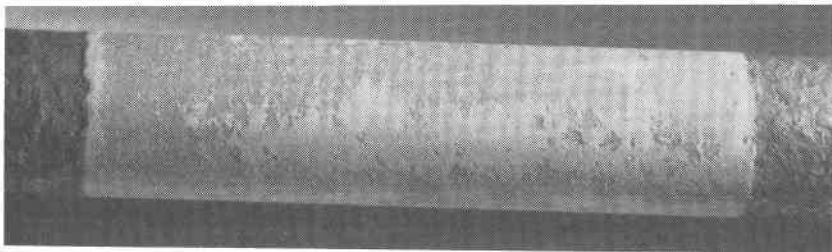
The appearance of the plasma sprayed coatings is shown in Figure 14. The ZrO<sub>2</sub>.8Y<sub>2</sub>O<sub>3</sub> coating with the CoCrAlY base coat failed by either spallation or attack on the bond coat. The other two coatings showed various degrees of spallation but afforded significant protection to the substrate.



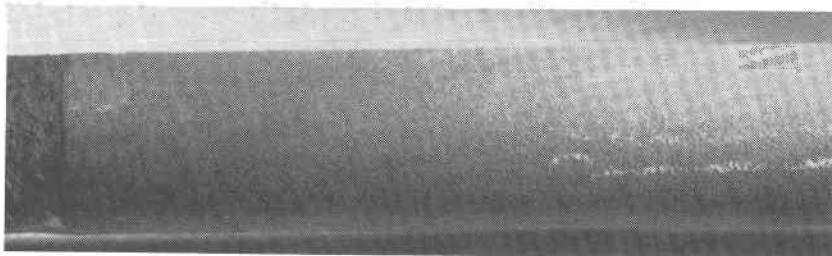
A. Uncoated



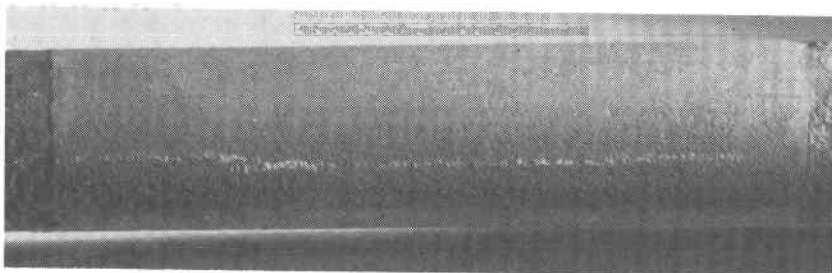
B. Solaramic S6100M



C. Solaramic S6100

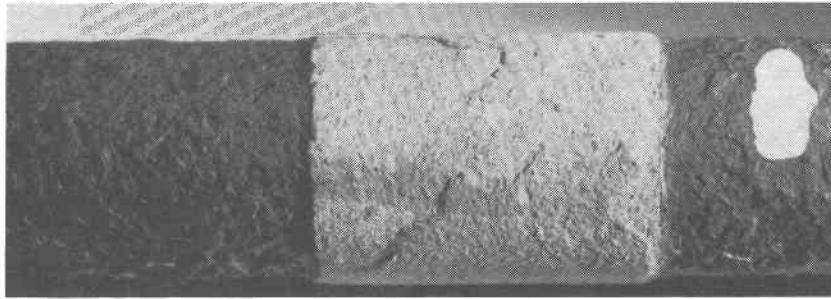


D. Metal/Ceramic S20-180NC-1

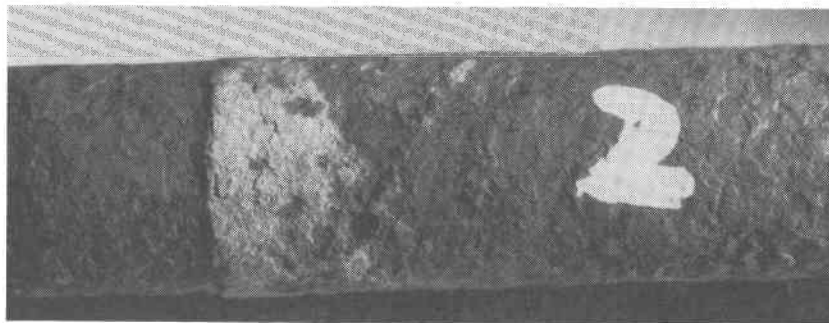


E. NBS A418

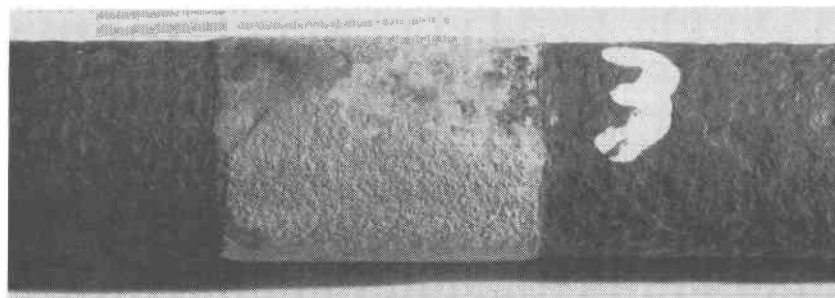
Figure 13. 240-Hour Test of Thin Vitreous or Vitreous/Metallic Coatings on Incoloy 800 in Combustion Products of Municipal Waste (Metal Temperature 1300°-1600°F)



A.  $ZrO_2 \cdot 8Y_2O_3$  (NiCrAlY)



B.  $ZrO_2 \cdot 8Y_2O_3$  (CoCrAlY)



C.  $CaTiO_3$  (NiCrAlY)

Figure 14. Plasma Sprayed Coatings on Incoloy 800 After 240-Hour Testing in Combustion Products of Municipal Waste

#### Conclusions for Municipal Waste Exposures

The combustion products of municipal waste are extremely corrosive in the temperature range of this investigation, i.e., 1300° to 1600°F. Alloys such as AISI 310 and Incoloy 800 are penetrated to a depth of 50 mils in less than 400 hours. Vitreous ceramic coatings have shown that they can afford complete protection for times up to 400 hours. There is significant need for longer testing times and optimization of the coatings, particularly to increase the softening temperature of

the vitreous phases to prevent ash-coating reaction. Plasma sprayed coatings also showed promise in resisting ash attack but the cyclic performance resulted in significant coating spallation. The vitreous coating showed no evidence of spallation under these test conditions.

The superior performance of the vitreous coatings as compared to the oxide on the alloys or to the aluminum-enriched surface probably is due to the extreme severity of environmental attack and the relatively low test temperature. The ceramic coating is thick enough to resist attack, whereas the coatings requiring diffusion to repair damage can't handle the rate of attack, probably, by both alkali sulfate and chlorides.

#### THERMAL BARRIER COATINGS FOR COMBUSTION CANS BURNING SRC-II

As indicated previously, ceramic coatings and the underlying substrate are subject to attack by the turbine environment. Typically, the variations due to specific fuel-air ratios will significantly affect coating performance. In a recently completed DOE/NASA contract to develop low NO<sub>x</sub>, heavy fuel combustors for advanced gas turbines, calcium titanate and yttria stabilized zirconia were compared qualitatively. The coatings were evaluated on a go/no-go basis for their ability to resolve local overtemperature problems being encountered in the primary combustion zone. A sketch of this combustor is shown in Figure 15 and the fuel composition is given in Table 3. This combustor operates in a fuel-rich (reducing) condition. A typical set of operating parameters using solvent refined coal (SRC) as the fuel is given below:

<u>Primary Zone Combustion Conditions</u>	
Fuel	SRC-II
Combustor Pressure	160 psig
Inlet Temperature	500°F
Exit Temperature	1850°F
Air Flow	0.65 lb/sec
Fuel/Air Ratio	0.156
Fuel/Stoichiometric Ratio	2.31

During testing combustor conditions were varied using fuel/air ratios ranging from 0.052 to 0.152.



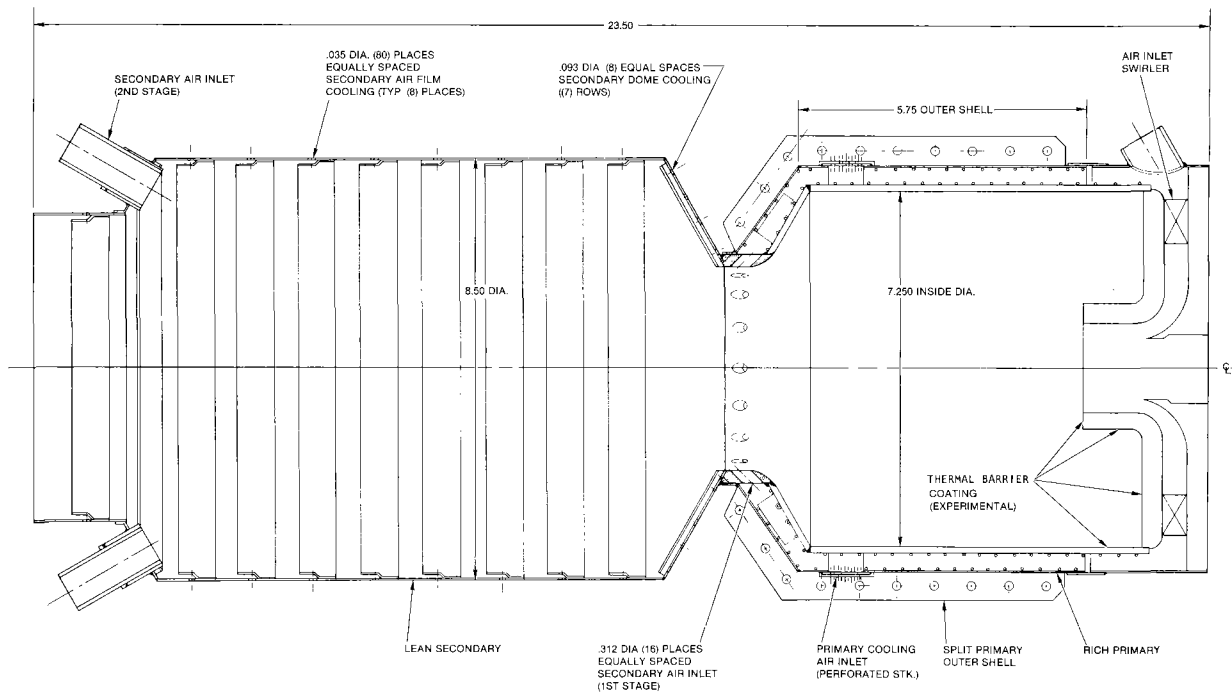


Figure 15. Experimental Low  $\text{NO}_x$  Combustor

Table 3

Major Components and Impurities of SRC-II Fuel

Component	
Nitrogen: %W	0.9- 1.1
Oxygen: %W	3.6-4.3
Sulfur: %W	<0.2
Carbon: %W	86.0
Hydrogen: %W	9.1
Hydrocarbon groups (HPLC): %V	
Saturates	35.0-38.0
Aromatics and polar compounds	62.0-65.0
Nickel: ppm	<0.1
Vanadium: ppm	<0.1
Sodium: ppm	-

Results of these tests showed a significant difference in the performance of the zirconia and calcium titanate coatings. Initially, a  $ZrO_2 \cdot 8Y_2O_3$  coating 0.010" thick was applied to the internal surfaces of the combustor using a Ni-19Cr-6Al-0.2Y bond coat to improve adherence and reduce interfacial corrosion. This coating system proved to be unsuitable for use in the fuel-rich environment. After a brief period of operation the coating structure was destroyed (probably by reduction) and the coating was lost as a fine powder.

A second TBC using calcium titanate as the ceramic overlay with a NiCrAlY bond coat was applied to the combustor. This coating remained intact throughout the combustor test program. After an initial 40 hours of operation the unit was inspected and the coating was found to be intact. Loss of the Hastelloy X liner through overheat had been eliminated. No problems were encountered for the remainder of the SRC-II fuels test program.

#### THERMAL BARRIER COATINGS USED WITH DOPED DIESEL NO. 2 FUEL

Currently gas turbines are operated on fuels with a closely controlled composition. This composition limit for liquid fuel, and that of four fuels under consideration by customers, is given in Table 4. As is evident in the table, a need exists for coatings that are stable in the presence of materials containing alkali metals, vanadium and sulfur. Products of combustion from these impurities such as vanadates and alkali sulfates have been found to attack ceramics such as zirconia and severely corrode turbine components. As part of the coating development program three ceramics were selected for evaluation as candidates for TBC usage. Properties of these materials along with those of a current turbine alloy are given in Table 5.

The stabilized zirconia has been found empirically to be one of the most promising materials tested for use as TBCs in clean fuel and was selected to provide a baseline.

The basis for selection of  $MgAl_2O_4$  and  $CaTiO_3$  can best be illustrated by consideration of problems that have been encountered with the  $MgO-ZrO_2$  and  $ZrO_2-Y_2O_3$  compositions currently in use. With these last two coatings, chemical attack by  $SO_4$ ,  $V_2O_5$  and/or  $P_2O_5$  has produced volume growth and/or destabilization of structure that results in ultimate coating spall. The two new coating systems were selected as being single compound with the potential for being more stable than the two-phase  $ZrO_2 \cdot 24MgO$  or the solid solution  $ZrO_2-8Y_2O_3$  composition. Both spinel and Pervoskite compounds have lower melting temperatures than  $ZrO_2$  and thus in application will

Table 4

## Proposed Fuels for Industrial Turbine Use

	<u>Solar Diesel No. 2 Specification</u>	<u>Fuel A</u>	<u>Fuel B</u>	<u>Fuel C</u>	<u>Fuel D</u>
Sulfur	1% max.	1.9	2.0	1.9-2.3	1.4-2.7
Vanadium	0.5 ppm max.	25.0	18.0	2.0-9.0	3.0-13.0
Sodium + Potassium	1.0 ppm max.	10-15	2.0	0.1-25.0	2.0-6.0
Lead	2.0 ppm max.	NR*	NR*	NR*	NR*
Ash	5.0 ppm max.	30-100	50.0	20-2200	1.4-2.7

\*NR - not reported

Table 5

## Physical Properties of Selected Materials

	<u>ZrO<sub>2</sub> Stabilized</u>	<u>MgAl<sub>2</sub>O<sub>3</sub> Spinel</u>	<u>CaTiO<sub>3</sub> Perovskite</u>	<u>MAR-M421 Alloy</u>
Melting temperature	4700°F	3875°F	3580°F	2300-2500°F
Thermal conductivity (Btu/hr/Ft°F)	1.0 (RT-2000°F)	8-2 (RT-2000°F)	N.A.	10-16 (800-1600°F)
Crystalline form	Cubic	Cubic	Cubic	Cubic
Hardness (mohs)	5.0-6.0	7.5-8.0	4.0-4.3	--
Coefficient of expansion x 10 <sup>6</sup> /°F	6.3 (1000-1400°F)	4.72 (1000-1000°F)	6.8 (500-1300°F)	8.7 (800-1600°F)
Young's modulus x 10 <sup>-6</sup> psi	20.0-14.0 (RT-2000°F)	34.0-28.0 (RT-2000°F)	16 (est)	29.4-20.4 (RT-2000°F)

be operating at a higher percentage of their homologous temperature, perhaps providing greater strain accommodation at operating temperature.

Thermal expansion comparisons can be made between the various oxide coatings and a typical turbine blade superalloy, MAR-M421. All of the oxides are significantly lower in expansion than the superalloy with cubic  $ZrO_2$  and  $CaTiO_3$  having the best match. If fully dense coatings were to be sprayed on MAR-M421 (assuming zero strain in the coating at an equilibrium point of 2000°F) the calculated compressive stress in the coating would be 50 ksi at room temperature for  $CaTiO_3$ , over 200 ksi for  $MgAl_2O_4$ , and an intermediate stress for cubic  $ZrO_2$ . Although these data are unfavorable to  $MgAl_2O_4$ , the hardness of the spinel (and consequent greater erosion resistance), the relatively high thermal conductivity, good chemical and structural stability are strong points for developing coatings based on this compound. The zero strain temperature of 2000°F was selected as the maximum long-term equilibrium temperature for purposes of illustration. The true zero stress level will vary with coating composition and deposition techniques.

Further, both  $CaTiO_3$  and  $MgAl_2O_4$  are lower density materials than  $ZrO_2$  and consequently will provide, at comparable thickness, less added weight to blades. The 10-20 mil TBCs will add significant weight to the airfoil in small industrial gas turbine engines, increasing blade and root stresses.

To determine the effect of the various elements on the stability of each coating a 100-hour furnace test at 1600°F was conducted. MAR-M421 specimens 0.5" in diameter by 0.2" thick were plasma sprayed with the coatings under test. Solutions containing the salts being tested were applied to the test specimens and dried to provide a salt deposit of 2 mg/cm<sup>2</sup>. These specimens were then furnace heated to 982°C for 100 hours with the salt deposit being renewed every 24 hours to ensure continuing attack. Results of these tests are summarized in Tables 6, 7 and 8. From Table 6 the effect of the cubic stabilizer on coating performance is illustrated. The magnesia stabilized coating is virtually destroyed while the yttria stabilized coating shows little damage under the test conditions. Table 7 is illustrative of the performance of calcium titanate where a slight loss of stability is evidenced. Two tests were conducted on this material to determine repeatability of results. The third table, Table 8, reports the results of testing with sulfur, vanadium and phosphorus simultaneously. Two factors are evident. Under the test conditions the calcium titanate is relatively unaffected. Secondly, reducing porosity (surface area) of the zirconia coatings enhances stability. The conventional zirconia coating is representative of the open structure now in use. The high density coating is applied at higher power levels using fused material. As is evident, the latter is less subject to attack.

Table 6

Effect of Vanadium and Sulfur on Zirconia Coatings at 982°C

Ceramic material	<u>Before Test</u>	<u>After Test</u>	<u>Before Test</u>	<u>After Test</u>
	MgO.ZrO <sub>2</sub>	MgO.ZrO <sub>2</sub>	8Y <sub>2</sub> O <sub>3</sub> .ZrO <sub>2</sub>	8Y <sub>2</sub> O <sub>3</sub> .ZrO <sub>2</sub>
Cubic ZrO <sub>2</sub> (%)	79.0	12.0	89.0	89.0
Monoclinic ZrO <sub>2</sub> (%)	-	49.0	-	-
Tetragonal ZrO <sub>2</sub> (%)	-	12.0	-	-

Table 7

Effect of Vanadium and Sulfur on Two CaTiO<sub>2</sub> Coatings at 982°C

Ceramic material	<u>Before Test</u>	<u>After Test</u>	<u>Before Test</u>	<u>After Test</u>
	CaTiO <sub>3</sub>	CaTiO <sub>3</sub>	CaTiO <sub>3</sub>	CaTiO <sub>3</sub>
Cubic CaTiO <sub>3</sub> (5)	96.0	84.0	97.0	93.0
Sum of intensities of identified reflections	229.0	253.5	286.5	234.0

Table 8

Furnace Corrosion Test Results With Phosphorus Additives After Test at 982°C

Ceramic material	<u>Coating After Na<sub>2</sub>SO<sub>4</sub>, NaVO<sub>3</sub>, Na<sub>3</sub>PO<sub>4</sub> Test</u>	<u>Coating After Na<sub>2</sub>SO<sub>4</sub>, NaVO<sub>3</sub>, Na<sub>3</sub>PO<sub>4</sub> Test</u>	<u>Baseline Coating As-Received</u>	<u>Baseline Coating After Na<sub>2</sub>SO<sub>4</sub>, NaVO<sub>3</sub>, Na<sub>3</sub>PO<sub>4</sub> Test</u>	<u>Coating After Na<sub>2</sub>SO<sub>4</sub>, NaVO<sub>3</sub>, Na<sub>3</sub>PO<sub>4</sub> Test</u>	<u>Baseline Coating After Na<sub>2</sub>SO<sub>4</sub>, NaVO<sub>3</sub>, Na<sub>3</sub>PO<sub>4</sub> Test</u>
	CaTiO <sub>3</sub>	CaTiO <sub>3</sub>	ZrO <sub>2</sub> .8Y <sub>2</sub> O <sub>3</sub>	ZrO <sub>2</sub> .8Y <sub>2</sub> O <sub>3</sub>	ZrO <sub>2</sub> .MgO	ZrO <sub>2</sub> .8Y <sub>2</sub> O <sub>3</sub>
Cubic CaTiO <sub>3</sub>	87	87	-	-	-	-
Cubic ZrO <sub>2</sub>	-	-	87	26	17	50
Monoclinic ZrO <sub>2</sub> (%)	-	-	4	64	82	30
Tetragonal ZrO <sub>2</sub> (%)	-	-	9	5	-	-

## COMPARISON OF THERMAL BARRIER COATINGS FOR GAS TURBINES

As the result of literature review, engine tests, combustor tests and laboratory evaluations, a comparison can be made between zirconia and calcium titanate TBCs. This is summarized in Table 9.

Table 9

Comparison of Zirconia and Calcium Titanate Thermal Barrier Coatings

<u>Property</u>	<u>ZrO<sub>2</sub>.8Y<sub>2</sub>O<sub>3</sub></u>	<u>CaO.TiO<sub>2</sub></u>
Crystal structure	Cubic	Cubic
Spall resistance	Good	Excellent
Erosion resistance	Good	Fair
Chemical stability	Fair	Good
Application	High velocity, clean environments (blades)	Dirty fuels in lower velocity areas (combustors and nozzles)

The two coating systems each have areas in which they exhibit superior performance. Generally, calcium titanate is the better material for TBCs on combustors where its erosion is not a major problem and chemical attack is encountered, but the zirconia system is better in high erosion areas such as turbine blades. Thermal shock resistance was not found to be a major problem on operating components but erosion was severe on turbine blades.

## COMPARISON OF THERMAL BARRIER COATINGS IN BURNER RIGS

Several burner rig tests are being conducted on thermal barrier coatings (TBCs) using both clean and contaminated Diesel No. 2. The coatings now in test are ZrO<sub>2</sub>.8Y<sub>2</sub>O<sub>3</sub>, CaTiO<sub>3</sub> and CaSiO<sub>3</sub>. The tests are still in progress and a complete summary of the results is not yet available.

The burner rig used in this test normally employs a 2.5 cm diameter exit nozzle. Calibration tests were performed with this nozzle. A gas temperature of 1149°C was maintained in the specimen location and cooling air was used to reduce metal temperatures to the specified level. Placement of the control thermocouple for coating endurance was based on the results obtained in the initial calibration tests using a 2.5 cm nozzle. A typical thermocouple placement is shown in Figure 16. The method used to place the thermocouple tip consists of first milling a 1.5 mm diameter hole through the specimen wall at an angle of 45 degrees in the desired location. The

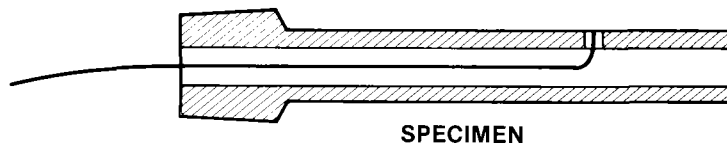


Figure 16. Plasma Spray Sealed Thermocouple Tip

Inconel sheath of the thermocouple is stripped back to expose the chromel and alumel wires. These wires are welded to the specimen in close proximity (0.25 mm) to the specimen surface. The opening is then sealed by plasma spray with a nickel chromel alloy and ground flush prior to application of the test coating. Practical engine instrumentation experience has shown that this approach gives accurate metal temperature in close proximity to the surface and minimizes the effect of thermal conduction down the wires or hot gas impingement. Thermocouples were located in individual test specimens on the surface directly exposed to the hot gas stream, as follows: 35mm from the base; 47 mm from the base; and 54 mm from the base.

In addition a thermocouple was located 32 mm from the base on the surface facing the center of rotation and a final thermocouple was used 35 mm from the base facing the adjacent specimen. The first three thermocouples were used to provide data on longitudinal temperature variations and the last two indicated circumferential variations. The highest temperatures occurred 32-35 mm from the base and initial burner rig testing will be conducted using this location for thermocouple placement. It was found that metal temperatures ranged from 740° to 815°C. The 815°C temperature location (32-35 cm from the base) was selected for control instrumentation during coating testing.

Several fuels have been used with various levels of vanadium, alkali metals, lead, sulfur and magnesium. A typical fuel composition contains the following impurity levels:

Magnesium	-	150 ppm
Vanadium	-	50 ppm
Sodium	-	1 ppm
Lead	-	0.5 ppm
Calcium	-	0.5 ppm

Except for the the sodium, which is emulsified in the fuel as a water solution of sulfate and chloride upstream of the burner nozzle, the additives are incorporated as fuel soluble organic compounds. Heavy deposits are developed by this fuel mixture on both the test specimens and the fuel nozzle. The flame temperature is set

at  $1150 \pm 10^\circ\text{C}$ . Fine temperature control is primarily by adjustment of air flow once the basic operating parameters have been established.

Under these conditions optical measurements give a specimen temperature in the hot zone of  $790^\circ\text{C}$ . At 120 hours the specimens and holder were removed for examination. Figure 17 illustrates the appearance of the specimens at this time. The heavy deposits at the base of the specimens are readily apparent. This particular test had a 500-hour duration with specimens being removed periodically after various exposure periods.

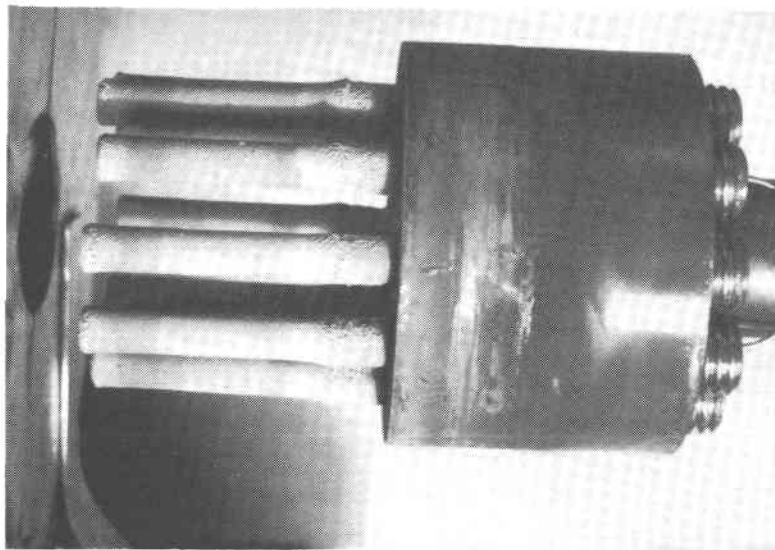


Figure 17. Burner Rig Specimens After 120 Hours Exposure at a Flame Temperature of  $1150^\circ\text{C}$ ; Magnification 0.95X

The test bars, exposure time and visual appearance are summarized in Table 10. Preliminary X-ray diffraction work indicates that the deposits are magnesium vanadate ( $\text{Mg}_3\text{V}_2\text{O}_8$ ). Crystallographic changes are now being determined. The visual examinations indicate that all of the coatings remained intact. Diametrical measurements of the specimens show that the high-density  $\text{ZrO}_2.8\text{Y}_2\text{O}_3$  has maintained a constant dimension throughout the test while the specimens prepared with conventional  $\text{ZrO}_2.8\text{Y}_2\text{O}_3$  shows a volume change and the diameter of the coated pin is greater at completion than at initiation of the test. These results are preliminary and metallographic examination will be required before a meaningful evaluation of the results can be made.



Table 10

## Burner Rig Test Bars at End of 500 Hours Test

Holder Number	Coating	Test Duration (hrs)	Remarks (Visual Appearance)
1	ZrO <sub>2</sub> .8Y <sub>2</sub> O <sub>3</sub> / NiCrAlY (Solar)	400	Some slight surface flaking of deposit.
2	CaO.TiO <sub>2</sub> / NiCrAlY	190	Coating intact, heavy deposits.
3	CaO.TiO <sub>2</sub> / NiCrAlY	400	Coating intact, heavy deposits.
4	ZrO <sub>2</sub> .8Y <sub>2</sub> O <sub>3</sub> / NiCrAlY (Solar)	190	Coating intact, flaking of deposits.
5	Uncoated	190	Heavy deposits.
6	CaO.TiO <sub>2</sub> / NiCrAlY	514	Coating intact, heavy deposits.
7	CaO.TiO <sub>2</sub> / CoCrAlY	514	Coating intact, heavy deposits.
8	ZrO <sub>2</sub> .8Y <sub>2</sub> O <sub>3</sub> / NiCrAlY	514	Coating intact, deposits spalled.
9	ZrO <sub>2</sub> .8Y <sub>2</sub> O <sub>3</sub> / NiCrAlY	400	Coating intact, deposits spalled.

## THERMAL BARRIER COATINGS IN GAS TURBINES BURNING CLEAN FUEL

This test and development program, conducted at Solar Turbines, Inc. under DOE/NASA sponsorship (Contract DEN3-109), for thermal barrier coatings (TBCs) is organized to meet three objectives while reducing heat input to engine components:

1. survive the thermal and mechanical stresses developed during engine operation;
2. resist attack by corrosive elements, e.g., Na, K, V, in the gas stream; and
3. maintain stability under both oxidizing and reducing atmospheres at 2500°F.

To establish the engine performance of the coatings, eight TBC first-stage turbine blades were subjected to engine test. This was an endurance test of the Mars engine encompassing operation on liquid and gaseous fuels with at least one stop-start cycle every 24 hours of operation.

Four coating systems (two blades with each system) were run in this test. Each coating listed in Table 11 was applied to two Mars first-stage turbine blades. The eight coated blades were installed in pairs at 90-degree spacings.

Table 11  
Thermal Barrier Coatings Applied to First-Stage Turbine Blades

<u>Bond Coat</u>		<u>Ceramic Coat</u>		
<u>Composition</u>	<u>Thickness (cm)</u>	<u>Composition</u>	<u>Thickness (cm)</u>	<u>Source</u>
Ni-14Cr-14Al-0.2Y	0.013	2CaO.SiO <sub>2</sub>	0.025	NASA
Ni-14Cr-14Al-0.2Y	0.013	ZrO <sub>2</sub> .8Y <sub>2</sub> O <sub>3</sub>	0.025	NASA
Ni-19Cr-6Al-0.2Y	0.013	CaO.TiO <sub>2</sub>	0.025	Solar
Ni-19Cr-6Al-0.2Y	0.013	ZrO <sub>2</sub> .8Y <sub>2</sub> O <sub>3</sub>	0.025	Solar

The spacing and pairing of the blades was selected to minimize rotor balance effects due to the coatings. Calculation of coating weight effects indicated that 100 percent ceramic coating loss from more than two adjacent blades would be required to exceed the design values for rotor imbalance at maximum operating speed. In addition, positioning the blades with identical (e.g., Solar ZrO<sub>2</sub>.8Y<sub>2</sub>O<sub>3</sub>) coatings at 180-degree intervals further reduced the probability of imbalance due to coating loss since equivalent coatings were expected to provide similar weight losses in the event of failure by a given TBC under test. Cooling air flow for coated and uncoated blades was maintained at the same level, as established by flow checking, to further guard against problems generated by coating failure.

Engine conditions during test are given in Table 12.

During test an optical pyrometer was used to monitor blade temperature. The resulting data indicated that TBCs increased the average surface temperature 83°C due to reduced heat loss to the cooling air.

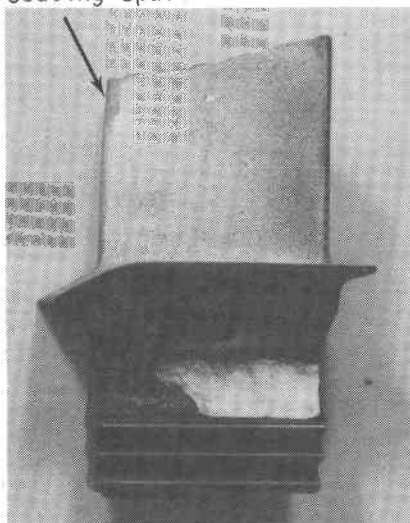
The most satisfactory overall results in this were obtained with the ZrO<sub>2</sub>.8Y<sub>2</sub>O<sub>3</sub> coating system. A blade coated with this system is shown in Figure 18. Except for loss of coating at the leading edge, Figure 19, the coating has maintained its integrity. This coating structure is shown in Figure 20. The calcium silicate coating exhibited severe spallation on the pressure face and the calcium titanate was subject to some particulate erosion and thinning during test, but less spalling was observed with this system than with the others.

Table 12

Mars Cyclic Endurance Engine Test

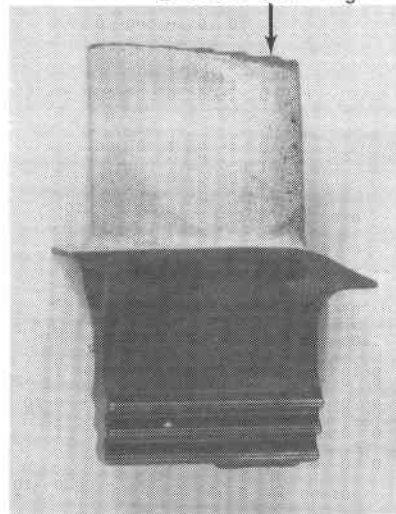
Duration: Calibration	50 hours
Run	500 hours
Rotor inlet temperature	1850° to 2035°F
Blade thermal cycle (surface)	600° to 1670°F (hot restart)
Blade temperature (bulk)	1490°F (maximum)
Blade tip speed	1400 fps
Tip shoe rub depth (design)	0.030 inch
Restarts (hot or cold)	Every 24 hours
Time to maximum blade temperature	Cold, 120 secs; hot, 50 secs
Inspection	50, 100, 250 and 550 hours
Fuel	50% diesel, 50% natural gas

Coating Spall



Pressure Face

Eroded Coating



Suction Face

Figure 18. Solar  $ZrO_{2.8}Y_{2}O_{3}$  Coated Blade After 500-Hour Engine Endurance Test

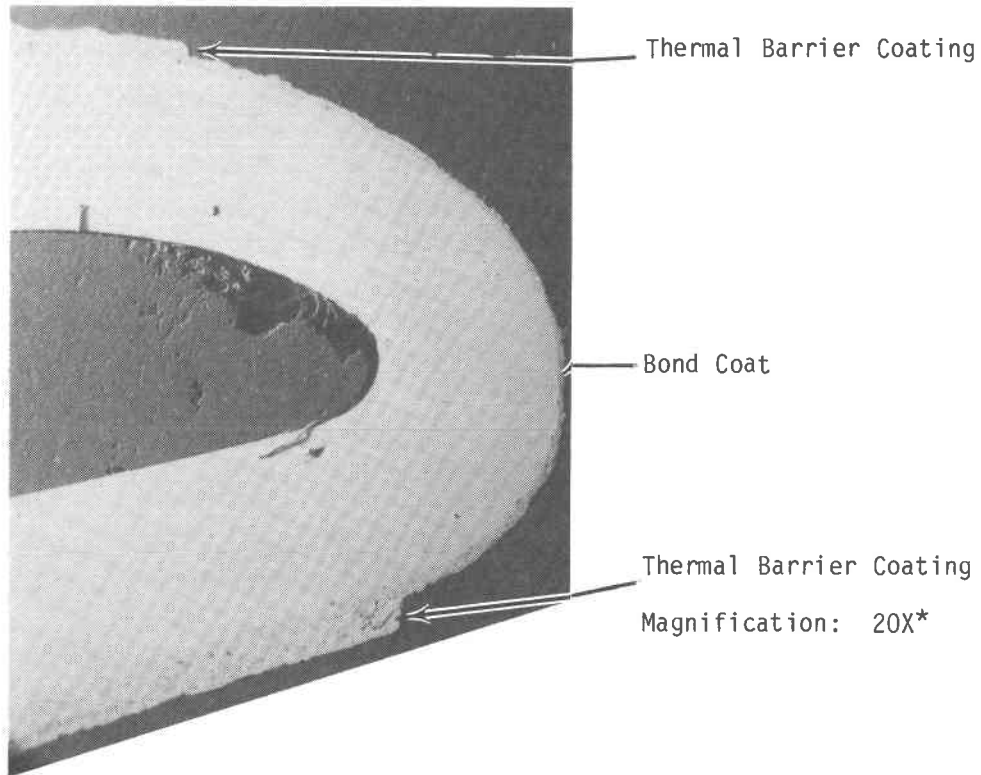


Figure 19. Solar  $ZrO_{2.8}Y_{2O_3}$  Coated Blade Leading Edge After 500-Hour Endurance Test

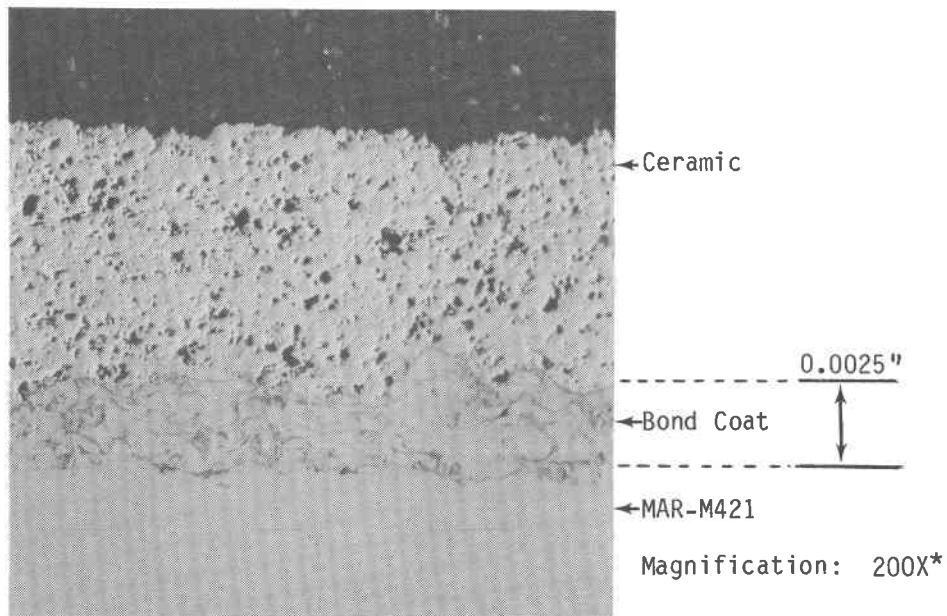


Figure 20.  $ZrO_{2.8}Y_{2O_3}$  Thermal Barrier Coating After 500-Hour Engine Endurance Test Showing 0.0025" Bond Coat

\*Please note that the illustration(s) on this page has been reduced 10% in printing.

In addition to metallographic and visual examination, X-ray diffraction analyses were used to determine if crystallographic changes had occurred during engine operation. The results of these tests are presented in Table 13.

Table 13  
X-ray Diffraction Data Before and After  
500-Hour Engine Test

Weight % $Y_2O_3$	7.2- 9.9	8.5
Mole % tetragonal $ZrO_2$ , non-transformable	66.0-80.0	76.0
Mole % monoclinic $ZrO_2$	5.0-11.0	10.0
Mole % cubic $ZrO_2$	Balance	14.0

\* Limits measured for plasma spray control specimens

The baseline data was from five sets of X-ray diffraction data and represents the range of values measured. Normal coatings have been found to be within these limits. The after-test values were determined on the test blades. No measurable change in crystal structure was found to have occurred. The non-transformable tetragonal nomenclature is based on work conducted at NASA-Lewis. The crystal lattice dimensions closely approximate the cubic structure and this material is frequently reported as cubic. For comparison with data reported from earlier work, where the non-transformable tetragonal is not reported, this value should be added to the cubic value.

#### CONCLUSIONS

Coatings applied to the primary zone of the staged combustion are subject to reducing conditions. These rapidly degrade the zirconia-base systems, resulting in coating loss. The calcium titanate is stable under these conditions and provides superior protective coatings.

When subjected to burner rig testing with contaminated fuels (i.e., Na, K, V, etc.) or attack by metallic salts in furnace corrosion testing, zirconia-base coatings are subject to crystallographic phase changes that degrade their properties. Calcium titanate coatings subjected to the same test conditions remain stable (cubic) enhancing their life.

In a gas turbine engine operated on clean fuel, calcium silicate coatings are susceptible to thermal stresses when compared with zirconia or calcium titanate. No evidence of phase change was found in the zirconia coatings and their greater hardness gives better erosion resistance than the calcium titanate and calcium silicate coatings. However, none of the coatings were fully able to survive the particulate and debris impingement stresses developed on the blade leading edge during the engine test cycle.

## STUDIES OF THERMAL BARRIER COATINGS FOR HEAT ENGINES

R. J. Bratton, S. K. Lau, C. A. Andersson and S. Y. Lee  
Westinghouse Research and Development Center  
Pittsburgh, PA 15235

### ABSTRACT

This paper summarizes studies conducted on the high-temperature corrosion resistance of  $ZrO_2 \cdot Y_2O_3$ ,  $ZrO_2 \cdot MgO$  and  $Ca_2SiO_4$  plasma sprayed coatings that are candidates for use as thermal barrier coatings in heat engines. Coatings were evaluated in both atmospheric burner rig and pressurized passage tests using GT No. 2 fuel and that doped with corrosive impurities such as sodium, sulfur and vanadium. The test results showed that the coatings perform very well in the clean fuel, pressurized passage tests as well as burner rig tests. With impure fuels, the test results revealed that while the coatings encountered greater damage in pressurized passage tests, the fuel sensitivity of each coating system exposed to both types of tests were qualitatively similar. It was found that chemical reactions between the ceramic coatings and combustion gases/condensates played the critical role in coating degradation. The degradation mechanism for each coating system is discussed. This work was conducted for NASA and EPRI under contract NAS3-21377. Advanced coating development studies have also been conducted for NASA and DOE under contract DEN3-110. A brief discussion of the progress being made in improving coating durability towards impure fuels is given.

## INTRODUCTION

The potential benefits of ceramic thermal barrier coatings for gas turbines have been well documented<sup>(1-4)</sup>. They include increased engine reliability by reducing metal temperature by 50-220°C; increased engine efficiency by reducing cooling air requirements; reduced fabrication cost by eliminating elaborate cooling schemes; and most of all, significant performance improvement and thus large cost saving by increasing the turbine inlet temperatures. However, while plasma sprayed ceramic coatings have been used for over ten years in aircraft burners and after burners, a ceramic coating that possesses the desired chemical and physical properties for turbine airfoil applications in clean or lower grade fuel burning environments has yet to be fully demonstrated.

Plasma sprayed zirconia compositions, due to their refractoriness, low thermal conductivities and high thermal expansion coefficients, have been of most interest for thermal barrier coatings. NASA-Lewis demonstrated that a simple two-layer plasma-sprayed ceramic/metal system<sup>(5,6)</sup> has the potential for protecting high temperature air-cooled gas turbine components. Of the initially examined coatings, the most promising system for aircraft gas turbines was composed of a Ni-16Cr-6Al-.6Y bond coating and a ZrO<sub>2</sub>-12 wt % Y<sub>2</sub>O<sub>3</sub> thermal barrier coating.

Although the NASA coating performed well in clean combustion gases such as natural gas and jet aircraft fuel, preliminary studies conducted at NASA<sup>(4)</sup> and Westinghouse<sup>(7)</sup> showed that in the presence of sea-salt or vanadium, the coating deteriorated through severe cracking and eventual spalling indicating potential hot corrosion problems.

Much work has been conducted to improve the performance of duplex ZrO<sub>2</sub>·Y<sub>2</sub>O<sub>3</sub>/NiCrAlY coating system. Included are modification of zirconia compositions by increasing or decreasing the yttria content<sup>(8)</sup> or by using stabilizers other than yttria, e.g., magnesia<sup>(9)</sup>; structural improvement by introducing a graded intermediate region of ceramic/metal to minimize the thermal expansion mismatch between the MCrAlY bond coat and the ceramic overcoat<sup>(10)</sup>; variation of MCrAlY compositions and thicknesses<sup>(11)</sup>; and the search for ceramic materials other than zirconia such as Ca<sub>2</sub>SiO<sub>4</sub><sup>(12)</sup>.

The purpose of this paper is to review the findings of a recent Westinghouse study conducted to evaluate the resistance of some of these present day thermal barrier coating systems to combustion gases that contain corrosive impurities such as sodium, vanadium, phosphorus and sulfur. Both atmospheric burner rig and pressurized passage tests were used for this purpose. The likely coating degradation mechanism identified will also be presented.



EXPERIMENTAL

Coating Systems

Nine coating systems were evaluated in this study (Table 1). They included both duplex and graded coatings; and with the exception of  $\text{Ca}_2\text{SiO}_4$ , all the overcoats were based on zirconia compositions. Both the bond coat and oxide overcoat of each of the coating systems were deposited by plasma spraying. The substrate alloys used were Udimet 720, a nickel base blade alloy and ECY 768, a cobalt base vane alloy.

Table 1

Thermal Barrier Coating Systems

<u>Oxide*</u> <u>Thermal Barrier</u>	<u>Coating** Description</u>	<u>Oxide Phase</u>
1. $\text{ZrO}_2 \cdot 8\text{Y}_2\text{O}_3$	Duplex- Two Layers: 5 mil NiCrAlY Bond Coat 15 mil Oxide Overcoat	95 Tetragonal/cubic 5 monoclinic
2. $\text{ZrO}_2 \cdot 15\text{Y}_2\text{O}_3$		Tetragonal/cubic
3. $\text{ZrO}_2 \cdot 20\text{Y}_2\text{O}_3$		Tetragonal/cubic
4. $\text{ZrO}_2 \cdot 24.65\text{MgO}$		82 Tetragonal/cubic 18 monoclinic and Free MgO
5. $\text{Ca}_2\text{SiO}_4$		$\text{Ca}_2\text{SiO}_4$
* * * * *		
1. $\text{ZrO}_2 \cdot 8\text{Y}_2\text{O}_3$	Graded - Three Layers: 4 mil NiCrAlY 8 mil Graded Zone 8 mil Oxide Overcoat	Tetragonal/cubic monoclinic
2. $\text{ZrO}_2 \cdot 15\text{Y}_2\text{O}_3$		Tetragonal/cubic
3. $\text{ZrO}_2 \cdot 20\text{Y}_2\text{O}_3$		Tetragonal/cubic
4. $\text{ZrO}_2 \cdot 24.65\text{MgO}$		82 Tetragonal/cubic 18 Monoclinic and Free MgO

\* Nominal oxide compositions in wt%

\*\* Nominal NiCrAlY compositions (wt%): Ni-20Cr-11Al-0.4Y

The as-deposited phases present in the oxides as determined by X-ray diffraction analysis are also shown in Table 1. It should be noted that due to the rapid cooling from the melt during plasma spraying, the as-sprayed zirconia phases do not reach equilibrium. Both the partially stabilized and fully stabilized  $ZrO_2(Y_2O_3)$  compositions consisted primarily of tetragonal  $ZrO_2(Y_2O_3)$  phases. They possibly also contained cubic  $ZrO_2(Y_2O_3)$  phase. However, its determination was uncertain because the diffraction peaks obtained were rather broad and the lattice parameters of the yttria doped cubic and tetragonal zirconia phases differed only very slightly. The partially stabilized  $ZrO_2 \cdot 8$  w/o  $Y_2O_3$  also contained a minor amount of monoclinic  $ZrO_2(Y_2O_3)$  phase. The  $ZrO_2 \cdot 24.65$  w/o MgO composition, in addition to tetragonal/cubic and monoclinic  $ZrO_2(MgO)$ , also contained some free MgO.

#### Experimental Equipment

The specimen geometry and the atmospheric barrier rigs used in this study have been fully described previously<sup>(13,14)</sup>. Briefly, air-cooled cylindrical specimens were cycled every hour in atmospheric rigs burning GT No. 2 fuel doped to various levels of impurities that included sodium, vanadium, phosphorus, calcium, potassium, iron, magnesium and sulfur.

For pressurized passage testing, a rig capable of operating at pressures up to twelve atmospheres was used. The test section consisted of six cylindrical specimens mounted in an electrically actuated traveler assembly to allow thermal cycling. Five thermocouples were located in the gas stream immediately upstream of the test section. Two thermocouples were mounted in the wall of each test specimen to measure the metal temperature during operation.

The test specimens were cooled by internal air flow. Individual cooling air tubes permitted the specimen metal temperatures to be adjusted externally during test passage operation. The rig allowed a maximum temperature difference of about 280°C between the combustion gas temperature and the test specimen maximum metal temperature. Under normal conditions, the maximum metal temperature for all six test specimens were maintained within  $\pm 11^\circ C$  during steady state operation.

Combustion was achieved using a cut-down version of the Westinghouse 1/4 scale B-4 combustor and fuel nozzle. Ignition was achieved using a propane ignitor. A fireeye infra-red flame detection system was used as a safety interlock on the fuel system.

Two different levels of thermal cycling were used. The first consisted of inserting the specimen traveler assembly directly into the gas stream held at 1066°C and keeping the metal temperature at 800°C for a total exposure time of 55 minutes. The specimens were then extracted and allowed to cool to 90-150°C for five minutes

before they were reinserted into the gas stream. The thermal transient experienced by specimens during this operation was far more severe than the normal start-up and shut-down transients expected for turbine blades in an operating utility gas turbine.

The second level of thermal transient conditions was more realistic. It involved air/fuel flow and temperature ramps to closely simulate the normal start-up and shut-down transients expected in actual gas turbines. Each cycle consisted of a 30-minute cooling down period. The time at steady-state with specimen temperature at 800°C was 40 minutes.

## RESULTS AND DISCUSSION

### Burner Rig Tests

Both clean-fuel and impurity-doped fuel sensitivity tests were conducted in atmospheric burner rigs. Results of clean-fuel tests were described in earlier papers<sup>(14,15)</sup>. The impurity-doped fuel tests and results are discussed more fully in this paper.

The fuel sensitivity tests were conducted by maintaining the gas/metal temperatures at 1150°C/800°C, respectively. The ceramic coating surface temperatures, measured by an optical pyrometer, were between 870 to 900°C. GT No. 2 fuel doped to four levels of impurities to simulate crude and residual oils were used in the tests. Following commercial turbine practice, a magnesium additive was added to fuels that contained vanadium. All testings were terminated after 500 one-hour cycles.

Figure 1 shows the results of the burner rig fuel sensitivity tests in terms of the minimum number of one-hour cycles to initiate coating spalling. It is clear from these results that the partially stabilized  $ZrO_2 \cdot 8$  w/o  $Y_2O_3$  coating performed better than the fully stabilized  $ZrO_2 \cdot 15$  w/o  $Y_2O_3$  and  $ZrO_2 \cdot 20$  w/o  $Y_2O_3$  coatings.

A possible explanation for the better performance of the partially stabilized  $ZrO_2(Y_2O_3)$  coatings is that<sup>(16)</sup> with an optimum fraction of monoclinic  $ZrO_2(Y_2O_3)$ , the microscopically stressed, two-phase  $ZrO_2(Y_2O_3)$  system can relieve thermal stresses by developing small cracks throughout the ceramic.

Test results shown in Figure 1 also reveal that graded coatings outperformed their duplex counterparts regardless of their compositions. This resulted from the reduction of thermal expansion mismatch between the ceramic overcoat and the NiCrAlY bond coat and the prevention of crack propagation. While it is clear from Figure 1 that graded  $ZrO_2 \cdot 8Y_2O_3$  and duplex  $Ca_2SiO_4$  coatings performed the best, none of the coating systems tested could survive the most severe test with 180 ppm V, 9 ppm Na, and 2.25 w/o S.

A general result of these tests is that vanadium appears to be particularly detrimental to the coatings. Accelerated failures occurred with increasing vanadium content even when all the other contaminants including the Mg/V ratio remained constant as in Tests 1 to 3. The relationship between fuel vanadium content and coating failure time is illustrated in Figure 2.

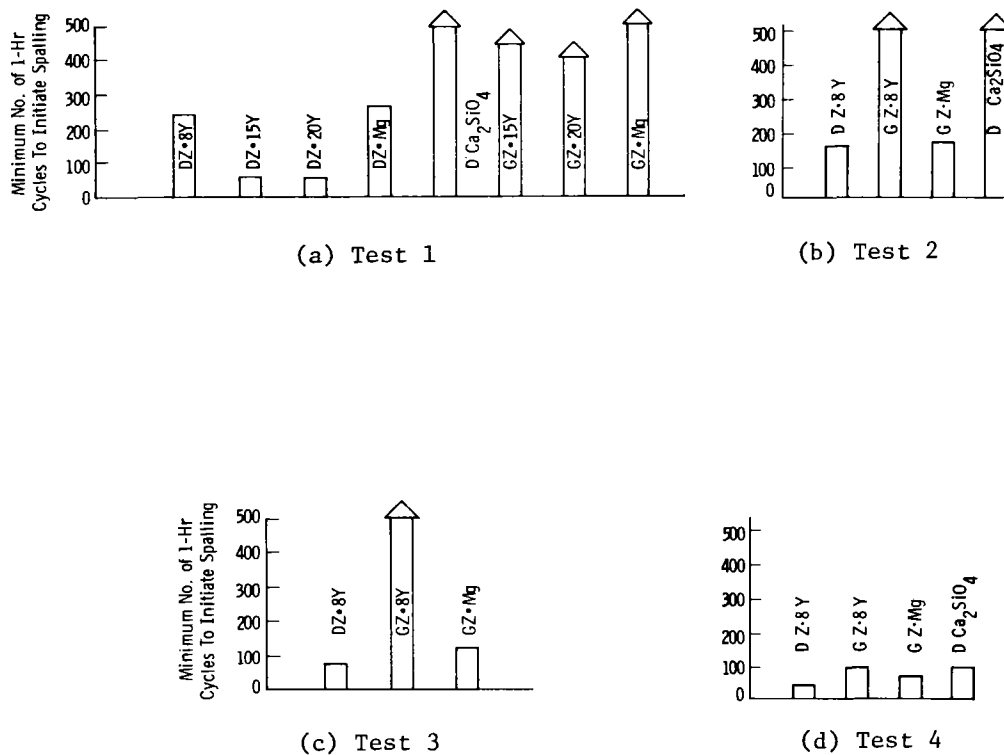


Figure 1 - Atmosphere burner rig fuel sensitivity test results at a gas temperature of 1150°C and a metal temperature of 800°C. The fuel was GT No. 2 doped to as follows:

- (a) 1 ppm Na, 2 ppm V, 2 ppm P, 0.5 ppm Ca, 2 ppm Fe, 6 ppm Mg, 0.25 w/o S
- (b) 1 ppm Na, 20 ppm V, 2 ppm P, 0.5 ppm Ca, 2 ppm Fe, 66 ppm Mg, 0.25 w/o S
- (c) 1 ppm Na, 50 ppm V, 2 ppm P, 0.5 ppm Ca, 2 ppm Fe, 150 ppm Mg, 0.25 w/o S
- (d) 9 ppm Na, 180 ppm V, 18 ppm P, 4.5 ppm Ca, 2 ppm Fe, 594 ppm Mg, 2.25 w/o S

### Pressurized Passage Tests

All pressurized passage tests were conducted at the nominal steady-state condition of 135 psig, 1066°C gas temperature and 800°C metal temperature. The gas velocity was 430 ft/sec, which was almost 40 times faster than that in the burner rig. These testing conditions were very similar to those found in an actual utility gas turbine.

As in atmospheric burner rigs, both clean fuel and impurity-doped fuel sensitivity tests were conducted. Clean fuel tests were conducted using GT No. 2 fuel.

Impurity-doped fuel tests were conducted using GT No. 2 fuel doped to 1 ppm Na, 20 ppm V, 2 ppm P, 0.5 ppm Ca, 2 ppm Fe, 66 ppm Mg and 0.25% S. This was the same fuel used for Test 2 of the atmospheric burner rig tests. Six specimens which

included two each of duplex  $ZrO_2 \cdot 8Y_2O_3$ , graded  $ZrO_2 \cdot 8Y_2O_3$  and duplex  $Ca_2SiO_4$  were evaluated in each test. After 20 cycles, the specimens were extracted for examination. Due to the high operating cost, all the pressurized passage tests were terminated after 50 cycles.

Results of pressurized passage tests are shown in Figures 3a-b. Regardless of which thermal cycle was used, all three coating systems tested in the undoped GT No. 2 fuel passed the 50 cycles without failure. However, in the contaminated fuel test, they all encountered gross coating spalling after testing for less than 20 cycles.

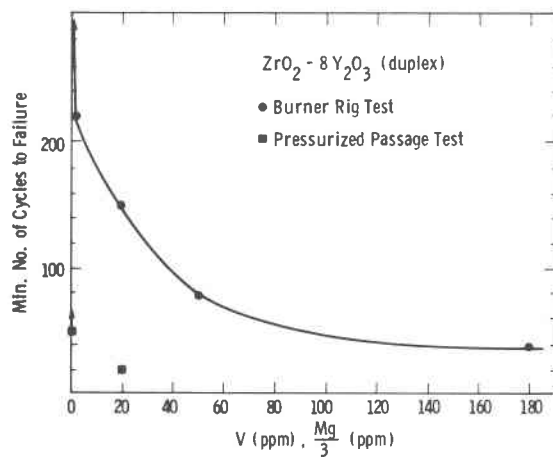


Figure 2 - Coating failure time as a function of fuel vanadium content

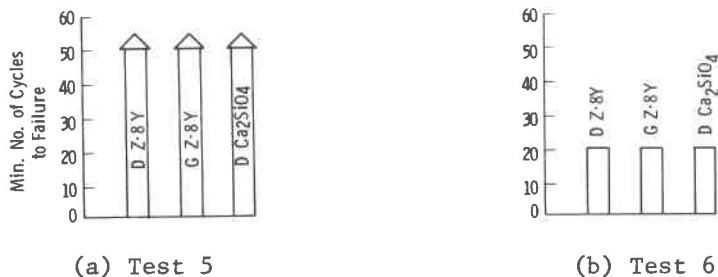


Figure 3 - Pressurized passage test results

Temperature - 1066°C gas/800°C metal

Pressure - 135 psig

Fuel - (a) GT No. 2

(b) GT No. 2 doped to 1 ppm Na, 20 ppm V, 2 ppm P, 0.5 ppm Ca, 2 ppm Fe, 66 ppm Mg, 0.25 w/o S

Comparison between pressurized passage and atmospheric burner rig tests conducted using the same fuel (Figure 3b vs. Figure 2b) clearly illustrates the greater severity of the pressurized passage test. Due to the higher total pressure, the impurity elements have a much higher partial pressure in the pressurized passage and likely account for the accelerated initiation of failures. Indeed, by using higher dopant levels, the failure times observed in atmospheric burner rig Test 4 (Figure 1d) were approaching those observed in the pressurized passage test (Figure 3b). Figure 4 shows the post-test conditions of two graded  $ZrO_2 \cdot 8Y_2O_3$  specimens. It can be seen that the specimen tested for only 20 cycles in the pressurized passage has suffered more extensive damage than the one tested for 350 cycles in the burner rig using a fuel with 9X dopant concentrations. The difference can be attributed to the higher gas velocity, mass flow rate, and thermal stress condition that existed in the pressurized tests. These factors are important in imparting damage once failures initiate due to reactions with the condensate. In the clean fuel test failure did not initiate and coating damage was not encountered.

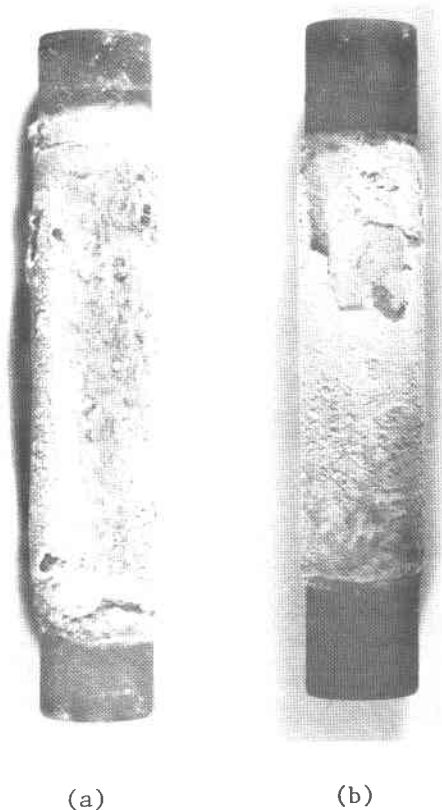


Figure 4 - Post-test appearance of graded  $ZrO_2 \cdot 8Y_2O_3$ /NiCrAlY specimens exposed to

- (a) Pressurized passage test for 20 cycles, Test 6
- (b) Atmospheric burner rig test for 350 cycles, Test 4

## Post-Test Analysis

Detailed post-test analyses, which included X-ray diffraction, chemical, metallographic as well as electron microprobe analysis, have been conducted on representative specimens from all tests.

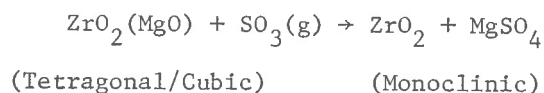
Results of Test 1 using the fuel with the lowest dopant level (1 ppm Na, 2 ppm V) were presented in earlier papers<sup>(14,15)</sup>. It was concluded that in combustion environments containing Na, Mg and S impurities, the formation and penetration of molten  $\text{Na}_2\text{SO}_4$  and  $\text{MgSO}_4$  into the coating interior can lead to coating failure through several possible mechanisms<sup>(14,15)</sup>. Among them, the mismatch of thermal expansion between the  $\text{ZrO}_2(\text{Y}_2\text{O}_3)$  coating and the entrapped solidified salt condensate is a very viable one<sup>(15)</sup>. The degradation mechanisms of the coating systems exposed to the other three burner rig tests and the pressurized passage test using fuels with higher vanadium dopant levels are discussed here in detail.

Metallographic examination showed that specimens exposed to both burner rig and pressurized passage tests usually encountered more extensive damage at the leading edges that were directly facing the gas stream. It was also found that duplex coatings always spalled in the ceramic coating very close to the ceramic/NiCrAlY interface (Figure 5). However, for graded specimens tested in contaminated fuels, cracking and eventual spalling occurred only near the oxide/graded zone interface, and as a result, a graded zone which can provide protection was left adhering to the specimen (Figure 6). This is different from the failure mode of the graded coatings encountered in clean fuel tests<sup>(14,15)</sup> at higher metal temperatures (845°C) where failure occurs at the graded zone/NiCrAlY bond coat interface.

The chemical behavior of specimens exposed to the pressurized passage test and the three burner rig tests were very similar. The surface condensates collected on all the specimens were identified as  $\text{Mg}_3\text{V}_2\text{O}_8$ ,  $\text{MgSO}_4$  and  $\text{MgO}$ . Furthermore, it was found that chemical reactions which occurred between the ceramic coatings and the combustion gases/condensates played a critical role in coating degradation. Detailed degradation mechanism for each coating system is described below.

### (a) $\text{ZrO}_2 \cdot 24.65 \text{ MgO}$ Coating Systems

X-ray diffraction analysis revealed that a large fraction of  $\text{MgO}$  contained in the original duplex and graded  $\text{ZrO}_2 \cdot 24.65 \text{ MgO}$  coatings had reacted with  $\text{SO}_3(\text{g})$  of the combustion gases to form  $\text{MgSO}_4$ . A result of removing the  $\text{MgO}$  stabilizer from the  $\text{ZrO}_2(\text{MgO})$  solid solution was destabilization of  $\text{ZrO}_2(\text{MgO})$  according to the reaction:





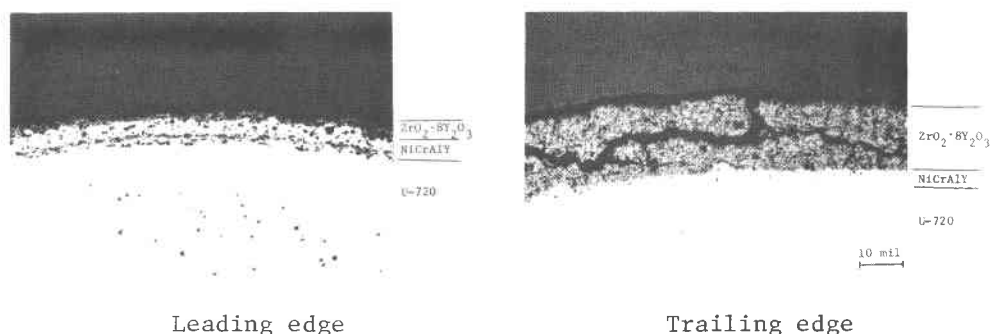


Figure 5 - Cross-section of a failed duplex  $ZrO_2 \cdot 8Y_2O_3/NiCrAlY$  specimen exposed for 50 cycles in Test 6

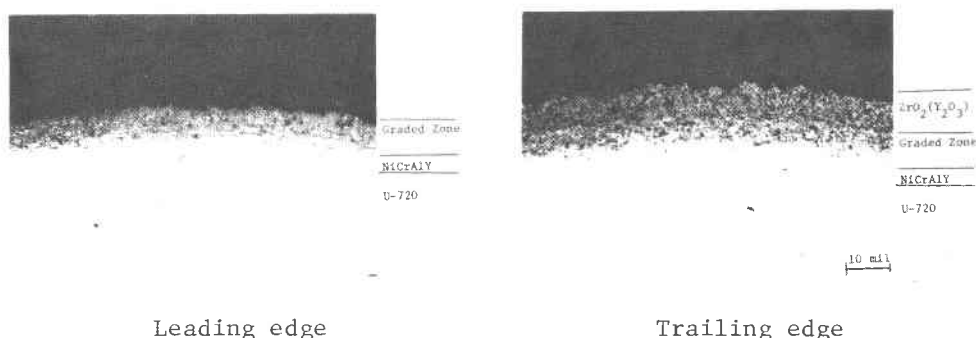
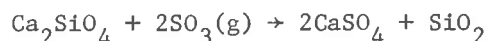


Figure 6 - Cross-section of a failed graded  $ZrO_2 \cdot 8Y_2O_3/NiCrAlY$  specimen exposed for 20 cycles in Test 6

This observed destabilization as well as the volume change associated with the  $MgSO_4$  formation were probably responsible for the coating failure. However, it should be noted that from phase-equilibria considerations, tetragonal/cubic  $ZrO_2(MgO)$  is actually metastable at temperatures below  $\sim 900^\circ C$ <sup>(17)</sup>. Thus it should undergo an eutectoid decomposition and form  $MgO$  and monoclinic  $ZrO_2(MgO)$  when thermally cycled. The reaction with  $SO_3$  gas therefore accelerates this destabilization.

#### (b) $Ca_2SiO_4$ Coating System

X-ray results in the duplex  $Ca_2SiO_4$  coating, which performed quite well in most of the burner rig tests, suggested the occurrence of extensive reactions. In the first place,  $Ca_2SiO_4$  was found to be extremely susceptible to the attack of  $SO_3$  gas. A soft and powdery  $CaSO_4$  phase was found throughout the coating. The reaction which occurred was:



It can be shown that at  $\sim 900^\circ C$  (the coating surface temperature), this reaction is thermodynamically possible at  $P_{SO_3} > 6 \times 10^{-6}$  atm. This is one to two orders of

magnitude lower than the  $P_{SO_3}$  levels normally found in utility gas turbines ( $10^{-5} \sim 10^{-4}$  atm) burning fuels containing 0.1 to 1 wt % sulfur. Thus, even when relatively clean fuels such as GT No. 2 fuel (typically contains 0.25 wt % S) are used, reaction between  $SO_3$  gas and  $Ca_2SiO_4$  coating may still occur.

There is also evidence that a ternary magnesium-calcium silicate was formed on the  $Ca_2SiO_4$  coating surface after exposure to combustion environments containing magnesium-vanadium impurities. Although X-ray diffraction analysis could not identify the exact reaction product because broad amorphous peaks were obtained, the overlapping of Mg, Si and Ca concentrations (Figure 7) strongly suggests the formation of a magnesium-calcium silicate. This illustrates the possibility that  $Ca_2SiO_4$  is also chemically unstable toward turbine condensates such as  $Mg_3V_2O_8$  and  $MgSO_4$ .

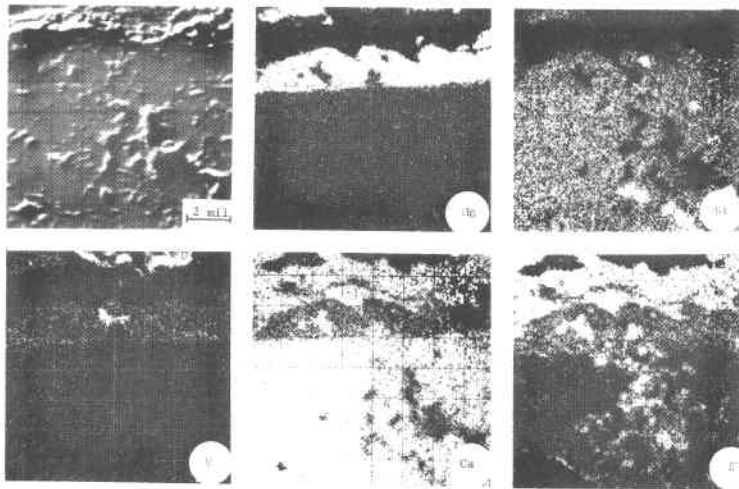


Figure 7 - EMP scans on a duplex  $Ca_2SiO_4$  coating exposed for 500 cycles in Test 2

The chemical reactivity of  $Ca_2SiO_4$  toward combustion gases and condensates may therefore explain the failure of this coating in both burner rig and pressurized passage tests.

#### (c) $ZrO_2(Y_2O_3)$ Coating Systems

Post-test analysis on  $ZrO_2(Y_2O_3)$  coatings exposed to combustion environments containing vanadium impurities revealed that the destabilization of  $ZrO_2(Y_2O_3)$  induced by the reaction with combustion condensates played a very important role in coating degradation.

$ZrO_2 \cdot 8Y_2O_3$  specimens (both graded and duplex) that failed in atmospheric burner rig Tests 2-4 and the dirty fuel fired pressurized passage test invariably showed an

increase in monoclinic  $ZrO_2(Y_2O_3)$ , (greater amounts with increased vanadium contamination). Using careful sampling procedures, this destabilization process of tetragonal/cubic  $ZrO_2(Y_2O_3)$  to monoclinic  $ZrO_2(Y_2O_3)$  has been examined in detail. Table 2 shows the results of post-test X-ray analysis on a failed graded  $ZrO_2 \cdot 8Y_2O_3$  specimen exposed in burner rig Test 4 for 350 one-hour cycles. X-ray samples were taken at various depths of the coating from both leading and trailing edges.

Table 2

X-Ray Results on Specimen 1B3\* ( $G-ZrO_2 \cdot 8Y_2O_3$ )

<u>X-Ray Sample</u>	<u>Pre-Test Phase</u>	<u>Post-Test Phase</u>
Surface deposits (L.E.)	-	M - $MgSO_4 \cdot 6H_2O$ m - $MgO, Mg_3V_2O_8$
Coating surface just below deposits (L.E.)	M- $ZrO_2(Y_2O_3)$ (tetra/cubic) m- $ZrO_2(Y_2O_3)$ (monoclinic)	M - $ZrO_2(Y_2O_3)$ (monoclinic) m - $ZrO_2(Y_2O_3)$ (tetra/cubic) T - $MgSO_4$
Deep coating interior (L.E.)	M- $ZrO_2(Y_2O_3)$ (tetra/cubic) m- $ZrO_2(Y_2O_3)$ (monoclinic)	M - $ZrO_2(Y_2O_3)$ (tetra/cubic) m - $ZrO_2(Y_2O_3)$ (monoclinic)
Back of spalled chip(L.E.)	M- $ZrO_2(Y_2O_3)$ (tetra/cubic) m- $ZrO_2(Y_2O_3)$ (monoclinic)	M - $ZrO_2(Y_2O_3)$ (tetra/cubic) m - $ZrO_2(Y_2O_3)$ (monoclinic)
Surface deposits (T.E.)		T - $MgSO_4 \cdot 6H_2O$
Coating surface just below deposit (T.E.)	M- $ZrO_2(Y_2O_3)$ (tetra/cubic) m- $ZrO_2(Y_2O_3)$ (monoclinic)	M - $ZrO_2(Y_2O_3)$ (tetra/cubic) m - $ZrO_2(Y_2O_3)$ (monoclinic)

L.E. = leading edge

T.E. = trailing edge

M = Major

m = Minor

T = Trace

\*Test Temperature = 1150°C gas/800°C metal

Fuel: GT No. 2 doped to (ppm) Na - 9, V-180, P - 18,

Ca - 4.5, Fe - 2, Mg - 594, S - 2.25%

Test Time - 350 one-hour cycles

As may be seen from Table 2, the destabilization of tetragonal/cubic  $ZrO_2(Y_2O_3)$  occurred predominantly at regions close to the surface while the coating interior remains unaffected. It is also evident that the destabilization reaction tends to occur preferentially at the specimen leading edge where more combustion condensates ( $Mg_3V_2O_8$ ),  $MgSO_4$  and  $MgO$ ) are collected. Another important observation is that the back of a chip spalled from the leading edge showed no observable destabilization. These observations suggest that in combustion environments containing vanadium impurity, destabilization of tetragonal/cubic zirconia occurs as the result of chemical reactions with combustion deposits collected on the specimen surface.

There are reports<sup>(7,18,19)</sup> that molten vanadates such as  $Na_2V_2O_6$  or  $V_2O_5$  are responsible for the leaching of  $Y_2O_3$  stabilizer from the tetragonal/cubic  $ZrO_2(Y_2O_3)$  to form monoclinic  $ZrO_2(Y_2O_3)$  and  $YVO_4$ . It is interesting to find from the present study that in combustion environments burning magnesium treated fuels where  $V_2O_5$  or  $Na_2V_2O_6$  condensates do not form, destabilization of tetragonal/cubic  $ZrO_2(Y_2O_3)$  was still observed. Electron microprobe analysis has found heavy vanadium concentration in the  $ZrO_2(Y_2O_3)$  coating below the  $MgSO_4$  and  $Mg_3V_2O_8$  deposits (Figure 8). It was therefore assumed that the destabilization process was induced by the reaction of  $ZrO_2(Y_2O_3)$  with vanadium compounds, gaseous  $V_2O_5$  or solid  $Mg_3V_2O_8$ .

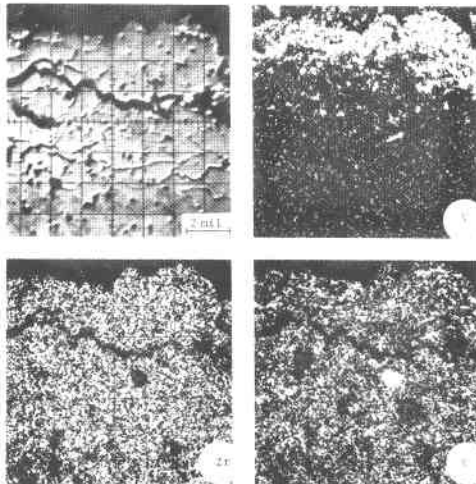
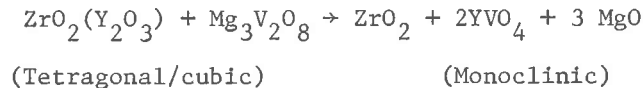


Figure 8 - EMP scans on a graded  $ZrO_2 \cdot 8Y_2O_3$  coating exposed for 500 cycles in Test 3

A recent laboratory study<sup>(20)</sup> conducted by the authors clearly showed that solid  $Mg_3V_2O_8$  is the major reactant causing destabilization. While the details of this study will be published later, a summary is given here. A powder mixture of  $ZrO_2 \cdot 8Y_2O_3$  and  $Mg_3V_2O_8$  was heated in air at  $930^\circ C$ , a temperature close to the coating surface temperature established in the burner rig tests. The  $ZrO_2 \cdot 8Y_2O_3$  powder initially contained 82% tetragonal/cubic  $ZrO_2(Y_2O_3)$  phase and 18% monoclinic

ZrO<sub>2</sub>(Y<sub>2</sub>O<sub>3</sub>) phase. After 335 hours, the ZrO<sub>2</sub>(Y<sub>2</sub>O<sub>3</sub>) powder was found to contain 94% monoclinic ZrO<sub>2</sub>(Y<sub>2</sub>O<sub>3</sub>) phase and only 6% tetragonal/cubic ZrO<sub>2</sub>(Y<sub>2</sub>O<sub>3</sub>) phase, YVO<sub>4</sub> and MgO were also found. The reaction occurred was:



It is well known that monoclinic ZrO<sub>2</sub> undergoes phase transformation on heating and cooling with an associated disruptive volume change<sup>(21)</sup> (reported between 4 to 6%). This reaction can therefore initiate coating cracking. The degradation mechanism of ZrO<sub>2</sub>·Y<sub>2</sub>O<sub>3</sub> coating can be described in the following steps: (1) solid Mg<sub>3</sub>V<sub>2</sub>O<sub>8</sub> deposit collected on the specimen leading edge; (2) reaction of Mg<sub>3</sub>V<sub>2</sub>O<sub>8</sub> and ZrO<sub>2</sub>(Y<sub>2</sub>O<sub>3</sub>) removes Y<sub>2</sub>O<sub>3</sub> stabilizer and leads to monoclinic ZrO<sub>2</sub> formation at the coating surface; (3) with sufficient monoclinic ZrO<sub>2</sub> formed, cracks are initiated at the coating surface when the monoclinic ZrO<sub>2</sub> undergoes phase transformation on thermal cycling; (4) these surface cracks propagate and branch into the coating interior and eventually lead to coating spalling.

It is therefore concludes that the magnesium additives that can effectively control vanadium corrosion attack on gas turbine metal parts are not useful in protecting ceramic coatings such as ZrO<sub>2</sub>(Y<sub>2</sub>O<sub>3</sub>). They may, however, delay the coating failure somewhat by avoiding the more aggressive molten V<sub>2</sub>O<sub>5</sub> or Na<sub>2</sub>V<sub>2</sub>O<sub>6</sub> attack, and converting to a slower solid-solid reaction between Mg<sub>3</sub>V<sub>2</sub>O<sub>8</sub> and ZrO<sub>2</sub>(Y<sub>2</sub>O<sub>3</sub>).

A mechanistic study on the degradation of ZrO<sub>2</sub>(Y<sub>2</sub>O<sub>3</sub>) coatings in Na and S contaminated fuels will be presented in a future paper<sup>(20)</sup>.

#### Advanced Ceramic Coating Development

In this study an initial screening test of a host of ceramic coating candidates revealed that partially stabilized porous zirconia plasma sprayed coating showed the best combination of thermal stress resistance and corrosion resistance. However, since it was clearly demonstrated in our previous work (NAS3-21377) that the zirconia coatings had limited durability in combustion products containing the sulfur, sodium and vanadium contaminants, the concept of high density overcoats to seal off the surface of the porous zirconia was tested. This concept resulted in coating lifetimes better than 2.70 x those of the baseline ZrO<sub>2</sub>·8Y<sub>2</sub>O<sub>3</sub> duplex coating when tested in high sodium fuel, and 1.5 x improvement in high vanadium fuel.

Improved stress resistance under corroding conditions of the zirconia baseline coatings was accomplished by the incorporation of mechanical locking/crack arresting layers intermediate to the NiCrAlY bond coat and porous zirconia. A 2.2 x improvement was made for high sodium fuels. By combining intermediate and top

coats lifetimes were further improved to 4 x the baseline coating.

In addition to the advanced coating development work, a preliminary design study was made to evaluate TBC benefits for improving metal blading life and turbine performance. For Westinghouse utility turbines operating in the field today, a 15 mil ceramic coating would reduce metal temperature by 100°F. The effect of this is to improve both creep and low cycle fatigue life by an order of magnitude, and to reduce metal corrosion by one half. An improvement in specific power and efficiency can be obtained by operating under conditions such that the metal temperatures are maintained constant and the cooling flow is reduced.

## CONCLUSIONS

1. In a pressurized passage test conducted at pressure and temperature conditions simulating those of an actual utility gas turbine, both duplex and graded  $ZrO_2 \cdot 8 \text{ w/o } Y_2O_3$  and duplex  $Ca_2SiO_4$  coating systems performed satisfactorily when clean GT No. 2 fuel was used.
2. None of the coating systems evaluated survived the pressurized passage test conducted with a fuel containing 20 ppm V and 66 ppm Mg; nor the ambient pressure burner rig test using a fuel containing 180 ppm V and 594 ppm Mg.
3. While coating systems encountered more massive damage in pressurized passage tests than in atmospheric burner rig tests using the same fuel, the chemical behavior of the coatings exposed to both types of tests was qualitatively similar.
4. In the presence of sulfur, the principle cause of failure of the  $ZrO_2 \cdot 24.65MgO$  coating is the reaction of MgO contained in  $ZrO_2(MgO)$  with  $SO_3(g)$  to form monoclinic  $ZrO_2$  and  $MgSO_4$ .
5.  $Ca_2SiO_4$  was found to be chemically reactive with combustion gases and condensates obtained from burning fuels containing sulfur, vanadium and magnesium. The formation of  $CaSO_4$  and ternary silicates may be responsible for the coating failure.
6. The failure mechanism of  $ZrO_2(Y_2O_3)$  coating systems in vanadium contaminated fuels treated with magnesium was identified. Reaction of  $Y_2O_3$  contained in  $ZrO_2(Y_2O_3)$  with  $Mg_3V_2O_8$  deposit leads to the removal of yttria stabilizer from  $ZrO_2(Y_2O_3)$  to form monoclinic  $ZrO_2$ . The phase transformation of monoclinic  $ZrO_2$  on thermal cycling then initiates coating spalling.

#### ACKNOWLEDGMENTS

This work is being performed for NASA-Lewis Research Center under the sponsorship of EPRI and DOE. The NASA Technical Manager for contract NAS3-21377 is Dr. Robert A. Miller and the EPRI Program Manager is Dr. A. Cohn, whose helpful contributions are acknowledged. The NASA Technical Manager for contract DEN3-110 is G. E. McDonald and the DOE Program Manager is John Fairbanks.



## REFERENCES

1. Amos, D.J., "Analytical Investigation of Thermal Barrier Coatings on Advanced Power Generation Gas Turbines," NASA CR-135146, March 1977.
2. Carlson, N., and Stone, B.L., "Thermal Barrier Coatings on High Temperature Gas Turbine Engines," NASA CR-135147, February, 1977.
3. Clark, J.S., Nainiger, J.J., and Heyland, R.E., "Potential Benefit of a Ceramic Thermal Barrier Coating on Large Power Generation Gas Turbines," NASA TM 73712, June, 1977.
4. Levine, S.R., and Clark, J.S., "Thermal Barrier Coatings—A Near Term High Payoff Technology," NASA TM X-73586, 1977.
5. Stecura, S., and Liebert, C.H., "Thermal Barrier Coating System," U.S. Patent, 4,055,705, October 25, 1977.
6. Stecura, S., "Two-Layer Thermal Barrier Coating for High Temperature Components," Am. Ceram. Soc., Bull. Vol. 56, No. 12, Dec. 1977, pp. 1082-1089.
7. Singhal, S.C., and Bratton, R.J., "Stability of a  $ZrO_2(Y_2O_3)$  Thermal Barrier Coating in Turbine Fuel with Contaminant," Eng. for Power, Vol. 102, No. 4, October 1980, pp. 770-775.
8. Stecura, S., "Effects of Compositional Changes on the Performance of a Thermal Barrier Coating System," NASA TM78976, 1978.
9. Taylor, T.A., Price, M.O., and Tucker, R.C., "Plasma-Deposited Thermal Barrier Coatings," in Proceedings of the First Conference on Advanced Materials for Alternative Fuel Capable Directly Fired Heat Engines, Castine, Maine, 1976, p. 606.
10. Cavanagh, J.R., et al, "The Graded Thermal Barrier - A New Approach for Turbine Engine Cooling," AIAA Paper 72-361, April, 1972.
11. Stecura, S., "Effects of Yttrium, Aluminum and Chromium Concentrations in Bond Coatings on the Performance of Zirconia-Yttria Thermal Barriers," NASA TM-79206, 1979.
12. Hodge, P.E., et al., "Thermal Barrier Coatings: Burner Rig Hot Corrosion Test Results," DOE/NASA/2593-78/3, NASA TM-79005, 1978.
13. Bratton, R.J., Lau, S.K., Lee, S.Y., and Andersson, C. A., "Ceramic Coating Evaluations and Developments," in Proceedings of the First Conference on Advanced Materials for Alternative Fuel Capable Directly Fired Heat Engines, Castine, Maine, July 31 - August, 1979.
14. Bratton, R.J., and Lau, S.K., "Zirconia Thermal Barrier Coatings," in Proceedings of First International Conference on the Science and Technology of Zirconia, Cleveland, OH, June 16-18, 1980.
15. Bratton, R.J., Lau, S.K., and Lee, S.Y., "Evaluation of Present-Day Thermal Barrier Coatings for Industrial/Utility Applications," Thin Solid Films, 73 (1980), pp. 429-437.

16. Cook, R.G., and Lloyd, D.Z., "Fabrication of Zirconia Bodies and Some Considerations of Their Thermal Shock Properties," in Proceedings of the Fifth Symposium on Special Ceramics, Poppev, P., Ed., The British Ceramic Research Association, 1972, pp. 125-134.
17. Viechnicki, E., and Stubican, V., J. Am. Ceram. Soc., 48, (292), 1965.
18. Zaplatynsky, I., "Reactions of Yttria-Stabilized Zirconia with Oxides and Sulfates of Various Elements," DOE/NASA/2593-78/1, NASA TM-78942, 1978.
19. Palko, J.E., and Luthra, K.L., and McKee, D.W., "Evaluation of Performance of Thermal Barrier Coatings Under Simulated Industrial/Utility Gas Turbine Conditions," Final Report, General Electric Co., 1978.
20. Lau, S.K., and Bratton, R.J., to be published.
21. Gupta, T.K., et al, "Stabilization of Tetragonal Phase in Polycrystalline Zirconia," J. of Matrls. Sci., 12 (1977) pp. 2421-2426.

PROCESSING TECHNOLOGY FOR  
ADVANCED METALLIC AND CERAMIC  
TURBINE AIRFOIL COATINGS

D. S. DUVALL  
PRATT & WHITNEY AIRCRAFT  
COMMERCIAL PRODUCTS DIVISION  
EAST HARTFORD, CT. 06108

INTRODUCTION

Future gas turbine powerplants will require greater protection against surface attack because of increasingly harsh operating environments. During the 1980's decade, combustion gas temperatures in aircraft propulsion systems will steadily be increased to achieve the maximum available fuel efficiency. This will also be the trend in land-based gas turbines because of similar motivations. However, the most drastic change could be the introduction of alternate fuels with an attendant major increase in the corrosiveness and/or erosiveness of the combustion environment. The already durability-limited turbine airfoils in such machines may require substantially improved surface protection to resist these effects.

Ceramic coatings provide an attractive means for obtaining greater turbine airfoil surface stability and heat resistance. Relatively thin (e.g., 0.005-0.020 inches) layers of zirconia, for instance, can provide 100<sup>0</sup>-300<sup>0</sup>F or more thermal insulation on air-cooled components in modern high pressure gas turbines. Ceramic coatings may also provide increased hot corrosion resistance since many of the candidate ceramic compositions per se are much less rapidly attacked than current metallic coatings. In addition, due to thermal insulation effects, the surfaces of ceramic airfoil coatings will be hotter than current metallic coated airfoil surfaces. This will tend to reduce condensation of corrosive species onto the airfoils.

Ceramic coatings (based on alumina, silica, or zirconia) have been employed for over 20 years as thermal barriers on combustors and afterburners in aircraft gas turbines to reduce metal temperatures and thermal fatigue cracking. Unfortunately, the coatings have never been sufficiently spall resistant to permit their use on turbine-section blades and vanes. Currently, considerable efforts are underway to increase ceramic coating durability so that they can be successfully used on turbine airfoils.

## CERAMIC COATING FAILURE MODES

Today, failure of a ceramic coating invariably means premature removal of all or part of the ceramic layer due to:

- stresses from thermal cycling
- metallic underlayer oxidation
- effects from corrodents
- particulate erosion

Conceivably, future spall-resistant ceramic coatings may have sufficiently long lives to be prone to gradual chemical degradation in an analogous failure mode to current turbine metallic coatings. However, today's problems must be solved first.

### Spalling from Cyclic Thermal Stresses

Most contemporary **ceramic turbine coatings** are plasma sprayed zirconia systems with a metallic underlayer (to provide substrate oxidation protection and a rough surface for ceramic adhesion). At Pratt & Whitney Aircraft, the metallic layer is typically an MCrAlY (NiCoCrAlY or CoCrAlY). Partially or fully cubic-stabilized zirconia is favored as the ceramic because of its low thermal conductivity and relatively large coefficient of thermal expansion.

Nevertheless, the mismatch in thermal expansion between ceramic and metallic substrate can sufficiently stress the ceramic to propagate flaws in the plane of the coating during repeated thermal cycling. Flaw propagation and link-up leads to spalling; the location usually being in the ceramic just next to the metal-ceramic interface for plasma sprayed deposits. Figure 1 shows a JT9D-7F first stage turbine blade with an experimental zirconia coating which partially spalled from cyclic thermal stresses after 264 hours/1424 cycles of engine endurance testing. In particularly friable zirconia coatings, thermal cycling may cause gradual loss of ceramic through separation of poorly bonded sprayed particles--a "microspalling" phenomenon which may be confused with loss by particulate erosion (see below). Temperature exposure during thermal cycling can also cause phase transformations in partially stabilized zirconia coatings; the attendant internal volume changes can create and propagate flaws leading to massive ceramic spalling.

### Spalling from Metallic Layer Oxidation

Oxygen can penetrate ceramic coatings through connecting voids or cracks in the ceramic and oxidize the underlying metal during high temperature exposure. The problem is enhanced in zirconia coatings due to the rapid transport rate of oxygen through the zirconia lattice itself. Oxidation of the metallic underlayer can create enough volume of oxidation product to buckle and spall a structurally sound ceramic top layer. The zirconia coating on the burner rig test specimen shown in Figure 2 spalled in this manner after excessive localized oxidation of the underlying NiCoCrAlY coating.

### Spalling from Hot Corrosion Effects

Several experimenters have observed that the spall resistance of zirconia coatings is greatly reduced when corrodents (sulfur, sodium, vanadium, lead et.al.) are present in the combustion gas stream (1)(2)(3)(4). A frequent proposed mechanism is that liquid corrodent deposits penetrate flaws in the ceramic; upon cooling they freeze and produce severe internal stresses (3)(4). Gas turbine corrodent species can also chemically remove yttrium and magnesium additions from zirconia leading to crystallographic destabilization and spall-inducing phase transformations (3)(5). To date, hot corrosion attack of the metallic underlayer has not seemed to have been a problem.

### Removal by Particulate Erosion

Although particulate erosion is not a severe problem in most gas turbine operations today, it could become more important in the future depending on the nature of any alternate fuels which are adopted. Some ceramic coatings may be extremely sensitive to such attack. Recently, specimens coated with 0.010 inch thick zirconia were subjected to 20° angle impingement of 27 micron alumina particles in a 30 psi room temperature air stream. The poorest performing ceramic coatings were completely removed in less than 9 seconds, while specimens with 0.0005 inch thick NiCoCrAlY as the coating exhibited no erosion after 90 seconds.

Despite these numerous problems, there are considerable reasons to suggest that ceramic coatings will begin to be successfully employed on hot-section turbine airfoils in the relatively near future. A substantial research and development effort launched by encouraging NASA engine tests in the mid 1970's (6) has already resulted in considerable increases in ceramic coating durability. In large part, the improvements have been achieved through processing rather than coating composition development.

## PROCESS IMPROVEMENTS TO INCREASE DURABILITY

Most contemporary ceramic turbine airfoil coatings consist of MCrAl-type underlayers with zirconia-based ceramic outer surfaces. The state-of-the-art at Pratt & Whitney Aircraft in 1977, for instance, consisted of plasma sprayed systems such as: 1) CoCrAlY plus graded/mixed CoCrAlY and 21 w/o magnesia-stabilized zirconia; 2) NiCoCrAlY plus 21 w/o magnesia-stabilized zirconia (i.e. 2-layer system); and 3) NiCoCrAlY plus 20 w/o yttria-stabilized zirconia (2-layer system). Since then, the resistance of the 2-layer coatings to thermal-stress induced spalling has been significantly increased strictly through process developments. Figure 3 illustrates the 20:1 improvement in thermal stress spall resistance achieved by process changes in plasma sprayed NiCoCrAlY + 20 w/o yttria-stabilized zirconia and the greater than 40 times improvement obtained with the same coating system when deposited by electron-beam physical vapor deposition.

### Plasma Sprayed Coatings

The effects of various process procedures on plasma sprayed ceramic coating microstructures and resistance to thermal cycling are shown in Figure 4. In these examples, resistance to cyclic thermal stresses was measured by testing the coatings (0.005 inch thick Ni-23 w/o Co-18 w/o Cr-12 w/o Al-0.6 w/o Y plus 0.010 inch thick 20 w/o yttria-stabilized zirconia) on solid, uncooled superalloy test bars. The coated specimens were exposed to the exhaust of a Jet-A fueled burner rig and cycled to 1850<sup>0</sup>F for 4 minutes followed by 2 minutes of forced air cooling. The tests indicated that ceramic coating durability was increased by two basic approaches: 1) increasing the strain tolerance of the ceramic layer by tailoring the microstructure; and, 2) control of the ceramic layer's stress state (7).

High density (e.g., less than 10% porosity) 20 w/o yttria-stabilized zirconia coatings were found to be extremely prone to spalling and failed in less than 1000 cycles. Such coatings were fabricated with "high energy input" conditions such as high gun power settings, close gun-to-substrate distances, and fine ceramic particle sized sprayed powder. At the other processing extreme, "low energy input" coatings were somewhat more spall resistant (e.g., 3000-4000 cycles) but were excessively friable, very porous (greater than 25%) and consisted of poorly bonded deposited particles with numerous faults (easily cracked interfaces) in the plane of the coating. Those coatings fabricated with energy input process conditions in between these extremes exhibited approximately 15-25% porosity and cyclic lives of about 6000 cycles. In this case, strain tolerance was achieved by the low modulus

of the porous but well bonded ceramic structure. Similar energy input process effects on cyclic durability have been observed on other types of plasma sprayed zirconia coatings which rely on microcracking or segmentation rather than porosity to achieve strain tolerance.

Another potent process effect involves the residual stress state imparted to the ceramic layer upon deposition (7). It was found that heating of the bulk substrate to temperatures above 1000<sup>0</sup>F during coating resulted in excessive compressive stressing of the ceramic upon post-coating cooling. Such stresses cause buckling failure of the ceramic layer immediately following coating or within a few thermal cycles thereafter. By restricting substrate temperature to 70<sup>0</sup>-600<sup>0</sup>F during coating, a neutral or slightly tensile stress is imposed on the deposited ceramic and a two-to-four fold improvement in spall resistance is achieved. Combining the best of these process variables (to produce stress-controlled, strain-tolerant microstructures) resulted in 20 w/o yttria-stabilized zirconia coatings with lives of approximately 20,000 cycles in the Jet-A fueled 1850<sup>0</sup>F burner rig tests (Figure 4).

When ceramic-layer tolerance to thermal stress is achieved, the oxidation resistance of the underlying layer can govern coating durability in "clean" fuel turbine environments. The specimen in Figure 2 is a strain-tolerant plasma sprayed zirconia coating which spalled after burner rig cyclic testing because of excessive localized oxidation of the NiCoCrAlY underlayer. A relatively small area of oxidation-penetrated NiCoCrAlY caused separation of a much larger area of overlying ceramic. On this specimen, the NiCoCrAlY was deposited by a conventional "air spraying" plasma process. Burner rig tests have revealed that it is possible to double the oxidation resistance of MCrAlY coatings by utilizing high energy, low pressure vacuum chamber spraying as an alternative deposition process (8). Figure 5 compares the microstructural differences and relative oxidation lives of NiCoCrAlY coatings fabricated by "air" and "vacuum chamber" plasma spraying. The difference in oxidation resistance between the coatings is believed to be caused by the amounts of porosity and oxygen content introduced by the two types of processes. The effect of this process variable on ceramic coating durability is currently being evaluated in a NASA contract (9).

These recent process improvements related to ceramic coating thermal stress and oxidation resistance will significantly assist the incorporation of thermal barrier coatings on turbine airfoils in aircraft powerplants. However, it is unclear whether these improvements will increase ceramic coating resistance to more corrosive engine environments. A program is currently being conducted under Depart-

ment of Energy/Battelle Institute sponsorship to evaluate the hot corrosion and hot corrosion/erosion resistance of strain-tolerant plasma sprayed ceramic coatings (10). The initial testing has involved evaluation of plasma sprayed zirconia, mulite ( $\text{Al}_2\text{O}_3 + \text{SiO}_2$ ), calcium silicate, and  $\text{ZrSiO}_4$  coatings of 0.003 and 0.010 inch thicknesses in "clean-fuel" cyclic burner rig tests to establish a durability baseline. Results to date have shown the beneficial effect of the relatively high thermal expansion coefficient of zirconia and the increased durability of 0.003 inch versus 0.010 inch thick ceramic layers. Hot corrosion tests are in progress using the ducted burner rigs and test conditions described in Figure 6. The results to date in the hot corrosion tests at  $1300^\circ\text{F}$  (Figure 6) show that strain-tolerant zirconia coatings (0.003 and 0.010 inch thickness) provide much greater substrate protection than is obtainable from 0.005 inch thick NiCoCrAlY plasma sprayed coatings. However, coatings with low-thermal-expansion ceramics such as  $\text{ZrSiO}_4$  have exhibited limited durability due to ceramic layer spalling despite "strain-tolerant" process techniques (Figure 6). Tests at  $1600^\circ\text{F}$ , which are currently being conducted, are expected to reveal the effects of corrosive infiltration on "strain-tolerant" ceramic coatings because of the increased liquid state of sodium-vanadium-sulfur-oxygen deposits at this higher test temperature.

Testing is also being conducted in this program to examine the consequence of combined hot corrosion attack and particulate erosion. The burner rig test methods used (Figure 7) are similar to those employed in a previous metallic coating study where severe interactive corrosion/erosion degradation was observed (11). The initial test results at  $1300^\circ\text{F}$  (Figure 7) indicate that the ceramic coatings are subject to erosive degradation while metallic NiCoCrAlY plasma sprayed coatings fail equally quick due to erosion-accelerated corrosion attack. Further testing is currently in progress.

#### Electron-Beam Physical Vapor Deposited Coatings

Electron-beam physical vapor deposition has been successfully used for over a decade to fabricate MCrAlY turbine airfoil coatings for aircraft, marine, and industrial gas turbines. Experiments have shown that it is possible to also use this process to form ceramic coatings with unique microstructures favorable for spall resistance. For instance, it is possible under certain process conditions to create columnar structured (perpendicular to the surface) ceramic layers with excellent tolerance to differential ceramic/metallic substrate expansion and contraction. This tolerance results from each column being strongly attached to the substrate at its base yet unbonded with, and free to move, relative to neighboring columns.



When fabricated properly, electron-beam physical vapor deposited NiCoCrAlY plus 20 w/o yttria-stabilized zirconia coatings have demonstrated substantially greater spall resistance in "clean" fuel burner rig tests than comparable thickness, identical composition plasma sprayed coatings (Figure 4). Unfortunately, these preliminary experiments have also revealed a reproducibility problem with electron-beam physical vapor deposited zirconia coatings. While some are extremely durable, others made under seemingly identical conditions either spall following deposition or upon a few cycles of thermal exposure.

Electron metallographic analyses have suggested that slight coating microstructural differences may account for this behavior. This in turn, may be caused by subtle processing variations not controlled by present techniques. For instance, zirconia columnar growth on oxidized NiCoCrAlY coatings is different, especially near the zirconia/NiCoCrAlY interface, than on NiCoCrAlY coatings polished to remove surface oxides (Figure 8).

A research study has recently been initiated under DOE/Battelle Institute sponsorship to investigate the effects of electron-beam physical vapor deposition process parameters on ceramic coating microstructure and spall resistance (12). This study is systematically examining a range of substrate starting conditions, in-process coating parameters, and post-coating treatments on zirconia coating microstructures and spall resistance. Once the process conditions which give reproducibly good performance are established, it will be possible to initiate a detailed evaluation of the thermal stress spalling, oxidation, hot corrosion, and erosion properties of vapor deposited ceramic coatings to ascertain their engineering utility.

#### SUMMARY

Ceramic coatings offer a promising means to protect gas-turbine airfoils against future higher temperature and/or corrosive combustion environments. However, considerable improvements must be achieved in the durability of these coatings before they can be reliably utilized. Wide variations in spall resistance have been observed with current systems depending on coating fabrication techniques. Plasma sprayed MCrAlY plus zirconia coatings have exhibited 20-to-1 differences in life depending upon processing variables which affect the strain tolerance, stress state, and oxidation resistance of coating microstructures. Some zirconia coatings fabricated by the electron-beam physical vapor deposition possess considerably greater durability. To date, the greatest improvements in ceramic coating durability have been achieved through processing rather than composition development. Programs are

currently underway to determine the utility of these process-improved ceramic coatings for future aircraft and industrial gas turbines.

#### REFERENCES

1. D. W. McKee, K. L. Luthra, P. Siemers, J. E. Palko, Proceedings of First DOE/EPRI Conference on Advanced Materials for Alternative Fuel Capable Directly Fired Heat Engines, Castine, ME., 1979, p. 258.
2. R. J. Bratton, S. K. Lau, S. Y. Lee, C. A. Andersson, Proceedings of First DOE/EPRI Conference on Advanced Materials for Alternative Fuel Capable Directly Fired Heat Engines, Castine, ME., 1979, p. 582.
3. P. E. Hodge, R. A. Miller, M. A. Gedwill, Thin Solid Films, 73 (1980), p. 447.
4. S. R. Levine, P. E. Hodge, R. A. Miller, Proceedings of First DOE/EPRI Conference on Advanced Materials for Alternative Fuel Capable Directly Fired Heat Engines, Castine, ME., 1979, p. 667.
5. R. H. Barkalow, F. S. Pettit, Proceedings of First DOE/EPRI Conference on Advanced Materials for Alternative Fuel Capable Directly Fired Heat Engines, Castine, ME., 1979, p. 704.
6. C. H. Liebert, R. E. Jacobs, S. Stecum, R. C. Morse, NASA TM X-3410, 1976.
7. I. E. Sumner, D. Ruckle, Paper AIAA-80-1193, AIAA/SAE/ASME 16th Joint Propulsion Conference, Hartford, CT., 1980.
8. F. J. Pennisi, D. K. Gupta, "Tailored Plasma Sprayed MCrAlY Coatings for Aircraft gas Turbine Applications," Final Report, NASA Contract NAS3-21730, 1981.
9. NASA Contract NAS3-22548
10. DOE/Battelle Institute Contract B-A0747-A-Z
11. R. H. Barkalow, F. S. Pettit, Proceedings of First DOE/EPRI Conference on Advanced Materials for Alternative Fuel Capable Directly Fired Heat Engines, Castine, ME., 1979, p. 270.
12. DOE/Battelle Institute Contract B-A0762-A-E

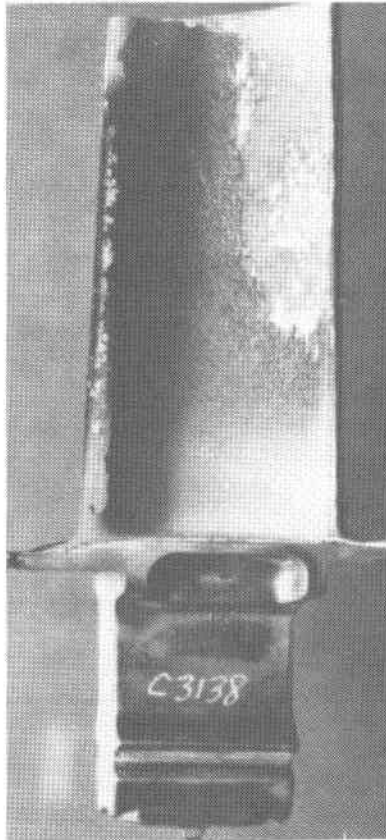


FIGURE 1

NiCoCrAlY plus 20 w/o yttria-stabilized zirconia coating which spalled after cyclic experimental testing on a high pressure turbine blade in a JT9D-7F aircraft gas turbine.

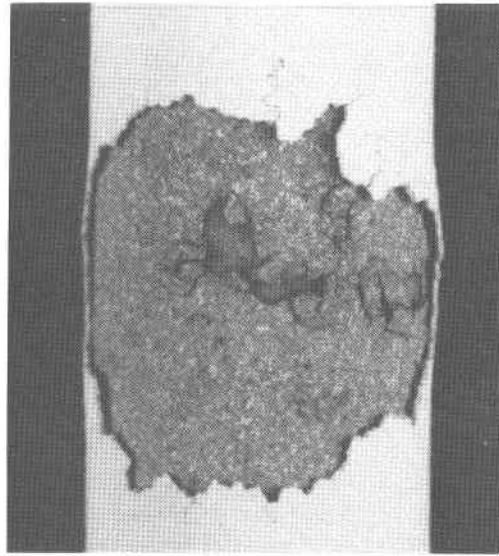


FIGURE 2

Yttria-stabilized zirconia coating which spalled during cyclic burner rig testing due to local oxidation of the underlying air plasma sprayed NiCoCrAlY coating.

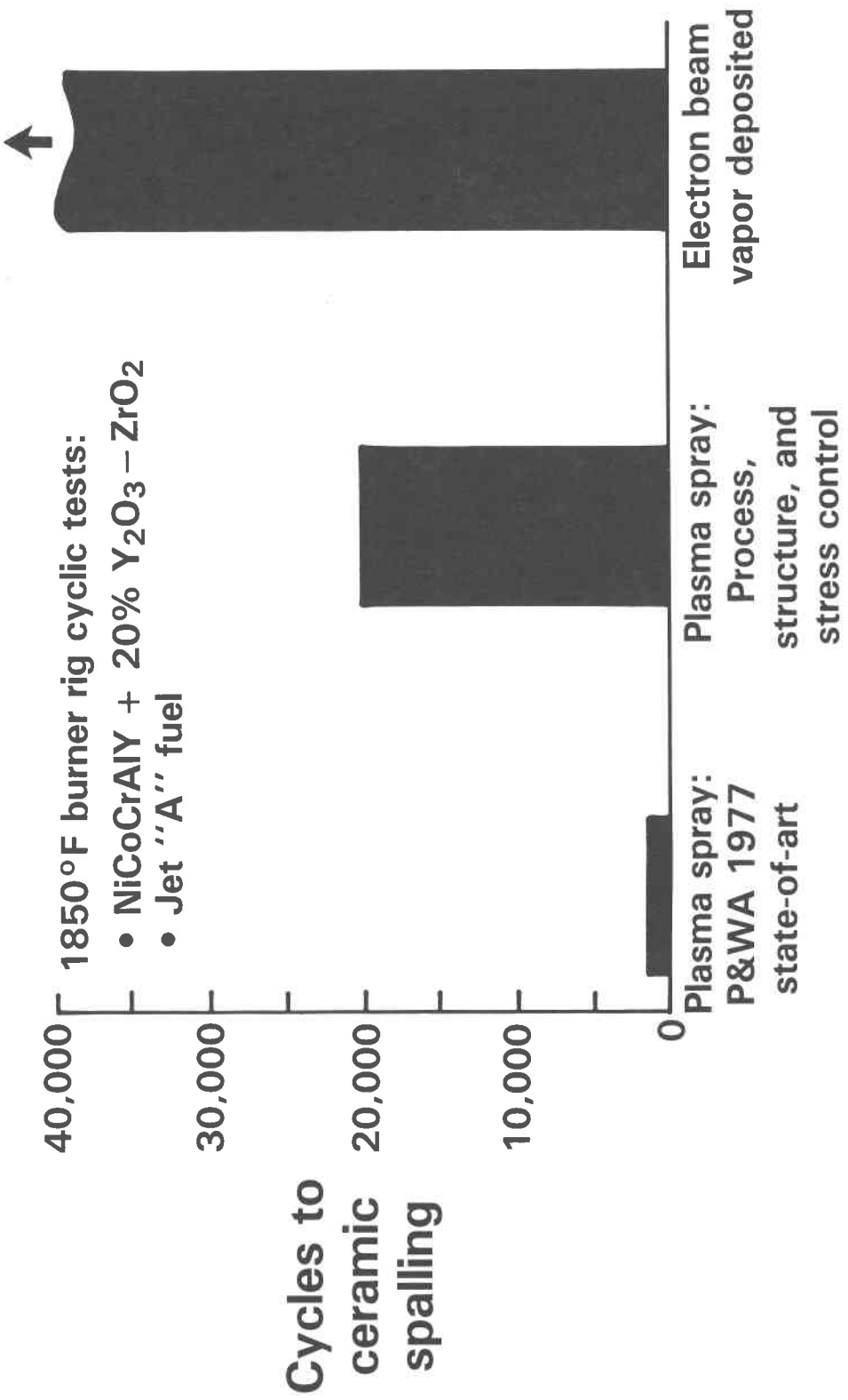
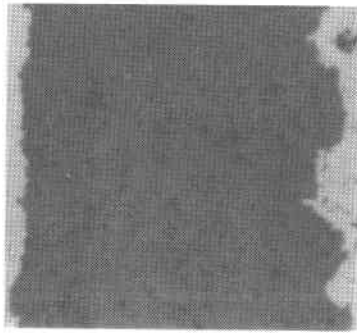


FIGURE 3

Effect of processing on cyclic spall resistance of 0.010 inch thick zirconia coatings

Plasma sprayed NiCoCrAlY + 20% Y<sub>2</sub>O<sub>3</sub> - ZrO<sub>2</sub>

**High density**



• 200-1000  
cycles

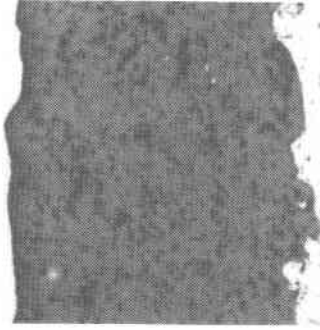
200X

**Low energy**



• 3000-4000  
cycles

**Balanced process**



• 20,000  
cycles

FIGURE 4

Effect of plasma spray processing variables on the microstructure and spalling resistance of 20 w/o yttria-stabilized zirconia coatings evaluated in "clean" fuel burner rig tests.

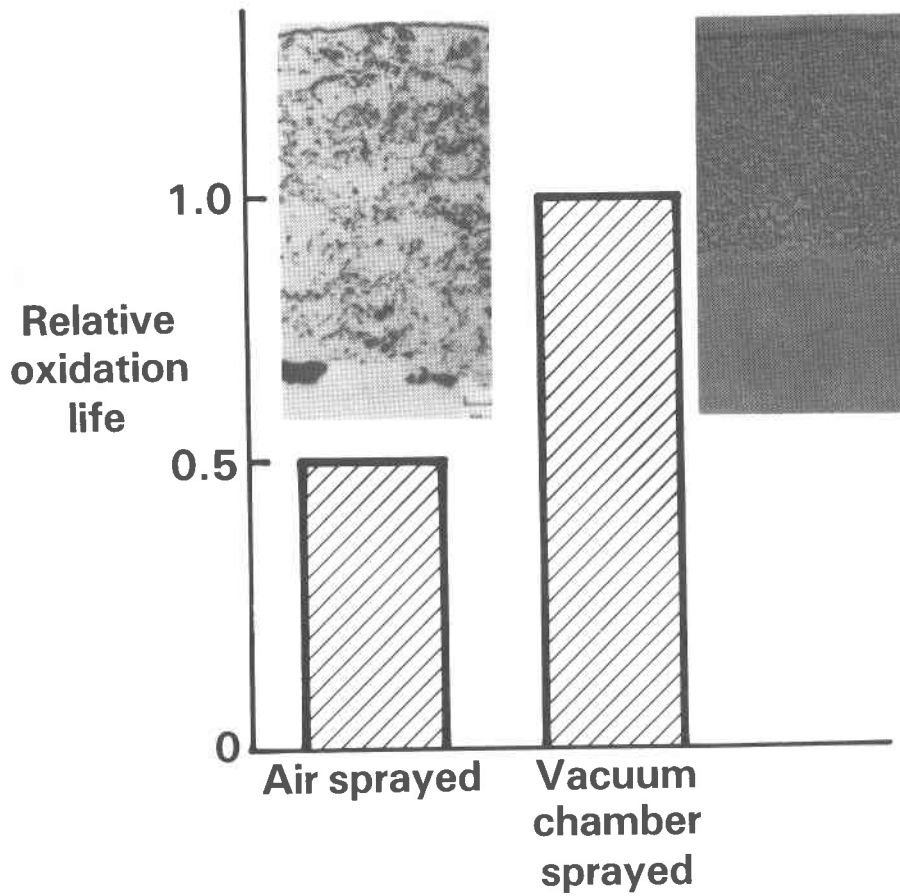
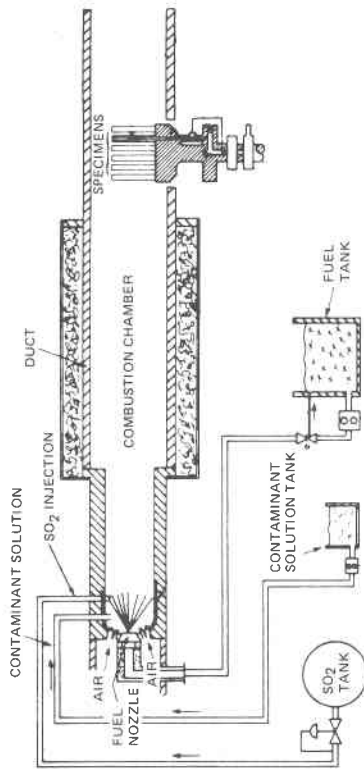


FIGURE 5

The effect of the type of plasma spray process on the microstructure and relative oxidation resistance of NiCoCrAlY coatings.

## Test facility



- 1300°F; 1600°F
- GT2 fuel contamination:
  - 1.3% Sulfur
  - 0.5 PPM Vanadium
  - 0.5 PPM Sodium
  - 0.5 PPM Potassium
  - 0.5 PPM Lead
- 20 PPM Sea Salt

## 1300°F test results

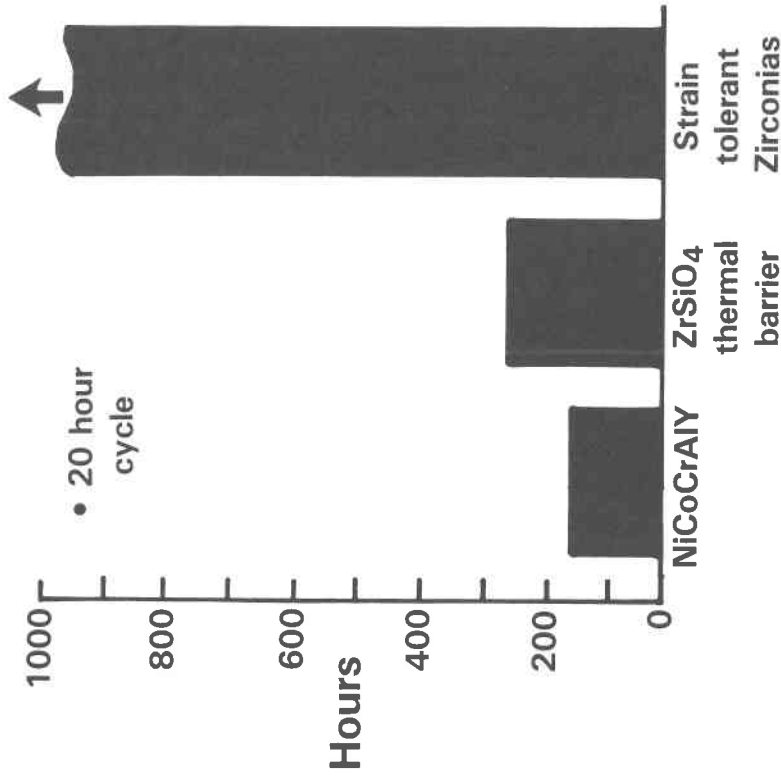


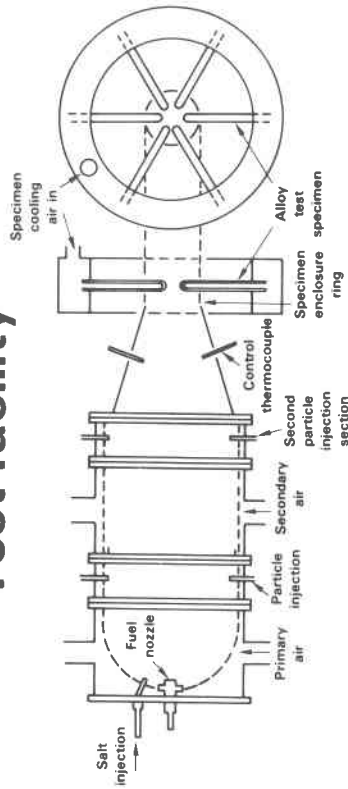
FIGURE 6

Facility and test conditions being used for hot corrosion testing of metallic and ceramic coatings. In 1300°F tests, plasma sprayed zirconia coatings have provided much greater protection (no failure after 1000 hours) than NiCoCrAlY coatings (failure after 180 hours).

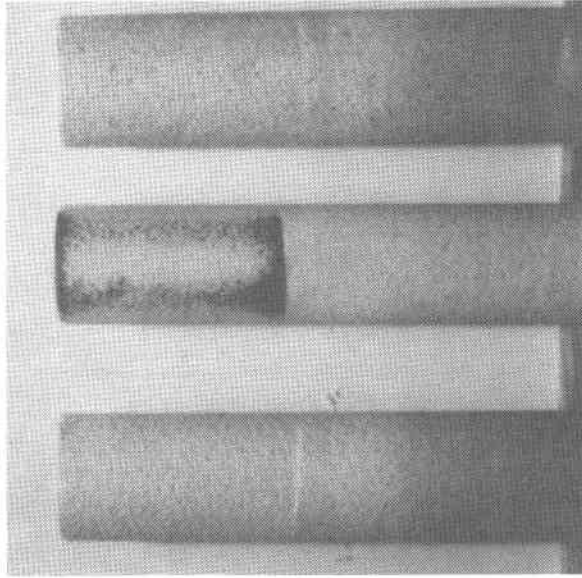


# Test facility

# 1300°F test results



- 1300°F; 1600°F
- GT2 fuel plus:
  - 60 liters/hr SO<sub>2</sub>
  - 11 PPM Sea Salt
  - 2.5 micron Al<sub>2</sub>O<sub>3</sub> at:
    - 3 grams/min.
    - 225 m/sec.

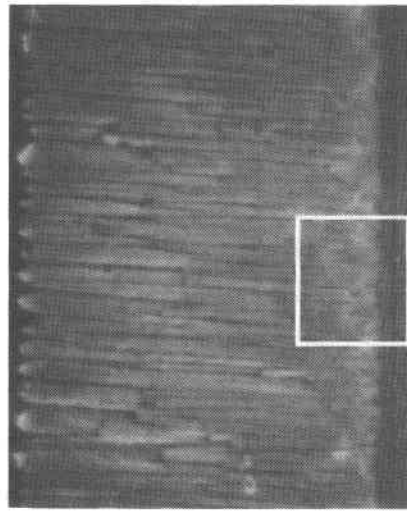


- 6 hours exposure

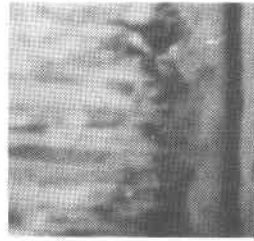
FIGURE 7

Facility and test conditions being used for erosion/corrosion testing of metallic and ceramic coatings. The initial tests indicate substantial differences in ceramic erosion rates depending upon ceramic layer composition (right hand photograph).

## Polished NiCoCrAlY

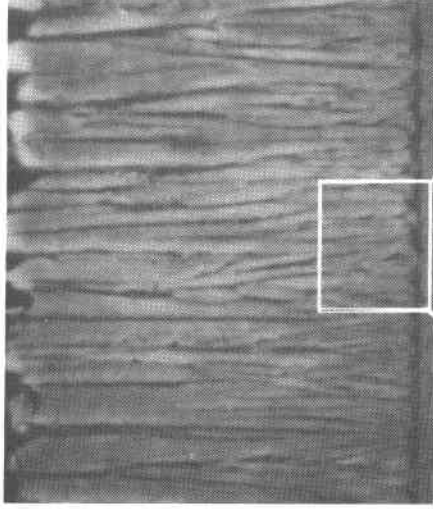


1000X\*

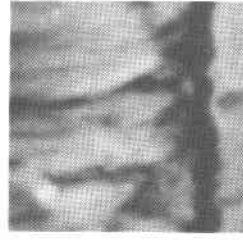


5000X\*

## Polished + oxidized NiCoCrAlY



1000X\*



5000X\*

FIGURE 8

The effect of NiCoCrAlY surface condition on the microstructure of 20 w/o yttria-stabilized zirconia coatings fabricated by electron-beam physical vapor deposition.

\* Please note that the illustration(s) on this page have been reduced 10% in printing.

## SPUTTERED CERAMIC COATINGS AND SEALING LAYERS\*

J.T. Prater, J.W. Patten, D.D. Hays, and R.W. Moss  
Pacific Northwest Laboratory,\*\* Richland, WA 99352

Progress on the development of hybrid ceramic/metal sputter deposited coatings which are designed to be adherent to metal substrates in gas turbine hot sections is reported. The ceramic materials investigated are  $ZrO_2 + 20\% Y_2O_3$  and pure  $Al_2O_3$ . The metal is CoCrAlY. In general, a CoCrAlY layer is sputter deposited first. The composition is then graded so that the ceramic content increases towards the coating surface. This transition zone has a segmented (columnar) structure, and varies in thickness. In some cases, the coating surface still contained some CoCrAlY. Heat treatments have been conducted on these deposits in an effort to provide a continuous metal (minority phase) matrix along the ceramic grain boundaries. For other deposits, the grading is continued until no metal is present, and a thick layer of pure ceramic has been deposited over the graded material. Preliminary thermal cycle results, microstructural characterization and composition profile data are presented.

---

\* This research supported by U.S. Department of Energy under Contract DE-AC06-76RLO-1830.

\*\* Operated by Battelle Memorial Institute

## INTRODUCTION

The durability of directly fired heat engines operating on minimally processed coal-derived liquid fuels is expected to depend on the hot corrosion and erosion resistance of the combustion zone components. Several ceramic coating materials have been shown to have excellent resistance to aggressive hot corrosion environments,<sup>(1-3)</sup> but retaining adherence of these coatings to metallic components has been difficult. This research examines two coating designs that offer promise.

The adherence problem arises from: 1) the inability of brittle ceramic materials (particularly dense coatings) to accommodate modulus and thermal expansion mismatches with metal substrates, and 2) the entrainment of corrosion products or condensates in coating porosity followed by thermal cycling which stresses the surrounding ceramic coating and induces spallation. For example, a porous, partially stabilized  $ZrO_2 \cdot 8Y_2O_3$  coatings, prepared by plasma spraying, have been found to do well in accommodating the modulus and thermal expansion mismatches that occur between a ceramic coating and a metal substrate.<sup>(4)</sup> However, these coatings are compromised when used in engines operated on low grade fuels where condensates and corrosion products collect in the coating porosity. These stress the coating<sup>(5)</sup> and leach the coating of the phase stabilizing  $Y_2O_3$ .<sup>(6-8)</sup> Coating spallation results during subsequent thermal cycles. To minimize entrainment of these contaminants, a dense, and if possible self healing, outer layer is clearly desirable.

The need for a ceramic coating that is both adherent to a metal substrate and impermeable to liquid and gaseous combustion products has been long recognized at PNL.<sup>(9)</sup> For the past eight years a number of approaches to coating design have been examined in an effort to obtain an adherent and impervious ceramic deposit.<sup>(10,11)</sup> This earlier work has identified that a segmented ceramic structure and a graded transition zone that separates the metal and the ceramic layers are useful techniques in improving coating adherence. A broad transition zone is considered to be beneficial in diffusing the sharp discontinuity in modulus and thermal expansion properties that occurs at the metal-ceramic interface. The columnar structure in the ceramic regions is considered to be beneficial in accommodating the lateral strains generated near the metal-ceramic interface. Based on these results, two coating designs have been prepared for the present study. Both coatings start with the sputter deposition of a 50  $\mu m$  thick CoCrAlY layer. The ceramic material, either  $ZrO_2 + 20\% Y_2O_3$  or pure  $Al_2O_3$  is then co-sputtered with the CoCrAlY to produce a broad transition zone with a segmented (columnar) structure. The ceramic composition has been gradually increased towards the coating surface. In one case,

the grading has been continued until a pure ceramic is achieved. A thick layer of segmented ceramic followed by a dense (non-segmented) ceramic layer has been deposited over the graded material as an impermeable closeout layer. Previous experiments with similar coatings show that spallation in these coatings occurs by the propagation of cracks, in the pure ceramic layer, parallel to the deposit surface.<sup>(12)</sup> Based on these results a second group of coatings has been prepared in which deposition of the transition zone has been stopped before a pure ceramic is obtained. The outer surface composition is approximately 5% CoCrAlY and 95% ceramic. It is expected that the retained metal will provide the ceramic coating with greater ductility and crack resistance, and help close the coating to penetration by combustion products.

## EXPERIMENTAL

A dual-target combined mode (r.f. and d.c.) sputtering system capable of coating seven substrates simultaneously was used in the present study. The use of this sputtering system to deposit metal layers, graded metal to ceramic deposits and ceramic layers has been described in detail elsewhere.<sup>(11)</sup> Briefly, the deposits were prepared with two independent, opposing flat plate targets of CoCrAlY and either  $ZrO_2 + 20\% Y_2O_3$  or  $Al_2O_3$ . Each target was covered with a shutter when not in use. The substrates (X-40 and In 792) were burner rig wedge test specimens, approximately 9 x 16 x 63 mm. These substrates were continuously rotated during deposition. This enhanced the growth of voids or leaders through the coating thickness. These developed by a geometrical shadowing mechanism.<sup>(13)</sup> By selecting sputtering parameters conducive to the formation of coatings with a very large number of leaders oriented perpendicular to the substrate it was possible to prepare coatings with the desired columnar (segmented) structure. Application of a small negative bias voltage to the substrates during deposition disrupted the columnar growth structure and permitted formation of a dense defect-free layer.

Supported discharge triode sputtering was used for deposition of the pure metal layers. A d.c. voltage was applied to the metal target. The ceramic layers were deposited using either r.f. diode or r.f. supported discharge techniques. The triode (supported discharge) method generated a richer plasma at lower gas pressures and permitted a 30% increase in sputtering rates for the ceramic. At the lower gas pressures used in the triode mode, the mean-free-path distance for collisions between sputtered material and sputtering gas was increased. This would be expected to affect the adatom incidence vectors and alter the stress state of the deposit. Also when sputtering ceramic in the triode mode,  $O_2$  gas was added to

the Kr sputtering gas in a ratio of 1:1. Thus, substantial differences in the stoichiometry and the internal stress levels of the ceramic layers prepared by these two methods were expected.

A total of forty-nine hybrid coatings were sputter deposited in seven deposition experiments. Seven representative samples, listed in Table I, were selected for preliminary evaluation. Two different types of coatings were prepared. All of the coatings started with the deposition of a CoCrAlY base followed by the deposition of a graded ceramic layer in which the ceramic content increased towards the coating surface. In the first group of coatings (samples 1-3) the deposition of the graded zone continued until pure  $ZrO_2 + 20\% Y_2O_3$  was obtained. The thickness of the transition layer was varied from 19  $\mu m$  in sample 1 to 3  $\mu m$  in sample 3. Then a thick layer of pure  $ZrO_2 + 20\% Y_2O_3$  was deposited. These coatings were deposited onto hollow X-40 substrates. The second group of coatings, represented by samples 4-7, were prepared with a thick graded zone. Deposition was terminated on these coatings before pure ceramic was obtained. Coatings 4 and 6 were prepared with  $Al_2O_3$  as the ceramic material. Samples 5 and 7 were made with  $ZrO_2 + 20\% Y_2O_3$  as the ceramic material. Samples 4-7 were deposited onto solid In 792 substrates following a trial experiment in which it was found that the hybrid CoCrAlY/ $Al_2O_3$  coatings failed to adhere to hollow X-40 substrates.

Characterization of the microstructure, composition, heat treatment behavior and thermal cycle durability was conducted on the samples listed in Table I. Three 10 mm sections were cut from the end of each of the seven samples for characterization. Two of the sections were used to prepare metallography samples, one in the as-deposited condition, and one following an 8 hour vacuum heat treatment at 1080°C. The third specimen section was subjected to a series of twelve 10-minute thermal cycles between ambient temperature and 1000°C. The sequence consisted of eight cycles where the coating was cooled in air followed by four cycles in which the samples were quenched into water. Structural and composition studies were conducted using the optical and scanning electron microscope (SEM), equipped with an energy dispersive spectrometer for chemical analysis.

## RESULTS AND DISCUSSION

The samples selected for characterization are described in Table I. All coatings examined started with the sputter deposition of a 50  $\mu m$  thick CoCrAlY layer. The ceramic material, either  $ZrO_2 + 20\% Y_2O_3$  or pure  $Al_2O_3$ , was then co-sputtered with the CoCrAlY to produce a transition zone where the composition was

graded from pure metal to nearly pure ceramic. The thickness of the transition layer was varied for the different samples. In samples 1-3, a thick layer of  $Zr_2O_3 + 20\% Y_2O_3$  was sputter deposited over the transition layer. For specimens 4-7 the transition zone was broader than those in the other coatings, but deposition was stopped before a pure ceramic, either  $Al_2O_3$  or  $ZrO_2 + 20\% Y_2O_3$ , was obtained. The outer surface of these samples contained about 5% CoCrAlY. The  $Al_2O_3$  was deposited with the cubic  $\gamma-Al_2O_3$  structure, which was in agreement with previous work.<sup>(14)</sup> The graded layers in samples 4 and 5 were prepared by r.f. diode sputtering. The graded zones in samples 6 and 7 were r.f. triode sputtered with  $O_2$  gas added to the sputtering gas. With the exception of the outermost closeout layer on sample 1, all of the coatings were sputter deposited with a densely packed columnar structure extending through the coating thickness. A fracture surface perpendicular to the plane of deposit 1 shows this segmented structure (Figure 1).

Vacuum heat treatments of these coatings at  $1080^\circ C$  for 8 hours produced a series of changes in the coating microstructure. Recrystallization in the CoCrAlY layer resulted in a much coarser grain structure and a more ductile fracture behavior after heat treatment, as shown in Figures 2 and 3. In the metal-to-ceramic transition zone a very fine distribution of metallic and ceramic phases developed. As a continuous metal matrix developed in the graded zone during heat treatment, this layer did develop some ductility, especially in the  $Al_2O_3$  deposits ( samples 4 and 6). Following heat treatment, the as-deposited columnar structure was no longer present in the transition zone, though it did persist in the pure outer ceramic layer. Brittle fracture behavior was displayed in the pure ceramic layers.

After heat treatment at  $1080^\circ C$ , differences were observed between the graded regions prepared by r.f. diode and r.f. triode sputtering. The graded ceramic coatings, samples 6 and 7, which were prepared using the r.f. triode sputtering mode and had  $O_2$  added to the sputtering gas during deposition were much more adherent and much less prone towards cracking after heat treatment than coatings 4 and 5 which were prepared using the r.f. diode mode and had no  $O_2$  added. Metallography which compares two of these coatings is shown in Figure 4. After heat treatment, both samples formed a graded zone where the ceramic phase was incorporated in a metal matrix. In addition, the triode sputtered coatings developed a nearly pure ceramic layer above the intermediate zone. In general, during thermal cycling of samples 4-7, cracking and spallation occurred in the graded region. It is important to note, however, that no specimens heat treated for 8 hours at  $1080^\circ C$  were thermal cycled. If heat treatment sufficient to modify the graded layers

had been conducted on thermal cycled specimens, then greater durability to thermal cycles would be expected.

The thermal cycling experiment and post-heat treatment metallography indicated that sample 1, a fully graded  $ZrO_2 + 20\% Y_2O_3$  sample with a broad transition layer and a pure ceramic outer layer was much less prone to cracking than any of the other coatings, as seen in Figure 5. In fact, after the fourth water quench this sample was examined in the SEM and it was observed that no spallation or surface cracks were present. Some cracks were observed in the cross section of the heat treated sample. However, these cracks ran vertically into the coating and usually stopped at the top of the graded zone. None were observed to penetrate into the CoCrAlY layer. In comparison, sample 2, which contained a thinner transition zone, did spall during the thermal cycling experiment. Spallation occurred at the small radius end of the wedge, as seen in Figure 5. The metallography sample prepared from the heat treated section showed vertical cracking similar to that observed on sample 1. Sample 3, which contained almost no graded region, spalled badly during thermal cycling. Metallography on the heat treated section showed that this sample developed a series of cracks in the pure ceramic layer parallel to the deposit surface, as shown in Figure 6. These findings supported previous results<sup>(12)</sup> which showed that a broad transition zone was beneficial in accommodating the strains that arose from the modulus and thermal expansion mismatches at the metal-ceramic interface.

All of the coatings in which deposition was terminated at the top of the graded zone, i.e. samples 4-7, performed poorly in the thermal cycling experiment. Multiple cracking and spalling of the scale was observed on all four of these samples. Small amounts of spallation occurred in the graded layer of samples 4 and 5. In addition, the  $Al_2O_3$  coating on sample 4 was severely cracked. This cracking was attributed to the phase transformation of the sputtered  $\gamma-Al_2O_3$  to  $\alpha-Al_2O_3$  upon heating, a phase transformation that would have been accompanied by a 10% volume decrease. It was surprising that sample 5 did not perform better under the thermal cycling. This coating was very similar to the lower portion of deposit 1, the sample which showed such excellent thermal cycle durability. The substitution of In 792 substrates for the X-40 wedges might account for the poorer performance. However, it was also possible that the absence of the outer ceramic layer resulted in a more severe thermal cycling of the graded layer than that which occurred when the layer was protected by a thick ceramic layer. This might have produced higher stress levels in the coating and resulted in more severe cracking of the deposits.



Major portions of the outer ceramic layer on samples 6 and 7 spalled. This spallation appeared to be restricted to the outermost, ceramic-rich region of the graded zone. It appeared that the inner portion of the graded layer, a region that was richer in metal and, as seen in Figure 4, formed a continuous metal matrix, remained intact. It is expected that the thermal cycle durability of these samples can be improved by increasing the amount of metal in the surface region slightly. Also, as previously mentioned, a heat treatment prior to thermal cycling may be beneficial in developing a continuous metal matrix which can provide the ceramic layer with greater ductility at the start of the cycling experiment, and thereby avert premature failure. This belief is reinforced by inspection of the metallography on heat treated samples 6 and 7 which shows them to be virtually crack free. It remains to be determined whether these coatings can provide improved hot corrosion and erosion resistance.

#### SUMMARY

A hybrid  $\text{CoCrAlY/ZrO}_2 + 20\% \text{Y}_2\text{O}_3$  sputter deposited coating that remains adherent to a metallic substrate after relatively severe thermal cycling has been designed. The current study shows that a broad transition zone is important in accommodating the modulus and thermal expansion mismatches that exist at the ceramic-metal interface. Also, the selection of substrate material, the addition of extra  $\text{O}_2$  and the use of triode sputtering techniques are all important factors that affect ceramic coating adherence. While it may be possible to retain a few discrete composition steps across a coating thickness, this study shows that the segmented structure and the gradual composition gradients that have been deposited in the transition layers of the present coatings are transient features above  $1000^\circ\text{C}$ . The present study also suggests that it may be possible to obtain improved adherence in ceramic coatings by retaining small amounts of a metallic second phase in the ceramic layer.

#### ACKNOWLEDGMENTS

This work was supported by the U.S. Department of Energy, Office of Coal Utilization, under Contract DE-AC06-76RL0-1830. Scanning electron microscopy facilities were provided by H.E. Kjarmo.

## REFERENCES

- 1) D.W. McKee and P.A. Siemers, "Resistance of Thermal Barrier Ceramic Coating to Hot Salt Corrosion", Thin Solid Films, 73 (1980), p. 439-445.
- 2) D.L. Ruckle, "Plasma Sprayed Ceramic Thermal Barrier Coatings for Turbine Vane Platforms", Thin Solid Films, 73 (1980), p. 455-461.
- 3) S.J. Dapkunas and R.L. Clarke, "Evaluation of Hot-Corrosion Behavior of Thermal Barrier Coatings", U.S. Naval Ship Research Development Center Report NSRDC-4428 Nov. 1974.
- 4) S.J. Grisaffe and S.R. Levine, "Review of NASA Thermal Barrier Coating Programs for Aircraft Engines", Proceedings of First Conference on Advanced Materials for Alternative Fuel Capable Directly Fired Heat Engines (1979), Castine, Maine, July 31-Aug. 3, 1979; NTIS Rep. CONF-790749, U.S. Dept. of Energy, Washington D.C., 1979, p. 680-703.
- 5) R.J. Bratton, S.K. Lau and S.Y. Lee, "Evaluation of Present-Day Thermal Barrier Coatings For Industrial/Utility Applications", Thin Solid Films, 73 (1980), p. 429-437.
- 6) D.W. McKee, K.L. Luthra, P.A. Siemers and J.E. Palko, "Resistance of Thermal Barriers to Hot Salt Corrosion", Proceedings of First Conference on Advanced Materials for Alternate Fuel Capable Directly Fired Heat Engines, Castine, Maine, July 1979; NTIS Rep. CONF-790749, U.S. Dept. of Energy, Washington D.C., 1979, p. 258-269.
- 7) R.H. Barkalow and F.S. Pettit, "Mechanism of Hot Corrosion Attack of Ceramic Coating Materials", Proceedings of First Conference on Advanced Materials for Alternate Fuel Capable Directly Fired Heat Engines, Castine, Maine, July 1979; NTIS Rep. CONF-790749, U.S. Dept. of Energy, Washington D.C., 1979, p. 704-714.
- 8) P.E. Hodge, R.A. Miller and M.A. Gedwill, "Evaluation of the Hot Corrosion Behavior of Thermal Barrier Coatings", Thin Solid Films, 73 (1980), p. 447-453.
- 9) J. Fairbanks, R. Busch, J. Patten and E. McClanahan, "High-Rate Sputter Deposition of Protective Coatings on Marine Gas Turbine Hot-Section Superalloys", Proceedings of 1974 Gas Turbine Materials In the Marine Environment Conference, Castine, Maine, July 1974; NTIS Report MCIC-75-27 (1975), p. 429-456.
- 10) M.A. Bayne, R. Busch, J.W. Fairbanks and J.W. Patten, "Improvement of Sputtered Oxide Coating Adherence and Integrity for Turbine Airfoil Applications", Proceedings of the First Conference on Advanced Materials For Alternative Fuel Capable Directly Fired Heat Engines, Castine, Maine, July 1979; NTIS Report CONF-790749, U.S. Dept. of Energy, Washington D.C., 1979, p. 629-657.
- 11) J.W. Patten, M.A. Bayne, D.D. Hays, E.D. McClanahan and J.W. Fairbanks, "Sputter-Deposited Multilayered Ceramic/Metal Coatings", Thin Solid Films, 64 (1979), p. 337-343.

- 12) J.W. Patten, J.T. Prater, D.D. Hays, R.W. Moss and J.W. Fairbanks, "Mechanical Behavior of Segmented Oxide Protective Coatings", Thin Solid Films, 73 (1980), p. 463-470.
- 13) J.W. Patten, "The Influence of Surface Topography and Angle of Adatom Incidence on Growth Structure in Sputtered Cr", Thin Solid Films, 63 (1979), p. 21-129.
- 14) W.T. Pawlewicz, D.D. Hays and P.M. Martin, "High Band Gap Oxide Optical Coatings for 0.25 and 1.06  $\mu\text{m}$  Fusion Lasers", Thin Solid Films, 73 (1980), p. 169-175.

TABLE 1. HYBRID METAL-CERAMIC COATINGS

SAMPLE NO.	SPUTTERING RUN	SUBSTRATE	COGRALY		TRANSITION ZONE		CERAMIC LAYER				
			THICKNESS ( $\mu\text{m}$ )	STRUCTURE	SPUTTERING DESCRIPTION	THICKNESS ( $\mu\text{m}$ )	STRUCTURE	SPUTTERING DESCRIPTION			
1	MC-13-7	HOLLOW X-40	50	SEGMENTED	TRIODE	19	SEGMENTED	R.F. DIODE, $\text{ZrO}_2$	15 + .5 OUTER	SEGMENTED DENSE	$\text{O}_2$ ADDED TRIODE
2	MC-14-6	HOLLOW X-40	50	SEGMENTED	TRIODE	8	SEGMENTED	R.F. DIODE, $\text{ZrO}_2$	15	SEGMENTED	DIODE
3	MC-15-5	HOLLOW X-40	50	SEGMENTED	TRIODE	3	SEGMENTED	R.F. DIODE, $\text{ZrO}_2$	24	SEGMENTED	DIODE
4	MC-17-7	SOLID IN 792	50	SEGMENTED	TRIODE	20	SEGMENTED	R.F. DIODE, $\text{Al}_2\text{O}_3$			
5	MC-18-7	SOLID IN 792	50	SEGMENTED	TRIODE	20	SEGMENTED	R.F. DIODE, $\text{ZrO}_2 + 20\% \text{Y}_2\text{O}_3$			
6	MC-19-6	SOLID IN 792	50	SEGMENTED	TRIODE	30	SEGMENTED	$\text{O}_2$ ADDED, R.F. TRIODE $\text{Al}_2\text{O}_3$			
7	MC-20-6	SOLID IN 792	50	SEGMENTED	TRIODE	30	SEGMENTED	$\text{O}_2$ ADDED, R.F. TRIODE $\text{ZrO}_2 + 20\% \text{Y}_2\text{O}_3$			

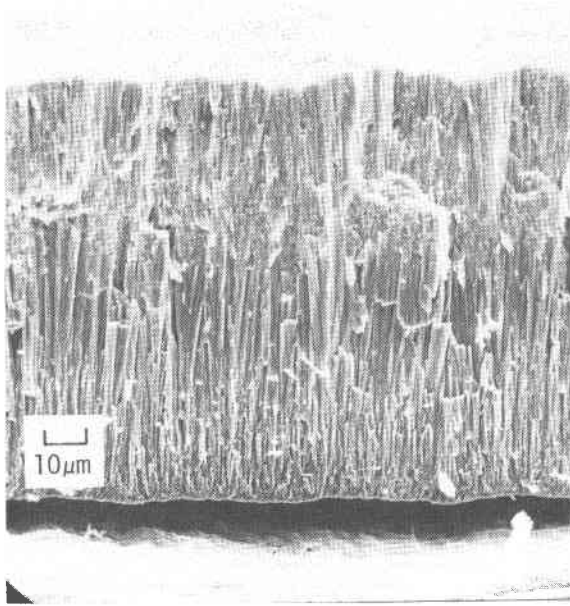


Figure 1.

SEM micrograph of a fracture surface showing the segmented structure of Sample 1 in the as-deposited condition.

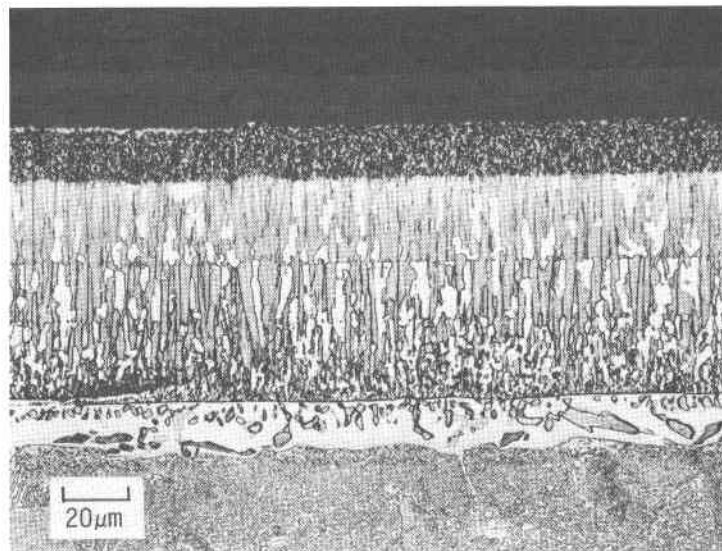


Figure 2. Optical micrograph of Sample 1 following heat treatment for eight hours at 1080°C. The polished sample has been lightly etched. The freckled zone is the metal-to-ceramic transition layer and above this is the dark gray layer that is pure ZrO<sub>2</sub> + 20% Y<sub>2</sub>O<sub>3</sub> ceramic.

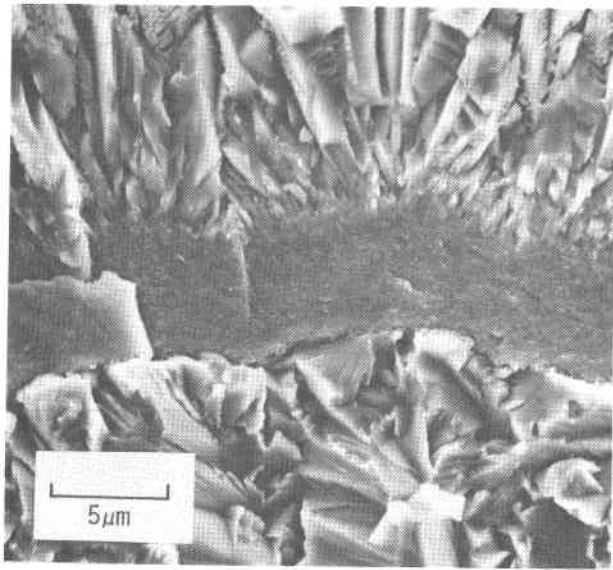


Figure 3.

Fracture surface of Sample 2 following heat treatment for eight hours at 1080°C. The metal-to-ceramic transition zone is located at the center of the micrograph. The CoCrAlY region is below and the  $ZrO_2 + 20\% Y_2O_3$  zone is above the transition layer.

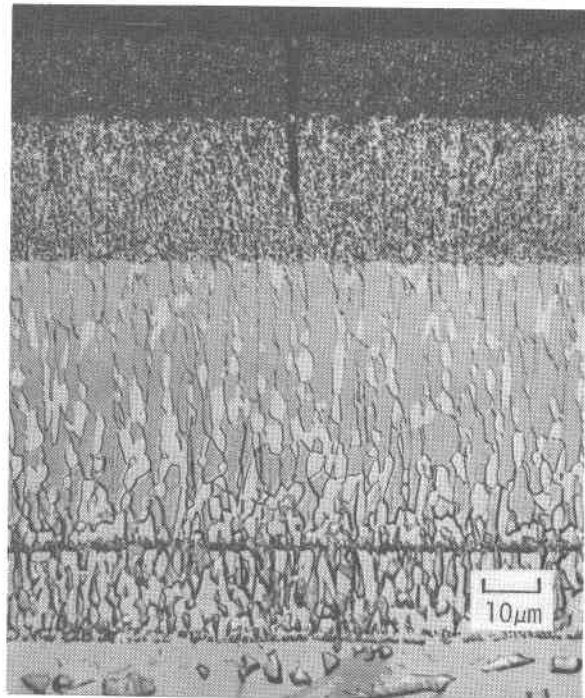
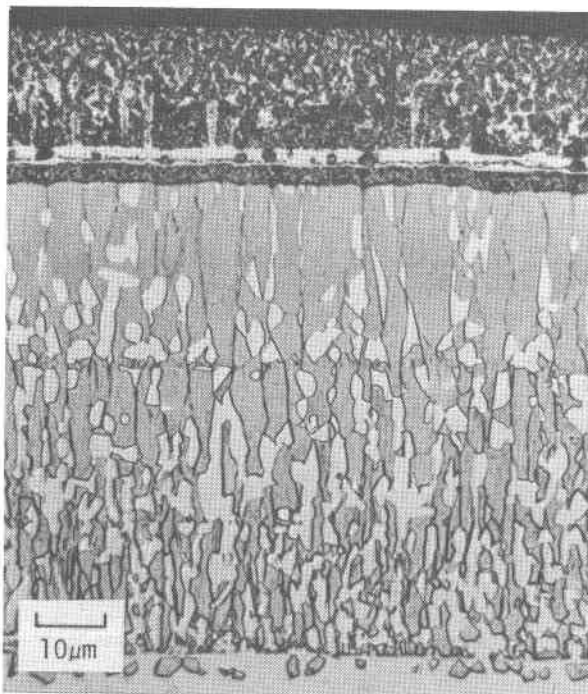


Figure 4. Optical micrographs of two CoCrAlY/ $Al_2O_3$  coatings in which deposition was terminated at the top of the graded zone. Both have been heat treated for eight hours at 1080°C. The transition layer for Sample 4, (on the left) was prepared using the r.f. diode mode; Sample 6 (on the right) was sputtered in the r.f. triode mode and had  $O_2$  gas added during ceramic deposition.

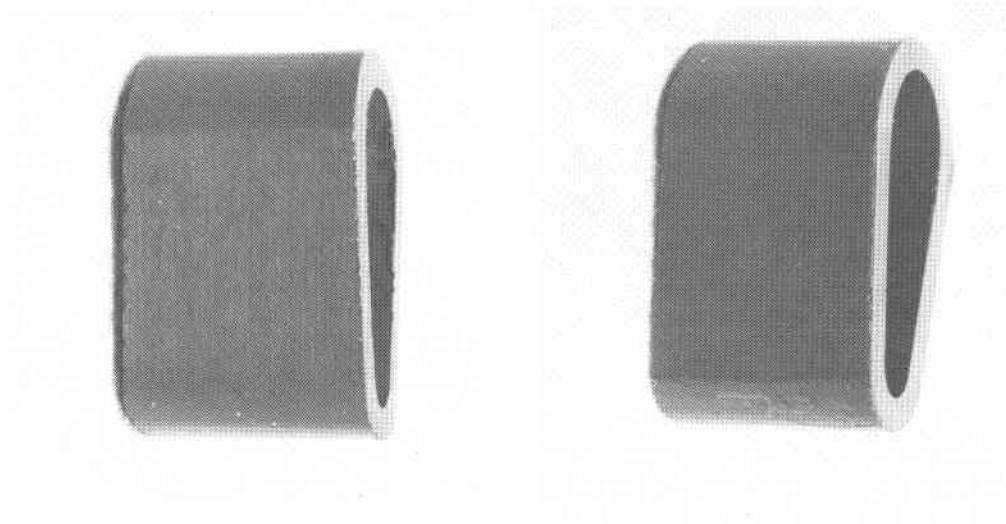


Figure 5. Sample 1 (left) and Sample 2 (right) are shown following the thermal cycle experiment. No spallation or cracking is observed on Sample 1. A small amount of spallation occurred at the smaller radius end of Sample 2.

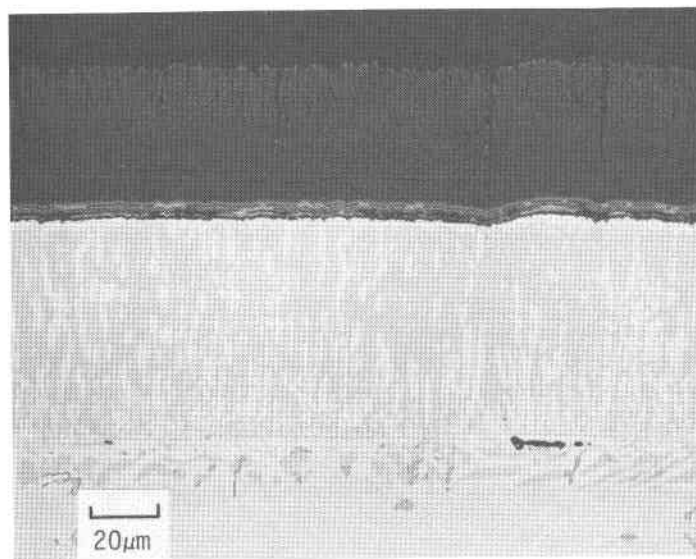


Figure 6. Optical micrograph showing Sample 3 after a heat treatment for eight hours at 1080°C. Both vertical and horizontal cracks are present in the  $ZrO_2 + 20\% Y_2O_3$ . The thin metal-to-ceramic transition layer can be observed just below the cracks.

Response of Plasma Sprayed  $\text{MgO}\cdot\text{ZrO}_2$  and  $\text{ZrO}_2\text{-6.6Y}_2\text{O}_3$   
Thermal Barrier Coatings to Thermal Fatigue and Hot Corrosion

T. A. Taylor, M. O. Price & R. C. Tucker, Jr.

To be presented at  
Second Conference on Advanced Materials for  
Alternative-Fuel-Capable Heat Engines  
August 27, 1981

Coatings Service  
Linde Division  
Union Carbide Corporation  
1500 Polco Street  
Indianapolis, Indiana 46224



## Section I

### INTRODUCTION

Thermal barrier coatings on gas turbine blade and vane gas-path surfaces offer several potential advantages; higher operating efficiency because higher gas temperatures or less cooling air can be used, reduced fabrication cost through the elimination of airfoil cooling holes, reduced corrosion rates, etc. Both simple gaseous oxidation and "hot" corrosion due to condensed compounds, such as  $\text{Na}_2\text{SO}_4$ , may be reduced with an appropriate thermal barrier system. The rate of gaseous oxidation may be lowered by a thermal barrier, even if the oxide layer is porous, simply because the metal undercoat temperature is reduced. More likely, however, higher gas temperatures will be used with the metal temperature still at an elevated temperature. Then a sealed undercoat must be incorporated in the thermal barrier system (if the oxide is porous) to protect the blade or vane alloy. Hot corrosion can be reduced if the thermal barrier oxide is resistant to the condensed compounds and effectively impermeable or by maintaining a high enough surface temperature to prevent condensation. If a thermal barrier oxide is permeable, but corrosion resistant, it may still be useful if it is accompanied by a corrosion resistant undercoat.

Plasma deposition appears to be the most economical and flexible method of producing thermal barrier coatings. Virtually any oxide and metallic undercoat can be deposited. The density and structure of the oxide can be controlled, and the metallic undercoat can be effectively sealed to provide oxidation protection for the blade or vane alloy (1). Moreover, highly automated equipment is already available to reliably apply these coatings on a production basis. The final goal of the work described here was to develop a plasma-deposited duplex (two layer) thermal barrier coating with improved resistance to thermal shock and corrosion by sodium and vanadium sulfate, impurities which are likely to exist in utility gas turbine fuels.

The present program was carried out in two phases. In phase I, thermal barrier coatings with twenty-two variations in oxide coating density, thickness, oxide type and with and without intermediate layers of Cr or Ni-20Cr, were made. These were subjected to a combined thermal fatigue and isothermal air oxidation test. The samples for initial and final microstructures were determined metallographically and using x-ray diffraction phase analysis.

The results of phase I were used to select a final set of six thermal barrier coatings for further thermal fatigue testing and for cyclic corrosion testing in phase II.

## Section 2

### TEST PROGRAM AND RESULTS

#### PHASE I

The samples for phase I are listed in Table I. In all cases, the coatings were deposited on 0.75 inch diameter Hastelloy C-276\* alloy tubing segments and subsequently vacuum heat treated at 1975°F for 4 hours. A set of four samples were tested at one time in an apparatus that cyclically rotated from a heating position to a blast cooling position. The heat was provided by an oxygen-methane burner. After 140 seconds of heating the oxide surface temperature reached 1950-2000°F, then, switched to the cooling position for 60 seconds, it dropped to about 400°F. The tubes were internally cooled with individual airflows to limit the inside metal temperature to about 1800°F. In an effort to accelerate the failure point, an isothermal exposure at 1850°F in air was carried out after the first 200 thermal fatigue cycles. The test concluded with 600 additional thermal fatigue cycles.

The results can be summarized as follows. A much higher percentage of  $ZrO_2-20Y_2O_3$  samples spalled than did  $MgO \cdot ZrO_2$  samples. Sample failure always involved shearing within the oxide near the undercoat interface. The  $ZrO_2-20Y_2O_3$  samples appeared to be more prone to shear failure because they had a more lamellar structure as compared with the more interlocking structure of the  $MgO \cdot ZrO_2$ . Surprisingly, although the  $MgO \cdot ZrO_2$  converted primarily to monoclinic during testing, destabilization did not seem to impair thermal fatigue performance in this test sequence. The  $ZrO_2-20Y_2O_3$  did not significantly change from the original cubic  $ZrO_2$  structure during testing.

Regarding density, the isothermal exposure overstressed the high density (90% theoretical)  $ZrO_2-20Y_2O_3$  samples, resulting in sample failure. The low (86% theoretical) and medium (88% theoretical) density  $ZrO_2-20Y_2O_3$  samples looked better in this test sequence. In contrast, a greater percentage of high density (94.5% theoretical)  $MgO \cdot ZrO_2$  samples survived than did low (86% theoretical) or medium (89% theoretical) density  $MgO \cdot ZrO_2$ . In addition, the spalling mechanism of the high density  $MgO \cdot ZrO_2$  coatings tended to be more self-limiting than did that of the lower density coatings, (i.e., the high density coating formed smaller chips with "feathered" edges).

The two oxide types also exhibited opposite behavior as a function of oxide thickness. Among medium density  $ZrO_2-20Y_2O_3$  samples, the thinner the coating (in the 4-12 mil range), the better the performance. In contrast, for the  $MgO \cdot ZrO_2$  coatings, increasing thickness over the 4 to 12 mil range seems to improve performance.

Finally, regarding the effect of a middle layer, the Cr middle layer oxidized excessively during the 1850°F air isothermal exposure and these samples spalled during the air cool to room temperature. In addition, no advantage was gained from the use of a NiCr middle layer.

\*Trademark of Cabot Corporation, referred to subsequently as C-276.

## PHASE II

The results of the first phase indicated that an improved microstructure would be required for yttria-stabilized zirconia if it were to be successful. The ZrO-20 wt %  $Y_2O_3$  coating revealed in the SEM a laminar collection of oxide splats, poorly mechanically interlocked. The high purity of this material probably allowed a narrow freezing range and limited flow upon deposition. A different source of powder was found that was less pure, containing 1.5 wt %  $HfO_2$ , among other impurities, and 6.6 wt %  $Y_2O_3$ . The resulting structure using this powder was more like the MgO-ZrO<sub>2</sub> coating.

The medium to high densities were selected for phase II, partially due to the good thermal fatigue performance of MgO-ZrO<sub>2</sub>, and as one means to possibly reduce the oxide's permeability to liquid NaSO<sub>4</sub>-type salts. Only the 12 mil thickness was pursued. The negative results in phase I with Cr or NiCr inner layers eliminated their further consideration.

The coatings selected for phase II are listed in Table II, with their measured densities.\* A new variable, a controlled microcrack population, was added to counter balance the expected high elastic modulus of the high density coatings. (A high modulus would generate higher thermal stresses in the oxide for a given thermal expansion mismatch.) The microcrack patterns obtained in the high density MgO-ZrO<sub>2</sub> and ZrO<sub>2</sub>-6.6Y<sub>2</sub>O<sub>3</sub> coatings are shown in the SEM micrographs of their surfaces in Figure 1. In these coatings the microcrack pattern was enhanced by modified plasma spray parameters. In fact, all the zirconia coatings made and tested in this program have had a microcrack pattern, but to a lesser degree. This pattern is on a much finer scale than the segmented pattern generated by Ruckle<sup>(2)</sup>, which had about a 1mm crack spacing in ZrO<sub>2</sub>-6Y<sub>2</sub>O<sub>3</sub>.

All the thermal barrier coatings were vacuum heat treated, 4 hours at 1975°F. The primary reasons are to densify and seal the metallic layer and to form a diffusion bond between it and the substrate. In addition, the aluminum in the MCrAlY layer can form Al<sub>2</sub>O<sub>3</sub> by reduction of ZrO<sub>2</sub>. In these coatings, it is found that an aluminide depletion layer forms in LCO-22 during the vacuum heat treatment. It is up to 0.08 mils wide in contact with ZrO<sub>2</sub>-6.6Y<sub>2</sub>O<sub>3</sub> and 0.1 to 0.4 mils wide in contact with MgO-ZrO<sub>2</sub>. A thin layer of Al<sub>2</sub>O<sub>3</sub> between the LCO-22 and the zirconia layer can be seen at high magnification using differential interference contrast. This added bond formation is another reason for using a vacuum heat treatment cycle for thermal barrier coatings.

The thermal fatigue testing was modified by using higher oxide temperatures in the cycle and eliminating any isothermal cycle. The cycle was increased to 150 seconds heating with a hotter burner condition to reach 2260°F, followed by 130 seconds blast cooling to reach about room temperature. A lower burner temperature was used to generate a 2100°F oxide temperature for part of the samples tested.

The cycles to failure results for thermal fatigue tests are given in Table III. Three tests were done at 2260°F for each of the 6 different coatings, and one of each was tested at 2100°F. These results are shown graphically in Figure 2. The failure criterion used here was very conservative. Any spallation or microchipping visible to the eye was considered a failure, whether the area affected was large or small. It was found that for the medium density coatings MgO-ZrO<sub>2</sub> is superior to ZrO<sub>2</sub>-6.6Y<sub>2</sub>O<sub>3</sub> at 2260°F, but they were equal in 2100°F testing. At either test

\*The medium density MgO-ZrO<sub>2</sub> is designated UCAR LTB-8B. The high density and high density + microcracks ZrO<sub>2</sub>-6.6Y<sub>2</sub>O<sub>3</sub> coatings have been designated UCAR LTB-12 and UCAR LTB-13, respectively. UCAR is a trademark of Union Carbide Corporation.

temperature the  $ZrO_2-6.6Y_2O_3$  is greatly superior to  $MgO-ZrO_2$  when both are in the high density or high density plus microcracked conditions. The coating most resistant to thermal fatigue was found to be  $ZrO_2-6.6Y_2O_3$  coated at high density with microcracks. This coating had not failed in the 2100°F test at 3200 cycles when the test was terminated. If the average cycles-to-failure data are analyzed, it is found that the temperature dependence is greater for the  $ZrO_2-6.6Y_2O_3$  family of coatings, and their superiority should increase over  $MgO-ZrO_2$  group as the test temperature is decreased. At higher temperatures the two oxide types may tend toward the same life.

The same group of thermal barrier coatings was tested in a cyclic corrosion test. A temperature gradient was maintained during heating by gas impingement cooling on the inside of the C-276 substrate. A typical test cycles' temperature history is shown in Figure 3. The holding period at 1600°F was 4 hours. After each fifth cycle of 4 hours the group of coatings under test was removed from the furnace and coated with an aqueous solution of sodium sulfate and vanadium sulfate. It was dried and held to a weight gain of 0.5-1.0 mg/cm<sup>2</sup>. The solution had Na, S and V concentrations of 75, 35 and 17.5 grams/liter. Evaporated to dryness, the salt had an approximate melting range of 1410 to 1535°F.

The cyclic corrosion test was run for 50 cycles, equivalent to 200 hours at 1600°F. None of the six final coating candidates of phase II spalled during the test, although a gradual color change was observed for the  $ZrO_2-6.6Y_2O_3$  family of coatings. Two corrosion specimens were made of the high purity  $ZrO_2-20Y_2O_3$  oxide from phase I, and these samples spalled massively within 60 hours.

Polished cross-sections of the high density coatings of  $MgO-ZrO_2$  and  $ZrO_2-6.6Y_2O_3$  were examined with an SEM equipped with an x-ray analyzer. At the time of examination the samples had completed 200 hours of corrosion testing, and they had been tested 20 hours at 1600°F since their last application of the salt solutions. In either the  $MgO-ZrO_2$  or  $ZrO_2-6.6Y_2O_3$  coatings, no indication of Na, S, or V could be found.

However, analysis of the oxide surface of the same types of coatings after 85 cycles (340 hours at 1600°F) showed a moderate amount of V and a small amount of Na, only on the  $MgO-ZrO_2$  surface. The surface morphology appeared similar to the starting condition. In contrast, the surface of the  $ZrO_2-6.6Y_2O_3$ , which appeared green to the eye, had no indication of Na, S or V, but moderate concentrations of Cr and Al, and weak indications of Co and Mg were recorded. The surface morphology was changed considerably from the starting condition, with the appearance of an oxidized metallic alloy. Crystals of  $Cr_2O_3$  were identified on the surface, probably contributing to the green color. Other complex Al, Co, and Cr oxides were present. These oxides do not appear in the polished cross-section and are apparently a very thin surface layer. Similar surface oxides on  $ZrO_2-12Y_2O_3$  have been analyzed by Singhal and Bratton<sup>(3)</sup>. The transport method for the elements, apparently from the LCO-22 undercoat to the surface of the  $ZrO_2-6.6Y_2O_3$  layer is not clear, but thought to occur by surface diffusion from the ends of the coated tube sections where the green colors first appeared. While this is an interesting effect, it does not change the general result that none of the zirconia oxides failed mechanically in the 200 hours of corrosion testing.

The x-ray diffraction phase analyses are summarized for the starting and tested coatings in Table IV. The  $MgO-ZrO_2$  family of coatings was found to be principally cubic  $ZrO_2$  with a cubic  $MgO$  minor phase and an indication of monoclinic  $ZrO_2$ , both as-heat treated and after the 2260°F test. After the 2100°F thermal fatigue test and the 1600°F cyclic corrosion tests, monoclinic  $ZrO_2$  was found to be the major phase, with cubic  $ZrO_2$  and cubic  $MgO$  the minor phases. The  $ZrO_2-6.6Y_2O_3$  material

always maintained a cubic  $ZrO_2$  as the major phase throughout all tests. A minor phase, not found in the powder, was generated in coating and also remained through the tests. This phase is identified as Unk. T in the Table, and represents a very poor intensity match to tetragonal  $ZrO_2$ , but does have many of the tetragonal reflections present. A minor monoclinic  $ZrO_2$  phase was present in the powder, and remained in all coatings.

The polished cross-sections of the tested coatings were examined with the metallograph. In the 2260°F thermal fatigue specimens there was no oxidation of the substrate, but on the hotter, burner-facing half of the tube circumference, the aluminide phase of the LCO-22 metallic layer was depleted. Internal oxide had formed in a 0.5-1 mil layer of the LCO-22 next to the oxide overcoat, but the bulk of the LCO-22 was oxide-free. A typical microstructure is shown in Figure 4. In the 1600°F corrosion samples, there was no attack of the C-276, and very little change in the aluminide depletion layer of the LCO-22, compared to the heat treated, not tested, condition.

The mode of oxide spallation for all  $MgO \cdot ZrO_2$  coatings in both the 2100 and 2260°F thermal fatigue tests was by large area spalls, with the fracture at the oxide-metallic interface or slightly within the oxide, but near the undercoat. This type of spall is shown in Figure 5. In phase I for a 1950°F test, high density  $MgO \cdot ZrO_2$  failed by small chipping which produced a tapered edge around the spall zone. In the 2100°F cycle, the medium density  $ZrO_2-6.6Y_2O_3$  layer failed by a progressive enlargement of a spall zone formed from very small chips. The high density variant developed widely spaced shallow chips, from cracks running parallel to the surface, shown in Figure 6. The yttria stabilized high density plus microcracks did not spall by 3200 cycles at 2100°F. The medium density  $ZrO_2-6.6Y_2O_3$  coatings in the 2260°F test showed shallow microchip formation (Figure 7), and deeper, larger chip formation for the higher densities (Figure 8).

Thus there is a trend toward spall growth by microchipping at the lower temperatures, and large area spalls down to the undercoat at higher temperatures. The  $ZrO_2-6.6Y_2O_3$  materials have a higher transition temperature for this change of failure mode than the  $MgO \cdot ZrO_2$  coatings. In the  $ZrO_2-6.6Y_2O_3$  family, the lower densities can maintain the microchip mode to even higher temperatures, but their time to first failure is less than the higher densities as described earlier.

### Section 3

#### DISCUSSION

The failure observations in this program have shown several different mechanisms strongly dependant upon the structure of the oxide. As the coating/substrate system is stressed in a thermal cycle the weakest point will be the first to fail. In these duplex coatings the metallic layer interface roughness was already nearly optimized<sup>(1)</sup> from the mechanical attachment standpoint. There are additional chemical bonding forces developed, due to the aluminum-zirconia reaction mentioned. A good diffusion bond between the metallic undercoat and the substrate eliminates this interface as a failure point.

If the mechanical and chemical bonds at the oxide/undercoat interface are well established, initial spallation will be dependant upon the properties of the oxide. If the oxide is porous and composed of poorly interlocked oxide particles, like the lamellar structure of high purity  $ZrO_2-20Y_2O_3$ , long running cracks are easily propagated. It appears that in fully stabilized cubic materials there is less toughness or crack blunting ability of the structure, compared to multiphase oxides such as  $MgO \cdot ZrO_2$  or in partially stabilized zirconia.

If crack propagation is made difficult by a dense, highly interlocked particle structure, which also has a toughened matrix, the failure mechanism may have to find the next weakest path. If the oxide is too dense and has a high elastic modulus, it is possible to exceed its fracture strength by thermal expansion mismatch strain from a single cycle to a high temperature (thermal shock) or to create a flaw which grows cyclically at a somewhat lower temperature (thermal fatigue). The latter condition appears satisfied in the high density  $ZrO_2-6.6Y_2O_3$ , which fails slowly from surface originated cracks by slow growth and microchipping. When the high density structure is given microcracks, part of the high modulus may be reduced as well as provide sites for growing cracks to stop at an internal interface.

If the properties of the oxide resist internal crack growth, the site of failure may again seek the interface area near the metallic layer, but after longer times. It is believed that part of a duplex thermal barriers success in withstanding thermal cycles is due to the softening of the MCrAlY layer as its temperature exceeds about 1500<sup>o</sup>F. The yield strength of MCrAlY coatings falls quickly in this temperature range and should be able to relieve mismatch strains that have accumulated. It is really the substrate alloy and oxide layer mismatch that is important and whether the metallic coating layer can absorb some of the difference plastically. One would expect that the undercoat should be at least some critical thickness to obtain this compliance. Finally, the near interface failure mechanism comes in to play when the metallic undercoat has its oxidation resistance decreased to a point where internal oxides form, which harden the metallic layer and reduce its ductility. Then stresses can be generated without relief at the interface and the oxide will fail near the interface. The choice of an undercoat composition which maximizes its own oxidation resistance, while maintaining a low brittle-to-ductile transition should extend the life of a thermal barrier. Several of these aspects can be

interpreted from others<sup>(4)</sup>, relating MCrAlY composition and metallic layer thickness to thermal barrier life. However, on the basis of the above model, an internally oxidized, air-sprayed MCrAlY layer would have already forfeited some of its life.

It also appears possible that the use of high density, low porosity oxide coatings has a chance of prolonging the life of thermal barriers in the presence of corrosive salts. The higher porosity and weak internal structure of the phase I  $ZrO_2-20Y_2O_3$  material lead to rapid failure in the corrosion test, possibly due to mechanical rupturing by solidified salt within the porosity, as was found by Bratton, et al<sup>(5)</sup>. The higher density coatings of phase II may have at least forced the corrosion effects to stay at the surface, without substantial penetration into the oxide. Substantially longer cyclic tests over a range of temperatures would be desirable to fully investigate the corrosion resistance of these coatings.

## Section 4

### CONCLUSIONS

The goals of this thermal barrier improvement program were achieved. A new thermal barrier coating was identified which had much superior thermal fatigue resistance than previous base-line thermal barrier coatings. The high density plus micro-cracked  $ZrO_2-6.6Y_2O_3$ , lasted about three times longer in a 2260<sup>o</sup>F thermal fatigue test, and more than five times longer in the 2100<sup>o</sup>F test than the current standard, medium density  $MgO \cdot ZrO_2$ . Both the  $MgO \cdot ZrO_2$  and  $ZrO_2-6.6Y_2O_3$  families of coatings passed the cyclic corrosion test without failure. The same corrosion test caused massive spallation in a porous  $ZrO_2-20Y_2O_3$  coating.

This work also demonstrated the usefulness of a controlled microcrack population and an internally strong oxide microstructure. Each of these elements of structure control improved the thermal fatigue life of the base-line medium density coatings. In the case of the  $ZrO_2-6.6Y_2O_3$  system these improvement factors were the most impressive. The present microcrack pattern greatly improves thermal fatigue life, while the work by Ruckle<sup>(2)</sup> using a segmented, wide crack pattern was also successful.



## Section 5

### REFERENCES

1. R. C. Tucker, T. A. Taylor and M. H. Weatherly, 3rd Conference on Gas Turbine Materials in a Marine Environment, Bath University, Bath, Great Britian, 1976.
2. D. L. Ruckle, Thin Solid Films, 73 (1980) 455-461.
3. S. C. Singhal and R. J. Bratton, Trans. ASME, Volume 102, October 1980, p. 770.
4. S. Stecura, Thin Solid Films, 73, (1980) 481-489.
5. R. J. Bratton, S. K. Lau and S. Y. Lee, Thin Solid Films, 73, (1980) 429-437.

Table I  
THERMAL BARRIER COATINGS\*  
FOR PHASE I

<u>Intermediate Layer Type</u>	<u>Oxide Type</u>	<u>Oxide Density %Theoretical</u>	<u>Oxide Thickness, mils</u>	
None	MgO·ZrO <sub>2</sub>	94	4	
			8	
			12	
		89	4	
			8	
			12	
		86	8	
	NiCr	MgO·ZrO <sub>2</sub>	94	8
			89	8
86			8	
Cr	MgO·ZrO <sub>2</sub>	94	8	
		89	8	
None	ZrO <sub>2</sub> -20Y <sub>2</sub> O <sub>3</sub>	90	4	
			8	
			12	
		88	4	
			8	
			12	
NiCr	ZrO <sub>2</sub> -20Y <sub>2</sub> O <sub>3</sub>	86	8	
		90	8	
		88	8	
	86	8		

\*All specimens have an 0.003 to 0.005 thick undercoat of UCAR LCO-22 (Co-32Ni-21Cr-8Al-0.5Y). Theoretical densities used: MgO·ZrO<sub>2</sub> (5.01), ZrO<sub>2</sub>-20Y<sub>2</sub>O<sub>3</sub> (5.97).

Table II  
THERMAL BARRIER COATINGS  
FOR PHASE II

Coating Type	Coating Thickness			
	LCO-22 Undercoat Average	Std. Dev.	Oxide Overcoat Average	Std. Dev.
<u>Thermal shock samples</u>				
<u>MgO·ZrO<sub>2</sub></u>				
MD*	6.4	0.3	15.2	0.4
HD	6.2	0.6	12.8	0.7
HD + MC	6.6	1.0	13.8	0.8
<u>ZrO<sub>2</sub>-6.6Y<sub>2</sub>O<sub>3</sub></u>				
MD	6.4	0.3	12.3	0.6
HD	6.7	0.6	12.9	0.8
HD + MC	6.7	0.5	14.4	0.4
<u>Cyclic corrosion samples</u>				
<u>MgO·ZrO<sub>2</sub></u>				
MD	4.6	0.8	12.9	0.9
HD	4.6	0.5	14.0	1.1
HD + MC	4.4	0.7	13.2	0.4
<u>ZrO<sub>2</sub>-6.6Y<sub>2</sub>O<sub>3</sub></u>				
MD	4.9	0.6	14.4	0.4
HD**	4.5	0.4	13.6	0.5
HD + MC***	4.3	0.4	12.2	0.5
<u>Density</u>				
<u>Density samples</u>	<u>gm/cm<sup>3</sup></u>	<u>%Theoretical</u>		
<u>MgO·ZrO<sub>2</sub></u>				
MD	4.40	88.7		
HD	4.54	91.5		
HD + MC	4.60	92.7		
<u>ZrO<sub>2</sub>-6.6Y<sub>2</sub>O<sub>3</sub></u>				
MD	5.28	87.3		
HD	5.36	88.6		
HD + MC	5.30	87.6		

Notes: All values in mils. MD=medium density; HD=high density; MC=microcracks. 5-6 readings per average thickness. 3 readings per average density. All specimens for density were given the same 4 hr., 1975°F vacuum heat treatment that was given the test samples. Theoretical densities used: MgO·ZrO<sub>2</sub> (4.96), ZrO<sub>2</sub>-6.6Y<sub>2</sub>O<sub>3</sub> (6.05 gm/cm<sup>3</sup>).

\* UCAR LTB-8B  
\*\* UCAR LTB-12  
\*\*\* UCAR LTB-13

Table III  
CYCLES TO FAILURE IN THERMAL FATIGUE

<u>Thermal Barrier</u>	<u>2260°F Maximum Average Life*</u>	<u>Standard Deviation</u>	<u>2100°F Maximum Life, One Test</u>
<u>MgO-ZrO<sub>2</sub></u>			
Medium density**	195	38	638
High density	184	41	834
High density + microcracks	233	24	769
<u>ZrO<sub>2</sub>-6.6Y<sub>2</sub>O<sub>3</sub></u>			
Medium density	96	13	653
High density***	378	25	2924
High density + microcracks****	566	24	> 3208

\* of three tests  
 \*\* UCAR LTB-8B  
 \*\*\* UCAR LTB-12  
 \*\*\*\* UCAR LTB-13

Table IV

 X-RAY DIFFRACTION PHASE ANALYSIS  
 OXIDE LAYER OF THERMAL BARRIER COATINGS

Coating Type	As Heat Treated		2260°F Thermal Shock		2100°F Thermal Shock		1600°F Corrosion	
	Major	Minor	Major	Minor	Major	Minor	Major	Minor
MgO·ZrO <sub>2</sub>								
MD*	C	C-MgO; M					M	C; C-MgO
HD	C	C-MgO; M	C	C-MgO; M	M	C; C-MgO	M	C; C-MgO
HD + MC	C	C-MgO; M	C	M; C-MgO	M	C; C-MgO	M	C; C-MgO
ZrO <sub>2</sub> -6.6Y <sub>2</sub> O <sub>3</sub>								
MD	C	M; Unk. T					C	Unk. T; M
HD**	C	Unk. T; M	C	Unk. T; M	C	Unk. T	C	Unk. T
HD + MC***	C	Unk. T; M	C	Unk. T; M	C	Unk. T; M	C	Unk. T; M

Notes: Diffraction sample was surface of 0.75" diameter coated tube held in special fixture. C:cubic ZrO<sub>2</sub>; M:monoclinic ZrO<sub>2</sub>; Unk. T:poor fit but probably tetragonal ZrO<sub>2</sub>; C-MgO:cubic MgO, typically 4.21Å lattice parameter in all cases. The cubic ZrO<sub>2</sub> lattice parameter was 5.11Å in the MgO·ZrO<sub>2</sub> material and 5.13Å in the ZrO<sub>2</sub>-6.6Y<sub>2</sub>O<sub>3</sub> coatings.

\* UCAR LTB-8B

\*\* UCAR LTB-12

\*\*\* UCAR LTB-13

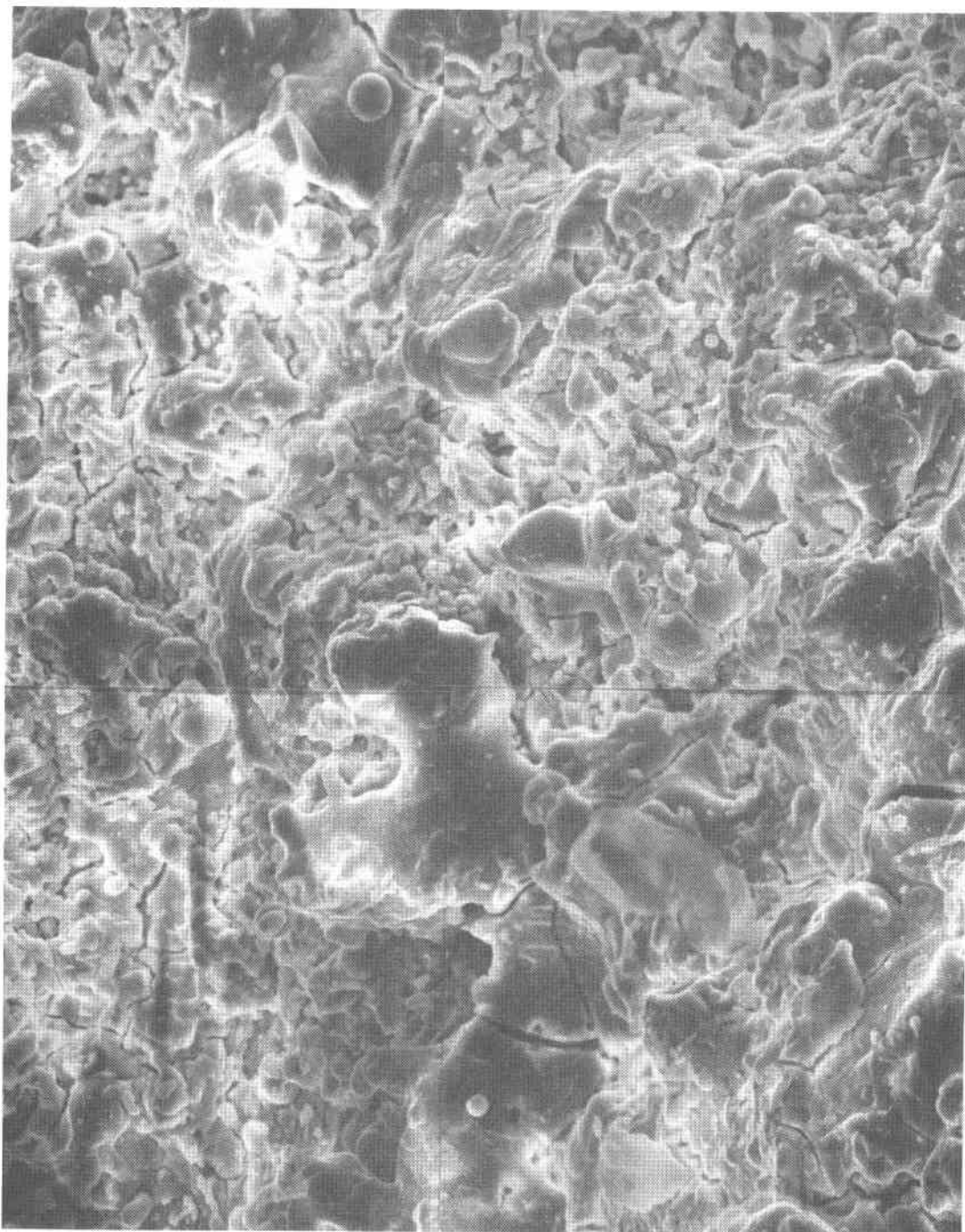



Figure 1A. Surface of MgO·ZrO<sub>2</sub> high density + microcracked coating, after 4 hour vacuum heat treatment at 1975<sup>o</sup>F. SEM. 5 microns: 

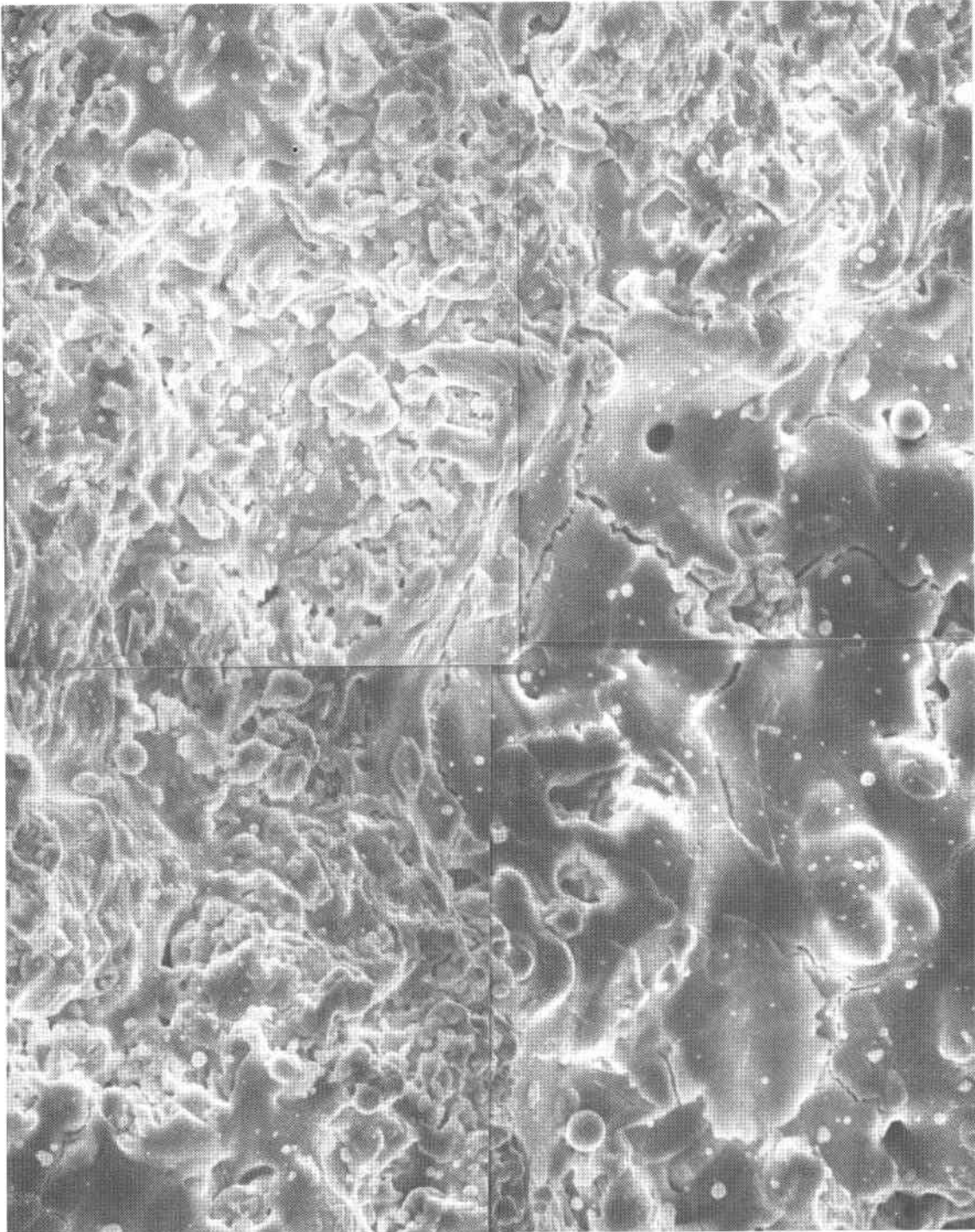


Figure 1B. Surface of  $ZrO_2-6.6Y_2O_3$  high density + microcracked coating, after 4 hour vacuum heat treatment at 1975<sup>o</sup>F. SEM.  
5 microns: —

## AVERAGE FAILURE CYCLES: THERMAL FATIGUE

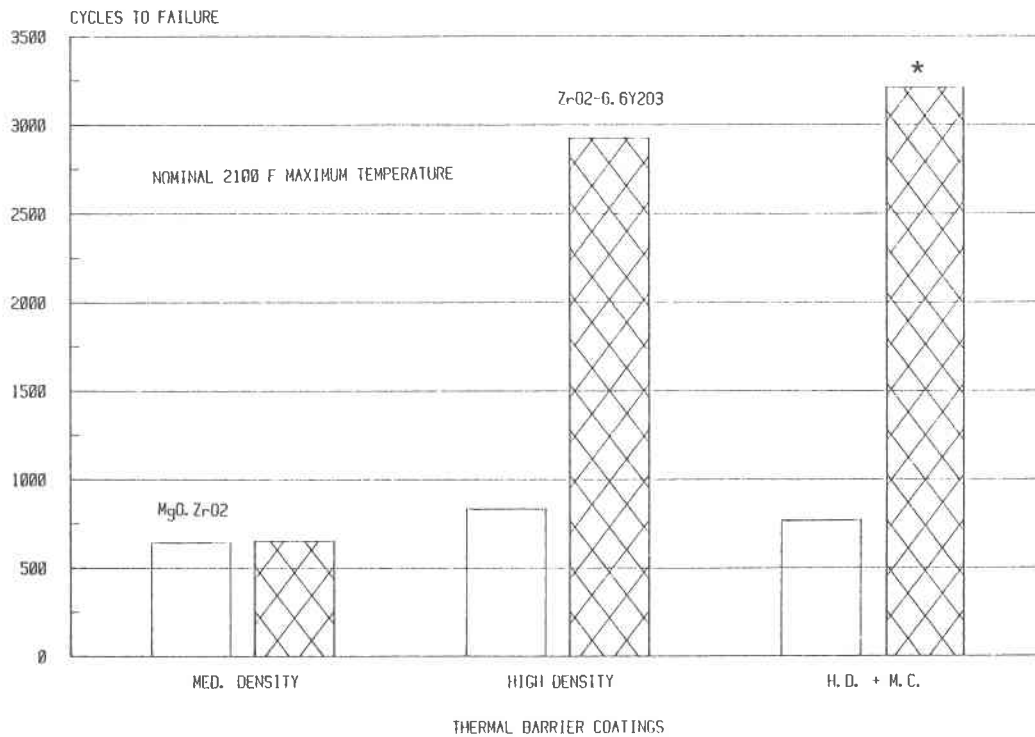
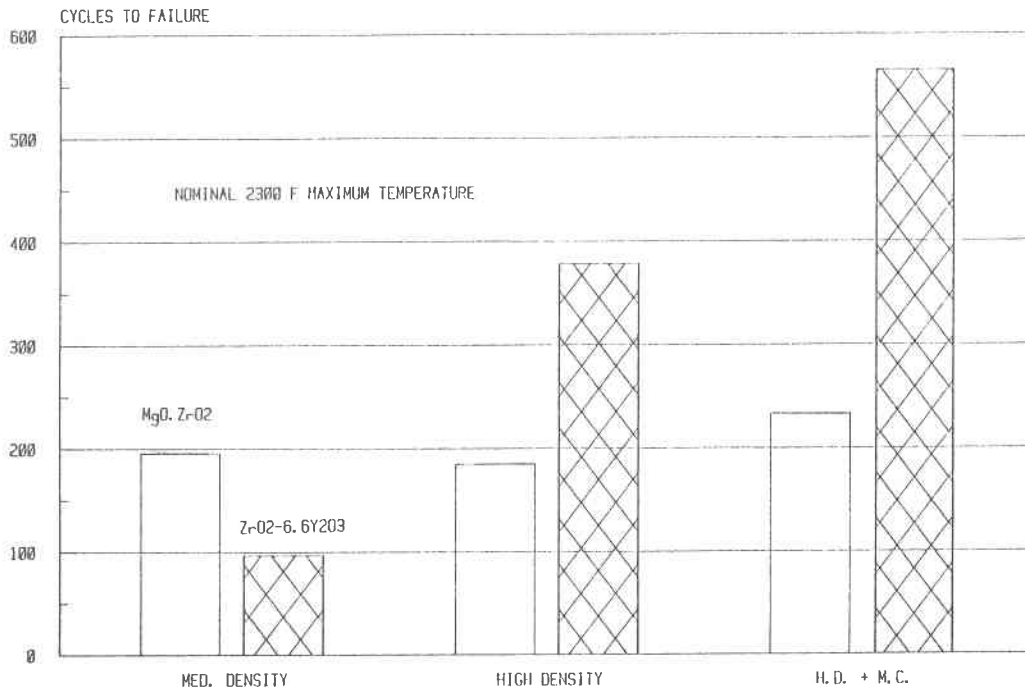


Figure 2. Cycles to failure results for the 2260<sup>o</sup>F thermal fatigue test (above) and for the 2100<sup>o</sup>F test (below). \*No failure at 3208 cycles.



ZrO<sub>2</sub>-6.6%Y<sub>2</sub>O<sub>3</sub> H. D. + M. C. THERMAL BARRIER

CYCLIC HOT CORROSION TEST

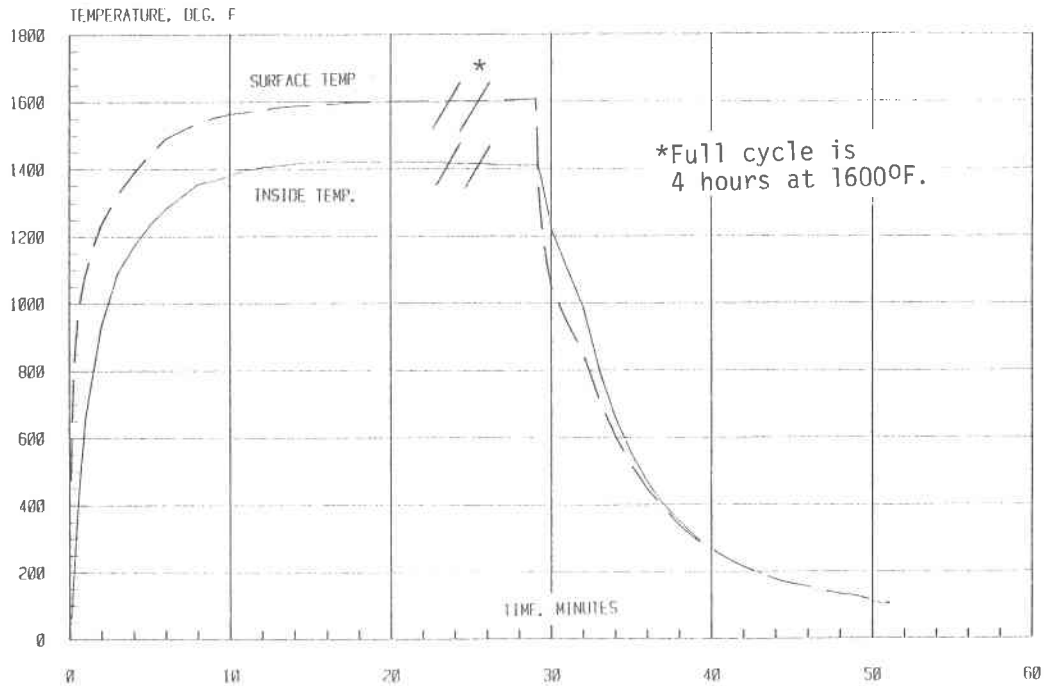


Figure 3. Heating and cooling temperatures for the cyclic corrosion test. Actual time at maximum temperature is 4 hours. Oxide surface and inside diameter substrate metal temperature by thermocouple measurement.

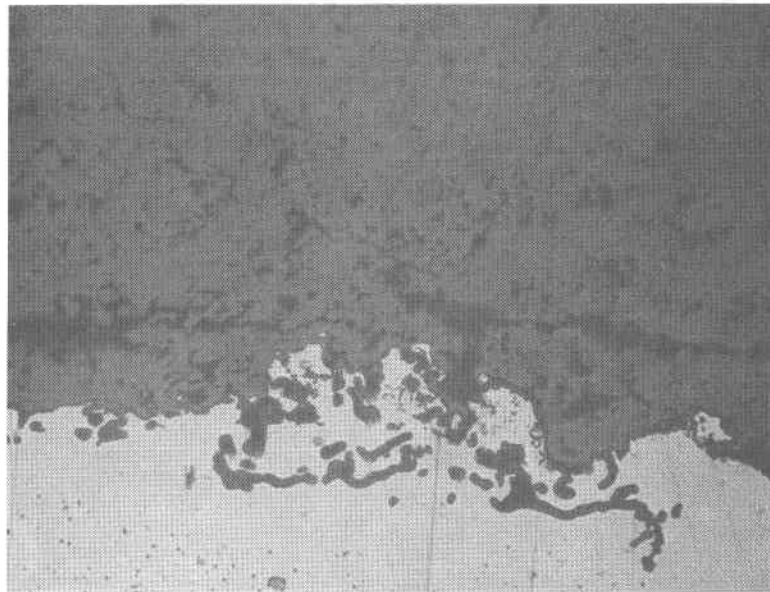


Figure 4. Polished cross-section of ZrO<sub>2</sub>-6.6Y<sub>2</sub>O<sub>3</sub> high density + microcracked thermal barrier, after 583 cycles of the 2260°F thermal fatigue test. 50 microns:  $\longleftarrow$

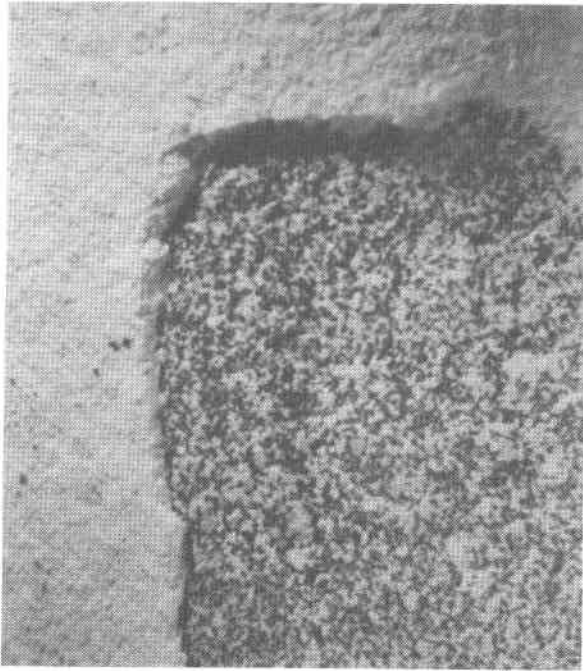



Figure 5. Spall zone of  $MgO \cdot ZrO_2$  HD + MC coating, failed after 250 cycles to  $2260^{\circ}F$ . Optical. 0.1 inch: 

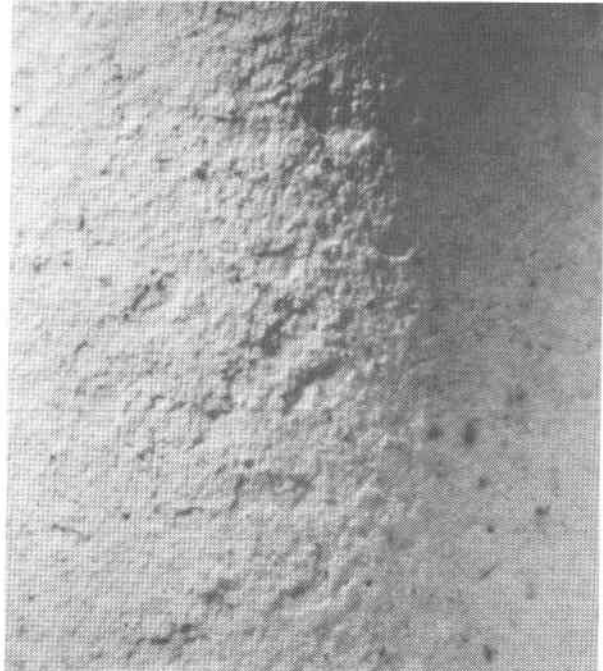



Figure 6. Spall zone of  $ZrO_2 - 6.6Y_2O_3$  HD coating, after 2924 cycles to  $2100^{\circ}F$ . Optical. 0.1 inch: 





Figure 7. Spall zone of  $ZrO_2 - 6.6Y_2O_3$  MD coating, failed after 99 cycles to  $2260^{\circ}F$ . SEM. 0.02 inch: 



Figure 8. Spall zone of  $ZrO_2 - 6.6Y_2O_3$  HD + MC coating, after 583 cycles to  $2260^{\circ}F$ . SEM. 0.1 inch: 

DEVELOPMENT OF ELECTRON BEAM  
PHYSICAL VAPOR DEPOSITION OF CERAMIC COATINGS

R.E. Demaray  
W.K. Halnan  
S. Shen  
Turbine Coating Group, Airco Temescal Division

## SUMMARY

Under subcontract to the Division of Fossil Fuel Utilization of the Department of Energy, the Turbine Coating Group of Airco Temescal Division has developed a dedicated e-beam physical vapor deposition (P.V.D.) ceramic coater furnace with enhanced capability for the production of ceramic coatings by reactive oxide deposition. This equipment, together with the associated process development, is reviewed. The results of physical metallography and process development are correlated. The influence of deposition cycle parameters on the columnar oxide morphology and, in particular, the attendant resistance of the thermal barrier coating to thermochemical aging, is related.

The desirability of ceramic thermal barrier coatings for application to turbine engine hot section components, particularly blades and vanes, has been widely discussed with respect to fuel energy conversion efficiency, i.e., combustion temperature elevation, and engine component lifetime. The requirements for such a coating are very demanding in materials properties and deposition process technology. Ceramic materials such as zirconia and alumina possess the necessary low thermal conductivity and high oxidation resistance relative to turbine blade superalloys. However, their relatively low coefficient of thermal expansion (C.T.E.), low ductility, and relatively poor erosion resistance militate against their ready application to turbine components. The difference in the respective C.T.E. values for the ceramic and alloy materials results in thermal cycle stress mis-match for one or both of the two extremes of the thermal cycle: tensile expansion stress or residual compression stress. Due to the much higher modulus of the ceramic material, it accrues the greater portion of the stress. This generally results in strain accommodation, and tensile or compressive damage to the oxide coating.

Progress toward the reconciliation of these conflicting thermal properties has been made with each of the three major coating processes: plasma spray, planar magnetron sputtering, and e-beam physical vapor deposition. The latter two methods produce a "columnar" ceramic morphology by an adatom line of sight shadowing mechanism. This structure has columnar boundaries that are macroscopic in size and normal or vertical to the substrate surface. This columnar structure continues to provide bench-

mark thermal cycle to failure standards in burner rig testing of "advanced" and "residual stress control" ceramic coatings due to its capacity to accommodate strain without catastrophic structural effects.

Both sputtering and P.V.D. are "adatom" deposition techniques, and they both produce columnar structured ceramic morphology. The higher deposition rates (i.e., power) and the small source distension (i.e., power density and imaging) of the e-beam process offer two advantages. One is commercially utilizable deposition rates. The other is optimization of the "shadowing" mechanism through the collimation that results from the small virtual source size, i.e., the smaller solid angle of the substrate that is subtended by the evaporant source. Other deposition parameters are also distinctively different.

Briefly, e-beam vacuum reduction of the ceramic zirconia feedstock produces a melt ( $T \geq 3500^{\circ}\text{C}$ ) and associated vapor that is reduced in oxygen stoichiometry. Consequently, oxygen partial pressure must be maintained during deposition to provide reactive re-oxidation of the vapor. In order to operate a high tension D.C. electron discharge gun, a large, 2-3 orders, partial pressure differential between the reactor portion of the furnace and the e-beam chamber is required and differential baffling and pumping arrangements must be arranged. The substrate surface temperature must be a function of the adatom flux to provide a matched rate of re-oxidation for the substoichiometric adatom vapor. The e-beam emission current (power) is tied to both the adatom flux and the source radiation distribution. Unlike MCrAlY evaporation, ceramic feedstock insulates the water cooled, bottom-fed crucible. This results in re-radiation of a very large fraction, perhaps 80-90 percent, of the e-beam incident energy of approximately 30 kilowatts. In steady state, useful evaporation rates accompany substrate oxide surface deposition temperatures of more than  $1500^{\circ}\text{F}$  for an eight-inch source to substrate distance with no additional over-source heating. Surface deposition temperatures of  $2100^{\circ}\text{F}$  to  $2300^{\circ}\text{F}$ , i.e., in service combustion temperatures, require that additional heating be available on a multiple-loop feedback basis with e-beam emission current, i.e., evaporation rate, oxygen mass flow, and oxide surface temperature.

In this highly coupled system, two contradictory deposition process objectives must be met: reproducibility and stability, on the one hand, and process variability, i.e., flexible process variation from sample to sample, on the other. The computer control of the process accomplishes both these criteria in an intensive data acquisition, i.e., parameter documentation, environment. The completed ceramic coater has unique capabilities for specimen production variation and reproducibility.

Interrupt-driven process control, multichannel data logging, and data formatting techniques are utilized.

Initial process design strategy aims at two objectives. One is residual stress control by production of an optimized columnar ceramic coating morphology. The second is columnar basal adhesion and resistance to oxidation-related adhesion failure. This is accomplished through optimization of bond coat, surface pretreatment, and process control of the early stages of deposition.

## Section 1

### INTRODUCTION

The desirability of "ceramic thermal barrier coatings" for use with turbine engine hot section components has been widely discussed (1-4, 6). With respect to fuel energy conversion efficiency and engine durability, the advantages of an oxidation-resistant, durable, thermal barrier coating that would provide temperature differential between the combustion zone surface and the turbine components of the order of several hundred degrees Fahrenheit, is widely- and well-appreciated (1,6). However, the application of the most promising yttrium stabilized zirconia to nickel-based superalloy and MCrAlY coated components has resulted in coatings of less than acceptable thermal cycle durability having uncertain oxidation properties (2,6).

Three major coating processes have been used to produce zirconia thermal barrier coatings: plasma spray, planar magnetron sputtering, and e-beam physical vapor deposition. The latter two methods produce a "segmented" or "columnar" ceramic by an "adatom," line-of-sight, shadowing mechanism enhancement of the tendency of ceramic materials of high melting points to form leadered growth structures when deposited from the vapor phase. This structure has cylindrical columnar boundaries that are macroscopic in size and normal to the substrate surface; see Figure 20. The substrate surface temperature must be matched to the adatom flux to provide a matched rate of "reactive" re-oxidation at the accumulating adatom flux. The e-beam emission current is tied to both the adatom flux as well as the source radiation distribution and flux. Unlike MCrAlY evaporation, ceramic feedstock insulates the water-cooled, bottom-fed crucible, resulting in re-radiation of a very large fraction, perhaps 90 percent, of the e-beam incident energy which is on the order of 30 kilowatts. In steady state, useful evaporation rates accompany substrate oxide surface deposition temperatures of more than 1500°F for an eight-inch source to substrate distance. Surface deposition temperatures of 2100 to 2300°F, i.e., in service combustion temperatures, require that additional heating capability be available on a multiple loop feedback basis with the emission current, the oxygen mass flow (partial pressure), and the oxide surface temperature.

In this highly coupled system, two contradictory process objectives must be met: reproducibility and stability on the one hand, and process variation from sample to sample on the other. The computer control of the process accomplishes both these criteria in an intensive data acquisition, i.e., documentation, environment. As discussed below, the completed coater has unique capabilities for ceramic thermal barrier specimen variation and reproducibility.



## Section 2

### INSTRUMENTAL CONSIDERATIONS AND APPARATUS

Baffling for the stagnation of  $O_2$  feed gas surrounds the furnace hot section, water-cooled baffles. A first burnthrough plate in the vertical wall of this baffle connects this "reactor" region to a "discharge separation" region. The discharge region is pumped by a 20-inch diffusion pump. A second burnthrough plate in the horizontal floor of the discharge region allows the e-beam 270 degrees curvature access from the gun chamber below, i.e., over the horizon. The gun chamber is differentially pumped by a separate 10-inch diffusion pump. This allows the e-beam gun to operate at  $5 \times 10^{-5}$  torr while the reactor baffled region above the crucible can be maintained at 1 to 100 microns  $O_2$  partial pressure. A mass flow of approximately 200 SCCM of  $O_2$  produces  $2\mu$  reactor pressure and  $1 \times 10^{-5}$  torr e-beam gun chamber pressure. The two chambers have upleak rates of .01 to .02 microns per minute. Terminal pressures of  $5 \times 10^{-7}$  torr after bakeout are obtained.

The electron beam gun and main magnet assembly were assembled and rebuilt from production components. The spacing of the gun and crucible in the small vacuum chamber required that the e-beam trajectory radius be less than eight inches. The resulting beam parameters, radius, current distribution (focus), and momentum, produce a collimated one-inch diameter power distribution. This distribution yields a dark, shiny metallic "semioxide" zirconia reduction, melt condition of several millimeters depth; see Figure 14. Outgassing begins at approximately 800 milliamps, 30 kV. Samples have been coated for thirty minutes at values of emission current between 800 and 1200 milliamps, resulting in coating deposition thickness of from .002 inches to .015 inches. Power above 1500 milliamps without sweeping or diffusing the power distribution results in superheating of the submerged superoxide and "spitting" of the semioxide melt. The oxidation stoichiometry of the semioxide is unknown. However, it should be emphasized that when cooled, it is a conductor, supporting point contact impedances as low as several kilo-ohms. "Per-square" impedance measurements are under way. Under oxygen bleed, the recrystallization of the semioxide incorporated deep, clear, translucent sections in the glossy dark, evanescent semioxide seen in Figures 14 and 15.

An oversource heater assembly utilizes a 60 kW power supply and water-cooled high-amp feedthroughs. The eight heating elements subtend three sides of the crucible over-cube, passing perpendicularly three inches above the sample rotation height of eight inches. The inner radiation shield, the water-cooled copper shield, a suspended "ersatz" substrate thermal mass, and the horizontal baffle plate upon which the oversource, baffle assembly sits, are instrumented with K-type thermocouples. In addition, a K-type thermocouple, with a rotational feedthrough, is fixtured through the center of the water-cooled feedshaft into the rotating sample substrate.

A residual gas analysis (RGA) unit has been rebuilt and added to the system by the Turbine Coating Maintenance Department to monitor the mass spectra of the residual gas components. System operation for sample coating requires a ratio of 3:1 for indicated  $H_2O:N_2$  content. The C-100 UTI, RGA unit is differentially pumped by a Veeco MS90 leak detector through choke flow tubeulation and samples the upper chamber "reactor section." Computer remote scan and data logging of the residual gas mass spectra before and during coating is plotted for each sample before (Figure 11) and after (Figure 12). Peak heights are available in virtual file form to the process control software.

Two units make up the system software control system. One is an instrument controller, which has a broad range of signal handling capabilities and data transfer types; it supports stored program execution. The other is a host computer that supports an independent processor and touch-sensitive paging of software utilities. This functions are foreground and acts to provide interrupt-driven processing (8). The background program is stored as data statements at the beginning of the foreground program.

Process variation is achieved by modification of the foreground program using Basic Editor utilities. The basic program is then put in core image form by a Fortran-like compiler for high-speed execution. When the foreground program is loaded from memory at system power-on, the background program data statements are transferred over the connecting IEEE-488 bus and the background program is "downloaded" to the control link. Input channels are defined as temperature, voltage, or status input and their units and thermocouple type are defined, together with A to D sample rates and autorange conditions. The foreground program requests such information as the coat cycletime lengths, delays, preheat steady state or ramps, and e-beam emission current profile from the operator in a friendly way. It asks whether virtual process parameter data arrays should be created and what the part number and history are. It checks status for vacuum map and high voltage interlock relays; several

CRT pages of conditions must be sequentially set or executed. It then initiates the part shaft-feed procedure. In each case, the operator must respond by touching the appropriate software-labeled key on the touch-sensitive computer CRT screen. The foreground and background clocks are set. There is a cycle parameter download handshake. The foreground system implements a "BEGIN" bus command.

As the coat cycle progresses, the background program scans and linearizes the analog channel inputs and stores them in its memory. It checks the cycle time conditions and executes a remote interrupt bus command to the foreground computer. The foreground program handshakes and requests the data array using the high-speed 25 megabyte synchronous talk-listen bus mode. It then updates the analog input screen display page with the present input values: four (4) temperatures, two (2) ionization gauges, and two (2) thermocouple pressures, the e-beam emission current, the cycle time, and cumulative cycle (coat) time. It also displays the value of the current subscript index of the virtual arrays if data logging is proceeding. Analog sample times for any one channel are on the order of three (3) seconds for refresh. Array reaggregation and asynchronous transfer development has achieved a high degree of foreground transparency to the background process control tasks such as scanning the RGA or providing feedback to the e-beam filament supply controller. Analog output control of the emission current or remote monitoring of the residual gas analyzer does not add extra time to the cycle due to the relatively high speed of stored program execution relative to the scan or bus transfer times.

Data recording proceeds for 512 cycles of approximately six seconds each, or about one hour, 3600 seconds. Virtual files of four to eight arrays are recorded. Each array contains 512 eight (8) byte, floating point variables. Each production part is documented by these arrays in 17-block production records. One mini floppy disc can contain the records of four (4) sample runs.

At the end of each coating production cycle, the files are accessed by a graphics utility foreground program that reads the files and controls the printer-plotter, also on the IEEE-488 bus, to plot the multi-channel plots that accompany the parts production reports. See Figures 1-6 and 9.

Section 3  
CERAMIC COATING PROCESS DEVELOPMENT

A number of separate process control issues must be addressed and brought into balance in order to reactively deposit physical vapor produced by electron-beam evaporation of ceramic feedstock.

Perhaps the most critical is the electron beam emission current, as discussed above. Figure 1 shows the correlation of a number of process parameters that are plotted in color against similar color ordinate scales in the original documentation graphics. Each of the small ticks on the independent axis corresponds to one minute. The axis is labeled in seconds up to one hour, 3600 seconds. The graph that rises from the abscissa at six minutes represents the electron beam emission current against the left-hand ordinate, 2 amps full scale. The sawtooth relaxation behavior is a result of changing filament surface condition. The emission current is developed by changing the temperature of the tungsten electron gun filament. Figure 1, Graph 023, represents the best ramp and hold behavior that can be obtained by manual operation of the filament D.C. power supply (9). At constant filament current (9), and therefore constant filament temperature, the changing oxidation state of the filament in the reactive ceramic application yields a decrease in thermionic emission from the initial value. This "droop" relaxation and associated longer-term D.C. drift can be seen from about 17 minutes to 47 minutes. The inverted spikes in the trace represent two arcs of the e-beam gun assembly. Two operator interventions adjust the emission current at 25 and 43 minutes, each by about 100 milliamps, to recover evaporation rate.

The significance of this drift in evaporation rate can be appreciated given that the total useful range of evaporation begins at about 1.000 amps and ends at about 1.300 amps, i.e., the manual mode instrument stability was initially something like half the dynamic process range. Also note the graph just above the emission current: it is the rotating substrate temperature and corresponds to the right-hand ordinate in degrees Fahrenheit. Note the 150°F drift in the substrate bulk temperature associated with the source re-radiation of the drifting e-beam energy.

Figure 2, Graph 028, represents the first trial of a computer-driven analog feedback loop designed to modulate the e-beam gun filament supply so as to obtain constant output current in the presence of changing filament surface state. The computer provides an analog output voltage that is phased for wait, ramp, hold, and cease portions of the coat cycle. Figure 3, Graph 029 shows a reproducible ramp and a D.C. hold emission current of  $1.109 \pm .003$  amps over the 25-minute coat cycle. Note the upper curve, reactor chamber pressure with a constant 170 sccm  $O_2$  mass flow, against the semilog ordinate,  $\sim 9 \times 10^{-4}$  torr. Outgassing and melting of the ceramic feedstock begins at about .850 amps e-beam ramp current. Also note the relative thermal stability of the rotating substrate temperature against the far right-hand ordinate, in °F, under the influence of the constant source re-radiation from the stabilized e-beam current. Figure 3 represents the temperature, evaporation rate, and  $O_2$  partial pressure conditions of the middle ground of the initial process parameter space.

Ceramic feedstock "conditioning," i.e., premelting, prior to coating reduces outgassing and the associated arcing behavior of the emission current observed in Figures 1-5. See Figure 8, the graph for Part No. 035. Part No. 035 is shown in Figure 16, as parted for metallurgical examination. Note the stabilized parameters in Figure 8. Also note the substrate temperature quench rate against the right-hand side ordinate. This part was produced with 300 sccm  $O_2$  mass flow. The ceramic coating deposited was approximately .004 inches thick and the weight gain was 1.01 grams. An SEM of the coating at the diamond saw parting face, the free basal substrate plane, and the "cauliflower" surface of the columnar field are shown for Part No. 035 in Figure 16.

Figure 16 also shows two interesting variants of the columnar morphology in the lower right frame. This is the ceramic interface region. Approximately one-micron layers cross the columnar structure at right angles. A divergent non-columnar "bush" structure can also be seen on the right. Surface contamination is thought to account for the bush-like structures.

The cross-hatched structure can be seen more clearly in Figures 17 and 18, SEM photographs of Part No. 042.

A comparison of Figure 7, showing the cross-hatched or "beaded" columns, with the process data graph for the same part (Figure 8), shows that the beads persist long after the temperature has equilibrated. Figure 9 shows a preheat pulse preceding ceramic evaporation. This process variation of initial substrate temperature left

the beaded structure intact. Rotational frequency can be seen to play a part in the number of beaded layers. At 6 Hz for 30 minutes, the number of layers indicates that the layers correspond to single rotational depositions. Varying the rotational frequency results in a change in the beaded layer thickness. Rotational speeds above 15 Hz result in the structure shown in Figures 19 and 20 for Part No. 054. It is clear that the epi-interfacial ceramic structure is fully columnar.

A bootstrap matrix of surface process variations, reactive processing parameters, and substrate cooling variants has been produced and shipped for burner-rig evaluation by NASA Lewis.

A deposition model accounting for the beaded structure has been developed and is in the process of experimental confirmation. Optical remote sensing of the nascent surface, in deposition, as a potential rate feedback parameter is planned.

Initial quantitative Bragg diffraction showing exclusive face-centered cubic lattice type for both melted and quench source material, as well as the deposited coating for 8-10 w/o  $Y_2O_3 \cdot ZrO_2$  feedstock, in agreement with the results for e-beam PVC ceramic coatings cited in Ref. (7). See the x-ray diffraction  $2\theta$  spectra for the sub-stoichiometric pool material (Figure 21), and see Figure 22 for the as-deposited blade. Note the orientation enhancement of the  $(h,k,l) = (0,0,2)$  and  $(h,k,l) = (0,0,4)$  peaks over the source material. This may indicate substantial cubic micro-crystalline orientation within the larger columnar morphology.

## Section 4

### REFERENCES

1. E.S. Lassow and D.L. Ruckle. Program for Development of Strain Tolerant Thermal Barrier Coating Systems. Second Quarterly Progress Report, January 1, 1981 to March 31, 1981. Prep NASA Contract NAS3-22548, Pratt & Whitney Aircraft Group Report PWA-5777-6.
2. I.E. Sumner and D. Ruckle. Development of Improved Durability Plasma Sprayed Ceramic Coatings for Gas Turbine Engines. AIAA/SAE/ASME 16th Joint Propulsion Conference 1980. NASA Lewis Research Center, Pratt & Whitney Aircraft, East Hartford, Connecticut.
3. M.A. Gedwill. Burner Rig Evaluation of Thermal Barrier Coating Systems for Nickel-Based Alloys. U.S. Department of Energy Report DOE/NASA/2593-26, NASA TM-81684.
4. R. Busch. Develop Sputter Deposited, Graded Metal-ZrO<sub>2</sub> Coating Technology for Application to Turbine Hot Section Components. Periodic Tech Report, November 1975 to September 1976, Naval Sea Systems Command Contract #N00024-75-C-4333, Battelle Pacific Northwest Laboratories.
5. Dr. J. Patten. Personal communication. Battelle Pacific Northwest Laboratories.
6. P. Valentine and R.D. Maier. Microstructure and Mechanical Properties of Bulk and Plasma-Sprayed Y<sub>2</sub>O<sub>3</sub>-Partially Stabilized Zirconia. NASA Contractor Report T65126. August 1980.
7. N.P. Anderson and D.L. Ruckle. Program for Development of Strain Tolerant Thermal Barrier Coating Systems. Third Quarterly Report, NASA Lewis Research Center, Contract NAS3-22548. August 1981.
8. John Fluke Mfg. Instrument Controller Model 1720A and Measurement and Control Link Model 2400A.
9. Standard high power, constant-voltage electron beam (30 kilovolts, 0-6 amps) metallurgical evaporation equipment of the type associated with vacuum deposition of the MCrAlY type alloys utilizes constant demand set filament current to achieve constant thermoionic emissions, i.e., beam current.

WESTINGHOUSE PART # 023

SLIDE NO. 23

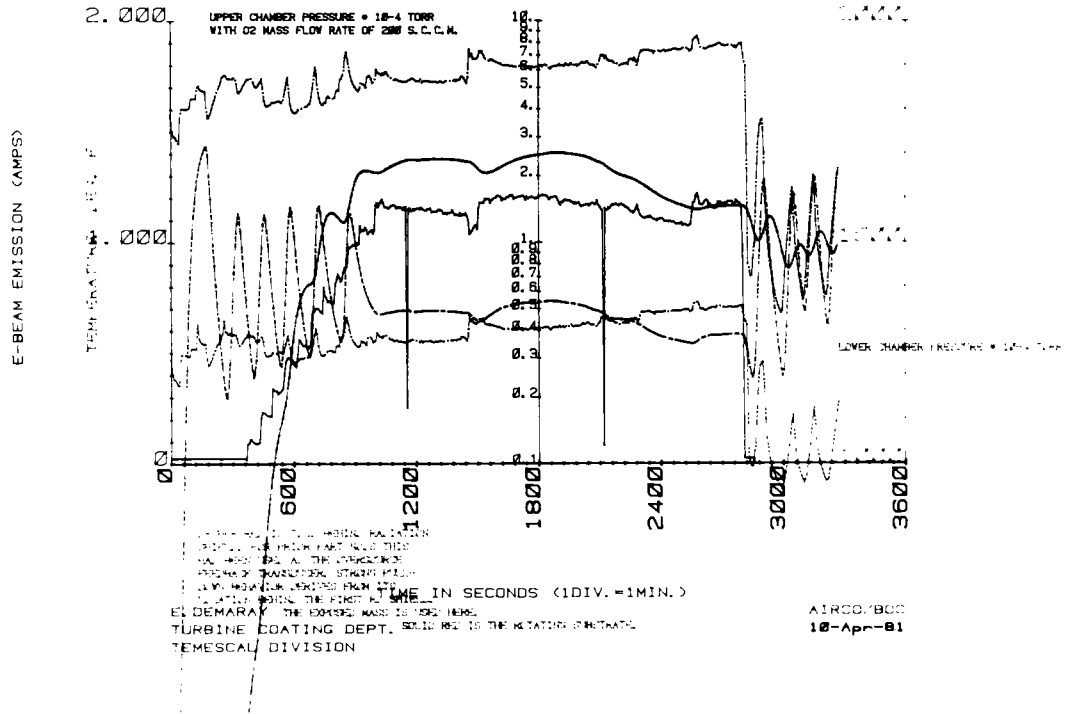


Figure 1. Best case response curve for manual operation of e-beam ramp and hold coat cycle third trace from top.



WESTINGHOUSE PART #028

SLIDE NO. 28

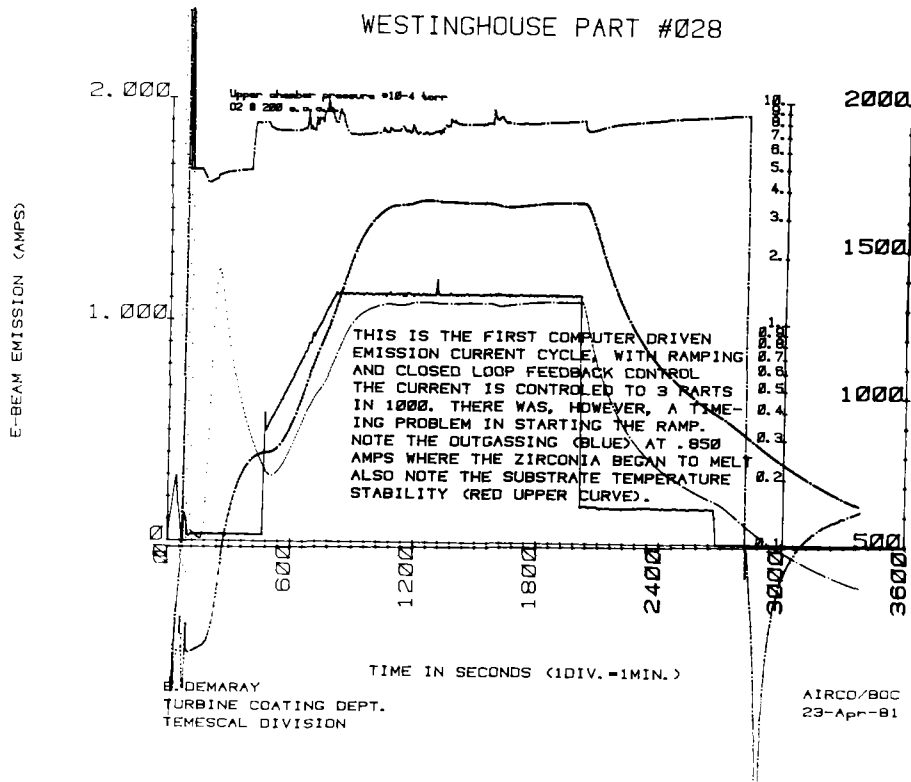


Figure 2. First computer-driven coat cycle. Note ramp begins when new filament supply switch placed in "auto" mode half-way through ramp.

Westinghouse Part #029

SLIDE NO. 29

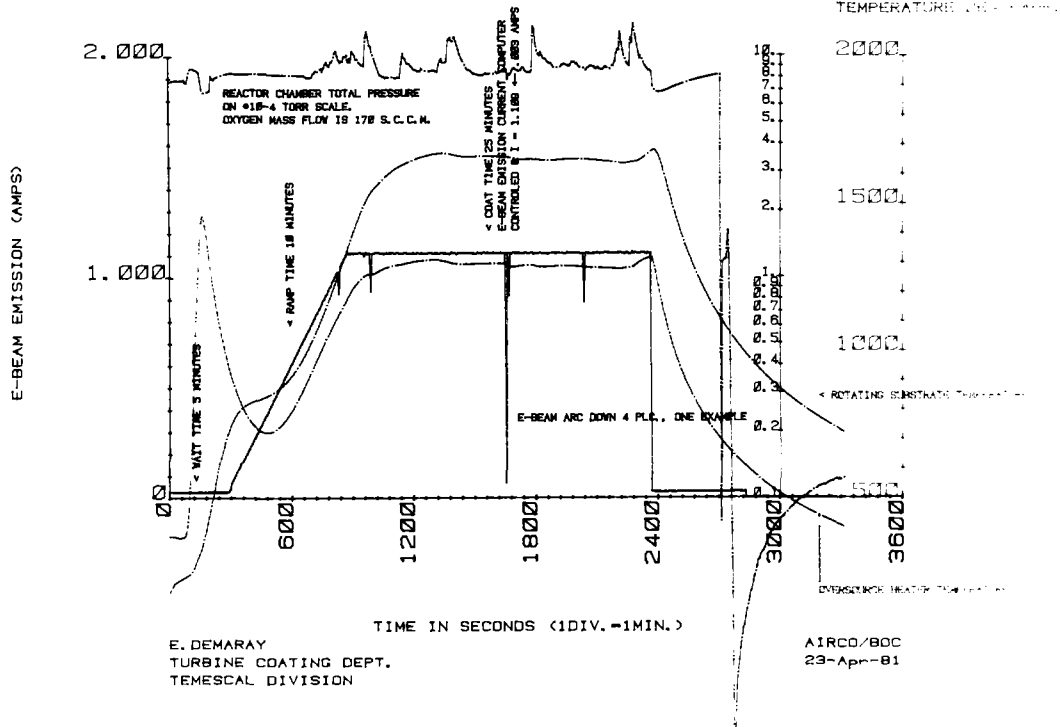


Figure 3. Reactive coat cycle with pre-heat pulse and feed-back stabilized emission current. Melting, deposition, and outgassing onset simultaneously. 10-minute ramp.

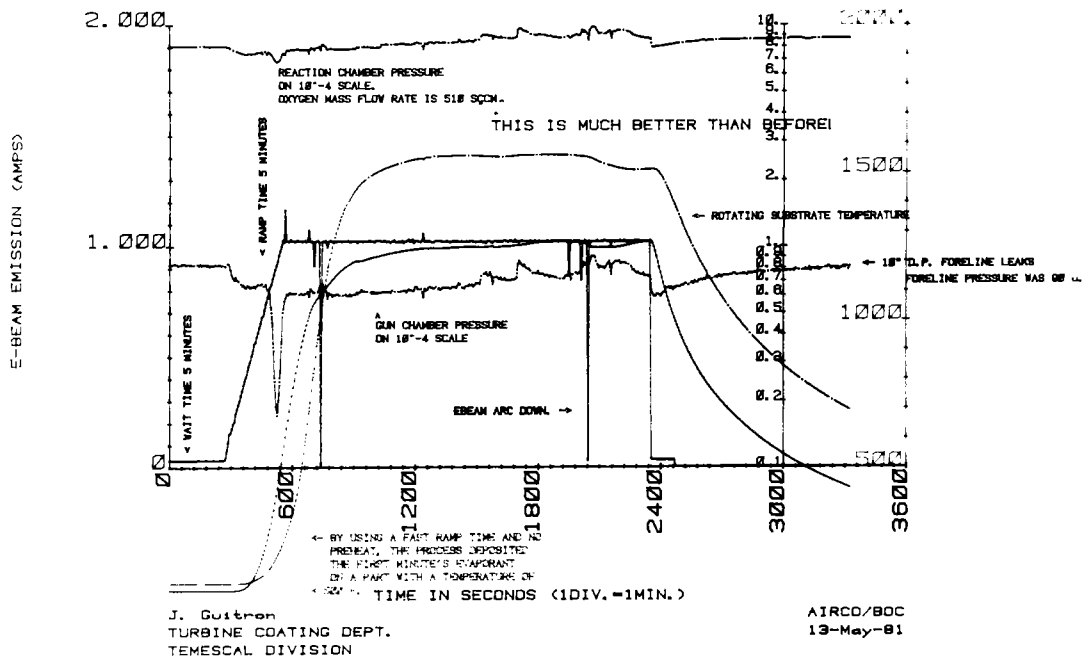


Figure 4. 5-minute ramp without pre-heating provides lower initial deposition temperature.

Westinghouse Part # 031

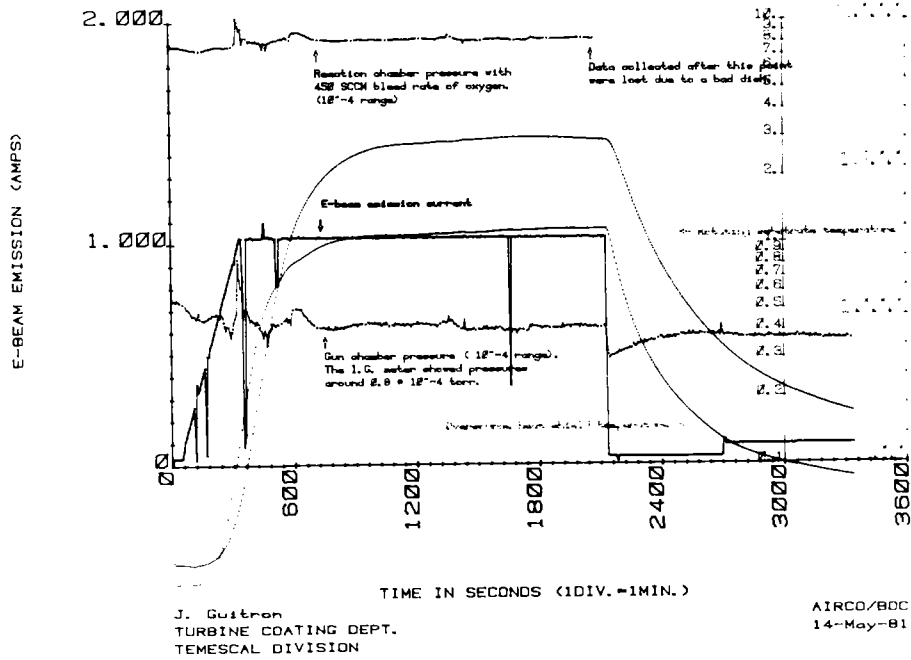


Figure 5. Arcing behavior due to un-preconditioned ceramic feedstock causes stoichiometry "shock" layering similar to beaded structure.

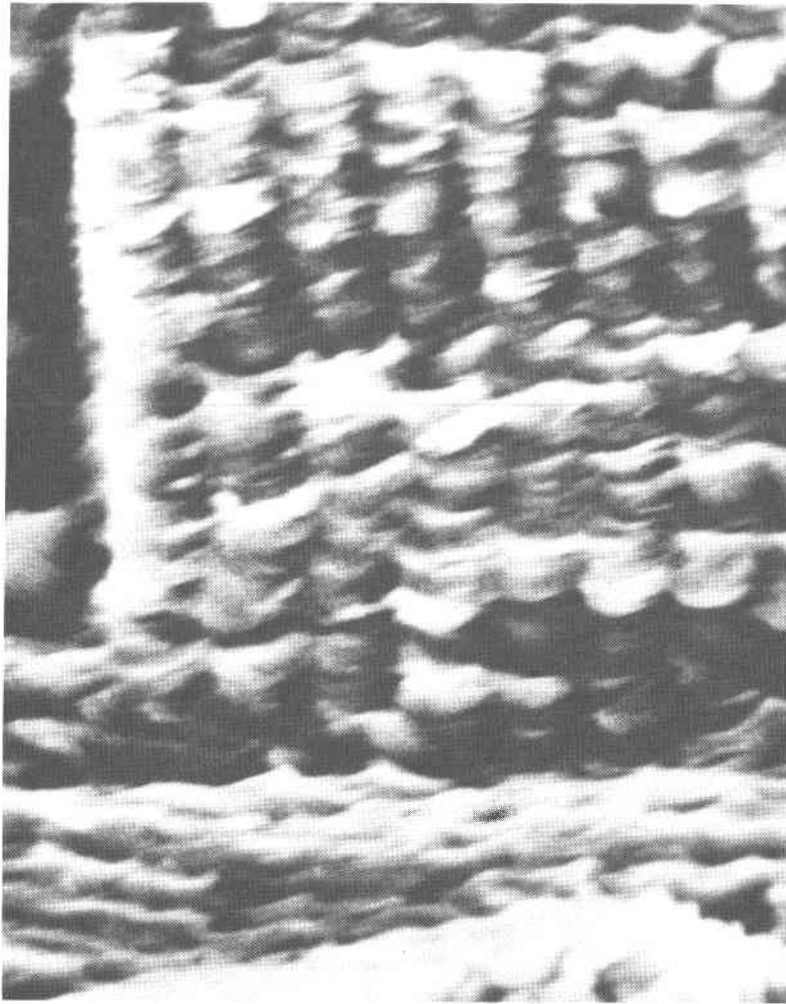


Figure 7. SEM, Part No. 032, 5000X\*. Note "beaded" structure.

\*Please note that the illustration(s) on this page has been reduced 10% in printing.

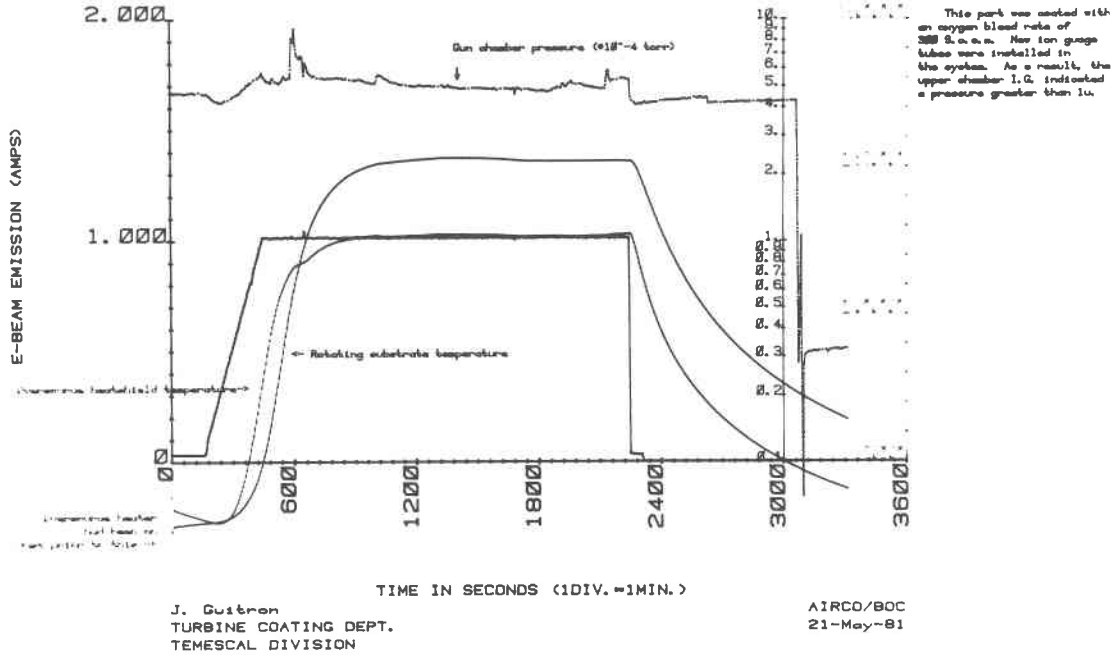


Figure 8. Graph for Part No. 035. Typical outgassing of conditioned feedstock with 300 sccm O<sub>2</sub> mass flow. Correlate with SEM and x-ray data for Part No. 035.

NASA THICK CYLINDER #67 (0, 1)

SLIDE NO. 67

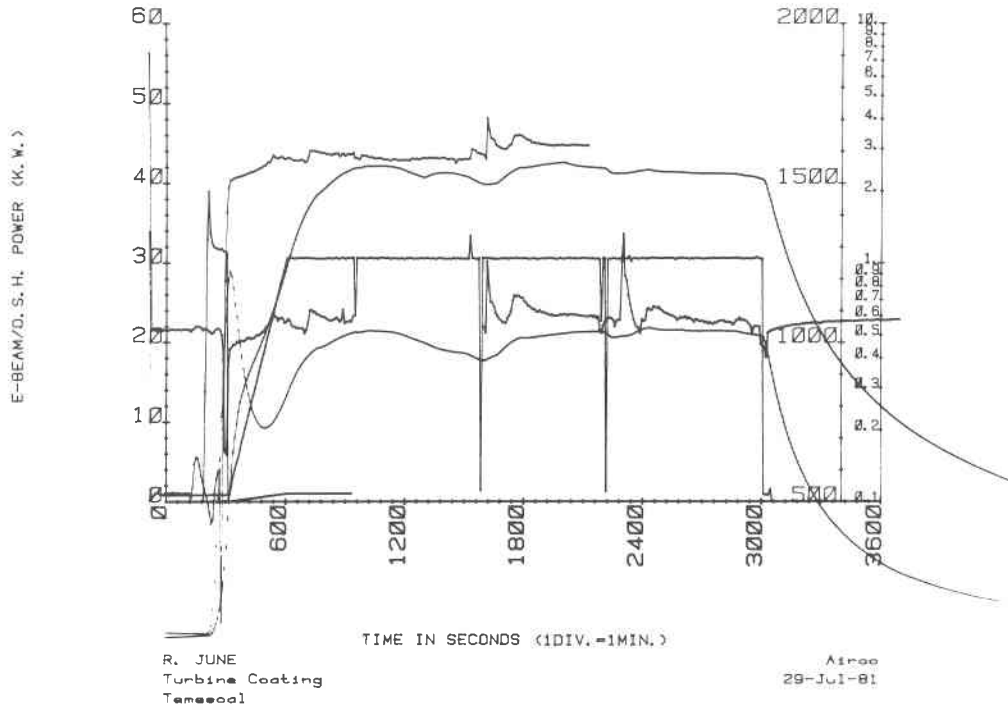


Figure 9. Graph for Part No. 067. Energy ordinate scale converted to kilo-joules for both e-beam and oversource enthalpy input traces.

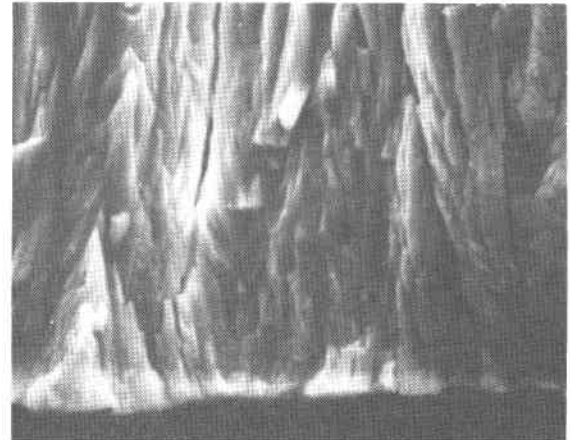
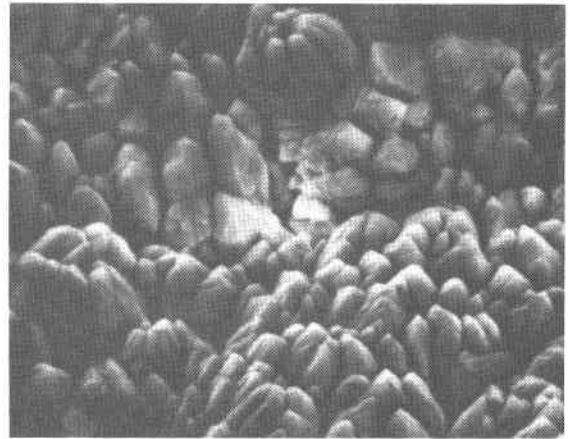


Figure 10. SEM at High Rotational Velocity,  $\omega \approx 15$



# RESIDUAL GAS ANALYSIS

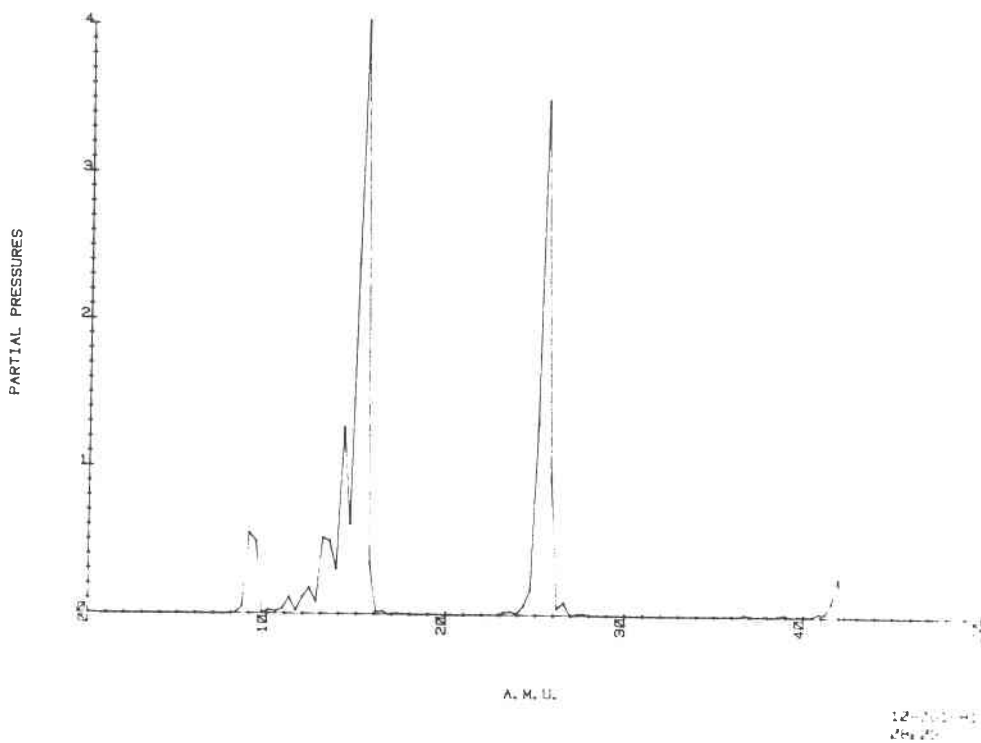


Figure 11. Computer-driven and data logged RGA of vacuum environment before coat cycle.

# RESIDUAL GAS ANALYSIS

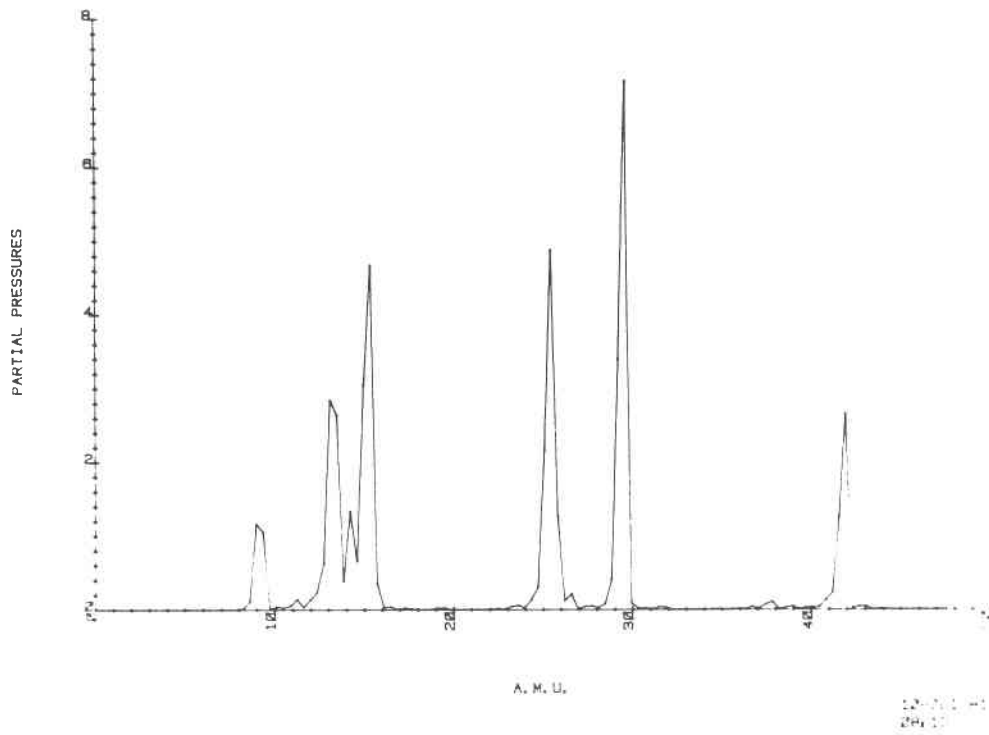


Figure 12. RGA vacuum environment during coating. Note  $O_2$  presence and hydrocarbon fragmentation pattern below  $amu=17$ .

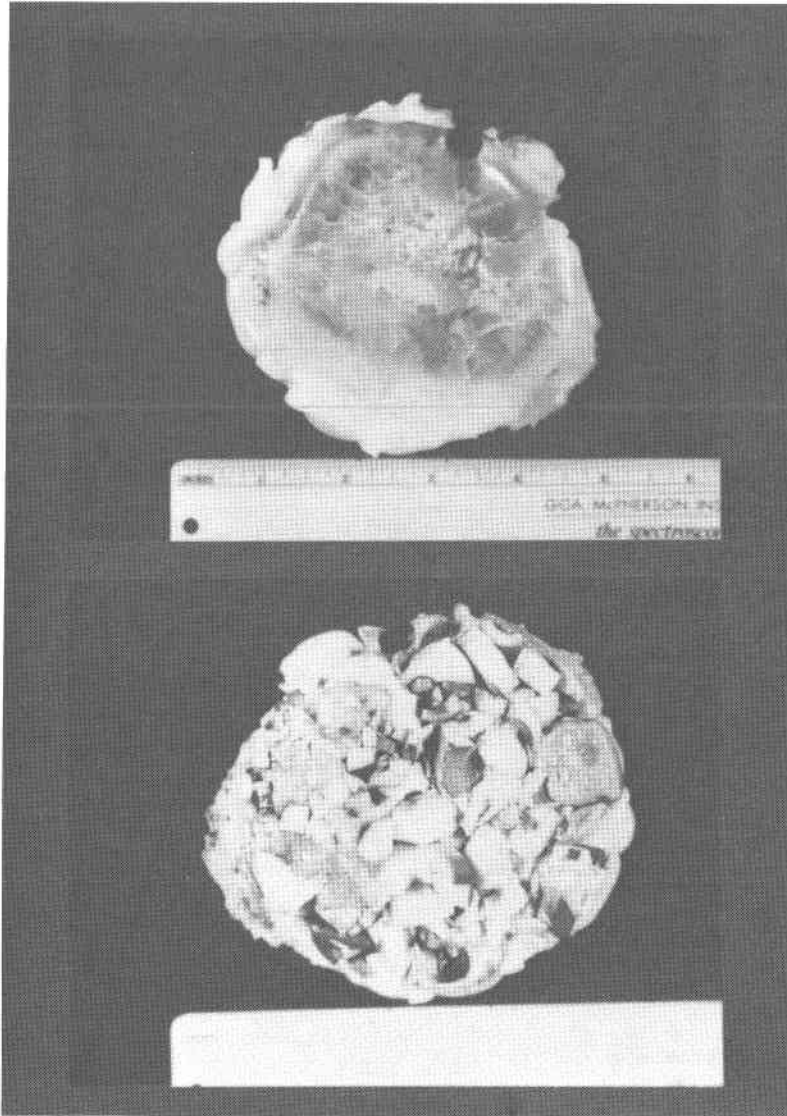


Figure 13. Al<sub>2</sub>O<sub>3</sub> e-beam Melted Source Material using Low Frequency x-y sweep.

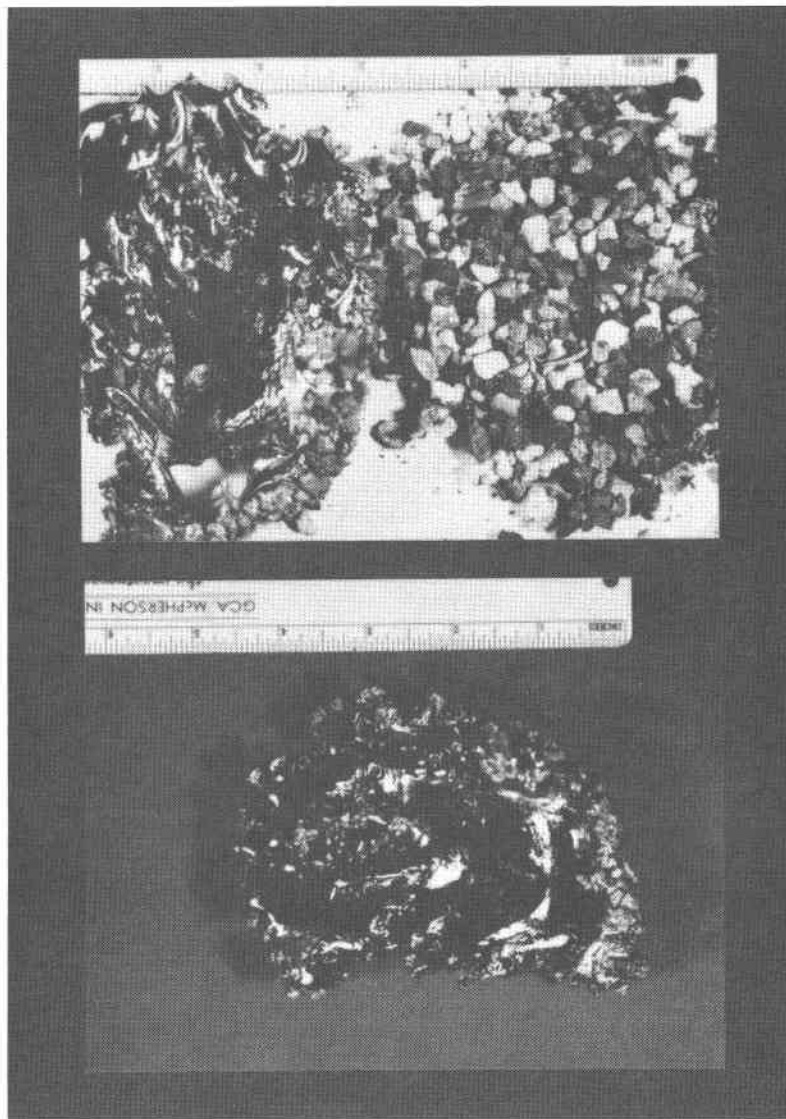


Figure 14.  $Y_2O_3.ZrO_2$  e-beam Melted Source Material using Low Frequency x-y Sweep.

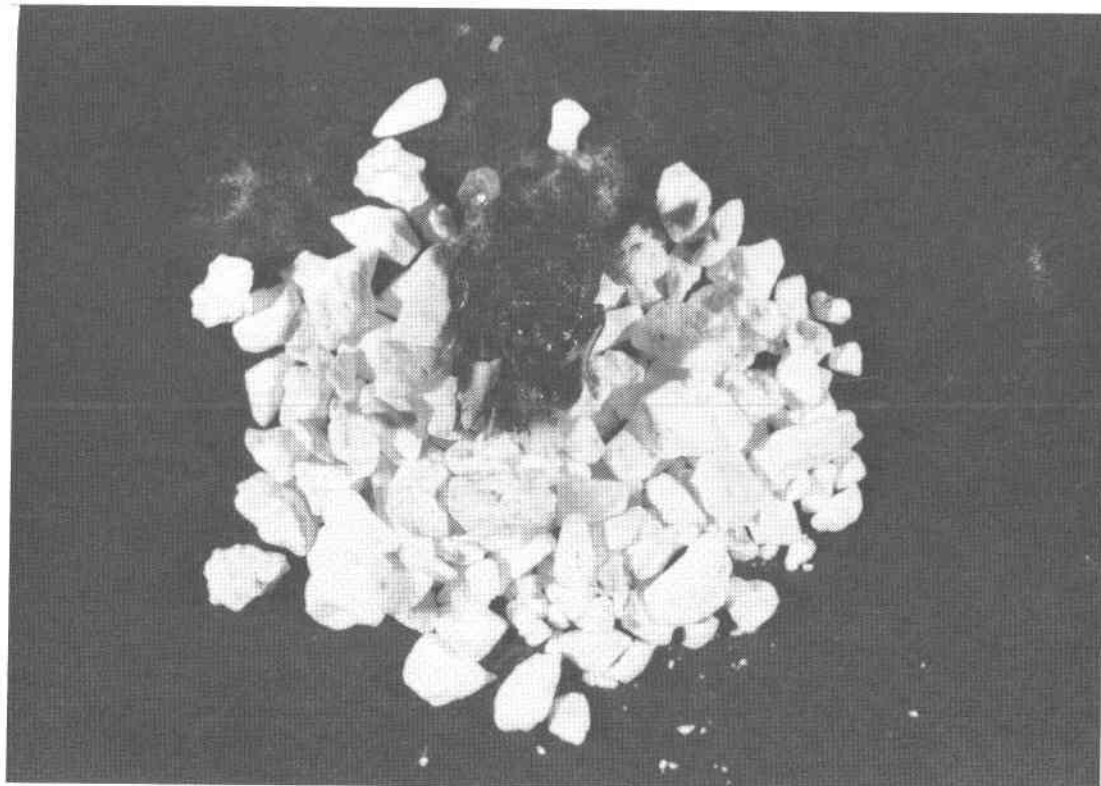


Figure 15. Recrystallized 10 w/o  $Y_2O_3.ZrO_2$  below glassy, substoichiometric evaporant melt, on as-received feedstock.

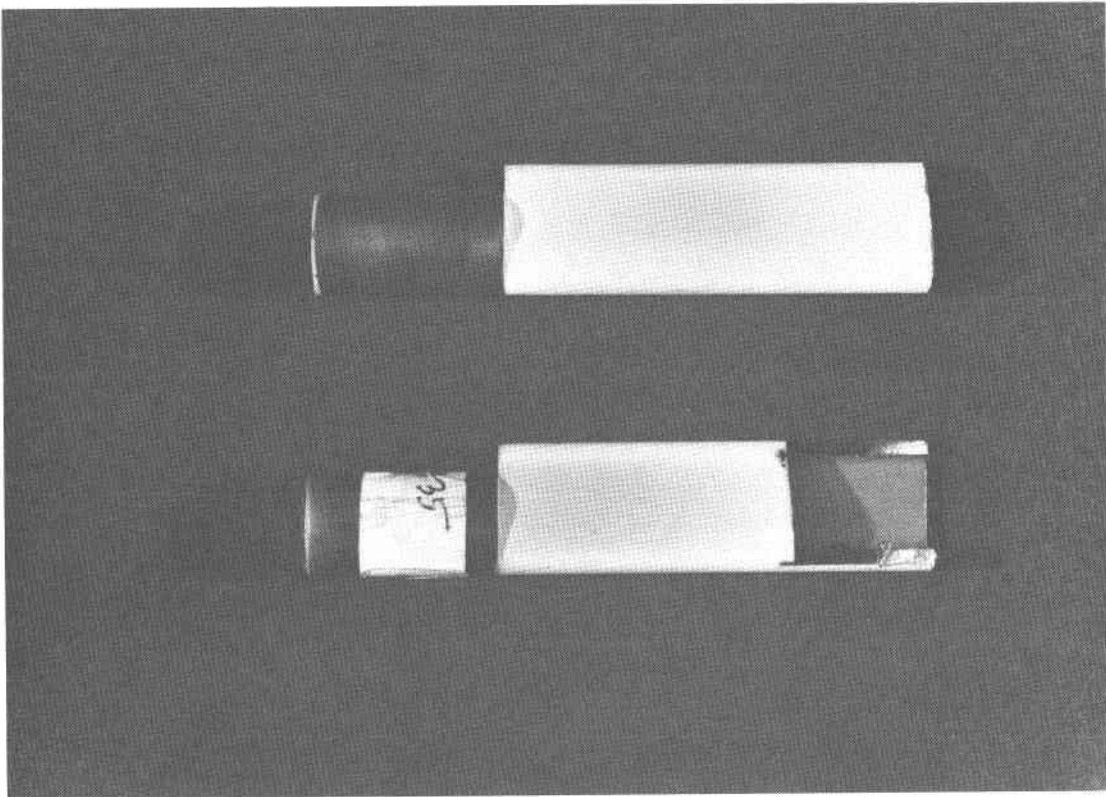


Figure 16. Part No. 035, SEM, and Part No. 035 as parted by diamond saw for metallography.

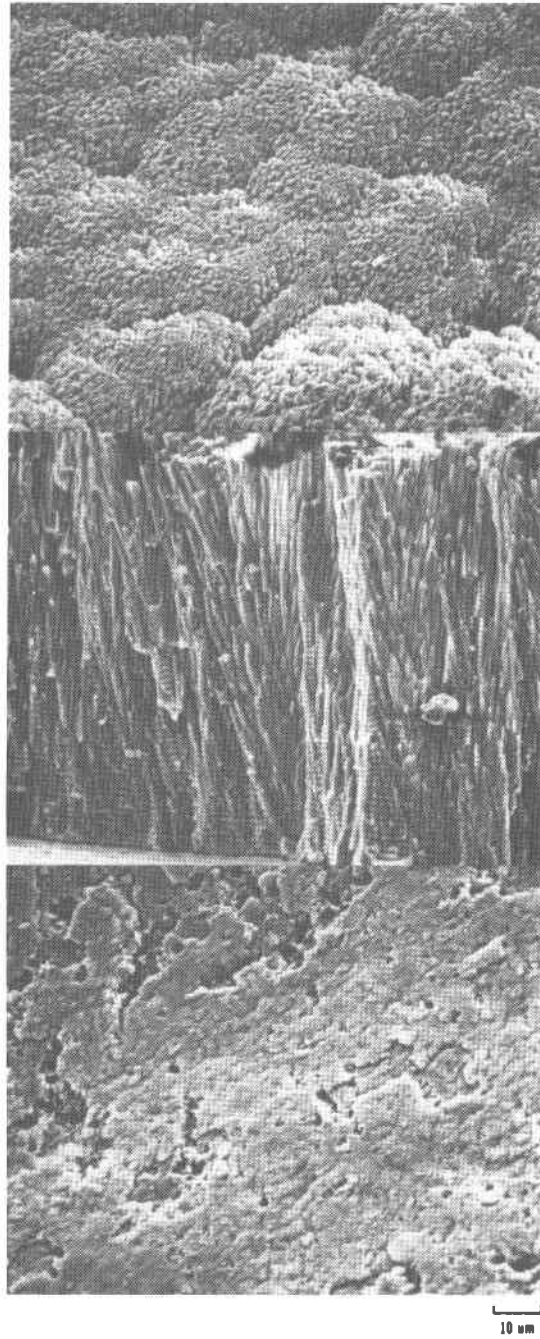


Figure 17. SEM, Part No. 042. Note "beaded" striations extending through coating.

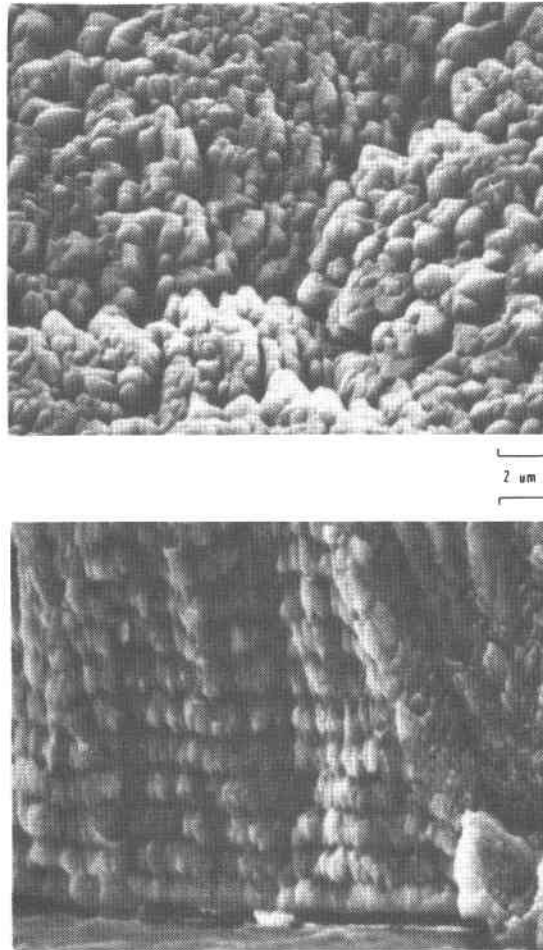


Figure 18. SEM, Part No. 042. Detail of "beaded" structure near surface. Note fully developed bead from first revolution at full e-beam emission current. Bonding is due to ramp phase evaporant which is over-stoichiometric from adsorbed initial  $O_2$ .



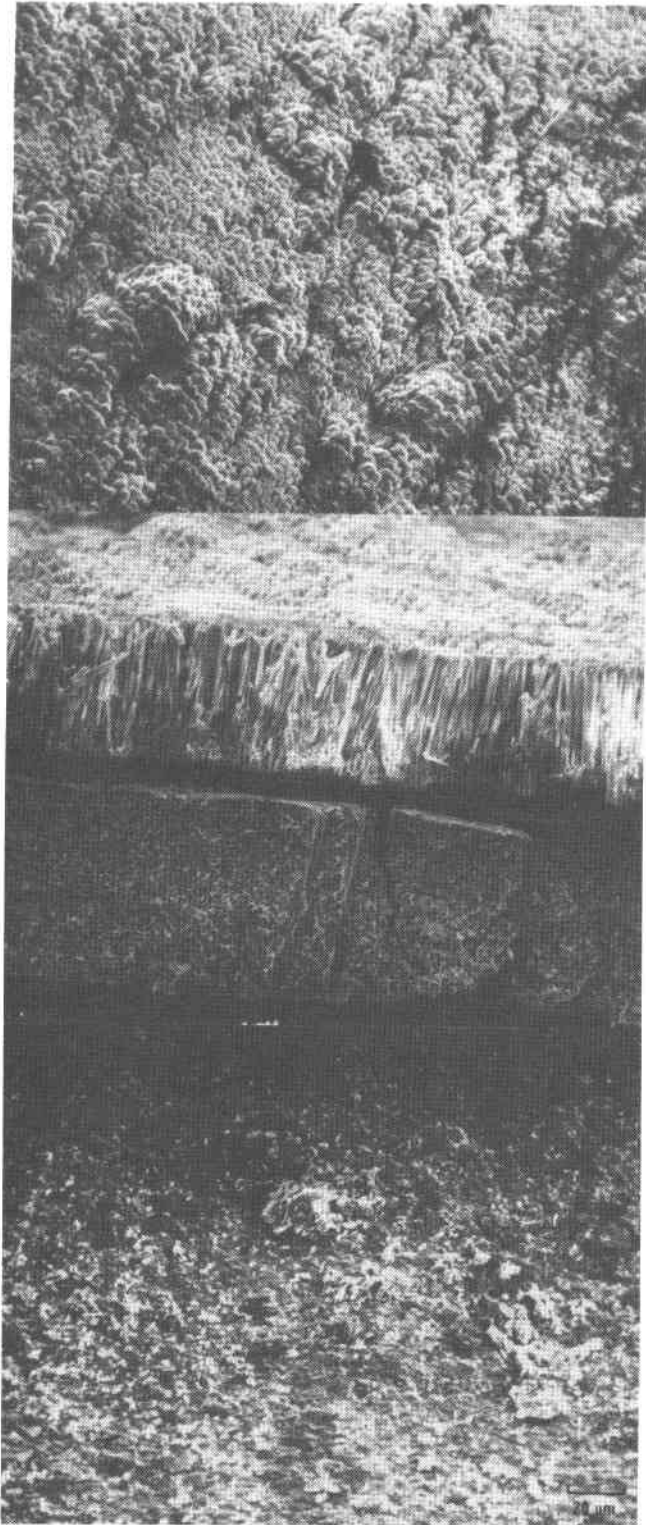


Figure 19. SEM, Part No. 054. Note lack of "beaded" structure. w 15.

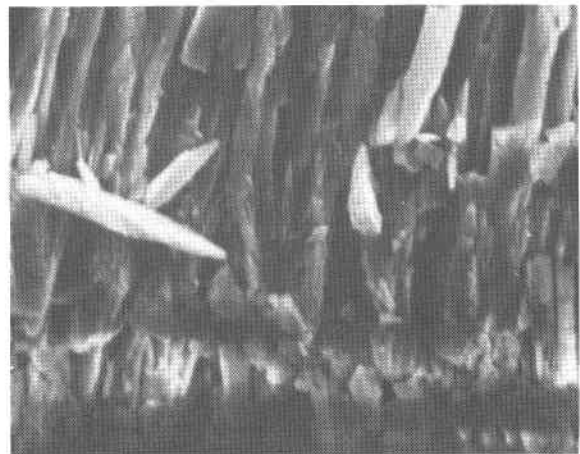
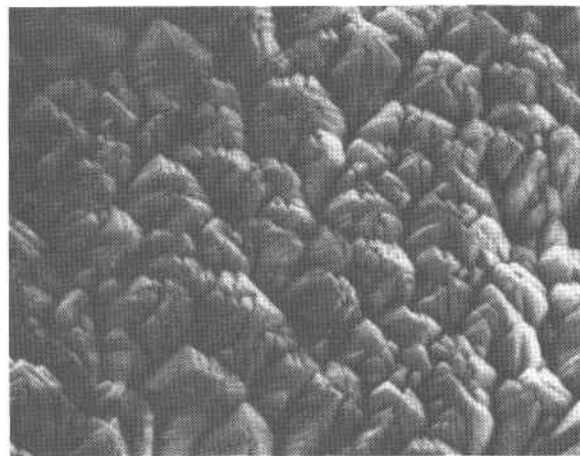
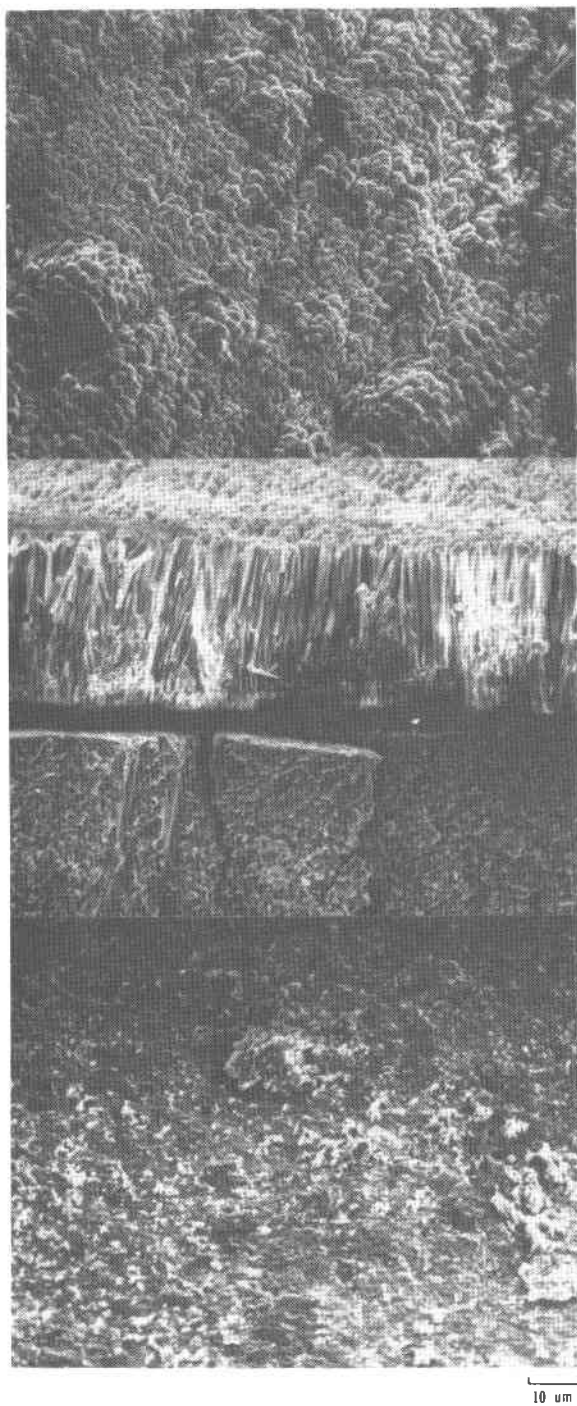


Figure 20. SEM, Part No. 054. Note difference in superficial cauliflower surfaces of Figures 18 and 20. Also note  $l/d$  for columns is 40 here.

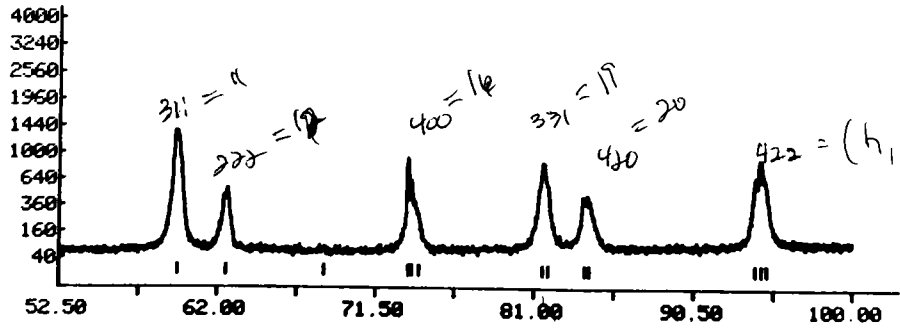
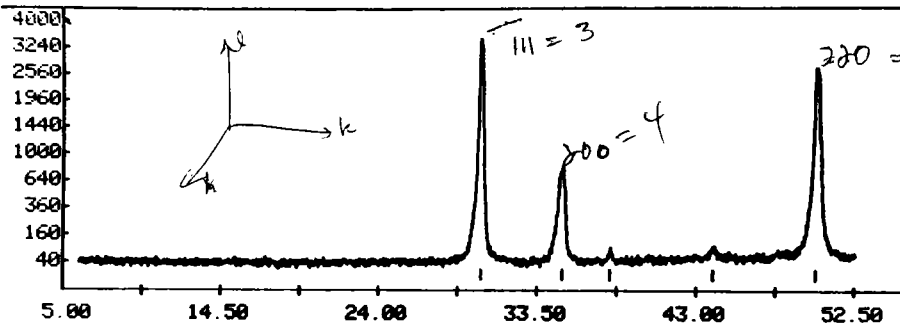
$\vec{G} \perp$  to planes  $\vec{G} = \left( \frac{h}{a_x}, \frac{k}{a_y}, \frac{l}{a_z} \right)$ ,  $|\vec{G}| = \frac{1}{d}$

face centered  
cubic  $3, 4, 8, 12, 16$   
 $(1, 2, 0)$

FILENAME: ZROB.RD

SAMPLE: ZROB

8/11/81



FILENAME: ZROW.RD  
FILENAME: ZROB.RD

SAMPLE: ZROW

8/12/81

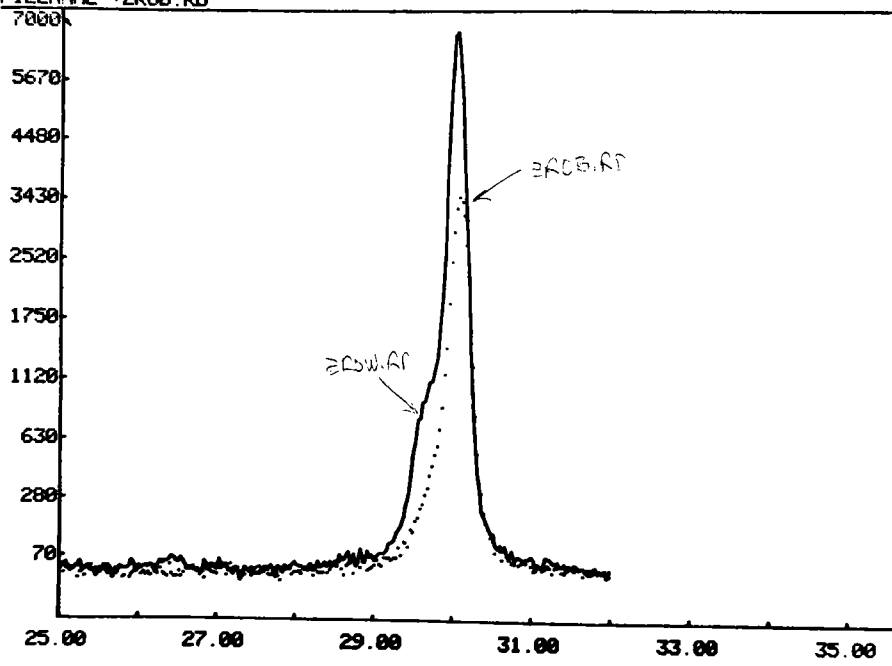
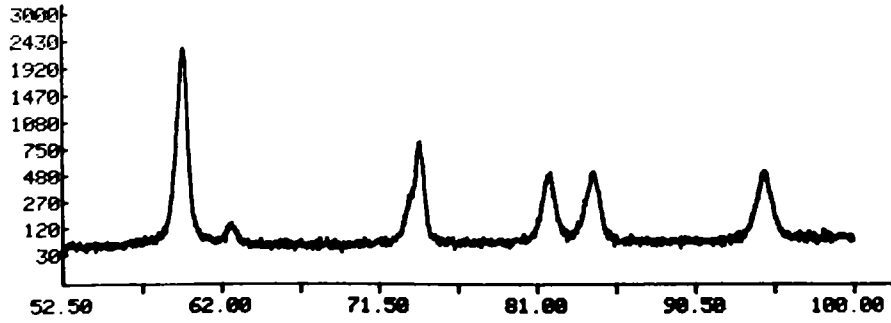
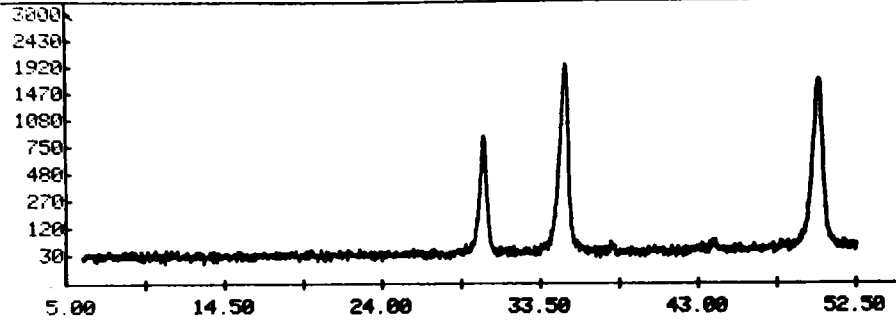


Figure 21. x-ray diffraction spectra of black glassy pool material indicates fully face-centered cubic with 8 w/o YSZ.

FILENAME: 200SCCM.RD      SAMPLE: 200SCCM      8/12/81



FILENAME: 300SCCM.RD      SAMPLE: 300SCCM      8/13/81

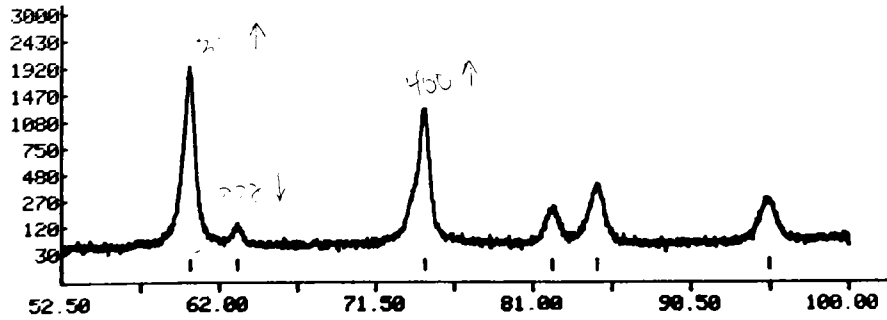
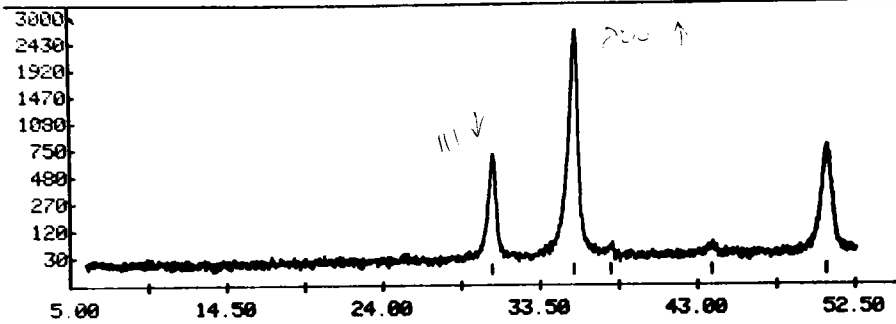


Figure 22. x-ray diffraction spectra for as-deposited coating sample 035 shown above.

## Thermal Barrier Coatings Research at NASA Lewis

Stanley R. Levine

Robert A. Miller

Michael A. Gedwill

NASA Lewis Research Center

### ABSTRACT

Thermal barrier coatings can give effective thermal protection to air-cooled heat engine components. The future use of these coatings in the turbine sections of aircraft and electric utility gas turbine engines can provide significant gains in efficiency or durability. Much of the impetus for current research into thermal barrier coatings came from the successful gas turbine engine test of a two-layer coating system applied to first stage blades. The plasma-sprayed coating consisted on a zirconia-yttria ceramic layer over a NiCrAlY alloy bond coat layer.

In this paper, the status of ceramic coatings research at NASA Lewis will be reviewed. The major thrusts are: modeling of coating thermo-mechanical behavior, understanding coating adherence and degradation mechanisms in clean and dirty combustion gases, understanding the phase stability and properties of the coating materials, improving coating strain tolerance through structure modification, and improving plasma spraying technology. In addition, engine evaluations of coatings are being used to augment laboratory experience.

## INTRODUCTION

Thermal barrier coatings (TBCs), i.e. thin ceramic thermally insulative coatings, offer an attractive approach for improving the durability and/or efficiency of the hot section of heat engines. These coatings typically consist of an inner oxidation/hot corrosion resistant alloy bond coating on the order of 0.01 cm thick and an outer ceramic layer, which is most commonly a stabilized zirconia, with a thickness of 0.01 to 0.05 cm. A 0.025 cm thick TBC on a cooled component can have as much as a 100 to 300<sup>o</sup>C temperature drop across its thickness. Thus, the TBC concept can provide a relatively large improvement in hot section component performance. In comparison, hot section improvements are currently limited by the 10<sup>o</sup>C per year rate of improvement in the high-temperature strength capability of superalloys (1).

Much of the impetus for current research into thermal barrier coatings came from the successful NASA Lewis J-75 gas turbine engine test of two-layer, plasma-sprayed coating systems having a zirconia-based ceramic layer over a NiCrAlY alloy bond coat layer (2). However, subsequent engine tests under more severe and realistic conditions have demonstrated that plasma-sprayed thermal barrier coatings are not yet ready for use on airfoils of advanced aircraft gas turbines (3). Here, thermo-mechanical stresses exceed the capability of plasma sprayed ceramics. Also temperatures are high enough for the ceramic to undergo sintering, creep and phase changes, and for significant bond coat oxidation. Finally, the presence of corrosive air- or fuel-derived impurities in combustion gases must be considered. Deposition and reaction of corrodents can alter the coating materials or their thermo-mechanical response.

Several difficult technology hurdles must still be overcome to attain bill-of-material status for thermal barrier coatings on gas turbine airfoils. In the

materials area, ceramic thermo-mechanical stress, condensed salt, erosion resistance and bond coat oxidation resistance must be upgraded so that ceramic adherence is extended in both time and temperature. The magnitude of each of the above hurdles depends on the specific application. However, for any application, an improved understanding of failure mechanisms must be attained so that airfoils can be designed to take maximum advantage of a thermal barrier coating. Reliable coating properties are also required to accomplish such a design. Finally, the coating has to be applied reproducibly, economically, and to design specifications for thickness, quality and surface roughness.

The current in-house, grant, and contractual research program at NASA Lewis addresses all of the above critical elements of thermal barrier coatings technology. The purpose of this paper is to discuss the progress that has been made at NASA Lewis over the past several years and to assess the readiness of such coatings for stationary gas turbines.

#### THERMO-MECHANICAL STRESS CONSIDERATIONS

Thermal stress is a primary consideration for monolithic ceramic and metallic heat engine materials. With a composite, such as a two-layer thermal barrier coating on a superalloy, consideration must be given to a thermal expansion mismatch component as well as a thermal gradient induced component in solving a thermal stress problem. In addition, the plasma spray process produces coatings with significant levels of residual stress and these stresses should also be taken into account in the solution of the thermal stress problem. The stress state of the ceramic layer at room temperature may be either compressive or tensile depending on the effective substrate temperature during deposition and the thermal expansion mismatch between the ceramic and substrate. Furthermore, the stress state is subject to change due to ceramic sintering, creep and microcracking while the

coating is in use. Thus, at present it is not possible to vigorously treat all aspects of the thermal stress problem.

Conventional wisdom with regard to bulk ceramic materials tells us that compressive stresses are favorable. For ceramic coatings, the conventional wisdom does not apply. For example, consider a stabilized zirconia coating on a solid, relatively large diameter, superalloy rod. If this composite is slowly heated to the operating temperature,  $T_o$ , e.g.  $1100^{\circ}\text{C}$ , from ambient temperature,  $T_a$ , the thermal stress in the ceramic can be calculated from (4).

$$\sigma_c = \frac{E_c (\bar{\alpha}_m - \bar{\alpha}_c) (T_o - T_a)}{1 - \mu_c}$$

where  $E_c$  is the elastic modulus of the plasma sprayed ceramic,  $2.1 \times 10^4$  MPa at  $1100^{\circ}\text{C}$ (3), and  $\mu_c$  is Poisson's ratio, 0.25. Over the temperature interval from ambient to  $1100^{\circ}\text{C}$ , stabilized zirconia has a mean coefficient of thermal expansion,  $\bar{\alpha}_c$ , of  $12.2 \times 10^{-6}/^{\circ}\text{C}$  while a typical superalloy has a mean coefficient of thermal expansion,  $\bar{\alpha}_m$ , of  $18.5 \times 10^{-6}/^{\circ}\text{C}$  (3). Thus, the calculated ceramic layer thermal stress is 190 MPa while the strain is about 0.7 percent. Since the thermal expansion mismatch strain exceeds the reported fracture strain of zirconia by about 120 percent (3), the ceramic will be stress relieved by cracking under these conditions, but it will still adhere.

However, thermal barrier coatings, when used in applications such as on gas turbine blades, are not given the luxury of being slowly heated and cooled. As a matter of fact, heating rates are such that the coatings can be subjected to high compressive stresses during the heat-up transient in spite of the fact that the thermal expansion coefficient mismatch between zirconia and a typical austenitic



superalloy favors development of tensile stresses in the ceramic. Two examples illustrate this point.

In the first, solid 1.25 cm diameter Rene' 41 bars were coated with either a Ni-16Cr-6Al - 0.3Y\* or Ni-18Cr-12Al-0.3Y bond coating and either a ZrO<sub>2</sub>-8 Y<sub>2</sub>O<sub>3</sub>\* or ZrO<sub>2</sub>-12 Y<sub>2</sub>O<sub>3</sub> ceramic. Bond and ceramic coating thicknesses were 0.013 and 0.038 cm, respectively. Eight specimens were placed in a rotating carousel and rapidly cycled between room temperature and a 1040°C leading edge temperature in a Mach 0.3 atmospheric pressure burner rig firing Jet A fuel. The heating part of the cycle was either 4 minutes in the flame followed by a 3 minute forced air cool or 57 minutes followed by the same forced air cool. Results are presented in Figure 1 (5). With the less oxidation resistant Ni-16Cr-6Al-0.3Y bond coat, life was governed by the number of thermal cycles since life in terms of cycles to failure was insensitive to cycle heating time. With the more effective Ni-18Cr-12Al-0.3Y bond coat, life is controlled by both time-at-temperature and the number of thermal cycles. One should note that failures occurred not at the leading edge, but at the 60°C hotter trailing edge.

Two analyses of this experiment were performed - an elegantly simple short stress analysis which will be described here and a confirmatory finite element heat transfer and stress analysis which is described in reference 5. The short stress analysis is based on consideration of the early moments of the heat-up cycle where the ceramic is responding by going into compression before the metal shows any significant thermal response. The mean thermal stress in the ceramic coating, is equated to the hoop or radial detachment stress. The detachment stress was calculated as 4.4 MPa. This value is on the order of the reported adhesive/cohesive strength of 6.2 MPa for an as-deposited ZrO<sub>2</sub>-12 Y<sub>2</sub>O<sub>3</sub> coating.

---

\*Compositions are in weight percent

Undoubtedly, coating bond strength changes with thermal exposure and the composition of the oxide scale formed between the ceramic and the bond coat.

The second example is a ground based JT9D engine test of the early NASA coating:  $ZrO_2-12 Y_2O_3/Ni-16Cr-6Al-0.6Y(3)$ . A 0.018 cm ceramic layer over a 0.009 cm bond coat was applied to first-stage turbine blades. The engine was run for 264 hours of which 190 hours were cyclic endurance in which 1424 thermal cycles were accumulated. Typical accelerated endurance cycles consisted of 2 minutes at take-off power with maximum turbine inlet temperature reaching about  $1425^{\circ}C$  and 5 minutes at idle power. After 39 hours (327 cycles), coating failure occurred only at the highest temperature locations at the leading edge. At test completion, ceramic spallation was also noted on the blade upper pressure surface near the trailing edge. Heat transfer and structural analyses were carried out (3). The analyses revealed that ceramic failures occurred in regions of combined high temperature and compressive strain.

Figure 2 illustrates the calculated leading edge ceramic strain during an endurance test cycle. The maximum compressive strain during the acceleration from idle to take-off is about 0.005 cm/cm. Going back to the thermal stress/detachment stress concepts of the earlier example, the stress in the coating can be calculated and equated to the detachment stress

$$\epsilon E_C = \frac{Pd}{2t}$$

With a leading edge diameter of about 0.3 cm and a zirconia modulus of  $2.4 \times 10^4$  MPa, P turns out to be about 14 MPa which greatly exceeds the adhesive/cohesive strength of the coating. However, if we consider a large utility gas turbine operating at about half the pressure ratio of a JT9D, with slower transients, a more generous leading edge diameter and an appreciably lower turbine inlet temper-

ature during transients, current TBCs might perform quite well. For further details, see the paper by Bratton et al. in these proceedings.

From the results of the JT9D engine test and analysis, several clear directions for improvement of thermal barrier coatings are apparent. First, the coatings should be deposited so as to minimize residual compressive stress or even make the residual stresses tensile. Second, the coating structure should be segmented to improve compressive stress accommodation. Third, adhesive/cohesive strength should be increased. Fourth, improved bond coatings are needed to eliminate coating disruption as a result of bond coating oxidation. Finally, because of the compressive stress sensitivity of TBCs, attention should be paid to thermal expansion coefficient mismatch optimization.

#### PERFORMANCE IN NON-CORROSIVE ENVIRONMENTS

Since the JT9D engine test discussed in the previous section, a substantial improvement was made to the durability of the  $ZrO_2$ - $Y_2O_3$ /NiCrAlY system (8). This was accomplished by decreasing the  $Y_2O_3$  level from 12 w/o, where the ceramic is essentially single-phase, to the 6 to 8 w/o range, where the zirconia is multiphase. Also, the yttrium level in the NiCrAlY was reduced from 0.6 w/o to the 0.15 to 0.3 w/o range. This modification is believed to enhance the stability of the zirconia/bond coat interface region. These compositional effects are illustrated in Figure 3 which summarizes the results for coated, solid specimens exposed to a cyclic torch test. In more severe Mach 1.0 burner rig tests, air-cooled turbine blades coated with  $ZrO_2$ -8  $Y_2O_3$ /Ni-17Cr-5Al-0.35Y survived 2000 one-hour cycles without failure at a surface temperature of 1450°C and a substrate temperature of 920°C. The early  $ZrO_2$ -12  $Y_2O_3$  based system failed after 800 hours at somewhat lower temperatures (8).

Two studies of the  $ZrO_2-8 Y_2O_3$  system have been carried out to elucidate its behavior as a TBC. In the first, the constitution of plasma sprayed  $ZrO_2-8 Y_2O_3$  was investigated as a function of aging time and temperature (9). The as-sprayed material was determined to consist of 80 percent of a tetragonal phase which was nontransformable with respect to a martensitic conversion to the low temperature monoclinic phase, but which was diffusionally unstable at high temperatures. Another 12 percent of the as-sprayed material was cubic while the remaining 8 percent was found to be the martensitically transformable tetragonal phase. The latter phase is detected as the monoclinic phase at room temperature. A large and possibly disruptive volume increase is associated with this transformation. The trade-off between this volume transformation and the possible benefits of transformation toughening as we go to very low levels of yttria stabilization (10) remains to be determined. However, the decrease in life at 4 w/o yttria shown in Figure 3 can be attributed to the volume change associated with the formation of the monoclinic phase (8).

In the second study (11) it was demonstrated that  $1500^{\circ}C$  aging of solution annealed bulk  $ZrO_2-8Y_2O_3$  results in a gradual increase in hardness with aging time. This hardness is associated with the formation of coherent-tetragonal precipitates. At aging times greater than about 100 hours, hardness drops due to the formation of grain boundary monoclinic precipitates. There was no evidence that transformation toughening, which is observed in very low yttria  $ZrO_2-Y_2O_3$  (10), plays a role in the properties of bulk (11) or as-plasma sprayed (9)  $ZrO_2-8Y_2O_3$ .

Additional TBC life improvements have been obtained by improving the oxidation resistance of the bond coating. For example life can be doubled either by increasing the bond coat Cr content from 16 to 25 w/o or by increasing the bond coat Al content from 6 to 10 w/o (12). Further improvements can be obtained by

increasing the density of the plasma sprayed bond coatings by increasing the power level and adding hydrogen to the arc gas (13, 14). Further improvements can be expected by going to inert gas shrouding or by going to low pressure plasma spraying. Using the latter technique, overlay metallic coatings having environmental resistance equivalent to or better than electron-beam physically-vapor-deposited (EB-PVD) coatings have been obtained (15).

The structure and composition of the zirconia coating also have an effect on the oxidation kinetics of the bond coating. Increasing the density to above about 88 percent of theoretical and decreasing the yttria content reduce the bond coat oxidation rate (16). However, higher zirconia density can adversely affect thermal shock resistance while being beneficial in corrosive environments. Further research is required to explore these trade-offs.

As discussed earlier, the structure and residual stress state of a TBC are important parameters. An investigation of both of these factors has been carried out at Pratt and Whitney as part of the NASA Engine Component Improvement Project. Coating segmentation via the EB-PVD process and residual stress control were most effective as illustrated in Figure 4 (17).

Three coatings were subjected to a JT9D cyclic endurance engine exposure on first stage vane platforms having a cooling system redesigned to take advantage of the TBC. The coatings tested were 0.038cm thick  $ZrO_2-20 Y_2O_3$ ,  $ZrO_2-6 Y_2O_3$ , and  $ZrO_2-21 MgO$  over a Ni-22Co-18Cr-13Al-0.7Y bond coat. Except for those vanes exposed in a severe hot streak, the coatings survived with no apparent damage. In a current contract effort with Pratt and Whitney (NAS 3-22548) this technology is being extended to turbine blades. It should be noted that the thermal conditions on first-stage vane platforms are about one-third as severe as on first-stage

blade leading edges in an aircraft gas turbine and comparable to conditions on first-stage blade leading edges in a typical non-aircraft derivative stationary gas turbine.

#### PERFORMANCE IN CORROSIVE ENVIRONMENTS

The durability of the  $ZrO_2-12Y_2O_3/NiCrAlY$  coating system is greatly diminished when trace inorganic contaminants such as Na, V, and S - as found in many industrial/utility gas turbine fuels - are present in the combustion products (18-20). The results of burner rig exposure tests conducted at NASA-Lewis with sodium and vanadium additions to the fuel are given in Figure 5. The observed early failures are thought to be due to the deposition of liquid salts such as  $Na_2SO_4$ . These liquid salts are believed to enter the open pores of the coating and permeate parts of the coating where the temperature exceeds the melting point of the salt. Since sodium sulfate does not react with  $ZrO_2-Y_2O_3$  under the conditions of these experiments (21), it is believed that this salt adversely affects the ability of the ceramic to accommodate cyclic thermal stress (22). The mechanism may involve the infiltration of molten salts into the pores and microcracks of the plasma sprayed ceramic coating thereby greatly decreasing its thermal stress resistance. Recently it has been shown that an understanding of the thermochemistry of salt deposition can aid in the interpretation of coating failure induced by impurities derived from the fuel or air. For example, in Figure 6, the case in which 5 ppm of Na was present in the fuel is considered (22). The sketch shows that the observed location of spalling can be correlated with the dewpoint of  $Na_2SO_4$  for these conditions. It also shows that the observed depth of failure within the ceramic layer can be correlated with the depth in the coating at which the melting point of  $Na_2SO_4$  is reached. In contrast, in clean fuels failure nearly always occurs in the ceramic very close to the bond coat.

The results of the tests just described, as well as the results of other investigations, indicated a need to identify ceramic coatings having improved resistance to fuel and air impurities (19, 20, 23, 24). An initial step toward this goal was taken when a series of coating systems was tested in a Jet-A fuel-fired Mach 0.3 burner rig with the flame doped to the fuel-equivalent impurity level of 5 ppm Na + 2 ppm V (18). Ceramic coating thickness was maintained at 0.038 cm, and bond coat thickness was maintained at 0.013 cm. Results are summarized in Figure 7. Various thermal and chemical treatments of the  $ZrO_2-12Y_2O_3/Ni-16Cr-6Al-0.6Y$  system resulted in little or no improvement. A more oxidation/hot corrosion resistant bond coat (Ni-21Co-19Cr-13Al-0.6Y) and a dense  $Y_2O_3$  top-coat with the baseline coating offered some improvement. The  $ZrO_2-8Y_2O_3/Ni-16Cr-5Al-0.15Y$  coating offered an even greater improvement. The most promising duplex ceramic coating identified was 1.8 CaO-SiO<sub>2</sub>/Ni-16Cr-6Al-0.6Y. A higher thermal conductivity cermet coating consisting of 50 volume percent MgO in Ni-20Cr-17Al-1.0Y over the standard bond coating survived 1000 one-hour cycles without spalling. However, coating thickness was reduced about 50 percent by erosion.

Further studies of the behavior of  $ZrO_2-Y_2O_3$  and  $Ca_2SiO_4$  were carried out using a slightly more severe burner rig test (25). The effects of bond coat and zirconia compositions and ceramic coating thickness were investigated. Results are presented in Figure 8. In this test  $ZrO_2-8Y_2O_3$  was more durable than  $ZrO_2-6Y_2O_3$  and  $ZrO_2-12Y_2O_3$ . Increased bond coat Cr and Al content and reduced ceramic coating thickness were both beneficial for  $ZrO_2-8Y_2O_3$ . With  $Ca_2SiO_4$ , increased bond coat Cr and Al were ineffective for nickel-base bond coats, but effective for cobalt-base bond coats. Once again, reduced ceramic thickness was beneficial. The improved durability of the thinner coatings may be attributed in part to the fact that they are operating at a higher bond coat temperature and thus condense less salt. Another factor is the reduced detachment stress resulting from the reduced ceramic thickness as discussed earlier.

Analyses of tested specimens by X-ray diffraction and electron microprobe elemental mapping revealed condensation of  $\text{Na}_2\text{SO}_4$  as can be seen from the coincidence of Na and S in Figure 9 and formation of  $\text{YVO}_4$  in  $\text{ZrO}_2\text{-8Y}_2\text{O}_3$ . For  $\text{Ca}_2\text{SiO}_4$  coatings,  $\text{Na}_2\text{SO}_4$  and  $\text{V}_2\text{O}_5$  or  $\text{Na}_2\text{V}_2\text{O}_6$  condensation were confirmed and reaction of  $\text{Ca}_2\text{SiO}_4$  with sulfur to form  $\text{CaSO}_4$  and  $\text{CaSiO}_3$  was detected.

The behavior of the duplex  $\text{Ca}_2\text{SiO}_4$  system, duplex and graded zirconia systems, and a duplex and graded  $\text{ZrO}_2 - 24.7\text{MgO}$  system have also been investigated by Bratton et.al. in an EPRI-funded, NASA-managed contract (26). Clean fuel, low velocity burner rig tests of air-cooled specimens were carried out at substrate temperatures of 800, 845, and  $900^\circ\text{C}$  for 500 one-hour cycles. At  $845^\circ\text{C}$ , bond coat oxidation in the graded coatings limited ceramic coating life. In a dirty fuel (1 ppm Na, 2 ppm V, 2 ppm P, 0.5 ppm Ca, 2 ppm Fe, 6 ppm Mg) at  $800^\circ\text{C}$  substrate temperature, only the graded coatings and the duplex  $\text{Ca}_2\text{SiO}_4$  survived 500-hour exposures. When the V level was increased to 50 ppm and the Mg level to 150 ppm to simulate a water washed and treated residual oil, failures were observed in about 100 hours with a duplex  $\text{ZrO}_2\text{-8Y}_2\text{O}_3$  coating and a graded  $\text{ZrO}_2\text{-24.7 MgO}$  coating, while the graded  $\text{ZrO}_2\text{-8Y}_2\text{O}_3$  coating survived 500 one-hour cycles under these relatively mild thermal conditions. However, in 9 atmosphere pressurized burner rig tests, TBC durability in a simulated water washed and treated residual fuel (20ppm V) was drastically reduced (Bratton et al., this proceedings).

In summary, the condensation of combustion gas-borne salts in porous thermal barrier coatings drastically reduces their tolerance to thermal cycling. Exclusion of these salts via a platinum overlay as has been demonstrated by Clarke (27) one approach that appears to be feasible at low temperatures and flow rates. Other sealants would be required at higher temperatures and gas velocities due to the volatility of platinum oxide. Also, the viability of this approach on erosion



prone components is questionable. Laser sealing now appears to be another promising technique (I. Zaplatynsky, private communication). A preferable approach would involve the development of TBC structures that are immune to mechanical degradation by condensed salts. One step in this direction is to increase coating density. However, trade-offs against thermal stress tolerance are involved.

Finally, it must be noted that severe degradation of TBC life has been observed with levels of combustion gas contamination representative of industrial or marine applications. For aircraft gas turbine applications where the fuels are clean and relatively little sea salt is ingested, thermal barrier coatings appear to have adequate tolerance. For example, the results of Hodge et.al. (18) show that at the 0.5 ppm fuel equivalent Na level, the early  $ZrO_2-12Y_2O_3/Ni-16Cr-6Al-0.6Y$  TBC did not fail after 1300 one-hour cycles (Figure 5). Also, in furnace corrosion tests at  $900^{\circ}C$  (28), pre-coating of specimens with  $5\text{ mg/cm}^2$  of  $Na_2SO_4$  caused no coating distress in 100 hours. However, distress was observed with as little as 10 percent  $NaVO_3$  in the deposit (28).

#### CONCLUDING REMARKS

The performance of thermal barrier coating systems is governed by many complex and interrelated factors. Coating structure and properties control the ability of the coating to tolerate thermal stress. Compressive thermal stresses which arise on rapid heating are more difficult to accommodate than tensile stresses. The ability of the ceramic to tolerate thermal stress is severely compromised by combustion gas impurities condensed in coating pores. In addition, factors such as phase stability and bond coat oxidation arise in situations where corrosion and thermal stress are at least initially overcome. Often the obvious direction for coating improvement to cope with one problem aggravates another. For example, increased coating density would limit coating permeation by condensed combustion gas

impurities, but thermal stress resistance may be sacrificed. To more effectively make these trade-offs, far more must be learned about coating structure/property/failure mechanism relationships so that further coating improvements can be made. Such improvements are required for the most stringent gas turbine applications such as aircraft gas turbine airfoils and stationary gas turbines firing dirty fuels. However, for stationary gas turbines firing clean fuels—for example gasifier-combined-cycle systems with cold gas clean-up – thermal barrier coatings are sufficiently developed to warrant field testing. Such an effort would require further coatings evaluation to select the currently most promising systems, development of coatings deposition technology, generation of coating property data for design analysis and field service testing in the blade durability improvement (rather than the performance improvement) mode.

#### ACKNOWLEDGEMENT

This paper was written with support from the Department of Energy, Heat Engines and Heat Recovery Division, under DOE/NASA Interagency Agreement DE-AI01-77ET-13111. Some of the work discussed herein was performed under DOE/NASA Interagency Agreement DE-AI01-77ET-10350.

#### REFERENCES

1. R. A. Signorelli, et al., NASA CP-2092, p. V-1, 1979.
2. C. Liebert, et al., NASA TMX-3410, 1976.
3. W. R. Sevcik and B. L. Stoner, NASA CR 135360, 1978.
4. W. D. Kingery, et al., Introduction to Ceramics, 2nd Edition, John Wiley and Sons, New York, 1976, p. 609.
5. G. McDonald and R. C. Hendricks, Thin Solid Films, Vol. 73, 1980, p. 491-496.

6. S. R. Levine, NASA TM-73792, 1978.
7. R. S. Colladay, Turbine Cooling, Vol. 3, Ch. 11, NASA SP-290, 1975.
8. S. Stecura, NASA TM-78976, 1978.
9. R. A. Miller, et al., Proceedings of the First Inter. Conf. on the Science and Technology of Zirconia, 1981.
10. T. K. Gupta et.al., J. Mat. Sci., Vol. 12, 1977, p. 2421-2426.
11. P. G. Valentine and R. D. Maier, NASA CR-165126, 1980.
12. S. Stecura, NASA TM-79206, 1979.
13. M. A. Gedwill, NASA TM-81567, DOE/NASA/2593-18, 1980.
14. M. A. Gedwill, NASA TM-81684, DOE/NASA/2593-26, 1981.
15. F. J. Pennisi, and D. K. Gupta, NASA CR-165234, 1981.
16. S. Stecura, Private Communication.
17. I. E. Sumner and D. L. Ruckle, NASA TM-81512, 1980.
18. P. E. Hodge, et al., DOE/NASA/2593-78/3, NASA TM-79005, 1978.
19. R. J. Bratton, et al., EPRI RP 421-1, 1979.
20. J. E. Palko, et al., DOE EC-77-C-05-5402, 1978.
21. I. Zaplatynsky, DOE/NASA/2593-78/1, 1978.
22. R. A. Miller, DOE/NASA/2593-79/7, NASA TM-79205, 1979.
23. S. R. Levine and J. S. Clark, ERDA CONF-770110, 1977, p. 331.
24. S. J. Dapkunas and R. L. Clarke, NSRDC-4428, 1974.
25. P. E. Hodge, et al., DOE/NASA/2593-16, NASA TM-81520, 1980.
26. R. J. Bratton, et al., Thin Solid Films, Vol. 73, 1980, p. 429-437.
27. R. L. Clarke, DTNSRDC/TM-28-80-164, 1980.
28. D. W. McKee and P. A. Siemers, Thin Solid Films, Vol. 73, 1980, p. 439-445.

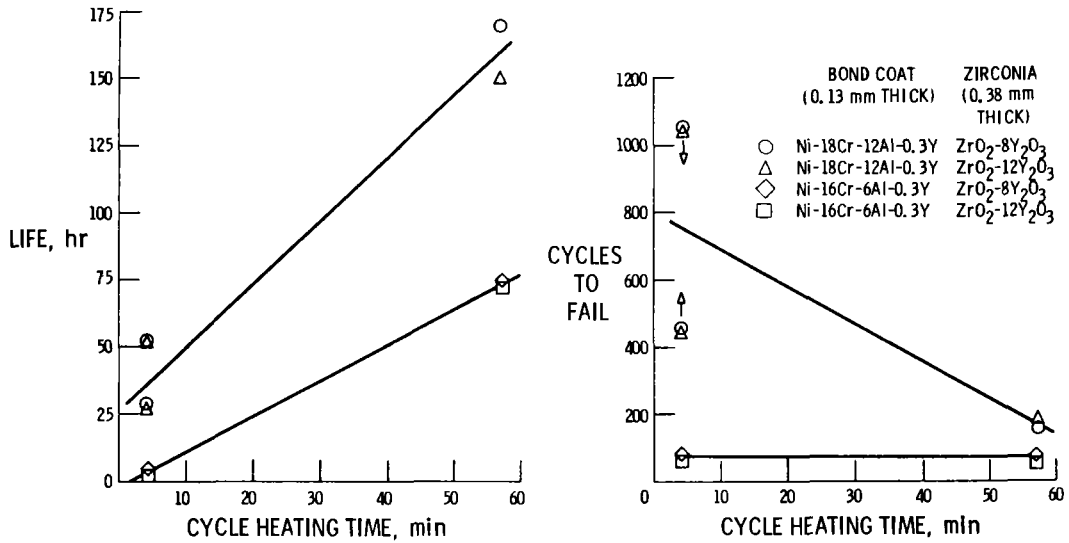


Figure 1. Effect of cycling on life of thermal barrier coating. Heating-cooling cycle: 4 min heat - 3 min forced cool; 57 min heat - 3 min forced cool. Optical surface temperature, 1040°C.

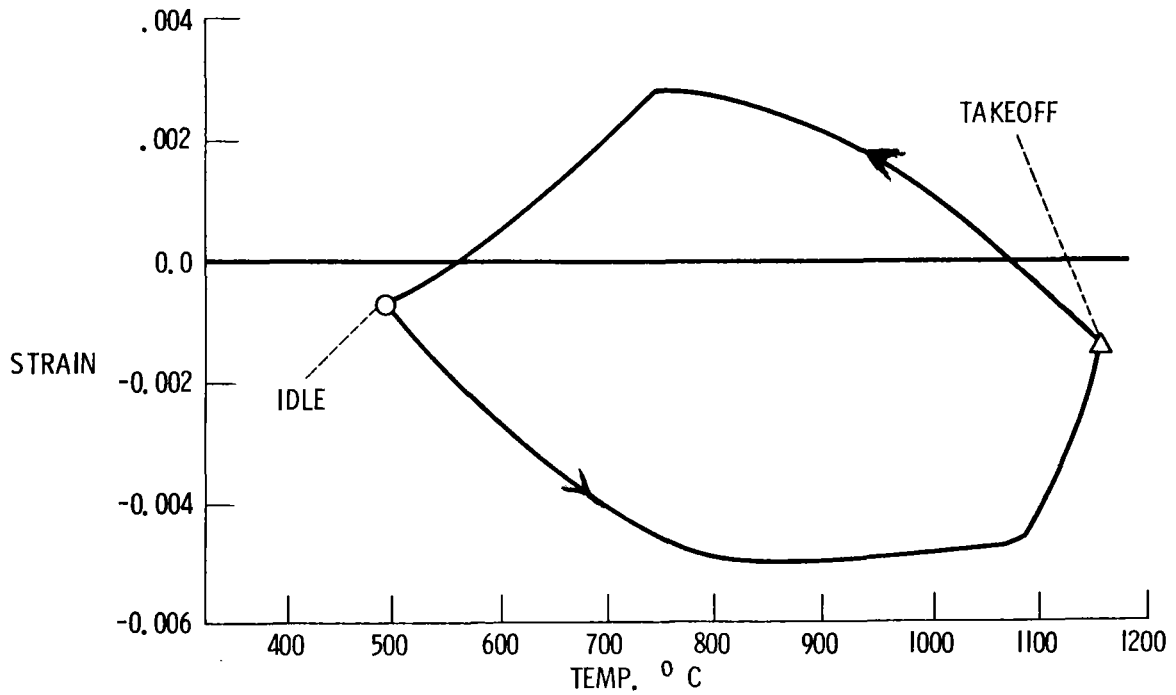


Figure 2. Strain in 0.018cm ZrO<sub>2</sub>-12Y<sub>2</sub>O<sub>3</sub>/0.009cm NiCrAlY TBC at the 70 percent span leading edge of a JT9D first stage blade.

CYCLIC NATURAL GAS TORCH TEST DATA

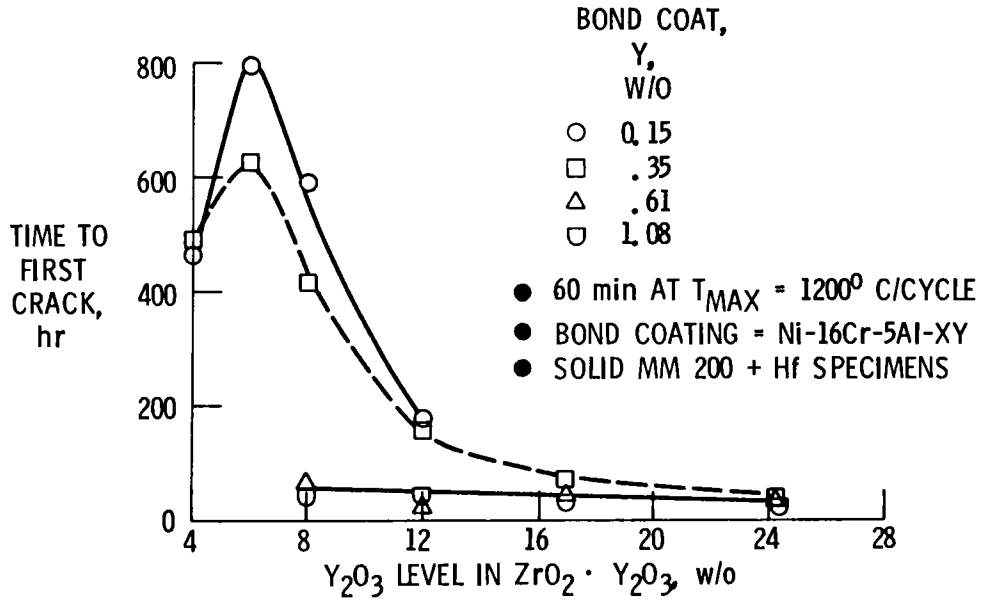


Figure 3. Effects of bond coat and zirconia composition on coating life.

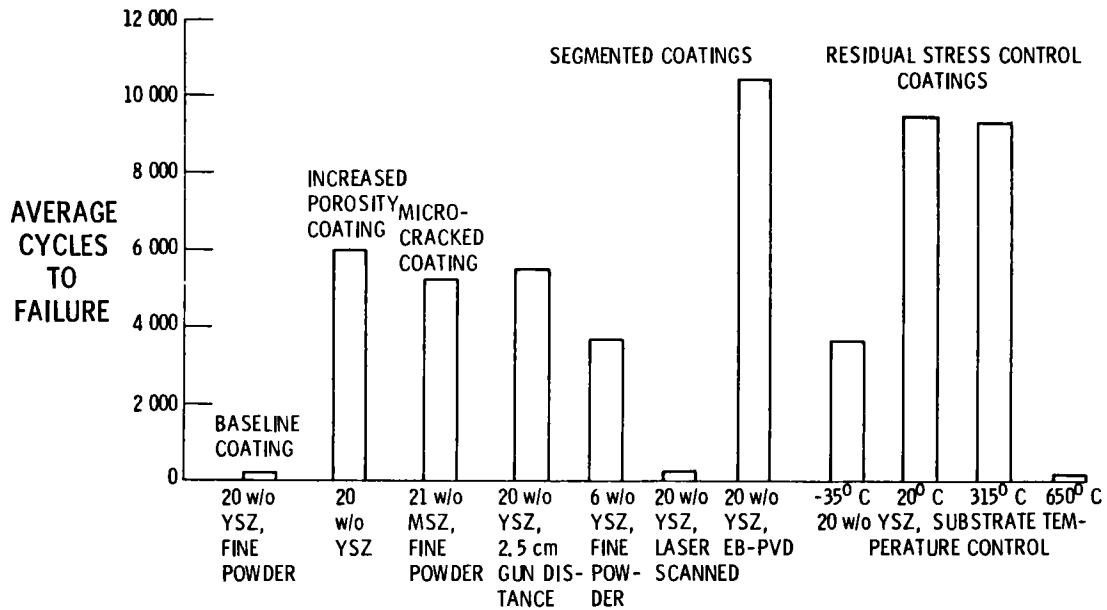


Figure 4. Average number of thermal cycles to failure for several thermal barrier coating systems. Thermal cycle: 4 minutes of heating to 1010°C in a Mach 0.3 burner rig followed by 2 minutes of forced air cooling to 260°C or less.

MACH 0.3 BURNER RIG, 0.05 w/o S IN FUEL;  
 SURFACE TEMP, 980° C; BOND COAT TEMP, 850° C

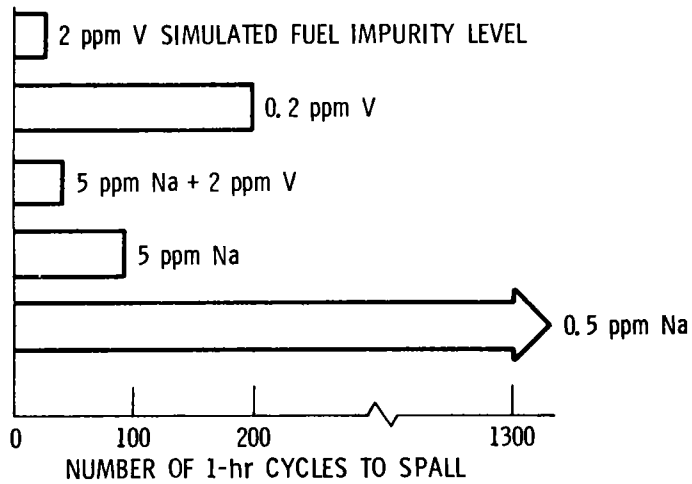


Figure 5. Effect of fuel impurities on a 0.038cm  $ZrO_2-12Y_2O_3/0.013cm Ni-16Cr-6Al-0.6Y$  thermal barrier coating.

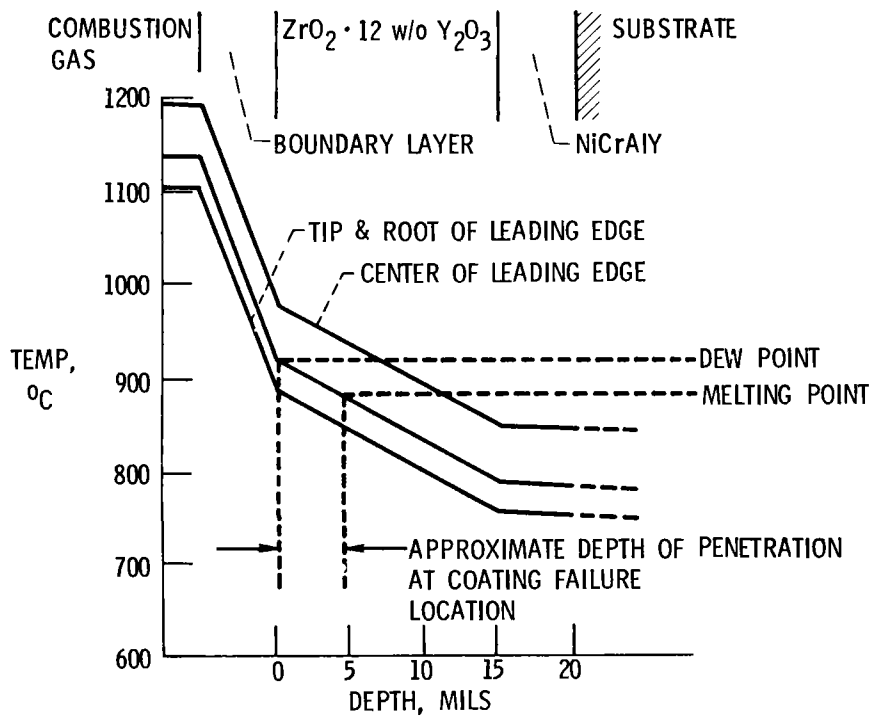


Figure 6. Predicted depth of penetration of  $Na_2SO_4$  for 5ppm Na simulated fuel impurity level.

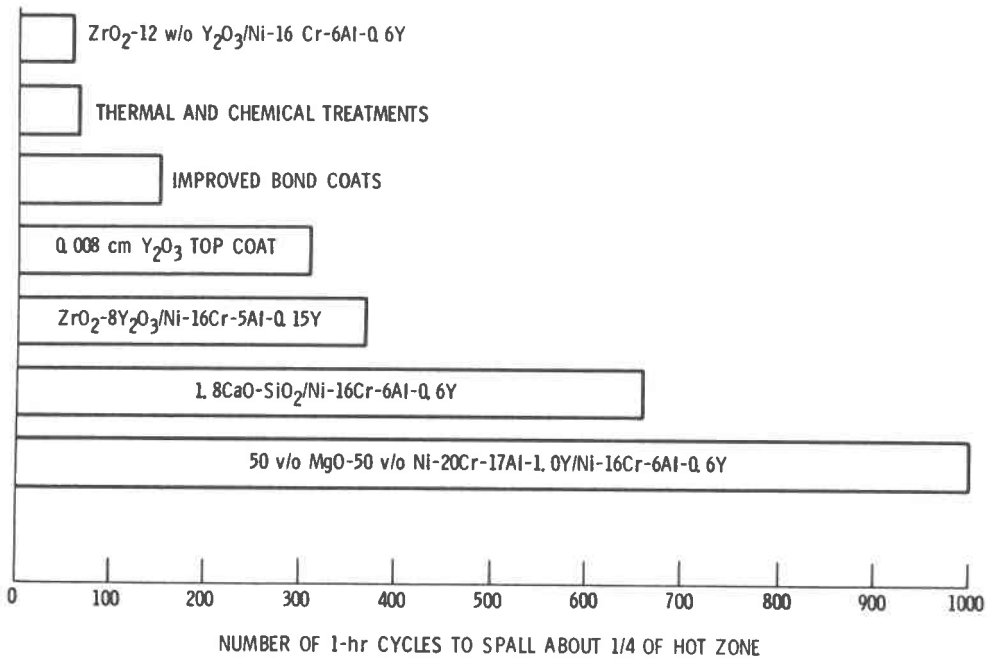


Figure 7. Improved thermal barrier coatings. Exposure in a Mach 0.3 burner rig firing fuel doped to 5 ppm Na plus 2 ppm V. Flame temperature, 1370°C; ceramic surface temperature 980°C; metal temperature, 840°C.

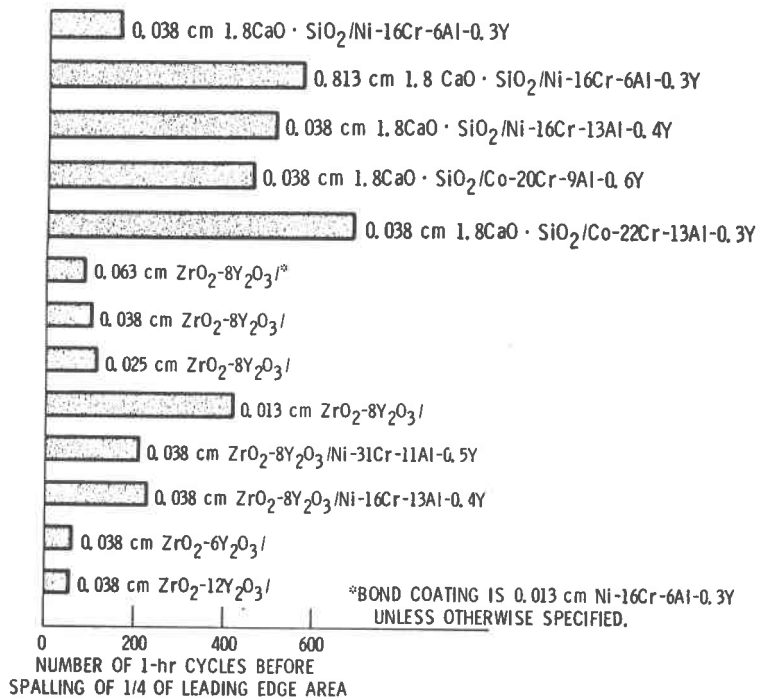
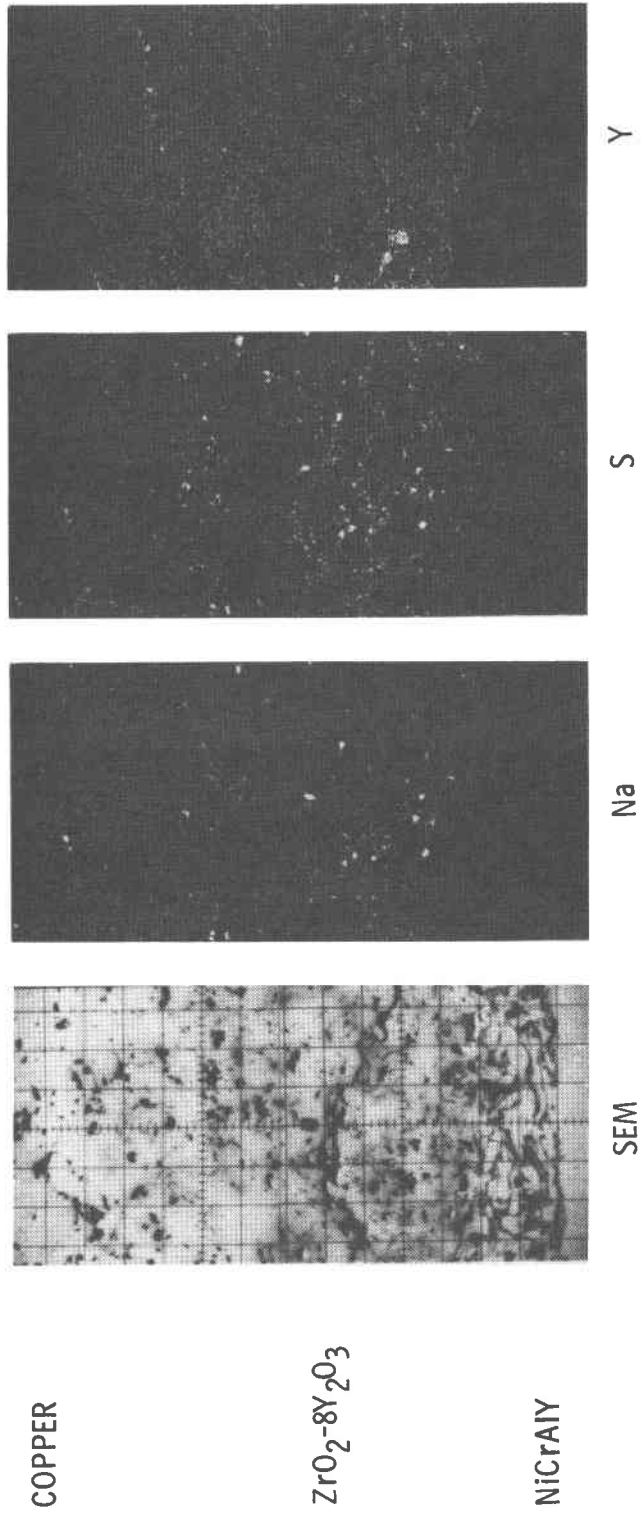


Figure 8. Effects of ceramic thickness and bond coat composition on doped fuel Mach 0.3 burner rig lives of thermal barrier coatings. Fuel impurity level: 5 ppm Na plus 2 ppm V. Fuel to air ratio: 0.046. Ceramic surface temperature: 980°C. Substrate temperature: 840°C.



ZrO<sub>2</sub>-8Y<sub>2</sub>O<sub>3</sub>

NiCrAlY

Figure 9. Electron microprobe maps for ZrO<sub>2</sub>-8Y<sub>2</sub>O<sub>3</sub>/Ni-16Cr-6Al-0.3Y after 120 one-hour cycles of exposure to Mach 0.3 Na plus V doped combustion gases.



Session VII

**METALLIC ALLOYS**

## PROTECTIVE COATINGS FOR ELECTRIC UTILITY GAS TURBINES

by

J.A. Goebel, C.S. Giggins  
United Technologies Corp.,  
Pratt & Whitney Aircraft

M. Krasij  
United Technologies Corp.,  
Power Systems Division

J. Stringer  
Electric Power Research Institute

### Introduction

Sulfate-induced hot corrosion continues to be a major cause of turbine airfoil deterioration for industrial and utility gas turbines. Moreover, hot corrosion can be expected to be a continuing problem even for engines operating on relatively pure fuels. The reason for this is that airborne impurities present in the combustion air can contribute significantly to the formation of the types of sulfate deposits which cause hot corrosion. In this regard it has been observed that the use of more efficient inlet air filtration systems has led to substantial reductions of turbine hot corrosion, particularly in environments where the air may contain sea salt aerosols<sup>(1)</sup>. Nevertheless, it cannot be expected that inlet air filtration will eliminate hot corrosion, but merely reduce the severity. The important point is that in spite of the prospect that coal-derived fuels can be made to relatively high purity standards<sup>(2)</sup> gas turbines operating on such fuels will probably suffer hot corrosion at least to the degree currently experienced with clean distillate fuels.

Airfoil coatings used in today's industrial and utility gas turbines have in most cases been developed for aircraft engine applications. Experience with these coatings at United Technologies has shown that they lack the desired hot corrosion resistance when operated in industrial type engines which characteristically have lower turbine airfoil temperatures. The temperature range of concern has been 1100 to 1400<sup>o</sup>F, approximately, where conventional coatings such as the CoCrAlY-type (20% Cr-12% Al) have performed more poorly than expected. Anticipated performance had been based on laboratory hot corrosion tests at 1650<sup>o</sup>F or higher.

The initial phase of this coating development program involved the optimization of MCrAlY type overlay coatings for industrial/utility corrosion service. Particular emphasis was placed on laboratory testing to evaluate the hot corrosion resistance of modified MCrAlY compositions at low temperatures (i.e., 1200-1400°F). It was found that substantial improvements in coating life could be obtained at chromium concentrations in the range 30-35 w/o<sup>(3)</sup>. A farther-term parallel effort has been carried out concurrently, which has studied the corrosion resistance of more advanced coating compositions. Of special interest has been the evaluation of silicon-containing alloys and coatings for possible use as airfoil coatings.

Utility engine verification testing is an important part of the program, and two improved MCrAlY coatings have been selected for turbine airfoil hot corrosion testing in Pratt & Whitney FT4 engines. As reported previously<sup>(3)</sup>, Co-35Cr-8Al-0.5Y and Ni-20Co-35Cr-8Al-0.5Y coating compositions exhibited improved hot corrosion resistance compared to conventional Co-20Cr-12Al-0.5Y coatings in laboratory hot corrosion tests.

Engine testing has only recently been initiated at the Oakland, California Plant of Pacific Gas and Electric Company. Coatings are being tested on first turbine vanes in an FT4 engine operating on No. 2 distillate fuel. The test plan calls for a 1000h test, with an interim vane inspection at 500h. Experimental MCrAlY performance will be rated against standard, baseline CoCrAlY coatings inserted at the same time.

The primary purpose of this paper is to report on the progress of work to develop more advanced coatings under this program. The effort has been directed primarily toward evaluating duplex or two-layer coatings of the MCrAlY/Si and MCr/Si type. The objective of this test has been to evaluate both conventional and improved MCrAlY underlayers, applied by electron beam physical vapor deposition (PVD) and by low pressure chamber spray (LPCS) processes. In addition we are evaluating three methods to develop the silicon-rich overlayers. While this phase of the testing has not yet been completed, we are able to report on the results of burner rig testing of Co-20Cr-12Al-0.5Y (EB-PVD)/Si type duplex coatings.

## Experimental

Developmental coatings were applied on Mar-M509 test bars and exposed in ducted burner rigs at 1350<sup>0</sup>F and 1650<sup>0</sup>F. A description of the burner rigs and of the test conditions was provided previously<sup>(3)</sup>. PVD underlayers of Co-20Cr-12Al-0.5Y (nominal) composition were applied in the conventional manner: post-deposition glass bead peening, followed by heat treatment for 4h at 1975<sup>0</sup>F in hydrogen. Development of the siliconized outerlayer was accomplished in a separate operation using either PVD, slurry, or LPCS methods.

The fabrication of PVD CoCrAlY/PVD Si type overlay coatings has been described in detail elsewhere<sup>(4)</sup>. Siliconized overlayers are developed in a separate step using PVD to deposit pure silicon on the underlayer. The substrate is maintained at about 1850<sup>0</sup>F during and after deposition, in order to accomplish reaction of the silicon with the CoCrAlY underlayer. A typical duplex coating of this type has two metallographically discernable layers, Figure 1. Microprobe analysis of similar coatings has shown that the silicon concentration can be as high as 30% in the outerlayer; the layer itself consists of silicides of chromium and cobalt<sup>(4)</sup>.

Duplex coatings of similar structure and composition were successfully fabricated using an activated slurry technique to develop the outer silicide layer, Figure 1. It can be seen that the outer layers of the slurry Si coatings were slightly thinner (0.5-0.75 mils) than the PVD Si coatings (0.75-1.0 mils), but otherwise appeared very similar. The slurry was applied by air spraying and consisted of a mixture of silicon powder and lithium fluoride (activator) in a cellulose binder. Test specimens prepared in this manner were reaction heat treated in argon at 1800<sup>0</sup>F for 15 minutes. Two applications were found necessary to develop the required silicide thickness.

The fabrication of silicide overlayers by the direct LPCS application of silicon was unsuccessful. Silicon applied in this manner apparently did not react with the CoCrAlY underlayer and spalled off as the substrate cooled to room temperature. Conditions developed during deposition (time and temperature) were insufficient to permit reaction of silicon with the CoCrAlY underlayer. Only a single attempt at applying pure silicon was made.

As an alternate approach, the application of thin layers of pre-alloyed CoCrAlYSi on PVD CoCrAlY underlayers was attempted. These efforts were much more successful, and the microstructure of such a coating is shown in Figure 2. The structure of these outerlayers was very similar to those made by PVD or slurry, aside from being much rougher. The surface roughness is largely characteristic of plasma sprayed coatings in the as-deposited condition. The composition of the plasma spray powder (Co-10Cr-5Al-25Si-0.5Y) was selected to model the average composition of PVD silicide outerlayers as determined by electron beam microprobe analysis<sup>(4)</sup>.

### Results and Discussion

The degradation of PVD and slurry silicon duplex coatings was significantly less than for the single-layer CoCrAlY coatings in the 1350<sup>o</sup>F hot corrosion test. Figure 3 shows a plot of maximum depth of coating attack versus time in this burner rig test. Characteristically all of these coatings exhibited approximately linear rates of degradation after about the first 100h of exposure; actual curves were determined from a linear regression analysis of the data. It can be seen that the maximum depth of attack of PVD and slurry silicon coatings was only about 1.5 and 2 mils respectively after 1000h of testing. In contrast to this the monolayer CoCrAlY coatings suffered this amount of degradation in less than 100h.

Typical post-test corrosion microstructures for these coatings are shown in Figure 4. Degradation of the CoCrAlY coating, generally referred to as Type 2 attack, was characteristically severe. Attack of the PVD silicon duplex coating was confined to the outer, Si-enriched layer. Attack of the slurry silicon coating was slightly more severe, having penetrated the Si-enriched layer in several places. The fact that the slurry siliconized layers were somewhat thinner than the PVD layers is believed to be the reason for the deeper corrosion penetration. In general the degradation of these duplex coatings was much more uniform (less localized) than was found for (and is typical of) CoCrAlY monolayer coatings in this test. This is believed to be important because it means that the behavior of the duplex coatings is more predictable than is conventional CoCrAlY coatings. Although long term predictions of duplex coating behavior based on only 1000h of testing are considered risky, abrupt changes in the apparent rate of coating degradation are not expected. It was observed for example, that the slurry silicon outerlayers were penetrated in some areas as early as 600h of exposure. In spite of this, no significant change in the corrosion rate was observed.

In contrast to the performance of PVD or slurry duplex coatings, those with LPCS CoCrAlYSi overlayers performed poorly in the 1350<sup>0</sup>F burner rig test. As shown in Figure 5, one sample of this type of coating failed after only 300h, which is little better than conventional CoCrAlY coatings. A second sample also performed poorly; its corrosion rate increased continuously with time, behavior uncharacteristic of other coatings in this test.

Examination of the post-test microstructures of PVD CoCrAlY/LPCS CoCrAlYSi duplex coatings has provided an explanation for the unexpectedly poor performance of these coatings. Figure 6 shows the corrosion features of one sample after 600h of exposure at 1350<sup>0</sup>F. Attack of the overlayer has occurred along interfaces between successive layers of the plasma deposit built up as the substrate was rotated during the deposition process. In addition, corrosion has proceeded along the original PVD innerlayer/overlayer interface and into the innerlayer. This interface degradation is a direct cause of coating failure and has undoubtedly occurred because of insufficient bonding between successive plasma deposit layers. It is believed that a diffusion bonding heat treatment, if it had been performed after plasma deposition, would probably have prevented this mode of degradation.

In the high temperature hot corrosion test the corrosion resistance of the PVD silicon and slurry silicon duplex coatings was significantly lower than that of the conventional CoCrAlY baseline coating. Depth of attack data for the duplex coatings as a function of time, Figure 7, were essentially identical. The slurry silicon coating showed evidence of local penetration to the substrate after 100h of exposure. In contrast to this, the CoCrAlY baseline coating suffered only about one mil of attack after 1000h.

Typical microstructural features of the baseline CoCrAlY and a duplex coating are compared in Figure 8 after 600h exposure at 1650<sup>0</sup>F. Shown is the microstructure of the PVD silicon coating, however the features of the slurry silicon coating were very similar. Two important points must be made about the duplex coatings. First of all, the more severe degradation compared to the CoCrAlY coating is evident in Figure 8. Secondly, the microstructure of non-corroded portions has changed significantly when compared to the pretest condition, Figure 1, or to the 1350<sup>0</sup>F post-test microstructure, Figure 4. This change is due to the diffusion of silicon into the CoCrAlY underlayer during burner rig exposure. In fact, after 600h at 1650<sup>0</sup>F diffusion of silicon has occurred beyond the Mar-M509/coating interface to a depth of about 0.3-0.5 mils in the Mar-M509 substrate alloy.

The corrosion resistance of the CoCrAlY/LPCS CoCrAlYSi was poor in the 1650°F burner rig test. After 300h of testing localized corrosion penetration to the alloy/coating interface had occurred. Microstructural features have provided no obvious basis for the poor performance of this coating in the high temperature test. In contrast to the low temperature degradation of this coating, for example, there was no evidence that lack of bonding of the LPCS outerlayer to the PVD underlayer accelerated the degradation process.

#### Summary and Conclusions

The present studies have confirmed earlier ones which have shown that duplex CoCrAlY/Si type coatings are significantly more resistant to low temperature hot corrosion when compared to conventional CoCrAlY coatings. They have also shown that at high temperatures the corrosion resistance of the duplex coatings is actually less than that of monolayer CoCrAlY coatings. These results show that this type of coating has a maximum potential benefit on airfoils operating at temperatures lower than 1650°F. The reason for the improved low temperature hot corrosion resistance of silicon-enriched coatings is not known. It is believed, however that coatings of this type may form oxide scales containing SiO<sub>2</sub> and that these scales may be more resistant to the effects of molten salt deposits compared to Al<sub>2</sub>O<sub>3</sub> formed on conventional CoCrAlY coatings. In this regard, experiments have been performed to identify the composition of the oxide scales on these types of materials. Figure 9 shows a scanning electron micrograph of the surface of a coupon of Ni-40Cr-5Al/PVDSi after 500h oxidation at 1650°F. In areas where the oxide scale did not spall, Area "C" of Figure 9, energy dispersive x-ray analysis shows the presence of Si along with Cr, Ni, and Al in the oxide scale. Microprobe spectrometer mapping for oxygen has confirmed that the silicon detected is in the oxide scale.

The test results have also provided a comparison of the corrosion resistance of duplex coatings for which the siliconizing was achieved by three different methods. Overall, the PVD silicon outerlayer coatings performed best. Slurry type outerlayer coatings were only slightly less resistant, making this an attractive approach chiefly because of the simplicity of the method. As tested, LPCS plasma spray outerlayers performed poorly. Lack of a post-deposition diffusion heat treatment is suspected to be the basis for the poor performance, particularly in the low temperature test.

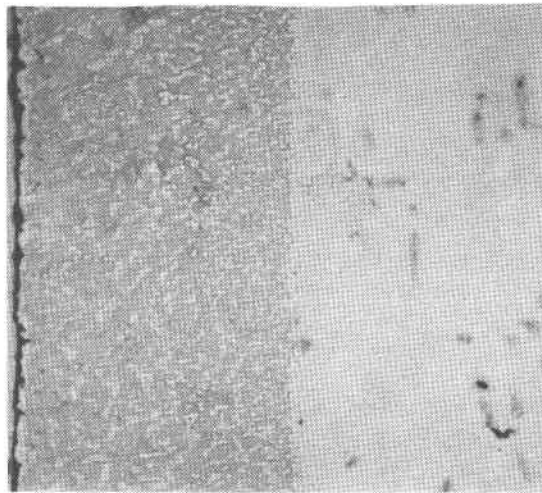
#### References

1. Hawkins, P., Proceedings of the 4th Conference on Gas Turbine Materials in a Marine Environment (1979); pp 49-67.
2. Neal, J.W., Proceedings of the First Conference on Advanced Materials for Alternative Fuel Capable Directly Fired Heat Engines (1979); pp 2-17.
3. Goebel, J.A., Ibid; P473.
4. Vargas, J.R., Ulion, N.E., and Goebel, J.A., Thin Solid Films vol. 73 (Nov. 1980); pp 407-413.

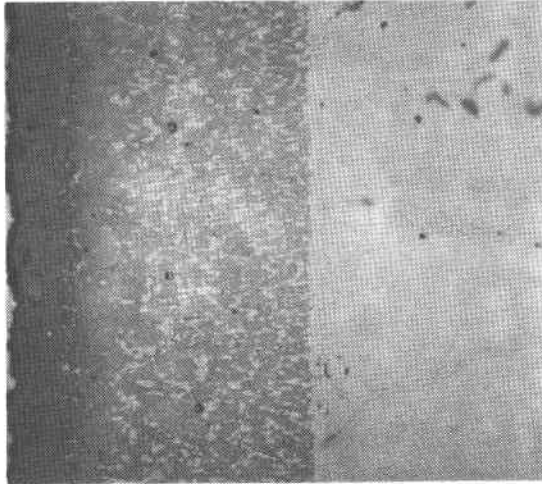


# PRETEST COATINGS ON MAR-M509

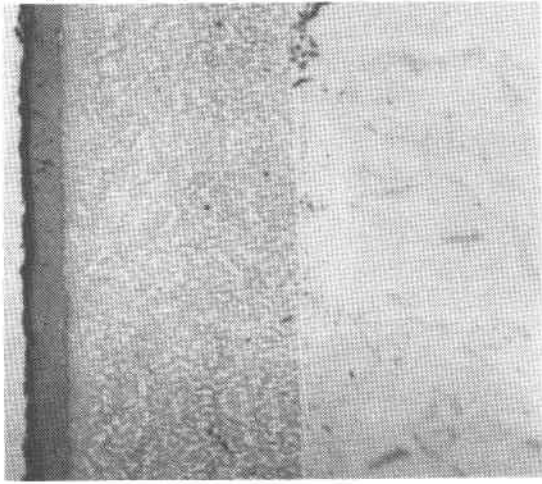
CoCrAlY: 20% Cr — 12% Al



**PVD CoCrAlY**



**PVD CoCrAlY/PVD Si**



**PVD CoCrAlY/Slurry Si**

Figure 1. Photomicrographs showing typical pretest microstructures of PVD CoCrAlY and PVD CoCrAlY/Si coatings.

# PRE-TEST PVD CoCrAlY/LPCS CoCrAlYSi ON MAR-M509

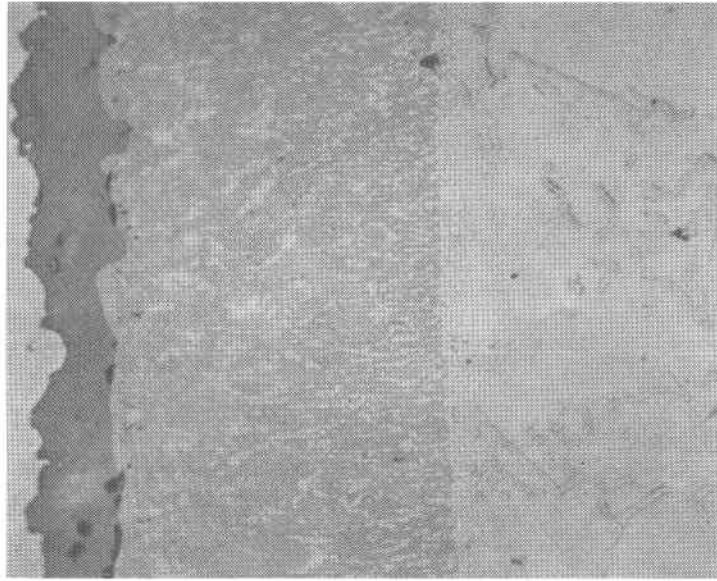


Figure 2. Photomicrograph showing typical microstructure of PVD CoCrAlY/LPCS CoCrAlYSi duplex coating. LPCS refers to low pressure plasma spray process. CoCrAlY: 20%Cr-12%Al; CoCrAlYSi: 10%Cr-5%Al-25%Si.

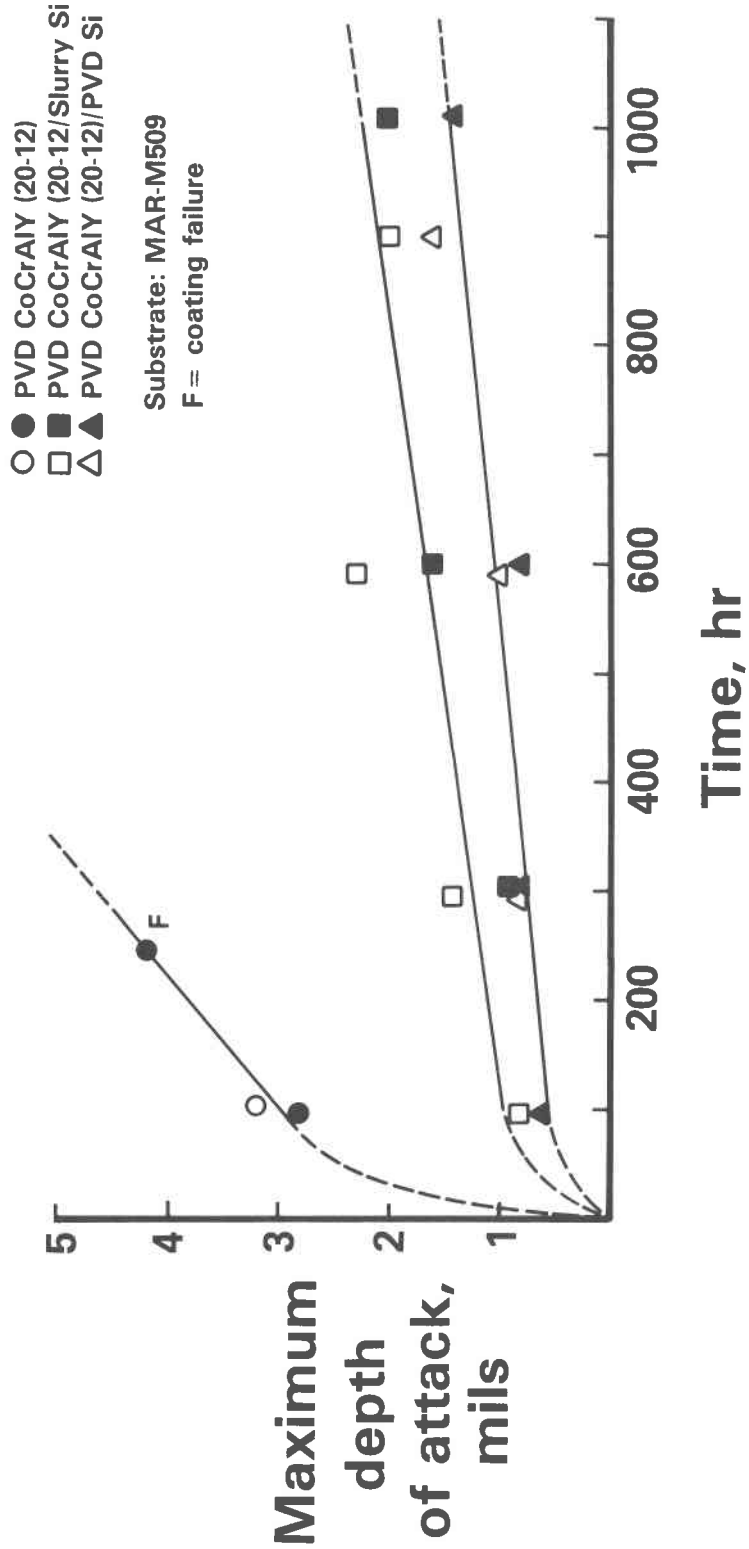
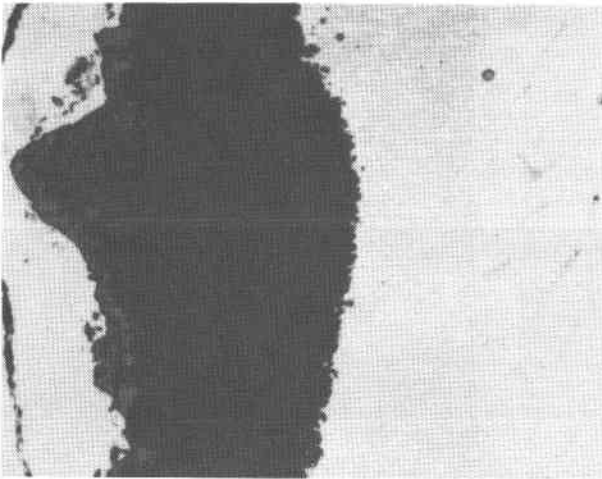
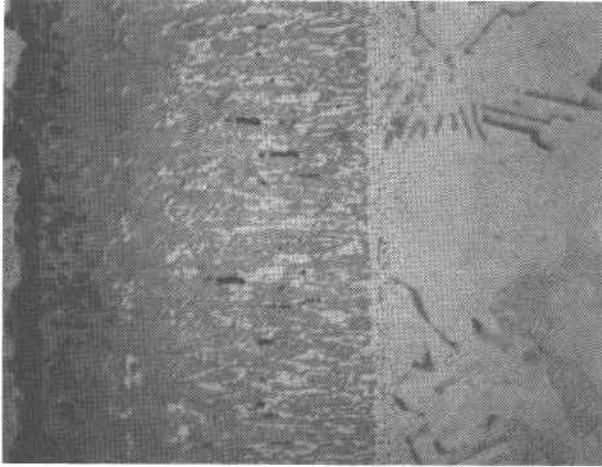


Figure 3. Plot of depth of maximum corrosion attack versus time for PVD CoCrAlY and PVD CoCrAlY/Si coatings in 1350°F ducted burner rig test: 20 ppm sea salt, 2.6% sulfur.



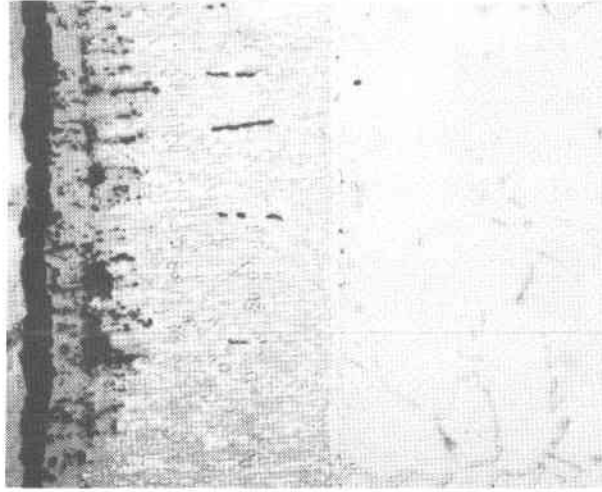
**PVD CoCrAlY**

**96 h**



**PVD CoCrAlY/PVD Si**

**1010 h**



**PVD CoCrAlY/Slurry Si**

**1010 h**

Figure 4. Photomicrographs showing typical hot corrosion microstructures from 1350°F burner rig test. Features of PVD CoCrAlY were typical for Type 2 attack.

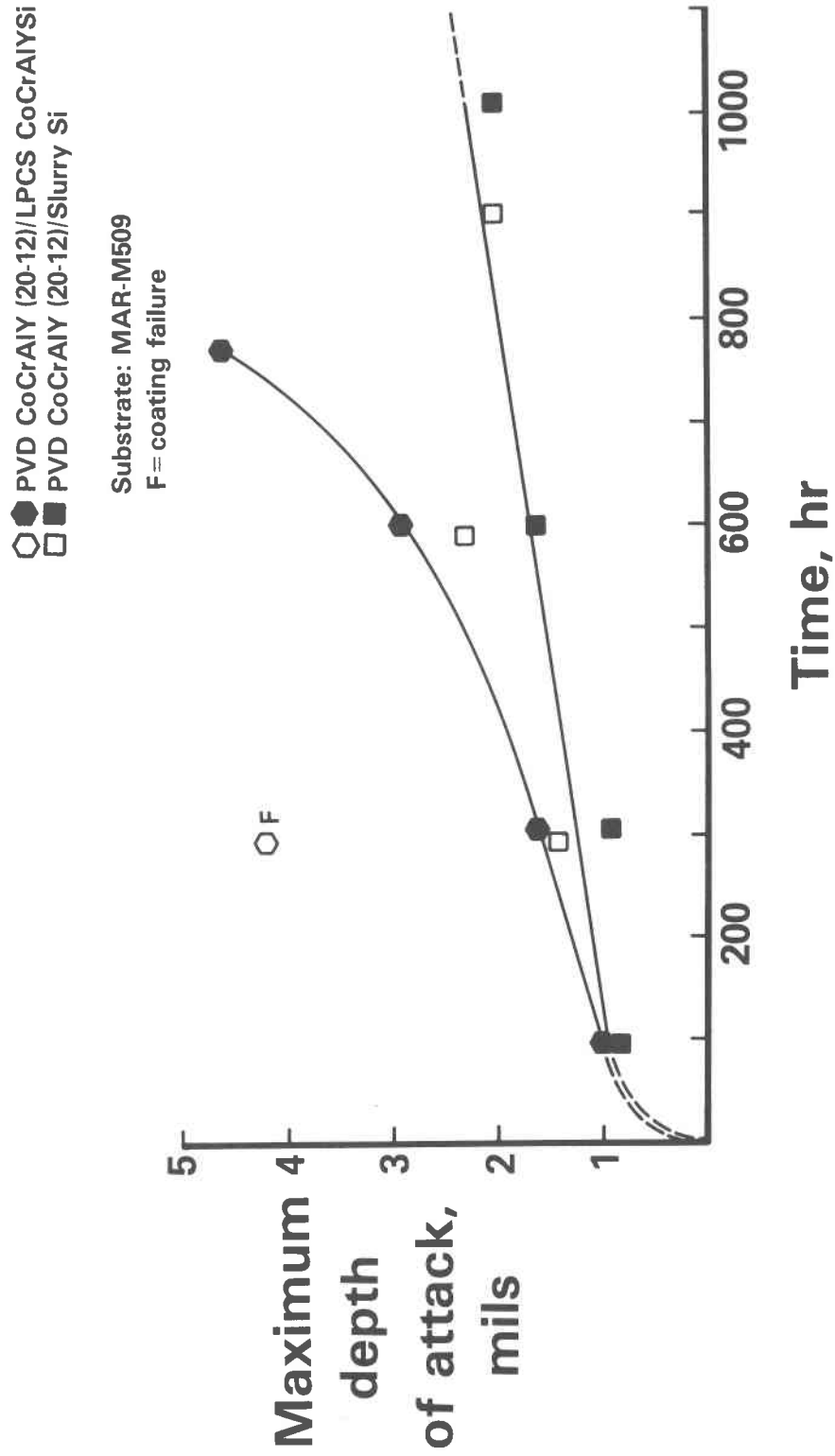


Figure 5. Plot of depth of maximum corrosion penetration versus time in 1350°F burner rig test (20 ppm sea salt, 2.6% sulfur). Data for PVD CoCrAlY/slurry Si coatings have been re-plotted from Figure 3 for comparison purposes.

## MAR-M509/PVD CoCrAlY/LPCS CoCrAlYSi

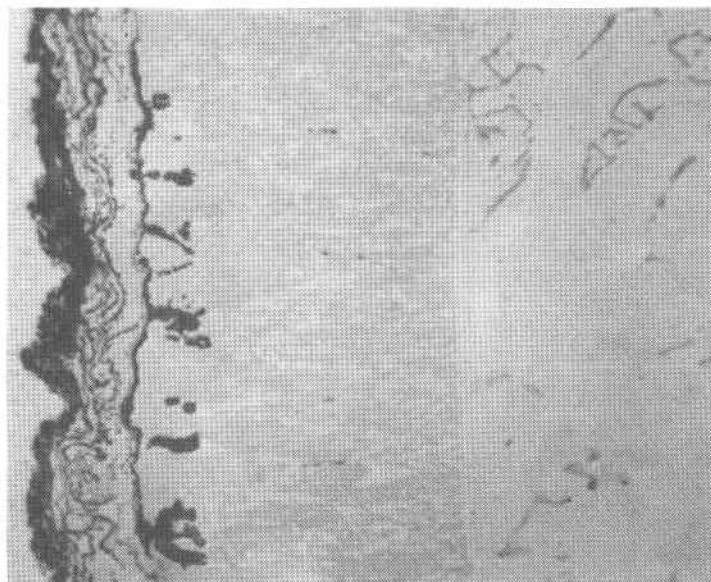


Figure 6. Photomicrograph showing typical hot corrosion microstructure from 1350°F burner rig test after 600h of exposure. Degradation of low pressure chamber spray (LPCS) Co-10Cr-5Al-25Si-0.5Y outer layer has occurred along poorly-bonded LPCS layers.

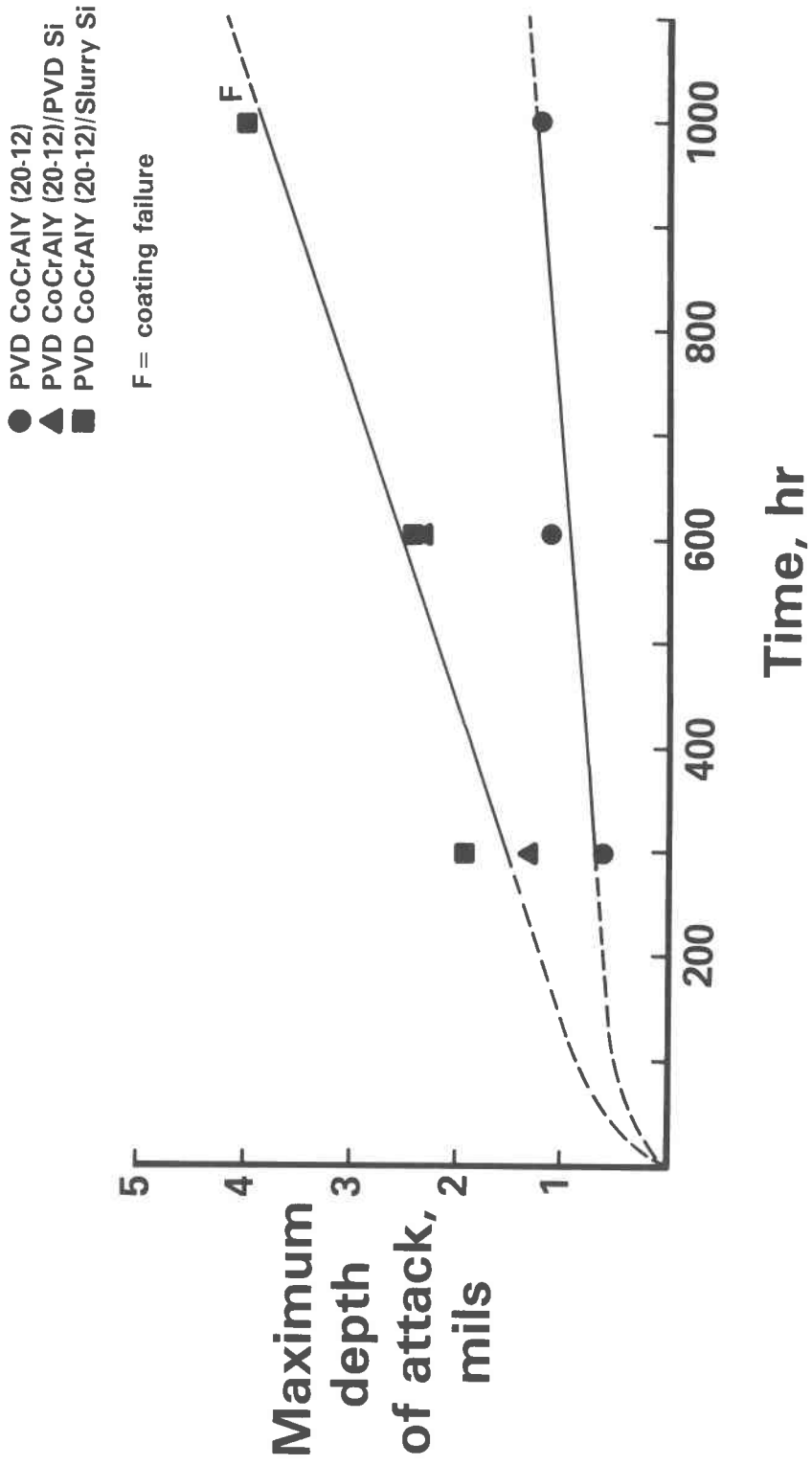
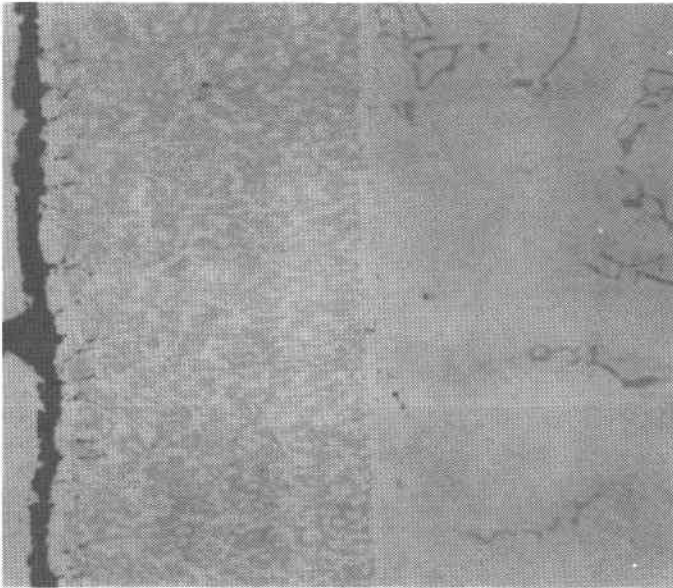
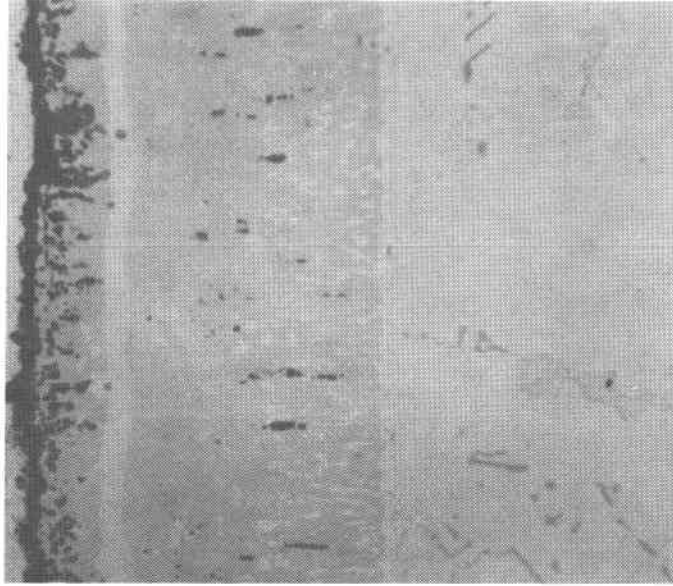


Figure 7. Plot of depth of maximum degradation versus time in 1650°F burner rig test (20 ppm sea salt, 1.3% sulfur) for PVD CoCrAlY and PVD CoCrAlY/Si coatings.



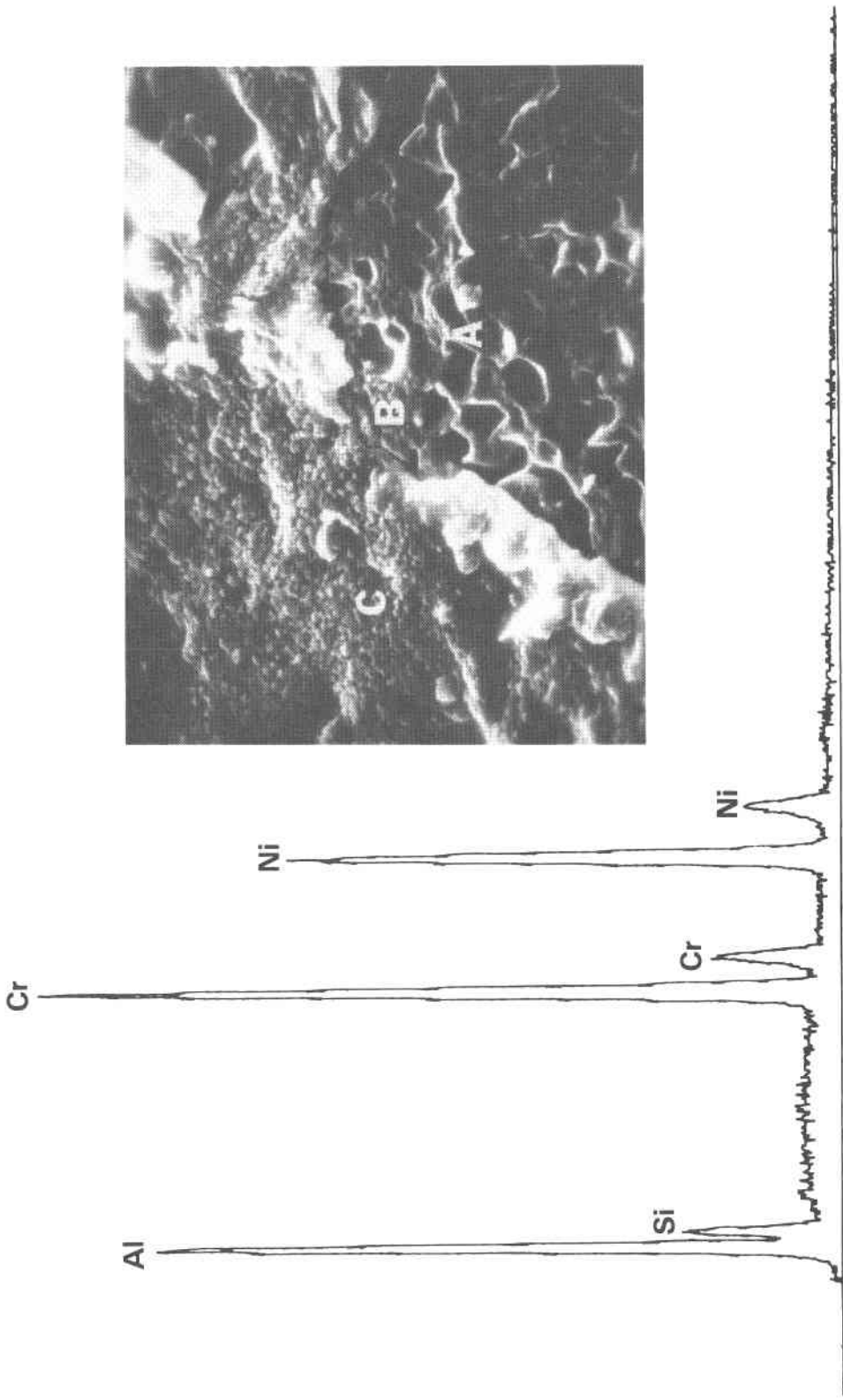
**PVD CoCrAlY**  
**600 h**



**PVD CoCrAlY/PVD Si**  
**600 h**

Figure 8. Photomicrographs showing hot corrosion microstructures of PVD CoCrAlY and PVD CoCrAlY/PVD Si after 600h in 1650°F burner rig test. Altered microstructure of duplex coating is due to interdiffusion between inner and outer layers.





20 kev

### EDX analysis

0 kev

Figure 9. Scanning electron micrograph and energy dispersive x-ray (EDX) analysis of in situ oxide scale from Ni-40Cr-5Al/Si coupon. Specimen was oxidized for 500h at 1650°F in air. EDX analysis from area C shows the presence of Si in an oxide scale which also contains Cr, Al and Ni.

Behavior of NiCrSi Coating Alloys  
in  $\text{Na}_2\text{SO}_4$ ,  $\text{V}_2\text{O}_5$ , and Mixed Salt Hot Corrosion

R. G. Corey,\* R. H. Barkalow, A. S. Khan, and R. J. Hecht  
Pratt & Whitney Aircraft Group  
Government Products Division  
West Palm Beach, FL 33402

INTRODUCTION

This program was initiated to address a fuel availability scenario which anticipated near-term utilization of low grade petroleum fuels and eventual switch-over to coal-derived liquids. This scenario depicted the need for turbine coatings capable of resisting both the hot corrosion and ash erosion effects due to vanadium, sulfur, and alkali metals in residual oils as well as the oxidation/interdiffusion degradation resulting from cleaner but hotter burning coal derived fuels. Since the former of these regimes appears inherently aggressive to thin alumina scales (1,2), it seems desirable to attempt coating development from alloys which depend for their environmental stability on scales other than alumina. The potential for improved durability of other scales is that chromia is thicker, while silica is believed to be essentially immune to acidic dissolution in molten salts.

High chromium coatings have successfully applied to superalloy substrates by pack, vapor deposition, and plasma spraying techniques, and it is clear that improved low temperature hot corrosion resistance can be obtained by increasing the chromium content of MCrAlY coatings (1). The feasibility and potential for good resistance to vanadium-induced hot corrosion of silicon diffusion coatings has also been demonstrated (3-5). Fundamental studies of the oxidation behavior of high chromium, silicon containing alloys have been carried out (6), and alloying additions which improve the stability of chromia scales and the mechanical properties of silicon diffusion coatings have been identified. Especially interesting from the point of view of both oxidation resistance and mechanical behavior are such concepts as pack- or PVD-siliconizing of the surface of MCrAlY coatings or coating compositions which result in the formation of an alumina or silica skin under a chromia scale, thus reducing environmental interactions by slowing diffusion across the scale as well as sealing the porous chromia against penetration by liquid salt deposits.

\*Now at Allied Corporation, Morristown, NJ, 07960

From this background, a program of furnace and burner rig testing was devised to evaluate the behavior of the following alloys in  $\text{Na}_2\text{SO}_4$ ,  $\text{V}_2\text{O}_5$ , and mixed salt hot corrosion:

- a) NiCrSi alloys of varying Cr and Si content
- b) Quarternary and active element additions to NiCrSi
- c) Cr-base alloys
- d) Si-34Cr-23Ta

Fundamental information about the corrosion behavior of these is being sought by determining material consumption and degradation microstructure versus the major hot corrosion variables (temperature, type and amount of salt, air versus  $\text{SO}_3$  and  $\text{V}_2\text{O}_5$  in the gaseous environment), with the ultimate goal of identifying systems and compositions suitable for further alloy and process development.

#### PROGRAM DESCRIPTION

The program is organized into the following four tasks:

##### Task I

Candidate coating alloys were subjected to furnace hot corrosion testing in air with deposits of  $\text{Na}_2\text{SO}_4$  and  $\text{V}_2\text{O}_5$ . Tests were run at temperatures of 700 to 900°C and salt quantities of approximately 1 to 10 mg/cm<sup>2</sup>. Severity of attack and degradation microstructure versus alloy composition were documented to identify promising systems and seek basic information on hot corrosion mechanisms.

##### Task II

Approximately 12 candidate coating alloys - selected directly from Task I compositions or modified slightly as suggested by Task I data - are being tested with mixed salt deposits ( $\text{Na}_2\text{SO}_4$  with additions of  $\text{V}_2\text{O}_5$ ,  $\text{K}_2\text{SO}_4$ , and PbO). Test temperatures and salt quantities parallel those of Task I so that results will establish the manner in which the components of the mixed salt interact to enhance or inhibit severity of attack.

##### Task III

Four candidate coating alloys and baseline MCrAlYs - applied by plasma spraying to superalloy substrates - will be subjected to tube furnace hot corrosion testing with  $\text{Na}_2\text{SO}_4$  and  $\text{V}_2\text{O}_5$  deposits and gaseous environments with controlled partial pressures of  $\text{V}_2\text{O}_5$  and  $\text{SO}_3$ . The presence of these gaseous species in the combustion products of contaminated fuels is known to affect the aggressiveness of condensed salt deposits.

##### Task IV

The Task III coatings will be applied to burner rig bars and exposed to high

velocity (approximately 250 m/sec) solid particle erosion in the combustion products of jet fuel. The test is designed to simulate the erosion, erosion-corrosion, and/or fouling effect of ash particles expected to be present in some types of residual oil and coal-derived fuels.

The outcome of this program will be the identification of coatings or coating systems with increased durability in the erosion/oxidation/hot corrosion environments to which industrial gas turbine engines may be exposed. Hopefully a contribution to fundamental knowledge of material behavior under these conditions will also emerge from a systemic analysis of the iterative results on the various trial compositions.

#### MATERIALS AND PROCEDURE

The candidate coating compositions were prepared as cast buttons from high purity elemental charges. Rationale for choice of the compositions was a systematic variation of Cr and Si content plus addition of elements such as Al, Mn, Ta, Nb, and Zr expected to modify oxidation behavior or effect improvements in mechanical properties or diffusional stability of high Cr, high Si coatings. The as-cast buttons were annealed for 24 hours at temperatures from 1080 to 1205°C for homogenization and stress relief.

Baseline materials for use in selected experiments were uncoated MAR-M509 (Co-23Cr-10Ni-7W-3Ta-0.6C), uncoated IN 671 (Ni-47Cr-0.2Ti), cast CoCrAlY (Co-23Cr-12Al-0.5Y), and CoCrAlY-coated MAR-M509.

Also tested under selected conditions were co-sputtered CrSi coatings (Cr-3.3Si and Cr-6.5Si) on MAR-M509 substrates.

Surfaces of bulk materials were prepared by grinding on 600 grit SiC paper. Deposits of  $\text{Na}_2\text{SO}_4$  and  $\text{NH}_4\text{VO}_3$  were applied by swabbing or spraying an aqueous solution; heavier deposits of  $\text{V}_2\text{O}_5$  were applied with a cellulose nitrate binder.

#### RESULTS AND DISCUSSION

##### 900°C Oxidation

To confirm expected oxidation behavior and gain experience in the metallography of the NiCrSi compositions, the alloys listed in Table I were exposed isothermally for 120 hours in static air. Visual inspection and weight changes identified most of the alloys as chromia formers, while Ni-12Cr and Ni-8Si formed mixed product layers. Metallography of the NiCrSi alloys showed no internal oxidation. Ni20Cr8Si appeared to have formed a thin layer, presumably  $\text{SiO}_2$ , beneath the

external  $\text{Cr}_2\text{O}_3$  scale; however the  $\Delta M/A$  value was not perceptibly changed.

Alloy wt%	$\frac{\Delta M}{A} \frac{mg}{cm^2}$	Products-Subjective*
Ni	8.30	NiO
Ni-2Cr	11.49	NiO
Ni-5Cr	5.95	NiO
Ni-12Cr	3.11	Mixed
Ni-20Cr	0.17	$\text{Cr}_2\text{O}_3$
Ni-30Cr	0.37	$\text{Cr}_2\text{O}_3$
Ni-40Cr	0.45	$\text{Cr}_2\text{O}_3$
Ni-50Cr	0.47	$\text{Cr}_2\text{O}_3$
Ni-75Cr	0.60	$\text{Cr}_2\text{O}_3$
Cr	0.78	$\text{Cr}_2\text{O}_3$
Ni-40Cr-2Si	0.19	$\text{Cr}_2\text{O}_3$
Ni-40Cr-5Si	0.19	$\text{Cr}_2\text{O}_3$
Ni-40Cr-8Si	0.25	$\text{Cr}_2\text{O}_3$
Ni-20Cr-2Si	0.28	$\text{Cr}_2\text{O}_3$
Ni-20Cr-5Si	0.24	$\text{Cr}_2\text{O}_3$
Ni-20Cr-8Si	0.72	$\text{Cr}_2\text{O}_3$
Ni-2Si	3.49	NiO
Ni-8Si	0.64	Mixed

\*Based on visual examination

Table 1. Weight gains of NiCr, NiSi, and NiCrSi alloys in isothermal oxidation; 120 hours at  $900^\circ\text{C}$ .

#### $900^\circ\text{C}$ $\text{V}_2\text{O}_5$ Hot Corrosion

The same alloys were exposed isothermally for 50 hours with deposits of  $3 \text{ mg/cm}^2$  of  $\text{V}_2\text{O}_5$ ; weight gains and the nature of the corrosive scales are listed in Table 2. Post-test metallography showed that scale/metal interfaces were generally more irregular with greater incidence of internal oxidation than in the initial oxidation experiment. Also, the data suggest a transition from a uniform to a layered

Alloy, wt%	$\frac{\Delta M}{A} \frac{mg}{cm^2}$	Product morphology in cross section
Ni	3.70	Uniform homogenous
Ni-2Cr	5.86	Uniform heterogenous
Ni-5Cr	4.98	Uniform heterogenous
Ni-12Cr	*	Uniform heterogenous
Ni-20Cr	4.94	Uniform heterogenous
Ni-30Cr	5.16	Uniform heterogenous
Ni-40Cr	4.13	Two layered
Ni-50Cr	4.37	Two layered
Ni-75Cr	4.66	Compact inner layer
Cr	15.33	Thick porous
Ni-40Cr-2Si	4.04	Two layered
Ni-40Cr-5Si	3.19	Two layered
Ni-40Cr-8Si	3.28	Irregular
Ni-20Cr-2Si	1.98	Two layered
Ni-20Cr-5Si	2.35	Two layered
Ni-20Cr-8Si	4.27	Compact inner layer
Ni-2Si	*	Largely homogenous
Ni-8Si	3.53	Two layered

Table 2. Weight gains of NiCr, NiSi, and NiCrSi alloys in isothermal hot corrosion; 50 hours at  $900^\circ\text{C}$  with  $3 \text{ mg/cm}^2$   $\text{V}_2\text{O}_5$ . \* = not meaningful; oxide spalled in handling.

scale morphology at Cr contents near 40% in binary alloys, and formation of layered structures at lower Cr contents in ternary NiCrSi compositions. However the layered structures did not bring about lower values of  $\Delta M/A$ .

### 815°C V<sub>2</sub>O<sub>5</sub> Hot Corrosion

Alloys listed in Table 3 were exposed for 512 hours (8 cycles of 64 hours each) at 815°C with deposits of 10 mg/cm<sup>2</sup> of V<sub>2</sub>O<sub>5</sub>; the specimens were washed and lightly

	Wt Change After 7 Cycles mg/cm <sup>2</sup>	Metal Loss mils	After No. Cycles	Comments
Ni-40Cr-8Si	+ 4.0	2	8	Liquid retained. Rough protrusions.
Ni-25Cr-8Si	-27.9	11	8	Regular spalling of oxide sheets.
Ni-60Cr-8Si	+62.8 <sup>1</sup>	1	8	Liquid retained. Smooth faces, bulging edges.
Ni-40Cr	-24.3	6	8	Regular spalling of oxide sheets.
Co-40Cr-8Si	ND <sup>2</sup>	4	4	Regular spalling. Alloy cracking.
Ni-32Cr-8Al-8Si	+44.6	2	8	Liquid retained. Rough appearance.
Ni-32Cr-8Nb-8Si	-25.2	12	8	Regular spalling of oxide sheets.
Ni-40Cr-8Si-1Zr	+10.7	1	8	Liquid retained. Smooth surface.
Ni-40Cr-12Si	+14.9	3	8	Liquid retained. Mounds develop.
Ni-50Nb-8Si	ND <sup>3</sup>	39	1	Failed at 1st-cycle.
Cr-18Ni-15Si	- 2.1	11	8	Spongy oxides. Occasional spalling.
Cr-20Ni-5Si	+39.1 <sup>1</sup>	5	8	Spongy oxides. Occasional spalling.
Cr-20Ni-5Si-5Al	+40.2 <sup>1</sup>	ND	NA	Spongy oxides. Occasional spalling.
Cr-20Ni-5Si-10Nb	+48.6 <sup>4</sup>	4	6	Spongy oxides. Occasional spalling.
Cr-20Ni-5Si-1Zr	+48.6	5	8	Spongy oxides. Occasional spalling.
Ni-40Cr-12Ta-8Si	-19.3 <sup>5</sup>	4	8	Regular spalling of oxide sheets.
Ni-40Cr-8Mn-8Si	+43.1 <sup>6</sup>	2	7	Thick products. Powdery spall.
Si-34Cr-23Ta	NA <sup>7</sup>	NA	NA	No evident attack.
Cr-3.3Si/MAR-M 509	-45.7 <sup>8</sup>	5	4	Spongy products, occasional spalling.
Cr-6.5Si/MAR-M 509	-52.1 <sup>8</sup>	3	4	Spongy products, regular spall to metal.
MAR-M 509	-51.6	11	8	Regular powdery spalls.
CoCrAlY/MAR-M 509	-40.1 <sup>8</sup>	60% <sup>9</sup>	4	Coating defeat at 1st-cycle and growing.
Bulk CoCrAlY	-112.4	8	8	Regular spalling of oxide sheets.

<sup>1</sup> Chipping of specimen or change of broken wire required extrapolation from values unaffected by the weight change produced other than by corrosion.

<sup>2</sup> Specimen chipped regularly preventing extrapolation of weight change.

<sup>3</sup> Specimen completely defeated after 1 cycle.

<sup>4</sup> After 5 cycles.

<sup>5</sup> Specimens attacked preferentially at casting inhomogeneity on first cycle. Reported value is from second to eighth cycles.

<sup>6</sup> After 6 cycles.

<sup>7</sup> Testing continuing, metallography not performed.

<sup>8</sup> After 4 cycles.

<sup>9</sup> Percent coating defeat.

Table 3. 815°C hot corrosion of cast coating alloys; 512h with 10 mg/cm<sup>2</sup> V<sub>2</sub>O<sub>5</sub>.

brushed to remove loose scale prior to reapplication of fresh salt after each exposure cycle. Weight changes, depth of corrosion penetration, and a qualitative assessment of the morphology and adherence of the reaction products are also listed in the Table.

For the purpose of initial screening of promising systems, significance was attached to the retention of apparently unreacted  $V_2O_5$  on some of the specimens versus complete reaction of the deposit on most of the alloys. The compositions which retained unreacted melt after each exposure cycle were:

Ni-40Cr-8Si	Ni-40Cr-8Si-1Zr
Ni-60Cr-8Si	Ni-40Cr-12Si
Ni-32Cr-8Si-8Al	Si-34Cr-23Ta

The obvious trend in this listing is the relatively good performance of the high chromium, silicon-containing alloys.

The silicon effect was also evident in X-ray element maps of the corroded Si-containing compositions. Figure 1, for example, shows Si-rich inclusions in the scale formed on Ni40Cr8Si, while Figure 2 shows greater amounts of the Si-rich oxide and suggests the possibility of forming a continuous  $SiO_2$  underlayer at sufficiently high Si contents. The corrosion products on the quaternary Ni32Cr8Al8Si sample also contain  $SiO_2$  inclusions and Al-rich subscale (Figure 3), although their morphology and distribution do not appear to be protective.

#### 900°C $Na_2SO_4$ Hot Corrosion

The alloys listed in Table 4 were exposed in the same manner (8 cycles of 64 hours, with water washing and reapplication of fresh salt between cycles) with deposits of  $5 \text{ mg/cm}^2$  of  $Na_2SO_4$ . As expected, these deposits were found to be much less aggressive than the  $V_2O_5$  of the preceding test, although four of the samples suffered severe attack. The ternary and quaternary Si-containing alloys exhibited mixed reaction products, but the mixed scales appeared to be generally adherent and protective.

#### WORK IN PROGRESS

The high chromium, high silicon alloys which showed potential for good resistance to vanadium-induced corrosion in the Task I experiments will be evaluated as described in the program plan.

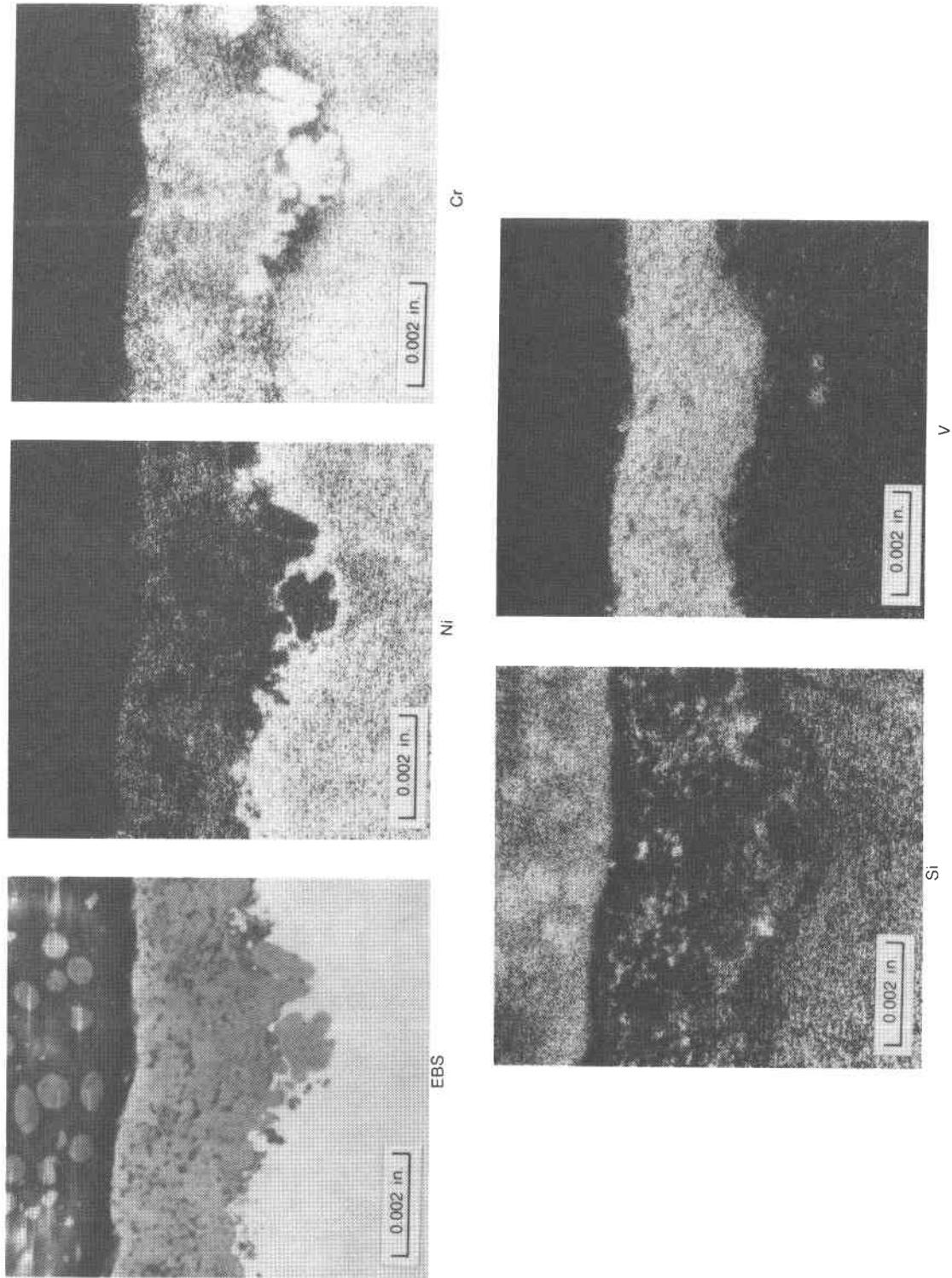


Figure 1. X-ray microprobe analysis of Ni-40Cr-8Si after 8-64 hour cycles,  $10 \text{ mg/cm}^2 \text{ V}_2\text{O}_5$ ,  $815^\circ\text{C}$ .



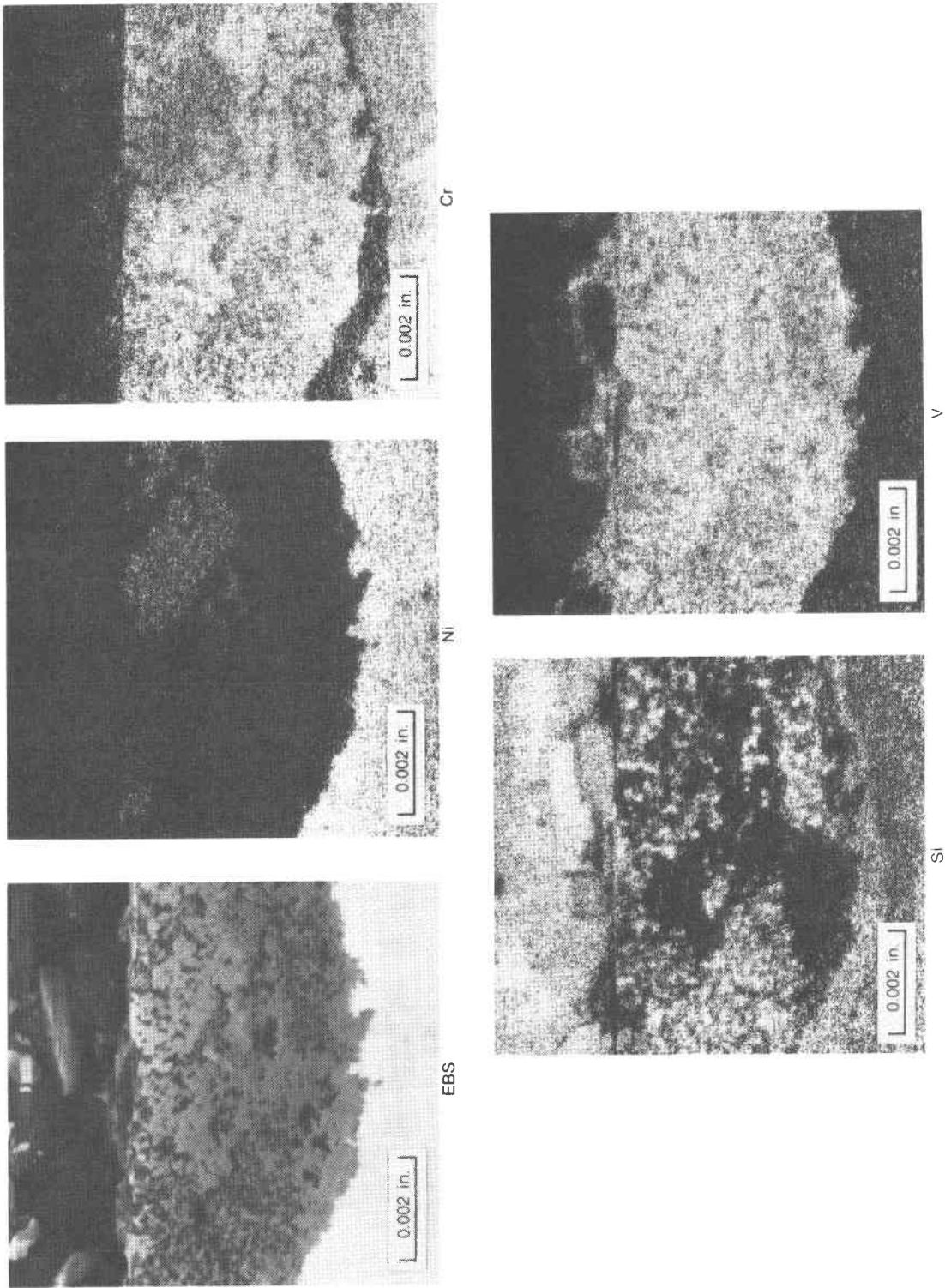


Figure 2. X-ray microprobe analysis of Ni-40Cr-12Si after 8-64 hour cycles,  $10 \text{ mg/cm}^2 \text{ V}_2\text{O}_5$ ,  $815^\circ \text{C}$ .

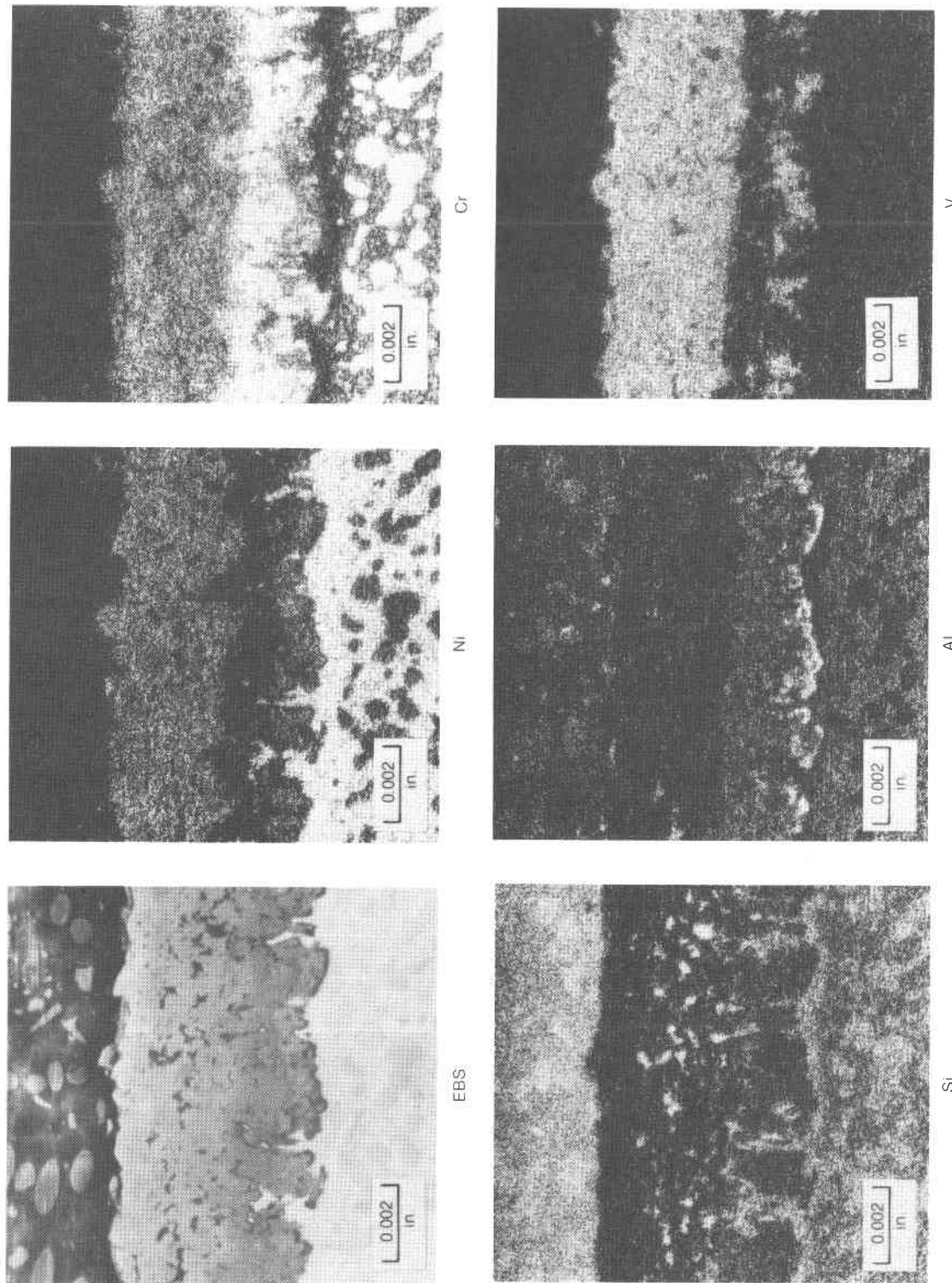


Figure 3. X-ray microprobe analysis of Ni-32Cr-8Al-8Si after 8-64 hour cycles, 10 mg/cm<sup>2</sup> V<sub>2</sub>O<sub>5</sub>, 815°C.

Alloy	Total Wt Change 8 Cycles mg/cm <sup>2</sup>	Comments*
Ni-40Cr-8Si	- 7.6	Cr <sub>2</sub> O <sub>3</sub> former
Ni-25Cr-8Si	+16.9 <sup>1</sup>	Rapid attack upon 1st cycle
Ni-60Cr-8Si	- 7.4	Cr <sub>2</sub> O <sub>3</sub> former
Ni-40Cr	- 4.9	Cr <sub>2</sub> O <sub>3</sub> former
Co-40Cr-8Si	- 7.4	Cr <sub>2</sub> O <sub>3</sub> former
Ni-32Cr-8Si-8Al	- 0.3	Al <sub>2</sub> O <sub>3</sub> former
Ni-32Cr-8Si-8Nb	- 4.8	Cr <sub>2</sub> O <sub>3</sub> former
Ni-40Cr-8Si-1Zr	- 6.0	Cr <sub>2</sub> O <sub>3</sub> former
Ni-40Cr-12Si	- 8.0	Cr <sub>2</sub> O <sub>3</sub> former
Ni-50Nb-8Si	NA	Failed in 2 cycles
Cr-18Ni-15Si	- 5.8	Cr <sub>2</sub> O <sub>3</sub> former
Cr-20Ni-5Si	- 5.2	Cr <sub>2</sub> O <sub>3</sub> former
Cr-20Ni-5Si-5Al	- 2.9	Al <sub>2</sub> O <sub>3</sub> first 3 cycles
Cr-20Ni-5Si-5Nb	- 3.9	Cr <sub>2</sub> O <sub>3</sub> former
Cr-20Ni-5Si-1Zr	- 4.1	Cr <sub>2</sub> O <sub>3</sub> former
Ni-40Cr-8Si-12Ta	- 4.0	Cr <sub>2</sub> O <sub>3</sub> former
Ni-40Cr-8Si-8Mn	-12.5	Black scale, pitted
Ni-17Ta-19Cr-15Si	- 1.0	Mixed products
Si-34Cr-23Ta	- 0.3 <sup>2</sup>	Mixed products
Ni-23Cr-26Ta-16Si	- 4.1 <sup>3</sup>	Mixed products
Co-20Ni-5Si-5Mn	- 4.1 <sup>3</sup>	Black scale
MAR-M 509	- 1.6	Black scale
CoCrAlY/MAR-M 509	- 0.04	Al <sub>2</sub> O <sub>3</sub> former
Bulk CoCrAlY	+ 0.3	Cr <sub>2</sub> O <sub>3</sub> former
Cr-3.3Si/MAR-M 509	-10.4 <sup>4</sup>	Rapid attack
Cr-6.5Si/MAR-M 509	-11.2 <sup>4</sup>	Rapid attack

\* Scale products based on visual examination.

<sup>1</sup> Following 1st cycle. Subsequent weight changes were erratic.

<sup>2</sup> Rapid attack at casting heterogeneity on 1st cycle. Reported value is between 2nd and 8th cycles.

<sup>3</sup> Extrapolated from values unaffected by change of support wire.

<sup>4</sup> After 4 cycles.

Table 4. Hot corrosion of cast coating alloys; 512 hours (8 cycles of 64 hours) at 900°C with 5 mg/cm<sup>2</sup> Na<sub>2</sub>SO<sub>4</sub>.

#### REFERENCES

1. C.S. Giggins and R.J. Fenton: Interim Technical Reports on Contract No. N00024-78-C-5337, Metallic Coating Development and Evaluation Program, P&WAG/GPD for Naval Sea Systems Command.
2. R.H. Barkalow and F.S. Pettit: High Temperature Erosion and Erosion-Hot Corrosion with Various Types of Solid Particles. Proc. 5th Int. Conf. on Erosion by Solid and Liquid Impact, Cavendish Laboratory, Univ. of Cambridge, Sept. 1979, paper #44.
3. E. Fitzner and J. Schwab: Attack of Scaling-Resistant Materials by Vanadium Pentoxide and Effect of Various Alloying Elements thereon. Corrosion, Vol. 12, (sept. 1956) pp. 459-464.
4. R. Bauer, H. Grunling, and K. Schneider: Silicon and Chrome Base Coatings for Stationary Gas Turbines. Proc. First Conf. on Advanced Materials for Alternative Fuel Capable Directly Fired Heat Engines, J.W. Fairbanks and J. Stringer, Eds., NTIS No. CONF 790749 (Aug. 1979), p. 505.
5. E. Fitzner et al: Aluminum and Silicon Base Coatings for High Temperature Alloys - Process Development and Comparison of Properties. Proc. Int. Conf. on Metallur-

gical Coatings, San Diego, CA; 23-27 April 1979, Elsevier Sequoia S.A., J.N. Zemel, Ed., 1979, pp. 305-320.

6. K. Ledieff, A. Rahmel, und M. Schorr: Oxidation und Aufkohlung hochgelierter Werkstoffe für Crackrohre; Teil 1: Das Oxidationsverhalten in Luft. Werkstoffe und Korrosion 30, 767-784 (Mai 1979).

#### ACKNOWLEDGEMENTS

This work was supported by the U.S. Department of Energy under Contract No. DE-AC03-79ET15322.

CHANGES IN HOT CORROSION DUE TO COMPOSITION MODIFICATIONS  
IN CoCrAlY COATINGS\*

J.T. PRATER, J.W. PATTEN, D.D. HAYS, AND R.W. MOSS  
Pacific Northwest Laboratory,\*\* Richland, WA 99352

J.W. FAIRBANKS  
Heat-Engine and Heat Recover Division, Office of Coal Utilization,  
Department of Energy, Washington D.C.

Burner rig and engine test which describe differences in the hot corrosion resistance of sputter deposited CoCrAlY coatings with varied compositions and coating designs are presented. The objective of this study is to determine the potential of modifying CoCrAlY coatings to provide significantly longer lifetimes for gas turbine engine components operating on alternative fuels or in marine environments. Modified coatings that contain a high chromium surface composition, a gradient in chromium and aluminum composition, and a platinum underlayer or graded platinum addition have been examined. Twenty-nine different samples have been burner rig tested for 500 hours at 677°C (1250°F) in an aggressive, marine-type hot corrosion environment and then ranked according to their performance. Also, four chromium rich coatings have been tested for 20 hours in a Rolls Royce Olympus C turbine engine operated at 1067°C on residual fuels. Results from these tests indicate that a high chromium surface composition, and composition gradients through the coating thickness can improve the hot corrosion resistance of coatings in aggressive, low temperature environments.

---

\* This research supported by U.S. Department of Energy under  
Contract DE-AC06-76RLO-1830

\*\* Operated by Battelle Memorial Institute

## INTRODUCTION

Gas turbine hot-section vanes and blades operating with current light distillate fuels are often life-limited by hot corrosion effects (oxidation/sulfidation), particularly in marine environments or in the presence of fuel contaminants such as sulfur and vanadium<sup>(1)</sup>. The severity of these effects is multiplied by the use of more plentiful residual fuels and may be drastically increased by the use of minimally processed coal-derived liquid fuels. The plentiful supply of coal in the continental United States balanced against decreasing reliability and increasing expense of petroleum fuel sources further emphasizes the need to develop coating systems capable of withstanding long-term use of minimally processed coal-derived fuels and other potentially dirty fuels. Currently it is not technically feasible to use ceramic materials for airfoils<sup>(2,3)</sup>, and although ceramic coatings for airfoils hold great potential<sup>(4-6)</sup>, development of these coatings to the production stage is a long-term effort. Because of this, it is necessary to aggressively pursue improvements in existing protective coatings to permit expanded near-term use of residual fuel and coal-derived liquid fuels.

Present state-of-the-art production coatings for protection of gas turbine hot section vanes and blades from hot corrosion are variations of MCrAlY (frequently CoCrAlY) compositions. Extensive research efforts historically have been concentrated on those coatings prepared by electron beam physical vapor deposition (PVD) techniques<sup>(7-9)</sup>. More recently, coatings with these same compositions have been deposited by high-rate sputter deposition at Pacific Northwest Laboratory (PNL). These coatings are strongly bonded to the substrates, are defect- or leader-free and are very fine grained with a very uniform composition distribution<sup>(10,11)</sup>. Engine and burner rig tests of early sputter deposited coatings show their performance to be comparable to the most advanced PVD coatings. The present study seeks to utilize the unique advantages offered by PNL sputter-deposition equipment and techniques to establish improved coating compositions and structures for use in marine environments and for operation with residual and coal-derived fuels.

Several modified coating designs have been included in the present study. Half of the coatings have been prepared with a high chromium and a high chromium to aluminum concentration ratio at the coating surface. Especially at operating temperatures below 850°C the selection of these parameters is important. The optimum value is expected to be one that promotes the rapid formation of a

chromium oxide scale for early protection, with an aluminum oxide gradually replacing the chrome oxide at longer times. Several of the present coatings have been prepared with an aluminum composition gradient which increases the aluminum concentration at greater depths into the coating. This design provides for a gradual shift towards increased aluminum content in the coating surface region at longer service times. This should enhance the transition of the scale from the initial chromium oxide to aluminum oxide at longer service times. Besides affecting the corrosion behavior the presence of Cr and Al composition gradients in these coatings is expected to affect the coating durability by influencing coating ductility and thermal expansion coefficients at the coating-substrate interface. As a possible method for reducing the problems that arise from coating - substrate interdiffusion many of the samples have been prepared with a platinum underlayer deposited on the substrate before the CoCrAlY coating is sputter deposited. The formation of platinum compounds, e.g. platinum aluminides, is expected to restrict the mobility of selected elements. Coatings with graded platinum additions have also been prepared to establish the optimum distribution of platinum. The importance that each of these modifications will have on improving coating corrosion resistance will depend on such factors as service temperature, hot corrosion environment, coating and substrate compositions, coating microstructure, etc.

#### Experimental Procedures

Dual target, d.c. supported discharge, high rate sputter deposition techniques developed at PNL have been used to prepare the CoCrAlY coatings for this study. The sputter deposition equipment and procedures are described in detail elsewhere<sup>(10)</sup>. Briefly, CoCrAlY deposits with different compositions and composition gradients are prepared with two independent, opposing flat plate targets of CoCrAlY and either Al, Cr, or Pt. The platinum underlayers are deposited between two concentric cylindrical Pt targets.

To date, 210 coatings have been prepared for testing and metallographic characterization. The different processing parameters used are: variations in the Cr and Al concentration, composition gradients through the coating thickness, the presence or absence of platinum underlayers and graded platinum deposits, deposition on X-40, Marz-M-509, In 792, or In 738 substrates, and the choice of different heat treatments prior to testing.

Twenty-nine sputter coated pins, ~ 3 mm in diameter and 35 mm long, and three PVD control samples, listed in table I, were tested at Annapolis Naval Ship Research and Development Center (NSRDC). The test ran for 500 hours in a low velocity, atmospheric pressure burner rig operated on marine diesel fuel containing 2% sulfur<sup>(12)</sup>. An aggressive, low temperature, hot corrosion environment was induced by making 10 ppm salt additions to the inlet air. During the test, the samples were cycled from an operating temperature of 677°C (1250°F) to room temperature every 24 hours.

In addition to this burner rig test, four high chromium CoCrAlY coatings, listed in Table II, were tested for 20 hours in a Rolls Royce Olympus C turbine operated on commercially available residual heating fuels. Blade temperatures ranged from 500-840°C. Each of the In 738 C turbine blades was first coated with a 5 µm platinum underlayer and then covered with an 145 µm CoCrAlY coating. The coating was graded such that the chromium composition was a maximum at the coating surface. Three of the blades were preoxidized for one hour at 1080°C in air before the start of the test.

## Results and Discussion

The Annapolis burner rig test provided an aggressive, low temperature, hot corrosion environment for evaluation of the samples. Following the test, a surface examination of the upper portion of each of the test pins by Auger Electron Spectroscopy and X-ray Photoelectron Spectroscopy revealed that the pins were almost completely covered with  $\text{Na}_2\text{SO}_4$ ,  $\text{CaSO}_4$ , and mixed silicates. Only trace signals of sulfides and oxides were observed. A subsequent study with a scanning electron microscope (SEM), equipped with energy dispersive spectrometry for composition analysis, showed that the oxide scale was covered by a heavy deposition of sodium, calcium, and magnesium sulfates; calcium and magnesium silicates; potassium sulfate and potassium chloride. X-ray diffraction confirmed the presence of  $\text{Na}_2\text{SO}_4$  and the existence of oxide spinels, either  $\text{CoAl}_2\text{O}_4$  or  $\text{Co}_2\text{CrO}_4$ . Following a water wash of the surface only the oxide scale and oxide particles remained. The oxide was found to contain P and Si (up to 9 wt%) and a small amount of sulfur (typically 1 wt%). Examination of the pins in cross section showed that the corrosion product consisted of a dense scale that contained sulfides. There was no appreciable depletion zone in the alloy below the pit, as shown in Figure 1.



The samples that were burner rig tested at Annapolis are listed in Table I. These coatings have been ranked according to post-test metallography results which measured the average and the deepest penetration of corrosion product. All of the pins from the burner rig tests were sectioned at three locations for metallographic examination. These sections were taken 6.35 mm from the top; 6.35 mm from the test carousel, and in the middle of the exposed 22 mm test length. If a localized area of corrosion would have been missed by these sectioning locations, they were modified so as to include that area. For each sample, depth of corrosion attack measurements were made every 20 degrees around the circumference of each of the three cross-sections. These 54 measurements were then averaged to yield an average depth of attack for each coating. The maximum observed depth of attack found on any of the cross-sections was also recorded.

Analysis of the depth of attack data showed that coating composition was the dominant factor in determining the corrosion resistance of the coatings. The lack of redundancy in the samples made it impossible to determine whether the use of different substrate materials or the deposition of a platinum underlayer had a minor effect on coating performance. However, it was clear that in this test the effect was very small when compared to the effect of coating composition. Table III presents the depth of attack results for the six general types of coating compositions studied. In general, the sputtered coatings were superior to similar control PVD coatings. Samples with a low surface concentration of aluminum, i.e. 1-4 wt% Al, were found to be more resistant to the variety of hot corrosion experienced in this test than samples with 8-11 wt% Al at the coating surface. Excellent corrosion resistance was obtained from the CoCrAlY coating that had a starting surface composition of 29 wt% Cr, 4 wt% Al, 1.2 wt% Y and the balance as cobalt (see samples 1021, 5034 and 5005). This coating is shown in Figure 2. The graded Pt-CoCrAlY samples were also found to have very good corrosion resistance (see samples 1048, 2014 and 5007). These coatings, shown in Figure 3, contained a platinum gradient that peaked at 90% near the center of the coating thickness and then decreased to 10% at the coating surface. The scale that formed on these samples was a mixed Cr-Al-Co oxide that contained no platinum.

A gradient in the Al composition that increased its concentration as a function of coating depth appeared to be beneficial in minimizing the occurrence of deep localized attack. This was dramatized by the group II coatings (see samples 2042, 2010 and 5003) which contained a concentration gradient in which the aluminum composition increased from 3% up to 19% as a function of depth into

the coating, as shown in Figure 4. Homogenization of this coating occurred during the course of the 500 hour test and eventually brought the coating composition to a uniform 20% Cr and 15% Al, i.e. during the test the surface composition increased gradually from 3% to 15% Al. In general, test results showed that the graded coating performed better than either the homogeneous 3% Al (starting surface composition of the graded coating) or the 9% Al (intermediate surface composition of the graded coating) samples (see samples 1005, 2047, 5012, 2051, 2035 and 2054). It appears that a composition gradient in which the aluminum content was increased into the coating thickness was beneficial.

Interdiffusion between the coating, the substrate pins and the platinum underlayers was examined with SEM. Composition profiles across the coating showed that by the conclusion of the 500 hour test, substrate alloying elements, in particular Ta, W and Ni, had permeated through the coating thickness (~ 130  $\mu\text{m}$ ) at a concentration of about 1%. The presence of a platinum underlayer did not affect the diffusion of these three elements. Also, by the conclusion of the 500 hours at 677°C the platinum underlayers had broadened to a width of 45  $\mu\text{m}$  and were present in the CoCrAlY as a second phase, rich in aluminum and titanium, as shown in Figure 5. After 500 hours at 677°C very little aluminum had diffused out of the coating and into the substrate. In this study, the presence of a platinum underlayer actually accelerated aluminum depletion of the coating since aluminum diffused rapidly to the platinum rich phase. However, the effect that the Pt underlayer would have on the long-term loss of aluminum from the coating after longer times, or at higher temperatures was not established.

Titanium and molybdenum are superalloy element additions, present in In 792, that are considered to aggravate the hot corrosion<sup>(13)</sup> of alloys if they are present at the surface. Therefore, it is important to devise coating designs that can minimize the outward diffusion of substrate elements through a coating. In this study the platinum phase was observed to attract the titanium. Thus, the platinum underlayer might be expected to have long term significance on coating performance. Regrettably, in the present study the time was too short and the temperature too low to have tested this hypothesis. Neither Mo nor Ti had diffused appreciably into any of the coatings examined. This is believed to be the reason the depth of attack data did not show any significant dependence on the choice of substrate or the presence of platinum additions.

Four turbine blades, listed in Table II, were tested for 20 hours in a Rolls Royce Olympus C engine. Each of the blades was first coated with a 5  $\mu\text{m}$  platinum underlayer and then uniformly covered with a 145  $\mu\text{m}$  graded CoCrAlY coating. Three of the blades were preoxidized for one hour at 1080°C in air before the start of the test. None of the four blades showed any significant attack at the conclusion of the test. The leading edge of a preoxidized blade and a blade which received no treatment prior to testing are compared in Figures 6 and 7. A protective  $\text{Cr}_2\text{O}_3$  scale formed on both samples. The peppered appearance of the preoxidized sample is a result of internal oxidization and precipitation of  $\text{Al}_2\text{O}_3$  during the oxidation pretreatment.

#### SUMMARY

Burner rig and engine test results indicate that the hot corrosion resistance of sputter deposited CoCrAlY coatings to aggressive low temperature environments is very dependent on coating composition. Coatings with a high chromium surface concentration, a high chromium to aluminum ratio at the surface and a gradient in the aluminum composition that increases its concentration into the coating thickness all improve the corrosion resistance of the coating. Deposits containing platinum additions also provide good low temperature protection. The test results also suggest that platinum underlayers may be effective in inhibiting the diffusion of aluminum and titanium through the formation of intermetallic compounds.

#### ACKNOWLEDGMENTS

\*This work was supported by the U.S. Department of Energy, Office of Coal Utilization, under Contract DE-AC06-76RLO-1830. The burner rig test and depth of attack measurements were conducted by L.F. Aprigliano at the David W. Taylor Naval Ship Research and Development Center. Scanning electron microscopy facilities were provided by H.E. Kjarmo.

## REFERENCES

- 1) J. Stringer, "Hot Corrosion of High Temperature Alloys", Properties of High Temperature Alloys, ed. Z.A. Foroulis and F.S. Pettit, ECS Proceedings, Vol. 77-1, 1976, p. 513-556.
- 2) J.W. Fairbanks, "Ceramic Coating Development - A Technical Management Perspective", Proceedings of 4th Conference on Gas Turbine Materials In The Marine Environment, Vol. II, June 1979, p. 749-770.
- 3) V. deBiasi, Gas Turbine World, July 1977, p. 12-18.
- 4) R.J. Bratton, S.K. Lau, S.Y. Lee and C.A. Anderson, "Ceramic Coating Evaluations and Developments", Proceedings of First Conference on Advanced Materials for Alternative Fuel Capable Directly Fired Heat Engines, July 1979; NTIS Rep. CONF-790749, U.S. Dept. of Energy, Washington D.C., 1979, p. 582-605.
- 5) S.R. Levine, P.E. Hodge and R.A. Miller, "NASA Progress on Ceramic Coatings For Industrial/Utility Gas Turbines", Proceedings of First Conference on Advanced Materials for Alternative Fuel Capable Directly Fired Heat Engines, July 1979; NTIS Rep. CONF-790749, U.S. Dept. of Energy, Washington D.C., 1979, p. 667-679.
- 6) J.W. Patten, J.T. Prater, D.D. Hays and R.W. Moss and J.W. Fairbanks, "Mechanical Behavior of Segmented Oxide Protective Coatings", Thin Solid Films, 73 (1980), p. 463-470.
- 7) G.W. Goward, Thin Solid Films (1978), p. 223-224.
- 8) S. Shen, D. Lee and D. Boone, Thin Solid Films 53, (1978), p. 233.
- 9) W. Grossklaus, N.E. Ulion, and H.A. Beale, "Some Effects of Structure and Composition on the Properties of Electron Beam Vapor Deposited Coatings for Gas Turbine Superalloys", Thin Solid Films, 40, (1977), p. 281-290.
- 10) J.W. Patten, D.D. Hays, R.W. Moss, and J.W. Fairbanks, Proceedings of the 1977 Tokyo Joint Gas Turbine Congress, Gas Turbine Society of Japan, October 1977, p. 527-537.
- 11) J.W. Patten, R.W. Moss, D.D. Hays and J.W. Fairbanks, "Development of Graded Composition CoCrAlY (+ Pt) Sputtered Coatings", Proceedings of First Conference on Advanced Materials for Alternative Fuel Capable Directly Fired Heat Engines, Castine, Maine, July 1979; NTIS Rep. CONF-790749, U.S. Dept. of Energy, Washington D.C., 1979, p. 459-472.
- 12) L.F. Aprigliano, "Burner Test Results of Department of Energy/Battelle Northwest Coatings", Naval Ship R&D Center Report 10310, Annapolis, MD.
- 13) J.A. Goebel, F.S. Pettit and G.W. Goward, "Mechanism for the Hot Corrosion of Nickel-Base Alloys", Met. Trans, Vol. 4, Jan. 1973, p. 261-278.

TABLE I: BURNER RIG PINS TESTED AT NAVAL SHIP R&D CENTER, ANNAPOLIS, MARYLAND

Sample No.	Depth of Aver.	Attack Maxi.	Coating Composition <sup>(1)</sup>	Thermal Treatment	Pt Underlayer Thickness( $\mu\text{m}$ )	Coating Thickness( $\mu\text{m}$ )	Substrate Alloy
1021	0	0	Cr: 27-29 Al: 6-4	Vac H.T. 4 hrs @ 1080°C	12.5	120	X-40
5034	0	0	Cr: 27-29 Al: 6-4	"	0	120	In 792
5005	0	0	Cr: 27-29 Al: 6-4	"	5	120	In 792
1005	0	0	Cr: 34 Al: 3	"	5	102	X-40
5014	0	5	Cr: 35 Al: 1	"	12.5	105	In 792
1048	0	5	Cr: 12-3-21 Pt: 68-87-17 Al: 1-0-2	"	0	135	X-40
2014	0	5	Cr: 12-3-21 Pt: 68-87-17 Al: 1-0-2	"	12.5	135	Mar-M-509
2042	0	5	Cr: 24-30 Al: 19-3	"	0	125	Mar-M-509
2010	0	5	Cr: 24-30 Al: 19-3	"	12.5	125	Mar-M-509
5003	0	7.5	Cr: 24-30 Al: 19-3	"	5	125	In 792
2047	0	12.5	Cr: 34 Al: 3	"	0	102	Mar-M-509
5012	0	25	Cr: 34 Al: 3	"	12.5	102	In 792
1007	0	25	Cr: 35 Al: 1	"	5	105	X-40
5037	0	25	Cr: 35 Al: 1	"	0	105	In 792
1001	2.5	5	Cr: 19-26 Al: 18-9	"	5	133	X-40
2051	2.5	5	Cr: 22 Al: 9	Sputter etched after nitriding 4 hrs @ 900°C	5	35	Mar-M-509
5007	2.5	20	Cr: 12-3-21 Pt: 68-87-17 Al: 1-0-2	Vac H.T. 4 hrs @ 1080°C	12.5	135	In 792
1040	2.5	23	Cr: 19-26 Al: 18-9	"	0	133	X-40
2035	5	5	Cr: 22 Al: 9	Sputter etched after nitriding 4 hrs @ 900°C	0	35	Mar-M-509
2054	5	7.5	Cr: 32-34 Al: 9	"	5	175	Mar-M-509
2031	5	10	Cr: 30 Al: 9.5	Vac H.T. 4 hrs @ 1080°C	0	150	Mar-M-509
2027	5	12.5	Cr: 33 Al: 9.4	"	0	163	Mar-M-509
2018	5	15	Cr: 25-30 Al: 9-8	"	0	115	Mar-M-509
1019	5	137	Cr: 19-26 Al: 18-9	"	12.5	133	X-40
2038 <sup>(2)</sup>	5	135	Cr: 23 Al: 9	H.T. 2 hrs @ 1052°C	0	88	Mar-M-509
5027	7.5	220	Cr: 25-30 Al: 9-8	None	0	175	In 792
1037	10	10	Cr: 25-30 Al: 9-8	None	0	175	X-40
2020	10	65	Cr: 25-30 Al: 9-8	Vac H.T. 4 hrs @ 1080°C	0	138	Mar-M-509
2001	12.5	113	Cr: 25-30 Al: 9-8	"	5	117	Mar-M-509
2003	12.5	135	Cr: 25-30 Al: 9-8	"	5	138	Mar-M-509
2058 <sup>(2)</sup>	12.5	138	Cr: 23 Al: 9	H.T. 2 hrs @ 1052°C	5	88	Mar-M-509
DTSNRDC <sup>(3)</sup>	23	275	Cr: 24	H.T. 4 hrs @ 1052°C	0	125	Rene 80

(1) CoCrAlY composition at substrate - at outer surface.

(2) PVD control coating

(3) PVD control coating provided by Naval Ship R&D Center, Annapolis, MD.

TABLE II. ROLLS ROYCE TURBINE BLADE COATINGS

<u>BLADE No.</u>	<u>COATING COMPOSITION</u>	<u>THERMAL TREATMENT</u>	<u>PT UNDERLAYER THICKNESS (<math>\mu\text{m}</math>)</u>	<u>COATING THICKNESS (<math>\mu\text{m}</math>)</u>	<u>SUBSTRATE ALLOY</u>
23	CR: 43-48 AL: 8-7	SPUTTER ETCHED AFTER NITRIDING @ 900°C + 1HR. @ 1080°C IN AIR	5	150	IN 738 C
25	CR: 43-48 AL: 8-7	SPUTTER ETCHED AFTER NITRIDING @ 900°C + 1HR. @ 1080°C IN AIR	5	150	IN 738 C
68	CR: 43-48 AL: 8-7	VAC. H.T. 4 HRS. @ 1080°C + 1 HR. @ 1080°C IN AIR	5	150	IN 738 C
70	CR: 43-48 AL: 8-7	VAC. H.T. 4 HRS. @ 1080°C	5	150	IN 738 C

TABLE III. COATING COMPOSITION TYPES - ANNAPOLIS BURNER RIG TEST RESULTS

<u>GROUP</u>	<u>COMPOSITION</u>	$\frac{\text{DEPTH OF ATTACK } (\mu\text{m})}{\bar{X}}$	$\frac{\text{MAX}}{\bar{X}}$
I	27-29% CR, 6-4% AL	0	0
II	24-30% CR, 19-3% AL	0	8
III	12-3-21% CR, 2% AL 68-87-17% Pt	0	20
IV	34% CR, 3% AL	0	25
V	19-26% CR, 18-9% AL	3	120
VI	28 ( $\pm$ 5) % CR, 9% AL	10	218
VII	CONTROL SPECIMENS 2 PVD: 23 CR, 9% AL PVD: 24 CR, 11% AL	9 23	140 275

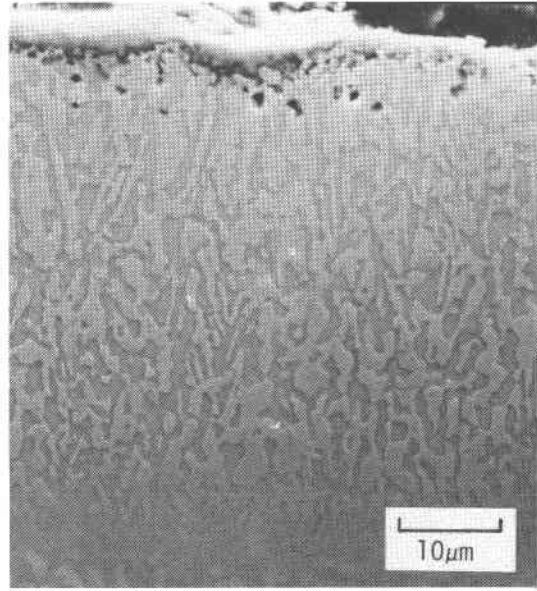
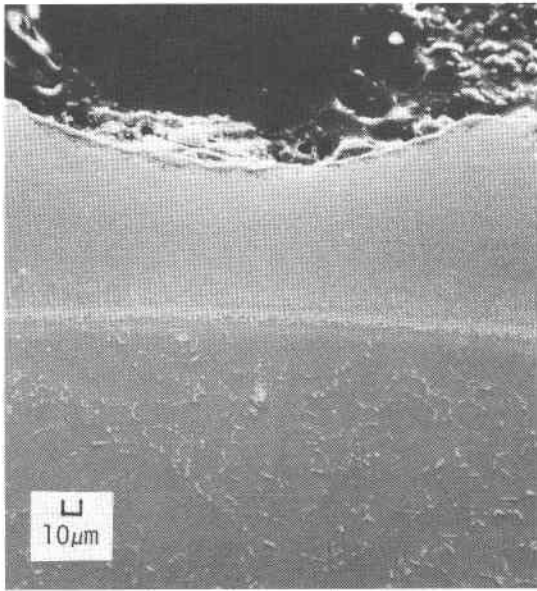


Figure 1. Typical corrosion pit found on burner rig pins. The absence of a depletion zone in the underlying metal is shown on the right.

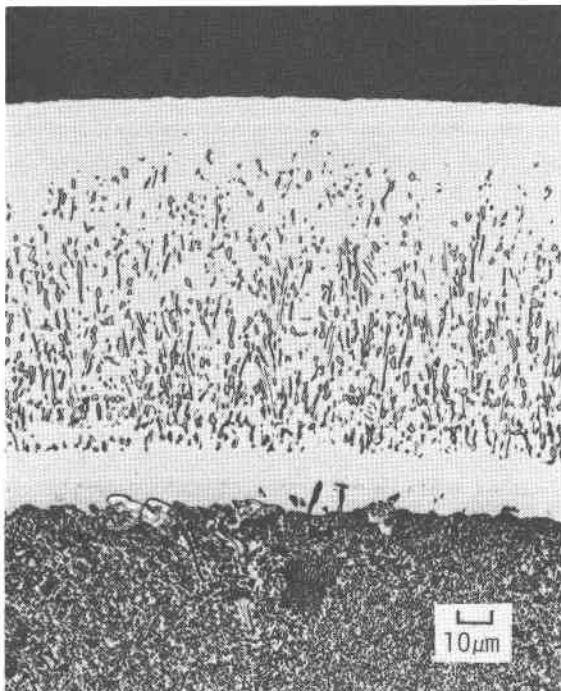


Figure 2. Optical micrograph showing a cross section of the graded 27-29% Cr, 6-4% Al coating. The coating has been heat treated at 1080°C for 4 hours and then polished and etched.



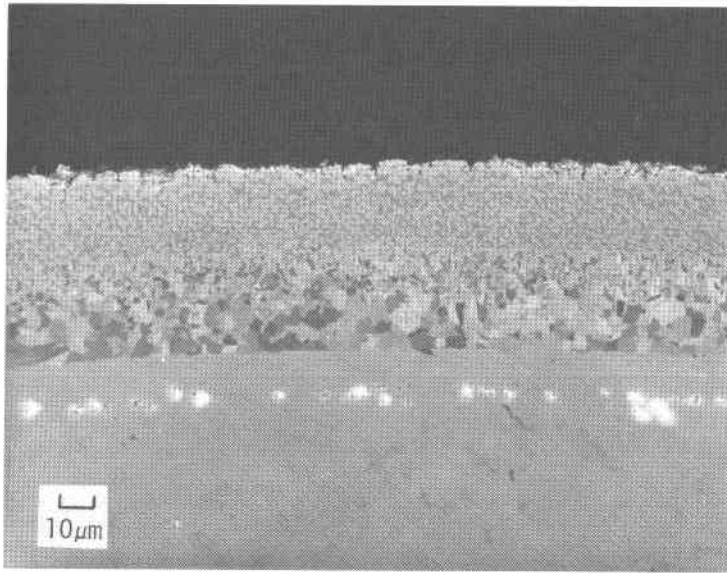


Figure 3. Optical cross section of the graded Pt - CoCrAlY coating, following burner rig testing.

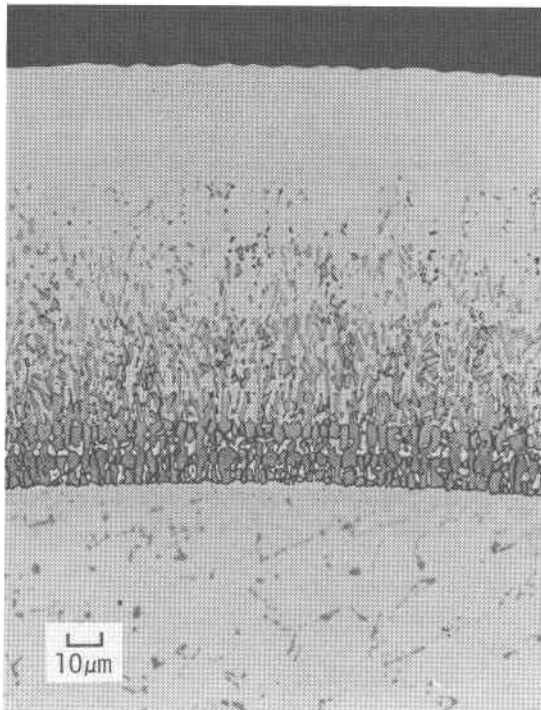


Figure 4.

Optical micrograph showing the graded 24-30% Cr, 19-3% Al coating. The deposit has been heat treated at 1080°C for 4 hours and then polished and etched.

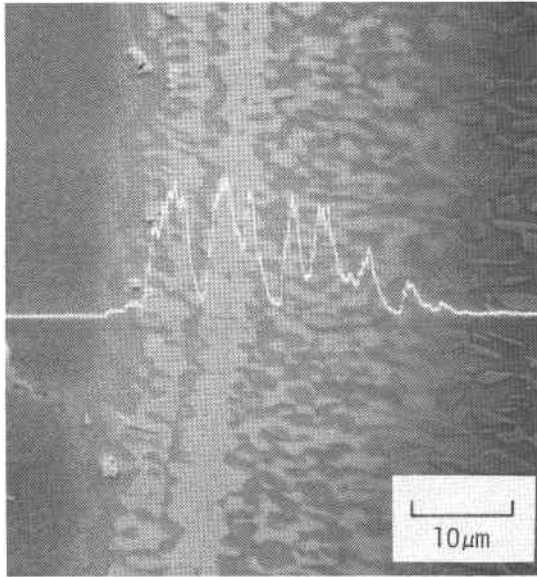


Figure 5.

SEM micrograph showing the platinum underlayer following the 500 hour burner rig test. A line trace shows the platinum concentration. The layer broadened from an original 5 micrometers thickness to 33 micrometers. Aluminum and titanium are concentrated in the platinum rich phase.

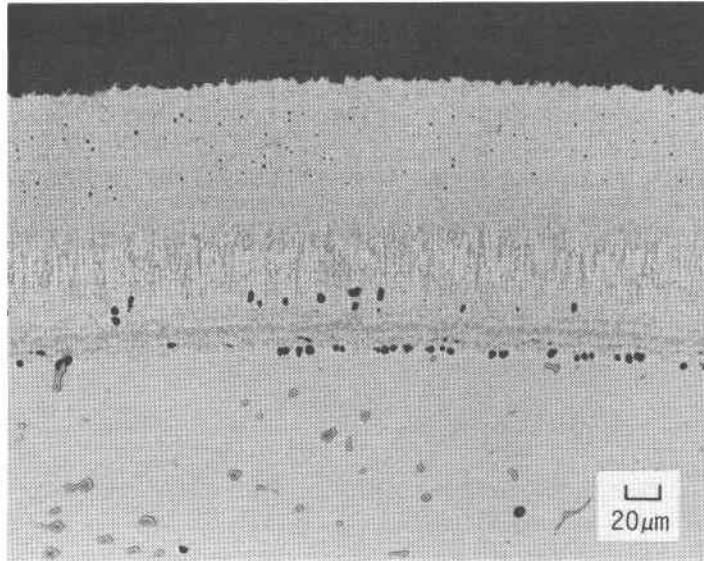


Figure 6. Optical micrograph of CoCrAlY coating after testing in Rolls Royce turbine for 20 hours.

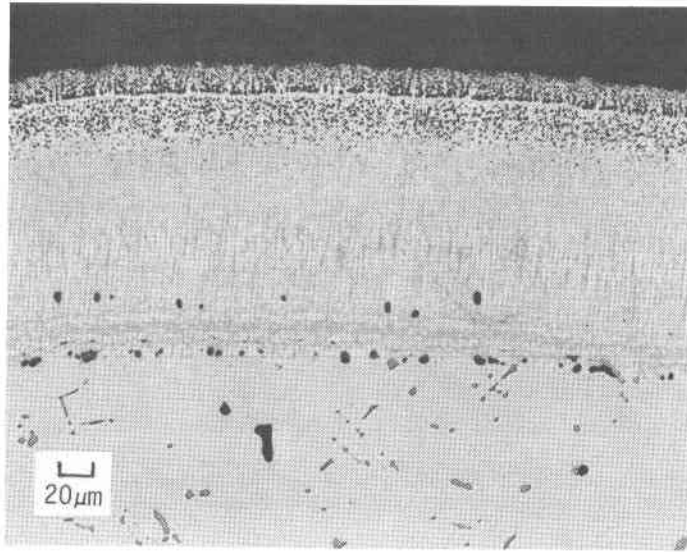


Figure 7. Optical micrograph of CoCrAlY coating tested in Rolls Royce turbine for 20 hours. Preoxidation of 1 hour at 1080°C before testing resulted in internal oxidation at top of coating.

## DEVELOPMENT OF DIFFUSION BONDED CLADDINGS FOR LARGE GAS TURBINE APPLICATIONS

J.H. Wood, T.R. Farrell, A.M. Beltran, W.F. Schilling and W.J. Ostergren  
General Electric Company, Schenectady, New York

### I. INTRODUCTION

Since 1970, the General Electric Company's Gas Turbine Division has been investigating diffusion-bonded, corrosion-resistant sheet claddings as an alternate means of protecting gas turbine bucket airfoils from the corrosion encountered in the more severe service environments. This effort has involved sheet cladding alloy composition development, cladding process development, laboratory burner rig corrosion testing, and field evaluation of clad gas turbine bucket airfoils. Each of these topics has been discussed to some extent previously in the literature (1-6). The earliest work, sponsored in part by the Maritime Administration-Department of Commerce (1,2) later evolved into the General Electric Lynn Rainbow Rotor Program (3) in which two cladding compositions, along with a number of different coatings, were evaluated after approximately 19,000 hours service in an MS5001 turbine burning treated residual fuel. A subsequent field evaluation program involving General Electric and ARAMCO (Arabian American Oil Co.) also included three different cladding compositions; results of an investigation after 13,051 hours in an MS5002 turbine located in Saudi Arabia have been reported upon (3,4,5). Additional alloy composition development and testing, including mechanical property testing of clad composite specimens, was performed under the DOE funded CFCC contract EX-76-C-01-2357, while a current EPRI contract (RP 1460-1) is aimed at developing clad processing techniques for large utility-sized gas turbine buckets and extending the scope of mechanical property testing of clad materials.

Specifically, the purposes of this paper are to:

- a.) Describe in more detail than previously reported the performance of various cladding alloys during burner rig testing, as a function of temperature, time, and fuel contaminant levels.
- b.) Report the initial results of an investigation of the effects of cladding on the mechanical properties of clad substrates.
- c.) Update the results of the "rainbow rotor" field trials in which clad buckets have now reached approximately 26,000 hours in service lifetime.

### II. BURNER RIG CORROSION BEHAVIOR OF CLAD ALLOYS

Previous investigations of clad superalloys by Gedwell<sup>(7)</sup> and Grisaffe and Gedwell<sup>(8)</sup> demonstrated that oxidation-resistant cladding alloys such as Fe-25Cr-4Al-1Y and Ni-20Cr-4Al-1Si afforded excellent protection to WI-52 and IN-100 at 1038 and 1093C in normal oxidizing environments for exposures up to 400 hours. The primary objective of this present study, however, was to provide longer-term hot-corrosion resistance between 732C and 982C, the temperature regime wherein hot corrosion is particularly severe due to condensed corrodents such as Na<sub>2</sub>SO<sub>4</sub>. The more promising cladding systems were also exposed to normal oxidizing environments at 982C and 1038C.

#### A. Clad Alloy Selection

Extensive burner rig test experience with various Fe, Ni and Co-base sheet alloys narrowed the choice of cladding alloys to Inconel 671, S-57, PFB-6 and GE 2541

(Table I). Inconel 671, a Ni-base alloy containing essentially 50 wt. % Cr, was obtained as 0.3175 cm thick hot-rolled plate from Huntington Division of International Nickel Company. This material was annealed and cold-rolled to produce 0.25 mm sheet; final annealing was conducted at 1260°C for 30 minutes in very dry H<sub>2</sub> (dew point -73°C).

GE 2541 is an Fe-base alloy containing 25% Cr, 4% Al, and 1% Y (wt. %). Initially, ingots of the alloy were vacuum induction melted, and hot-and cold-rolled to 0.25 mm thick sheet. Prior to the fabrication of specimens, the sheet was vacuum annealed ( $5 \times 10^{-5}$  Torr) at 1093°C for 30 minutes. More recently, GE 2541 sheet has been fabricated from hot-isostatically pressed ingots of prealloyed powder, which improves alloy ductility and formability.

S-57 and PFB-6 are Co-base alloys with 25% Cr, and 3 or 5% Al, respectively (Table I). Sheet fabricability is also ductility limited in these alloys; both have benefited from HIP powder metallurgy processing. IN-738, a  $\gamma'$ -strengthened Ni-base investment-cast superalloy, was selected as the substrate material for this study (Table I).

### B. Burner Rig Specimen Fabrication

Diffusion-bonded clad specimens were prepared by the "glass-HIP" process.<sup>(9)</sup> Small "packages" of three to six clad corrosion discs were fabricated by spot-welding the substrate discs between two clad sheets, and securely spot-welding the clad-to-clad seams to prevent glass penetration during the HIP cycle (Figure 1). The cladding packages were loaded into mild steel containers filled with soda-lime glass cullet, and mild steel covers with an evacuation tube were GTA-welded in place. The containers were leak-checked on a He mass spectrometer and outgassed at 316°C for 16 hours at a vacuum of  $10^{-3}$  Torr followed by forge-welding of the evacuation tube. Diffusion bonding was accomplished in an argon-pressurized autoclave by hot-loading the containers at 982°C, closing the vessel, and simultaneously increasing temperature and pressure to the preset levels of 1149°C, 10.5 kg/mm<sup>2</sup>. Following a one-hour hold, the autoclave was depressurized and furnace power shut off, permitting removal of the containers at approximately 870°C. The containers were directly water-quenched to fracture the glass, allowing easy removal of the cladding packages and subsequent final cleanup of the specimens by glass-bead blasting.

In an attempt to improve cladding oxidation and hot-corrosion resistance, a pack aluminide coating was applied to S-57 and PFB-6 using a pack mixture of 1% Al, balance Al<sub>2</sub>O<sub>3</sub> with an HF activator at 1060°C for 3 hours in flowing argon (Figure 2a). An alternate procedure was developed to enhance the resistance of GE-2541. An inner layer of Al foil was incorporated between the cladding and IN-738 substrate, and the HIP-bonding cycle controlled to first apply pressure to the assembly; temperature was then raised to melt the Al foil while under this constraint. Diffusion-bonding occurred simultaneously with the formation of a  $\beta$ -NiAl reaction zone at the bondline, thus providing an Al source beneath the cladding for added protection<sup>(10)</sup> (Figure 2b).

### C. Testing and Evaluation

The clad IN-738 corrosion discs were evaluated in simulated gas turbine environments using small combustion burner rigs. Tests were conducted in a normal oxidizing environment at 982 and 1038°C in combusted undoped propane, and in a hot-corrosion environment at 732, 871 and 982°C, produced by burning diesel oil containing 1% S and doped with artificial sea salt mixed with the fuel to yield approximately 8 ppm Na in the combustion products. In order to simulate coal-combustion environments such as might be encountered in pressurized fluidized beds, tests were also run with K in partial substitution for Na. The aim was to generate a fused salt deposit with equal molar fractions of Na<sub>2</sub>SO<sub>4</sub> and K<sub>2</sub>SO<sub>4</sub>. The burner rigs operate at atmospheric pressure, 20 mps gas velocity, and a maximum air:fuel ratio of 50:1 at 871°C. The specimens, which are stationary during test, are cycled to room temperature every 24-48 hours, depending on the type of test being run.

Following test, the specimens were examined metallographically at 100 times magnification to determine (i) maximum depth of attack, (ii) average surface loss of the cladding, and (iii) depth of internal oxide, nitride or sulfide formation in the substrate below the bondline. Data were obtained on the basis of the original disc and cladding dimensions, using the clad/substrate bondline as the reference point. Selected specimens were examined on a Cameca electron microprobe analyzer to determine the extent of clad/substrate interdiffusion, cladding composition gradients, and the composition of precipitate phases.

#### D. Results

1. Hot-Corrosion Tests - Tests in Na,S-doped diesel oil at 871C, the temperature of greatest interest, produced the following ranking of cladding systems: aluminided S-57 and aluminided PFB-6 (most resistant), GE-2541 and IN-671 (least resistant) (Figure 3). After 5000 hours of exposure, GE-2541 exhibited a moderate degree of internal sulfide and oxide penetration, while the aluminided S-57 and PFB-6 claddings showed little cladding penetration; however, the added  $\beta$ -CoAl surface layer had essentially been consumed (Figure 4). Both IN-671 and GE-2541 exhibited a "breakaway" corrosion behavior, where an accelerated rate of penetration occurred after approximately 3000-4000 hours for IN-671 and 5000-6000 hours for GE-2541. Penetration of the IN-671 cladding in the longer exposures generally resulted in the formation of nitrides and oxides in the IN-738 substrate. Conventional pack aluminide coatings applied directly to IN-738 also exhibit breakaway behavior in this exposure, with failure generally occurring after just 500 to 1000 hours.

Hot-corrosion attack at 982C was significantly greater for all cladding systems, however, the ranking of alloys remains the same as at 871C. IN-671 fails completely in approximately 1500 hours, indicating that  $\text{Cr}_2\text{O}_3$  is not as protective or stable as  $\text{Al}_2\text{O}_3$  at this temperature (Figure 5). Penetration of GE-2541 occurred in 2500 hours, whereas the surface aluminide layers on S-57 and PFB-6 last for almost 3000 hours, while marked cladding attack becomes evident after 4000 hours.

Although fewer hot-corrosion tests have been conducted at 732 or 760C, IN-671 is clearly the most resistant cladding alloy with minimal attack after 2000 hours, by virtue of a stable, protective  $\text{Cr}_2\text{O}_3$  surface oxide (Figure 6). GE-2541 is somewhat less resistant, while the un-aluminided Co alloys S-57 and PFB-6 suffer severe pitting attack in some cases in as few as 100 hours. These tests were conducted with the additional ingestion of  $\text{SO}_2$  to raise the sulfur ( $\text{SO}_3$ ) partial pressure to produce a more realistic simulation of turbine environments. The Co alloys suffer the greatest attack since a stable sulfate eutectic is formed between  $\text{CoSO}_4$  and  $\text{Na}_2\text{SO}_4$ ;  $\text{CoSO}_4$  appears to be stable in this temperature regime by reaction of  $\text{SO}_3$  with  $\text{CoO}$ (1f).

2. Oxidation Tests - In undoped oxidizing environments of combusted natural gas or propane at 982 and 1038C, the high Al concentration alloys once again offer the greatest protection. GE-2541 exhibits excellent resistance for about 10,000 hours at 982C, while IN-671 suffered internal oxide/nitride penetration after just 4000 hours (Figure 7). At 1038C, aluminided S-57 showed very little effect of exposure on the cladding or surface  $\beta$ -CoAl layer after 4000 hours, while GE-2541 developed internal oxides throughout the cladding in 2000 hours and IN-671 was almost totally consumed in this time, allowing significant substrate attack.

Substantial improvement in the life of GE-2541 cladding in the 982C hot-corrosion and 1038C oxidation exposures has been generated by providing an Al source at the bondline with the substrate (i.e., "under aluminiding"). Burner rig hot-corrosion tests at 980C produced little cladding attack after 8300 hours, although scattered internal oxide and sulfide particles were found to a depth of 125  $\mu$  (Figure 8).

Similarly, a 4000 hour oxidation exposure at 1038C produced only 65  $\mu$  of cladding penetration. Hence, a bondline Al source produces a factor of four gain in GE-2541 cladding life, and this composite compares very favorably with the aluminided S-57 or PFB-6 cladding systems.

3. Simulated Coal-Fired Tests - In the simulated coal-fired burner rig tests involving partial substitution of K for Na, hot-corrosion attack appeared to be more severe than Na alone at 982C, however, the ranking of alloys remained: aluminided PFB-6, aluminided S-57, GE-2541 and IN-671. Useful cladding lives were reduced by approximately 1500 hours compared to the Na-only tests. Severe edge corrosion also occurred for these laminated disc specimens, which may have also influenced the results. A cladding-alloy ranking reversal occurred at 760C even though SO<sub>2</sub> ingestion was employed, with IN-671 substantially more resistant than the remaining alloys, most of which suffered severe pitting attack in less than 300 hours. However, a non-Al containing Co-base cladding alloy also showed good corrosion resistance without signs of pitting, possibly indicating a harmful effect due to Al in this particular fused salt environment.

#### E. Discussion

This study has demonstrated that diffusion-bonded claddings are a viable means of providing long-term oxidation and hot-corrosion protection to the Ni-base superalloy IN-738 in simulated oil and coal-fired atmospheres. Hot-corrosion burner rig testing indicates that IN-671 is the most corrosion resistant cladding alloy at 760C, while aluminided S-57 and PFB-6 suffer severe pitting attack and GE-2541 is intermediate in resistance. At 871 and 982C, however, the reverse is true and aluminided S-57 and PFB-6 last substantially longer than GE-2541 and IN-671. This suggests that the alloying systems which rely upon Al diffusion to the surface to form Al<sub>2</sub>O<sub>3</sub> are more stable and protective at these higher temperatures, while Cr<sub>2</sub>O<sub>3</sub> forming systems such as IN-671 afford reliable protection only at the lower temperatures. All of these cladding systems, however, are significantly more corrosion resistant in these exposures than conventional aluminide coatings.

All of the cladding alloys appear to exhibit a type of "breakaway" corrosion behavior, that is, the onset of a higher corrosion penetration rate before approximately two-thirds of the cladding is actually penetrated by sulfide, oxide or nitride precipitate. This undoubtedly is related to the consumption of the key elements Al or Cr in the outer portion of the cladding and the establishment of sharp concentration gradients. Surface oxide stability and adherence become increasingly difficult to maintain. The presence of added Al-sources in the case of pack aluminided S-57 and PFB-6 or the "under-aluminided" GE-2541 is clearly beneficial, significantly enhancing corrosion life of the cladding system up to 982C, and oxidation resistance to 1038C.

Another important observation from these studies is the significantly higher rate of Fe:Ni interdiffusion between GE-2541 and IN-738 compared to Co:Ni interdiffusion for S-57 or PFB-6 clad IN-738, as indicated metallographically by the width of the  $\gamma'$ -denuded zone beneath the cladding:substrate bondline (Figure 7). Ni injection from IN-738 promotes the matrix transformation of body-centered-cubic (ferritic) GE-2541 to face-centered cubic austenite, while the counterflux of Fe into IN-738 gives rise to sigma-phase formation after just 2000 hours at 871C. Although Co is also regarded as a sigma-phase stabilizer, slower Co:Ni interdiffusion rates between S-57 or PFB-6 and IN-738 apparently delay sigma formation, as it did not form after 5000 hours exposure. This is further evidenced by the slow rate of growth of the  $\gamma'$ -denuded zone (Figure 4).

### III. GE/ARAMCO FIELD TESTING

The performance of MS5002 gas turbine buckets clad with three different sheet cladding alloys which had operated for 13,051 hours in desert environments involving high concentrations of alkali salts and sulfur-containing fuels was discussed in References 3-5. Since then,

additional clad buckets have been evaluated following a total of 26,069 service hours in the same environment. The claddings evaluated included IN-671 which had been subjected to a pack aluminiding cycle following cladding, S-57 which had also been overaluminided, and GE-2541.

The earlier evaluation, after 13,051 hours, had indicated that both the Fe and Co-base cladding alloys had performed in outstanding fashion with approximately 15  $\mu$  of corrosion attack occurring on the original 250  $\mu$  thick cladding. By contrast, the Ni-base IN-671 cladding alloy had suffered nearly complete corrosion penetration with only 50  $\mu$  of the original 200  $\mu$  remaining. Over-aluminiding appeared to have significantly improved the performance of the IN-671 cladding with approximately 125  $\mu$  remaining following service.

The latest evaluation, following 26,069 hours in the same machine, indicated that aluminided S-57 was still in very excellent condition. The maximum localized corrosion penetration did not exceed approximately 50  $\mu$  (of the original 250  $\mu$  thickness), with most of the airfoil surface exhibiting less than 25  $\mu$  of corrosion penetration (Figure 9). The Fe-base GE-2541 did not fare quite so well, however, as localized areas now showed internal oxidation/corrosion which had penetrated as much as 175  $\mu$  of the 250  $\mu$ -thick cladding (Figure 10). This penetration had not resulted in gross scale formation or destruction of the cladding, but rather consisted largely of fine, discrete, internal oxide particles. Penetration was greatest at the bucket leading edge with lesser depths (up to approximately 90-100  $\mu$ ) occurring on the pressure face aft of the bucket mid-chord. Elsewhere, little of this internal attack was present; thus, it seemed to be delineating those areas of the airfoil which were subject to the more severe environmental conditions.

The third bucket examined was clad with IN-671 which had been over-aluminided; no unaluminided bucket with comparable service was available for comparison. Corrosion attack of up to 100-125  $\mu$  was observed in localized areas on the leading edge and pressure face aft of the bucket mid-chord (Figure 11). From a corrosion standpoint, this bucket appeared no worse than the comparable one examined after only 13,051 hrs.<sup>(3-5)</sup> (Slight differences in thickness of the as-applied cladding due to stretching or thinning during clad forming may have had some bearing on this result.) Overall, based on the latest evaluation, the performance of the over-aluminided IN-671 would be ranked slightly ahead of that for the GE-2541 cladding. Neither of these performed nearly as well as the aluminided S-57 Co-base cladding, however.

An observation worth noting is that several areas of cladding unbond were observed for both the IN-671 and S-57 claddings, but not for the GE-2541 cladding. In a given cross-section these unbonded areas could exceed approximately 2.5 cm in length; their presence presumably reflects the difficulty in achieving shape conformity between the cladding and the substrate airfoil prior to HIP diffusion bonding. Most probably, the greater ductility and consequent ease of fabrication of the GE-2541 material lessens the chance for such areas of unbond. Interestingly, however, neither of those clad buckets which did contain areas of unbond gave any evidence of potential cladding tearing or loss as a result of that lack of bonding, even after 26,069 hours of service.

#### IV. EFFECT OF CLADDINGS ON MECHANICAL PROPERTIES

The objective of mechanics of materials work on clad systems is to determine the effect of claddings on component mechanical properties. Information of this type is required before any surface protection system is committed to long-term commercial service. This insures that the cladding, which is applied to give added environmental protection, does not dramatically reduce bucket mechanical properties. It also serves to identify areas where mechanical properties are enhanced by use of a clad system.

The objective of the work presented in this section was to provide an evaluation of the impact of claddings on bucket tensile and creep properties, utilizing stress-strain analysis and available test data. Clad test specimen behavior was analyzed using a stress-strain computer model and compared to test results obtained on IN-738 specimens clad with S-57, GE-2541, IN-671, PFB-5PM, and PFB-6PM.<sup>(12)</sup> The calculated behavior of clad test specimens was



found to be in good agreement with the test results, confirming the validity of the developed stress-strain model. From this, the potential impact of claddings on the mechanical properties of clad buckets has been developed.

The stress-strain model was developed under the current EPRI contract RP1460-1 for the purpose of understanding the mechanical behavior of clad test specimens and components. The data used in substantiating the calculated results were generated under the DOE funded contract EX-76-C-01-2357.<sup>(12)</sup> Additional test data to be obtained under the current EPRI contract will be generated by the end of 1981. Testing will include both isothermal and thermal-mechanical fatigue testing.

#### A. The Model

In order to fully understand test results from clad test specimens and to properly relate test specimen behavior to the component, the development of a stress-strain model of the clad system became necessary. The model identifies where the largest effects would be expected, provides an understanding of why these effects occur, and provides the basis for the translation of these effects on test specimens to the component.

A uniaxial stress-strain computer program was used to model clad test specimen and clad bucket mechanical behavior. This program utilizes physical, tensile and creep inputs to calculate stress-strain behavior under selected conditions and was developed within the General Electric Company to handle investigations of this type. The program calculates the behavior of the individual materials, as well as the composite, allowing examination of each material's contribution to the composite's behavior. During an actual test of a clad test specimen, it is only possible to monitor the behavior of the composite. However, it is important in understanding the observed behavior of the composite to determine the behavior of the individual materials which make up the composite.

An idealized clad test specimen configuration is shown in Figure 12. Due to the bond existing between the substrate and cladding, the clad test specimen can be assumed to be under generalized plane strain constraint (i.e., the ends displace a uniform but constant amount). The stress-strain computer program models this configuration as two cylinders attached at each end to a rigid plate. The two plates remain parallel to one another producing generalized plane strain constraint. By simulating a specified load/stress or strain sequence, the mechanical behavior of cladding/substrate systems can be studied. Also, the relationship between clad test specimens and clad components can be derived through their relative cross-sectional areas.

#### B. Clad Tensile Behavior

The tensile behavior of a cladding/substrate system as calculated by the stress-strain model can be described in terms of stress by the relationship:

$$P = \sigma_{COMP} A_{COMP} = \sigma_S A_S + \sigma_C A_C \quad (1)$$

Equation (1) relates the load carried by the composite ( $\sigma_{COMP} A_{COMP}$ ) to the sum of the loads carried by the substrate ( $\sigma_S A_S$ ) and the cladding ( $\sigma_C A_C$ ). It can be seen from Equation (1) that the composite behavior is simply a weighted average of the two individual materials. Figure 13 shows in general the calculated stress-strain behavior of a cladding/substrate system where a relatively weak 0.25 mm thick cladding is bonded to a relatively strong 6.25 mm diameter substrate. The stress-strain behavior of the composite was found to be intermediate to that of the cladding and substrate and varied with substrate cross-sectional area for a constant cladding thickness, the effect of the cladding decreasing with increasing substrate cross-sectional area.

Estimates of the 871C stress-strain behavior of the two cladding alloys, S-57 and GE-2541, were made based on tensile results<sup>(12)</sup> and input into the computer program for analysis. S-57 was chosen to represent one of the stronger cladding alloys, and GE-2541 was chosen to represent a weak cladding alloy.

Simulated tensile tests ( $\dot{\epsilon} = 0.5\%/min.$ ) were performed on the computer for 6.25 mm diameter IN-738 tensile specimens clad with 0.25 mm of either S-57 or GE-2541. The results of these simulations are shown in Figures 14 and 15. It can be seen from these figures that the weaker claddings should result in a greater loss of composite strength. It can be inferred from this that at low temperatures the negative effect of claddings on composite strength would diminish as the cladding alloys exhibit strengths more comparable to that of the substrate alloy. In fact, the strength of the composite would be expected to increase relative to the substrate should the strength of the cladding exceed that of the substrate.

The 0.2% yield strengths at 871C of S-57 and GE-2541 clad IN-738 were obtained from the calculated behavior shown in Figures 14 and 15 and tabulated in Table III. The results obtained from tensile tests on 6.25 mm diameter clad tensile specimens<sup>(12)</sup> are also provided in Table III for comparison. (Results from specimens clad with five different alloys, using fabrication techniques similar to those described in Section II.B., are included.) The percent loss of yield strength determined from the test results of Table III are seen to be in fairly good agreement with the calculated results (Figure 16).

From Equation (1) a theoretical limit to the percent loss in strength at a given strain of clad systems as compared to unclad can be formulated. If the cladding is assumed to offer no strength contribution to the composite, Equation (1) can be reduced to the following expression:

$$\sigma_{COMP} A_{COMP} = \sigma_S A_S \quad (2)$$

The loss in strength at a given strain becomes related to the area ratio  $A_S/A_{COMP}$ . For a 6.25 mm diameter tensile specimen with a 0.25 mm thick cladding, the area ratio  $A_S/A_{COMP}$  becomes 0.857. Thus, clad 6.25 mm diameter test specimens should not have an average strength which is less than 85.7% of the substrate material at a given strain.

For the case of a large bucket like the MS7001 stage 1 bucket, the area ratio becomes approximately 0.98. Therefore, the maximum expected impact of a 0.25 mm thick cladding on this bucket would result in strengths which are approximately 98% of the unclad. Admittedly, this effect is rather small indicating that claddings should have little or no effect on bucket tensile properties.

### C. Clad Creep Behavior

The creep behavior of cladding/substrate systems, as calculated by the stress-strain model, can be described by the following relationships:

$$@ \text{time} = 0;$$

$$\sigma A = P = P_S + P_{CI} = \sigma_S A_S + \sigma_{CI} A_{CI} \quad (3)$$

$$@ \text{time} = t_1;$$

$$\sigma A = P = (P_S + \Delta P) + (P_{CI} - \Delta P) = (\sigma_S + \Delta \sigma_S) A_S + (\sigma_{CI} - \Delta \sigma_{CI}) A_{CI} \quad (4)$$

It can be seen from these equations that with time there is a calculated load shift from the weaker cladding to the stronger substrate. In other words, the weaker cladding creeps rapidly at first, giving up most of its load (or stress) to the substrate. As the creep strain in the cladding increases, the elastic strain in the substrate increases accordingly. This causes clad creep test specimens to creep faster than unclad specimens during the load shift.

Clad test specimen creep behavior was compared to unclad through constant load testing, wherein the same load was applied to both clad and unclad test specimens. Figure 17 shows the calculated creep response of a 6.25 mm diameter test specimen with a 0.25 mm thick cladding in comparison to an unclad test specimen. Constant load testing results in the composite behavior converging with the unclad behavior, indicating little effect of the cladding at the higher creep strains.

This behavior can be explained easily using the illustration in Figure 18 which shows the expected time/stress response for constant load testing of a clad test specimen compared to an unclad. At time equal to zero, the same load as applied to the unclad test specimen results in a lower initial stress for the clad test specimen. As time progresses, the weaker cladding gives up most of its load to the stronger substrate causing the substrate's stress level to increase until this stress nearly equals that in the unclad test specimen. Thus, at high creep strains, after the load shift is complete, the clad test specimen behavior very closely resembles the unclad. It was found through the modelling of clad test specimen creep behavior that the creep properties of the weaker cladding alloy alter only the time required to complete the load shift. Generally, the load shift was found to be nearly complete before the clad test specimen reached 0.1% creep strain.

Using data from earlier stress-rupture testing,<sup>(12)</sup> constant load testing of S-57 and GE-2541 clad IN-738 was simulated on the computer and compared to unclad IN-738. The results of these calculations are tabulated in Table IV, and the S-57 clad IN-738 results are plotted in Figure 19. Similar results were obtained for the GE-2541/IN-738 composite.

Test results obtained on creep specimens (6.25 mm diameter with 0.25 mm thick claddings of several different alloys) tested under constant load conditions are also shown in Table IV. The results of these tests are plotted in Figure 20 showing the clad test specimen data closely surrounding the single unclad baseline test. The scatter of the data shown in Figure 20 is typical of creep data on cast IN-738. At the strain levels included in this graph, this scatter far outweighs any expected effects of the cladding on creep behavior. (Strain levels less than 0.1%, where composite behavior should differ significantly from the substrate, are not included in these data.) The above test data from constant load testing of clad test specimens is in reasonable agreement with the calculated behavior. This tends to substantiate the stress-strain model as applied to the creep behavior of clad test specimens.

To determine the effect of claddings on bucket creep properties, one must take into account the increased centrifugal loading on the bucket due to the presence of the cladding. To account for this effect, the comparison between clad and unclad bucket creep behavior is made assuming the same initial stress is applied in each case. As discussed previously, the weaker cladding gives up its load to the stronger substrate. This results in a higher stress in the substrate of the clad bucket in comparison to the unclad bucket. To illustrate this point, Figure 21 compares the time/stress response, under equivalent initial stress, of a clad bucket and an unclad bucket. The clad bucket at time equals zero receives a greater load than the unclad bucket to achieve the same initial stress in each. As time progresses, the load shift from the weak cladding to the substrate results in a greater stress in the substrate bucket alloy as compared to the unclad. Thus, the clad bucket should behave similar to an unclad bucket loaded to a higher stress level.

A theoretical limit to the calculated increase in the substrate's stress level can be determined. The maximum percent increase in substrate stress of a clad system compared to the unclad is related to the area ratio  $A_{COMP}/A_S$  and is governed by the following expression:

% Increase in Substrate Stress =

$$\left[ (A_{COMP}/A_S) - 1 \right] \times 100\% \quad (5)$$

Thus, for a large bucket like the MS7001 stage 1 bucket, there is a calculated maximum substrate stress increase due to a 0.25 mm cladding of approximately 2%. This calculated stress increase can also be thought of in terms of a loss in creep strength. Thus, for this bucket, the maximum expected impact of claddings on bucket creep properties is a loss of approximately 2% of its creep strength. This is a small loss of creep strength indicating that claddings are expected to have little or no impact on the creep strain characteristics of this bucket. However, claddings may have a significant beneficial impact on creep cracking due to the added environmental protection. This may result in higher achievable creep strains before creep cracking occurs.

Under the current EPRI contract, creep testing of clad specimens will be conducted with results expected by early 1982. Testing up to 10,000 hours is planned to evaluate the potential benefits.

#### D. Discussion

The above results obtained from modelling the effects of claddings on tensile and creep properties have been shown to be in good agreement with test results. The negative impact of claddings on bucket tensile and creep properties is calculated to be minimal.

One area not addressed by this paper is the impact of claddings on the fatigue characteristics of clad specimens or components as compared to unclad. The above stress-strain modelling of clad systems is useful in the evaluation of cladding/substrate hysteretic behavior. However, the model can not solely be used in studying cladding/substrate fatigue behavior as fatigue properties are highly dependent upon the crack initiation and propagation characteristics of the composite. In view of this, the only viable way to determine the true impact of claddings on fatigue behavior is through specimen testing. Under the current EPRI contract, isothermal as well as thermal-mechanical fatigue testing will be conducted with results expected by late 1981.

#### V. SUMMARY

This paper has reviewed some of the recent activity in General Electric's ongoing study of sheet metal claddings as a means of providing corrosion protection for gas turbine bucket airfoils. The environmental resistance of several cladding alloys, including Co, Fe, and Ni-base compositions, was evaluated in burner rig testing under conditions of varying temperature and fuel contamination level. In general, the Ni-base alloy IN-671 was found to be most corrosion resistant at the lower temperature (i.e., 760°C), while the over-aluminided Co-base alloys, S-57 and PFB-6, were found to be superior at the higher temperatures. The Fe-base alloy GE-2541 proved to be intermediate in corrosion resistance in both test temperature regimes. These burner rig results have been corroborated quite well by the results of field testing of clad buckets. The over-aluminided S-57 alloy proved to be the best of the claddings after approximately 26,000 hours service at maximum temperatures which probably did not exceed 1550-1600°F. Unaluminided IN-617 was the poorest, while GE-2541 and over-aluminided IN-671 were intermediate in resistance.

Finally, a study of the possible effects of claddings on mechanical properties was presented. Results obtained from computer modeling of cladding/substrate systems were shown to be in fairly good agreement with the available test data. Based on these results, claddings are expected to have minimal impact on clad bucket tensile and creep strain behavior; the maximum expected decrease in both tensile and creep strength for a clad MS7001 first stage bucket should not exceed approximately 2%. The environmental protection afforded by claddings may also have a beneficial effect on creep cracking behavior.

## VI. REFERENCES

1. S.M. Kaplan, Heavy Duty Marine Gas Turbine Development Project, Task 1/6 (Operational Performance and Maintenance Improvement): Volume B (Materials Development), Final Report prepared for U.S. Department of Commerce, Maritime Administration, Contract No. 0-35510, Gas Turbine Division, General Electric Co., Schenectady, N.Y., November, 1, 1974.
2. S.M. Kaplan, Operational Performance Verification of Advanced Gas Turbine Technology, Final Report prepared for U.S. Department of Commerce, Maritime Administration, Contract No. 4-37123, Gas Turbine Division, General Electric Co., Schenectady, N.Y., December 31, 1975.
3. W.F. Schilling, H.M. Fox, and A.M. Beltran, "Field Testing and Evaluation of Next Generation Industrial Gas Turbine Coatings," Proceedings of the First Conference on Advanced Materials for Alternate Fuel Capable, Directly-Fired Heat Engines, Castine, Maine, July 1979.
4. A.M. Beltran and W.F. Schilling, "The Development and Evaluation of Diffusion-Bonded Clad Gas Turbine Buckets," Proceedings of the Fourth International Symposium on Superalloy, Seven Springs, Pa., September 1980.
5. N.R. Lindblad *et. al.*, "Gas Turbine Bucket Protection Developments," ASME Paper No. 79-GT-47, December 1978.
6. A.M. Beltran and W.F. Schilling, "The Diffusion Bonding of Corrosion-Resistant Sheet Claddings to IN-738," Proceedings of the Third International Symposium on Superalloys, Seven Springs, Pa., September 1976.
7. M.A. Gedwell, NASA Report TND-5483, October 1969.
8. M.A. Gedwell and S.J. Grisaffe, Metals Engr. Quarterly, May 1972.
9. W.F. Schilling, A.M. Beltran, and G.E. Wasielewski, U.S. Patent No. 3,952,939, April 1976.
10. W.F. Schilling and A.M. Beltran, U.S. Patent No. 4,218,007, August 1980.
11. D.V. Wortman, R.E. Fryxell, and I.I. Bessen, "A Theory for Accelerated Corrosion at Intermediate Temperatures," 3rd Conference on Gas Turbine Materials in a Marine Environment, Bath U.K., 1976.
12. PFB Coal-Fired Combined Cycle Development Program, "Turbine Materials Evaluation - Final Report Task 3.0", U.S. DOE Contract EX-76-C-01-2357, March 1980.

**TABLE I**  
**NOMINAL SUBSTRATE AND CLADDING**  
**ALLOY COMPOSITIONS (In Wt.%)**

<u>Alloy</u>	<u>Ni</u>	<u>Co</u>	<u>Fe</u>	<u>Cr</u>	<u>Al</u>	<u>Other</u>
IN-738	Bal.	8.5	-	16	3.4	3.4Ti, 1.75Mo, 2.6W, 0.9Cb, 1.75Ta, 0.1C
GE-2541	-	-	Bal.	25	4	1Y
S-57	10	Bal.	-	25	3	5Ta, 0.3Y
PFB-5	-	Bal.	10	25	5	0.15Y
PFB-6	10	Bal.	-	25	5	0.3Y
IN-671	Bal.	-	-	48	-	0.2Ti

**TABLE II**  
**BURNER RIG OXIDATION DATA**

<u>Clad Alloy</u>	<u>Temp.</u>	<u>Time, hrs.</u>	<u>Max. Penetration mm x 10<sup>2</sup></u>	<u>Surface Loss, mm x 10<sup>2</sup></u>	<u>Internal Oxidation, mm x 10<sup>2</sup></u>
IN-671	982	4,006	13.7	4.8	24.4
		9,452	Destroyed		
	1038	2,113	25.4	18.0	25.7
GE-2541	982	4,006	0.7	0.7	-
		9,452	5.1	1.3	-
	1038	2,113	14.2	0.7	13.5
S-57 Aluminided	982	2,002	3.6	1.5	-
		4,000	3.3	2.0	-

**TABLE III**  
**YIELD STRENGTH OF CLAD IN-738 AT 871°C\***

<u>Substrate Alloy</u>	<u>Cladding Alloy</u>	<u>0.2% YS MPa</u>	<u>% of Unclad</u>
<u>Calculated</u>			
IN-738	-	497.9	-
IN-738	S-57	462.8	92.9
	GE-2541	431.0	86.6
<u>Test Results</u>			
IN-738	-	424.1	-
IN-738	IN-671	360.7	85.0
		357.9	84.4
IN-738	S-57	360.7	85.0
		366.9	86.5
		393.8	92.8
IN-738	PFB-5PM	351.7	82.9
		355.2	83.7
IN-738	GE-2541	362.1	84.9
		364.8	86.0
IN-738	PFB-6PM	376.6	88.8
		361.4	85.2

\* Test Specimen Dimensions: Substrate Diameter - 6.25 mm  
Cladding Thickness - 0.25 mm  
Gage Length - 31.25 mm

**TABLE IV**  
**CREEP PROPERTIES OF CLAD IN-738 AT 871°C**  
**UNDER CONSTANT LOAD TESTING\***

Load (P) = 668.7 kg.

<u>Substrate Alloy</u>	<u>Cladding Alloy</u>	<u>Hrs. to 0.2% <math>\epsilon</math></u>	<u>Hrs. to 0.3% <math>\epsilon</math></u>	<u>Hrs. to 0.5% <math>\epsilon</math></u>	<u>Hrs. to 1.0% <math>\epsilon</math></u>
<u>Calculated</u>					
IN-738	-	38.3	68.3	143.3	391.7
IN-738	S-57	35.1	65.5	141.3	391.0
	GE-2541	35.8	66.1	141.7	391.1
<u>Test Results</u>					
IN-738	-	31.5	66.0	150.0	390.0
IN-738	IN-671	34.0	78.0	170.0	420.0
IN-738	IN-671	34.0	76.0	162.0	360.0
IN-738	S-57	14.5	35.0	98.0	335.0
IN-738	S-57	56.0	140.0	290.0	770.0
IN-738	PFB-5PM	24.0	56.0	140.0	350.0
IN-738	PFB-5PM	43.0	82.0	172.0	400.0
IN-738	GE-2541	22.0	51.0	130.0	335.0
IN-738	PFB-6PM	15.0	35.0	100.0	340.0

\* Test Specimen Dimensions: Substrate Diameter - 6.25 mm  
Cladding Thickness - 0.25 mm  
Gage Length - 31.25 mm



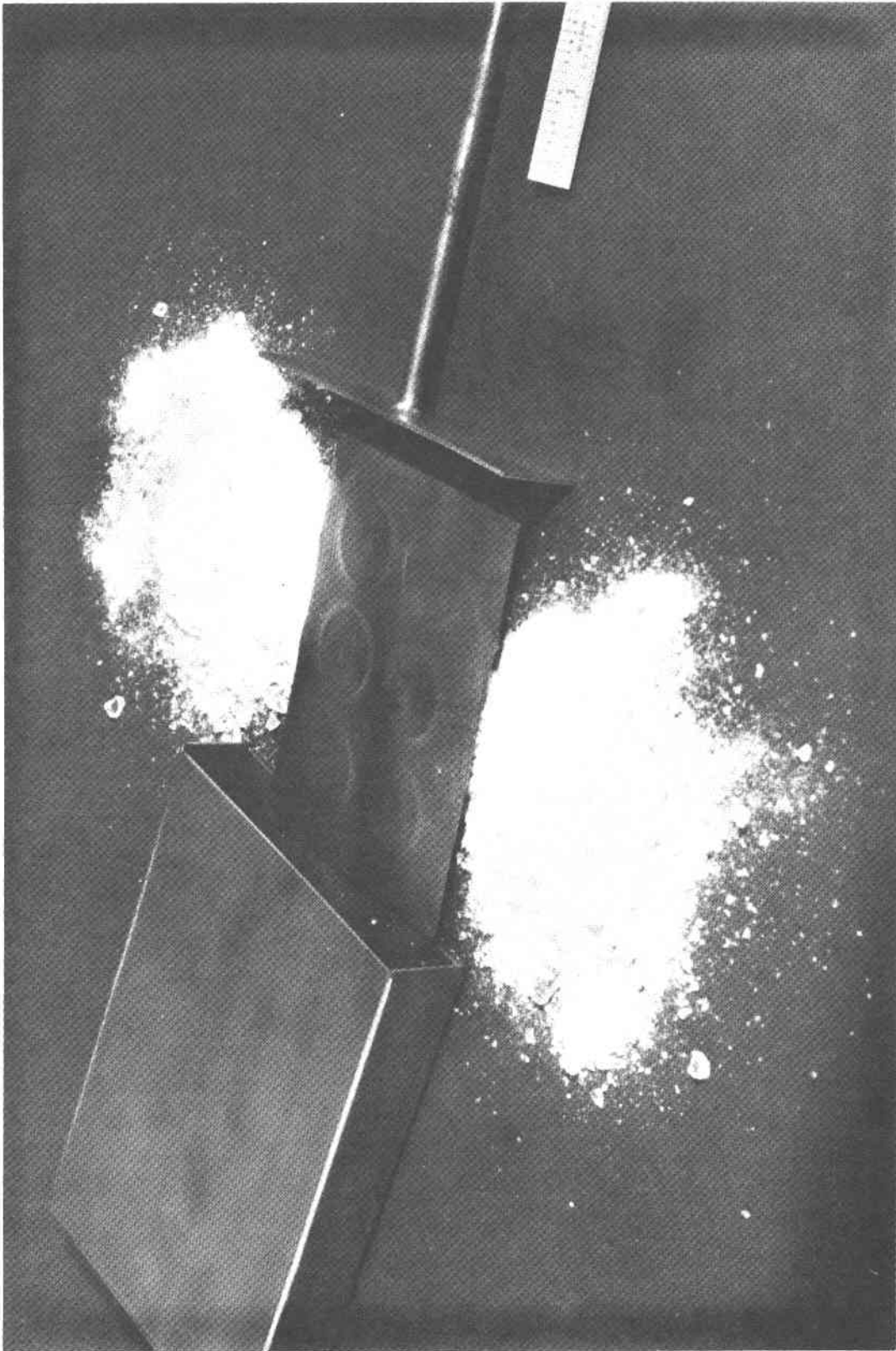
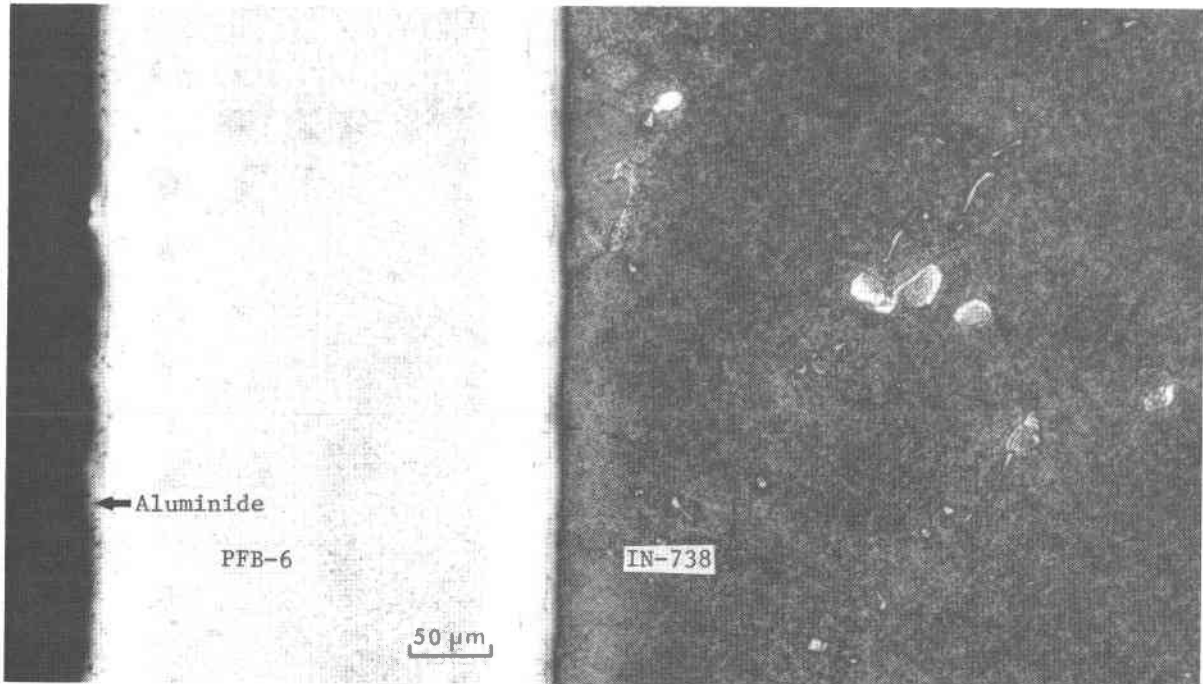
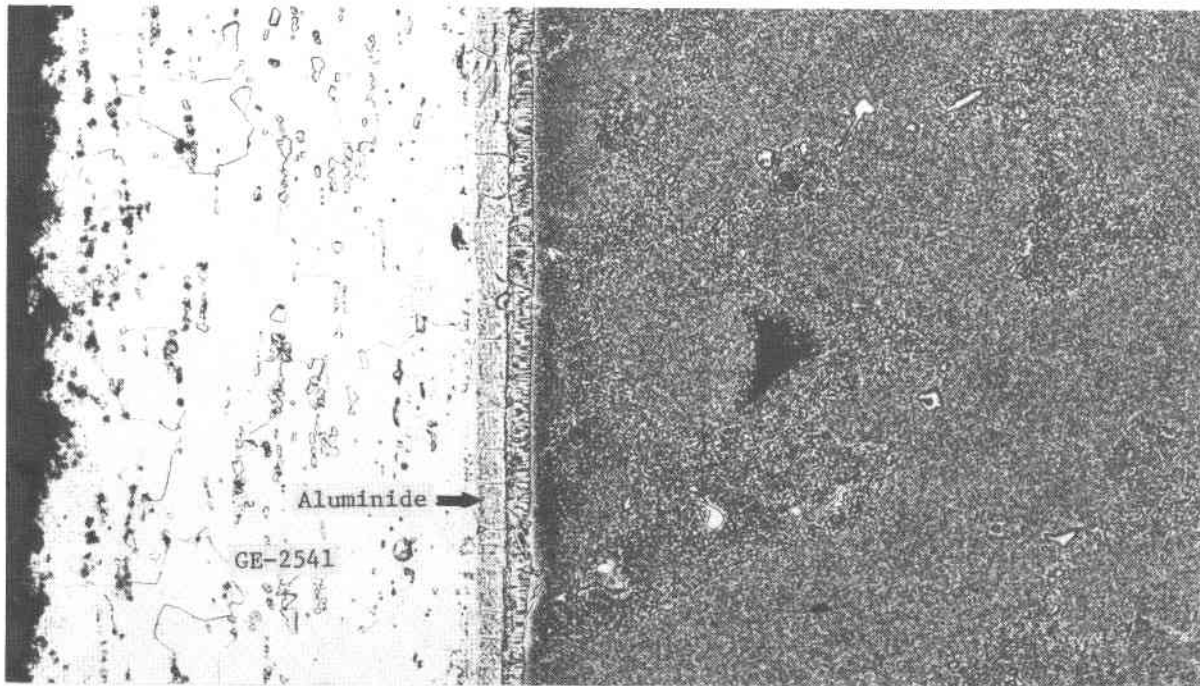


FIGURE 1. CLAD CORROSION DISC ASSEMBLY



Pack-Aluminided PFB-6



Under-Aluminided GE-2541

Figure 2. Addition Of Al Sources To Extend Cladding Life

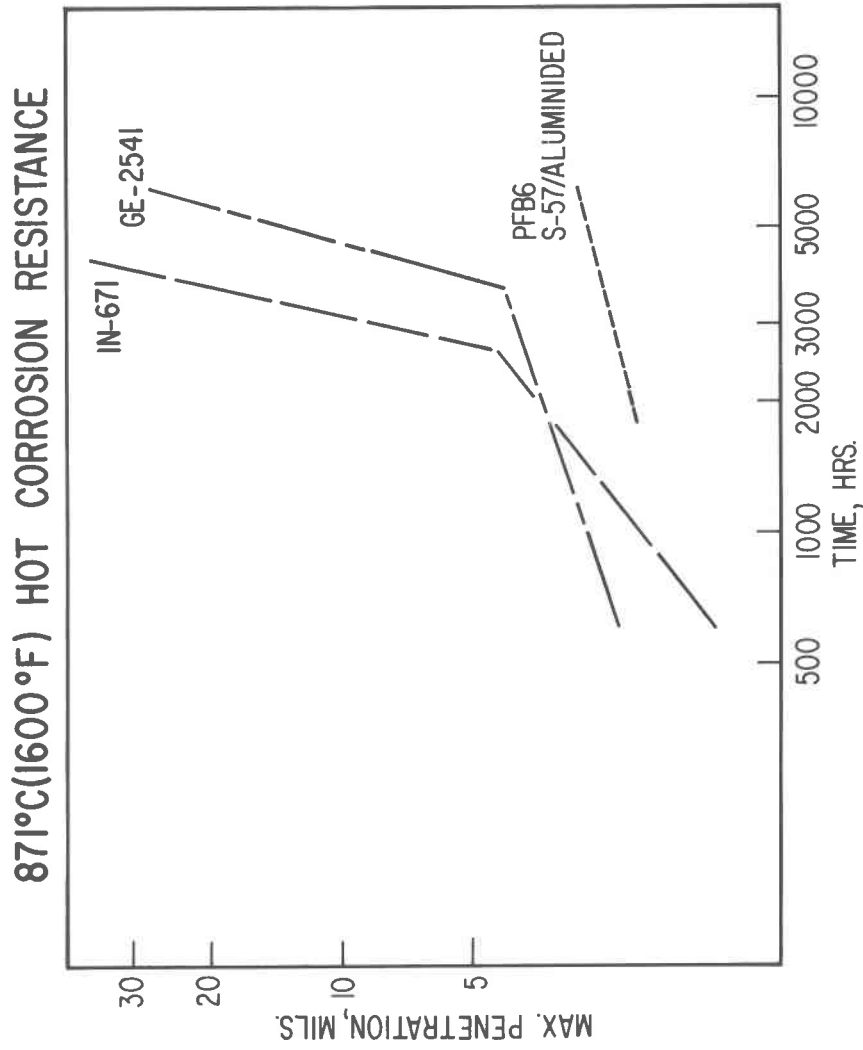
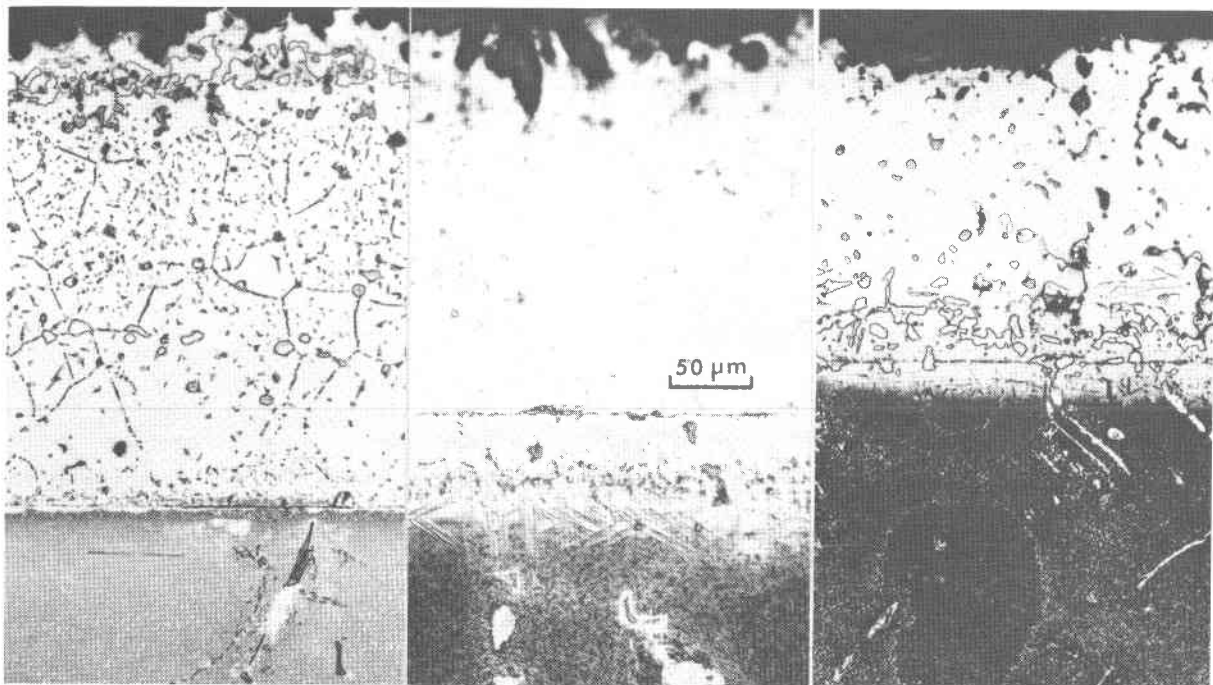


FIGURE 3. 871C HOT-CORROSION RESISTANCE

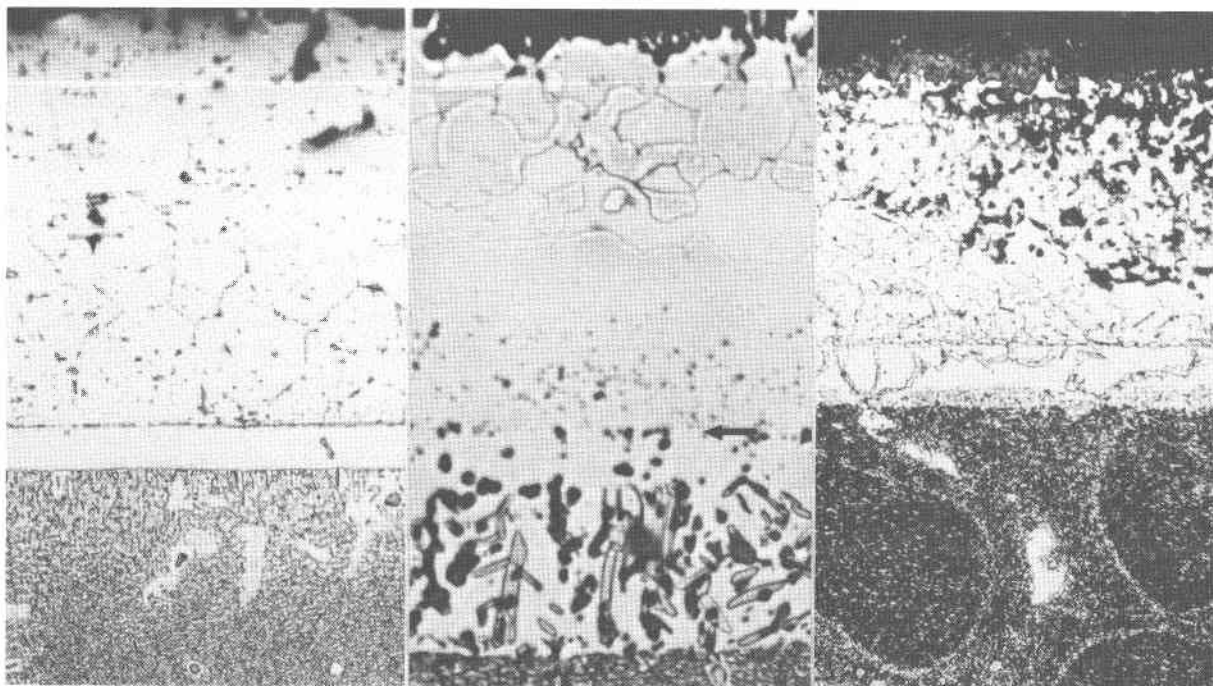


Aluminided S-57

GE-2541

IN-671

Figure 4. Hot-Corrosion Behavior After 5000 Hours At 871°C

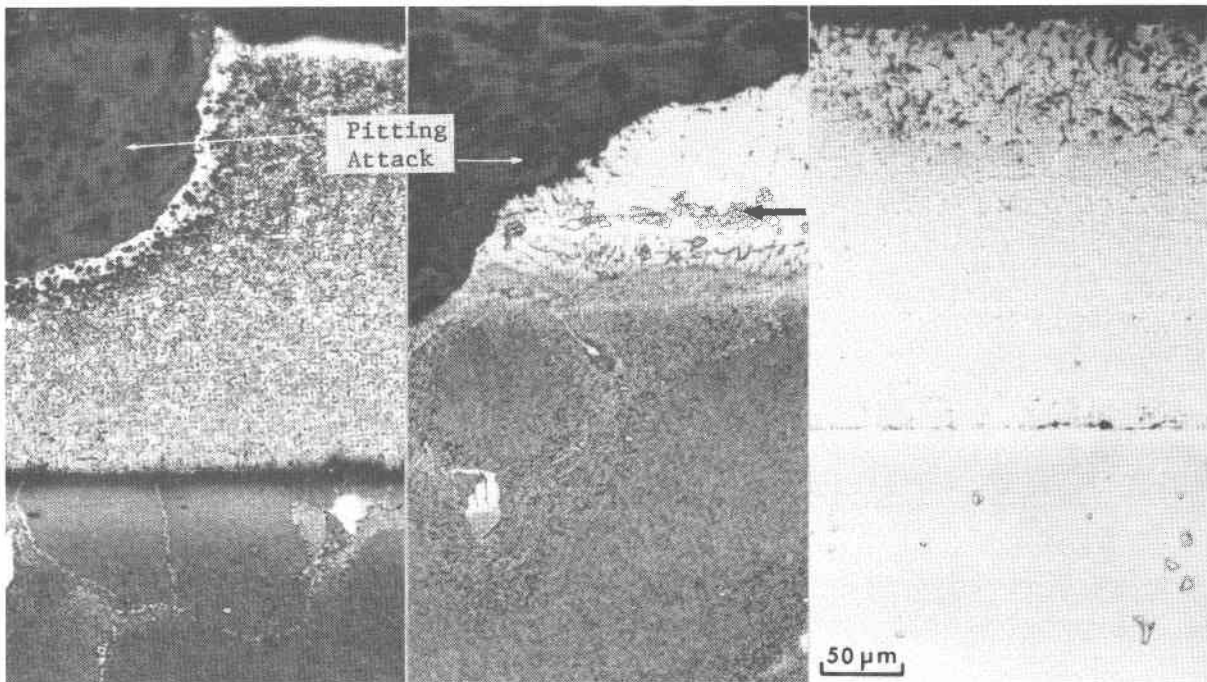


Aluminided S-57

GE-2541

IN-671

Figure 5. Hot-Corrosion Behavior Of Claddings At 982 C

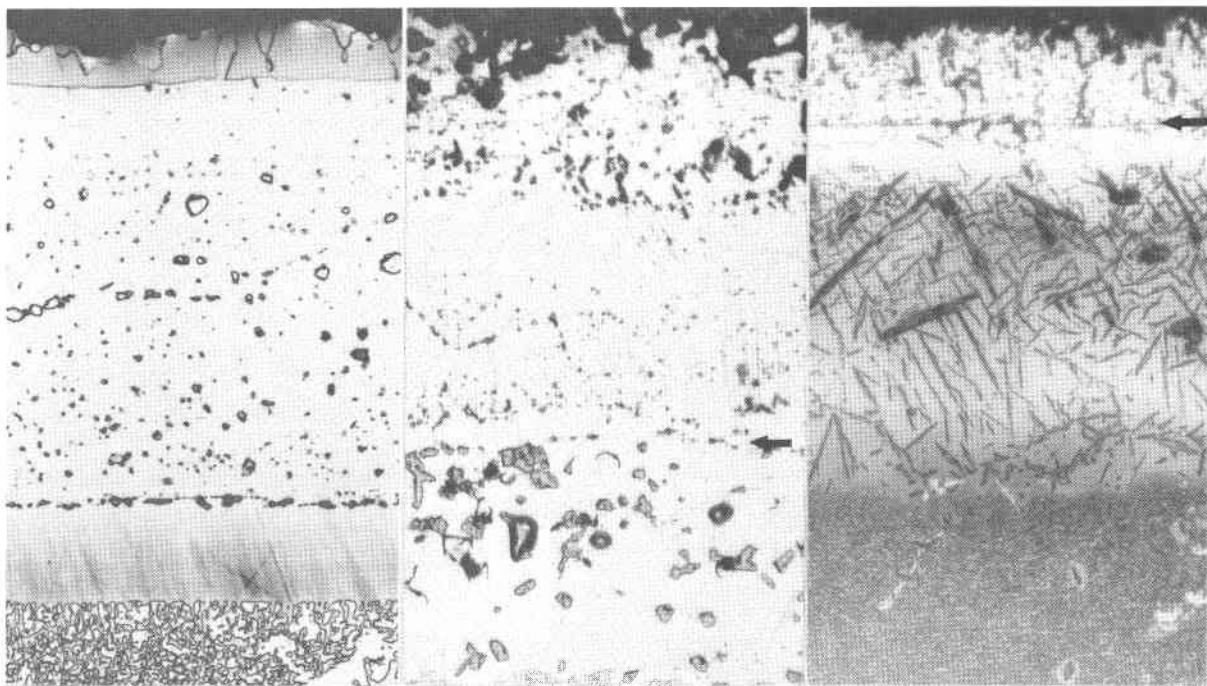


PFB-6  
499 Hr.

GE-2541  
613 Hr.

IN-671  
4132 Hr.

Figure 6. Hot-Corrosion Behavior Of Claddings At 732 C

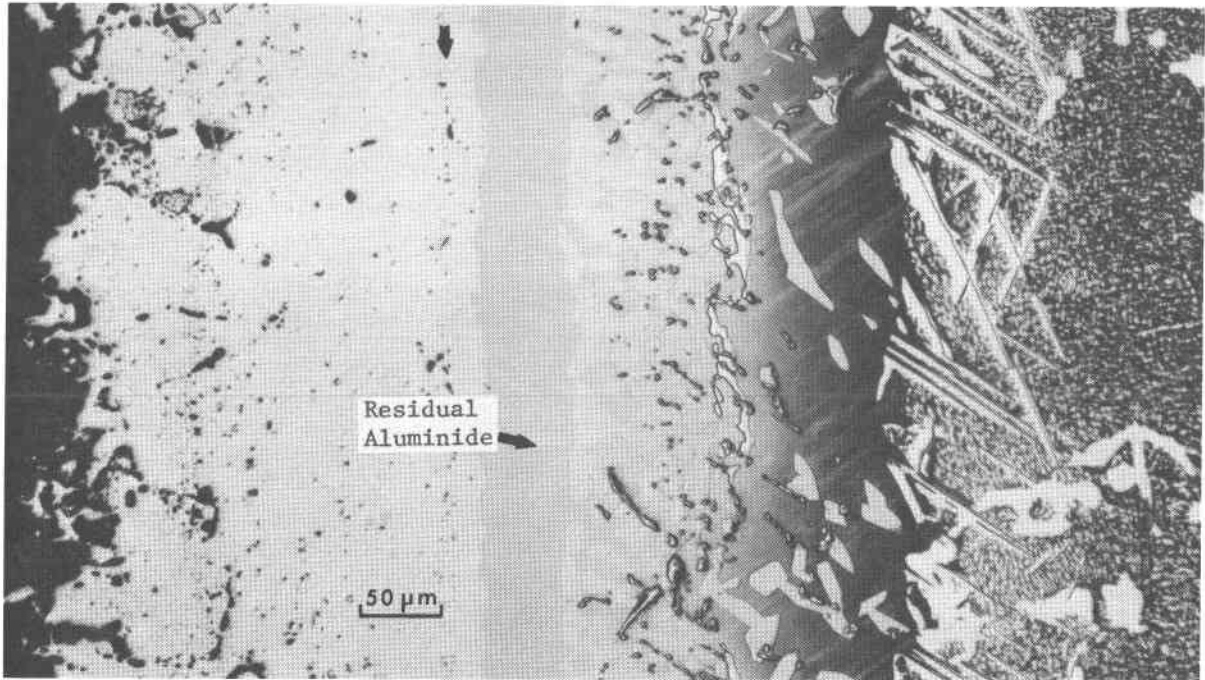


Aluminided 5-57  
1038°C/4000 Hr.

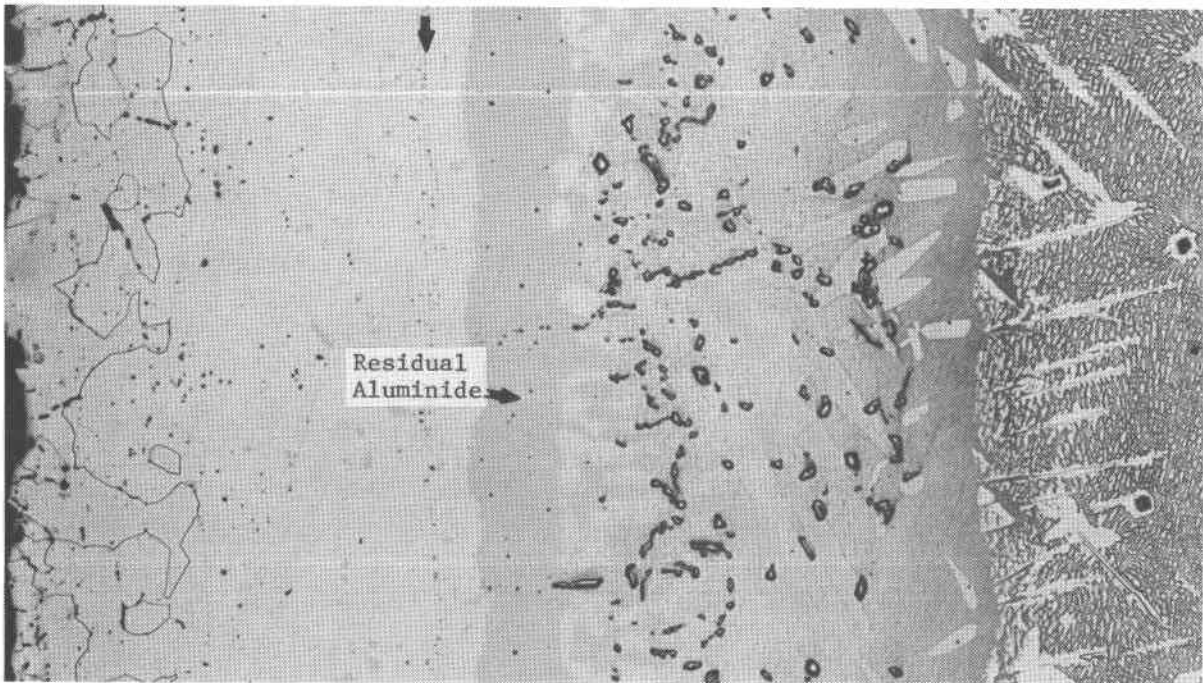
GE-2541  
1038°C/2000 Hr.

IN-671  
982°C/4500 Hr.

Figure 7. Oxidation Behavior Of Claddings



982°C/8277 Hr. Hot-Corrosion



1038°C/4000 Hr. Oxidation

Figure 8. Effect Of Al Source On GE-2541 Cladding Life



FIGURE 9. LEADING EDGE, S-57 CLADDING + OVERALUMINIDE AS POLISHED

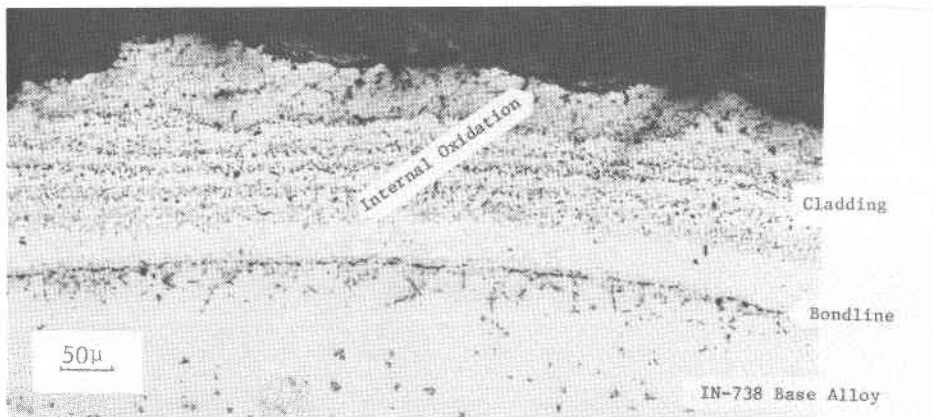


FIGURE 10. LEADING EDGE, GE-2541 CLADDING AS POLISHED

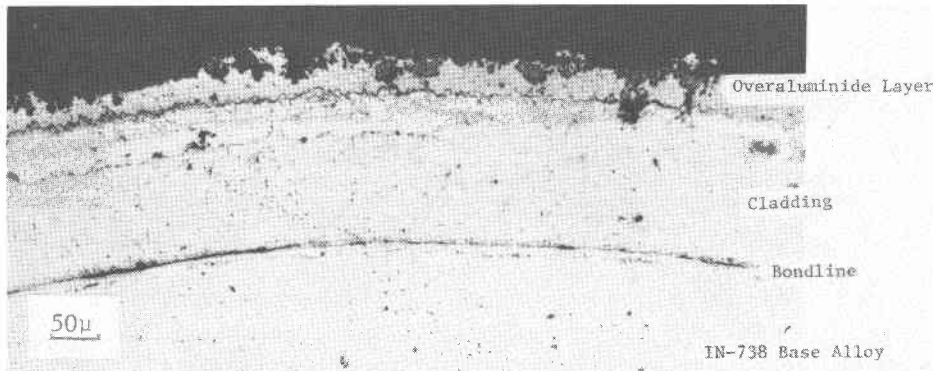


FIGURE 11. LEADING EDGE, IN-671 CLADDING + OVERALUMINIDE AS POLISHED

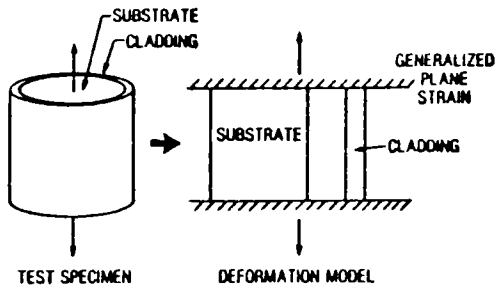


FIGURE 12. DEFORMATION MODEL OF TEST SPECIMEN

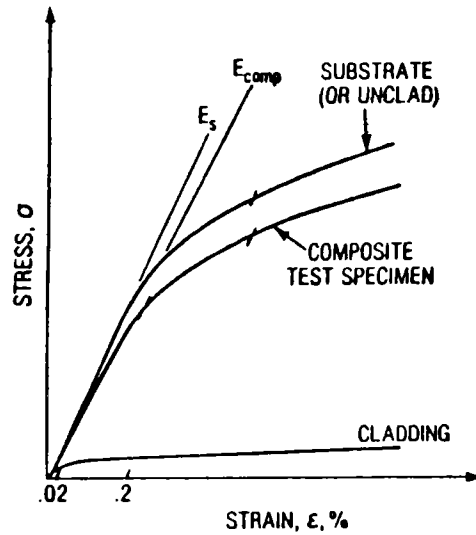


FIGURE 13. CALCULATED CLAD BAR TENSILE BEHAVIOR

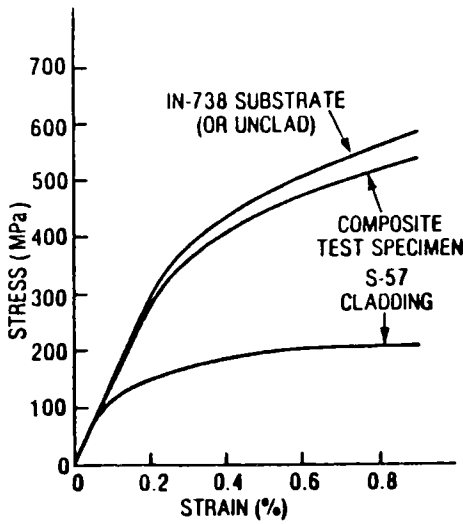


FIGURE 14. CALCULATED 871°C TENSILE BEHAVIOR OF S-57 CLAD IN738 TENSILE BAR

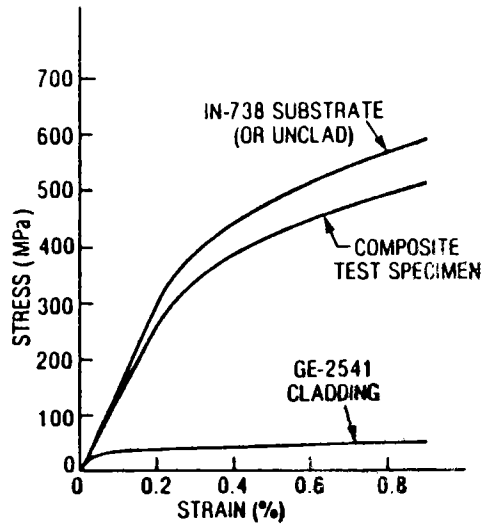


FIGURE 15. CALCULATED 871°C TENSILE BEHAVIOR OF GE-2541 CLAD IN738 TENSILE BAR



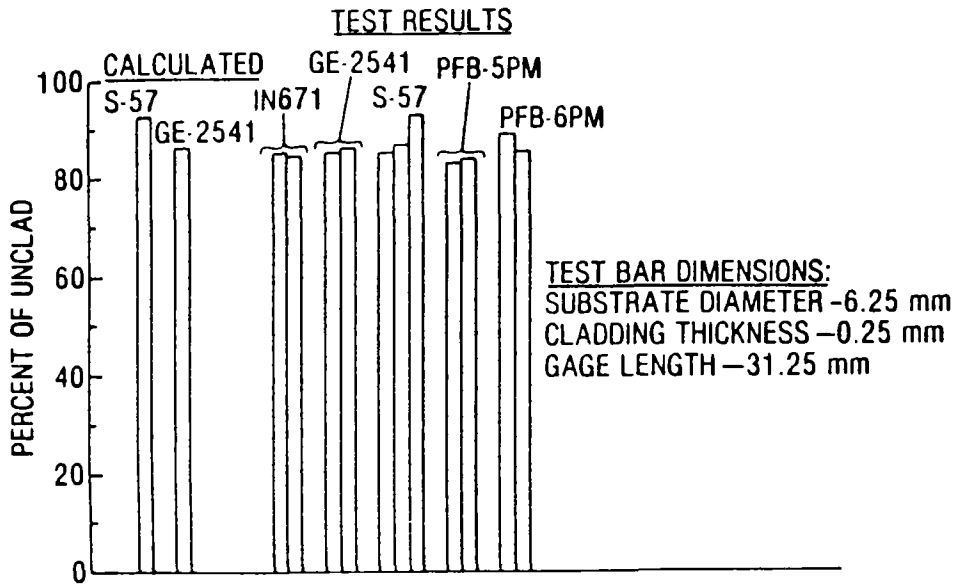


FIGURE 16. 0.2% YIELD STRENGTH OF CLAD IN738 TENSILE BARS AT 871°C

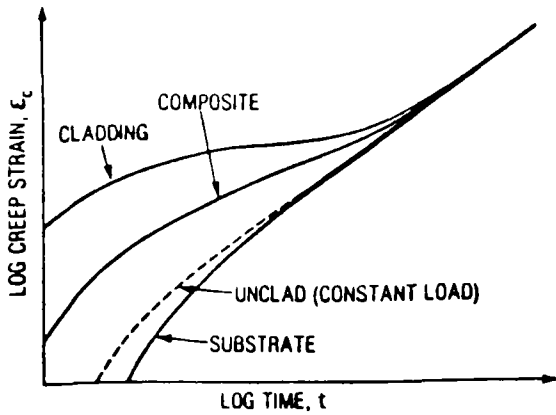


FIGURE 17. CALCULATED CLAD BAR CREEP RESPONSE

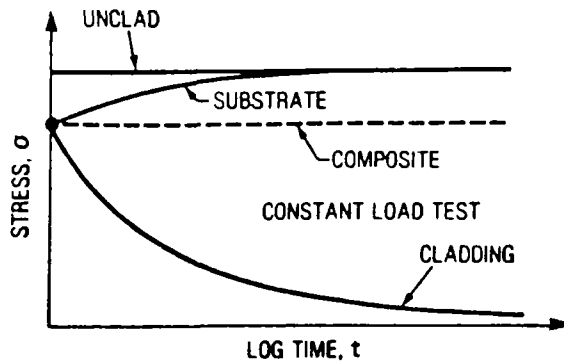


FIGURE 18. CLAD BAR CREEP STRESS RESPONSE UNDER CONSTANT LOAD TESTING

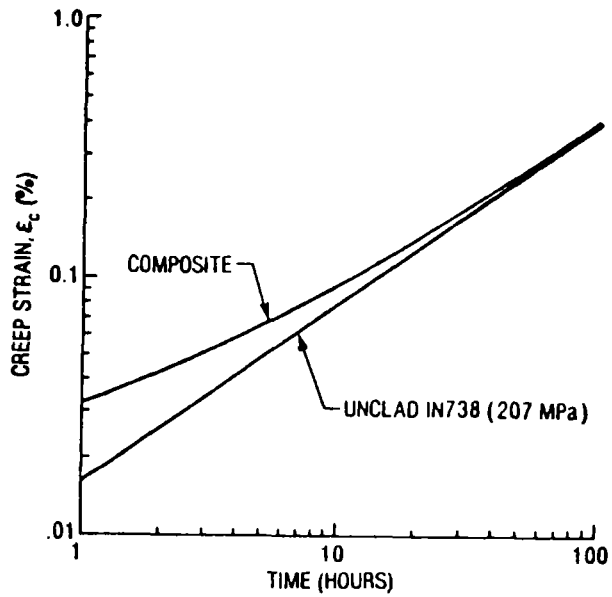


FIGURE 19. CALCULATED CONSTANT LOAD CREEP BEHAVIOR OF S-57 CLAD IN738 CREEP BARS AT 871°C

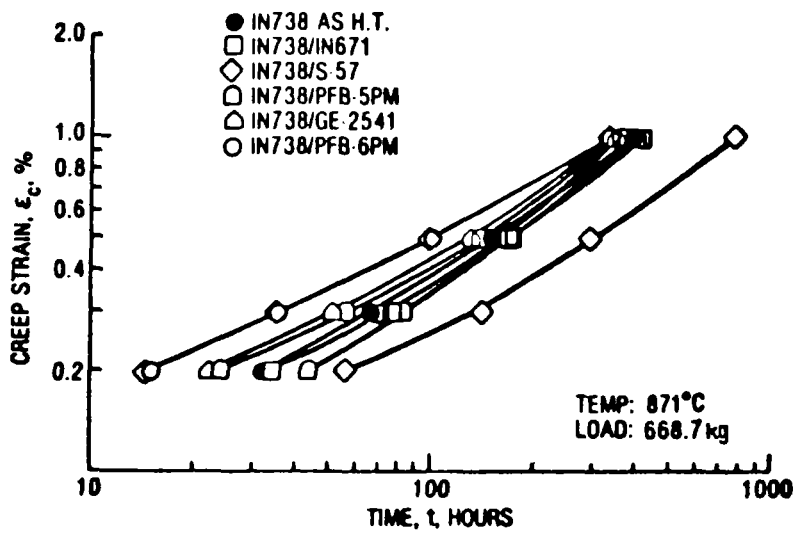


FIGURE 20. CREEP PROPERTIES OF CLAD IN738 CREEP BARS

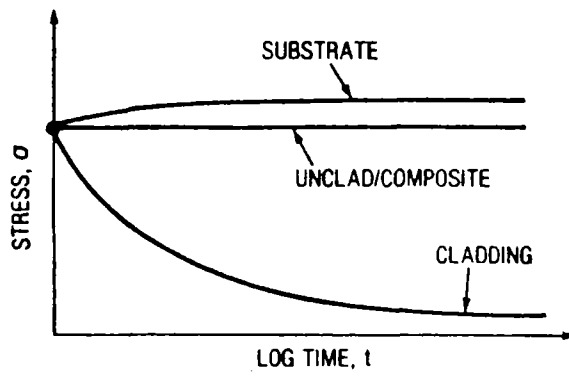


FIGURE 21. CLAD BAR CREEP STRESS RESPONSE UNDER EQUIVALENT STRESS

# INTERACTIONS BETWEEN COATINGS AND SUBSTRATES AT ELEVATED TEMPERATURES

by

D. P. Whittle  
D. H. Boone

University of California  
Lawrence Berkeley Laboratory  
Materials and Molecular Research Division  
Berkeley, California 94720

## INTRODUCTION

The durability of directly fired heat engines operated on minimally processed coal-derived liquid fuels is expected to be dependent on the surface stability of combustion zone components. From previous experience with gas turbine engines burning highly refined fuels in both clean environments such as experienced in aircraft propulsion, as well as in marine and industrial environments where a variety of types and levels of contaminants are present, it was found that the use of some type of protective coating is mandatory. As a result, three principal types of protective coatings have developed: diffusion aluminide coatings in the early fifties, overlay-type coatings in the sixties and finally, the recent, ceramic or thermal barrier coatings. At first sight, this order of development also represent what might be anticipated to be an increasing independence of the substrate, and indeed this was one of the driving forces in the evolution of newer coatings. As the superalloy substrates became stronger and more complex, and in the process less corrosion resistant their ability to provide beneficial elements and "coatability" to diffusion-type coating systems was drastically reduced. Nevertheless, as discussed in what follows, it is slowly being realized that overlay coatings particular metallic overlays and probably also the ceramic thermal barrier-types are far from independent of the substrate, and there is a real need to understand the type and extent of interactions which can occur. In essence, it is now no longer possible to develop superalloy substrate compositions independently of considerations of the need to apply a coating.

This paper then examines the three major types of coatings - diffusion aluminide, overlay and thermal barrier coatings, and in particular concentrates on the effects

of substrate elements interfering with or enhancing the corrosion resistance properties of the coating. The effects of coating elements diffusing into the substrate and influencing its mechanical properties are not considered.

#### DIFFUSION ALUMINIDE COATINGS

Diffusion aluminide coatings are produced principally via a pack cementation process. The extent of substrate interaction depends critically on the process used and two types have been identified (1): 'inward' and 'outward' coatings formed in high and low Al activity packs respectively. The inward, and to a lesser extent the outward, type coating has an external zone which is strongly dependent on the initial substrate. This is a significant feature that can both improve or degrade the oxidation and hot corrosion resistance. For example, the MC-type carbides of the base alloy often extend out to the coating surface providing the origin for defects which can favor the local oxidation of the coating. In addition, loss in nickel from the substrate to the coating can result in  $\sigma$ -phase formation. Improvements in the protectivity of simple aluminides can sometimes be achieved via some form of pre-treatment. For example, the adverse effect of titanium from the substrate interfering with protective oxide formation can sometimes be avoided by depositing a 15-30  $\mu\text{m}$  of a nickel-base alloy on the component prior to aluminizing (2).

In a more positive sense, however, addition of elements such as chromium or noble metals like platinum are considered. While the level of chromium enrichment which can be achieved is limited, enrichment of the substrate in chromium followed by a separate or sequential inward aluminizing step can result in enhanced hot corrosion resistance, particularly in the low and intermediate temperature regime. An alternative method of introducing chromium into aluminide-type coatings involves the incorporation of chromium-rich particles from the pack using a low aluminum activity pack, and hence an outward growing aluminide. However, it is difficult to control the inclusion mechanism, since the quantity of chromium-rich particles included depends on the quality of the pack-component contact.

The incorporation of platinum or possibly other noble metals by predepositing 5-10  $\mu\text{m}$  of Pt prior to aluminizing, either via a high or low activity process leads to coatings of excellent quality. Lifetime improvements, particularly in the intermediate temperature range, 800-1000°C, can be achieved.

The mechanism by which chromium and platinum improve the protectivity of the simple aluminides is not well understood, but is being related to their effect on the structure and behavior of the initial  $\text{Al}_2\text{O}_3$  layer which forms on exposure to an oxidizing environment. Using a deep etching technique, which selectively removes the coating, allows direct examination of the underside of the surface oxide at its

interface with the coating. Figure 1 shows a typical example of the underside of an  $Al_2O_3$  scale formed in 100 h at 1000°C on a platinum-modified coating on IN 738. Comparison with other systems, and at various stages of exposure indicates that one difference is the much finer  $Al_2O_3$  grain size found on the platinum modified aluminide. Studies are continuing.

Currently, there is also considerable interest in active element additions to aluminide coatings, similar to those in overlay coatings. Again, one route to achieve this, is via additions to the substrate. It has been reported (3) that Hf diffusing from the substrate alloy to the coating was responsible for the improvement in oxidation resistance of Rene 125 over Rene 80. Recent work on aluminized IN 738 containing different levels of Hf indicates that indeed the active element can have an effect on the coating behavior, but that this again depends on the type of aluminide coating.(4)

Aluminide coating of more advanced alloy substrates, such as directionally solidified and oxide dispersion strengthened alloys produces additional problems. The development of unwanted porosity between coating and substrate is often observed. Recent studies with oxide dispersion strengthened alloys (5) have indicated coating void formation and the resulting spallation occurs primarily in the coating inner zone and is delayed, but not prevented, by a larger more dispersed zone produced by outward type coatings on high aluminum content alloys. In addition, the thickness and structure of aluminide coatings particularly the inner coating zone on ODS alloys was a strong function of substrate alloy composition. Increased aluminum levels and possible refractory strengthening elements appeared to be beneficial. For all the ODS alloys and aluminide coatings studied, the coating systems appeared to have insufficient protectivity to match the available mechanical properties. The lack of stability was manifested by both coating void formation and resulting spallation and aluminum diffusion into the substrate.

#### OVERLAY COATINGS

Overlay coatings, applied by physical vapor deposition, both electron beam and sputtering, and plasma spraying, allow more flexibility in composition selection. Substrate effects are still observed. However, the amount of published information available is rather limited, since these interaction effects are only just being recognized. In addition, the complexity of the system and various proprietary interests are also involved. Hf from IN 738+Hf was found to improve the hot corrosion resistance of a CoCrAlY type coating (6). The coating process also has an influence, Gupta (7) found that diffusion of Hf from a DS MAR-M200+Hf substrate into an EB PVD coating occurred at a substantial faster rate than into a NiCoCrAlY

coating prepared by plasma spraying. Ti has also been found to diffuse rapidly into EB PVD CoCrAlY coatings and accumulate at the interface between the surface  $Al_2O_3$  and the coating.

At this point, it is of interest to briefly examine which elements from the substrate are likely to influence, either in a beneficial or detrimental way, the corrosion resistance of the coating. Some of these are listed in Figure 2. Elements like tungsten, molybdenum and niobium may contribute to acid fluxing in conjunction with sulfate deposits on the surface. Titanium and hafnium may contribute to improved scale adhesion in some instances, but in others may compete with the aluminum in scale formation and reduce the protectivity of the surface oxide. In general, it is not possible to broadly classify a particular element as beneficial or deleterious. It depends on the concentration of the element concerned, and perhaps more critically, on the type of conditions being considered: at high temperature, oxidation is the primary degradation mode, whereas at lower temperatures hot corrosion due to the presence of molten salts is more important with the nature of the deposit also being critically temperature dependent.

Equally, it is important to examine how fast the various elements can diffuse through a typical overlay coating. Figure 3 shows very approximately the time taken for the concentration of an element from the substrate to reach 10% of its value in the substrate at the surface of a 125  $\mu m$  thick coating. These calculations are based on diffusion coefficients taken from Diffusion Data (8), and consequently, do not take into account the possible variation of diffusion coefficients with composition, or perhaps more importantly with coating structure, as discussed later. It is clear from Figure 3 that at temperatures above 1100°C, virtually any substrate element can penetrate the surface coating in a relatively short period, while below 1000°C, it is perhaps surprising to see any effect of the substrate on the surface properties of the coating.

Studies at the Naval Postgraduate School (6, 9) of the potentially beneficial effects of platinum as an interlayer between the superalloy substrate and the EB-PVD applied CoCrAlY coating suggest that the essential effect of platinum may be its strong interaction with Ti (forming an Engel-Brewer type phase (10)). In this manner, platinum limits the movement of Ti through the coating to the surface either during the coating process or during subsequent exposures at elevated temperatures. The effect of substrate composition and the presence of a platinum interlayer is shown qualitatively in Figure 4. Since these results are for accelerated (<100 hr) hot corrosion testing at 700°C any effect on the surface oxide protectivity must have been present in the as-coated condition or very shortly thereafter.

Studies of the PVD process has indicated the occurrence of a certain amount of surface mixing during the deposition process. The presence of any bias, so-called ion plating, is known to accelerate this interaction (11).

The as-deposited coating structure consists of an open, columnar oriented grain structure through which substrate elements could rapidly move by surface diffusion (12). Subsequent processing is used to densify this structure, but may be microscopically incomplete; Jacobsen reports the presence of  $\sim 100 \text{ \AA}$  diameter channels through several type of "fully dense" overlay coatings (13). Increased deposition times, temperatures and the presence of surface ion activity could accelerate this movement. Crane and Boone detected the presence of platinum,  $\sim 2\%$ , on the surface of a  $150 \text{ \mu m}$  thick EB-PVD CoCrAlY coating as applied over a  $5 \text{ \mu m}$  platinum layer (14). Previously, calculated diffusion rates do not predict this very high rate of substrate interaction.

The potential effect of coating structure is also seen in the studies by Gupta (7). An oxide at the "splat" boundaries of a plasma deposited MCrAlY might serve to accelerate the substrate diffusion of some elements (although the grain boundary path length from the substrate to the surface of a plasma deposited structure is clearly longer and more tortuous than for the perpendicularly aligned PVD boundaries). However, if the diffusing species is more oxygen active than the boundary oxide, interaction can occur, thereby effectively blocking the movement of certain elements such as Hf as proposed by Gupta. The possibility thus exists for selective transport of substrate elements to the coating-oxide surface. Hf moves much more rapidly in an EB-PVD coating than a plasma sprayed system. However, less potentially beneficial elements than Hf such as Ti may also be found at the surface of a PVD coating. Also, the "beneficial" effect of a platinum interlayer on high Ti content substrates may be deleterious if it blocks the movement of Hf as it would be predicted to do (6). The variables of substrate composition, coating composition and processing, and the use of interlayers appear to be increasing and additional studies and information are required to optimally use these systems in increasingly severe environments.

Another important effect, that of coating thickness, on the degree and rate of interaction has been recently noted by Morral and Barkalow together with development of a method of normalizing measurements on coatings of varying thicknesses (15). Diffusion distances and the "reservoir" of coating elements are considered in their calculations. Such effects may account for some of the apparent scatter in results observed in some test programs.



Finally, in such discussions as this, it is appropriate to note that in these phenomena where extremely small levels of certain elements can have very large effects on protectivity, it is important to consider some of the inherent limitations of analytical techniques often used in their study. In a multi-phase, columnarly oriented structure with potential channel like diffusion paths, the critical levels of substrate elements such as Ti may be undetected by all but, the most sensitive (time consuming and expensive) techniques. For these and other reasons, little hard data are available as yet on the specific elements and their threshold levels for detectible effects on coating protectivity.

#### CERAMIC THERMAL BARRIER COATINGS

Finally, ceramic coatings are currently being actively considered since these provide both a thermal barrier, allowing hotter gas temperatures, and an apparent inert barrier to isolate the metallic components from the corrosive environment. Potential substrate effects are still evident. Most ceramic coating designs use an intermediate metallic bond coating to improve the adhesion of the ceramic coating. This, of course, is susceptible to all the interactions referred to above. The bond coating is usually pre-oxidized before the ceramic coating is applied but the effects of this, and the influence of the substrate, on the mechanism of adhesion, oxide to oxide are not well understood. In addition, there is also the possibility of destabilization of the ceramic, especially  $ZrO_2$  a prime candidate, by elements diffusing from the substrate and into the ceramic.

#### CONCLUDING REMARKS

Table 1 summarizes the various observations which have been discussed. From this it is clear that there is a real need for a coordinated study of the interaction between coating and substrate and its subsequent effect on coating behavior is of vital importance. Considerably more understanding and data are required, particularly relating to the effects of low, but significant, concentrations of elements such as titanium, hafnium, platinum, etc., although it is recognized that there are some analytical limitations. The initial oxide, and in particular its interface with the surface coating, appears to be the critical area.

#### ACKNOWLEDGEMENT

This work was supported by the Director, Office of Energy Research, Office of Basic Energy Sciences, Materials Sciences Division of the U. S. Department of Energy under Contract Number W-7405-ENG-48.

## REFERENCES

1. G. W. Goward and D. H. Boone, *Oxid. of Metals*, 3 (1971).
2. R. Pichoir, "High Temperature Alloys for Gas Turbines," *App. Sci. Publ.* (1979) pg. 191.
3. P. Aldred, paper presented at the National Aerospace Engineering and Manufacturing Meeting, Los Angeles, November 1975.
4. J. R. Exell, M. S. Thesis, Naval Postgraduate School, Monterey, CA. (1981).
5. D. H. Boone, D. A. Crane and D. P. Whittle, *Thin Solid Films*, to be published.
6. R. N. King, M. S. Thesis, Naval Postgraduate School, Monterey, CA. (1980).
7. D. K. Gupta, *Thin Solid Films*, 73 (1980) 477.
8. *Diffusion Data*, Ed. F. H. Wohlbier, *Trans. Tech. Publ.*
9. D. E. Bush, M. S. Thesis, Naval Postgraduate School, Monterey, CA. (1979).
10. L. Brewer and P. R. Wengert, *Met. Trans.* 4, 83 (1973).
11. R. D. Bland, G. J. Kominiak and D. G. Mattox, *J. Vac. Sci. and Tech.* 11, 4 (1974).
12. D. H. Boone, T. E. Strangman and L. W. Wilson, *J. Vac. Sci. Technol.* 11, (1974) 641.
13. B. E. Jacobson, private communication, 1981.
14. D. A. Crane and D. H. Boone, Lawrence Berkeley Laboratory unpublished work (1981).
15. J. E. Morrel and R. H. Barkalow, submitted for publication, *Scripta Met.* (1981).

TABLE I  
OBSERVATION SUMMARY

- \* A strong effect of substrate composition exists on the protectivity of the applied coating.
  - either beneficial or detrimental depending upon specific elements.
- \* The substrate effect is greatest for diffusion aluminides.
  - depends on type of aluminide and use of addition elements.
- \* The substrate effect is less for overlay type coating.
  - Cladding Systems
    - depends on thermal diffusion and could be predictable with sufficient data.
    - interdiffusion a significant factor at high temperatures.
  - Thermal Spray Systems
    - grain boundary effects important
      - selective barriers for oxygen active elements.
      - selective paths for other elements?
  - Physical Vapor Deposition Systems
    - aligned boundaries - short circuit diffusion, can be beneficial or detrimental.
    - process sensitive.
- \* The use of platinum (or possibly other) intermediate layers can be beneficial or detrimental.
  - can act as a selective barrier depending upon substrate elements.
- \* Ceramic thermal barrier coating systems.
  - intermediate layer dependence similar to overlay systems.
  - ceramic-oxide bonding possibly dependent on interaction (not well understood).
  - degree of ceramic stability dependent on interaction.

## FIGURE CAPTIONS

- Figure 1. SEM examination of underside of protective  $Al_2O_3$  oxide grown on platinum modified aluminide coating using LBL deep etching technique. Structural features of oxide-metal interface surface are being compared with oxides grown on other aluminide and overlay coatings to understand differences caused by interaction with substrate elements.
- Figure 2. Schematic drawing of coating-substrate interactions and potential elements of interest.
- Figure 3. Plot of calculated substrate diffusional interaction time for an element to appear at the surface of a  $125\ \mu m$  single phase fully dense coating layer, as function of temperature.
- Figure 4. Qualitatively comparison of relative  $700^\circ C$  hot corrosion resistance of  $125\ \mu m$  thick EB-PVD applied CoCrAlY coating as affected by substrate composition, and presence of platinum interlayer (6).

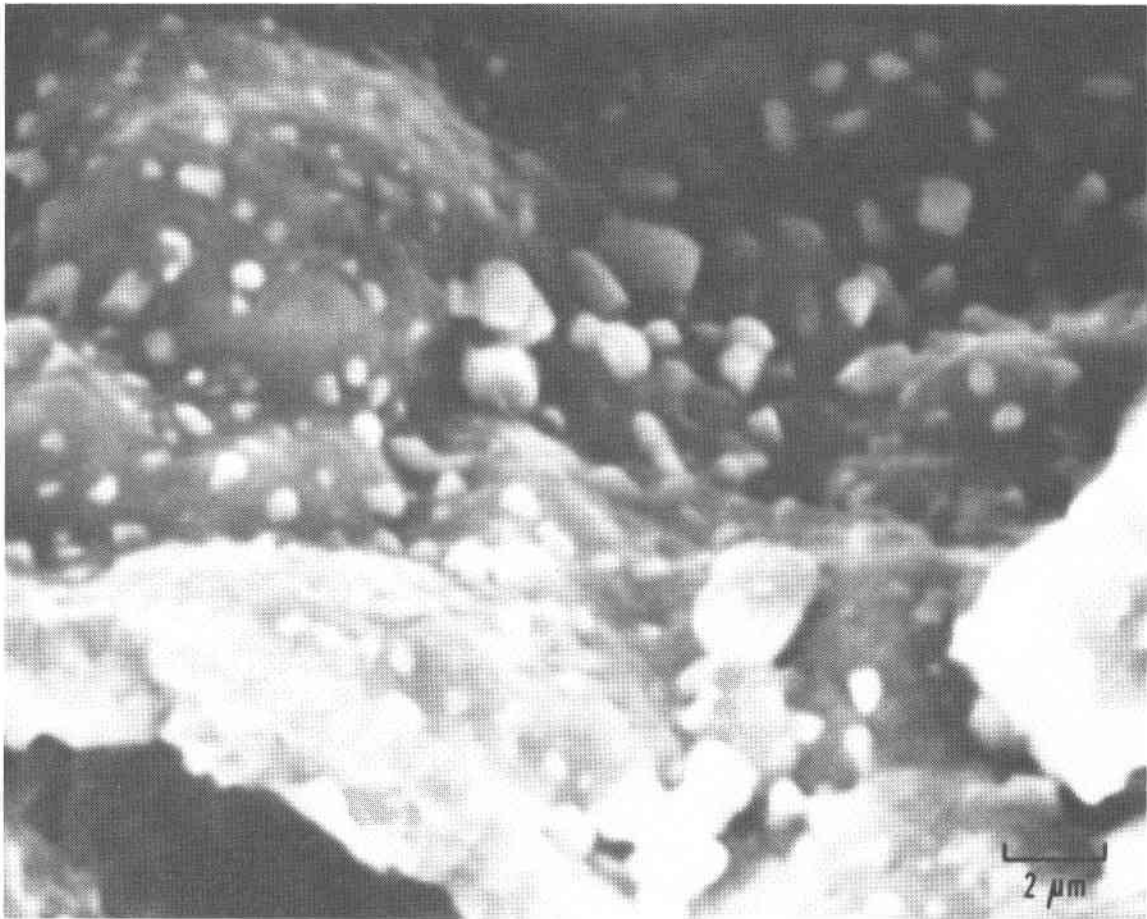
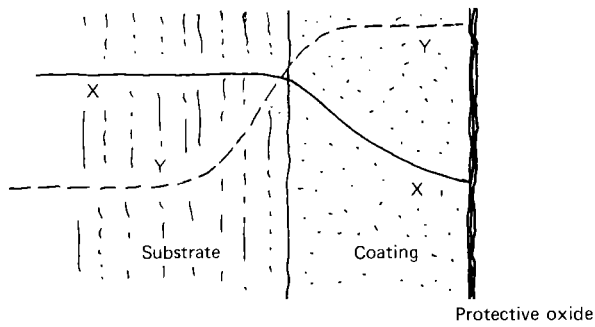


Figure 1.



Typical X elements

- |    |  |
|----|--|
| W  | } May contribute to acid fluxing   |
| Mo |  |
| Nb |  |
| Ta | } Active elements may contribute to scale adhesion or compete with $Al_2O_3$ formation |
| Ti |  |
| Hf |  |
| Pt |  |

Typical Y elements

- Al  
Cr  
Y  
Pt

Figure 2.

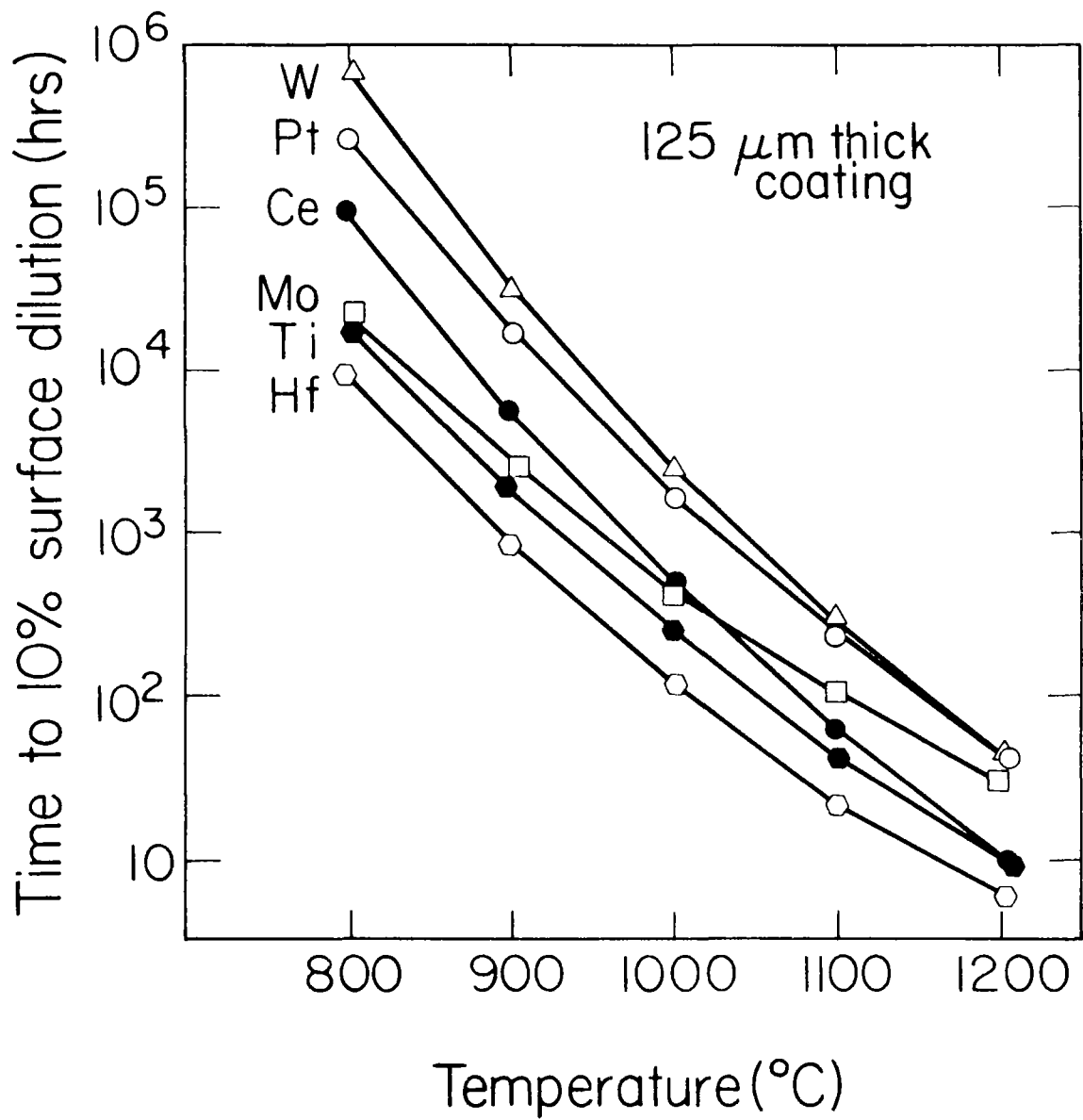


Figure 3.

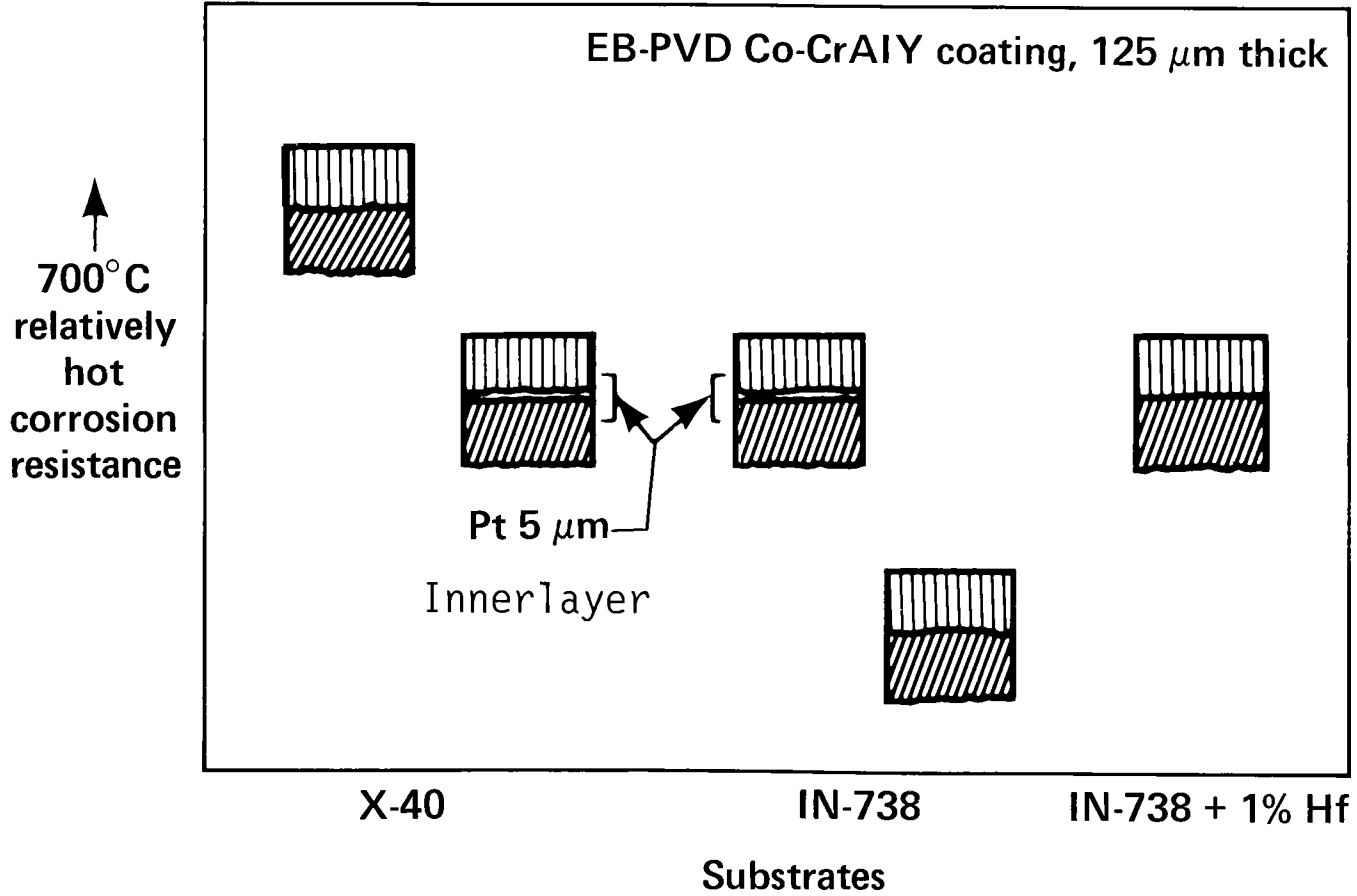


Figure 4.



TURBINE BLADE MATERIALS RESEARCH  
AT SANDIA NATIONAL LABORATORIES

by

R. E. Benner, J. C. Hamilton,  
A. S. Nagelberg, and P. L. Mattern

Introduction

Large payoffs are associated with increasing the operating temperature of gas turbines and using coal-derived fuels. Motivated by these possibilities, DOE/OBES is supporting programs at Sandia National Laboratories, Livermore, California, to develop and use new diagnostic techniques for the in-situ study of turbine blade materials and coatings. A major goal is to use the developed techniques to augment the present understanding of corrosion processes at elevated temperatures in realistic combustion environments.

In order to obtain a better understanding of failure mechanisms, we need to be able to characterize the chemical species present on and in turbine blade materials and coatings, as well as in the surrounding gaseous environment. In addition, measurements of structural symmetry, stoichiometry, impurity content, and temperature are required. To be of practical importance, experimental techniques under development should possess high overall sensitivity and adequate spatial and temporal resolution. With such diagnostic capabilities, the process of evaluating the corrosion resistance of a given turbine blade composition for a particular application should be greatly simplified and made significantly more reliable.

Most of the in-situ methods being evaluated at Sandia rely on a form of laser light scattering called spontaneous Raman spectroscopy. These techniques are supplemented by post-exposure surface analytical tools optimized for combustion-related materials studies. Advantages of the Raman method include the capability of characterizing samples at high temperatures ( $>1050^{\circ}\text{C}$ ) and high pressures (1 atm. or higher), identifying chemical compounds -- rather than the elemental constituency -- determining compound symmetries, providing good lateral resolution ( $\sim 1$  micrometer), and giving adequate sensitivity for the identification of thin corrosion scales ( $<50$  Å for some materials of practical importance).

This paper summarizes recent experimental results which demonstrate some of the capabilities of the Raman method. In the following section, we present a brief description of Raman spectroscopy and describe a combustion environment simulator which has been modified for materials studies. Later sections emphasize applications to gas phase studies, analysis of zirconia-based thermal barrier coatings, alloy oxidation, and molten salt attack.

### Experimental Techniques

Raman spectroscopy relies on the interaction of incident monochromatic light with vibrational/rotational excitations within a sample to produce frequency-shifted scattering radiation. Measured frequency shifts are directly correlated with vibrational/rotational mode energies. Scattered light intensities are proportional to the concentration of scattering species in the probe volume. This volume is usually determined by the lateral extent of the incident laser beam, and the depth of penetration of the laser light into the sample. Since vibrational mode energies are species-specific, Raman data provide molecular or compound signatures which can be used for identification. Comparison of collected spectra with data from reference standards is required to complete the identification process.

The major components of a Raman apparatus optimized for in-situ materials studies are indicated in Fig. 1. Excitation radiation from an argon ion laser is incident through the combustion chamber either vertically (for gas phase studies) or horizontally at an angle of incidence of  $\sim 30^\circ$  (for the characterization of opaque solids). Raman-scattered light is collected by the lens L1 and imaged onto the entrance slit of a triple grating monochromator for analysis of the frequency components present in the scattered light. Detection is accomplished with a photomultiplier and photon counting electronics.

The atmospheric combustion exhaust simulator (ACES) schematically represented in Fig. 1 provides combustion exhaust gases at high temperatures ( $\sim 1200^\circ\text{C}$ ) with a variable flow velocity (0.5 - 100m/sec). Provisions are also included for injection of particulates and/or trace species, and physical probe access. The simulator has been modified to include sample chambers with good optical access for laser-based studies of materials being exposed to the combustion exhaust flow.

### Gas Phase Analysis

To understand the details of corrosive attack, it is necessary to characterize the gas-phase environment. Figure 2 shows Raman scattering data which provide a quantitative description of the ACES gas phase composition, when the combustion

simulator was burning methane  $\text{CH}_4$  at a fuel/air equivalence ratio of  $\sim 0.03$  and operating at  $600^\circ\text{C}$ . The peaks observed correspond to  $\text{CO}_2$  (centered about  $\sim 1285\text{ cm}^{-1}$  and  $\sim 1385\text{ cm}^{-1}$ ),  $\text{O}_2$  ( $\sim 1550\text{ cm}^{-1}$ ),  $\text{N}_2$  ( $\sim 2330\text{ cm}^{-1}$ ) and  $\text{H}_2\text{O}$  ( $\sim 2650\text{ cm}^{-1}$ ). As expected (for the operational fuel/air ratio) unburned hydrocarbons from the  $\text{CH}_4$  fuel were not detected when the combustor was operating at  $600^\circ\text{C}$ . Based on the relative cross section for  $\text{CH}_4$  (1), unburned  $\text{CH}_4$  -- if present -- should have been detectable at the 0.1% level.

For comparison, a Raman spectrum also was recorded just after the burner was extinguished, resulting in an air temperature of  $\sim 330^\circ\text{C}$ . The  $\text{N}_2/\text{O}_2$  concentration ratio was then determined using the known Raman cross sections (1) to be 3.7 (in excellent agreement with the expected result for air) in comparison with the oxygen-lean value of 5.3 obtained in the exhaust when the burner was operating at  $600^\circ\text{C}$ . Also, as expected, the primary combustion products  $\text{CO}_2$  and  $\text{H}_2\text{O}$  were no longer observed in significant quantities.

Gas phase Raman data from diatomic molecules such as  $\text{N}_2$  also can provide a measurement of local temperature (1). This type of Raman thermometry is accomplished by comparing Raman data with calculated spectra which account for allowed transitions between different vibrational/rotational levels. The sensitivity to temperature occurs via the thermally-determined population factors for each level. An example is shown in Fig. 3, which compares a "best" fit result of  $629\text{K} \pm 25\text{K}$  with a thermocouple-measured temperature of  $625\text{K}$ . While the closeness of agreement is probably fortuitous, it is nevertheless evident that Raman spectroscopy provides a characterization of temperature as well as the composition of the gas-phase environment in realistic combustion environments.

### Thermal Barrier Coatings

Higher turbine operating efficiencies can be obtained with existing high temperature, high strength alloys by coating the turbine blades with a ceramic thermal barrier (2). The coating reduces metal surface temperatures and limits the interaction of corrosive species with the metallic substrate. Among the coatings being considered for use as thermal barriers are zirconia-based materials containing from 8-12 wt%  $\text{Y}_2\text{O}_3$ . The yttria serves to stabilize the coating in a fixed structure. Without the stabilizing additive, the coatings are susceptible to spallation initiated by large, thermally driven, volume-changing phase transitions (tetragonal or cubic to monoclinic) inherent in pure  $\text{ZrO}_2$  (3). Even with the addition of yttria,  $\text{ZrO}_2$ -based coatings are subject to failure, generally attributed to destabilization caused by thermal cycling or reaction with fuel impurities.

Raman spectroscopy can be used to determine the degree of stabilization of  $ZrO_2$ - $Y_2O_3$  ceramics. The ability to obtain this information remotely, while the sample is at temperature in a hostile environment, is an important advantage for Raman scattering over conventional techniques in this application. To illustrate the relative ease of phase identification in zirconia-based systems, room temperature Raman data obtained from  $ZrO_2$  crystals (4) containing various weight percentages of  $Y_2O_3$  are shown in Fig. 4. Dramatic differences are seen to exist between the samples containing 3%  $Y_2O_3$  (primarily monoclinic) and those containing 4-8%  $Y_2O_3$  (primarily tetragonal). Some regions of tetragonal symmetry exist within the 3% samples, evidenced by weak peaks at  $\sim 150\text{ cm}^{-1}$  and  $275\text{ cm}^{-1}$  in the spectrum from the 3% sample. Less pronounced changes arise during the tetragonal to cubic transition. In phase changes from tetragonal to cubic, the mode at  $\sim 625\text{ cm}^{-1}$  is displaced to lower frequency shifts, and the intensities of the remaining peaks approach zero, as can be seen by comparing the 8%, 12%, and 20% data.

Raman scattering can also be used to monitor the symmetry of the lattice structure as a function of temperature. The data shown in Fig. 5 are from a sintered pellet of  $ZrO_2$  containing 1 wt%  $Y_2O_3$ . The spectrum obtained at room temperature clearly is characteristic of the monoclinic phase of zirconia. The peaks associated with the monoclinic structure are quite sharp at room temperature, but broaden significantly upon heating to  $1050^\circ\text{C}$ . Interpretation of high temperature Raman data may be somewhat hampered by this type of thermal broadening; in some cases it may be necessary to obtain reference spectra at several temperatures. Nevertheless, as is expected for a 1% doping, the monoclinic structure is indicated in Fig. 5 as the predominant phase at ambient and elevated temperatures.

For the  $ZrO_2$ -based ceramics with higher levels of yttria addition, phase transitions have been observed by Raman scattering, while samples are heated or cooled at a constant rate. To minimize structural changes occurring during the acquisition of individual spectra, a multichannel Raman instrument was used. This apparatus consisted of a zero-dispersion premonochromator and third-stage spectrograph with an SIT vidicon detector. Using this system, spectra could be recorded in times as short as 15 ms and at a rate of several/sec. Figure 6 shows data obtained from a  $ZrO_2$ -2.5%  $Y_2O_3$  sample upon heating (a) and cooling (b) at a rate of  $6^\circ/\text{min}$ . The best indication of the monoclinic to tetragonal phase transition is the appearance of the peak at  $\sim 275\text{ cm}^{-1}$ . In agreement with previous studies (5), large hysteresis effects were observed in the phase transition temperature depending upon whether the sample was being heated (a) or cooled (b).

Deriving a surface temperature from solid-phase Raman data is based on a different approach than for the gas phase, since the temperature dependence of solid spectra cannot (usually) be calculated directly. One possible means of

obtaining a surface temperature from Raman data is illustrated in Fig. 7. Stoke's (vibrational excitation creation) and anti-Stoke's (vibrational excitation annihilation) spectra are shown for a  $ZrO_2$ -8%  $Y_2O_3$  pellet at 500°C (a) and 25°C (b). At low temperatures, a high degree of asymmetry is observed in the relative intensities of the Stoke's (negative frequency shift) and anti-Stokes (positive frequency shift) portions. The anti-Stokes spectrum is weak at low temperatures because the excited vibrational states are not populated. Thus, the annihilation scattering process, wherein the scattered photon gains energy from the destruction of a quantum of lattice energy, is not likely to occur. With increasing temperature, the system gains sufficient thermal energy to populate higher lying vibrational states, causing the spectra to become more nearly symmetric. By assuming a Boltzmann population distribution of the form  $\exp(-E/kT)$ , where E is the vibrational mode energy, k is Boltzmann's constant, and T is the absolute temperature, it becomes possible to calculate a surface temperature from measurements of Stoke's/anti-Stoke's intensity ratios. As before, the depth to which the temperature is sampled is determined primarily by the optical properties of the near-surface region. Preliminary results from applying this procedure are in agreement with thermocouple data. At present, we are refining the calculational procedures to improve accuracy and reproducibility.

Raman scattering has been shown to provide both solid-state surface and gas-phase temperatures, as well as chemical identification of surface compounds and gas species. A logical and relevant application of this technique will be to relate measured corrosion rates to the distribution of temperature and species in a boundary layer and adjacent to materials exposed in high temperature flows.

### Alloy Oxidation

For turbine applications not requiring thermal barrier coatings, the corrosion resistance of structural alloys relies heavily on the formation of a protective, adherent oxide scale. To date, we have applied Raman techniques primarily for investigating the oxidation characteristics of Fe-Cr-Ni alloys. Typical results are shown in Fig. 8, which displays Raman spectra obtained at room temperature from 304 SS coupons after oxidation in air for 3 hrs. at temperatures between 350°C and 1050°C. For temperatures below 650°C, the primary oxide components are found to be  $\alpha$ - $Fe_2O_3$  (peaks labelled Fe) and an Fe-rich spinel, probably  $Fe_3O_4$  [peak labelled Fe(S)]. At 750°C and 850°C,  $Cr_2O_3$  (peaks labelled Cr) is the major oxide constituent. In addition, increasing amounts of  $MnCr_2O_4$  [peaks labelled Mn(s)] are observed between 650°C and 850°C. Visual examination of the oxide scale formed at 950°C indicated significant amounts of spallation. The

Raman data suggest the presence of  $\text{Fe}_2\text{O}_3$  and a spinel phase. At  $1050^\circ\text{C}$ ,  $\text{MnCr}_2\text{O}_4$  is the dominant species detected.

Scanning electron microscopy and Auger analysis of the oxidized 304 SS samples indicated that many of the oxide scales had a lateral microstructure with dimensions ( $\sim 20$  micrometers), corresponding approximately to the grain size of the underlying alloy. However, the Raman data of Fig. 8 give only the average composition at the oxide surface, since the laser probe beam was focused on the sample over an area  $\sim 0.25$  mm x  $\sim 50$   $\mu\text{m}$ . To remove the ambiguities introduced by this averaging process, it would be highly desirable to obtain Raman data with sub-grain resolution. A microscope-based system currently is being assembled which will have a resolution  $\sim 1$   $\mu\text{m}$ , enough to resolve the lateral microstructure of many oxide scales.

The quantitative analysis of data from complex oxide scales requires a knowledge of the probe depth and relative sensitivity of Raman scattering for the different oxides. Many of the oxides of interest, including  $\text{Fe}_2\text{O}_3$  and  $\text{Cr}_2\text{O}_3$ , are opaque semiconductors at the visible wavelengths conventionally used in Raman investigations. As a consequence, if the outermost component of a complex scale strongly attenuates the probe laser radiation, Raman data obtained from the scale surface would not (necessarily) reveal the presence of an inner oxide component. On the other hand, the laser penetration depth in many opaque oxides is strongly wavelength-dependent. The use of tunable laser sources, now routinely available, permits to some degree the ability to control the effective depth of the probed volume.

The depth resolution of Raman scattering also depends on the strength of the scattered radiation. Due to a combination of processes which depend on the electronic structure, the relative scattering cross sections for different oxides can vary widely. For example, our results indicate that  $\text{Fe}_2\text{O}_3$  can be detected in thicknesses of  $\sim 50$   $\text{\AA}$ , whereas  $\sim 500$   $\text{\AA}$  of  $\text{Cr}_2\text{O}_3$  are required to obtain a recognizable spectrum.

In order to obtain compositional and structural depth profiles analogous to the elemental profiles obtained by sputter-Auger or SIMS, we have combined Raman scattering with Ar ion sputtering. As a result, we obtain depth-resolved spectra which minimize the ambiguities associated with oxide-dependent penetration depths. An example is shown in Figs. 9 and 10, which compare an Auger depth profile for the 304 SS coupon oxidized in air at  $450^\circ\text{C}$  with Raman results recorded after various amounts of ion sputtering. The Auger data (Fig. 9) indicate that the oxide thickness was approximately  $240$   $\text{\AA}$ . The uniformity of the Raman spectra (Fig. 10) with depth suggest that the oxide composition is relatively constant.

Furthermore, the decrease in Raman intensity with increased sputtering indicates that the optical penetration depth exceeds the total oxide thickness.

One ambiguity remains in the data of Fig. 10: the increasing Cr concentration revealed by the Auger profile between 60 and 100 Å below the surface does not appear to be reflected directly in the Raman spectra. To address this question, additional experiments were performed with mixed  $\text{Fe}_2\text{O}_3$ - $\text{Cr}_2\text{O}_3$  solid solutions. Some preliminary results are shown in Fig. 11. Even though pure  $\text{Fe}_2\text{O}_3$  and  $\text{Cr}_2\text{O}_3$  have the same structure, their Raman spectra are quite distinct, as can be seen by comparing the 0% and 100%  $\text{Cr}_2\text{O}_3$  curves in Fig. 11. As additional Cr is added, the spectra evolve in a continuous way to the spectrum of pure  $\text{Cr}_2\text{O}_3$ . Note that the highest frequency-shift peak ( $>650\text{ cm}^{-1}$ ) appears only in the mixed Fe-Cr solid solutions, and coincides with the dominant peak of  $\text{Fe}_3\text{O}_4$  and  $\text{FeCr}_2\text{O}_4$  spinels. It also can be seen in Fig. 11 that the incorporation of as much as 20% Cr in  $\text{Fe}_2\text{O}_3$  yields a spectrum quite similar to those in Fig. 10 with the high Cr content regions. Thus, the Cr content indicated by the Auger profile of Fig. 9 can be reconciled with the Raman data of Fig. 10 by postulating the incorporation of Cr as  $\text{Cr}_2\text{O}_3$  (as much as 20%) in a solid solution of  $\text{Fe}_2\text{O}_3$  and  $\text{Cr}_2\text{O}_3$  or in a mixed Fe-Cr spinel phase.

A number of additional aspects of the Raman technique are illustrated by the 304 SS oxidation data. First, the detection of  $\sim 50\text{ Å}$  of  $\alpha\text{-Fe}_2\text{O}_3$  demonstrates that the method can be quite sensitive compared to x-ray diffraction or SEM-EDAX. (Sensitivity, however, is strongly dependent upon oxide composition.) The interpretation of data from complex oxide scales also may be complicated by oxide-dependent probe depths. However, this problem can be circumvented by recording data as a function of depth using the sputter/Raman method. Lateral resolution can be adjusted for the study of microstructural effects ( $\sim 1\text{ }\mu\text{m}$ ) or to attain an averaged characterization of the oxide scale (0.25 mm). Uniqueness questions also can arise in the interpretation of Raman data. Among the oxides formed on Fe-Cr-Ni alloys,  $\text{Fe}_2\text{O}_3$  and  $\text{Cr}_2\text{O}_3$  have quite distinct spectra, even though these two oxides have the same structure. However, many of the commonly-formed spinels appear to have quite similar spectra, suggesting the need for careful measurements and reliable reference standards.

Application of Raman techniques to other systems, such as the alumina-forming MCrAlY alloys used for turbine blades, requires generating the relevant reference spectra and determining Raman sensitivities for the oxides of interest. These studies are currently in progress.

## Molten Salt Corrosion

Raman methods are not limited to simple oxidizing environments, but can be extended easily to mixed-oxidant studies. As an added benefit, the technique can be utilized to characterize the environment as well as corrosion products. Preliminary experiments which demonstrate this capability have been performed with  $\text{NaNO}_3$  and  $\text{Na}_2\text{SO}_4$ -coated  $\text{Cr}_2\text{O}_3$ -forming alloys. Results from molten nitrate studies showed that significantly different oxide scales formed on 304 stainless when the exposure temperature was raised from 450°C to 550°C. Analysis of post-exposure Raman data revealed that the principal constituents of the outer scale layer for exposure at temperatures less than 450°C were  $\text{Fe}_2\text{O}_3$  and  $\text{Fe}_3\text{O}_4$ . In contrast, molten nitrate attack at 550°C resulted in the formation of a layer of  $\text{NaFeO}_2$ . Moreover, during exposure, Raman monitoring of the salt chemistry revealed the formation of  $\text{NaNO}_2$ , and the dissolution of Cr into the salt.

The use of laser "cavity dumping" and gated detection were necessary to obtain useful signals from the corrosion scales in the presence of the large background of thermally-induced radiation. Figure 12(b) shows the Raman data (dominated by thermally-induced contributions) obtained without gated detection from Ni-20% Cr alloy spray coated with  $\text{Na}_2\text{SO}_4$  (6). For comparison, the spectrum recorded with gated-detection is shown in Fig. 12(a). The dramatic improvement in sensitivity is self-evident. Figure 12(c), obtained by subtracting the thermal contribution from the in-situ data, is the Raman spectrum of the Ni-Cr alloy at 900°C.

## Conclusion

Turbine blade materials research at Sandia currently emphasizes the development of in-situ techniques for characterizing turbine blade materials and their service environments. For this purpose, spontaneous Raman spectroscopy has been demonstrated as a promising technique, especially when used in conjunction with complementary surface analysis methods. Future studies will be aimed at improving sensitivity and extending results to new alloy systems and varying environmental conditions.

As the diagnostics-oriented program matures, we plan to apply the methods we have developed to specific materials problems with high potential payoff to energy-producing technology. At present, we foresee a good overlap of the capabilities of Raman scattering with studies on thermal barrier coatings, structural alloys, molten salt attack, and deposition phenomena which may arise with higher service temperatures and the use of coal-derived fuels.



This work was supported by the Department of Energy, Office of Basic Energy Science. Acknowledgment is made to J. C. F. Wang for assistance with construction and operation of the combustion simulator, to B. E. Mills for use of ultra-high vacuum chamber, and to L. A. Selberg for assistance throughout the experiments.

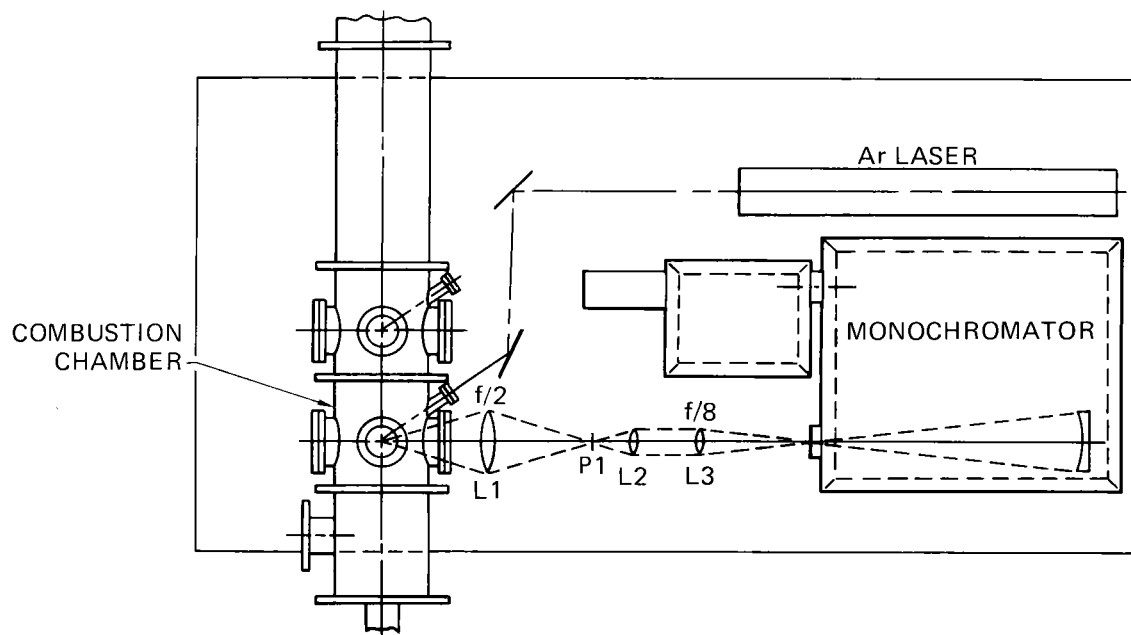
### References

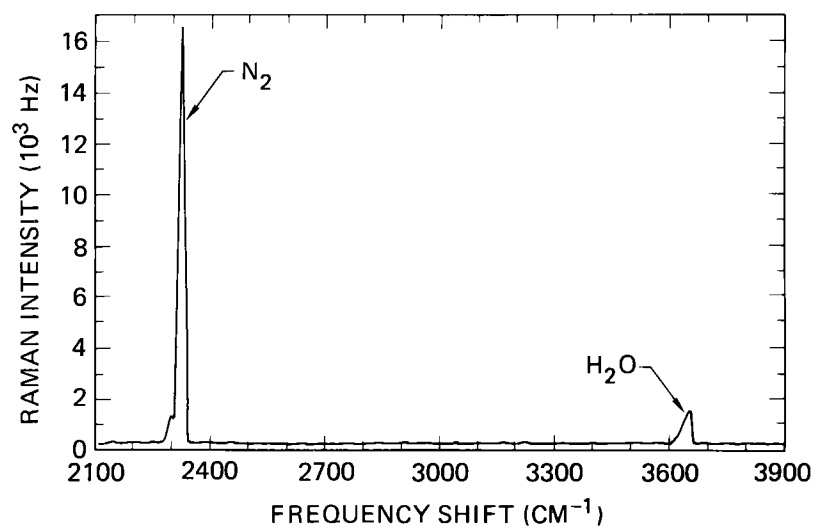
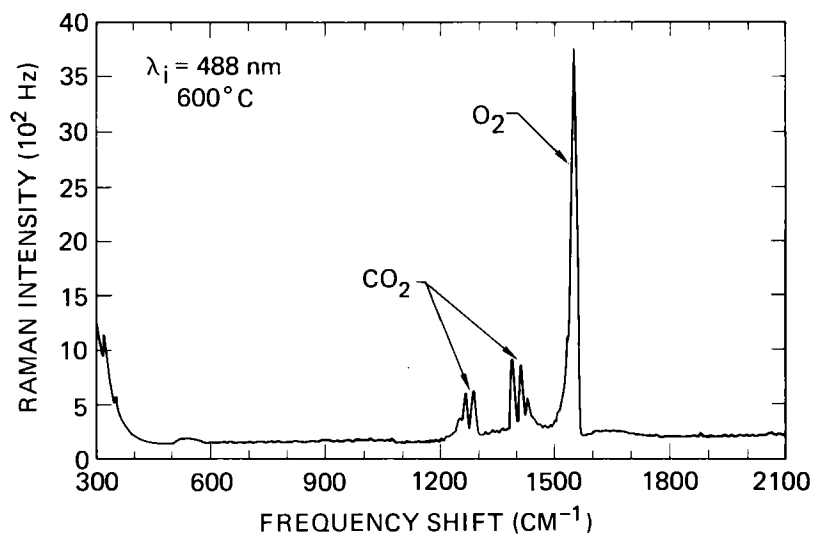
1. See, for example, Laser Raman Gas Diagnostics, ed. Marshall Lapp and C. M. Penney, Plenum Press, New York, 1974.
2. J. W. Fairbanks, Proceedings of the First Conference on Advanced Materials for Alternative Fuel Capable Directly Fired Heat Engines, J. W. Fairbanks and J. Stringer, ed., Castine, Me (1979) 527.
3. S. R. Levine, P. E. Hodge, and R. A. Miller, Proceedings of the First Conference on Advanced Materials for Alternative Fuel Capable Directly Fired Heat Engines, J. W. Fairbanks and J. Stringer, ed., Castine, Me (1979) 667.
4. Samples obtained from and work in conjunction with R. Rice and R. Ingel, Naval Research Laboratory.
5. Yu. K. Voron'ko, B. V. Igant'ev, E. E. Lomonova, V. V. Osiko, and A. A. Sabol, Sov. Phys. Sol. State 22, 603 (1980).
6. Samples obtained from and work in conjunction with J. Truhan and S. Aceves, Lawrence Livermore Laboratory.

### Figure Captions

- Figure 1. Schematic representation of the Raman apparatus used for in-situ studies of gases and solids of the Atmospheric Combustion Exhaust Simulator (ACES).
- Figure 2. Gas phase Raman data obtained with ACES operating at  $\sim 600^\circ\text{C}$  indicating the relative concentrations of  $\text{CO}_2$ ,  $\text{O}_2$ ,  $\text{N}_2$ , and  $\text{H}_2\text{O}$ .
- Figure 3. Theoretical fit of Raman data from  $\text{N}_2$  gas within the ACES exhaust. The theory indicates a temperature of  $629^\circ\text{C}$  in good agreement with the thermocouple-measured temperature of  $625^\circ\text{C}$ .
- Figure 4. Comparison of Raman spectra of  $\text{ZrO}_2\text{-Y}_2\text{O}_3$  crystals containing various weight percentages of  $\text{Y}_2\text{O}_3$  showing the spectra of the monoclinic, tetragonal, and cubic phases.
- Figure 5. Raman spectra from  $\text{ZrO}_2\text{-1 wt\% Y}_2\text{O}_3$  at  $1050^\circ\text{C}$  and  $25^\circ\text{C}$  showing the effect of thermal broadening.

- Figure 6. Raman data obtained at heating (a) and cooling (b) rates of 6°/min. from  $ZrO_2$ -2.5 wt%  $Y_2O_3$  pellets. The monoclinic to tetragonal phase transition is best indicated by the appearance of the peak at  $\sim 275\text{ cm}^{-1}$ . Hysteresis effects are also observed.
- Figure 7. Stokes and anti-Stokes Raman spectra from  $ZrO_2$ -8%  $Y_2O_3$  demonstrating a technique for extrapolating temperature from solid phase Raman data.
- Figure 8. Post-exposure Raman data from 304 SS coupons heated in air for 3 hrs. at the indicated temperatures ( $Fe=Fe_2O_3$ ,  $Cr=Cr_2O_3$ ,  $Fe(s)=Fe_3O_4$ ,  $Mn(s)=MnCr_2O_4$ ).
- Figure 9. Auger depth profile for 304 SS exposed in air at 450°C for 3 hrs. The arrows indicate points at which Raman spectra were obtained.
- Figure 10. Raman spectra from 304 SS exposed in air at 450°C after removal of varying amounts of oxide by ion sputtering. The spectra correspond with arrow labels in Fig. 9.
- Figure 11. Raman spectra from mixed  $Fe_2O_3$ - $Cr_2O_3$  solid solutions showing the spectra evolution from pure  $Fe_2O_3$  to pure  $Cr_2O_3$ .
- Figure 12. Comparison of Raman data obtained from a Ni-20%Cr sample coated with  $Na_2SO_4$  at 900°C with gated detection (a), without gated detection (b), and (c) by subtracting the blackbody contribution (b) from spectrum (a).

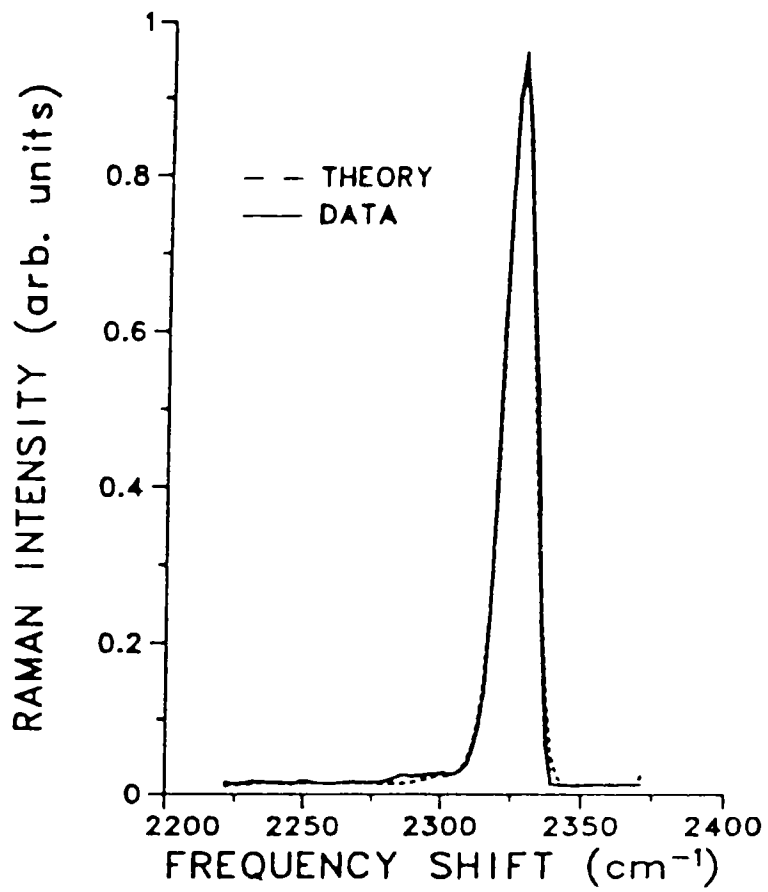




NITROGEN TEMPERATURE

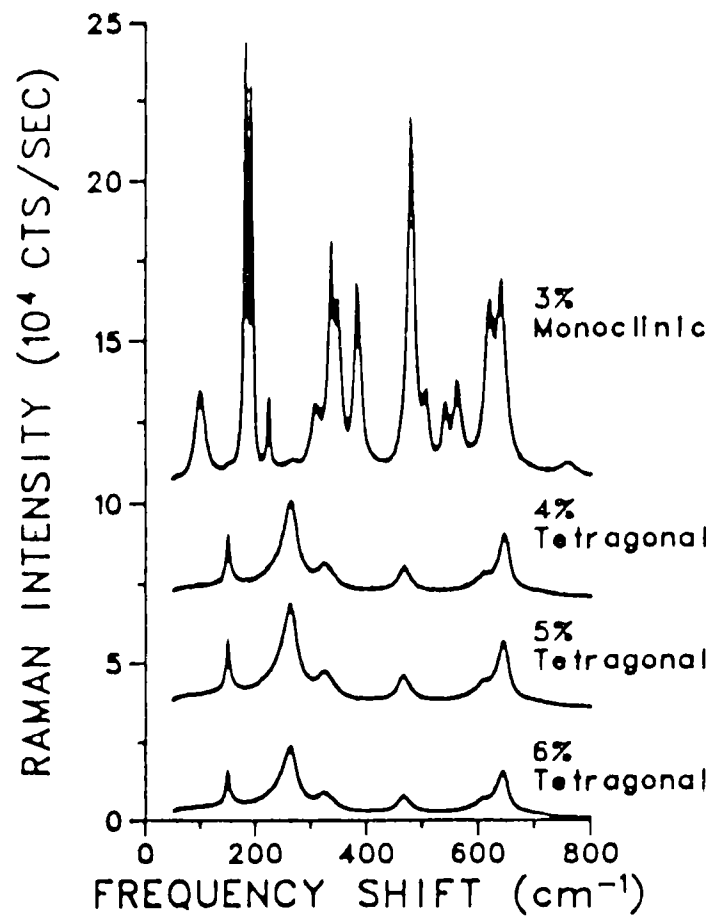
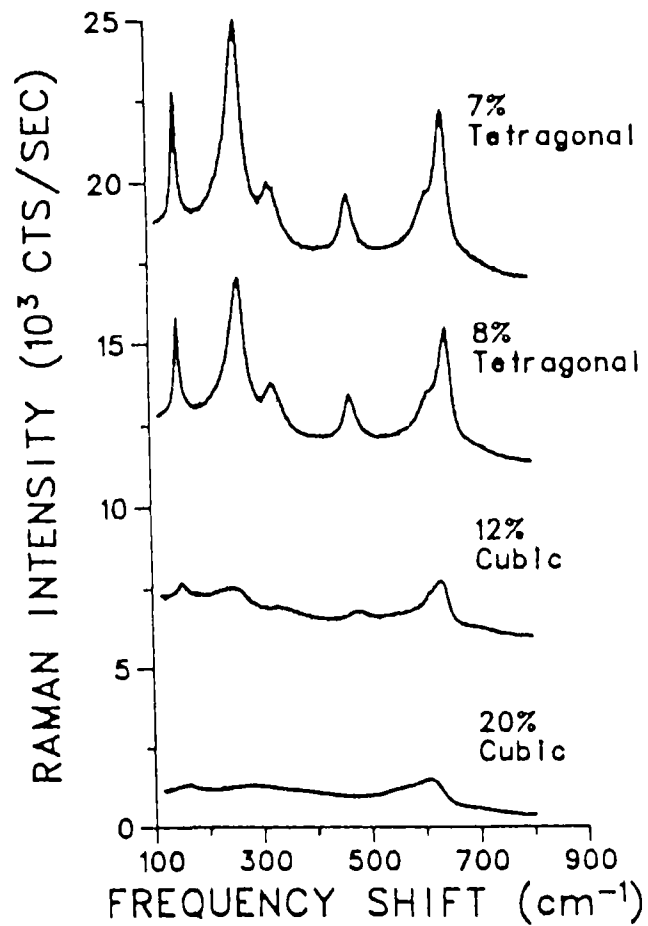
THERMOCOUPLE = 625K

THEORY FIT = 629K

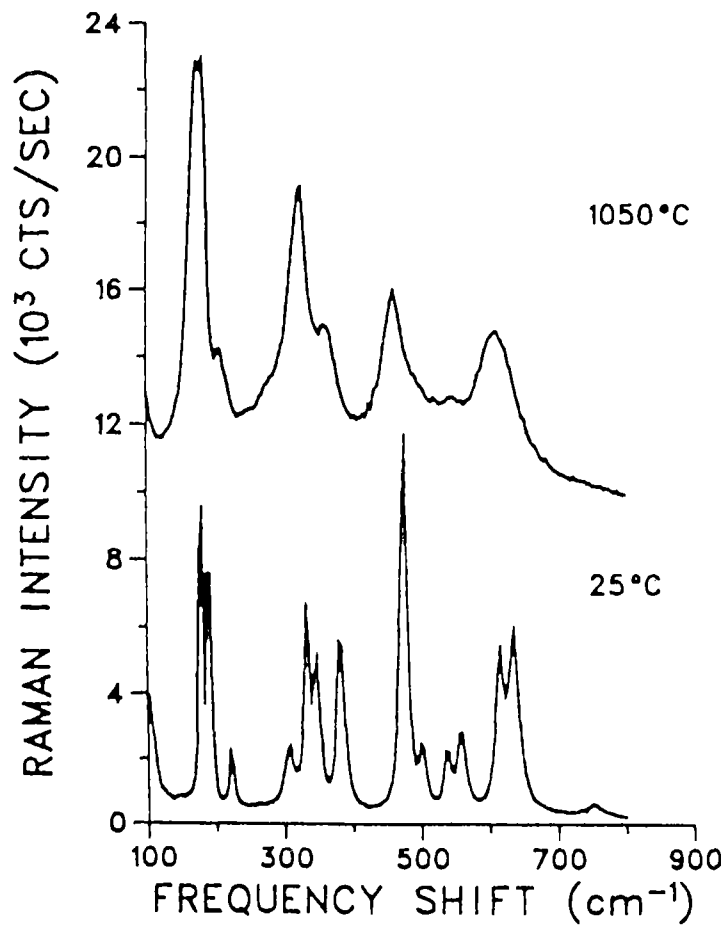


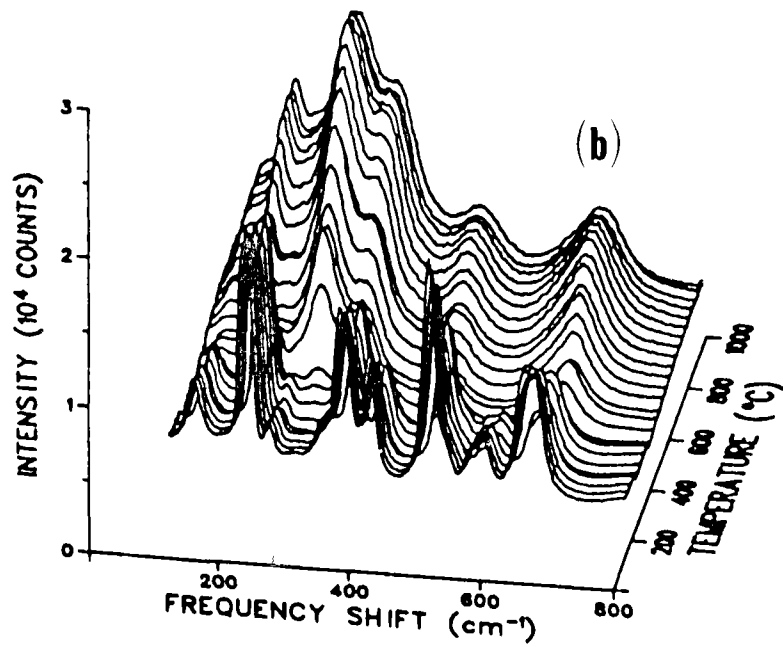
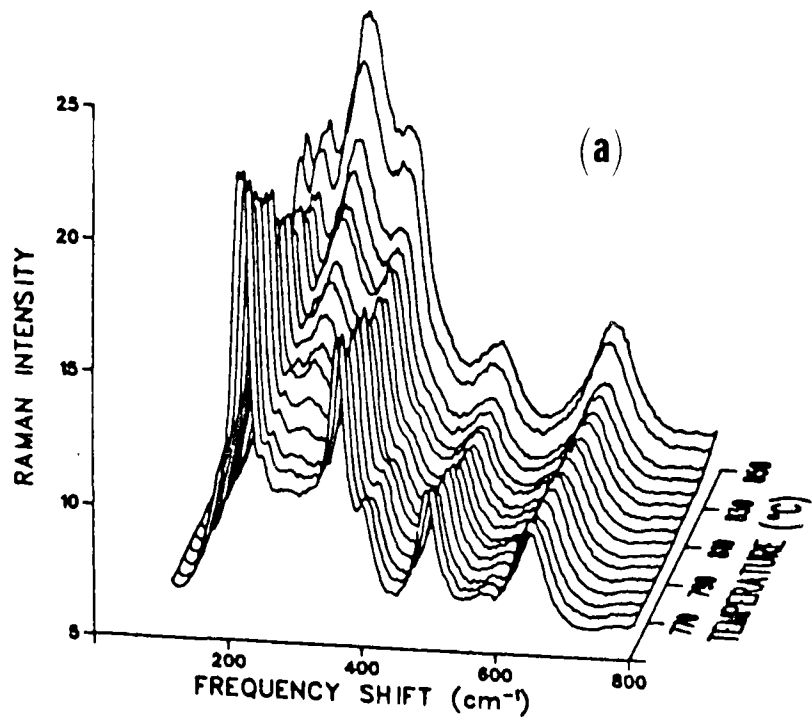


7-96



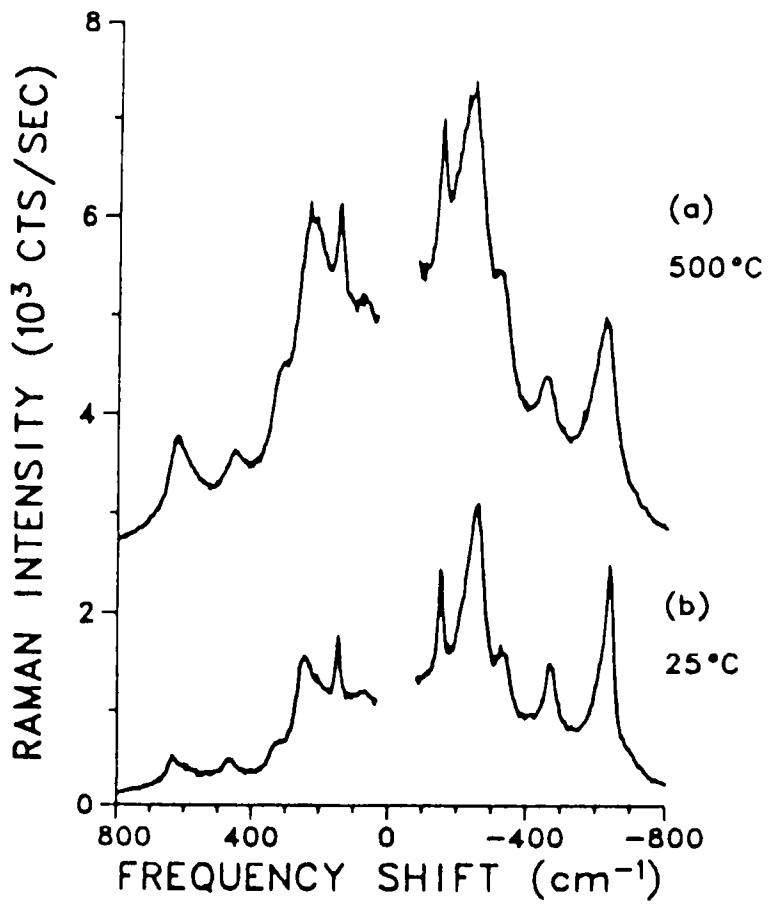
ZrO<sub>2</sub> - 1% Y<sub>2</sub>O<sub>3</sub>



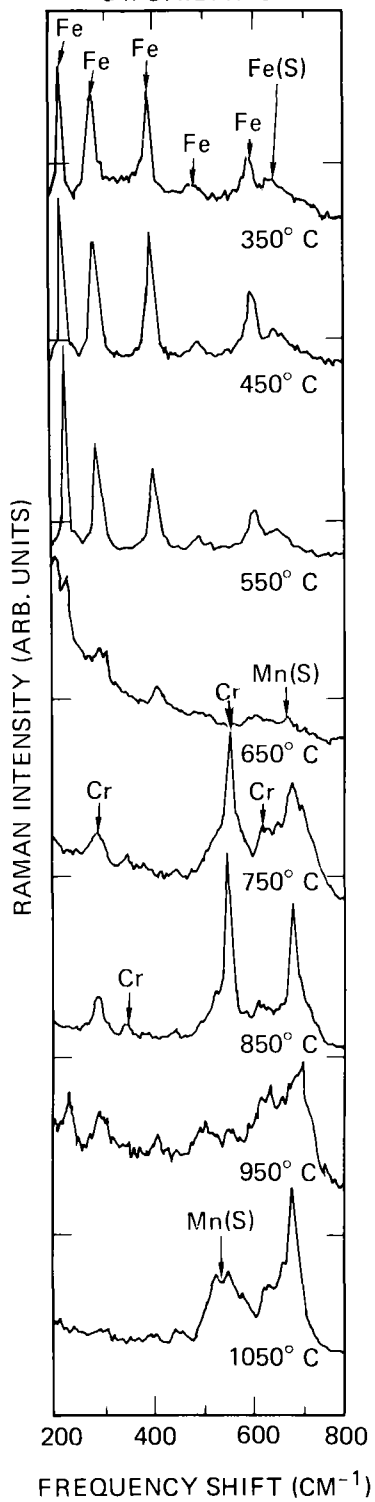


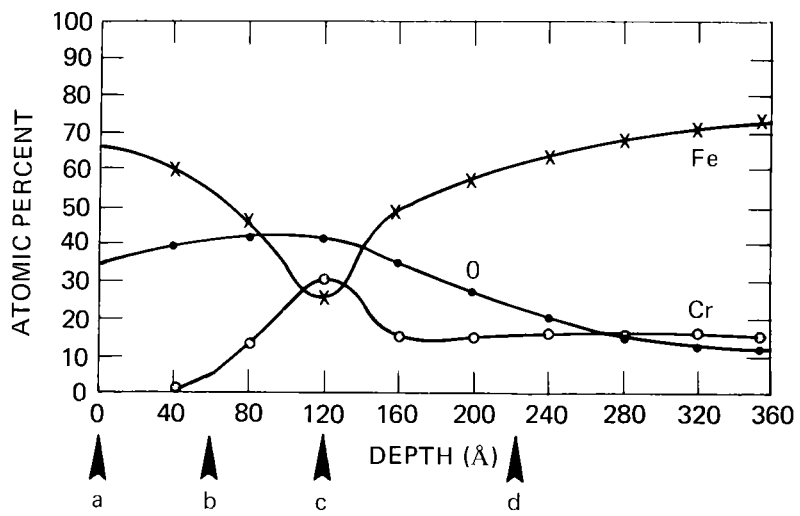


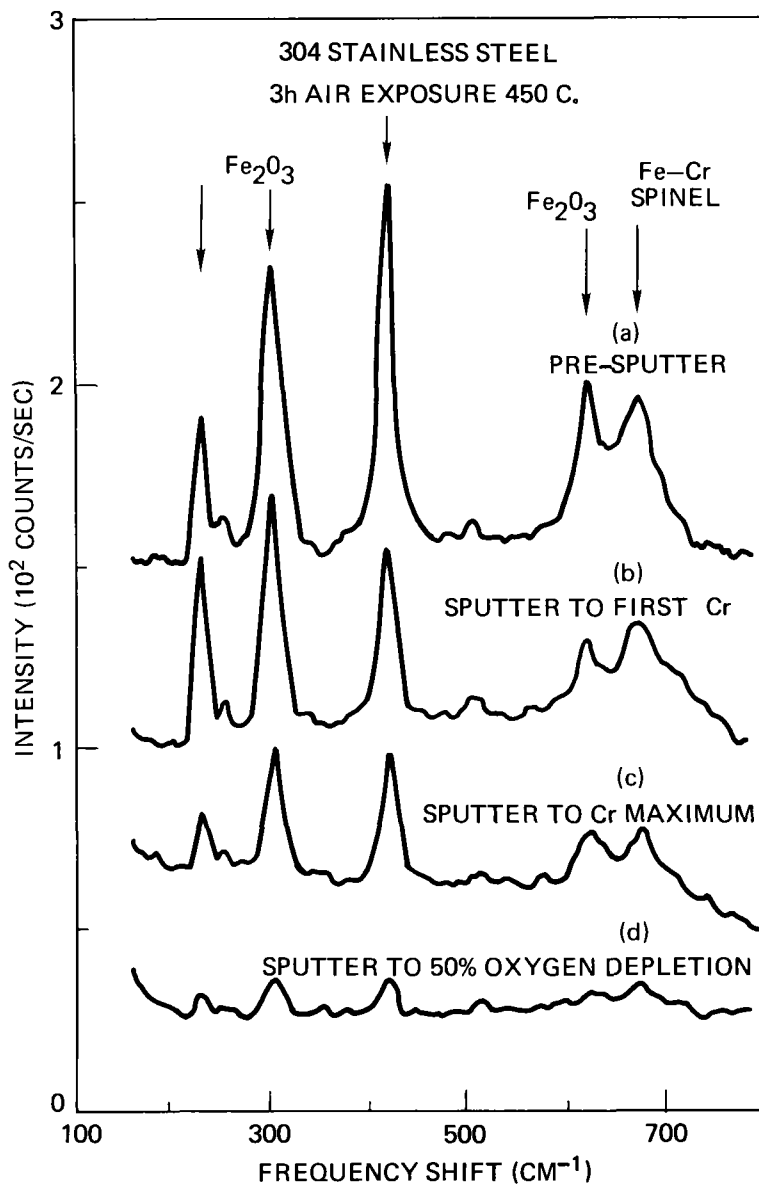
ZrO<sub>2</sub> - 8% Y<sub>2</sub>O<sub>3</sub>



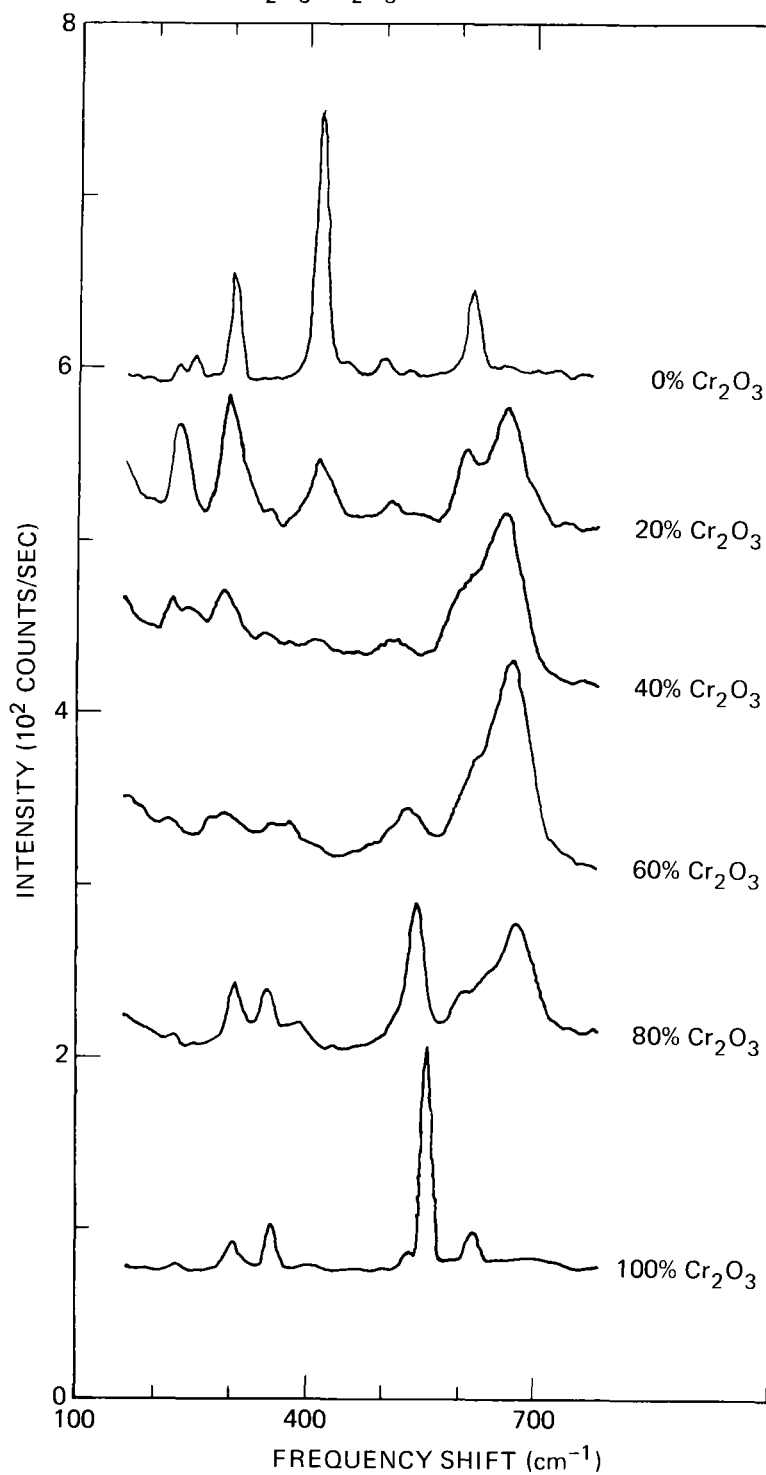
304 STAINLESS STEEL  
3 h OXIDATION



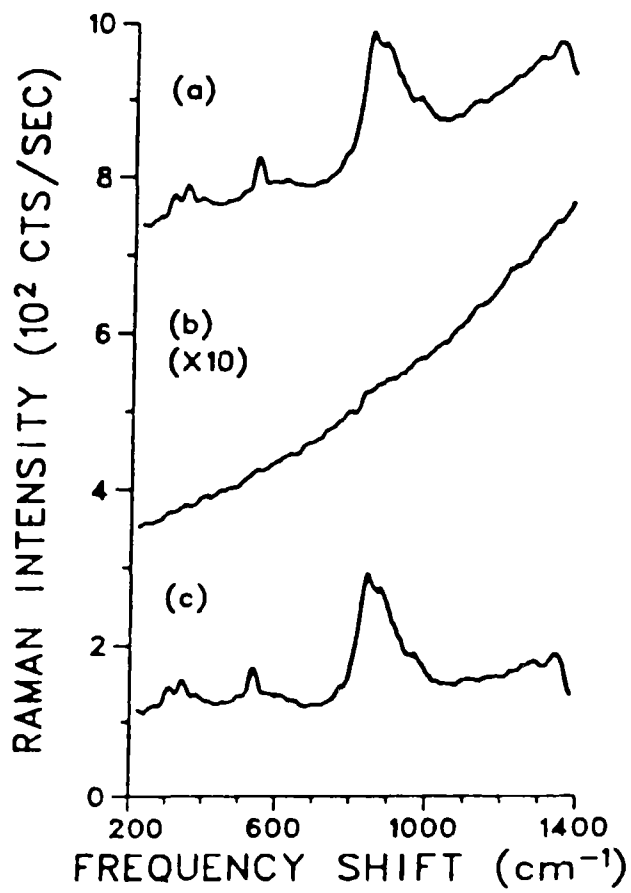




Fe<sub>2</sub>O<sub>3</sub>-Cr<sub>2</sub>O<sub>3</sub> SOLID SOLUTIONS



NI-Cr/Na<sub>2</sub>SO<sub>4</sub>



## RAPIDLY SOLIDIFIED SUPERALLOYS

by

E. C. van Reuth and L. A. Jacobson

### Introduction:

The development of superalloys with improved capability has historically depended on the introduction of new processing technologies. Major improvements were realized through the use of vacuum melting, and, more recently, directional solidification of airfoil castings. Superalloy powder processes have been successfully applied to the production of gas turbine engine disks through the superplastic forming operation known as Gatorizing, and disks made from hot isostatically pressed powder have also been developed and used. A new method of making superalloy powder, based on centrifugal atomization and helium gas quenching has opened up a new arena for superalloy improvement through additions of larger amounts of molybdenum and aluminum. The new technique, termed Rapid Solidification Rate, or RSR, gives cooling rates in the range of  $10^5$  to  $10^6$  °C/second and has stimulated a large amount of effort to apply rapid solidification processing to a number of other structural alloy systems, most notably, aluminum alloys.

Efforts to develop new and improved alloys by rapid solidification have been consolidated within the Department of Defense into a thrust area for Rapid Solidification Technology (RST). The specific definition of what constitutes RST presently includes all solidification methods which give a cooling rate in excess of  $10^3$  °C/second. This definition admits most methods of making alloy powders, and all the techniques for forming ribbon or flake product (melt-spinning, planar casting or melt extraction). The processes considered as a part of RST could be expanded considerably if the

definition were changed somewhat to encompass processes for achieving solidified alloys which have finer, more uniform microstructures than those associated with conventional ingot processing. It is the purpose of this paper to present the current and near-term planned efforts on RST superalloys, not only for DoD, but for other Government agencies as well. Overall objectives and approaches will be discussed, and some examples of accomplishments to date will be highlighted. Programs underway in Fiscal Year 1981 will be briefly described, along with the general results which are anticipated. While the program descriptions do not detail the specific resources involved, it is important to note that the total Government agency expenditures on RST superalloys were nearly \$9 million in FY 81, and this is expected to grow to \$11 million in FY 82. The out-year estimates for FY 83 through FY 85 fall between \$7 million and \$9 million per year, giving a five year total of nearly \$44 million of Government sponsored R&D on rapidly solidified superalloys.

Objectives:

The overall objectives of programs in rapidly solidified superalloys can be grouped into several areas of emphasis--performance, producibility and national need. The development of alloys which depend to a lesser degree on critical or strategic elements, defined as those for which this country must rely almost entirely on foreign sources, clearly relates to the latter emphasis. Alloys with better formability, or which allow for a broader range of processing conditions or heat treatments address the area of improving superalloy producibility. Finally, the efforts to develop alloys with higher temperature capability, as measured by higher creep and stress rupture properties, alloys with improved oxidation resist-



ance, and alloys with increased resistance to cyclic loading, are aimed at improving the performance of these materials. The improved performance translates directly into higher efficiency, more durable, lighter weight gas turbine engines.

Approaches:

Realization of the benefits of rapid solidification processing of superalloys requires better understanding of the fundamental aspects of several phenomena which bear on alloy capability. A few of these are: Factors influencing the strength of gamma prime; The long term phase stability of alloys saturated with solution strengthening elements; The partitioning of alloying elements between phases; and The control of grain size and recrystallization during thermal treatment. Rapid solidification allows new approaches to alloy development, including the possibility of adding larger quantities of strengthening elements, reducing or eliminating the use of critical or strategic elements, and maintaining excellent compositional homogeneity. This homogeneity extends also to minor alloying additions that give significant improvement in oxidation resistance. Obtaining useful hardware components from rapidly solidified superalloys requires improvements in processing. Current programs are addressing issues related to high volume powder production, including uniformity, cleanliness and the yield percentage of desired size fractions. Consolidation processes are being studied in order to achieve good powder particle bonding, to develop useful models for the full densification of complex shapes, and to devise ways of retaining the unique microstructures resulting from rapid solidification. Forming operations are being developed that will lead to near net shape components, or exploit the improved workability of consolidated powder alloys.

Accomplishments:

Government support of very rapidly solidified superalloys began some five years ago with a major effort sponsored by Defense Advanced Research Projects Agency to perform research on alloys made by the Pratt & Whitney, Government Products Division, RSR process. A follow-on program to scale up the process and demonstrate manufacturing methods for gas turbine engine blades and vanes was initiated two years ago with joint DARPA and Air Force support. The highlighted accomplishments which follow come principally from these programs, since they represent the most concentrated attempts to exploit the potential benefits which rapid solidification could bring to the next generation of superalloys.

Significant improvement in alloy homogeneity has been demonstrated, as indicated by the comparison of microstructures shown in Figure 1. This level of homogeneity would be realized in conventional castings only after long time annealing at very high temperature. It translates directly into a 100<sup>0</sup> F or greater increase in alloy incipient melting point, as shown in Figure 2, giving the RS superalloys a wider heat treatment window and simplifying the production of elongated grain structures.

An improvement of some 150<sup>0</sup> F in alloy capability for 100 hour, 1% creep deformation at stress levels equivalent to those experienced at the mid-span of a turbine blade, is illustrated in Figure 3. This is also approximately the same temperature improvement for equivalent stress rupture life that has been achieved for RSR alloys over the current bill-of-material blade alloy for the F-100 engine, DS MAR-M-200+Hf.

The improvement in oxidation resistance that has been achieved for modifications of alloy 185 (Ni-Al-Mo-W) is shown in Figure 4. The cyclic test is more severe than a static test due to the increased spalling of the oxide scale. While specific improvement in hot corrosion resistance is not a major program goal, testing has shown that RSR alloys are at least as capable as the newest DS single crystal blade and vane alloy, designated PWA 1480.

A key requirement for blade and vane alloys produced from RS powder is the ability to grow elongated grains in the principal loads experienced by the part. It is also important to achieve control of the orientation of such grains in order to maximize mechanical properties. Since the consolidated rapidly solidified powder can be cold rolled, the ability to develop strong textures in fine grained sheet has led to significant improvement in the control of desired orientation during directional grain growth. In fact, single crystal sheets have been prepared. Cold rolled sheet has also been diffusion bonded into blocks, which then can be directionally recrystallized into nearly single crystals. Another procedure, currently under investigation, is the diffusion bonding of single crystal sheet. If successful, this process will allow a high degree of control in orientation and properties of finished airfoil parts.

Additional improvement in component temperature capability is realized through the employment of new cooling designs, based on the radial wafer blade construction illustrated in Figure 5. The combination of convection and film cooling is achieved by etching the passage configurations in wafers, then diffusion bonding the wafers together, and machining the final part from the diffusion bonded wafer block.

The entire process is shown in Figure 6 which the directional recrystallization is indicated as occurring after the diffusion bonding step. As mentioned earlier, the possibility of achieving controlled orientation single crystal wafers by performing this operation on cold rolled sheet may change the order of the blade manufacturing sequence.

A major milestone was recently achieved with the successful run of two RSR radial wafer blades in an F-100 core engine. The blades experienced 25 Tactical Air Command cycles which involve an engine start, running under various power settings including full military power, and engine shutdown.

The thermal cycling involved in a TAC cycle imposed great demands on the ability of blades to withstand transverse stresses, and it was therefore most gratifying that the RSR Radial Wafer blades showed no signs of distress after the engine testing.

### Current Programs:

This brief description of currently active programs conveniently divides into major areas of emphasis previously presented; fundamental understanding, alloy development, and process development. Efforts related to alloy phase stability and texture/recrystallization control are being performed by the Air Force Materials Laboratory and the Naval Research Laboratory in direct support to the RSR Blade and Vane effort. The study of  $\text{Ni}_3\text{Al}$  ductility improvement is being supported by the Department of Energy.

Navy supported programs related to alloy development include effort to improve the oxidation and sulfidation resistance of nickel base alloys through rapid solidification, and exploration of possibilities of achieving better intrinsic oxidation resistance in niobium based alloys. A large portion of the RSR Blade and Vane effort is devoted to alloy development, both for improved oxidation resistance and for high temperature strength.

Both DARPA and NASA are supporting efforts to develop improved processes for increasing the low cycle fatigue life of gas turbine engine disks, and the Navy is continuing a program to demonstrate satisfactory structural components made by layer deposition methods. The manufacturing process development effort of the RSR Blade and Vane program is also identified under the process improvement area. A new DARPA sponsored effort will demonstrate the ability to fabricate a radial turbine disk from powder of two alloy compositions--one chosen for high burst strength for the disk interior, and the other for high creep strength needed at the disk rim. The component has been designed by the Norwegian firm of Kongsberg Vapenfabrikk for use in a new turbine power source which could have thermal efficiency equal to a diesel engine, at only half

the weight and size of the diesel. Finally, a DARPA supported effort has been initiated with the objective of demonstrating that useful shapes can be formed directly by plasma spray deposition of superalloy powder. By selecting different alloy compositions for various sections of a component, thermal stresses could be minimized, with obvious payoff in terms of extended lifetimes for components such as combustors.

Conclusions:

The anticipated benefits of rapid solidification processing of superalloys have been described earlier--higher performance, lower cost, less dependence on critical/strategic elements, improved durability, and the ability to use advanced component designs. A major area of concern, which will pace the ability to achieve the maximum benefits from rapid solidification, is the exercise of proper control over all aspects of superalloy powder processing, especially those related to cleanliness, handling, consolidation and forming. It is anticipated that such topics will be addressed in most near-term future government sponsored programs.

Acknowledgements:

The authors wish to express their appreciation to Mr. Atwell Adair, Air Force Wright Aeronautical Laboratories, Materials Lab, and Mr. John Miller, Pratt & Whitney, Government Products Division, for their invaluable assistance in the preparation of this paper.

# REVOLUTIONARY POWDER METALLURGY OFFERS NEW DIMENSION FOR SUPERALLOY DEVELOPMENT

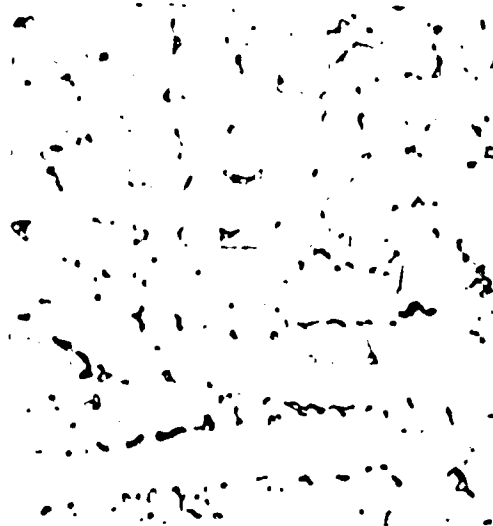
---

0.01°/sec  
Cooling Rate



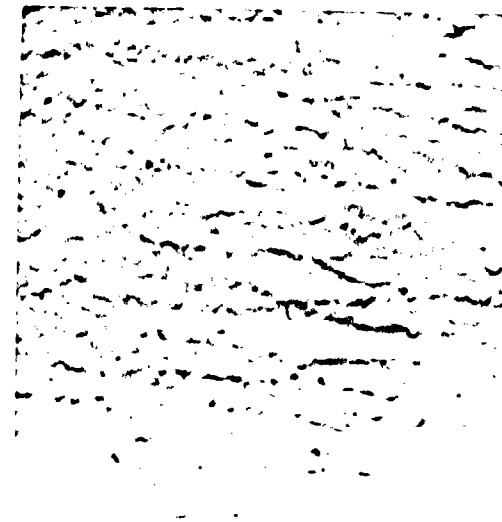
Mag: 100X\*

100°/sec  
Cooling Rate



Mag: 1000X\*

1,000,000°/sec  
Cooling Rate



Mag: 10,000X\*

FIGURE 1

\*Please note that the illustration(s) on this page have been reduced 10% in printing.

# INCIPIENT MELTING POINT OF RSR POWDER-PROCESSED ALLOYS VS CAST ALLOYS

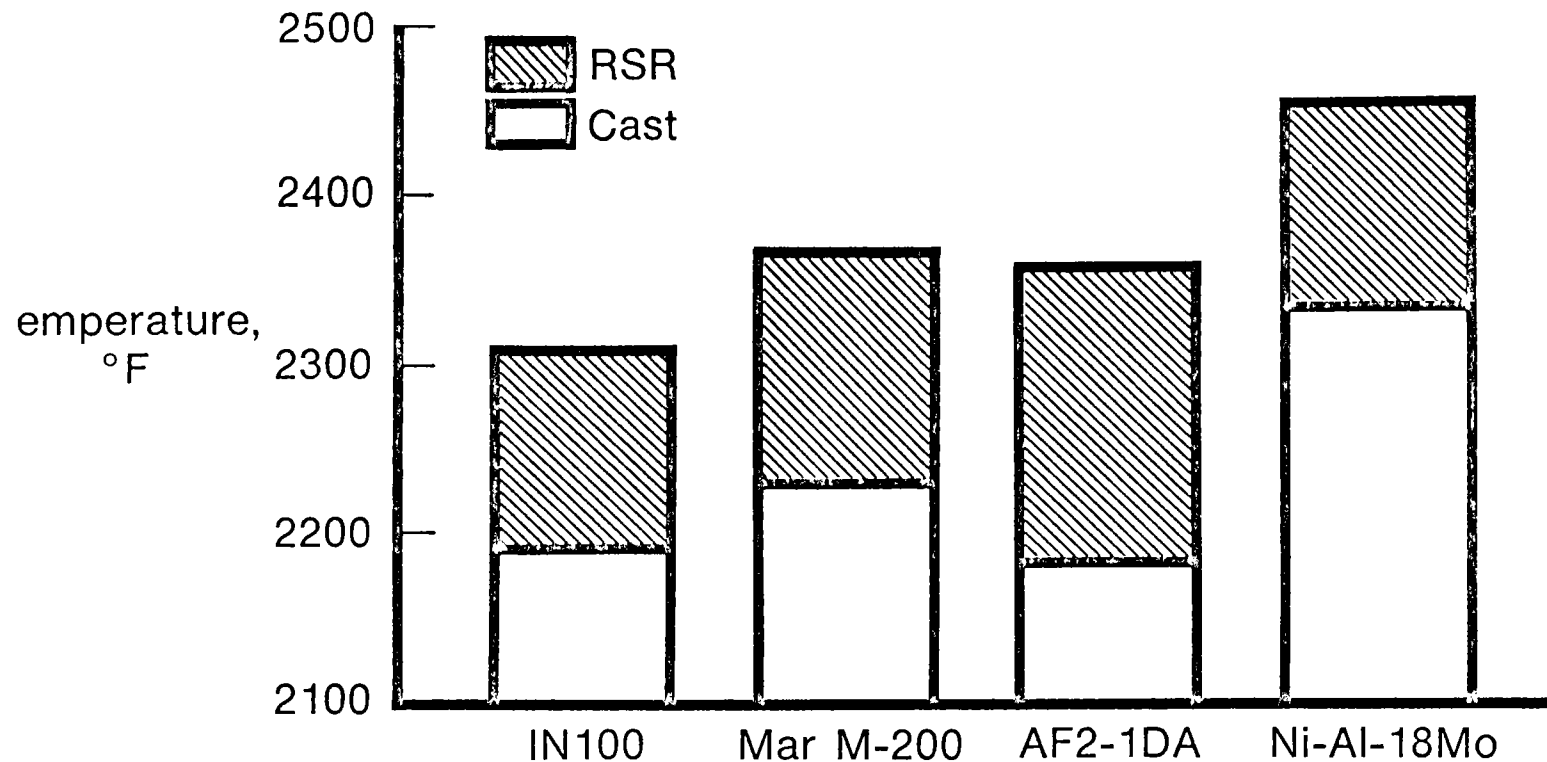


FIGURE 2



# CREEP RESISTANCE OF SUPERALLOYS

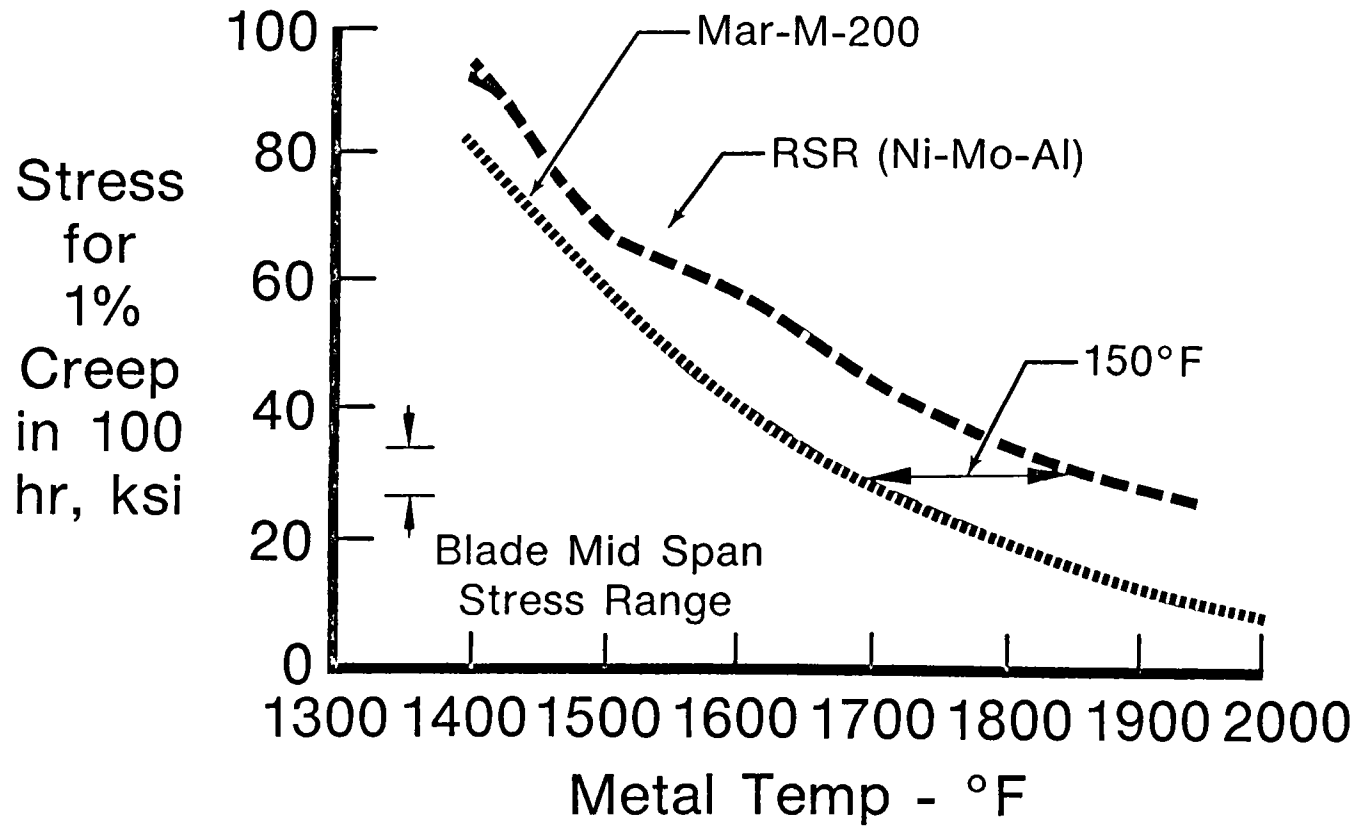


FIGURE 3

# BLADE ALLOY OXIDATION - 2100°F CYCLIC FURNACE TEST

*Significant Improvement in Oxidation Resistance Made  
With Minor Alloying Additions*

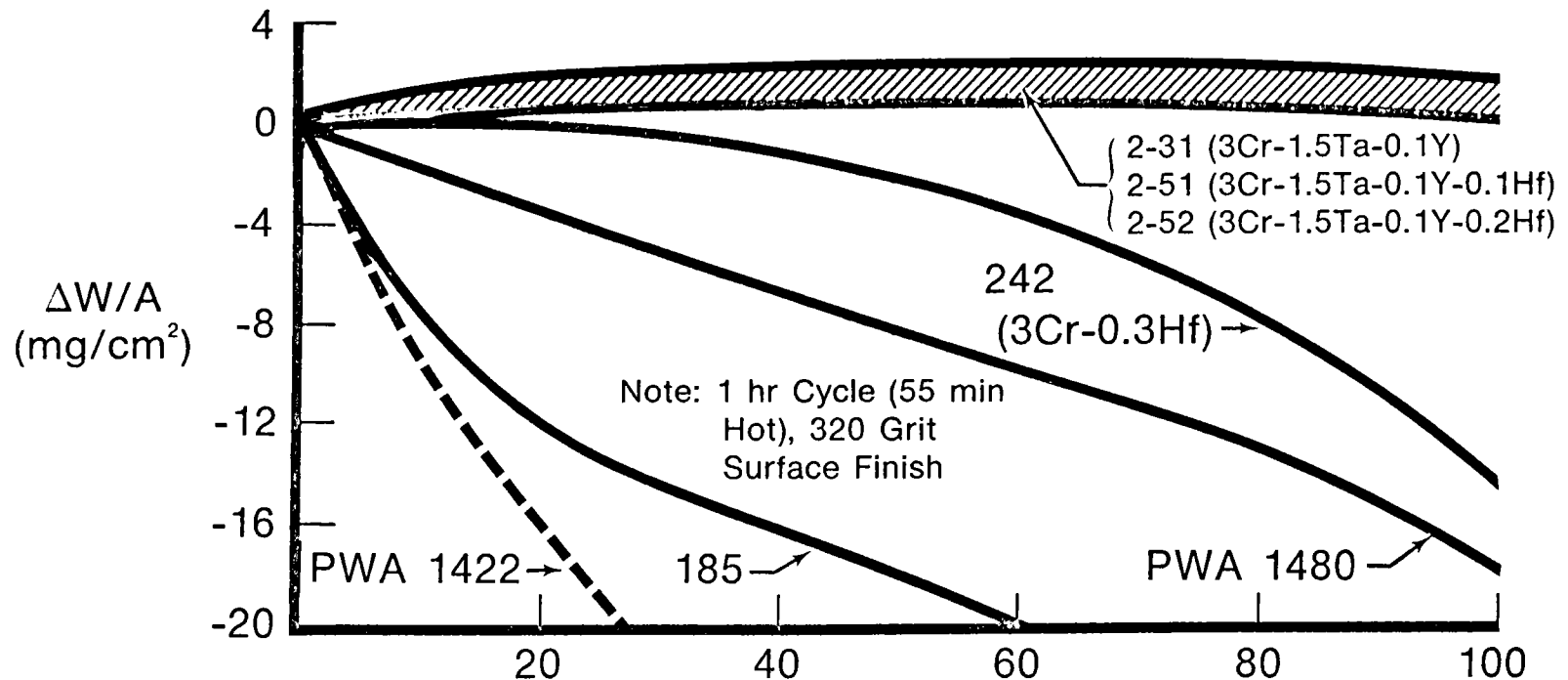


FIGURE 4

# RADIAL WAFER BLADE CONSTRUCTION

---

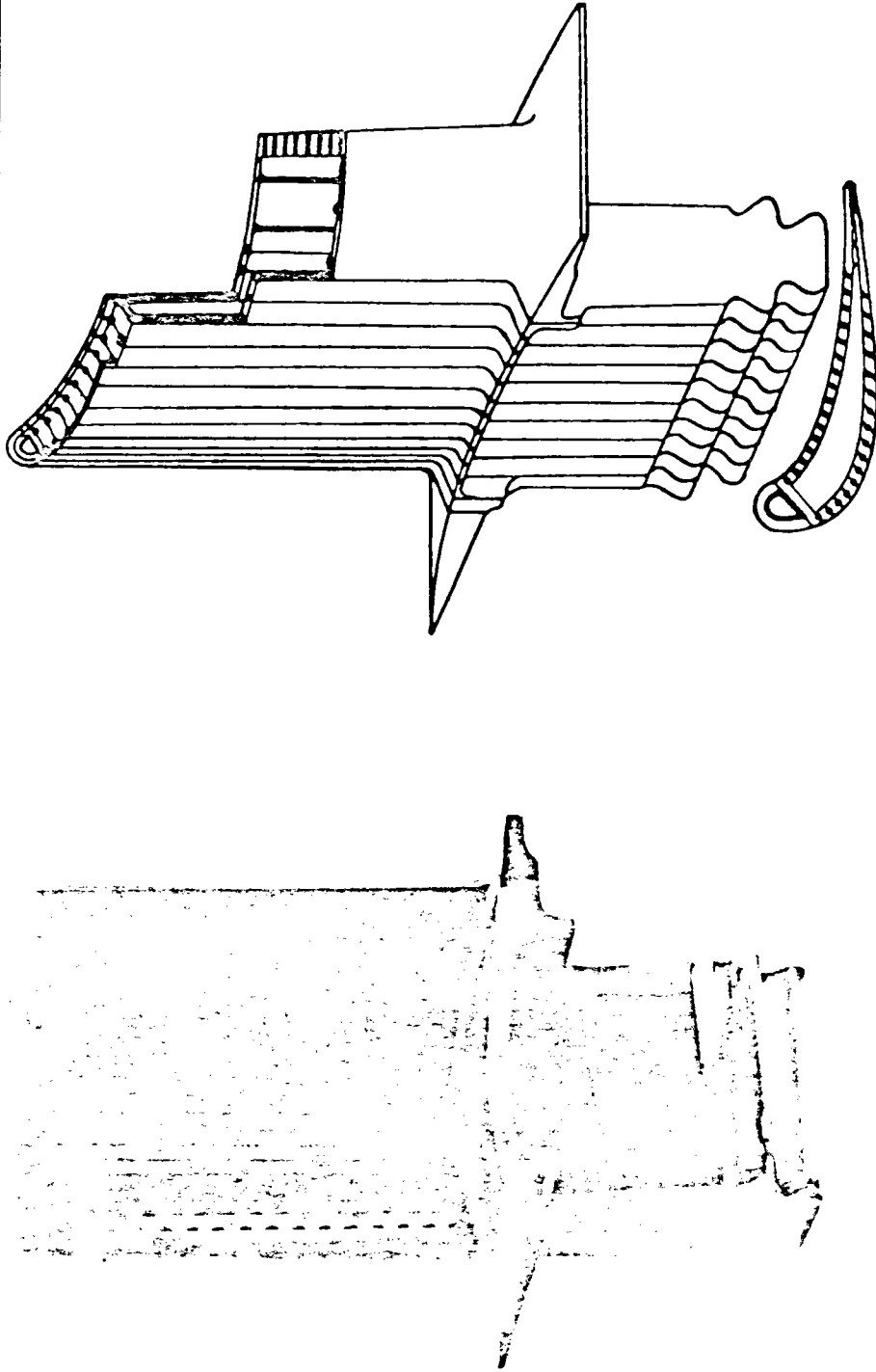
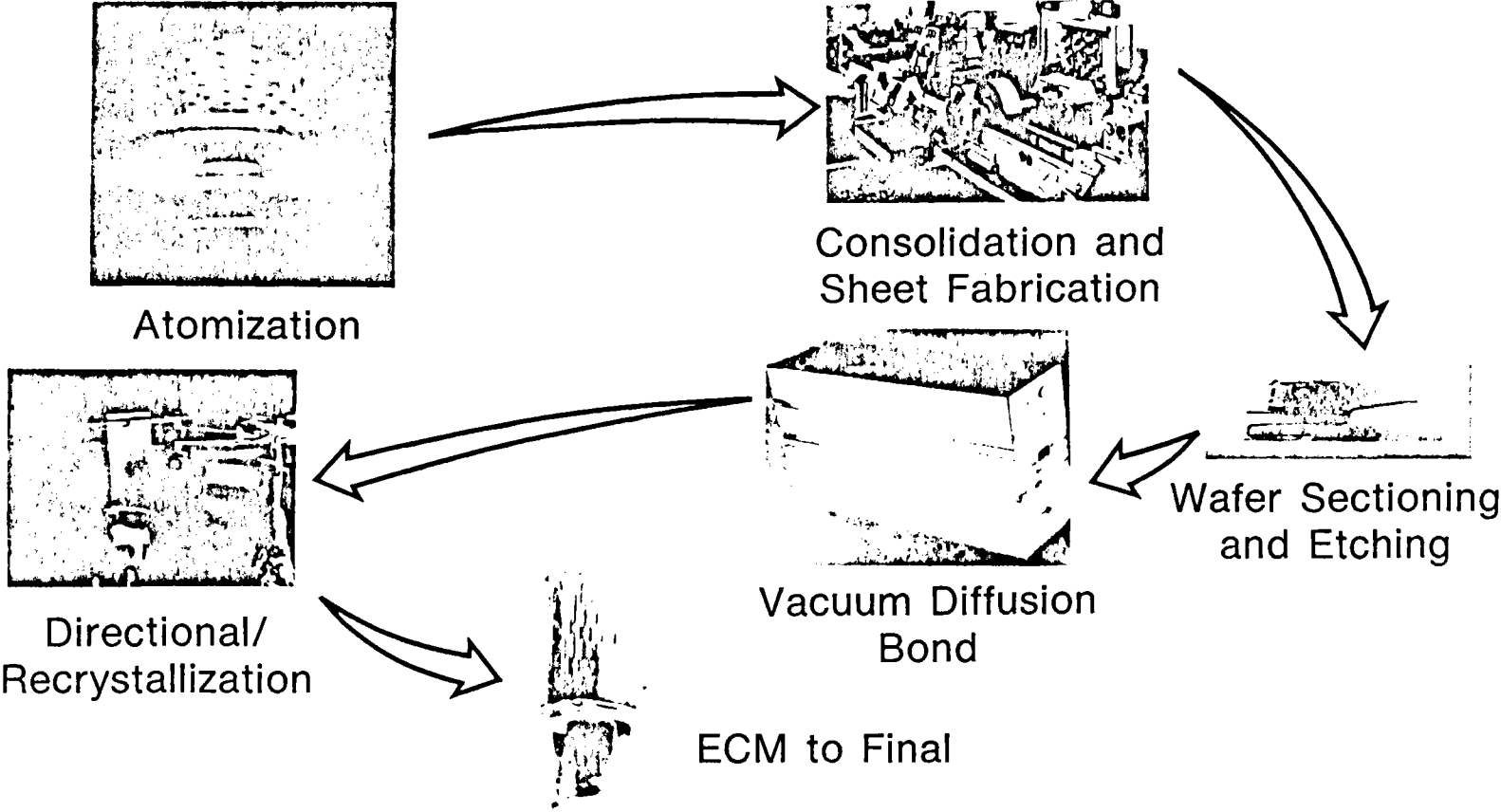


FIGURE 5

# MANUFACTURING SEQUENCE FOR RSR RADIAL WAFER BLADE



7-118

FIGURE 6

Development of a Directionally Solidified  
Composite Industrial Gas Turbine Airfoil

William Schilling  
General Electric, Schenectady, New York

John Fairbanks  
U.S. Department of Energy, Washington, D.C.

Superalloys for aircraft gas turbine were steadily improved from the mid-50's through to the early 60's by optimizing metallic phases, heat treatment, carbides and gamma-prime strengthening. These conventionally cast superalloys provided the combined high temperature oxidation resistance and mechanical properties required for engine use. However, the operating temperatures for these superalloys reached a temperature plateau of about 1750°F in the early 60's. Unfortunately these aircraft engine alloys sacrificed hot-corrosion resistance, primarily in reduced Cr content, to achieve high temperature strength. Towards the end of the 60's, alloys emerged that were developed specifically for the industrial/marine gas turbine engine. These alloys had about twice the hot-corrosion resistance but somewhat lower strength than the aircraft engine superalloys. It was shown in the 70's that hot-corrosion resistance could not be satisfactorily achieved for marine gas turbine use by coating aircraft engine superalloys with either diffused aluminide or overlay coatings if the CoCrAlY type. Satisfactory hot-corrosion resistance required a moderately corrosion resistive superalloy with a highly resistive coating.

A major improvement in aircraft turbine alloys was achieved by Pratt & Whitney in the 60's with the directional solidification process. Directional solidified (D.S.) involves pouring superheated liquid metal into the mold such that grains are nucleated and grow normal to a water cooled copper chill. The mold is removed from the furnace at a controlled rate that maintains the desired solidification at a line of baffles which shield thermal radiation from the furnace. The chill heat sink enhances grain alignment in a singular direction by maintaining the heat flow and temperature gradient in the liquid metal.

DS turbine airfoils developed for aircraft gas turbine engines have 10X greater thermal fatigue life, and 2X greater creep-rupture ductility. DS turbine airfoils are bill-of-material for five aircraft engines. DS offers a spin-off technology which could have major advantages for industrial gas turbines.

Coal gasification should provide a relatively clean combustion gas to the turbine. In the proximity to the coastal areas, sea salts in the engine ingested air will introduce a moderate hot-corrosion problem. With the reduction of hot-corrosion activity anticipated with coal gasification, industrial gas turbine airfoils will be life limited by mechanical properties, primarily thermal fatigue. DS alloys could provide either of the following advantages with coal gasification; life improvement at current temperatures of a factor of 2 to 3X or a 150°F increase in turbine inlet temperature with at least current airfoil life. In fact, the DS alloy currently used in aircraft engines, MARM-200+Hf could be a candidate for the industrial engine. The problem is that current DS techniques cannot adequately control the heat transfer with the very large gas turbine blades.

The Department of Energy is supporting a program at the General Electric Company to develop the techniques of bonding a turbine airfoil section to a powder metallurgy dovetail. This approach allows optimization of the high tensile strength and ductility requirements in the root to wheel attachments and the high temperature creep-rupture strength, thermal fatigue resistance and high temperature oxidation. Thus, each of the two sections is optimized without the current compromises with conventionally cast blades. Successful bonding techniques would have the growth potential to single crystal alloys. Also, if hot-corrosion/erosion is a more severe problem with any of the coal derived liquid or coal slurry fuels, a DS alloy can be developed to improve engine life. Bonding techniques also allow fabrication of the airfoil section using complex turbine blade cooling schemes such as the wafer blade concept or a clam shell scheme that could not be done with a large single piece conventionally cast blade. In addition, if erosion becomes a severe problem with coal slurry fuels an erosion resistant leading edge might be bonded. Thus, the bonding approach can provide considerable range of improvements in the industrial gas turbine, not only the airfoil section bonded to the root attachment but also bonding of segments of the airfoil. The big objective is to take advantage of DS airfoils in large industrial gas turbine engines to enhance operation on coal base fuels.

The report work is of an interim nature as the program has just passed its mid-point at conference time.

#### BACKGROUND

Generally speaking, the increasing firing temperature trend has placed greater demands on the high temperature capability of hot section components of industrial gas turbines. Air cooling has mitigated these demands somewhat but the trend still persists. In fact, as a result of the need for improved high temperature strength, vacuum investment casting technology is now widely employed throughout the industry for hot section components. Major processing developments were required in order to successfully scale up vacuum investment casting technology to reach capability for hardware sizes currently in routine use. Figure 1 shows a size comparison between aircraft and industrial first stage turbine blading. Latter stage blading weighing approximately 70 kilograms (30 pounds) are presently produced by investment casting. Areas which received particular attention during development of vacuum investment casting technology for large gas turbine components included:

- control of solidification behavior
- dimensional tolerance
- elimination of post-casting straightening
- compositional modifications to improve castability

It was observed early in the development of large section superalloy castings that there were major differences in the structure of thin section (arbitrarily < .25 in.) versus thick section (> .25 in.) castings. These differences included:

- carbide size and shape
- dendritic arm spacing
- volume percent of  $\gamma/\gamma'$  eutectic
- primary  $\gamma'$  size
- extent of coring and presence of unwanted phases

Figure 2 shows the relative structural differences between investment cast thin and thick sections of IN-738.

Importantly, these significant structural differences give rise to a phenomena known as "section size effect." Typically, tensile properties are affected most strongly, however, it is believed that low cycle fatigue strength can also be influenced. Reductions in yield and tensile strength of about 20% have been observed for typical superalloy castings when comparing properties derived from cast-to-size bars versus bars machined from actual turbine hardware. Table 1 gives some typically observed properties for thick and thin section sizes. A schematic representation of the effect of section size on superalloy tensile strength and ductility is given in Figures 3a and 3b. Frawley and Pedersen in unpublished work at General Electric have shown a strong correlation of the tensile properties of investment cast IN-738 with primary dendritic arm spacing with lower properties being obtained with larger spacings. It is clear that the slow solidification rates associated with large superalloy investment castings play a major role in the section size effect.

As higher strength alloys have been introduced, the issues associated with the investment casting of them have become more critical. More highly alloyed compositions give rise to greater levels of segregation and a significant disparity between the actual properties of the component and those which the alloy is truly capable of. Process technology which has been utilized for aircraft gas turbines is now being evaluated for industrial gas turbine applications. A major area of interest centers on the evaluation of directional solidification for large parts. Directional solidification offers important potential opportunities for industrial gas turbine applications including:

- attainment of part properties which approach optimum alloy properties
- increase in bucket alloy strength
- increased alloy ductility
- increased control of solidification behavior
- potential for future growth in alloy strength

As will be apparent in the next section, potential processing difficulties associated with the directional solidification of the entire part make alternative methods for incorporating a directionally solidified airfoil section in what is termed a hybrid structure attractive options. In any case, additional costs associated with the use of directional solidification must be mitigated by enhanced turbine performance.

Rotating, directionally solidified hardware currently produced for the aircraft industry represents state-of-the-art technology. Stress-rupture advantages of DS MAR-M200+Hf over conventionally cast, equiaxed structures can be seen in the mechanical property comparison shown in Figure 4. Technology needed to cast these alloys, whether they be IN-738 or MAR-M247 is also in place. However, utilization of DS technology to produce rotating components for land based gas turbines may require hybrid structure technology in order to successfully fabricate large section parts.

Directional solidification is achieved through the presence of a steep temperature gradient between the molten alloy and the solidified material. Too low a temperature gradient will allow nucleation of new grains in advance of the solidification front. As ceramic molds for DS castings are made larger and the volume of molten metal increases, the relationship between the rate of heat extraction through the solidified material behind the advancing solidification front and the rate of heat loss from the molten metal ahead of the solidification front will begin to change. At some point within the casting the distance from the chill will be great enough that the temperature gradient will no longer drive the columnar grain growth perpendicular to the chill.

Grain growth will then revert to an equiaxed structure. Figure 5 demonstrates this transition from a DS to equiaxed structure in a land based gas turbine first stage bucket.

Though Figure 5 is only a trial casting, continued development to produce a completely columnar structure beyond the platform region could be difficult. An alternative to producing a complete DS blade would be to bond some other alloy to the blade below that region where an equiaxed grain zone begins. The forerunner of such a structure was conceived and fabricated at General Electric's Gas Turbine Division. The resultant hybrid blade with an IN-738 airfoil section and P/M Rene 80 for the shank/dovetail portion is shown in Figure 6. Conventional equiaxed castings were used for the airfoil. Clearly a hybrid blade concept should be capable of growth beyond the idealized cost to size properties of conventional turbine bucket alloys like IN-738.

Selection of DS casting for the airfoil section will not only eliminate the discrepancy between cast to size and machined from blade MFB data, but will enable increased operational blade-temperature capability. This is to be achieved by eliminating grain boundaries normal to the direction of highest stresses. This in turn then limits preferred stress-rupture fracture paths within the bucket.

In addition to improving blade properties through directional solidification, selection of a material and process to improve shank and dovetail can be made. Alloys capable of sustained high temperature operation (1000 to 1200°F) while still maintaining a fine grain size (25 $\mu$ ) at bonding temperatures of 2200°F can be obtained through the combination of powder metallurgy and hot isostatic pressing.

Design of such a turbine blade would depend heavily on the airfoil to shank/dovetail bond performance. Strains applied to the joint would be a function of bond location, shape, operating temperatures, and mechanical loading from the rotating blade. Bond integrity would be dependent on alloy compatibility (airfoil to dovetail) and bonding techniques.

#### MATERIAL AND PROCESSES

Fabrication of a hybrid gas turbine blade will be achieved using hot isostatic pressing to diffusion bond a DS airfoil to a powder dovetail. The use of DS alloys could produce increases in operating temperatures by as much as 150°F while still maintaining stress levels imposed on conventionally cast buckets. P/M superalloys were chosen due to their inherently fine grain size, high temperature exposure capability without grain growth and their ability to be HIP consolidated to an approximate shank/dovetail shape. DS alloys MAR-M200 + HF, Rene 80H and 441 were chosen while API (low carbon Astroloy) and PA-101 (low carbon IN-792) represent the powder alloys. All alloys have property improvements over IN-738 in their intended area of use. These property improvements include low cycle fatigue life and creep rupture for the airfoil and high temperature tensile strength and ductility for the dovetail.

Bonding of all alloy combinations is accomplished using hot isostatic pressing. HIP temperatures were selected based on alloy solutioning temperatures. Eighteen HIP combinations involving 5 alloys and 3 HIP temperatures for each alloy combination are under investigation. Additional studies will include variations in bonding techniques (activated diffusion bonding) and material parameters (heat treat cycle, surface preparation).



Results to date are encouraging. Preliminary tensile results for heat treated DS alloys, Table II, show MAR-M200 + Hf to be the best choice from a strength/ductility standpoint. All cast MAR-M200 + Hf test bars showed good columnar grain structure with minimal porosity and off axis growth. From a casting feasibility viewpoint results are also favorable since the perimeter to surface area ratio for these test bars is lower than the first stage bucket root section ratio. Powder alloys have not been tested; however, HIP'ed microstructures show no presence of TIP, no formation of prior particle boundaries, and no excess carbide formation around grain boundaries.

All HIP bonded alloy combinations have been completed. Metallography for as HIP'ed (2200°F/2 hr.) MAR-M200 + Hf to API, Figure 7, show clean bondlines with no continuous film or carbide precipitation along the boundary. This alloy combination possesses the least amount of embrittling elements along the bondline. In addition, some grain growth and twinning is taking place across the boundary. For these reasons it has been selected as the combination to be used for LCF testing.

Design studies center on two bondline configurations, Figure 8. Location of these bonds will be in the shank region close to the bucket platform. Finite element analysis of these configurations will help to plot stress distributions around the bondline. In conjunction with bondline stress analysis, new designs of shank and dovetail sections are being done to make bucket geometry more compatible with HIP consolidated P/M techniques.

Tensile testing of HIP'ed powder and all bonded combinations have yet to be done. Extensive evaluation including prove, TEM, SEM and hardness plots of bondline regions are in progress. Additional evaluation of the prime alloy combination will include alternate aging/solution heat treat cycles to affect the bonded structure.

TABLE 1

Typical IN-738 Mechanical Properties  
Using Cast-to-Size Specimens and  
Specimens Machined from Buckets

	Cast-to-Size Specimens	Specimens Machined from Buckets
982°C/151.7 MPa (22 ksi) Rupture		
Hours to rupture	47	34
% RA	14	11.5
% EI	9	11
649°C Tensile		
Ultimate (ksi/MPa)	157/1082.7	126/868.9
0.2% Yield (ksi/MPa)	114/786.2	95/655.1
% RA	10	10
% EI	8	8
Room Temperature Tensile		
Ultimate (ksi/MPa)	156/1075.8	121/834.4
0.2% Yield (ksi/MPa)	129/889.6	110/758.6
% RA	8	8.5
% EI	7	5.5

TABLE 2

## Directionally Solidified Tensile Results

Material	Test Temp. °F	Yield (0.2) KSI	Ulti- Mate KSI	Elongation %	R/A %
IN738	1200	110.9	172.1	12.2	16.9
	1600	67.2	113.0	20.8	42.2
MAR-M200+Hf	1400	145.4	175.3	13.9	22.7
	1600	130.3	141.4	14.8	22.8
RENE 80H	1400	111.4	159.4	24.7	38.1
	1600	84.9	114.8	20.8	46.3

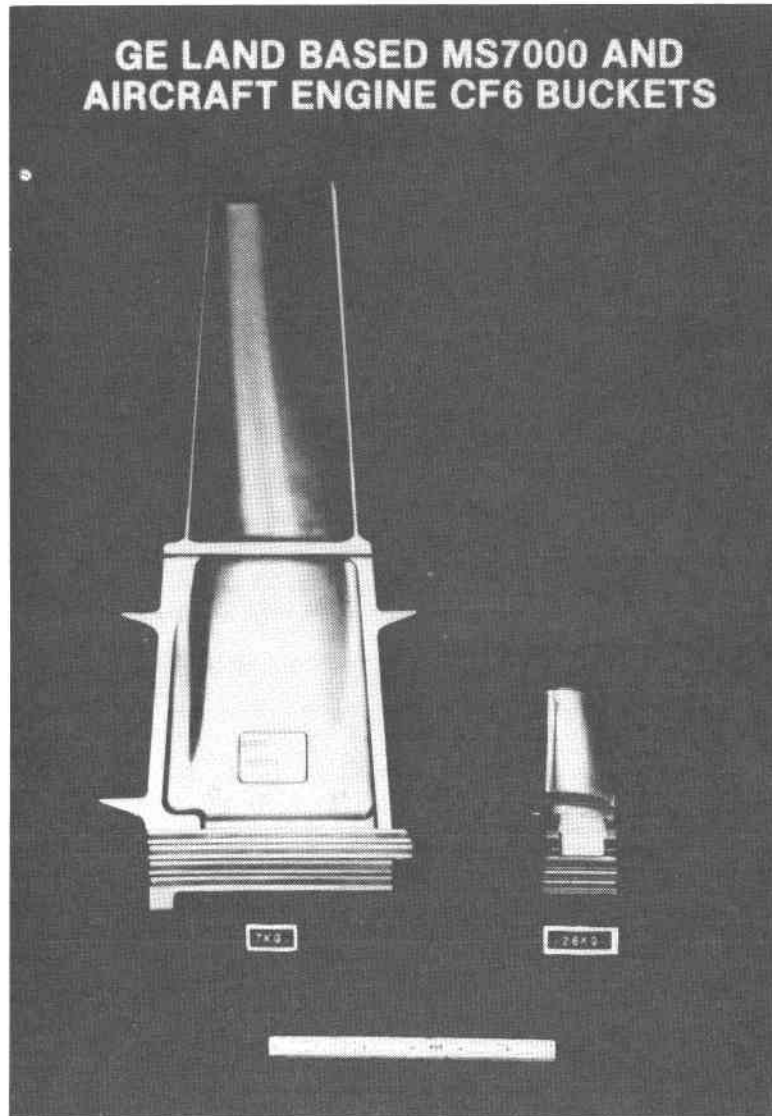


Figure 1. GE Land Based MS7000 and Aircraft Engine CF6 Buckets (Blades).

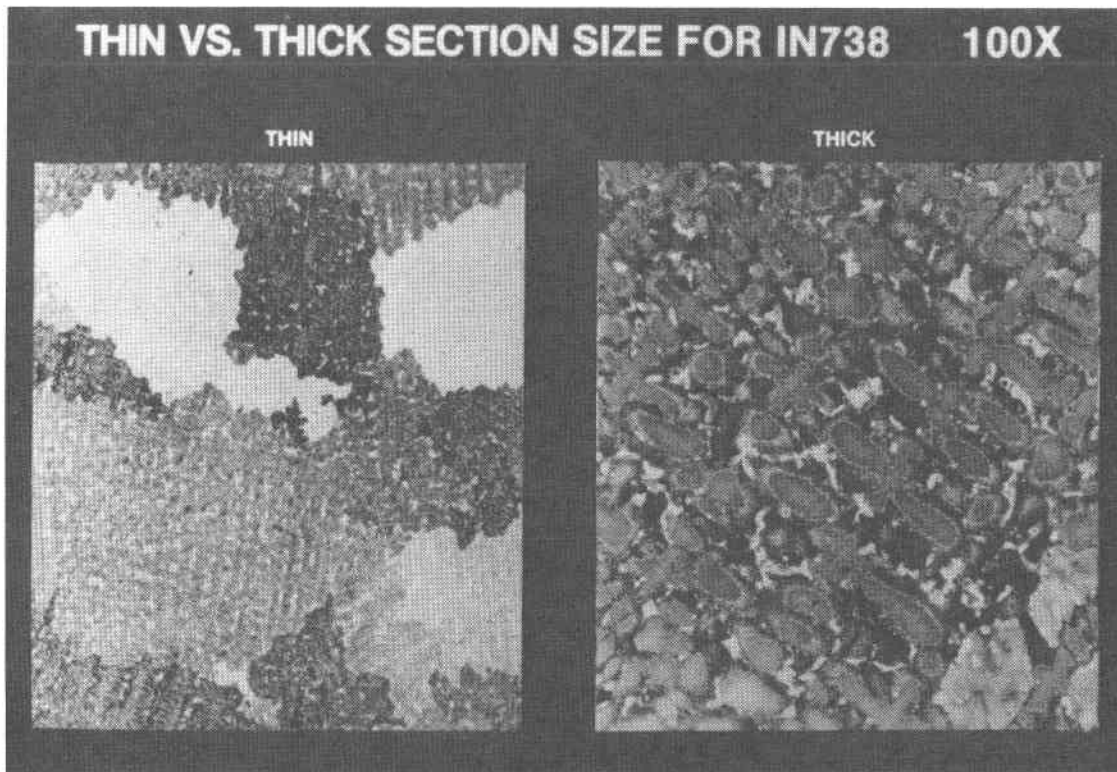


Figure 2. Thin vs. Thick Section Size for IN738

\*Please note that the illustration(s) on this page have been reduced 10% in printing.

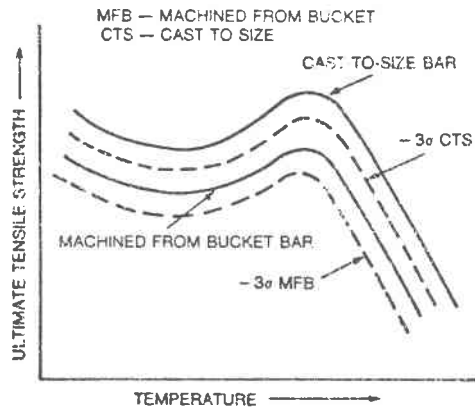


Figure 3a. SCHEMATIC REPRESENTATION OF UTS vs. TEMPERATURE FOR CAST-TO-SIZE AND MACHINED FROM BUCKET TEST BARS

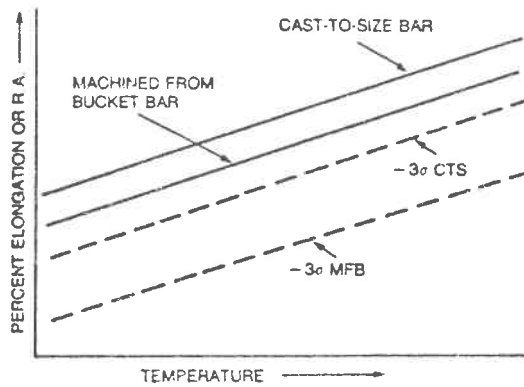


Figure 3b. SCHEMATIC REPRESENTATION OF PERCENT ELONGATION OR R.A. FOR CAST-TO-SIZE AND MACHINED FROM BUCKET TEST BARS

Figure 3. Effect of Section Size on Superalloy Tensile Strength and Ductility.

# COMPARATIVE THERMAL FATIGUE RESISTANCE OF VARIOUS SUPERALLOYS IN NASA TESTS

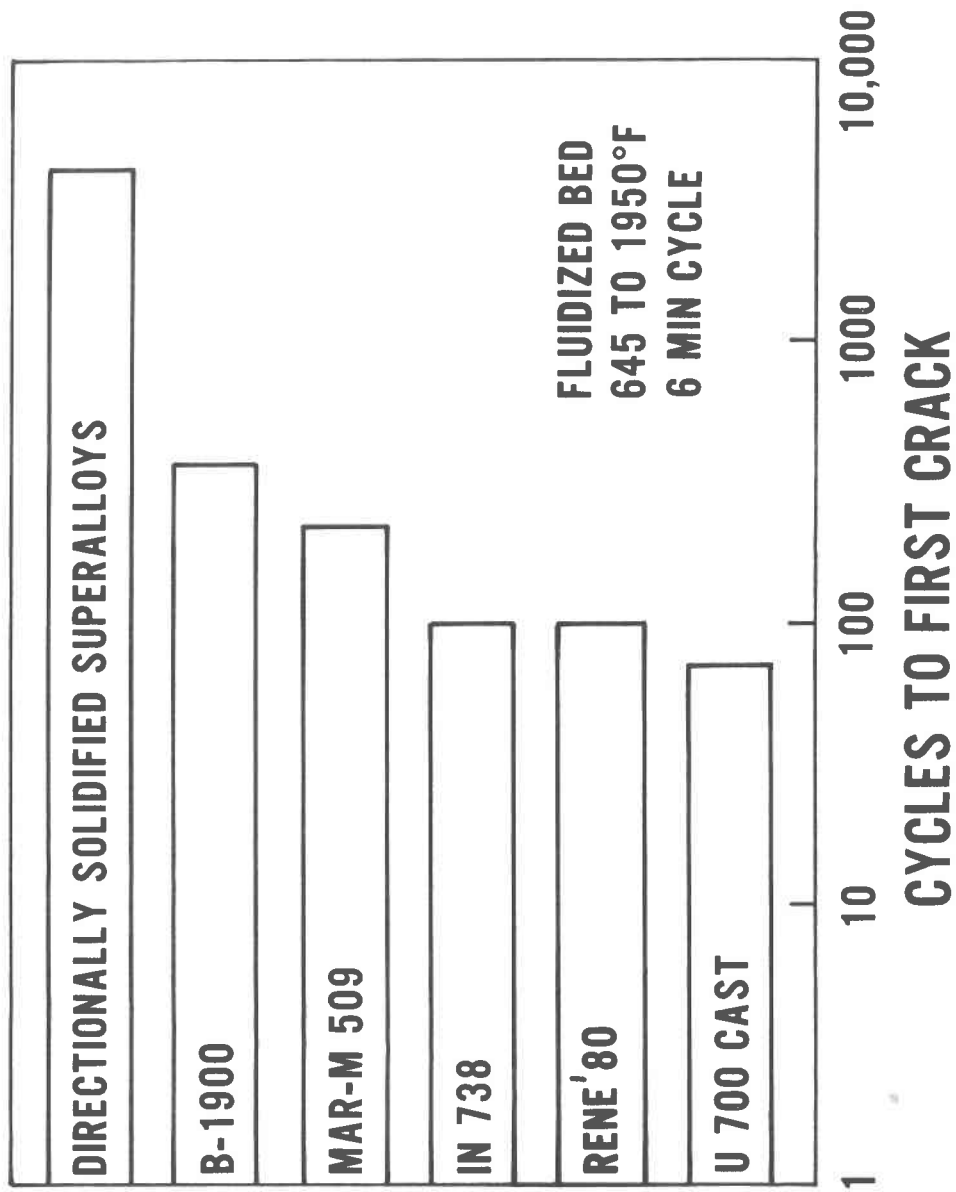


Figure 4

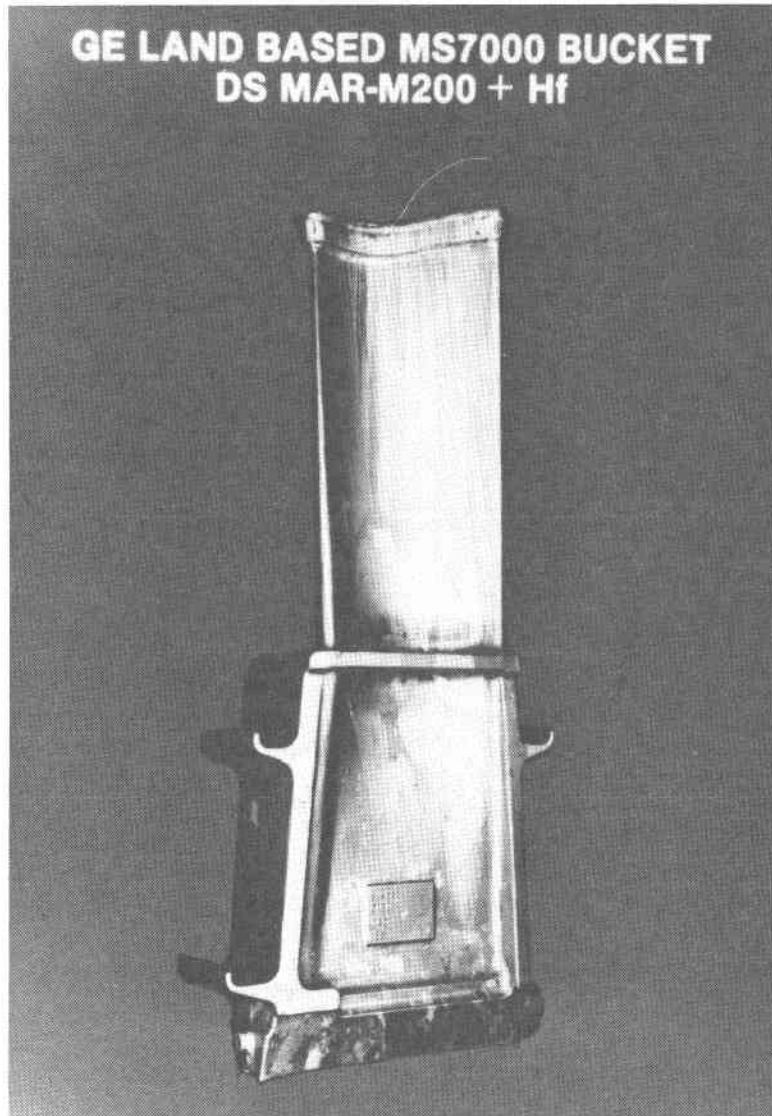


Figure 5. GE Land Based MS7000 Bucket DS MAR-M200 + Hf



**COMPOSITE BUCKET  
CAST EQUIAXED GRAIN IN738 TO  
P/M RENE 80 DOVETAIL**

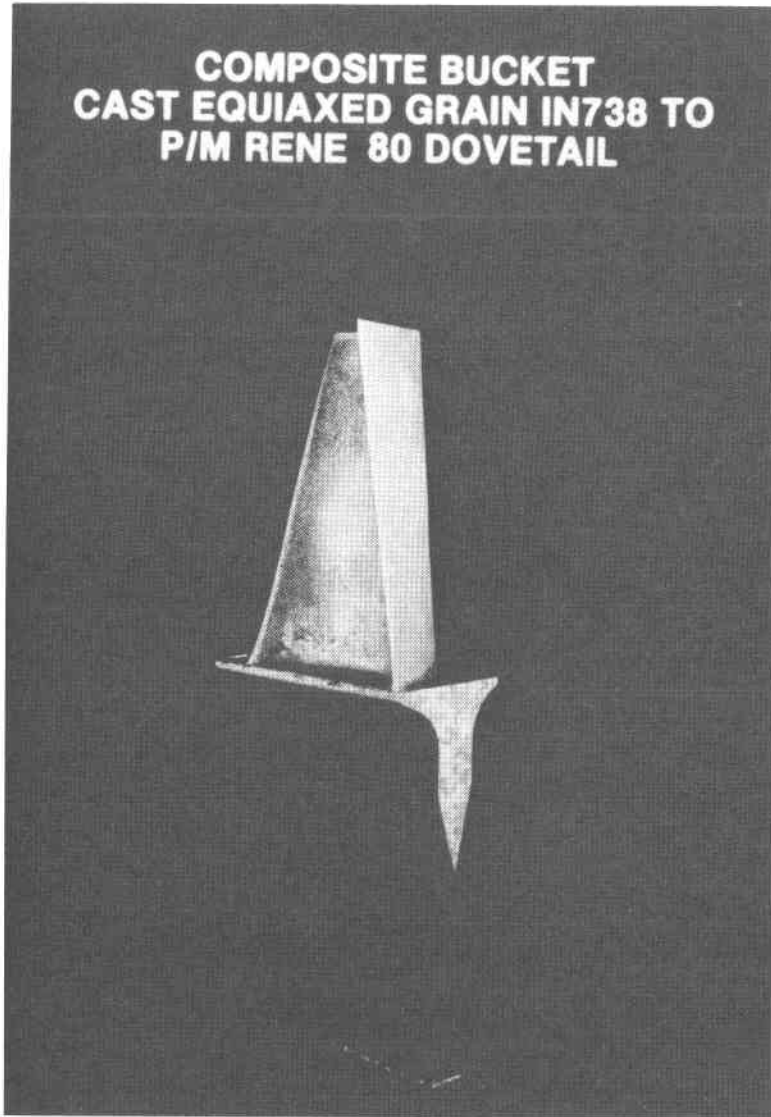


Figure 6. Composite Bucket Cast Equiaxed Grain IN738 to P/M Rene 80 Dovetail

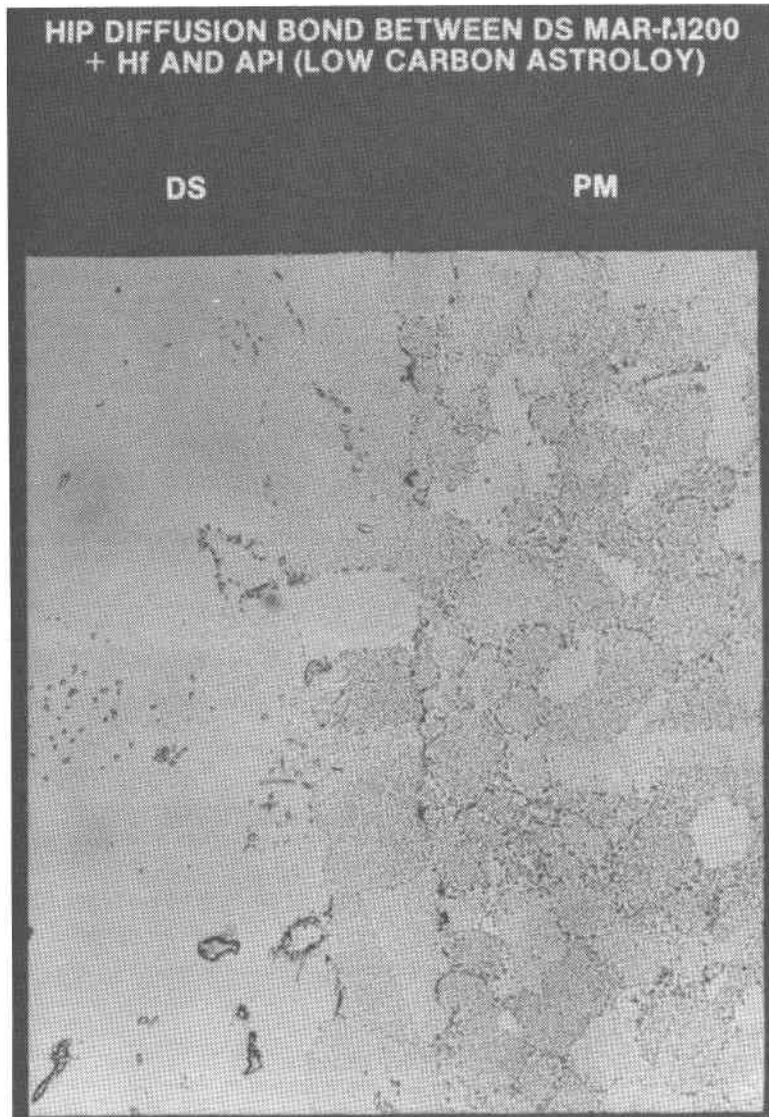


Figure 7. HIP Diffusion Bond Between DS MAR-M200 + Hf and API (Low Carbon Austenitic)

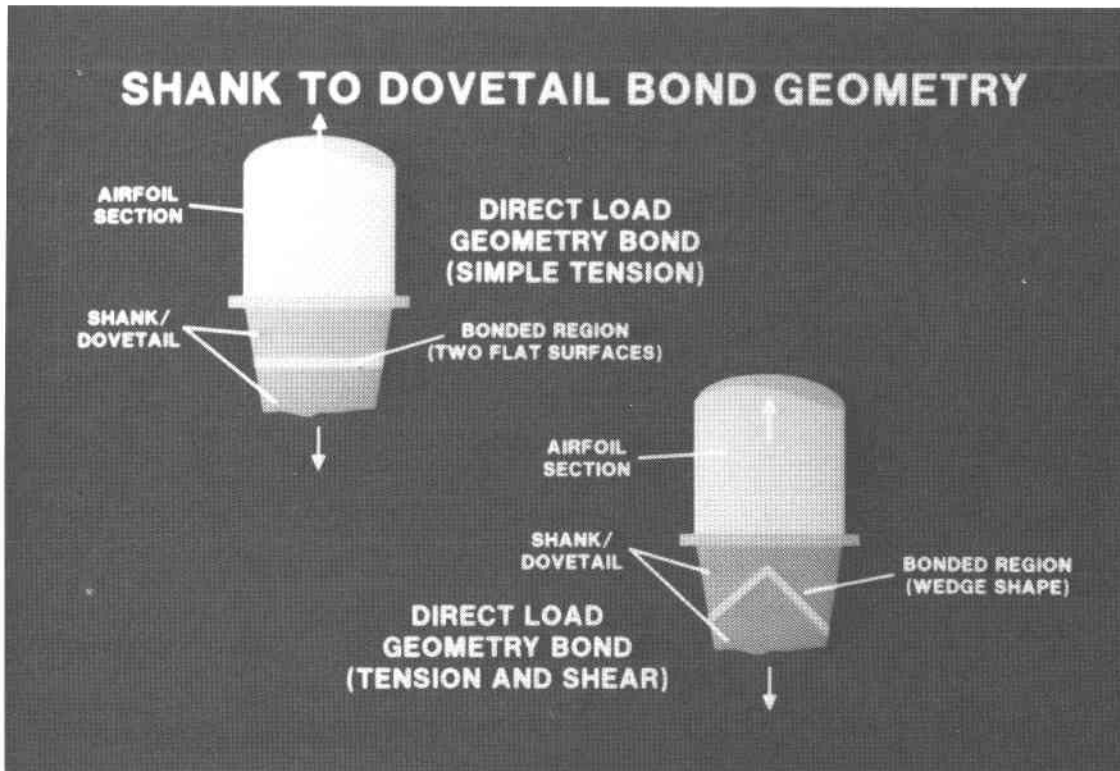


Figure 8. Shank to Dovetail Bond Geometry

## Conclusions and Recommendations

Directional solidified (DS) turbine airfoils have provided very significant improvements in aircraft gas turbine performance and life. DS technology has matured to the point where spin-off to industrial gas turbines can be achieved with moderate cost. The DS turbine blade alloy which has undergone 15 years of development and use in aircraft gas turbines, MAR M-200+Hf, could provide either a 150°F increase in turbine inlet temperature with at least current life or a 2 to 3X increase in blade life operating with coal gasification. There is a need to develop or modify an alloy with the DS process to optimize hot-corrosion resistance.

The problem this program addresses is the inability of maintaining adequate heat transfer to maintain DS with the very large turbine blades. Early work with large turbine airfoils regularly encountered "freckles" or random grain orientation in very thick areas of the blade such as the platform area and the dovetail section. The solution pursued was to bond a DS airfoil to a powder metallurgy root section. HIP diffusion bonding appears very promising at the mid-point in the program.

This approach allows optimization of the high tensile strength and ductility requirements in the root attachment to the turbine disc area and the higher temperature creep-rupture strength, thermal fatigue resistance and higher temperature oxidation requirements of the airfoil section. This bonding approach allows optimization of each section without the compromises necessary with conventionally cast single piece turbine blades. This bonding method would also be compatible with single crystal airfoil sections.

Bonded turbine airfoils enables much more sophisticated air cooling technology be applied to large industrial gas turbine airfoils. Based on achievements with convectively cooled bonded turbine blades using wafer construction technology, bonded composite turbine airfoils with advanced air cooling could accomodate 2600°F (1427°C) combustor exit temperatures with life equivalent to that currently obtained. Bonding techniques allowing optimization of material requirements in specific sections of engine hot-section components has very major promise not only in advanced turbine airfoils but in disc fabrication and radial turbine fabrication.

## Second Conference on Advanced Materials for Alternative-Fuel-Capable Heat Engines

August 24-28, 1981  
Monterey, California

### List of Attendees

Ibrahim Allam  
SRI International  
333 Ravenswood Avenue  
Menlo Park, CA 94025  
415-859-5208

S. B. Alpert  
Electric Power Research Institute  
3412 Hillview Avenue  
Palo Alto, CA 94303  
415-855-2512

Leonard C. Angello  
Electric Power Research Institute  
3412 Hillview Avenue  
Palo Alto, CA 94303  
415-855-2873

L. F. Aprigliano  
David Taylor Naval Shipyard  
R&D Center  
Annapolis, MD 21012

Dr. Wate Bakker  
Electric Power Research Institute  
3412 Hillview Avenue  
Palo Alto, CA 94303  
415-855-2462

Walter Bauer  
Sandia National Laboratories  
Livermore, CA 94550  
415-422-2994

Dr. D. H. Boone  
Lawrence Berkeley Laboratories  
Bldg. 62  
University of California  
Berkeley, CA 94720  
415-486-4914

Norman Bornstein  
United Technologies Corporation  
P. O. Box 109  
South Windsor, CT 06074  
203-727-7487

Michael Brands  
Cummins Engine Company  
P. O. Box 3005  
Columbus, IN 47201  
812-379-5977

R. J. Bratton  
Westinghouse Research & Dev. Center  
1310 Beulah Road  
Pittsburgh, PA 15235  
412-256-7000 x 7335

Bruce Brown  
Pratt & Whitney Aircraft  
12850 S. Shore Drive  
Lake Park, FL 33410  
305-840-6631

Walter H. Buttrill  
Detroit Diesel Allison  
P. O. Box 894 T-27  
Indianapolis, IN 46206  
317-242-7186

Anthony Caruvana  
General Electric Company  
1 River Road - 56-200  
Schenectady, NY 12345  
518-385-2269

Arthur Cohn  
Electric Power Research Institute  
3412 Hillview Avenue  
Palo Alto, CA 94303  
415-855-2525

Kathy Davis  
Meeting Planning Associates  
883 Santa Cruz Avenue #24  
Menlo Park, CA 94025  
415-854-2186

S. M. DeCorso  
Westinghouse Electric Company  
Concordville, PA 19331  
215-358-4624

Dr. R. Ernest Demaray  
Airco Temescal  
2850 7th Street  
Berkeley, CA 94710  
415-841-5720

R. L. Derby  
Dow Chemical Company  
Res. Adm. B-1214  
Freeport, TX 77541  
713-238-2057

D. Scott Duvall  
Pratt & Whitney Aircraft  
400 Main Street  
East Hartford, CT 06108  
203-565-7775

Michael Edwards  
Royal Military College of Science  
Shrivenham  
Swindon, Wiltshire, England  
0793-782551 x 279

John W. Fairbanks  
Office of Coal Utilization  
U. S. Department of Energy  
MS E-178  
Germantown, MD 20767  
301-353-2822

Nancy Fitzroy  
General Electric Company  
1 River Road, Bldg. 500-224  
Schenectady, NY 12345  
518-385-9013

Diane Foster  
Meeting Planning Associates  
883 Santa Cruz Avenue #24  
Menlo Park, CA 94025  
415-854-2186

Robert M. Giannini  
U. S. Department of the Navy

Michael Gluckman  
Electric Power Research Institute  
3412 Hillview Avenue  
Palo Alto, CA 94303  
415-855-2493

T. G. Godfrey  
Oak Ridge National Laboratory  
P. O. Box X  
Oak Ridge, TN 37830  
615-574-4455

Joseph A. Goebel  
Pratt & Whitney Aircraft  
400 Main Street  
East Hartford, CT 06108  
203-565-3154

G. W. Goward  
Coatings Technology Corporation  
2 Commercial Street  
Branford, CT 06405  
203-481-5371

Professor Peter Hancock  
Department of Engineering Metallurgy  
Cranfield Institute of Technology  
Cranfield, Bedford MIL430AL  
England

Darrell D. Hays  
Battelle - Pacific Northwest Laboratories  
P. O. Box 999 231-Z/200-W/97  
Richland, WA 99352  
509-373-2829

William R. Heater  
Cooper Energy Services  
N. Sandusky Street  
Mt. Vernon, OH 43050  
614-397-0121

Ralph J. Hecht  
Pratt & Whitney Aircraft  
P. O. Box 2691 M-26  
West Palm Beach, FL 33402  
305-840-3228

L. D. Hoblit  
Dow Chemical U.S.A.  
Freeport, TX 77541  
713-238-2468

Robert A. Holzl  
San Fernando Laboratories  
10258 Norris Avenue  
Pacoima, CA 91331  
213-899-7484

Dr. M. J. Humphries  
Exxon Research & Engineering  
P. O. Box 45  
Linden, NJ 07036  
201-474-2966

Dr. Robert I. Jaffee  
Electric Power Research Institute  
3412 Hillview Avenue  
Palo Alto, CA 94303  
415-855-2453

Ray Kamo  
Cummins Engine Company  
1900 McKinley Avenue  
Columbus, IN 47201  
812-372-7211

Fred S. Kemp  
Power Systems Division  
UTC  
P. O. Box 109  
South Windsor, CT 06074  
203-727-2212

Jack Kittle  
Plasma Technics, Inc.  
3000 Taft Street  
Hollywood, FL 33021  
305-963-3316

Alex Korosi  
Stone & Webster  
P. O. Box 2325  
Boston, MA 02107  
617-973-5728

Arnold Kossar  
Curtiss-Wright Corporation  
Wood-Ridge, NJ 07075  
201-717-2900

Dr. Richard Krutenat  
Exxon Research & Engineering  
Bldg. 101, Room H133  
Florham Park, NJ 07932  
201-765-3126

Dr. Ingard Kvernes  
Central Institute for Industrial Research  
Forskningssvn. 1,  
P.B. 350, Blindern  
Oslo 3, Norway  
02/69 58 80

Ivan H. Landes  
General Electric Company  
3172 Porter Drive  
Palo Alto, CA 94304  
415-494-7693

Dr. Jay M. Larson  
Eaton Corporation  
463 N. 20th Street  
Battle Creek, MI 49016  
616-962-7571

S. Y. Lee  
Westinghouse Research Laboratory  
1310 Beulah Road, Churchill  
Pittsburgh, PA 15235  
412-256-3358

Stanley R. Levine  
NASA-Lewis  
21000 Brookpark Road  
Cleveland, OH 44135  
216-433-4000 x 6150

Charles Lewis  
Metco, Inc.  
3340 Del Sol Blvd., #190  
San Diego, CA 92154  
714-690-5938

Lynn Lundberg  
Los Alamos National Laboratory  
P. O. Box 1663  
Los Alamos, NM 87545  
505-667-6540

George B. Manning  
Office of Coal Utilization  
U. S. Department of Energy  
MS GTN, E-178  
Washington, DC 20545  
301-353-2816

Peter L. Mattern  
Sandia National Laboratories  
Livermore, CA 94550  
415-422-2520

Sundarajan Mutialu  
Plasma Technics, Inc.  
3000 Taft Street  
Hollywood, FL 33021  
305-963-3316

R. L. McCarron  
General Electric Company  
Bldg. 23, Room 278  
One River Road  
Schenectady, NY 12345  
518-385-4005

D. McKnight  
Rolls-Royce Ltd.  
Ansty, Coventry  
England  
Cov. 613211

Alan S. Nagelberg  
Sandia National Laboratories  
Division 8313  
Livermore, CA 94550  
415-422-3361

Richard Niedzwiecki  
NASA Lewis Research Center  
MS 86-6  
2100 Brookpark Road  
Cleveland, OH 44135  
216-433-4000 x 6132

Iten Oskar  
Brown Boveri Company Ltd.  
CH-8401 Baden  
Switzerland  
056/756239

Dr. W. J. Ostergren  
General Electric Company  
Bldg. 53 - Room 316  
One River Road  
Schenectady, NY 12345  
518-385-7170

Dr. James Patten  
Battelle-Pacific Northwest Laboratories  
P. O. Box 999 231-Z/200-W/95  
Richland, WA 99352  
509-373-2603

Kenneth R. Pearce  
Transamerica Delaval Inc.  
550-85th Avenue  
Oakland, CA 94621  
415-577-7577

Max W. Pepper  
Exxon Research & Engineering Company  
P. O. Box 51  
Linden, NJ 07036  
201-474-3371

Roy R. Peterson  
The MITRE Corporation  
1820 Dolley Madison Blvd.  
McLean, VA 22102  
703-827-6865

Commodore Pichini  
U.S. Coast Guard  
630 Sansome Street  
San Francisco, CA 94126  
415-556-3530

William R. Pierson  
Battelle Columbus Laboratories  
3010 Greenvale Dr.  
Worthington, OH 43085  
614-424-4780

John T. Prater  
Battelle - Pacific Northwest Laboratories  
P. O. Box 99  
Richland, WA 99352  
509-373-2000

Dr. G. E. Provenzale  
Exxon Research & Engineering Company  
P. O. Box 101  
Florham Park, NJ 07932  
201-765-1647

J. R. Rairden  
General Electric Company  
P. O. Box 8  
Schenectady, NY 12345  
518-385-8248

George Ray  
Union Carbide Corporation  
1011 Camino Del Mar, Suite 232  
Del Mar, CA 92024  
714-755-2576

David Rigney  
General Electric Company  
Mail Code D/83  
Evendale, OH 45215  
513-243-6340

William C. Rovesti  
Electric Power Research Institute  
3412 Hillview Avenue  
Palo Alto, CA 94303  
415-855-2519

Professor Arthur Sarsten  
Norwegian Institute of Technology  
MTS, Haakon Haakonsensgt 34  
N7000 Trondheim  
Norway  
075-95515

Dr. W. F. Schilling  
General Electric Company  
Bldg. 53 - Room 316  
One River Road  
Schenectady, NY 12345  
518-385-7170



Michael A. Schleigh  
Cooper Energy Services  
N. Sandusky Street  
Mt. Vernon, OH 43050  
614-397-0121

Rolland Scholl  
Caterpillar Tractor Company  
100 N.E. Adams Street  
Peoria, IL 61629  
309-578-8197

Clifford E. Seglem  
Westinghouse Electric Company  
P. O. Box 251  
Concordville, PA 19331  
215-358-4638

W. E. Shannon  
Synthetic Oil Corporation  
20380 Town Center Lane, Suite 170  
Cupertino, CA 95014  
408-257-3907

Tom Sherlock  
Westinghouse Electric Company  
P. O. Box 251 - L200  
Concordville, PA 19113  
215-358-4602

Erik Skog  
United Stirling  
Box 856  
21080 Malmo  
Sweden  
40/100950

Ralph Slone  
Cummins Engine Company  
P. O. Box 3005  
Columbus, IN 47201  
812-379-5977

Dr. Charles J. Spengler  
Westinghouse Electric Company  
1310 Beulah Road  
Pittsburgh, PA 15235  
412-256-3622

Anton Steiger  
Sulzer Brothers  
8401 Winterthur  
Switzerland  
4152/812360

R. W. Stepien  
General Electric Company  
One River Road, Bldg. 500-224  
Schenectady, NY 12345  
518-385-4411

A. R. Stetson  
Solar Turbines International  
P. O. Box 80966  
San Diego, CA 92138  
714-238-6731

Dr. Jacob J. Stiglich  
San Fernando Laboratories  
10258 Norris  
Pacoima, CA 91331  
213-899-7484

T. E. Strangman  
Garrett Turbine Engine Company  
111 S. 34th Street  
Phoenix, AZ 85010  
602-267-4399

John Stringer  
Electric Power Research Institute  
3412 Hillview Avenue  
Palo Alto, CA 94303  
415-855-2472

Jack C. Swearengen  
Sandia Laboratories  
East Avenue  
Livermore, CA 94550  
415-422-3022

R. J. Taylor  
Rolls-Royce Ltd.  
Ansty, Coventry  
England  
Cov. 613211

Dr. Thomas A. Taylor  
Union Carbide Corporation  
1500 Polco Street  
Indianapolis, IN 46224  
317-240-2614

Dr. Robert C. Tucker, Jr.  
Union Carbide Corporation  
1500 Polco Street  
Indianapolis, IN 46224  
317-240-2539

Harald Valland  
Norwegian Institute of Technology  
Husebyveien 64D  
7078 Saupstad  
Norway  
075-82396

E. C. vanReuth  
Defense Advanced Research Projects Agency  
1400 Wilson Boulevard  
Arlington, VA 22209  
202-694-4750

Robert L. Vogt  
Sulzer Brothers, Inc.  
200 Park Avenue  
New York, NY 10166  
212-949-0999

Richard A. Wenglarz  
Westinghouse R&D Center  
1310 Beulah Road  
Pittsburgh, PA 15235  
412-256-3253

Dr. Graham A. Whitlow  
Westinghouse Electric Company  
1310 Beulah Road  
Pittsburgh, PA 15235  
412-256-3622

Jerry M. Winter  
NASA Lewis Research Center  
21000 Brookpark Road  
Cleveland, OH 44135  
216-433-4000 x 5207

John C. Wolf  
Curtiss-Wright  
1 Passaic Street  
Wood-Ridge, NJ 07075  
201-777-2900

Stanley M. Wolf  
Materials Sciences Division  
U.S. Department of Energy  
Washington, DC 20545

I. G. Wright  
Battelle Columbus Laboratories  
505 King Avenue  
Columbus, OH 43201  
614-424-4377

Below are five index cards that allow for filing according to the four cross-references in addition to the title of the report. A brief abstract describing the major subject area covered in the report is included on each card.

EPRI

Proceedings of the Second Conference on Advanced Materials for Alternative-Fuel-Capable Heat Engines

Electric Power Research Institute

EPRI and DOE cosponsored this second conference that addressed the problems that may be encountered by structural materials in heat engine systems burning alternative fuels. The conference was held in Monterey, California, on August 24-28, 1981. This Proceedings presents materials that were discussed in the following sessions: alternative fuels, alternative fuels combustion, heat engines and heat recovery, heat engine combustion zone materials problems, airfoil cooling, ceramic coatings and monolithic ceramics, and metallic alloys. 916 pp.

EPRI Project Manager: J. Stringer

Cross-References:

- 1. EPRI RD-2369-SR 2. Proceedings 3. Materials Support Group 4. Coal Gases

ELECTRIC POWER RESEARCH INSTITUTE Post Office Box 10412, Palo Alto, CA 94303 415-855-2000

EPRI RD-2369-SR

EPRI

Proceedings of the Second Conference on Advanced Materials for Alternative-Fuel-Capable Heat Engines

Electric Power Research Institute

EPRI and DOE cosponsored this second conference that addressed the problems that may be encountered by structural materials in heat engine systems burning alternative fuels. The conference was held in Monterey, California, on August 24-28, 1981. This Proceedings presents materials that were discussed in the following sessions: alternative fuels, alternative fuels combustion, heat engines and heat recovery, heat engine combustion zone materials problems, airfoil cooling, ceramic coatings and monolithic ceramics, and metallic alloys. 916 pp.

EPRI Project Manager: J. Stringer

Cross-References:

- 1. EPRI RD-2369-SR 2. Proceedings 3. Materials Support Group 4. Coal Gases

ELECTRIC POWER RESEARCH INSTITUTE Post Office Box 10412, Palo Alto, CA 94303 415-855-2000

PROCEEDINGS

EPRI

Proceedings of the Second Conference on Advanced Materials for Alternative-Fuel-Capable Heat Engines

Electric Power Research Institute

EPRI and DOE cosponsored this second conference that addressed the problems that may be encountered by structural materials in heat engine systems burning alternative fuels. The conference was held in Monterey, California, on August 24-28, 1981. This Proceedings presents materials that were discussed in the following sessions: alternative fuels, alternative fuels combustion, heat engines and heat recovery, heat engine combustion zone materials problems, airfoil cooling, ceramic coatings and monolithic ceramics, and metallic alloys. 916 pp.

EPRI Project Manager: J. Stringer

Cross-References:

- 1. EPRI RD-2369-SR 2. Proceedings 3. Materials Support Group 4. Coal Gases

ELECTRIC POWER RESEARCH INSTITUTE Post Office Box 10412, Palo Alto, CA 94303 415-855-2000

MATERIALS SUPPORT GROUP

EPRI

EPRI RD-2369-SR Proceedings May 1982

Proceedings of the Second Conference on Advanced Materials for Alternative-Fuel-Capable Heat Engines

Electric Power Research Institute

EPRI and DOE cosponsored this second conference that addressed the problems that may be encountered by structural materials in heat engine systems burning alternative fuels. The conference was held in Monterey, California, on August 24-28, 1981. This Proceedings presents materials that were discussed in the following sessions: alternative fuels, alternative fuels combustion, heat engines and heat recovery, heat engine combustion zone materials problems, airfoil cooling, ceramic coatings and monolithic ceramics, and metallic alloys. 916 pp.

EPRI Project Manager: J. Stringer

Cross-References:

- 1. EPRI RD-2369-SR 2. Proceedings 3. Materials Support Group 4. Coal Gases

ELECTRIC POWER RESEARCH INSTITUTE Post Office Box 10412, Palo Alto, CA 94303 415-855-2000

COAL GASES

EPRI

EPRI RD-2369-SR Proceedings May 1982

Proceedings of the Second Conference on Advanced Materials for Alternative-Fuel-Capable Heat Engines

Electric Power Research Institute

EPRI and DOE cosponsored this second conference that addressed the problems that may be encountered by structural materials in heat engine systems burning alternative fuels. The conference was held in Monterey, California, on August 24-28, 1981. This Proceedings presents materials that were discussed in the following sessions: alternative fuels, alternative fuels combustion, heat engines and heat recovery, heat engine combustion zone materials problems, airfoil cooling, ceramic coatings and monolithic ceramics, and metallic alloys. 916 pp.

EPRI Project Manager: J. Stringer

Cross-References:

- 1. EPRI RD-2369-SR 2. Proceedings 3. Materials Support Group 4. Coal Gases

ELECTRIC POWER RESEARCH INSTITUTE Post Office Box 10412, Palo Alto, CA 94303 415-855-2000

